PROCEEDINGS

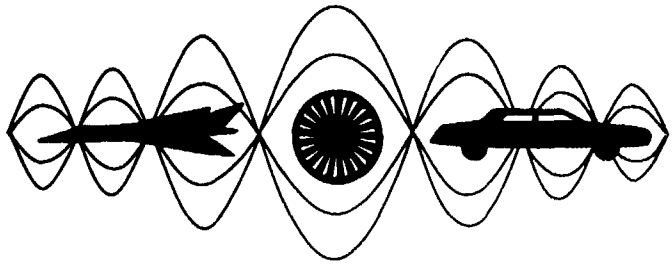

SECOND INTERNATIONAL CONGRESS ON RECENT DEVELOPMENTS IN AIR- AND STRUCTURE-BORNE SOUND AND VIBRATION

MARCH 4-6, 1992 AUBURN UNIVERSITY, USA

Edited by
Malcolm J. Crocker
P. K. Raju

Volume 3

DISCLAIMER NOTICE

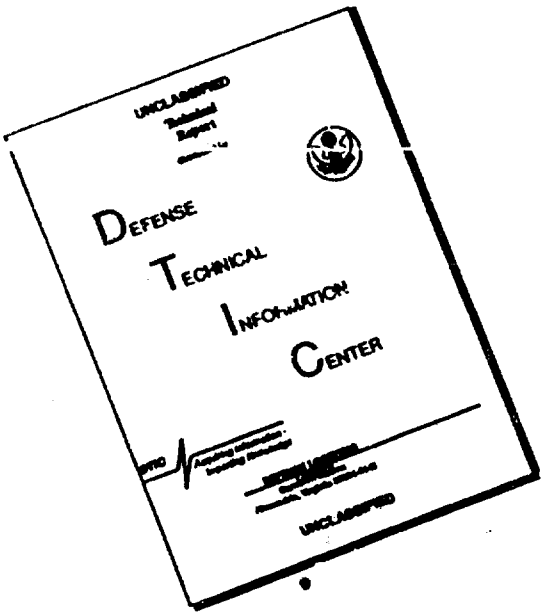

THIS DOCUMENT IS BEST QUALITY AVAILABLE. THE COPY FURNISHED TO DTIC CONTAINED A SIGNIFICANT NUMBER OF PAGES WHICH DO NOT REPRODUCE LEGIBLY.

PROCEEDINGS

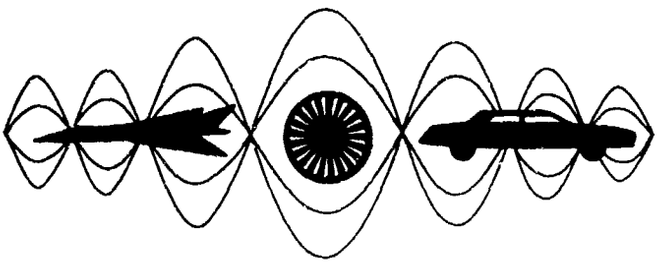

SECOND INTERNATIONAL CONGRESS ON RECENT DEVELOPMENTS IN AIR- AND STRUCTURE-BORNE SOUND AND VIBRATION

MARCH 4-6, 1992 AUBURN UNIVERSITY, USA

N00014-92-J-1525
ONR

Edited by
Malcolm J. Crocker
P. K. Raju

Volume 3

Printed in the United States of America
Cover design by Malcolm J. Crocker and Wally Ridgeway

Copies may be ordered from:
International Sound & Vibration Congress Editors
Mechanical Engineering Department
202 Ross Hall
Auburn University, AL 36849-5331, USA

Available only as a set of three volumes at the price of $125 each plus $30 each set for airmail.

SECOND INTERNATIONAL CONGRESS ON RECENT DEVELOPMENTS IN AIR- & STRUCTURE-BORNE SOUND AND VIBRATION

MARCH 4-6, 1992

Auburn University
USA

Sponsored by **AUBURN UNIVERSITY** in cooperation with
THE INTERNATIONAL COMMISSION ON ACOUSTICS OF IUPAP
and with the following professional societies:

ACOUSTICAL SOCIETY OF AMERICA
ACOUSTICAL SOCIETY OF THE NETHERLANDS
ACOUSTICAL SOCIETY OF THE RUSSIAN FEDERATION
AMERICAN HELICOPTER SOCIETY
AMERICAN SOCIETY OF MECHANICAL ENGINEERS
ASSOCIATION BELGE DES ACOUSTICIENS
ASSOCIAZIONE ITALIANA di ACUSTICA
AUSTRALIAN ACOUSTICAL SOCIETY
THE CANADIAN SOCIETY FOR MECHANICAL ENGINEERING
DEUTSCHE ARBEITSGEMEINSCHAFT FÜR AKUSTIK (DAGA)
INSTITUTE OF ACOUSTICS, UNITED KINGDOM
INSTITUTE OF NOISE CONTROL ENGINEERING/JAPAN
INSTITUTE OF NOISE CONTROL ENGINEERING/USA
INSTITUTION FOR MECHANICAL ENGINEERS, UNITED KINGDOM
THE AMERICAN SOCIETY FOR NONDESTRUCTIVE TESTING, INC.
VEREIN DEUTSCHER INGENIEURE (VDI-EDV), GERMANY
THE SOUTH AFRICAN ACOUSTICS INSTITUTE
SOCIÉTÉ FRANÇAISE D'ACOUSTIQUE
SOVIET ACOUSTICAL ASSOCIATION
ACOUSTICAL COMMISSION OF THE HUNGARIAN ACADEMY OF SCIENCES

General Chairman—Malcolm J. Crocker, Mechanical Engineering Department
Program Chairman—P. K. Raju, Mechanical Engineering Department

Financial Support

Financial support for these international congresses has been provided by:

National Science Foundation
Office of Naval Research
Office of Naval Research—Europe
Alabama Space Grant Consortium
National Aeronautics and Space Administration
College of Engineering (Auburn University)
Department of Mechanical Engineering (Auburn University)

FOREWORD

This three-volume book of proceedings includes the written versions of the papers presented at the Second International Congress on Recent Developments in Air- and Structure-Borne Sound and Vibration held at Auburn University March 4-6, 1992. The Congress was sponsored by Auburn University in cooperation with the International Commission on Acoustics of IUPAP and the 29 professional societies in 14 countries listed at the beginning of each volume. The support of this Commission and the professional societies has been invaluable in ensuring a truly international congress with participation from 30 countries. This support is gratefully acknowledged. In addition, the organizing committee would like to thank the National Science Foundation, the Office of Naval Research, the Office of Naval Research—Europe, the Alabama Space Grant Consortium, NASA, the College of Engineering and the Department of Mechanical Engineering of Auburn University for financial assistance.

Topics covered in the Proceedings include Sound Intensity, Structural Intensity, Modal Analysis and Synthesis, Statistical Energy Analysis and Energy Methods, Passive and Active Damping, Boundary Element Methods, Diagnostics and Condition Monitoring, Material Characterization and Non-Destructive Evaluation, Active Noise and Vibration Control, Sound Radiation and Scattering, and Finite Element Analysis.

The order in which the 217 papers appear in these volumes is roughly the same as they were presented at the Congress although the order is modified somewhat so they can be grouped in the topics above. There are also six keynote papers, including Professor Sir James Lighthill on Aeroacoustics and Atmospheric Sound, Professor Frank J. Fahy on Engineering Applications of Vibro-Acoustic Reciprocity; Dr. Louis Dragonette on Underwater Acoustic Scattering, Professor Robert E. Green on Overview of Acoustical Technology for Non-Destructive Evaluation, Professor David Brown on Future Trends in Modal Testing Technology and Professor Lothar Gaul on Calculation and Measurement of Structure-borne Sound. The papers in this book cover all major topics of interest to those concerned with engineering acoustics and vibration problems in machines, aircraft, spacecraft, other vehicles and buildings.

In the last 30 years, improvements in computers have allowed rapid developments in both theoretical and experimental analysis of acoustics and vibration problems. In the early 1960s statistical energy analysis (SEA) was first applied to coupled sound and vibration problems. In the early 1970s the finite element method (FEM) was first used in acoustics problems. In recent years considerable progress has been made with the boundary element method (BEM) in which discretization is confined to two-dimensional surfaces instead of three-dimensional fields. Some of these approaches have been combined for instance in SEA-FEM. The 1980s, which have also seen rapid advances in improved measurement techniques, could be called the decade of sound intensity, as it can now be used for rapid measurements of the in-situ sound power of a machine, to rank noise sources and determine transmission loss of structural partitions. Power flow in structures also now can be determined with the use of structural intensity measurements. Sound

and vibration signals are being used increasingly to diagnose the condition of machinery and to detect faults or to determine the properties of materials through non-destructive evaluation. There is also increased knowledge in sound radiation and scattering; in particular advances have occurred in scattering theory and in numerical solution techniques.

The organization and hosting of a conference is a considerable undertaking, and this Congress is no different. We would firstly like to thank all the authors who submitted their contributions promptly making publication of this book before the Congress possible. We would also like to acknowledge the assistance of the scientific committee and organizing committee who helped to completely organize some sessions. The staff of the Mechanical Engineering Department of Auburn University also provided valuable assistance. Our special thanks are extended to Rose-Marie Zuk who worked untiringly and efficiently on all aspects of the Congress program and this book, to Julia Shvetz who provided invaluable expert assistance in all areas of Congress planning in particular with travel arrangements for foreign guests, and to Olga Riabova for her hard work on Congress communications.

Malcolm J. Crocker, General Chairman
P.K. Raju, Program Chairman

TABLE OF CONTENTS

KEYNOTE ADDRESSES

KEYNOTE ADDRESS

UNDERWATER ACOUSTIC SCATTERING

Louis R. Dragonette

SECOND INTERNATIONAL CONGRESS ON
RECENT DEVELOPMENTS IN AIR- AND
STRUCTURE-BORNE SOUND AND VIBRATION
MARCH 4-6, 1992 AUBURN UNIVERSITY USA

UNDERWATER ACOUSTIC SCATTERING

Louis R. Dragonette
Naval Research Laboratory
Washington, D.C. 20375-5000 U.S.A.

ABSTRACT

The detection and classification of man-made objects underwater is a continuing topic of major interest in acoustics scattering research. A variety of analytic/numerical methods have been developed to describe the scattering from objects that approach the complexity of the targets of interest, and experimental work, as performed in facilities such those at NRL, produces scattering data of high precision and accuracy. In the ideal world, important scattering mechanisms are isolated from the computed or measured inputs and these form the foundation of physics based algorithms used to identify the target. Exploitation algorithms include novel new methods as well as modified versions of very old signal processing techniques. This paper will review the impact of some basic mechanisms, as predicted by experimental and analytic/numerical methods, on target scattering, and consider some of the techniques employed for exploitation of these mechanisms.

INTRODUCTION

Underwater scattering encompasses a broad area of interest which includes bottom, surface, and medium interactions. This paper focuses on the scattering by finite targets in an isotropic medium, and will emphasize the detection and classification features associated with the scattering.

Mechanisms associated with simple shapes are reviewed. It is noted that often the overall effect of the interference between shape dominated and elastic dominated scattering mechanisms is a pronounced null in the scattering. These nulls are easily observed in the laboratory or in high signal-to-noise environments, but are susceptable to degredation by noise. Separation techniques such as suggested by resonance theory are indicated and displays generated by a physics-based processing scheme, which might be the basis of automated identification systems are presented.

DETECTION

The physics of the scattering process is for the most part a secondary issue for detection purposes; the major emphasis being placed on source level and processing gain. The active sonar equation is given its most basic form as

$$EL = SL - TL1 + TS - TL2 \quad (1)$$

where EL and SL are source and echo level respectively, $TL1$ and $TL2$ are the transmission loss from source to target and target to receiver respectively, and TS in the target strength of the scatterer All of the quantities are in dB, and TS is defined as:

$$TS = 20\log\frac{p_s}{p_i} + 20\log\frac{r}{r_o} \tag{2}$$

Here p_s and p_i are the amplitudes of the measured scattered pressure and pressure incident at the target respectively, r is the range from target to receiver, and r_o is the reference distance of 1m from the target. The r_o is generally dropped, and it is understood that TS is referenced back to a distance of 1m.

The major interests in a detection problem involve source level and the gains that may be achieved by source/receiver directivity and by processing techniques. Gross estimates are generally made of TS, and methods for obtaining these estimates include tables of geometrical acoustics approximations, the Kirchhoff approximation, and other high frequency schemes. Eqs. 3 and 4 give the geometrical acoustics predictions of the TS of a rigid sphere and rigid cylinder respectively as found in Urick.[1]

$$(TS)_s = 20\log\frac{a}{2} \tag{3}$$

$$(TS)_c = 10\log\left\{\frac{al^2}{2\lambda}\left(\frac{\sin[kl\sin\theta]}{kl\sin\theta}\right)^2\cos\theta\right\} \tag{4}$$

In Eqs. 3 and 4, a is the radius, l is the cylinder length, λ is the wavelength of the incident sound, θ is the angle measured from normal incidence (0°) to axial incidence (90°), and k is $2\pi/\lambda$.

Estimates of the TS of a finite cylinder with hemisperical end caps as calculated from a combination of the geometrical optics Eqs. 3 and 4 and by the Kirchhoff approximation are given in Fig. 1. The cylinder has total length of 50m and a diameter of 5m, the frequency, f = 600 Hz.

CLASSIFICATION

The term classification as used here involves the physics of scattering. In the "forward" sense, this involves the prediction of echo characteristics from a knowledge of the incident wave coupled with an understanding of scattering mechanisms; in the "inverse" sense, the problem is to predict the physical parameters of the scatterer from analysis of the scattered echo.

Much of the understanding of scattering mechanisms and the development of physics-based-processing techniques has come from the studies of simple shapes, for which exact scattering solutions can be obtained. Normal mode series (Rayleigh series) solutions for the pressure scattered by spheres[2,3] and cylinders[2,4] have been published . Generally descriptions are presented as form functions. The form function is a dimensionless form of the scattered pressure defined as

$$f_\infty = A\frac{p_s}{p_i} \tag{5a}$$

where A is a normalization factor that involves target dimensions and range. For a sphere and cylinder

$$(f_\infty)_s = \frac{2r}{a}\frac{p_s}{p_i} \tag{5b}$$

$$(f_\infty)_c = \sqrt{\frac{2r}{a}}\frac{p_s}{p_i} \tag{5c}$$

Normal mode series solutions in the form

$$f_\infty = \sum_{n=0}^{\infty} f_n \tag{5d}$$

are given in Refs. 3, 4 and in many others. For a rigid sphere and rigid cylinder, these solutions have in the backscatterer direction the simple forms:

$$f_\infty^c = \frac{-2}{(i\pi ka)^{\frac{1}{2}}} \sum_{n=0}^{\infty} (2-\delta_{no}) \frac{J_n'(ka)}{H_n'(ka)} \tag{5e}$$

$$f_\infty^s = \frac{-2}{ka} \sum_{n=0}^{\infty} (2n+1)(-1)^n \frac{j_n'(ka)}{h_n'(ka)} \tag{5f}$$

For an infinite solid-elastic cylinder, the backscattered form function has the general form:

$$f_\infty(ka) = A \sum_{n=0}^{\infty} (2-\delta_{no}) \frac{b(n,ka)}{D(n,ka)} \cos n\varphi H_n^{(1)}(kr) \tag{6a}$$

where $b(n,ka)$ and $D(n,ka)$ are 3×3 determinants which depend on the elastic parameters of the material and the fluid. Resonances in $f_\infty(ka)$ occur for ka values that satisfy:

$$D(n,ka) = 0 \tag{6b}$$

The Rayleigh series is the preferred method for computing the response of these canonical shapes; although, it does not directly illuminate the scattering mechanisms

Interest in circumferential waves became acute because of the experimental work carried out at ARL Texas[5], and this distinctive view of scattering was formalized by Überall and collaborators,[7,8] who transformed the Rayleigh summation over n into an integral in the complex ν plane using the Watson transformation. The residues of poles which occurred at values $\nu_l(ka), [l = 1, 2 \cdots m]$ which satisfy

$$D[\nu, ka] = 0 \tag{6c}$$

were associated with circumferentially traveling surface waves having a phase velocity

$$c_l(ka) = \frac{(ka)c_w}{Re\nu_l}. \tag{6d}$$

"Franz" or "Creeping" waves were associated with geometrical diffraction, and of the Franz type poles only $l = 1$ is significant for underwater scattering. Rayleigh type, R_l, waves were associated with the elasticity of the material. The R_1 label is associated with the "leaky" Rayleigh surface wave on a flat-infinite-half space. Associations of the higher $R_{l=2,\ m}$ poles, with elastic phenomena has been the subject of several papers.[9,10]

Form function curves, computed by the Rayleigh series, for solid-elastic spheres are given in Fig. 2 Features in these form functions are related to both the geometry and to material parameters. The rigid body curve (Fig. 2a) shows peaks and nulls associated with the creeping wave. The elastic form functions have a low frequency region similar to that of the rigid body; as ka increases this is followed by characteristics related to their shear and longitudinal velocities. The ka position of the initial form function peak and the Δka between peaks are characteristics of the shape and size of the target. The amplitude of the initial peak is related to the density. The deviations from the rigid are related to the natural modes of vibration of the target [2,11]

The resonances are labeled (n,l) where the $l's$ are the eigenfrequencies associated with the modal numbers, n. For solid spheres and cylinders whose densities $\rho_s > \rho_w$ and whose shear speeds $c_s > c_w$, the initial deviation from the rigid is caused by the excitation of the (2,1) "spheroidal mode", and the ka position at which this is observed is related to the shear speed of the material. Vogt separated the

Rayleigh series describing the pressure scattered by solid sphere into rigid and resonance portions and his plot of the modulus of the elastic portions for three materials is seen in Fig. 3. The ka position of the (2,1) resonance nulls were shown to have a direct relationship to the relative shear speeds in the materials, and as will be described below, this is true because the position of the (2,1) mode and the relative positions of the (n,1) modes in general are related to the leaky-Rayleigh wave speeds in the material.

The relationship between these free body resonances (n,ℓ) and the surface wave description derived from the Watson transformation was presented in a joint Catholic U/NRL paper.[12] In brief, resonances labelled (n,ℓ) are related to the R_ℓ^{th} elastic circumferential wave. The eigenfunction index, n, represents the circumferential mode number, i.e., there are 2n nodes on the surface, and the eigenfrequency number, ℓ, represents the number of nodes along the radius. The significant member of the family of R_ℓ waves is the circumferential wave related to the leaky Rayleigh-surface wave $R_1 \leftrightarrow (n,1)$. Fig. 4 shows a computation of the normal node series solution for a solid steel cylinder and for a steel cylinder with a hole, whose diameter is 0.1d drilled in the center of the cylinder.

Note that the (2,1) mode position is altered by the presence of the hole, while the (3,1) and higher (n,1) modes are far less effected. The surface wave penetrates $\sim \lambda/2$ into the target. At Low frequency the hole interacts with the wave, at higher frequency it does not.

The resonance theory of scattering was formalized in a second joint Catholic University/NRL paper,[13] in which the scattering by solid elastic spheres and cylinders was described in the form:

$$f_\infty(ka) = \sum_n f^{Rigid}(ka) + \sum_n f^{res}(ka), \tag{7a}$$

where f^{res} is in the form:

$$f_n^{res} \propto \frac{1}{k - k_n + i\Gamma_n} \tag{7b}$$

In the case of solid-elastic metal targets, the isolation of the background term as, $f^{rigid}(ka)$, (see Eq. 7a) is straightforward. The identification of a proper background term for most targets particularly shells, is not so straightforward. Werby[14] has written a recent paper on this significant topic.

The identification of the relevant background term is a powerful analysis tool because the background term is generally large, and masks an easy isolation of significant elastic mechanisms. As is seen in many examples discussed in this paper, the effects of elastic mechanisms often appear as nulls in the total form function, but as large peaks when the proper background is subtracted.

Fig. 5 shows form function computation for steel cylindrical shells, and for a rigid and soft cylinder. The figure illustrates the complications involved in choosing a background response, but also the interesting variations in the low frequency response of shells as a function of thickness. The initial slope of the form function approaches, in magnitude, the "perfectly soft" limit at thickness, $h = .005a$ ($\frac{b}{a} = .995$); it moves toward the rigid slope for $\frac{b}{a} = 0.99$, and approaches zero as $\frac{b}{a} \approx 0.96$. As thickness is further increased it returns toward the rigid value.

Only two terms in the Rayleigh series the $n = 0$, and $n = 1$ term are important in describing the form function for a hollow cylindrical shell for $ka < 1$ as seen in Fig. 6 which shows the form function f_∞, and the partial wave terms f_0, f_1, and f_2 for the steel shell with $\frac{b}{a} = 0\ 96$. The relative null in the form function is caused by the cancellation between the f_0 term which is dominated by the compressibility of the shell and the f_1 term which is dominated by the mass of the shell. A recent paper by Gaumond[15] describes the low frequency responses of shells in terms of their compressibility and mass relative to that of the displaced water volume.

The examples of form function presented here, have been for simple shapes, but are representative of the scattering mechanisms and the effects of scattering mechanism on the response of targets Many of the major identification features are destructive interference nulls in the form function magnitude caused by the interaction of geometric and elastic effects. These nulls are easily isolated in the laboratory, but are strongly effected by noise Additionally, the phase of the scattering form

function is strongly impacted by the elastic mechanisms, but these phase changes are obscured by the consistent increase in phase angle with frequency, that results from the time delay bias between scattered and incident waves. Examples of the magnitude effects (i.e. form function nulls) have been seen throughout this paper; the phase effects are illustrated in Fig. 7 which shows the form function magnitude (Fig. 7a) and form function phase (Fig. 7b) for a solid steel sphere, along with a plot of the rate of phase change with respect to frequency (Fig. 7c). In Fig. 7c three distinct features, no longer obscured by the time delay bias, can be observed. There is a slowly oscillating region associated with the rigid body/creeping wave response; there are single-step changes associated with the Rayleigh/shear wave speeds; and there are single-cycle swings associated with the longitudinal speed in the material

A joint time/frequency analysis approach sensitive to scattering mechanisms was described by Yen.[16,17] The technique is based on the Wigner distribution function (WDF). The properties of the Wigner function and the description of the time-frequency-analysis processing scheme, based on a local average of the WDF, is given in Ref. 17. Vein diagram displays that result from an implementation of Yen's scheme are given for solid spheres and hollow spherical shells in Figs. 8 and 9 respectively. In these black and white versions of the vein diagram, the thickness of the lines is related to the magnitude. The displays in Fig. 8 show dark lines (SR) associated with the specular reflection for aluminum oxide and steel at $t \approx 0.3$; creeping wave lines (CW) are found near $t \approx 1$, and remain to much higher ka for aluminum oxide because of its very high shear velocity. The shear speeds may be estimated directly from the relative positions of the Rayleigh wave lines (SW) in Figs. 8a and 8b. The interference patterns within the specular reflection lines–more visible in color plots–give longitudinal speed estimates. The vein diagram for the plastic sphere (Fig. 8c) is much different in character. The specular (SR) line is not the largest in magnitude. There is no creeping wave line. A compressional wave (LW) line is visible, and both the LW and shear (SW) lines are at positions which indicate the relatively low sound speeds in lucite. The largest magnitudes are associated with the LW and SW lines which shows that penetration, refraction, and reradiation produce the main echo response.

The vein diagrams for shells, seen in Fig. 9, were all obtained for stainless steel. Thicknesses of $\frac{b}{a} = 0.99$, $\frac{b}{a} = 0.94$, and $\frac{b}{a} = 0.90$ are represented in Figs. 9a–c respectively. The character of lines associated with specular reflection (SR), and with compressional (SFM) and flexural (AFM) waves within the shell indicate the thickness related differences. It is believed that schemes, such as the vein diagrams, derived from the modified WDF will be robust against noise, and this is an on-going topic of research at NRL.

CONCLUSION

There have been hundreds of articles and papers that have described acoustic scattering mechanisms, and the implications of these mechanisms on the prediction of either the characteristics of an acoustic echo and/or the isolation of target parameters from an echo. A few mechanisms and target-identification features and techniques were discussed in this paper. In all of the examples discussed here the frequency response and/or the time response of the echo could be obtained by exact analytic means. It is clear from the difficulties associated with the exploitation of these well understood situations, that even as high quality scattering solutions for non-canonical targets become available through boundary element and finite element techniques, as well as through high quality experimental measurements, the development of physics-based algoritms for target identification is still a wide open area of investigation.

REFERENCES

1. Urick, R.J., **Principles of Underwater Sound, 3rd Edition**, McGraw-Hill, New York, p. 291, (1983).

2. Faran, J.J., "Sound Scattering by Solid Cylinders and Spheres," J. Acoust. Soc. Amer. 23, p. 405, (1951).

3. Hickling, R., "Analysis of Echoes From a Solid Elastic Sphere in Water," J. Acoust. Soc. Amer. 34, p. 1582, (1962).

4. Flax, L. and Neubauer, W.G., "Acoustic Reflection From Layered Elastic Absorptive Cylinders," J. Acoust. Soc. Amer. 61, p. 307, (1977).

5. Barnard, G.R. and McKinney, C.M., "Scattering of Acoustic Energy by Solid and Air-Filled Cylinders in Water," J. Acoust. Soc. Amer. 33, p. 226, (1961).

6. Horton, C.W. and Mechler, M.V., "Circumferential Waves in a Thin-Walled Air-Filled Cylinder in a Water Medium," J. Acoust. Soc. Amer. 51, p. 295, (1971).

7. Überall, H. *et al*, "Use of Sound Pulses for a Study of Circumferential Waves," J. Acoust. Soc. Amer. 39, p. 564, (1966).

8. Doolittle, R.D., *et al.*, "Sound Scattering by Elastic Cylinders," J. Acoust. Soc. Amer. 43, p. 1, (1968).

9. Überall, H., "Surface Waves in Acoustics," in *Physical Acoustics*, edited by W.P. Mason and R.N. Thurston, vol. 10, Academic Press, New York, pp. 1-60, (1973).

10. Dickey, J.W., *et al.*, "Whispering Gallery Wave Modes on Elastic Cylinders," J. Acoust. Soc. Amer. 59, p. 1339, (1976).

11 Vogt, R. and Neubauer, W.G., "Relationship Between Acoustic Relfection and Vibrational Modes of Elastic Spheres," J. Acoust. Soc. Amer. 60, p. 15, (1976).

12. Überall, H. *et al.*, "Relationship Between Creeping Waves and Normal Modes of Vibration of a Curved Body," J. Acoust. Soc. Amer. 61, p. 711, (1977).

13. Flax, L., *et al.*, "Theory of Elastic Resonance Excitation by Sound Scattering," J. Acoust. Soc. Amer. 63, p. 723, (1978)

14 Werby, M.F., "The Acoustical Background for a Submerged Elastic Shell," J. Acoust. Soc. Amer. 90, p. 3279, (1991).

15. Gaumond, C.F. and Dragonette, L.R., "Form Function Dependence on Rigidity and Mass," J Acoust. Soc Amer. 90, p. 2692, (1991)

16 Yen, N., "Time and Frequency Representation of Acoustic Signals by Means of Wigner Distribution Function: Implementation and Interpretation," J Acoust. Soc Amer. 81, (1987).

17. Yen, N., *et al.*, "Time-Frequency Analysis of Acoustic Scattering From Elastic Objects," J. Acoust. Soc. Amer. 87, p. 2359, (1990).

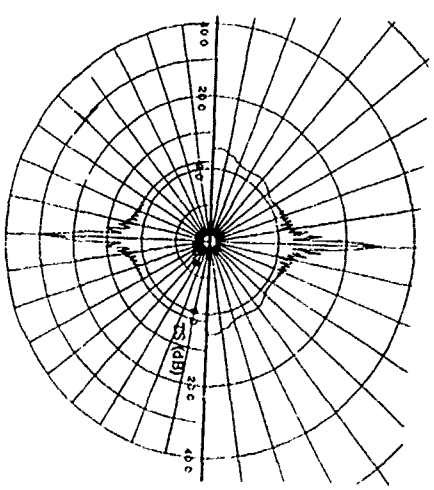

Fig. 1 An approximation to the target strength of a rigid finite cylinder with hemispherical end caps as produced from geometrical acoustics tables (left) and the Kirchhoff approximation (right).

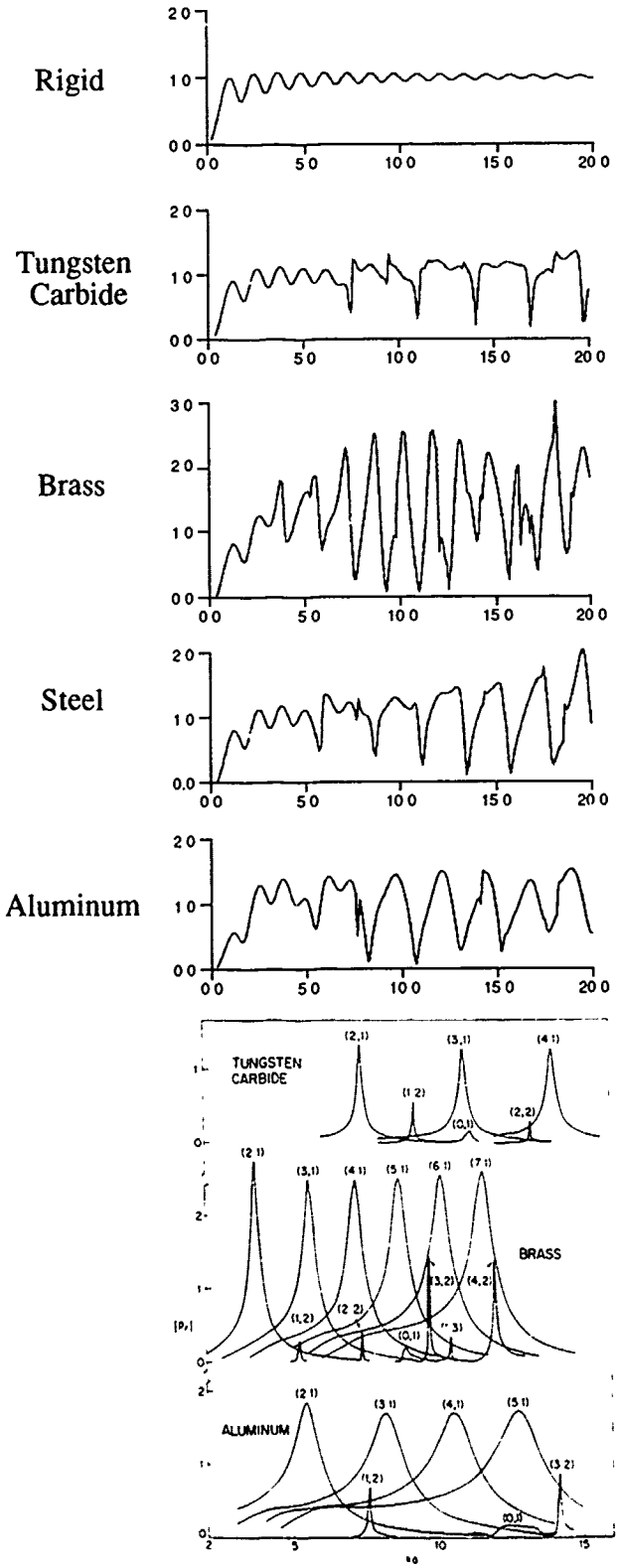

Fig. 2 The form-function for a rigid sphere, and for solid-elastic spheres of tungsten carbide, brass, steel, and aluminum.

Fig. 3 The description of the scattering by tungsten carbide, brass, and aluminum spheres that remain when the rigid-body contributions are subtracted.

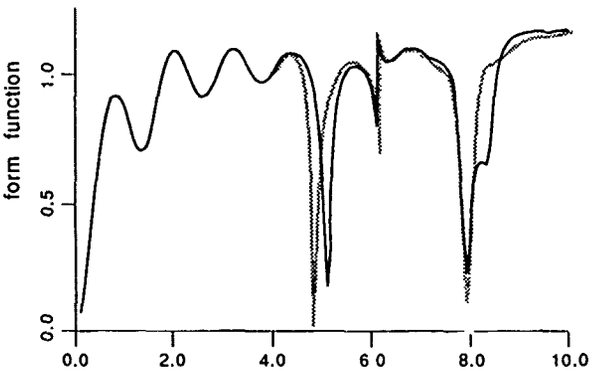

Fig. 4 An example of the effect of a hole on the "leaky Rayleigh-wave" contribution to the scattering. The form -functions compared are infinite aluminum cylinders. The solid curve is competed for a solid body; the dashed curve for a body with $\frac{b}{a} = 0.9$.

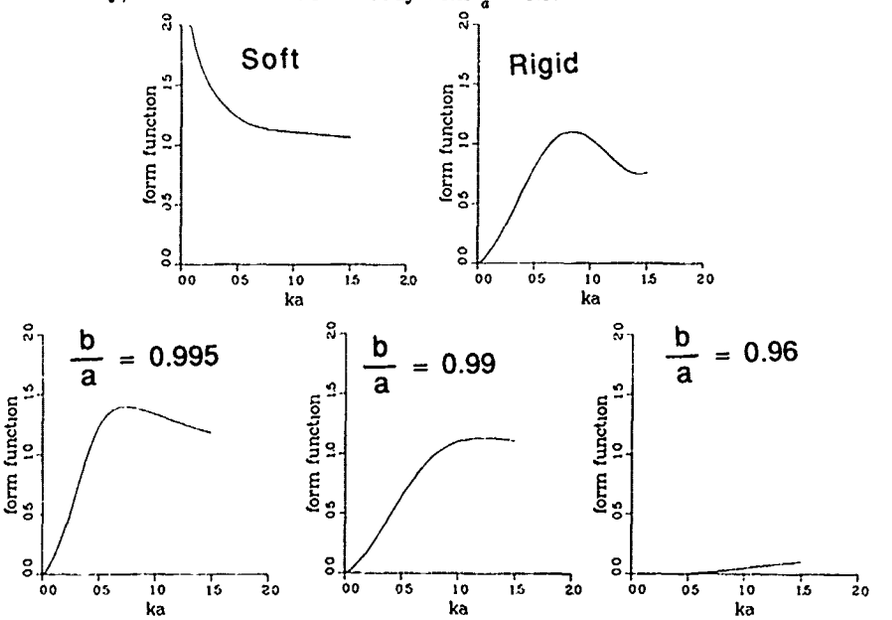

Fig. 5 The form-function for a rigid and soft infinite cylinder, and for cylindrical-steel-shells with $\frac{b}{a} = 0.995, \frac{b}{a} = 0.99$, and $\frac{b}{a} = 0.96$.

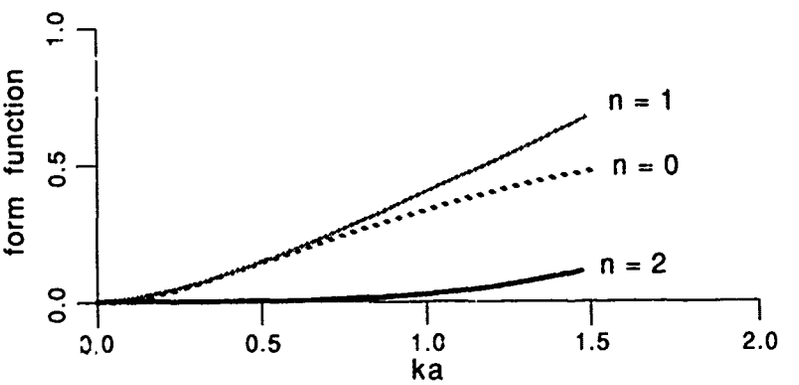

Fig. 6 The form-function for an infinite-cylindrical-steel shell with $\frac{b}{a} = 0.96$ and the magnitudes of individual partial-wave terms f_0, f_1, f_2.

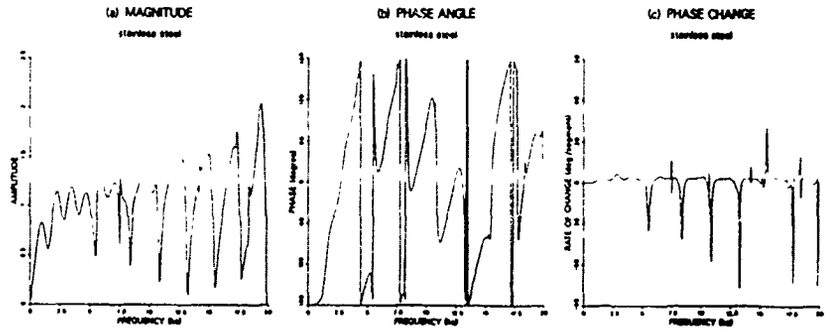

Fig. 7 The form-function magnitude (a) and phase (b) for a solid steel sphere, and the rate of change of the phase with frequency (c).

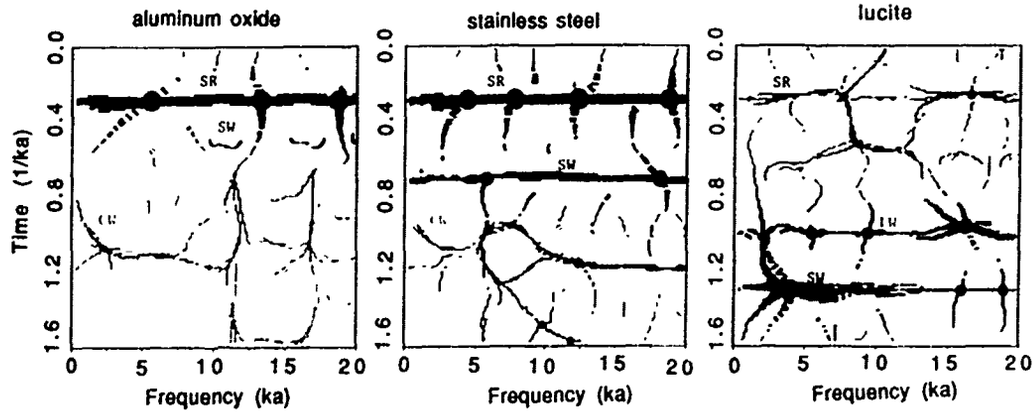

Fig. 8 The Vein diagrams for solid elastic spheres of aluminum, steel, and lucite.

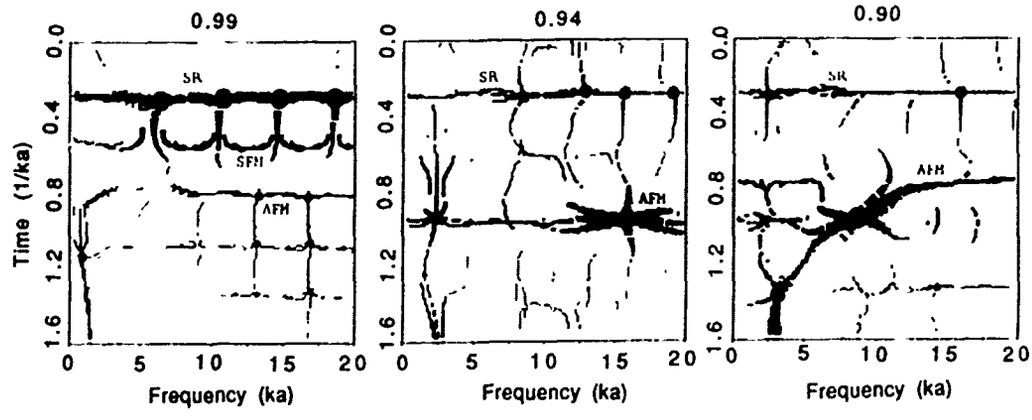

Fig. 9 The Vein diagrams for spherical shells of stainless steel; thicknesses are (a) $\frac{b}{a} = 0.99$, (b) $\frac{b}{a} = 0.94$, and (c) $\frac{b}{a} = 0.90$.

SOUND PROPAGATION, RADIATION AND SCATTERING

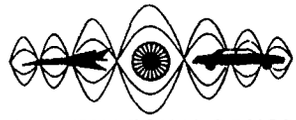

SECOND INTERNATIONAL CONGRESS ON
RECENT DEVELOPMENTS IN AIR- AND
STRUCTURE-BORNE SOUND AND VIBRATION
MARCH 4-6, 1992 AUBURN UNIVERSITY USA

SOUND BACKSCATTERING FROM OCEAN BOTTOM

Anatoly N. Ivakin
N. N. Andreev Acoustics Institute
Shvernik 4, Moscow 117036
USSR

ABSTRACT

Analysis of theoretical and experimental research of backscattering of sound from the ocean bottom is presented. Geoacoustic model of scattering is proposed, in which the bottom is considered to be irregular stratified medium with scatterers of two types : irregularities of bottom relief and volume inhomogeneities of bottom medium - random fluctuations of the acoustical parameters. Two cases of high and low frequences are considered. At high frequencies sound penetration into the sediments is so small, that bottom stratification is not taken into account. The influence of sedimentary stratification on sound scattering is studied for low frequencies. The results are used for interpretation of characteristic and distinctive features of sound scattering from the bottom in shallow and deep regions of the ocean.

INTRODUCTION

Acoustic scattering from the ocean bottom is a process of interest and considerable importance, due to its effect on acoustic propagation, operation of underwater acoustic systems, and as a means of remotely obtaining information on seabed sediment properties.

The prediction of acoustic scattering from the bottom and remote measuring of its parameters are possible only if there is geoacoustic model of sound scattering, i.e., the model which, on the one hand, is to be based on up-to-date geological and geophysical studies of sediment medium and, on the other hand, makes it possible to explain characteristic and distinctive features of sound scattering from the bottom.

The purpose of this paper is to analyze a number of models, applicable for high and low frequencies. The bottom is considered to be irregular medium with scatterers of two types : irregularities of bottom relief and volume inhomogeneities of bottom medium (random fluctuations of the acoustical parameters). Two cases of high and low frequencies are considered. At high frequencies sound penetration into the sediments is so small, that bottom stratification is not taken into account, i.e., the bottom may be assumed to be homogeneous on the average. In this case analysis of bottom backscattering is presented for both types of scatterers and for main types of bottom medium: muds, silts, sands and rocks. The influence of sedimentary stratification on sound scattering is studied for low frequencies. The results are used for interpretation

of some typical and distinctive features of experimental frequency-angle dependences of the backscattering coefficient observed in shallow and deep regions of the ocean.

ANALYSIS OF BACKSCATTERING EXPERIMENTS

We now discuss the scattering properties of the ocean bottom experimentally observed in shallow water and deep sea. They are characterized by the so-called scattering coefficient, which is measured in far (Fraungofer) zone relative to the scattering part of the bottom and is defined as

$$m_b = \frac{W_{scat}}{I_{inc} A} \qquad (1)$$

where W_{scat} is the average acoustic power scattered by part of the bottom with surface area A in a specified direction per unit solid angle, and I_{inc} is the intensity of the incident sound wave near the scattering part of the bottom.

In most cases experimental studies of backscattering only are carried out to investigate the dependence of quantity m on the grazing angle of the incident sound wave relative to the bottom, and its frequency. Let us consider most typical frequency-angle dependences of thebackscattering coefficientstrength observed in shallow and deep regions of the ocean with bottom sediments of several types.

Shallow water

The paper [1] gives generalized (averaged) dependences of m_b on the grazing angle χ , obtained by a number of authors in shallow seas and coastal regions of the ocean in the frequency range 10 - 100 kHz for grazing angles of 5 - 50°. It is shown that for sandy sediments angular dependence of m_b is rather close to the Lambert law

$$m_b \sim \sin^2 \chi \, . \qquad (2)$$

For silts and muds m_b is close to the Lommel-Seeliger law

$$m_b \sim \sin \chi \, . \qquad (3)$$

For $\chi \leq 6^\circ$ the scatter of experimental points usually increases and there is no regular dependence $m_b(\chi)$ [2]. Besides frequency independence of m_b is observed in most bottom backscattering experiments.

Deep sea

Some typical dependences of m_b on χ , obtained in deep ocean regions in the frequency range 0.8 - 6.4 kHz for grazing angles of 1 - 60° are analyzed in [1]. It is shown, that m_b is almost frequency independent and its angular dependences are between the Lommel-Seeliger law and the Lambert law.

GEOACOUSTIC MODELING OF SOUND SCATTERING

To explain typical features of sound backscattering from the ocean bottom the geoacoustic model of scattering is needed. This model should

be based on up-to-date geological and geophysical studies of sediment medium, as to its fundamental physical properties, stratification and spatial inhomogeneity, etc. [3]. Let us consider the bottom as irregular stratified medium. This model takes into account two types of sound scatterers : irregularities of bottom relief and volume inhomogeneities of bottom interior (random fluctuations of the acoustical parameters).

Since attenuation of sound in the sediments varies directly as sound frequency, only a shallow sedimentary surface layer having a thickness inversely proportional to the radiation frequency is effectively irradiated by sound and scatters it. At higher frequencies, owing to strong absorbtion of sound in the bottom, it is rather a thin layer. In this case the bottom in geoacoustic models may be assumed homogeneous on the average, i.e., it is assumed that the mean values of its acoustical parameters (sound velocity, density, and absorbtion coefficient) do not depend on the depth. For this case of sufficiently high frequencies the analysis of the bottom scattering coefficient is presented below for both types of scatterers and for main types of ocean bottom medium : muds, silts, sands, and rocks (basalts).

As the frequency is lowered, the penetration depth of sound in the bottom increases, and the mean values of the acoustical parameters vary with depth within the insonofied layer, i.e., stratification can no longer be neglected, since it induces a qualitative change in the spatial structure of the sound field in the sediments. This is caused by the onset of waves associated with refraction as the sound velocity in the sediments increases with depth, along with waves reflected from internal interfaces in the bottom and interference between these waves. It is shown below that sedimentary stratification can influence the scattering properties of the bottom significantly, and the allowance for this influence makes it possible to explain the distinctive features observed in the frequency and angular dependence of the sound-scattering coefficient of the bottom in shallow- and deep-water regions of the ocean, in particular at small grazing angles.

High frequency

First let us consider the case of sufficiently high frequencies, when the bottom may be assumed to be homogeneous on the average, i.e., bottom stratification is not taken into account. Besides, water-saturated sediments of the upper surface layer in most cases may be supposed to be a liquid medium, i.e., influence of shear elasticity of the bottom is to be neglected. But it is not justified in the case of sufficiently dense sands and rocks, which will be considered separately. There are two types of sound scatterers, roughness of water-bottom interface and volume inhomogeneities of bottom medium, which we will take into account. If volume inhomogeneities are rather weak, the approximation of volume single scattering may be used. In this case it may be shown that

$$m_b = m_v + m_s \qquad (4)$$

where m_v and m_s are the coefficients of sound scattering by volume and surface irregularities.

Volume scattering. The scattering of high frequency sound by inhomogeneities of liquid sediments has been investigated in papers [1,4]. An equation has been derived [4] for the coefficient of backscattering of sound from the bottom in the case of a plain water-sediment interface ($m_s = 0$)

$$m_b = m_v = (|W|^4/m^2)m_o h_{eff} \qquad (5)$$

where $W = 2m \sin\chi / [\, m \sin\chi + (n^2 - \cos^2\chi)^{1/2} \,]$ is the pressure coefficient of sound transmission from the water into the bottom, m is the ratio of the densities of the bottom to the water, $n = n_o(1 + i\alpha)$ is the complex refractive index, α is the loss tangent ($0 < \alpha << 1$), m_o is the volume sound-scattering coefficient in the bottom, and h_{eff} is the effective thickness of the scattering layer (penetration depth of sound into the bottom)

$$h_{eff} = \mathrm{Re}(n^2 - \cos^2\chi) / (2\beta n_o) \qquad (6)$$

where the symbol Re denotes the real part, $\beta = 2kn_o\alpha$ is the energy coefficient of absorbtion in the bottom, k_o is the wave number of the sound in the water. For m_o we have

$$m_o = 2\pi k^4 G(q) \qquad (7)$$

where $G(q)$ is the spatial spectrum of the inhomogeneities, q is the scattering vector, $k = k_o|n|$ is the modulus of the wave number in the bottom. It may be shown, particularly, that in the case of water-saturated sediments, for not very small angles, when $|n^2-1| << \sin^2\chi$, "Eq.5" leads to

$$m_v = \frac{8\, m_o \sin\chi}{m^2 (m+1)^4 \beta} \qquad (8)$$

that is in agreement with the observed Lommel-Seeliger law. For sands, the calculations predict a sharp decrease of m_v at $\chi < \chi_o = \arccos n_o$ (critical angle), because of the decrease of the sound penetration into the sediments. But experiments usually do not show such a sharp decrease. It may be partially explained if roughness of the bottom surface or its shear elasticity is taken into account.

Influence of shear elasticity. Sound scattering by volume inhomogeneities of an elastic half-space has been investigated in our recent paper [5]. The angular dependence of the backscattering coefficient has been calculated for typical parameters of several ocean media such as ice, basalt, and a sandy ocean bottom. It is shown, particularly, that shear elasticity radically alters the form of the angular dependence of the scattering coefficient for basalt and ice. This influence is also fairly strong in the case of a dense sandy medium ($m = 2.2$), for which the backscattering coefficient increases by 5-7 dB at grazing angles $\chi \leq 40^o$. Calculations show that the influence of shear elasticity on angular characteristics of the scattered field can be disregarded for less dense marine sediments with a relative density $m \leq 2$, in which case the increase is less than 3 dB.

Surface roughness scattering. Scattering of sound by roughness of water-sediments interface without volume inhomogeneities has been investigated in adequate detail. There are two main approaches to this problem [6]. The Kirchhoff approximation requires that the scattering interface irregularities be relatively large and smooth in the sense that their radii of curvature must not be much smaller than acoustic wavelength. The small-roughness perturbation approximation is valid, when the interface relief is smaller than the acoustic wavelength.

The analysis of surface scattering from the bottom without volume inhomogeneities shows, that it can not explain the typical experimental

dependences of m_b, which are discussed above, such as the Lommel-Seeliger and Lambert laws.

Volume - surface scattering. A complete model for high frequencies should consider scattering from within the volume of the bottom medium along with its surface roughness, i.e., volume - surface scattering.

In our paper [7] it is shown that there is sufficient influence of large smooth roughness on the value of the volume backscattering coefficient m_v in the angle region $\chi \leq \chi_0$ (for $n_0 < 1$). Physically, this result is explained by the fact that the roughness of the surface greatly enhances the penetration of sound into the medium over those parts of rouhgness in the vicinity of which local grazing angle $\chi > \chi_0$, and therefore intensifies the scattering of sound by volume inhomogeneities of the bottom. It may partially explain the fact that experimentally observed decrease for sands is not so sharp at $\chi < \chi_0$, as it might be expected.

Low frequency

Now we consider the case of low frequencies, when bottom stratification can no longer be neglected. In our paper [8] an equation has been derived for backscattering coefficient

$$m_v = m_0 \int_0^h |g(z)|^4 dz \qquad (9)$$

where m_0 is an effective (depth-averaged) volume scattering coefficient, h is thickness of the scattering layer, and function g(z) is normalized unperturbed sound field in the sediments (without volume inhomogeneities). Here we discuss the results for specific models of the bottom stratification [8].

Continuous stratification. Let us consider the influence of continuous stratification of the bottom medium, when the averaged acoustical parameters are the continuous functions of depth. Some general properties of sound-scattering coefficient of the bottom can be established without specifying the explicit form of these functions. For the case, when they are sufficiently smooth, the modified WKB approximation for the unperturbed field in the bottom has been used, which is valid in the neighborhood of the depth level of the turning point as well as outside it. It is shown, that if the turning point exists (sound velocity grows with depth, grazing angles are not too large), the bottom scattering coefficient closely corresponds to the Lambert law $m_v \sim \sin^2\chi$. We add here that, as it is mentioned above, an appreciable growth of the sound velocity with depth in the upper sedimentary layer and the Lambert law scattering are most typical of the indicated sandy-type sediments.

Influence of internal boundaries. To analyze the influence of internal reflecting boundaries in the sediment on the bottom-scattered field, a bottom model has been investigated in the form of a randomly inhomogeneous layer situated on a reflecting surface [8]. It has been shown, that both the frequency and angular dependence of the scattering coefficient m_v are rapidly oscillating in this case. The amplitude of the oscillations of m_v increase abruptly at small grazing angles in

the case $n_0 > 1$. This means that the scatter of the experimental points due to individual oscillations of the frequence and angular dependence of m_v will necessarily increase sharply at small angles in the measurement of m_v by means of receiving and radiating systems with sufficiently high frequency-angle resolution. This effect is indeed observed in experiments on the backscattering of sound by the bottom, as it is mentioned above, and can be explained within the scope of the above described bottom model, because many types of bottom media are known [3] to be characterized by the existence of a surface sedimentary layer in which the sound velocity is smaller than in water ($n_0 > 1$).

The frequency and angular dependences of the scattering coefficient, averaged over the rapid oscillations, are of practical interest insofar as they can be logically compared with the experimental dependences obtained by averaging the data over a certain frequence band and an interval of grazing angles, as is customary in practice. Such averaging is also realized automatically with the application of insufficiently narrow systems and the use of wideband filters. As a result we obtain [8], that the scattering coefficient averaged over rapid oscillations is close to the Lommel-Seeliger law $m_v \sim \sin\chi$, which frequently is observed experimentally.

REFERENCES

1. A.N. Ivakin. Backscattering of sound by the ocean bottom. Theory and experiment. In: Acoustics of ocean medium / Ed. by L.M. Brekhovskikh, I.B. Andreeva. Moscow: Nauka, 1989, p. 160-169.

2. A.V. Bunchuk and Yu.Yu. Zhitkovskii. Sound scattering by the ocean bottom in the shallow-water regions (review). Sov. Phys. Acoust., v. 26, N5, 1980, p. 363-370.

3. E.L. Hamilton. Geoacoustic modeling of the sea floor. J. Acoust. Soc. Am., v. 68, N5, 1980, p. 1313-1340.

4. A.N. Ivakin. Sound scattering by random volume inhomogeneities and small surface irregularities of underwater ground. Voprosy sudostroenija, Akustika, N17, 1983, p. 20-25.

5. A.N. Ivakin. Sound scattering by inhomogeneities of an elastic half-space. Sov. Phys. Acoust., v. 36, N4, 1990, p. 377-380.

6. F.G. Bass and I.M. Fuks. Wave Scattering from Statistically Rough Surfaces. Pergamon, Oxford, 1979, p. 438.

7. A.N. Ivakin and Yu.P. Lysanov. Underwater sound scattering by volume inhomogeneities of a bottom medium bounded by a rough surface. Sov. Phys. Acoust., v. 27, N3, 1981, p. 212-215.

8. A.N. Ivakin. Sound scattering by random inhomogeneities of stratified ocean sediments. Sov. Phys. Acoust., v. 32, N6, 1986, p. 492-496.

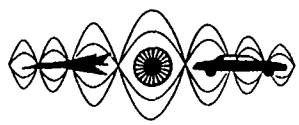

SECOND INTERNATIONAL CONGRESS ON
RECENT DEVELOPMENTS IN AIR- AND
STRUCTURE-BORNE SOUND AND VIBRATION
MARCH 4 6 1992 AUBURN UNIVERSITY, USA

Laboratory Simulation of Point Monopole and Point Dipole Sound Sources

K. K. Ahuja*
Georgia Institute of Technology
GTRI/Aerospace Laboratory and
School of Aerospace Engineering
Atlanta, GA 30322-0800
U. S. A.

ABSTRACT

Simulation of point monopole and dipole sound sources is often needed for a number of laboratory experiments. Availability of a true point sound source is particularly useful in evaluating a range of theoretical formulations and to validate computational aeroacoustics codes. This paper will describe the construction of a device that provides laboratory simulation of point monopole sound sources. Addition of two such sources with suitable phase differences enables the simulation of point dipoles. Directivity measurements of a point monopole and a point dipole sound source made in an anechoic chamber are presented. Selected examples of how the devices have been used to verify theoretical calculations are also provided.

NOMENCLATURE

U	Particle velocity	ρ	Instantaneous density
ρ_0	Equilibrium density	P	Instantaneous pressure
P_0	Equilibrium pressure	p	Excess or acoustic pressure = $P - P_0$
c	Velocity of sound propagation	t	Time
k	Wave member	ω	Circular frequency in radians/sec

INTRODUCTION

In this paper we shall consider the laboratory simulation of two of the acoustic point sound sources, namely, a monopole and a dipole. The monopole is the simplest of the point sound sources and is classically regarded as a small pulsating sphere. Two such sources, pulsating in antiphase, are combined to form a dipole. The monopole source can be considered as a source of time varying mass injection. In the dipole source, on the other hand, while there exists no net mass flux, it can be represented by a fluctuating force.

There are a number of applications that require simulation of a point monopole or a dipole sound source in the laboratory. Over the last 15 years, this author and his colleagues have utilized such sources for applications to a range of acoustics problems. Some of these applications include: (1) calibrating the acoustic quality of anechoic chambers [1]; (2) studying refraction of sound through jets and verifying the existence of Snell's law for sound propagation through a flow discontinuity [1,2]; (3) studying convective amplifications applicable to high-speed, low-flying aircraft [3]; (4) exciting instability waves in mixing layers of a model-scale jet [4,5]; (5) generating sound waves at the focus of a paraboloidal reflector to obtain plane waves [6]; and others.

The details of the design of these sources and their performance characteristics are provided in this paper. A summary of how these sources were applied to various research problems and where these sources can be used in the future is also given.

* *Head: Acoustics Branch, GTRI/AERO and Professor, School of Aerospace Engineering*

DESIGN OF THE POINT MONOPOLE SOUND SOURCE

Theoretical Requirements

The monopole may be classically regarded as a pulsating sphere giving rise to a system of acoustic waves whose amplitude and phase is a function only of the distance from the source. A simple, two dimensional analogue is the waves emanating from a rock dropped into an otherwise calm pond.

The wave equation given by

$$\frac{\partial^2 p}{\partial t^2} = c^2 \nabla^2 p \tag{1}$$

must be satisfied

where, in spherical coordinate system

$$\nabla^2 = \frac{1}{r^2}\frac{\partial}{\partial r}\left(r^2 \frac{\partial}{\partial r}\right) + \frac{1}{r^2 \sin\theta}\frac{\partial}{\partial \theta}\left(\sin\theta \frac{\partial}{\partial \theta}\right) + \frac{1}{r^2 \sin^2\theta}\frac{\partial^2}{\partial \phi^2} \tag{2}$$

Since, for a monopole source, the amplitude and phase are a function of distance, r, alone and independent of θ and ϕ, the wave equation (1) can be reduced to

$$\frac{\partial^2 p}{\partial t^2} = c^2 \frac{1}{r^2}\frac{\partial}{\partial r}\left(r^2 \frac{\partial p}{\partial r}\right) \tag{3}$$

which can be further simplified to

$$\frac{\partial^2 (rp)}{\partial t^2} = c^2 \frac{\partial^2 (rp)}{\partial r^2} \tag{4}$$

The general solution of this equation can be shown to be

$$rp(r,t) = f_1(ct - r) + f_2(ct + r) \tag{5}$$

or

$$p(r,t) = \frac{1}{r} f_1(ct - r) + \frac{1}{r} f_2(ct + r) \tag{6}$$

The first term of this equation represents a disturbance traveling outboards from the origin at the sound speed c and the amplitude decays inversely with distance r from the source. It can be shown that this is merely a result of the acoustic power being spread over spheres of increasing radius. The second wave is not so important in acoustics as it represents a wave converging on the origin, and will not be considered further.

By assuming a sinusoidal form for $f_1(ct - r)$, equation 6 can be written as

$$p(r,t) = \frac{A}{r} e^{j(\omega t - kr)} \tag{7}$$

where A is a constant and can be specified from the knowledge of the pressure amplitude variations at some point in the sound field.

Furthermore, by regarding the source as a small sphere of mean radius r_o which is small compared with the acoustic wavelength so that

$$kr_o << 1 \tag{8}$$

it can be shown that

$$p(r,t) = \frac{1}{4\pi r}\frac{\partial M}{\partial t}(t - r/c) \tag{9}$$

where M is the mass flux from the source and can be written as the product of the surface area of the sphere with the fluid density ρ and the surface velocity U_0.

Equation 9 describes the pressure disturbance associated with a point monopole sound source whose amplitude is inversely proportional to the distance and directly proportional to the rate of change of mass flux from the source. Clearly, an ideal monopole is expected to be omnidirectional.

Construction of a Point Monopole Source

The point monopole sound source used by the author consisted of a commercially available acoustic driver unit coupled to a straight tube via an inverse conical horn section. The other end of the tube terminated into a 0.635 cm diameter opening. A typical source is shown in Figure 1. It should be noted that the requirement of equation 8 was met by selecting a very small source opening. The requirement of fluctuating mass flux of equation 9 was met by adding a driver at one end of the inverse conical horn. Movement of the driver coil provided mass flux variation with time from the source opening. The strength of the monopole source was changed by changing the movement of the driver coil which in turn changed the rate of change of mass addition at the point source opening.

A number of source configurations were tested. The configuration shown in Figure 1 has a straight tube connected to the conical termination. Another configuration shown in Figure 2, terminated into a smooth right angled bend and was equipped with a fairing. This source was used to study the effect of flow on sound propagation within a jet. The portion of the source stem consisting of the fairing was immersed in the flow with the opening facing the direction of the flow. This point source, shown schematically in Figure 3, was subjected to extensive calibrations. These calibrations carried out to evaluate the performance of the source are described below.

Point Source Directivity Calibration

A calibration test to determine the directivity of the point source radiation in the absence of any surrounding flow was conducted in an anechoic chamber with the experimental setup shown in Figure 2. Using white noise excitation signal for the driver, 1/3-octave SPL spectra were measured at 15° intervals on a circular arc of radius 0.305m. The directivity was measured in two orthogonal planes (shown in Figure 4) as follows:

Plane #1: Perpendicular to the axis of point source tube.

Plane #2: Passing through the axis of point source tube.

Typical directivity plots at various frequencies for measurements in plane #1 and plane #2 are shown in Figures 5 and 6, respectively. As seen in these figures, the point source is fairly omni-directional over the frequency range considered in these tests. We have thus met the requirements of a point monopole sound source and have succeeded in laboratory simulation of such a source.

Effect of Vibration on Point Source

As mentioned earlier, the point sound source described here is amenable to immersion in flows to study sound propagation characteristics in a moving medium. It was not clear if the characteristics of the point monopole source would change significantly if the source started to vibrate by any impinging flow disturbances. To determine the order of magnitude of the effect of such vibrations on the characteristics of point source radiation, a separate test was conducted where artificial vibrations were imposed on the point source stem. This was achieved by attaching the source stem to a motor-cam operated shaker through a 0.635 cm diameter rigid bar, and operating the shaker at various frequencies. Typical results showing the effects of vibrating the point source at a frequency of 10 Hz are presented in Figure 7. It was concluded from these tests that the changes in levels and directivity of the point source due to vibration are negligible.

DESIGN OF THE DIPOLE SOUND SOURCE

Theoretical Requirements

A dipole can be represented by two monopoles pulsating in antiphase, placed a distance L apart as shown in Figure 8.

If each source acting independently is assumed to produce a sinusoidal signal at the observer O of amplitude $\frac{A}{r_1}$ and $\frac{A}{r_2}$ respectively, then the acoustic pressure at O is given by

$$p(r,\theta,t) = \frac{A}{r_1}\cos\omega(t - r_1/c) - \frac{A}{r_2}\cos\omega(t - r_2/c) \qquad (10)$$

Note that the retarded times are used indicating that the pressure at the observer location measured at time was generated at the origin at earlier or retarded times $(t - r_1/c)$ and $(t - r_2/c)$, respectively for r>>L, equation (10) can be approximated to produce the following expression for dipole sound field:

$$p(r,\theta,t) = \frac{2A}{r} \sin \omega (t - r/c) \sin\left(\frac{\omega L \cos\theta}{2c}\right) \qquad (11)$$

It is clear from this equation that unlike the sound field of a single monopole which was constant at a given distance r in any direction, now the amplitude of the signal can vary anywhere between zero and 2A/r depending upon the value of $\left(\frac{\omega L \cos\theta}{2c}\right)$

Clearly, the final amplitude at the observer location (r,θ) depends upon whether the sources are interfering constructively or destructively. However, when the two monopole sources are very close together such that

$$\omega L/c << 1 \qquad (12)$$

the same term in equation (11) can be replaced by its argument so that

$$p(r,\theta,t) = \frac{A}{r}\left(\frac{\omega L \cos\theta}{c}\right) \sin \omega (t - r/c) \qquad (13)$$

The pressure amplitude now shows an angular dependence, being zero at $\theta = 90°$ and rising to a maximum at $\theta = 0°$. This is because now at $\theta = 90°$, the retarded time differences for both antiphase monopole sources are identical and as such the radiation from the two antiphase monopole sources reaches the observer at the same time and adds destructively. As the angle θ is decreased, the radiation from one source leaves at progressively earlier times compared to that from the other if they are to reach the observer simultaneously. Thus less complete cancellation occurs and a larger signal is measured as the time difference increases.

To simulate a dipole sound source in the laboratory, we thus need two point monopole sound sources operating in antiphase and placed as close as possible. Keeping these requirements in mind, a point dipole sound source, described below, was built and tested.

Construction of a Point Dipole Source

The point dipole consisted of two point monopoles described above. As shown in Figure 9, the two source units were mounted in a housing such that the openings of the two single sources faced each other. The distance between the openings could be varied by operating a hinge-support located near the acoustic drivers. All of the results presented here were obtained with a gap (l) of 0.16 cm (1/16 inch).

Calibration of the Dipole Source

These measurements were made with the dipole unit mounted in the Georgia Tech anechoic chamber as shown in Figure 10. As shown in Figure 11, two microphone arcs, one for azimuthal measurements and another for polar measurements were used. The microphones are for the polar measurements, which is out of view in the photograph of Figure 10, was located directly underneath the point dipole source.

The dipole source was calibrated at selected discrete tones.The frequencies of these tones were 350, 500, 750, 1000, 2000, 3000, 4000, 5000, and 6000 Hertz.

Strictly speaking the phases of the sound at the opening of each of the two monopole sources should have been measured and adjusted so that they were in antiphase Because of the small size of the source opening and difficulty of placing a microphone between the gap, a different approach described below was adopted.

As shown earlier, the dipole should produce a maximum sound pressure level along the line joining the centers of the openings of the two sources, that is at ϕ or $\theta = 0°$ and a minimum perpendicular to it at ϕ or $\theta = 90°$ (see Figure 11). Keeping this requirement in mind, the phase of the electronic signal fed to one of the the acoustic drivers with respect to that of the other was adjusted until a minimum sound pressure level was recorded at the microphone located at $\theta = 90°$. As shown in Figure 12 for a frequency of 350 Hz, a dipole type directivity was indeed obtained in the azimuthal plane. The same was found to be true at other frequencies as seen in Figures 13 and 14 for 500 Hz and 1000 Hz, respectively

In the polar plane, defined earlier in Figure 11, although the trends of noise reduction in moving from $\theta = 0°$ to 90° were similar to those obtained in the azimuthal plane, the width of the directivity lobe was somehow much narrower in the polar plane. This is shown for the frequencies of 350 Hz and 500 Hz in Figures 15 and 16, respectively. The reason for this inconsistency is not quite clear.

SOME APPLICATIONS OF THE POINT MONOPOLE SOURCE

Some applications of the monopole point sound source are summarized below:

Calibration of Acoustic Chambers

It is a common practice to calibrate the performance of anechoic chambers by measuring the sound pressure level reduction as a function of distance. If a point monopole is used as the source of sound then if there are no reflections from the walls of the anechoic chamber, a 6 dB reduction for every doubling of distance will be obtained. Typical results obtained from a test using the point monopole source described here are presented in Figure 17.

Excitation of Instability Waves in Jets

Point monopole sound sources have been used to study the excitation of instability in jet flows [4, 5]. A point source allows a localized section of the jet to be affected by sound. A typical configuration that has produced some very interesting results [4, 5] on the subject of receptivity of jet flows to acoustic excitation is shown in Figure 18.

Sound Propagation in Flows

Point monopole sound source , because of its small size, it is amenable to immersion in flows. Because of its omnidirectionality, it is ideal for studying the effects of convection on sound directivity and on the effect of turbulence on sound absorption. Such point sources have been used by Ahuja et al [1, 2] to study ray paths of sound through a mixing layer, total internal reflection of sound at flow discontinuities, and to verify Snell's law and shear layer corrections applicable to anechoic free-jet facilities.

Confirmation of Theories and Computational Acoustic Codes

Since a point monopole source is the most basic source, a number of theories and computational acoustics codes are based upon the formulation by using point sound sources. For example, the diffraction of sound around a cylinder or an airfoil has been modeled by Khan et al [7] in this fashion. Likewise, any roster of theoretical sound generators includes a multiplicity of point monopole sound sources, for example see Levine [8-11]. These theories and computational codes can be tested by employing the point source (or a suitable combination thereof) described here.

Beam Forming

By a suitable spacing of a number of point monopoles and proper selection of their phases and amplitudes, it is possible to obtain a highly directive sound source [12] or to obtain a given radiation pattern. This is also referred to as acoustic beam forming. The basis of this capability lies in the so called *Huygens' principle* which states that any wave phenomenon can be analyzed by the addition of contributions from some distribution of simple point (monopole) sources, properly selected in phase and amplitude to represent the physical situation.We have been successful in the laboratory in obtaining a well defined lobe by using three point monopoles separated by half of the wavelength, each having equal amplitude, and appropriate phase delays.

Building Higher-Order Point Sources

As already shown, we were able to build a reasonable point dipole source. Likewise other higher order point sources (such as a quadrupole) can be built and used to test out theoretical formulations.

Energy Conversion From Low Frequencies to High Frequencies

The design of the point monopole source described here is particularly amenable to this relatively less known phenomenon of converting low frequency acoustic energy emitted at the acoustic driver location to a high frequency energy at the point source opening. This happens at high amplitude sound inputs from the acoustic driver. As the acoustic waves travel down the inverted conical horn, the intensity of the sound is increased because of a reduction in the duct cross-sectional area. Non-linear propagation takes place and is found to be responsible for converting a low frequency broadband noise to rather high frequency broadband noise. This is particularly useful in the laboratory testing for simulating broadband noise all the way to a frequency of 50 KHz by using acoustic drivers that may be rated to produce flat response only to a frequency of 10 KHz. This phenomenon is further enhanced by appropriate combination of the inverse conical horn convergence angle and the length of the straight tube. Details for this phenomenon are documented in [13].

Educational Tools

Building a point monopole source is quite easy and can be used as a very powerful educational tool in academic institutions.

SOME APPLICATIONS OF THE POINT DIPOLE SOURCE

Almost all of the comments given above for the point monopole source apply to a dipole as well. We have applied our dipole source to excite a jet by more directed acoustic beam generated by this dipole. A typical test configuration is shown in Figure 19.

CONCLUDING COMMENTS

To the author's knowledge, the only other experiments where sound generation phenomena for both monopoles and dipoles were realized in the laboratory are those by Lighthill and Ffowcs Williams [14], but these simulations were in one dimension and were performed in a tank filled with water. These experiments were not so much realizations of the sound-generation phenomena as simulations of them. In these simulations, the sound waves were replaced by ripples in a glass-bottomed tank filled with water to a depth of 5 mm.The dipole in these experiments were simulated by arranging two plungers above the surface of the water and letting them move up and down at the same frequency, and with the same amplitude but 180°out of phase.

We believe that ours is the first detailed calibration of a point sound source which has also been used for a number of advanced applications. We also believe that it is the first experimental simulation of a three dimensional dipole sound source in the laboratory. At the time these experiments were done, miniaturized microphones were not available. These microphones, particularly those based on fiber optics are now commercially available. It is recommended that additional experiments be conducted with the dipole sound source by mounting the miniature microphones at the source openings and monitoring their amplitudes and phases and adjusting them accordingly.

ACKNOWLEDGEMENTS

The author is grateful to a number of his colleagues, particularly Dr. P. D. Dean and W. H. Brown, for the design of the point sound sources.

REFERENCES

1. K. K. Ahuja, B. J. Tester, and H. K. Tanna, "The Free Jet as a Simulator of Forward Velocity Effects on Jet Noise," NASA CR-3056, 1978
2. K. K. Ahuja, H. K. Tanna, and B. J. Tester, "An Experimental Study of Transmission, Reflection, and Scattering of Sound in a Free Jet Flight Simulation Facility and Comparison with Theory," *Journal of Sound and Vibration*, 75, 1981 (Also see AIAA Paper No. 77-1266, 1977)
3. R. H. Burrin and K. K. Ahuja, "High Speed Flight Effects on Noise Propagation," AIAA-87-0013, AIAA 25th Aerospace Sciences Meeting, 1987
4. K. K. Ahuja and C. K. W. Tam,"A Note on the Coupling Between Flow Instabilities and Incident Sound," *Journal of Sound and Vibration*, 83, 1982
5. K. K. Ahuja, "Basic Experimental Study of the Coupling Between Flow Instabilities and Incident Sound," NASA CR-3789, 1984
6. M. Matheus and K. K. Ahuja, "Investigation of an Acoustic Denial System" Paper presented at the Second International Congress on Recent Developments in Air- and Structure-Borne Sound and Vibration, Auburn University, March 1992.
7. M. M. S. Khan, W. H. Brown, and K. K. Ahuja, "Computational Aeroacoustics as Applied to the Diffraction of Sound by Cylindrical Bodies," *AIAA Journal*, Vol. 25, No. 7, 1987, pp 949-956.
8. H. Levine, "On the Output of Acoustical Sources," Stanford University Report JIAA TR -16, 1979.
9. H. Levine, "A Note on Sound Radiation from Distributed Sources," Stanford University Report JIAA TR -25, 1979.
10. H. Levine, "On Source Radiation," Stanford University Report JIAA TR -29, 1980.
11. H. Levine. "On the Power Output of Some Idealized Source Configurations with One or More Characteristic Dimensions," Stanford University Report JIAA TR -46, 1982.
12. Theodor F. Hueter and Richard H. Bolt "Sonics - Techniques for the Use of Sound and Ultrasound in Engineering and Science," John Wiley and Sons, Inc,1955, pp. 59-85.
13. M. Salikuddin and K. K. Ahuja, "A Device to Generate High Frequency Noise from Commercially Available Low Frequency Acoustic Drivers," *Journal of Sound and Vibration*, Vol. 123, No. 2, 1988, pp. 261-280. *(Also appeared as AIAA Paper 87-2688, 1987)*
14 James Lighthill, " Waves in Fluids,"Cambridge University Press, 1990, pp. 41-50.

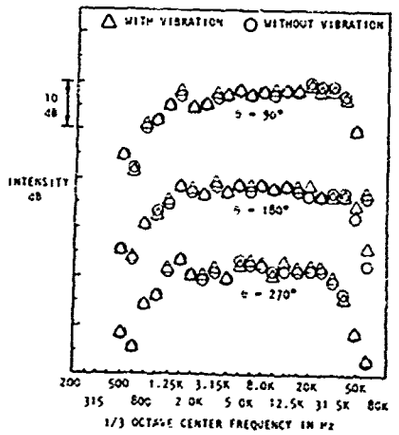

Figure 7 Insignificant effect of monopole source vibration.

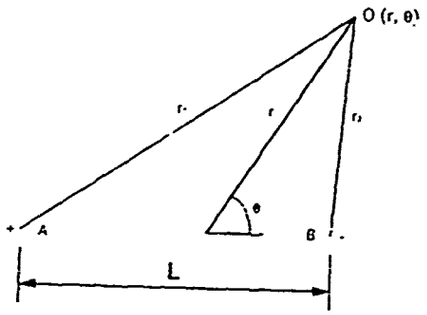

Figure 8 Two antiphase monopole sources of equal amplitude.

Figure 10 Measurement configuration for dipole directivity.

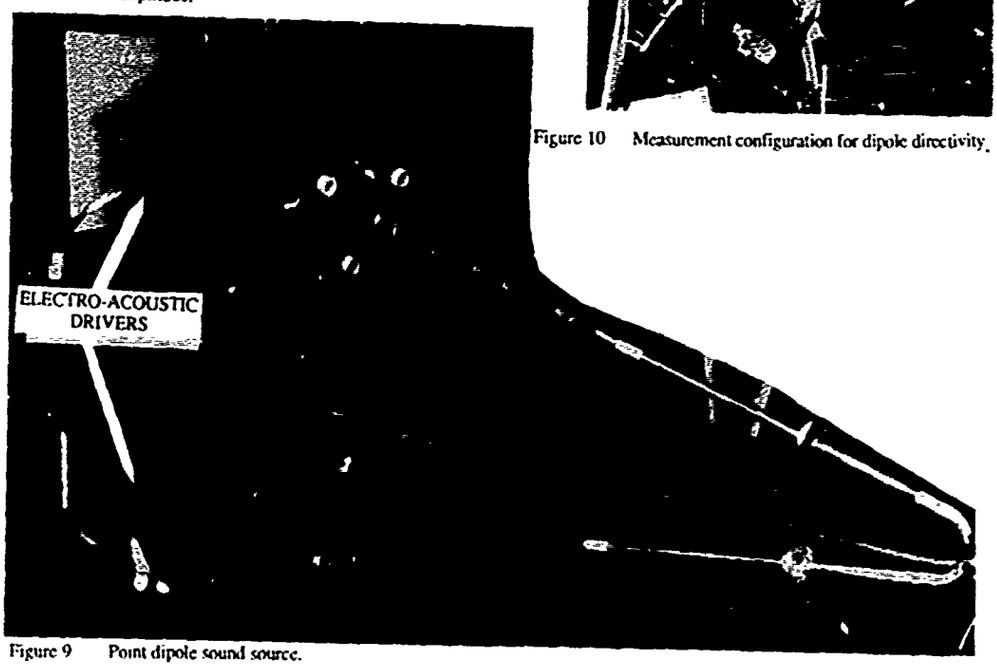

Figure 9 Point dipole sound source.

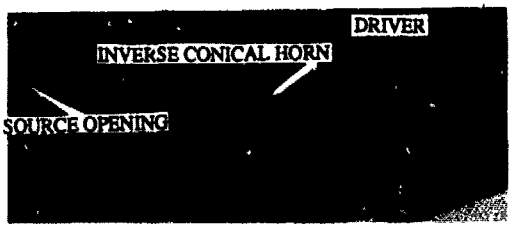

Figure 1 Point monopole source in an anechoic chamber.

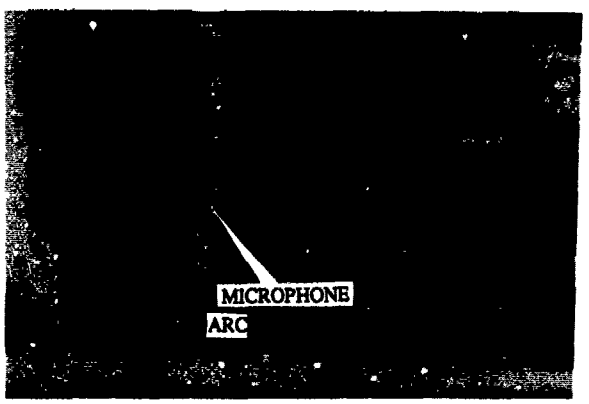

Figure 2 Point monopole sound source equipped with a fairing and mounted in an anechoic chamber. The circular arc used to mount microphones.

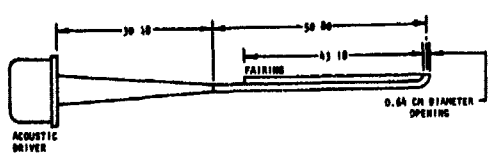

Figure 3 Point monopole sound source dimensions.

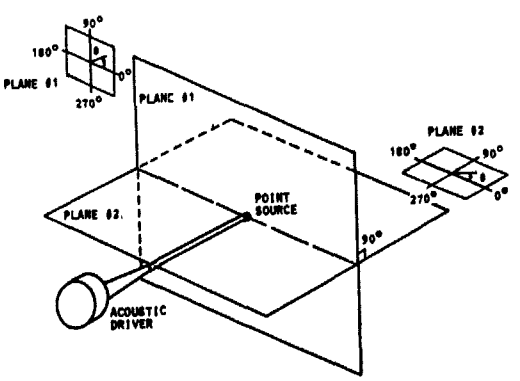

Figure 4 Two planes of calibration of the monopole source.

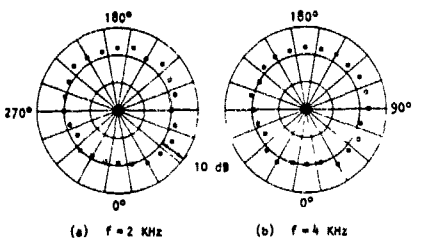

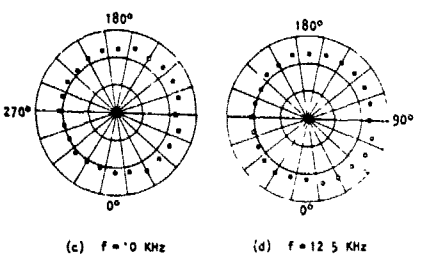

Figure 5 Monopole source directivity in plane #1.

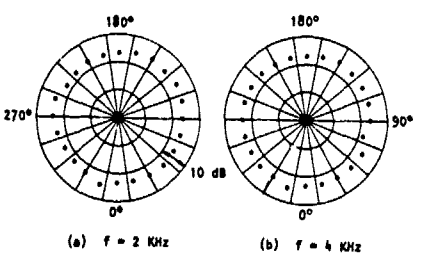

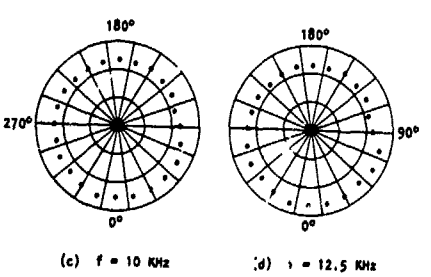

Figure 6 Monopole source directivity in plane #2.

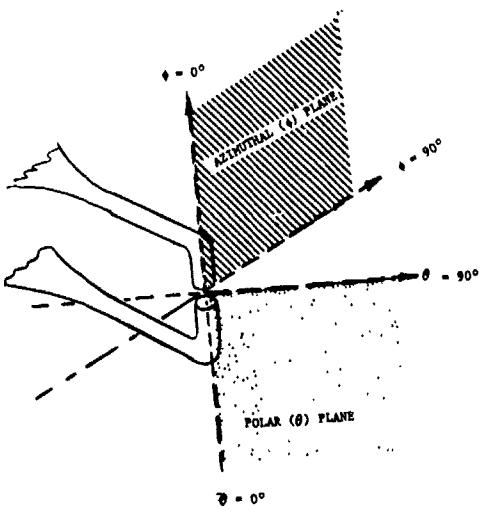

Figure 11 Two planes of calibration of the dipole source.

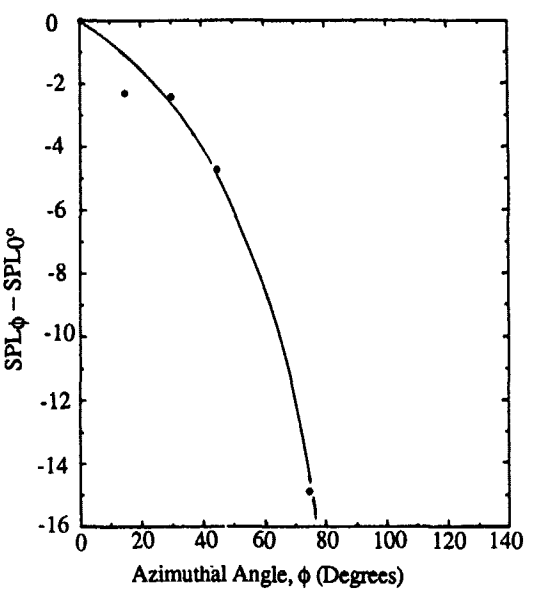

Figure 13 Azimuthal directivity of the dipole source at 500Hz.

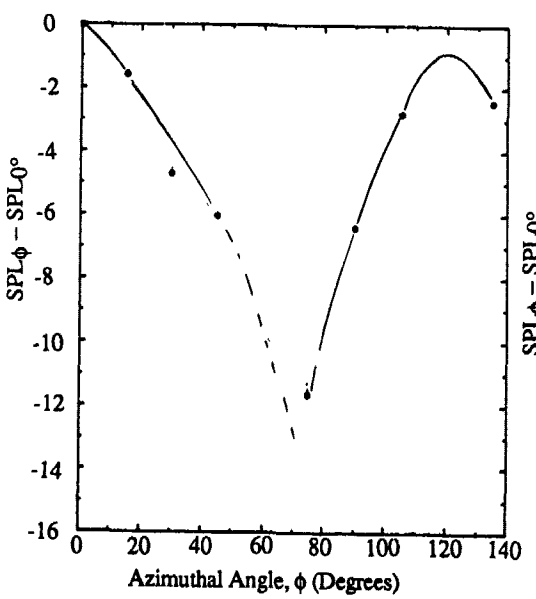

Figure 12 Azimuthal directivity of the dipole source at 350Hz.

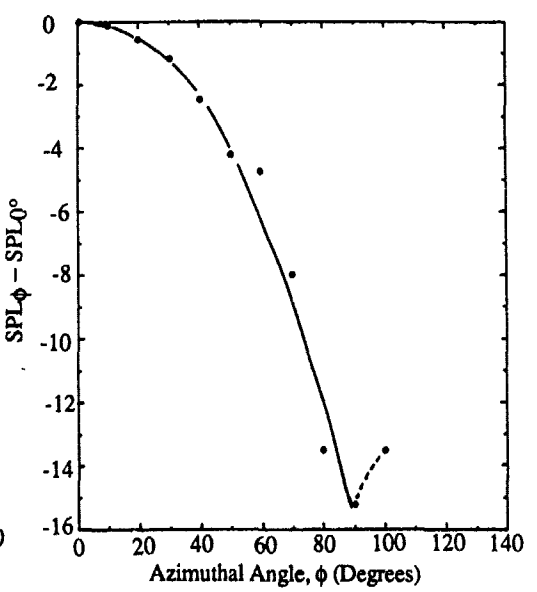

Figure 14 Azimuthal directivity of the dipole source at 1000Hz.

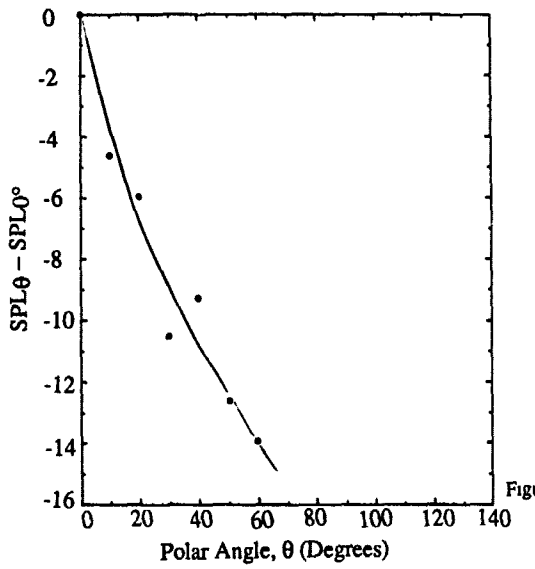

Figure 15 Polar directivity of the dipole source at 350Hz.

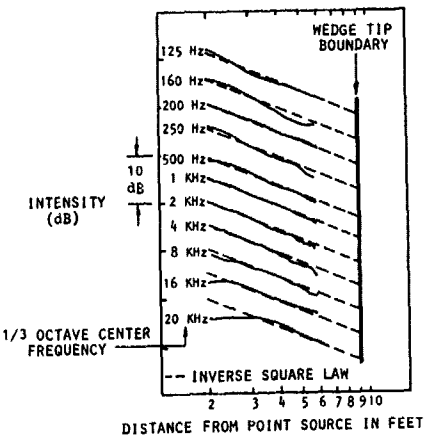

Figure 17 Typical intensity distance plots obtained using a point monopole to calibrate the acoustic characteristics of an anechoic chamber.

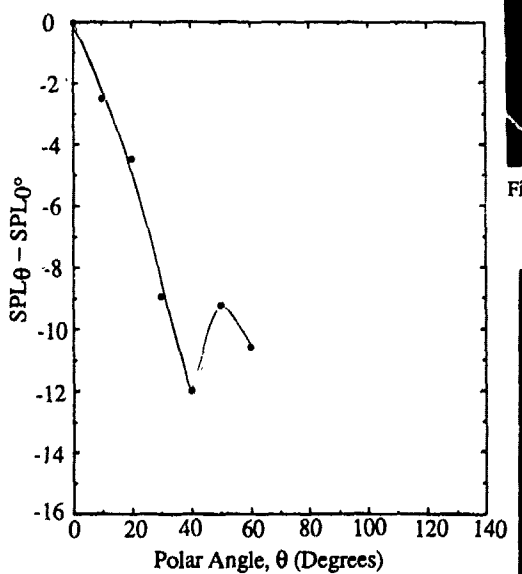

Figure 16 Polar directivity of the dipole source at 500Hz.

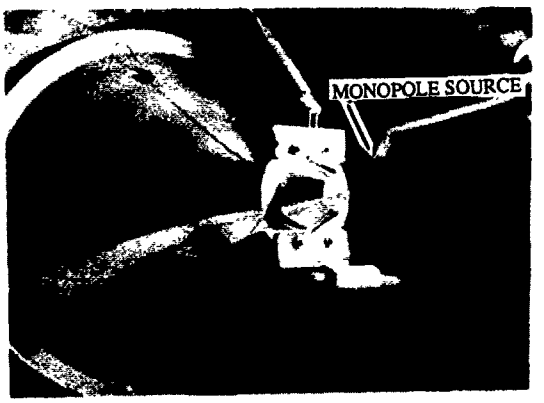

Figure 18 Point monopole source used to study jet receptivity to sound.

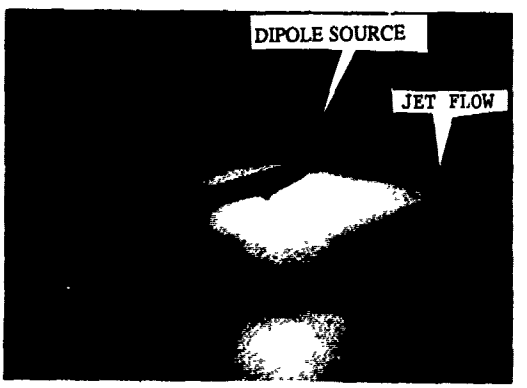

Figure 19 Point dipole source used to study jet receptivity to sound.

SECOND INTERNATIONAL CONGRESS ON
RECENT DEVELOPMENTS IN AIR- AND
STRUCTURE-BORNE SOUND AND VIBRATION
MARCH 4-6, 1992 AUBURN UNIVERSITY, USA

RECONSTRUCTION OF SURFACE ACOUSTIC FIELD FROM MEASUREMENTS OF PRESSURE OVER A LIMITED SURFACE

Angie Sarkissian, Charles F. Gaumond, Earl G. Williams, and Brian H. Houston
Naval Research Laboratory
Washington, D.C. 20375-5000
U.S.A.

ABSTRACT

The acoustic field on the surface of a radiating structure is reconstructed from measurements of pressure made on a limited region of space. The measurement surface is located very close to the structure to enable the reconstruction of evanescent-like modes that decay very rapidly away from the surface. This approach is different from conformal holography in that the measurement surface spans only a small region of space. The boundary-element method is applied to compute an operator that relates the pressure on the measurement surface to the normal velocity on the structure surface. The operator is inverted by applying singular value decomposition. The algorithm is developed for a structure with axial symmetry where the azimuthal dependence is separated to reduce computation time The result is the reconstruction of the acoustic field over a small region on the structure surface located under the measurement surface

INTRODUCTION

The boundary-element method may be applied to compute the acoustic field on the surface of a structure from measurements of pressure made on a surface far from the structure[1,2]. In this case, only limited resolution is attainable. Higher resolution may be attained by moving the measurement surface close to the structure by choosing, for example, a conformal surface to enable the reconstruction of evanescent-like field that decays very rapidly away from the surface[3,4]. In this case the acoustic field everywhere on the surface of the structure may be reconstructed If one is interested in computing the acoustic field on only a limited region on the structure surface, the measurement surface need not span entirely around the structure. A small measurement surface near the surface of interest is sufficient.

From experimental measurements of pressure over a small axisymmetric region near a cylinder, the surface normal velocity is reconstructed with high resolution over a small region under the measurement surface. The results are compared to the surface field computed from a conformal measurement surface spanning the entire structure surface

THEORETICAL FORMULATION

The Boundary-Element Method

Given an axisymmetric structure with surface ∂S, with the coordinate origin placed at its center and the z-axis along its axis of symmetry, with a time harmonic pressure field outside with an $e^{-i\omega t}$

time dependence suppressed. The pressure p_s on its surface is related to the normal velocity v by an integral equation

$$p_s(\vec{r'}) = \frac{1}{2\pi}\int_{\partial S}\Big\{\hat{n}\cdot\nabla\Big[\frac{e^{\imath k|\vec{r}-\vec{r'}|}}{|\vec{r}-\vec{r'}|}\Big]p_s(\vec{r}) - \imath\omega\rho\Big[\frac{e^{\imath k|\vec{r}-\vec{r'}|}}{|\vec{r}-\vec{r'}|}\Big]v(\vec{r})\Big\}dS \tag{1}$$

where

$$v(\vec{r}) = \frac{1}{\imath\omega\rho}\hat{n}\cdot\nabla p(\vec{r}), \tag{2}$$

$k = \omega/c$ is the wavenumber, c is the speed of sound in the fluid, ρ is the density and $\hat{n}$ is the unit normal pointing away from the surface. Separating the ϕ dependence,

$$p(\vec{r}) = \sum_{m=-\infty}^{\infty} p_m(r,\theta)e^{\imath m\phi} \tag{3}$$

$$v(\vec{r}) = \sum_{m=-\infty}^{\infty} v_m(r,\theta)e^{\imath m\phi}, \tag{4}$$

the relationship between surface pressure coefficients $p_m|_s$ and surface normal velocity coefficients v_m may be determined from Eq. (1),

$$\begin{aligned} p_m(r',\theta')|_s = \frac{1}{2\pi}\int_{\partial L}\Big\{ & p_m(r,\theta)\int_0^{2\pi}\hat{n}\cdot\nabla\Big[\frac{e^{\imath k|\vec{r}-\vec{r'}|+\imath m(\phi-\phi')}}{|\vec{r}-\vec{r'}|}\Big]d\phi \\ & - i\omega\rho v_m(\theta)\int_0^{2\pi}\Big[\frac{e^{\imath k|\vec{r}-\vec{r'}|+\imath m(\phi-\phi')}}{|\vec{r}-\vec{r'}|}\Big]d\phi\Big\}r\sin\theta dl, \end{aligned} \tag{5}$$

where ∂L is the meridian of the surface of revolution ∂S.

The boundary-element method[5] is next applied by discretizing the curve ∂L_s. It is divided to N segments of approximately equal length, segment j having length ∂l_j and containing point (r_j,θ_j), N being sufficiently large such that the pressure and velocity coefficients may be approximated to be constant within each segment. The integral equation above may then be approximated by a matrix equation,

$$\sum_{j=1}^{N} A_{ij}^m P_j^{ms} = \sum_{j=1}^{N} B_{ij}^m V_j^m \tag{6}$$

where matrices $\mathbf{A^m}$ and $\mathbf{B^m}$ are defined as

$$A_{ij}^m = \frac{1}{2\pi}\int_{\partial l_j}\int_0^{2\pi}\hat{n}\cdot\nabla\Big[\frac{e^{\imath k|\vec{r}-\vec{r_i}|+\imath m(\phi-\phi_i)}}{|\vec{r}-\vec{r_i}|}\Big]r\sin\theta d\phi dl - \delta_{ij}, \tag{7}$$

$$B_{ij}^m = \frac{i\omega\rho}{2\pi}\int_{\partial l_j}\int_0^{2\pi}\Big[\frac{e^{\imath k|\vec{r}-\vec{r_i}|+\imath m(\phi-\phi_i)}}{|\vec{r}-\vec{r_i}|}\Big]r\sin\theta d\phi dl \tag{8}$$

and column vectors $\mathbf{P^m}$ and $\mathbf{V^m}$ contain pressure and velocity coefficients,

$$P_i^{ms} = p_m(r_i,\theta_i)|_s, \tag{9}$$

$$V_i^m = v_m(r_i,\theta_i)|_s. \tag{10}$$

Matrix $\mathbf{Z^m}$, relating $\mathbf{P^m}$ to $\mathbf{V^m}$,

$$\mathbf{P^{ms}} = \mathbf{Z^m V^m}, \tag{11}$$

may be computed from Eq. (6)

$$\mathbf{Z^m} = [\mathbf{A^m}]^{-1}\mathbf{B^m} \tag{12}$$

An axisymmetric measurement surface $\partial S'$ is next chosen, having meridian $\partial L'$. The curve $\partial L'$ is discretized by dividing it into N' segments, segment i having length $\partial l'_i$ and containing point (r'_i, θ'_i) with pressure coefficient

$$P_i^m = p_m(r'_i, \theta'_i) \tag{13}$$

that is related to surface normal velocity on ∂S

$$P_i^m = \sum_{j=1}^{N} E_{ij}^m V_j^m, \tag{14}$$

where $\mathbf{E^m}$ may be computed from an integral equation similar to Eq. (5)

$$E_{ij}^m = \sum_{k=1}^{N} \frac{1}{4\pi} \int_{\partial s_k} \hat{n} \cdot \nabla \Big[\frac{e^{\imath k|\vec{r}-\vec{r}_i| + \imath m(\phi-\phi_i)}}{|\vec{r}-\vec{r}_i|} \Big] dS \; Z_{kj} - \imath\omega\rho \frac{1}{4\pi} \int_{\partial s_j} \Big[\frac{e^{\imath k|\vec{r}-\vec{r}_i| + \imath m(\phi-\phi_i)}}{|\vec{r}-\vec{r}_i|} \Big] dS, \tag{15}$$

where ∂s_k is the surface of revolution formed by rotating ∂l_k around the z-axis.

The Inverse Problem

From Eq. (14), the determination of the surface normal velocity from measurements of pressure requires the inversion of matrix $\mathbf{E^m}$. Due to the presence of evanescent-like waves that decay rapidly away from the surface, matrix $\mathbf{E^m}$ will be ill-conditioned even if the measurement surface is sufficiently large to surround the structure surface entirely. The conditioning of the matrix becomes worse as the size of the measurement surface decreases.

We next define diagonal matrices $\mathbf{W}$ and $\mathbf{W'}$ to contain integration weights along the structure surface and measurement surface respectively,

$$W_{ij} = \delta_{ij} \Big(2\pi \int_{\partial l_j} r \sin\theta dl \Big)^{\frac{1}{2}} \tag{16}$$

$$W'_{ij} = \delta_{ij} \Big(2\pi \int_{\partial l'_j} r \sin\theta dl \Big)^{\frac{1}{2}}, \tag{17}$$

and apply singular value decomposition[6] to matrix $\mathbf{W'E^mW^{-1}}$, given by

$$\mathbf{F^{m\dagger}(W'E^mW^{-1})G^m = S^m}, \tag{18}$$

where $\mathbf{F^m}$ and $\mathbf{G^m}$ are unitary matrices,

$$\mathbf{F^{m\dagger}F^m = 1} \tag{19}$$

$$\mathbf{G^{m\dagger}G^m = 1} \tag{20}$$

and $\mathbf{S^m}$ is a real, diagonal matrix containing positive singular values in order of decreasing magnitude,

$$S_{ij}^m = \delta_{ij}\sigma_{mi}, \tag{21}$$

$$\sigma_{mi} \geq \sigma_{mi+1} \geq 0. \tag{22}$$

Functions f_l^m defined as

$$f_l^m(r'_i, \theta'_i, \phi) = W'^{-1}_{ii} F_{il}^m e^{\imath m\phi} \tag{23}$$

will form an orthonormal set of functions on the measurement surface

$$\int_{\partial S'} f_l^{m*} f_{l'}^{m'} dS = \delta_{ll'}\delta_{mm'} \tag{24}$$

and functions g_l^m defined as

$$g_l^m(r_1, \theta_1, \phi) = W_{11}^{-1} G_{1l}^m e^{im\phi} \tag{25}$$

will form an orthonormal set of functions on the structure surface

$$\int_{\partial S} g_l^{m*} g_{l'}^{m'} dS = \delta_{ll'} \delta_{mm'}. \tag{26}$$

We assume above that the discretization of the structure surface and measurement surface is sufficiently fine such that functions f_l^m and g_l^m remain approximately constant within each segment.

The measured pressure may be expanded with functions f_l^m

$$p(r, \theta, \phi)|_{\partial S'} = \sum_{m=-M}^{M} \sum_{l=1}^{N'} a_l^m f_l^m(r, \theta, \phi), \tag{27}$$

where M is sufficiently large to insure convergence. The reconstructed normal velocity may be expanded with function g_l^m

$$v(r, \theta, \phi) = \sum_{m=-M}^{M} \sum_{l=1}^{q} b_l^m g_l^m(r, \theta, \phi), \tag{28}$$

where the coefficients a_l^m and b_l^m are related by the singular values

$$b_l^m = \frac{1}{\sigma_{ml}} a_l^m. \tag{29}$$

The coefficients a_l^m may be computed from measurements of pressure,

$$a_l^m = \int_{\partial S'} f_l^{m*} p dS \tag{30}$$

and the velocity coefficients b_l^m may next be determined from Eq. (29). The sum in Eq. (28) must be truncated to keep only q terms in the expansion to remove modes with negligible radiation.

Unlike previous algorithms[1-3], we apply singular value decomposition to matrix $\mathbf{W'E^mW^{-1}}$ rather than matrix $\mathbf{E^m}$. This insures that the orthonormal functions f_l^m and g_l^m have the normalization in Eqs. (24) and (26) and are independent of the discretization of the two surfaces.

IMPLEMENTATION

The algorithm is applied to the radiation problem where from experimental measurements of pressure near the structure surface, the normal velocity is reconstructed. Fig. 1 shows the structure and the location of the driver and measurement points The length of the cylinder is 33.88cm, its radius is 5.54cm. It is excited by a miniature driver located at a distance of 10.80cm from the left end, as shown in the figure

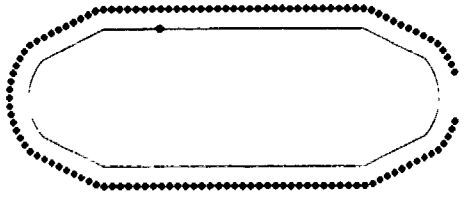

Figure 1 - - Geometry of the cylinder. the location of the measurement points and the location of the driver, shown by the dot

The measurement surface is located at a distance of 1.59cm from the shell. It contains 64 equally spaced points along the length of the structure and 64 equally spaced points in the circumferential direction. At each location, pressure time histories are measured and Fourier transformed to frequency space. The experiment is described in detail in Ref. 7. The description will not be repeated here.

First, we attempt to reconstruct the surface field from only the first 16 leftmost measurement points along the length, i.e. the measurement surface spans one fourth of the surface shown in fig. 1. Although the algorithm reconstructs the field at all points on the structure surface, we would expect the reconstruction to be valid only in the area beneath the measurement surface.

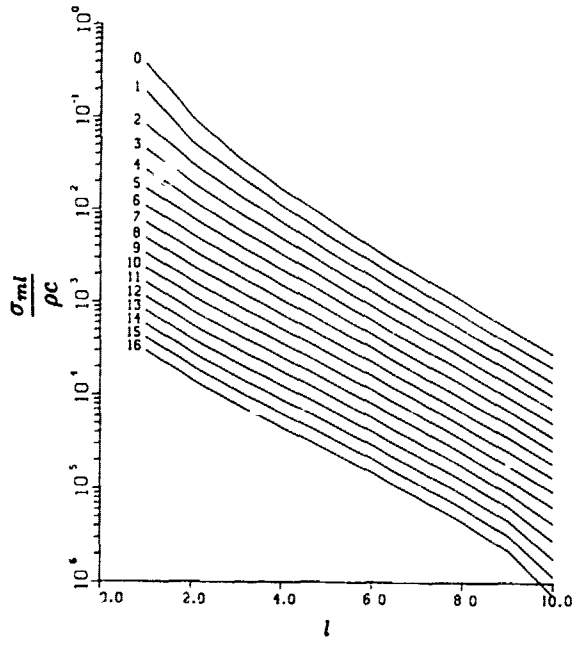

Figure 2 - - $\sigma_{ml}/\rho c$ versus index l. The value of m is given at the left end of each curve.

Fig. 2 shows the singular values at a frequency of 2.23kHz The dimensionless quantity $\sigma_{ml}/\rho c$ is plotted as a function of index l for $0 \leq m \leq 16$. If the measurement surface had been located in the farfield, there would be a sharp drop in the curves separating the radiating modes from the evanescent-like modes. Fig. 2 shows no such drop because the evanescent-like modes are present in the nearfield.

Figs. 3 and 4 show the functions g_l^m along the arclength of the structure at the same frequency with $m = 0$ and 5 and $l = 1, .., 5$ The real and the imaginary parts of g_l^m are shown. It can be seen that the functions are non-zero mainly in the region at the left end under the measurement surface The imaginary parts of functions g_l^m decrease with increasing index l. This corresponds to the decreasing singular value σ_{ml} at higher values of l shown in fig. 2.

Fig. 5(a) shows the reconstructed normal velocity field from the leftmost 16 axial measurement points, at the same frequency of 2.23kHz Fig. 5(b) shows the reconstructed field from the next 16 measurement points and 5(c) shows the reconstructed field from points 33 through 48. The surface field reconstructed from the entire measurement surface is shown in fig 5(d). It can be seen that in

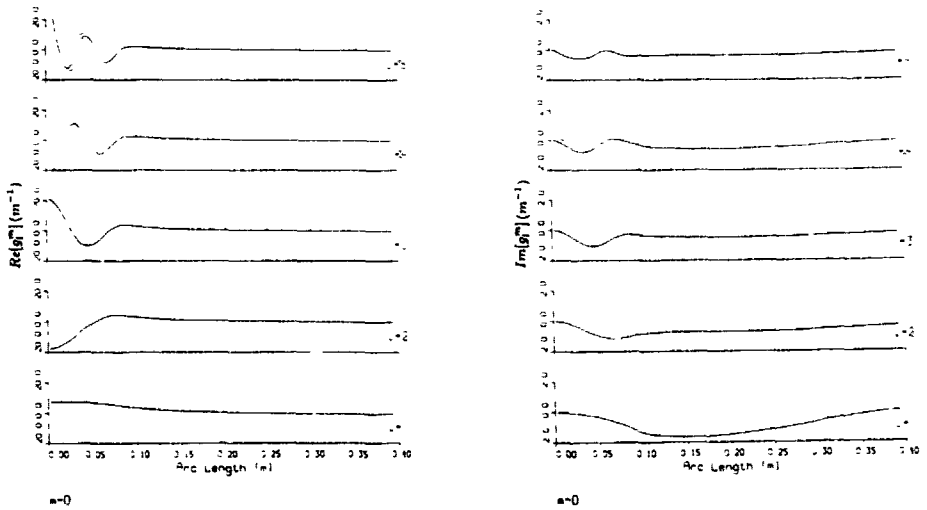

Figure 3 - - Real and Imaginary parts of g_l^m as a function of arclength for $m = 0, l = 1..5$

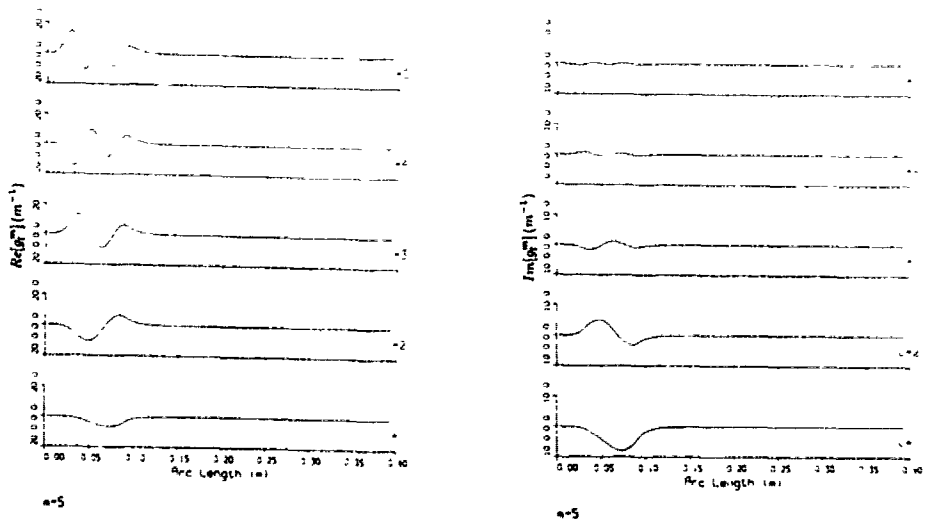

Figure 4 - - Real and Imaginary parts of g_l^m as a function of arclength for $m = 5, l = 1..5$

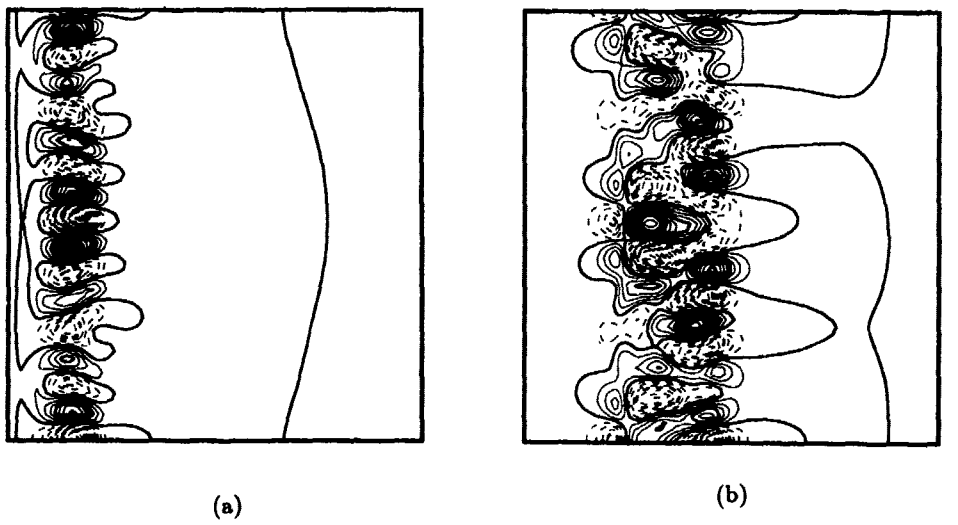

(a) (b)

(c) (d)

Figure 5 - - Reconstructed velocity contours from (a) the leftmost 16 axial measurement points, (b) measurement points 17 through 32, (c) measurement points 33 through 48 and (d) the entire measurement surface. The horizontal axis represents arclength, the vertical axis represents angle ϕ. Solid lines indicate positive values, dashed lines indicate negative values. Velocity is normalized by force giving contour interval of $2\text{x}10^{-3}$s/kg.

each case the reconstruction is accomplished beneath the measurement surface alone, the field values approach zero in the region far from the measurement surface.

CONCLUSION

We have shown how the normal velocity on the surface of a radiating, finite object can be reconstructed from samples of the pressure field taken over a limited area on a nearby surface. This method uses the boundary element method to generate a numerical Neumann Green's function from the Helmholtz integral equation, Eq. 5. This step requires the use of the shape of the whole radiator The singular value decomposition is then used to invert the direct Neumann radiation problem, Eq. 14. By limiting the number of singular values used in the reconstruction, the instability caused by the ill - conditioned inverse problem is overcome.

The operation of this method has been demonstrated with the case of a finite cylinder, shown in Fig. 1, excited by a point driver at 2.23 kHz. The reconstruction shown in Fig 5(a) is generated by data taken over the left endcap. This reconstruction is faithful to the complete reconstruction, shown in Fig. 5(d), over the portion surface which lies under the measurement surface. Over the reconstruction surface which does not lie under the measurement area, the reconstruction is small. In this area the reconstruction is less determined by the data. This behavior is characteristic of the singular value decomposition.

In conclusion this technique is useful for reconstructing the normal surface velocity on the surface of a known, finite radiator from data taken over an area which covers only the area of interest on the object.

REFERENCES

[1] W. A. Veronesi, and J. D. Maynard, "Digital Holographic Reconstruction of Sources with Arbitrarily Shaped Surfaces," J. Acoust Soc. Am. **85**, 588-598 (1989).

[2] G. T. Kim, and B. H. Lee, "3-D Sound Source Reproduction Using the Helmholtz Integral Equation," J. Sound Vib. **136**, 245-261(1990).

[3] G. Borgiotti, A. Sarkissian, E. Williams, and L. Schuetz, "Conformal Generalized Near-field Acoustic Holography for Axisymmetric Geometries," J. Acoust. Soc. Am. **88**, 199-209(1990).

[4] A. Sarkissian, "Near-field Acoustic Holography for an Axisymmetric Geometry· A New Formulation," J. Acoust. Soc. Am. **88**, 961-966(1990).

[5] G. Chertock, "Sound Radiation from Vibrating Surfaces," J. Acoust. Soc. Am. **36**, 1305-1313(1964).

[6] K. E. Atkinson, *An Introduction to Numerical Analysis* (Wiley, New York, 1978), pp.408-410

[7] E. G. Williams, B. H. Houston, and J. A. Bucaro, "Broadband nearfield acoustical holography for vibrating cylinders," J. Acoust. Soc Am. **86**, 674-679 (1989).

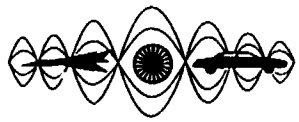

SECOND INTERNATIONAL CONGRESS ON
RECENT DEVELOPMENTS IN AIR- AND
STRUCTURE-BORNE SOUND AND VIBRATION
MARCH 4-6, 1992 AUBURN UNIVERSITY USA

SCATTERING OF SOUND BY STRONG TURBULENCE AND CONDITIONS OF CHERENKOV RADIATION

Vadim.I.Pavlov, Oleg.A.Kharin
Department of Acoustics
Faculty of Physics
Moscow State University
119899 Moscow
USSR.

ABSTRACT

The equation for the mean acoustic field has been obtained for random turbulent media using the Green's function approach. The correlation function $b(x)=\langle u_i u_j \rangle$ was described by the Karman distribution with the index $n = 2 \simeq 11/6$. Applying the Bourret's approximation, the exact expression for the mass operator $Z(q)$ has been calculated analytically. The frequency dependence of the scattering coefficient of the mean field has been derived. The conditions of Cherenkov radiation are analized.

INTRODUCTION

The problems associated with the emission [1-3] and propagation acoustic waves in turbulent media [4,5] occupy a key position in acoustics. It is sufficiently to refer, for example, to the acoustic radiation detection problem (project DUMAND) [6]. In this program the acoustic emission arisen by a particle beams in the turbulent stratum of the Ocean is registered. In this conditions the generation of patches of turbulence has marked effect on diminishing acoustic propagation underwater.

The theory of wave propagation and emission in random media has received contributions from various branches of physics: acoustics, optics, atmospheric physics, etc.

One can point out that a variety of mathematical methods have been employed in studies of present phenomena in random media [4,5].

The analysis of propagation through turbulence and wave emission in inhomogeneous media is better performed in a multiple scattering regime. In the present work we use a Green's function method that permits, in principle, any effects of multiple scattering to be take into account.

The purpose of the present paper is to examine the acoustic wave excitation in inhomogeneous (turbulent) media by a fast moving objects, and to derive an exact expression for the Green's function in the framework of turbulence model proposed.

GOVERNING EQUATIONS

Let us write down the complete set of hydrodynamic equations, together with the equation of state of the liquid:

$$\frac{d\mathbf{V}}{dt} = -\frac{1}{\rho}\nabla p, \qquad \frac{d\rho}{dt} = -\rho\, div\, \mathbf{V}, \qquad \frac{d\ln\rho}{dt} = \frac{p}{c^2\rho}\frac{d\ln p}{dt} - q.$$

where $\mathbf{V}$ is the velocity of the liquid, p is pressure, ρ is density. The quantity q is the power density of thermal sources due to absorption in the liquid, for example, of electromagnetic radiation. The operator $\frac{d}{dt}$ is the material derivation in time. Final-

ly, c is the speed of sound.

We will assume that the acoustic disturbances caused by a sources (for example, ρ) is forced on background of the turbulent motion in medium. We suppose also that the frequencies of the turbulent velocity pulsations are small in comparison with the characteristic acoustic frequencies. We assume as well that in the region in question the values of the hydrodynamic (not associated with density perturbations) velocities $\mathbf{U}$ is considerably higher then the acoustic one $\mathbf{S}$, i.e. $\mathbf{V} = \mathbf{U} + \mathbf{S}$, where $div\ \mathbf{U} = 0$.

After calculations, the basic set of equations can be reduced to the governing equation for the Fourier component of the pressure variations in the linear approximation:

$$\Delta p + k^2 p = \frac{i\omega}{c^2} q - \hat{L}p, \tag{1}$$

where $k = \omega/c$ denotes the wave number, Δ is the Laplace's operator, the operator $\hat{L}$ is defined by the relation:

$$\hat{L}p = \frac{2}{i\omega} (\nabla \cdot (\mathbf{U} \cdot \nabla)\nabla)p.$$

The equation (1) is basic for the problem under consideration.

MEAN FIELD ACCOMPANIED SOURCE

Let now $p = \langle p \rangle + p'$, where $\langle \ldots \rangle$ denotes the operator of a statistical average. Applying this operation to (1), one obtains the equation:

$$\Delta \langle p \rangle + k^2 \langle p \rangle = \frac{i\omega}{c^2} q - \langle \hat{L}p' \rangle \tag{2}$$

and the equation for the fluctuating component of p':

$$\Delta p' + k^2 p' = - \hat{L}\langle p \rangle - \left\{ \hat{L}p' - \langle \hat{L}p' \rangle \right\}. \tag{3}$$

In the Bourret's approximation [7], only the first term $-\hat{L}\langle p \rangle$ of equation (3) is taken, and following expression

$$p' = - \int d\mathbf{X}_1 \, G_0(\mathbf{X}-\mathbf{X}_1) \, \hat{L} \, \langle p(\mathbf{X}_1) \rangle \tag{4}$$

is introduced in (3).

The function $G_0(\mathbf{X},\mathbf{X}_1)$ is the free Green's function, that obeys the equation

$$\Delta G_0 + k^2 G_0 = \delta^{(3)}(\mathbf{X}-\mathbf{X}_1).$$

where $\delta^{(3)}(\mathbf{X})$ is the Dirac delta function.

Inserting the expression (4) into eq. (2) the equation for mean field $\langle p \rangle$ accompanied source can be obtained:

$$\Delta \langle p \rangle + k^2 \langle p \rangle - \int d\mathbf{X}_1 \, \langle \hat{L} G_0(\mathbf{X}-\mathbf{X}_1) \hat{L}_1 \rangle \langle p(\mathbf{X}_1) \rangle = \frac{i\omega}{c^2} Q. \tag{5}$$

COMPLETE GREEN'S FUNCTION

Let the positions of the source and the receiver be fixed by the vector $\mathbf{X}_0$ and $\mathbf{X}$ respectively. The Green's function $G(\mathbf{X},\mathbf{X}_0)$ describes the acoustic field (pressure p) at the point $\mathbf{X}$. Thus, in the present paper the complete Green's function $G(\mathbf{X},\mathbf{X}_0)$ obeys the following equation (see eq. (5)):

$$(\Delta + k^2)G(\mathbf{X}-\mathbf{X}_0) + \frac{4}{c^2R^2}\theta_i\theta_j\int d\mathbf{X}'\,\theta_l G_0(\mathbf{X}-\mathbf{X}')\,\theta'_l\left\{b_{kl}(\mathbf{X}-\mathbf{X}')\theta'_i\theta'_j G(\mathbf{X}'-\mathbf{X}_0)\right\} =$$

$$= \delta^{(3)}(\mathbf{X}-\mathbf{X}_0).$$

The correlation function of the fluctuations $\mathbf{V}(\mathbf{X})$ is defined by the formulae:

$$b_{kl}(\mathbf{X}_1-\mathbf{X}_2) = \langle v_k(\mathbf{X}_1)v_l(\mathbf{X}_2)\rangle.$$

If the inhomogeneities are caused by turbulence, the correlation between medium velocity inhomogeneities is described by the expression:

$$b_{ik}(\mathbf{X}) = \int\frac{d\mathbf{p}}{(2\pi)^3}\,b(p)\left(\delta_{ik} - \frac{p_i p_k}{p^2}\right)\exp(i\mathbf{p}\cdot\mathbf{X}).$$

Via Fourier transformation, one obtains the Dyson's equation

$$\left[k^2 - q^2 + \Sigma(q)\right]G(q) = 1,$$

in which the mass operator $\Sigma(q)$ has the form:

$$\Sigma(q) = \frac{4}{(2\pi)^3c^2}\,\frac{1}{k^2}\int d\mathbf{p}\,\frac{(\mathbf{p}\cdot\mathbf{q})^2}{p^2 - k^2 - i0}\,b(|\mathbf{q}-\mathbf{p}|)\,\frac{p^2q^2 - (\mathbf{p}\cdot\mathbf{q})^2}{(\mathbf{p}-\mathbf{q})^2}. \quad (6)$$

The term $-i0$ determines the rule of pole moving in the free Green's function.

Introducing a spherical coordinate system, after integrating over the angles, formulae (6) takes the form:

$$\Sigma(q) = \frac{q^4}{\pi^2c^2k^2}\int_0^\infty dp\,\frac{p^6}{p^2 - k^2 - i0}\int_{-1}^{1}dt\;b\left(\sqrt{q^2 + p^2 - 2pqt}\right)\,\frac{t^2(1-t^2)}{p^2 + q^2 - 2pqt}.$$

CHOICE OF THE CONCRETE MODEL

It can be considered exact calculations only with the concrete form of the function $b(p)$.

For turbulent random media, the correlation function $b(p)$ is described then by the Kolmogorov-Obuchov formulae. On spectral decomposition of the fluctuation correlation function, one obtains $b(p) \sim p^{-11/3}$, which is valid in the range $L^{-1} < p < l^{-1}$. The parameter l is the minimum inhomogeneity size (e.g., for air $l \simeq 10^{-3} \div 10^{-2}$m), L is the typical flow dimension ($L \sim 100$m).

In the present paper we take into consideration the modeling function $b(p) = b_0(p_0^2 + p^2)^{-3}$, which is not far from Kolmogorov's distribution in the range $p \gg p_0 \sim L^{-1}$. One can see that with the exception of the pole of second order at the points $\pm ip_0$, $b(p)$ is an analytical function for all complex values p.

Thus, the mass operator $\Sigma(q)$ is given by the following expression

$$\Sigma(q) = \frac{bq^4}{\pi^2c^2k^2}\int_0^\infty dp\,\frac{p^6}{p^2 - k^2 - i0}\cdot$$

$$\int_0^1 \frac{dt}{(p_0^2 + q^2 + p^2 - 2pqt)^2}\,\frac{t^2(1-t^2)}{(p^2 + q^2 - 2pqt)}. \quad (7)$$

In the fin, one can write the following equation, which determines the poles of the function G_k.

$$k^2 - q^2 + Z(q) = 0.$$

In zero order approximation we have $q = k$. The first order approximation is given by the condition: $Z(q) \approx Z(k)$. Using the expansion $(1 + \Omega)^n \simeq 1 + n\Omega$, one obtains the expression for the effective wave number of the mean acoustic field:

$$k_{eff} \simeq k + \frac{Re\ Z(k)}{2k} + i\,\frac{Im\ Z(k)}{2k}.$$

In this case, the scattering coefficient representing attenuation of the intensity of the mean acoustic field is given by the formulae:

$$\delta = 2\ Im\ k_{eff} = \frac{1}{k}\ Im\ Z(k).$$

PARTICULAR CASE: CONDITION OF CHERENKOV RADIATION

Let us consider a source uniformly moving in the turbulent medium with velocity $V = cM$ (M is Mach number) along Z axis. Cherenkov radiation may arise if

$$k^2 - q_\perp^2 - q_z^2 + Z\left(\sqrt{q_z^2 + q_\perp^2}\right) = 0 \text{ and } q_z = k/M. \qquad (9)$$

Here we analyze the case when $p_0 \to 0$. Then exp.(8) can be simplified:

$$Z(q) \approx \frac{ibk}{32\pi p_0^2 \omega^2}\left[k^2 + q^2\right]^2. \qquad (10)$$

Existence of propagating waves is determined by the following condition $Re\ q_\perp \geq Im\ q_\perp$. Hence, making use exps.(9),(10), critical Mach number from which Cherenkov radiation channel is open can be written as

$$M_{cr}^2 = \frac{2^{3/2}\varepsilon}{\sqrt{(1 + 64\varepsilon^2)^{1/2}} - 2^{3/2}\varepsilon}, \qquad \varepsilon = \frac{bk}{32\pi p_0^2 c^2}.$$

If the turbulence level ε is equal to $\sqrt{3/4}$ then $M_{cr} \to \infty$. It means that Cherenkov radiation channel is closed at sufficiently high ε for all Mach numbers (fig.2).

PHYSICAL INTERPRETATION OF THE APPROXIMATION

The consideration used for studying an acoustic wave propagation in turbulent media by means Green's function method can be given a simple interpretation using Feynman's diagrams. It can be shown [5,7] that if the Bourret's approximation is used, an infinite subsequence of the perturbation theory series is summed up. Analytically this corresponds to condition for fine grained random media only.

CONCLUSIONS

The consideration presented using a Green's function method permits the attenuation of the mean acoustic field to be calculated. Employing the Karman formulae for turbulence, the scattering produced by the turbulence has been calculated in the Bourret's approximation. In the limit $k \gg p_0$, the analysis gives a simple expression for the δ. The conditions when Cherenkov radiation exists are found.

The integral can be calculated by the method of contour integration. Integrating preliminary over variable t one obtains

$$Z(q) = \frac{b}{64p_0^4\pi^2\omega^2 q}\int_C dp\left\{\frac{1}{p-k-i0}+\frac{1}{p+k+i0}\right\}\left[\Phi_1(p)+\Phi_2(p)+\Pi(p)\right].$$

where:

$$\Phi_1(p) = -\left\{\ln\left[\frac{p-i\sqrt{q^2+p_0^2}}{p-q-ip_0}\right]\Pi_1(p)+\ln\left[\frac{p-iq}{p-q}\right]\Pi_2(p)\right\}$$

$$\Phi_2(p) = -\left\{\ln\left[\frac{p+i\sqrt{q^2+p_0^2}}{p-q+ip_0}\right]\Pi_1(p)+\ln\left[\frac{p+iq}{p-q}\right]\Pi_2(p)\right\}$$

Polynoms $\Pi(p)$, $\Pi_1(p)$, $\Pi_2(p)$ have the following expressions:

$$\Pi(p) = 2p_0^2pq\left[5p^2p_0^2+3pqp_0^2+5q^2p_0^2+3p_0+p^4+2p^3q+2p^2q^2+2pq^3+q^4\right].$$

$$\Pi_1(p) = \left[p_0^2+p^2+q^2\right]\cdot$$

$$\left[(p^2-q^2)^2p_0^2+5(p^2+q^2)p_0^4+3p_0^6-p^6+p^4q^2+p^2q^4-q^6\right].$$

$$\Pi_2(p) = (p^4-q^4)^2.$$

Contour C consists of the real axis $(-\infty,+\infty)$ and arc of infinite radius (Fig.1). The function $\Phi_1(p)$ is analytical one for all complex p except two cuts along lines $\gamma_1 = \left[i\sqrt{q^2+p_0^2}, q+ip_0\right]$ and $\gamma_2 = (iq, q+i0)$. On the other hand, the function $\Phi_2(p)$ is analytical one except two cuts along lines $\gamma_3 = (iq, q+i0)$ and $\gamma_4 = \left[i\sqrt{q^2+p_0^2}, q+ip_0\right]$. The poles η_+ at the point $k+i0$ and η_- at the point $-k-i0$ are originated by free Green's function. Since the singularities of terms in integral (8) lie within different sides from real axis it is possible to deform the contour C into infinite radius circle C_0 and circles around poles η_+ and η_-.

Thus, after calculations, one can obtain that

$$Z(q) = \frac{b}{48p_0^3\pi\omega^2}\cdot\left[-3k^6+3k^4p_0^2-3k^4q^2+15k^2p_0^4+10k^2p_0^2q^2+3k^2q^4+9p_0^6+21p_0^4q^2+15p_0^2q^4+3q^6\right]+$$

$$+\frac{ib}{32p_0^4\pi\omega^2 q}\left\{\ln\left[\frac{k-q+ip_0}{k+q+ip_0}\right]\Pi_1(k)+\ln\left[\frac{k-q}{k+q}\right]\Pi_2(k)\right\}+ \qquad (8)$$

$$+\frac{ib}{16p_0^2\pi\omega^2}\left[5k^3p_0^2+5kq^2p_0^2+3kp_0^4+k^5+2k^3q^2+kq^4\right].$$

The consideration presented, using a Green's function method, are of interest as far as the expression obtained for $Z(p)$ is exact.

Critical to be calculation is the choice of the correlation function model for the turbulence.

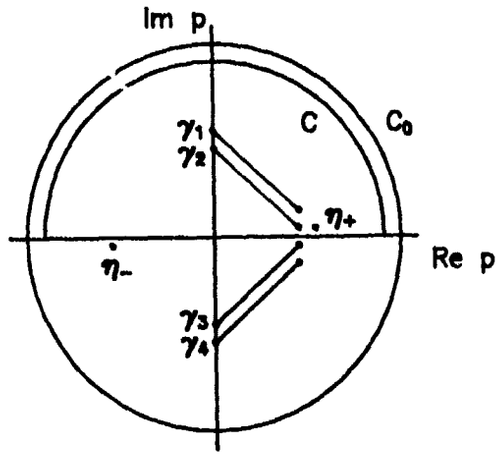

Fig.1. Integrating contours and singularities of functions under integral on the complex plane.

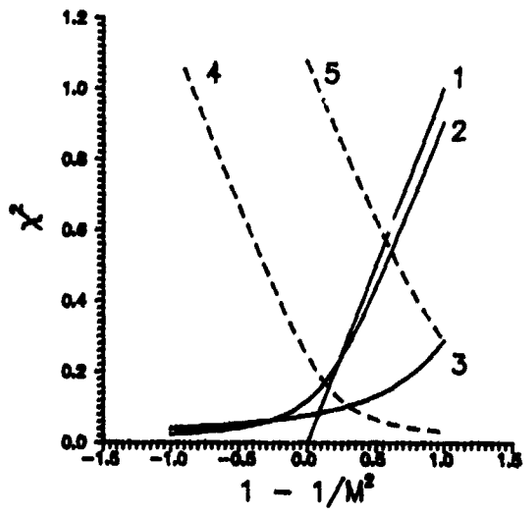

Fig.2. Conditions of Cherenkov radiation existence. Line 1 corresponds to $\varepsilon \to 0$, curves 2,3 describe $(Re\ q_\perp)^2$ and these 4,5 describe $(Im\ q_\perp)^2$ for $\varepsilon = 0.1$ and $\varepsilon = \sqrt{3/4}$ respectively.

REFERENCES

1. V.I.Pavlov, A.I.Sukhorukov. Sov. Phys. - Usp. (USA), vol.28, no.9, p.584-802. (1985).
2. V.I.Pavlov, O.A.Kharin. Sov. Phys. - JETP. (USA), vol.71, no.2, p.211-216. (1990).
3. V.I.Pavlov, O.A.Kharin, S.V.Kholodova. Sov. Phys. - Acoust. (USA), vol.37, no.5. (1991)
4. A.Ishimaru. Wave Propagation and Scattering in Random Media. Academic press. New York. 1978.
5. V.I.Tatarskii. The effects of the Turbulent Atmosphere on Wave Propagation. Edited by J.W.Strobehn.
6. V.S.Berezinskii, B.T.Zatsepin. Sov. Phys. - Usp. (USA), vol.20, no.5, pp.361-380. (1977).
7. S.M.Rytov, V.I.Tatarskii et al. Principles of statistical radiophysics. - Berlin etc. 1989.

SECOND INTERNATIONAL CONGRESS ON
RECENT DEVELOPMENTS IN AIR- AND
STRUCTURE-BORNE SOUND AND VIBRATION
MARCH 4-6, 1992 AUBURN UNIVERSITY, USA

IDENTIFICATION OF UNDERWATER TARGETS BY MEANS OF RESONANCES IN THEIR SONAR ECHOES

Guillermo C. Gaunaurd
Naval Surface Warfare Center (R 12)
Research Department, White Oak Lab.
Silver Spring, MD 20903-5000 U.S.A.

Hans C. Strifors
National Defense Research
Establishment (FOA 2)
S 17290, Sundbyberg, Sweden

ABSTRACT

We deal with the inverse scattering problem of extracting physical information (i.e., composition, shape, size,...) from the echoes returned by an underwater elastic target insonified by a pulsed active sonar. The target identification is to be accomplished in the intermediate (or resonance) spectral region of the body. In this region, low or high frequency approximations do not hold, and either exact solutions or new approximations are required. We have achieved some success by exploiting the presence of certain resonance features that manifest themselves in the resonance or middle region of the backscattering cross section (i.e.,BSCS) of submerged elastic targets. The extraction of resonance features from echoes has been extensively documented (i.e., see references 7 and 8). The main interest over the years has been the isolation and extraction of the resonance features, theoretically, experimentally and computationally, by means of either time or pulsed interrogating waveforms. In the present work we will show examples of how these resonances can be used to characterize the scatterer by identifying its physical characteristics. It also serves to expose this community to the method, and to give a more detailed list of pertinent and updated references to prospective users. This is a generic method, and thus, it applies to any active return from any sensor.

INTRODUCTION

The scattering of sound waves by elastic, fluid filled shells in water was first studied by Goodman and Stern [1] followed by Hickling and his co workers [2,3]. Since then, numerous works have addressed the many aspects of the general interaction of incident sound waves with submerged structures [4-34]. Parallel efforts have studied analogous problems dealing with electromagnetic waves interacting with conducting and dielectric bodies [35,36,41,42,44,45]. Most of this body of work has addressed the direct scattering problem, in which the goal is to predict the acoustic or electromagnetic fields scattered by the structure, once the incident wave and the structure itself have been both specified. There has been an immense volume of work along this line. There are low and high frequency approximations that can be used at both ends of the spectrum that introduce substantial simplifications in the analysis. Some of these simplifications have been taken advantage of in some of the above works [i.e.,13], but in the middle or intermediate or resonance region of the BSCS of any target, such simplifications no longer hold, and either novel approximations or exact solutions must be used. In these resonance scattering situations we have established that within each echo there is always a smooth, mostly geometry dependent background that interacts with a superimposed, discrete, set of prty, mostly composition-dependent, resonance features. The resonance [illegible] of any penetrable scatterer seems to extend above the Rayleigh

region with no apparent upper bound. All the above situations have been analyzed for many geometrical shapes (i.e., flat, multilayered, spherical, cylindrical, spheroidal, etc.,), and for various fluid or solid target compositions, in cases in which the scatterers are embedded in either fluid (i.e., gaseous /liquid) or solid (i.e., elastic / viscoelastic), boundless, host media. Longitudinal and transverse c.w. incidences have also been considered, as well as cases in which the targets are inside bounded host fluid media. There are several hundred of these cases, and they have all been catalogued and updated in recent reviews [4,5,7,8]. There is still considerable interest in the direct scattering problem, partly mainly in cases in which the scattering structure is not only non separable, but quite complicated with internal ribs, loads, and/or attached masses, and having, in general, weird non canonical shapes. The principal difficulties in these cases are mainly of the computational type since only numerical solutions are possible for them. At present the scientific interest seems to have shifted to the much harder inverse scattering problem, in which the scattering structure is unknown, and one tries to predict its physical characteristics from the known echoes it returns when it is insonified with known waveforms. Even for very simple shaped objects, having very simple internal structure, this has turned out to be quite a formidable problem, often lacking unique solutions. Some advances have been reported [i.e., 34,36,40,41 43,45,46,49,50] using both c.w. [36] and pulsed [31] incident waveforms. The concepts of impulse sonar [32] and impulse radar [41] have emerged as strong candidates to achieve many target ID goals. The required short pulses must be very energetic and, therefore, some advances in the development of sources are required. The "identification" has to be based on a clearly understood method in order to be implemented either manually or automatically. In the following pages we will use an example from under water acoustics in which the physical characteristics of a simple structure are all remotely identified, "in situ", from the examination of the echoes it returns. The structure could be insonified by either a c.w. waveform (i.e., the steady state case), or by a long or short sonar pulse (i.e., the transient case). We study the limitations of these alternatives and repeat that the example given is merely an illustration of a powerful methodology that applies to considerably more general cases, in the areas of both sonar and radar. We first review the theory for the chosen problem, and then give its solution in both the steady-state and transient cases. We conclude by examining the resonances in the return, in order to extract from them the physical parameters of the scatterer that identify it.

THEORETICAL BACKGROUND

A thin, elastic, spherical shell of outer (inner) radius a (or b) is air filled and submerged in water. It is then insonified at its South pole (defined by the spherical coordinate $\Theta=\pi$) by a plane sound wave emerging from a distant source. Its normalized BSCS is given by [9,10]

$$\frac{\sigma}{\pi a^2} = |f_\infty(\pi,x)|^2 = \left|\sum f_n(\pi,x)\right|^2 = \left|\frac{2}{ix}\sum (-1)^n (2n+1)\, A_n(x)\right|^2, \qquad (1)$$

where $f_\infty(\pi,x)$ is the form function in the backscattering direction $\Theta=\pi$. We define $x=k_1 a$, where $k_1=\omega/c_1$ is the wavenumber. The circular frequency is ω and c_1 is the sound speed in the outer medium (i.e., #1, the water). The shell is medium # 2, and the inner fluid (i.e., the air) is medium # 3. See Fig. 1. For each value of n, the "normal mode" coefficients $A_n(x)$ are all determined from the six boundary conditions available at the two interfaces r=a,b, as ratios of two 6x6 determinants in the form

$$A_n(x) \equiv \begin{vmatrix} A_1^* & d_{12} & d_{13} & d_{14} & d_{15} & 0 \\ A_2^* & d_{22} & d_{23} & d_{24} & d_{25} & 0 \\ 0 & d_{32} & d_{33} & d_{34} & d_{35} & 0 \\ 0 & d_{42} & d_{43} & d_{44} & d_{45} & d_{46} \\ 0 & d_{52} & d_{53} & d_{54} & d_{55} & d_{56} \\ 0 & d_{62} & d_{63} & d_{64} & d_{65} & 0 \end{vmatrix} \Big/ \begin{vmatrix} d_{11} & d_{12} & d_{13} & d_{14} & d_{15} & 0 \\ d_{21} & d_{22} & d_{23} & d_{24} & d_{25} & 0 \\ 0 & d_{32} & d_{33} & d_{34} & d_{35} & 0 \\ 0 & d_{42} & d_{43} & d_{44} & d_{45} & d_{46} \\ 0 & d_{52} & d_{53} & d_{54} & d_{55} & d_{56} \\ 0 & d_{62} & d_{63} & d_{64} & d_{65} & 0 \end{vmatrix}, \qquad (2)$$

where the 30 non zero elements d_{ij} and A_1^*, A_2^* have all been listed elsewhere

[10,14]. All the elements of the determinants depend directly or indirectly on x. The partial waves $f_n(\pi r, x)$ for n= 0,1,2,... defined above in Eq. (1), are the "normal-modes" that make up the form-function $f_\infty(\pi r, x)$. The above formulation is exact, since the shell motions are described by the (exact) three-dimensional equations of dynamic elasticity [21], rather than by any approximate "shell theory". The above solution was programmed for numerical evaluation in quite broad frequency bands. The backscattered pressure as a function of time is [23],

$$p_{sc}(r,\theta=\pi,t) = \frac{a}{2r}\exp[i(k_1 r-\omega t)]\,[\frac{2}{a}f_\infty(\theta=\pi,x)], \qquad (3)$$

which completes the steady state solution for c.w. incidences. To generalize to the case of a transient (i.e., pulsed) incidence, we introduce the additional canonical variable $\tau=c_1 t/a$. If $g(\tau)$ is the incident pulse and G(x) is its spectrum (i.e., its Fourier transform), then the scattered pressure pulse can be eventually expressed as, [26,28,32,42]

$$p_{sc}(\pi,\tau)\,r = \frac{1}{2\pi}\int_{-\infty}^{+\infty} G(x)\,f_\infty(\pi,x)\,e^{-ix(\tau-r/a)}\,dx. \qquad (4)$$

Hence, in the non dimensional time domain τ , the backscattered pulse is (proportional to) the inverse Fourier transform of the (steady-state) form function given in Eq.(1), weighted by the spectrum G(x) of the incident pulse, $g(\tau)$. Equation (4) resembles a filter type of integral [51]. The corresponding result in radar has been known since the sixties [24]. If the incident pulse is a (Dirac) delta function (i.e., if $g(\tau)=\delta(\tau)$), then G(x)=1, and the (unit) impulse response of the scatterer is then defined by

$$h(\tau) = p_{sc}(\pi,\tau)\,r = \frac{1}{2\pi}\int_{-\infty}^{+\infty} f_\infty(\pi,x)\,e^{-ix(\tau-r/a)}\,dx. \qquad (5)$$

as the inverse Fourier transform of the form function in the (retarded) variable τ r/a. Equation (4) can also be expressed in convolution form as

$$p_{sc}(\pi,\tau)\,r = g(\tau) * h(\tau) = \int_{-\infty}^{+\infty} g(\tau')\,h(\tau-\tau')\,d\tau', \qquad (6)$$

which means that the time domain structural response to any pulse $g(\tau)$ is the convolution of the impulse response of the structure $h(\tau)$, and that pulse. In the frequency domain x, the normal mode expression for the (modulus of the) backscattered pressure spectrum is:

$$\left|p_{sc}(\pi,x)\,r\right| = \left|G(x)\,f_\infty(\pi,x)\right|. \qquad (7)$$

which is the quantity which was inverted in Eq.(4). These linear systems concepts which are here applied to scattering problems were first given in the sixties [24], and only hold within certain limitations. The above completes all the required theory for the steady-state and transient cases.

NUMERICAL RESULTS

Let the shell be made of steel of parameters: ρ_2= 7.8 g/cm, c_{d_2}= 5.88 km/s, and c_{s_2}=3.14 km/s, and let it have relative thickness: h/a=2.5%. The external water has: ρ_1=1 g/cm^3, and c_1=1.5 km/s, while the internal air has: ρ_3=0.0012 g/cm^3 and c_3=0.34 km/s. The magnitude of the form function of this structure, as computed by Eqs. (1) and (2), is given in Fig. 2 (top), within the frequency band: $0 \leq x \leq 50$. This spectrum has numerous peaks and dips, broad "bumps" and narrow "spikes" which have all been analyzed before [14,23,26] in a series of papers. They are all caused by the various types of Lamb waves, water borne, curvature, and creeping waves circumnaigating the shell either in the water, or in the shell's metal. The broad "bump" centered at x = 45 is due to the "coincidence" effect [15], and the large amplitude spike near x=2 is caused by a peculiar curvature wave induced there. The unit impulse response of the shell, as computed by Eq. (5), is given in Fig.(2) (bottom). This completes the steady-state analysis.

We proceed to investigate the conventional use of long pulses to interrogate targets. Consider a c.w.-pulse (i.e., a sinusoidal wave-train of finite length) of the form: $g(\tau) = \sin x_o \tau$, defined in the time interval: $0 \leq \tau \leq \tau^*$, where x_o is the carrier frequency. If $x_o = 19.92$ units and N=100 cycles, then this pulse has duration: $\tau^* = 2\pi N/x_o \cong 31.5$. The modulus of the complex-valued spectrum of this pulse, $|G(x)|$, is displayed in Fig. 3 (top). Since this pulse is so long (i.e., 100 cycles), its spectrum is very narrow and resembles a spike at $x = x_o = 19.92$. This carrier frequency was chosen because it corresponds to one of the target resonances, as we see in Fig. 2 (top). This "dip" in the form-function corresponds to the n = 5 resonance caused by the s_o Lamb wave in the shell. This is the "generalized" zeroeth order symmetric Lamb wave in the shell, accounting for its curvature and fluid loaded condition on both surfaces. The backscattered pressure pulse returned by the shell is computed from Eq. (4), and is displayed in Fig. 4 in the time domain. This response shows its characteristic double transient behavior [22,30], which resembles the impulse response of a "notch" filter [51], and displays the double exponential decay after each transient that we have encountered before in many investigations [30,31,25]. The two transient peaks in the return shown in Fig.4 are here separated by 31.5 units, which is the incident pulse duration. The "ringing" of the excited resonance at x_o, occurs after the second transient in the "free vibration" region of the response. The spectrum of the backscattered pulse in Fig. 3 is obtained from Eq.(7), and it is shown in Fig. 3 (bottom). This spectrum exhibits some low amplitude contributions caused by the multipole nature of the low frequency resonance spike at x=2 [13]. This concludes the transient analysis for long pulses.

Consider a short, amplitude modulated pulse: $g(\tau) = \sin x_o \tau \sin x_1 \tau$, with carrier frequency $x_o = 35$, envelope frequency $x_1 = 7$, and N =2.5 cycles. This pulse has duration $\tau^* = 2\pi N/x_o \cong 0.45$, as can be seen in Fig. 5 (top). Its spectrum $|G(x)|$ is quite broad as can be noted in Fig. 6 (top). Its spectral width covers the interval: $0.4x \leq x \leq 1.5x$, which represents a 53% relative bandwidth. Since this exceeds 10%, this is an ultra wideband (UWB) system. Conventional sonar has bandwidth of order 2%, or less. This is an "impulse sonar" [41,32]. The backscattered pulse is computed from Eq. (4), and the result is shown in Fig. 5 (bottom). The spectrum of the backscattered pulse is found from Eq.(7), and it is shown in Fig.6 (bottom). We note that the response to a short pulse consists of a series of wave packets (cf., Fig.5 (bottom)). Many of the resonance features of the form function in Fig.2 (top) are present in Fig. 6 (bottom) within the band: $15 \leq x \leq 50$, which is the bandwidth of the incident pulse (cf., Fig. 6 (top)). The wave packets seen in Fig. 5 (bottom) appear so clearly delineated because the carrier frequency $x_o = 35$ was chosen as one of the shell's "generalized" a_o Lamb resonances (cf., Fig.2, (top)). Therefore, interrogating the structure with a short pulse activated many target resonances that can be recovered in the spectrum of the backscattered pulse, and then used for target ID. An experimental technique was developed to implement this method (originally for the c.w. incidences and the long pulses) that has been repeatedly described elsewhere [22,30,31,41]. Many of these experiments were carried out at the N.S.W.C., in the mid eighties. Its extension to short pulse incidences is also available [10]. This concludes the portion of the transient analysis of the incident short pulses that is possible to include here.

TARGET IDENTIFICATION

Once as broad a portion of the form function as possible has been extracted from the backscattered pressure pulse, as shown above, one can use the resonance features in it to determine specific target characteristics. For example, the low frequency, large amplitude, resonance feature present at $x \cong 2$, fixes the target size. Hence, if the incident frequency is known to be, say, 6.1 kHz, then $x = 2$ fixes the outer shell diameter at 2a = 1 m. The "coincidence bump" centered at $x = 15$ (see Fig.2 (top)) fixes the shell thickness. The "coincidence" condition [19, (9)], $c_{ph} = c_1$, is usually satisfied whenever $C x_c (h/a) \sim 1$, where x_c is the coincidence frequency and C is a material dependent parameter that for steel has the value $C = 0.9$. Since x_c is seen to be 45 in Fig.2 (top), then the above condition yields: $h/a \cong 2.5\%$, which was indeed the value used to generate Fig. 2 (top).

With the outer radius and the relative thickness known, the shell thickness comes out to be h = 12.5 cm. The shell composition can be found from the separation between the initial resonance "dips" in Fig. 2 (top). That spacing is read there to be: $\Delta x_1 = 3.6$. That spacing was also shown to be given by: $\Delta x_1 = c^{pl}/c_1$ where c^{pl} is the "plate velocity" of "plate waves" in the metal [52]. In terms of E, ν, and ρ, the plate velocity is: $(E/[\rho(1-\nu^2)])^{\frac{1}{2}}$.

In the present case it comes out to be: $c^{pl} = 1.5 \times 3.6 = 5.4$ km/s, which can be used as a rough classifier of the steel. Thus, the size, thickness, and elastic composition of the shell have been found from the information in Fig.6 (bottom). It remains to determine the composition of the filler-fluid. This can be done in various ways. One is from the spectrograms in the context we have used them in this work [11,8]. Another is by analysis of the large quasi-thickness resonance feature that appears at high frequencies when the critical frequency of the s_1 -Lamb wave is activated [14]. Still a third method is by measuring the shell's reflection coefficient "V". This is the amount by which the specularly reflected portion of the time return is reduced in amplitude relative to that of the incident wave. It turns out that the impedance $\rho_3 c_3$ of the filler-fluid is given by the relation: $\rho_3 c_3 = \rho_1 c_1 [(1-V)/(1+V)]$, at the critical frequency of the s_1 Lamb wave. Hence, the impedance so found serves as a filler classifier from tables of impedances of fluids. We note that at this frequency, the formula for $\rho_3 c_3$ is the same as that for a plane boundary separating the two dissimilar fluids #1 and #3, as if the shell were not present. We conclude by repeating that this type of analysis is generic and that it applies to many shapes, compositions, incident waves, and types of sensors.

CONCLUSIONS

We presented a resonance scattering analysis of the echoes that are returned by a submerged shell when insonified by (active) sonar pings. Our approach is equally effective in the frequency and time domains. We have compared the returned echoes produced by various types of incidences. We examined the pulse duration effects, and showed that long pulses of narrow spectra, excite resonances in the (BSCS of) targets, only when the carrier frequency of the incident pulse coincides with (any) one of the target's resonances. A good way to approximate the (steady state) results obtained with c.w incidences is to use long interrogating pulses (of any shape). On the other hand, short pulses have broad spectra and can excite many target resonances provided they are energetic enough (i.e., impulse sonar). We also showed an example of how all the physical characteristics of the shell and its filler can be extracted from the resonance features in its BSCS, once a good portion of the cross section has been isolated and pulled out from the returned echo, in a band as broad as possible, by the use of short incident pulses. This generic method applies to many types of sensors.

REFERENCES

1. R. Goodman and R. Stern, J. Acoust. Soc. Am., 34, 338-341, (1962).
2. R. Hickling, J. Acoust. Soc. Amer., 36, 1124-1137, (1964).
3. R. Hickling and R. Means, J. Acoust. Soc. Am., 44, 1246-1257, (1968).
4. G. Gaunaurd, "Resonance acoustic scattering from underwater elastic bodies", in Proceed. of (Second) IUTAM Symposium on: Elastic Wave Propagation, North Holland Publishers, 335-347, (Invited, 1988).
5. D. Brill & G. Gaunaurd, "Resonance theory of elastic waves ultrasonically scattered from an elastic sphere", J.Acoust. Soc. Am., 81, 1-21, (1987).
6. D. Brill et al., "The influence of natural resonances on scattering and radiation processes", J. Wash. Acad. of Sciences 72, 55-65, (1987).
7. G. Gaunaurd, "Elastic and acoustic resonance wave scattering", Applied Mechanics Reviews 42, 143-192, (1989, and references therein).
8. G. Gaunaurd and M. Werby, "Acoustic resonance scattering by submerged elastic shells", Applied Mechanics Reviews 43, 171-208, (1990).
9. G. Gaunaurd & A. Kalnins, "Resonances in the sonar cross sections of coated spherical shells", Intern.J. Solids & Struct., 18, 1083-1102, (1982).
10. V. Ayres et al.,"The effects of Lamb waves on the sonar cross sections of elastic spherical shells", Intern.J.Solids & Struc., 23, 937-946, (1987).

11. C. Gaunaurd & D. Brill, "Acoustic spectrograms and complex frequency poles of a resonantly excited tube", J.Acoust.Soc.Am.,75,1680-1693, (1984).
12. G. Gaunaurd, "Techniques for sonar target identification", IEEE Trans. Ocean. Engr., OE-12, 419-423, (Special issue on "Scattering"), (1987).
13. H. Strifors and G. Gaunaurd, "Multipole character of the large-amplitude, low frequency resonances in the sonar echoes of submerged spherical shells", Intern. J. Solids & Structures 29, 121-130, (1992).
14. G. Gaunaurd and M. Werby, "Lamb and creeping waves around submerged spherical shells resonantly excited by sound scattering", J. Acoust. Soc. Amer., 82, 2021-2033, (1987); also, ibid, "Resonance response of submerged, acoustically excited, thick and thin shells", J.Acoust. Soc. Am., 77, 2081-2093, (1985); also, ibid, "Lamb and creeping waves around submerged spherical shells resonantly excited by sound scattering II.Further applications", J. Acoust. Soc. Am., 89, 1656 1667, (1991); also, ibid, "Similarities between various Lamb waves in submerged spherical shells and Rayleigh waves in elastic spheres and in flat half spaces", J. Acoust. Soc. Am., 89, 2731-2739, (1991); also, ibid, "Sound scattering by resonantly excited, fluid loaded, elastic spherical shells", J.Acoust.Soc.Am., 90, 2536-2550, (1991).
15. M. Junger and D. Feit, Sound, Structures, and their Interaction, MIT Press, Cambridge, MA (1986).
16. I. Viktorov, Rayleigh and Lamb Waves, Plenum Press, New York, (1967).
17. K. Williams and P. Marston, J. Acoust. Soc. Am., 79, 1702-1708, (1986).
18. P. Jackins and G. Gaunaurd, "Resonance acoustic scattering from stacks of bonded elastic plates", J. Acoust. Soc. Amer., 80, 1762-1776, (1986).
19. M. C. Junger, "Normal modes of submerged plates and shells", in Fluid-Solid Interaction, Proced., ASME Symp.(J. Greenspon, Ed.), N. York, (1967).
20. L. Brekhovskikh, Waves in Layered Media, Academic, 1st. Edit., (1960).
21. N. Veksler, Information Analysis in Hydroelasticity, Acad. Sciences Estonian S.S.R., Valgus Publishers, Tallinn, (1982, in Russian).
22. Examples of French work on this subject have appeared in the volume: La Diffusion Acoustique, Edited by the "Groupe d'Etudes Sur la Propagation Acoustique (GESPA)", Cedocar Publishers, Paris, France, (1987, in French).
23. G. Gaunaurd and W. Wertman, "Transient acoustic scattering by fluid-loaded elastic shells", Intern. J. Solids & Structures 27, 699 711, (1991).
24. E. Kennaugh and D. Moffatt, Proceed., IEEE, 53, 893-901, (1965).
25. V. K. Nigul, Echo Signals from Elastic Objects, Acad. Sciences Estonian S.S.R., Valgus Publishers, Tallinn, (2 Vols., In Russian, 1974).
26. H. Strifors and G. Gaunaurd, "Transient scattering of sound pulses by underwater viscoelastic bodies", Proceed., 1st. Pan American Congress of Applied Mechanics (PACAM), Rio de Janeiro, Brazil, 756 760, (1989).
27. M. Talmant et al., J. Acoust. Soc. Amer., 88, 2720-2735, (1990).
28. E. McDaid & G. Gaunaurd, "Signal processing of ideal echoes resonantly scattered by underwater structures", J.Acoust.Soc.Am.,88,2720-2735, (1990).
29. V. Ayres and G. Gaunaurd, "Inverse scattering from an elastic sphere", J. Acoust. Soc. Amer., 82, 1291 1302, (1987).
30. G. Gaunaurd and C.Y. Tsui, "Transient and steady-state target resonance excitation by sound scattering", Applied Acoustics 23, 121-140, (1988).
31. C. Tsui, G. Reid & G. Gaunaurd, "Resonance scattering by elastic cylinders and its experimental verification", J. Acoust. Soc. Am., 80, 382-390, (1986); also, ibid, "Bistatic measurements of target scattering at resonance", J. Acoust. Soc. Amer., 83, 1946-1951, (1988).
32. G. Gaunaurd and H. Strifors, "Transient resonance scattering resulting from the interaction of sound pulses with submerged elastic shells", in Computational Acoustics, IMACS'91, D. Lee et al, Eds., (to appear, 1992).
33. D. Brill et al., "Backscattering of sound pulses by elastic bodies underwater", Appl. Acoustics 33, 87-107, (1991, and references therein).
34. G. Gaunaurd, "Inverse scattering techniques for material characterization", Procced., Ultrasonics International '87, Butterworth Scientific Ltd., Surrey, U.K., 520 525, (1987).
35. G. Gaunaurd et al., "Resonances of dielectrically coated conducting spheres and the inverse scattering problem", J.Appl.Phys., 52,35-43, (1981)
36. G. Gaunaurd et al., "Inverse scattering and the resonances of visco-viscoelastic and electromagnetic systems", in: Wave Propagation in Viscoelastic Media, Pitman Publ., London, F. Mainardi, Ed., 234-257, (1982).
37. M. Werby & G. Gaunaurd, "Transition from soft to rigid behavior in scattering from submerged, elastic shells" Acoust. Lett., 9, 89-93, (1986).

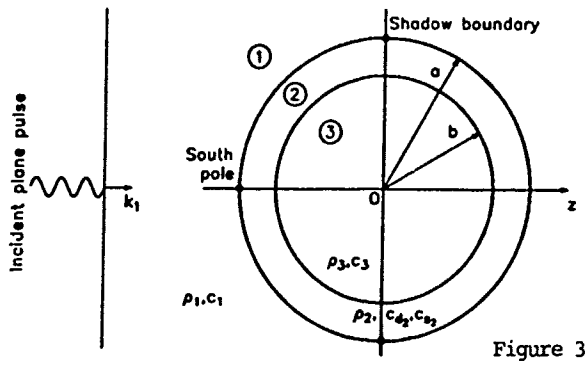

Figure 1. The geometry.

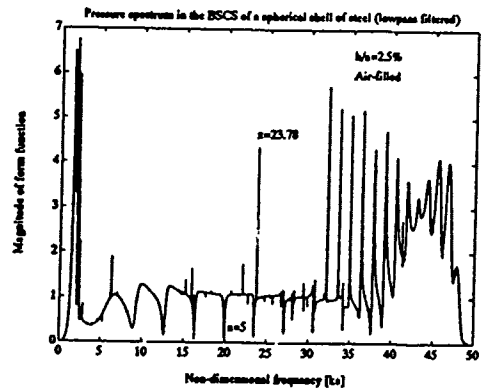

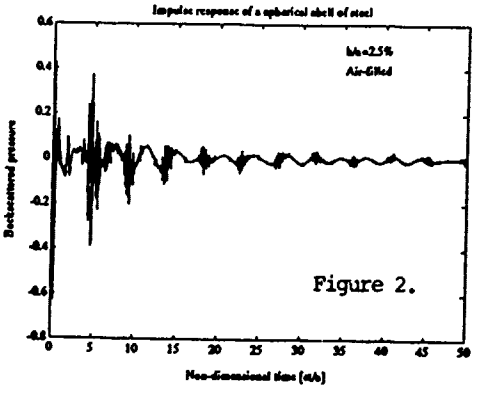

Top: The form-function. Bottom: The Unit impulse response of the shell.

Figure 3. Top: Spectrum of incident pulse. Bottom: Spectrum of the backscattered pulse.

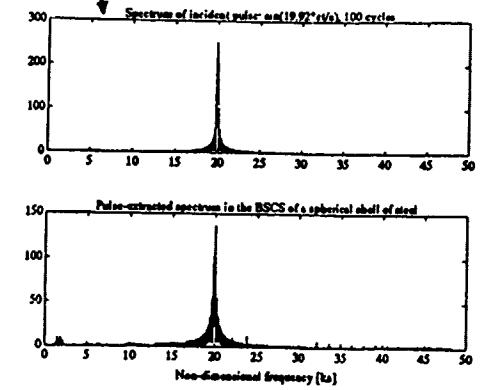

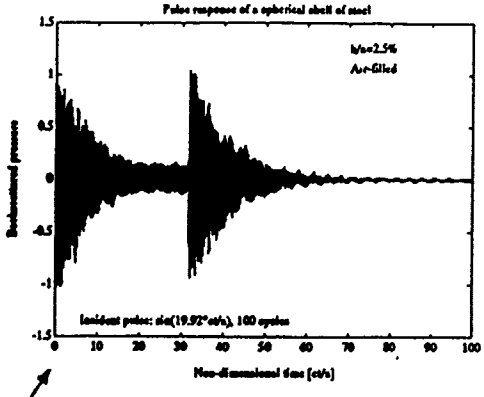

Figure 4. Backscattered pressure pulse when the incident pulse is a long c.w. pulse.

REFERENCES (CONTINUED)

38. R. Wyker & D. Dudley, IEEE J. Ocean. Engr., OE-12, 317-326, (1987).
39. H. Uberall et al., "Acoustic surface wave pulses and the ringing of resonances", J. Acoust. Soc. Amer., 72, 1014-1017, (1982).
40. G. Gaunaurd, "Inverse scattering problems in the acoustic resonance region of an underwater target", Proceed., SPIE Conference on Automatic Object Recognition, Vol. 1471, pp. 130 141, (1991).
41. S. Abrahamsson et al., "Target identification by means of impulse radar", Proceed., SPIE Conference on Automatic Object Recognition, Vol. 1471, pp. 130 141, (1991).
42. G. Gaunaurd et al., "Transient of arbitrary electromagnetic pulses by dielectric targets", J. Electrom. Waves & Applic., 5, 75 92, (1991).

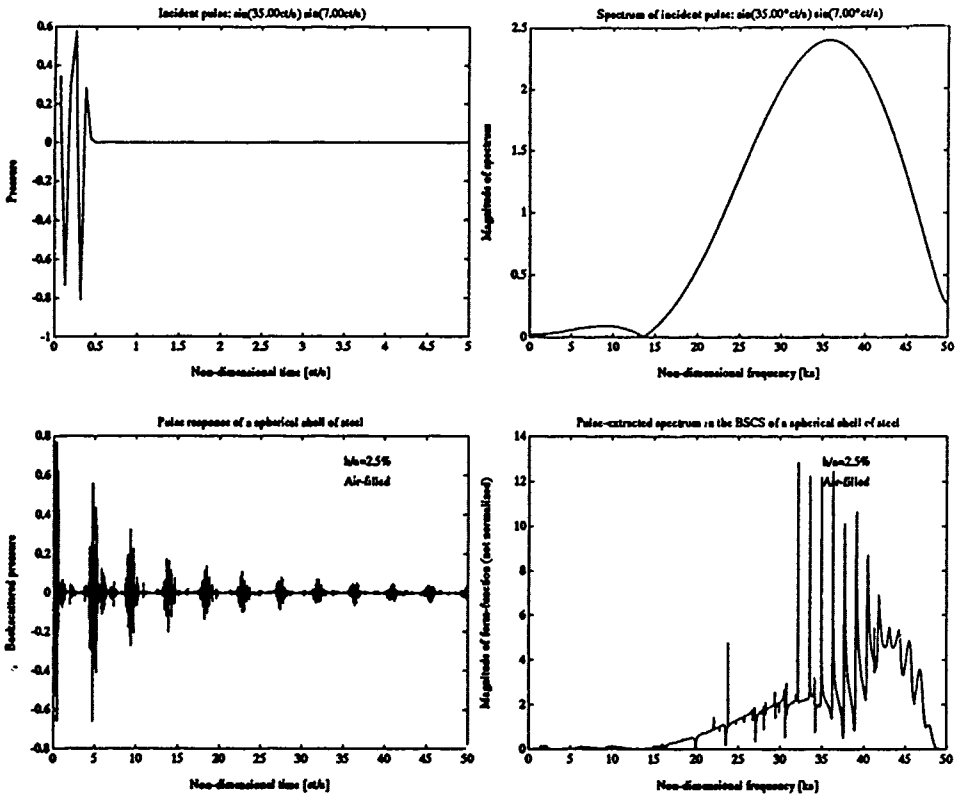

Figure 5. Top: Short incident pulse on shell. Bottom: Corresponding backscattered pulse.

Figure 6. Top:Spectrum of the short incident pulse. Bottom: The backscattered spectrum.

REFERENCES (CONCLUDED)

43. M. Werby and G. Gaunaurd "Critical frequencies for large scale resonance signatures from elastic bodies", Proceed., SPIE Conference on Automatic Object Recognition, Vol. 1471, pp. 2 17, (1991).
44. H. Ikuno & L. Felsen, IEEE Trans.Anten.& Prop.,AP-36,1272-1280, (1988).
45. H. Strifors et al., "Scattering of arbitrary electromagnetic pulses by dielectric spherical targets", Proceedings, URSI Symposium on Electromagnetic Theory, Stockholm, 488-490, (1989).
46. G. Quentin, "Resonance scattering studies in underwater acoustics: The direct and inverse problems", Proceed., IEEE Ultrasonics Symposium, B. McEvoy, Editor, 849-859, (1990). (Lists many references to French works).
47. L. Flax et al., in: Physical Acoustics, Vol. 15, Ch. 3, Academic Press, (1981). (This early review has been updated by references 7 and 8).
48. M. Talmant and G. J. Quentin, J. Applied Physics 63, 1857 1863, (1988).
49. M. Werby and G. Gaunaurd, "Classification of resonances for acoustic scattering at arbitrary incident angles from a submerged spheroidal shell", J. Acoust. Soc. Amer., 82, 1369-1377, (1987).
50. F.A. Sadjadi, Editor, Proceed., SPIE Conference # 1471 on Automatic Object Recognition, SPIE Press, 476 pp., (1991).
51. M. Gardner and J. Barnes, Transients in Linear Systems, J. Wiley & Sons Inc., (2 Vols.), New York, (1942).
52. H. Strifors & G. Gaunaurd, "Differences in the acoustic echoes from submerged elastic shells containing different fluids" (J. Ultrasonics, to be published, 1992).

Note: At about 15 references per page, a comprehensive list would be over 60 pages long. The above list is a bit arbitrary, but representative. For additional recent ones see, for example, refs. 5, 7, 8, 22 and 46, above.

ACKNOWLEDGEMENTS

The authors thank the Independent Research Program Office of their respective Institutions, and the Office of Naval Research for support.

SECOND INTERNATIONAL CONGRESS ON
RECENT DEVELOPMENTS IN AIR- AND
STRUCTURE-BORNE SOUND AND VIBRATION
MARCH 4-6, 1992 AUBURN UNIVERSITY, USA

HIGH-FREQUENCY ELASTIC WAVES EXCITED WITHIN THE STRUCTURE OF A SPHERICAL SHELL BY INCIDENT SOUND IN WATER

Robert Hickling and James F. Ball
National Center for Physical Acoustics
University of Mississippi
Coliseum Drive, University, MS 38677.

ABSTRACT

Previous work has shown the nature of the elastic waves excited within the structure of a spherical shell, by continuous incident sound at low and intermediate frequencies. It was shown that these waves are consistent with thin-shell theory. In this paper the nature of the elastic waves is examined at higher frequencies where there is a departure from thin-shell theory. It is shown, for continuous-wave excitation, that the elastic waves in the shell structure separate into surface waves at the inner and outer surfaces of the shell, particularly at the back of the shell away from the incident sound. At high frequencies, the principal reaction appears to occur on the side of the shell closest to the sound source.

INTRODUCTION

Until recently the elastic response of canonical spherical and cylindrical bodies to incident sound has largely been inferred from the scattered field, even though the elastic response has been available directly from the solution of the scattering problem. With the advent of supercomputers and graphics software it has become easier to compute the elastic behavior directly. In a recent paper on scattering by solid spheres and cylinders [1], it was shown that the elastic response is characterized by rotational waves (i.e. waves whose displacement vector is oriented along lines around a center of rotation), interacting in a manner similar to the meshing of gears. For free or natural modes of vibration, this behavior contrasts with the surface-wave descriptions inferred from the scattered field (i.e. Rayleigh waves and whispering-gallery waves). The fundamentals of the natural modes do indeed tend to Rayleigh waves but only at high frequencies [2]. The harmonics bear no relation to whispering-gallery waves; their elastic behavior involves a significant displacement amplitude at all depths within the solid structure. In the same paper [1] it was shown that individual natural modes can be excited in a solid sphere by continuous sound at the frequency of the mode. In contrast, for a thin spherical shell excited by continuous sound in water, it was shown [3] that individual natural modes apparently cannot be excited because the frequencies of the fundamentals congregate closely together when the shell is thin and radiation damping in the water causes a strong overlap between these fundamentals, making it impossible or certainly very difficult to excite an individual mode.

In the present paper, elastic waves excited in a thin shell are examined at higher frequencies, in the region where thin-shell theory does not apply.

SCATTERING THEORY

It is assumed that a continuous train of plane waves in water is incident on a solid spherical shell of outer radius a and inner radius b. There is a vacuum in the interior of the shell. The spherical shell and the coordinate system used in the analysis are shown in Fig. 1. The incident plane pressure waves are given by

$$p_i = P_o \sum_{n=0}^{\infty} (2n + 1) i^n j_n(kr) P_n(\cos\theta), \tag{1}$$

where the j_n are spherical Bessel functions and the P_n are Legendre polynomials. The scattered sound pressure waves are given by

$$p_s = P_o \sum_{n=0}^{\infty} c_n h_n(kr) P_n(\cos\theta), \tag{2}$$

where the h_n are spherical Hankel functions and the c_n are coefficients determined from the boundary conditions. The time dependence which is not shown in the equations is exp $(-i\omega t)$ where ω is the circular frequency equal to kc, k is the wave number and c is the speed of sound in water. The vibrational displacement vector $\mathbf{u}$ is given by

$$\mathbf{u} = -\nabla\psi + \nabla \times \mathbf{A} \ , \tag{3}$$

where ψ is a scalar quantity representing compressional waves and $\mathbf{A}$ is a vector representing shear waves. Because of axisymmetry

$$u_\phi = 0 \ \text{ and } \mathbf{A} = (0,0,A_\phi) \ , \tag{4}$$

where u_ϕ and A_ϕ are respectively the ϕ components of the displacement vector $\mathbf{u}$ and the vector $\mathbf{A}$. All quantities are independent of the ϕ coordinate. Hence ψ and A_ϕ can be expressed as

$$\psi = \sum_{n=0}^{\infty} \{a_n j_n(k_1 r) + a_n' n_n(k_1 r)\} P_n(\cos\theta) \tag{5}$$

and

$$A_\phi = \sum_{n=0}^{\infty} \{b_n j_n(k_2 r) + b_n' n_n(k_2 r)\} \frac{dP_n(\cos\theta)}{d\theta} \ , \tag{6}$$

where $k_1 = \omega/c_p$ and $k_2 = \omega/c_s$, and c_p is the compressional wave velocity and c_s is the shear wave velocity. It follows that the components of $\mathbf{u}$ in the shell are

$$u_r = -\frac{1}{r} \sum_{n=0}^{\infty} \{a_n k_1 r j_n'(k_1 r) + a_n' k_1 r n_n'(k_1 r) + n(n+1)\{b_n j_n(k_2 r) + b_n' n_n(k_2 r)\}\} P_n(\cos\theta) \tag{7}$$

$$u_\theta = -\frac{1}{r} \sum_{n=0}^{\infty} \{a_n j_n(k_1 r) + a_n' n_n(k_1 r) + b_n\{j_n(k_2 r) + k_2 r j_n'(k_2 r)\} + b_n'\{n_n(k_2 r) + k_2 r n_n'(k_2 r)\}\} \frac{dP(\cos\theta)}{d\theta}$$

where the primes on the j_n and n_n functions denote differentiation with respect to the argument. The interior of the shell is a vacuum. Solutions for the exterior scattered field and the displacement vector $\mathbf{u}$ in the shell are obtained by applying the boundary conditions at the inner and outer surfaces of the shell to obtain the coefficients a_n, a_n', b_n, b_n', and c_n. The procedure has been presented in a number of papers [4-6].

The properties for water are assumed to be: density, $\rho = 10^3 kgm^{-3}$; sound velocity, $c = 1440 s^{-1}$. The shell is assumed to be made of aluminum with elastic properties:

density, $\rho_s = 2.965 \times 10^3 kgm^{-3}$; Lamé constant, $\lambda = 6.1 \times 10^{10} Pa$

and shear constant, $\mu = 2.5 \times 10^{10} Pa$,

from which are derived

compressional velocity, $c_p = 6418\ ms^{-1}$; shear velocity, $c_s = 3046\ ms^{-1}$

All quantities are nondimensionalized with respect to the radius a of the sphere and the density r and speed of sound c of the water. Nondimensional forms of the quantities used in the computed results are

$$r' = \frac{r}{a}\ ;\ u_r' = \frac{u_r}{a}\left(\frac{\rho c^2}{P_0}\right)\ ;\ u_0' = \frac{u_0}{a}\left(\frac{\rho c^2}{P_0}\right) \qquad (8)$$

and ka is used as the nondimensional frequency parameter. In the above analysis, the primes have been omitted. The nondimensional parameter $P_0/\rho c^2$ is necessarily a small quantity in acoustics.

EXCITATION OF THE SHELL BY CONTINUOUS SOUND AT HIGH FREQUENCIES

The vibrations in an aluminum shell with b/a = 0.98 were computed for incident sound at frequencies corresponding to ka = 300 and 600. The vibrations are shown graphically by plotting the flowlines indicating the direction of the displacement vector and contour lines indicating the magnitude of the displacement amplitude. In a thin shell with b/a = 0.98, a special transformation has to be used to present the data in a form that is clearly visible. The transformation is shown schematically in Fig. 2 where the shell is transformed into a rectangular section. This section is divided into six rectangular segments each covering 30 degrees of the angular dimension θ, between θ = 180 and 0 degrees. Each rectangular segment has a narrow segment above it showing the pressure waves in the liquid next to the shell, consisting of both incident and scattered sound. Shading indicates positive pressure. Figure 3(a) shows the displacement flowlines and Figure 3(b) shows the contours of the displacement amplitude, for ka = 300. Figures 4(a) and (b) present the same data for ka = 600. In Figs. 3(b) and 4(b), the positions of the maximum and minimum points are indicated twice, once at the front of the shell, between 180 and 90 degrees and again at the back of the shell, between 90 and 0 degrees. This separation was made because the displacement amplitude at the front of the spherical shell is an order of magnitude greater than at the back, and the contours at the back would not have been seen on the same contour scale as the front. Ten contours are shown between the maximum and minimum (which is essentially zero). Figures 3 and 4 show the displacement in the shell and the adjacent pressure in the liquid at the beginning of the cycle of excitation, i.e. at $\omega t = 0$. During successive cycles, the waves in the shell and the adjacent liquid move in the direction of decreasing θ. Videos of the computed data show that the movement does not occur at a steady speed but at a rate that appears sinusoidal. During each cycle of the steady-state excitation, the direction of the displacement flowlines changes twice.

As the frequency increases from ka = 300 to ka = 600, it is seen that the wave structure begins to separate with surface waves, particularly towards the back of the shell away from the incident sound. The amplitude of the waves on the outer surface of the shell next to the liquid is greater than that on the inner surface. The pattern of the pressure waves in the liquid next to the shell is seen to be quite complicated in places.

Figures 5 and 6 show the transition from anti-symmetric behavior, characteristic of thin-shell theory [7], at low and intermediate frequencies [3], and symmetric behavior characteristic of higher frequencies. Figure 5(a) shows a comparison between the radial component of displacement on the outer surface of the shell (dotted line) and the inner surface (solid line). Only 40 degrees of the circumferential coordinate θ are shown; the remainder of the θ range is similar. Figure 6 shows symmetric behavior of the radial components in more detail, for ka = 600. Figure 5(b) shows a comparison between the circumferential component of displacement at the middle surface (dotted line) and the arithmetic average of the circumferential components on the inner and outer surfaces (solid line). At low and intermediate frequencies these circumferential components are the same, agreeing with thin-shell theory [3]. As frequency increases the agreement with thin-shell theory disappears, as shown in Fig. 5(b).

CONCLUDING COMMENTS

Further exploration of high-frequency behavior is needed. In particular, it is necessary to determine how well ray theory predicts high-frequency behavior.

An important need is to relate the elastic waves inside the structure of the acoustic target with the scattered sound field. Resonance scattering theory (RST) [8] provides a significant insight into the nature of the scattered field. Direct computation of the elastic waves should be combined with RST to develop a complete understanding of the manner in which the scattered field is formed from the vibrations of the acoustic target.

ACKNOWLEDGEMENTS

The authors gratefully acknowledge the assistance of the Mississippi Supercomputer Center at the University of Mississippi. This work was partially supported by the Office of Naval Research.

REFERENCES

1. R. Hickling, R.K. Burrows and J.F. Ball, "Rotational Waves in the Elastic Response of Spherical and Cylindrical Acoustic Targets in Water," J. Acoust. Soc. Amer. 89, 971-979 (1991).

2. E.R. Lapwood and T. Usami, "Free Oscillations of the Earth," (Cambridge UP, Cambridge, U.K., 1981).

3. R. Hickling, J.F. Ball, R.K. Burrows, and M. Petrovic, "Computational Structural Acoustics Applied to Scattering of Sound by Spherical Shells," to be published J. Acoust. Soc. Amer. (1992).

4. R.R. Goodman and R. Stern, "Reflection and Transmission of Sound by an Elastic Spherical Shell," J. Acoust. Soc. Amer. 34, 338-344 (1962).

5. R. Hickling, "Analysis of Echoes from a Hollow Metallic Sphere in Water," J. Acoust. Soc. Amer 36, 1124-1137 (1964).

6. G.C. Gaunaurd and M.F. Werby, "Lamb and Creeping Waves Around Submerged Spherical Shells Resonantly Excited by Sound Scattering," J. Acoust. Soc. Amer. 82, 2021-2033 (1987).

7. H. Kraus, "Thin Elastic Shells," (John Wiley and Sons, Inc., New York, 1967).

8. L. Flax, G.C. Gaunaurd and H. Uberall, "Theory of Resonance Scattering," in Physical Acoustics, W.P. Mason and R.M. Thurston (eds.), Vol. XV, Chapt. 3, (Academic Press, New York, 1981).

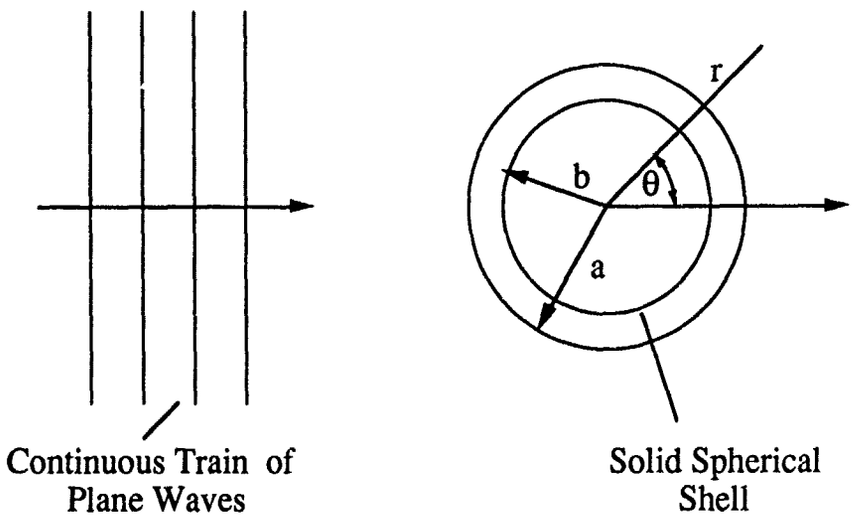

Fig. 1 Continuous train of plane waves incident on a spherical shell.

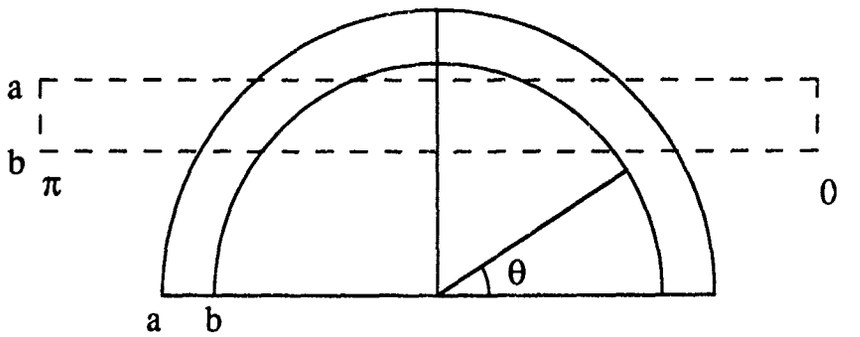

Fig. 2 Transformation of section of spherical shell into a rectangular section.

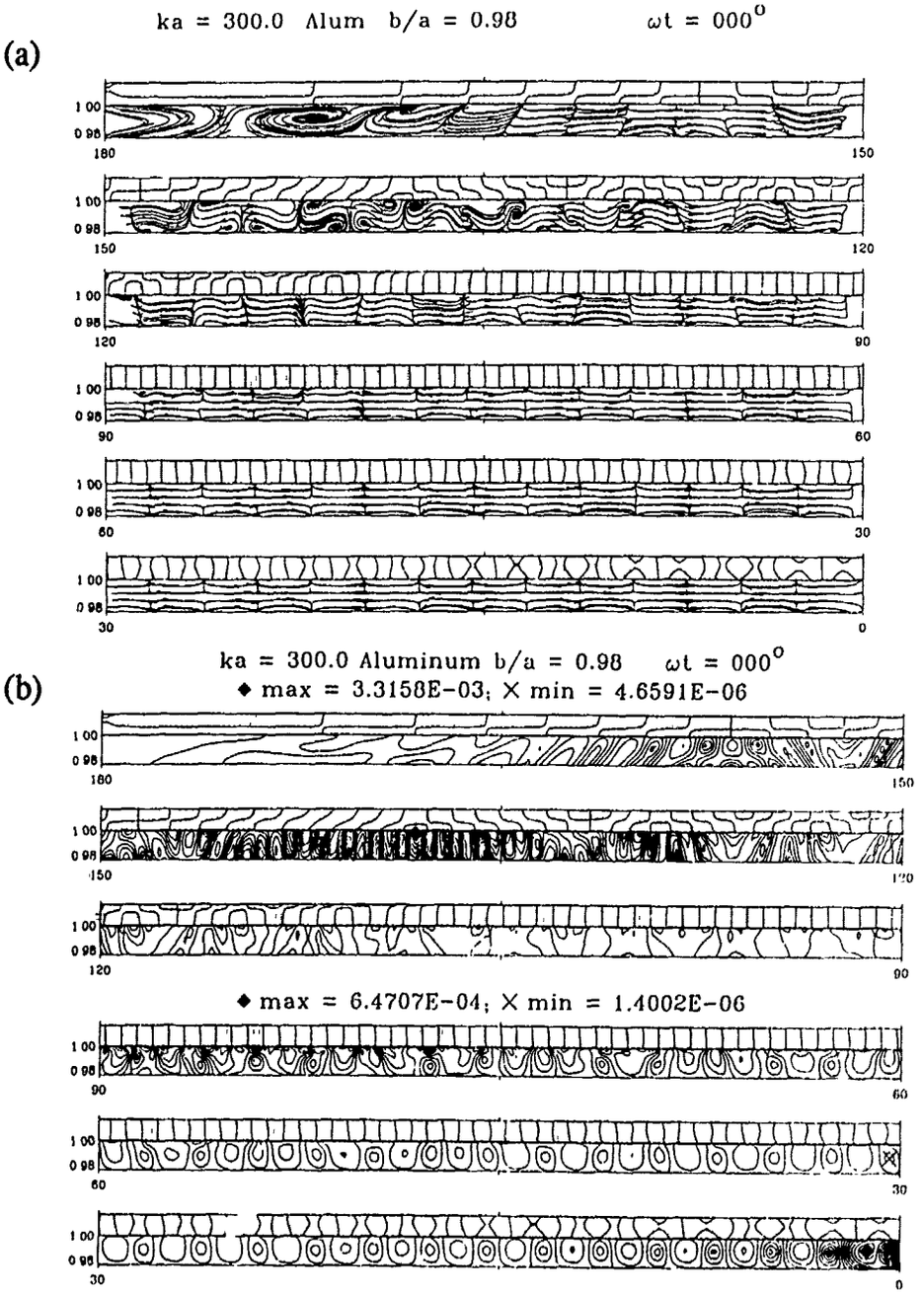

Fig. 3 Two sequences of 6 plots, each covering 30 degrees of the angular dimension θ of the shell, showing:

(a) the flowlines of the displacement vector direction and

(b) contour plots of the amplitude of the displacement between the max and min values of the amplitude.

The shell is excited by incident sound at ka = 300. The thin layer at the top of each section shows the pressure field in the water next to the shell, positive pressure indicated by shading. The sequence occurs at ωt = 0 at the beginning of the cycle of excitation.

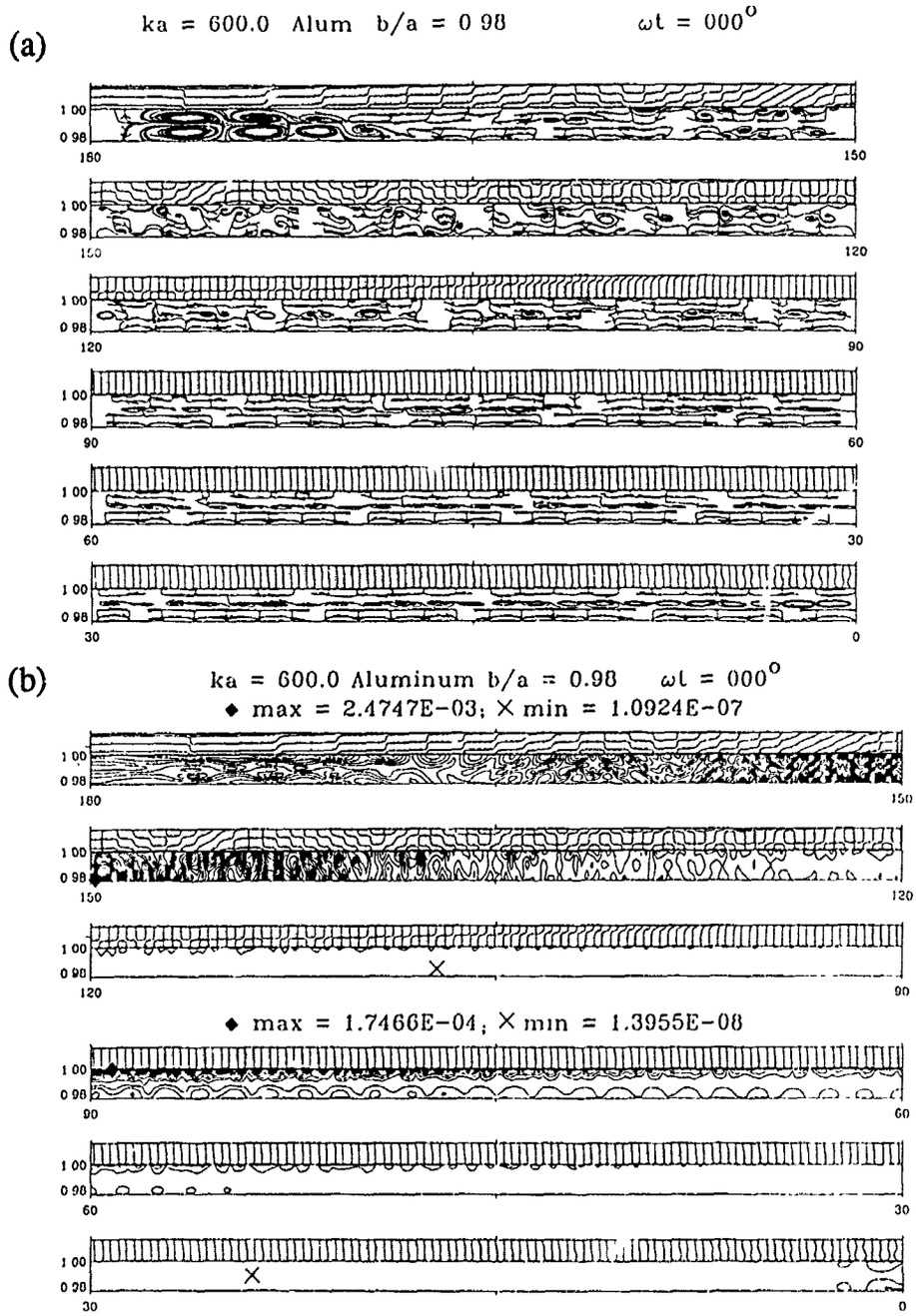

Fig. 4 Two sequences of 6 plots, each covering 30 degrees of the angular dimension θ of the shell, showing:

(a) the flowlines of the displacement vector direction and

(b) contour plots of the amplitude of the displacement between the max and min values of the amplitude.

The shell is excited by incident sound at ka = 600. The thin layer at the top of each section shows the pressure field in the water next to the shell, positive pressure indicated by shading. The sequence occurs at ωt = 0 at the beginning of the cycle of excitation.

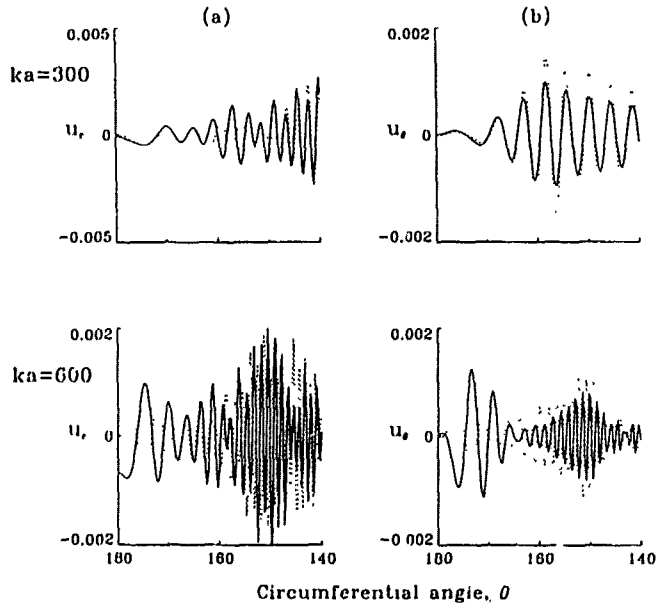

Fig. 5 Comparison of:

(a) the radial component of displacement on the outer surface of the shell (dotted line) with that on the inner surface of the shell (solid line)

(b) the circumferential component of displacement on the middle surface of the shell (solid line) with the arithmetic average of the circumferential components on the inner and outer surfaces of the shell (dotted line).

The shell has b/a = 0.98 and the excitation frequencies in water are ka = 300 and 600. The curves are for the beginning of the cycle of excitation at $\omega t = 0$. Only the part of the shell closest to the source of incident sound is shown.

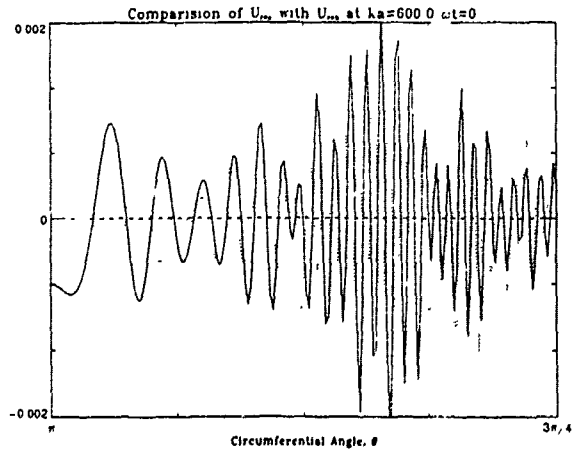

Fig. 6 Comparison for ka = 600 of the radial component of displacement on the outer surface of the shell (dotted line) with that on the inner surface of the shell (solid line) showing the development of symmetric motion in the shell.

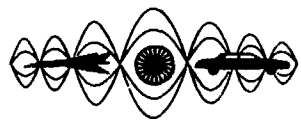

SECOND INTERNATIONAL CONGRESS ON
RECENT DEVELOPMENTS IN AIR- AND
STRUCTURE-BORNE SOUND AND VIBRATION
MARCH 4-6, 1992 AUBURN UNIVERSITY, USA

ELEMENTS, EIGENFUNCTIONS AND INTEGRAL EQUATIONS IN FLUID–STRUCTURE INTERACTION PROBLEMS

R. P. Shaw
Dept. of Civil Engineering
S. U. N. Y. at Buffalo

ABSTRACT:

A review is given of various integral equation formulations and some general solution methods, including element and eigenfunction expansion approaches.

INTRODUCTION:

Integral equations in modern engineering may be viewed as a tree with many branches and, under our current educational system, unfortunately few roots. Boundary element methods (BEM), T matrix methods (TMM), Embedding element methods (EEM) and many others are all based on this concept. It is clear that integral equation formulations are really not new in classical physics, i.e., solid mechanics, fluid mechanics, electromagnetics, thermodynamics, etc. of continua (now the purview of engineering) since the search for "the" Green's functions for specific problems, geometries and boundary conditions, going back about 150 years, is based on an integral form. This approach leads to a complete and exact solution in the form of a quadrature of prescribed boundary values, e.g., Morse and Feshbach[1]. The breakthrough to boundary integral equations, BIE, came when it was recognized that the same formulation could be used with any Green's function satisfying the governing equation, regardless of geometry and boundary conditions, and led to an equation of reduced dimensionality by placing the solution point on the boundary. The price paid for this generality was that the resulting equation was an integral or even integro--differential equation. The many integral equation methods are distinguishable by the solution technique used such as approximate, i.e. expansions in terms of continuous functions with arbitrary coefficients, and numerical, i.e. local approximation of the dependent variables at discrete points, methods as well as other methods, i.e. eigenfunction expansions, elements and everything else (this last category includes iteration, asymptotic expansions and other rarely used approaches). They are further distinguished by various "organizations" of the location of integration or "source" points and solution or "field" points. The main claim of integral equation formulations is that they are boundary rather than volume methods, thereby distinguishing them from the standard methods of finite differences and finite elements. Each of these has its own advantages and disadvantages, e.g. in a coupled fluid-structure interaction problem, it may be advantageous to use a volume method for a complicated structure, possibly heterogeneous and/or nonlinear, with the boundary integral equation form serving as a generalized closing "boundary condition" to

that structure. The emphasis here then will be on the BIE itself rather than the actual coupling. This review will discuss a) the general integral equation formulation for wave problems, including some unusual forms, b) some solution techniques including i) elements, ii) eigenfunction expansions and iii) "other" solution methods.

a) THE "BOUNDARY" INTEGRAL EQUATION FORMULATION

It should be noted that the term "formulation" rather than "solution method" is used here. This is because these integral equation forms are completely equivalent to the differential equation form; there are no "new", i.e. other than the original physical assumptions, approximations made and thus the integral equation form contains all of the same information as does the differential equation form. For example, Shaw[2] uses such a formulation to obtain dispersion equations for an infinite elastic plate. Many of the same techniques, e.g. elements, eigenfunction expansions, asymptotic expansions, iterations, etc., are used to solve both differential and integral formulations.

The Helmholtz equation for time harmonic acoustic waves in a homogeneous medium is

$$\nabla^2 \phi(\vec{r}) + k^2 \phi(\vec{r}) = Q(\vec{r}) \quad \text{in } V \tag{1}$$

with a dependent variable, ϕ, a forcing term, Q, and appropriate boundary conditions

$$\phi(\vec{r}) = f_1(\vec{r}) \text{ on } S_1 \; ; \; \partial\phi(\vec{r})/\partial n = f_2(\vec{r}) \text{ on } S_2 \; ; \; K\,\phi(\vec{r}) + \partial\phi(\vec{r})/\partial n = f_3(\vec{r}) \text{ on } S_3 \tag{2}$$

where $S_1 \cup S_2 \cup S_3$ is the total boundary to the acoustic domain, V. A time harmonic dependence proportional to $\exp(-i\omega t)$ is taken. Corresponding transient formulations are also available, e.g. Friedman and Shaw[3].

Green's functions for the Helmholtz equation are defined by

$$\nabla^2 G(\vec{r}, \vec{r}_0) + k^2 G(\vec{r}, \vec{r}_0) = -\delta(\vec{r} - \vec{r}_0) \quad \text{in } V \tag{3}$$

with the boundary conditions left unspecified at this point. For an infinite domain, the Green's function is well known in terms of $R = |\vec{r} - \vec{r}_0|$ as

$$G_0(\vec{r}, \vec{r}_0) = \exp(i k R)/(4\pi R) \quad \text{in 3-D}; \quad = (i/4) H_0^{(1)}(k R) \quad \text{in 2-D} \tag{4}$$

Green's third integral theorem with an outward (from $V(\vec{r}_0)$) normal, $\vec{n}_0$, gives

$$\int_S \{G(\vec{r}, \vec{r}_0)\, \partial\phi(\vec{r}_0)/\partial n_0 - \phi(\vec{r}_0)\, \partial G(\vec{r}, \vec{r}_0)/\partial n_0\} dS(\vec{r}_0) = \int_V \{\phi(\vec{r}_0)\, \delta(\vec{r} - \vec{r}_0) + Q(\vec{r}_0)\, G(\vec{r}, \vec{r}_0)\} dV(\vec{r}_0) \tag{5}$$

Here, $\vec{r}$ represents the solution or field point while $\vec{r}_0$ is the integration or source point. For exterior acoustic scattering problems, there is a contribution from a closing surface at infinity since the total acoustic field is not zero there; to use the form given here, either ϕ must represent the scattered field which does vanish at infinity or an incident wave field must be used for an equivalent $Q(\vec{r})$.

If the field point $\vec{r}$ is within $V(\vec{r}_0)$, the first volume integral yields $\phi(\vec{r})$ while if $\vec{r}$ is

outside of $V(\vec{r}_0)$ it yields zero due to the nature of the delta function. If however, $\vec{r}$ is on the boundary surface $S(\vec{r}_0)$, i.e. neither inside nor outside of V, the boundary integration includes the source point $R = 0$ and leads, with care, to $(1/2)\,\phi(\vec{r})$ at a smooth boundary location and some other fraction of ϕ at a sharp corner. One way to view this is that only a fraction of the delta function operates for a solution point on the boundary; this can of course be rigorously established. For $\vec{r}$ on S, the integrals are taken in a Cauchy principle value sense, i.e. excluding the point $\vec{r} = \vec{r}_0$ from the integration. The advantage to this latter "boundary integral equation" form is that all unknowns are required only on the boundary, i.e. the problem has been reduced by one dimension. Furthermore, the infinite domain often required in exterior radiation and scattering problems has been reduced to a solution on the finite boundary S. Once this boundary integral equation has been solved, the solution at $\vec{r}$ in V is expressed in terms of known quadratures. The boundary integral equation formulation is then

$$c\,\phi(\vec{r}) = \int_S \{G(\vec{r}, \vec{r}_0)\partial\phi(\vec{r}_0)/\partial n_0 - \phi(\vec{r}_0)\partial G(\vec{r}, \vec{r}_0)/\partial n_0\} dS(\vec{r}_0) - \int_V Q(\vec{r}_0)\, G(\vec{r}, \vec{r}_0)\, dV(\vec{r}_0) \qquad (6)$$

where $c = (1, 1/2, 0)$ for $\vec{r}$ within V, on S and not within V respectively (with some other fraction replacing 1/2 at corners). Frequently $Q(\vec{r})$ is zero, i.e. no field sources and no volume integration is required at all. In exterior scattering problems, the total wave field may be used as the dependent variable if the Q integral represents $-\phi_{incident}$. This may be established by examining the interior solution, i.e. outside of V, which should be zero everywhere, e.g. Friedman and Shaw[2]. Note that if ϕ were prescribed on S and G were chosen in a form to be zero on S, the exact solution would follow for field points anywhere in V; this would then be "the" Green's function solution to this problem, with other boundary conditions requiring other "the" Green's functions. In boundary integral equations, G is usually taken as the free-space or infinite domain Green's function given above. Then if ϕ were given on S, eq. (6) with $c = 1/2$, would be an integral equation of the first kind on $\partial\phi/\partial n$, which appears only under the integral, on S. Once $\partial\phi/\partial n$ on S is determined, eq. (6) with $c = 1$ yields results at any field point within V, etc. It is also worth noting here that the unknown boundary values could also be determined by placing the field point anywhere outside of V; then eq. (6) will always have $c = 0$ and thus always be an integral equation of the first kind. This "null field"or "extinction" approach avoids the Cauchy principle value but has some numerical solution difficulties, along with the question of where best to locate the field points, e.g. Bates and Wall[4].

Before examining these in detail, it is valuable to consider the physical interpretation of eq. (6) in terms of distributions of sources and doublets on the surface S which replace the original physical object by a "saltus" problem, i.e. one with fluid everywhere and allowable discontinuities in the dependent variable at the original surface. The first surface integral may be considered as a distribution of simple sources, $G(\vec{r}, \vec{r}_0)$, of strength $\partial\phi/\partial n$ on S while the second term may be thought of as a distribution of doublets, $\partial G(r, \vec{r}_0)/\partial n$, of strength $-\phi$. These surface distributions cause a discontinuity in the dependent variable and its normal derivative as a field point moves from within V to outside of V such that the dependent variable ϕ and its normal derivative go from their actual values within V to zero values outside of V. Their value on S will be defined to be that of the interior of V since there is no meaning here to a value "at" a discontinuity. This is the "direct" boundary integral formulation. An equally useful "indirect" formulation can be made in terms of distributions

either sources alone or doublets alone. In this case the "jump" is only in the normal derivative or the variable itself respectively and the solution goes from the required one interior to V to some nonzero artificial one outside of V. These are NOT new concepts. Lamb[5] discussed such discontinuities at some length in his classic text on hydrodynamics. The direct formulation is essentially the "mathematical statement of Huygens' principle" as described by Baker and Copson[6]. It is only the use of digital computers for numerical solutions that has changed their role in engineering. To illustrate the indirect approach, consider the doublet source formulation for the Helmoltz equation for an exterior Dirichlet problem;

$$\phi(\vec{r}) = \int_S \sigma(\vec{r}_0) \quad \partial[G(\vec{r},\vec{r}_0)]/\partial n_0 \; dS(\vec{r}_0) \tag{7}$$

which represents the acoustic velocity potential, ϕ, at a field point $\vec{r}$ in terms of a distribution of point doublets of strength σ on the obstacle surface S. ϕ is discontinuous across such a surface, although the normal derivative of ϕ is still continuous, i.e. as $\vec{r}$ approaches S from the fluid ($\vec{r}_+$) and from the interior of the obstacle ($\vec{r}_-$),

$$\phi(\vec{r})_- = + (1/2)\,\sigma(\vec{r}) + \int_S \sigma(\vec{r}_0)\,\partial[G(\vec{r},\vec{r}_0)]/\partial n_0 \; dS(\vec{r}_0) \tag{8}$$

$$\phi(\vec{r})_+ = - (1/2)\,\sigma(\vec{r}) + \int_S \sigma(\vec{r}_0)\,\partial[G(\vec{r},\vec{r}_0)]/\partial n_0 \; dS(\vec{r}_0) \tag{9}$$

Clearly as $\vec{r}$ approaches the obstacle surface, there is a discontinuity of $-\sigma$ in ϕ across S from the fluid to the interior of the obstacle. For a Dirichlet problem where ϕ is given on S, eq. (9) allows σ to be found and eq. (7) allows ϕ to be found in the field once σ is known; similar approaches hold for a surface of simple sources.

One other formulation seems appropriate to mention here. There is no actual need to place these source surfaces, i.e. discontinuities, on the original boundary. They could be placed in the region outside of the original volume and their source and/or doublet strengths adjusted to satisfy the original boundary conditions on the original boundary. This approach is called the "embedding" integral equation formulation since the original volume is now embedded in a larger domain and was actually one of the first integral equation formulations used, albeit for potential flow rather than acoustics, e.g. Munk[7] and Von Karman[8]. Here a typical representation would have

$$\phi(\vec{r}) = \int_{S_e} \sigma(\vec{r}_0)\, G(\vec{r},\vec{r}_0) \; dS(\vec{r}_0) + \int_{V_e} Q(\vec{r}_0) \; G(\vec{r},\vec{r}_0) \; dV(\vec{r}_0) \tag{10}$$

where S_e would be some convenient "embedding" surface such as a circle in 2D or a sphere in 3D placed outside of the original volume and V_e is the new total volume which includes the original domain plus the added volume to extend the domain up to the embedding surface. Even if there are no sources within the original volume, there may still be occasion to introduce them in the added domain. If Dirichlet conditions are given on $S(\vec{r}_e)$, i.e. $\phi(\vec{r}_e)$ is known, eq. (10) allows for the solution of $\sigma(\vec{r}_0)$. Once σ is known, eq. (10) with $\vec{r}$ at any field location in V allows the solution for $\phi(\vec{r})$ just as a normal derivative of eq. (10) with respect to $n(\vec{r})$ allows $\partial\phi/\partial n$ to be found everywhere in the original domain. Clearly other boundary conditions could be handled in much the same manner. While this embedding approach avoids

the singular integrals and Cauchy principal values of the "standard" boundary integral equation method, it has its own advantages and disadvantages. It has been used in some acoustic problems, e.g. Shaw and Huang[9] for eigenvalue problems and Shaw and Huang[10] for radiation and scattering problems.

b) SOME SOLUTION TECHNIQUES

The classical techniques for the solution of integral equations tend to be overlooked in engineering practice along, unfortunately, with the available theory. For example, the "interior eigenvalue" problem, inherent in boundary integral equation formulation itself rather than any numerical technique, where an exterior radiation or scattering solution by this approach fails at the eigenvalues of an interior problem with the same geometry and a related boundary condition, e.g. Schenck[11], is most clearly understood in terms of integral equation theory.

i) ELEMENT METHODS: This boundary element method, BEM, approximates both the surface of integration and the dependent variables by simpler geometrical forms, i.e. shape functions, over subregions, i.e. boundary elements. For the dependent variable, this implies a functional variation determined by numerical values at appropriate nodes while for the geometry this implies certain orders of smoothness for the connectivity of the elements. In the simplest case, the dependent variables are approximated by a constant "shape function" on each element and the elements are taken as straight lines in 2D and flat triangles in 3D, i.e. linear "shape functions" which have constant normal directions; this "jargon" is a direct outgrowth from finite elements and may not always be the best description of what actually is being done in boundary elements. Consider eq. (6) with $Q = 0$, for $\vec{r} = \vec{r}_i$; $i = 1, 2, .. M$ on S at a smooth location with S segmented into M elements. Typically, $\vec{r}_i$ is chosen at the center of the geometrical element.

$$(1/2)\,\phi(\vec{r}_i) = \sum_{k=1}^{M} \int_{S_k} \{G(\vec{r}_i, \vec{r}_0)\,\partial\phi(\vec{r}_0)/\partial n_0 - \phi(\vec{r}_0)\,\partial G(\vec{r}_i, \vec{r}_0)/\partial n_0\} dS(\vec{r}_0) \qquad (11)$$

Approximating ϕ and $\partial\phi/\partial n$ as "constants" on each element S_k, regardless of the approximation of the geometry, this becomes

$$(1/2)\phi_i = \sum_{k=1}^{M} \{(\partial\phi/\partial n)_k \int_{S_k} G(\vec{r}_i,\vec{r}_0) dS(\vec{r}_0) - \phi_k \int_{S_k} \partial G(\vec{r}_i,\vec{r}_0)/\partial n_0 dS(\vec{r}_0)\} = \sum_{k=1}^{M} \{(\partial\phi/\partial n)_k G_{ik} - \phi_k \tilde{H}_{ik}\} \qquad (12)$$

While this is the "standard" explanation of the lowest order approximation, it must be pointed out that this is computationally equivalent to using a mean value theorem from integral calculus with the approximation in eq. (12) being that the unknown location of these mean values is taken to be the center of the element, Shaw[12]. The arithmetic does not change from the "constant" shape function concept, but the interpretation of physical results does. The constant shape function requires a "ziggurrat" or stepped representation while the mean value approach only requires that the mean value of the unknown over the element occur at the midpoint, thereby allowing other constraints such as continuity of the solution from element to element to be added. Moving the last term to the left hand side of this equation and calling $H_{ik} = \delta_{ik} + \tilde{H}_{ik}$ leads to the "standard" boundary element form

$$\sum_{k=1}^{M} \phi_k \, H_{ik} = \sum_{k=1}^{M} (\partial\phi/\partial n)_k \, G_{ik} \; ; \; i = 1, 2, \ldots, M \tag{13}$$

For any M boundary conditions on the 2 M unknown variables ϕ_i and $(\partial\phi/\partial n)_i$, this set of M equations may be solved for the remaining M unknowns. The "influence coefficients" G_{ik} and H_{ik} are integrals of G and $\partial G/\partial n$ over S_k for a field point at $\vec{r}_i$ and are obtained for $i \neq k$ by standard Gauss integration formulas. For $i = k$, G_{ii} is obtained by a modified Gaus mula, while for "flat elements" H_{ii} is zero. This latter result is based on the fact that G is a function of R and $\partial G/\partial n$, which is thus proportional to $\partial R/\partial n$, is zero for all points on a "flat" S_i where $\hat{n}_i$ is always perpendicular to R, excluding the point $R = 0$ since this is a Cauchy principle value integral. Many reviews of boundary element methods applied to wave problems are available, e.g. Shaw[13]. Embedding element methods have been applied to some acoustic scattering problems but are still in the process of development, e.g. Shaw and Huang[10].

ii) EIGENFUNCTION METHODS: The direct application of eigenfunction expansions to the governing boundary integral equation, eq. [6], suffers from the drawback that the eigenfunction expansions for $G_0(\vec{r}, \vec{r}_0)$, given in standard references such as Morse and Feshbach[1], have distinct forms for $\vec{r} > \vec{r}_0$ and $\vec{r} < \vec{r}_0$ but no mention is ever made of what happens at $\vec{r} = \vec{r}_0$. While G_0 itself is continuous, its derivatives are not. This difficulty can clearly be resolved, but this does not appear to be a "method of choice" in the engineering community. Rather, the T matrix met' d or TMM, introduced into acoustics by Waterman[14], seems to dominate this approach. T: method uses eigenfunction expansions based on simple geometries for the solution of other more complicated geometries, which in a sense is the basis of the classical Trefftz method. The TMM is applied primarily to exterior problems, i.e. scattering or radiation into an infinite exterior domain, and has been applied to a variety of problems, e.g. acoustic, elastodynamic, water and electromagnetic waves. Consider an infinite homogeneous acoustic domain, V, with a submerged rigid obstacle of finite surface, S. Take the standard problem of the scattering of plane time harmonic waves incident on this obstacle; the resulting scattered wave field is sought. Choosing an appropriate orthogonal set of basis functions, $\Psi_n(\vec{r})$, the following expansions may be made for a typical exterior scattering problem:

$$\phi_w(\vec{r}) = \sum_{p=0}^{\infty} a_p \, \mathrm{Re}[\, \Psi_p(\vec{r}) \,] \tag{14}$$

$$\phi_s(\vec{r}) \quad \phi(\vec{r}) - \phi_w(\vec{r}) = \sum_{n=0}^{\infty} f_n \, \Psi_n(\vec{r}) \tag{15}$$

$$G(\vec{r},\vec{r}_0) = \beta \sum_{n=0}^{\infty} \begin{cases} \Psi_n(\vec{r}) \, \mathrm{Re}[\, \Psi_n(\vec{r}_0) \,] \; ; \; r > r_0 \\ \Psi_n(\vec{r}_0) \, \mathrm{Re}[\, \Psi_n(\vec{r}) \,] \; ; \; r_0 > r \end{cases} \tag{16}$$

The factor β, (i/4 in 2D), is typical of the T matrix notation. The governing integral equation is then written twice, once for $\vec{r}$ on the circumscribed surface and once for $\vec{r}$ on the inscribed surface; note that neither of these points is on the original boundary surface,

$$\phi(\vec{r}) - \phi_w(\vec{r}) = \phi_s(\vec{r}) = -\int_S \Phi(\vec{r}_0) \, \partial G(\vec{r},\vec{r}_0)/\partial n_0 \, dS(\vec{r}_0) \; ; \; r > r_0 \tag{17}$$

$$\phi_w(\vec{r}) = \int_S \phi(\vec{r}_0) \, \partial G(\vec{r},\vec{r}_0)/\partial n_0 \, dS(\vec{r}_0) \; ; \; r_0 > r \tag{18}$$

If the field on the scattering surface, $\phi(\vec{r}_0)$, were itself expanded in an appropriate set of basis functions, e.g. $Y_m(\vec{r}_0)$ where Y_m might be Ψ_m, Re[Ψ_m], etc.,

$$\phi(\vec{r}_0) = \sum_{m=0}^{\infty} \alpha_m \, Y_m(\vec{r}_0) \tag{19}$$

then f_n and a_p could be related to each other through the elimination of α_m. For real basis functions, Y_m, the definition of the Q matrix as

$$Q_{mn} = \int_S Y_m(\vec{r}_0) \, \partial\Psi_n(\vec{r}_0)/\partial n_0 \, dS(\vec{r}_0) \tag{20}$$

leads to the equations

$$f_n = -\beta \sum_{m=0}^{\infty} \alpha_m \, \mathrm{Re}[Q_{mn}] \tag{21}$$

$$a_p = \beta \sum_{m=0}^{\infty} \alpha_m \, Q_{mp} \tag{22}$$

$$f_n = -\sum_{p=0}^{\infty} \sum_{m=0}^{\infty} a_p \, Q_{mp}^{-1} \, \mathrm{Re}[Q_{mn}] = \sum_{p=0}^{\infty} a_p \, T_{pn} \tag{23}$$

Thus given an appropriate set of basis functions, $Y_m(\vec{r}_0)$, and the scattering geometry S, the matrix Q and thus the matrix T can be computed. For a complex set of basis functions Y_m, the details are modified somewhat, e.g. Martin[15]. It is clear that this procedure could have been halted at eq. (21) where α_m could be found in terms of f_n, i.e. the surface potential coefficients in terms of the known incident wave coefficients. This would correspond to the 'null-field' method arising from the location of field or solution points outside of the acoustic domain where the field should be identically zero. Since the TMM is based on the same integral equation formulation as the BEM, it should also be subject to the "fictitious interior eigenvalue" failure problem. While this problem was also recognized early on in the development of the TMM, e.g. Waterman[14], and in methods for circumventing it such as the use of the full complex form of Ψ_m for the basis set Y_m by Martin[15], which implicitly recognizes the existence of the 'fictitious interior eigenvalue' problem when only the real part of Ψ_m or its normal derivative is used for Y_m, it does not seem to be of great concern in practice. This may be seen for example in a typical recent discussion of the relative merits of the TMM and BEM, Tobocman[16], where this difficulty is pointed out for the BEM but not mentioned for the TMM. In fact, Waterman[17] recommended the use of the real part of Ψ_m for the basis set Y_m. This disparity between principle and practice led to a study illustrated by an example of 2D scattering by a circular cylinder of radius a, i.e. Shaw and Huang[18]. Embedding methods based on eigenfunction expansions turn out to be nothing other than the well known Trefftz method, but with a clearer understanding of the physical meaning of this time honored approach, Shaw and Huang.[19]

iii) OTHER METHODS: These include such classical methods as iteration, e.g. Chertock[20], asymptotic expansions in either frequency or geometry, e.g. Shaw[21], etc. While of interest, these do not seem general enough for standard methods, but do have theoretical significance.

Coupled interior structure-exterior fluid problems are a direct extension of these concepts.

REFERENCES:

1. Morse, P. and H. Feshbach, METHODS OF THEORETICAL PHYSICS, I AND II, McGraw - Hill Book Co., N.Y.C., N.Y., 1953,

2. Shaw, R. P., Elastic Plate Vibrations by Boundary Integral Equations, Part I: Infinite Plates, Res Mechanica, 4, pp. 83 - 88, 1982,

3. Friedman, M. B. and Shaw, R. P., Diffraction of a Plane Shock Wave by an Arbitrary Rigid Cylindrical Obstacle, ASME 61 --WA--55, 1961; also Jour. App. Mech. 29, pp. 40-46, 1962,

4. Bates, R. H. T. and Wall, D. J. N., Null Field Approach to Scalar Diffraction, Phil. Trans. R. Soc. Lond., A, 287, pp 45-78 (Part I) and pp 79-95 (part II), 1977.

5. Lamb, H., HYDRODYNAMICS, Cambridge Univ. Press, Cambridge, U. K., 1932,

6. Baker, B. B. and Copson, E. T., THE MATHEMATICAL THOERY OF HUYGEN'S PRINCIPLE, Oxford Univ. Press, Oxford, U. K., 1939,

7. Munk, M. M., "The Aerodynamic Forces on Airship Hulls", NACA Tech. Rep. 184, 1924,

8. von Karman, T., Calculation of Pressure Distribution on Airship Hulls, NACA TM 574, 1930,

9. Shaw, R. P. and Huang, S-C, Helmholtz Eigenvalues by Embedding Methods, Wave Motion, 7, pp. 367-370, 1989,

10. Shaw, R. P. and Huang, S-C, The Embedding Integral Equation Formulation with Applications to Acoustics Problems, COMPUTATIONAL ACOUSTICS, ed. D. Lee, A. Cakmak and R. Vichnevetsky, Elsevier Pub., N.Y., pp. 83-99, 1990,

11. Schenck, H. A., "Improved Integral Formulation for Acoustic Radiation Problems", J. Acoust. Soc. Am., 44, pp. 41 - 58, 1968,

12. Shaw, R. P., Boundary Element Methods as Weighted Mean Values, Math. Comput. Mod., 15, pp. 279-283, 1991,

13. Shaw, R. P., Boundary Integral Methods in Acoustics, Chap. 7, BOUNDARY ELEMENT METHODS IN MECHANICS, ed. D.E. Beskos, North Holland-Elsevier Pub., Amsterdam, 1989,

14. Waterman, P. C., "New Formulation of Acoustic Scattering", J. Acoust. Soc. Am., 45, pp. 1417 - 1429, 1969,

15. Martin, P. A., "Acoustic Scattering and Radiation Problems, and the Null-Field Method", Wave Motion, 4, pp. 391 - 408, 1982,

16. Tobocman, W. , "Comparison of the T Matrix and the Helmholtz Integral Equation Methods for Wave Scattering Calculations", J.Acoust..Soc..Am., 77, pp. 369 - 374, (1985),

17. Waterman, P.C., "Survey of T Matrix Methods and Surface Field Representations", pp. 61-78 in ACOUSTIC, ELECTROMAGNETIC AND ELASTIC WAVE SCATTERING - FOCUS ON THE T MATRIX APPROACH, ed. V. K. Varadan and V.V. Varadan (1979), Pergamon Press, N.Y.C., N.Y., 1979,

18. Shaw, R. P. and S-C Huang, The Fictitious Eigenvalue Difficulty in the T Matrix and the BEM Methods for Exterior Wave Scattering, J. Acous. Soc. Am., 86, pp. 839-842, 1989,

19. Shaw, R. P., Huang, S-C and Zhao, C-X, The Embedding Integral and the Trefftz Method for Potential Problems with Partitioning, Engineering Analysis, (in press-1992),

20. Chertock, G., Convergence of Iterative Solutions to Integral Equations for Sound Radiation, Quar. App. Math. 26, pp. 268 - 271, 1968,

21. Shaw, R. P., Time Dependent Acoustic Radiation from a Submerged Elastic Shell Defined by Nonconcentric Circular Cylinders, J. Acous. Soc. Am., 64, pp. 311-317, 1978.

**SECOND INTERNATIONAL CONGRESS ON
RECENT DEVELOPMENTS IN AIR- AND
STRUCTURE-BORNE SOUND AND VIBRATION**
MARCH 4-6, 1992 AUBURN UNIVERSITY USA

FAR-FIELD SOUND RADIATION FROM A LINE-DRIVEN FLUID-LOADED INFINITE FLAT PLATE WITH ATTACHED RIB STIFFENERS HAVING ADJUSTABLE ATTACHMENT LOCATIONS

Benjamin A. Cray
New London Laboratory
Naval Underwater Systems Center
New London, CT 06320

ABSTRACT

Previous research has determined the far-field sound pressure radiated from the upper surface of a line-driven, fluid-loaded infinite flat plate with attached rib stiffeners spaced periodically.

In this study, the plate is configured to have two sets of rib stiffeners, though the formulation may be extended to include additional rib stiffener sets. The stiffeners composing a given set are identical and are spaced periodically with distance ℓ. However, one set of ribs is shifted by an amount Δ from the other set. In this manner, portions of the plate may be configured with repeating sections having nonperiodic rib spacing.

The research shows that a periodically stiffened plate produces a symmetrical far-field directional radiation pattern. Whereas, a nonperiodic rib-stiffened plate generates unsymmetrical radiation characteristics.

INTRODUCTION

Acoustic radiation from stiffened plates has been investigated over the past thirty years with a primary focus on far-field solutions of the radiated acoustic pressure from periodically stiffened structures. Romanov [1] calculated the radiated power from an infinite plate due to a field or random line forces driving the plate between two frames spaced a distance 2ℓ apart and symmetric about the origin. Both sides of the plate were fluid loaded. Evseev [2] determined the far-field radiation from an infinite thin plate with attached frames periodically spaced at a distance ℓ. The fluid-loaded plate was driven by a harmonic point force. The effect of the attached frames was modeled as a reaction force applied at each attachment location. The frames were allowed to have mass and bending stiffness properties, but not rotational stiffness. Garrelick [3] presents results that show the far-field radiated pressure from a two-framed, a four-framed, and a plate stiffened by an infinite set of periodic frames over a wide band of frequencies. Mace [4] considered the far-field radiated pressure from an infinite fluid-loaded plate having two sets of rib stiffeners, one set spaced an integer multiple of the periodic spacing of the other set. A harmonic point force was applied to the unloaded surface of the plate and the far-field pressure was obtained by the method of staionary phase. The frames did not exert moment reactions on the plate. Burroughs [5] extended the formulation given by Mace to analyze the far-field radiation from a fluid-loaded infinite cyclindrical shell having periodic and identical circular intermediate ring supports and bulkhead supports.

This paper investigates the far-field sound pressure radiated from the upper surface of a line-driven, fluid-loaded stiffened infinite flat plate. The formulation presented here allows for one set of identical periodically spaced rib-stiffeners to be offset from another set of periodically spaced rib-stiffeners. The method can be extended to many sets of frames, all of which have a different offset from one another. Hence, composite sections of the plate may be designed, over any length scale, to possess nonperiodic frame spacing.

FORMULATION

Figure 1 is a conceptual illustration of the fluid-loaded, rib-stiffened infinite flat plate under investigation. The plate is fluid-loaded on the upper surface only; the lower surface is in vacuo. An external time harmonic line force of magnitude F_0 is applied perpendicularly to the plate's lower surface.

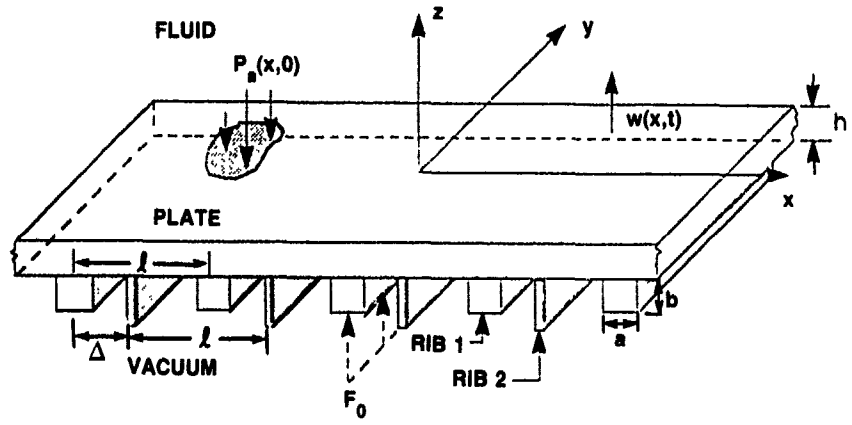

Fig. 1. Geometry of flat plate showing two sets of rib-stiffeners and the external forces acting on the stiffened plate.

Two sets of attached rib-stiffeners are shown and both are spaced periodically with a distance denoted as ℓ. One set of stiffeners is offset from the other set by a distance denoted as Δ. The stiffeners composing a given set are identical, i.e., they have the same cross-sectional areas and material properties. The properties of one set, however, can differ from that of the other set.

The elastic plate is of uniform thickness, h. It is isotropic, homogeneous, and its transverse motion is assumed to be govered by Euler-Bernoulli's equation of motion. Rotary inertia and shear deformation effects within the plate are neglected. The plate has structural damping which has been included by allowing for a complex Young's modulus having a loss factor η.

The rib-stiffeners exert reactive forces upon the plate, but not angular moments. Eatwell [6] and Mace [7] have included angular displacements or rotations of the rib-stiffeners and the extension is not difficult. For simplicity, though, this analysis neglects angular displacements of the stiffeners and the angular moments their displacements produce. The time variation, $e^{-i\omega t}$, of all of the applied loads is suppressed throughout the analysis.

Given the above conditions, the governing equation of motion for the surface displacement of the plate, w(x,y), is

$$D\frac{d^4w(x)}{dx^4} - m\omega^2 w(x) = P_e(x) - P_a(x) - \{P_1(x) + P_2(x)\}, \qquad (1)$$

where D is the plate's rigidity, m is the plate's mass per unit area, and ω is the applied excitation frequency.

The external pressure due to the applied line force is denoted $P_e(x)$ and the acoustic pressure acting on the upper surface of the plate is $P_a(x,0)$. The total pressure exerted by all of the sets of rib stiffeners are $P_1(x)$ and $P_2(x)$.

Equation (1) is transformed, term by term, using Exponential Fourier transforms, which are defined as

$$\tilde{w}(k) = \int_{-\infty}^{\infty} w(x)\, e^{-ikx} dx,$$

and

$$w(k) = \frac{1}{2\pi} \int_{-\infty}^{\infty} \tilde{w}(k)\, e^{ikx} dk.$$

Equation (1) can be immediately transformed and the result is given as

$$(Dk^4 - m\omega^2)\, \tilde{w}(k) = \tilde{P}_e(k) - \tilde{P}_a(k) - \{\tilde{P}_1(k) + \tilde{P}_2(k)\}, \qquad (2)$$

where the ~ denotes the transformed expressions.

The transform of the external pressure due to the applied line force, which acts along a line parallel to the rib-stiffeners, at some distance x_0, with constant force, F_0, is simply

$$\tilde{P}_e(k) = F_0 e^{-ikx_0}. \tag{3}$$

The acoustic pressure, $P_a(x,0)$, applied to the plate's upper surface is determined in the usual manner, i.e., through the acoustic wave equation and the condition of continuity of momentum at the interface of the plate and the fluid medium. The transformed response of the fluid loading pressure is well-documented, Junger [8], and can be written as

$$\tilde{P}_a(z,k) = \frac{-i\rho_0\omega^2\,\tilde{w}(k)}{\sqrt{k_0^2-k^2}}\; e^{\,i\sqrt{k_0^2-k^2}\;z} \qquad |k| \le k_0$$

and

$$\tilde{P}_a(z,k) = \frac{-\rho_0\omega^2\,\tilde{w}(k)}{\sqrt{k^2-k_0^2}}\; e^{\,-\sqrt{k^2-k_0^2}\;z} \qquad |k| \ge k_0,$$

where $k_0 = \frac{\omega}{c}$, which is the acoustic wavenumber.

Substituting these values into the inverse transform integral for the physical radiated pressure from the fluid-loaded stiffened plate's surface gives

$$P_a(x,z) = -\frac{i\rho_0\omega^2}{2\pi} \int_{-\infty}^{\infty} \frac{\tilde{w}(k)}{\sqrt{k_0^2-k^2}}\; e^{\,i\sqrt{k_0^2-k^2}\;z}\; e^{ikx} dk. \tag{4}$$

The transformed acoustic pressure acting on the surface of the plate is

$$\tilde{P}_a(0,k) = \frac{-i\rho_0\omega^2\tilde{w}(k)}{\sqrt{k_0^2-k^2}} \qquad |k| \le k_0, \tag{5a}$$

and

$$\tilde{P}_a(0,k) = \frac{-\rho_0\omega^2\tilde{w}(k)}{\sqrt{k^2-k_0^2}} \qquad |k| \ge k_0. \tag{5b}$$

It is assumed that the reaction force produced by each rib-stiffener acts over an infinitely narrow region and each set of stiffeners produces a total reactive pressure of

$$P_1(x) = -\sum_{n=-\infty}^{\infty} m_1'\,\omega^2 u_1(x)\,\delta(x-n\ell), \tag{6a}$$

and

$$P_2(x) = -\sum_{n=-\infty}^{\infty} m_2'\,\omega^2 u_2(x)\,\delta(x-(n\ell+\Delta)), \tag{6b}$$

where m_1' and m_2' are the mass per unit length of each of the rib stiffener sets. The displacement of each set of rib stiffeners is denoted $u_1(x)$ and $u_2(x)$.

Both of the above equations are transformed with respect to x and, assuming the order of integration, may be interchanged with the summations, the following is obtained:

$$\tilde{P}_1(k) = -m_1'\,\omega^2 \sum_{n=-\infty}^{\infty} w(n\ell)\, e^{-ikn\ell}, \tag{7a}$$

and

$$\tilde{P}_2(k) = -m_2'\,\omega^2 \sum_{n=-\infty}^{\infty} w(n\ell+\Delta)\, e^{-ik(n\ell+\Delta)}. \tag{7b}$$

Notice that the plate's displacement, $w(n\ell)$ and $w(n\ell+\Delta)$, has been substituted for the displacement of the rib's displacement, $u(n\ell)$ and $u(n\ell+\Delta)$, since the plate and ribs are rigidly attached at $x_n = n\ell$ and $x_n = n\ell+\Delta$. Also notice that equations (7a) and (7b) are not in terms of the transformed variable, k, but are in terms of a physical displacement variable, $n\ell$ and $n\ell+\Delta$.

By introducing a new transformation domain, denoted as the ζ domain, manipulations may be performed to write equations (7a) and (7b) in terms of the wavenumber, k.

The manipulation is accomplished by introducing the transform shown below:

$$w(n\ell) = \frac{1}{2\pi} \int_{-\infty}^{\infty} \hat{w}(\zeta) e^{i\zeta(n\ell)} d\zeta. \tag{8}$$

Substituting equation (8) into equations (7a) and (7b) and incorporating Poisson's summation formula gives

$$\tilde{P}_1(k) = \frac{-m_1'\omega^2}{2\pi} \int_{-\infty}^{\infty} \hat{w}(\zeta) \left\{ \frac{2\pi}{\ell} \sum_{n=-\infty}^{\infty} \delta\left(\zeta - (k + \frac{2\pi n}{\ell})\right) \right\} d\zeta, \tag{9a}$$

$$\tilde{P}_2(k) = \frac{-m_2'\omega^2}{2\pi} \int_{-\infty}^{\infty} \hat{w}(\zeta) \left\{ \frac{2\pi}{\ell} e^{i\Delta(\zeta - k)} \sum_{n=-\infty}^{\infty} \delta\left(\zeta - (k + \frac{2\pi n}{\ell})\right) \right\} d\zeta, \tag{9b}$$

Interchanging the order of the summation and integration, the integrals of equations (9a) and (9b) can be evaluated exactly, yielding

$$\tilde{P}_1(k) = K_1 \sum_{n=-\infty}^{\infty} \tilde{w}(k + nk_\ell) \tag{10a}$$

$$\tilde{P}_2(k) = K_2 \sum_{n=-\infty}^{\infty} \tilde{w}(k + nk_\ell) e^{ink_\ell \Delta}, \tag{10b}$$

where

$$K_1 = \frac{-m_1'\omega^2}{\ell} \qquad K_2 = \frac{-m_2'\omega^2}{\ell} \qquad k_\ell = \frac{2\pi}{\ell}.$$

Note that k_ℓ is a constant wavenumber corresponding to the periodic inter-rib spacing, ℓ. The other terms, K_1 and K_2, represent the dynamic mass of the attached rib stiffeners.

Substituting all of the transformed external pressures, equation (3), equations (5a) and (5b), equations (10a) and (10b) back into equation (2) yields the fluid-loaded stiffened plate's wavenumber response, though not in an explicit form, i.e.,

$$\tilde{w}(k) = F(k) - K_1 Y(k) \sum_{n=-\infty}^{\infty} \tilde{w}(k + nk_\ell) - K_2 Y(k) \sum_{n=-\infty}^{\infty} \tilde{w}(k + nk_\ell) e^{ik_\ell n\Delta}. \tag{11}$$

where

$$F(k) = \frac{F_0 e^{-ikx_0}}{S(k)} \qquad Y(k) = \frac{1}{S(k)},$$

$$S(k) = \begin{cases} D(k^4 - k_b) - \dfrac{i\rho_0\omega^2}{\sqrt{k_0^2 - k^2}} & |k| \le k_0 \\ D(k^4 - k_b^4) - \dfrac{\rho_0\omega^2}{\sqrt{k^2 - k_0^2}} & |k| \ge k_0, \end{cases}$$

and $k_b = \frac{m\omega^2}{D}$, the free "in vacuo" plate wavenumber. Note that if additional sets of rib stiffeners, of different size and offset, had been included, equation (11) would simply become

$$\tilde{w}(k) = F(k) - Y(k) \left\{ \sum_{n=-\infty}^{\infty} (K_1 + K_2 e^{ink_\ell \Delta_1} + \ldots + K_N e^{ink_\ell \Delta_{N-1}}) w(k + nk_\ell) \right\}. \tag{12}$$

The difficulty now lies in determining an explicit expression for the plate's wavenumber response, $\tilde{w}(k)$. That is, it is necessary to manipulate equation (11) such that the summations that contain the wavenumber response, $\tilde{w}(k + nk_\ell)$, must be written in terms of known quantities.

The following summation expressions are defined, where the subscript p denotes the integer value in the summation exponent.

$$W_p(k) \equiv \sum_{n=-\infty}^{\infty} \tilde{w}(k + nk_\ell)\, e^{ikn_\ell \Delta p},$$

$$F_p(k) \equiv \sum_{n=-\infty}^{\infty} F(k + nk_\ell)\, e^{ikn_\ell \Delta p},$$

$$Y_p(k) \equiv \sum_{n=-\infty}^{\infty} Y(k + nk_\ell)\, e^{ikn_\ell \Delta p}.$$

Each summation defined above has the following key property:

$$G_p(k + mk_\ell) = Gp(k)\, e^{-imk_\ell p\Delta}.$$

The expression for the summed plate response, $W_p(k)$, is substituted into equation (11) and yields

$$\tilde{w}(k) = F(k) - K_1 Y(k)\, W_0(k) - K_2 Y(k)\, W_1(k). \tag{13}$$

To explicitly solve for $\tilde{w}(k)$ in equation (13), let $k = k + k_\ell m$, and sum both sizes of equation (13) over all m, which, considering the above relationship, yields

$$W_0(k) = F_0(k) - K_1 Y_0(k) W_0(k) - K_2 Y_{-1}(k) W_1(k). \tag{14}$$

Returning to equation (13), both sides are now multiplied by $e^{ik_\ell m}$, the substitution $k = k + k_\ell m$ is made, and both sides are summed over all integers m, which yields

$$W_1(k) = F_1(k) - K_1 Y_1(k) W_0(k) - K_2 Y_0(k) W_1(k). \tag{15}$$

Equations (14) and (15) are solved simultaneously for $W_0(k)$ and $W_1(k)$ and are substituted back into equation (13). Hence, the explicit wavenumber response of the fluid-loaded, infinite flat plate having two sets of attached rib stiffeners is

$$\tilde{w}(k) = F(k) - Y(k) * \left\{ \frac{K_2(1+K_1Y_0(k))\, F_1(k) + K_1(1+K_2Y_0(k))\, F_0(k) - K_1K_2\,(F_0(k)Y_1(k) + F_1(k)Y_{-1}(k))}{1 + (K_1+K_2)Y_0(k) + K_1K_2(Y_0^2(k) - Y_1(k)Y_{-1}(k))} \right\} \tag{16}$$

For the special case of identical rib stiffeners spaced periodically with distance ℓ (for example $K_2 = 0.0$), equation (16) simplifies to

$$\tilde{w}(k) = F(k) - \frac{Y(k)K_1\, F_0(k)}{1 + K_1 Y_0(k)}. \tag{17}$$

Each additional set of rib stiffeners introduces an additional summation, $W_p(k)$, which must be solved simultaneously with the other summation terms to obtain the explicit form of the plate's wavenumber response. For example, ten independent rib-stiffener sets, nine of which have different offset, would generate ten equations in ten unknowns, $W_0(k)$, $W_1(k)$, ..., $W_9(k)$.

FAR-FIELD ACOUSTIC RADIATION

The inversion integral, equation (4), may be evaluated in the far-field by introducing a cylindrical coordinate transformation and employing the method of stationary phase, Junger [8]. The stationary phase asymptotic expansion, for an applied line force is,

$$P(R,\Theta) \sim \frac{-\rho_0\omega^2\tilde{w}(\bar{k})\, e^{iRk_0(1+i)}}{2\sqrt{Rk_0\pi}}.$$

The geometric, material, and acoustic fluid properties used for the numerical calculations are given in Table 1. Two configurations are considered, i.e., the BASELINE design and the ALTERNATE design. Both configurations will be compared to each other and with an unstiffened plate, which is simply referred to as an UNRIBBED configuration. Throughout this section, as an aid to the reader, the configurations will be capitalized.

Table 1. Geometric, Material, and Acoustic Properties

Geometrical Properties:	
Plate Thickness (h)	0.0254 m (1.0 in.)
Periodic Rib Spacing (l)	
Baseline	0.6035 m (23.75 in.)
Alternate	0.30175 m(11.8 in.)
Cross-Sectional Rib Area (a x b)	
Baseline	0.004215 m^2 (6.5 $in.^2$)
Alternate	0.001935 m^2 (3.0 $in.^2$)
Material Properties:	
Young's Modulus (Steel, E)	19.5 10^{10} Pa (27.7 10^6 psi)
Modulus Loss Factor (Steel, η)	0.02
Density (Steel, ρ_S)	7.7 10^3 kg/m^3 (475 lbf/ft^3)
Poisson's Ratio (Steel, ν)	0.28
Fluid Properties:	
Density (Water, ρ_O)	1.0 10^3 kg/m^3 (62 lbf/ft^3)
Sound Speed (Water, c_O)	1.5 10^3 m/s (4921 ft/s)

The magnitude of the line force is 1 kN (224 lbf), and the force is applied directly beneath a rib-stiffener at the plate's origin. The frequencies of excitation were chosen as 250 Hz, 500 Hz, 1000 Hz, and 2000 Hz. All of these frequencies are below coincidence for the plate investigated.

Figures 2 through 5 are directionality patterns that show, in decibels, the difference in far-field sound pressure level of the BASELINE and ALTERNATE plate configurations, with and without periodic offset, relative to the UNRIBBED plate. The directionality refers to the change in the magnitude of the radiated pressure with variation of polar angle, Θ. The angle varies from –89 degrees to 89 degrees at a fixed radial distance, R, of 1 meter. For all of the figures, the applied line force is fixed at the plate's origin.

For the UNRIBBED plate, the radiation pattern in omnidirectional, showing no preference for radiation at any angle, for frequencies less than the coincidence frequency. At coincidence, which for the UNRIBBED plate is approximately 9800 Hz, the radiated pressure becomes strongly directional.

Figure 2 illustrates the directionality pattern of the BASELINE plate at a frequency of 250 Hz. As might be expected, the low frequency radiation characteristics of the BASELINE and UNRIBBED plates are similar. Both configurations radiated pressure equally in all directions at low frequency, with the ribbed BASELINE being only a moderately stronger radiator than the UNRIBBED plate.

At 2,000 Hz, the directionality pattern shown in Figure 3 shows a strong dependence of acoustic radiation with direction. The BASELINE design is no longer omnidirectional. Radiation peaks are seen at approximately ±5 degrees; nulls occur at ±10 degrees. Notice, over much of the angular space, the BASELINE design radiates less acoustic pressure into the far-field than the UNRIBBED plate.

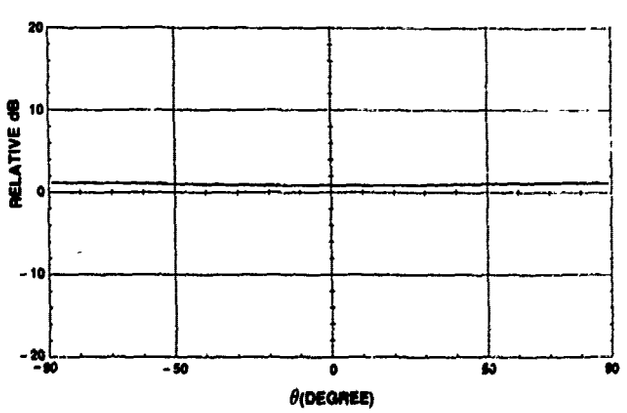

Fig. 2. Directionality pattern showing the difference in the far-field radiation of the BASELINE plate relative to the UNRIBBED plate at a frequency of 250 Hz.

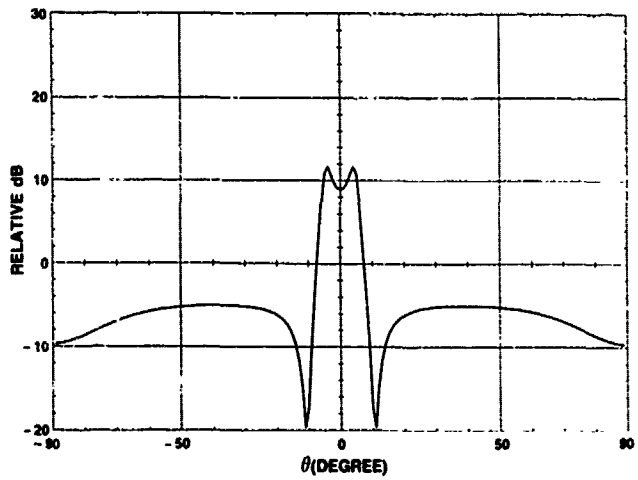

Fig. 3. Directionality pattern showing the difference in the far-field radiation of the BASELINE plate relative to the UNRIBBED plate at a frequency of 2000 Hz.

At 2,000 Hz, as shown in Figure 4, the radiation pattern of the ALTERNATE plate relative to the UNRIBBED plate is strongly directional. The overall pattern shown, with a radiation peak at 0.0 degrees or normal to the plate's surface, is similar to that shown at 500 Hz for the BASELINE plate in Figure 5. Notice in Figure 4, except for a narrow angular region centered about 0.0 degrees, the ALTERNATE plate radiates less sound than that which is radiated by the UNRIBBED plate for an excitation frequency of 2,000 Hz.

Figure 5 compares the directionality patterns of the BASELINE plate and a "30% shifted" BASELINE plate, both relative to the UNRIBBED plate, at an excitation frequency of 500 Hz. The "30% shifted" BASELINE plate has an offset, $\Delta=1.3(\frac{b}{2})$ which produces overall nonperiodic frame spacing.

The radiation patterns for the periodic rib spacing given by the BASELINE and ALTERNATE configurations all were symmetric in polar angle about the applied line force. It is apparent ,then, in Figure 5 that the "30% shifted" BASELINE configuration, which has nonperidoic rib spacing, is slightly unsymmetrical at 500 Hz with a narrow radiation peak that occurs at approximately 2 degrees.

Many investigators, such as Gorman [9], Romanov [1], and others, have recognized that the plate's internal structural damping alters the magnitude of the radiated acoustical pressure from that of a stiffened plate. Increasing the structural loss factor,η, will decrease the magnitude of the radiation peaks, while decreasing damping will increase the magnitude of these radiation peaks. The effect is noted here, though, in typical engineering applications, a plate material is specified by other considerations and the structural damping factor is fixed. Hence, it is unlikely that this effect can be exploited.

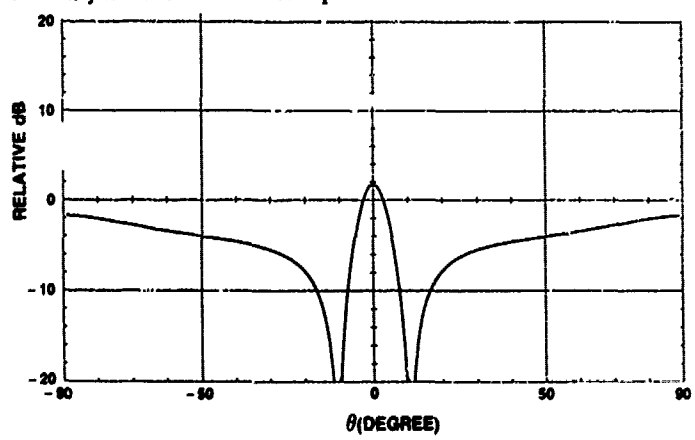

Fig. 4. Directionality pattern showing the difference in the far-field radiation of the ALTERNATE plate relative to the UNRIBBED plate at a frequency of 250 Hz.

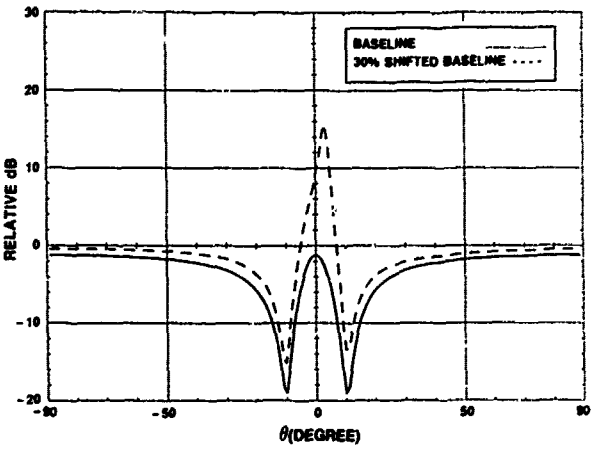

Fig. 5. Comparison of the directionality patterns of the BASELINE plate and the "30% shifted" BASELINE plate at a frequency of 500 Hz.

CONCLUSIONS

It was shown in Figure 4, the ALTERNATE configuration at 2,000 Hz, that less far-field sound is radiated from the stiffened plate than from the unstiffened plate over most of the angular radiation space. Therefore, the attachment of rib-stiffeners to a plate may reduce, at selected frequencies, the radiated sound compared to that generated by an unstiffened plate.

All of the directional radiation patterns of the periodic stiffened plate were symmetric in polar angle. For an offset which introduced nonperiodic spacing, the directionality patterns were no longer symmetric. It would appear that the stiffeners may act as an array of sources radiating pressures that constructively and destructively interfere in the far-field. A recommendation for future work would be to determine whether an equivalent source strength for a rib-stiffener could be obtained and used as an acoustical source in an array of sources. The directionality patterns given here could then be compared to those generated from an array of equivalent sources.

REFERENCES

[1] V. N. Romanov, Radiation of sound by an infinite plate with reinforcing beams, Sov. Phys. Acous., vol. 17, 1971, 92-96.

[2] V. N. Evseev, Sound radiation from an infinite plate with periodic inhomogeneities, Sov. Phys. Acoust., vol. 57, 1973, 370-373.

[3] J. M. Gerrelick and Gaw-Feng Lin, Effect of the number of frames on the sound radiaton by fluid-loaded, frame-stiffened plates, J. Acoust. Soc. Am., vol. 48, no. 2, 1975, 499-500.

[4] B. R. Mace, Sound radiation from a plate reinforced by two sets of parallel stiffeners, J. Sound Vib., vol. 71, no. 3, 1981, 435-441.

[5] C. B. Burroughs, Acoustic radiation from fluid-loaded infinite circular cylinders with doubly periodic ring support, J. Acoust. Soc. Am., vol. 75, no. 3, 1984, 715-722.

[6] G. P. Eatwell, The response of a fluid-loaded, beam stiffened plate, J. Sound Vib., vol. 84, no. 3, 1982, 371-388.

[7] B. R. Mace, Periodically stiffened fluid-loaded plates, I: Response to convected harmonic pressure and free wave propagation, J. Sound Vib., vol. 73, no. 4, 1980, 473-486.

[8] M. C. Junger and D. Feit, Sound, Structures, and Their Interaction, MIT Press, Cambridge, MA, 1986, 112-119.

[9] R. M. Gorman, Vibration of and acoustic radiation from line-excited rib-stiffened damped plates in water, PH.D. dissertation, the Pennsylvania State University, 1974.

SECOND INTERNATIONAL CONGRESS ON
RECENT DEVELOPMENTS IN AIR- AND
STRUCTURE-BORNE SOUND AND VIBRATION
MARCH 4-6, 1992 AUBURN UNIVERSITY, USA

THE EFFICIENCY OF LAYERED HOUSINGS WITH ARBITRARY SHAPE

Samuil A. Rybak
N. N. Andreyev Acoustics Institute.
Shvernik st., 4,
Moscow, 117036, USSR,
Tel.: (095) 126-9872, Fax.: (095) 126-8411.

ABSTRACT

Method of calculating of sound transmission loss by using layered housings with different viscous and elastic layeres of arbitrary shape is developed. The dynamics of layeres is described by means of correct relations of elasticity without simplifications. The effectivenes of the structure is measured by energy flow method like described by M.Crocker.

THEORETICAL METHOD

When we have an elastic layer in a pakage of layers then its garmonical vibrations can be described by means of matrix presentation. Let us introduce a vector B_1 :

$$B_1 = \begin{vmatrix} V_{n1} \\ V_{\tau 1} \\ P_1 \end{vmatrix} \qquad (1)$$

This means the boundary conditions on one side of the layer. Then on the other side of the layer of thickness h we have $B_2(h)$, which is connected with B_1 by relation :

$$B_2(h) = B_1 S , \qquad (2)$$

where S is the transition matrix. Its elements a_{ik} we determined earlier in [1]:

$$S = \begin{vmatrix} 1 & a_{12} & a_{13} & \left[-\frac{i\omega h}{\lambda+2\mu}\right] \\ a_{21} & 1 & \left[-i\omega\frac{h}{\mu}\right] & a_{24} \\ a_{31} & M & 1 & a_{43} \\ \left[1-\frac{k^2h^2M}{4}\right] & a_{42} & a_{43} & 1 \end{vmatrix} \qquad (3)$$

where

$$a_{12} = a_{34} = \frac{\lambda}{\lambda+2\mu} ikh ;$$

$$a_{13} = a_{24} = -i\omega\frac{ikh^2}{2\mu}\frac{\lambda+\mu}{\lambda+2\mu} ;$$

$$a_{21} = a_{43} = ikh\ ;$$

$$a_{31} = a_{42} = \frac{ikh}{2} M\ ;$$

$$M = -\frac{1}{i\omega}\left[-\rho h \omega^2 + \frac{4\mu(\lambda+\mu)}{\lambda+2\mu} hk^2\right]\ ;$$

$$L = -\frac{1}{i\omega}\left[-\rho h \omega^2 + \frac{4\mu(\lambda+\mu)}{\lambda+2\mu} \frac{h^3}{12} k^4\right]\ .$$

For the whole pakage which has N layers the resulting transition matrix Σ is :

$$\Sigma = \prod_{n=1}^{N} S_n\ . \qquad (4)$$

It is necessary to note that the matrix (3) describes arbitrary motion of thin viscoelastic layer and when we suppose $P_1 = P_2 = \tau_1 = \tau_2 = 0$ then from Eqs.(2) one can obtain a dispersive equation of free vibrations of the layer. The viscousity is described by introducing imaginary parts in parameters Lame λ, μ :

$$\lambda = \lambda_0 (1 - i\eta_1)\ , \quad \mu = \mu_0 (1 - i\eta_2)\ . \qquad (5)$$

where viscous coefficients η_1 and η_2 may be functions of ω .

When we have into the pakage a liquid or gas layer then for it the transition matrix is:

$$\sigma = \begin{vmatrix} \cos(qh) & i\frac{\sin(qh)}{\rho c}\cos\theta \\ i\rho c\frac{\sin(qh)}{\cos\theta} & \cos(qh) \end{vmatrix} \qquad (6)$$

Here : $q = (\omega^2/c^2 - k^2)^{1/2}$, c – sound velocity in considered layer, and $\theta = \operatorname{arctg}(q/k)$ – the incident angle.

For this case :

$$\tau_1 = \tau_2 = 0\ , \qquad (7)$$

and due to this condition we obtain from vector $B_{1,2}$ a vector :

$$A_{1,2} = \begin{vmatrix} V_{n1,n2} \\ P_{1,2} \end{vmatrix}\ . \qquad (8)$$

which is necessary in calculating the sound transmition through the liquid layer.

Relative to the incident sound wave $P_1 = 1 + R$, $V_{n1} = (1/\rho c)(1 - R)\cos\theta$, and $P_2 = D$, $V_{n2} = (1/\rho c) D\cos\theta$, where R is the reflection amplitude, and D is the transmision amplitude, $q_D = (1/2)\,\mathrm{Re}(P_2, V_{n2}^*)$.

CONCLUSION

With the help of special software based on described above algorithm we can calculate sound transmission through arbitrary pakage of layers and make the optimization the sound insolation of a partition. When the partition is of cylindrical shape we developed our method on the case of cylindrical layers [2].

REFERENCE

[1] S.A.Rybak & B.D.Tartakovsky,"Some applications of transition matrix to the theory of plane waves in the system of elastic layers", Sov. Phys. Acoust., No.1, V.8, (1962).

[2] G.M.Avilova & S.A.Rybak,"Normal waves in layered cylindrical shell", Sov. Phys. Acoust. No.1, V.25, (1979).

SECOND INTERNATIONAL CONGRESS ON
RECENT DEVELOPMENTS IN AIR- AND
STRUCTURE-BORNE SOUND AND VIBRATION
MARCH 4-6, 1992 AUBURN UNIVERSITY, USA

SOUND RADIATION BY STRUCTURES WITH DISCONTINUITIES

Korotin P.I., Lebedev A.V.
Institute of Applied Physics Academy of Sciences of the USSR,
603600, N Novgorod, USSR.

ABSTRACT

Sound radiation by an arbitrary structure, affected by discontinuities is analysed. A discontinuity strongly influences the structure radiation, small inhomogeneity being not a sign of slight variations of the acoustic field. Its effect depends on the Q-factor of the structure and its kind. A structure can have too many discontinuities that influence its radiation. Therefore one must search for a simple qualitative solution rather than complicate the calculation scheme by additional terms. This report is concerned with such qualitative analysis.

INTRODUCTION

The sound radiation by structures is of interest for noise control. One of the possible methods to solve the structure sound radiation problem is the method of limited differences. Evidence shortcoming of this method is its complexity caused by a great number of coupling elements. Moreover it is difficult to interpret results obtained and to prognosis of these variations under the alternation of the structure construction.

Because of that it is more convenient separate the structure by simple subsystems that can have arbitrary wave size and analyse their coupling [1,2]. If in the sound radiation some one of the subsystems predominates, other subsystems can be described as discontinuities. This important case is analysed in the present paper.

The most interesting frequency region includes frequencies up to $\lambda_0 \approx L$, where λ_0 is the sound wavelength and L is the characteristic size of the structure noise active element. Radiation losses in this region are small in comparison with the structural damping. Therefore radiation on resonance can have the great magnitude. At frequency $\lambda_0 \gtrsim L$ sound radiation of the structure is equivalent to the superposition of multipole radiation. The contribution of each multipole decreases as its order grows [3]. Sound radiation is determined by a small order of multipole sources, while the vibration field is determined by the highest multipole orders. Hence, the discontinuities that causing elastic wave scattering can lead the energy canalization from high to low order of multipole.

RESULTS AND DISCUSSION

Now we'll obtain the conditions of sound radiation increasing under the presence of discontinuities and determine the class of structures that are more sensible to them.

Let us have complete information about homogeneous structures (natural frequency and form of vibration modes, acoustic impedances, etc.). Using the method of small disturbances one can represent a normal component of velocity as an asymptotic row:

$$W(\vec{x}) = W^{(0)}(\vec{x}) + W^{(1)}(\vec{x}) + W^{(2)}(\vec{x}) + \dots , \qquad (1)$$

where the j-th term has the order $O(\delta^j)$ and $\delta = Z_e/Z_c$, Z_e is the impedance of discontinuity (its wave size is assumed less than 1), Z_c is the characteristic impedance of structure.

A nonresonant component weakly depends on δ if $\delta \ll 1$. Therefore, a corresponding equation for the acoustic power of the structure with discontinuities has the same form that for a homogeneous structure:

$$N = \frac{1}{2} \mathrm{Re}\left\{ \sum_{\substack{mn, \\ lq}} Z_{mnlq}\, W_{lq}^{(0)}\, W_{mn}^{(0)*} \right\} , \qquad (2)$$

where Z_{mnlq} is the acoustic impedance of modes (mn) and (lq).

On resonant frequencies of the structure with discontinuities (ω'_{kj}) the resonant component of radiation is determined by the sum of the own radiation of mode (kj) and reradiation by discontinuities.

$$N_{kj} = N_{kj}^{(0)} + \Delta N_{kj} \qquad (3)$$

The ΔN_{kj} value can be represented in the following form [4]: $\Delta N_{kj} = \alpha + \beta + \gamma$, where α, β, γ have orders $O(\delta Q)$, $O(\delta^2 Q^2)$, $O(\delta^2 Q)$, Q is Q-factor. From eq. for α, β, γ one can make the following conclusions (see Appendix):

1. If $\mathrm{Re}(Z_{lqlq}) \gg \mathrm{Re}(Z_{kjkj})$ the $\Delta N_{kj}/N_{kj}^{(0)}$ ratio can have a great magnitude. Therefore it is possible to enrich radiation frequency response characteristics.
2. A dissipative discontinuity (α term) changes the radiation level stronger than the inertial one.
3. A single ($n=1$) discontinuity always increases radiation while in case ($n>1$) both increasing and decreasing are possible.

Now we'll analyse the simplest case of single inertial discontinuity and determine the conditions under which the increasing of radiation takes place. In ref. [5] the expression for effective value of radiation resistance was obtained:

$$R_{kj}^{*} = R_{kj} + \sum_{lq \neq kj} R_{lq}\, z_{lq}^2 \frac{\omega_{kj}^4}{(\omega_{lq}^2 - \omega_{kj}^2)^2} \frac{(\phi_{kj}(B)\,\phi_{lq}(B))^2}{\phi_{lq}^4(A)} \qquad (4)$$

where $z_{lq} = M/m_{lq}$ is the mass of discontinuity to mode mass ratio, ω_{lq} are the natural frequencies, $\phi_{lq}(\vec{x})$ are eigen functions, A is the point of excitation, B is the point of discontinuity localization.

Note that the radiation increase is possible only in case when radiation resistances (R_{kj}) are less than structural resistances. Already

this condition restricts the number of cases which are worth analysing. The most important cases are cases where sound radiation is determined by slow flexural waves.

In the A=B case discontinuity leads to decrease of vibration amplitude because the structure's input impedance increases. In the $z_{1q}<1$ case the input impedance increases as the first power of z_{1q}, while (R^{*}_{1q}) increase as the second power of z_{1q}. Hence we can always search for z_{1q} that corresponds to equal values of these terms. From the other hand $\omega M/Z_c$ must be less than a unit. From this condition we determine the highest possible magnitude of M.

One can be convinced that the radiation level growth takes place under the following condition (5):

$$R_{1q}/R_{kj} > 4\ (\omega_{1q}-\omega_{kj})^2/(\omega_{kj}-\omega'_{kj})\omega_{kj} \quad , \qquad (5)$$

where ω'_{kj} is the frequency nearest to ω_{kj} $(\omega'_{kj}<\omega_{kj})$. The eq. (5) was obtained under the assumption $|\omega_{1q}-\omega_{kj}|/\omega_{kj}<1$.

The eq. (5) restricts the class of structures whose radiation is sensibile to discontinuity. Let $\omega_{1q}=\omega'_{kj}$ and rewrite (5) in the following form:

$$R_{1q}/R_{kj} > 4/\omega G(\omega) \quad , \qquad (6)$$

where G(ω) is the function of resonance density. Eq. (6) has a general form, that allow us to analyse the structures of different kind.

The comparative analysis for beams, plates and shells show that shells are the most sensibile to discontinuity. Here it is both high resonance density and strong difference between radiation resistances.

Now we'll analyse the sound radiation dependence on the distribution function of discontinuities. For simplicity, we consider sound radiation of a flat plate. In a more common case, variations are qualitative rather then quantitative.

The space spectrum of the vibration field is represented as follows:

$$w(\vec{k})= \frac{1}{4\pi^2} \sum_{1q} w_{1q}\ S_{1q}(\vec{k}) \quad , \qquad (7)$$

where $S_{1q}(\vec{k})=\iint_{\Sigma} \phi_{1q}(\vec{x})\exp(i\vec{k}\cdot\vec{x})d\vec{x}$ is the form function.

The expression for the sound radiation has a form:

$$P(z,\vec{x})= \sum_{1q} \frac{i\,\rho_o c_o P}{2\pi\, m_{1q}(\omega^2_{1q}(1-i/Q)-\omega^2)} \iint_{-\infty}^{\infty} \frac{S_{1q}(\vec{k})\ \exp(i\vec{k}\cdot\vec{x} + z\cdot\sqrt{k_o^2-\vec{k}^2})}{\sqrt{k_o^2-\vec{k}^2}}\, d\vec{k} \quad , \qquad (8)$$

where ρ_o, c_o is the density of fluid and sound velocity, respectively, $k_o=\omega/c_o$, z is the normal to the plate surface Σ, P is the exciting force.

We use the results of ref. (6) and rewrite eq. (8) in the following form:

$$P_o = \frac{k_o F \exp(ik_o R)}{2\pi R} \cdot \frac{\rho_o c_o S(\bar{K})}{Z_o}, \qquad (9)$$

where $R=\sqrt{z^2 + x^2}$, $k_o R \gg 1$, $\bar{K}=k_o z/R$.

One can see from eq. (9) that the sound radiation is proportional to characteristic impedance ratio. Acoustic impedance depends on the magnitude of the form-function at the stationary phase point of the integral (8). It is evident that $S(\bar{K})$ corresponds to the square of the acoustic active region.

Under $S(\bar{K})$ definition it is the convolution of Fourier transforms of $\tilde{\psi}_{1q}(\vec{x})$ function and the weight function $\theta(\vec{x})$. Function $\tilde{\psi}_{1q}(\vec{x})$ is the prolongation of $\psi_{1q}(\vec{x})$ on the infinite plane, $\theta(\vec{x})=1$ if $x \propto \Sigma$ and $\theta(\vec{x})=0$ outside Σ region. In the case of the structure with discontinuities whose mass distribution is given by expression $m_s=M\cdot\Phi(\vec{x})$, where $\int\Phi(\vec{x})d\vec{x}=1$, the eigen-functions of such system have the following form [6]: $\psi'_{1q}(\vec{x})=\psi_{1q}(\vec{x})/\Phi^{1/2}(\vec{x})$.

Therefore the form-function can be expressed by the convolution of three Fourier transforms:

$$S_{1q}(\bar{K})=G(\tilde{\psi})*G(\theta)*G(\Phi^{-1/2}) \qquad (10)$$

If the radiation is caused by slow flexural waves, $G(\tilde{\psi})\sim\delta$. Hence the cause of radiation is either edges (θ function) or discontinuities (Φ function). The width of the space spectrum increases proportional to the width of θ, Φ spectra. Thus one can state that the greatest alternation of sound radiation pattern takes place for a single local discontinuity. We note that similar results were obtained earlier by an other method of analysis (eq. 3).

In conclusion, we represent the results of calculation of the frequency response (FR) characteristic of a cylindrical shell. A steel shell of finite length is submerged in water. The parameters of the shell: L/R=5, h/R=0.01, Q=100, M=1% of the total mass of the shell (L is the shell length, h is the shell walls thickness). A thin line corresponds to M=0 case, while a thick line, to M=1%. On the first hand we point, that the FF is enreached. The high order multipole modes of the vibration field are displayed in radiation. Here the radiation directivity of appearing peaks has a simple dipole shape and doesn't depend on the order of the vibration field mode. It means that the energy is canalized by dipole modes. Moreover, one can prove that the directivity coincides with the characteristic directivity that has a simple dipole shape in the frequency range, which corresponds to Fig. 1 [7].

SUMMARY

Now we formulate the main results of our paper.

1. It was shown that discontinuity can be the cause of extremely high level of noise and the mechanism of radiation increase was explained.
2. The conditions of radiation increase were obtained and the class of structures whihc are the most sensible to discontinuity was determined.
3. The influence of discontinuity distribution was analysed. A single local discontinuity leads to the most alternation of radiation pattern.

All these results can be used for the rough estimation of sound radiation level. The eq. (4) allow us to evaluate the contribution of the each channel of energy canalization. Thus we can determine the

directivity of sound radiation from structures with discontinuities.

Authors believe that their results can help to solve of the important problem of human protection against high level noise.

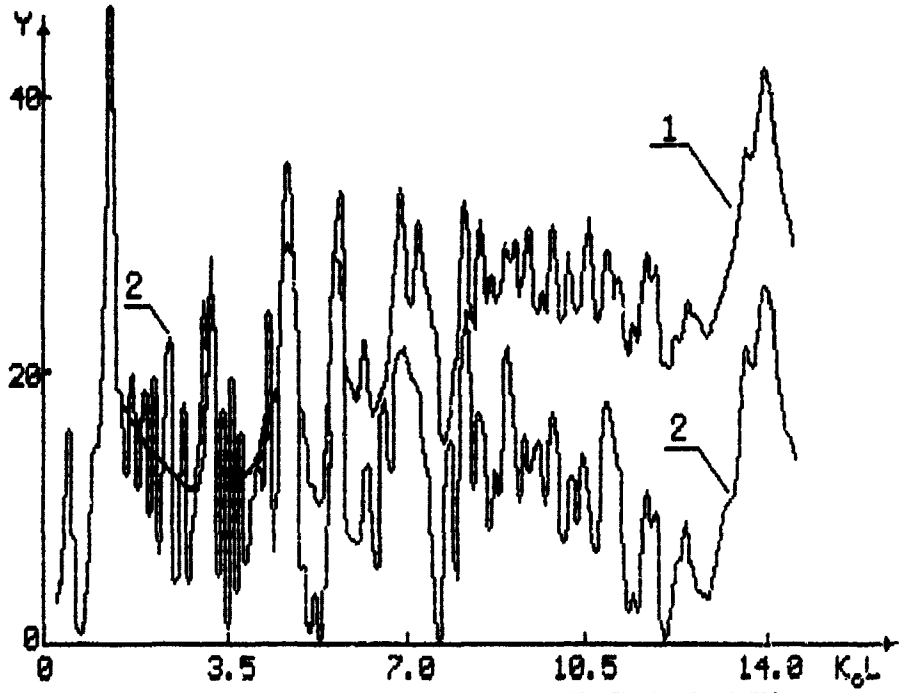

Fig. 1--Frequency response. $Y=P/(ik_0F/4\pi r)$ (dB)
Line 1 corresponds to homogeneous shell,
Line 2 - the shell with mass M=1%.

REFERENCES

1. Maidanik G., Maga L.J. "Response of coupled basic one-dimensional dynamic system", J. Sound Vibr., **111**, N3, 1986, 361-375.

2. Maidanik G., Dickey J. "Response of coupled one-dimensional dynamic system", J. Sound Vibr., **121**, N2, 1988, P.187-194.

3. Skudrzyk E. The Foundation of Acoustics. Springer, Vienna, 1968.

4. Korotin P.I., Lebedev A.V. "Sound radiation by inhomogeneous mechanical system with distributed parameters", Vibroacoustic fields of complex objects and their diagnosics. Collected art. ed. B.M.Salin, Ins. Appl. Phys. Ac. Sci. USSR, Gorky, 1989, 8-33, (in russian).

5. Lebedev A.V. "Influence of local inertial inhomogeneity on the sound radiation of complex mechanical system", Akust. J. **35**, 1989, 689-695, (in russian), Sov. Phys. Ac. **35**, 1989 (in english).

6. Skudrzuk E. Simple and Complex Vibratory Systems, Pennsylvania State U.P., State College, PA, 1968.

7. Lebedev A.V. "The peculiarities of the sound radiation by thin cylindrical shells of finite length", Preprint N253, Ins. Appl. Phys., Ac. Sci. USSR, Gorky, 1990 (in russian).

APPENDIX

The α, β, γ values are determined by the following expressions [4]:

$$\alpha = -\frac{1}{2}\,\mathrm{Re}\left\{ \sum_{\substack{lq\neq \\ kj}} Z_{lq} \sum_{p=1}^{n} \frac{(\omega'_{kj})^3 \langle F|\psi_{lq}\rangle \langle F|\psi_{kj}\rangle}{m_{lq}^2 |\Omega^2_{kjlq}|^2 m_{kj}^2 \omega_{kj}^2 \eta'_{kj}} (Z_p + Z_p^*) \cdot \psi_{lq}(\vec{r}_p)\, \psi_{kj}(\vec{r}_p) \right\} ,$$

$$\beta = \frac{1}{2}\,\mathrm{Re}\left\{ \sum_{\substack{lq\neq \\ kj}} Z_{lq} \sum_{p=1}^{n} \sum_{r=1}^{n} \frac{(\omega'_{kj})^4 (\langle F|\psi_{kj}\rangle)^2 Z_p Z_r^*}{m_{lq}^2 |\Omega^2_{kjlq}|^2 m_{kj}^2 \omega_{kj}^4 \eta'^2_{kj}} \cdot \psi_{lq}(\vec{r}_p)\, \psi_{kj}(\vec{r}_p)\, \psi_{lq}(\vec{r}_r)\, \psi_{kj}(\vec{r}_r) \right\} ,$$

$$\gamma = -\frac{1}{2}\,\mathrm{Im}\left\{ \sum_{\substack{lq\neq \\ kj}} Z_{lq} \sum_{p=1}^{n} \sum_{r=1}^{n} \frac{(\omega'_{kj})^4 \langle F|\psi_{kj}\rangle \langle F|\psi_{lq}\rangle}{m_{lq}^2 |\Omega^2_{kjlq}|^2 m_{kj}^2 \omega_{kj}^2 \eta'_{kj}} \cdot \psi_{lq}(\vec{r}_p) \psi_{kj}(\vec{r}_r) \sum_{\substack{st\neq \\ kj}} \frac{\psi_{st}(\vec{r}_r)}{m_{st}} \left(\frac{Z_p Z_r}{\Omega^2_{kjlq}} - \frac{Z_p^* Z_r^*}{\Omega^{*2}_{kjlq}} \right) \right\} ,$$

where ω'_{kj}, η'_{kj} are natural frequncies and decrements of the structure with discontinuities, $\Omega^2_{kjlq} = \omega'^2_{kj} - \omega^2_{lq}$, n is the number of discontinuities. The angle parentheses mean the scalar multiplication operation. All equations were obtained under $Z_{lqst} = Z_{lq}\delta_{ls}\delta_{qt}$ condition (δ_{ls} - Kroneker symbol).

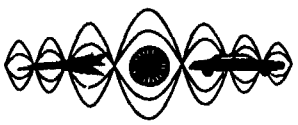

SECOND INTERNATIONAL CONGRESS ON
RECENT DEVELOPMENTS IN AIR- AND
STRUCTURE-BORNE SOUND AND VIBRATION
MARCH 4-6, 1992 AUBURN UNIVERSITY, USA

A NEW APPROACH TO THE ANALYSIS OF SOUND RADIATION FROM FORCED VIBRATING STRUCTURES

T.M. Tomilina

Blagonravov Institute of Engineering Research,
Griboedov St.,4, Moscow 101830, USSR

ABSTRACT

A new approach and fast numerical algorithm based on the Equivalent Sources Method are presented for solving the radiation problem of a forced vibrating structure in medium for the case of known linear operator describing the elastic sourface vibrations in vacuum. It is obtained the one-step solution to this problem with controlled accuracy. In this way both the structure surface vibration in medium and the sound field are described by the same system of functions — Green's functions of simple sources, placed inside the structure. This algorithm is mathematically backgrounded and its peculiarities are investigated in details. The answer to the question, how to choose the optimal values of its parametrers, is obtained. Several new results are presented which are concerned with the sound energy characteritics of force vibrating beams and open shells with known loss factor and their dependencies on geometric and physical parameters.

1 INTRODUCTION

In various branches of acoustics it is often required to solve the acousto-elastic problem of sound radiation from a finite elastic structure vibrating in a medium under the action of kinematic or force exitation. There is a large body of literature on the problem where a number of methods have been proposed, the Boundary Element Method (in combination with the Finite Element Method) being the most commonly used (see, e.g.,[1]).

Recently, a comparativily new approach was introduced in acoustics for treating the problem, which accured to be, from numerical point of view, more efficient when applied to structures of complex geometry [2–9]. The principal idea of the approach is in replacing the structure under study by an ensembly of point sources (equivalent sources — ES) located inside the structure.

This Equivalent Sources Method — the ESM (in the American literature it is called the Method of Superposition — SUP) was proposed in 1930-ies by V.D.Kupradze for obtaining an approximate solution of the boundary value problem of the Neumann or Dirichlet type[2]. It was widely used in Russian pubblications in 1960–70-ies for solving the Neumann problem in electrostatics, elastostatics and electrodynamics. There are several works of this period where the method was mathematically backgrounded (see review in [3]). The extention of the ESM to the radiation problem for a forced vibrating body (with prescribed external forces) was given in [3]. It was shown in the work that the equivalent sources, with properly defined amplitudes, are good modelling not only the radiated sound field outside the structure but the structure suface vibration as well. The main numerical features of the method were also investigated in this paper.

The fact that both the structure vibration and the sound field are described, in the ESM, by the same system of functions (i.e., by the ES) greatly simplifies the corresponding numerical algorithms and reduces considerably the computation time (compared to the commonly used methods). Its high efficiency was confirmed in the paper [8] were the ESM was compared with the BEM in the scattering problem for elastic shells.

There is one more important feature of the ESM. It has a controlled accuracy, and one can easily find the necessary compromise between the accuracy of the results obtained and the volume of computations.

It is the objective of the report to show how to choose the optimal values of the parameters of the ESM algorithm. Several results are presented which are obtained bythe ESM and concern the sound energy characteristics of forced vibrating beams and open shells with known loss factor and their dependencies on geometric and physical parameters.

2 THE ESM ALGORITHM AND ITS PARAMETERS

The mathematical formulation of the acousto-elastic problem is as follows.Considering the forced vibrating structure as an elastic body of finite size V with a closed surface S and trying to predict its harmonic field in the boundless medium one has to find a solution to the Helmholts equation

$$\Delta p + k^2 p = 0, \tag{1}$$

satisfying the radiation condition

$$\lim_{r\to\infty} r(dp/dr - \imath kp) = 0 \tag{2}$$

and two boundary conditions on the body surface S:

$$v_n = (\imath\omega\rho)^{-1}\partial p/\partial n = v \qquad on\ S \tag{3}$$

$$Lv + p = f \qquad on\ S \tag{4}$$

Here p is the sound pressure, k is the wave number, v denotes the medium particles velocity in n-direction, v denotes the elastic body particles velocity in n-direction, n is the outward normal, L is a linear operator describing the elastic structure surface vibrations in vacuum, f is the prescribed external force acting on the structure (factor $\exp(-\imath\omega t)$ is suppressed). In this problem the amplitudes of surface vibration v and pressure p are unknown, and the external force is known.

It should be emphasised that the known operator L in eq.(4) is defined with respect to the structure surface. It might be a differential operator (as for beams and thin plates) or matrix operator resulting from a finite element procedure after eliminating all inner degrees of freedom.

Let us consider the extention of the ESM to the acousto-elastic problem (1)–(4). According to the ESM one must approximately represent the pressure field radiated from the surface S by a sum of simple fields generated by N point sources (monopoles or dipoles) placed inside V on an auxiliary surface S_0 or on a line l_0 (Fig.1.):

$$p(r) \simeq \sum_{j=1}^{N} \mu_j g(r, r_j), \qquad r_j \in S_0 \tag{5}$$

It is assumed that the coordinates r_j of the equivalent sources are prescribed, but their amplitudes m_j are to be found. The Green's function g is known: e.g. for a monopole $g(r, r_j) = \exp\imath k|r - r_j|)/4\pi|r - r_j|$. The modelling sound pressure (5) produces on S the normal velocity function

$$v_n(s) \simeq \sum_{j=1}^{N} \mu_j h_j(s), \tag{6}$$

where $h_j = (\imath\omega\rho)^{-1}\partial g(s, r_j)/\partial n$ is the normal velocity created on $S(s)$ by a unit source at the point r_j.

The pressure in the form (5) satisfies already the Helmholts equation (1) and the radiation conditions (2), it rests to satisfy the boundary conditions (3),(4). Subtituting equations (5) and (6) into these conditions one obtains on S approximately:

$$f(s) \simeq \sum_{j=1}^{N} \mu_j[Lh_j(s) + g_j(s)] = \sum_{j=1}^{N} \phi_j(s) \tag{7}$$

Thus, the unknown amplitudes are to be found as a coefficients of the expansion of prescribed function f in nonorthogonal functions $h_j(s)$ and $g_j(s)$. The fundamental theoretical result underling this type of expansion is that the functions $h_j(s)$, $g_j(s)$ are linearly independent and form complete function systems (in the least mean square sence) [1]. It means that the quadratic functional

$$J_f = \int\int |f - \sum_{j=1}^{N} \mu_j \phi_j|^2 \tag{8}$$

tends to zero when number of functions encreases ($N \to \infty$). As a result of the completeness, every finite function f on S can be expanded in these functions with arbitrary high accuracy depending on the number N. Minimisation of the functional (8) by varying m_j leads to the system of N linear algebraic equations for N unknown amplitudes of the equivalent sources

$$A\vec{\mu} = \vec{b}, \tag{9}$$

where $\vec{\mu} = \{\mu_1, ..., \mu_N\}$ is N-vector of amplitudes, N x N-matrix A and N-vector $\vec{b}$ have the following components:

$$A = \{A_{kj}\} = \{\frac{1}{S}\int_S\int \phi_j^* \phi_k dS\},\ b = \{b_j\} = \{\frac{1}{S}\int_S\int \phi_j^* f dS\}, \tag{10}$$

For a given number N the accuracy of the field modelling (5) can be estimated with the help of the magnitude of the functional J_f. The minimized value of functional (8) was taken as a measure of the accuracy of the algorithm. It was verified by some test calculations that the computational error for the sound field quantities (pressure and particle velocities) does not exceed this error in boundary conditions (8).

If the model parameters μ_j are found from the Eq.9 and if the calculation accuracy (the corresponding values of J_f) is accepted as satisfactory, then both the acoustic field parameters and vibrating amplitudes can be calculated easily with the help of the representations (5) and (6'.

3 PROPERTIES OF THE METHOD

As one can see from what was said above, the ESM solution is composed of two parts: determination of the equivalent sources amplitudes and calculations of sound field characteristics.

The solution of the system (9) is, in its sense, a typical inverse problem or a back radiation problem which, as a rule, is associated with nonstable numerical algorithms. For the given case it was investigated in details in [3]: analytically (for an infinite cylinder) and numerically (for a finite cylinder). The main phisical aspectes are as follows. When the given function f to be expanded in series (7) on S are smooth enough, the amplitudes of the equivalent sources are rather small. But high space frequency components of these functions might give the equivalent sources of great amplitudes and they oscilate over the auxiliary surface S_0 (or line l_0) with high frequencies. It is the case for example when the given functions f have random experimental or numerical errors. Numerically this peculiarity displays itself in bad conditioning of the matrix A in equation (9).

The next peculiarity of the method is that the high frequency oscillations of the equivalent sources does not show itself in the sound field outside the structure surface S. The reason is that the evanescent waves generated by such sources decay rapidly and practically vanish at the nearest distance from S. As a result the whole numerical algorithm of the ESM demonstrates the stable work over the wide range of numerical parameters variance.

The accuracy of the method depends most of all on the parameters of the auxiliary surface So on which the ES are located. Theoretically, the question of the finding necessary surface S_0 is not investigated. Practically it can be found as a compromise between the computation time and the required accuracy. Making S_0 closer to S reduces the error, but increases the number N and the computing time. (The computing time is determined by the time of inversion of NxN-matrix A). Since the error can be readily checked, the necessary combination of accuracy and computing time is obtained by running several test calculations. By the same way, one can avoid an icrease in the error at the natural frequencies of the volume enveloped by S_0.

The error of the algorithm strongly depends on the discretisation parameter M of the structure surface S and on the number N of the ES. It should be noted that a number of authors (e.g.[7]) determine

amplitudes μ by the collocation method ($M = N$). We have found that in some cases this method gives an error of thousand percent due to descrepancy in the interstices though at the colocation points the boundary conditions are satisfied almost exactly.

The dependence J_f on M is associated with the accuracy of integration in Eqs.(10). Fig.2 presents the typical diagrams of decay of the relative error $\Delta = J_f^{1/2}/f_{max}$, while the number M increases. It is useless to increase M without increasing the number of sources N. The optimal discretization number M_0 of the radiator sourface is two or three times the number N: $M_0 = 2.5N$.

Typical dependences of the error on N are shown in Fig.3. The optimal number N_0 corresponds to the beginning of the mildly sloping part of the curve $\Delta(N)$ which can be easily obtained by several testtest calculations. It is worth noting that the accuracy of the method increases as the frequency gets higher (see Fig.3). Other properties of the ESM see in Ref.[3].

4 EXAMPLES

In the acoustic design of structures the most important are the energy characteristics, that is to say, total sound power flow and its equivalent — radiation impedance or admittance. Fig.1 presents some structures for which all these characteristics and their dependences on geometric and physical parameters have been investigated [3,4,9]. Here are two general observations concerning these dependences.

It is surprising how strongly the total power flow emitted from an open thin-walled structure depends on the thickness of the structure. As an example Fig.4 shows the real part of radiation impedance $Re(Z)$ vs frequency for an open thin-walled tube. The total flow of radiated sound energy $W = \frac{1}{2}|v_0|^2 Re(Z)$ is proportional to the tube thickness.

It is practically important to know the amount of energy emitted with noise and absorbed in the structure due to damping of material. Investigations we carried out for finite beams and plates performing flexural vibration in medium under the action of external forces yield the following general conclusion: at low frecuencies the behaviour of the structure, e.g. the quality factor of the structure resonances, is determined by internal damping; at high frequencies the losses are due to the sound radiation; in the frequency range around the coincidence frequency these two types of energy losses are comparable. This obeervation is well illustrated in Fig.5 where the real part of the input admitance $Y = v/f_0$ if presented, η beeng the loss factor of the material. One more is illustrated in Fig.6. Eight piezoceramic rings which are interacting with each other through the surrounding medium (water) are drived independently by eight external forces (voltages) of the same amplitude and phase. Fig.6 shows the amplitudes distribution of the radial velocity of the rings which noticably depends on the frequency. The observations concerning the energy mentioned above are valid for this structure as well.

5 CONCLUSION

The results of study of the ESM properties and its applications have showed that this method of solving the noise prediction problem poseses the remarcable features: simplicity, controlled accuracy, small computing time. The advantages of the method become impressing when it is applied to the radiation problem for a complicated structure driven by external forces. This makes the Equivalent Sources Method to be a useful tool for predicting of sound fields in noise control engineering, in hydroacoustics and other branches of acoustics.

REFERENCES

1. M.C.Junger and D.Feit, Sound, Structures, and Their Interactions. MIT, Cammbridge, MA, 1986.

2. V.D.Kupradze, An approximate solutions to problems of mathematical phisycs. Uspehi matematicheskikh nauk (Progress in math.sciences), v.22(1), 1967, p.59–107.

3. Y.I.Bobrovnitskii and T.M.Tomilina, Application of ESM to a calculation of a finite elastic structure radiation. Soviet Physics acoust., v.36(4), 1990, p.334–338.

4. T.M.Tomilina and Y.I.Bobrovnitskii, Modelling by point sources and sound field analysis of machines and vibrating structures. Proc. Inter-Noise 1990, v.2, p.895-898.

5. M.Heckl, Bemerkung zur Berechnung der Schallabstrahlung nach der Methode der Kugelfeldsynthese. Acustica,v.68, 1989, p.251–257.

6. M.Ochmann, Die Multipolstrahlersynthese - ein effektives Verfahren sur Berechnung der Schallabstrahlung von schwingenden Strukturen beliebiger Oberflachengestalt. Acustica, v.72, 1990, p.233–245.

7. G.H.Koopmann ,L.Song, and J.B.Fahnline, A method for computing acoustic fields based on the principle of wave superposition. The Journal of the Acoust. Soc.of America, v.86(6), 1989, p.2433–2438.

8. R.D.Miller, E.T.Moyer,Jr., H.Huang, and H.Uberall, A comparison between the Boundary Element Method and the Wave Superposition approach for the analysis of the scatterred fields from rigid bodies and elastic shells. The Journal of the Acoustical Society of America, v.89(5), 1991, p.2185–2196.

9. T.M.Tomilina, Radiation impedance of a hollow cylindrical radiator. Soviet Physics Acoustics,v.35(1), 1989, p.73–75.

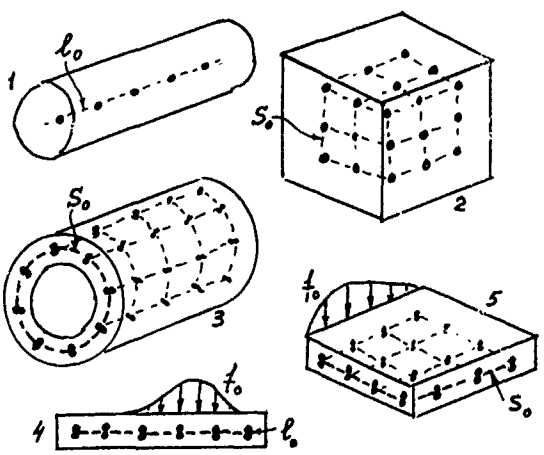

Fig.1 Modeling of vibrating structure by monopoles or dipoles placed on auxiliary surface S_0 or line l_0
1-pulsating cylinder;
2-elastic box with given vibration amplitudes;
3-pulsating open tube;
4-forced vibrating beam (4) and plate (5)

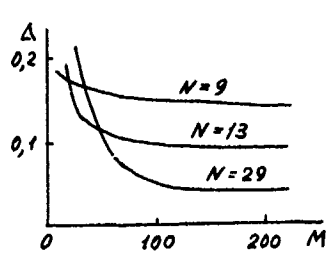

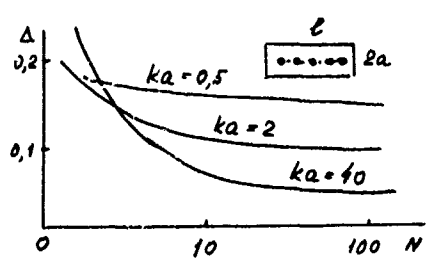

Fig.2,3 The error of the algorithm as a function of discretisation number M of the radiated surface S and of number N of the equivalent sources for pulsating cylinder ($l/a = 4$)

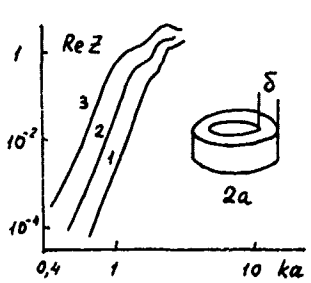

Fig.4 Radiation impedance of a pulsating ring with thickness $\delta = 0.02a(1)$, $\delta = 0.2a(2)$, $\delta = 0.2a(3)$

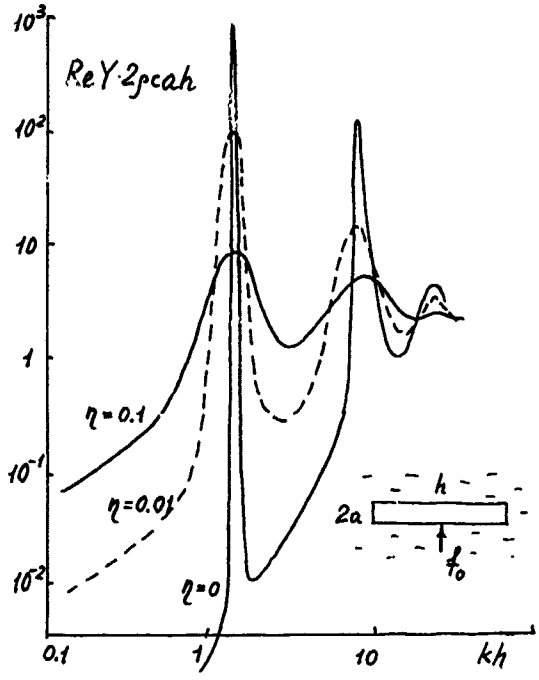
10^3
ReY·2pcah
10^2
10
1
10^{-1}
10^{-2}
η=0.1
η=0.01
η=0
h
2a
t_0
0.1
1
10
kh

Fig. 5

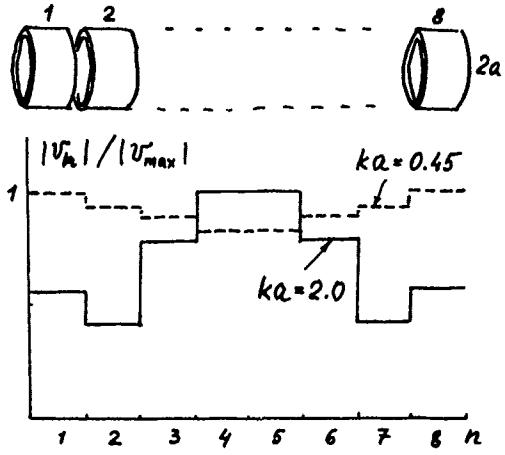
1
2
8
2a
$|V_n|/|V_{max}|$
ka=0.45
1
ka=2.0
1 2 3 4 5 6 7 8 n

Fig. 6

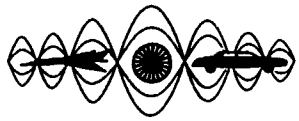

SECOND INTERNATIONAL CONGRESS ON
RECENT DEVELOPMENTS IN AIR- AND
STRUCTURE-BORNE SOUND AND VIBRATION
MARCH 4-6, 1992 AUBURN UNIVERSITY, USA

THE ASYMPTOTIC METHOD FOR PREDICTING ACOUSTIC RADIATION FROM A CYLINDRICAL SHELL OF FINITE LENGTH.

Lebedev A. V.
Institute of Applied Physics Academy of Sciences of the USSR,
603600, N. Novgorod, USSR.

ABSTRACT

This report is concerned with acoustic radiation by a thin cylindrical shell of a finite length. In spite of a great number of publications dealing with this problem, until now there is no effective method of its analysis in a general case. Our method is based on the idea which was proposed by Skudrzuk [1] for the dynamic response analysis of complex structures. The main aim of this paper is to represent the solution as asymptotic row.

Results of the calculation within the frames of the proposed model are compared with the known data. The agreement between the calculations allows us to use the model as the first approximation in more accurate studies of structure radiation.

INTRODUCTION

It is known that correct solution the problem of sound radiation by a structure includes joint solution of integral and differential equations. Such a method isn't convenient because it leads to very complicated calculations, requiring the great volume of memory and the high speed of computation.

In our paper the scheme of simple asymptotic theory is given. The choice of geometry and the kind of structure are explained by the model of the sound radiation problem of cylindrical shell.

The small parameter is the relation of acoustic power to the total energy of the shell. The main term of the asymptotic row corresponds to the solution of the self-consistent problem without radiation losses. The sense of this assumption is evident. The radiation losses determine the amplitudes of continuous spectrum waves, while these waves describe far distance coupling between shell pieces. The main term of the asymptotic row corresponds to adjacent piece coupling, while each next term describes high and high order coupling.

MAIN APPROXIMATION AND THE SCHEME OF SOLUTION

We will derive the expressions describing the shell radiation on the basis of Kirchhoff's integral. Assume that the driving force is directed normally to the side surface. We also use the symmetry of the problem.

All values which enter the integral are expressed by the superposition of different order polar-angle modes. But we express their amplitudes not by the superposition of longitudinal modes, as it is often made, but by the superposition of the primary and different order secondary *(reflected at the shell ends)* wave contributions. Due to the linearity of the problem the final equation for the m-th order polar-angle mode radiation field will have the following form:

$$P_m(\omega,\vec{r})=P_m^{(o)}(\omega,\vec{r})\ (1 + G_m(\omega,\vec{r})), \qquad (1)$$

where $\vec{r}$ is the radius-vector originating from the drive point towards the observation point, $P_m^{(o)}(\omega,\vec{r})$ is the contribution of the primary source (the waves running from the drive point), and $P_m^{(c)}(\omega,\vec{r})\cdot G_m(\omega,\vec{r})$ is the contribution of the waves reflected at the shell ends (resonant component).

We will assume that (i) the radiation loading on elastic motion of the shell is small in comparison with the inertia loading and (ii) the shell length (L) is large as compared to its radius (R).

A low value of the radiation loading means that we can neglect radiation losses and continuous-spectrum waves in the solution of the self-consistent problem of the shell vibration. This assumption is justified by the condition $c_f/c_o \ll 1$, where c_f is the velocity of the flexural wave and c_o is the velocity of the sound wave. In most cases c_o is less than the velocity of the longitudinal (c_l) and the torsional (c_t) waves. Because of that $c_f \ll c_o$, c_l, c_t and we can suppose that the flexural waves are *weakly coupled* to other kinds of wave motions. This relation for flexural waves occurs under the condition $h/R<0.1$, where h is the thickness of the shell walls [2].

When the second condition is fulfilled, the density of the hydrodynamic forces of the reaction to the shell vibration is, in fact, independent of the parameter L/R. Note that the first condition is quite a general one and does not depend on the shape of the structure, while the second condition is specified for an elongated body.

By virtue of the absence of the singularities in the integral expressions for sound radiation in the far zone, we can change the order of summing and integration and rewrite the expression derived from Kirchhoff's integral in the form:

$$P(\omega,\vec{r})=iP_d(\omega,\vec{r})\cdot\rho_o c_o R/\rho_s c_l h \sum_m i^{-m}\{\hat{w}_m(\theta)J_m(\xi\cos(\theta)) + i\cos(\theta)\hat{p}_m(\theta)J_m'(\xi\cos(\theta))\}\cos(m\phi)\ , \qquad (2)$$

$$\hat{w}_m(\theta)=R/L\int_{s_1}^{s_2} w_m(s)\cdot\exp(-i\xi\cdot s\cdot\sin(\theta))ds\ ,$$

$$\hat{p}_m(\theta)=R/L\int_{s_1}^{s_2} p_m(s)\cdot\exp(-i\xi\cdot s\cdot\sin(\theta))ds\ ,$$

where $P_d=ik_oF\exp(i\vec{k}_o\vec{r})/4\pi r$ determines the radiation of an infinitely small element of fluid under the action of the excited force F; ρ_s, ρ_o are the densities of the shell material and fluid, respectively; c_l, c_o are the sound velocity magnitudes in the shell and in the fluid; Ω is the dimensionless frequency; $\Omega=\omega R/c_l$, $\xi=k_oR$; $w_m(s)$ and $p_m(s)$ are, respectively, the complex amplitude of the velocity and pressure at the shell surface in the m-th wave harmonic, the velocity is normalized to

$V_0=\iota F/2\pi\rho_s RLh\omega$ while the pressure to $\rho_0 c_0 V_0$; $s=x/R$, $s=0$ corresponds to the drive point, and s_1, s_2, to the shell ends; $J_m(y)$ and $J'_m(y)$ are the m-th order Bessel function and its derivative; θ is the angle between normal to the shell surface and radius-vector $\bar{r}$, ϕ is the polar angle.

The expression (2) as a whole can be considered as the superposition of different-order polar-angular multipole contributions. The terms proportional to Bessel's functions describe the contribution of the monopole sources distributed over the surface, and the terms proportional to the derivatives of Bessel's function, the contribution of the same dipole sources.

We will now analyze the characteristic radiation, or the radiation from the shell whose resonant peaks are overlapped. If we determine this component of radiation we can determine resonant component using a multireflection method.

When solving the problem we will use the Fourier transform technique and obtain the relation between the mean-value (characteristic) velocities, pressures and dispersion relation of the structure. The fluid-loading will be determined under the condition of weak compressibility ($c_f/c_0<1$). The absence of acoustic losses allows us to reduce the Fourier integral to the sum of four residues. The two first residues correspond to the flexural travelling and decaying waves, the other two, to the torsional and longitudinal decaying waves. A relatively complicated procedure for the determination of the roots of the denominator in the Fourier integrals may be simplified by neglecting the transverse inertia terms and by using a small value of parameter h/R (see Appendix). The first assumption means that we, in fact, neglect longitudinal and torsional waves. The second one allows us to divide the dispersion relation into two weakly coupled terms which correspond to *the membrane* and *the plate* regions in the frequency response of shell vibration [1].

When determining the poles in the case m=0 (monopole mode-shapes), we encounter the difficulties that are associated with two branches of the dispersion curve. One of them corresponds to slow waves weakly coupled to radiation ($c_f/c_0<1$), while the other one, to fast waves strongly coupled to radiation ($c_f/c_0>1$). The description of acoustically fast modes needs an exact expression for acoustic impedance, taking into account the fluid compressibility (the k_0L parameter), and the diffraction peculiarities that occur at the shell ends.

Monopole forms are an exception to the rule and do not keep within the frames of a simple model. Therefore we will estimate monopole modes contribution.

We will first estimate the lower frequency of monopole vibrations. Apparently, it can be determined as the ordinate of the intersection point of the dispersion curves which correspond to flexural and sound waves ($\Omega=\sigma\cdot c_1/c_0$). The branch below the curve $\Omega=\sigma\cdot c_1/c_0$ corresponds to slow waves [3]: $(\Omega^2-1)\cdot\sigma\cdot\mathrm{sign}(\mathrm{Re}(\sigma))+\delta\cdot\Omega^2=0$, where $\delta=\rho_0 R/\rho_s h$ and $\sigma=k_x R$, k_x is the axial component of the structure's wave number.

Therefore the lower monopole frequency is $\Omega_0=(1+g^2)^{1/2}-g$. One can see that the frequency is determined only by the relative stiffness of the shell $g=\rho_0 c_0 R/2\rho_s c_1 h$.

The vibration amplitude in monopole modes at frequencies lower than Ω_0 is determined by the shell rigidity to overall stress, therefore $V_{mon}\sim V_0(\Omega/\Omega_0)$. Consequently, the radiation will have the form:

$$P_{mon}\sim\iota P_d\rho_0 c_0 R\Omega/\rho_s c_1 h\Omega_0^2$$

Below we will see that P_{mon} is smaller than the dipole radiation at

low frequencies. At high frequency ($\Omega \geq 1$) $k_0 L \gg 1$ because $L/R \gg 1$ too. Therefore we can use asymptotic equation for acoustic impedance and estimate monopole radiation in high frequency region. One can be also convinced that the magnitude of monopole radiation in $\Omega > 1$ region is small too [4].

When the conditions $\sigma_j \ll \xi$ (i.e. slow elastic waves) or $\mathrm{Im}(\sigma_j) \gg \xi$ (i.e. high decaying waves) are met, the Fourier transforms $w_m(s)$ and $p_m(s)$ are equal to

$$\int_{-\infty}^{\infty} A \exp(i(\sigma_j|s| - \xi \cdot s \cdot \sin(\theta))ds \approx 2iA/\sigma_j \qquad (3)$$

Thus, the characteristic radiation is a result of the superposition of the m-th order multipoles that are spread uniformly over the rings λ_j/π-wide.

Note that this is quite a general representation of the solution, which is a consequence of the low speed of elastic waves [4]. But in contrast to a plate or a beam, where the travelling and decaying waves have equal lengths, the shell has different λ_j, owing to the finiteness of its curvature, which results in interesting peculiarities in resonance shell radiation (fig. 2 below).

In the frequency range $\Omega \ll 1$, the equation determing the pole position can be simplified essentially taking into account $|\sigma| \ll m$ for flexural waves and $|\sigma| \gg m$ for torsional and longitudinal decaying waves.

Using these approximate equations for σ_j and eq. (3), we will determine the contribution of the m-th order sources to the characteristic radiation in the low frequency region:

$$p_m^{(c)}(\omega,r) = \rho_0 c_0 R\, i^{1-m}\, \Omega/\rho_s c_1 h \{J_m(\xi\cos(\theta))\,[(a/(a+b)b^2)$$

$$(1+(a+b/a-b)) - 2/(a^2-b_0^2)] + \xi\cos(\theta)J_m'(\xi\cos(\theta))\,[(a/a+b)^{1/2}$$

$$(1+(a+b/a-b)^{1/2})/mb^2 - (2\beta)^{1/2}(a^2-b_0^2)^{-5/4}])\cos(m\phi),\quad m>0 \qquad (4)$$

where $b^2=\Omega^2(\varepsilon_m+\delta/m)-\hat{\Omega}_m^2$, $b_0^2=\Omega^2\varepsilon_m+\hat{\Omega}_m^2$, $a^2=1-\nu^2$, $\varepsilon_m=1+1/m^2$, $\Omega_m^2=\beta^2(m^2-1)^2$, $\hat{\Omega}_m^2=\beta^2(2m^2-1)$, $\beta^2=h^2/12R^2$, ν is the Poisson ratio.

One can easily see that the dipole radiation is predominant in $\Omega \ll 1$ region, while the monopole radiation magnitude is more smaller and displays in neighborhood of $\theta, \phi \approx \pi/2$.

The eq. (4) also shows that the contribution of travelling flexural waves (the terms proportional to (a+b)/(a-b) ratio) becomes predominant when the frequency increases. The contribution of longitudinal and torsional waves is a resonant one and is displayed at the frequencies $\Omega \gg 1$, where different wave motions are strongly coupled. Since the longitudinal and torsional waves have high σ_j, their radiation in the low frequency region is lower than the flexural wave radiation.

We will now determine the resonant radiation component. The wavelength on the order of the shell length L corresponds to lower resonant frequencies, therefore we can ignore the reflection of primary decaying waves at the shell ends, without restricting the generality of the problem. Then employing the successive reflection method and the condition of the acoustic short circuit of flexural waves, we can show that the presence of boundaries provokes the appearance of two additional radiation sources. For example, when the drive point coincides with the middle of the shell, we obtain the expression for the secondary source

amplitude:

$$q_s = -q_0\cos(\xi a\sin(\theta)/2)\exp(i\sigma_1 a/2)[1- V_1- V_2\sigma_1/\sigma_2]/ \quad (5)$$
$$(1 - V_1\exp(i\sigma_1 a)),$$

where q_0 is the contribution of the primary source that corresponds to a travelling flexural wave, V_1 is the reflectivity of the travelling flexural wave, and V_2 is the transform coefficient, which describes the excitation of the secondary decaying wave by the primary travelling wave. For simplification, the secondary longitudinal and torsional waves (V_3 and V_4 coefficients) are not considered; $a=L/R$.

To determine the resonant component of radiation, we must distinguish the contribution of the travelling flexural wave. Therefore we will represent the characteristic radiation in terms of equivalent sources (the eq. (3), (4)):

$$k_1=[\hat{w}_m(\theta)]_{travel}/[\hat{w}_m(\theta)]_{total}= z_1/z_1+z_2+z_3+z_4$$

$$k_2=[\hat{p}_m(\theta)]_{travel}/[\hat{p}_m(\theta)]_{total}= \Delta_1/\Delta_1+\Delta_2+\Delta_3+\Delta_4 \quad (6)$$

$$\Delta_j=z_j/\gamma_j \cdot \quad \gamma_j^2= m^2+\sigma_j^2 \cdot$$

$$z_j=\gamma_j^2/[\sigma_j^2((8\sigma_j/\gamma_j)^2+2\beta^2\gamma_j^4-\varepsilon_m\Omega^2+\bar{\Omega}_m^2-38\Omega^2/4\gamma_j], \ m>0$$

Using eq. (6), we can determine the total radiation of the m-th mode-shape of the shell as follows:

$$P_m(\vec{r}) = P_{1m}^{(c)}(\vec{r}) \ (1+k_1 q_s/q_0) + \quad (7)$$
$$P_{2m}^{(c)}(\vec{r}) \ (1+k_2 q_s/q_0),$$

where $P_{1m}^{(c)}(\vec{r})$ is the distributive monopole source contribution to the characteristic shell radiation (the terms are proportional to Bessel's function in (2), (4)) and $P_{2m}^{(c)}(\vec{r})$ is the same dipole source contribution.

In the frequency region $\Omega<1$, where different types of waves are weakly coupled, we have $k_1=k_2=0.5$. Consequently, eq. (7) will take on the form:

$$P_m(\vec{r})=P_m^{(c)}(\vec{r})\cdot(1 + G_m(\Omega,\theta)) \ , \quad (8)$$

where for Navier boundary conditions ($V_1=-1$, $V_2=0$) function $G_m(\Omega,\theta)$:

$$G_m(\Omega,\theta)=-\cos(\xi a\sin(\theta)/2)/\cos(\sigma_1 a/2)$$

The function $G_m(\Omega,\theta)$ is a decaying oscillatory function of the frequency Ω and the angle θ. Since it enters eq. (8) additively for each m, we can say that the characteristic radiation, indeed, describes the shell radiation without the elastic wave diffraction effects. In a more general case, the contribution of the simple and dipole layers must be analysed separately. The functions $G_m(\Omega,\theta)$ are slightly different for each of this terms.

The amplitude of the resonant component of the shell radiation in the low frequency region has the following form (where Q is the Q-factor of the shell vibration):

$$P_m^{(c)}/2\mathrm{sh}(\pi(1+2n)/8Q)\approx 4QP_m^{(c)}/\pi(1+2n), \ Q\gg\pi(2n+1)/8, \ n=1,2,...$$

One can see that as the frequency increases the resonance contribution decreases exponentially as $\exp(-\pi n/4Q)$ and complete radiation slightly

differs from the characteristic level.

When the drive point does not coincide with the middle of the shell the expression describing the shell radiation will have the following form (Navier conditions):

$$G_m(\Omega,\theta)=-\{\sin(\sigma_1(\alpha/2+\Delta s))\exp(-\imath\xi\alpha\sin(\theta)/2)+ \quad (9)$$
$$\sin(\sigma_1(\alpha/2-\Delta s))\exp(\imath\xi\alpha\sin(\theta)/2)\}/2\sin(\sigma_1\alpha),$$

where Δs is the distance from the drive point to the middle of the shell.

When $\theta=0$ we have the following expression:

$$G_m(\Omega,\theta)=-\cos(\sigma_1\Delta s)/2\cos(\sigma_1\alpha/2)$$

In other words, the solution has the structure that is similar to the one described above, but the result of the interference of the secondary source is described by the multiplier $\cos(\sigma_1\Delta s)$ rather than $\cos(\xi L\sin(\theta)/2R)$. In a more common case (9) the solution combines two multipliers. One of them describes the delay of acoustic waves travelling from secondary sources, while the second one, the phases of sources. In other words expressions (7), (9) describe the sound radiation of one dimensional acoustic antenna that is consisted of three groups of multipole sources.

Finally, we will perform a comparative analysis for the calculations by the formulas that were presented above and in ref. [5]. We will neglect the mode coupling and take the Navier conditions as the boundary conditions. Figure 1 shows results of the computations of dipole radiation (m = 1), that are based on the suggested *"three sources"* model (the expressions were presented above) and on the well-known traditional *"mode method"*. The dashed line depicts the characteristic level corresponding to the dipole radiation. One can see that the calculations within the two models yield similar results particularly in the low-frequency region. The divergence is caused by the influence of the *continuous-spectrum waves* and manifests itself in the frequency region $k_0L\gg1$. These waves cause acoustic coupling between sources of radiation. For example, at $k_0L\cong2\pi$ the secondary sources which are $\lambda_0/2$-distant from the primary source damp it by their radiation. Characteristic frequencies slightly differ from $2\pi n$; so we have a possibility to make our solution more accurate by taking into account the radiation coupling of the sources that are placed in free space. But this specification is beyond the scope of our paper.

Summing up we can say that small value of radiation efficiency allows us to simplify the solution essentially. The solution is factorized. As a result, the peculiarities caused by dispersion relation and the characteristics of boundaries or other elastic waves scatterers can be separated. The solution becomes more illustrative and comprehensible. Using the suggested method we can simply analyse the boundary conditions influence on the shell's radiation. It seems that in contrast to plates and beams the level of shell radiation has the maximum in the case of free ends [3] (fig. 2).

ACKNOWLEDGEMENTS

The author wishes to thank Prof. L.A.Ostrovsky, Dr. B.M.Salin and Dr. R.A.Dudnik for their support and constructive criticism that helped to improve results of this paper.

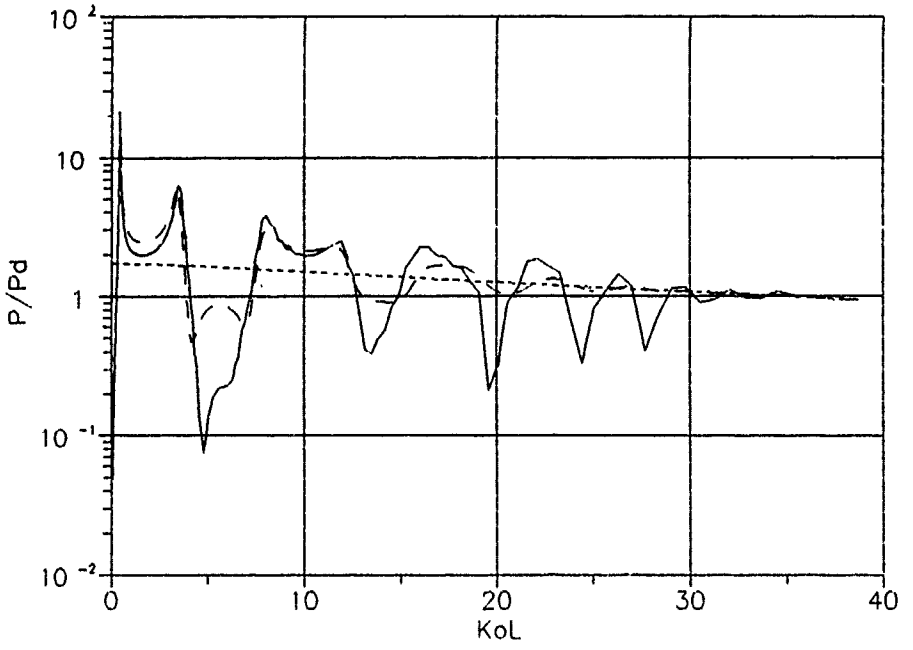

Fig. 1--Sound radiation by steel shell submerged in water
Shell's parameters: L/R=20, h/R=0.01, Q=10.
Solid line - modal solution, long dash - suggested model.

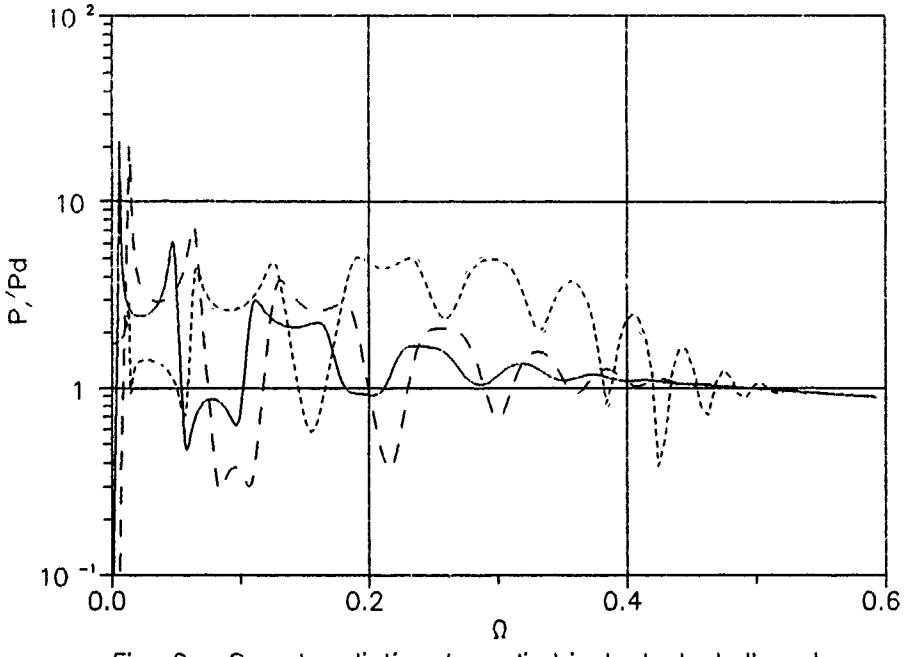

Fig. 2--Sound radiation by cylindrical steel shell under different boundary conditions. Solid line - Navier cond., long dash - rigidly fixed ends, short dash - free ends.

REFERENCES

1. Skudrzyk E. "The mean-value method of predicting the dynamic response of complex vibrations", J. Acoust. Soc. Am. **64**, 1980, 1105-1135 .
2. Muzychenko V.V., Paniklenko A.P., Rybak S.A., "Dispersion curves for normal wave in a cylindrical shell and the conditions for spatial coincidence near critical frequencies", Akust. J. **30**, 1984, 83-88 (in russian), Sov. Phys. Ac. **30**, 1984 (in english).
3. Lebedev A.V. "The peculiarities of the sound radiation by thin cylindrical shells of finite length", Preprint N**253**, Ins. Appl. Phys., Ac. Sci. USSR, Gorky 1990 (in russian).
4. Junger M.C., Feit D. Sound, Structures and Their Interaction, MIT Press, Cambridge, 1972.
5. Lebedev A.V. "On the mode coupling of the thin cylindrical shell of finite length", Akust. J. **34**, 1988, 1087-1094 (in russian), Sov. Phys. Ac. **34**, 1988 (in english).
6. Liessa A.W. The Vibration of Shells, US Government Printing Office, Washington, NASA SP-**288**, 1973.

APPENDIX: THE EQUATIONS DETERMING THE POLE POSITION

The dispersion relation for the shell has the following form [6]:

$$\Omega^2(\varepsilon_m+\delta\mu_m)=a^2\sigma^4/(m^2+\sigma^2)^2 \quad +\beta^2((m^2-1)^2+2m^2\sigma^2+\sigma^4), \qquad (A1)$$

where $\varepsilon_o=1$ and $\varepsilon_m = 1 + 1/m^2$; μ_m is the added mass coefficient.

The fluid motion is weakly compressible, so μ_m is equal to [4]:

$$\mu_m \approx (m^2+\sigma^2)^{1/2} \qquad (A2)$$

Substituting $\gamma^2=m^2+\sigma^2$ and taking a small value of β^2, we get an approximate relation determining the two first σ_j, which correspond to flexural waves:

$$\Omega^2(\varepsilon_m\gamma^4+\delta\gamma^3 sign(Re\gamma))=a^2(\gamma^2-m^2)^2+\Omega_m^2\gamma^4 \qquad (A3)$$

The relation describing the longitudinal and torsional waves can be derived by dividing the complete equation (A1) by the (A3):

$$C^2\gamma^4-C\delta\Omega^2\gamma^3 sign(Re\gamma)+(\delta\Omega^2+2Cm^2a^2)\gamma^2-$$
$$(4Cm^2a^2+\delta^2\Omega^4)\delta\Omega^2\gamma sign(Re\gamma)+C^3/\beta^2=0\ , \qquad (A4)$$
$$C=a^2-(\Omega^2\varepsilon_m+\hat{\Omega}_m^2)$$

The residue of this division is of the order of $O(\beta^2/a^2-\Omega^2)$. It means that equations (A3) and (A4) are valid when $|a^2-\Omega^2| \ll \beta$. One can see that (A3) corresponds to the "membrane" region of the shell vibration, while (A4) corresponds to the "plate" region of the shell vibration in the normal direction. In the low frequency region ($\Omega \ll 1$) σ_j which correspond to the flexural waves are determined from (A3), while in the high frequency region ($\Omega \gg 1$), from (A4).

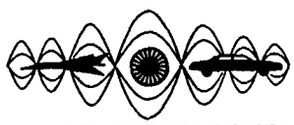

SECOND INTERNATIONAL CONGRESS ON
RECENT DEVELOPMENTS IN AIR- AND
STRUCTURE-BORNE SOUND AND VIBRATION
MARCH 4-6 1992 AUBURN UNIVERSITY USA

STRUCTURAL RESPONSE AND RADIATION OF FLUID-LOADED STRUCTURES DUE TO POINT-LOADS

Chafic M. Hammoud
Per G. Reinhall
Mechanical Engineering Department
University of Washington
Seattle, WA 98195
U.S.A.

The spatial decay of the response and acoustic radiation of a submerged infinite beam excited by a time-harmonic point-load are investigated using Fourier transfroms and asymptotic approximation for above and below coincidence conditions. For vey lightly internally damped beams, the spatial decay of the flexural waves is shown to undergo a large increase as the driving frequency is increased beyond the coincidence frequency. Moderately damped beams are found to not exhibit this behavior in that the decay rate of flexural waves undergo only a small increase as the forcing frequency goes from below to above coincidence. The decay rate is also shown to be sensitive to the amount of internal damping of the beam for both above and below coincidence frequencies.

I. INTRODUCTION

In the modeling of large submerged structures it is often necessary to truncate the structure in order to facilitate the analysis. For example, in investigating the radiation and response of a submarine hull due to a point-load, it is necessary to limit the region of study to a small section of the hull, at the location of the point-load. It is assumed however, that the behavior of the cutout section approximates the response of the entire structure. For this to be the case, there must be an insignificant amount of vibratory motion at the truncation boundaries. The decay of the vibratory motion over the structure must therefore be estimated before deciding the size of the truncated section.

The present study addresses this problem by investigating the structural response and radiation of a submerged infinite beam excited by a time-harmonic point-load. The vibration and the radiation of the beam are derived as a function of the distance to the excitation point. The spatial decay of the response is studied for both below and above coincidence conditions. Criteria pertaining to truncation are discussed.

The determination of the structural response and acoustic radiation of vibrating submerged structures represent an issue of considerable mathematical complexity. Numerous investigators have developed a diversity of solution approaches. Feit [1], for instance, derived the farfield directivity pattern of the radiated pressure for a point-excited plate using Fourier transform representations and asymptotic expansions of the solution. Nayak [2] studied the drive line admittance for a thin infinite fluid-loaded plate excited by a force and moment input through the use of Fourier transform. His results show that the plate admittance is considerably reduced by the fluid-loading, especially for ratios of acoustic to structural wavenumber less than 0.3. Nagaya et al.,[3] proposed a new technique for solving vibration problems of arbitrarily shaped plates by utilizing a Fourier expansion collocation technique. Their method produces the equations for finding the natural frequencies, the displacement, and the pressure field. Stepanishen et al.,[4,5] suggested another technique based on the use of modal expansion and wave-vector/time-domain method, to evaluate the time dependent acoustic loading on submerged vibrating structures. This approach portrays the fluid-loading as a modal sum in which each of the modal pressures is expressed as a sum of convolutions involving modal impulse response that are dependent on Mach number and modal velocity components. Extensive numerical results are presented to illustrate the characteristics of modal impulse response and the radiation impedances for a simply supported plate. In this paper, we have chosen a solution method which involves spatial Fourier transforms and an asymptotic approximation technique described by Nayak [2] and Crighton [6] in order to solve for both the beam response and the acoustic pressure field.

II. MATHEMATICAL ANALYSIS

Consider an infinite, thin elastic beam, and bending stiffness EI. The beam lies in the plane $z=0$, and it is driven by a time-harmonic point force, $Fe^{-i\omega t}$, at $x=0$, and $y=0$ (as shown in Fig. 1). The upper half space, $z \geq 0$ is occupied by an inviscid uniform fluid of density ρ, sound speed c. The bottom half of the beam at $z<0$ is assumed to be exposed to a vacuum.

Fig. 1. Thin elastic beam in fluid

The differential equation governing the displacement of the beam in the transverse direction is given

$$EI \frac{\partial^4 W}{\partial x^4} + \rho_s A \frac{\partial^4 W}{\partial t^2} = q(x,t) , \tag{1}$$

where E is the Young's modulus of the beam, I is the moment of inertia, ρ_s is the beam density , A is the cross-sectional area , and q(x.t) is the sum of loads applied to the beam surface. Assuming the beam is excited by a point-force $Fe^{-i\omega t}\delta(x)$, where $\delta(x)$ is the delta function, one may consider a solution of the form

$$W(x,t) = W(x) \exp(-i\omega t) , \tag{2}$$

where W(x) is the spatial dependence of displacement of the beam. Substituting Eq.(2) into Eq.(1) and suppressing all time-dependent variables $e^{-i\omega t}$, one may express Eq.(1) as

$$EI \frac{\partial^4 W}{\partial x^4} - \rho_s A \omega^2 W = F\delta(x) - p(x,0) , \tag{3}$$

where p(x,0) is the fluid reaction force acting on the beam surface.

The wave equation for the resulting acoustic pressure p(x,z) in the fluid is determined from the Helmholtz equation

$$\frac{\partial^2 p}{\partial x^2} + \frac{\partial^2 p}{\partial z^2} + K^2 p = 0 , \tag{4}$$

where $K = \omega/c$ is the acoustic wavenumber. The pressure field is coupled to the beam wave motion by the requirement that the normal component of the acceleration of the fluid particles must be equal to the acceleration of the beam

$$\left.\frac{\partial p}{\partial z}\right|_{z=0} = h\rho\omega^2 W(x) . \tag{5}$$

Equations (2)-(5) may be solved using the Fourier transforms pair

$$\tilde{f}(\gamma_x,\gamma_y)=\int_{-\infty}^{+\infty}\int_{-\infty}^{+\infty}f(x,y)e^{-i(\gamma_x x+\gamma_y y)}dx\,dy\,, \tag{6}$$

$$f(x,y)=\frac{1}{(2\pi)^2}\int_{-\infty}^{+\infty}\int_{-\infty}^{+\infty}\tilde{f}(\gamma_x,\gamma_y)e^{i(\gamma_x x+\gamma_y y)}d\gamma_x d\gamma_y\,. \tag{7}$$

As a result, the inverse Fourier transform of the beam displacement and the pressure field become

$$W(x)=\frac{F}{2\pi EI}\int_{-\infty}^{+\infty}\frac{\sqrt{K^2-\gamma^2}\,e^{i\gamma x}}{(\gamma^4-K_b^4)\sqrt{K^2-\gamma^2}-\dfrac{ih\rho\omega^2}{EI}}d\gamma\,, \tag{8}$$

and

$$p(x,z)=-\frac{ih\rho\omega^2F}{EI}\int_{-\infty}^{+\infty}\frac{e^{i(\gamma x+z\sqrt{K^2-\gamma^2})}}{(\gamma^4-K_b^4)\sqrt{K^2-\gamma^2}-\dfrac{ih\rho\omega^2}{EI}}d\gamma\,. \tag{9}$$

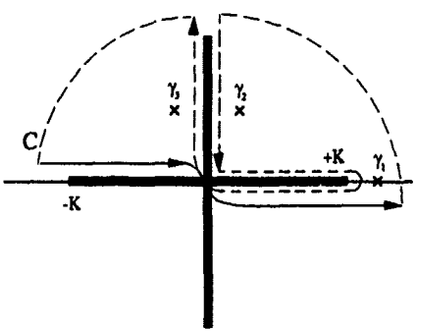

Fig. 2. Path of integration of the displacement and pressure integrals

These integrals are evaluated by an integration technique developed by Crighton[6]. A contour C is assigned in the upper half of the complex plane γ, shown in Fig. 2. The path of integration consists of an integral along the real axis excluding the singularities on the positive real axis γ, a second integral along the circular arc which vanishes as the arc radius $\rightarrow\infty$, and a third integral along the branch cuts from $\gamma=\pm K$. Since C is a closed contour, Eqns.(8) and (9) are then evaluated by considering residue contributions to C and the branch cut integral.

The necessity of employing a branch cut integration rises from the fact that the numerator of both Eqs. (8) and (9) are multivalued functions because of the term $(K^2-\gamma^2)^{1/2}$. The branch cut contour satisfies $Re(K^2-\gamma^2)^{1/2}>0$ for $K>|\gamma|$, and $Im(K^2-\gamma^2)^{1/2}>0$ for $K<|\gamma|$. These conditions, also defined by Nayak[2] as the causality requirements, ensure the appropriate decay of the beam displacement field and the acoustic pressure at infinity. The poles of the residues are found by numerically solving for the roots of the characteristic equation and then selecting only the appropriate roots satisfying $Im(K^2-\gamma^2)^{1/2}>0$. In this case, we always have a positive real root γ_1, and two complex conjugate roots γ_2, γ_3 (as indicated in Fig. 2). The characteristic equation is given by

$$EI\left(\gamma^4-K_b^4\right)\sqrt{K^2-\gamma^2}\;=\;ih\rho\omega^2.$$

Rewriting Eqs.(8) and (9) in terms of the residues and the branch cut integral followed by a substitution of γ by $K+iu$, one obtains

$$W(x) = \frac{F}{2\pi EI}\left[2\pi i\left(\sum_{j=1}^{3}\text{Residues}_j\right)_{\text{displacement}} - 2\left(\frac{h\rho\omega^2}{EI}\right)e^{iKx}\int_0^{\infty}\frac{\sqrt{u}\sqrt{u-2iK}\,e^{-ux}}{u\left((K+iu)^4 - K_b^4\right)^2(u-2iK)+\left(\frac{h\rho\omega^2}{EI}\right)^2}du\right],$$

and

$$p(x,z) = -\frac{ih\omega^2 F}{2\pi EI}\left[2\pi i\left(\sum_{j=1}^{3}\text{Residues}_j\right)_{\text{pressure}} + 2i\,e^{iKx}\left(\frac{ih\rho\omega^2}{EI}\right)\int_0^{\infty}\frac{\cos\left(z\sqrt{u^2-2iKu}\right)e^{-ux}}{\left((K+iu)^4 - K_b^4\right)^2\left(u^2-2iKu\right)+\left(\frac{h\rho\omega^2}{EI}\right)^2}du - 2e^{iKx}\int_0^{\infty}\frac{\sin\left(z\sqrt{u^2-2iKu}\right)e^{-ux}}{\left((K+iu)^4 - K_b^4\right)^2\left(u^2-2iKu\right)+\left(\frac{h\rho\omega^2}{EI}\right)^2}du\right]$$

The latter two expressions may now be asymptotically evaluated as $x \to \infty$ using Watson's Lemma integral [7].

$$W(x) \cong \frac{Fi}{EI}\left[\sum_{j=1}^{3}\frac{e^{i\gamma_j x}}{4\gamma_j^3 + \frac{\gamma_j(\gamma_j^4 - K_b^4)}{(\gamma_j^2 - K^2)}}\right] - \frac{F}{2h\rho\omega^2}\sqrt{\frac{2K}{\pi}}\,x^{-3/2}\,e^{i(Kx - \pi/4)}, \tag{10}$$

and

$$p(x,z) \cong \left(\frac{h\rho\omega^2 F}{EI}\right)\left[\sum_{j=1}^{3}\text{Residues}_j\Big|_{\text{displacement}}\frac{e^{iz\sqrt{(K^2-\gamma_j^2)}}}{\sqrt{(K^2-\gamma_j^2)}}\right] + \left(\frac{F\,e^{iKx}}{2\pi}\right)\left[\frac{-2\,e^{-i\pi/2}}{x} + \pi\sqrt{\frac{2K}{\pi}}\,e^{i3\pi/4}\,\frac{z}{x^{3/2}}\right]. \tag{11}$$

Internal dissipation in the beam is introduced by using a complex modulus of elasticity, $E = E(1-i\mu)$, where μ being the loss factor. This will force the real pole γ_1 to displace off the real axis in a counterclockwise fashion in relation to the origin. Thus, a minor adjustment must be made to the path of integration when material damping is considered.

III. Numerical Results

When the beam wavenumber exceeds the acoustic wavenumber (below coincidence), no acoustic pressure field is radiated. This is shown by examining the integrand of Eq.(9). When $K^2 < \gamma^2$, ζ becomes imaginary ($\zeta = i(\gamma^2 - K^2)^{1/2}$), indicating that no propagative plane wave can emerge from the source plane with a real angle of incidence. The exponent of the function shown in the integrand of Eq.(9) becomes negative and real which yields an exponential decay as the distance from the source plane increases. The resulting non-propagating waves are called evanescent waves because they stay closeto the source and die out just a few wavelengths away from the source. It should be noted that for a real, finite structure there is always some radiation into the ambient fluid below coincidence. This can be shown in an intuitive fashion by noting that the lack of radiation from a perfect, infinite, and undamped structure below coincidence is due to the symmetry of the flexural motion. Figure 3i illustrates the cancellation of the pressure wave due to symmetry in the case of an infinite beam. For a damped and finite structure, this symmetry

In order to obtain an estimate of the spatial decay of the vibratory motion of the beam, the amplitude of the transmitted waves along the beam surface, at a variable point B normalized with respect to the amplitude at a fixed point A, is considered (see Fig. 8).

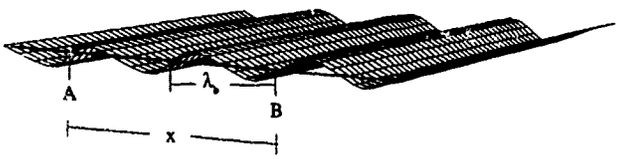

Fig. 8. Flexural waves in the beam

In Figures 9-12 this normalized amplitude is shown as a function of x/λ_b, where x is the separation of points A and B along the beam and λ_b is the wavelength of the structural propagating wave. In order to satisfy the condition of the asymptotic expansion, it is necessary to choose point A at a location that is significantly removed from the application point of the harmonic load (this requirement does not hinder our analysis due to the linear nature of the problem). Figures 9 and 10 show the spatial decay of the beam response for below and above coincidence, respectively, for a range of internal damping values (ω_c is taken to be the coincidence frequency). These figures clearly illustrate the role of acoustic radiation in the damping of flexural vibration of the beam. Figure 9 shows the decay of flexural motion for below coincidence, i.e. small amounts of acoustic radiation. Any small amount of radiation in this case is due to the "spatial unsymmetry" induced by the internal damping.

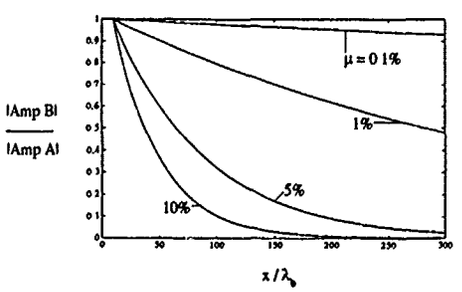

Fig. 9. Amplitude ratio of an infinite steel beam in water below coincidence, $\omega/\omega_c = 0.2$

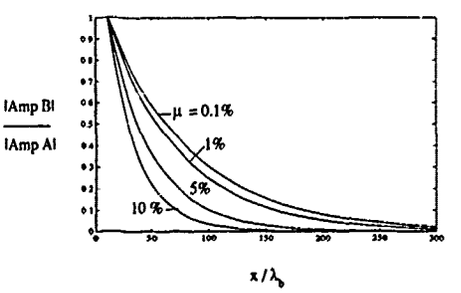

Fig. 10. Amplitude ratio of an infinite steel beam in water over coincidence, $\omega/\omega_c = 1.5$

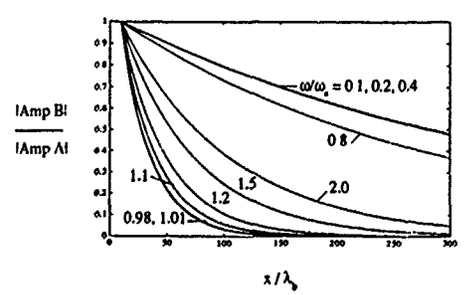

Fig. 11. Amplitude ratio of an infinite steel beam in water with 1% structural damping at various frequency ratio

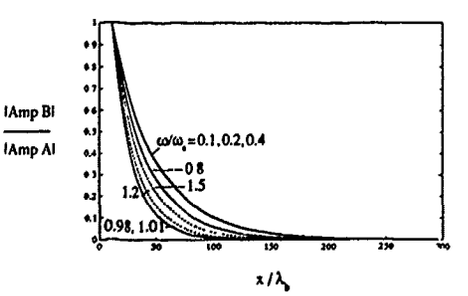

Fig. 12. Amplitude ratio of an infinite steel beam in water with 10 % structural damping at various frequency ratio

is broken and one has to expect some radiation of acoustic energy at all frequencies (as illustrated in Fig. 3ii).

When the frequency is over coincidence, the traveling waves in the beam decay more rapidly. This is due to the fact that the energy created from the vibration is leaked into the fluid medium in the form of acoustic radiation. This can also be shown from the integrand of Eq.(9). When $K^2 > \gamma^2$, ζ is real, a plane wave emerges from the source and propagates. In this case, the exponent of the function is imaginary and it is responsible for the phase change of the plane wave.

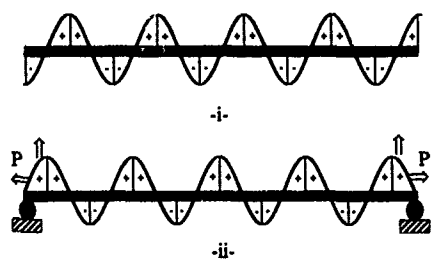

Fig. 3. i. Flexural waves of infinite beam below coincidence;
ii. Edges radiation of a finite beam below coincidence.

Using Eq.(11), the acoustic pressure field of a steel beam in water is shown in Figures 4-7 for different structural damping and frequencies. Below coincidence, the acoustic pressure field displays a rapid exponential decrease going away from the beam surface; no energy is radiated due to the absence of any discontinuity in the beam and the presence of evanescent plane waves. In contrast, the pressure field for frequency above coincidence (Fig. 5) is substantially influenced by the structural damping embedded in the beam, as anticipated. Figures 6 and 7 show the pressure distribution for below and above coincidence.

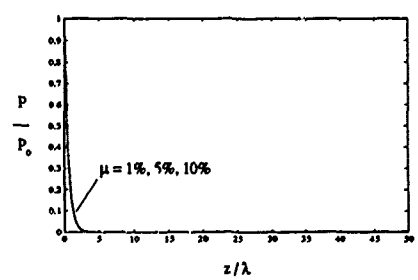

Fig. 4. Pressure ratio from an infinite steel beam in water, below coincidence, $\omega/\omega_c = 0.2$. z is the normal distance away from the beam, λ is the acoustic wavelength and λ_b is the beam wavelength, μ is the beam loss factor. $x/\lambda_b = 10$

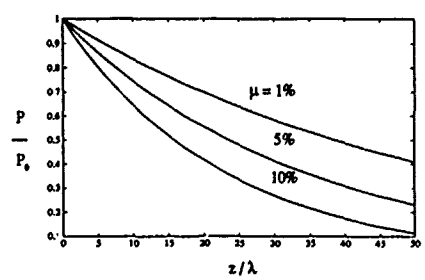

Fig. 5. Pressure ratio from an infinite steel beam in water, over coincidence, $\omega/\omega_c = 1.5$. $x/\lambda_b = 10$

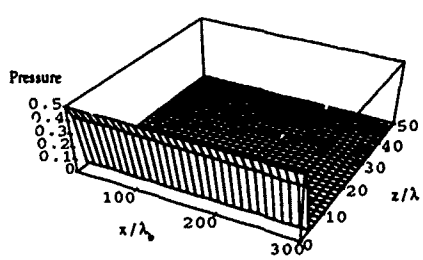

Fig. 6. Pressure distribution from an infinite steel beam in water, below coincidence, $\omega/\omega_c = 0.2$. $\mu = 1\%$

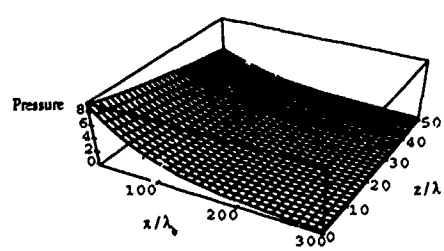

Fig. 7. Pressure distribution from an infinite steel beam in water, overcoincidence, $\omega/\omega_c = 1.5$. $\mu = 1\%$

Figure 10 shows the decay of the structural motion for an above coincidence situation ($\omega/\omega_c = 1.5$). Comparing this figure with Figure 9, it is apparant that for very low values of internal damping the structure is sensitive to the crossing of the coincidence frequency. However, for moderately low internal damping of 5% or higher it is seen that the spatial decay becomes rather insensitive to this increase in driving frequency. Furtheremore, it can be seen that by increasing the structural damping of the beam we can significantly increase the decay for both below and above coincidence situations.

Figures 11 and 12 further illustrate the difference between light and moderate structurally damped beams. Figure 11 shows the significant effect of the acoustic radiation on the spatial decay rate of a lightly damped beam (1%). It is worth noting that the decay rate is at maximum when the forcing frequency is equal to the coincidence frequency. The behavior of a beam with 10 % structural damping is shown in Figure 12. In this case, the added acoustic radiational efficiency in going from low frequencies to frequencies above coincidence produces a surprisingly small variation in the decay rates.

IV. SUMMARY AND CONCLUSIONS

The flexural displacement and the corresponding radiated field of a fluid-loaded infinite beam excited by a harmonic point-load have been obtained using an analytical contour integration method. The decay rate of flexural waves traveling down the beam has been obtained for a range of forcing frequencies and structural damping values. For very lightly damped beams (<1%) the spatial decay rate of flexural waves is shown to experience a large increase as the driving frequency is increased through the coincidence frequency. The damping of the flexural waves above coincidence is almost entirely due to the acoustic radiation from the beam into the fluid medium. Moderately damped beams (>5%) are found to not exhibit this behavior. The decay rate of flexural waves undergo only a modest increase as the forcing frequency is increased to exceed the coincidence frequency.

The decay rate of the transverse vibration along the beam is shown to exhibit sensitivity to the amount of structural damping for both above and below coincidence conditions. As expected, it was found that the damping of the motion below coincidence is highly dependent on the internal damping of the beam due to the lack of significant energy loss in the form of acoustic radiation. Less expected was the significant sensitivity to internal damping above coincidence where the beam can function as an efficient radiator. The implication is that the addition of structural damping to submerged structures, for example with the help of constraint layer damping, may have beneficial effects for a wide range of frequencies, spanning both above and below coincidence conditions.

In the modeling of large submerged structures, it is often necessary to truncate the structure in order to facilitate the mathematical analysis. It is shown here that this truncation must be done with care in that the flexural waves require a travel distance of several hundred wavelengths before their amplitude can be considered negligible. If the size of truncated structure is chosen without consideration of the decay rate of the flexural waves, there is a possibility that the imposed boundary conditions can overly degrade the accuracy of the analysis.

For above coincidence frequencies, the propagation distance along the beam required for a 90% decrease of the wave amplitudes is between 100 and 200 wavelengths. For below coincidence frequencies, this is only true if the beam has an internal damping which exceeds 5%. Selecting a truncation size of this order of magnitude is unfortunately most often prohibitive, requiring therefore a careful evaluation of the influence of the imposed boundary conditions and the possible use of dissipative boundaries.

Finally, it should be noted that the consideration of the decay rate of transverse motion is crucial in the design of silent submerged structures. Care must be taken in the placement of excitation sources in relationship to holes, stiffeners, and other irregularities responsible for acoustic radiation below coincidence. This research effort indicates that structural damping may play an important role in addressing this issue.

V. References

[1]Feit, D., "Pressure radiated by a point-excited elastic plate," J.Acous.Soc.Am. **40**, 1966, 1489-1494.
[2]Nayak, P.R., "Line admittance of infinite isotropic fluid-loaded plates," J.Acous.Soc.Am. **47**, 1970, 191-201.
[3]Nagaya, K., and Takenchi, J., "Vibration of a plate with arbitrary shape in contact with a fluid," J.Acous.Soc.Am. **75**, 1984, 1511-1518.
[4]Liand, D.J., and Stepanishen, P.R., "Transient and harmonic fluid loading on vibrating plates in a uniform flow field via a wave-vector/time domain field," J.Acous.Soc.Am. **83**, 1988, 474-482.

[5]Ebenezer, D.D., and Stepanishen, P.R., "Transient response of fluid loaded elastic plates via an impulse response method," J.Acous.Soc.Am. **82**, 1987, 659-666.
[6]Crighton, D.G., "The free and forced waves on a fluid-loaded elastic plate," J.Sound and Vibration.**63**, 1979, 225-235.
[7]Bleistein, N., Mathematical Methods For Wave Phenomena, Academic Press, Inc.,.1984, 204-205.

SECOND INTERNATIONAL CONGRESS ON
RECENT DEVELOPMENTS IN AIR- AND
STRUCTURE-BORNE SOUND AND VIBRATION
MARCH 4-6, 1992 AUBURN UNIVERSITY, USA

ACOUSTICAL IMAGES OF SCATTERING MECHANISMS FROM A CYLINDRICAL SHELL

Charles F. Gaumond and Angie Sarkissian
Naval Research Laboratory
Washington, D.C. 20375-5000 U.S.A.
Tim Yoder
SFA, Inc.
Landover, MD 20785 U.S.A.

ABSTRACT

The bistatic form function of an end-ensonified, hemispherically endcapped cylindrical shell was computed using a boundary element method program over the frequency range from $ka = 2$ to 6. The ratio of the total length to diameter is eleven. In a display of the form function versus angle and frequency, three scattering mechanisms - *viz* reflection, diffraction and elastic wave propagation - are evident. Because these mechanisms radiate sound predominantly into different directions, single frequency acoustical images which display each of these mechanisms can be created by angular windowing. Reflection can be seen occurring at the ensonified endcap; diffraction along the whole length; and fast elastic waves with non-constant amplitude along the length. Furthermore, interference between reflection and elastic wave propagation is also evident in the form function display. Several images from the cylinder, as well as idealized targets such as a point and line, are shown at relevant frequencies.

INTRODUCTION

This paper shows the analysis of acoustic scattering from a finite, cylindrical shell with the use of acoustical imaging to understand the important, underlying scattering processes. Understanding can be obtained from acoustical images because different scattering mechanisms manifest themselves differently in the image. Once the appearance of a mechanism is known, the mechanism can often be discerned in an apparently complicated, acoustical image. Previous work has shown the appearance of reflections from curved surfaces, reflections from collections of points, internal reflections inside elastic bodies and radiation from waves propagating along long line sources[1-3]. These images were made at a single frequency from rigid and elastic spheres and from theoretical / hypothetical scatterers such as points and lines. Single frequency images are useful for investigation of frequency dependent phenomena such as dispersive waves on structures.

This paper uses this accumulated understanding of acoustical images to analyze numerically generated bistatic scattering from an end - ensonified, hemispherically endcapped cylindrical shell. The scattered pressure field is measured by a receiver which is scanned from the back-scattered direction into the forward direction. In the frequency interval $2 < ka < 6$ of interest, several phenomena are observed in bistatic angular intervals. These phenomena are analyzed by generating acoustical images from scattering data in each of the bistatic angular intervals. The basic scattering mechanisms are then displayed pictorially.

Following this introduction a plot of the bistatic form function is discussed, brief definition of the imaging method is given, several images are generated and discussed and a conclusion ends the paper.

BISTATIC FORM FUNCTION

Consider a finite, cylindrical shell composed of hemispherical endcaps with 5 m radii connected to a right circular cylindrical shell of radius $a = 5$ m and length $L = 100$ m. The thickness h is a uniform 0.05 m. This cylinder is ensonified with a uniform plane wave $P_i = p_0 e^{ikz}$ along the cylindrical axis and the scattered pressure field $P_s(\theta)$ is measured in the far field at an angle θ from the incident direction. Thus $\theta = 0°$ is in the direction of the incident wave and $\theta = 180°$ is in the back-scattered direction. The dimensionless form function is defined by the relation $P_s = p_0 a f(\theta) e^{ikr}/2r$. The form function $f(\theta)$ was generated using the boundary element code DAXESAR[4] and is shown in fig. 1.

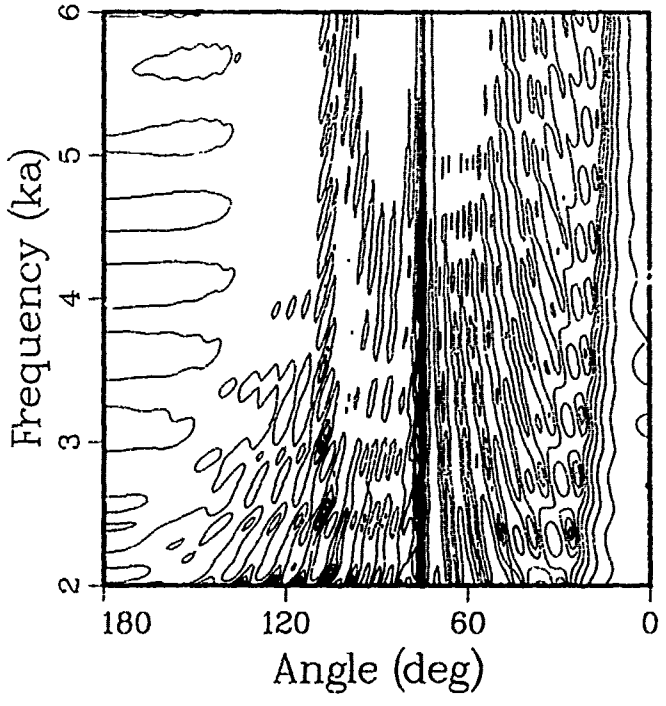

Figure 1 - - Contour plot of $20\log|f|$ as a function of frequency and angle.

The bistatic form function is plotted as $20\log|f|$ with the the horizontal axis as bistatic angle θ and the vertical axis being dimensionless frequency ka, where $ka = 2\pi a/\lambda$ and λ is the wavelength in the surrounding fluid. Contours of equal form function are plotted every 3 dB. This interesting frequency interval contains three distinct angular regions which encompass different patterns. The first region has gentle variations with frequency and angle in the interval from $\theta = 180°$ to $\theta = 130°$. In the second region there are vertical features at $\theta = 73°$ and $108°$ caused by radiation from waves propagating at the plate speed c_p[5]. The third region shows large values of the form function in the forward direction from $\theta = 50°$ to $0°$.

The pattern in the back-scattered region from 180° to 130° appears as frequency dependent stripes with a level of approximately 0 dB. This level and lack of angle and frequency dependence is consistent with a specular reflection from the hemispherical endcap. The small variations in frequency have minima which are separated by approximately $ka = 0.47 \pm 0.03$. Let us assume that this striation is caused by the interference of the specular reflection and the reradiation of sound which has traveled from the ensonified endcap to the other and back again. The total path length of this elastic wave is approximately $2L = 22a$. It follows that the ratio of the speed of this assumed wave to the speed of sound in water is $c_l/c = 3.3 \pm 0.2$. This value is consistent with the plate speed of a steel cylinder $\sim$ (5000 m/s) / (1500 m/s) = 3.3. This intermediating wave would radiate sound in the next angular region.

The next angular region extends from 130° to 50°. This region is dominated by a vertical ridge with form function of ~ 7 dB at $\theta \simeq 73°$ and a vertical stripe of hash marks at $\theta \simeq 108°$. These features are primarily due to radiation from a disturbance propagating at a speed of $c_l/c \simeq 1/\cos(73°)$. This is just the plate speed in the steel cylinder. This lends confirmation to the intermediation of the plate wave in the frequency striations of the form function from 180° to 130°. Closer inspection of the radiation peak at $\theta = 73°$ shows that the pattern is not symmetric around 73°. Instead much more sound is projected into the forward direction and relatively little is projected into angles > 73°. This is quite different from the radiation caused by a uniform wave propagating along the length of the cylinder from $z = -L/2$ to $z = L/2$. This uniform wave would radiate a pattern with angular dependence of $\sin(x)/(x)$, $x = kL(\cos\theta - \cos 73°)/2$ which is symmetric around 73°. The cause of this asymmetry will be shown with acoustical images to be an interaction between the specular reflection from the bow and radiation from the plate wave along the length of the cylinder.

The third and last angular region in the pattern lies in the forward scatter direction extending from $\theta \sim 50°$ to 0°. The form function here exceeds 25 dB. The form function in this region has been compared to scattering, or more properly diffraction, through an aperture[6]. The acoustical image from the forward scattered interval shows that the forward scattering from an extended structure such as this apparently originates from along the length of the body, not just at the ensonified end.

REVIEW OF IMAGING METHOD

The method of forming these acoustical images is based on the underlying assumption that the origin of the scattered field is a fictitious source distribution Q_i, namely

$$P_s(\vec{r}_s, \vec{k}_i) = -\frac{1}{4\pi}\int d\vec{\rho}\frac{e^{ikr}}{r}e^{-ik\vec{r}_s\cdot\vec{\rho}/r}Q_i(\vec{\rho}, \vec{k}_i) \tag{1}$$

where $\vec{k}_i$ is the incident wave vector, $\vec{r}_s$ is the far-field observation point where P_s is measured and single frequency ω is assumed. Thus the scattered field is assumed to come from a spatially extended source of any shape, not from the surface of a known shape. Experience has shown that the shape of the source distribution reveals the true location of acoustic radiation from an extended structure. Although Eq. 1 cannot be exactly inverted to determine Q_i from P_s, a filtered version Q_{ic} of this source distribution can be generated from far-field data as

$$Q_{ic}(\vec{r}, \vec{k}_i) = -\left[\frac{k^2 a P_s}{2\pi}\right]\frac{1}{2\pi}\int_0^{2\pi} d\phi_s \int_0^{\pi} d\theta_s \sin(\theta_s)e^{i\vec{k}_s\cdot\vec{r}}f(\vec{k}_i, \theta_s, \phi_s) \tag{2}$$

where f is the form function - $f = P_s 2r/aP_i$ - at scattered angle (θ_s, ϕ_s). a is the radius of the cylinder, $\vec{k}_s$ is the wave-vector in the direction of $\vec{r}_s$ and P_i is the amplitude of the incident wave at the center of the cylinder. Because there is no dependence on ϕ_s with bow-ensonification this formula simplifies to

$$Q_{ic}^N(\vec{r}, \vec{k}_i) = -\int_0^{\pi} d\theta_s \sin(\theta_s)e^{ikr\cos\theta\cos\theta_s}J_0(kr\sin\theta\sin\theta_s)f(\vec{k}_i, \theta_s) \tag{3}$$

where the source distribution has been normalized by the quantity in the square brackets of Eq. (2).

An inspection of Eq. 3 shows that the normalized, filtered source distribution Q_{ic}^N is a way of spatially displaying the complex data. In other words imaging is a linear transformation similar to the Fourier transform. Some phase information which does not appear in the amplitude display of f in fig. 1 is used to generate the spatial dependence of Q_{ic}^N. This formula can be used to determine the location of the sources of the scattered field within the limits of the resolution of the method. The limits of integration in Eq. 3 cover the whole bistatic angular interval. By constraining the limits of integration, the location of the sources of a particular feature of the scattered field in a particular angular interval can be determined up to the limits of resolution. Of course as the interval becomes smaller, the resolution becomes poorer; a trade-off is required. Limiting the aperture creates a major benefit in image understanding because it often limits the number of different acoustical processes in the picture. Some processes radiate predominantly in one direction, such as the forward direction. The form function is so large in the forward direction that these processes tend to dominate an image formed which includes this interval. With a judicious choice of values, the angular aperture can be thought of as a mechanism filter.

ACOUSTICAL IMAGES

Eq. (3) is used to generate acoustical images in a plane which cuts through the center line of the cylinder. These are displayed as contour plots in figs. 2 to 4. The horizontal axis is parallel to the axis of ensonification; the cylinder is positioned along the horizontal axis from -55 m to 55 m in the middle of each panel. All of the acoustical images shown are formed from data at $ka = 3.55$, which is a local maximum in the back-scattered direction $\theta = 0°$). In each of the figures an image of the data is shown on the left and an image from a simple model on the right. The simple model consists of a point scatterer, the form function of which is $f = A_p e^{ikz_p - kz_p \cos\theta}$ where A_p is a complex constant and z_p is the position of the point, and of a line radiator, the form function of which is $f = A_l \sin(x)/x$ with $x = (k_l L - kL\cos\theta)/2$ where A_l is a complex constant and $k_l = kc/c_l$.

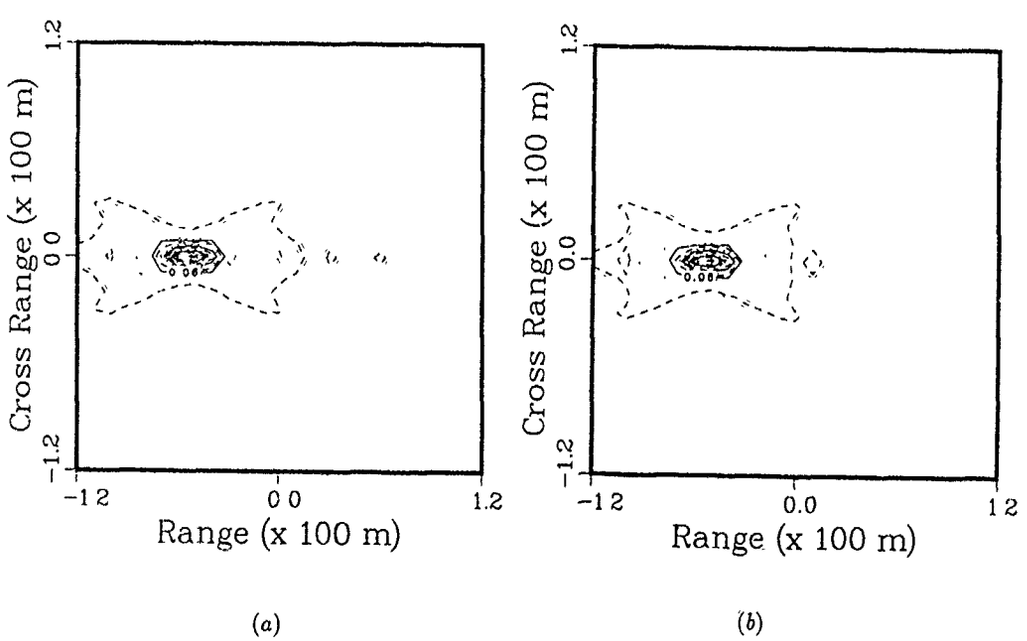

Figure 2 - - Acoustic image of (a) the cylinder with aperture 150°< θ <180°, (b) a point source with amplitude A_p = .712 and position z_p = .50m.

On the left, fig. 2(a) shows the acoustical image of the cylinder with aperture of 150°< θ <180°. The image consists of a single highlight located at approximately (-55 m, 0 m). This image strongly resembles the image shown in fig. 2(b) on the right of an idealized point scatterer with amplitude A_p = 0.712 and position z_p = -50 m. This amplitude is comparable to that of a soft or rigid sphere, which is 1. These values were determined by adjusting them until the images were nearly identical. The image of the point scatterer, incidentally, shows the resolution or point spread function of the image at this frequency with this specific aperture. It should be noted that there is sufficient resolution to confirm that the source of the scattered field is from the ensonified end of the scatterer as expected from physical intuition. Apparently the major source of reflected sound in the angular interval from 180° to 150° is simple reflection from the hemispherical endcap.

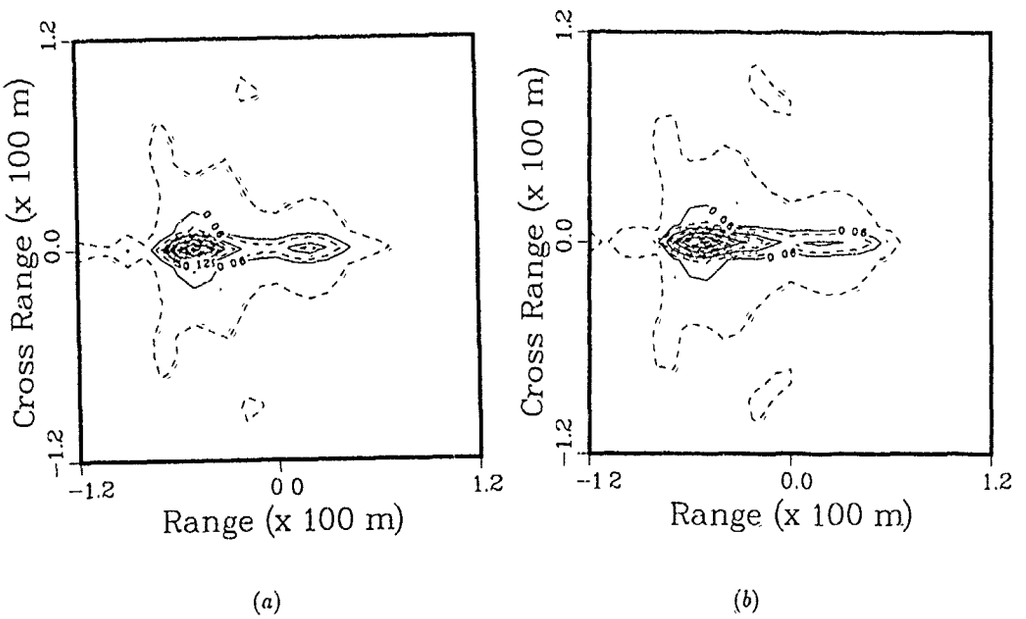

Figure 3 - - Acoustic image of (a) the cylinder with aperture 63°< θ <83°, (b) a point source with amplitude A_p = 92 and position z_p = −.50m and a uniform line source with amplitude A_l = −1.26, length L = 100m and c_l/c = 3.5.

Fig. 3(a) on the left shows the acoustical image of the cylinder with an aperture 83°< θ <63°. This aperture includes the large vertical feature at 73° in fig. 1 which is due in part to radiating waves propagating at the plate speed along the length of the cylinder. The image clearly shows the full extent of the cylinder from (-55 m, 0 m) to (55 m, 0 m). The image is very similar to the image of a point source connected to a uniform line radiating sound into a cone defined by $c_l/c = 1/\cos 73°$ shown in fig. 3(b). The values of the parameters used in the image are A_p = 0.92, z_p = -50m, A_l = -1 26, L = 100m and c_l/c = 3.5. This comparison clearly shows that the asymmetry of the pattern in the form function is caused by interference between the radiation from the plate wave and a reflection from the ensonified end. The phases of the two patterns are such that the $\sin(x)/x$ pattern of the line is canceled by the asymmetric $\sin(x)$ portion pattern of the point for angles greater than θ = 73°.

The last set of images is shown in fig. 4. These were each generated with an aperture 0°< θ <30°. Fig. 4(a) on the left shows a localized highlight at the ensonified end and an extended highlight along the length of the cylinder. The image on the right is composed of a point scatterer with amplitude

$A_p = 2.44$ at position $z_p = -.55$ m and of a line radiator with amplitude $A_l = 13.5$, length $L = 110$ m and speed $c_l/c = 1.0$. The value of the point scatterer is comparable with the maximum value of the pattern derived from scattering from a circular disc using the Kirchoff approximation.[7,8] The forward scattered amplitude in that approximation is simply $(2/a)\,(\pi a^2/\lambda) = 2\pi a/\lambda \simeq 3.6$ as compared with $A_p = 2.4$. However the dominant contribution to the form function in this region comes not from the the highlight located at the ensonified end, but rather from along the length of the scatterer.

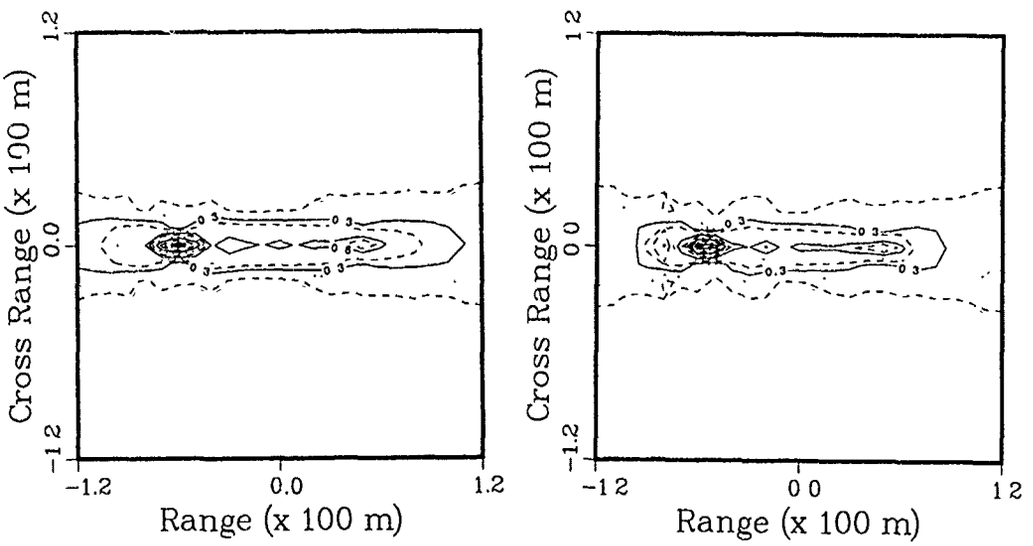

(a) (b)

Figure 4 - - Acoustic image of (a) the cylinder with aperture $0° < \theta < 30°$, (b) a point sources with amplitude $A_p = 2.44$ and position $z_p = -.55$m and a uniform line source with amplitude $A_l = 13.5$, length $L = 110$m and $c_l/c = 1$.

CONCLUSION

Several images were generated from the scattered acoustic field from a finite cylindrical shell with hemispherical endcaps, ensonified on the end. These images were generated using specific angular apertures which were meaningful in light of the acoustic phenomena involved in the scattering. The apertures included one or two side-lobes of the phenomena.

Several physical results are obtained from the analysis. One is that specular reflection from the ensonified end is present at all angles studied. The magnitude of the scattering from this end is consistent with a sphere of that size. The specular reflection interferes with sound radiated from a plate wave propagating along the length of the cylinder and creates an asymmetric pattern near 73°. Finally, the forward scattering is generated from sources along the whole length of the cylinder.

In conclusion, imaging has been used to understand the scattering from a finite body with end ensonification. This ensonification angle creates a symmetry which allowed the imaging algorithm to be simplified as Eq. 3. This method can also be used for a scatterer of any shape and ensonification angle.

REFERENCES

[1]P. B. Abraham, and C. F. Gaumond, "Reflection Tomography," J. Acoust. Soc. Am., **82**, 1303-1314 (1987).
[2]C. F. Gaumond, and P. B. Abraham, "Reflection Tomography Imaging," Proceedings of Noise-Con 87, Noise Control Foundation, p. 617(1987).
[3]C. F. Gaumond, B. H. Houston, and S. Woo, "Acoustical Images of a Submerged Aluminum Sphere," J. Acoust. Soc. Am. **86**, S6(1989).
[4]J. Shirron, "AXSAR User's Guide," Naval Research Laboratory Internal Report (June, 1991).
[5]M. C. Junger, and D. Feit, *Sound, Structures and Their Interaction, 2nd ed.* (MIT Press, Cambridge, 1986), p. 38.
[6]J. George, "Physical Optics Interpretation of Forward Scattering from Infinite Cylindrical Elastic Shells," J. Acoust. Soc. Am. **90**, 2309(1991).
[7]A. D. Pierce, *Acoustics: An Introduction to Its Physical Principles and Applications*, (Acoustical Society of America, Woodbury, NY 1989), pp.213-218.
[8]M. Born, and E. Wolf, *Principles of Optics, 5th ed.* (Pergamon Press, Oxford, 1975), pp.382-395.

SECOND INTERNATIONAL CONGRESS ON
RECENT DEVELOPMENTS IN AIR- AND
STRUCTURE-BORNE SOUND AND VIBRATION
MARCH 4-6, 1992 AUBURN UNIVERSITY, USA

CALCULATION OF SOUND RADIATION FROM COMPLEX STRUCTURES USING THE MULTIPOLE RADIATOR SYNTHESIS WITH OPTIMIZED SOURCE LOCATIONS

Martin Ochmann
Technische Fachhochschule Berlin, Department of Mathematics and Physics
Luxemburger Strasse 10
W - 1000 Berlin 65
Germany

ABSTRACT

The sound radiation from vibrating machine structures of arbitrary shape into three-dimensional space will be calculated by approximating the normal velocity on the surface as a superposition of velocities generated by multipoles, which are distributed over the interior of the radiator. The resulting surface velocity error can be minimized in different ways. The standard approach is to fix the origin-coordinates of the multipoles and to solve the resulting linear least squares problem for the unknown amplitudes of the multipoles. In addition we also try to find optimal positions for the multipole locations, because this choice has a strong influence on the surface velocity error. A nonlinear least squares problem has to be solved to find the optimal multipole positions in the interior of the radiator automatically. This has been done numerically by using the Levenberg-Marquardt method. Advantages of the multipole radiator synthesis with optimally located auxiliary sources are an improved accuracy and a highly adaptive approximation. The sound radiation of a cube and a cylinder will be investigated in order to compare these benefits with the price of having to solve a nonlinear least squares problem.

1. INTRODUCTION

With the help of commercially available finite-element programs (FEM programs) the vibration behavior of complex structures like gearboxes or engine blockes can be determined very accurately. However, the calculation of sound radiated by vibrating structures into the infinite free space encounters some difficulties, since the FEM is especially suited for the treatment of finite domains. A second, often used approach - the boundary element method (BEM) - leads to a fully populated complex and asymmetric system of linear equations of high dimension, which can be solved only by using a big amount of solution time on high speed computers. Therefore, we have developed a fast numerical method for solving the radiation problem - the multipole radiator synthesis or shorter: the multipole method (MPM). The basic idea of the MPM is to replace the vibrating structure by a system of multipoles, which are located in the interior of the radiating body. The number, amplitudes, locations, types and orders of the multipoles have to be chosen in such a way, that the difference between the prescribed normal velocity on the surface and the velocity field generated by the multipoles is as small as possible. For minimizing this surface velocity error different techniques have been used. All of them have in common that they try to determine the amplitudes of the multipoles while keeping unchanged the multipole positions and other parameters. In this case the MPM can be considered as a method of weighted residuals. Depending on the choice of weighting functions different variants of the MPM like the null field method, the method of Cremer or a linear least squares approximation is obtained (see [1]). However, in many appli-

cations the choice of the multipole locations can have a strong influence on the surface velocity error. Therefore we try to find optimal values for the amplitudes and for the multipole positions. For the determination of the amplitudes we use the linear least squares approximation (called MPQUAD, see [1]). For finding the optimal multipole positions automatically a nonlinear least squares problem has to be solved, which we did iteratively by applying the Levenberg-Marquardt method. The extended MPM is used to calculate the sound radiation from a cube and a cylinder in order to compare the advantage of higher accuracy with the disadvantage of solving a nonlinear least squares problem. The results of a "one-point-source test" (OPS-test) and a "one-line-source test" (OLS-test) show an enormous gain of accurancy. For the future more detailed investigations are planned. Especially the comparison with experimentally obtained data seems to be of great interest. We found the mathematical idea of optimizing the source locations and using the Levenberg-Marquardt method in the work of Mathon and Johnston [2]. In contrast to this approach they propose the use of fundamental solutions as trial functions - in acoustic language: the use of monopoles - , while we are working with multipoles of arbitrary order.

2. STATEMENT OF THE RADIATION PROBLEM

If harmonic time dependence of the field quantities is considered with an angular frequency ω, the complex amplitude p of the sound pressure has to satisfy the scalar Helmholtz equation

$$\Delta p + k^2 p = 0 \qquad (1)$$

in the exterior B_+ of the radiating body B (see Fig. 1), where $k = \omega/c$ is the wavenumber, c the speed of sound and Δ the Laplace operator; the time factor $\exp(- i \omega t)$ with $i^2 = -1$ is supresssed in all field quantities. On the surface S the normal velocity v and therefore the normal derivative of the pressure

$$\partial p / \partial n = i\omega\rho v \qquad (2)$$

is prescribed, where ρ is the fluid density and $\partial / \partial n$ is the derivative in the direction of the outward normal n. In addition, the pressure p has to satisfy the Sommerfeld radiation condition,

$$\lim_{r \to \infty} r\left[\frac{\partial p}{\partial r} - ikp\right] = 0, \qquad (3)$$

which can be interpreted as a boundary condition at infinity. Therefore, the Neumann boundary value problem represented by Eqs. (1) - (3) has to be solved.

3. THE MULTIPOLE METHOD WITH OPTIMIZED AMPLITUDES (MPA)

For the sound pressure p we make the substitution

$$p = \sum_{k=1}^{N} c_k \varphi_k, \qquad (4)$$

where the trial functions φ_k are radiating wave functions, which by definition satisfy Eqs. (1) and (3). The c_k are yet unknown coefficients. By substituting the series (4) into the boundary condition (2), one obtains the error, or the so-called residue

$$e = i\omega\rho v - \sum_{k=1}^{N} c_k \frac{\partial \varphi_k}{\partial n} \qquad (5)$$

at the surface of the radiator, which we require to be minimal. To carry out the minimization we follow the method of weighted residuals. By multiplying e with N so-called weighting functions w_j and integrating over the surface S, we obtain the following system of linear equations for the determination of the N unknown coefficients c_k:

$$\sum_{k=1}^{N} c_k \int_S \frac{\partial}{\partial n} \varphi_k(y)\, w_j(y)\, ds(y) = i\omega\rho \int_S v w_j(y)\, ds(y). \qquad (6)$$

As trial functions we use the spherical wave functions $\psi_k(x - x_q)$ with different locations x_q for the origin of the wave functions. This enables us to treat arbitrary geometries, e.g. L-shaped structures. If we use only one origin for all ψ_k, we are limited to the treatment of sphere-like geometries. Depending on the choice of the weighting functions, we obtain different variants of the MPM: If $w_j = \psi_j(x - x_q)$, we obtain generalized null field equations. For $w_j = [\partial\psi_j(x - x_q) / \partial n]^*$ we get the method of the least squares approximation (MPQUAD). The asterisk denotes complex conjugation. More detailed information can be found in [1]. We recommend the MPQUAD, since it minimizes the radiated sound power in a certain way [1].

4. THE MULTIPOLE METHOD WITH OPTIMIZED AMPLITUDES AND SOURCE LOCATIONS (MPAS)

Since the sound pressure p is a superposition of spherical wave functions $\psi_k(x - x_q)$ with variable source locations as desribed in Eq. (4), the corresponding normal velocity on S is

$$w(x;c,X_q) = \frac{1}{i\omega\rho} \sum_{q=1}^{Q} \sum_{k=1}^{N} c_{k,q} h_k(x - x_q), \qquad (7)$$

where we have used Eq. (2) and the definitions

$$h_k(z) = \frac{\partial \psi_k}{\partial n}(z), \qquad (8)$$

$$c = (c_{1,1}, \ldots, c_{1,Q}; \ldots\ldots; c_{N,1}, \ldots, c_{N,Q}) \quad \text{and} \quad X_q = (x_1, \ldots, x_Q).$$

Here Q is the number of source locations and N the number of the multipoles. The least squares error has the form

$$\chi^2(c, X_q) = \int_S |v - w|^2 ds \approx \sum_{i=1}^{M} |v_i - w_i(x_i;c,X_q)|^2 \Delta F_i, \qquad (9)$$

where the surface S was discretized into M elements F_i with area ΔF_i. All field quantities are supposed to be constant over one element; for instance $v = v_i$ on ΔF_i. Now we have to choose c and X_q in such a way that the error χ^2 becomes minimal. To find the vector of amplitudes c we use the linear least squares approximation MPQUAD (see [1]). For determining the X_q we need another algorithm, since the X_q depend nonlinearly on these parameters.

5. THE NUMERICAL METHOD

For solving the nonlinear least squares problem we use the Levenberg-Marquardt algorithm, which we describe only briefly by following the detailed representation given in [3]. First we have to determine the quantities

$$\beta_k = -\frac{1}{2}\frac{\partial \chi^2}{\partial u_k}, \quad \alpha_{kl} = \frac{1}{2}\frac{\partial^2 \chi^2}{\partial u_l \partial u_k}(1 + \delta_{lk} \cdot \lambda), \tag{10}$$

where δ_{ik} is the Kronecker symbol and the u_k are a suitable arrangement of the 3Q source coordinates of the multipole locations x_q in the three dimensional space (e.g.: $x_{q=1} = (u_1,u_2,u_3)$). The parameter λ depends on the result of the actual iteration. If λ goes to 0, we get the inverse Hessian method; if λ becomes very large, we get the steepest descent method. The calculation of the components α_{kl} and β_k requires to know the gradient of the functions h_k with respect to the u_k (see (7), (8)). As shown in [3] it is not necessary to compute the second derivatives explicitly. For the determination of the gradient we proceed in a similar manner as described in [1, Eq. (35)]. By solving the linear system of equations for the increments E_q of the multipole positions

$$A \cdot E_q = b \tag{11}$$

with the matrix $A = (\alpha_{kl})$ and the vector $b = (\beta_k)$ we get the new source positions $X_{q,new} = X_q + E_q$.
The main steps of the algorithm are:

1. Compute the amplitudes c and χ^2 for estimated starting values X_q.
2. Choose a certain value for λ (e.g. $\lambda = 0.0001$).
3. Solve system (10) for the increments E_q.
4. Compute new amplitudes c by using the MPQUAD with new source locations $X_{q,new} = X_q + E_q$ and evaluate the new surface velocity error χ^2_{new}.
5. If $\chi^2_{new} < \chi^2$ the iteration step was succesful. λ is decreased by a certain factor and the next iteration is performed by setting $X_q = X_{q,new}$ and going back to point 3.
6. If $\chi^2_{new} > \chi^2$ λ must be increased. We again go back to 3, but now we have to use the old X_q.
7. As suggested in [3], the iteration process is stopped if $|\chi^2_{new} - \chi^2|$ is small enough during a few successive iterations.

6. RESULTS

6.1 Results for a cube

The first test structure we have investigated is the cube shown in Fig. 2. The surface of the cube is divided into 96 equally-sized squares. The length of one edge is 0.25 m. The origin of the coordinate system (x,y,z) = (0,0,0) is identical with the centroid of the cube. For constructing the velocity field on the surface we performed a so-called OPS-test. That means: we set an (imaginary) point source - in this case a monopole - in the origin and evaluate the generated normal velocity on the surface of the radiator. The resulting velocity field was used as an input for the program. To reconstruct the sound field with the help of the MPAS we put another monopole near one corner of the cube at the position (0.1 m, 0.1 m, 0.1 m). After nearly 30 iteration steps this source has reached the optimal location (0,0,0) as shown in Fig. 3 and 5. In Fig. 4 the corresponding surface velocity error χ^2 is shown, which decreases with an increasing number of iterations. In all calculations ka is the Helmholtz number with a = 0.1m and k = wavenumber. It is interesting to note that the wandering monopole escaped from the cube in the vicinity of iteration 4. However, this effect does not disturb the convergence behavior towards the optimal position (0,0,0).

6.2 Results for a cylinder

The geometry of the cylinder is shown in Fig. 6. The length of the cylinder is 0.8 m, its diameter 0.2 m. The

structure consists of 160 elements. First we performed an OPS-test for three different frequencies as desribed in chap. 6.1. After nearly 20 iterations the monopole source has moved from the starting position at (0.3m, 0.3m, 0.3m) to the optimal position (0,0,0), where the "imaginary" point source is located (see Fig. 7). Fig. 8 shows that the corresponding χ^2-error goes to 0 - as expected.
We also performed an OLS-test. The situation is scetched in Fig. 11. We put a pulsating line source into the cylinder and proceed as if we would perform an OPS-test (details can be found in [1]).The results are shown in Fig. 9-11: We worked with two multipoles up to order one. Therefore each multipole consists of one monopole and three dipoles. Starting and end positions are shown in Fig. 9 and 11. It is obvious that the end positions are optimal for simulating an line source with two multipoles. This can also be seen from the decreasing χ^2-error (Fig. 11).

7. CONCLUDING REMARKS

The investigation of idealized radiating structures like cubes and cylinders with simply generated surface velocity fields demonstrates that the additional optimization of the multipole locations has a strong effect on the surface velocity error and improves the quality of the sound field approximation and prediction remarkably.Therefore, the application of the MPAS is very promising and the higher amount of computer time is justified. Real structures with complicated shapes often consist of a few thousand elements, and the surface velocity is only known from measurements or FEM caculations. Therefore, optimal positions are not known a priori. It seems to be possible to improve the accuracy of the sound field prediction for machine structures by using the MPAS in a similar order of magnitude as found in the investigation presented. Such investigations of real structures are planned for the near future.

8. ACKNOWLEDGEMENT

The author gratefully acknowledges the support of the Akustik Kontor in Berlin (AKB) with computer equipment for carrying out this study.

9. REFERENCES

[1] M. Ochmann, Multipole radiator synthesis - an effective method for calculating the radiated sound field of vibrating structures of arbitrary surface configuration (in German), Acustica, Vol. 72, 1990, 233-246.
[2] R. Mathon, R. L. Johnston, The approximate solution of elliptic boundary-value problems by fundamental solutions , SIAM J. Numer. Anal., Vol. 14, 1977, 638 - 650.
[3] W. H. Press, B. P. Flannery, S. A. Teukolsky, W. T. Vetterling, Numerical recipes, the art of scientific computing, Cambridge University Press, Cambridge, 1990.

10. FIGURES

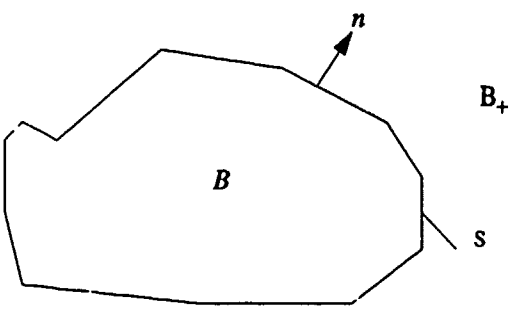

Fig. 1: Geometry of the radiation problem.

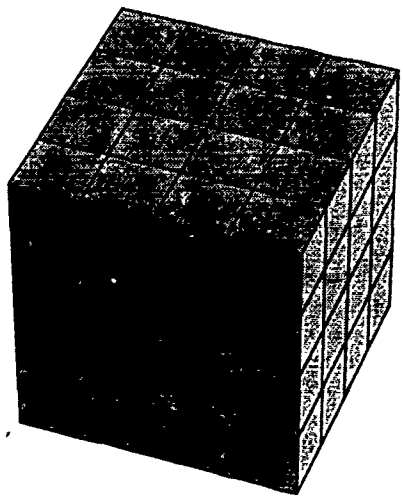

Fig. 2: Grid of the cube

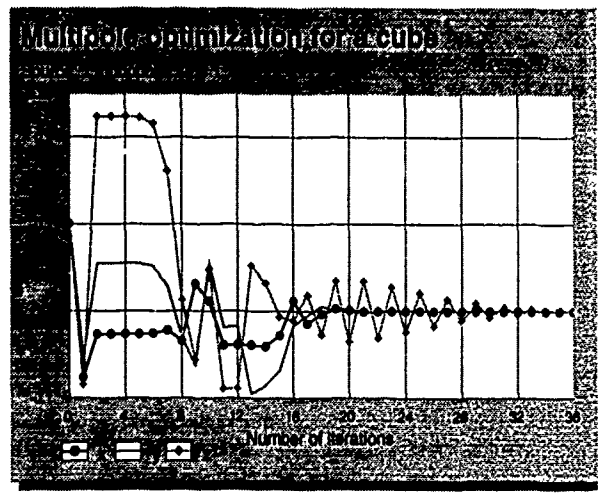

Fig. 3: OPS-test for the cube; starting position of the variable monopole is (0.1m,0.1m,0.1m). Optimal position is the origin.

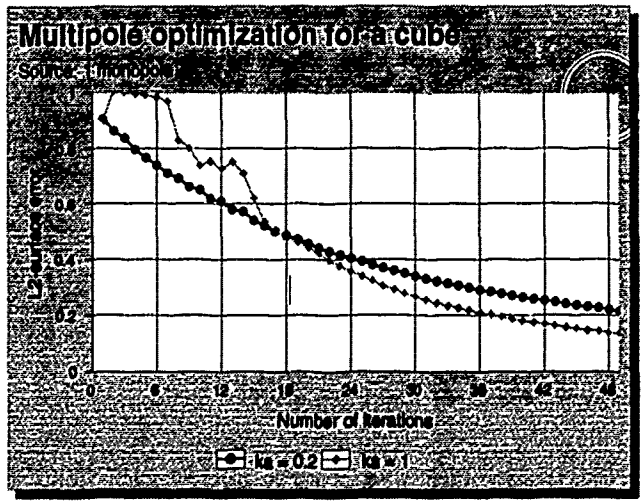

Fig. 4 : OPS-test for the cube: L2-error χ^2 over number of iterations (situation as in Fig. 3)

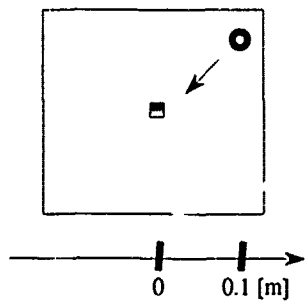

Fig. 5: Movement of the monopole

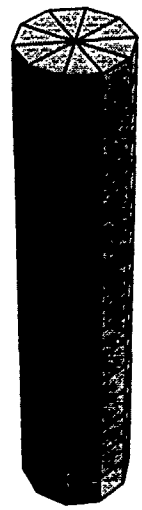

Fig. 6: Grid of the cylinder

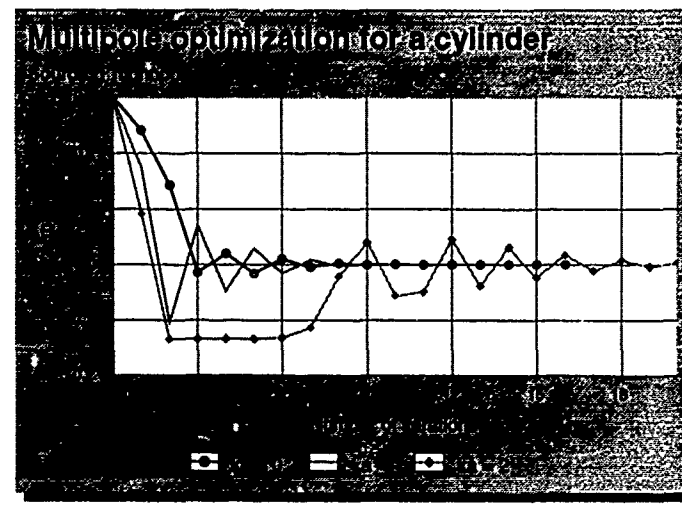

Fig. 7: OPS-test for the cylinder: starting position of the monopole is (0m,0m,0.3m); optimal position is the origin.

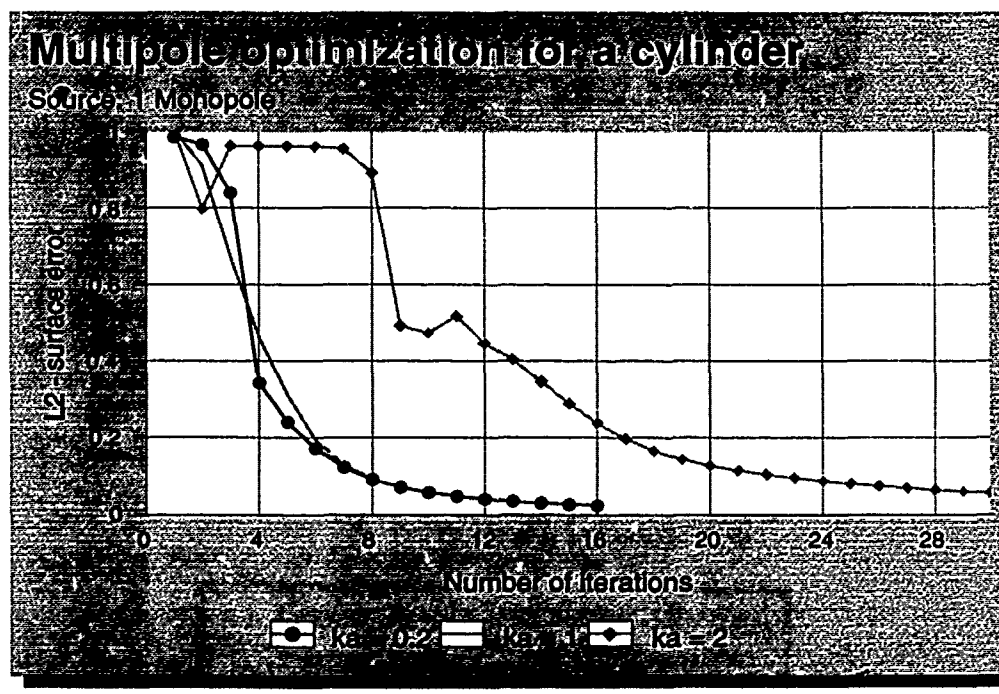

Fig. 8 : OPS-test for the cylinder: L2-error χ^2 over number of iterations (situation as in Fig. 7)

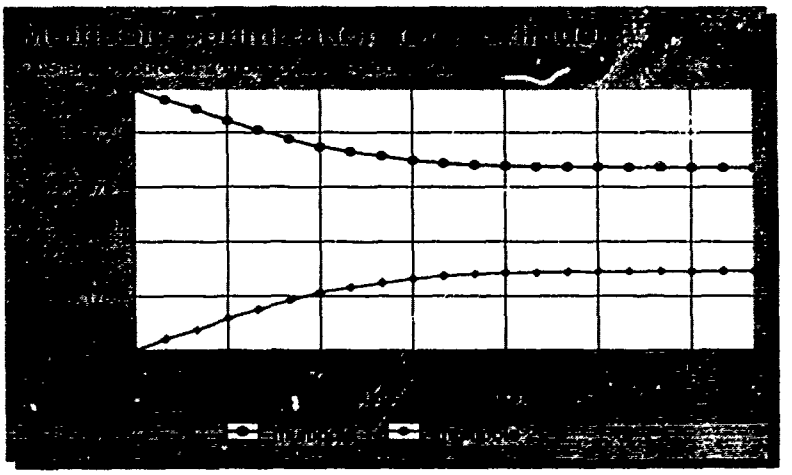

Fig. 9: OLS-test for the cylinder: starting position of the two multipoles are (0m,0m,+0.3m) and (0m,0m,-0.3m), optimal position is the origin. Position of the line source as in Fig. 11.

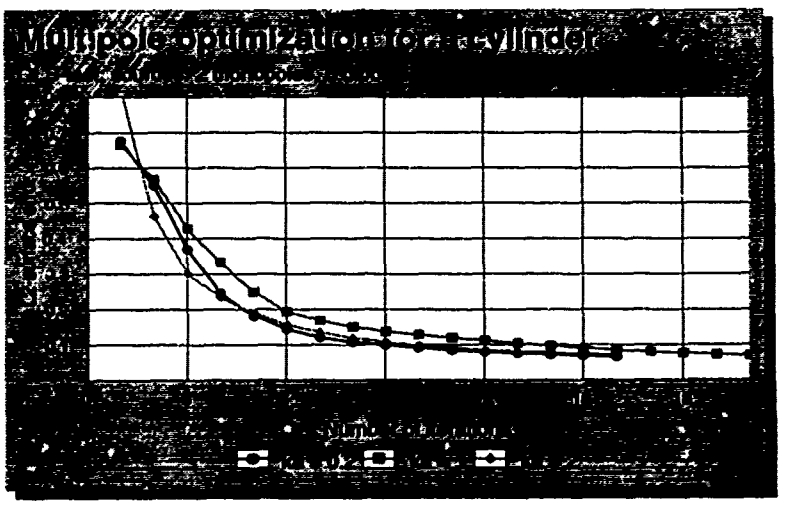

Fig. 10 : OLS-test for the cylinder: L2-error χ^2 over number of iterations (situation as in Fig. 9)

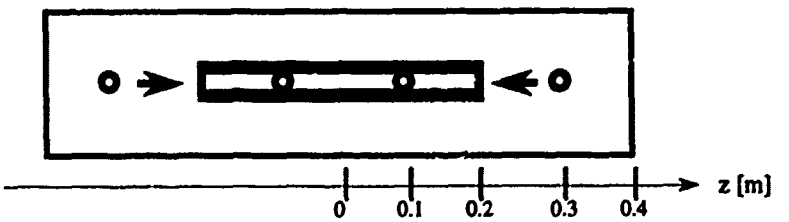

Fig. 11: Draft of the location of the line source and the journey of the multipoles

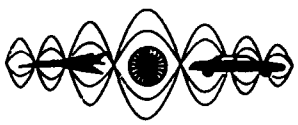

SECOND INTERNATIONAL CONGRESS ON
RECENT DEVELOPMENTS IN AIR- AND
STRUCTURE-BORNE SOUND AND VIBRATION
MARCH 4-6, 1992 AUBURN UNIVERSITY, USA

RADIATION AND SCATTERING AT OBLIQUE INCIDENCE FROM SUBMERGED OBLONG ELASTIC BODIES

Herbert Überall and X. L. Bao
Department of Physics
Catholic University of America, Washington, DC 20064, USA

Russel D. Miller
NKF Engineering
Arlington, VA 22203-1800, USA

Michael F. Werby
NRL, Numerical Modeling Branch
Stennis Space Center, MS 39529-5000, USA

ABSTRACT

The resonant behavior of solid or hollow oblong submersed elastic objects is studied both theoretically and experimentally. The resonances have been studied directly, by a calculation of surface wave displacements, or inferentially, by calculations or observations of echoes from plane incident acoustic waves with axial, broadside, or general oblique incidence onto the submersed objects. For the latter, we considered solid or hollow spheroids, or cylinders with flat or with hemispherical ends. Resonances are obtained theoretically from the phase matching of surface waves, which physically form standing waves in this case. A bar wave picture of resonant vibration has also been considered; it is shown to apply in the low-ka region while surface wave pictures apply in the high-ka region, and the two pictures merge in the intermediate region. The dispersion of surface waves along the object for axial incidence is t,eated exactly. For broadside incidence, simultaneous excitation of meridional and circumferential surface wave is noted. The same surface wave picture applies for sound radiation from these objects following point excitation.

INTRODUCTION

Experimental studies on the resonant behavior of submersed elastic objects, subject to incident acoustic waves and pulses, have been carried out for about a decade at US [1-3], German [4], and especially at French acoustics laboratories [5-8]. These studies were motivated by the establishment of the acoustic Resonance Scattering Theory (RST) [9-11] which, together with the physical interpretation of the elastic-body resonances in terms of phase-matching surface waves [12], has been brilliantly verified by the experiments. The outcome of these studies, of which the above references [1-8] just constitute a small, representative selection (for more recent updates on the extensive investigations that have been performed on this subject, see the books quoted in Refs. [3] and [11]) consists in the following information:

(a) The eigenfrequencies of elastic objects were determined from the observed resonance spectra. This was done first for the simplest objects such as solid spheres and infinite (i.e.) very long cylinders, but subsequently also for solid and hollow objects of more complex shapes, mainly for spheroids and finite cylinders with flat or hemispherical endcaps. This also includes the strength of the acoustic excitation (i.e., the peak heights), and the widths of the resonance peaks.

(b) Using phase matching arguments, the observed resonances were classified in terms of the surface waves that generated them (a surface wave launched by the incident wave, which is circumnavigating the object on a closed path, causes a resonant buildup of the surface wave amplitude, and hence resonant scattering, if phase matching takes place upon each circumnavigation). This led immediately to a classification of the various kinds of surface waves that the submersed elastic object can support, and that were in fact excited by the incident wave.

(c) The spacing of the resonance families belonging to a given type of surface waves permitted a prediction of the dispersion curves of each of these surface wave types; both phase and group velocities, and the losses due to radiation could be obtained in this way.

(d) A convenient way of representing the above data consists in plotting the "Regge trajectories" of each surface wave type, where the successive mode numbers in each wave are graphed vs. the frequency values at which the mode resonates.

In addition to such studies of the surface waves on elastic objects, excited by incident acoustic waves and inferred from the resonances they generate as observed in scattered echoes, the surface waves have also been examined when generated by mechanical forces acting on the elastic object, leading to acoustic radiation that displays related resonance effects [13]. Both scattering and radiation-generated resonances will be discussed in the following.

SURFACE WAVE GENERATION: BROADSIDE VS. END-ON

It was shown for cylinder and sphere scattering that analytically, resonances in the scattering amplitude are described [9, 10] by terms of the form

$$1/(x_{n\ell} - x - i\Gamma_{n\ell}/2) \qquad (1)$$

where $x = ka$, k being the wave number in the ambient fluid and a the cylinder or sphere radius. For oblong bodies, e.g. spheroids, one may instead use the variable $X = kL/2$, L being the length of the object. Equation (1) shows that the resonant amplitude has poles in the complex frequency plane located at

$$x = x_{n\ell} - i\Gamma_{n\ell}/2, \qquad (2)$$

i.e. in the fourth quadrant. For electromagnetic waves, this has been noted by Baum [14], who based his "Singularity Expansion Method (SEM)" of electromagnetic scattering on this concept. On the other hand, it was shown by Franz [15] by applying the Watson transformation to the modal series of scattering, that circumferential ("creeping" or "surface") waves arise in the scattering process, which e.g. for a cylinder have the

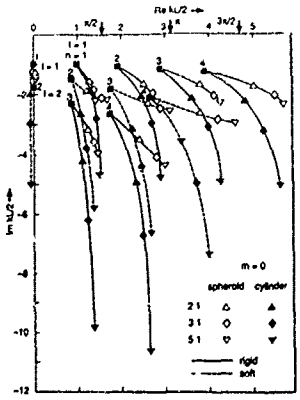

Fig. 1. Complex eigenfrequencies of rigid and soft elongated bodies.

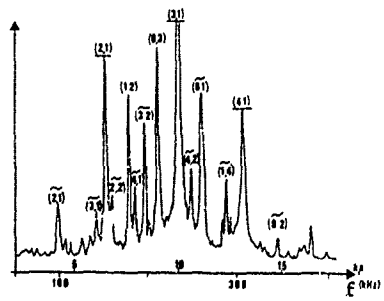

Fig. 2. Resonances of WC cylinder (experimental, broadside incidence).

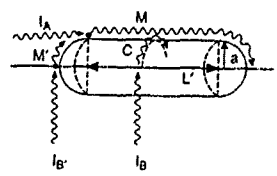

Fig. 3. Generation of circumferential and meridional surface waves by broadside incidence on a hemispherically-capped cylinder.

form $\exp(i\nu\phi)$, with a circumferential propagation constant ν given by $\nu = \nu_\ell$, which are the location of poles of the scattering amplitude in the complex ν-plane obtained from the Watson transformation; these are known as the "Watson poles" in electromagnetics, or "Regge poles" in nuclear physics. The connection between SEM poles and Watson-Regge poles was established by Dickey and Uberall [16] in 1978.

The ℓth surface wave $\exp(i\nu_\ell\phi)$ becomes resonant at $\nu_\ell = n$ because then, an integer number of wavelengths fits the circumference of the scatterer. This "principle of phase matching" [12,17] can be used to determine the nth modal resonance frequency (i.e., the position of the corresponding SEM pole) from the resonance condition

$$\nu_\ell = n. \tag{3}$$

This leads to the physical picture of the resonances, showing that a resonance originates from the resonant buildup of a multiply circumnavigating surface wave when it matches phase after each encirclement of the scatterer. This principle can be used in order to determine the resonance frequencies of bodies of arbitrary shape [17], the task here is mainly to obtain the surface paths of resonating surface waves. As an example of this approach, we show in Fig. 1 the complex resonance frequencies $X_{n\ell} = (L/2a)x_{n\ell}$ obtained by the phase matching condition for rigid or soft spheroids and hemispherically-endcapped cylinders of length L and radius a, for aspect ratios 2:1, 3:1, and 5:1 and assuming meridionally propagating surface waves, i.e., axial incidence of the acoustic wave generating these surface waves [18].

The results of an experimental study on the resonances of a solid tungsten carbide cylinder of finite length, terminated by hemispherical endcaps, are in press [8]. Both axial and broadside incidence was employed here. The interesting features appearing in Fig. 2 which shows the backscattering spectrum at broadside incidence, are the fact that not only the resonances that correspond to the phase matching of surface waves propagating circumferentially around the cylinder are visible [labeled by (n,ℓ) where n = mode number, ℓ = 1, 2, 3 surface-wave family index], but also those of meridionally propagating surface waves, labeled by $(n,\tilde{\ell})$. All the latter resonances are those, and only those, seen in the backscattering spectrum for axial incidence in the same experiment [8]. The reason for the broadside excitation of both types of closed-path surface wave phase-match resonances is schematically shown in Fig. 3 (although this figure refers to an impenetrable cylinder, hence tangential excitation of the surface waves): the meridional wave gets excited on the endcaps.

Graphs analogous to Fig. 2, obtained from a T-matrix calculation of backscattering for axial and broadside incidence for a 4:1 nickel spheroid, are shown e.g. in Ref. [19], reproduced below in Fig. 4, (a) for axial and (b) for broadside incidence. The form function (a) shows the n = 2 Rayleigh-wave peak at kL/2 = 7.0, caused by the phase matching of a meridionally propagating Rayleigh wave. The same peak also appears at broadside incidence (b), indicating that even in this case, meridional waves were

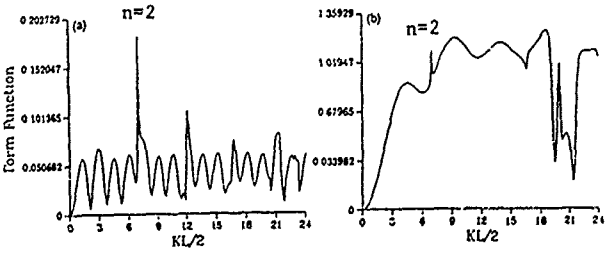

Fig. 4. Residual response vs. kL/2 for a 4:1 nickel spheroid: (a) end-on incidence, (b) broadside incidence.

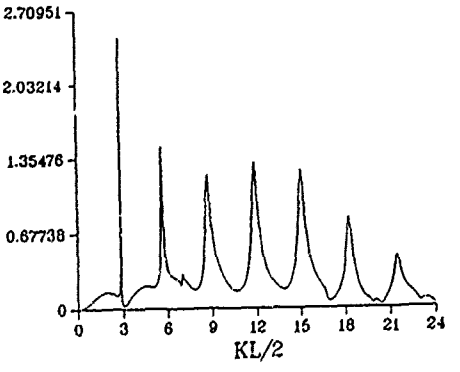

Fig. 6. As in Fig. 4, incidence at 50° to symmetry axis.

generated (while generally, the surface waves generated here propagate equatorially around the object, see Fig. 3).

In Fig. 4a, the first resonance frequency is lower than in the broadside case of Fig. 4b. This is because in broadside incidence, the surface waves follow a minimal path around the spheroid, i.e., parallel to the equator. For end-on incidence, the surface waves follow a maximal path, i.e. around a meridian. Thus the resonance frequency is higher for broadside incidence.

SURFACE WAVES FROM OBLIQUE INCIDENCE

Experiments on the excitation of surface waves on elastic cylinders and cylindrical shells by obliquely incident waves have been carried out at French laboratories since 1986 [20,21]. The important discovery here was the observation of resonances caused by axially propagating waves ("guided waves"), analogous to the above-mentioned meridional waves. The combination of circumferential and guided waves can be viewed as leading to helically propagating waves [2",23]. An example for these is given in Fig. 5, where the simplest closed geodesics ("helicoidal paths") for spheroids are shown; these paths were used to predict by phase matching the electromagnetic resonance frequencies of conducting spheroids [24].

In the elastic-body case, Fig. 6 shows resonances excited by oblique acoustic

In the elastic-body case, Fig. 6 shows resonances excited by oblique acoustic incidence, at 50° to the symmetry axis, in the nickel spheroid mentioned above. Here, bending resonances are dominant in which the spheroid (at 4:1 being sufficiently long and bar-like) undergoes bending vibrations about its long axis; and these are strongly excited by obliquely incident waves.

The question has been brought up [25] whether the resonances generated by axially incident signals can also be interpreted in terms of (longitudinal) bar waves. In the surface wave picture, the resonances are determined by the phase matching condition.

$$\oint k_\ell \, ds = 2\pi (n + \tfrac{1}{2}), \quad n = 1,2,3... \tag{4}$$

integrated over a closed surface path, while bar waves require

$$2 \int_0^L k_\ell{}^b \, dx = 2\pi m, \qquad m = 1,2,3..., \tag{5}$$

k_ℓ and $k_\ell{}^b$ being the wave numbers of the corresponding waves and m the number of half-wavelengths along the overall length L of the object. For $k_\ell{}^b$, we use the wave number for an infinite cylinder, while for k_ℓ in Eq. (4) one can employ the "tangent sphere" approximation where e.g. on a spheroid, the surface wave path is locally approximated by that on a tangent sphere [17], with known values of k_ℓ. In that method, a constant (Rayleigh-type) wave number can be employed on the cylindrical portion of e.g. a cylinder with hemispherical endcaps. This will be referred to as PM-TS. However, the known wave number on an infinite solid cylinder can be used for this purpose (an example being shown in Fig. 7 for a steel cylinder, the phase velocity tending to that of the Rayleigh were at high frequencies), thereby taking the transverse curvature into account. This model will be called PM-IC. Using the dispersion curve of Fig. 7, one may also employ the "bar wave" resonance condition Eq. (5); that model can be called LBW. We have applied all these models [26] to hemispherically capped steel cylinders as shown in Fig. 8. Here, the Regge trajectories indicate, by comparison with experimental results shown as circles, the correctness of phase matching (PM-IC and PM-TS) at high frequencies. Low frequency experiments are not available in this case, but for other examples these showed that both the bar wave and especially the PM-IC

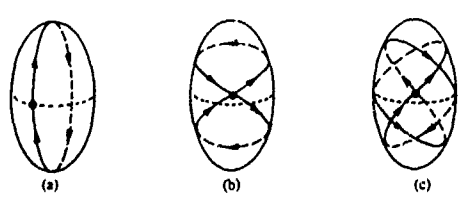

Fig. 5. Examples of simple closed geodesics on a prolate spheroid.

model fit the data well at low frequencies.

RADIATION PROBLEMS

We next consider the radiation and scattering from a stiffened cylindrical shell with flat flexible endcaps [27]. The NASTRAN/SIERRAS code was used to perform mobility, radiation and scattering analysis for the shell. The NASTRAN program is a general purpose finite element code. In the NASTRAN/SIERRAS approach it is used to obtain the structural matrices used by SIERRAS to represent the dynamic response of the structure in vacuo. The SIERRAS (Surface Integral Equation Radiation and Scattering) code is an advanced boundary element code for analyzing the radiation and scattering from arbitrary structures [28,29].

The NASTRAN finite element model consists of approximately 10000 degrees of freedom (DOF). It includes four plate elements between stiffeners and grid points every five degrees around the circumference. Guyan reduction was used to reduce the analysis set to 813 DOF prior to running SIERRAS. The analysis set included one grid point between stiffeners and a point every ten degrees around the circumference.

The SIERRAS boundary element model uses 437 wet fluid degrees of freedom in the analysis. The fluid element is a nine-noded superparametric boundary element.

The measured and computed radial drive point mobility is shown in Figure 9. The forced point was on the center stiffener at the midpoint of the shell in the radial direction. The peaks shown on the figure are the (1,2), (1,3), (1,1), and (1,4) modes of the shell, respectively. The mode numbers refer to the number of longitudinal half waves and the number of circumferential whole waves. Therefore the 1,4 wave consists of one longitudinal half wave along the shell and four whole waves around the circumference.

The radiated noise from the shell is given in Figure 10. Measured and computed results are shown for a location 60 feet in the radial direction from the drive point. The (1,1) mode is responsible for the wide peak at 300 Hz and corresponds to the bending mode of the cylinder.

Finally, the scattering for the shell for broadside incidence is shown in Figure 11. Although no measured results are provided, the comparisons with radiated noise measurements above and previous scattering analyses [28,29] yield a reasonable level of confidence in the results. The scattering results are normalized by a factor of R/a where R is the distance of the observation point and a is the radius of the cylinder. Note that while the frequencies of the resonances are comparable, the magnitudes or response are different. The maximum radiated noise was obtained for the (1,2) mode

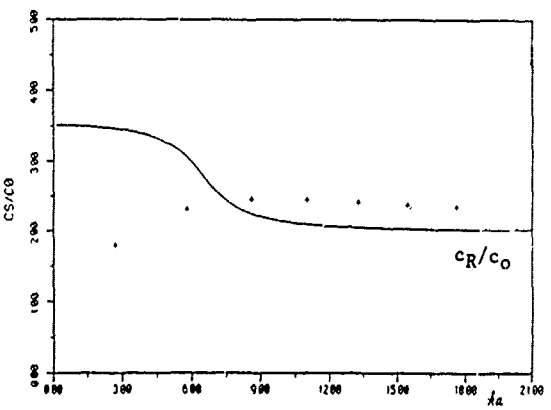

Fig. 7. Dispersion curves of the lowest axisymmetrical mode for an infinite steel cylinder (curve) and a steel sphere (crosses).

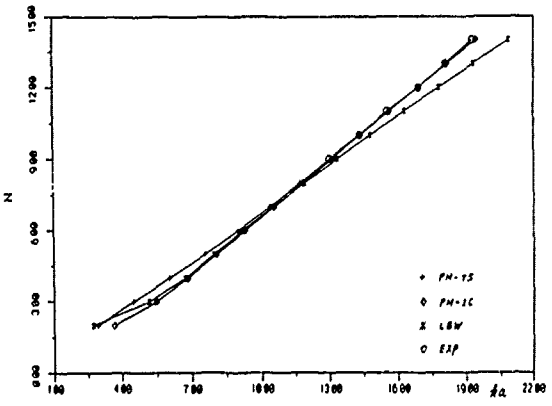

Fig. 8. Regge trajectory (number of resonating mode vs. frequency) for solid steel cylinde with hemispherical endcaps, aspect ratio = 2, end-on incidence.

while the maximum scattering was found for the (1,1) bending mode. Scattered pressure favors the lowest modes of the shell. The reason for this difference lies in the fact that the incident plane wave will tend to excite the resonance in a more pure form than a point force. Therefore, below coincidence, the cancellation of lobes over the surface is more likely to occur with scattering than for point excitation.

REFERENCES

[1] S. K. Numrich, W. E. Howell, J. V. Subrahmanyam, and H. Überall, "Acoustic ringing response of the individual resonances of an elastic cylinder," J. Acoust. Soc. Am. 80 (1986) 1161-1169.

[2] S. G. Kargl and P. L. Marston, "Observations and modeling of the backscattering of short tone bursts from a spherical shell: Lamb wave echoes, glory, and axial reverberations," J. Acoust. Soc. Am. 85 (1989) 1014-1028.

[3] X. L. Bao, H. Überall, and J. Niemiec, ""Experiments on the excitation of resonances of elastic objects by acoustic pulses, and theoretical interpretation," in Mechanics Pan-America, special issue of Applied Mechanics Reviews, 1991 (in press); X. L. Bao and H. Überall, "Experimental study of acoustic resonances of elastic spheres and hemispherically endcapped cylinders," in Acoustic Resonance Scattering, H. Überall, ed., Gordon and Breach, New York, 1992 (in press).

[4] H. Peine, Diplomarbeit, III. Physikalisches Institut, Universität Göttingen, Germany (1988).

[5] G. Maze and J. Ripoche, "Méthode d'isolement et d'identification des résonances (MIIR) de cylindres et de tubes soumis à une onde acoustique plane dans l'eau," Rev. Phys. Appl. 18 (1983) 319-326.

[6] M. Talmant and G. Quentin, "Backscattering of a short ultrasonic pulse from thin cylindrical shells," J. Appl. Phys. 63 (1988) 1857-1863.

[7] M. Talmant, G. Quentin, J. L. Rousselot, J. V. Subrahmanyam, and H. Überall, "Acoustic resonances of thin cylindrical shells and the resonance scattering theory," J. Acoust. Soc. Am. 84 (1988) 681-688.

[8] G. Maze, F. Lecroq, D. Decultot, J. Ripoche, S. K. Numrich, and H. Überall, "Acoustic scattering from finite cylindrical elastic objects," J. Acoust. Soc. Am., in press.

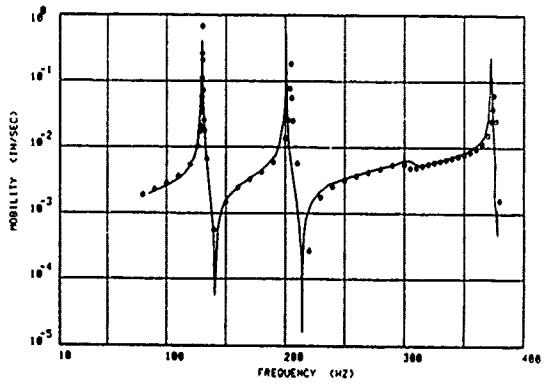

Fig. 9. Drive point mobility of a stiffened cylindrical shell (curve: measured; circles: NASTRAN/SIERRAS theoretical results).

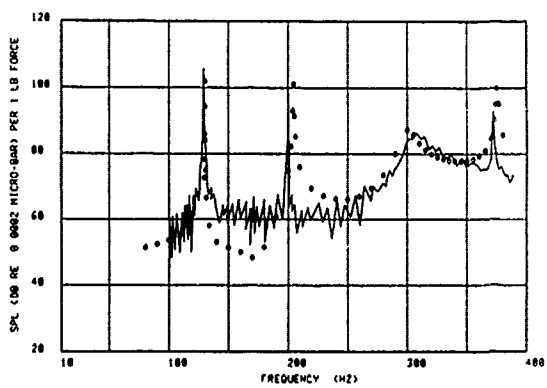

Fig. 10. Radiated noise of a force-excited stiffened cylindrical shell at a radial distance of 60' from drive point (curve: measured; circles: NASTRAN/SIERRAS).

[9] H. Überall, "Modal and surface-wave resonances in acoustic-wave scattering from elastic objects and in elastic-wave scattering from cavities, in Int. Union Theoret. and Applied Mecl. (IUTAM) Symposium: Modern Problems in Elastic Wave Propagation, edited by J. Miklowitz and J. Achenbach, Northwestern Univ., Sept. 1977; Proceedings publ. by Wiley (1978) 239-263.

[10] L. Flax, L. R. Dragonette, and H. Überall, "Theory of elastic resonance excitation by sound scattering," J. Acoust. Soc. Am. 63 (1978) 723-731.

[11] A. Derem, "Théorie de la matrice S et transformation de Sommerfeld-Watson dans la diffusion acoustique," in N. GESPA, La Diffusion Acoustique, edited by B. Poiree, CEDOCAR, Paris (1987) 189-279.

[12] H. Überall, L. R. Dragonette, and L. Flax, "Relation between creeping waves and normal modes of vibration of a curved body," J. Acoust. Soc. Am. 61 (1977) 711-715.

[13] P. Pareige, "Spectroscopie des résonances acoustiques," Thesis, University of Le Havre, 1988.

[14] C. E. Baum, in Transient Electromagnetic Fields, L. B. Felsen, ed., Springer, Berlin/Heidelberg 1976, 129-179.

[15] W. Franz, Über die Greenschen Funktionen des Zylinders und der Kugel," Zeits. f. Naturforsch. 9a (1954) 705-716.

[16] J. W. Dickey and H. Überall, "Surface wave resonances in sound scattering from elastic cylinders," J. Acoust. Soc. Am. 63 (1978) 319-320.

[17] H. Überall, Y. J. Stoyanov, et al., "Resonance spectra of elongated elastic objects," J. Acoust. Soc. Am. 81 (1987) 312-316.

[18] X. L. Bao, C. R. Schumacher, and H. Überall, "Complex resonance frequencies in acoustic wave scattering from impenetrable spheres and elongated objects," J. Acoust. Soc. Am. 90 (1991) 2118-2123.

[19] M. F. Werby et al., "Sound scattering from submerged elastic objects and shells of general shape," Proc. 3rd IMACS Symposium on Computational Acoustics, Harvard University, Cambridge, MA, June 1990.

[20] J. L. Izbicki, "Diffusion acoustique par des cylindres et des tubes," Thesis, University of Le Havre, 1986.

[21] P. Rembert, O. Lenoir, F. Lecroq, and J. L. Izbicki, "Oblique scattering by cylindrical shells," Phys. Lett. A157 (1991) 495-502.

[22] H. Überall et al., "Complex acoustic and electromagnetic resonance frequencies of prolate spheroids and related elongated objects and their physical interpretation," J. Appl. Phys. 58 (1985) 2109-2124.

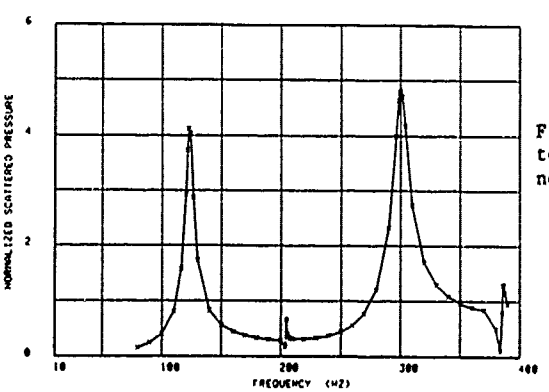

Fig. 11. Normalized form function (backscattering) for a stiffened cylindrical shell at normal distance (NASTRAN/SIERRAS results).

[23] J. M. Conoir, "Resonance scattering theory for oblique incidence," in Electromagnetic and Elastic Scattering, World Scientific, Singapore (1988).

[24] B. L. Merchant, A. Nagl, and H. Überall, "Eigenfrequencies of conducting spheroids and their relation to helicoidal surface wave paths," IEEE Trans. Antennas Propagat. 37 (1989) 629-634.

[25] R. Hackman, G. Sammelmann, K. Williams , and D. Trivett, "A reanalysis of the acoustic scattering from elastic spheroids," J. Acoust. Soc. Am. 83 (1988) 1255-1266.

[26] X. L. Bao, H. Überall and J. Niemiec, "Sound scattering and resonance prediction for a finite elastic cylinder immersed in water," J. Acoust. Soc. Am. (to be published).

[27] L. H. Chen, "Acoustic emission from submerged structures," Developments in Boundary Element Methods 2, edited by P. K. Banerjee and R. P. Show, Applied Science Publishers, Ltd., England, 1982.

[28] R. D. Miller, H. Huang, E. T. Moyer, and H. Überall, "The analysis of the radiated and scattered acoustic fields from submerged shell structures using a modal finite element/boundary element formulation," in Numerical Techniques in Acoustic Radiation (American Society of Mechanical Engineers, New York, NCA vol. 6 (1989), 83-94.

[29] R. D. Miller, E. T. Moyer, and H. Überall, "A comparison between the boundary element method and the wave superposition approach for the analysis of the scattered fields from rigid bodies and elastic shells," J. Acoust. Soc. Am. 89 (1991) 2185-2196.

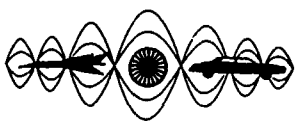

**SECOND INTERNATIONAL CONGRESS ON
RECENT DEVELOPMENTS IN AIR- AND
STRUCTURE-BORNE SOUND AND VIBRATION**
MARCH 4-6, 1992 AUBURN UNIVERSITY, USA

RAY REPRESENTATIONS OF THE BACKSCATTERING OF TONE BURSTS BY SHELLS IN WATER: CALCULATIONS AND RELATED EXPERIMENTS

Philip L. Marston, Ligang Zhang[1], Naihua Sun[2], Greg Kaduchak, and David H. Hughes
Department of Physics
Washington State University
Pullman, WA 99164-2814
USA

ABSTRACT

Ray methods are considered for the understanding of scattering by thin and thick hollow shells. The present research examines features of the backscattering from spheres and circular cylinders and emphasizes the use of exact elastic equations for determining guided wave properties. One of the prominent features described is the midfrequency enhancement of thin shells that is also evident in experiments and in exact scattering calculations. That feature is associated with a wave packet in the exact impulse response and is evident in a smoothed Wigner time-frequency analysis of the impulse response. The enhancement is caused by a strongly coupled slightly subsonic wave guided by the shell. Other features considered are the reasons for minima in the radiation damping of supersonic fluid-loaded Lamb waves that result in weak coupling with acoustic fields.

INTRODUCTION

Quantitative ray representations of amplitudes for the scattering of sound by hollow elastic shells in water were considered at the 1990 congress [1]. The emphasis of that discussion was on leaky Lamb wave contributions to scattering by thick spherical shells and on representations of steady-state scattering or form functions. Related publications discuss computational [2-4] and experimental [2,5] tests of the ray representations. The discussion given below summarizes recent work to broaden the range of scattering situations for which ray representations give quantitative predictions or useful insight into the response of shells to incident sound. The emphasis is on contributions that become important for thin shells and on the time domain response though other progress is also summarized. The discussion below emphasizes simple smooth shapes (hollow spheres and cylinders) though the echo structure was also studied near caustics produced by reflecting ultrasonic transients and tone bursts from a different shape of thin shell [6,7].

DISTINCTION BETWEEN LEAKY AND SUBSONIC GUIDED WAVES

Figure 1 illustrates the usual ray picture for backscattering contributions by the lth guided wave where the phase velocity of the wave along the outer surface of the shell c_l exceeds the speed of sound c in the surrounding water [1,3,5]. Such supersonic waves usually continuously leak or radiate sound at an angle $\theta_l = \arcsin(c/c_l)$ relative to the shell normal determined by the trace velocity matching condition (see however, discussion below). To facilitate the extension of midfrequency ray methods to thin shells, it is necessary to allow for subsonic guided waves where $c_l < c$. Figure 2 shows the modified ray picture [8,9] where the coupling is through an evanescent region having a thickness $(b_l - a) = (ac/c_l)(1 - c_l/c)$ that diverges as the outer radius a of the shell diverges. Apparent from truncations or other inhomogeneities, the subsonic waves considered would not radiate in this flat plate limit and are sometimes described as "trapped". The existence of such waves for plates in water has long been known [10-12]. The radiation and coupling with acoustic fields introduced by curvature is analogous with the bending losses of fiber-optic waveguides [7].

---

[1] Present Address: School of Electrical Engineering and Computing Science, Washington State University, Pullman, WA 99164.
[2] Present Address: EXP Group, Inc., 44063 Fremont Blvd., Fremont, CA 94538-6045.

MIDFREQUENCY ENHANCEMENT OF THE BACKSCATTERING OF TONE BURSTS

The contribution of a subsonic guided wave to the backscattering by thin spherical shells is especially significant when ka is in the general vicinity of a/h where $h = a - b$ is the shell thickness and $k = \omega/c$. For the purpose of illustrating a ray model for such contributions [9], consider the example of a stainless steel 304 shell with $a/h = 40$. The relevant guided wave properties are computed by finding the complex ν roots of $D_\nu(ka) = 0$ as previously described [2,3,5] where D_n is the denominator of the nth term of the exact partial wave series for the form function. (The method is based on the Watson transform.) The resulting properties for the case under consideration are shown in Fig. 3. The wave labeled with long and short dashes, designated by $l = a_{0^-}$, is subsonic throughout the region of interest but displays a noticeable rise in the radiation damping parameter β_l as c_l approaches c. This rise in coupling appears to be associated with the decrease in the thickness of the evanescent region near coincidence [9] and causes an enhanced backscattering as may be seen from the ray analysis summarized below. Analysis of guided wave scattering contributions by distinct leaky waves [5,13] to the present case of subsonic waves is possible by appreciating the importance of the caustic radius b_l to the backscattering amplitude [9]. The resulting contribution of the mth circumnavigation to the form function f has the magnitude

$$|f_{ml}| \approx 8\pi\beta_l (c/c_l) \exp(-\pi\beta_l - 2\pi m\beta_l), \tag{1}$$

where for m = 0, the wave has traveled only around the backside of the sphere as shown in Fig. 2. The solid curve in Fig. 4 gives $|f_{0l}|$ for $l = a_{0^-}$ while the dashed curve omits the factor c/c_l: $|f_{0l}|$ for the a_{0^-} wave shows a strong enhancement that peaks near $ka = 46.3$ where the value of $|f_{0l}| \approx 3.17$. It may be shown [9] that the value of $|f_{0l}|$ at such a peak depends only weakly on the shell thickness and material parameters since the ka dependance is dominated by that of β_l. The peak $|f_{0l}|$ occurs close to where β_l is $1/\pi$.

Equation (1) is directly applicable to the calculation of the enhanced backscattering by tone bursts that are sufficiently short that the echoes associated with different values of m don't overlap. The incident burst must be sufficiently long that the effects of dispersion are weak. The time domain echoes for such tone bursts were calculated by a Fourier synthesis that used the exact partial wave series [9,14]. This was done for several bursts of different ka. Figure 5 shows the resulting calculated amplitude for a 20 cycle burst with $ka = 46$. The dimensionless time units are $T = ct/a$. The normalization is such that specular reflection by a fixed rigid sphere of radius a has a unit amplitude. The earliest contribution from the shell in Fig. 5 is a specular reflection of close to unit amplitude. This is followed by the m = 0 and m = 1 contributions of the $l = a_{0^-}$ wave where the amplitude of the m = 0 echo of 3.07 is close to the aforementioned predicted enhancement. The identity of these echoes was also confirmed by comparison of their arrival times with ray theory. The amplitude of the m = 0, $l = a_{0^-}$ echo was similarly determined for several other values of ka and are plotted as the points in Fig. 4. The comparison with Eq. (2) gives strong support for the ray model of the enhancement. It is noteworthy that the later or m = 1 echo in Fig. 5 is weaker by a factor close to the expected value of $\exp(-2\pi\beta_l) \approx \exp(-2) \approx 0.135$. Furthermore, the predicted amplitudes are weak for the distinct ray contributions of the $l = a_0$ and s_0 guided waves whose properties are also shown in Fig. 3. Consequently those contributions only weakly affect the time record in Fig. 5. The earliest contribution to the backscattering by the a_{0^-} wave and its midfrequency enhancement may be especially useful for inverse problems [9].

LABORATORY OBSERVATIONS OF THE MIDFREQUECNY ENHANCEMENT

The existence and general magnitude of the enhancement described above was confirmed with experiments in a large redwood tank of water [15]. The volume of water available, approximately 6500 gallons, was such that reflections from the sides, top, and bottom of the tank did not occur in the time region of interest. The target was a stainless steel 304 shell with a radius $a = 38.1$ mm and a radius-to-thickness ratio $a/h = 43.8$. The predicted enhancement is for frequencies near 310 kHz. Figure 6 shows a representative time record in the region of greatest enhancement of the guided wave echo which is the second of the echoes. This record, which is for 318 kHz manifests the important features of Fig. 5. A substantial shift of the carrier frequency was observed to cause a reduction in the guided wave echo magnitude relative to that of the specular reflection and the observed behavior is in at least qualitative agreement with the shape of $|f_{0l}|$ predicted in Fig. 4. While the analysis of the measurement is incomplete at the time of this writing, the present results are supportive of the ray model.

MIDFREQUENCY ENHANCEMENT OF THE FORM FUNCTION

The ray model was also used to synthesize the exact form function f for steady-state backscattering in the region of the midfrequency enhancement for the spherical shell considered in Fig. 3 with $a/h = 40$. The dashed curve in Fig. 7 shows the |f| from the exact partial wave series and the solid curve shows $|f_{ray}|$ where

$$f_{ray} = f_{sp} + f_{a_{0^-}} + f_{s_0} + f_{a_0} \tag{2}$$

where f_{sp} is the specular contribution (here neglecting a small curvature correction) and f_l for $l = s_0$ and a_0 are leaky wave contributions computed as discussed previously [3]. In the region shown $|f_l|$ is negligible for $l = a_0$ but for $l = s_0$ it gives rise to the vary narrow resonance spikes. The enhancement is associated with the $l = a_0$. term which is computed by summing ray terms of the form f_{ml} as in Eq. (1) but including phase information. The result reduces to

$$f_l = \frac{-G_l \exp\left[-\pi\beta_l + i\eta_l\right]}{\left[1 + \exp\left(-2\pi\beta_l + i2\pi xc/c_l\right)\right]} \quad , \quad G_l = \frac{8\pi\beta_l c \exp(i\phi_l)}{c_l} \quad , \tag{3,4}$$

where $\eta_l = xc/c_l - (\pi/2)$, $x = ka$, and except for the expression for $\arg(G_l) = \phi_l$, the generalization to this case of a subsonic wave follows from the ray geometry in Fig. 2 and related considerations [9,13]. The approximation for ϕ_l used in Fig. 7 was obtained by assuming that ϕ_l varies linearly with c_l as c_l approaches c,

$$\phi_l \left(Rc \le c_l \le c\right) \approx \pi\left[(3/2) - (2F/3)\right], \quad F = \left[\left(c_l/c\right) - R\right] / (1 - R), \tag{5,6}$$

but that ϕ_l becomes constant for c_l/c below a particular value of $R < 1$ so that $\phi(c_l < Rc) = 3\pi/2$. Note that F varies from 0 to 1 in the domain of Eq. (5). Results of Ho and Felsen [8] were used as a guide for formulating the limiting values of ϕ_l though the value of $R = 0.91$ used for the synthesis in Fig. 7 was determined empirically. Inspection of Fig. 3(b) shows that for ka near 40, β_l is sufficiently small for the a_0. wave that contributions from repeated circumnavigations are important giving rise to a distinct resonance structure. With increasing ka there is an enhancement in $|f_l|$ associated primarily with the $m = 0$ contribution plotted in Fig. 4. For $ka \gtrsim 50$, β_l is so large that repeated circumnavigations are no longer important and the gradual periodic variations in |f| shown in Fig. 7 are due to the interference with the specular reflection. This was verified with a simple ray calculation of the quasiperiod $\Delta ka \approx 2\pi[2 + (\pi c/c_l)]^{-1} \approx 1.2$. A ray synthesis was also demonstrated for backscattering from a circular cylindrical stainless steel shell also with $a/h = 40$ and the agreement with the exact result was slightly improved over that of Fig. 7 [16]. The magnitude of the enhancement relative to the strength of the specular contribution is weaker for cylinders than for spheres due to the absence of axial focusing in the cylinder case [9,13].

TIME-FREQUENCY ANALYSIS OF BACKSCATTERING BY SPHERICAL SHELLS

Yen et al. [17] explored the use of a modified version of the Wigner distribution function (WDF) for displaying a time-frequency analysis of transients scattered by elastic objects. The present research applies methods of smoothing the WDF discussed by Nuttall [18] to scattering by spherical shells [19]. The example considered below is that of backscattering by the same shell considered in Figs. 3-5. The response to an impulse is computed for the time domain in Ref. 9 where it is shown that in addition to the specular reflection, there is a large wave packet associated with the $l = a_0$. wave with the $m = 0$ ray path shown in Fig. 2. Considering the impulse response in the time-frequency domain displays the spectral evolution of this and other wave packets. Figure 8 shows the smoothed WDF for the impulse response based on the exact f from the partial-wave series. The axes are in dimensionless ka and $T = tc/a$ where the time offset used is the same as that of Fig. 4 so that the earliest contribution is the specular reflection at $T = 1$ in the narrow time resolution limit. Various contributions can be identified by comparing the time of the contribution with predictions from ray theory as discussed e.g. in Ref. 5 and 9. The dark bar centered on $T = 1$ is the specular reflection and the dark patch centered near $T \approx 5.5$ and $ka \approx 46$ is from the $l = a_0$., $m = 0$ wave packet associated with the midfrequency enhancement. Leaky wave contributions that can be easily identified include those due to the $l = s_0$ and a_1 generalizations of Lamb waves to the present case of a hollow fluid-loaded shell. In addition, there is a large prompt contribution to the backscattering for ka in the region from approximately 455 to 485. This enhancement is in the vicinity of the threshold for the s_1 Lamb wave as well as the longitudinal resonance discussed in Ref. 3 and 4 that, for the present shell, is at $ka = 482$. Since Fig. 8 shows that this contribution is close in time to the specular reflection, a surface guided wave does not have sufficient time to travel around the backside of the sphere. A novel alternative prompt guided-wave mechanism is from rays with the group velocity directed opposite to the phase velocity [20] and Fig. 8 is generally supportive of such a mechanism.

WEAKLY- OR NON-RADIATING SUPERSONIC LAMB WAVES ON FLUID-LOADED PLATES AND SHELLS

Consider again the conventional leaky ray picture for backscattering by spheres and cylinders shown in Fig. 1. The associated contributions have been used to synthesize the exact f for thick hollow spherical [1,3] and cylindrical [21] shells. In those ray calculations, the leaky lamb wave properties $c_l(ka) > c$ and $\beta_l(ka)$ are calculated from the exact elastic equations as discussed above in conjunction with Fig. 3. One curious result of those calculations is that for certain leaky rays, the function $\beta_l(ka)$ can exhibit a minimum where β_l can be as

small as 10^{-4} Np/rad which means that the supersonic guided wave only weakly leaks energy. In the region of ka where β_l is small, the resonances associated with that leaky wave are narrow [3,13]. For the examples of a thick stainless steel shell with h/a = 0.162 considered in Ref. 3 (Fig. A1) and 21 (Fig. 2(b)), such minima occur at $ka \approx 18$ and 73 for the $l = s_0$ and a_1 waves, respectively. Insight into the cause of such minima can be found by first considering the particle displacement at the surface of a flat plate in a vacuum. Worlton [22] has shown that when the phase velocity c_{lP} of the lth Lamb mode of the plate is equal to the longitudinal wave speed c_L of the bulk material, then there is no normal displacement at the plate's surface. For a supersonic wave to radiate or leak sound into the surrounding inviscid fluid, it is essential that surface displacements occur perpendicular to the plate. Consequently, it is to be expected that the radiation damping vanish exactly when $c_{lP} = c_L$ for fluid loaded plates. Inspection of the exact dispersion equations given in Ref. 12 and 11 for the case of (inviscid) fluids on one or both sides, respectively, shows that is indeed the case: when $c_{lP} = c_L$, there is no radiation damping of the lth Lamb wave and c_{lP} does not depend on the density of the fluid! A corresponding analysis of the exact displacements at the (curved) surface of a shell has not been carried out however it is to be anticipated on physical grounds that locally normal surface displacements are essential either for radiation by a given mode or for excitation of that mode by an incident sound wave. For leaky waves with $ka >> 1$ on shells with $h/a << 1$, the effects of curvature should be small so that β_l should be small when $c_l \approx c_L$. One approximation to allow for curvature effects is to compare c_l with the projection of c_L from an imagined middle surface of the shell to the outer surface in contact with the fluid. (A similar projection is described in Ref. 23 for the purpose of relating plate and thick shell phase velocities.) Comparisons for the thick shells considered in Ref. 3 and 21 indicate that this projection only roughly approximates the curvature correction for estimating exactly where $\beta_l(ka)$ is minimized for thick shells but that the general condition that c_l is close to c_L is applicable [24].

CLOSING COMMENTS AND ACKNOWLEDGMENT

The summary given here considers the application of ray methods to backscattering from shells with an emphasis on understanding those contributions which are either very large or very weak. In related work the underlying formalism of resonance scattering theory has also been investigated with a product expansion of the S-matrix for symmetric scatterers [25]. Recent advances in the extension of ray approximations to low frequencies, briefly reviewed in Ref. 7, would suggest that modified ray methods may be applicable down to ka of 2 or smaller. Especially relevant is a correction recently investigated by Rumerman for cylindrical shells [26].

In other recent research pertaining to the influence of structures on fluid flow, interactions resulting from rotational oscillations of a circular cylinder about its axis were investigated [27]. For certain frequencies of oscillation that depend on the Reynolds number, waves were excited in the viscous shear layers that separate from the cylinder.

This work was supported by the U.S. Office of Naval Research.

REFERENCES

[1] P. L. Marston and S. G. Kargl, "Scattering from hollow shells: quantitative ray representations of amplitudes," *Proceedings of the International Congress on Recent Developments in Air- and Structure-Borne Sound and Vibration* (M. J. Crocker, editor, Auburn, AL., 1990) pp. 565-568.

[2] S. G. Kargl and P. L. Marston, "Ray synthesis of Lamb wave contributions to the total scattering cross section for an elastic spherical shell," J. Acoust. Soc. Am. **88** (1990), 1103-1113.

[3] S. G. Kargl and P. L. Marston, "Ray synthesis of the form function for backscattering from an elastic spherical shell: Leaky Lamb waves and longitudinal resonances," J. Acoust. Soc. Am. **89** (1991), 2545-2558.

[4] S. G. Kargl and P. L. Marston, "Longitudinal resonance in the form function for backscattering from a spherical shell: Fluid shell case," J. Acoust. Soc. Am. **88** (1990), 1114-1122.

[5] S. G. Kargl and P. L. Marston, "Observations and modeling of the backscattering of short tone bursts from a spherical shell: Lamb wave echoes, glory, and axial reverberations," J. Acoust. Soc. Am. **85** (1989), 1014-1028; erratum **89** (1991), 2462.

[6] C. K. Frederickson, "Wavefields near transverse cusp caustics produced by reflecting ultrasonic transients and tone bursts from curved surfaces," Ph.D. Thesis, Department of Physics, Washington State University (1991).

[7] P. L. Marston, "Geometrical and catastrophe optics methods in scattering," to appear in *Physical Acoustics* vol. XXI (R. N. Thurston and A. D. Pierce, eds.) Academic Press.

[8] J. M. Ho and L. B. Felsen, "Nonconventional traveling wave formulations and ray-acoustic reductions for source-excited fluid-loaded thin elastic spherical shells," J. Acoust. Soc. am. **88** (1990), 2389-2414.

[9] L. G. Zhang, N. H. Sun, and P. L. Marston, "Mid-frequency enhancement of the backscattering of tone bursts by thin spherical shells," J. Acoust. Soc. Am. (accepted for publication).

[10] M. F. Osborne and S. D. Hart, "Transmission, reflection, and guiding of an exponential pulse by a steel plate in water. I. Theory," J. Acoust. Soc. Am. **17** (1945), 1-18.

[11] W. M. Ewing, W. S. Jardetzky, and F. Press, *Elastic Waves in Layered Media* (McGraw-Hill, 1957) pp. 288-293.

[12] A. Grabowska, "Propagation of elastic waves in solid-liquid system," Archives of Acoustics **4** (1979), 57-64.
[13] P. L. Marston, "GTD for backscattering from elastic spheres and cylinders in water, and the coupling of surface elastic waves with the acoustic field," J. Acoust. Soc. Am. **83** (1988), 25-37.
[14] Ligang Zhang, "Scattering of tone bursts from spherical shells: Computations based on Fourier transform method," M.S. thesis, Department of Physics, Washington State University (1991).
[15] G. Kaduchak and P. L. Marston, in preparation.
[16] N. H. Sun and P. L. Marston, "Ray synthesis of backscattering by thin cylindrical shells (abstract)," J. Acoust. Soc. Am. **89** (1991), 1949.
[17] N. Yen, L. R. Dragonette, and S. K. Numrich, "Time-frequency analysis of acoustic scattering from elastic objects," J. Acoust. Soc. Am. **87** (1990), 2359-2370.
[18] A. H. Nuttall, *Signal Processing Studies*, Naval Underwater Systems Center (1989).
[19] D. H. Hughes and P. L. Marston, in preparation.
[20] P. L. Marston, N. H. Sun, and L. Zhang, "Backward-wave model of the high-frequency enhancement or quasiresonance in the backscattering from spherical shells (abstract)," J. Acoust. Soc. Am. **90** (1991) 2341.
[21] N. H. Sun and P. L. Marston, "Ray synthesis of leaky Lamb wave contributions to backscattering from thick cylindrical shells," J. Acoust. Soc. Am. (accepted for publication).
[22] D. C. Worlton, "Experimental confirmation of Lamb waves at megacycle frequencies," J. Appl. Phys. **32** (1961), 962-971.
[23] P. L. Marston, "Phase velocity of Lamb waves on a spherical shell: Approximate dependence on curvature from kinematics, J. Acoust. Soc. Am. **85** (1989), 2663-2665.
[24] P. L. Marston, in preparation.
[25] P. L. Marston, S. G. Kargl, and N. H. Sun, "Elastic resonance amplitudes described by generalized GTD and by product expansions of the S-matrix," to appear in *Acoustic Resonance Scattering* (H. Uberall, editor) Gordon and Breach Publishers.
[26] M. L. Rumerman, "Increased accuracy in the application of the Sommerfeld-Watson transformation to acoustic scattering from cylindrical shells," J. Acoust. Soc. Am. **90** (1991), 2739-2750.
[27] J. R. Filler, P. L. Marston, and W. C. Mih, "Response of the shear layers separating from a circular cylinder to small-amplitude rotational oscillations," J. Fluid Mech. (1991), 481-499.

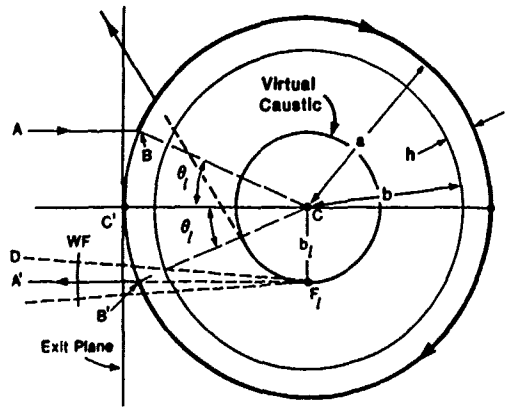

Figure 1 -- Ray diagram for sound backscattered due to a leaky Lamb wave of type *l* excited near B traveling repeatedly around a spherical or cylindrical shell.

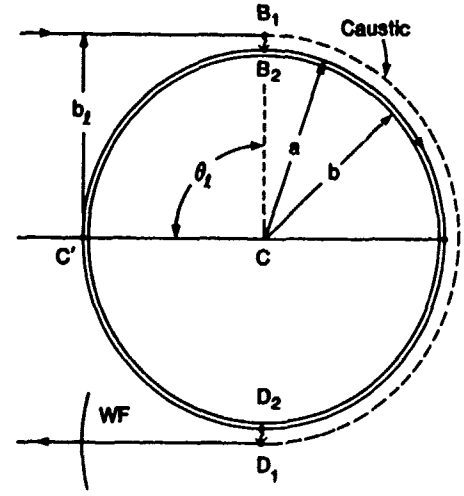

Figure 2 -- Like Fig. 1 but for a guided wave whose phase velocity along the outer surface of the shell is subsonic with respect to the surroundings. WF denotes a section of wavefront that appears to be radiated from an external caustic of radius b_l.

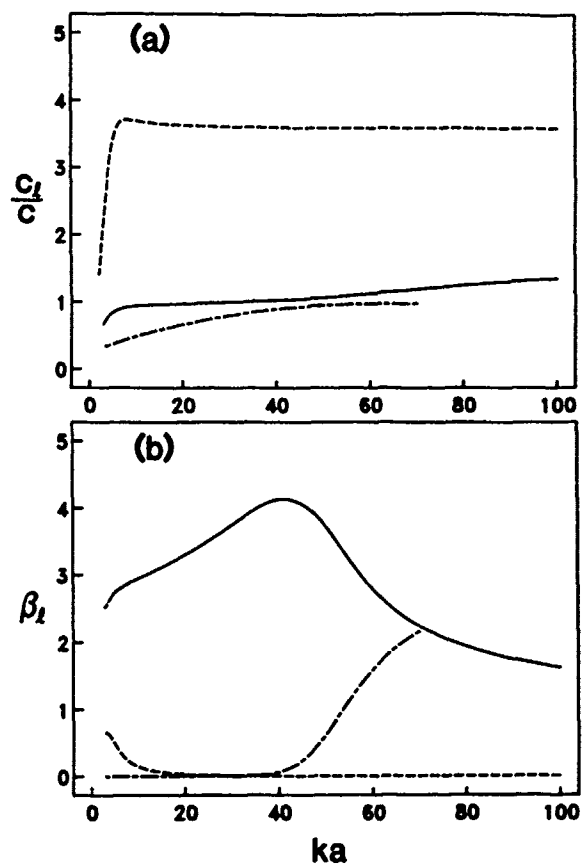

Figure 3 -- Normalized phase velocity (a) and radiation damping (b) of surface guided waves on a 304 stainless steel shell in water with $h/a = 0.025$. The curves are identified as follows: long and short dashes ($l = a_0$.), dashes ($l = s_0$), and solid ($l = a_0$).

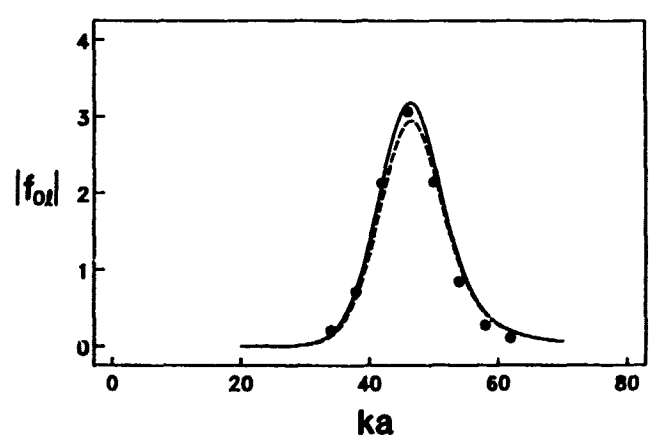

Figure 4 -- The solid curve gives the ray model in Eq. (1) for the a_0. guided wave echo amplitude in the region of the enhancement near $ka = 46$. The points are from the exact echo amplitude determined by a Fourier synthesis as illustrated in Fig. 5.

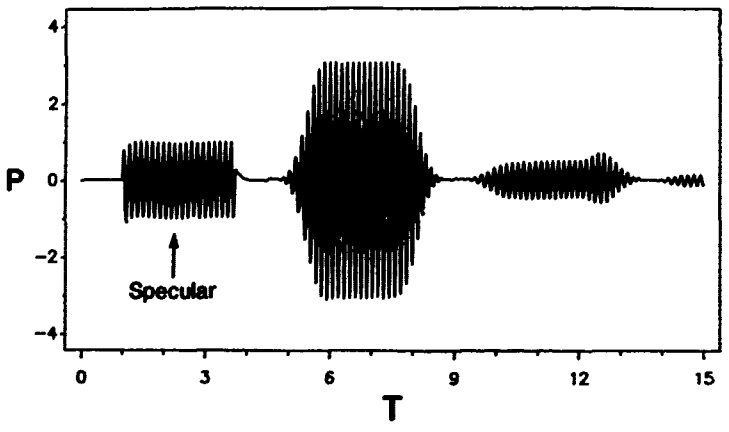

Figure 5 -- Farfield scattered normalized pressure P(T) calculated by Fourier synthesis from the exact of partial-wave series for 20 cycle incident burst with a carrier k*a* of 46 for the shell considered in Fig. 3. The large second echo is enhanced as predicted in Fig. 4.

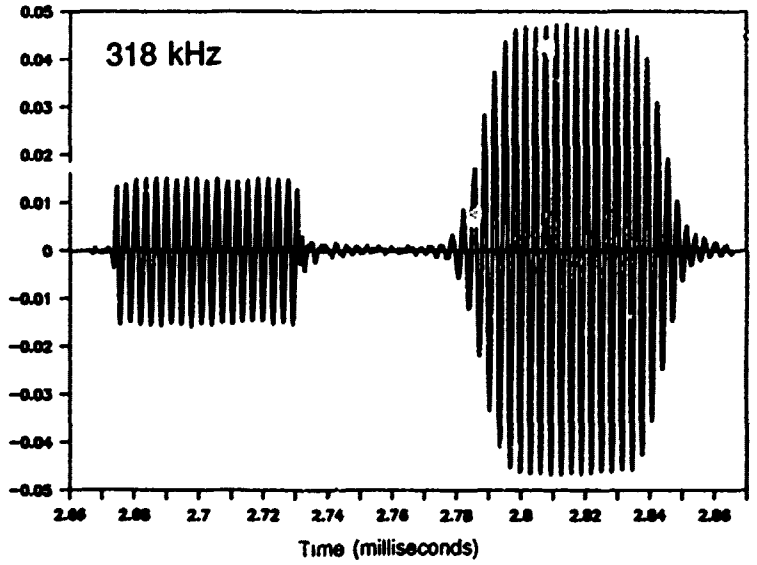

Figure 6 -- Experimental confirmation of the midfrequency enhancement of the earliest subsonic guided wave echo for a thin spherical shell (see text). The echo on the left is the specular reflection.

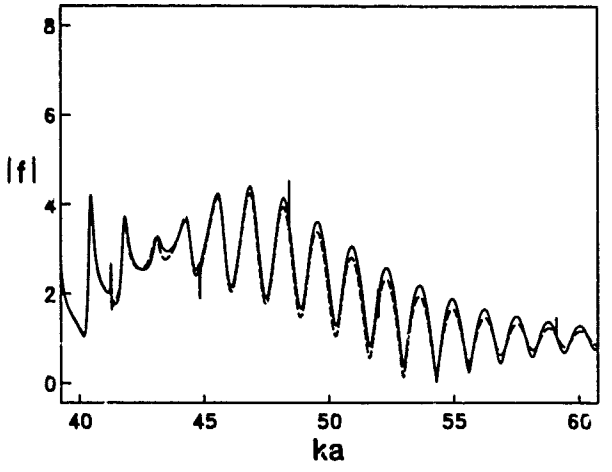

Figure 7 -- The dashed curve gives the exact |f| for steady-state backscattering by the hollow spherical shell considered in Figs. 3-5. The solid curve gives ray approximation based in Eq. (3) that manifests the enhancement.

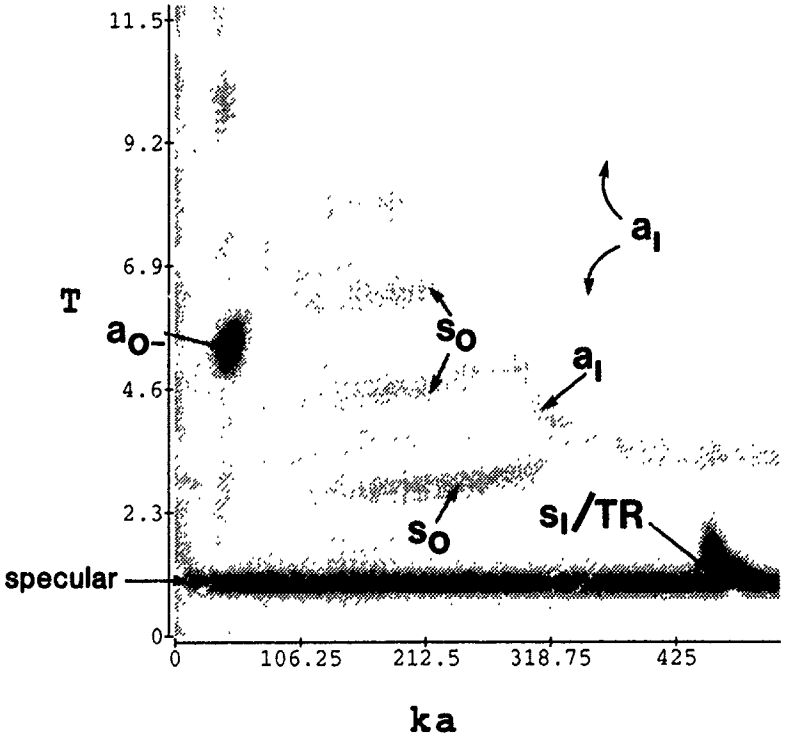

Figure 8 -- Time-frequency analysis of the impulse response for backscattering by the 2.5% thick shell considered in Figs. 3-5. The dynamic range is such that the darkest regions correspond to signals that are orders-of-magnitude larger than the light regions. The earliest and strongest of a sequence of a_0 wave packets is labeled as is the prompt large thickness-resonance/s_1-wave-threshold feature, both of which are stronger in this plot than the specular reflection. Features associated with circumnavigations of dispersive leaky Lamb waves are also evident.

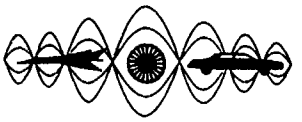

SECOND INTERNATIONAL CONGRESS ON
RECENT DEVELOPMENTS IN AIR- AND
STRUCTURE-BORNE SOUND AND VIBRATION
MARCH 4-6, 1992 AUBURN UNIVERSITY, USA

VIBRATIONS, SOUND RADIATION AND SCATTERING BY SHELLS WITH ARBITRARY SHAPE

Vadim V. Muzychenko
N. N. Andreyev Acoustics Institute.
Shvernik st., 4,
Moscow, 117036, USSR,

ABSTRACT

An analitical and calculating method describing the dynamics of arbitrary shells in the fluid is developed. This method permits to investigate radiated and scattered field. First of all real solution of the dispersion relation for a thin cylindrical elastic shell are obtained in application to the sound-scattering problem. Then the system of shell equations is obtained from the equations of elastic equilibrium of thin shell. The density of simply sources is defined from the system of boundary integral equations. For the case of circular contour there is a calculative example of scattering amplitude. Using this method we calculated the scattering amplitude for bistatic case.

INTRODUCTION

The low-frequency resonance radiation and scattering of sound by elastic shells has emerged as a timely problem in recent years. Various methods have been developed for the solution of the sound vibration, radiation and scattering problems, including the T-matrix method, the Boundary Element Method, Method of Moments, Matching of Asimptotical Expansions, etc. We note that the practical application of any method is limited either by insufficient speed and storage capacity of present-day computers or by the difficulty of using it for physical analysis of the structure of the fields. In addition to these methods it is useful to have model analytical method [1]. This method is based on the Kirchhoff integral . In this paper the analitical and calculating model method describing the dynamics of arbitrary shells is developed. First of all real solutions of the dispersion relation for a thin cylindrical elastic shell are obtained [2] it is shown that the reaction of medium has a significant influence only on flexural waves. The experimentally observed increase in the low-frequency scattering amplitude in the region of angles of incidence of a plane sound wave on the shell close to the axis of the cylinder is also explained. Radiation impedance of limited cylindrical area is calculated in [3] A scattering problem of sound wave, which falls normaly to infinite thin cylindrical shell with arbitrary contour of cross-section is considered too. The sistem of shell equations may be obtained from the equations of elastic equilibrium of thin shell by

V.Z Vlasov. The analitical expression for Green function of shell is found with help of simply layer potential. The density of simply sources is defined from the system of boundary integral equations. In partial cases (absolutely rigid and absolutely soft boundary, elastic shell with circular contour) the known expressions are followed

INFLUENCE OF THE REACTION OF THE MEDIUM

It is generally known that the amplitude of a plane sound wave scattered by a cylindrical elastic shell increases abruptly when the condition

$$\mathrm{Im}\,(Z_y^m + Z_a^m) = 0 \qquad (1)$$

holds [1], where Z_y^m and Z_a^m are the Fourier components of the mechanical impedance of the shell and the radiation impedance respectively:

$$Z_y^m = \frac{i}{\omega}\frac{c_{10}^2 h \rho_M}{R^2}\left(\frac{D_0^m}{D_{33}^m}\right);\quad Z_a^m = i\rho_{11}\omega R\frac{H_m^{(1)}(\varkappa R)}{(\varkappa R)H_m^{(1)'}(\varkappa R)}. \qquad (2)$$

Here c_{10} - is the longitudinal wave velocity in a plate of the same material as the shell; $c_{10}^2 = E/\rho_M(1-\nu^2)$; E, ρ_M, ν -are the Young's modulus, density, and Poisson ratio of the shell material; h and R are the thickness and radius of the centroidal surface of shell; D_0^m and D_{33}^m are the principal determinant and corresponding minor of the system of equations of motion describing the free vibrations of "dry" infinite thin cylindrical shell [1]; $\varkappa = (k_{11}^2 - k^2)^{1/2}$; $H_m^{(1)}(\varkappa R)$ and $H_m^{(1)'}(\varkappa R)$ are the Hankel function of the first kind of order and its derivative with respect to the argument, $H_m^{(1)}(\tilde{z}) = J_m(\tilde{z}) + iY_m(\tilde{z})$, and the branches of the Bessel function $J_m(\tilde{z})$ and the Neumann function $Y_m(\tilde{z})$ are chosen so that $J_m(\tilde{z})$ and $Y_m(\tilde{z})$ are real functions for positive real values of the argument $\tilde{z}$.

The objective of the present study is to analyze the conditions under which Eq. (1) is valid and the scattering amplitude thus acquires resonance maxima. Inasmuch as we investigating the scattering of a plane sound wave $\Phi = A_0\exp(ik_x x + ik_y y + ik_z z)$, which is determined by the wave vector $\vec{k} = (k_x, k_y, k_z)$ and which has a fixed frequency ω, we are interested only in the real solution of Eq. (1). Moreover, the function $k(\omega)$ obtained in the present study will be used to analyze the resonant vibrations of a bounded simply supported shell with eigenfunction $\Psi_p(z) = \sin[k_p(z + L/2)]$, $k_p = \pi p/L$. We require $k(\omega)$ in the interval $[0, \omega]$, because resonant vibrations of the indicated type $\Psi_p(z)$ are excited by an incident wave with any $k = k_{11}\cos\theta_0$ (θ_0 is the angle between the direction of sound incidence and the longitudinal axis of the shell). Here a discrete series of values of k_p corresponds to points situated on very curves $k(\omega)$ calculated below over the entire range of variation of k. We consider the function $F(y, \Omega_{10}, m) = Z_y^m + Z_a^m$. On the basis of Eq. (2) it has the form :

$$F(y, \Omega_{10}, m) = i\rho_M c_{10}\left[\frac{D_0^m}{D_{33}^m} + \beta\frac{\Omega_{10}^2}{(12\delta)^{1/2}}\frac{H_m^{(1)}([\Omega_{10}^2 - y^2]^{1/2})}{[\Omega_{10}^2 - y^2]^{1/2}H_m^{(1)'}([\Omega_{10}^2 - y^2]^{1/2})}\right], \qquad (3)$$

where $\delta = h^2/12R^2$; $\Omega_{10} = k_{10}R = \omega R/c_{10}$; $\Omega_{11} = k_{11}R = \omega R/c_{11}$; $y = kR$; $\beta = \rho_{11}/\rho_M$;

$D_j^m = \det L_j^m$; $D_{33}^m = L_{11}^m L_{22}^m - L_{12}^m L_{21}^m$; $L_{11}^m = [\Omega_{10}^2 - y^2 - am^2]$; $L_{22}^m = [\Omega_{10}^2 - ay^2 - m^2]$;

$L_{12}^m = L_{21}^m = -bmy$; $L_{13}^m = L_{31}^m = i\nu y$; $L_{33}^m = [1 - \Omega_{10}^2 + \delta(y^2 + m^2)^2 - \delta(2m^2 - 1)]$;

$L_{23}^m = L_{32}^m = im$; $a = (1-\nu)/2$; $b = (1+\nu)/2$.

Separating the function Eq. (3) into real and imaginary parts, we obtain the equations :

$$\mathrm{Im}\,Z_y^m = (12\delta)^{1/2}\rho_M c_{10}(1/\Omega_{10})F_y^{(1)}(y,\Omega_{10},m)\,; \tag{4}$$

$$\mathrm{Im}\,Z_s^m = (12\delta)^{1/2}\rho_M c_{10}(1/\Omega_{10})F_s^{(1)}(y,\Omega_{10},m)\,; \tag{5}$$

$$\mathrm{Im}\,Z_s^m = (12\delta)^{1/2}\rho_M c_{10}(1/\Omega_{10})F_s^{(r)}(y,\Omega_{10},m)\,; \tag{6}$$

where $F_y^{(1)}(y,\Omega_{10},m) = v_0^m/v_{s0}^m = [1-\Omega_{10}^2+\delta(y^2+m^2)^2-\delta(2m^2-1)]+$

$$+\left[\frac{m^2(\Omega_{10}^2-y^2-am^2)+2bvm^2y^2+v^2y^2(\Omega_{10}^2-ay^2-m^2)}{(\Omega_{10}^2-y^2-am^2)(\Omega_{10}^2-ay^2-m^2)-b^2m^2y^2}\right], \tag{7}$$

$$F_s^{(1)}(y,\Omega_{10},m) = \begin{cases} \beta\dfrac{\Omega_{10}^2}{(12\delta)^{1/2}}\dfrac{1}{t}\dfrac{[J_m(t)J_m'(t)+Y_m(t)Y_m'(t)]}{[J_m(t)]^2+[Y_m(t)]^2}\,; & y\le\Omega_{11}, \\ \beta\dfrac{\Omega_{10}^2}{(12\delta)^{1/2}}\dfrac{1}{t^*}\dfrac{K_m(t^*)}{K_m'(t^*)}\,, & y>\Omega_{11}, \end{cases} \tag{8}$$

$$F_s^{(r)}(y,\Omega_{10},m) = \begin{cases} \beta\dfrac{\Omega_{10}^2}{(12\delta)^{1/2}}\dfrac{2}{\pi t^2}\dfrac{1}{[J_m(t)]^2+[Y_m(t)]^2}\,, & y\le\Omega_{11}, \\ 0\,; & y>\Omega_{11}. \end{cases} \tag{9}$$

Here $J_m(t)$, $Y_m(t)$ and $K_m(t^*)$ are Bessel and Neumann functions and modified Bessel functions of the third kind (Macdonald functions) ; $t=(\Omega_{11}^2-y^2)^{1/2}$, $t^*=(y^2-\Omega_{11}^2)^{1/2}$. The following identity for the Wronskian of the Bessel and Neumann functions is taken into account in the derivation of Eq. (9) : $W(J_m(\tilde z),Y_m(\tilde z)) = J_m(\tilde z)Y_m'(\tilde z)-J_m'(\tilde z)Y_m(\tilde z) = 2/\pi\tilde z$.

We thus seek the real solution $y(\Omega_{10})$ of the equation :

$$F_y^{(1)}(y,\Omega_{10},m)+F_s^{(1)}(y,\Omega_{10},m) = 0\,. \tag{10}$$

The solution of Eq. (10) has been investigated previously for $\beta = 0$, i.e., when the reaction of the medium surrounding the shell is disregarded [$F_s^{(1)}(y,\Omega_{10},m) = 0$] [1]. In the present report we find the solutions of Eq. (10) for $\beta \neq 0$ [2]. We first consider the case $m = 0$.

The asimptotic behavior of the function $F_s^{(1)}(y,\Omega_{10},0)$ defined by Eq. (8) in the neighborhood of the line $y = \Omega_{11}$ follows from the properties of the functions $H_0^{(1)}(z)$, $K_0(z)$ and their derivatives occurring in the function :

$$F_s^{(1)}(y,\Omega_{10},0) \approx \beta\frac{\Omega_{10}^2}{(12\delta)^{1/2}}\ln\left[(|\Omega_{11}^2-y^2|)^{1/2}\right]\,;\ y\to\Omega_{11}\,. \tag{11}$$

Substituting Eqs. (11) and (7) with $m = 0$ in Eq. (10), we obtain (in the limit $y\to\Omega_{11}$) :

$$F_y^{(1)}(y,\Omega_{10},0)+\beta\frac{\Omega_{10}^2}{(12\delta)^{1/2}}\ln\left[(|\Omega_{11}^2-y^2|)^{1/2}\right] =$$

$$= \left[(1-\Omega_{10}^2+\delta y^4+\delta)+\frac{v^2y^2}{(\Omega_{10}^2-y^2)}\right]+\beta\frac{\Omega_{10}^2}{(12\delta)^{1/2}}\ln\left[(|\Omega_{11}^2-y^2|)^{1/2}\right] = 0\,. \tag{12}$$

Inverting Eq. (12) and invoking the expansion $(1-x)^{1/2}\approx 1-x/2$ for $x<<1$, we find that the solution $y(\Omega_{10}) = \Omega_{11}$ is a two-valued solution of Eq. (10) for the case $\beta = 0$, $m = 0$ in the limit $\beta\to 0$.

$$y_{1\pm}(\Omega_{10}) = \lim_{\beta\to 0}\left[\Omega_{11}\pm\frac{1}{2\Omega_{11}}\exp\left(-\frac{2(12\delta)^{1/2}}{\beta\Omega_{10}^2}F_y^{(1)}(\Omega_{11},\Omega_{10},0)\right)\right], \tag{13}$$

where the plus sign corresponds to one solution, and the minus sign corresponds to the other. It shoud be noted that β tends to zero from the left or right in the case, depending on the sign of the function $F_y^{(1)}(\Omega_{11},\Omega_{10},0)$. For example, β tends to zero from the right $(\beta\to 0+0)$ for values of the frequency Ω_{10} such that $F_y^{(1)}(\Omega_{11},\Omega_{10},0)$ is positive. In the case of negative values of $F_y^{(1)}(y,\Omega_{10},0)$, on the other hand, β tends to zero from the left $(\beta\to 0-0)$. We note that $\beta > 0$ in

the real physical problem ($\beta = \rho_{II} / \rho_M$ is the ratio of the density of the medium surrounding the shell to the material density of the latter). Consequently, the indicated two-valued solution $y_{I\pm}(\Omega_{Io}) = \Omega_{II}$ will exist whereve the function $F_y^{(1)}(\Omega_{II}, \Omega_{Io}, 0) > 0$ in the limit $\beta \to 0$ for $m = 0$, with the exception of solutions of the equation $F_y^{(1)}(y, \Omega_{Io}, 0) = 0$, which correspond to quasiflexural and quasilongitudinal waves.

We now consider the solutions of Eq. (10) for $\beta > 0$. The two-valued solution $y(\Omega_{Io}) = \Omega_{II}$ branches into two solutions $y_{I,II}(\Omega_{Io})$ in accordance with the asymptotic relation Eq.(13) for values of the frequency Ω_{Io} such that the function $F_y^{(1)}(\Omega_{II}, \Omega_{Io}, 0) > 0$ (this is the segment OA in Fig. 1), i.e., when the mechanical impedance of the shell Z_y^m exhibits elastic behavior. The two-valued solution $y(\Omega_{Io}) = \Omega_{II}$ branches into two complex-conjugate solutions for values of the frequency Ω_{Io} such that the function $F_y^{(1)}(\Omega_{II}, \Omega_{Io}, 0) < 0$ (this is the segment AB in Fig. 1), i.e., when the mechanical impedance of the shell Z_y^m is a mass reactance. Figure 1 shows the real solutions of Eq.(10) calculated on a computer in the case $m = 0$ and $m = 1$ for steel shells in water ($\nu = 0.3$; $E = 2 \cdot 10^{11}\ N/m^2$; $\rho_M = 7.8 \cdot 10^3\ kg/m^3$; $h/R = 0.1$ and $h/R = 0.2$; $c_{II} = 1500\ m/s$; $\rho_{II} = 1 \cdot 10^3\ kg/m^3$) The solution I and II have the line $y = \Omega_{II}$ as an asymptote in the limit $\Omega_{Io} \to 0$. As in the case $\beta = 0$, the solution III has a low-frequency asymptotic behavior corresponding to longitudinal waves in an unbounded rod in the limit $\Omega_{Io} \to 0$: $y \approx (1 - \nu^2)^{1/2}\, \Omega_{Io}$. As the frequency Ω_{Io} is increased from zero, the solutions II and III move away from the origin, diverge, and then begin to converge with a further increase in Ω_{Io} untill, at a certain value of Ω_{Io}, they form a branch point at some point C with coordinates (y_c, Ω_c), when $y_{II}(\Omega_c) = y_{III}(\Omega_c) = y_c$. In the neighborhood of the branch point C the asimptotic behavior of the solutions II and III has the form:

$$(y_{II,III} - y_c) \approx \pm A_c(\Omega_c - \Omega_{Io})^{1/2};\ \Omega_{Io} \to \Omega_c, \qquad (14)$$

where $A_c > 0$ is a constant. As mentioned, the solutions II and III become complex conjugates with a further increase in the frequency Ω_{Io} ($\Omega_{Io} > \Omega_c$).

It must be added here that, a qualitative restructuring of the solutions of Eq. (10) does not take place for $\beta \neq 0$ in the cases $m = 1, 2, \ldots$ This result is attributable to the fact, which follows from Eq. (8), that

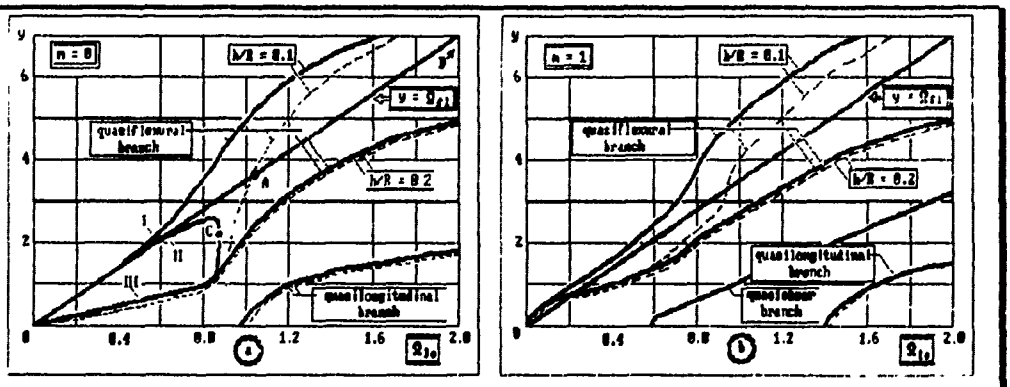

Fig.1 Real roots of the equations: (-) $\mathrm{Im}(Z_y^m + Z_e^m) = 0$ and (···) $\mathrm{Im}(Z_y^m) = 0$.

the function $F_e^{(1)}(y, \Omega_{Io}, m)$, $m \geq 1$, does not any singularities for real values of Ω_{Io} and y.

Thus, several results can be drawn from the foregoing analysis : The reaction of the medium has a significant influence only on flexural modes. It is evident from the graphs in Fig 1 that this influence causes a major change in the angular and frequency ranges where the condition for spatial coincidence holds for these waves [1] :

$$k = k_{fl} \cos\theta \quad \text{or} \quad y = \Omega_{fl} \cos\theta \ . \tag{15}$$

Here θ is the angle between the wave vector of the incident wave and the positive z direction, which coincides with the longitudinal axis of the shell. For example, the spatial coincidence condition Eq.(15) does not hold for any angles of plane-wave incidence for sufficiently thin shells ($h/R \le 0.1$) in the case $m = 1$ (see Fig. 1). This means that resonance maxima corresponding to the first mode will be absent in the experimental directivity patterns for the backscattering (echo return) of sound by thin cylindrical steel shells in water. Consequently, the positions of the resonance maxima (in the angular scattering patterns) corresponding to flexural modes must be determined by solving the dispersion relation Eq.(1), i.e., with allowance for the reaction of the medium. The analysis shows that the scattering-amplitude maxima corresponding to shear and longitudinal modes (see Fig.1) are determined very accurately by the positions of the dispersion curves for the "dry" shell [1].

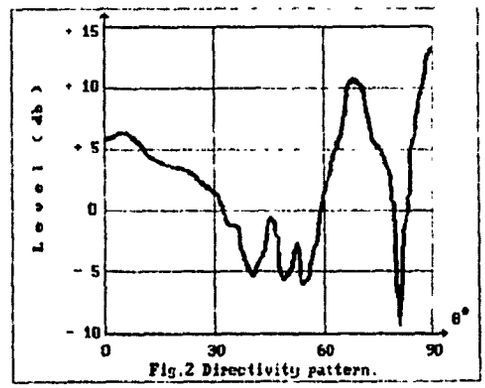

Fig.2 Directivity pattern.

The emergence of a new branch (see Fig. 1, branch II) of the dispersion equation Eq.(1) in the case $m = 0$ for sufficiently thin shells ($h/R \le 0.1$) in the low-frequency range ($\Omega_{10} < 1$) will cause the scattering amplitude to increase in the vicinity of angles of sound incidence close to the cylinder axis ($\theta \to 0^0$). This conclusion is also confirmed by experiments on the backscattering (echo return) of sound by cylindrical steel shells in water [1]. Fig. 2 shows experimental directivity patterns for the backscattering of sound by cylindrical steel shells $L/R \approx 9.126$; $h/R \approx 0.011$; $\Omega_{10} \approx 0.73$. It is evident from the patterns that the scattering amplitude increases in the vicinity of angles of sound incidence close to the cylinder axis ($\theta \to 0^0$).

TO THE THEORY OF SOUND SCATTERING

When the cross-sectional contour is an arbitrary plane curve the equations of thin cylindrical shell are very complicated, and their coefficients are alternative if the plane sound wave falls normally on the infinite cylindrical shell its vibrations depend only from coordinate φ, and the vector of elastic deformation has only two components: tangential U_1 and normal U_3. Then due to [4] the motion equations are (in asymptotical approach:)

$$\begin{cases} \dfrac{\partial^2 U_1}{\partial X^2} - \dfrac{\partial}{\partial X}(qU_3) + p^2 U_1 = 0, \\ (-q)\dfrac{\partial U_1}{\partial X} + \dfrac{h^2}{12}\dfrac{\partial^4 U_3}{\partial X^4} + q^2 U_3 - p^2 U_3 = \dfrac{1}{B}(P_0 + P_s) \end{cases} \tag{16}$$

Here: $p^2 = \rho_M h \omega^2 (1-\nu^2)/Eh$; ρ_M – the density of material , h – shell thickness ; ω – circular frequency ; $E = E_0(1 - i\eta)$; ν – Young's modulus and Poisson ratio; η – damping coefficient ; P_0 and P_s amplitudes of incident and scattering sound waves (inside the shell there is no medium);

$B = Eh/(1-\nu^2)$; $q(\varphi) = 1/R(\varphi)$; $dx = R\,d\varphi$. We suppose that the time dependence of all quantities is $\exp(-i\omega t)$. Note, that the only quantity which depends on x is curvature q. Last years the problem of sound scattering and radiation on cylindrical area with arbitrary contour of cross-section the method of simply sources (monopoles) is used [5], which density σ may be found by means of integral equations solved on computers.

For absolutely soft boundary we have.

$$P = P_0 + P_s = 0, \tag{17}$$

and the integral equation is :

$$\frac{1}{i\rho\omega} P_s(\vec{r}) = \int_{(s)} \sigma(\vec{r}\,') G(\vec{r}, \vec{r}\,')\, ds \ . \tag{18}$$

And when the boundary is absolutely rigid :

$$V_n = V_0 + V_s = 0 \ , \quad V_0 = \frac{1}{i\rho\omega}\left[\frac{\partial P_0(\vec{r})}{\partial n}\right] \ , \ V_s = \frac{1}{i\rho\omega}\left[\frac{\partial P_s(\vec{r})}{\partial n}\right] \tag{19}$$

and the integral equation is :

$$\frac{\sigma}{2} \quad \int_{(s)} \sigma(\vec{r}\,') \frac{\partial G(\vec{r}, \vec{r}\,')}{\partial n} ds' \quad V_0 \ , \tag{20}$$

where $G(\vec{r}, \vec{r}\,') = (1/4\pi) \exp(ik|\vec{r} - \vec{r}\,'|)/|\vec{r} - \vec{r}\,'|$ – Green function for Helmgoltz equation in three dimension case; $k = \omega/c_{11}$ – wave number of sound medium in two dimension case the Green function is $G(\vec{r}, \vec{r}\,') = (i/4) H_0^{(1)}(k|\vec{r} - \vec{r}\,'|)$, where $H_0^{(1)}(k|\vec{r} - \vec{r}\,'|)$ – is a Hankel function of the first kind.

In this report the method of boundary integral equations is derived for the case when the contour S is thin elastic shell described by equations Eq.(16). It is necessary to find Green function $U_3 = K(x, \xi)$ of system Eq.(16). It means their solution when in right part we change $(P_0 + P_s)$ by Dirac's function $\delta(x - \xi)$. When ω is arbitrary the problem has no analitical solution. But in the asimptotical (WKB) case function $K(x, \xi)$ can be obtained by next method.

We seek the solution in form :

$$U_{1,3}(x) = \exp[i\Phi(x)] \ , \tag{21}$$

where $\Phi(x) = \int_{\zeta}^{x} K(x)\,dx$, $K(x) = (2\pi)/\lambda(x)$.

The conditions of applicability are : $\lambda/R \quad . \ 1$, $(\lambda/R) \cdot (\partial R/\partial x) < \ll 1$.

The substitution of Eq.(21) into Eq.(16) gives a dispersion equation which has six roots. The point source $\delta(x - \xi)$ generates waves which run in the directions $\pm|x - \xi|$ and are of following types: flexible uniform waves ($K_1(x) = [p^2/(h^2/12)]^{1/4}$), flexible nonuniform waves ($K_2(x) = i K_1(x)$) and logngitudinal waves ($K_3(x) = [p^2 \ q^2(x)]^{1/2}$). Note, that roots $K_{1,2}$ are functions of x only if the parameters E, ρ, h depend on x in considered model only curvature $q = q(x)$ and, hence, only root K_3 is a function of x .

The corrections to the roots $K_{1,2,3}(x)$ are being found by WKB method :

$$\delta K_{1,2}(x) = \frac{3}{2} i \left[\frac{\partial K_{1,2}/\partial x}{K_{1,2}}\right] \ , \quad \delta K_3(x) = \frac{1}{2} i \left[\frac{\partial K_3/\partial x}{K_3}\right] \ . \tag{22}$$

By integrating the equation Eq.(16) on x in limits $[\xi - \varepsilon, \xi + \varepsilon]$. when $\varepsilon \to 0$ we have :

$$\begin{cases} [U_{1+} \quad U_{1-}] - q[U_{3+} - U_3] = 0 \ , \\ -q[U_{1+} - U_{1-}] + \dfrac{h^2}{12}\left[\dfrac{\partial^3 U_{3+}}{\partial x^3} - \dfrac{\partial^3 U_{3-}}{\partial x^3}\right] = \dfrac{1}{B} \end{cases} \tag{23}$$

In addition, the conditions of continuity are fulfilled in the point $x = \xi$: $U_{1+} = U_{1-}$: $U_{3+} - U_{3-}$, and the rotation angle of section is zero : $\partial U_{1+}/\partial x = 0$, $\partial U_{3-}/\partial x = 0$

We seek $K(x,\xi)$ in form (when $x > \xi$ and when $x < \xi$):

$$K(x,\xi) = U_{3\pm} = A_{1\pm}\exp\left[\pm i\int_{\xi}^{x}[K_1(x') + \delta K_1(x')]dx'\right] +$$

$$+ A_{2\pm}\exp\left[\pm(-1)\int_{\xi}^{x}[K_2(x') + \delta K_2(x')]dx'\right] + A_{3\pm}\exp\left[\pm i\int_{\xi}^{x}[K_3(x') + \delta K_3(x')]dx'\right]. \quad (24)$$

The wave $U_{1\pm}$ is bound with every wave $U_{3\pm}$ and its amplitude is $B_{j\pm} = \beta(\pm K_j)A_{j\pm}$; $j = 1;2;3$, where $\beta(\pm K_j) = (\pm K_j)[q/(K_j^2 - p^2)]$ is defined by substitution Eq (21) into the first equation of system Eq.(16). Six quantities $A_{j\pm}$ we fined after substituting expressions Eq.(24) in six conditions Eq.(23) and so on. Then we have:

$$K(x,\xi) = \frac{i}{4Dk_1^3(x)}\left[\frac{K_1(\xi)}{K_1(x)}\right]^{\frac{3}{2}}\exp\left[i\left|\int_{\xi}^{x}K_1(\xi)\,d\xi\right|\right] -$$

$$- \frac{i}{4Dk_1^3(x)}\left[\frac{K_1(\xi)}{K_1(x)}\right]^{\frac{3}{2}}\exp\left[-i\left|\int_{\xi}^{x}K_1(\xi)\,d\xi\right|\right] +$$

$$+ \frac{iq^2(x)}{2Bp^2[p^2 - q^2(x)]^{1/2}}\left[\frac{K_3(\xi)}{K_3(x)}\right]^{\frac{1}{2}}\exp\left[i\left|\int_{\xi}^{x}K_3(\xi)\,d\xi\right|\right] \quad (25)$$

where $D = Eh^3/12(1-\nu^2) = B(h^2/12)$.

Note, the multipliers $[K_1(\xi)/K_1(x)]^{3/2}$ and $[K_3(\xi)/K_3(x)]^{1/2}$ appear from Eq.(22), and when $x = \xi$ they turn to one. In the case when only parameter q depends on x in Eq.(25) only multiplier $[K_3(\xi)/K_3(x)]^{1/2}$ differs from one when $x \neq \xi$. With the help of analitical expression for Green function Eq.(25) we obtain the relation on the contour S:

$$\frac{\partial U_3}{\partial t} = V_0(x) + V_s(x) = -(i\omega)\int_S K(x,\xi)[P_0(\xi) + P_s(\xi)]d\xi \quad (26)$$

If now we introduce the density $\sigma(x)$ according to the integral equation

$$\frac{1}{i\rho\omega}P_s(x) = \int_S \sigma(x)G(x,\xi)\,d\xi, \quad (27)$$

then using Eq.(19) the system of integral equations Eqs.(26) and (27) is sufficient to solve the radiation or scattering problem for cylindrical shell with arbitrary cross-sectional contour. This system of equations may be performed to one integral equation on the contour S:

$$-(i\omega)\int_S K(x,\xi)\left[P_0 + i\rho\omega\int_S \sigma(\xi')G(\xi,\xi')\,d\xi'\right]d\xi$$

$$- \int_S \sigma(\xi)\frac{\partial G(x,\xi)}{\partial n}\,d\xi = \frac{1}{i\rho\omega}\left(\frac{\partial P_0}{\partial n}\right). \quad (28)$$

Note, that in the case of absolutely soft boundary $K(x,\xi) = \infty$ we have the problem Eq.(18), and in the case of absolutely rigid boundary $K(x,\xi) = 0$ we have the problem Eq.(20)

THE PARTICULAR CASE OF CIRCULAR CONTOUR

When the contour S is a circle of radius R it is convenient to use an expansion for P_0, V_0, P_s, V_s. $P_j = \sum_{m=-\infty}^{+\infty} P_j^m \exp(im\varphi)$ and so on. Using the relations. $V = \partial\Phi/\partial n$, $P = i\rho\omega\Phi$; $Z_s = -i\rho\omega[\partial\Phi/(\partial\omega/\partial n)]$ (Here: Φ and $(\partial\Phi/\partial n)$ - field potential and its normal derivative; Z_s - radiation impedance) we have:

$$V_0^m = -P_0^m/Z_0^m; \quad V_s^m = -P_s^m/Z_s^m \quad (29)$$

and from Eq.(26): $$V_0^m + V_s^m = (1/Z_y^m)[P_0^m + P_s^m], \quad (30)$$

where

$Z_y^m = -(i\omega) \int_S [K(X,\xi) \cdot \exp[i(\vec{n}/R)(X-\xi)]d\xi]$,

and $d\xi = R\, d\varphi$.

Note, that expressions Z_0^m and Z_y^m have a sense of impedance of incident wave and mechanical impedance of elastic vibration of shell correspondingly [1]. For the m-component of Fourier transform of P_s we have from Eqs. (29) and (30) :

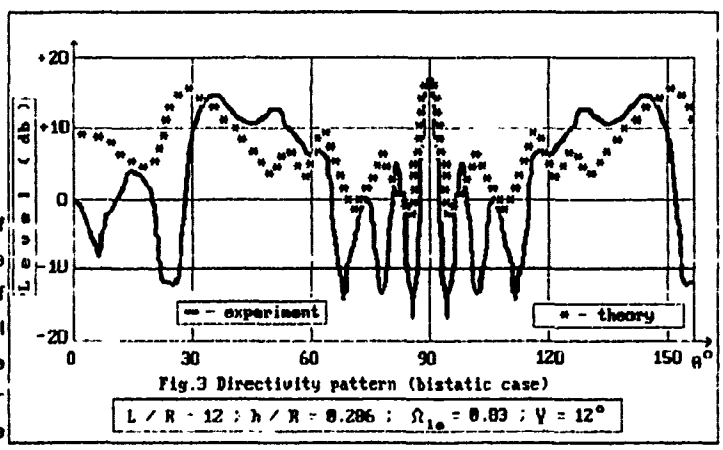

Fig.3 Directivity pattern (bistatic case)

L / R = 12 ; h / R = 0.286 ; Ω_{1e} = 0.83 ; ψ = 12°

$$P_s^m \quad P_0^m \frac{Z_s^m}{Z_0^m}\left[1 + \frac{Z_0^m - Z_s^m}{Z_y^m + Z_s^m}\right] \qquad (31)$$

The last expression is identical to the formulae Eq.(13) from [1]. Note, that for circular contour it is not necessary to find the density σ of simply sources

In particular case of circular contour we calculated the scattering amplitude for bistatic case. We used the analitical method described in the papar [1] and the report [3] presented to the FIRST AUBURN INTERNATIONAL CONGRESS ON RECENT DEVELOPMENTS IN AIR AND STRUCTURE-BORN SOUND AND VIBRATION. The results are given on Figure 3.

CONCLUSION

This method can be used to relate the characteristic features of the radiated and scattered fields to the geometrical and elastic parameters of a finite cylindrical shell. Method permits to investigate radiated and scattered fields in different cases. The theoretical and experimental results are in a good agreement.

REFERENCES

[1] V.V.Muzychenko & S.A.Rybak , "Low-frequency resonance scattering of sound by finite cylindrical shells (review)", Sov. Phys. Acoust., 34(4) , p325 (1988).

[2] V.V.Muzychenko & S.L.Skorokhodov , "Influence of the reaction of the medium on low-frequency resonance sound scattering by cylindrical shells", Sov. Phys. Acoust , 34(2) , p161 (1988).

[3] V.V.Muzychenko & S.A.Rybak , "Sound scattering by limited elastic shells", In: Proc.Int Congr.on Recent Developments in Air & Structure Born Sound & Vibration, Auburn Univ., AL, USA, Vol.2 , p751 (1990).

[4] S.A.Rybak , "Vibrations of double-curvature shells", Sov. Phys. Acoust., 2 , 148-153 (1973).

[5] S.M.Rao & P.K.Raju, "Application of the method of moments to acoustic scattering from multiple bodies of arbitrary shape", J. Acoust. Soc. Amer., 3 , 1143-1148 (1989).

SECOND INTERNATIONAL CONGRESS ON
RECENT DEVELOPMENTS IN AIR- AND
STRUCTURE-BORNE SOUND AND VIBRATION
MARCH 4-6, 1992 AUBURN UNIVERSITY, USA

SOUND RADIATION AND PROPAGATION IN CENTRIFUGAL MACHINES PIPING

Danielius Guzhas

Environmental Department
Vilnius Technical University
Vilnius 232040, Saulėtekio Alėja 11,
Lithuania

ABSTRACT

The paper deals with propagation of vibration and noise through piping in centrifugal machines. The results obtained reveal that a stationary field is achieved at a certain distance from a noise source. An excellent correlation between theoretical calculations with experimental data has been obtained.

The given study presents an analysis of semiinfinite cylindrical shell filled by gas. Because of intensive gas flow pulsation at the edge of the waveform, an excitation occurs. This calculation model is bound with the simultaneous solution of wave equations for a medium filled elastic cylindrical shell and elasticity theory equations. The aim of this study is to define noise level characteristics to the extent of source distance. By space coordinate z noise intensity in a pipe is not a stationary statistical process, though, according to our experiments, it may be achieved at a certain distance from a noise source. Such processes are called ergodicities. Space size of transitional phenomenon are bound with physical qualities of waveforms and with the length of frequency spectrum excited at the noise source.

First let us analyse simultaneously the wave equation with the equation of dynamic theory of elasticity for thinwalled shell, "Eq.(1)"

$$\frac{\partial^2 p}{\partial t^2} = c_0^2 \left\{ \frac{\partial^2 p}{\partial z^2} + \frac{1}{r}\frac{\partial}{\partial r} r \frac{\partial p}{\partial r} \right\}, \quad p = p_1 + p_2 \qquad (1)$$

$$D\frac{\partial^4}{\partial z^4} u + \frac{Eh}{R^2} u + \varrho h \frac{\partial^2 u}{\partial t^2} = p_1(z,R) + p_2(z,R)$$

and corresponding boundary conditions

$$\frac{\partial p_2}{\partial r} = 0, \qquad \frac{\partial p_1}{\partial r} = -\rho_0 \frac{\partial^2 u}{\partial t^2} \qquad \text{by} \quad r = R.$$

Sound pressure component p_1 is conditioned by shell oscillations; p_2 - by excitation of sound waves in the medium from supercharger, "Eq.(2)"

$$u = \sum u_m e^{-i\omega_m t} \qquad \text{by} \quad z = 0, \tag{2}$$

$$\frac{\partial u}{\partial z} = 0 \qquad \text{by} \quad z = 0.$$

Here c_0 - sound velocity in medium, D, E, h, R, ρ - shell parameters (cylindrical rigidity, Young's modulus, wall thickness, radius and density correspondingly), u_k - Fourier components of noise excited in the shell of radiator, z, r - pole coordinates. The flow has a constant component u_0 which is not essential and alternating pulsations, which for a definite model of supercharger may be approximated by exci - tation of shell vibration, "Eq.(3)"

$$u_k = \frac{u_{max}}{\pi} \frac{(-1)^{n-1}}{m}; \quad \omega_m = m\omega. \tag{3}$$

Let us assume that by such excitation $p_2 = 0$.

In a waveform /1/ normal waves may propagate with wave number k, which meet the so called dispersive equation, "Eq.(4)"

$$Dk^4 - \left(\rho h \omega_k^2 - \frac{Eh}{R^2}\right) = \rho_0 \omega^2 \frac{J_0\left(\sqrt{\frac{\omega^2}{c_0^2} - k^2} \cdot R\right)}{\sqrt{\frac{\omega^2}{c_0} - k}\, \dot{J}_0\left(\sqrt{\frac{\omega^2}{c_0^2} - k^2} \cdot R\right)}. \tag{4}$$

For shell vibration calculation wave number k, defined by this equation greatly differs from wave number ω/c_0 in a medium. Therefore, for these waves, due to low air density ρ_0, the right part of equation is not significant, "Eq.(5)"

$$k = \left[\frac{\rho h \omega_k^2 - (Eh/R^2)}{D}\right]^{\frac{1}{4}} \tag{5}$$

Thus, for low frequencies by $\omega_k < c/R$ (where c - sound velocity of shell material) field is heterogeneous and dies-out at source distance, "Eq.(6)"

$$u = u_{max} e^{-\beta z} \cos \beta z, \tag{6}$$

where "Eq.(7)"

$$\beta = \left[\left| \frac{Eh/R^2 - \rho h \omega_k^2}{4D} \right| \right]^{\frac{1}{4}} , \qquad (7)$$

and for a high frequency spectrum part by $\omega_k > c/R$ we have, "Eq.(8)"

$$u = u_{max} \left\{ \frac{e^{-kz}}{1-i} + \frac{e^{ikz}}{1+i} \right\} , \qquad (8)$$

what shows that there is a homogeneous wave energy flow along the shell axis.

Thus, heterogeneous spectrum consists of two parts: $S(t)$ and $S(\infty)$ and correspondingly, "Eq.(9)"

$$\left. \begin{aligned} J(z) &= \sum_{m=1}^{n} S_m e^{-2\beta_m z} \cos^2 \beta_m z + \sum_{m=n}^{\infty} \frac{e^{-k_m z}}{2} S_m , \\ J(\infty) &= \frac{1}{2} \sum_{m=n}^{\infty} S_m , \end{aligned} \right\} \qquad (9)$$

where $S_m = \frac{u_{max}^2}{\pi^2 m^2}$ - noise spectrum,

n - harmonic number, where heterogeneous field passes to homogeneous one, $n = \frac{c}{R\omega}$, where ω - main pulsation frequency which equals to the product of angular velocity of rotation of supercharger to blade number. Thus, we have the following final expressions for heterogeneous and homogeneous parts of vibration field:

$$J(z) = \frac{u_{max}^2}{\pi^2} \sum_{m=1}^{n} \frac{e^{-\frac{[3(1-\nu^2)]^{\frac{1}{4}}}{\sqrt{Rh}} z \left[1-\left(\frac{\omega m R}{c}\right)^2\right]^{\frac{1}{4}}}}{m^2} \cdot \cos^2 \left(\frac{[3(1-\nu^2)]^{\frac{1}{4}}}{\sqrt{Rh}} \cdot z \cdot \left[1-\left(\frac{\omega m R}{c}\right)^2\right]^{\frac{1}{4}} \right) + \frac{u_{max}^2}{2\pi^2} \cdot \sum_{m=n}^{\infty} \frac{1}{m^2}$$

by $\Omega = 310 \frac{radian}{sec}$, $\nu = 14$ - blade number, we have $\omega = 11 \cdot 10^3$,

$n = \frac{5 \cdot 10^3}{0{,}41 \cdot 11 \cdot 10^3} \cong 1$. Consequently,

$$J(z) = \frac{u_m^2}{\pi^2} \left\{ e^{-\frac{[3(1-\nu^2)]^{\frac{1}{4}}}{\sqrt{Rh}} \cdot z\,(0{,}19)^{\frac{1}{4}}} \cdot \cos^2 \frac{[3(1-\nu^2)]^{\frac{1}{4}} z}{\sqrt{Rh}} (0{,}19)^{\frac{1}{4}} + \right.$$

$$\left. + \frac{1}{2} \sum_{m=2}^{\infty} \frac{e^{-\frac{[12(1-\nu^2)]^{\frac{1}{4}}}{\sqrt{Rh}} z^2 \sqrt{\frac{\omega m R}{c}}}}{m^2} \right\} ,$$

$$S(\infty) = \frac{u_m^2}{2\pi^2}\left(\frac{\pi^2}{5} - 1\right)$$

Section length of heterogeneous field equals approximately to one meter. Thus, leaving part of energy constitutes only one sixth of the general reactive oscillation capacity.

The given evaluations show that excited shell vibrations synthesize heterogeneous noise field what cannot be explained by the obtained experimental data testifying that heterogeneous section length is five times greater. Thus, to describe a heterogeneous noise field, it is necessary to take into account the heterogeneous medium field along with the shell edge effect, i.e., one cannot neglect pressure p_2.

For this part of field we have the following edge problem, "Eq.(10)"

$$\left.\begin{aligned} &\frac{\partial^2 p_{2,1}}{\partial t^2} = c_0^2\left\{\frac{\partial^2 p_{2,1}}{\partial t^2} + \frac{1}{r}\frac{\partial}{\partial r} r \frac{\partial p_{2,1}}{\partial r}\right\}, \\ &\qquad \frac{\partial p_2}{\partial r} = 0 \qquad \text{by} \quad r = R, \\ &D\frac{\partial^4 u}{\partial t^4} u + \frac{Eh}{R^2} u + \rho h \frac{\partial^2 u}{\partial t^2} = p_1 + p_2, \\ &\qquad \frac{\partial p_1}{\partial r} = -\rho_0 \frac{\partial^2 u}{\partial t^2} \qquad \text{by} \quad r = R. \end{aligned}\right\} \tag{10}$$

In this case we assume, that "Eq.(11)"

$$\left.\begin{aligned} p_2 &= \sum_{m,k} p_{mk}^{(2)} J_0\left(\gamma_k \frac{r}{R}\right) e^{i\sqrt{\frac{\omega_m^2}{c_0^2} - \frac{\gamma_k^2}{R^2}}\, z - i\omega_m t}, \\ p_1 &= \sum_k p_k^{(1)} J_0\left(\sqrt{\frac{\omega_m^2}{c_0^2} - k^2}\, \frac{r}{R}\right) e^{ikz - i\omega_m t}. \end{aligned}\right\} \tag{11}$$

As the part of field bound with radiation and described above is not significant for this problem and may be omitted at this stage, we have the following problem, "Eq.(12)"

$$\left.\begin{aligned} &\frac{\partial^2 p_2}{\partial t^2} = c_0^2\left\{\frac{\partial^2 p_2}{\partial t^2} + \frac{1}{r}\frac{\partial}{\partial r}\frac{\partial p_2}{\partial r}\right\}, \\ &D\frac{\partial^4 u}{\partial z^4} u + \frac{Eh}{R^2} u + \rho h \frac{\partial^2 u}{\partial t^2} = p_2. \end{aligned}\right\} \tag{12}$$

By using first solution of (11), where μ_k - roots of Bessel function of first order, i.e., $J_1(\mu_k) = 0$, we get, "Eq.(13)"

$$D\frac{\partial^4 u}{\partial z^4} + \left(\rho h\,\omega_k^2 - \frac{Eh}{R^2}\right) u = \sum P_{mk}\, J_0(\mu_k) e^{i\sqrt{\frac{\omega_k^2}{c_0^2} - \frac{\mu_k^2}{R^2}}\cdot z}, \quad (13)$$

where size P_{mk} is defined as generalized Fourier - components of pressure pulsation at the outlet of supercharger, "Eq.(14)"

$$p(r,t,0) = \sum_{\substack{m=0\\k=1}}^{\substack{k=\infty\\m=\infty}} P_{mk}\, J_0\left(\mu_k \frac{r}{R}\right) e^{-i\omega_k t} \quad (14)$$

Here k - heterogeneous wave number. Consequently, for shell flexure (u_{mk}) we have heterogeneous equation which is solved in the following way, "Eq.(15)"

$$u_{mk} = \frac{P_{mk}\, J_0(\mu_k)}{D\left[\frac{\omega^2}{c_0^2} m - \frac{\mu_k^2}{R^2}\right]^2 + \left(\rho h \omega_k^2 - \frac{Eh}{R^2}\right)}. \quad (15)$$

Thus, heterogeneous part of field according to (11) and (15) is expressed by the sum

$$J_u(z) = \sum_{\substack{k=k_{max}\\m=0}}^{\substack{k=\infty\\m=\infty}} \frac{P_{mk}^2\, J_0^2(\mu_k)\, e^{-2\sqrt{\frac{\mu_k^2}{R^2} - \frac{\omega_m}{c_0^2}}\cdot z}}{\left\{D\left[\frac{\omega_m^2}{c_0^2} - \frac{\mu_k^2}{R^2}\right]^2 + \left(\rho h \omega_k^2 - \frac{Eh}{R^2}\right)\right\}^2},$$

where k_{max} is defined from the condition $\mu_{k+1} < \frac{\omega R}{c}$, homogeneous part of shift intensity is given in the form:

$$J_u(\infty) = \sum_{\substack{k=1\\m=0}}^{\substack{m=\infty\\k=k_{max}}} \frac{P_{mk}^2\, J_0^2(\mu_k)}{\left\{D\left[\frac{\omega^2}{c_0^2} m - \frac{\mu_k^2}{R^2}\right]^2 + \left(\rho h \omega_k^2 - \frac{Eh}{R^2}\right)\right\}^2}.$$

Significantly lengthy section of heterogeneous oscillation intensity may be explained by an unpropagated part of nearest pole, though, for this lengthy transitional period, coincidence (at least that of closeness) of wave parameter $\frac{\omega R}{c_0}$ with critical meaning μ_k (transversal resonance) is necessary.

μ_1	μ_2	μ_3	μ_4
3,8317	7,0156	10,1735	13,3237

For example, in the case of $f = 7806$ (RPM), $R = 0{,}4\,m$, $c_0 = 450$ m/sec (methane (gas) under pressure) we have

$$L = \frac{R}{\sqrt{\mu_3^2 - \left(\frac{\omega R}{c_0}\right)^2}} \approx 3\ m.$$

This points to the significance of the length of heterogeneous field sections.

Actually, in a plate loaded medium, the coefficient β defining field heterogeneity is defined by taking into accour: loading from the side of medium

$$\beta = \sqrt[4]{\frac{3(1-\nu^2)}{R^2 h^2}} \left\{ 1 - \left(\frac{\omega R}{c}\right)^2 \left[1 + \frac{\rho_0 R}{\rho h} \left(\frac{\omega R}{c_0}\right)^{-1} \cdot \frac{J_0\left(\frac{\omega R}{c_0}\right)}{\dot{J}_0\left(\frac{\omega R}{c_0}\right)} \right] \right\}^{\frac{1}{4}}.$$

Thus, the size of heterogeneous field in a shell will be

$$L = \frac{\frac{3\pi}{2}\sqrt{R \cdot h}}{\left[3(1-\nu^2)\right]^{\frac{1}{4}} \left\{ 1 - \left(\frac{\omega R}{c}\right)^2 \left[1 + \frac{\rho_0 R}{\rho h} \left(\frac{\omega R}{c_0}\right)^{-1} \frac{J_0\left(\frac{\omega R}{c_0}\right)}{\dot{J}_0\left(\frac{\omega R}{c_0}\right)} \right] \right\}^{\frac{1}{4}}}.$$

By analysing the above given conditions, we get $L \cong 5\ m$.

Here $c_0 = 466{,}9$ m/sec ; $c = 4864$ m/sec ; $\Omega = 7900$ RPM;
$\nu = 14$; $R = 0{,}4$ m ; $h = 20 \cdot 10^{-3}$ m.

The experiment was carried out at the natural gas compressor station where centrifugal compressors have been used. Piping gas pressure increased by compressor was sent to a gas main. Technical characteristics of the compressor are: blade wheel shaft (RPM) $n = 9800$; wheel blade number $\nu = 14$, 7 being short and 7 long ones; gas sucking and compressing pipes in diameter $D = 820$ mm .

At intervals of 1 m from the compressor along 50 m piping length oscillation acceleration in dB has been measured. Oscillation acceleration spectrum at the first point is given in Figure 1, where oscillation maximum at frequency is

$$f = \frac{n \cdot z}{60} = \frac{9800 \cdot 14}{60} = 2286\ Hz.$$

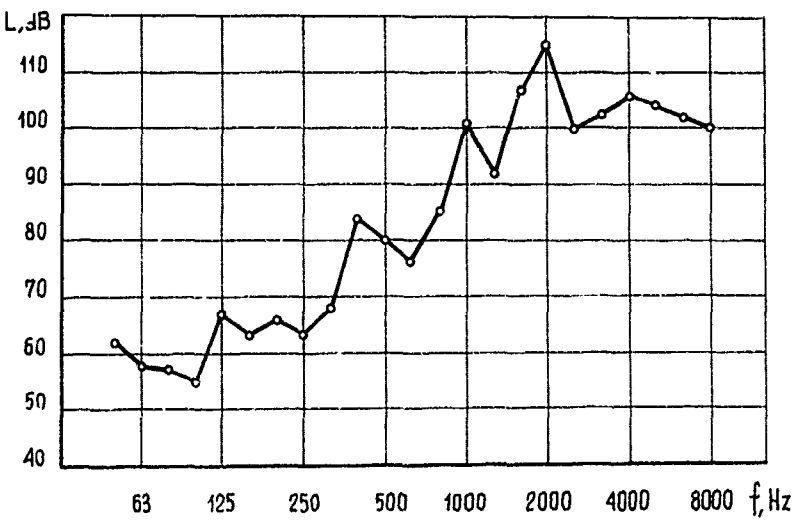

Figure 1. Vibration acceleration spectrum at the first point.

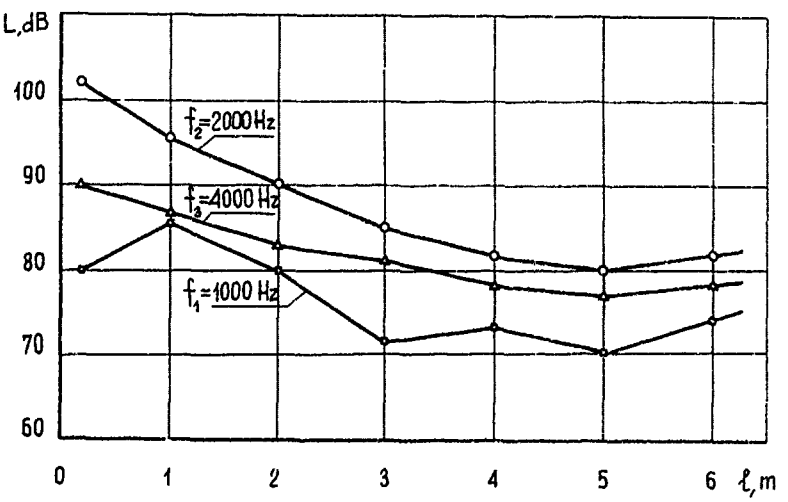

Figure 2. Vibration damping to the extent of source distance (in meters)

and its first harmonic is 4000 Hz. Spectrum composite at 1000 Hz shows the frequency of long blades. Figure 2 shows the vibration damping at 6 m distance from the compressor at the frequency of 1000 Hz, 2000 Hz and 4000 Hz. As it is seen from the curves, vibration damping occurs at 5 m distance. Further vibration level is of approximately the same level along 50 m distance from the compressor. An excellent correlation between theoretical calculations with experimental data has been obtained.

CONCLUSIONS

The physics of a heterogeneous state in a noise field of gas filled piping may be explained by the presence of acoustical heterogeneous normal waves and the dynamic edge effect in a gas piping. Acoustical edge effect, owing to the heterogeneous normal waves, exhibits a very unstable characteristics due to transversal resonance, i.e., at critical frequencies of the waveform. Edge effect in media filled piping occurs at a wide frequency range to null frequencies in a static conditioned but a relatively long section is required to explai the experimental data at the critical ring frequency of a piping $\left(\frac{\omega R}{C}=1\right)$.

REFERENCES

1. Guzhas D. Sound proofing of cylindrical pipes for normal modes. Vibration Engineering, 2:235-241, NY.,1988.

components (u_1, u_2) , and another to the symmetric component u_3 of the displacements. Finally the total pressure field can be found in the form

$$p=p^0+p_a^*[u_1(\theta_s), u_2(\theta_s)]+p_S^*[u_3(\theta_s)] \quad (2)$$

In the framework of the Timoshenko-Mindlin theory of plates and shells three types of waves can be observed: S_0 Lamb type wave (membrane propagation type), A_0 Lamb type wave (bending propagation type) and S_1 Lamb type wave (shear propagation type).

NUMERICAL RESULTS AND DISCUSSION

The calculations refer to the scattering of a plane wave of unit amplitude by an aluminium shell ($E=70GPa, \nu=0.335, \rho_1=2.7g/cm^3$) with the relative thickness $h=0.02R$. The shell is supported by the axial rib (stringer) with thickness equal to the thickness of the shell and with the radial dimension $l_s=R$ The angle between the direction of the incidence and the rib is $\theta_s=60°$.

Stiffener-borned sound pressure

Figure 1 gives the amplitude of the backscattered pressure field as a function of frequency kR (form function). Deep antiresonances on the form function of the unstiffened shell belong to the S_0 wave in the shell. The group velocity of this wave is approximately equal to the velocity of the longitudinal wave in the plate. The A_0 wave resonances do not appear in the farfield in the given frequency band as their phase velocity is subsonic. The stiffener generates additional sound pressure marked by multiple resonances. Considerable part of these resonances appear with the interval which is proper to the A_0 wave. To help interprete the wave generation processes the contributions of the antisymmetric and symmetric forms of vibrations of the shell are considered separately.

In Fig.2 the form function for the sound pressure field contribution p_a^* is presented. Resonances in this form function appear in groups concentrated around the antiresonances of the S_0 wave in the shell. However this function is rather difficult to interpret.

The contribution p_S^* of the symmetric forms of vibrations in the total sound pressure field is presented in Fig.3. This form function has very regular structures which tends to indicate the domination of two types of waves. First of them is the A_0 wave forming the series of the peaks. Two valleys at the frequencies $kR=12., 24....$ where form function changes character, mean interference of an another wave. Considering velocity of this wave approximately equal to that of the longitudinal wave in the shell, the path of this wave in the structure could be estimated Calculations show that this path is nearly equals to $2R$. It means that this is a longitudinal (in radial direction) resonance in the rib. To verify this statement another form function for the rib witch is two times shorter in the radial direction (height $h_s=0.5R$) is presented. It can be seen in Fig.4 that first valley occurs at the frequency $kR=24.$, which is twice as high. By this one should state that the longitudinal resonance in the rib highly attenuates the symmmetric resonance of the shell. Directivity pattern shows that at these frequences the rib does not radiate in any other direction.

Consequently for every given frequency the rib could be designed so that the stiffener-borned sound (at least the contribution of the symmetric forms of vibrations) is attenuated due to the longitudinal resonance of the rib.

In addition to that there are much other "zeroes" in the form functions of both contributions. They correspond to the position of the rib at the node of the symmetric and at the loop of the antisymmetric form of vibrations. The frequencies where the rib does not affect the shell can be seen in Fig.5 where the total contribution of the stiffener in thepressure field is presented. These zero rib-contribution frequencies could also be useful to the design of the nonradiating rib although most of them are very close to the resonance frequencies.

Reactions of the rib

As the ribs are assumed to be attached along lines they could be considered as the line forces (reactions). These reactions may be found for every given freqiency. The problem of the active sound radiation control can be formulated as the compensation of these reactions by the line control forces applied to the ribs. Furthermore line reactions are calculated and plotted versus frequency.

force to the rib is discussed.

STATEMENT OF THE PROBLEM

Let a thin-walled elastic circular cylindrical shell of centroidal radius R and thickness h be immersed in an ideal fluid medium with theHxdensity ρ and sound velocity c. The shell material is isotropic and has a density ρ_1 Young's modulus E and Poisson's rat o ν. A shell is supposed to be air-filled and supported by an arbitrary set of S longitudinal internal ribs and walls which are not in contact with each other. The radial dimension of the rib is l_s and its thickness is h_s. Subscript s denotes characteristics of the ribs. The shell is insonified by a plane acoustic wave p_i of normal incidense. Required is to determine the reactions of the stiffeners and also outer sound pressure field p caused by an incident wave in order to reduce the stiffener-borne sound.

Given 2D problem is formulated in polar coordinates (ρ,θ) attached to the shell.

Sound pressure p in the fluid must satisfy wave equation, radiation condition and a boundary condition at the shell surface

$$\frac{\partial}{\partial r}(p_i+p)|_{r=R}=-\rho k^2 u_3$$

where u_3 is the shell normal displacement and k is the wave number. The Timoshenko-Mindlin theory of plates and shells[1] considering shear deformation and rotational inertia is used to describe the motion of the stiffened shell. If the thickness of the stiffening members and the thin-walled shell are of the same order one can assume them to be joined along lines.

Equations of the motion of the structure acquire the form

$$L_{ij}u_j=\delta_{i3}(p_i+p)\ |_{r=R}+\sum_{s=1}^{S} f_{ijs}u_j\delta(\theta-\theta_s),\quad i,j=1,2,3$$

where L_{ij} are differential operators[1], u_1 and u_3 are tangential and normal displacements respectively, u_2 is angular in the radial plane displacement, δ_{ij} is kronecker's symbol, f_{ijs} denotes the stiffeners reaction per unit displacement of the shell. These equations together with the conditions of the continuity of the displacements at the junction lines form a closed system of differential equations.

SOLUTION OF THE PROBLEM

The unknown functions of displacements and pressure are expanded in series of the normal modes on angular coordinate θ. Displacements of the shell at the junction lines can be written in the form

$$u_j(\theta)\delta(\theta-\theta_s)=\frac{1}{2\pi}u_j(\theta_s)\sum_{m=-\infty}^{\infty}\exp[im(\theta-\theta_s)],\quad j=1,2,3 \qquad (1)$$

Due to the linearity the problem devides into two parts: p^0 corresponding to the well known solution for the unstiffened cylindrical shell and p^* describing contribution of the stiffeners or stiffener-born sound. Hence superscript zero denotes the contribution of the unstiffened shell and asterisk * contribution due to stiffener. Displacements $u_j(\theta_s)$ from Eq.(1) must be detrmined from the condition of the continuity of the deformations at the junction line

$$u_j(\theta_s)=\sum_{m=-\infty}^{\infty}(u^0_{jm}+u^*_{jm})\exp(im\theta_s),\quad j=1,2,3.$$

These conditions form a set of $3J$ linear equations, where J is a number of junctions. After the determination of the displacements $u_j(\theta_s)$ the additional forces $f_{ijs}u_j(\theta_s)$ (reactions of the ribs) are also determined. To solve this system one has to sum the series which may be regularized by extraction of singularities. In special case when the stiffeners lie entirely along one diameter, the matrix of coefficients of governing system of equations decomposes into two subsystems, one corresponding to the antisymmetric

components (u_1, u_2) , and another to the symmetric component u_3 of the displacements. Finally the total pressure field can be found in the form

$$p=p^0+p_a^*[u_1(\theta_s), u_2(\theta_s)]+p_S^*[u_3(\theta_s)] \quad (2)$$

In the framework of the Timoshenko-Mindlin theory of plates and shells three types of waves can be observed: S_0 Lamb type wave (membrane propagation type), A_0 Lamb type wave (bending propagation type) and S_1 Lamb type wave (shear propagation type).

NUMERICAL RESULTS AND DISCUSSION

The calculations refer to the scattering of a plane wave of unit amplitude by an aluminium shell ($E=70GPa, \nu=0.335, \rho_1=2.7g/cm^3$) with the relative thickness $h=0.02R$. The shell is supported by the axial rib (stringer) with thickness equal to the thickness of the shell and with the radial dimension $l_s=R$ The angle between the direction of the incidence and the rib is $\theta_s=60°$.

Stiffener-borned sound pressure

Figure 1 gives the amplitude of the backscattered pressure field as a function of frequency kR (form function). Deep antiresonances on the form function of the unstiffened shell belong to the S_0 wave in the shell. The group velocity of this wave is approximately equal to the velocity of the longitudinal wave in the plate. The A_0 wave resonances do not appear in the farfield in the given frequency band as their phase velocity is subsonic. The stiffener generates additional sound pressure marked by multiple resonances. Considerable part of these resonances appear with the interval which is proper to the A_0 wave. To help interprete the wave generation processes the contributions of the antisymmetric and symmetric forms of vibrations of the shell are considered separately.

In Fig.2 the form function for the sound pressure field contribution p_a^* is presented. Resonances in this form function appear in groups concentrated around the antiresonances of the S_0 wave in the shell. However this function is rather difficult to interpret.

The contribution p_S^* of the symmetric forms of vibrations in the total sound pressure field is presented in Fig.3. This form function has very regular structures which tends to indicate the domination of two types of waves. First of them is the A_0 wave forming the series of the peaks. Two valleys at the frequencies $kR=12.,24....$ where form function changes character, mean interference of an another wave. Considering velocity of this wave approximately equal to that of the longitudinal wave in the shell, the path of this wave in the structure could be estimated Calculations show that this path is nearly equals to $2R$. It means that this is a longitudinal (in radial direction) resonance in the rib. To verify this statement another form function for the rib witch is two times shorter in the radial direction (height $h_s=0.5R$) is presented. It can be seen in Fig.4 that first valley occurs at the frequency $kR=24.$, which is twice as high. By this one should state that the longitudinal resonance in the rib highly attenuates the symmmetric resonance of the shell. Directivity pattern shows that at these frequences the rib does not radiate in any other direction.

Consequently for every given frequency the rib could be designed so that the stiffener-borned sound (at least the contribution of the symmetric forms of vibrations) is attenuated due to the longitudinal resonance of the rib.

In addition to that there are much other "zeroes" in the form functions of both contributions. They correspond to the position of the rib at the node of the symmetric and at the loop of the antisymmetric form of vibrations. The frequencies where the rib does not affect the shell can be seen in Fig.5 where the total contribution of the stiffener in thepressure field is presented. These zero rib-contribution frequencies could also be useful to the design of the nonradiating rib although most of them are very close to the resonance frequencies.

Reactions of the rib

As the ribs are assumed to be attached along lines they could be considered as the line forces (reactions). These reactions may be found for every given freqiency. The problem of the active sound radiation control can be formulated as the compensation of these reactions by the line control forces applied to the ribs. Furthermore line reactions are calculated and plotted versus frequency.

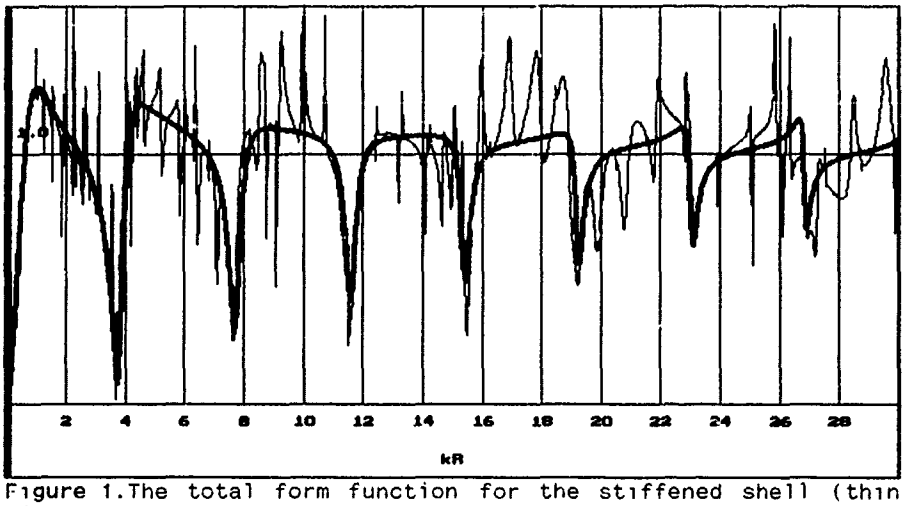

Figure 1.The total form function for the stiffened shell (thin line) and unstiffened shell (thick line).

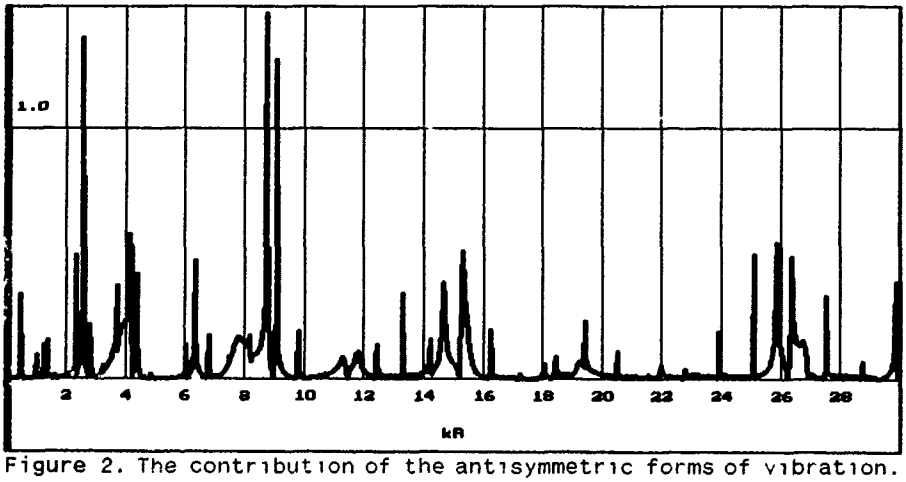

Figure 2. The contribution of the antisymmetric forms of vibration.

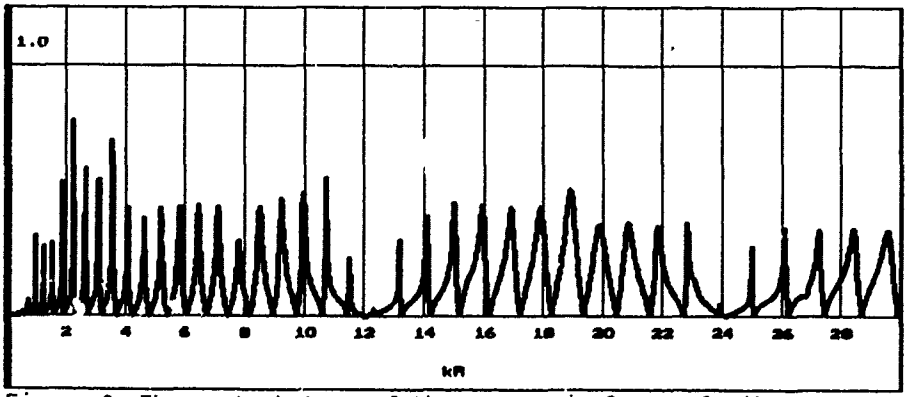

Figure 3. The contribution of the symmetric forms of vibrations.

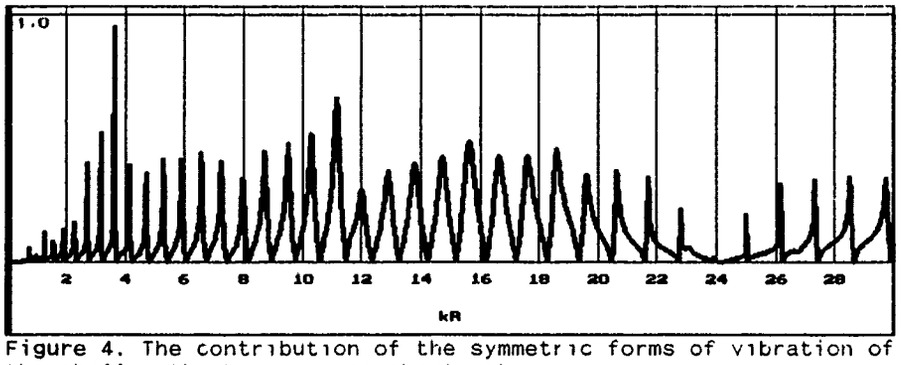

Figure 4. The contribution of the symmetric forms of vibration of the shell with the twice as short rib.

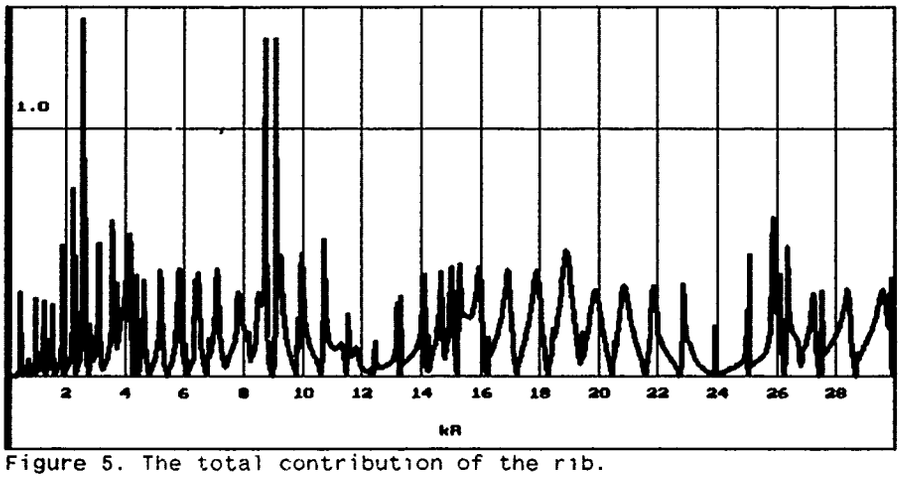

Figure 5. The total contribution of the rib.

In Fig.6 the amplitude of the tangential reaction F_t as a function of frequency is shown. This reaction can be defined as

$$F_t = f_{11s}u_1(\theta_s) + f_{12s}u_2(\theta_s)$$

In Fig.7 the amplitude of the momentum reaction M_θ as a function of frequency is presented which may be presented as

$$M_\theta = f_{21s}u_1(\theta_s) + f_{22s}u_2(\theta_s)$$

In Fig.8 the amplitude of the normal (radial) reaction F_n as a function of frequency is shown. This reaction can be defined as

$$F_n = f_{33s}u_3(\theta_s)$$

It can be seen from Figs.6-8 that the form functions of the reactions are allmost identical to the corresponding pressure form functions. In principle these reactions could be compensated by the control force applied to the rib. Although magnitude, direction, phase and the coordinate of the point of application of the control force can be found for every given frequency, the efficiency of such a method seems to be problematic, at least at the lower resonance frequencies.

Reactions F_t and M_θ can be decomposed and by that an interesting result can be achieved. In Figs.9-10 two parts of the reaction M_θ due to transversal and rotational motion respectively are presented. In the both figures the series of the sharp resonances appear.

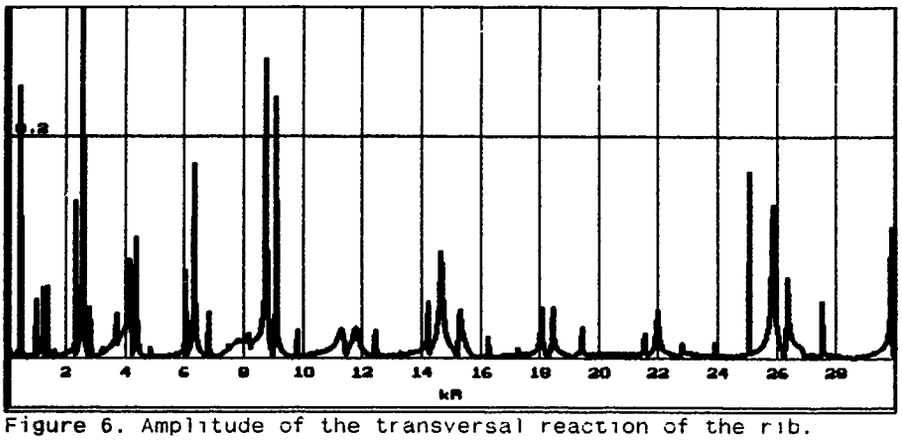

Figure 6. Amplitude of the transversal reaction of the rib.

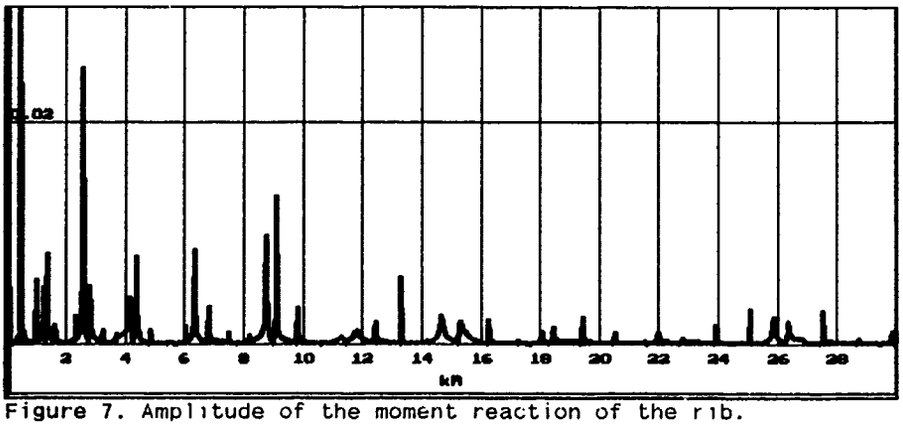

Figure 7. Amplitude of the moment reaction of the rib.

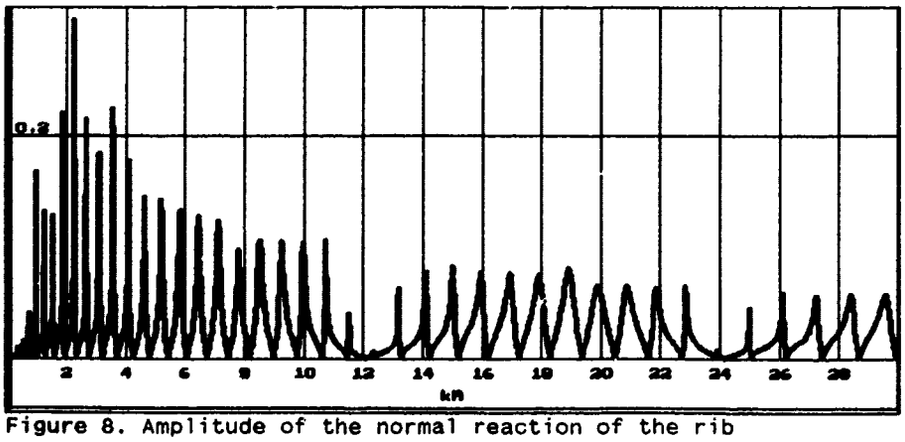

Figure 8. Amplitude of the normal reaction of the rib

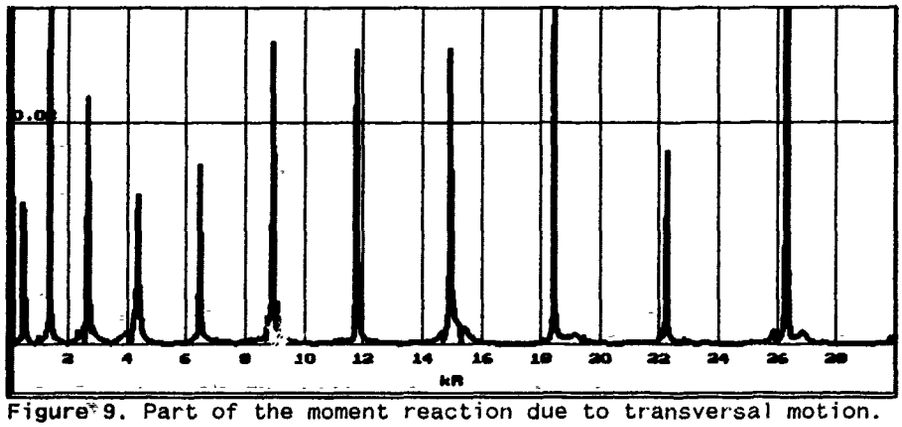

Figure 9. Part of the moment reaction due to transversal motion.

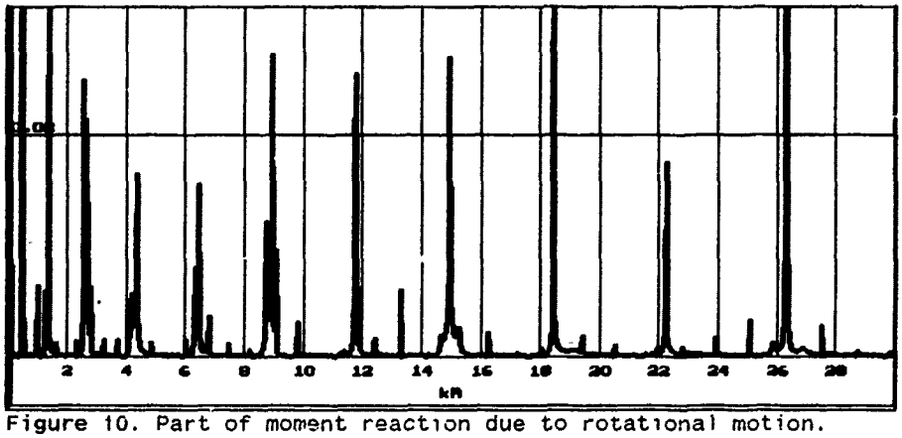

Figure 10. Part of moment reaction due to rotational motion.

Their position in the form function indicates that they correspond to the A_0 wave resonances in the rib. Nevertheless they do not visibly affect the total pressure form function as well as in the form function of the antisymmetric forms of vibrations.

To determine the dimensions of the reactions' amplitudes F_t and F_n should be multiplied by $Eh/R^2(1-\nu^2)$ and M_0 by $Eh/R(1-\nu^2)$ respectively.

CONCLUSIONS

On the active sound radiation control

The line reactions of the ribs in the ribbed shell can be found for every given frequency. Although magnitude, direction, phase and the point of the application of the line control force compensating reactions can be calculated, the effectiveness of this approach is greatly dependent on the position of the nearest resonances. At the higher frequencies, where the contribution of the symmetric with respect to the rib forms of vibrations prevail and attenuation is considerable, this approach may give better results. In any case the spectrum of the external load can not be broad.

On the frequencies where a rib does not radiate

Shown is that the series of the frequency bands exist where the rib does not radiate in any direction. Theoretically, when the rib is located in the node of the form of vibration the symmetric contribution tends to zero and when the rib is in the loop of the form of vibration the antisymmetric contribution tends to zero. The total contribution of the rib in the pressure field in that situation could not be zero. However it can be seen in Fig.5 that narrow frequency bands exist where the total contribution is very small.

In addition to that more large frequency bands exist where the rib does not radiate. These frequencies could be estimated by the expression

$$\omega_n = \frac{\pi n}{h_e}\sqrt{\frac{E}{\rho(1-\nu^2)}}, \quad n=1,2,3.... \quad (3)$$

representing the resonances of the longitudinal vibrations of the rib with the free ends. In that case the vibrating rib will not affect the vibrating shell. By choosing appropriate height of the rib according to the Eq.3, the nonradiating at the given frequency rib can be designed.

REFERENCES

1. G.Maidanik, "Surface-Impedance Nonuniformities as Wave Vector Convertors". J.Acoust.Soc.Am. 46, 1062-1073 (1969).

2. D.G.Crighton, G.Maidanik, "Acoustic and Vibrational Fields Generated by Ribs and Fluid-Loaded Panel. I: Plane Wave Problem for a Single Rib". J.Sound and Vibrat. 75(3), 437-452 (1981).

3. R.H.Lyon, "Sound Radiation from a Beam Attached to a Plate", J.Acoust.Soc.Am. 34(9), 1265-1268 (1962).

4. B.P.Belinskii, "Sound Radiation by Plate with a Set of Sailient Stiffeners under the Action of the Force". Sov.Phys.Acoust. 29, 420-427 (1983).

5. B.R.Mace, "Sound Radiation from Fluid-Loaded Orthogonally Stiffened Plates". J.Sound and Vibrat. 79(3), 439-452 (1981).

6. M.V.Bernblit, "Sound Radiation from a Ribbed Cylindrical Shell". Sov.Phys.Acoust 21, 518-521(1976).

7. C.B.Burroughs, "Acoustic Radiation from Fluid-Loaded Infinit Circular Cylinder with Doubly Periodic Ring Supports". J.Acoust.Soc.Am. 75(3), 715-722 (1984).

8. G.Maidanik ,J.Dickey "Reflection of Incident Pressure Waves by Ribbed Panels". J.Acoust.Soc.Am. 90(4), 2124-2138 (1991).

9. Y.Gu, C.R.Fuller, "Active Control of Sound Radiation due to Subsonic Wave Scattering from Discontinuities on Fluid-Loaded Plates. I: Far Field Pressure." J.Acoust.Soc.Am. 90(4), 2020-2026 (1991).

10. A.Klauson, J.Metsaveer, "Sound Scattering by a Langthwise-Reinforced Cylindrical Shell." Sov.Phys.Acoust. 35(1), 42-44 (1989).

11. A.Klauson, J.Metsaveer, "Sound Scattering by a Cylindrical Shell Reinforced by Lengthwise Ribs and Walls." J.Acoust.Soc.Am. (to be published).

12. I.Mirsky, G.Herrmann, "Nonaxially Symmetric Motions of Cylindrical Shells." J.Acoust.-Soc.Am. 29(10), 1116-1123(1957).

SECOND INTERNATIONAL CONGRESS ON
RECENT DEVELOPMENTS IN AIR- AND
STRUCTURE-BORNE SOUND AND VIBRATION
MARCH 4-6, 1992 AUBURN UNIVERSITY, USA

SPACE TIME ANALYSIS OF SOUND RADIATION AND SCATTERING

C.CLERC

METRAVIB R.D.S.
64, Chemin des Mouilles
F-69130 ECULLY

D.VAUCHER de la CROIX

METRAVIB R.D.S.
64, Chemin des Mouilles
F-69130 ECULLY

I. INTRODUCTION -

In many industrial problems, the acoustical and dynamical behavior of various structural components is taken into account as soon as possible in the design steps. The reasons underlying this preoccupation are numerous : that may be comfort problems such as the interior noise problem in a car or a plane ; that may be a sound pollution problems such as the engines radiated noise ; that may be a mechanical stresses problems such the fluid-structure interaction on satellite equipments located in the launcher's fairing.

In order to understand the relevant physical behaviors, and to predict the overall structural behavior, numerical methods has been developed in the last years. ASTRYD is one of those. This code allows to compute radiation, scattering and fluid-structure coupling problems with 3-dimensional structures of any shape. The method's originality, time domain computation coupled with boundary elements methods in space domain, gives ASTRYD a large computational power. For fluid-structure interaction problems, the mechanical behavior is taken into account by using modal representation. The modal characteristics computation can be performed by any classical F.E.M software. Thus, the acoustic software is independent of the mechanical modelization.

Primary results of ASTRYD are obtained as time functions ; secondary results are obtained as frequency functions by using classical Fourier Transform algorithms. Hypothesis and used methods are described in the first part of this paper. Some validations of the methods are presented in the second part. In the third and last part, methods capabilities are illustrated by some industrial applications.

II.HYPOTHESIS AND METHODS -

* II.1. - Acoustic computations -

Assumed are the classical hypothesis of linear acoustics. The fluid domain is infinite or half-infinite. The structures are bounded by closed surfaces. The normal motion of these surfaces may be imposed. Acoustic excitations are generated by monopoles located at any point of the fluid domain. In the time domain, the equations of acoustics lead to the Kirchhoff's formula, also called retarded potentials equation. Under these conditions, this equation, applied to the scattering and radiation problem in the external fluid, can be written as follows (ref [1], [2], [3]) :

$$\varepsilon\, p(M_0,t_0) = \int_\Sigma \{p^*\,\mathrm{grad}\,(1/d) - (1/cd)\,\dot{p}^*\,\mathrm{grad}\,d\}\; n_M\, d\sigma$$

$$+ 4\Pi \sum_k S_k^*/r_k + \rho_0 \int_\Sigma w^*/d\; d\sigma) \qquad (1)$$

where
- M_0 = Calculation point on Σ
- M = Arbitrary point on Σ
- Q_k = Location of the k^{th} acoustic pressure point source S_k
- d = $|MM_0|$, $r_k = |Q_k M_0|$
- n_M = outward normal vector to Σ in M.
- ε = 4Π if $M_0 \notin \Sigma$, 2Π if $M_0 \in \Sigma$

The asterisc means that the corresponding variable has to be evaluated at the retarded time $\tau = t_0 - d/c$ or $\tau_k = t_0 - r_k/c$, and the point denotes time derivative. p is the surface pressure field, and w specifies the normal acceleration on Σ.

The space discretization of the structures surface consists in plane triangular meshes. The acoustic pressure (and acceleration) are assumed constant on each mesh and computed at its gravity center. Thus, equation (1) becomes :

$$\varepsilon\, P_i(t_0) = \sum_{j=1}^{n_e} (A_{ij}.P_j(t_{ij}) + B_{ij}\;\dot{P}_j(t_{ij}) + C_{ij}\,\ddot{w}(t_{ij})) + 4\Pi \sum_k S_k^*/r_u \qquad (2)$$

where A_{ij}, B_{ij} and C_{ij} are space integration terms computed by a semi-analytical method.

The time discretization is based on a first order finite differences technique with a constant time step δt. The acoustic pressure on the i^{th} element (or at the i^{th} point in the fluid) is written, at time $t_0 = k_0\,\delta t$, as follows

$$P_i^{ko} = \sum_{j=1}^{ne} \left(D_{ij}.P_j^{k1} + E_{ij}.P_j^{k2} + C_{ij}.\ddot{W}_j \right) \qquad (3)$$

The results are obtained by solving a semi-implicito scheme :

$$[A]\,\{P\}^{ko} = [B]\,\{P\}^{ko-n-1} + \{P_e\}^{ko} \qquad (4)$$

where :
- $\{P\}^k$ is the acoustic pressures vector at the k^{th} time step
- $\{Pe\}^k$ is calculated explicitely as indicated by equation (3)
- n is a stability parameter of the numerical scheme.

II.2. - Fluid-structure interaction -

General hypothesis are those mentionned previously. The hypothesis of linear mechanics are assumed for the structure. For the coupled system, the mechanical behavior is not supposed very different from the in vacuo behavior. Mainly, it means that the modal base, computed in vacuo, is a good description base for the immersed structure's behavior. Indeed, this assumption is very well adapted for solving coupled problems involving light structures in air.

The acoustical scheme has been described previously ; now, an iterative structural response computation is performed, at each time step, in order to obtain the mechanical equilibrium (ref [5]). Practically, the mechanical computation is based on a classical modal superposition method ; the modal characteristics are obtained by FEM computation. In most cases, the convergence of the iterative scheme is reached very soon. Then, the computational cost is quite bound to the computational cost of the acoustical contribution. However, the modal characteristics have to be computed before the coupled system is solved with ASTRYD.

Important remark -

Quite generally, acoustic meshing and mechanical meshing have no reason to be identical. For some simplified structures shapes, it is possible to superpose the meshings. This approach is no more suitable for complex structures shapes because of possible numerical problems and prohibitive computational costs.

Thus, a specific numerical tool has been developed in the ASTRYD software package. It allows to convert a initial field (accelerations, modal displacements, etc...) -given at the modal points of the mechanical meshing- in a final field computed at the gravity centers of the acoustic meshing elements. The interpolation methods and topologic algorithms used in order to perform this task will not be detailed in this paper.

III.ASTRYD SOFTWARE VALIDATION -

III.1. - Analytical validation -

ASTRYD was applied to solve many different problems and the obtained results were compared to either analytical results or acoustic measurements. An illustration of a purely acoustic computation is given on figure 1. The directivity of a pulsating sphere is calculated in a half-space medium. ASTRYD results are compared to analytical results and to other numerical results (ref [6]). This comparison shows the good accuracy of the method.

III.2. - Comparison between numerical results and measurements -

The aim of this case was to evaluate the shock wave effects on buildings. The problem is quite easy to solve with one building with simple geometry (rectangular or cylindrical), but it is more difficult with many buildings with a narrow space between them. Particularly, overpressures can be generated by the reverberations between buildings.

In order to examine this phenomena, computations are run on a two-buildings group (figure 2) and corresponding measurements are performed on a scale model. In both cases, the pressure time evolution is observed between the buildings.

The results are shown on figure 3 ; the presented pressure levels (as time functions in Pascal units) show good agreement between ASTRYD results and measurements.

IV. ASTRYD APPLICATIONS -

IV.1.- Space application : fluid/structure coupled problem -

The proposed example hereafter concerns the vibroacoustic behavior of an aluminium honeycomb sandwich panel. During a work performed for the account of the CNES/TOULOUSE (ref [5]), a test panel typical for spatial applications has been studied. Different configurations have been analyzed : two types of boundary conditions and three distinct loading cases were considered.

One of these cases is illustrated by the table hereafter :

12 first modal frequencies related to a sandwich test panel. Simply supported edges - no additional equipment

IN VACUO	IN AIR	MEASURES
35.4	31	28.5
65 9	61	59
108.7	104	108
116.4	111	112
138.6	133	134
186.1	180	180
226.0	215	223
254.7	243	249
274.0	261	261
302.2	289	286
341.9	326	312
367.7	357	351

These results highlight the frequential shift generated by the fluid. This shift, foreseen by acoustic theory and confirmed by measurements, ranges between 3% and 14%. This phenomena is also illustrated by the response spectrum presented on figure 4. ASTRYD capabilities are also illustrated by these results. The average value of the differences between computations and measurements -performed in an anechoïc chamber- is 2,5%. The most important relative difference is about 9% for the first mode (only 3.5 Hz in absolute value).

IV.2. - Automotive application : interior noise problem -

Though the time domain computation was firstly used to solve transient problems in external fluid, the ASTRYD code is also able to solve interior noise problem. In fact, the considered problem couples a structure to an internal and an external acoustical fluid. The internal fluid is bounded by a thin structure, which consists in the assembly of one flexible panel and rigid walls. The excitations are mechanical or acoustic point sources located in the internal fluid or in the external fluid. ASTRYD allows to compute the coupled system response and delivers acoustic pressures in both fluids (including wall pressures).

The hereafter described application regards a research program performed for the automotive industry. The structure is not a real car but a rigid box (figure 5), only one face of which is a flexible structure.

The meshing of the structure, illustrated by figure 5, is made by MOSAIC software*. This graphic code is also used for the presentation of the color maps results. The first aim of these computations is to obtain the modal shapes at discrete eigenfrequencies and not to have very accurate results about the acoustic pressure level.

Thus, a simplified method is used in order to compute the fluid structure interaction. In first approximation, only the inertia of the flexible panel is considered, its stiffness is neglected. The other panels are thick steel panels and consequently much stiffer and heavier ; that is the reason why they are assumed as rigid walls.

The excitation is a point source acoustic excitation, with a quasi-Dirac time profile, which ensures a large frequency band spectrum. This point source is located out of the symmetry's plans of the problem in order to make as large a number of eigenmodes as possible concurring in the response.

The eigenfrequencies are obviously shown by response spectra such as the ones presented on figure 6. Eigenfrequencies and eigenshapes are compared to measured values and analytical values (as obtained by theoretical calculations applied to a rectangular with rigid walls box). The box sizes are the same that the maximum dimensions of the real structure.

These results are presented in the table hereafter :

MODE * (Theory)	COMPUTED EIGENFREQUENCY	MEASURED EIGENFREQUENCY	ANALYTICAL EIGENFREQUENCY
1,0,0	69,1	70	65
2,0,0	121	131	130
0,1,0	137	136	130
1,1,0	154	152	145
2,1,0	179	189	183
3,0,0	202	201	195

* Each number means the mode's order (number of pressure acoustic modes) in the three space directions (length, width, height)

The differences between numerical and analatycal results are explained both by the geometrical differences and by the fluid structure interaction's effects. The differences between numerical computations and measured values are explained by the simplifying assumption concerning the fluid-structure interaction. However, the overall good agreement for these different results proves the ASTRYD capabilities to solve this kind of problem.

Two internal pressure maps are shown on figures 7 and 8. The associated frequencies are those of the mode (1,0,0) and of the (0,1,0). Obviously, if the acoustical pressure levels were required with a very good accuracy, it would be neccessary to use the iterative coupling scheme mentionned in paragraph IV.1. With this one, it is possible to study the interior noise in an aircraft cabin or in a real car as well as the noise under the launcher's fairing caused by the rockets external sources during launching.

* Trademark of FRAMASOFT+C.S.I. French Corporation.

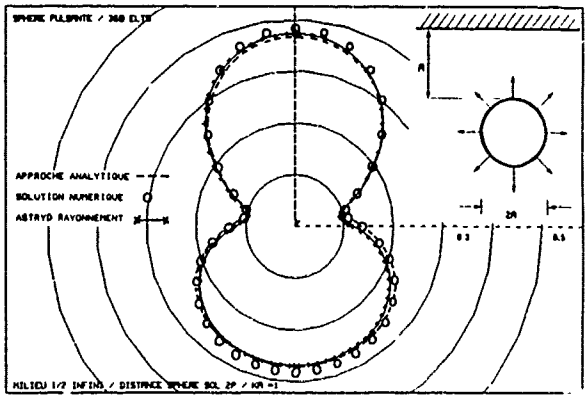

FIGURE 1 : Pulsating sphere directivity in half-space medium

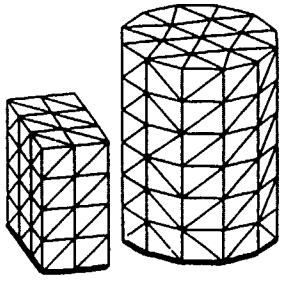

FIGURE 2 : Shock wave : buildings meshing

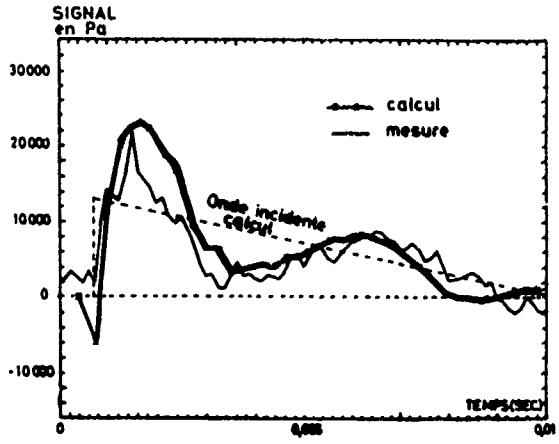

FIGURE 3 : Shock wave : acoustic pressure between both buildings

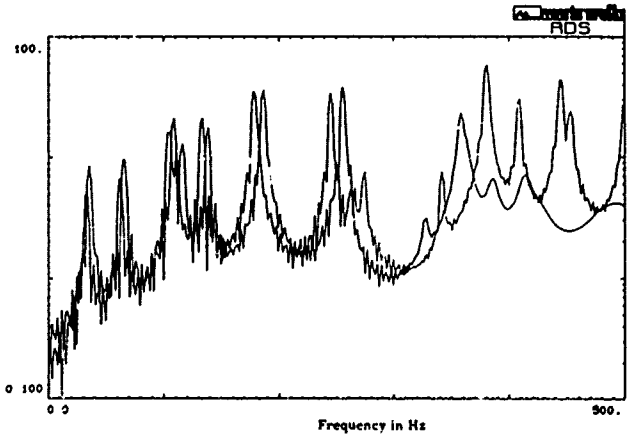

FIGURE 4 : Mean values of normal surface displacement on a simply supported panel
____ in vacuo --- in air

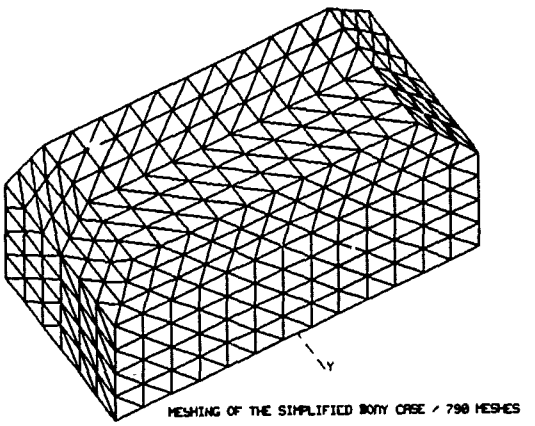

FIGURE 5 : Testing structure : meshing for acoustic computations

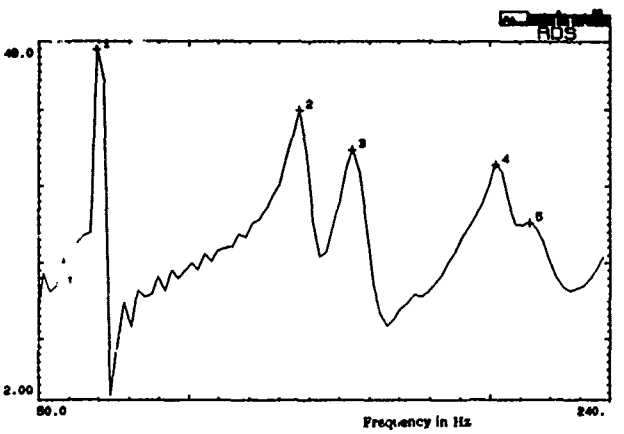

FIGURE 6 : Typical spectrum of interior walls pressure

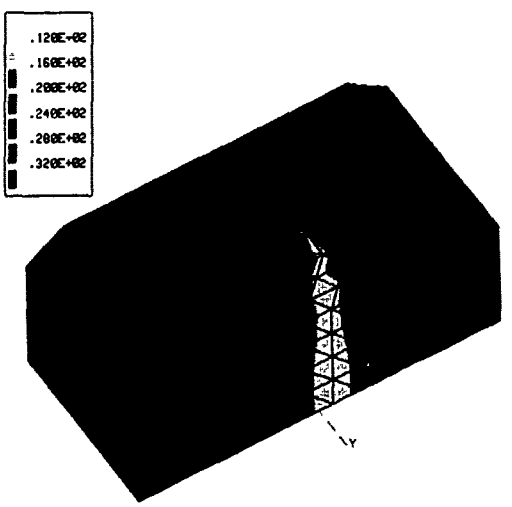

FIGURE 7 : Mode (1,0,0) : Interior walls pressure

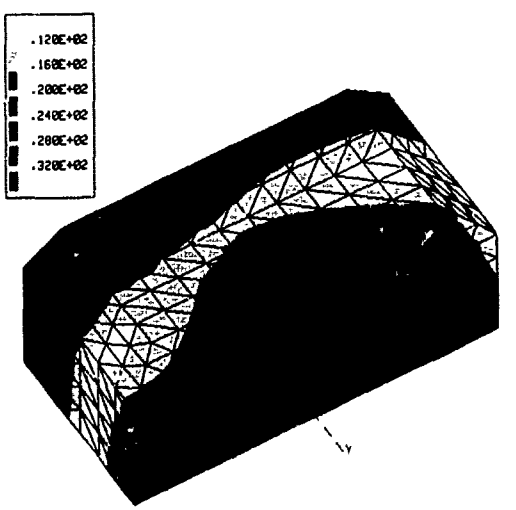

FIGURE 8 : Mode (0,1,0) : Interior walls pressure

V. CONCLUSION -

ASTRYD's original approach -time domain method- allows to perform computations on a large variety of acoustic problems.

This method is very efficient for solving transient phenomena in external fluid. It is able to solve acoustic problems characterized by a large adimensional wavenumber such as shock waves on buildings, engine radiation, acoustical loading on satellite equipments,....

Presently, the introduction of an iterative method, which couples the structural behavior to the acoustics, made ASTRYD able to study the whole vibroacoustic problem. Adaptations of the initial algorithm allow to consider interior noise problems and even fully coupled problems with both internal and external fluids. Though ASTRYD 's efficiency is about the same as the one related to classical frequency domain methods, the time domain method can be much faster for this kind of problems, provided there is a consequent damping (structural damping, wall impedance, radiation in the external fluid). This is the case for most industrial structures and ASTRYD reveals an efficient numerical tool for these problems. It can be easily used for evaluating interior noise in the plane 's cockpits, in the car's body cases or under the launcher's fairings.

VI. REFERENCES -

[1] E.SKUDRZYK
The Foundations of Acoustics / chap.24&27 - Springer Verlag-Wien New York - 1971

[2] C.BENNET & H.MIEVAS
Time domain integral equation solution for acoustic scattering from fluid targets.
JASA - Vol. 69(5) - 1981

[3] Ph.AILLAUD - P.VERPEAUX - JM.PAROT & B.BARBE
Calcul de diffraction d'onde par un corps de forme quelconque
11ième ICA PARIS- 1983

[4] C.CLERC & J.N.GIRAUDBIT
Acoustic prediction on satellite structure
International Conference on Spacecraft Structures and Mechanical Testing
ESA/ESTEC - NOORDWIJK (THE NETHERLANDS) - 24/26 April, 1991

[5] D.VAUCHER de la CROIX - L.PERRET - JM.PAROT
Fluid-Structure Interaction applied to the Analysis of a Test Sandwich Panel
International Conference on Spacecraft Structures and Mechanical Testing
ESA/ESTEC - NOORDWIJK (THE NETHERLANDS) - 24/26 April, 1991

[6] AF.SEYBERT - B.SOENARKO
Radiation and scattering of acoustic waves from bodies of arbitrary shape in three dimensional half space. - Transaction of ASME - Vol 110 - January 1988

[7] D.VAUCHER de la CROIX - C.CLERC - JM.PAROT
Time domain approach of fluid-structure interaction phenomenas
Application to satellite structures.
Air/Structure borne sound and vibration Congress - AUBURN, 4-6 March 1992.

SECOND INTERNATIONAL CONGRESS ON
RECENT DEVELOPMENTS IN AIR- AND
STRUCTURE-BORNE SOUND AND VIBRATION
MARCH 4-6, 1992 AUBURN UNIVERSITY, USA

VIBRATIONAL AND ACOUSTIC RESPONSE OF A RIBBED INFINITE PLATE EXCITED BY A FORCE APPLIED TO THE RIB

Ten-Bin Juang
Anna L. Pate
Alison B. Flatau
Department of Aerospace Engineering and Engineering Mechanics
Iowa State University
Ames, IA 50011

ABSTRACT

Vibrational and acoustic responses caused by application of a point or a line force to the rib of a single-ribbed, infinite plate with negligible fluid loading are investigated. Results show that the rib significantly reduces the plate displacement and acoustic responses. The results show that the structural intensity in the ribbed plate is an excellent tool for force localization and that the real, in-plane acoustic intensity can also be useful for that purpose.

INTRODUCTION

The vibrational and acoustic responses due to a general excitation of a submerged, infinite and periodically stiffened plate were formulated and solved with the Fourier transform method by Evseev [1]. Rumerman [2] started from plane wave excitation of a dry, infinite, periodically stiffened plate, and he then extended this model to include the vibrational response to general excitations by using a spectral impedance approach. Mace [3] adopted the Fourier transform method to formulate the vibrational and acoustic responses of a periodically stiffened infinite plate subjected to different types of excitation, including plane wave, line force, and point force excitation sources. Numerical integration was performed to calculate these responses both with and without fluid loading.

Referring to Mace's work [3], a similar technique is performed in this paper to investigate the vibrational and acoustic responses caused by application of a line or point force to a rib that is attached to an infinite plate submerged in air (i.e. negligible fluid loading).

Theoretical Derivations

Consider an infinite, thin, elastic ribbed plate, Fig. 1, lying in the plane $z = 0$ with plate thickness h_p, density ρ_p, and rib cross-sectional dimensions as shown in Fig. 1. The top half-space is occupied by air of density ρ_o and sound speed c_o. A vacuum is assumed to exist below the plate. The ribbed plate system is governed by the following equation

$$D_p(\nabla^4 - k_f^4)W(x,y,t) = f(x,y,t) - (P_a)_{z=0} - \delta(x)F_o + \frac{d\delta(x)}{dx} M_o \qquad (1)$$

where D_p is plate flexural rigidity, $D_p = \frac{E_p h_p^3}{12(1-\nu^2)}$. E_p is plate Young's modulus, ν is plate Poisson's ratio; $(P_a)_{z=0}$ is acoustic loading from air; $w(x,y,t)$ is plate transverse displacement response; $f(x,y,t)$ is excitation force; F_o and M_o are rib reaction force and moment; $\delta(x)$ is delta function; k_f is plate wavenumber where $k_f^4 = \frac{\rho_p h_p \omega^2}{D_p}$, ρ_p is plate density, and ω is angular frequency.

Assuming time harmonic excitation $f(x,y,t) = F(x,y)e^{i\omega t}$, the Fourier transform method is used to find the plate response to different excitations. With no acoustic loading and a line force excitation in parallel with the rib, the plate response is

$$W_L(x,y) = \frac{F_L \ell^3}{D_p}\left(\frac{-i}{4\Omega^2}\right)\cdot e^{-i\mu_y y}\left\{\left(\frac{e^{-i|x-x_o|\lambda_1}}{\lambda_1}+\frac{e^{-|x-x_o|\lambda_2}}{i\lambda_2}\right)-\frac{1}{\Delta(\mu_y)}\cdot\left[\frac{1}{K_R(\mu_y)}+iH'(o,\mu_y)\right]\cdot G(x,\mu_y)\cdot\left(\frac{e^{-i|x_o|\lambda_1}}{\lambda_1}+\frac{e^{-|x_o|\lambda_2}}{i\lambda_2}\right)+\mathrm{sgn}(x_o)\cdot\frac{1}{\Delta(\mu_y)}\cdot\left[\frac{1}{K_T(\mu_y)}+G(o,\mu_y)\right]\cdot H(x,\mu_y)\cdot\left(e^{-i|x_o|\lambda_1}-e^{-|x_o|\lambda_2}\right)\right\} \quad (2)$$

Similarly, for a point force excitation, the plate displacement response found after applying a contour integral on μ_x is

$$W_p(x,y) = \frac{F_p \ell^3}{D_p}\left(\frac{-i}{8\pi\Omega^2}\right)\cdot e^{-i\mu_y(y-y_o)}\cdot\left\{\int_{-\infty}^{\infty}\frac{e^{-i|x-x_o|\sqrt{\Omega^2-\mu_y^2}}}{\sqrt{\Omega^2-\mu_y^2}}+\frac{e^{-|x-x_o|\sqrt{\Omega^2+\mu_y^2}}}{i\sqrt{\Omega^2+\mu_y^2}}\right)d\mu_y-\int_{-\infty}^{\infty}\frac{1}{\Delta(\mu_y)}\left[\frac{1}{K_R(\mu_y)}+iH'(o,\mu_y)\right]\cdot G(x,\mu_y)\cdot\left(\frac{e^{-i|x_o|\sqrt{\Omega^2-\mu_y^2}}}{\sqrt{\Omega^2-\mu_y^2}}+\frac{e^{-|x_o|\sqrt{\Omega^2+\mu_y^2}}}{\sqrt{\Omega^2+\mu_y^2}}\right)d\mu_y+\int_{-\infty}^{\infty}\frac{1}{\Delta(\mu_y)}\left[\frac{1}{K_T(\mu_y)}+G(o,\mu_y)\right]\cdot H(x,\mu_y)\cdot\mathrm{sgn}(x_o)\cdot\left(e^{-i|x_o|\sqrt{\Omega^2-\mu_y^2}}-e^{-|x_o|\sqrt{\Omega^2+\mu_y^2}}\right)d\mu_y \quad (3)$$

where $\Delta(\mu_y) = \left[\frac{1}{K_T(\mu_y)}+G(o,\mu_y)\right]\left[\frac{1}{K_R(\mu_y)}+iH'(o,\mu_y)\right]$; $K_T(\mu_y)$ and $K_R(\mu_y)$ are rib translational and rotational stiffness parameters respectively; ℓ is a normalized length scale; Ω is the dimensionless excitation frequency, where $\Omega^4 = \frac{\rho_p h_p \omega^2 \ell^4}{D_p}$; μ_x and μ_y are the dimensionless wavenumber along x-axis and y-axis respectively; $\lambda_1 = \sqrt{\Omega^2-\mu_y^2}$ and $\lambda_2 = \sqrt{\Omega^2+\mu_y^2}$ are poles of the contour integral; x,y and x_o,y_o are the dimensionless coordinates for response and excitation points

respectively;

$$H'(o,\mu_y) = \frac{i}{4\Omega^2}(i\lambda_1 - \lambda_2);\ G(o,\mu_y) = \frac{i}{4\Omega^2}\cdot\ (-\frac{1}{\lambda_1} + \frac{i}{\lambda_2});\ H(x,\mu_y) = -sgn(x_o)(\frac{i}{4\Omega^2}).$$

$(e^{-i|x|\lambda_1} - e^{-|x|\lambda_2});\ G(x,\mu_y) = \frac{i}{4\Omega^2}\left(-\frac{e^{-i|x|\lambda_1}}{\lambda_1} + i\,\frac{e^{-|x|\lambda_2}}{\lambda_2}\right)$; and F_L and F_p are line and point forces respectively.

The acoustic pressure response is related to displacement response in the wavenumber domain as

$$\tilde{P}_a(\mu_x,\mu_y,z) = -\frac{\rho_o\omega^2}{\eta}\,\tilde{w}(\mu_x,\mu_y)\,e^{-\eta z} \tag{4}$$

where $\eta = \sqrt{\mu_x^2+\mu_y^2-\mu_f^2}$ and $\mu_f = k_f\ell$, which satisfies Euler's equation on the surface of the plate. Therefore, the pressure response for the $z \geq 0$ half space can be formulated by taking the inverse Fourier transform of (4) as

$$P_a(x,y,z) = (\frac{1}{2\pi})^2\int_{-\infty}^{\infty}\int_{-\infty}^{\infty}\frac{-\rho_o\omega^2}{\eta}\cdot\tilde{w}(\mu_x,\mu_y)\,e^{-i(\mu_x x+\mu_y y)}\cdot e^{-\eta z}\,d\mu_x\,d\mu_y \tag{5}$$

For line force excitation, a direct integration scheme is carried out requiring a single integration. Point force excitation presents a more difficult task, requiring a numerical double integration scheme using Eqs. (3) and (4). In this case a coordinate transformation from cartesian to polar coordinates is carried out and then a basic trapezoidal integration is performed in the angular variable and a Gaussian integration is carried out in the radial variable.

Based on these two basic types of response, of displacement and acoustic pressure, further response information can be developed. Structural intensity is calculated with the equation derived by Noiseux and Pavić [4], [5] as

$$I_\alpha = \langle D_p\left[\frac{\partial}{\partial\alpha}(\nabla^2 w\ V_z - \left(\frac{\partial^2 w}{\partial\alpha^2} + \nu\frac{\partial^2 w}{\partial\beta^2}\right)\frac{\partial V_z}{\partial\alpha} - (1-\nu)\frac{\partial^2 w}{\partial\alpha\partial\beta}\cdot\frac{\partial V_z}{\partial\beta}\right]\rangle_t \tag{6}$$

where spatial coordinates α,β can be represented as either x,y or y,x; $\langle\ \rangle_t$ indicates a time average; and V_z is the plate velocity response. Three-dimensional acoustic intensity is calculated as

$$I_x = \frac{1}{2}Re\left\{P_a\cdot\left(\frac{\partial P_a}{\partial x}\right)^*\right\},\ I_y = \frac{1}{2}Re\left\{P_a\cdot\left(\frac{\partial P_a}{\partial y}\right)^*\right\},\ I_z = \frac{1}{2}Re\left\{P_a\cdot\left(\frac{\partial P_a}{\partial z}\right)^*\right\} \tag{7}$$

where * denotes complex conjugate.

The acoustic pressure pattern due to a line force excitation is calculated by direct numerical integration, while the farfield pressure pattern due to a point force excitation is calculated by a stationary phase method [6]. Finally, acoustic power is calculated by first confirming that the farfield radial intensity obeys the spherical spreading law and then performing double integration over the semi-spherical surface [6], [7] as

$$W = \frac{R^2}{2\rho_o C_o}\int_o^{2\pi}\int_o^{\frac{\pi}{2}}|P_a(R,\theta,\phi)|^2\sin\theta d\theta d\phi \tag{8}$$

In [6], the authors use π in the integration limit, while here $\frac{\pi}{2}$ is used for the θ upper bound due to the fact that we are interested in the upper half space only, which is the same case as presented in [7].

NUMERICAL RESULTS AND DISCUSSIONS

The material for both the plate and rib is assumed to be aluminum, i.e. Young's modulus $E_p = E_b = 7.1 \times 10^{10}$ N/m^2; shear modulus $G_b = 2.4 \times 10^{10}$ N/m^2; Poisson's ratio $\nu = 0.33$; and density $\rho_p = \rho_b = 2700$kg/m^3. Additional parameters used are a plate thickness, $h_p = 3.175 \times 10^{-3}$m; a rib cross-sectional area of $0.05 \times 3.175 \times 10^{-3}$m^2; a rib eccentricity, $e_z = 0.0265875$ m; the density of air, $\rho_o = 1.21$kg/m^3; and the speed of sound in air, $c_o = 343$ m/sec.

The vibrational responses presented include displacement and structural intensity. Figure 2 shows the displacement response of a homogeneous plate due to a line force, which can be compared with the result of [8] in vacuo. Figure 3 shows displacement response of a ribbed plate due to the same line force applied on the rib. These two figures show similar behavior, except the ribbed plate has a smaller displacement response amplitude. Response due to a point force on the rib at the same frequency and with a 5.2 N magnitude is shown in Fig. 4. The plate response is symmetrical with respect to the rib as shown in the contour plot of Fig. 4. The structural intensity response due to a line force on the rib is shown in Fig. 5. In this case, the excitation wavenumber $k_y = 0$; thus, the plate's response becomes one-dimensional. The real part, or active intensity, shows a very useful feature for identifying the force location. On the side $x>0$, the value of the active intensity is always positive which means the intensity vector points to the right and on the side $x<0$, the value is always negative which means the intensity vector points to the left. Thus a rapid change in the sign of the active structural intensity occurs at the force location.

The acoustic responses include pressure patterns, acoustic power, and acoustic intensity. Figure 6 shows the pressure patterns due to a line force applied on a homogeneous plate and a ribbed plate. It can be seen in Fig. 6 that the pressure patterns change gradually from a hemi-circle into a bell shape. Moreover, at $\theta = \phi = 90^\circ$, on a surface along the rib, the pressure amplitude recovers to a constant as expected for a constant amplitude line force excitation. The pressure pattern due to a point force on the rib is shown in Fig. 7. Again, as ϕ is increased to 90° (the plane along the rib), an interesting pressure pattern is shown. At $\theta = \phi = 90^\circ$ the pressure amplitude does not equal to a constant; instead, it changes according to spherical spreading as expected for a point force excitation. Figure 8 compares the radiated acoustic power of the homogeneous and ribbed plates due to the same sinusoidal point force. The power radiated from the ribbed plate is reduced to about one-tenth of the homogeneous plate at the plate coincidence frequency. Above coincidence frequency, the radiated power for both cases is larger than below the coincidence frequency. In Fig. 8b, below the plate coincidence frequency, the rib coincidence frequency can be seen at about 260 HZ. Also, the normal acoustic intensity at the surface of the plate is shown in Fig. 9 for a line force applied to both a homogeneous and a ribbed plate. The in-plane acoustic intensity is shown in Fig. 10 for a ribbed plate only. Neither type of acoustic intensity data provides information that is as immediately useful as structural intensity information for force location. However, the in-plane active acoustic intensity looks much more promising for force localization than normal acoustic intensity when a line force is applied on the rib.

CONCLUSIONS

Expressions were derived for the vibrational and acoustic responses of an infinite, single-ribbed plate with negligible fluid loading. Results were presented for point and line force excitation applied to the rib and were compared with similar excitation of an infinite homogeneous plate.

The rib significantly changed the plate responses, causing a lowering in the magnitude of displacement and resultant acoustic pressure in comparison with homogeneous plate response magnitudes. Acoustic power radiated from a ribbed plate at the plate coincidence frequency is about ten times smaller than that radiated from a homogeneous plate with a similar point force excitation. Also, ribbed plate pressure directivity patterns are greatly changed from the patterns produced by a homogeneous plate, especially in a plane along the rib (at $\phi = 90^{\circ}$).

Structural intensity in the plate was compared with acoustic intensity on the surface of the plate. It was demonstrated that the structural intensity is an excellent tool for force localization and that the real, in-plane acoustic intensity can also be useful for that purpose. However, the normal acoustic intensity that is commonly used in practical noise control applications provides very poor information for the force localization in all cases considered in this paper.

ACKNOWLEDGEMENTS

The authors would like to thank the Office of Naval Research for the financial support of this research.

REFERENCES

1. V. N. Evseev, "Sound radiation from an infinite plate with periodic inhomogeneities," Sov. Phy. Acoust., Vol. 17, No. 3, Nov-Dec, 1973.
2. M. L. Rumerman, "Vibration and wave propagation in ribbed plates," J.A.S.A., Vol. 57, No. 2, Feb. 1975.
3. B. R. Mace, "Periodically stiffened fluid-loaded plates, I & II," J.S. & V., 73(4), 1980, p. 473-504.
4. D. V. Noiseux, "Measurement of power flow in uniform beams and plates," J.A.S.A., Vol. 47, No. 1, 1970, p. 238-247.
5. G. Pavić, "Structural surface intensity: An alternative approach in vibration analysis and diagnosis," J.S. & V., Vol. 115, No. 3, 1987, p. 405-422.
6. M. C. Junger and D. Feit, Sound, Structures, and their Interaction, 2nd edition, The MIT Press, Cambridge, Massachusetts, 1986, p. 114-116 & p. 66.
7. M. C. Junger, "Pressure radiated by an infinite plate driven by distributed loads," J.A.S.A., Vol. 74(2), No. 2, August 1983.
8. D. Feit and Y. N. Liu, "The nearfield response of a line-driven fluid-loaded plate," J.A.S.A., Vol. 78, No. 2, August 1985.

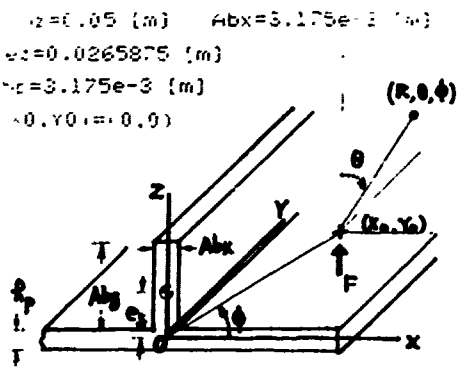

Fig 1. Geometry of a ribbed plate.

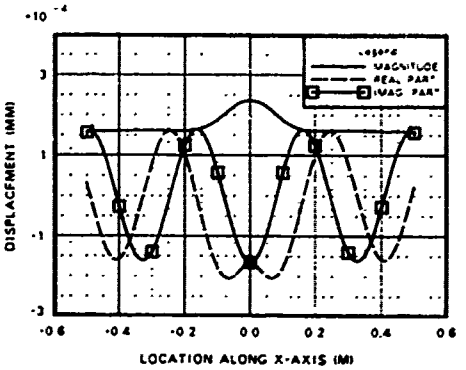

Fig 2. Displacement response of a homogeneous plate with 1.0 N/m, 292 HZ, and wavenumber k_y=0 1/m line force applied at x=0 m. Ribbed plate loss factor = 0.02, and fluid unloaded.

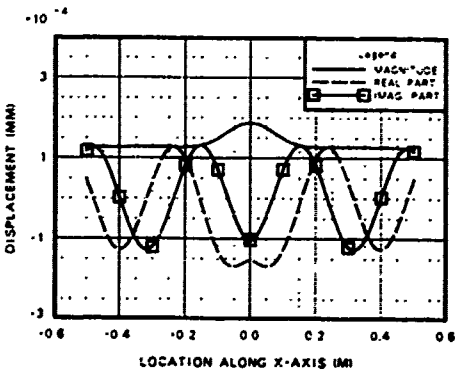

Fig 3. Displacement response of a ribbed plate with 1.0 N/m, 292 HZ, and wavenumber k_y=0 1/m line force applied at x=0 m. Ribbed plate loss factor=0.02, and fluid unloaded.

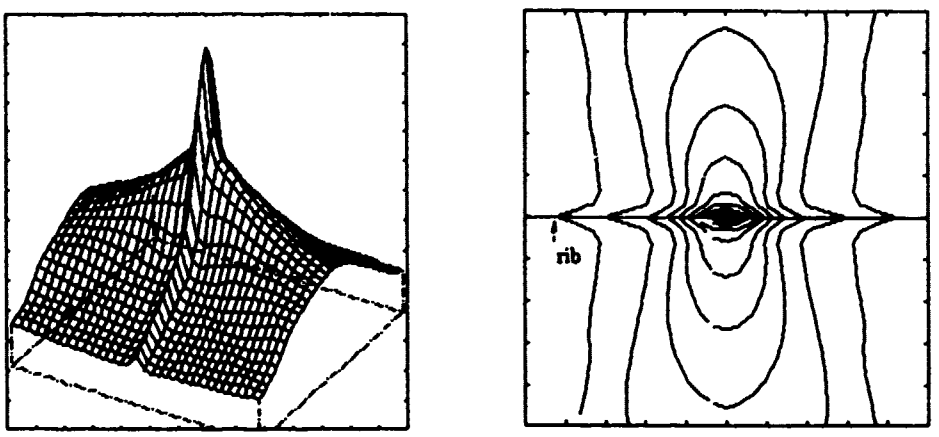

(a) (b)

Fig 4. Displacement response of a ribbed plate with 5.2 N, 292 HZ point force applied on the rib. Ribbed plate loss factor=0.02, and fluid unloaded (a) 3-D; (b) contour.

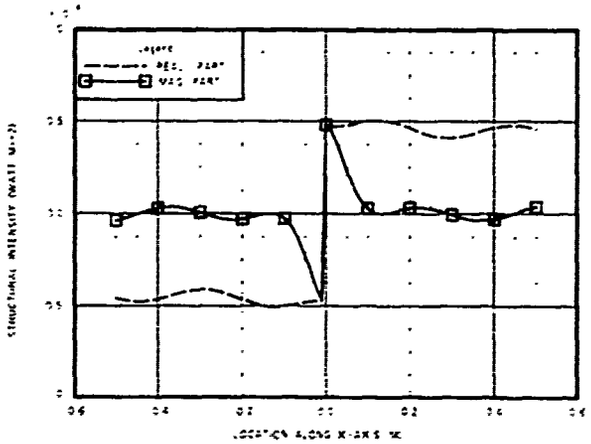

Fig 5. Structural intensity in x-direction when 1.0 N/m, 292 HZ, and wavenumber k_y=0 1/m line force is applied on the rib. Ribbed plate loss factor=0.02, and fluid unloaded.

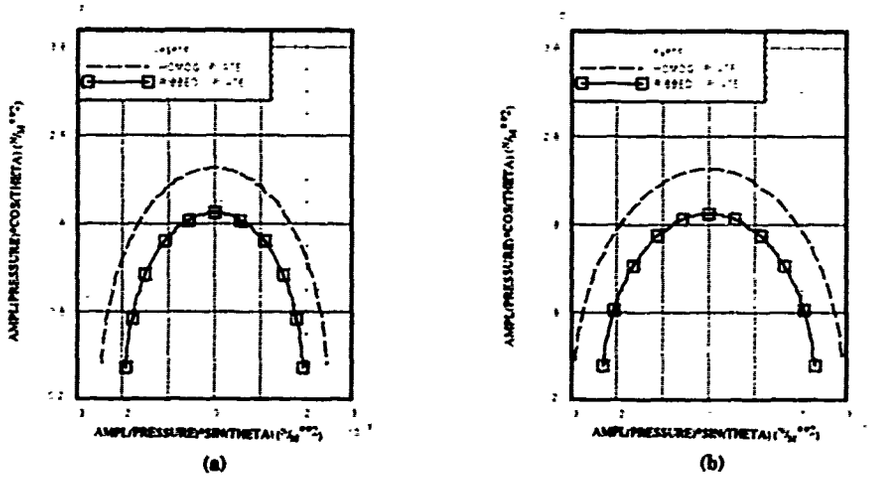

(a) (b)

(c)

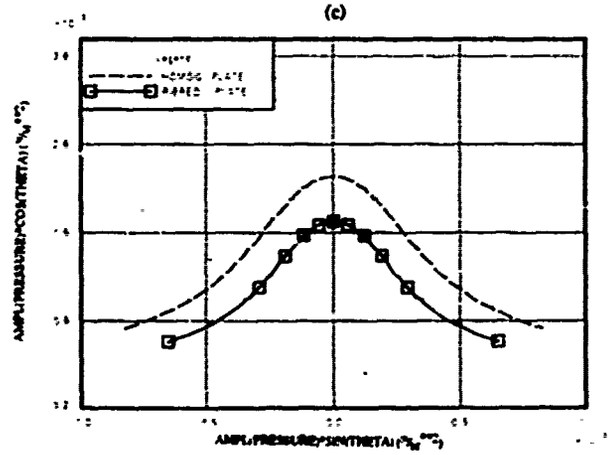

Fig 6. Farfield pressure directivity patterns at various planes (a) ϕ=0°; (b) ϕ=45°; (c) ϕ=90° when 1.0 N/m, 292 HZ, and wavenumber k_y=0 1/m line force is applied on the rib. Ribbed plate loss factor=0.02, and fluid unloaded.

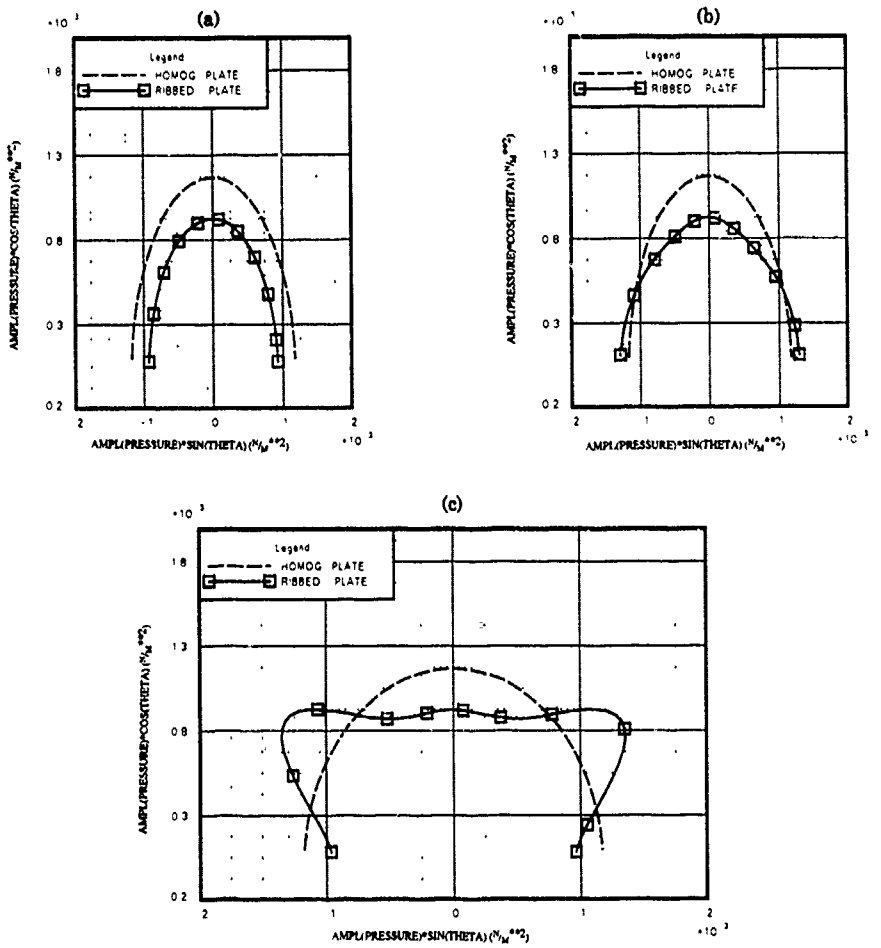

Fig 7. Farfield pressure directivity patterns for various planes (a) $\phi = 0°$; (b) $\phi = 45°$; (c) $\phi = 90°$ when 5.2 N, 292 HZ point force is applied on the rib. Ribbed plate loss factor = 0.02, and fluid unloaded.

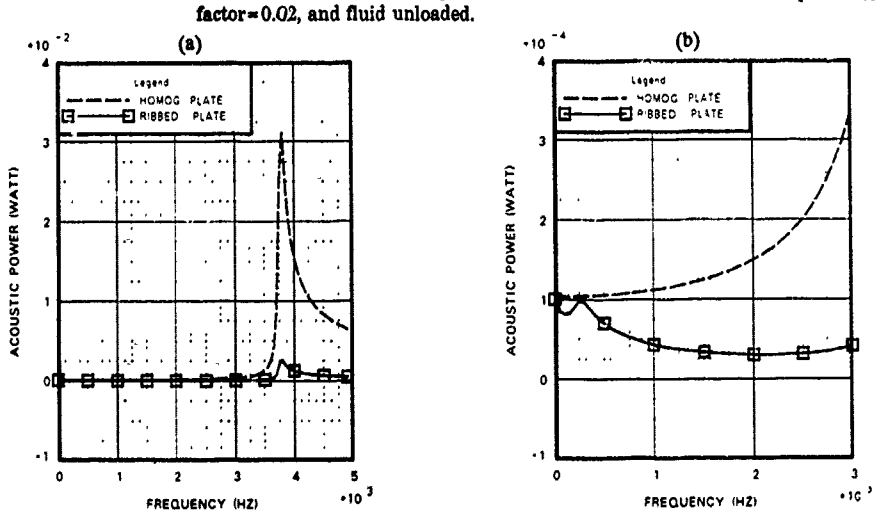

Fig 8. Acoustic power radiated of homogeneous and ribbed plates when 5.2 N, sinusoidal point force is applied on the rib. Ribbed plate loss factor = 0.02, and fluid unloaded.

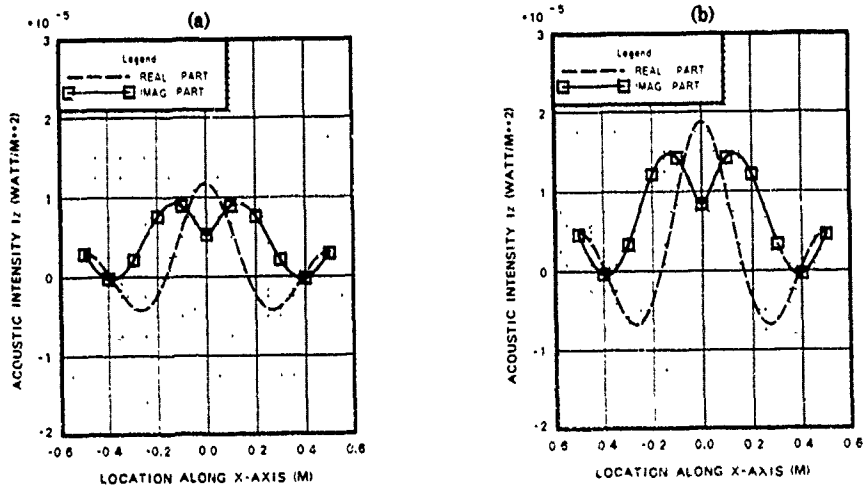

Fig 9. Normal acoustic intensity at the surface of the plate with a 1.0 N/m, 292 HZ, and wavenumber k_y=0 1/m line force excitation (a) homogeneous plate. (b) ribbed plate. Plate loss factor=0.02, and fluid unloaded.

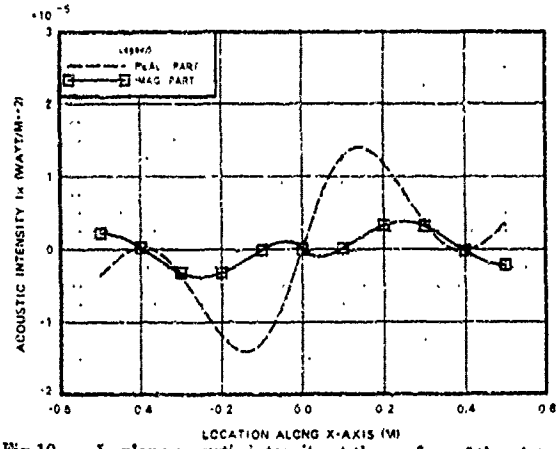

Fig 10. In-plane acoustic intensity at the surface of the plate with a 1.0 N/m, 292 HZ, and wavenumber k_y=0 1/m line force exictation. Plate loss factor=0.02, and fluid unloaded.

SECOND INTERNATIONAL CONGRESS ON
RECENT DEVELOPMENTS IN AIR- AND
STRUCTURE-BORNE SOUND AND VIBRATION
MARCH 4-6, 1992 AUBURN UNIVERSITY, USA

ANALYTICAL AND EXPERIMENTAL DETERMINATION OF THE VIBRATION AND PRESSURE RADIATION FROM A SUBMERGED, STIFFENED CYLINDRICAL SHELL WITH TWO END PLATES

A. Harari and B.E. Sandman
Naval Undersea Warfare Center Division, Newport
Newport, R.I. 02841

J.A. Zaldonis
Westinghouse Corporation
1310 Beulah Road, Pittsburgh, PA 15235

ABSTRACT

An analytical model of a finite, stiffened cylindrical shell with two end plates submerged in fluid was developed. Results obtained for the drive point and transfer point mobility as well as the pressure at various points in the fluid are compared with experimental results. Excellent agreement between the analytical and the experimental results are reported.

INTRODUCTION

The analysis presented here uses classical techniques to find the vibration and acoustic radiation from a finite, stiffened cylindrical shell with two end plates. The analysis considers Sanders-Koiter shell equation for the cylindrical part of the structure, classical bending and plane stress equations for the end plates and for the rectangular stiffeners. The shell is excited by harmonic forces. The force acting on the shell may be a distributed force or a point force acting in three directions or a moment in the axial direction.

The displacements on the shell are expanded by Fourier series in the circumferential direction. Since the structure is axisymmetric and the fluid infinite, the solution can be found for each circumferential mode separately. The shell is segmented at each stiffener location and at the location where a point force is acting on the shell. The end plates are also segmented if a point force is acting on one of the plates. The homogeneous and the particular solutions are found for each segment of the shell or the end plates. The value of the constants associated with the homogeneous solution are found by enforcing the boundary condition between the various structural elements. The boundary conditions between the various structural elements are a continuity of displacements/rotation and balance of forces at each interface. The boundary condition at an interface where the point force or line force is acting is the continuity of displacements and rotation and discontinuity of the appropriate stress resultant or moment. Since the analysis is conducted for each circumferential mode separately, the discontinuity of the stress resultant is equal to the Fourier component in the

circumferential direction of the forcing function. The fluid loading is approximated by neglecting the interaction between the velocity and pressure on the cylindrical part and the end parts of the cylindrical cavity. This is accomplished by considering a cylindrical cavity with rigid extension for the cylindrical part of the surface and half space with rigid extension for the end plates. For the purpose of solving the fluid/structure interaction problem, the normal to the surface vibration and the pressure on the shell are expanded by surface functions on the cylindrical shell and end plates. The general shell response is found in terms of the coefficients of the surface displacements and pressure on the shell. Similar expressions are found for the fluid cavity. The fluid/structure interaction is found in terms of the coefficients of expansion. Once the coefficients of expansion are found, the displacement/velocity on the shell or the pressure anywhere in the fluid can be found. The analysis in this paper is an extension of previous papers by the authors. Ref. 1 describes the method used for the fluid/structure interaction, Ref. 2 describes the analysis for the in vacuum vibration of a cylindrical shell with end plates excited by a point force and Ref. 3 describes the analysis of fluid loading of a cylindrical cavity. The experimental field test is described fully in Ref. 4.

ANALYSIS

To be presented

EXPERIMENT

To be presented

NUMERICAL RESULTS

To be presented

REFERENCES

1. A. Harari and B.E. Sandman "Radiation and Vibrational Properties of Submerged Stiffened Cylindrical Shells," J. Acoust. Soc. Am. 88 1817-1830 (1990).

2. A. Harari, "Dynamic Characteristics of a Non-Uniform Torpedo-Like Structure," The Shock and Vibration Bulletin, Bulletin 52, Part 5, pp 113-133 (1982).

3. B.E. Sandman, "Numerical Fluid Loading Coefficients for Modal Velocities of Cylindrical Shells," Comput. Structures 6, pp 467-473 (1976).

4. J.A. Zaldonis, "Structural Vibration and Sound Radiation Measurements on a Ribbed Cylindrical Shell," Stc Memo 90-1e7-nocon-ml, Westinghouse STC, Pittsburgh, PA 15235, (1990).

SECOND INTERNATIONAL CONGRESS ON
RECENT DEVELOPMENTS IN AIR- AND
STRUCTURE-BORNE SOUND AND VIBRATION
MARCH 4-6, 1992 AUBURN UNIVERSITY USA

SPREADING LOSSES IN OUTDOOR SOUND PROPAGATION

by

Louis C. Sutherland
Consultant in Acoustics
27803 Longhill Dr.
Rancho Palos Verdes, CA 90274

Introduction

Spreading losses are the fundamental starting point in sound propagation definition and this brief survey attempts only to collect, within one short paper, a minimum number of simple expressions to define spreading losses from various types of arrays of incoherent sources. These are commonly utilized to model community noise levels from large sources such as freeways or industrial plants. A few simplifications of some of the previous evaluations of this general problem are offered.

1. Linear Array of Point Sources.

Figure 1 shows the spreading loss along a line normal to the middle of an infinite and finite arrays of incoherent uniform point sources spaced at an equal distance b. Here, the spreading loss, A_s is expressed as the difference between the sound level L_s at a distance b along this line equal to the spacing between sources, and the sound level, L_s at any other distance a along this line. For an infinite array, this loss exhibits spherical spreading behavior (6 dB/DD) for values of a/b less than $1/\pi$ and cylindrical spreading loss behavior (3dB/DD) for larger values of a/b. For a finite number N of point sources, the spreading loss is essentially the same as for an infinite array for small values of a/b, regardless of the number of sources. However, at a normalized distance a/b greater than approximately (N-1)/2, the spreading loss for the finite array begins to change from cylindrical spreading back to spherical spreading as the finite size array begins to appear as a point source.

The values of A_s for these two cases are given by the following expressions.

Infinite array[1]
$$A_s = 10 \lg [(a/b)\coth(\pi)/\coth(\pi a/b)] \quad (1a)$$

Finite array of N(odd) sources[2]
$$A_s \approx 10 \lg \left[(a/b)\, \frac{\tan^{-1}[(N-1)/2]}{\tan^{-1}[(N-1)/(2a/b)]}\right] \quad (1b)$$

The expression for the finite array is an approximation valid only for N > 3 and a/b > 1/π for which the error is less than 1 dB.[1]. However, the values of A_s plotted in Figure 1 for the three different cases for N= 5, 25 and 125 point sources are exact and were computed by summing the mean square sound pressures from each of the N sources for each value of a/b considered.

2. Finite Continuous Line Source.

As the separation distance between the sources approaches zero, a linear array of point sources becomes a continuous line source. Consider the more general case of a finite line source of length L illustrated in the following sketch. For propagation along a line normal to the linear source axis but starting at a point displaced by a distance X from one end of the linear array, the spreading loss A_s at any distance a, relative to the level at a distance L along this line, is given by[1]:

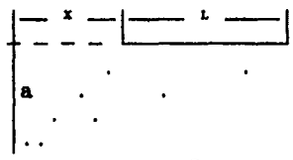

$$A_s = 10 \lg \left[(a/L) \frac{\tan^{-1}(X/L) - \tan^{-1}(X/L + 1)}{\tan^{-1}(X/a) - \tan^{-1}(X/a + L/a)} \right] \qquad (2)$$

3. Circular Planar Array of Incoherent Sources

A uniform plane array of incoherent sources is often used to model an extended source such as a large industrial plant. For a circular (disc) array with a radius R, define the spreading loss, A_s as the difference between a reference sound pressure level, for all of the sources operating, at a reference distance R equal to the array radius, and the level at any other distance, a from the disc array. Two different propagation paths are considered - 1) along the central axis normal to the disc plane and at a distance a from its center and 2) in the plane of the disc array at a distance a from the edge.

For the first case, the mean square sound pressure P^2_s at a distance a from the disc along its central axis can be given, for hemispherical radiation, by[3]

$$P^2_s = [\, W Z_o/(2\pi R^2)] \cdot \ln[(R/a)^2 + 1] \qquad (3)$$

where W is the total acoustic power output of the disc source, and Z_o is the characteristic acoustic impedance of air.

The spreading loss A_s for this case, at a distance a, relative to the sound level along the disc axis at a distance R, is simply:

$$A_s = 10 \lg[\, \ln(2)/\ln((R/a)^2 + 1) \,] \qquad (4a)$$

For the second case, the spreading loss A_s along a line in the disc plane at a distance a from the edge of the disc relative to the sound level along this line at a distance R from the edge is given by[1]

$$A_s = 10 \lg[\, \ln(4/3)/\ln\{(1 + (R/a))^2/((1 + (R/a))^2 - 1)\} \,] \qquad (4b)$$

These two cases for spreading loss are shown in Figure 2.

4. Rectangular Array of Incoherent Sources

Rectangular arrays of incoherent sources are also commonly used for modeling large distributed sources such as industrial plants. For example, the spreading propagation loss along the central axis normal to rectangular arrays has been evaluated for a range of rectangular array shapes[1,3,5], along with spreading losses along a line in the plane of the array[3]. Numerical integration has been employed to evaluate the spreading loss that would be measured on the ground, (ignoring ground effects) along a line normal to, and originating from, the mid-point of the lower edge of a vertical radiating wall of height b and length c with c >b[5]. Applying the same approach outlined earlier for a disc source, the spreading loss, A_s along this line at any distance a, relative to the level along the same line at a distance equal to the shortest dimension, b can be given as:

$$A_s = 10 \lg \left[\frac{(\pi/2) \tan^{-1}(c/b)}{\tan^{-1}(b/a) \cdot \tan^{-1}(c/2a)} \right] + K(a/b) \qquad (5a)$$

where K(a/b) is a "near field" correction factor that has been shown, graphically, to be a function of a/c with the aspect ratio c/b of the wall as a parameter.[5] However, as shown in Figure 3, this function can be expressed to a close approximation in terms of only the ratio a/b of the distance a from the wall to the length b of the shortest side and given by the following where $\beta = 1 - \lg(a/b)$:

$$K(a/b) = \begin{cases} 0.337 + 0.575\,\beta - 0.912\,\beta^2 & , a/b < 0.3 \\ 0 & , a/b \geq 0.3 \end{cases} \qquad (5b)$$

Eq. (5a) and (5b) were used to construct the curves in Figure 4 for the spreading loss along the median ground line for four different values of the aspect ratio c/b of the noise radiating wall -- 1,3,5 and 8. However, the abscissa for all of these curves is the non-dimensional distance a/R_s where R_s is the radius of a circle with the same area (b x c) as that of the wall. Thus, this normalized distance, a/R_s was simply equal to $(a/\sqrt{\pi/bc})$. As indicated in Figure 4, this method of evaluating the spreading loss for these various rectangular wall source arrays indicates that the spreading losses have roughly the same value for the same value of a/R_s. For comparison, the figure also shows the spreading loss from Figure 3 for the case of propagation along the central axis of a disc source. The close similarity between this curve and the curves for the rectangular wall source, when evaluated at the same value of a/R_s, is quite clear.

5. Spreading Loss from an Infinite Plane Source

To estimate the horizontal and vertical distribution of noise in a community, models have been developod to describe the average sound level measured in the plane of an infinite array of incoherent sources[6] and along a vertical line normal to such an infinite plane[7]. The latter model predicts the experimentally-measured low vertical gradient in high-density urban community outdoor noise at various floor levels of high rise buildings[7].

More complex spreading loss prediction models have been also been developed, analytically[8-10] and experimentally[11-13] to describe sound propagation in urban, built-up areas primarily from surface transportation but including V/STOL aircraft[13]. Some of these models include consideration of multiple reflections and shielding by high-rise urban buildings.

6. Summary

A limited number of expressions have been presented, and illustrated graphically, which summarize, and some cases, simplify, previously published models for predicting the spreading loss from various types of arrays of incoherent sources.

REFERENCES

1. RATHE, E.J. "Note on Two Common Problems of Sound Propagation," J.Sound Vib. 10, 472-479, 1969.

2. KURZE, U. and BERANEK, L.L. "Sound Propagation Outdoors," Chapter 7 in "Noise and Vibration Control", L.L .Beranek, (ed), McGraw-Hill Book Co., N.Y., 1971.

3. TATGE, R.B., "Noise Radiation by Plane Arrays of Incoherent Sources," J. Acoust. Soc. Am, 52, 732-736, 1972.

4. ELLIS, R.M. "Cooling Tower Noise Generation and Radiation," J. Sound Vib. 14, 171-182, 1971.

5. ELLIS, R.M. "The sound pressure of a uniform, finite, plane source," J. Sound Vib. 13, 503-508, 1970.

6. SHAW, E.A.G. and OLSON, N. "Theory of Steady-State Urban Noise for an Ideal Homogeneous City," J. Acoust. Soc. Am. 51, 1781-1793, 1971.

7. SUTHERLAND, L.C. "Ambient Noise Level Above Plane with Continuous Distribution of Random Sources," J. Acoust. Soc. Am. Vol 57, 1975, pp. 1540-1542.

8. DAVIES, H.G., "Multiple-Reflection Diffuse-Scattering Model for Noise Propagation in Streets," J. Acoust. Soc. Am. 64, 1978, pp. 517-521.

9. KURZE, U.J. "Noise Reduction by Barriers," J. Acoust. Soc. Am. 55, 504-518 (1974).

10. SHARP, B.H. and DONAVAN, P R. "Motor Vehicle Noise," Chap 32, Handbook of Noise Control, (1979) pp. 32-16.

11. WEINER, F.M., MALME, C.I. and GOGOS, C.M. "Sound Propagation in Urban Areas," J. Acoust. Soc., Am Vol. 37,(1965), pp. 738-747.

12. LAMURE, C. "Road Traffic Noise: Generation, Propagation and Control," Chap. 12, Noise Pollution, John Wiley and Sons, N Y. 1986, pp. 316-326.

13. DONAVAN, P.R. and LYON, R.H. "Model Study on the Propagation from V/STOL Aircraft into Urbans Environs," J. Acoust. Socy. Am," Vol. 55, 19174, pp 485(A).

FIGURE 1

SPREADING LOSS FOR LINEAR ARRAY OF POINT SOURCES

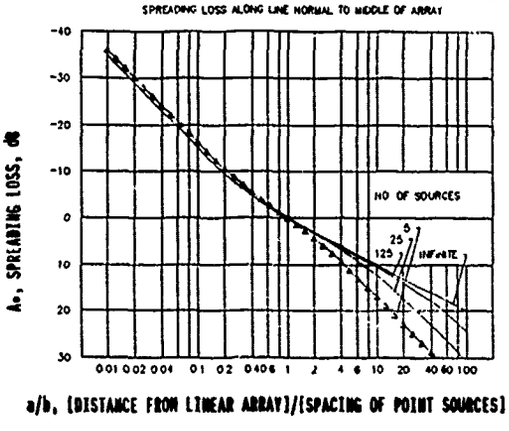

FIGURE 2

SPREADING LOSS FROM DISC SOURCE

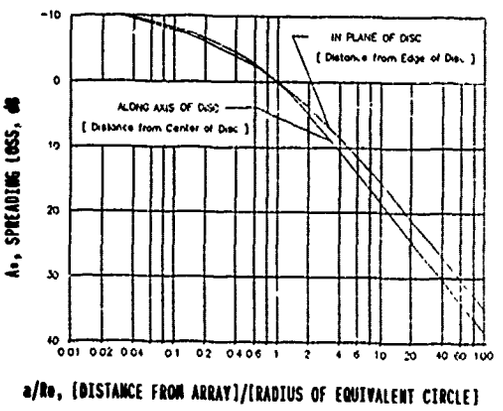

FIGURE 3

CORRECTION TO SPREADING LOSS FOR WALL

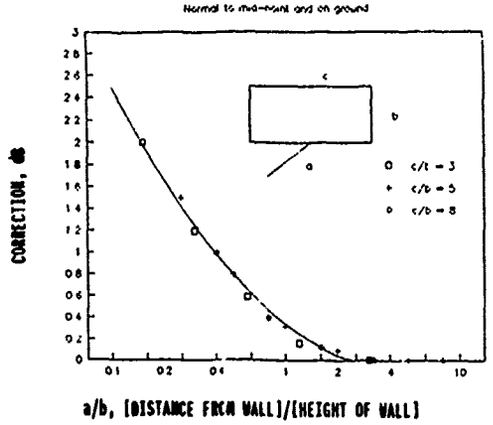

FIGURE 4

SPREADING LOSS FROM RECTANGLE OR DISC

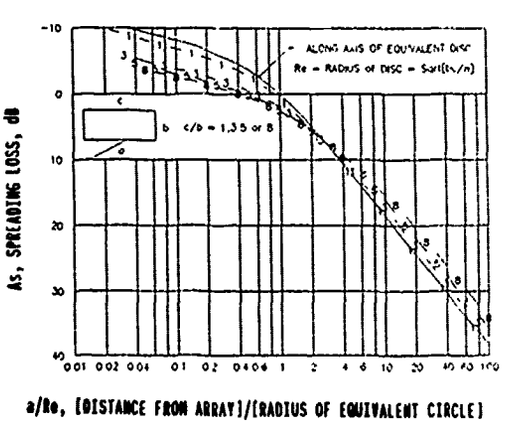

SECOND INTERNATIONAL CONGRESS ON
RECENT DEVELOPMENTS IN AIR- AND
STRUCTURE-BORNE SOUND AND VIBRATION
MARCH 4-6, 1992 AUBURN UNIVERSITY, USA

SOUND PROPAGATION

Marinus M. Boone
Delft University of Technology, Lab. of Seismics and Acoustics
P.O. Box 5046, 2600 GA Delft, The Netherlands

ABSTRACT

An overview is presented of our work on sound propagation models. These models are applied for the prediction of noise immission levels in the atmosphere as well as for studies on acoustic and elastic propagation through earth-layers for seismic exploration applications. The computational models that we use range from ray-tracing algorithms to finite difference techniques. Additionally, physical scale models are used.

In this paper our focus will be on near surface atmospheric sound propagation. The applicability of the various model approaches will be discussed and emphasis will be given to the effects of the influences of temperature and wind gradient profiles, decorrelation over large distances and ground absorption. It will also be discussed how these phenomena can be accounted for in the various models. Depending on the physical conditions to be studied and the required accuracy, it is discussed whether to use ray-tracing, beam-tracing, wave number domain techniques, full finite difference or a physical scale model.

1. INTRODUCTION

In this paper we will discuss some major phenomena that influence sound propagation. We will focus on outdoor situations, but some parts of the underlying theory and modeling schemes are applicable in other acoustic disciplines as well, i.e. in underwater acoustics and in seismics. For underwater acoustics this is quite obvious, as the same wave equation is applicable (neglecting shear forces). For seismics this is only partly true, because the earth solid can propagate both compressional and shear waves. However, if decomposition is applied to the data first, compressional and shear data can be analyzed separately. In our group much cross-fertilization takes place between the disciplines of acoustics and seismics, especially for computational schemes of wave propagation.

In the next sections we will first discuss the physical phenomena that influence outdoor sound propagation. Next we will summarize some important propagation modeling schemes and present a discussion on the different physical phenomena that can or cannot be introduced into such models. Finally, we will present scale model measurements and numerical results of the different models.

2. PHYSICAL PHENOMENA

Sound propagation is influenced by many different physical phenomena. To quantify the effects of these phenomena, we will need the related physical models; they are discussed in the next section. Here we will restrict ourselves to a qualitative description.

Screening One of the most important factors that influences sound propagation is given by the screening of the waves by obstacles. One makes practical use of that by constructing walls and barriers to diminish the propagation of traffic noise.
Air absorption Another important factor is given by the absorption of the medium, caused by molecular thermal relaxation, viscosity and heat conduction. It is well known that without this kind of absorption, we would live in a very noisy environment!
Ground absorption When propagation takes place close to the ground the so-called ground absorption plays an important role. In fact the term absorption is misleading. Most part of the extra attenuation due to the ground surface is not caused by absorption but by the destructive interference between direct and reflected sound.
Gradients Sound propagation is also strongly influenced by spatial and temporal inhomogeneities and moving of the medium. The wind- and temperature profiles are of particular importance. They can lead to acoustic shadow zones and to regions with very high immission levels.
Turbulence Another class of effects is given by wind turbulence and irregularly shaped temperature inhomogeneities. This can lead to longitudinal and transverse coherence loss.

3. PROPAGATION MODELING

Modeling of sound propagation is based on a simplified description of the real propagation process that takes place. From a theoretical point of view, one would like to solve the acoustic wave equation for an inhomogeneous, moving medium. This wave equation is given by

$$\rho_0 \nabla \cdot \left(\frac{1}{\rho_0} \nabla p \right) - \frac{1}{c^2} \left[\frac{\partial^2 p}{\partial t^2} + \frac{\partial}{\partial t} (\mathbf{v}_t \cdot \nabla) p \right] + \rho_0 \nabla \cdot (\mathbf{v}_t \cdot \nabla) \mathbf{v}_t = -s \ . \tag{1}$$

In this equation p is the sound pressure as a function of x, y, z and t, ρ_0 is the density of the medium which may be a function of x, y and z, c is the sound velocity, which may also be a function of x, y and z, s is a source function of x, y, z and t, and $\mathbf{v}_t$ is the total particle velocity, which is also a function of x, y, z and t. In many cases it is useful to distinguish between the medium velocity (in air: the wind velocity) $\mathbf{v}_0$ and the acoustic particle velocity $\mathbf{v}$:

$$\mathbf{v}_t = \mathbf{v}_0 + \mathbf{v} \ . \tag{2}$$

Analytical solutions of Eq. (1) are only possible for very simple boundary conditions and very simple functions of $\rho_0(x, y, z)$, $c(x, y, z)$ and $\mathbf{v}_0(x, y, z)$. For practical situations numerical solutions are needed. Such solutions are based on numerical integration of the wave equation or approximations of that. Besides that it must be mentioned that to include absorption effects, even a more complicated wave equation is needed.
The following modeling procedures are used in practice:

Wave field extrapolation in the time domain
This procedure is often used in seismic modeling and is based on a Taylor series expansion of $p(\mathbf{r}, t)$ as a function of t (here r represents the spatial coordinates x, y, and z). By application of the wave equation, the temporal differentiations are replaced by spatial differentiations. In two-dimensions this leads for $\mathbf{v}_0 = 0$ to the following expression [1]:

$$p(x,z,t+\Delta t) = -p(x,z,t-\Delta t) + 2\left[1 - \frac{(c\Delta t)^2}{\Delta^2}\right] p(x,z,t) + (c\Delta t)^2 s(x,z,t) +$$

$$\frac{(c\Delta t)^2}{\Delta^2} [p(x+\Delta,z,t) + (x-\Delta,z,t) + (x,z+\Delta,t) + (x,z-\Delta,t)] \ . \tag{3}$$

This solution is accurate and stable if $\Delta t c/\sqrt{2} < \Delta < \lambda_{min}/10$ in two dimensions or $\Delta t c/\sqrt{3} < \Delta < \lambda_{min}/10$ in three dimensions. λ_{min} is the minimum wave length to be considered.

Wave field extrapolation in the frequency domain

Transformation of the wave equation to the frequency domain gives a more simple expression, because the time differentiations are replaced by a multiplication factor $j\omega$, giving the well known Helmholtz equation in the case of a homogeneous, non-moving medium. In the x, y, z, ω domain, the Kirchhoff integral can be applied to compute the sound pressure at a point from the sound pressure and particle velocity at the boundary of a closed surface around that point. This general expression can be worked out for the special case of an infinite plane boundary, with the sound sources at one side and the point where the sound pressure is to be calculated at the other side. This approach results in the Rayleigh integrals. If we know the sound pressure at a plane $z = z_0$, then the sound pressure in a point A with coordinates x_A, y_A, z_A is given by [1]:

$$P(x_A,y_A,z_A,\omega) = \frac{1}{4\pi}\iint P(x,y,z_0,\omega)\frac{\partial G}{\partial n}dxdy \qquad (4)$$

where G is the Green's function for point A, assuming a pressure release surface at $z = z_0$. The Green's function depends on the properties of the medium. In the homogeneous case with no wind, Eq. (4) can be written as:

$$P(x_A,y_A,z_A,\omega) = \frac{jk}{2\pi}\iint P(x,y,z_0,\omega)\cos\phi\frac{1+jk\Delta r}{jk\Delta r}\frac{e^{-jk\Delta r}}{\Delta r}dxdy \ . \qquad (5)$$

The variables Δr and ϕ are defined in figure 1.

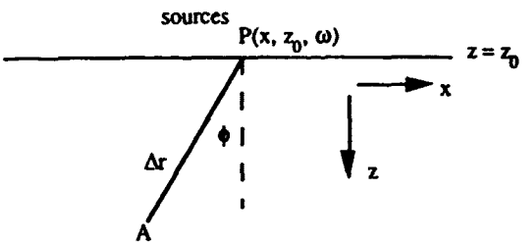

Figure 1: The sound pressure in point A can be found as a weighted sum over the sound pressures in the plane $z = z_0$. For simplicity a two dimensional situation is depicted here.

This result shows that the sound field extrapolation can be viewed as a summation over dipole sources with source strength $P(x,y,z_0\omega)$ over the surface $z = z_0$ (Huygen's principle).

Wave field extrapolation in the wave number domain

In the special case that the medium is laterally homogeneous between the planes $z = z_0$ and $z = z_A$, the Green's function G is spatially only dependent on Δr, which means that the wave field extrapolation between z_0 and z_A can be written as a spatial convolution. This means that if we take a spatial Fourier transform from x to k_x and from y to k_y, the extrapolation reduces from a convolution to a multiplication. The extrapolation is simply given by [1]

$$\tilde{P}(k_x,k_y,z_A,\omega) = \tilde{P}(k_x,k_y,z_0,\omega)e^{-jk_z\Delta z} \qquad (6)$$

with $\Delta z = |z_A - z_0|$ and $k_z = \sqrt{k^2 - k_x^2 - k_y^2}$. This result clearly shows that the spatial Fourier transform in the x and y direction results in a decomposition of the wave field into plane waves. When the medium is inhomogeneous between z_0 and z_A, also traveling waves in the opposite direction occur. Now a method similar to Eq. (6) can be used if the medium is built up from small homogeneous layers. Within each layer upgoing and downgoing waves appear simultaneously. At each interface the pressure and its derivative must be continuous, hence Eq. (6) turns into a matrix equation. As can be seen from Eq. (6), only inhomogeneities in the z-direction can be introduced, so only so-called stratified media can be dealt with.

Ray-acoustics

The wave field extrapolation methods rely on the computation of the wave propagation over a large spatial area. However, for the propagation of sound from a source to a receiver, only a part of this area is important: there are so-called propagation paths along which the acoustic energy is transported to the receiver. From that point of view it is obvious to try a ray approach. The ray approach is based on two principles:

1) Along a ray path the sound field may be locally approximated by a plane wave. The medium parameters determine how fast and in which direction the sound travels.
2) The acoustic energy is transported in the direction of the rays. Using this principle, the ray tube cross-section can be used to determine the intensity along a ray path. We call this procedure beam-tracing.

The ray paths can be computed from the ray-tracing equations [2]. The first ray-tracing equation gives the end point **r** of the ray as a function of time:

$$\frac{d\mathbf{r}}{dt} = c\mathbf{n} + \mathbf{v}_0 \ . \qquad (7.a)$$

n is the normal of the wave front and $\mathbf{v}_0$ is the wind velocity.

The second ray-tracing equation gives the changing of the angle α of the wave front normal as a function of time. In a moving medium this is a rather complicated equation. If we restrict ourselves to the x-z plane and a horizontal wind v_{ox}, it is given by:

$$\frac{d\alpha}{dt} = \sin\alpha\frac{\partial c}{\partial x} - \cos\alpha\frac{\partial c}{\partial z} + \cos\alpha\left(\sin\alpha\frac{\partial v_{0x}}{\partial x} - \cos\alpha\frac{\partial v_{0x}}{\partial z}\right) . \qquad (7.b)$$

This equation shows that the ray path is bended by the spatial derivatives of c and v_{ox}. Due to the bending of the rays a situation can occur where the reflected rays from the "skin" of a ray tube cross each other. This occurs in so-called caustics. Ray-tracing predicts infinite intensity at these points, which is certainly not correct. Ray theory is not valid here and needs to be corrected. The correction is obtained with a finite beam width around the caustic and a phase correction [2].

Physical scale model

The best way to test a computational model is to compare it with the real situation. However, under practical conditions it is often difficult to measure the important parameters as wind velocity and temperature. It may also be difficult to find a geometrical simple situation like an extended area with a flat ground that has the same impedance everywhere. For that reason it is sometimes advantageous to make a physical scale model where these parameters and the geometry are better under control. A physical scale model can also be used for geometrical situations that cannot easily be introduced in a calculation model.

4. IMPLEMENTATION OF THE PHYSICAL PHENOMENA IN THE MODELS

4.1 Screening

The effects of screening can be modeled as boundary conditions in the solution of the wave equation, or as reflecting and/or absorbing surfaces in ray models. Diffraction phenomena are rather complicated to account for in ray models. For complicated geometrical situations a physical scale model may be the best choice.

4.2 Air absorption

Because the models are based on the loss-free wave equation, air absorption is not included in the wave propagation models and in the ray model. However, the air absorption can easily be included because its effect is an attenuation expressed in dB/m. Its value depends on temperature, barometric pressure and humidity and it is frequency dependent. A calculation scheme to compute the air absorption is given by ISO Draft proposal 9613-1.

4.3 Ground absorption

The ground absorption is due to wave (or ray) reflections that take place on the ground surface due to the impedance contrast between the air and the ground. Much effort has been given to quantify its effect in different models. A fundamental quantity is the plane wave reflection coefficient, given by:

$$R_p = \frac{Z_b \cos\phi - Z_a \cos\phi}{Z_b \cos\phi + Z_a \cos\phi} \tag{8}$$

where ϕ is the angle between the wave front and the ground, Z_a is the specific acoustic impedance of air ($= \rho_0 c$) and Z_b is the specific acoustic impedance of the absorbing ground.
The ground impedance is strongly dependent on the surface layer. For open structure surfaces as for instance grass land, an adequate description is given by Delany and Bazley [3]. It is a function of frequency and of the flow resistivity σ.

In the wave extrapolation models, the ground impedance can be directly inserted as a boundary condition. This is most easily done in the wave number domain model, because here we are dealing with a plane wave decomposition. More difficulties are encountered in the ray model, which must rely on the reflection coefficients of the reflected rays. Direct application of the plane wave reflection coefficient is not allowed for frequencies below about 1000 Hz. In a homogeneous situation without wind the spherical reflection coefficient must be used as derived by Attenborough et al. [4]. In the *in*homogeneous case, where temperature and wind profiles are encountered, an exact solution is not known.

4.4 Wind and temperature profiles

An important effect of the meteorological processes that take place in the atmosphere near the ground is the occurrence of wind and temperature profiles. The wind leads to a direct convection of the medium that transports the acoustic energy, so the wave field itself is also transported. Hence, the wind has a *vectorial* influence on the wave field. The temperature changes have no direct influence on the wave propagation, but an indirect influence, because the sound velocity depends on the temperature. A good approximation is given by $c = 20\sqrt{T}$, with T the absolute temperature in Kelvin and c in m/s. Hence, the temperature has a *scalar* influence on the wave field. The effects of the wind and temperature profiles can be modeled with both the wave propagation models and the ray model. In the situation of a plane ground without any obstacles, it is a good approximation to assume only a horizontal wind and only vertical wind and temperature profiles (stratified medium). Under such conditions the equations are simplified considerably. It also means that the wave field extrapolation can be carried out in the wave number domain. An example is the wave field model of Nijs and Wapenaar [5]. In many ray-tracing models one also makes use of the assumption of a stratified medium. It is shown by Boone and Vermaas [2] that the ray-tracing equations can easily be solved numerically without making use of that property. The principle is illustrated in figure 2, showing how the wave front moves and bends under the influence of spatial variations in c and v. Using this approach, even vertical wind components can easily be included.

To obtain realistic values for the sound propagation under the influence of wind and temperature profiles, these quantities must be modeled in a realistic way [6, 7, 8].

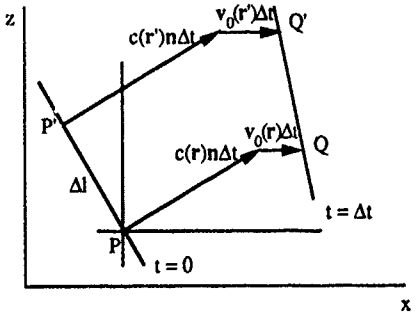

Figure 2: Ray-path and wave front construction in an inhomogeneous, moving medium.

4.5 Turbulence

The assumption of a stratified medium with wind- and temperature profiles that are independent of time is only partly valid. In reality the wind and temperature profiles may vary as a function of time. Besides that, the wind causes eddies of moving air and during day time there may be a vertical air flow in connection with thermal effects. Hence, the acoustic wave propagation takes place through a medium that contains irregularities in a spatial and in a temporal sense. These effects cannot directly be taken into account in the propagation models. Slow variations in the profile parameters can be studied by repeated modeling with changing of these parameters. The smaller irregularities, which also change as a function of time will have to be modeled in a statistical sense. The effects can be expressed in the longitudinal and transverse coherence loss of the medium [9]. The *longitudinal* coherence loss is important if a correlation procedure is used between a source and a receiver signal. Such coherence techniques strongly rely on the assumption of a time invariant linear transfer function of the medium. For noise control purposes this is of less importance. The *transverse* coherence loss is a measure for the decorrelation along a wave front or between two closely traveling rays. From this concept it can be understood that the interference dip of a direct and a reflected ray is less pronounced at larger distances. Such decorrelation effects can most easily be accounted for in a ray-tracing model.

5. RESULTS

At our laboratory, several modeling procedures have been studied for outdoor sound propagation. They have been presented by Boone and Vermaas [2] and Boone and Jabben [10]. The results of Boone and Jabben [10] are reproduced here to show a comparison between a physical scale model, the wave field extrapolation method of Nijs and Wapenaar [5] and the ray-tracing method of Boone and Vermaas [2]. The situation that was studied is a 1 : 100 scale model with a linear temperature profile above a hard ground surface. The ray patterns for a monopole source at x = 0 and z = 0.0223 m and a temperature profile of 84 K/m are shown in figure 3. Measurements and simulations were carried out for a receiver position at x = 2.32 m and z = 0.03 m and with different temperature profiles. Figure 4 shows the results for a temperature profile where the receiver is just in the shadow zone of the caustic. We see a good agreement between the wave field extrapolation model and the measurements but the ray-tracing gives results that are too low, because the diffracted field of the caustics is absent. Figure 5 shows the results for a temperature profile where the receiver is just behind the caustic. Now all three models agree very well.

We are presently involved in a study on the propagation of sound over large distances. In this study measurements are carried out outdoors which are compared with our calculation models. We are especially working on a realistic modeling of the temperature and wind profiles and the turbulence. Typical measured wind and temperature profiles are shown in figure 6. Notice the strong gradients in the region of 0 < z < 1 m. We found that our ray calculations are sometimes unstable due to these strong gradients, probably because of the finite difference approximations that are made. However, we must realize that for long wave

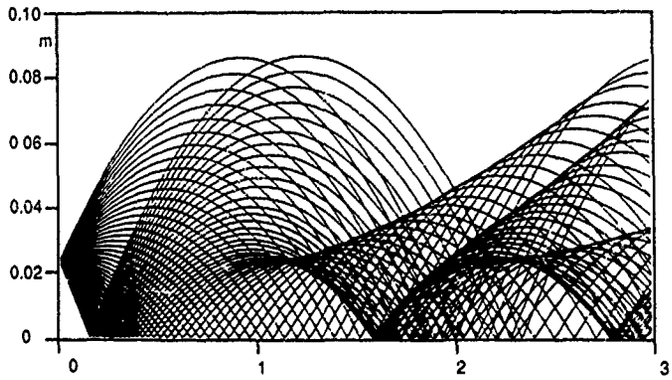

Figure 3: Ray-plot of the physical scale model measurements with $\partial T/\partial z$ = 84 K/m.

lengths the ray-tracing equations are not valid for such strong gradients. This can be understood by realizing that a spatial averaging takes place during the wave propagation, as shown in figure 1. This effect can be accounted for by applying a wave length dependent spatial low-pass filter over the gradients. At the congress our latest results on this study will be presented.

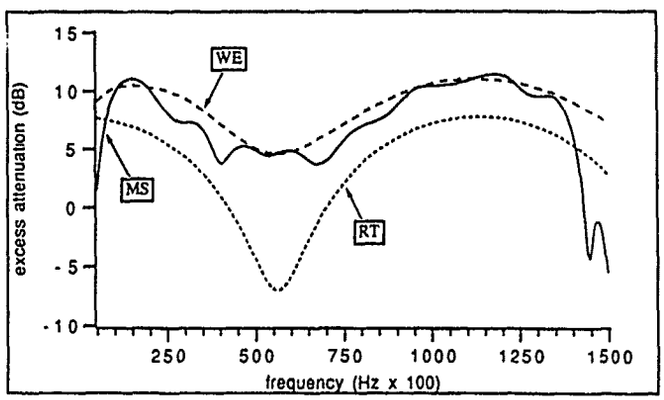

Figure 4: Source at (0,0.0223) and receiver at (2.32, 0.03). $\partial T/\partial z$ = 32 K/m.

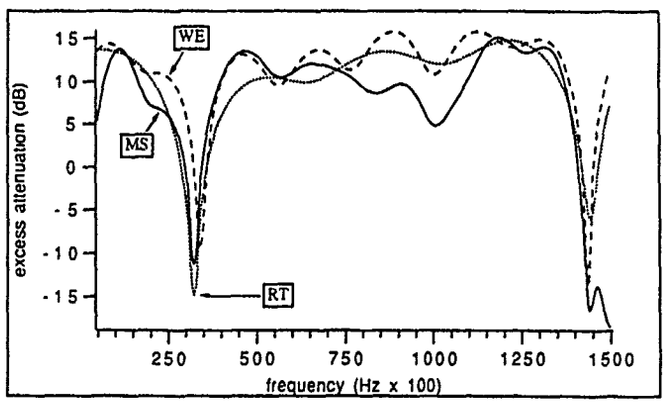

Figure 5: Source at (0,0.0223) and receiver at (2.32, 0.03). $\partial T/\partial z$ = 84 K/m.

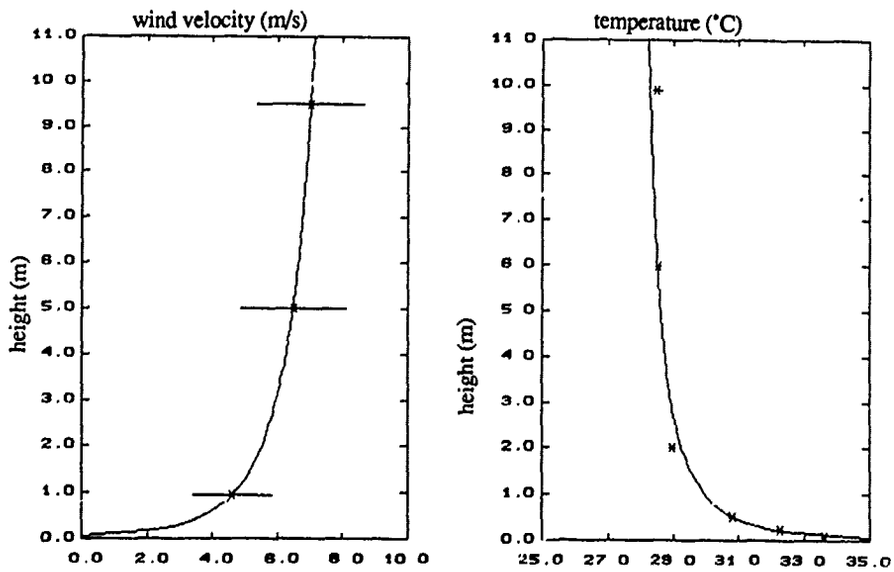

Figure 6: Typical measured wind and temperature profiles.

6. CONCLUSIONS

For the calculation of the outdoor sound propagation a choice has to be made between available numerical models. A compromise has to be found between complexity of the model and accuracy of the calculations. In those cases where the transfer function may be viewed as a time-invariant linear system caused by stratified temperature and wind profiles above a homogeneous plane ground surface, the wave field extrapolation model in the wave number domain is a good choice. This model works also good in shadow zones and caustics. In the case of complicated gradients and ground surfaces, ray-tracing is to be preferred, because the ray-tracing equations can easily be solved even under complicated circumstances. However, shadow zones cannot easily be handled and in caustic regions a special beam-tracing is required. For more complicated situations where also turbulence is involved, a modified beam-tracing algorithm is proposed.

7. ACKNOWLEDGEMENTS

Part of this work is carried out in cooperation with the Institute of Applied Physics, TUD-TNO.

8. REFERENCES

1. A.J. Berkhout, *Applied seismic wave theory,* Elsevier, Amsterdam, 1987.
2. M.M. Boone and E.A. Vermaas, "A new ray-tracing algorithm for arbitrary inhomogeneous and moving media, including caustics", J. Acoust. Soc. Amer. **90**, 2109–2117 (1991).
3. M.E. Delany and E.N. Bazley, "Acoustical Properties of Fibrous Absorbent Materials", Applied Acoustics, **3**, 105–116 (1970).
4. K. Attenborough, S.I. Hayek and J.M. Lawther, "Propagation of Sound above a Porous Half-space", J. Acoust. Soc. Amer. **68**, 1493–1501 (1980).
5. L. Nijs and C.P.A. Wapenaar, "The influence of wind and temperature gradients on sound propagation, calculated with the two-way wave equation", J. Acoust. Soc. Amer. **87**, 1987–1998 (1990).
6. R.E. Munn, *Descriptive micrometeorology,* Academic Press, New York/London, 1966.
7. F. Nieuwstadt, "The computation of the friction velocity u* and the temperature scale T* from temperature and wind velocity profiles by least-square methods", Boundary-Layer Meteorology, **14**, 235-246 (1978).
8. H. Klug, *Schallimpulse als Meßsunde zur Bestimmung meteorologischer Einflüsse auf die Schallausbreitung,* PhD. Thesis, Universität Oldenburg, Germany (1990).
9. M.M. Boone, *Design and development of a synthetic acoustic antenna for highly directional sound measurements,* PhD. Thesis, Delft University of Technology, 1987.
10. M.M. Boone and J. Jabben, "A physical scale model for sound propagation in an inhomogeneous medium with a plane boundary layer", Proc. InterNoise 90, Gothenburg, 317 – 320, (1990).

SECOND INTERNATIONAL CONGRESS ON
RECENT DEVELOPMENTS IN AIR- AND
STRUCTURE-BORNE SOUND AND VIBRATION
MARCH 4-6, 1992 AUBURN UNIVERSITY, USA

WEATHER EFFECTS ON SOUND PROPAGATION NEAR THE GROUND

Conny Larsson
Department of Meteorology
Uppsala University
Box 516, S-751 20 Uppsala
Sweden

ABSTRACT

The wind and temperature gradients cause refraction of the sound rays, and hence influence the sound level. The curvature of a nearly horizontal sound ray can be calculated by using measurements of wind and temperature. A method for estimating the curvature without profile measurements is given. An empirical connection between curvature and sound level has been determined. A way of examine if a specific set-up of source-receiver can be sensitive to the weather is presented.

INTRODUCTION

The understanding of sound propagation outdoors has increased during the past decades [1,2]. Today there exist different types of prediction schemes and propagation models for planning purposes. They are often restricted to certain meteorological conditions, e.g. 'moderate downwind', and do not take the local climate into consideration. How common these conditions are for an actual site is not taken into consideration. The predicted quantity is often a single value, e.g. the long-term average sound level, and gives no information about the highest noise levels and how often they occur.

The cumulative distribution ought to be a more useful tool for users. It contains more information needed for decision-making, e.g. the fraction of time a certain noise level is exceeded, or what noise level is exceeded, e.g. the worst 5 % of the time. The mean or the median sound level gives no information about the upper and lower tail of the distribution. Two distributions with different highest levels can have the same mean value.

They only way to obtain the distribution, without expensive long-time sound level measurements, is to include the effects of the weather and the climate for an area.

Since 1976, investigations concerning meteorological effects on sound propagation have been carried out at the Department of Meteorology at the Uppsala University. A number of experimental [3,4,5,6,7] and theoretical studies [8,9] have been performed. It was found that the meteorological effects were noticeable at a distance of 25 m from the source and increased with decreasing receiver height.

METEOROLOGICAL EFFECTS ON SOUND PROPAGATION

The three most significant meteorological effects on sound propagation are: *refraction, atmospheric absorption* and *scattering by turbulence.*

Refraction of sound rays occurs if the sound velocity and/or the wind speed change along the ray path, i.e. there are gradients of wind and temperature. The wind and temperature fields are horizontally homogeneous

in reasonably flat terrain. Thus wind speed and temperature depend on elevation (z) only. They are dependent on each other through the governing hydrodynamic equations. The refraction influences the sound level. The angle of incidence at the ground is changed, which results in varying ground attenuation with the radius of curvature, see Eq. (1). In downwind conditions and/or temperature inversion the sound rays are bent downwards, and in upwind conditions and/or lapse they are bent upwards. Upwind conditions and/or lapse create areas which no direct sound ray can reach, known as sound shadow zones. The refractive effects of the gradients of the temperature and the component of the wind in the direction of propagation are additive. A suitable parameter for characterizing the refraction is the curvature of near-horizontal sound rays, 1/R [10].

$$\frac{1}{R} = \frac{\frac{10}{\sqrt{T}}\frac{\partial T}{\partial z} + \frac{\partial u}{\partial z}}{c\left(1 + \frac{u}{c}\right)^2} \qquad (1)$$

where R is the radius of curvature (m), T is the temperature (K), c is the sound velocity (m/s) and u is the component of the wind vector (m/s) in the direction of the ray. To get values around unity for the curvature we introduce k:

$$k = 1/R\ 10^3 \qquad (2)$$

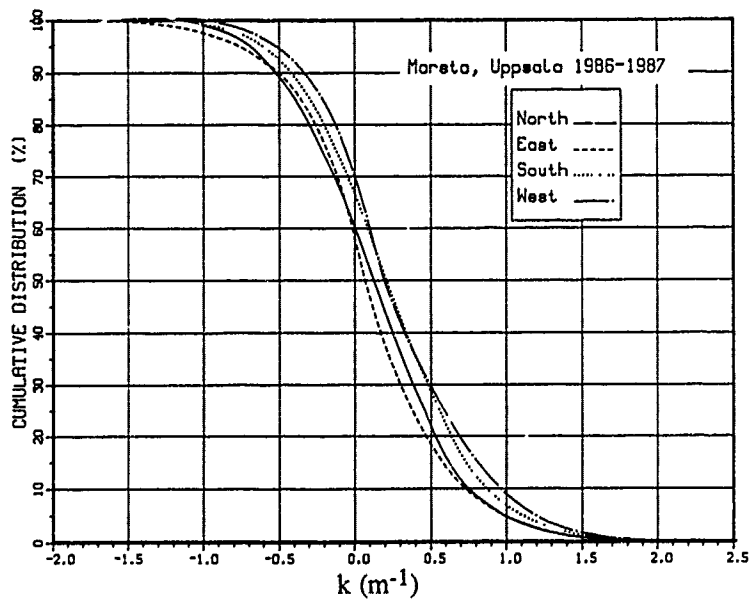

Figure 1. The cumulative distribution of the curvature for a source located north, east, south and west of the receiver, respectively.

All the parameters in Eq. (1) are functions of z. The largest variations of the curvature take place near the ground, where the gradients are steepest. To choose a representative height interval in order to determine the gradients is not easy. It is possible to calculate a mean value of the curvature in a layer where sound propagates but the layer will change with weather conditions and source and receiver heights. A simpler and more practical approach [3] is to use finite differences for the gradients, and hence obtain a k-value which, in some sense, is an average value. The heights 0.5 and 10.0 m seems to give values close to mean values determined from ray tracing. The lowest height is chosen close to the ground and 10 m is the meteorological standard height for wind speed measurements. Using the measuring heights 0.5 and 10 m Eqs. 1 and 2 can be simplified as

$$k \approx (0.6\,\Delta T + \Delta u)/3.2 \qquad (3)$$

where ΔT is the temperature difference in K or °C, and Δu is the wind component difference in m/s. Finite differences between 0.5 and 10 m have been used. The parameter could be used as an external parameter describing the sound propagation conditions. In studies of sound propagation up to 1 km [11,12] it was shown that the variations of the sound level under various meteorological conditions depend mainly on the influence of refraction on the ground effect. Comparisons with other investigations [13,14] were made [5] and qualitative agreement was found.

The distribution of k must be determined for different locations. Figure 1 display the curvature, k, from Marsta in Uppsala, Sweden during 1986 and 1987. Maintenance and instrumental errors reduced the data set to cover 97.8 % of the period.

Looking at the curvature that was exceeded for 5 % of the time, we conclude that the highest curvature is found for the source location west of the receiver. This is not surprising since the wind direction distribution for Marsta has a maximum around the south-west and a minimum around the east. In general, an increasing curvature means an increasing sound level, and thus this location will also give the highest sound levels. The best location for a source near Marsta must be in the sector between north and east. Very small differences between the curves are found for the highest curvatures, i.e. cases when the temperature stratification dominates over the wind stratification in Eq. (1), viz. mostly temperature inversions with low wind speed.

A cumulative plot of the curvature can be used for general planning purposes, since the sound level usually increases with increasing curvature. This is less costly and time-consuming than calculation of the sound level, in which case empirical or model results relating the sound level to the curvature must be used.

The *atmospheric absorption* depends on frequency, relative humidity, temperature and atmospheric pressure. The sound attenuation due to the absorption can be calculated [15].

Turbulence has a two-fold effect on sound propagation. First, the temperature fluctuations lead to fluctuations in the velocity of sound. Secondly, turbulence velocity fluctuations produce additional random distortions of the sound wavefront. Turbulence scatters sound into sound shadow zones and causes fluctuations of the phase and the amplitude of the sound waves, thus destroying the interference between different rays reaching the receiver. This gives higher sound levels than expected for frequencies where the ground effect has its maximum. The effect of turbulence can be disregarded for low frequencies and distances up to a few hundred meters.

VARIATIONS OF SOUND PROPAGATION CONDITIONS DURING A DAY WITH A SMALL AMOUNT OF CLOUDS

Wind and temperature profiles cause variations in the sound level especially during parts of a day with a small amount of clouds.

An example taken from such a day is given in Figs. 2-4. Acoustic and meteorological measurements were carried out at the Marsta Meteorological Observatory (59°55'N, 17°35'E Gr), which belongs to the Department of Meteorology of the Uppsala University. The site is a typical agricultural area with few obstacles. The area around the observatory is very flat, the level differing by few meters over the nearest km^2.

An anticyclone, centered over Scandinavia, gave fair weather at Marsta on 25 June 1986. The temperature and wind speed at 0.5, 1.5, 4.0, 9.8 and 17.6 m are given in Figs 2 and 3. The temperature roughly describes a sine curve, the minimum occurring around sunrise, and the maximum in the afternoon. Sunrise and sunset are indicated by vertical arrows. The wind direction is given at the top of the Figure. The temperature increases with height during the night (inversion) and decreases with height during the day (lapse) as a result of the balance between the incoming the outgoing radiation.

Wind speed normally increases with height above the ground. A diurnal wave of wind speed close to the ground was found even though the driving force, the large-scale pressure gradient, was constant. The temperature distribution, given in Fig. 2, influenced the wind speed distribution in Fig. 3, and the maximum wind speed was found in the afternoon. The stalling speed of the anemometers was around 0.5 m s^{-1}, influenced the wind speed values and gave some incorrect mean values during the night.

The described daily pattern of temperature and wind speed is very often masked by weather systems of different scales. The amount of incoming and outgoing radiation decreases with an increasing amount of clouds, resulting in smaller temperature gradients. The influence from wind fields associated with cyclones or land- and

sea-breeze circulations were usually much greater than the daily pattern described in Figs. 2 and 3.

In Fig. 4, examples from the results of the acoustic measurements during the day and the evening are presented. The distance was 100 m the source height was 1.4 m and the receiver height 1.25 m. The levels were corrected for atmospheric absorption using the standard ANSI band method.[15] The ground along the line-of-sight from the source to the receiver was covered with 5-10 cm high grass, over the nearest 50 m to the source, and the rest consisted of 40 cm high crops. The loudspeaker was directed towards 251°, nearly WSW, and the wind direction was from 256° and 185°, respectively, for the cases displayed in Fig. 4. Numerical ray tracing[5] was carried out for these periods to illustrate the propagation conditions. The temperature decrease with height, together with the light upwind, created a sound shadow during the period between 10^{15} and 10^{20}. The temperature increase with height during the evening made it possible for many sound rays to reach the receiver.

The sound level for the 500-4000 Hz octave bands showed increased sound pressure values between 10 and 20 dB. It did not change considerably in the lower octave bands. From this and other measurements, we conclude that the weather conditions influence the sound propagation close to ground mostly in octave bands from 500 Hz and higher. The variations during a day within an octave band were up to 20 dB.

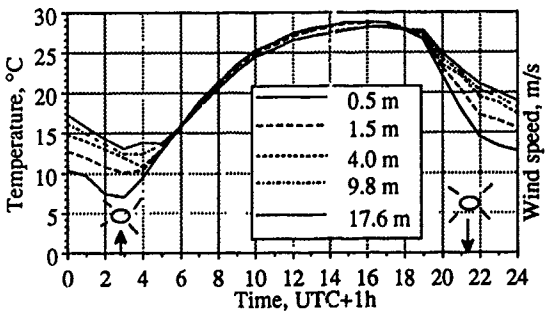

Figure 2. Temperature distribution near the ground.

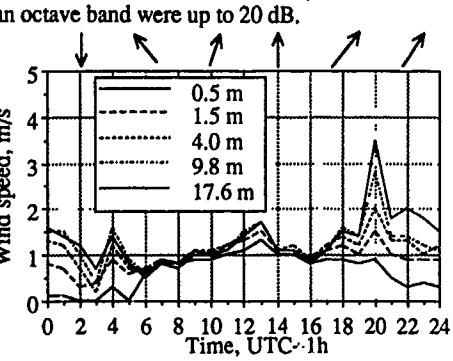

Figure 3. Wind distribution near the ground

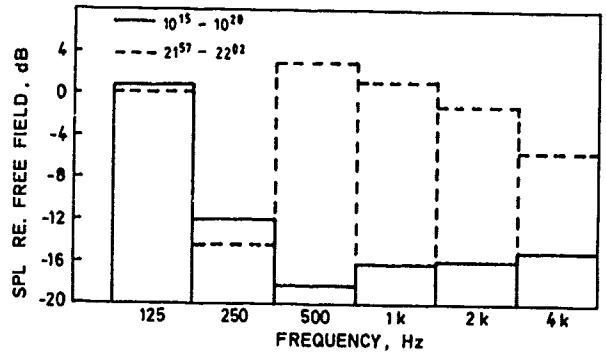

Figure 4. Examples of sound spectra during the day and the evening of 25. June 1986. Distance 100 m, source height 1.4 m; receiver height 1.25 m.

THE EMPIRICAL CONNECTION BETWEEN CURVATURE AND SOUND LEVEL

Results from simultaneous acoustic and meteorological measurements at the Department of Meteorology describes the empirical connection between curvature and sound level.[16,17]

The normalized sound level, level relative free field and corrected for the atmospheric absorption[15], and the curvature from Eq. (3) were computed

The sound levels are, for most octave bands, lowest for negative curvatures, i.e. when the rays were bent up from the ground and creating sound shadow, and highest for positive curvatures, see Fig. 5 where results from measurements at a distance 100 m from a source at 1.4 m and a receiver at 1.25 m are displayed. Such an empirical connection between sound level and refraction was shown earlier [3-5] and has also been used in a

method[18] for calculation of the conditions for sound propagation close to the ground. The regression coefficients varied between 0.89 and 0.94 for the curves in Fig. 5.

A straight line is the best fit for the 500 Hz octave band. The larger curvature the higher sound level is found. The other octave bands display a more wave-formed curve with a highest sound level for a specific value of k followed by a decrease in the sound level for higher curvatures.

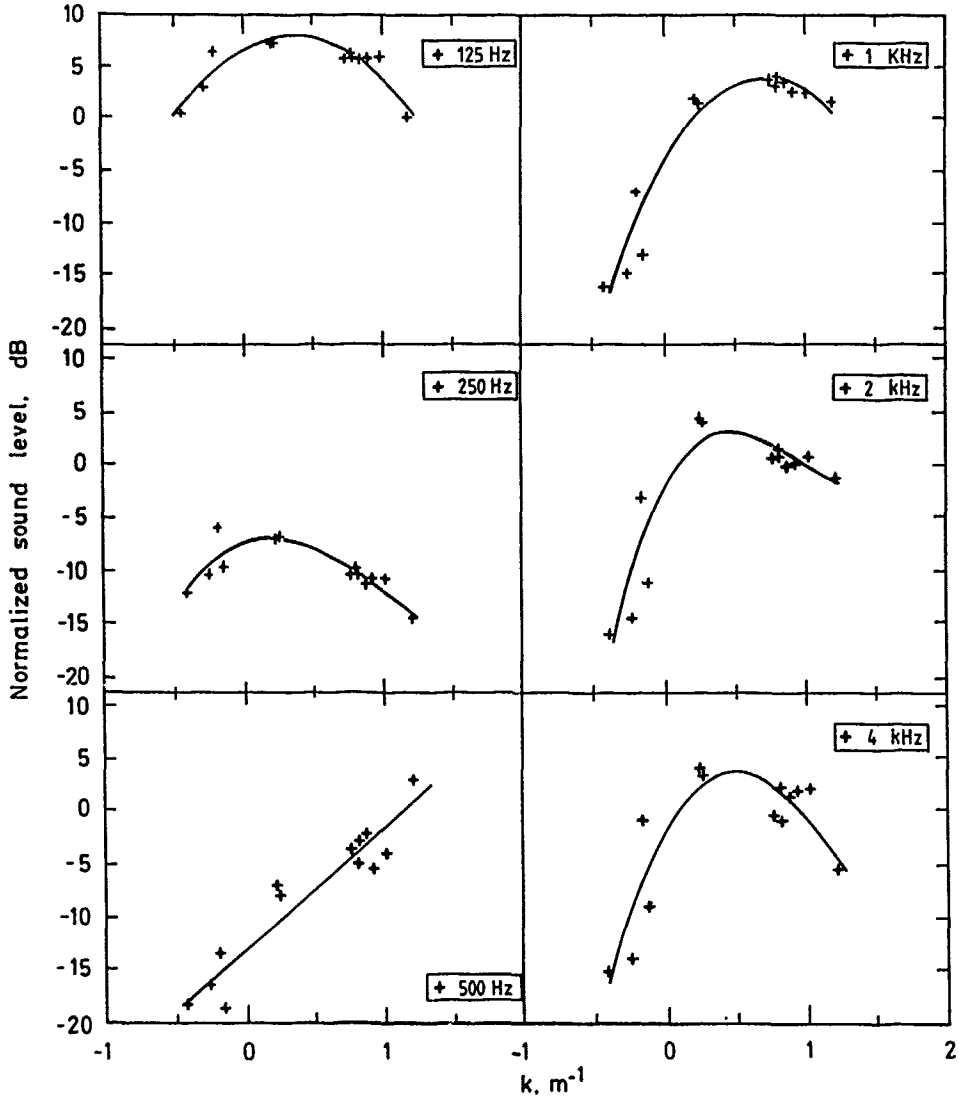

Figure 5. Sound pressure level relative free field, corrected for atmospheric absorption, versus k. Cultivated ground. Distance source-receiver 100 m; Source height: 1.4 m; receiver height: 1.25 m.

Some conclusions from all measurements carried out at the site can be drawn:

1. The highest sound level is found when source and receiver are close to ground and at a distance between 75 - 150 m. For larger distances too many sound rays propagate from source to receiver destroying maximum interference
2. There are a tendency for many of the curves that the maximum decreases and moves to lower k-values when the distance, source and receiver heights are increased. The reason for this is not completely

understood, but must have something to do with the most favorably combination of temperature and wind gradients giving a maximal focussing together with ground attenuation.

3. Measurement results for different distances, ground types, source and receiver heights are given in a supplement [17]

Estimation of curvature without profile measurements

A brief description of a method[19] for determination of the curvature, for nearly horizontal sound rays close to is be given here:

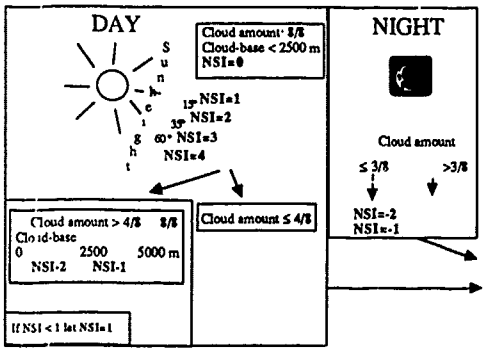

Wind speed, m/s	4	3	2	1	0	-1	-2	NSI
	Δt, °C 10-0.5 m							
< 0,8	-2.5	-2.5	-1 3	-0 2	-0 1	1 0	4 1	
0,8 - 1,8	-2.5	-1 3	-1 3	-0.2	-0 1	1 0	4 1	
1,9 - 2,8	2 5	-1.3	-1.3	-0.2	-0 1	1 0	4 1	
2,9 - 3,3	-1 3	-1.3	-0.2	-0 1	-0 1	0 0	1 0	
3,4 - 3,9	-1.3	-1.3	-0 2	-0 1	-0 1	-0.1	0 0	
4,0 - 4,9	-1 3	-0 2	-0 2	-0 1	-0 1	-0 1	0 0	
5,(5,4	-0 2	-0 2	-0 1	-0 1	-0.1	-0.1	0 0	
5,5 - 5,9	-0 2	-0 2	-0 1	-0 1	-0.1	-0 1	0 1	
> 5,9	-0 2	-0 1	-0 1	-0 1	-0 1	-0 1	0 1	

Figure 6. Scheme for estimation of Δt by use of sun-height, cloud amount and wind speed at 10 m.

The wind and temperature profiles are interrelated with each other. Neglecting the change in the wind profile due to the temperature profile we can calculate the wind speed, v, at the height z:

$$v(z)=\frac{u_*}{\kappa}\ln\frac{z}{z_0} \qquad (4)$$

where κ is von Kármán's constant ≈ 0.4 and the friction velocity u_*:

$$u_*=\frac{\kappa\, v(z_m)}{\ln\frac{z_m}{z_0}} \qquad (5)$$

is determined from wind speed measurements at the height z_m and z_0 is the roughness length, see Table 1.

Table 1. Values of z_0, m, for different type of terrain.

Forests	≈ 0.8
Fairly level wooded country	≈ 0.4
Farmland	between 0.02 and 0.1
Fairly level grass plains	between 0.007 and 0.02
Desert (flat)	≈ 0.0005

The wind speed difference between 10 and 0.5 m, Δv is given by:

$$\Delta v = v(10) - v(0.5) = \frac{u_*}{\kappa}\left(\ln\frac{10}{z_0} - \ln\frac{0.5}{z_0}\right) \qquad (6)$$

Δu in Eq. (3) can be calculated by measuring the angle, ϕ, between wind direction and the line source-receiver and using:

$$\Delta u = \Delta v \cos(\phi) \qquad (7)$$

Δt is taken from the scheme in Fig. 6. Equation 4 can be used when wind speed measurement not was taken at 10 m height. The method, described above, seems to work best for $k > 0$. The maximum errors in determining k from 50 observations during a two-year period were < 0.3 for $k > 0$ and < 0.5 for $k < 0$.

A way of testing the weather sensitivity for a specific source-receiver setup.

A disadvantage with using the empirical connection between sound level and curvature is that different regression constants depending on ground, distance, source and receiver heights has to be used.

A way of testing if a specific set-up can be sensitive to meteorological conditions is by using the sound propagation parameter, W:

$$W = \frac{k\,(z_s + z_r)^2}{d} \qquad (8)$$

The sound propagation parameter includes the weather sensitive parameter (k), see Eq 2, source and receiver heights (z_S, z_r) and distance (d). The sum of source and receiver heights are squared to make W dimensionless and stress the fact that the meteorological effects are larger close to the ground.

The sound propagation parameter, W, describes in a way the sound propagation conditions for a specific source-receiver set-up. The only distinction necessary for this parameter is ground condition and octave band.

Results with use of the sound propagation parameter, W are shown in t Fig. 7 for cultivated ground. The results show a great scattering of the data, especially close to W=0. Outside the interval $W = \pm 0.1$ the spread is less and we obtain more or less the same sound level for greater or smaller W. For many octave bands the levels for positive and negative values of W seems to be the same.

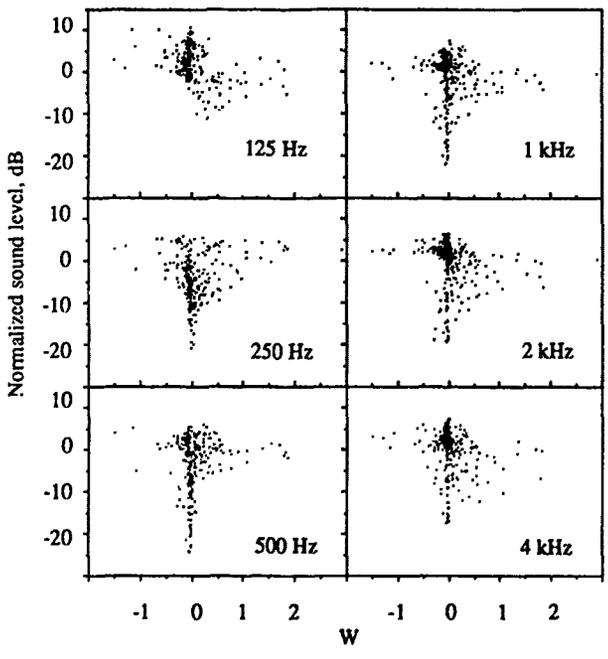

Figure 7. Sound pressure relative free field, corrected for atmospheric absorption, versus the sound propagation parameter, W. Cultivated ground.

CONCLUSIONS

The wind and temperature gradients cause refraction of the sound rays, and hence influence the sound level. The curvature seemed to be a suitable parameter describing the sound propagation conditions. A number of curves, showing the connection between sound level and curvature, showed very good correlation with the measurements. The curvature can be calculated by using measurements of wind and temperature or be estimated from observations of clouds and wind measurement from one height.

A new sound propagation parameter, W, which includes distance, source and receiver height were suggested to evaluate if a specific set-up can be sensitive to the meteorological condition.

ACKNOWLEDGEMENTS

This study was financially supported by the Swedish Environmental Protection Agency.

REFERENCES

1 Delany, M. E., Sound propagation in the atmosphere: a historical review. *Acustica*, **38** (1977), pp. 201-23.

2 Piercy, J. E., Embleton, T. F. W. & Sutherland, L. C., Review of noise propagation in the atmosphere. *J. Acoust. Soc. Am.*,**61**(6) (1977), pp. 1403-18.

3 Larsson, C. and Israelsson, S.: The influence of the meteorological parameters on the sound propagation from a traffic road. *Inter-Noise 79*, Warszawa, Poland (1979), pp. 513-516.

4 Larsson, C. and Israelsson, S.: The effects of meteorological parameters on sound propagation from a point source. *Report No. 67, Dept. of Meteorology, Uppsala* (1982).

5 Hallberg, B., Larsson, C. and Israelsson, S.: Measurements of meteorological effects on long-range sound propagation using m-sequence correlation. *J. Acoust. Soc. Am.* 78(3) (1985), pp. 1038-1044.

6 Larsson, C. and Hallberg, B.: Sound propagation over ground with a barrier - some meteorological effects. *Proceedings Inter-Noise 83*, Edinburgh, Great Britain (1983), pp. 271-274.

7 Larsson, C., Hallberg, B. and Israelsson, S.: Long-term audible noise and radio noise performance from an operating 400-kV transmission line. *IEEE. Transactions on Power Delivery*, Vol. 3, No 4 (1988), pp. 1842-1846.

8 Hallberg, B., Larsson, C. och Israelsson, S.: A numerical ray tracing model for sound propagation. *Department of Meteorology, Uppsala* (1988) (in Swedish).

9 Hallberg, B., Larsson, C. och Israelsson, S.: Numerical ray tracing in the atmospheric surface layer. *J. Acoust. Soc. Am.* **83(6)** (1988), pp. 2059-2068.

10 B. Gutenberg, "Propagation of sound waves in the atmosphere, *J. Acoust. Soc. Am.* **13** (1942), pp. 151-155.

11 Larsson, C.: Effects of meteorological parameters on sound propagation. Acta Universitatis Upsaliensis, *Abstracts of Uppsala Dissertations from the Faculty of Science*, 714 (1984).

12 Hallberg, B.: Meteorological effects on sound propagation near the ground. Acta Universitatis Upsaliensis, *Comprehensive Summaries of Uppsala Dissertations from the Faculty of Science*, 76 (1987).

13 Parkin, P. H. and Scholes, W. E.: The horizontal propagation of sound from a jet engine close to the ground, at Hatfield. *J. Sound. Vib.* **2**, (1965), pp. 353-374.

14 Sutherland, L. C. and Brown, R.: Static test of excess ground attenuation at Wallops Flight Center. *NASA Contractor Report 3435, Wyle Research, El Segundo, CA* (1981).

15 ASA, ANSI, Method for the calculation of the absorption of sound by the atmosphere. *ANSI S1.26 (ASA 23-1978)*, (1978).

16 Larsson, C. and Israelsson, S. (1991): Effects of meteorological conditions and source height on sound propagation near the ground. *Applied Acoustics* **33**, pp 109-121.

17 Larsson, C. and Israelsson, S.: Supplement to "Effects of meteorological conditions and source height on sound propagation near the ground". *Department of Meteorology, Uppsala* (1989).

18 Larsson, C., Hallberg, B. and Israelsson, S.: A method to estimate meteorological effects on sound propagation near the ground. *Applied Acoustics* **25**, pp. 17-31 (1988).

19 Larsson, C: Estimation of sound ray curvature close to the ground. *Department of Meteorology, Uppsala* (1991) (in Swedish).

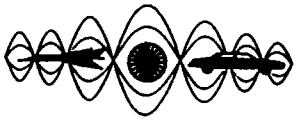

SECOND INTERNATIONAL CONGRESS ON
RECENT DEVELOPMENTS IN AIR- AND
STRUCTURE-BORNE SOUND AND VIBRATION
MARCH 4-6, 1992 AUBURN UNIVERSITY, USA

PROPAGATION OF SOUND THROUGH THE FLUCTUATING ATMOSPHERE

D. Keith Wilson
Graduate Program in Acoustics and Department of Meteorology
Pennsylvania State University
University Park, PA 16802

ABSTRACT

The emphasis of this talk will be on line-of-sight propagation through the turbulent atmospheric boundary layer. Among the topics discussed are: (1) New computational tools, such as parabolic equation propagation models and large-eddy simulations, which show promise for modelling the effects of constantly-changing atmospheric structure on acoustic signals. (2) Useful analytic and graphical tools for describing signal variability, including wavefunction phasor diagrams and chaotic attractor reconstructions. (3) Recently completed concurrent measurements of atmospherically-propagated sound and turbulence structure which indicate that the spatial scale of the fluctuations that drive acoustic signals is larger, by about two orders of magnitude, than previously had been thought. (4) Acoustic tomographic methods for reconstructing atmospheric turbulence fields.

INTRODUCTION

The title of this paper resembles, quite intentially, the title of the 1979 monograph by Flatté *et al.*, *Sound Transmission through a Fluctuating Ocean* [1]. That book is representative of a changed perception of propagation through the ocean: no longer can the acoustician solely focus his/her efforts on propagation physics; a firm understanding of the spatial and temporal structure of the propagation medium is also required.

Recent research in atmospheric acoustics also emphasizes realistic characterization of the propagation medium. This new focus, combined with progress in atmospheric measurement technology, atmospheric similarity scaling, and numerical propagation modelling, is creating many new and exciting research topics in atmospheric acoustics.

NUMERICAL PROPAGATION MODELLING

Numerical modelling of sound propagation through the atmosphere has progressed quickly during the past decade. For example, Raspet *et al.* [2] developed the Fast Field Program (FFP) for the atmosphere in 1985. This technique was originally developed by DiNapoli and Deavenport [3] for oceanic propagation in 1980. In the FFP, the solution is assumed to have cylindrical symmetry; i.e., the environment is assumed to be horizontally homogeneous. By approximating an inverse Hankel transform integral with a Fast Fourier Transform (FFT), the FFP computes fields with great efficiency for distances greater than a few wavelengths from the source. Refinements of the FFP for atmospheric propagation are also discussed by Lee *et al.* [4], Franke *et al.* [5] and Wilson [6].

Of course, the atmosphere, due to turbulence and ground surface inhomogeneities, is not horizontally stratified. But we still may ask whether there are circumstances when the FFP can provide useful information. For example, suppose one wishes to model propagation over approximately flat terrain. Can knowledge of the *mean* vertical profiles of wind and temperature be used to predict the spatial dependence

of the *mean acoustic field*? Because the two are nonlinearly related, this is not generally true. Recent research has provided tentative answers to this question [7,8,9]. It appears that appplication of the FFP should be limited to cases where there is only weak turbulence, and the receiver is not in a shadow zone (i.e., not reached by any geometric rays). This is because the primary mechanism by which acoustic energy reaches a receiver in a shadow zone appears to be turbulent scattering, as opposed to diffraction. The FFP cannot model the scattered component of the acoustic field.

More recently, Gilbert and White [10] applied parabolic equation (PE) methods to the atmosphere. Development of the PE for ocean acoustics goes back to Tappert [11]. PE calculations are somewhat slower than the FFP, but have the important advantage of being applicable to non-horizontally-stratified environments. This fact enabled Gilbert and Raspet [7] to model propagation through atmospheric turbulence.

It should be pointed out that neither the FFP nor the PE correctly models refraction by wind gradients. They are strictly applicable only to refraction by sound speed (temperature or humidity) gradients. In order to correctly model refraction by wind gradients, it is still necessary to resort to ray-tracing methods, which are strictly valid only at high frequency. Incorporation of wind velocity fields into ray tracing is discussed by Hallberg [12] and Pierce [13].

The new numerical propagation models promise to further understanding of atmospheric sound propagation, and improve methods for predicting environmental noise. But without adequate methods for characterizing the propagation medium, the atmosphere, even the best propagation models will yield poor results. Modelling of the atmosphere is the topic of the next section.

ATMOSPHERIC SIMILARITY SCALING AND PROFILE SHAPE

Meteorological models for the surface-layer profiles of wind and temperature have existed for some time. (The surface layer is typically 10–100 m high on a clear day.) The most successful models use similarity scaling techniques, based on threee significant parameters: the surface Reynold's stress τ, the surface heat flux Q, and the buoyancy $\beta = g/\theta_s$, where g is gravitational acceleration, and θ_s is the surface temperature. From these parameters, representative scales for velocity, temperature, and length can be developed. One choice for the velocity scale, called the *friction velocity*, is $u_* = \sqrt{\tau/\rho}$. The *surface-layer temperature scale* is proportional to the surface heat flux: $T_* = -Q/u_*$. The surface-layer length scale, usually called the *Monin-Obukhov length*, is $L_{mo} = -u_*^3/\beta Q$. This length scale represents the ratio of mechanical to buoyant forces. Monin and Obukhov [14] suggested that the statistics of the atmospheric surface layer, when properly normalized by u_*, T_*, and z, could be written as universal functions of a normalized height $\zeta = z/L_{mo}$. The mean wind and temperature gradients are, in normalized form,

$$\frac{\partial u}{\partial z} = \frac{u_*}{\kappa z}\phi_M(\zeta), \tag{1}$$

$$\frac{\partial T}{\partial z} = -\gamma_d + \frac{T_*}{\kappa z}\phi_H(\zeta), \tag{2}$$

respectively, where ϕ_M is the surface-layer momentum function, and ϕ_H is the surface-layer heat flux function. Over the past few decades, much experimental effort has been expended to determine empirical forms for the ϕ-functions. By far the most commonly used forms are due to Businger *et al.* [15] and Dyer [16]. These relationships (the reader is referred to Panofsky [17] for their explicit forms) have been used in acoustical applications, by Klug [18] and Wilson [8], among others. It is also possible to scale higher order statistics, such as variances, using the above scales.

Figure 1 shows mean wind and temperature profiles calculated using the Businger-Dyer equations, for conditions typical of a clear, sunny day. Also shown is the effective sound speed profile, defined as $c_{eff} = u\cos\alpha + 20\sqrt{\theta}$, where u is the wind speed, α is the angle between the propagation path and the mean wind, and θ is the temperature in Kelvin. In the downwind direction, the mean profile structure creates a waveguide with multipath acoustic arrivals. This is shown in Fig. 2, for a source and receiver separated by 200 m. The effect that changing the height of the transducers has on the ray turning height (the maximum height attained by the ray) is depicted. The numbering system used to identify the ray paths has the form "$N\pm$", where N indicates the number of turning points, and the postscript sign $\pm$ indicates the number of ground reflections. A "+" postscript means that the ray has one more ground reflection than turning points; a "−" means that the ray has one less ground reflection than turning points. The absence of a postscript indicates that the number of turning points and ground reflections are the same.

Large-scale turbulence, such as wind gusts, will of course cause the profile shapes to fluctuate about the mean. As a result, the number of ray paths reaching a stationary receiver can vary. Figure 3 shows some

experimental results which may exhibit this effect. In the experiment, a source and receiver were placed on 6 m towers, separated by a distance of about 200 m. The source transmitted a signal in the band 400–1000 Hz, with duration 0.1 s. Displayed is the cross correlation of the transmitted and received signals, at 30 s intervals. In the first record, there appears to be two ray paths: a direct one (1−), arriving first; and a ground reflected (0+), which has a lesser intensity due to absorption by the ground. The second record suggests the presence of more than one ground-reflected path. The third record has a structure similar to the first. In the fourth record, however, only one path (probably 1−) is evident. We observe that the refractive characteristics of the atmosphere can change significantly on scales as short as 1 min.

IMPORTANCE OF LARGE EDDIES

While the discussion in the previous section addressed the mean structure of the atmosphere, it also demonstrated the significance of fluctuations. Theoretical and experimental characterization of sound propagation through atmospheric turbulence has been an area of much recent activity [19]–[24].

Wavefunction phasor diagrams are a particularly fundamental graphical depiction of scattering [1]. These figures display samples of the wavefunction phasor, defined as $\psi = p/\langle p \rangle$, where p is the complex acoustic pressure, and the angle brackets represent the mean. Inspection of a wavefunction phasor diagram allows one to immediately characterize the propagation regime based on the relative importance of the phase and amplitude variances. In the *geometric acoustics* regime, the spatial scale of the turbulence ℓ is much greater than the wavelength, so that a deterministic ray paths continues to exist as coherent entity. Hence phase variance dominates. In the *Rytov extension* regime, the wavelength is larger than the turbulence scale, so that amplitude and phase variance are both evident. In *full saturation*, strong turbulent fluctuations cause deterministic raypaths to split into a number of micropaths, separated by distances on the order of ℓ. The statistics are incoherent. Dashen [25] has also identified a *partial saturation* regime, where the micropaths exist separated by distances smaller than ℓ. The statistics of the amplitude and phase fluctuations, as well as the boundaries between the regimes, can be described in terms of a strength parameter Φ and a diffraction parameter Λ [1]. Figure 4 shows numerically-simulated wavefunction phasor diagrams for the various fixed values of Φ and Λ.

Surprisingly, researchers have not yet been able to predict the regimes characteristic of acoustic propagation in the surface layer. For example, Fig. 5 compares simulated wavefunction phasor samples with results from an experiment performed by Bass *et al.* [23]. The simulation made use of Bass *et al.*'s experimentally-determined meteorological parameters, including their values of $\ell = 15$ m and index-of-refraction variance 1.6×10^{-6}. The acoustic frequency was 62.5 Hz, and the propagation path length was 91 m. These values lead to $\Phi = 0.15$ and $\Lambda = 0.71$. Note that the simulated wavefunction samples are characteristic of the geometric acoustics regime. However, comparison with Fig. 5(a) in Bass *et al.* reveals that the measured wavefunction samples were characteristic of the Rytov regime. Phase fluctuations in the experimental data were roughly twice as strong as the simulation, while the amplitude fluctuations were stronger by an order of magnitude. There is a difficulty here in reconciling theory and experiment: stronger phase fluctuations would result from using a larger ℓ, whereas stronger amplitude fluctuations would result from using a smaller ℓ. Hence the value of ℓ alone cannot be adjusted to agree with the data. Similar discrepencies occured with independent measurements made by this author [26].

Before attempting to explain the actual cause of this discrepency, let us first consider the question of what we should expect a realistic length scale for atmospheric turbulence to be. It turns out that there is drastic disagreement between the acoustics and atmospheric science communities on this matter. Most previous researchers in the acoustics community have suggested that the most significant eddies are isotropic, and have dimension on the order of the height from the ground, z. (This would be 1–10 m for most problems of interest.) It is well known to atmospheric scientists, however, that on a clear day the most energetic eddies will have dimensions approaching the boundary-layer thickness (100–1000 m), z_i.

Wilson [26] provides an extensive literature review of the meteorological literature on this matter, coming to the conclusion that both the scales z and z_i are relevant in determining turbulence scales near the ground. Measurements of horizontal length scales a few meters off the ground are typically on the order 100 m during the daytime, significantly larger than Bass *et al.*'s measurement. Although one may expect vortex stretching to make lengthen the eddies in the direction of the wind, that process alone cannot explain why the horizontal length scale is so much greater than z near the ground. Large, boundary-layer size eddies must play a significant role, even very near the ground.

Atmospheric turbulence can be generated either by shear or buoyancy instabilities. Højstrup [27,28] has suggested that the actual turbulence spectrum consists of two components, a low-frequency spectrum due to buoyant instabilities and the resultant large-eddy field, and a high-frequency spectrum due to shear instabilities.

The former scales with z_i; the latter with z. An implication of this hypothesis is that the integral length scale also consists of a sum of low- and high-frequency parts (denoted here by "L" and "H," respectively):

$$\ell = \frac{1}{\sigma_L^2 + \sigma_H^2}(\sigma_L^2 \ell_L + \sigma_H^2 \ell_H), \tag{3}$$

where σ^2 is the total variance, $\ell_L \sim z_i$, and $\ell_H \sim z$.

Most of the previous acoustical literature [20,22,23,24] has focused on the importance of the high-frequency structure. However, some authors have suggested the importance of boundary-layer-scale turbulence in acoustic propagation [32,33,34,26]. If boundary-layer size eddies indeed play a significant role, the implications for propagation modelling are fundamental. Since the large eddies tend to have their center at the middle of the boundary layer, assumptions of homogeneity in eddy field become invalid. The effect of the ground on the eddy field cannot be neglected. These considerations led Wilson to develop a new model based on fluctuating curvature in the sound speed profile [26,35]. Predictions from the model are quite similar to classical scattering theory, except that the vertical scale of the tubulence is characterized by z, whereas large eddies dominate the horizontal scale. The agreement between the model and existing experimental results is much better than if one uses z- or z_i-scale turbulence alone in an isotropic scattering model [26].

Computer simulations of large-scale boundary-layer turbulence, called large-eddy simulations (LES), have advanced considerably during the past decade. Such turbulence simulations may be very useful when used in conjunction with acoustic propagation models. C.-H. Moeng of the National Center for Atmospheric Research (NCAR) kindly provided the author with output from her state-of-the-art LES [29,30]. Moeng's LES was then used in conjunction with a ray-tracing code which could accomodate three-dimensional atmospheric structure [31]. It would be even better to use PE methods (discussed in Section 2) in conjunction with the LES fields. From the standpoint of acoustic studies, one limitation of the LES is its 20 m vertical resolution. In its present form, LES does not capture the near-surface structure well.

ACOUSTIC TOMOGRAPHY

The sensitivity of acoustic waves to atmospheric structure motivates consideration of acoustic techniques for probing the atmosphere. Wilson [26] has used tomographic methods to reconstruct atmospheric turbulence fields from acoustic transmissions. The basic idea is quite simple: one measures the time required for acoustic bursts to propagate between a number of sources and receivers. Since the travel time depends upon wind speed and temperature, information on the atmospheric fields is thus obtained.

Figure 6 shows the layout of the tomographic array, implemented at the R. E. Larson Agricultural Research Center at Rock Springs, PA. In the basic horizontal coniguration, there are three sources and five receivers, at 6 m height, providing a total of 15 ray paths. The dimensions of the array are approximately 200 m square. The reader is referred to Ref. [26] for more details of the experiment. That reference also explains the procedure for inverting the acoustic travel times to obtain the atmospheric fields.

Figure 7 shows an example field reconstruction. The dark area on the middle left of the figure is a region of cold air. In the lower right is a warm region. Arrows indicate wind speed and direction.

SYSTEM ATTRACTOR CHARACTERIZATON

An extensive program of low-frequency acoustic measurements was recently completed by the author, Edward Maniet, and Dennis W. Thomson of Penn State. These data were also at Rock Springs, PA. Most of the data sets consist of one-minute averages, recorded continuously over periods lasting from three to seven days. Measurements were made during fall, winter, and summer conditions. The propagated frequencies were 28 Hz, and the first three harmonics thereof. Typically there were two receivers, at heights of 2 and 6 m, separated by a horizontal distance of 770 m from the source. Additional micrometeorological measurements of the turbulent momentum, heat, and moisture fluxes were made adjacent to the path, and a Doppler sodar was used to monitor the boundary-layer wind profile. Figure 8 shows a characteristic record for the signal variation over the course of a day. The level of the signal tends to be elevated at night, presumably because of temperature inversions.

Harry Henderson of Penn State has studied the system attractor dynamics of a portion of our data set. The attractor was found to have a dimension of about 2.3. This value is somewhat lower than that computed for other atmospheric data sets, presumably because of the spatial and temporal averaging inherent to the acoustic measurement. The effect of such averaging is now being studied.

Reconstruction of the dynamical phase space revealed that most of the measurements fell within a small

possible the construction of filters which are based on the *dynamics* of the signal and noise, rather than *spectral* characteristics.

ACKNOWLEDGEMENTS

Many of the ideas in this paper originated during the author's work as a graduate student at Penn State. The author is particularly indebted to his thesis advisor, Dennis W. Thomson.

Financial support for this research was provided by the Office of Naval Research (Grant N00014-86-K-06880), and the U. S. Army Atmospheric Sciences Laboratory (Grant N00039-88-C-0051). The support and encouragement offered by Dr. Robert Olsen of ASL was particularly appreciated.

REFERENCES

[1] S. M. Flatté (ed.), R. Dashen, W. H. Munk, K. M. Watson, and F. Zachariasen, *Sound Transmission through a Fluctuating Ocean* (Cambridge University Press, Cambridge, 1979).

[2] R. Raspet, S. W. Lee, E Kuester, D. C. Chang, W. F. Richards, R. Gilbert, and N. Bong, "A fast-field program for sound propagation in a layered atmosphere above an impedance ground," *J. Acoust. Soc. Am.* **77**, 345–352 (1985).

[3] F. R. DiNapoli and R. L. Deavenport, "Theoretical and numerical Green's function field solution in a plane multilayered medium," *J. Acoust. Soc. Am.* **67**, 92–105 (1980).

[4] S. W. Lee, N. Bong, W. F. Richards, and R. Raspet, "Impedance formulation of the fast field program for acoustic wave propagation in the atmosphere," *J. Acoust. Soc. Am.* **79**, 628–634 (1986).

[5] S. J. Franke, R. Raspet, and C. H. Liu, "Numerical predictions of atmospheric sound-pressure levels in shadow zones," *J. Acoust. Soc. Am.* **83**, 816–820 (1988).

[6] D. K. Wilson, "Use of wave-number-domain windows in fast field programs," *J. Acoust. Soc. Am.* **89**, 448–450 (1990).

[7] K. E. Gilbert and R. Raspet, "Calculation of turbulence effects in an upward refracting atmosphere," *J. Acoust. Soc. Am.* **67**, 92–105 (1980).

[8] D. K. Wilson and D. W. Thomson, "Comparison of FFP predictions with measurements of a low frequency acoustic signal propagated in the atmosphere," in *Proceedings of the Fourth International Symposium on Long-Range Sound Propagation, NASA Conference Publication 3101* (Hampton, VA, 1990), pp. 187–200.

[9] R. K. Brienzo, "Effect of wind and temperature gradients on received acoustic energy," in *Proceedings of the Fourth International Symposium on Long-Range Sound Propagation, NASA Conference Publication 3101* (Hampton, VA, 1990), pp. 165–185.

[10] K. E. Gilbert and M. J. White, "Application of the parabolic equation to sound propagation in a refracting atmosphere," *J. Acoust. Soc. Am.* **85**, 630–637 (1989).

[11] F. D. Tappert, "The Parabolic Approximation Method," in *Wave Propagation and Underwater Acoustics*, J. Keller and J. S. Papadakis, eds., Lecture Notes in Physics, Vol. 70 (Springer-Verlag, Heidelberg, 1977).

[12] B. Hallberg, C. Larsson, and S. Israelsson, "Numerical ray tracing in the atmospheric surface layer," *J. Acoust. Soc. Am.* **83**, 2059–2068.

[13] A. D. Pierce, "Wave equation for sound in fluids with unsteady inhomogeneous flow," *J. Acoust. Soc. Am.* **87**, 2292–2299.

[14] A. S. Monin and A. M. Obukhov, "Basic laws of turbulent mixing in the ground layer of the atmosphere," *Tr. Akad. Nauk., SSSR Geophiz. Inst.* **151**, 1963-1987 (1954).

[15] J. A. Businger, J. C. Wyngaard, Y. Izumi, and E. F. Bradley, "Flux profile relationships in the atmospheric surface layer," *J. Atmos. Sci.* **28**, 181–189 (1971).

[17] H. A. Panofsky and J. A. Dutton, *Atmospheric Turbulence: Models and Methods for Engineering Applications* (Wiley & Sons, New York, 1984).

[18] H. Klug, "Sound-speed profiles determined from outdoor sound propagation measurements," *J. Acoust. Soc. Am.* **90**, 475-481 (1991).

[19] G. A. Daigle, "Correlation of the phase and amplitude fluctuations between direct and ground-reflected sound," *J. Acoust. Soc. Am.* **68**, 297-302 (1980).

[20] G. A. Daigle, J. E. Piercy, and T. F. W. Embleton, "Line-of-sight propagation through atmospheric turbulence near the ground," *J. Acoust. Soc. Am.* **74**, 1505-1513 (1983).

[21] S. F. Clifford and R. J. Lataitis, "Turbulence effects on acoustic wave propagation over a smooth surface," *J. Acoust. Soc. Am.* **73**, 1545-1550 (1983).

[22] M. A. Johnson, R. Raspet, and M. T. Bobak, "A turbulence model for sound propagation from an elevated source above level ground," *J. Acoust. Soc. Am.* **81**, 638-646 (1987).

[23] H. E. Bass, L. N. Bolen, R. Raspet, W. E. McBride, and J. Noble, "Acoustic propagation through a turbulent atmosphere: Experimental characterization," *J. Acoust. Soc. Am.* **90**, 3307-3313 (1991).

[24] W. E. McBride, H. E. Bass, R. Raspet, and K. E. Gilbert, "Scattering of sound by atmospheric turbulence: A numerical simulation above a complex impedance boundary," *J. Acoust. Soc. Am.* **90**, 3314-3325 (1991).

[25] R. Dashen, "Path integrals for waves in random media," *J. Math. Phys.* **20**, 894-920 (1979).

[26] D. K. Wilson, *Acoustic Tomographic Monitoring of the Atmospheric Boundary Layer*, Ph.D. Dissertation in Acoustics, Pennsylvania State University (University Park, Pennsylvania 1992).

[27] J. Højstrup, "A simple model for the adjustment of velocity spectra in unstable conditions downstream of an abrupt change in roughness and heat flux," *Bound. Layer Meteor.* **21**, 341-356 (1981).

[28] J. Højstrup, "Velocity spectra in the unstable boundary layer," *J. Atmos. Sci.* **39**, 2239-2248 (1982).

[29] C.-H. Moeng, "A large-eddy simulation model for the study of boundary-layer turbulence," *J. Atmos. Sci.* **41**, 2052-2062 (1984).

[30] C.-H. Moeng and J. C. Wyngaard, "Spectral analysis of large-eddy simulations of the convective boundary layer," *J. Atmos. Sci.* **44**, 3573-3587 (1988).

[31] D. K. Wilson, "Numerical studies of sound propagation in the atmospheric convective boundary layer using a large-eddy simulation," in *Proceedings of NOISE-CON 91* (Tarrytown, NY, 1991), pp. 189-196.

[32] C. I. Chessel, "Observations of the effects of atmospheric turbulence on low-frequency sound propagation," *J. Acoust. Soc. Am.* **60**, 29-33 (1976).

[33] S. D. Roth, *Acoustic Propagation in the Surface Layer under Convectively Unstable Conditions*, Ph.D. Dissertation in Acoustics, Pennsylvania State University (University Park, Pennsylvania, 1983).

[34] J. M. Noble, *Sound Field Fluctuations due to Large Scale Wind Driven Turbulence*, Ph.D. Dissertation in Physics, The University of Mississippi (University, Mississippi, 1989).

[35] D. K. Wilson, *Propagation through Anisotropic Atmospheric Turbulence*, submitted to *J. Acoust. Soc. Am.*

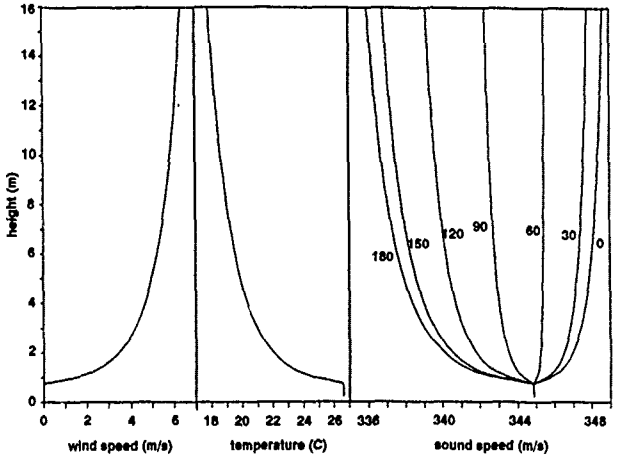

Figure 1: Profiles for a convective surface layer, with $u_* = 0.6$ m/s and $T_* = -0.4$ K.

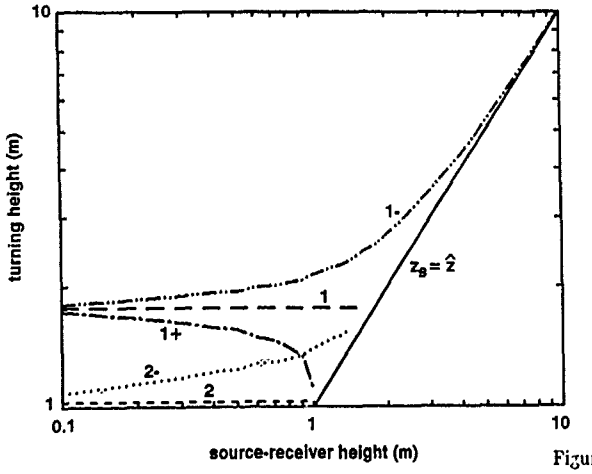

Figure 2 Ray multipath structure for downwind propagation in a convective surface layer. The source and receiver are separated by a horizontal distance of 200 m. See the text for an explanation ray identification scheme.

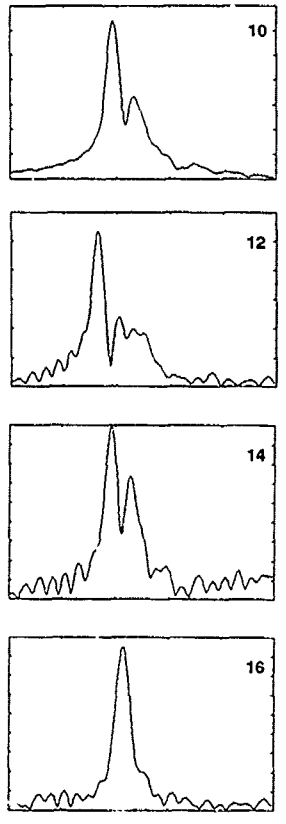

Figure 3: Cross correlation of transmitted and received acoustic signals. The transducers are at a height of 6 m, and separted horizontally by 200 m. The horizontal axis is time, spanning 24 ms. The vertical axis is amplitude in uncalibrated units.

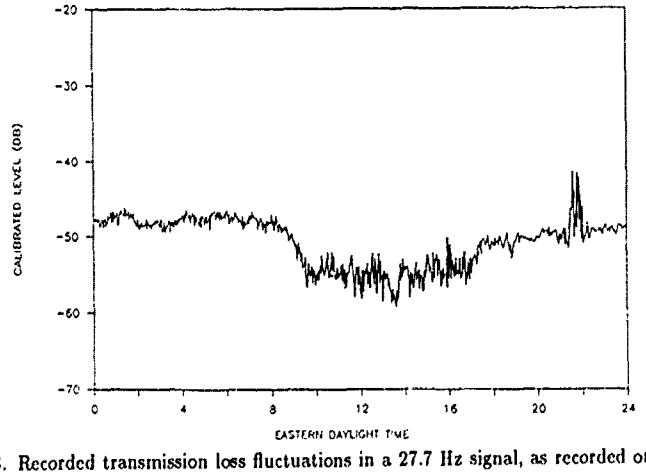

Figure 8. Recorded transmission loss fluctuations in a 27.7 Hz signal, as recorded on 10 March 1989.

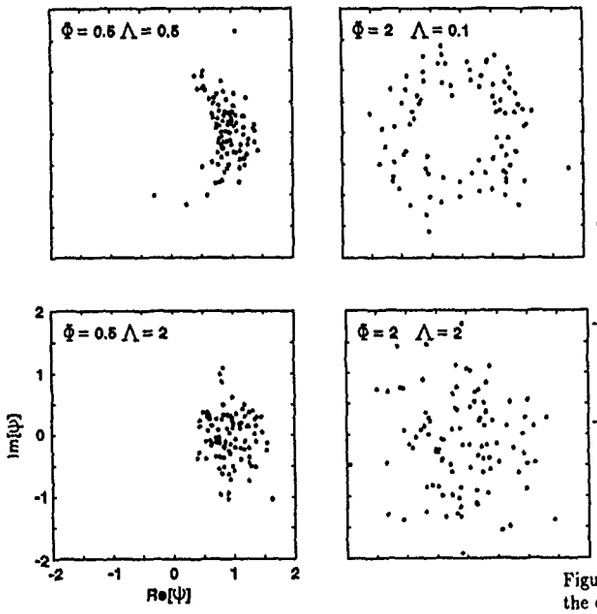

Figure 4: Simulated wavefunction phasor samples as a function of the strength-diffraction regime. Upper left: Geometric acoustics case, with $\Phi = 2$ and $\Lambda = 0.1$. Lower left: Geometric acoustics case, with $\Phi = 0.5$ and $\Lambda = 0.5$. Lower right : Rytov extension case, with $\Phi = 0.5$ and $\Lambda = 2$. Upper right: Fully saturated case, with $\Phi = 2$ and $\Lambda = 2$ The probability density functions were assumed to be Gaussian. One hundred random samples are shown.

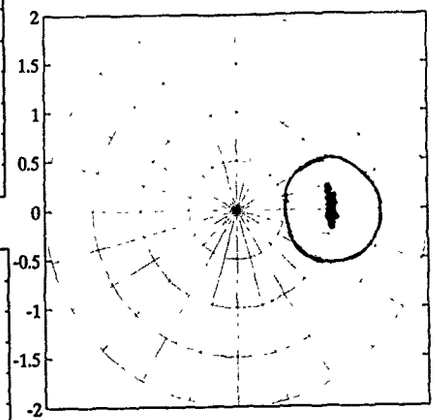

Figure 5. Simulated wavefunction phasor samples for the experiment of Bass *et al.* The closed curve would roughly enclose most of the actual experimental data (See Ref. 23.)

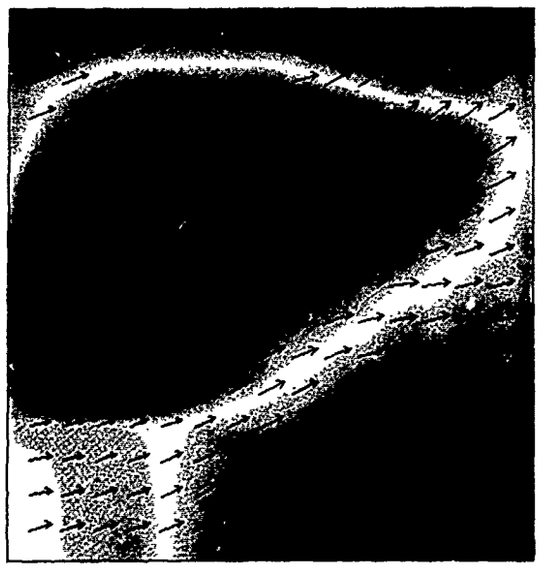

Figure 7. Tomographic reconstructions of the atmospheric temperature and wind velocity fields, in a 200 x 200 m horizontal plane.

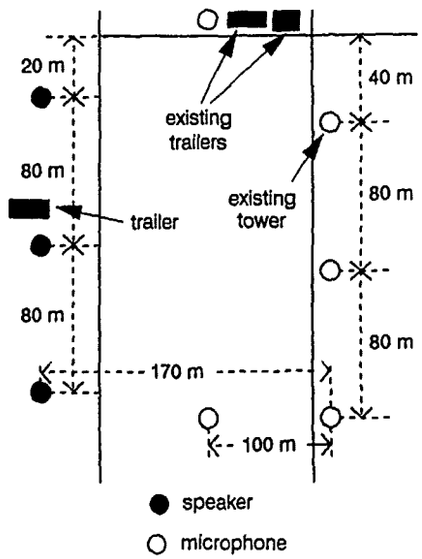

Figure 6: Tomographic array implemented at Rock Springs, PA.

SECOND INTERNATIONAL CONGRESS ON
RECENT DEVELOPMENTS IN AIR- AND
STRUCTURE-BORNE SOUND AND VIBRATION
MARCH 4-6, 1992 AUBURN UNIVERSITY, USA

SOUND SHIELDING BY BARRIERS WITH CERTAIN SPECIAL TREATMENTS

Kyoji FUJIWARA

Department of Acoustic Design
Kyushu Institute of Design
Shiobaru 4-9-1, Minami Fukuoka 815
JAPAN

ABSTRACT

This paper presents the answer to a question "is it possible to get more attenuation by thin barrier with certain special treatments than that by commonly used thin barrier?". The answer is "possible". There are some possibilities to make acoustical treatments, for example, to cover barrier surface with absorbing materials, to cover it with a lot of one quarter wave length acoustic tubes, to install hard, absorptive or soft cylinder at barrier edge. In this study the efficiencies of these acoustical treatments are numerically and experimentally examined.

1. INTRODUCTION

It is common to build a barrier for reducing the noise from motor way, rail road, factory, etc., and for such purpose noise barriers with absorbing material on the surfaces are currently used. To improve the efficiency of the barriers, it would be simple to make the barriers higher, but there is a limit to barrier height because of factors such as cost, shadow cast by the barriers, and blocking sight. The aim of this paper is to show how we can get more reduction by new types of thin barriers than by commonly used thin barriers. In this study a barrier with absorptive surface, a barrier with soft surface and barriers with hard, absorptive and soft round edge will be treated. Their cross-sections are shown in Fig.1. And general positions of a source, a receiving point and barriers are shown in Fig.2, and some parameters also in Fig.2.

2. EXCESS ATTENUATION BY THIN HARD BARRIER

A thin hard barrier is shown in Fig.1(a), the excess attenuation by this type of barrier is given by well known Maekawa's chart [1] and numerically calculated by Eq.(1). This equation was recently derived by the theoretical analysis [2]. The comparison between Maekawa's chart and the new numerical formula is shown in Fig.3. Dashed curve show Maekawa's chart and solid curve the numerical result by Eq.(1). Many points show the rigorous numerical results by the diffraction solution for the same conditions as Maekawa's experiments. The excess attenuation is here define by a term ${}_0[ATT]_{h0}$ and let it be the basic value of this study.

$$ {}_0[ATT]_{h0} = \begin{cases} 10\log(N) + 12 & 2 \leqq N \\ 5 \pm 9\sinh^{-1}(\,|\,N\,|^{0.45}) & -0.3 \leqq N < 2 \\ 0 & N < -0.3 \end{cases} \quad (dB) \quad (1) $$

3. EXCESS ATTENUATION BY BARRIER WITH ABSORPTIVE SURFACE

The excess attenuation by a barrier with absorptive surface is approximately obtained by the diffraction solution for the hard barrier, whose second term is multiplied by the

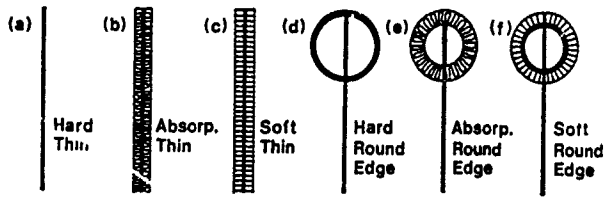

Fig.1 Cross-sections of different types of thin barriers with special treatments

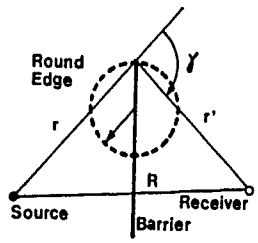

Fig.2 Geometry of barrier, sound source and receiving point

reflection coefficient of the surface [3], and when the surface is perfectly absorptive it is given by a half of the sum of solutions for hard barrier and soft one [4]. We can get a little more excess attenuation by this type of barrier than ${}_s[ATT]_{ho}$. The effect of absorption of barrier surface is defined by

$$ {}_s[EA] = {}_s[ATT]_{ao} - {}_s[ATT]_{ho} \qquad \text{(dB)} \qquad (2) $$

where ${}_s[ATT]_{ao}$ is the excess attenuation by an absorptive barrier. The values of the effect of absorption ${}_s[EA]$ are shown in Fig.4 as a function of the diffraction angle gamma shown in Fig.2. The parameter Q is the value of the sound reflection coefficient of the surface. When the barrier is perfectly absorptive, the effect of absorption is 4 to 5dB in the range of gamma 60° to 90°. This type of barrier is easily realized by covering the barrier surface with thin absorbing material as shown in Fig.1(b) and nowadays it is widely used. But the effect of absorption is not expected quantitatively at noise barrier designing and only the existence of the effect is expected.

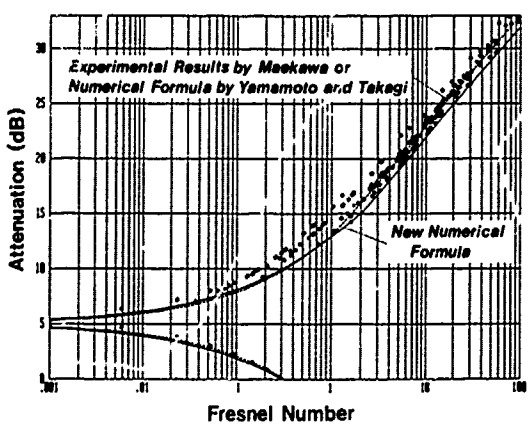

Fig.3 Excess attenuation by a thin barrier as a function of Fresnel Number N

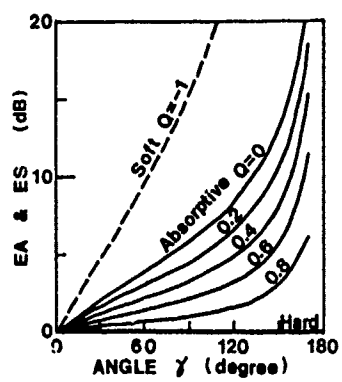

Fig.4 Effects of absorptive and soft surface as a function of the diffraction angle gamma

4. EXCESS ATTENUATION BY BARRIER WITH SOFT SURFACE

When the sound reflection coefficient of the barrier surface Q is -1, that is the case of soft barrier, the energy reflection coefficient is 1 and this means perfectly reflective. But the effect of soft surface is very great as shown by dashed curve in Fig.4. This effect is nearly double of that of perfectly absorbent barrier. In this case the effect of soft surface is defined by

$$ {}_s[ES] = {}_s[ATT]_{so} - {}_s[ATT]_{ho} \qquad \text{(dB)} \qquad (3) $$

where ${}_s[ATT]_{so}$ is the excess attenuation by a barrier with soft surface [5]. The realization of this type of barrier is not so easy. Recently I have tried to realize the soft barrier surface by covering the surface with the array of one quarter wave length acoustic tubes.

It is well known that the effect of thickness of barrier is quite a little when the thickness is less than half a wave length [6]. Then the barrier covered by these tubes at both sides and those openings are covered by thin hard plates is approximately comparable to thin barrier. But the surface covered by acoustic tubes can reflect the incident sound just 180° out of phase, that is the reflection coefficient of this surface is -1. The measured results are shown in Figs.5 and 6. The test barrier was designed for 5kHz and the cross-section is shown in Fig.1(c) and the detail is show in Fig.7. The measurements were performed in the anechoic chamber for some different conditions. In Fig.5 the distributions of the effect of soft surface behind the barrier are shown. In the left it shows the predicted contour and in the right the measured. There is about 3dB difference. In Fig.6 the effect of soft surface is plotted as a function of frequency. Dashed curve shows the predicted value, and black and open circles show the measured values in the cases when both sides and only source side were covered by acoustic tubes respectively. Locations of source and receivers are shown in Fig.8. Although there are some differences between predicted and measured values, the frequency responses are similar. In the calculation of these values the second term of diffraction solution was multiplied by the reflection coefficient

$$Q = -\frac{1 - j\cos\theta \cot(kd)}{1 + j\cos\theta \cot(kd)} \qquad (4)$$

where θ is the incident angle, d is the depth of acoustic tube and k is wave number.

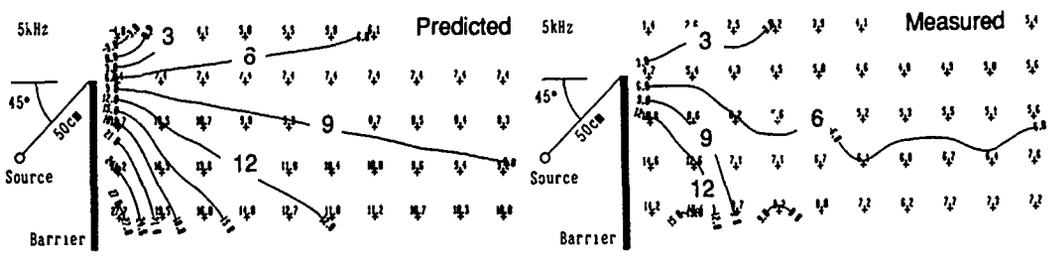

Fig.5 Contours of predicted and measured [ES] in the case of 5kHz

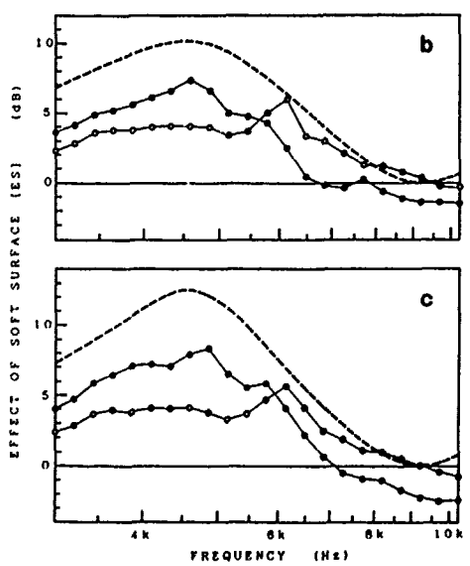

Fig.6 Comparisons of measured and predicted values of [ES] as a function of frequency
●——● : measured (both sides are soft), o—o : measured (source side is soft and receiver side is hard), ------ : predicted (both sides are soft)

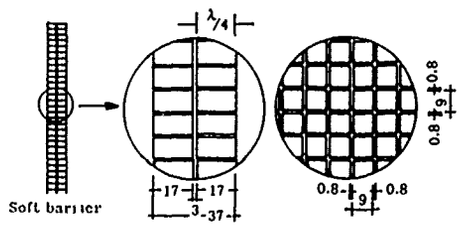

Fig.7 Detail of the cross-section of soft thin test barrier

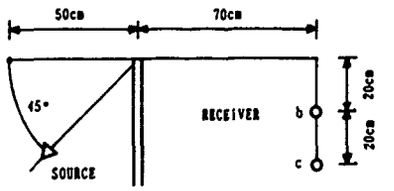

Fig.8 Location of source and receivers

5. EXCESS ATTENUATION BY BARRIER WITH HARD CYLINDER AT THE EDGE

The barrier with any obstacle at the edge can reduce the sound more than the commonly used thin barrier can. In this study the cylinders with different acoustic reflection characteristics are selected as the obstacles because of the simplicity and the practicality. When the cylinder is very hard, the solution of the diffraction field has been already obtained by Keller [7] and using this solution the effect of hard cylinder is defined by

$$ {}_c[EHC] = {}_c[ATT]_{hc} - {}_c[ATT]_{ho} \qquad (dB) \qquad (5) $$

where ${}_c[ATT]_{hc}$ is of course the attenuation by barrier with hard cylinder at the edge. The suffix c at the left side of variables means the incident sound is generated from the cylindrical line source. But in this study all effects predicted in two dimensional sound field are assumed to be equal to that predicted in three dimensional sound field, that is in the field of spherical sound wave incidence.

One of the numerical results is shown by dotted curve in Fig.9. The geometry for calculation is also shown in Fig.9. The value of ${}_c[EHC]$ is not so great, less than 3dB and sometimes it is minus value. Some measured values are shown in Fig.10 as a function of the relative size of cylinder ka, where "a" is the radius of cylinder. The cross-section of the barrier is shown in Fig.1(d). The distance of source from the edge was 40cm and the distance of receiving point from the edge was 60cm. Measured and predicted values are in fairly good agreement except for some cases. Specially when the diameter is half a wave length the effect of hard cylinder is very large.

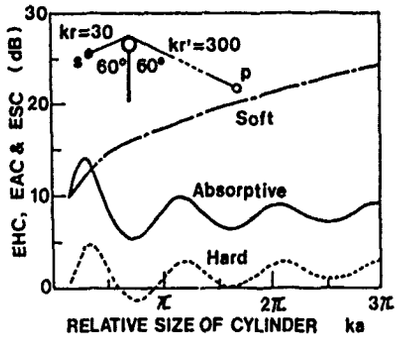

Fig.9 Comparison of numerically obtained effects of cylinder for different reflection characteristics

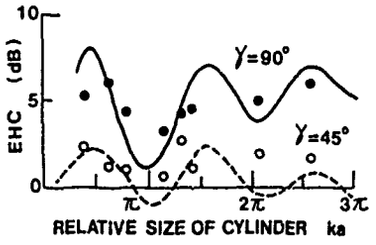

Fig.10 Comparison of measured and predicted effects of hard cylinder

6. EXCESS ATTENUATION BY BARRIER WITH ABSORPTIVE CYLINDER AT THE EDGE

When a barrier has an absorptive cylinder at the edge, the attenuation by this barrier may be lager than that by the barrier with hard cylinder. The solution of diffraction field by this type of barrier may be obtained by the same procedure in the case of thin barrier mentioned above. The solution by the barrier with soft cylinder at the edge has been also obtained by Keller [7]. The effect of absorptive cylinder is defined by

$$ {}_c[EAC] = {}_c[ATT]_{ac} - {}_c[ATT]_{ho} \qquad (dB) \qquad (6) $$

where ${}_c[ATT]_{ac}$ is the excess attenuation by the barrier with absorptive cylinder at the edge. One of the numerical results is shown by solid curve in Fig.9. The realization of this barrier is not so difficult and the cross-section of the barrier may be that shown in Fig.1(e).

One example of this type of barrier has been really produced for practical use [8 and 9]. Real construction is shown in Fig.11. The effect of absorptive cylinder was measured by the existing express way. The one of results is shown in Fig.12. This figure shows the difference between the sound pressure levels measured before and after setting the absorptive cylinder at barrier edge. And the sound pressure levels were measured for 5 to 7 nights and averaged. The effect of absorptive cylinder is roughly 2 to 3 dB. The

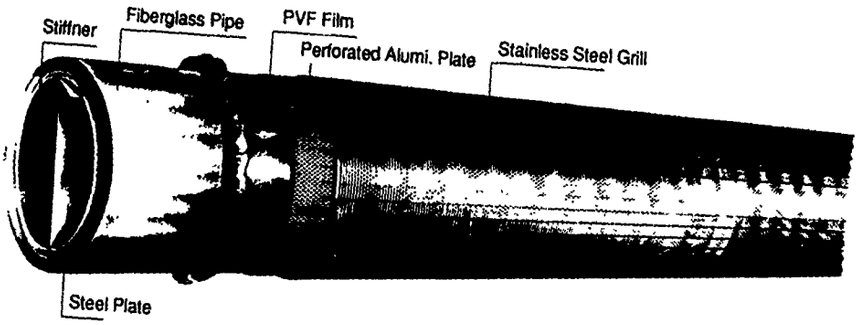

Fig.11 Construction of newly-developed absorptive cylinder for practical use

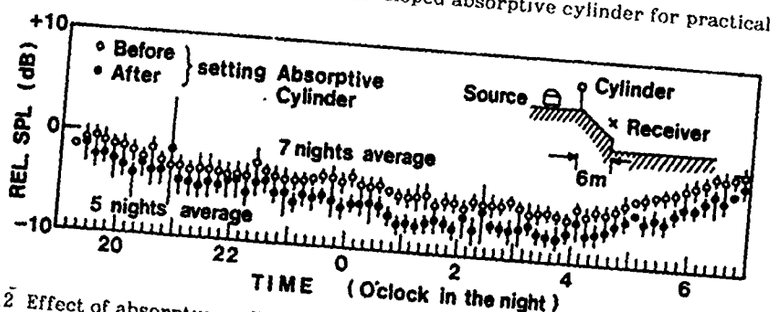

Fig.12 Effect of absorptive cylinder measured in the real situation. open circles show the sound pressure levels measured before the installation of the absorptive cylinder and averaged over 7 nights. Solid circles show the measured values after the installation and averaged over 5 nights. Thin lines show the standard deviations of each set of data

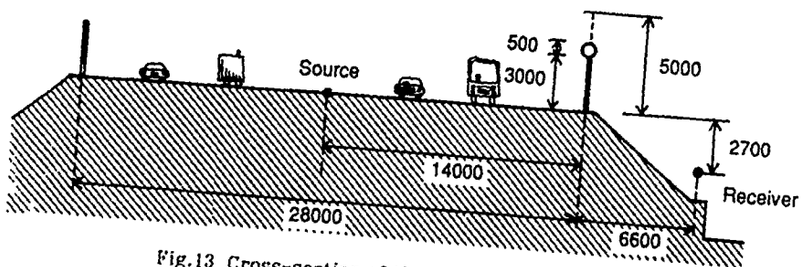

Fig.13 Cross-section of the measured field

cross-section of the measured field is shown in Fig.13. In this case the difference between the excess attenuations obtained by 5m and 3m barriers is about 2.7dB. So this 2 to 3 dB extra attenuation corresponds to the excess attenuation obtained by thin barrier of 2m higher without cylinder.

7. EXCESS ATTENUATION BY BARRIER WITH SOFT CYLINDER AT THE EDGE

At last, how is the effect of cylinder when the cylinder is soft? The numerical example is shown by chain curve in Fig.9. The effect of soft cylinder is defined by

$$\Delta[ESC] = \Delta[ATT]_{hc} - \Delta[ATT]_{hc} \qquad (dB) \qquad (7)$$

where $\Delta[ATT]_{hc}$ is the excess attenuation by a thin barrier with soft cylinder at the edge. The effect is considerably greater than that of absorptive and hard cylinders. When the

diameter is one wave length, the effect is about 18dB. But from the practical point of view we will have some problems to realize this type of barrier. One idea is that the cross-section of such barrier might be that shown in Fig.1(f), that is to cover a cylinder with one quarter wave length acoustic tubes.

8. CONCLUSIONS

The aim of this paper was to show whether it is possible to get more attenuation than that obtained by commonly used thin barrier. The answer is in some sense "possible" as shown above. One type of barrier is effective for all frequency band, but the effect is not so large. On the other hand, the effect of another type of barrier is very large, but the barrier effect is very frequency dependent. At the end of this paper we can say that much more effort is needed to invent a new type of barrier by which we can get more excess attenuation because of the requirements from the engineers.

REFERENCES

[1] Z.Maekawa; "Noise reduction by screens", Mem. Faculty Engi. Kobe Univ., 11 (1965) 29

[2] K.Fujiwara and A.Omoto; "A note on Maekawa's Chart", J. Acoust. Soc. Jpn. 47 (1991) 348 (in Japanese)

[3] K.Fujiwara, Y.Ando & Z.Maekawa; "Noise control by barriers, Part 2: Noise reduction by an absorptive barrier", Appl. Acoust., 10 (1977) 167

[4] G.F.Butler; "A note on improving the attenuation given by a noise barrier", J. Sound & Vib., 32 (1974) 367

[5] H.M.Macdonald; "A class of diffraction problems", Proc. Lond. Math. Soc., 14 (1915) 410

[6] K.Fujiwara, Y.Ando & Z.Maekawa; "Noise control by barriers, Part 1: Noise reduction by a thick barrier", Appl. Acoust., 10 (1977) 147

[7] J.B.Keller & D.G.Magiros; "Diffraction by a semi-infinite screen with round end", Commu. Pure & Appl. Math., 14 (1961) 457

[8] K.Yamamoto & M.Yamashita; "Reduction of road traffic noise by absorptive cylinder adapted at the top of a barrier", Inter-Noise 89 (1989) 349

[9] K.Fujiwara and N.Furuta; "Sound shielding efficiency of a barrier with a cylinder at the edge", Noise Control Engineering Journal 37 (1991) 5

SOUND INTENSITY, STRUCTURAL INTENSITY AND SOUND FIELD SPATIAL TRANSFORMATION

SECOND INTERNATIONAL CONGRESS ON
RECENT DEVELOPMENTS IN AIR- AND
STRUCTURE-BORNE SOUND AND VIBRATION
MARCH 4-6, 1992 AUBURN UNIVERSITY, USA

SOUND POWER DETERMINATION BY MANUAL SCANNING OF ACOUSTIC INTENSITY

*Michael Bockhoff, Ondrej Jiricek**
Department of Acoustics
CETIM
F - 60300 Senlis
FRANCE

ABSTRACT

Sound power determination by intensity measurements using manual scanning has become an attractive method, but for setting up a standard some more evidence is needed to relate the precision of the result to the measurement parameters. For this reason systematic measurements have been carried out and the influence of several parameters such as measurement distance, scanning speed, path configuration has been analysed, in comparison with point measurements, in order to select appropriate ranges for these parameters.

INTRODUCTION

Since the apparition of intensity techniques some 15 years ago, sound power determination by intensity measurements has been a matter of standardisation at national and international levels. Recently ISO has finalised a document [1] describing a procedure based on measurements at discrete points. This document has raised some criticism, mainly because of the indicators which have to be used for checking the precision of measurements.
Another method, based on continuous scanning of intensity, is actually discussed in standardisation. Many peoples have already used it successfully and the method seems to be more attractive than point measurements, because its application is much faster. Consequently it reduces some problems such as sound field fluctuation (source under test and extraneous noise) and last but not least the cost of the sound power determination. The main problem for standardisation is actually a lack of knowledge of its precision and of the appropriate way to obtain a wanted degree of precision. Since very few studies are published (for ex. [2] to [5]) we have carried out systematic measurements in order to get sufficiant data for analysing the influence of parameters such as measurement distance, scanning speed, path length and scanning pattern, scanning time, presence of extraneous noise etc.

* on leave from Dept. of Phys., Techn. Univ. Prague

EXPERIMENTAL SET UP AND TEST PROGRAM

Acoustic Environment :
Free field in front of reflecting plane as shown in figure 1 and excited by time-stationary white noise in the frequency band 100 Hz - 5000 Hz.

Measurement Surface :
Area of 1 m x 1 m parallel to the reflecting plane, distances between measurement surface and reflecting plane d = 0.10 m , 0.20 m, 0.40 m.

Scanning Path :
Four parallel (horizontal and / or vertical) lines turning at each edge, each of them is subdivided to four elements with length l_o = 0.25 m as shown in figure 2. Additional measurements have been made with a doubled line density.

Spatial Sampling :
- Scanning method
  - 1 complete trajectory 16 x l_o = 4 m
  - 4 lines 4 x l_o = 1m
  - 4 x 4 elementary lines l_o = 0.25 m

- Measurement at discrete points
  - 16 points uniformly distributed (4 x 4), as shown in figure 2
  - 64 points uniformly distributed (8 x 8)

Scanning Speed :
- 0.85 ms^{-1} which corresponds to 4.7 s scanning time
- 0.43 ms^{-1} which corresponds to 9.5 s scanning time
- 0.21 ms^{-1} which corresponds to 19 s scanning time
- 0.11 ms^{-1} which corresponds to 37.5 s scanning time
- 0.05 ms^{-1} which corresponds to 75 s scanning time

(depends on sampling frequency of analyser)

Measured Quantities :
L_p, L_I - for both scanning and discrete point measurements

Calculated Quantities (As Defined By ISO) :
F_2, F_3 - for both methods
F_4 - for sets of elementary lines and discrete points
L_W

Extraneous Noise :
A reference sound source producing white noise is placed as near as possible to the reflecting plane. Source of extraneous noise is adjusted by following choice :
- $L_{p,cent.} = \overline{L}_{p,16}$,
- $L_{p,cent.} = \overline{L}_{p,16} + 3$ dB,

where $L_{p,cent.}$ is sound pressure level in the middle of the measurement surface due to extraneous source only and $\overline{L}_{p,16}$ is mean sound pressure level calculated from 16 points measurement without extraneous noise.

Instrumentation :
FFT - intensity meter composed of

- two-channel real time analyser HP 3582 A
- desk computer HP 9826
- intensity probe made by two microphones (B & K 4165) and preamplifiers (B & K 2639)
- power supply (B & K 2807)
- intensity software CETIM-INTAC

RESULTS

Only a small part of the results can be presented here and we will merely highlight the influence of the dominant parameters which are measurement distance, scanning speed and scan pattern.

Measurement Distance
The sound powers determined by point measurements and by horizontal scanning under differents conditions are given in table 1 (1/3 oct. 500 Hz) and table 2 (1/3 oct. 4 kHz). The values for scanning indicate the differences with respect to point measurements. It is seen that at the low frequency, where directivity effects are quite moderate, the difference between point measurements and scanning is typically ≤ 1 dB for all three measurement distances. At 4 kHz, where directivity is stronger, the two techniques give similar results for the greatest distance d = 0.4 m, but there is a significant increase of the difference, up to 6 dB, at lower distances and this even in the presence of extraneous noise (the corresponding F3 - indicators are shown in tables 3 and 4). Allthough the error observed at small distances depends an other parameters too, a minimum distance of 0.2 m, which is actually discussed by ISO, seems to be a reasonable compromise.

Scanning Speed :
Results corresponding to those in tables 1 and 2 but determined with approximately half the scanning speed (0.05 m/s) are presented in tables 5 and 6. The comparison shows no significant differences due to scanning speed at the greater distances (0.2 and 0.4 m). Only for d = 0.1 m a slow scan reduces the errors observed more particularly at high frequencies. Nevertheless the conclusion that at greater distances fast scans do not affect the measurement precision would be erroneous : In fact, a more detailed analysis reveals that repeatability of results suffers at very high and very low scanning speeds. For 5 different speeds we have repeated the complete scan 8 times and determined both the mean sound power levels and the relative errors ε defined by :

$$\varepsilon = \frac{t_{\alpha/2,n-1} \cdot \sqrt{\frac{s^2}{n}}}{\overline{W}} \cdot 100 \quad [\%],$$

where $t_{\alpha/2,n-1}$ is the coefficient of Student t-distribution at $(1 - \alpha) \times 100\%$ confidence level (in our case it was 2.365), $\overline{W}$ is the mean sound power, s^2 the sample variance of sound power and n the number of independant samples.

Table 7 shows results for the measurement distance 0.4 m. It is seen that best repeatability in obtained in the medium range of speeds arround 0.2 m/s. The monotonous decrease of errors with the scanning speed that might be expected is not observed, probably because of increasing "personal errors" induced by the operator at long scanning times and very low speeds.

Scanning pattern :
The results presented above have been obtained by horizontal scans only. The comparison of various configurations (complete scans or division into elementary paths with a total number of FFT samples maintained constant) does not reveal significant differences but they all underestimate systematically the true (?) sound powers given by point measurements, especially at high frequency. This underestimation which is due to the choice of the scanning pattern cannot be reduced by increasing only the number of FFT samples (by a lower speed) without changing the path.
The influence of the scanning pattern is show in the table 8 and 9 where we compare horizontal and vertical scans with two path lengths : 4 and 8 m. At 4 kHz and with a path length of 4 m the horizontal scan produces an underestimation but the vertical scan an overestimation. The combination of both (h & v) fits very well to the point measurements.
With a double line density (path length 8 m) the differences are much smaller and either horizontal or vertical scannings are sufficient for a correct sound power estimate. Scanning on crossed paths seems to be an interesting technique to check whether the chosen line density is appropriate or not.

CONCLUSION

A rough analysis of the large number of collected data has allowed to show the influence of several measurement parameters on the calcuated sound power and to select reasonable ranges for some of them (measurement distance, scanning speed). These ranges fit quite well to the reommandations discussed actually by ISO.
A more detailed analysis of the data, especially with respect to the indicators which are already used in point measurements, should permit to quantify the measurement errors, to define classes of precision and to get guidance for improving insufficient estimates.

REFERENCES

[1] Acoustics - Determination of sound power levels of noise sources using sound intensity - part 1 : measurement at discrete points ISO/DIS 9614 - 1 (1990)

[2] Bockhoff M. Some remarks on the continuous sweeping method in sound power determination, Proc. of Inter-Noise 84, p.1173 - 1176

[3] Pettersen K.O., Newman M.J., An Intensity method for determining sound power in situ Noise Control Eng. J., 31 (2) 1988, p. 93 - 100

[4] Pettersen K.O., Newman M.J., Is our confidence in scanned intensity measurements justified ? Proc. of Inter-Noise 89, p.979 - 984.

[5] Olsen H., Pettersen K.O., Vigran T.E., Newmann M.J. Sound intensity field mapping using scanning technique Proc. of Inter-Noise 90, p.87 - 90.

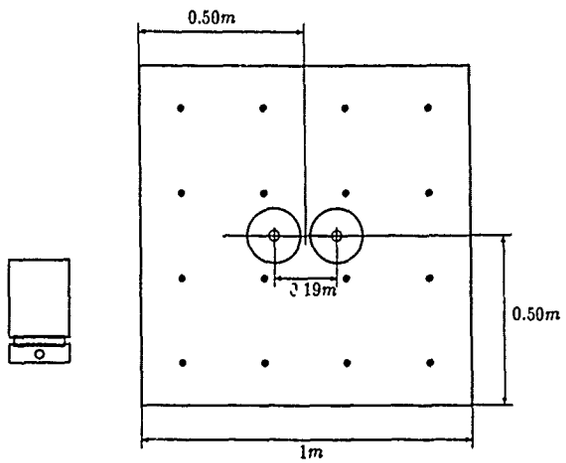

Figure 1 : Experimental set up of source under test (two loudspeakers) and extraneous noise source

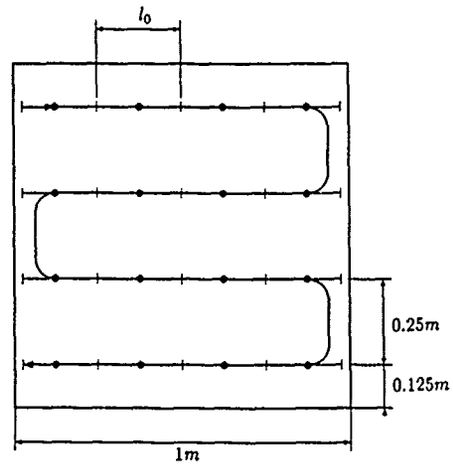

Figure 2 : Distribution of discrete points and scanning paths

Table 1 : Sound power levels for 1/3 oct. 500 Hz, $v_S = 0.11$ ms^{-1}

ext. noise dB	Ø			$L_{pq,c} = \overline{L}_{pq,16}$			$L_{pq,c} = \overline{L}_{pq,16} + 3dB$	
distance	0.1 m	0.2 m	0.4 m	0.1 m	0.2 m	0.4 m	0.1 m	0.2 m
16 points cor.	66.4	64.4	61.3	70.1	67.3	64.8	73.0	69.9
compl. scan	-0.9	0.2	0.3	-0.9	0.0	0.5	-0.4	-0.2
4 x 1*m*	0.0	-0.7	0.8	-0.5	0.6	-0.3	-0.6	-0.3
16 x l_0	-0.6	0.3	-0.7	-0.8	1.1	0.7	-1.4	

Table 2 : Sound power levels for 1/3 oct. 4 kHz, $v_S = 0.11$ ms^{-1}

ext. noise dB	Ø			$L_{pq,c} = \overline{L}_{pq,16}$			$L_{pq,c} = \overline{L}_{pq,16} + 3dB$	
distance	0.1 m	0.2 m	0.4 m	0.1 m	0.2 m	0.4 m	0.1 m	0.2 m
16 points cor.	71.3	72.3	71.4	72.4	72.5	71.6	73.2	72.1
compl. scan	-5.7	-3.1	0.4	-5.7	-3.8	-0.2	-2.7	-1.4
4 x 1*m*	-4.7	-2.1	-0.7	-5.5	-5.1	0.4	-4.3	-2.3
16 x l_0	-5.7	-3.1	0.2	-6.2	-5.6	0.0	-8.2	

Table 3 : Indicator F_3 for 1/3 oct. 500 Hz, $v_S = 0.11$ ms^{-1}

ext. noise dB	Ø			$L_{pq,c} = \overline{L}_{pq,16}$			$L_{pq,c} = \overline{L}_{pq,16} + 3dB$	
distance	0.1 m	0.2 m	0.4 m	0.1 m	0.2 m	0.4 m	0.1 m	0.2 m
16 points	1.5	0.6	-0.1	3.0	4.2	3.5	3.4	4.3
compl. scan	1.9	1.0	0.4	3.6	4.4	3.7	3.4	4.6
4 x 1*m*	1.8	0.7	0.2	3.5	4.3	3.8	4.1	4.9
16 x l_0	1.9	0.7	0.1	3.7	4.0	3.6	4.5	

Table 4 : Indicator F_3 for 1/3 oct. 4 kHz, $v_S = 0.11$ ms^{-1}

ext. noise dB	Ø			$L_{pq,c} = \overline{L}_{pq,16}$			$L_{pq,c} = \overline{L}_{pq,16} + 3dB$	
distance	0.1 m	0.2 m	0.4 m	0.1 m	0.2 m	0.4 m	0.1 m	0.2 m
16 points	3.3	2.3	1.5	8.2	8.4	3.8	9.9	10.7
compl. scan	4.6	2.3	1.4	10.9	9.3	5.0	9.4	8.8
4 x 1*m*	4.3	1.6	1.5	10.8	10.1	4.6	11.3	9.9
16 x l_0	4.3	2.1	1.3	11.5	10.2	4.8	14.9	

Table 5 : Sound power levels for 1/3 oct. 500 Hz, $v_S = 0.05\ ms^{-1}$

ext. noise dB	Ø			$L_{pq,c} = \overline{L}_{pq,16}$			$L_{pq,c} = \overline{L}_{pq,16} + 3dB$	
distance	0.1 m	0.2 m	0.4 m	0.1 m	0.2 m	0.4 m	0.1 m	0.2 m
16 points cor.	66.6	65.2	61.7	69.7	68.2	65.0	72.9	71.1
compl. scan	-0.1	0.0	0.0	0.4	0.3	-0.3	-0.2	-0.2
4 × 1*m*	0.0	-0.2	0.2	0.0	0.1	-0.3	-0.5	-0.4
16 × l_0	-1.1	0.0	0.7	0.3	0.5	0.1	-0.4	-0.3

Table 6 : Sound power levels for 1/3 oct. 4 kHz, $v_S = 0.05\ ms^{-1}$

ext. noise dB	Ø			$L_{pq,c} = \overline{L}_{pq,16}$			$L_{pq,c} = \overline{L}_{pq,16} + 3dB$	
distance	0.1 m	0.2 m	0.4 m	0.1 m	0.2 m	0.4 m	0.1 m	0.2 m
16 points cor.	71.3	72.7	71.4	72.9	73.6	71.9	73.1	73.6
compl. scan	-3.4	-2.2	0.5	-3.9	-2.3	-0.2	-4.6	-2.1
4 × 1*m*	-3.9	-2.5	0.1	-4.5	-3.3	0.1	-4.4	-3.5
16 × l_0	-4.7	-3.3	-0.6	-4.2	-2.8	0.2	-4.1	-5.3

Table 7 : Sound power levels for d = 0,4 m, without extraneous noise

freq. [Hz]	64 points	0.85m/s	0.43m/s	0.21 m/s	0.11m/s	0.05m/s
500	54.0	53.7	54.6	54.9	54.3	54.3
		26%	12%	13.5%	10.0%	10.5%
1000	64.6	63.2	64.1	64.7	64.6	64.7
		28%	8.0%	6.4%	9.5%	5.5%
2000	69.6	68.0	68.4	69.1	69.5	69.7
		37%	14.5%	6.4%	6.5%	7.2%
4000	69.9	69.8	68.4	69.5	69.6	69.8
		49%	21%	5.4%	8.3%	9.7%
lin	77.7	77.0	76.7	77.5	77.7	77.9
		28%	12%	5.8%	3.0%	6.2%
A	78.6	77.9	77.5	78.4	78.6	78.8
		30%	12.5%	6.5%	3.0%	6.6%

Table 8 : Sound power levels for 1/3 oct. 500 Hz, without extraneous noise

dist. [*m*]	0.1	0.2	0.4
16 points cor.	65.5	63.2	60.0
scan 4*m* (h.&v.)	65.5	63.6	61.0
scan 4*m* horizontal	65.2	63.7	60.8
scan 4*m* vertical	65.8	63.6	61.3
scan 8*m* (h.&v.)	65.5	62.9	60.4
scan 8*m* horizontal	65.6	63.5	60.5
scan 8*m* vertical	65.3	62.2	60.4

Table 9 : Sound power levels for 1/3 oct. 4 kHz, without extraneous noise

dist. [*m*]	0.1	0.2	0 4
16 points cor.	70 6	71.3	70.5
scan 4*m* (h.&v.)	70.8	70.1	70.4
scan 4*m* horizontal	66.5	68.3	69.1
scan 4*m* vertical	73.0	71.4	71.4
scan 8*m* (h.&v.)	70.4	70.6	70.2
scan 8*m* horizontal	70.1	70.0	70.1
scan 8*m* vertical	70.7	71.1	70.2

SECOND INTERNATIONAL CONGRESS ON
RECENT DEVELOPMENTS IN AIR- AND
STRUCTURE-BORNE SOUND AND VIBRATION
MARCH 4-6, 1992 AUBURN UNIVERSITY, USA

THE INFLUENCE OF ELECTRICAL NOISE ON MEASUREMENT OF SOUND INTENSITY

Finn Jacobsen
The Acoustics Laboratory
Technical University of Denmark, Building 352
DK-2800 Lyngby
Denmark

ABSTRACT

The influence of electrical noise from microphones and preamplifier circuits on sound intensity estimation is examined. Electrical noise has no systematic effect on the time averaged sound intensity, but it increases the random error associated with using a finite averaging time. The effect of electrical noise is shown to be far more serious than one would have expected; in fact, electrical noise may well make it virtually impossible to determine the sound power of relatively quiet low frequency sources with the intensity technique. It is shown theoretically and demonstrated experimentally that the additional random error that is due to the noise depends in a simple manner on four quantities: the signal-to-noise ratio of the microphone signals, the pressure-intensity index of the measurement, the frequency, and the distance between the microphones

NOMENCLATURE

B	bandwidth
c	speed of sound
C_{12}	real part of cross spectrum of microphone signals
I_r	sound intensity
$I_r(\omega)$	sound intensity spectrum
k	wavenumber at the centre frequency of the filter band
$\overline{n^2}$	mean square value of electrical noise in each channel
$\overline{p^2}$	mean square pressure
P_a	sound power
Q_{12}	imaginary part of cross spectrum of microphone signals
S	surface area
S_{11}, S_{22}	power spectra of noise free microphone signals
S_{nn}	power spectrum of electrical noise
S_{pp}	power spectrum of sound pressure
T	averaging time
γ_{12}^2	coherence of microphone signals
Δf	resolution bandwidth
Δr	microphone separation distance
ε	random error
ρ	density of air
φ_{12}	phase angle between microphone signals
ω	radian frequency
ω_a, ω_b	radian band limits

Subscripts

n	pertaining to electrical noise
r	component in the r-direction

Superscripts

$\hat{}$ an estimated value

INTRODUCTION

The most important application of the sound intensity technique is the determination of the sound power of source in the presence of other sources. Other important applications include localising or identifying regions of sources with particularly strong radiation, determining radiation properties and determining transmission loss. In typical measurement conditions the sound intensity level to be measured is relatively high, and electrical noise, that is, thermal noise from the microphones and the preamplifier circuits of the intensity probe, is of no importance. However, in some cases the sound intensity level to be measured can be fairly low. One might expect some effect of the electrical noise, say, in determining the sound insulation of a partition or in determining the sound power of a relatively quiet source, but whereas there is an obvious lower limit of the dynamic range in measurement of the sound pressure, there is no correspondingly obvious lower level in estimating the sound intensity. The purpose of this paper is to examine the matter, which seems to have been ignored in the sound intensity literature. In what follows it is assumed that the intensity is determined with the usual technique based on two closely spaced pressure microphones, and that the two pressure signals are contaminated by independent electrical noise signals.

THEORY

Bias of the Estimate

As shown by Fahy[1] and Chung[2] the sound intensity spectrum is proportional to the imaginary part of the cross spectrum of the two pressure signals:

$$I_r(\omega) = -Q_{12}(\omega)/(\omega\rho\Delta r) \tag{1}$$

The noise signals that contaminate the pressure signals have no influence on the cross spectrum since they are uncorrelated and uncorrelated with the pressure signals. Therefore, quite apart from whether the sound intensity actually is determined from measured cross spectra, the formulation given by Eq. (1) leads to the important conclusion that the sound intensity estimate is unbiased, irrespective of the signal-to-noise ratio of the microphone signals However, the noise affects *estimation* of the cross spectrum by increasing the random error, which means that the averaging time must be increased accordingly.

Random Error

Various expressions for the normalised random error of sound intensity estimates have been published.[3-7] All of them are based on the assumption that the microphone signals are normally distributed; this is also assumed in the following.

Pascal[4] derived the expression

$$\varepsilon\{\hat{I}_r(\omega)\} = \left(1 + 1/\gamma_{12}^2(\omega) + \cot^2\varphi_{12}(\omega)\left(1/\gamma_{12}^2(\omega) - 1\right)\right)^{\frac{1}{2}}/\sqrt{2\Delta f T}, \tag{2}$$

where γ_{12}^2 is the coherence and φ_{12} is the phase angle between the two microphone signals, Δf is the resolution bandwidth and T is the averaging time. (The expressions published by Seybert,[3] Elko[5] and Gade[6] are, in effect, identical. None of these expressions is suitable for predicting random errors from experimental data, as pointed out in Ref. 7. However, that is not the issue here.) The coherence will usually be close to unity.[8] On the other hand it is well known that the phase angle can be very small indeed, and therefore the random error can be considerably larger than the corresponding error in sound pressure measurements, $1/\sqrt{\Delta f T}$, even in the absence of electrical noise (that is, at levels where the influence of the noise is negligible).[3,7] It is obvious that electrical noise reduces the coherence, from which it follows that such noise increases the random error, in particular in conditions where the phase angle between the sound pressure signals is small.

The coherence is defined by the expression

$$\gamma_{12}^2(\omega) = \left(C_{12}^2(\omega) + Q_{12}^2(\omega)\right)/S_{11}(\omega)S_{22}(\omega) \tag{3}$$

where C_{12} is the real and Q_{12} is the imaginary part of the cross spectrum and S_{11} and S_{22} are the two power spectra. In the presence of electrical noise the coherence becomes

$$\gamma^2_{12n}(\omega) = \left(C^2_{12}(\omega) + Q^2_{12}(\omega)\right) \Big/ \left(\left(S_{11}(\omega) + S_{nn}(\omega)\right)\left(S_{22}(\omega) + S_{nn}(\omega)\right)\right), \tag{4}$$

where S_{nn} is the power spectrum of the noise in each channel. Since

$$1/\gamma^2_{12n}(\omega) = 1/\gamma^2_{12} + \frac{S_{nn}(\omega)\left(S_{11}(\omega)\, S_{22}(\omega)\right) + S^2_{nn}(\omega)}{C^2_{12}(\omega) + Q^2_{12}(\omega)}, \tag{5}$$

it can now be seen that the normalised variance of the estimate $I_r(\omega)$ can be divided into two parts: one part that depends on the sound field, and an additional part that is due to electrical noise. The former part is independent of the sound pressure (or sound intensity) level; the latter part does, of course, depend on the level.

The normalised random error corresponding to the additional variance due to electrical noise is obtained by combining Eqs. (2) and (5):

$$\varepsilon_n\{\hat{I}_r(\omega)\} = \left(\frac{S_{nn}(\omega)\left(S_{11}(\omega) + S_{22}(\omega)\right) + S^2_{nn}(\omega)}{\left(C^2_{12}(\omega) + Q^2_{12}(\omega)\right)\sin^2\varphi_{12}(\omega)}\right)^{\frac{1}{2}} \Big/ \sqrt{2\Delta f T}. \tag{6}$$

Assuming a reasonably large signal-to-noise ratio, that is, that

$$S_{pp}(\omega) = S_{11}(\omega) = S_{22}(\omega) = C_{12}(\omega) >> S_{nn}, \tag{7}$$

where S_{pp} is the power spectrum of the sound pressure, leads to the following simple expression,

$$\varepsilon_n\{\hat{I}_r(\omega)\} = \sqrt{\frac{S_{nn}(\omega)}{S_{pp}(\omega)}}\, \frac{1}{\sin\varphi_{12}(\omega)}\, \frac{1}{\sqrt{\Delta f T}}, \tag{8}$$

which clearly shows that the additional random error can be considerable when the phase angle is small, even when the signal-to-noise ratio is fairly large.

In practice it is often useful to determine sound intensity (or sound power) levels in frequency bands, one-third octave bands, for example. The normalised random error of an estimate of the form

$$I_r = -\frac{1}{\pi\rho\Delta r}\int_{\omega_a}^{\omega_b} \left(Q_{12}(\omega)/\omega\right) d\omega \tag{9}$$

can be written as[7]

$$\varepsilon\{\hat{I}_r\} = \frac{\left(\frac{\pi}{T}\int_{\omega_a}^{\omega_b}\left[\left(S_{11}(\omega)S_{22}(\omega) - C^2_{12}(\omega) + Q^2_{12}(\omega)\right)/\omega^2\right] d\omega\right)^{\frac{1}{2}}}{\left|\int_{\omega_a}^{\omega_b}\left(Q_{12}(\omega)/\omega\right)\right|}. \tag{10}$$

The random error of a frequency band estimate is larger than the random error of a spectral estimate unless the intensity spectrum is flat within the band.[7] The additional random error that is due to electrical noise can be shown to be[9]

$$\varepsilon_n\{\hat{I}_r\} = \frac{\overline{p^2}/\rho c}{I_r}\sqrt{\frac{\overline{n^2}}{\overline{p^2}}}\, \frac{1}{k\Delta r}\, \frac{1}{\sqrt{BT}}, \tag{11}$$

where $\overline{p^2}$ is the mean square pressure, $\overline{n^2}$ is the mean square value of the electrical noise, and B is the bandwidth. Since[10]

$$\varphi_{12} = k\Delta r I_r \rho c/\overline{p^2}, \tag{12}$$

it can be seen that the expression for the additional random error of a frequency-band estimate, Eq. (11), is in agreement with the corresponding expression for spectral estimates, Eq. (8).

In practice the global random error of the result of a complete sound power estimate based on measurement at discrete points or continuous averaging (scanning) is more important than the error of a point measurement. The additional random error of a sound power estimate in a frequency band can be shown to be[9]

$$\varepsilon_n\{\hat{P}_a\} = \left(\int_S \left(\overline{p^2}/\rho c\right) dS \Big/ \int_S \vec{I}\cdot d\vec{S}\right)\sqrt{\overline{n^2}/\frac{1}{S}\int_S \overline{p^2} dS}\, \frac{1}{k\Delta r}\, \frac{1}{\sqrt{BT_{tot}}}, \tag{13}$$

where T_{tot} is the total averaging time. (Note that it is the total averaging time that matters[11]; it does not matter whether the sound field is sampled at discrete points or

continuously along a scanning path.) It is evident that this expression resembles the expression for measurement at one point, Eq. (11). The only difference is that the intensity and the mean square pressure have been replaced by surface average values. (One cannot extend Eq. (8) in such a simple manner.)

DISCUSSION

It is apparent that the additional random error that is due to electrical noise depends on the signal-to-noise ratio, on the (local or global) pressure-intensity index of the sound field, on the frequency, and on the distance between the microphones. The relationship is illustrated in Figure 1, from which it can be seen that electrical noise is a problem mainly at low frequencies. Note that an increase of the pressure-intensity index of 5 dB has the same effect as a reduction of the signal-to-noise ratio of 10 dB.

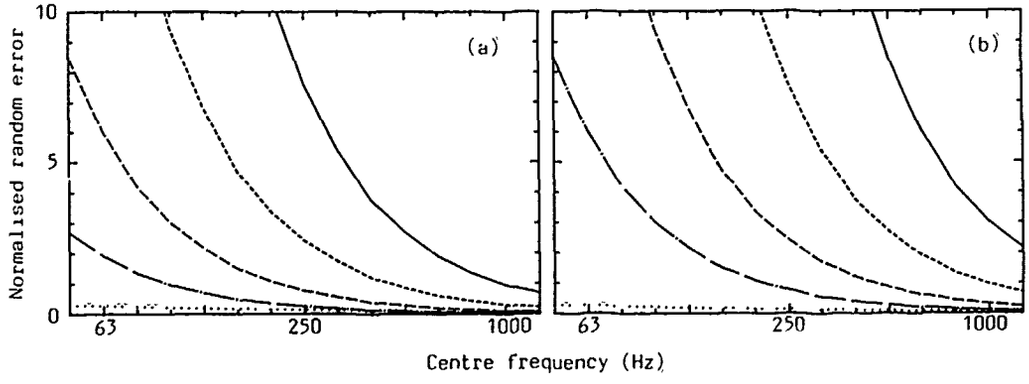

Figure 1. Normalised random error of sound intensity estimates in one-third octave bands with a microphone separation distance of 12 mm, and an averaging time of 1s. Signal-to-noise ratio: ——— , 0 dB; - - - , 10 dB; — — — , 20 dB; — • — , 30 dB. ••• , Theoretical minimum value, $1/\sqrt{BT}$. (a) Pressure-intensity index: 5 dB; (b) pressure-intensity index: 10 dB.

Typical pressure microphones used in sound intensity estimation have equivalent background noise levels of less than 20 dB re 20 μPa in one-third octave bands. One would therefore have expected the effect of electrical noise to be completely negligible in all but extreme measurement conditions, as it is in measurement of sound pressure levels. However, the effect can actually be considerable in quite realistic conditions.

This can be demonstrated by an example. If the sound intensity is determined with an intensity probe with a microphone separation distance of 12 mm in relatively mild conditions where the pressure-intensity index is 5 dB, and if the signal-to-noise ratio of the signals from the probe is 20 dB, then the normalised random error is 1.05 at 200 Hz with an averaging time of 1s. It would be reasonable to require that the error should be less than 0.058; in this case the intensity is, with a confidence level of 95%, determined within an interval of ±0.5 dB ($2 \cdot 4.34 \cdot 0.058 \approx 0.5$). To reduce the error to this level one would have to use an averaging time of about 5½ minutes ($(1.05/0.058)^2/60 \approx 5.5$). An averaging time of about five minutes is not unreasonable in a complete sound power measurement. However, to maintain the same accuracy at 100 Hz one should use an averaging time of 45 minutes. In less favourable measurement conditions the error would be larger, of course, and one would have to use a longer averaging time. If the pressure-intensity index of the sound field is 10 dB instead of 5 dB, then, with figures as above, one should use an averaging time of 55 minutes at 200 Hz and more than 7 hours at 100 Hz! In practice it is necessary to test the measurement conditions by determining various 'quality indicators' from preliminary measurements,[12-15] and therefore even a required averaging time of five minutes is rather inconvenient.

The most dramatic example of the influence of electrical noise occurs in measurement of the residual pressure-intensity index of intensity measurement systems. The residual pressure-intensity index is defined as the pressure-intensity index that is indicated by the instrument when the two microphones are exposed to the same sound pressure.[6] This quantity, which should be as large as possible, is a convenient way of describing the phase mismatch of the measurement system. At the present technical stage it is of vital importance that users of the intensity technique are aware of the influence of

phase mismatch on the measurement result, which means that the residual pressure-intensity index of the measurement system should be determined at regular intervals.[16,17] However, determining the index can be *rather* lengthy because of electrical noise. If, say, the residual pressure-intensity index of an intensity probe with a microphone separation of 12 mm is 20 dB, then an averaging time of more than twenty minutes would be required in order to determine the index within an interval of ±0.5 dB in the 125 Hz one-third octave band, even with a signal-to-noise ratio of 50 dB. With a signal-to-noise ratio of 40 dB one should use an averaging time of about four hours! Moreover, one cannot predict the averaging time that is needed owing to the fact that the residual pressure-intensity index itself enters into the prediction. (It is not self-evident that one can predict random errors from Eq. (11) when the indicated intensity is due to phase mismatch. That it is so is shown in Ref. 9.) This explains the observation that the sign of the residual intensity seems to vary randomly with time.[18] However, the problem is solved if one simply increases the sound pressure level in measuring the residual pressure-intensity index; a signal-to-noise ratio of, say, 70 dB should be sufficient.

With a microphone separation distance of 12 mm the upper frequency limit of the intensity probe is about 5 kHz.[19] The only way to extend the frequency range of 'two-microphone technique' upwards is to use smaller microphones separated by a correspondingly smaller distance. However, the smaller the microphone the higher the noise level. If, say, a microphone set of type Brüel & Kjær 4181 (i.e. ½" microphones) and a 12 mm spacer are replaced by a microphone set of type B&K 4178 (i.e. ¼" microphones) and a 6 mm spacer, then the random error will be about ten times larger,[9] from which it follows that the signal level should be about 20 dB higher if the accuracy should be maintained. The best compromise would probably be microphones with a diameter of about 9 mm separated by a 9 mm spacer.

EXPERIMENTAL RESULTS

To examine the validity of the expressions presented in the foregoing some experiments have been carried out. The sound intensity was determined with an intensity probe, B&K 3519, and a dual channel filter analyser, B&K 2133. The intensity probe was provided with three different microphone sets: a phase matched set of ½" microphones with high sensitivity, B&K 4177, a phase matched set of microphones specifically developed for intensity measurements, B&K 4181, and a phase matched set of ¼" microphones, B&K 4178. In all the measurements a microphone separation distance of 12 mm was used.

To predict the random error from Eq. (11) one must know the equivalent sound pressure level of the electrical noise. Measurements in an anechoic room gave the following results. The background noise level of the microphone set with high sensitivity is very low, less than 5 dB re 20 μPa in one-third octave bands; the corresponding noise level of the set of type B&K 4181 is about 12 dB re 20 μPa; and the ¼" microphones are rather noisy, with a noise level of about 30 dB.

The B&K 2133 analyser can be programmed to repeat a measurement any given number of times and calculate the normalised standard deviation of the results. This facility was used in determining the experimental results presented in Figure 2. The experiment took place in an anechoic room. The intensity probe was placed about 10 cm from an unenclosed loudspeaker driven with pink noise generated by the analyser, and the random error was estimated by repeating intensity measurements with an averaging time of two seconds one hundred times. These measurements were performed at three different intensity levels with the three microphone pairs. Also shown in Figure 2 are predicted values of the random error, calculated from the measured levels of the electrical noise and measured sound pressure and sound intensity levels using Eq. (11). The sound intensity level and the pressure-intensity index are shown in Figure 3.

Equation (11) seems to be confirmed; there is fair agreement between measured standard deviations and predicted random errors. Note the different ordinate axes. With the microphones of high sensitivity, B&K 4177, there is practically no influence of electrical noise; the random error approaches the theoretical minimum value of $1/\sqrt{BT}$. (The larger random error at 160 Hz is undoubtedly due to the sound field. Equation (11) does not take such random errors into account; that would require knowledge of measured power and cross power spectra.[7,11]) By contrast, it is evident that electrical noise has increased the random error significantly below 200 Hz in the measurements with the B&K - 4181 microphone set, and this effect is, of course, still more pronounced in the measurements with quarter inch microphones. It is obvious that one cannot use quarter microphones below 200 Hz even at fairly high signal levels since the averaging time must be increased prohibitively. If the normalised random error takes a value of two, say, then one would have to use an averaging time of 40 minutes ($(2/0.058)^2 \cdot 2/60 \approx 40$) in order to determine the sound intensity with 95% confidence within an interval of ±0.5 dB.

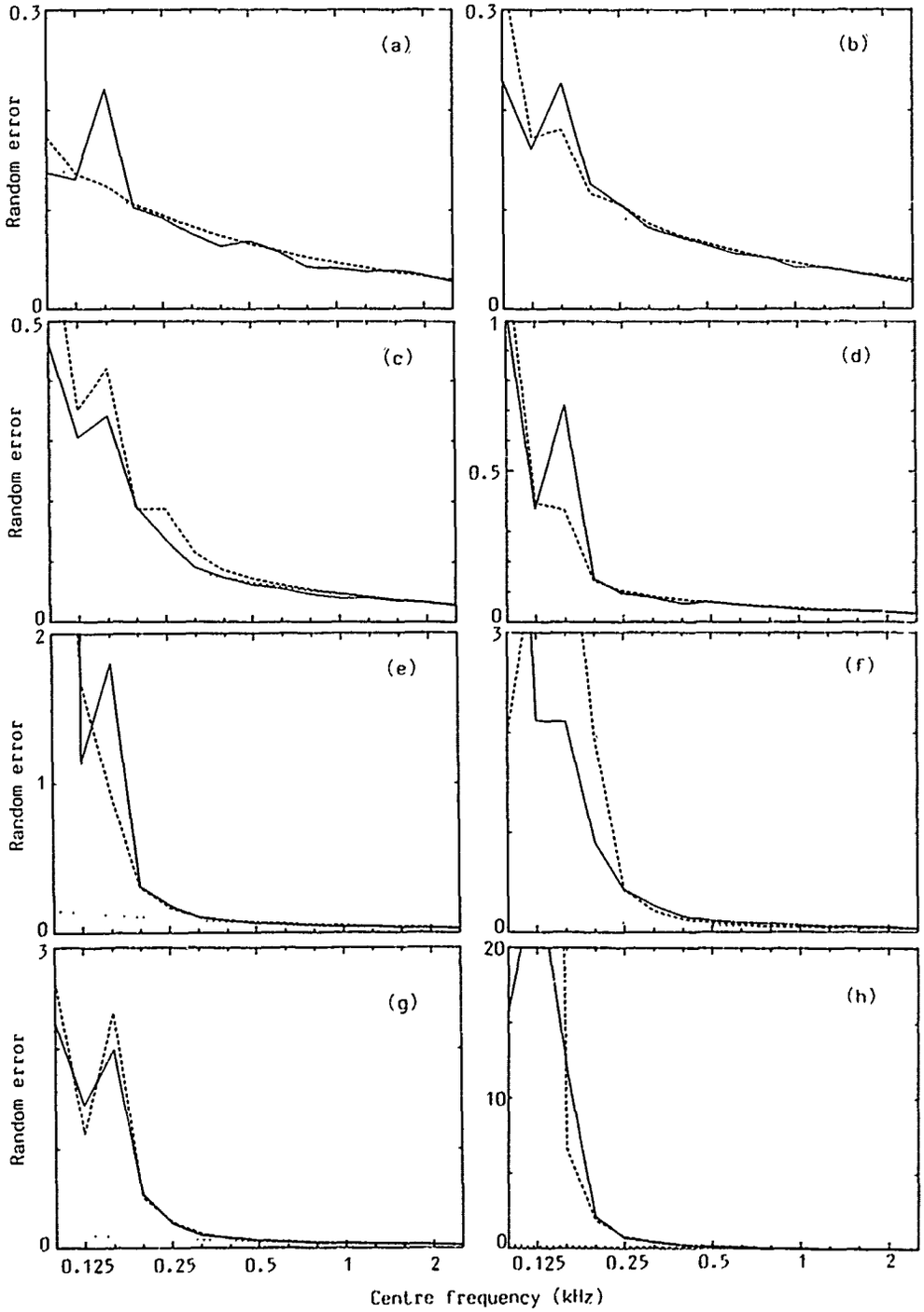

Figure 2. Normalised standard deviation of the results of 100 repeated intensity measurements near an unenclosed loudspeaker with an averaging time of 2s, compared with predicted random error. ——— , Measured standard deviation; - - - - , prediction; •••• , theoretical minimum value, $1/\sqrt{BT}$. (a),(b),(c) B&K 4177; (d),(e),(f) B&K 4181; (g),(h) B&K 4178. In (b),(e) and (h) the intensity level has been reduced by 10 dB; in (c) and (f) the intensity level has been reduced by 20 dB.

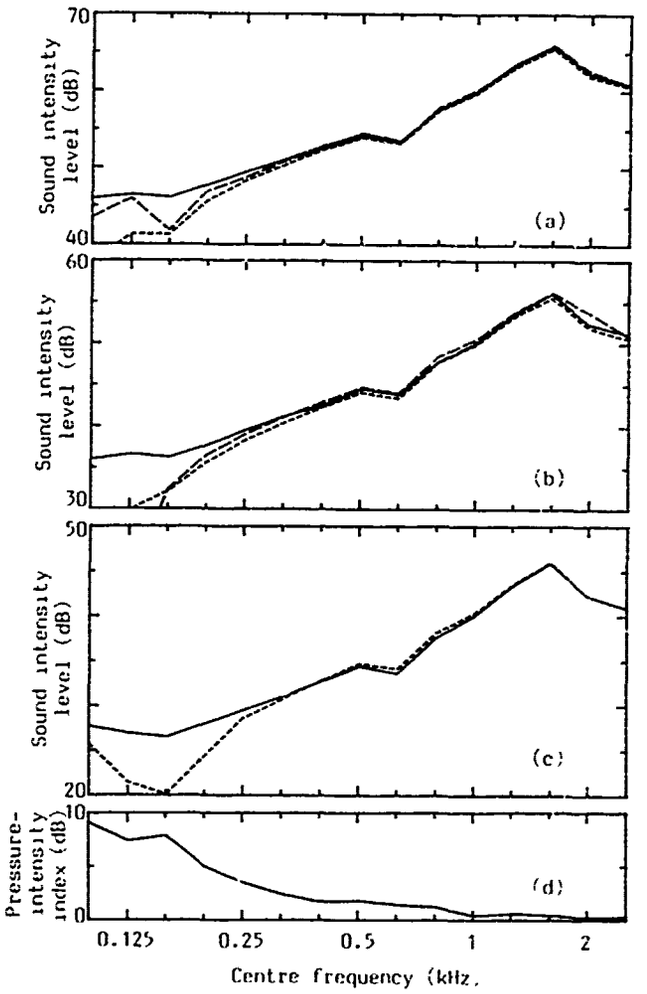

Figure 3. Measurement near an unenclosed loudspeaker driven with pink noise. (a),(b),(c) Sound intensity estimated with three different microphone sets using an averaging time of 3 minutes; in (b) the loudspeaker signal has been reduced by 10 dB; in (c) the loudspeaker signal has been reduced by 20 dB. —— , B&K 4177; - - - - , B&K 4181; — — — , B&K 4178. (d) Pressure-intensity index determined with B&K 4181.

CONCLUSIONS

Electrical noise from the microphones and preamplifiers of sound intensity probes has no systematic influence on the measured sound intensity, but it increases the random error, in particular at low frequencies, the more so the smaller the microphone separation distance. The effect of the noise is more serious than one would have expected: with standard equipment very large random errors are likely to occur if the sound power level is less than, say, 40 dB re 1 pW. The error is particularly large in adverse circumstances where the pressure-intensity index of the sound field assumes a large value, and this explains why extremely large random errors occur in measurements of the residual pressure-intensity index unless the sound pressure level is rather high.

Whereas it is possible to correct bias errors due to phase mismatch with considerable success, one cannot compensate for random errors. However, the random error - and thus the averaging time that is needed to ensure an acceptable value of the error - can easily be predicted from the intensity and the mean square pressure, provided that the equivalent sound pressure level of the electrical noise is known.

REFERENCES

1. F.J. Fahy: Measurement of Acoustic Intensity Using the Cross-Spectral Density of Two Microphone Signal. *Journal of the Acoustical Society of America* **62** (1977), 1057-1059.

2. J.Y. Chung: Cross-Spectral Method of Measuring Acoustic Intensity Without Error Caused by Instrument Phase Mismatch. *Journal of the Acoustical Society of America* **64** (1978), 1613-1616.

3. A.F. Seybert: Statistical Errors in Acoustic Intensity Measurements. *Journal of Sound and Vibration* **75** (1981), 519-526.

4. J.-C. Pascal: Mesure de l'intensité active et réactive dans differents champs acoustiques. *Proceedings of International Congress on Recent Developments in Acoustic Intensity Measurements* 1981, 11-19.

5. G.W. Elko: Frequency Domain Estimation of the Complex Acoustic Intensity and Acoustic Energy Density. Ph.D. Thesis, Pennsylvania State University 1984.

6. S. Gade: Validity of Intensity Measurements in Partially Diffuse Sound Field. *Brüel & Kjær Technical Review* **4** (1985), 3-31.

7. F. Jacobsen: Random Errors in Sound Intensity Estimation. *Journal of Sound and Vibration* **128** (1989), 247-257.

8. F. Jacobsen: Active and Reactive, Coherent and Incoherent Sound Fields. *Journal of Sound and Vibration* **130** (1989), 493-507.

9. F. Jacobsen: Sound Intensity Measurement at Low Levels. Submitted to *Journal of Sound and Vibration*.

10. U. Kurze: Zur Entwicklung eines Gerates für Komplexe Schallfeldmessungen. *Acustica* **20** (1968), 308-310.

11. F. Jacobsen: Random Errors in Sound Power Determination Based on Intensity Measurement. *Journal of Sound and Vibration* **131** (1989), 475-487.

12. G. Hübner: Sound Intensity Measurement Method - Errors in Determining the Sound Power Levels of Machines and Its Correlation With Sound Field Indicators. *Proceedings of Inter-Noise* **87** (1987), 1227-1230.

13. F. Jacobsen: Sound Field Indicators: Useful Tools. *Noise Control Engineering Journal* **35** (1990), 37-46.

14. ISO *International Standard* 9614-1 Acoustics - Determination of Sound Power Levels of Noise Sources Using Sound Intensity - Part 1: Measurement at Discrete Points (1989).

15. pANSI S12 12 Engineering Method for the Determination of Sound Power Levels of Noise Sources Using Sound Intensity (1989).

16. F. Jacobsen: A Simple and Effective Correction for Phase Mis-Match in Intensity Probes. *Applied Acoustics* **33** (1991), 165-180.

17. M. Ren and F. Jacobsen: A Simple Technique for Improving the Performance of Intensity Probes. *Noise Control Engineering Journal* (in press).

18. F.J. Fahy: Sound Intensity. Elsevier Applied Science 1989. See section 8.2.

19. S. Gade: Sound Intensity (Part II, Instrumentation and Applications). *Brüel & Kjær Technical Review* **4** (1982), 3-32.

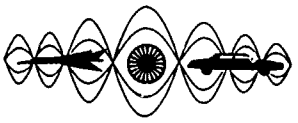

SECOND INTERNATIONAL CONGRESS ON
RECENT DEVELOPMENTS IN AIR- AND
STRUCTURE-BORNE SOUND AND VIBRATION
MARCH 4-6, 1992 AUBURN UNIVERSITY, USA

INTERFERENCE EFFECTS IN SOUND INTENSITY FIELD OF SIMPLE SOURCES

M.G. Prasad and W.S. Kim
Noise and Vibration Control Laboratory
Department of Mechanical Engineering
Stevens Institute of Technology
Hoboken, New Jersey 07030
U.S.A.

ABSTRACT

The use of sound intensity to describe acoustical field of sources is well known. The main advantage of sound intensity is in its vectorial nature. In presence of multiple simple sources, the interference effects could significantly influence the nature of the sound intensity field. This paper describes the analytical and experimental studies dealing with the effects on both sound pressure and intensity field of a point monopole source due to interference. The interference caused by interactions with other sources and/or boundary reflection are considered. The possible applications of such studies are discussed.

INTRODUCTION

The vector nature of complex acoustic intensity [1] has made intensity method useful with many applications such as source identification and ranking and sound power evaluation [2]. However, direct superposition of intensity does not hold when there are multiple coherent sources and/or nearby reflecting boundaries. Thus, the resultant intensity field of multiple sources should be obtained by not only the direct vectorial summation of intensity field of individual sources but also adding the interference due to the interaction among sources. Consequently, the intensities in near field tend to be severely influenced by interference. This interference effects on acoustic intensity field is one of the important factors which must be considered in intensity method [3,4,5].

A measurement surface with little interference is desired for power determination, source location and ranking. Therefore, an evaluation of interference in normal direction to measurement surface gives useful information both for source location and ranking and for uncertainty analysis in sound power determination. Also, the extent of interference can be used to classify the sound measurement environment. In this paper, two harmonically radiating point monopoles are used to study the interference nature in complex acoustic intensity field. The interference terms in both complex mean intensity and mean squared pressure field are formulated. Also the pressure ratio and intensity ratio are formulated to derive the practical interference indicator δ_{pI}. They are expressed as functions of acoustic frequency, geometrical parameters, relative source strength and phase difference.

The discussion on the use of δ_{pI} in this paper will be made under the assumption that the measured intensity does not suffer from the significant instrument nearfield measurements errors such as finite difference approximation errors [6] or phase mismatch error [7]. Indeed, fortunately the finite difference errors are not serious when compared to field errors introduced by interference in practical measurements and phase mismatch error can be eliminated [7,8].

The present investigation on the two simple sources offers some insight into the basic interference nature in acoustic fields and indicates that such studies of both active and reactive intensity interferences and the interference indicator δ_{pI} will have applications in both measurement and analysis aspects of acoustic intensity method.

FORMULATION OF INTERFERENCE

Based on the linearized acoustic wave equation, the pressure and particle velocity generated by two harmonic point sources can be obtained by direct superposition as long as they are point sources and thus there is no scattering due to the finite source itself.

$$\tilde{p} = \tilde{p}_1 + \tilde{p}_2 \ , \quad \tilde{u} = \tilde{u}_1 + \tilde{u}_2 \tag{1}$$

where $\tilde{}$ denotes the complex number. The mean squared pressure field and complex mean intensity field generated by two harmonic sources is given by

$$p_{rms}^2 = \tilde{p}\tilde{p}^*/2 = (\tilde{p}_1 + \tilde{p}_2)(\tilde{p}_1 + \tilde{p}_2)^*/2 \tag{2}$$

$$\tilde{I} = \tilde{p}\tilde{u}^*/2 = (\tilde{p}_1 + \tilde{p}_2)(\tilde{u}_1 + \tilde{u}_2)^*/2 \tag{3}$$

where * denotes the complex conjugate.
Above equations can be rewritten as

$$p_{rms}^2 = (p_{rms}^2)_d + (p_{rms}^2)_i \ , \quad \tilde{I} = \tilde{I}_d + \tilde{I}_i \tag{4}$$

where the subscripts d and i denote the direct term and interference term respectively.

The direct terms is obtained by superposition of fields of each individual source in free space.

$$(p_{rms}^2)_d = (p_{rms}^2)_1 + (p_{rms}^2)_2 = (p_1^2 + p_2^2)/2 \tag{5}$$

$$\tilde{I}_d = \tilde{I}_1 + \tilde{I}_2 = (\tilde{p}_1\tilde{u}_1^* + \tilde{p}_2\tilde{u}_2^*)/2 \tag{6}$$

Therefore the interference terms become

$$(p_{rms}^2)_i = (\tilde{p}_1\tilde{p}_2^* + \tilde{p}_2\tilde{p}_1^*)/2 \ , \quad \tilde{I}_i = (\tilde{p}_1\tilde{u}_2^* + \tilde{p}_2\tilde{u}_1^*)/2 \tag{7}$$

The real part of complex mean intensity vector $\tilde{I}$ is well known active intensity and the imaginary part of complex mean intensity vector $\tilde{I}$ is reactive intensity. From now on, active mean intensity vector will be denoted as **I** and the reactive mean intensity vector will be denoted as **J** in this paper.

The (nondimensional) geometrical description of the two simple sources is shown in Fig. 1 and given by,

$$(kr_2)^2 = (kr_1)^2 + (kh)^2 + 2(kh)(kr_1)\cos\theta \tag{8}$$

where k is wave number and r_1 is the distance of a primary source from a field point and r_2 is the distance of the secondary source from a field point and h is the separation distance between two sources and the angle θ represents the direction of a field point with regard to the line connecting the centers of sources.

The pressure and particle velocity vector of a primary point harmonic monopole with strength $Q_1(t)$ is given by,

$$\tilde{p}_1 = Q_1(t)\,\frac{e^{-jkr_1}}{r_1} \ , \quad \tilde{u}_1 = Q_1(t)\,\frac{(j - kr_1)}{kz_o}\,\frac{e^{-jkr_1}}{r_1^2}\,\hat{e}_1 \tag{9}$$

Likewise, for a secondary source we have

$$\tilde{p}_2 = Q_2(t)\,\frac{e^{-jkr_2}}{r_2} \ , \quad \tilde{u}_2 = Q_2(t)\,\frac{(j - kr_2)}{kz_o}\,\frac{e^{-jkr_2}}{r_2^2}\,\hat{e}_2 \tag{10}$$

where $\hat{e}_1$ denotes the radial unit vector in r_1 direction and $\hat{e}_2$ denotes the radial unit vector in r_2 direction and $z_o(=\rho_o c_o)$ denotes the specific impedance of medium. And $\hat{e}_2$ can be rewritten as

$$\hat{e}_2 = \delta\,\hat{e}_1 + \epsilon\,\hat{e}_\theta \tag{11}$$

where $\hat{e}_\theta$ is the transverse unit vector with regard to θ in Fig. 1, and δ and ϵ are given in Eq. (8) by

$$\delta = \frac{\partial r_2}{\partial r_1} = (r_1 + h\cos\theta)/r_2 \ , \quad \epsilon = \frac{\partial r_2}{r_1 \partial\theta} = -h\sin\theta/r_2 \tag{12}$$

The source strengths with a phase difference β are given by

$$Q_1(t) = Q_1\, e^{j\omega t} \quad , \quad Q_2(t) = Q_2\, e^{j(\omega t - \beta)} \tag{13}$$

The mean squared pressure and active and reactive mean intensity for a primary monopole without interference in free space are

$$(p^2_{\rm rms})_1 = \frac{Q_1^2}{2r_1^2} \quad , \quad \mathbf{I}_1 = \frac{Q_1^2}{2z_o r_1^2}\,\hat{e}_1 = \frac{(p^2_{\rm rms})_1}{z_o}\,\hat{e}_1 \quad , \quad \mathbf{J}_1 = \frac{Q_1^2}{2kz_o r_1^3}\,\hat{e}_1 = \frac{(p^2_{\rm rms})_1}{kz_o r_1}\,\hat{e}_1 \tag{14}$$

The similar expression for a secondary source without interference can be obtained.

Pressure Interference

From Eqs. (5) and (14), the direct term in mean squared pressure is

$$(p^2_{\rm rms})_{\rm d} = \frac{Q_1^2}{2r_1^2} + \frac{Q_2^2}{2r_2^2} \tag{15}$$

Plugging Eqs. (9) and (10) into Eq. (7), the interference in mean squared pressure fields is given by

$$(p^2_{\rm rms})_{\rm i} = \frac{Q_1 Q_2}{r_1 r_2}\cos\alpha \tag{16}$$

where $\alpha = (kr_1 - kr_2 - \beta)$. Defining the mean squared pressure divided by mean squared pressure of a primary source without interference as the pressure ratio $P_{\rm R}$, we have

$$P_{\rm R} = \frac{(p^2_{\rm rms})}{(p^2_{\rm rms})_1} = \frac{(p^2_{\rm rms})_{\rm d} + (p^2_{\rm rms})_{\rm i}}{(p^2_{\rm rms})_1} = 1 + Q_o^2 R_o^2 + 2Q_o R_o \cos\alpha \tag{17}$$

where $Q_o = Q_2/Q_1$ and $R_o = r_1/r_2$.

Intensity Interference

From Eqs. (11) and (14), the direct term in active intensity vector becomes

$$\begin{aligned} \mathbf{I}_{\rm d} &= \mathbf{I}_1 + \mathbf{I}_2 = I_1\,\hat{e}_1 + I_2\,\hat{e}_2 = (I_1 + \delta\, I_2)\,\hat{e}_1 + \epsilon\, I_2\,\hat{e}_\theta \\ &= \left(\frac{Q_1^2}{2z_o r_1^2} + \delta\,\frac{Q_2^2}{2z_o r_2^2}\right)\hat{e}_1 + \epsilon\,\frac{Q_2^2}{2z_o r_2^2}\,\hat{e}_\theta \end{aligned} \tag{18}$$

Likewise, the direct reactive intensity vector is

$$\begin{aligned} \mathbf{J}_{\rm d} &= \mathbf{J}_1 + \mathbf{J}_2 = J_1\,\hat{e}_1 + J_2\,\hat{e}_2 = (J_1 + \delta\, J_2)\,\hat{e}_1 + \epsilon\, J_2\,\hat{e}_\theta \\ &= \left(\frac{Q_1^2}{2kz_o r_1^3} + \delta\,\frac{Q_2^2}{2kz_o r_2^3}\right)\hat{e}_1 + \epsilon\,\frac{Q_2^2}{2kz_o r_2^3}\,\hat{e}_\theta \end{aligned} \tag{19}$$

Plugging Eqs. (9) and (10) with Eq. (11) into Eq. (7), the interference term in active intensity becomes

$$\mathbf{I}_{\rm i} = \frac{Q_1 Q_2}{2z_o r_1 r_2}\left[\left\{(1+\delta)\cos\alpha + (R_o\delta - 1)\frac{\sin\alpha}{kr_1}\right\}\hat{e}_1 + \epsilon\left\{\cos\alpha + \frac{\sin\alpha}{kr_2}\right\}\hat{e}_\theta\right] \tag{20}$$

And the interference term in reactive intensity becomes

$$\mathbf{J}_{\rm i} = \frac{Q_1 Q_2}{2z_o r_1 r_2}\left[\left\{(1-\delta)\sin\alpha + (R_o\delta + 1)\frac{\cos\alpha}{kr_1}\right\}\hat{e}_1 + \epsilon\left\{\frac{\cos\alpha}{kr_2} - \sin\alpha\right\}\hat{e}_\theta\right] \tag{21}$$

Defining the active intensity vector divided by active intensity of a primary source without interference as the active intensity ratio vector $\mathbf{I}_{\rm R}$ [4,9], we have

$$\begin{aligned} \mathbf{I}_{\rm R} &= \frac{\mathbf{I}}{I_1} = \frac{\mathbf{I}_{\rm d} + \mathbf{I}_{\rm i}}{I_1} \\ &= \left[1 + \delta Q_o^2 R_o^2 + Q_o R_o\left\{(1+\delta)\cos\alpha + (R_o\delta - 1)\frac{\sin\alpha}{kr_1}\right\}\right]\hat{e}_1 \\ &\quad + \epsilon\left[Q_o^2 R_o^2 + Q_o R_o\left\{\cos\alpha + \frac{\sin\alpha}{kr_2}\right\}\right]\hat{e}_\theta \end{aligned} \tag{22}$$

Likewise, the reactive intensity ratio vector $\mathbf{J}_R$ is

$$\begin{aligned}\mathbf{J}_R &= \frac{\mathbf{J}}{J_1} = \frac{\mathbf{J}_d + \mathbf{J}_i}{J_1} \\ &= [1 + \delta Q_o^2 R_o^3 + Q_o R_o\{(1-\delta)kr_1 \sin\alpha + (R_o\delta + 1)\cos\alpha\}]\,\hat{e}_1 \\ &\quad + \epsilon\,[Q_o^2 R_o^3 + Q_o R_o\{R_o\cos\alpha - kr_1\sin\alpha\}]\,\hat{e}_\theta \end{aligned} \tag{23}$$

The similar expressions of the intensity ratio are also found in Ref. [3,10,11].

Though the interference terms given by Eqs. (16), (20), and (21) may represent the amount or direction in interference, due to the difficulty in direct measurements of interference terms, a few indirect methods to evaluate the degree of *interference effects* has been sought in some references [4, 12]. For practical use, the most reliable one to indicate the interference seems to be δ_{pI} which is one of the field indicators for the characterization of environments [13]. Forssen and Crocker [14] have discussed the use of a pressure-intensity index δ_{pI} defined as $|L_p - L_I|$ in conjunction with the finite difference error in intensity measurements and Gade [15] describes the use of δ_{pI} referred to as an reactivity index in validity of intensity measurements. δ_{pI} is termed as an interference indicator in Ref. [12] and has good correspondence with the formulation of an interference index L_x in Ref. [5]. When the field point is in far field where the interference effect is assumed to be absent or very weak, the following relationship between the mean intensity and mean squared pressure is well known.

$$I \approx p_{rms}^2/z_o \quad \text{or} \quad \delta_{pI} \approx 0 \tag{24}$$

It is easily observed that the statement of Eq. (24) is equivalent to the fact that the interference terms are absent in Eqs. (16) and (20).

Using mean pressure ratio P_R in Eq. (17) and the magnitude of active intensity ratio vector $\mathbf{I}_R$ with regard to a specific direction in Eq. (22), the interference indicator δ_{pI} can be formulated as following.

$$\begin{aligned}\delta_{pI} &= |L_p - L_I| = |10\log\frac{p_{rms}^2}{400I}| \\ &\approx |10\log\frac{p_{rms}^2}{z_o I}| = |10\log P_R/I_R| = L_x \end{aligned} \tag{25}$$

The complete formulation of δ_{pI} for the case of two point monopoles is obtained from Eqs. (17) and (22).

EXPERIMENTAL WORK

In order to verify the theoretical formulations, some experiments were conducted. Two small enclosed speakers ($Q_o = 1$) were used as monopole sources. The evaluation of acoustic quantities for this study was carried out in an anechoic chamber using FFT analyzer and real time intensity analyzer (B&K Type 4433) and side-by-side two-microphone (phase matched) probe. Experimental set-up is shown in Fig. 2. The interference due to the secondary source was introduced using a on/off switch. P_R and I_R at a certain field point are obtained directly from the measured pressure level L_p and the measured intensity level L_I through two microphones placed along the radial direction. The phase change between two sources is done by the polarity switch.

RESULTS AND DISCUSSIONS

The experimental results in Figs. 3 and 4 are compared to the predicted value based on Eqs. (17) and (22), for the radial interference indicator as given by $(\delta_{pI})_r = 10\log(I_R)_r/P_R$. Fig. 4 is for the case of passive interference due to hard reflecting panel [5]. It is observed that as r_1/h increases, the interference amplitude increases because the intensity was measured in the radial direction of source 1. The experimental results show good agreement with the analysis.

Using Eqs. (18)-(21), the coupled acoustic intensity vector field with interference can be decomposed into direct pattern and interference pattern. Figs. 5 and 6 illustrate the decomposition of active and reactive intensity vector for the case of $Q_o = 2$ out of phase with nondimensional separation distance $kh = 0.5$ and $kh = 25$ respectively (the plotted vector magnitudes scales $\propto I^{1/8}$). At low frequency ($kh = 0.5$), it is observed in Fig. 5 that the active intensity vector field is severely distorted from the direct field whereas the reactive intensity vector field suffer less from the interference effect. At high frequency ($kh = 25$) in Fig. 6, the case is the reverse.

Fig. 5 clearly demonstrates the fact that the weaker radiator take a role of active power sink due to the interference field. This is because the power radiated from the weak source is affected by the pressure field

produced by the other nearby source with phase difference. However, it should be noted that the weak monopole still constitutes an active source when $kh = 25$ (in this case, the separation distance h is greater than wavelength as seen in Fig. 6). The intensity field contaminated by the strong interference in near field often makes it difficult identifying sources, and determining the individual power of primary source of interest or using the evaluated total power for noise control, especially when the measurement surface is close to the extended sources. The detail on the effect of interference in this respect is well discussed by Fahy [16]. Also, it is noted that the weak monopole is always reactive power source even though the wavelength is greater than h and the phase difference exists in Figs. 5 and 6. This nature indicates that reactive intensity may give useful information in source location and ranking. The possible use of reactive intensity mapping for better source location was discussed in Ref. [17,11].

The sound power radiated from a primary source is obtained by integrating the acoustic intensity over any surface enclosing the source. When there are two monopoles in free space and the measurement surface S encloses only primary source 1, the surface integration of complex mean intensity is

$$\begin{aligned} \int_S \tilde{\mathbf{I}}\, \mathbf{n} dS &= \int_S (\tilde{\mathbf{I}}_\mathrm{d} + \tilde{\mathbf{I}}_\mathrm{i})\, \mathbf{n} dS \\ &= \int_S (\tilde{I}_1 + \tilde{\mathbf{I}}_2)\, \mathbf{n} dS + \int_S (\tilde{\mathbf{I}}_\mathrm{i})\, \mathbf{n} dS = \int_S \tilde{\mathbf{I}}_1\, \mathbf{n} dS + \int_S (\tilde{\mathbf{I}}_\mathrm{i})\, \mathbf{n} dS \end{aligned} \tag{26}$$

As seen in above equation, if the interference term $\tilde{\mathbf{I}}_\mathrm{i}$ is negligible and consequently the total intensity is about the same as the direct intensity on measurement surface, main advantage of using intensity for power evaluation is that the measurement of intensities over the surface gives the power of primary source 1, regardless of the presence of other steady sources outside measurement surface. However, if the interference on measurement surface is considerable, the field error in sound power of the source is expected as much as

$$\int_S (\tilde{\mathbf{I}}_\mathrm{i})\, \mathbf{n} dS = \int_S (\tilde{p}_1 \tilde{\mathbf{u}}_2^* + \tilde{p}_2 \tilde{\mathbf{u}}_1^*)\, \mathbf{n} dS \tag{27}$$

As the estimation of sound power using intensity was based on Eq. (26), measurement surface in the region with strong interference should be avoided for more precise power evaluation of a source. It should be noted that the fact δ_pI is nearly zero ($L_\mathrm{I} \approx L_\mathrm{p}$) or interference is negligible does not necessarily imply the validity for use of sound pressure for sound power determination. It is evident that the sound pressure can be used to find power of primary source 1 when only $\tilde{\mathbf{I}}_1$ is nonzero in Eq. (26). The comparison of sound power evaluation, using both pressure and intensity is shown in [18].

The advantage of using intensity over using pressure in source location is well described in Fig. 7. It is evident that the intensity map gives clearer location of sources. However, even when the intensity is being used, it can be seen in Figs. 5 and 6 that the interference effects in near field makes it difficult simply locating and ranking the individual sources. The actual field is the direct field plus the additive interference field, and the negative effect of interference should be considered when the effective source identification is desired.

For δ_pI and intensity maps, the normal components of intensities to measurement surface will be taken and the measurement surface is d m above two monopoles. Fig. 8 shows the active intensity map and reactive intensity map in dB scale as well as interference indicator δ_pI when $d = 0.25$ m, $Q_o = 1$ in phase and the nondimensional separation distance kh is 0.5, 5, and 25 respectively. It is noted in Fig. 8 that δ_pI always shows minimum around the location of monopoles. This results suggest another possibility in use of δ_pI in source location. However, using the complex intensity (both active and reactive) together with δ_pI under the consideration of the effect of interference rather than depending only one of them will give better and more accurate source location and ranking in any case.

CONCLUSIONS

Given that the actual sound field which is produced by multiple sources and the reflecting boundaries surrounding sources is more complicated, the observations from present studies on ideal field by two simple sources reflect the nature of complexity of the interference. The study reported in this work has dealt with the nature of interference in complex intensity field. The interference terms in both mean squared pressure and complex mean intensity which are usually measured with dB scale in practice are separated from the total acoustic field and formulated. And the effect of interference was depicted by the means of visualization of the radiation pattern. Also, the relative intensity error was calculated as the interference term divided by the primary sound field.

Based on these formulations, the interference indicator δ_pI defined as the level difference between sound pressure and intensity can be formulated with respect to a certain direction (mostly the normal direction to measurement surface). Since the relative intensity error is unmeasurable, the use of δ_pI in source identification

and source power determination using intensity was examined in respects of interference effect represented by the relative intensity errors.

The formulations of δ_{pI} was confirmed with the experimental results for a few cases. The results indicate that δ_{pI} can be used for uncertainty analysis in sound power evaluation, and δ_{pI} can help the source identification together with the visualization of the interference in both active and reactive radiation patterns. Finally it should be mentioned that δ_{pI} may be inadequate to reflect these interference effects discussed in this paper if the instrument errors is significant on the measurement points.

REFERENCES

1. G.W. Elko and J. Tichy, "Measurement of the Complex Acoustic Intensity and the Acoustic Energy Density," *Proc. of Inter-Noise 84*, 1984, 1061-1064
2. J.C. Pascal, J. Lu, "Advantage of Vectorial Nature of Acoustic Intensity to describe Sound Fields," *Proc. of Inter-Noise 84*, 1984, 1111-1116
3. G. Krishnappa, "Acoustic Intensity in the Near field of Two Interferencing Monopoles," *J. Acoust. Soc. Am.* **74**(4), 1983, 1291-1294
4. S.Y. Ham, W. Kim and M.G. Prasad, "Interference Studies of Acoustic Pressure and Intensity Fields of Two Simple Sources," *J. Acoust. Soc. Am.* **90**(2), Pt. 1, 1991, 1149-1154
5. W.S. Kim and M.G. Prasad, "An Index to Characterize the Pressure-Intensity Field of an Acoustic Source with Interference," *Proc. of Inter-Noise 89*, 1989, 959-964
6. J.K. Thompson and D.R. Tree, "Finite Difference Approximation Errors in Acoustic Intensity Measurements," *J. Sound and Vibration*, **75**, 1981, 229-238
7. J.Y. Chung, "Cross-Spectral Method of Measuring Acoustic Intensity Without Error Caused by Instrument Phase Mismatch," *J. Acoust. Soc. Am.* **64**(6), 1978, 1613-1616
8. F. Jacobsen, "A Simple and Effective Correction for Phase Mismatch in Intensity Probes," *Applied Acoustics*, **33**, 1991, 165-180
9. W.S. Kim, "On the Development of an Index to describe the Acoustic Field of Interfering Sources with Applications to Intensity and Power Determination," Master's Thesis, Stevens Institute of Technology, 1989
10. G. Krishnappa, "Sound Intensity in the Near field of a Point Source Over a Hard Reflecting Plane," *Proc. of Second International Congress on Acoustic Intensity, Senlis, France*, September, 1985
11. M. Ren, "Complex Intensity and Nearfield Description," The Acoustic Laboratory, Technical University of Denmark, Report No. 46, 1991
12. Working Group S12-21, "Engineering Method for Determination of Sound Power Levels of Noise Sources Using Sound Intensity," Draft-Standard, 1986
13. G. Huebner, "Recent Development of Requirements for an Intensity Measurements Code Determining Sound Power Level of machines," *Proc. 2nd International Conference on Acoustic Intensity, CETIM, Senlis, France*, 1985, 307-318
14. B. Forssen and M.J. Crocker, "A General Formulation of Finite Difference Error and the Level Difference between Sound Pressure and Sound Intensity near an Arbitrary Source Distribution on a Surface," *Proc. of Inter-Noise 84*, 1984, 1071-1076
15. S. Gade, "Validity of Intensity Measurements," *Proc. of Inter-Noise 84*, 1984, 1077-1082
16. F.J. Fahy, "Sound Intensity," Elsevier, London and New York, 1989
17. F. Jacobsen, "Sound Field Indicators: Useful Tools," *Noise Control Engineering J.*, **35**, 1990, 37-46
18. D.M. Yeager, "A Comparison of Intensity and Mean Pressure Methods for Determining Sound Power Using a Nine Point Microphone Array," *Noise Control Engineering J.*, May-June, 1984, 86-95

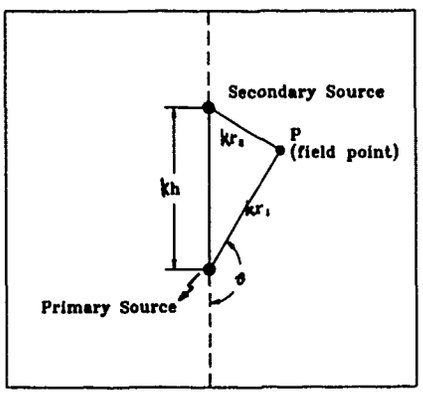

Fig. 1: The (nondimensional) geometrical configuration of two simple sources

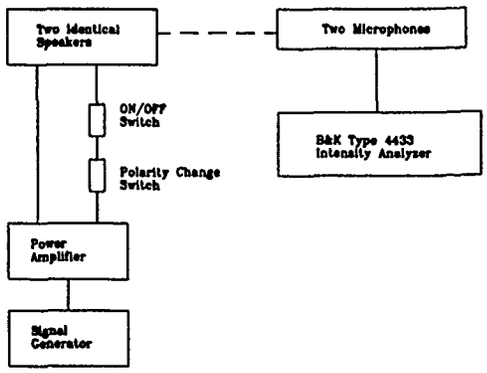

Fig. 2: Diagram of experimental setup.

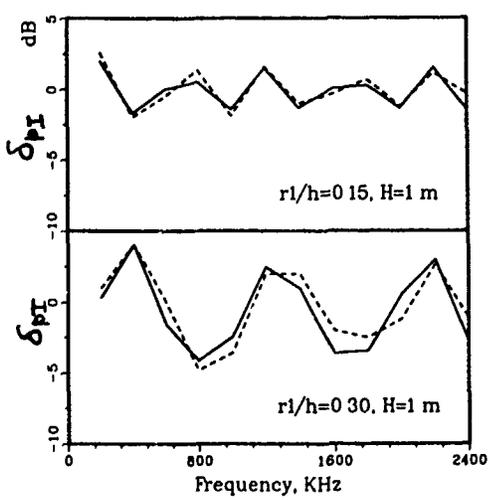

Fig. 3: Experimental results of radial component of δ_{pI} at field points ($\theta = \pi$), (a) $r_1/h = 0.15$ (b) $r_1/h = 0.3$, when $Q_s = 1$, in phase (solid lines: analysis, dashed lines:experiment).

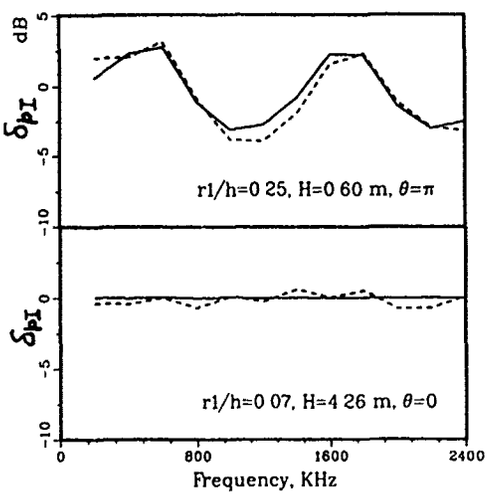

Fig. 4: Experimental results of radial component of δ_{pI} at field points (a) $\theta = \pi$, $r_1/h = 0.25$ (b) $\theta = 0$, $r_1/h = 0.07$, when $Q_s = 1$, in case of passive interference due to hard reflecting panel (solid lines: analysis, dashed lines:experiment).

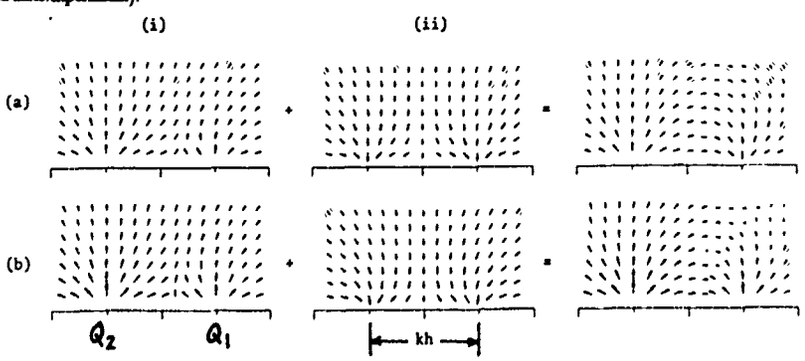

Fig. 5: Description of decomposition of actual (a) active intensity, (b) reactive intensity field into (i) direct field and (ii) interference field when $kh = 0.5$.

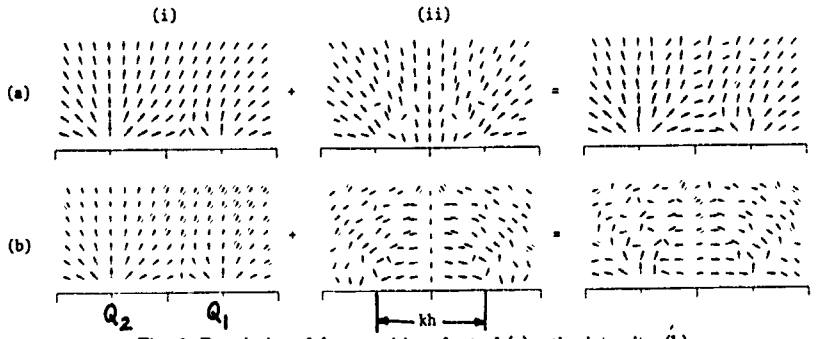

Fig. 6: Description of decomposition of actual (a) active intensity, (b) reactive intensity field into (i) direct field and (ii) interference field when $kh = 25$.

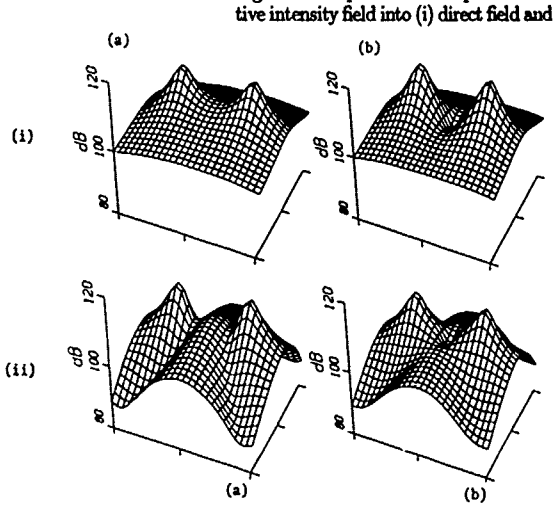

Fig. 7: Comparison between (a) pressure mapping and (b) intensity when $Q_o = 1$ in phase and (i) $kh = 0.5$, (ii) $kh = 5$.

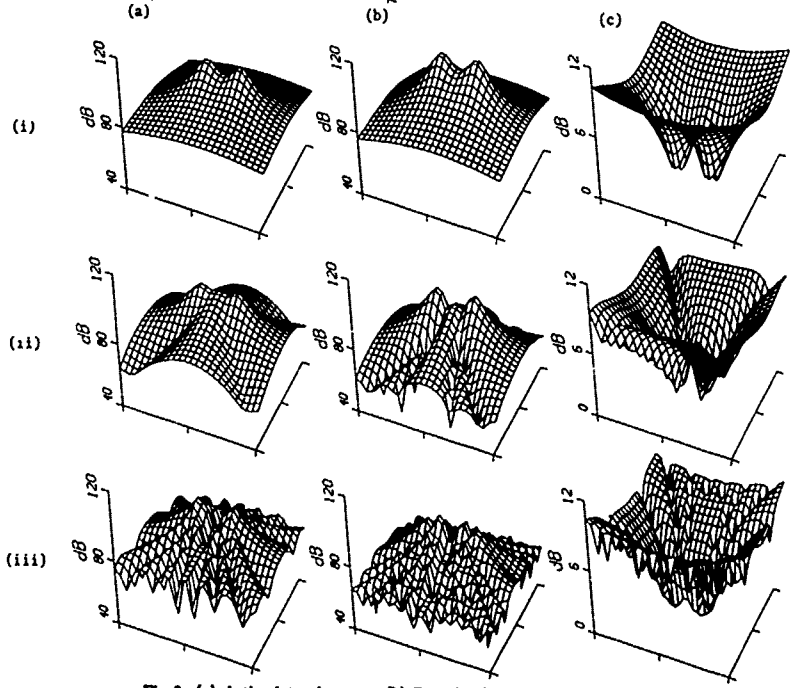

Fig 8: (a) Active intensity map, (b) Reactive intensity map, (c) δ_{pI} map for source locations when $Q_o = 1$ in phase and the measurement surface is 0.25 m above the sources and (i) $kh = 0.5$, (ii) $kh = 5$, (iii) $kh = 25$.

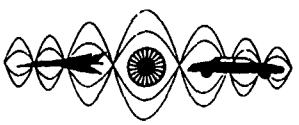

SECOND INTERNATIONAL CONGRESS ON
RECENT DEVELOPMENTS IN AIR- AND
STRUCTURE-BORNE SOUND AND VIBRATION
MARCH 4-6 1992 AUBURN UNIVERSITY, USA

EXPERIMENTAL STUDY ON THE APPLICATION OF UNDERWATER ACOUSTIC INTENSITY MEASUREMENTS

Eric Stusnick and Michael J. Lucas
Wyle Laboratories
Arlington, Virginia 22202
U.S.A.

ABSTRACT

This paper reports on the improvement in the signal-to-noise ratio of underwater sound measurements that is possible through the use of acoustic intensity measurements. These measurements were made in a lake and flooded dry dock. The acoustic intensity probe was made from a pair of hydrophones that was oriented to measure the horizontal component of sound. Simple sound sources were used to demonstrate that it is possible to obtain an improvement in the signal-to-noise ratio by reducing the background surface noise.

INTRODUCTION

With the increase in relatively inexpensive data processing hardware, acoustic intensity has become the method of choice in measuring airborne sound power. In the past several years, measurement of acoustic intensity has become a technique regularly used in field work and no longer has the flair of an innovative research tool. The common use of acoustic intensity has not occurred in underwater applications, however, and its use there still remains a research topic.

Acoustic intensity measurements offer benefits not easily attainable using traditional underwater instrumentation, such as ordinary and gradient hydrophones. Acoustic intensity instrumentation measures both the scalar sound pressure and the vector acoustic intensity. In many cases, acoustic intensity can improve the signal-to-noise ratio, as compared to pressure measurements, making it easier to discriminate between the source of interest and the background noise.

This can be seen in Figure 1, which shows the total acoustic intensity vector, $\vec{I}_T$, at the measurement point P. In the figure, $\vec{I}_T$ has been decomposed into two components: the acoustic intensity vector, $\vec{I}_S$, from the source of interest, S, and the ambient acoustic intensity vector, $\vec{I}_B$, from all background sources (e.g., sea source noise, oceanic turbulence, distant ship traffic).

An intensity component measurement made along the direction of $\vec{I}_S$ will consist of the sum of the source intensity and the component of the ambient intensity along the direction of the measurement. A scalar pressure measurement made at the point P will consist of the energy sum of the source pressure contribution and the total ambient pressure contribution. If the ambient intensity vector is oriented in a different direction than the source intensity vector, as shown in the figure, the result will be a smaller background contribution to the intensity component measurement than to the pressure measurement, with a corresponding improvement in signal-to-noise ratio.

This paper reports on demonstrations of the improvement in signal-to-noise ratio possible through the use of acoustic intensity rather than sound pressure to define underwater acoustic signatures. These demonstrations were conducted on a lake in central Virginia and in a coastal dry dock.

INSTRUMENTATION

Data collection, processing, and plotting were accomplished using a Wyle-developed hardware/software system called General Acoustic Intensity Measurement System (GAIMS). The system used in these experiments evolved from earlier systems that were developed for the U.S. Navy. This work dates back to the earlier 1980s and discussions on these earlier measurement programs and systems can be found in References 1 to 6.

GAIMS is hosted on a 9000 Series 300 Hewlett-Packard computer. By means of a IEEE-488 bus, GAIMS downloads spectral data from a Scientific-Atlanta Model SD380Z two-channel spectrum analyzer. Two Ithaco Model 451 amplifiers are used to condition the signal from the hydrophone pair before sampling by the analyzer.

The acoustic intensity probe is constructed from two International Transducers Corporation Model 6050C hydrophones. A distance of 0.7 meter separates the two elements. This probe configuration has a working frequency range of 1 to 10 kHz. The probe bias error exceeds 1.5 dB above 5 kHz and increases as the frequency increases. Probe bias error is the sum of the bias errors due to the finite gradient approximation, the existence of uncorrected phase differences between the signal channels, and the uncertainty in defining the distance between the two transducer elements.

DEFINITION OF EQUIVALENT PRESSURE

In order to be able to compare intensity measurements directly with pressure measurements, the vector intensity measurements were converted to scalar equivalent pressure measurements. The equivalent pressure corresponding to a given intensity (or component) is defined as the pressure that would be measured for that intensity if the wavefront of the sound signal were plane or spherical.

A simple relation exists between pressure, p, and the magnitude of intensity, $|\vec{I}|$, for a locally plane:

$$|\vec{I}| = p^2/\rho c \tag{1}$$

where ρ is the density of the medium through which the wave propagates, and c is the speed of sound in that medium. Values of the acoustic impedance, ρc, are on the order of 1,500,000 mks rayls for water. The equivalent pressure for all types of waves can be defined as:

$$p_e = \left(\rho c\,|\vec{I}|\right)^{1/2} \tag{2}$$

This equivalent pressure will only be equal to the measured pressure for intensity measurements made in local plane fields and along the direction of propagation of the acoustic energy. Along other directions in such fields, the equivalent pressure will always be less than the measured pressure, since it represents only the component of the energy flow along the direction of the intensity measurement while the pressure represents the total energy flow.

If p_S is the sound pressure corresponding to the acoustic energy from the source and p_B is the sound pressure corresponding to acoustic energy from the noise background, then the normal signal-to-noise ratio (in decibels) for a receiver in the far field is:

$$\text{SNR} = 10\log_{10}\frac{p_S^2}{p_B^2} = 10\log_{10}\frac{\rho c\,|\vec{I}_S|}{\rho c\,|\vec{I}_B|} = 10\log_{10}\frac{|\vec{I}_S|}{|\vec{I}_B|} \tag{3}$$

where $|\vec{I}_S|$ and $|\vec{I}_B|$ are the magnitude of the source and background acoustic intensity vectors, respectively.

The signal-to-noise ratio of the equivalent pressure of source background, $(p_e)_S$ and $(p_e)_B$, respectively, which correspond to intensity component measurements in the direction of $\vec{I}_S$ is:

$$(SNR)_e = 10 \log_{10} \frac{(p_e^2)_S}{(p_e^2)_B} = 10 \log_{10} \frac{\rho c \left|\vec{I}_S\right|}{\rho c \left|\vec{I}_B\right| \left|\cos\theta\right|} = SNR - 10 \log_{10} \left|\cos\theta\right| \quad (4)$$

where θ is the angle between the source intensity vector and the background intensity vector (see Figure 1) which, due to the nature of the ambient noise, will generally be a function of frequency.

Thus the improvement possible in signal-to-noise ratio by the use of equivalent pressure measurements is:

$$(SNR)_e - SNR = -10 \log_{10} \left|\cos\theta\right| \quad (5)$$

Although this simple model does not take into account many practical factors, such as the effects of changes in the direction and magnitude of both the source and background intensity vectors, while spectral measurements are being made, it does indicate that signal-to-noise improvements are at least feasible.

In general, the net horizontal intensity component of isotropic sea surface noise is expected to be small. This can be seen in Figure 2, which shows acoustic intensity components from two elements of sea surface symmetrically located on each side of the measurement point, P. The horizontal component, $\vec{I}_{H1}$, of the intensity vector due to element 1 is equal and oppositely directed to the horizontal component, $\vec{I}_{H2}$, of the intensity vector due to element 2. Thus the two components cancel, resulting in a zero net horizontal intensity component. If the sea surface is isotropic, then the net horizontal intensity components for all such pairs of elements are zero, so that no net horizontal sea state intensity component exists at the measurement point.

Thus measurements of the horizontal component of a source's radiated acoustic intensity will not be contaminated by background contributions from wave motion on the sea surface. Instead, the lowest measurable horizontal component of the source's radiated intensity will be governed by the net horizontal intensity component of distant ship traffic, which cannot be expected to be isotropic.

SURFACE NOISE CANCELLATION EXPERIMENT

Figure 3a shows the experimental setup used to demonstrate surface noise cancellation. Two water sprayers separated by a distance of 8 feet were attached to port and starboard sides of a pontoon boat. The boat was securely anchored in 9 feet of water. Water was pumped from the rear starboard of the boat to the sprayers. The sprayers were throttled to maintain equal flow in each sprayer. Water from one or both of the sprayers was directed into the air allowing the droplets to free fall onto the lake surface, thus generating lake surface noise.

The acoustic intensity probe was positioned midway between the two sprayers at a depth of 4.5 feet. The probe was oriented to measure the horizontal intensity component in the direction from port to starboard.

GAIMS was used to measure the narrowband intensity component and sound pressure spectra over a frequency range of 0 to 10 kHz with a bandwidth of 25 Hz. Each spectrum is an average of 100 ensembles, representing a time period of approximately 20 seconds.

Figures 4 and 5 show narrowband spectra measured in the lake. In each of the figures the upper trace is the pressure; the middle is the equivalent pressure; and the lower is the direction indicator. The direction indicator shows the direction of energy flow. A positive direction (+) indicates energy flow from port to starboard. A negative (-) direction indicates energy flow from starboard to port.

The lake ambient pressure and equivalent pressure are shown in Figure 4a. In Figure 4b are the spectra measured with both sprayers running. In this experiment, the lake ambient represents the background noise level, and the noise generated by the droplets landing on the lake surface represents the source. The source levels are seen to increase by 30 dB above lake ambient and the direction indicator shows no preferred direction as a function of frequency.

Figure 5 shows the pressure and equivalent pressure spectra with either the starboard (Figure 5a) or the port (Figure 5b) sprayer running. As expected, when only one sprayer is running the pressure spectrum is 3 dB down from when both sprayers are running. Also, as expected, the direction of energy flow at most frequencies is away from the source being operated.

When both sprayers are on, the acoustic intensities from the starboard and port sprayer should cancel. Comparing Figures 5a and 5b with Figure 4b it can be seen that the equivalent pressure with both sprayers on is 2 to 3 dB less than that with only one sprayer on. This reduction was not as significant as might be expected because of background intensity contribution from the submersible pump used to provide water to the sprayers. However, the results do show that cancellation does occur.

DRY DOCK MEASUREMENTS

Simultaneous sound pressure and acoustic intensity measurements of underwater background noise were carried out in a coastal dry dock. These measurements were made when other activities at the shipyard were minimal.

The data was processed using the GAIMS system, as before, except each spectrum is now an average of 999 ensembles. This averaging time represents approximately 3 minutes of data collection.

Intensity component measurements were made parallel to the main axis of the dry dock and perpendicular to that axis. All measurements were made at a depth of approximately 20 feet (see Figure 3b).

During the measurements the dry dock was empty but flooded. Water surface conditions during the measurement period ranged from calm to light rain to choppy.

Figure 6a shows typical narrowband pressure and equivalent pressure spectra at a measurement location close to the dry dock gate. A positive direction (+) indicates the energy flow is from the gate into the dry dock. A negative (-) direction indicates energy flow is from the dry dock toward the gate.

Note that the acoustic energy flow at most frequencies is directed from the gate into the dry dock. This would imply that the primary source of background noise in the dry dock at this time was harbor, rather than shipyard noise radiating from the sides of the dry dock.

The differences between the pressure and the equivalent pressure range from approximately 5 dB at 1000 Hz to approximately 10 dB at 10,000 Hz. This is typical of the measurements made during the first measurement period, during which the water surface was calm.

Figure 6b shows a similar plot for measurements made parallel to the dry dock gate. Note that the direction of energy flow is much more a random function of frequency than was the case in Figure 6a, indicating a more reverberant situation than along the major axis of the dry dock.

Note also that, while the pressure levels in Figure 6b are similar to those in Figures 6a, the equivalent pressure levels are approximately 5 dB lower. This would imply that most of the energy in the dry dock is flowing along its major axis rather than perpendicular to that axis.

The difference between pressure and equivalent pressure indicated in Figure 6a and 6b are representative of those occurring for calm water surface conditions. A second measurement was carried out in a light drizzle. In a third session, a west wind produced choppy waves on the water surface.

The average difference between pressure and equivalent pressure over the frequency range from 1 kHz to 10 kHz for the three surface conditions are summarized in Table 1.

Table 1

Typical Differences Between Pressure (L_p) and Equivalent Pressure (L_{ep}) Values

Direction	Surface	$L_p - L_{ep}$
Normal to Dry Dock Gate	Calm	4.0
	Drizzle	10.6
	Choppy	17.5
Parallel to Dry Dock Gate	Calm	14.1
	Drizzle	18.6
	Choppy	20.6

To further study the potential signal-to-noise improvements, a third hydrophone was used to inject a 5 kHz tone into the water 2 feet from the intensity probe. Figure 7 shows the resultant pressure and equivalent pressure spectra with a choppy surface condition. The signal-to-noise ratio for the pressure is 29.2 dB; the corresponding ratio for the equivalent pressure is 45.2 dB. The resultant increase in signal-to-noise is 16.0 dB.

CONCLUSION

The results described above clearly show that acoustic intensity measurements are a useful adjunct to sound pressure measurements in that they can improve the signal-to-noise ratio of the measurement. In addition, they provide information on the direction of the energy flow, which can be useful in discriminating between signal and background noise.

REFERENCES

1. Stusnick, E., "Acoustic Intensity Measurement Techniques", Wyle Research Technical Note TN 83-01, May 1983.

2. Stusnick, E., "An Investigation of the Application of Acoustic Intensity Measurement Techniques to the Study of Noise Radiated From Naval-Type Structures – Phase I", Wyle Research Report WR 83-29, August 1983.

3. Stusnick, E., "An Investigation of the Application of Acoustic Intensity Measurement Techniques to the Study of Noise Radiated From Naval-Type Structures", Wyle Research Report WR 85-4, March 1985 (C).

4. Jones, K., and Stusnick, E., "The Application of Acoustic Intensity Measurement Technique to the Improvement of the Signal-to-Noise Ratio of Underwater Sound Measurements", 36th Naval Symposium on Underwater Acoustics, April 1985 (C).

5. Stusnick, E., "An Investigation of the Application of Acoustic Intensity Measurement Techniques to the Study of Noise Radiated From Naval-Type Structures", Wyle Research Report WR 86-17, October 1986 (S).

6. Stusnick, E., and Lucas, M., "A Study of the Application of Acoustic Intensity Measurements to Overside Noise Screening Tests, Volume I, Volume II (C), Volume III, Wyle Research Report WR 89-10, July 1989.

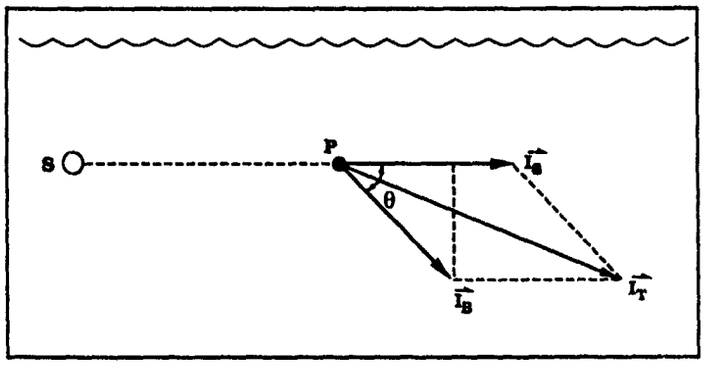

Figure 1. Reduction of the Background Contribution by the Use of Acoustic Intensity Measurements.

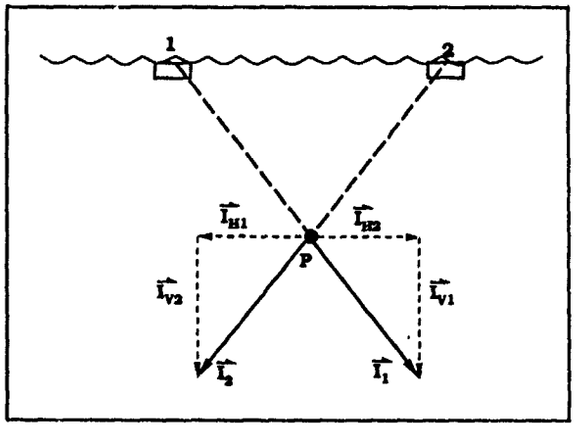

Figure 2. Cancellation of Horizontal Component of Sea Surface Intensity Contribution.

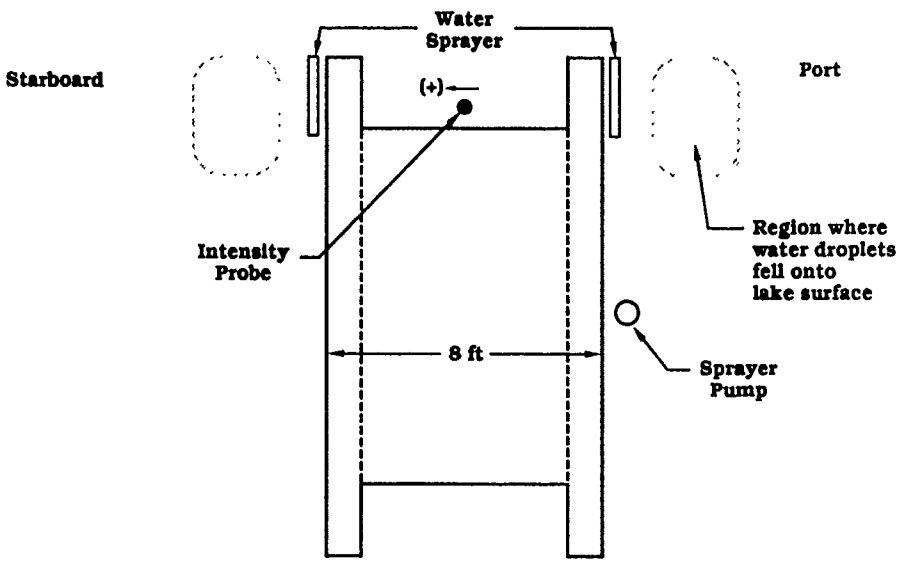

(a) Aerial View of Pontoon Boat on Lake.

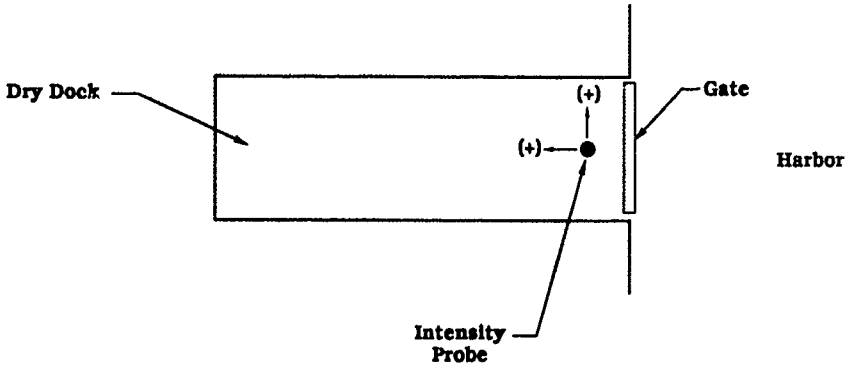

(b) Aerial View of Dry Dock.

Figure 3. Experimental Setup of Pontoon Boat and Drydock.

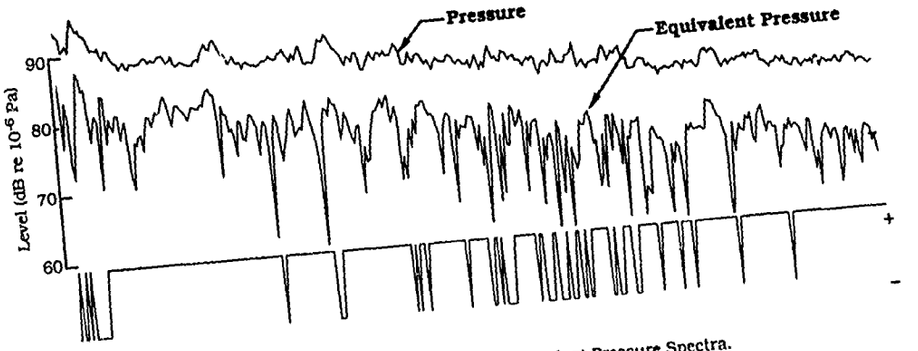

(a) Lake Ambient Pressure and Equivalent Pressure Spectra.

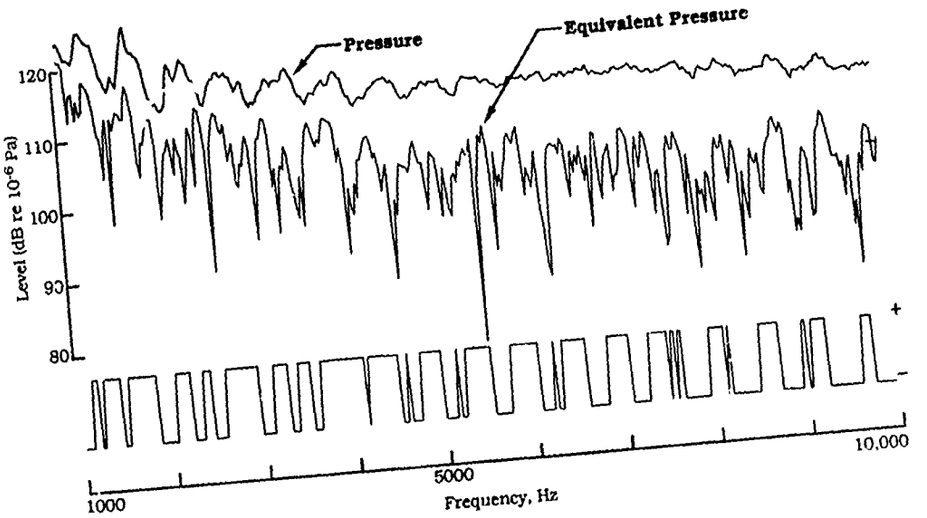

(b) Port and Starboard Water Sprayer Running. Pressure and Equivalent Pressure Spectra.

Figure 4. Narrowband Spectra Measured in the Lake.

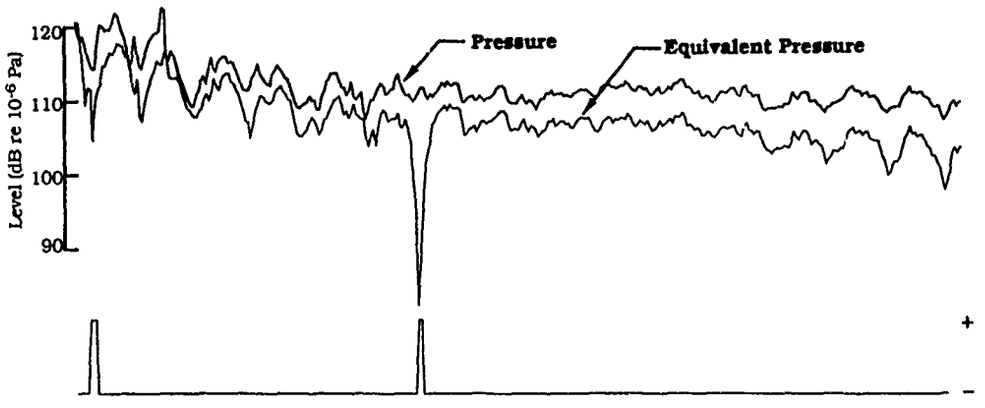

(a) Pressure and Equivalent Pressure Spectra, Starboard Water Sprayer Running.

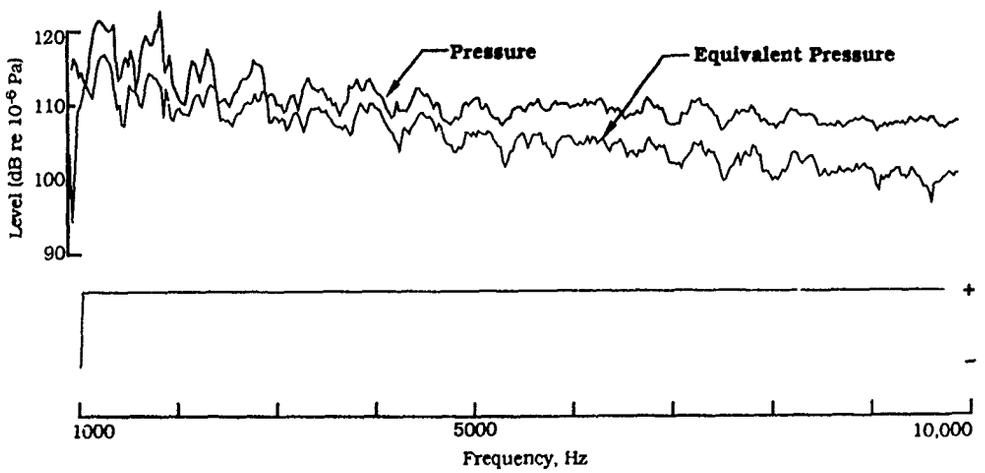

(b) Pressure and Equivalent Pressure Spectra, Port Water Sprayer Running.

Figure 5. Narrowband Spectra Measured With Water Sprayers Running.

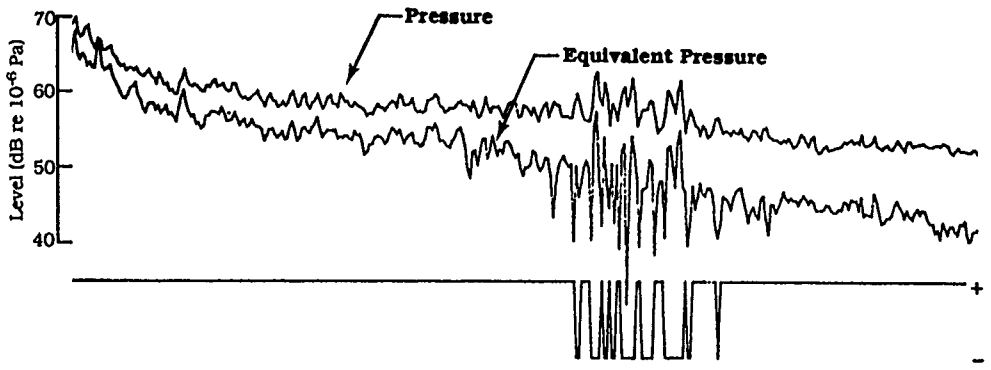

(a) Pressure and Equivalent Pressure Spectra, Energy Flow Normal to the Dry Dock Gate.

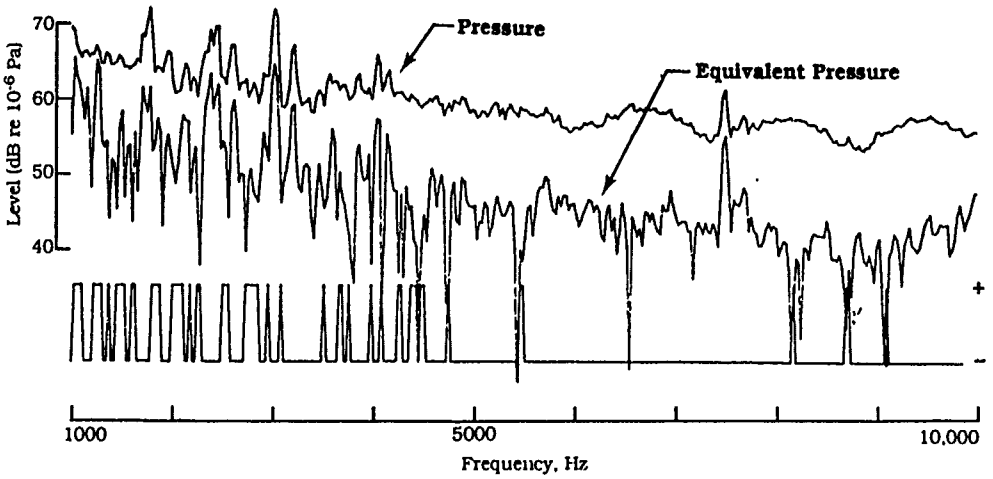

(b) Pressure and Equivalent Pressure Spectra, Energy Flow Parallel to the Dry Dock Gate.

Figure 6. Narrowband Spectra Measurements Close to Dry Dock Gate. (Positive direction corresponds to energy flow from the harbor into the dry dock.)

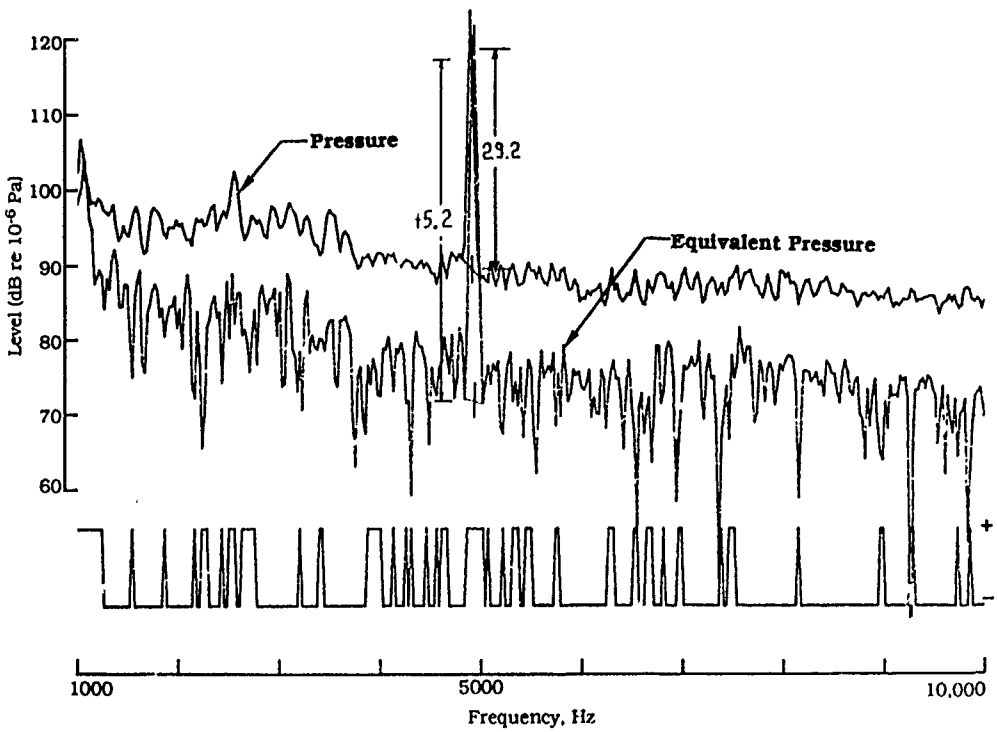

Figure 7. Pressure and Equivalent Pressure Spectra With 5 kHz Pure Tone.

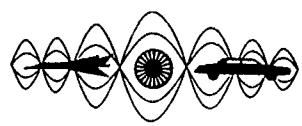

SECOND INTERNATIONAL CONGRESS ON
RECENT DEVELOPMENTS IN AIR- AND
STRUCTURE-BORNE SOUND AND VIBRATION
MARCH 4-6, 1992 AUBURN UNIVERSITY USA

INTENSITY MEASUREMENTS USING 4-MICROPHONE PROBE

I. V. Lebedeva, S. P. Dragan

Department of Physics

Moscow State University

Moscow, 119899, GSP,

USSR

ABSTRACT

Unlike the well known 2-microphone technique using the finite difference approximation a method of intensity measurements based on analytic solution of sound wave propagation equation is offered. Sound pressure level and phase difference between them are measured by means of 2 microphone located in arbitrary points of a field (1D case). Active and reactive parts of intensity in each of these points are estimated using the measured value of pressure and the calculated value of oscillating velocity. This condition ensures the independence of the upper frequency range on the chosen distance between the microphones. While with the gradient method the choice of the distance imposes restriction on the upper frequency range. As for the lower frequency range in the both methods the restriction is due to mismatch of measuring chains. Making use of regressive analysis method of mathematical modeling the equation of errors for the parameters determining were obtained, which showed the influence of the amplitude and the phase measurements accuracy as well as of the parameter $k \cdot l$ (where k is the wave number, l - microphone separation distance). For measurements of the intensity vector in 3D space the 4-microphone probe is suggested in which the microphones are mounted in such a way that their centers form a tetrahedron.

INTRODUCTION

Sound intensity measurements are widely used in practice, their usefulness is indisputable. In all existed sound intensity analyzers the finite difference approximation is used. Approximation error and errors due to phase mismatch of microphone channel lead to frequency range restriction [1].

A method of intensity measurements based on the analytic solution of sound wave propagation equation is offered in this paper. The intensity is computed using experimental data for sound pressure p_1 and p_2 and difference of phases $\Delta\varphi$ between them, measured in two arbitrary points situated at the distance l.

BASIC RELATIONS

Let us consider 1D case. A plane monochromatic wave propagates along a wave-guide which has a reflecting terminal. Taking into consideration

that sound wave propagates from the first to the second microphone we may write the expression for sound pressure in the area of the microphone location

$$p_1=p_0(1-r),\ p_2e^{i\Delta\varphi}=p_0e^{-ikl}\ (1-r\ e^{2ikl})\ , \tag{1}$$

where p_0 is the pressure in the incident wave, r is complex reflection coefficient $r=|r|e^{i\theta}$, θ is the phase of reflection coefficient in the position of the first microphone, k is a wave number.

After simple transformation of the Eq. (1) it is easy to derive the formula for absolute value and phase of reflection coefficient:

$$|r| = \frac{[(N^2-1)^2+4N^2(\cos^2kl+\cos^2\Delta\varphi)-4N(N^2+1)\cos\Delta\varphi\ \cos(kl)]^{1/2}}{N^2+1-2N\ \cos(\Delta\varphi+kl)}$$

$$\theta = \operatorname{arctg}\frac{2N\ \sin(kl)\ (N\cos(kl)\ -\ \cos\ \Delta\varphi)}{N^2-1-2N\cos(kl)\ (N\cos(kl)-\cos\Delta\varphi)} \tag{2}$$

where $N=p_1/p_2$.

Active I_a and reactive I_r components of intensity determined in the position of the first microphone may be written in the form

$$I_a=\frac{p_1^{\,2}}{\rho c}\ \frac{1-r^2}{1+r^2-2|r|\cos\theta}\ ,\qquad I_r=\frac{p_1^{\,2}}{\rho c}\ \frac{2|r|\sin\theta}{1+r^2-2|r|\cos\theta}\ . \tag{3}$$

ERRORS DUE TO CHANNEL MISMATCH

Usually instrumental errors are considered to be caused only by the phase channel mismatch and the amplitude characteristics are identical, which is not always correct. Let us consider errors caused as by phase as well as by amplitude channel mismatch. Influence of the parameter kl will also be considered.

Numerical modeling of free field condition for channel mismatch in the range $\pm3^0$ in phase ($\delta\varphi$) and ±2 dB in pressure (Δp) has been done. Parameter kl was changed from 1.8° to 90°.

Let us suppose that the relative errors of intensity measurements may be written in the form of functional dependence: $y=F(\delta\varphi,\Delta p,kl)$. Taking into account only first linear and nonlinear terms of expansion (quadratic terms are omitted due to their small value), we may write the equation of errors in the form

$$y = a_0+a_1\delta\varphi+a_2\Delta p+a_3/kl+a_4\delta\varphi\Delta p+a_5\delta\varphi/kl+a_6\Delta p/kl+a_7\delta\varphi\Delta p/kl \tag{4}$$

Coefficients a_0, a_1, ... a_7 are obtained by multiple regression method [2]. For practical evaluation the Eq (4) may be simplified by accounting for only the more important variables using stepwise regression procedure.

The dependence of the relative errors of the active intensity measurements for free field condition on the parameters under consideration may by written in the form

$$\Delta I_a/I_a = 0.1254 - \frac{0.995\ \delta\varphi}{kl}\ (1.008 + 0.131\ |\Delta p|) \tag{5}$$

The Eq. (5) differs from the known equation of errors by having an additional term, determined by the quantity $|\Delta p|$ which can not be neglected.

The measurement errors of reactive intensity was determined versus the quantity I_a (because in the running wave $I_r=0$). The simplified dependence has the form

$$\Delta I_r/I_a = -0.091 - \frac{8.115}{kl}\Delta p \qquad (6)$$

As follows from the Eq. (6) the phase mismatch practically does not influence the measurement errors of reactive intensity.

The dependence of relative errors of the intensity components determination on parameter kl was checked experimentally in the wave-guide in the running wave condition.

Theoretical and experimental dependencies of intensity components determination on parameter kl are represented on the fig.1,2. It is seen that experimental results coincide satisfactorily with the theoretical prediction. As it follows from the analysis of the error equation the errors of quantities under consideration decrease significantly for $kl>18^{\circ}$.

It is interesting to note that the theoretical dependence of errors on parameter kl in gradient method tends asymptotically to zero with the increasing kl. In our case when phase and amplitude channel mismatch taken into account under increasing kl quantity of $L_a=10\cdot lg(I_a/<I_a>)$ changes its sign and tends asymptotically to certain limiting value which is determined by the quantities $\delta\varphi$ and Δp. The theoretical predictions are in a good agreement with the experiment.

3D SYSTEM

For measurements of the intensity vector in 3D space it is sufficient to use the 4-microphone probe in which the microphones are mounted side by side in such a way that their centers form a tetrahedron. The procedure of processing of arbitrary form signal entering from 4 channel has been derived. It includes FFT analysis and the computer calculations. As a result of processing the amplitude specter of signal is determined for each channel as well as the phase-frequency specter between the first and each of remaining three microphones.

Using the relations derived the calculation of three intensity components in the position of first microphone is performed and then the procedure is repeated for each of three other microphones.

The generalization of above method to 3D space is connected, generally speaking, with the same approximation which exists in gradient method.

CONCLUSION

Unlike the gradient method the considered method of intensity measurements practically does not have frequency restrictions. Using the 4-microphone probe instead of 6 microphones for intensity vector measurements in 3D field has its own advantages. The measurement process may be designed for automatic performance.

BIBLIOGRAPHIC REFERENCES

1. S. Gade, Validity of intensity measurements, INTER-NOISE, Honolulu, USA, 1984, 1077-1082.
2. N. R. Draper, H. Smith, Applied regression analysis, J.W., N-Y, 1966.

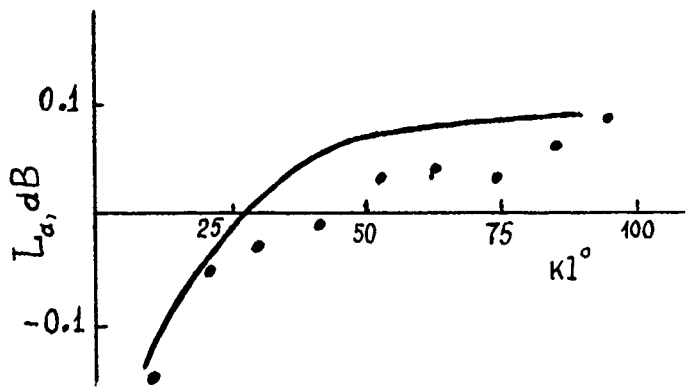

Fig. 1
The relative errors of the active intensity determination
(solid line - theory, dots - experiment)

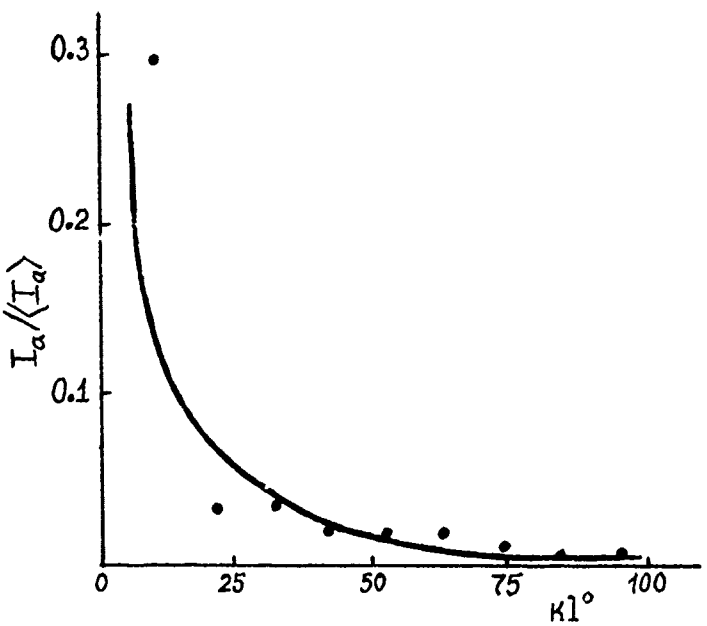

Fig. 2
The relative errors of the reactive intensity determination
(solid line - theory, dots - experiment)

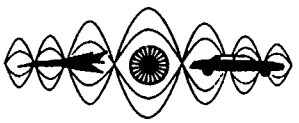

**SECOND INTERNATIONAL CONGRESS ON
RECENT DEVELOPMENTS IN AIR- AND
STRUCTURE-BORNE SOUND AND VIBRATION**
MARCH 4-6, 1992 AUBURN UNIVERSITY, USA

USE OF REFERENCES FOR INCLUSION AND EXCLUSION OF PARTIAL SOUND SOURCES WITH THE STSF TECHNIQUE

Jørgen Hald
Brüel & Kjær Industri A/S
Skodsborgvej 307
DK-2850 Nærum, DENMARK.

ABSTRACT

A brief introduction to the main principles of the Spatial Transformation of Sound Fields (STSF) technique is given before the use of reference signals in STSF is treated in more detail. The normal type of references determine the part of the total sound field to be included in the sound field model: Only the part coherent with these references will be included. At least one normal reference must always be applied. The second type of references applies for subtraction of undesired non-coherent sound field components from the model: The part of the sound field coherent with these references will be excluded from the model otherwise obtained. Examples are given showing how the exclude references apply for suppression of background noise and for suppression of certain independent components of a sound source.

INTRODUCTION

The STSF technique permits a 3D sound field mapping based on a 2D scan measurement in the near field of a source. By measurement of the cross spectra between a set of references and the cross spectra from each scan position to each of the references, a principal component representation of the sound field is extracted which can be applied for near-field holography and Helmholtz' integral equation calculations. Basically, this sound field representation includes only the part of the sound field, which is coherent with the reference signals. More precisely, only "views" of the independent parts of the sound field seen by the references are included. Therefore, provided the references do not pick up some possible background noise, the background noise will not become part of the sound field processed by STSF. However, if the background noise is picked up by the reference transducers, it will become part of the model and cause errors in the calculations. In order to overcome this problem, the possibility of using a set of "exclude references" has been implemented in the STSF system. These references should pick up only the uncorrelated background noise to be suppressed in the model. The exclude references can also be used to suppress an independent part or a "view" of a composite sound source to be mapped.

PRINCIPLE OF STSF

The principle of the STSF technique is illustrated in Fig.1. A certain stationarity of the source is assumed and correlation, phase and amplitude information is obtained by measuring the cross spectra during a scan over a plane close to the source under investigation. Based on these cross

spectra, a principal component representation of the sound field is extracted. Any power descriptor of the sound field (e.g. intensity, reactive intensity, pressure, particle velocity) can then be mapped over a 3D region extending from the surface of the source to infinity (Fig.1). The near field is predicted from the scan data using near-field acoustical holography while the more distant field is calculated using Helmholtz' integral equation. In addition to the 3D mapping capability based on the 2D measurements, STSF also provides the possibility of performing a simulation of partial source attenuation. The main advantage of the STSF technique compared to similar systems is that STSF can be used on broadband, non-coherent sources [1].

THE USE OF NORMAL "INCLUDE" REFERENCES

Ideally, the cross spectrum from every point to every other point over the scan area would have to be measured yielding an enormous amount of data. However, the amount of data to be measured, stored and processed can be considerably reduced by using some important properties of this enormous cross spectrum matrix to remove redundant information. Since in general the large matrix is strongly rank deficient, the whole matrix can be constructed from a relatively small number of linearly independent columns, obtained by measuring the cross spectra from the scan points to a number of reference transducers and the cross spectra between every pair of references [1].

The reference transducers will typically be placed between the sound source and the scan plane and should be distributed over the scan area. Too few reference transducers will generally misrepresent the sound field as certain important combinations ("views") of the uncorrelated partial fields will not be identified. This is illustrated by the following example taken from [1]. An STSF measurement is made over two identical loudspeakers using a single reference microphone placed on the symmetry plane between the two loudspeakers. The loudspeakers are excited by two identical, independent noise generators which are adjusted to produce equal sound pressure level at the reference. Thus, the total sound field consists of two mutually uncorrelated partial fields, each of which are spatially coherent. However, the use of one reference provides only one "view" of the two partial fields and therefore does not provide a complete representation of the total sound field. The sound field representation is based on the cross spectra from the reference to the individual scan positions, and at some positions in the scan plane the contributions to the cross spectrum from the two uncorrelated partial fields will tend to cancel each other. Thus, the sound field model will show an interference pattern which is not found in the true total sound field. With the reference on the plane of symmetry, the interference pattern will be as if the two speakers were excited in-phase from a single generator (Fig.2). To obtain a complete model of the sound field, a second reference needs to be added. Furthermore, the second reference must have a "view" of the two independent sources which is different to that of the first reference. The solid curve in Fig.2 shows the sound pressure level calculated from a measurement involving two references. Notice that the spurious interference pattern has been avoided.

If one or more partial sources can be identified before the references are selected then references can be positioned to pick up individual partial fields. As an example, assume that the vibration of a certain surface is suspected to be an important source. Then the sound field coherent with that vibration can be mapped by the use of a single reference which picks up the vibration signal, e.g. an accelerometer or a laser velocity transducer. The use of a vibration signal as reference has the advantage of providing a good suppression of uncorrelated background noise. A drawback is the possibility of measuring the vibration signal at a nodal line of the vibration pattern.

THE USE OF "EXCLUDE" REFERENCES

In cases where some uncorrelated background noise cannot be avoided at the normal reference transducers, the background noise will become part of the sound field model used by STSF for mapping of the field. In such cases, if a set of exclude references can be introduced picking up only the background noise, this noise can be removed from the model quite efficiently. The effect of using a set of exclude references is to subtract the part of the sound field coherent with these references from the sound field model. In case of more than one exclude reference, a set of principal components is extracted, and the dominating principal components are subtracted.

Effectively, the set of views of the different mutually uncorrelated parts of the sound field seen by the exclude references is subtracted from the field model.

The exclude references can also be applied to suppress the part of the sound field coherent with a set of reference signals measured on a composite sound source. In this case, the part of the sound field coherent with the exclude references is considered as background noise.

The exclusion is a process performed during the measurement. To obtain sufficient accuracy in the subtraction of the background noise, it is important that all signals involved in the subtraction (i.e. all reference and scan transducer signals) are measured simultaneously. Suitable instrumentation can be based upon the Multichannel Analysis System Type 3550, which enables up to 16 channels including all cross products to be measured at the same time. The use of the exclude reference mode does not inhibit any of the normal STSF calculations: The STSF data-base has exactly the same form, the only difference being that the field coherent with the exclude references has been subtracted from all data.

A major application of the exclusion technique is in the use of STSF in windtunnels during wind induced noise testing of motor vehicles. Often, the fan noise of the windtunnel itself is the principal undesirable noise source. Another application is the investigation of tyre/road noise under running conditions. In this case the noise due to the engine can be significantly suppressed by placing one or a set of exclude references in the engine compartment.

MEASUREMENTS

Two series of measurements shall be described, each involving the use of exclude references. The first measurement series employing two loudspeakers shows, how effectively a spurious source can be eliminated. The second measurement series shows the effect of using the technique for suppressing a component of a real-world sound source.

Speaker measurements

The first measurement series was performed using 10 x 8 scan positions in front of two loudspeakers, each one supplied with its own uncorrelated broadband noise. One loudspeaker (the leftmost) was considered to be the principal sound source, the other the interfering background noise source. Two normal reference microphones were positioned so that they had different views of the two loudspeakers. A third reference microphone, the exclude reference microphone, was positioned as close as possible to the background noise loudspeaker. Three measurements were performed for the following conditions:

1) No background noise. No exclude references (Figs.3 & 4).
2) Background noise. No exclude references (Figs.5 & 6).
3) Background noise. One exclude reference (Figs.7 & 8).

For all three measurements the principal source was on. From Figs. 3 & 4 and 7 & 8 it can be seen that the exclude reference mode accurately reconstitutes the unadulterated sound field from the principal sound source. This is seen quantatively in the total sound power, and qualitatively in the contour plots. All the plots represent a 50 Hz band around 1200 Hz.

Tank measurements

The second measurement series consisting of two measurements was performed using 32 x 10 positions along the left, rear part of a stationary tank, covering thereby the engine, the ventilation system and the exhaust outlet regions. Two normal references were used: one accelerometer on the belt drive wheel and another accelerometer on a rear panel plate, which was vibrating strongly. A single exclude microphone positioned close to the exhaust outlets behind the vehicle was used in the second measurement (Figs.10,12&14), whereas the first measurement was made without exclude references (Figs.9,11&13). Figs. 9 and 10 show the sound power spectrum through the scan area (shifted 0.3 m towards the source) without and with exclusion of the field coherent with the exhaust reference. It appears that an overall reduction around 4 dB is achieved over the frequency range 80-500 Hz by subtracting the field coherent with the exhaust reference. The remaining four figures contain plots of the active intensity for the 20 Hz band centred at 120 Hz. Figs. 11 and 12 contain contour plots of the normal component of the intensity vectors in a plane

very close to the surface of the tank. Clearly, the exclude reference suppresses the radiation from the upper rear region, where the exhaust outlets are located. The sound power is reduced from 92.2 dB to 87.5 dB. Figs. 13 and 14 show the tangential component of the active intensity vectors in the scan plane. Again the reduced radiation from the exhaust region is apparent.

CONCLUSIONS

The STSF technique employs an efficient principal component measurement technique to achieve a cross spectral representation of the sound field. Normal references and exclude references can be used to include and exclude, respectively, various uncorrelated parts of the total sound field. The technique also includes a validation procedure to evaluate the representation obtained by a specific set of references. The use of exclude references for suppression of uncorrelated background noise and independent parts of a source has been demonstrated.

ACKNOWLEDGEMENTS

I would like to thank the people at Bundeswehr in Meppen for good co-operation in connection with the tank measurements and for allowing us to use the results from the measurements.

REFERENCES

[1] *"STSF - a unique technique for scan based near-field acoustic holography without restrictions on coherence"*, J.Hald, Technical Review No. 1, 1989, B & K publication.

[2] *"Development of STSF with emphasis on the influence of bandwidth; Part I, Background & theory"*, J.Hald.

[3] *"Part II, Instrumentation and computer simulation"*, K.B.Ginn & J.Hald, Noise Con 88, Proceedings 529 (1988).

[4] *"Source location using accelerometers as reference transducers for the STSF technique"*, K.B.Ginn & J.Hald, ICA 89 (1989).

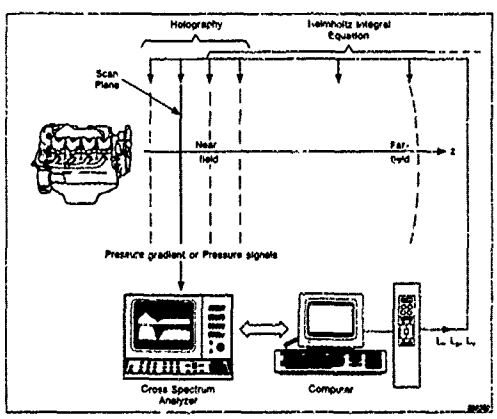

Fig.1. Principle of STSF based on Multichannel Analysis System Type 3550.

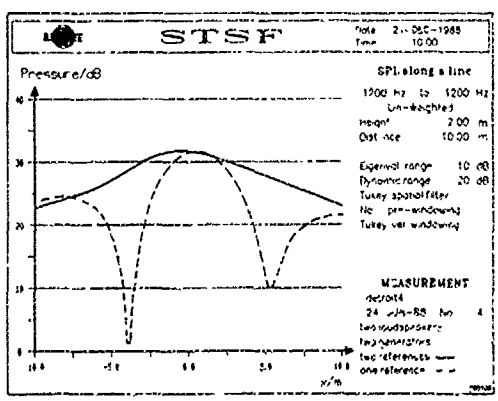

Fig.2. Calculated sound pressure level. Dashed: one reference (insufficient). Solid: two references (sufficient).

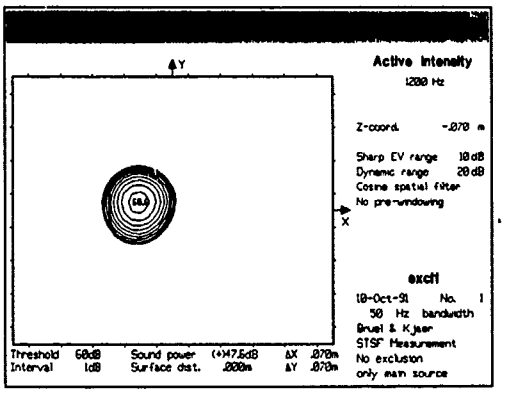

Fig.3. No background noise; no exclusion.

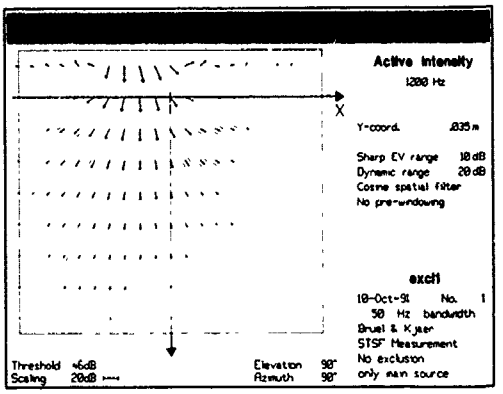

Fig.4. No background noise; no exclusion.

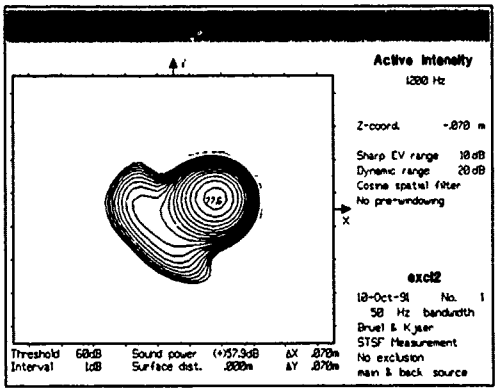

Fig.5. Background noise; no exclusion.

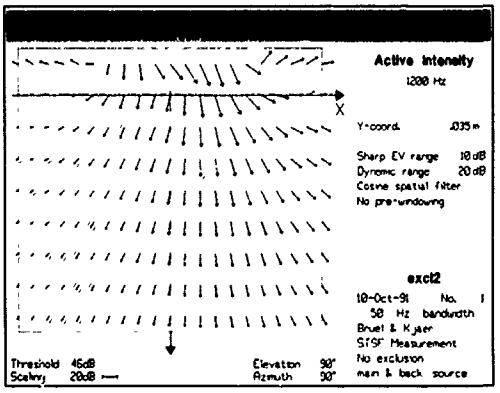

Fig.6. Background noise; no exclusion.

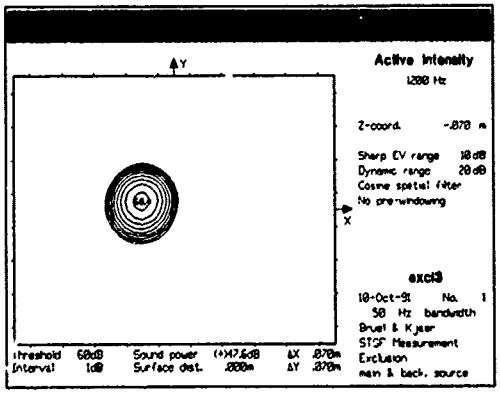

Fig.7. Background noise; exclusion.

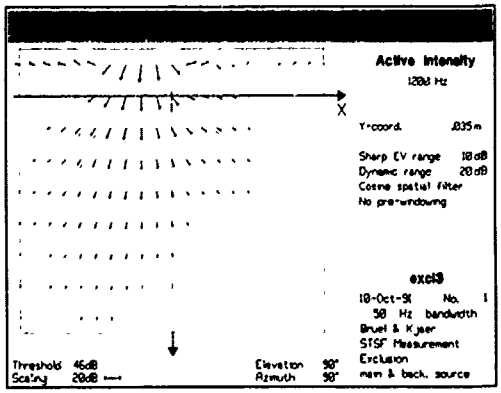

Fig.8. Background noise; exclusion.

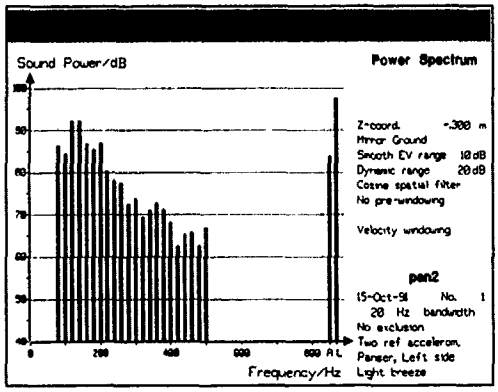

Fig.9. Sound power spectrum; no exclusion.

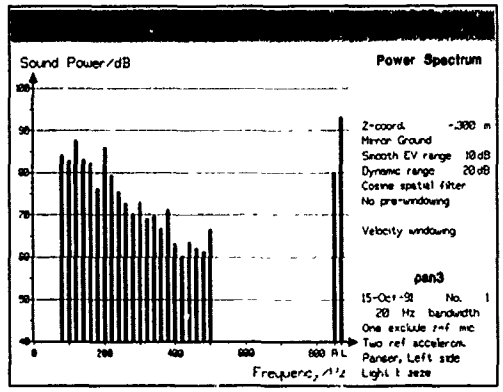

Fig.10. Power spectrum; exclusion of exhaust.

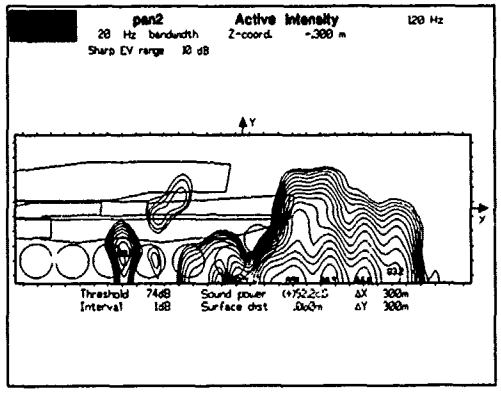

Fig.11. Intensity, 120 Hz; no exclusion.

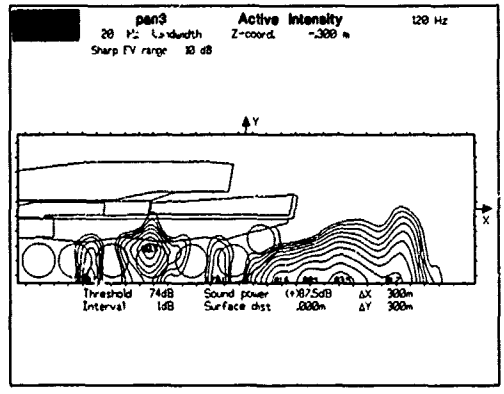

Fig.12. Intensity, 120 Hz; exclusion of exhaust.

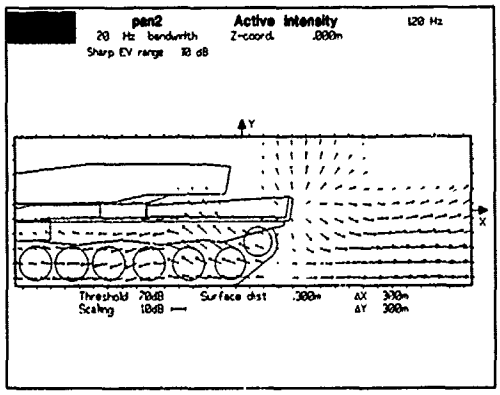

Fig.13. Intensity, 120 Hz; no exclusion.

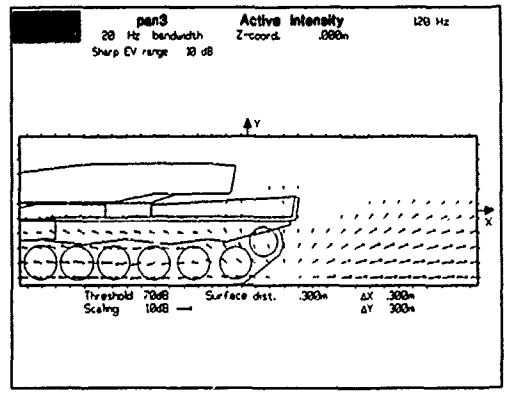

Fig.14. Intensity, 120 Hz; exclusion of exhaust.

SECOND INTERNATIONAL CONGRESS ON
RECENT DEVELOPMENTS IN AIR- AND
STRUCTURE-BORNE SOUND AND VIBRATION
MARCH 4-6, 1992 AUBURN UNIVERSITY, USA

IMPEDANCE-RELATED MEASUREMENTS USING INTENSITY TECHNIQUES

Tapio Lahti
Finnish Acoustics Centre Ltd
Mannerheimintie 168 A
SF-00300 HELSINKI
Finland

ABSTRACT

Three types of measurements are presented which are based on applying the intensity techniques to detect the impedance and other closely related quantities. The first type of application is the measurement of surface impedance with either the two-microphone acoustic intensity or the surface intensity instrumentation. The main advantage of the method is that the impedance can be determined in any sound field as a function of position. The technique is demonstrated with measurements of the impedance of mineral wool and and a window. The second type of application is the measurement of the incident intensity in an arbitrary incoming sound field. This method is based on the principle of reciprocity, and it is an extension of the measurement of impedance distribution on the surface of an insonified plane. The technique is used to measure the intensity incident on the wool and the window. The third type of application is the measurement of the impedance in a bending wave using the structural intensity technique. The method is applied to the determination of the impedance and the reflection coefficient of a narrow beam in laboratory conditions.

INTRODUCTION

The sound intensity techniques, and their counterpart in vibration measurements, the structural intensity technique have offered many new ways of looking at familiar problems in acoustical and mechanical testing. Three such methods are reviewed in this paper. They all have the common approach of turning the information from intensity measurement into the determination of the impedance, or other closely related descriptors of the field and the boundary or structure.

The measurement of the acoustic impedance using the two-microphone intensity technique was presented in [1]. Later, the method have been shown to work with absorbing surfaces by several researchers. Here two experiments are reviewed, using mineral wool and a window, the impedance of which can also be measured more directly with the surface intensity technique. Another acoustical application is the measurement of the incident intensity. This quantity would be needed for the determination of the transmission loss or the absorption coefficient. Using the distributions of intensity and impedance on the insonified surface, the incident intensity can be measured without *a priori* knowledge of the incoming sound field. The method was presented in [2], and it was later refined in [3], along with the first laboratory experiments. The applicability of the method was also investigated using the wool and the window as test specimens.

In structural intensity measurements, the application of the intensity technique to the determination of impedance-related quantities is also a logical extension, which parallels the similar development in acoustics. This approach was briefly mentioned in [4] and described more thoroughly in [5,6]. The impedance technique may be formulated generally as for sound fields, but the first tests which are reviewed here were made with a simple beam in the laboratory.

METHODS

Measurement of specific acoustic impedance

The sound intensity instrumentation gives signals which contain information on sound pressure p and (a component of) particle velocity u. Instead of forming their conjugate product, the intensity, one may as well

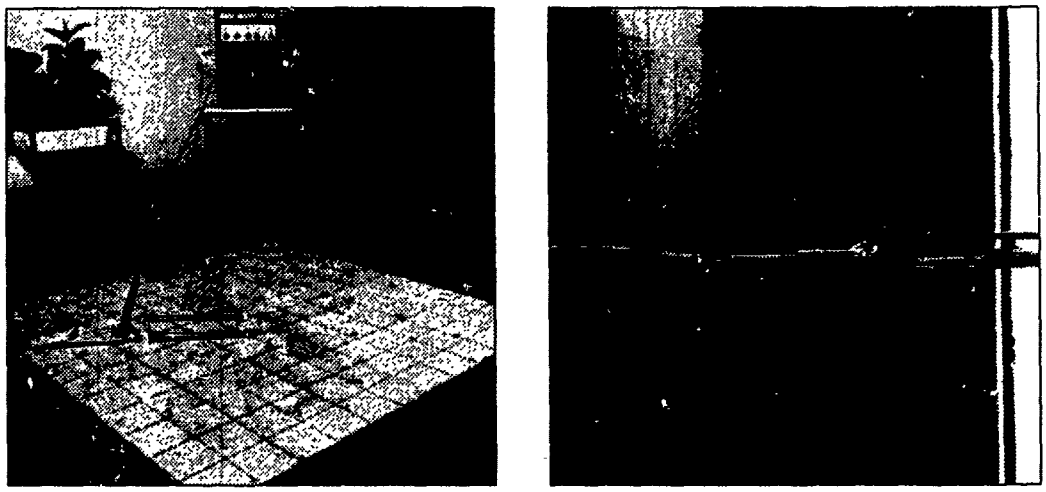

Figure 1—The arrangement of test specimens and transducers in the acoustic impedance and incident intensity experiments: (Left) The wool absorbent on the laboratory floor and the acoustic intensity probe. (Right) The surface intensity transducers on / near one of the panes of the window.

calculate their ratio — which is the specific acoustic impedance. The impedance is defined in the frequency domain with the Fourier transforms $p(f)$ and $u(f)$ as

$$Z(f) = \quad p(f)/u(f) \tag{1}$$

The impedance in the general (3-dimensional field) case can be estimated using the two-microphone intensity technique. This approach, presented in [1] and refined in [2], leads to the following optimum estimate for the impedance

$$Z(f) = \frac{j\omega\rho d}{2} \quad \frac{G_{11} + G_{22} + 2\,\mathrm{Re}\{G_{12}\}}{G_{11} - G_{22} - j2\,\mathrm{Im}\{G_{12}\}} \tag{2}$$

where ρ is the density of air and d microphone spacing. The subscripts of the auto- and cross-spectra G_{ij} refer to the pressure signals of microphones 1 and 2. By orientating the probe to detect normal intensity close to a boundary, one can measure its normal impedance. In the special case of surface intensity instrumentation, with one microphone and one accelerometer, the impedance is given directly by the frequency response function from velocity to pressure: $Z(f) = H_{up}(f)$.

Measurement of incident sound intensity

The common feature of all the standard methods for measuring incident intensity is that the form of the incoming sound field must be known beforehand. Outlining a method to determine the incident intensity of a truly arbitrary field was attempted in [2] and a more complete account was given in [3]. The development was based on the possibility opened by the intensity techniques, of obtaining directly the impedance, or complex velocity as well as pressure distributions, on a boundary between two media.

An arbitrary sound field incident on a boundary produces pressure $p(x,y)$ and velocity $u_z(x,y)$ on the surface. By the principle of reciprocity, the pressure can be decomposed into blocked pressure $2p_i$, where p_i is the incident pressure, and radiated pressure p_{rad}, which is produced by the surface vibrating with velocity distribution u_z. The incident pressure and the field (point) impedance at the surface are then given by

$$p_i(x,y) = \quad 1/2 \quad [p(x,y) - p_{rad}(x,y)] \qquad \text{and} \qquad Z_p(x,y) = \quad p_{rad}(x,y)/u(x,y) \tag{3}$$

The complex distributions of pressure $p(x,y)$ and velocity $u_z(x,y)$ on the surface can be measured. For solving the incident pressure $p_i(x,y)$, one needs the radiated pressure $p_{rad}(x,y)$. On a plane surface it can be computed from $u_z(x,y)$ using the Rayleigh integral. The incident power is given by

$$\Pi_i = \quad 1/\mathrm{Re}\{Z_{rad}\} \qquad \iint_S |p_i(x,y)|^2 \,dx\,dy \tag{4}$$

where Z_{rad} is the radiation impedance, defined by

$$Z_{rad} = \quad \iint_S p_{rad}(x,y)\, u_z^*(x,y)\,dx\,dy \quad / \quad \iint_S |u_z(x,y)|^2 \,dx\,dy \tag{5}$$

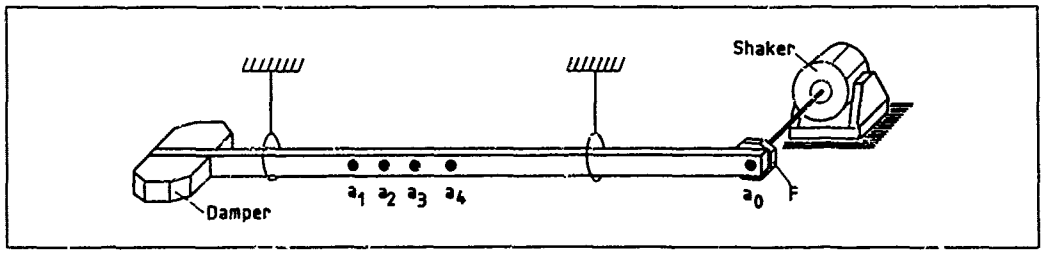

Figure 2 — Test arrangement in the structural impedance experiment: a steel beam, excited by a shaker at one end and heavily damped at the other end, and an array of four accelerometers.

The practical measurement of the complex distributions $p(x,y)$ and $u(x,y)$ [or $Z(x,y)$] require a common time origin, implying synchronised acquisition at all points. If this is done sequentially in time, a stationary field and good coherence to an external reference position are necessary. In the latter technique, data acquisition consists of the frequency response functions from the reference signal to a single transducer in one measurement position at a time. When using surface intensity instrumentation, the frequency responses $H_{Rp}(x,y)$ and $H_{Ru}(x,y)$ to the pressure microphone and the accelerometer signals are determined. With acoustic intensity instrumentation, one measures the frequency responses to the two pressure microphones. Thus pressure distributions $p_1(x,y)$ and $p_2(x,y)$ are acquired in the form $H_{Ri}(x,y)$, $i = 1,2$ for two different planes z_1 and z_2, with $d = z_2 - z_1$. The finite-difference approximation gives

$$H_{Rp}(x,y) = 1/2\ [H_{R1}(x,y) + H_{R2}(x,y)] \quad \text{and} \quad H_{Ru}(x,y) = 1/j\omega\rho d\ [H_{R1}(x,y) - H_{R2}(x,y)] \tag{6}$$

Measurement of bending wave impedance and reflection coefficient in a beam

As in acoustics, the structural intensity methods can also be extended to the determination of the mechanical impedance. The impedance at a point of the mechanical wave field is defined as the ratio of the force and motion type quantities. In a bending wave in a beam there are two quantities each, which results in an impedance matrix of four different combinations. As far as energy transmission is concerned, it is natural to concentrate on the two diagonal terms of the matrix which are directly related to the two components of bending wave power: the force impedance and the moment impedance. The force impedance relates (the Fourier transforms of) the shear force S to velocity v and the moment impedance relates the bending moment M to angular velocity w:

$$Z_S(f) = S(f)/v(f) \quad \text{and} \quad Z_M(f) = M(f)/w(f) \tag{7}$$

These may be expressed as functions of velocity and its spatial derivatives:

$$Z_S = \frac{B}{j\omega}\,\frac{1}{v}\,\frac{\partial^3 v}{\partial x^3} \quad \text{and} \quad Z_M = -\frac{B}{j\omega}\,\frac{1}{\partial v/\partial x}\,\frac{\partial^2 v}{\partial x^2} \tag{8}$$

where B is bending stiffness. In addition, the concepts of wave force impedance and wave moment impedance may be introduced in the farfield of an infinite beam. Taking directly the spatial derivatives, in the specific case of a single freely propagating wave, the wave impedances become

$$Z_{S0} = k^3 B/\omega \quad \text{and} \quad Z_{M0} = kB/\omega \tag{9}$$

Using the expression $k^4 = \omega^2 m/B$, where m is mass per unit length, one gets

$$Z_{S0} = m^{3/4} B^{1/4} \omega^{1/2} \quad \text{and} \quad Z_{M0} = m^{1/4} B^{3/4} \omega^{-1/2} \tag{10}$$

Thus the wave impedances are independent of the field quantities, and are functions of the wave direction and the material (and geometrical) properties of the beam only.

For determining the impedances, their estimates are basically given by

$$Z_S = H_{vS} = G_{vS}/G_{vv} \quad \text{and} \quad Z_M = H_{wM} = G_{wM}/G_{ww} \tag{11}$$

Inserting the expressions of the other field quantities in terms of velocity and evaluating the cross- and autospectra, one obtains (for force impedance)

$$Z_S = \frac{2B}{j\omega l^2}\,\frac{3G_{33} - 3G_{22} + j6\,\mathrm{Im}\{G_{23}\} + G_{21} - G_{24} + G_{31} - G_{34}}{G_{22} + G_{33} + 2\,\mathrm{Re}\{G_{23}\}} \tag{12}$$

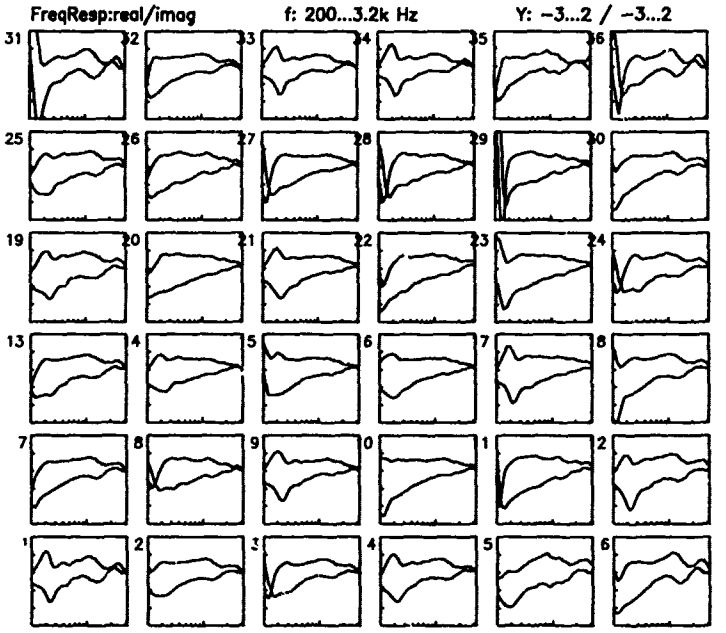

Figure 3 — Point-by-point map of the raw normal impedance above the wool surface measured with the two-microphone technique, providing a qualitative view over the spatial variations. Field: free plane wave of normally incident pulses.

and a similar heavy expression for Z_M, which both consist of 2 auto- and 5 cross-spectra. These spectra should all be measured simultaneously with a 4-channel FFT analyzer.

However, in a stationary situation, when neither the excitation nor the dynamic properties of the structure change during the measurement, the simultaneous measurement using a 4-transducer array can be avoided. The velocities can be measured sequentially, one at a time, with a 2-channel FFT. Then one again applies the frequency response method [7] which makes use of a reference signal. If the serial acquisition is applicable, the impedances become simpler to process:

$$Z_S = \frac{2B}{j\omega d^2}\,\frac{H_{R1} - 3H_{R2} + 3H_{R3} - H_{R4}}{H_{R2} + H_{R3}} \quad \text{and} \quad Z_M = -\frac{B}{2j\omega d}\,\frac{H_{R1} - H_{R2} - H_{R3} + H_{R4}}{H_{R2} - H_{R3}} \tag{13}$$

When the vibration energy propagates in one dimension only, the structural intensity methods can also be extended to the determination of the reflection coefficient. Using the analogy between the farfield of bending waves and the one-dimensional acoustic field, more compact results than those available in the literature can be achieved. The reflection coefficient for the bending wave in a beam can be defined on the basis of the wave equation. Its solution has four terms; e.g. for the velocity, the incident and reflected wave terms v_i and v_r and the respective nearfield terms. The reflection coefficient is a 2×2 matrix: $\{v_r\} = [R(f)]\{v_i\}$. Usually, however, one is interested in the farfield, where only the terms v_i and v_r are significant. Then the reflection coefficient refers to the farfield term of $[R]$, or in this case $v_r = R(f)\, v_i$.

For measuring the reflection coefficient, one can use the acoustic duct solution for plane sound waves by Chung and Blaser [8]. One easily sees that this efficient expression applies to beams as well. Adapting the subscript notation to the 4-accelerometer array,

$$R_3(f) = [H_{32}(f) - e^{-jkd}] \,/\, [e^{jkd} - H_{32}(f)] \tag{14}$$

The result refers to position 3. This equation is not restricted by the finite-difference approximation, but it is restricted to one dimension and the farfield only.

In a one-dimensional (far) field there exists a simple relationship between the impedance and the reflection coefficient. This provides an alternative, indirect way of determining the impedances via the estimated reflection coefficient. The results are:

$$Z_S(f) = [1 - R]/[1 + R]\, Z_{S0} \qquad \text{and} \qquad Z_M(f) = [1 + R]/[1 - R]\, Z_{M0} \tag{15}$$

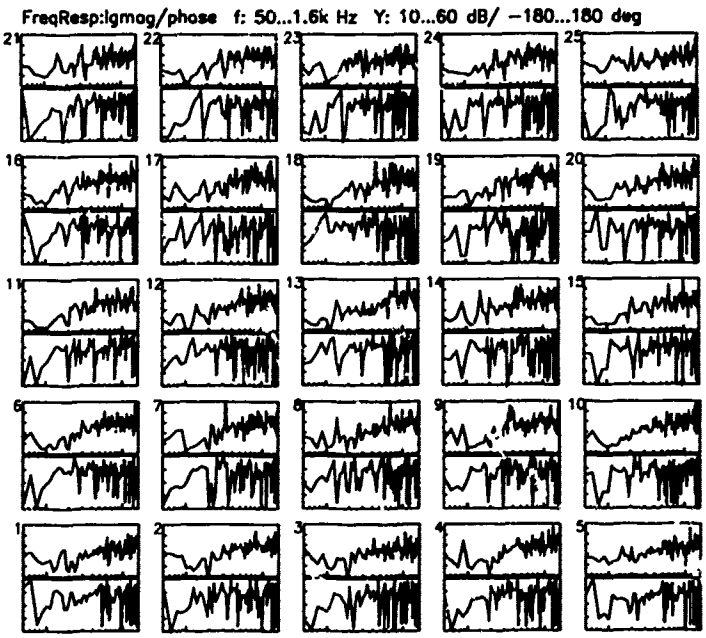

Figure 4 -- Point-by-point map of the normal impedance of the window surface (1st pane, incident side) providing a qualitative view of the spatial variations. Field: free plane wave of normally incident pulses. Normalised impedances, with log magnitude in dB re 1.

EXPERIMENTS

The acoustical impedance and the incident intensity techniques were both tested with two specimens common in building acoustics: a patch of mineral wool and a two-pane window (Fig. 1). The wool area was 1.2×1.2 m^2 and thickness 50 mm. The patch was lying on the hard floor in an ordinary laboratory room. The sound field consisted of normally incident plane wave pulses. The effects of reflections were removed from subsequent processing by suitable windowing. The two-microphone intensity probe with a 50 mm spacing was placed on the wool surface using a measurement grid of 6×6 positions. In the incident intensity test, the loudspeaker input was used as the necessary reference signal for constructing complex pressure distributions.

The gross area of the window was 1.2×1.2 m^2 and the air space between the two 4 mm panes was 100 mm. It was mounted in the partition wall in a laboratory transmission suite. The exciting sound field was again normally incident plane wave pulses. The effects of reverberation were again excluded by data windowing. The impedance measurements were repeated using also diffuse field excitation. Both acoustic and surface intensity transducers were used in the signal acquisition. Measurements were taken on a grid of 5×5 positions on the surface of the incident side of the window. The loudspeaker signal served again as the phase reference for the complex distributions.

The structural intensity methods were tested with a bending wave propagating in a steel beam (Fig. 2). The beam was excited by a point force at one end, and it was damped at the other end. An array of four accelerometers with spacing $d = 50$ mm was fixed in the middle of the beam. The frequency response of accelerations a_2 and a_3 were measured with a 2-channel FFT analyzer. For 4-channel measurements, the frequency responses from a reference signal (the input force signal) to the accelerations were measured.

RESULTS

Acoustic impedance

The spatial variations of the normal impedance above the wool surface are shown in the pointwise map of Fig. 3, meant to deliver a rough qualitative vision only. The edge and corner positions differed from the others, especially at high frequencies. Another feature was the instability of the real part at 200 Hz. Fig. 4 shows the respective variations of the normal impedance of the window surface in a normally incident pulse field. The comparison between the wool impedance obtained with the two-microphone impedance technique and two conventional methods, the standing wave tube and the separately known reflection of incident pulses,

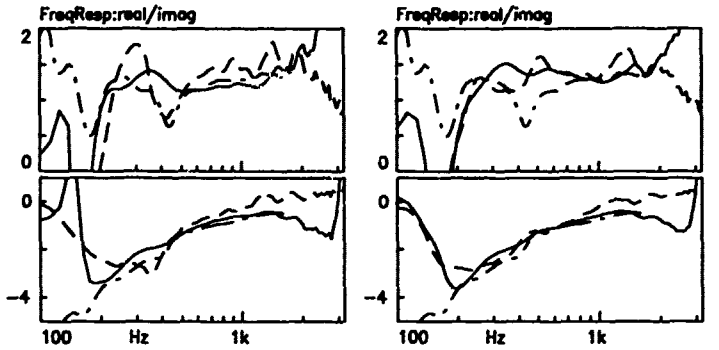

Figure 5—Normal impedance of the wool surface in a normally incident (plane wave) field, comparison between different methods. Spatial average over: (left) 4, (right) 16 centremost positions. Method: —— two-microphone, – – – pulse reflection, – · – rapid SW tube.

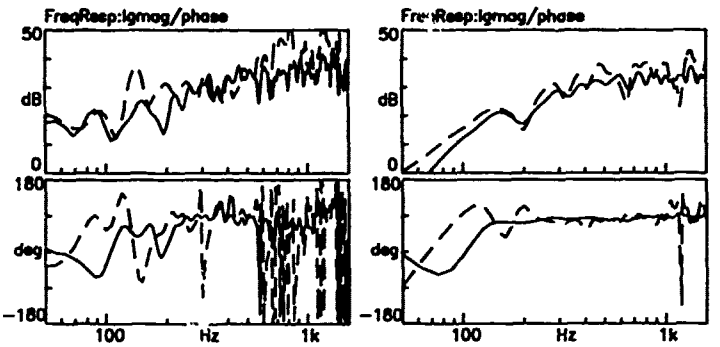

Figure 6 — Examples of the normalised surface impedance of the window. Excitation: (left) normally incident pulses, (right) diffuse field; Processing: – – – at the centrepoint, —— averaged over the 25 positions.

is shown in Fig. 5. The agreement between the curves was fairly good from 200 Hz upwards, and excellent between the tube and new methods between 500 Hz and 1.6 kHz. The result was satisfactory, bearing in mind the uncertainties involved in both the conventional methods.

In the early tests with the window, the acoustic two-microphone technique failed completely to detect correctly the velocity and impedance on the incident side of the window, as compared with the direct surface intensity method. This was obviously caused by insufficient dynamic range: trying to measure the normal velocity of a nearly hard surface is a most adverse test for the two-microphone technique. The pressure-intensity index exceeded 20 dB for most frequencies, indicating that the intensity technique cannot operate reliably.

Examples of window impedances detected using the surface intensity instrumentation are shown in Fig. 6 for the two different excitations. The impedance responding to the diffuse field was stabler and its phase nearer to that of a pure mass for most frequencies.

Incident intensity

The new method of measuring the incident intensity through reciprocity was assessed by comparing the absorption coefficients obtained with the new method and the conventional hard-surface pressure-doubling method. The principal test of the new method is seen in Fig. 7. The actual comparison should be confined to the frequency range 200 to 800 Hz, limited by the sound source and the spatial sampling resolution. The result of the comparison was encouraging. The new method was able to produce curves which followed reasonably close the results of the traditional method, up to its limit of validity.

In Fig. 8, estimates for the incident intensity are plotted, and compared with the method of halving the pressure on the window surface. The comparison showed a fair agreement between the new method and the conventional hard-surface estimate in the range 100 to 500 Hz. The difference was of the order of 3 dB, with the new method detecting more power coming towards the window. Further up the two curves practically coincide. The result was reasonable: The apparently tedious and cumbersome method, of measuring the incident intensity without prior knowledge of the incoming sound field, seemed to work with a promising

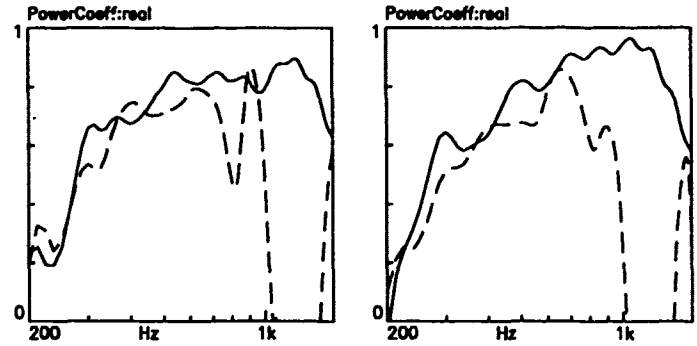

Figure 7—Absorption coefficient of the wool, measured using the new incident intensity method, and compared with the conventional reflection method. The absorbed intensity in both the curves is the same, from an ordinary intensity measurement. Incident intensity from: ——, pressure on hard floor, – – –, the new method. Spatial sums over: (left) 16 centremost, (right) all 36 positions.

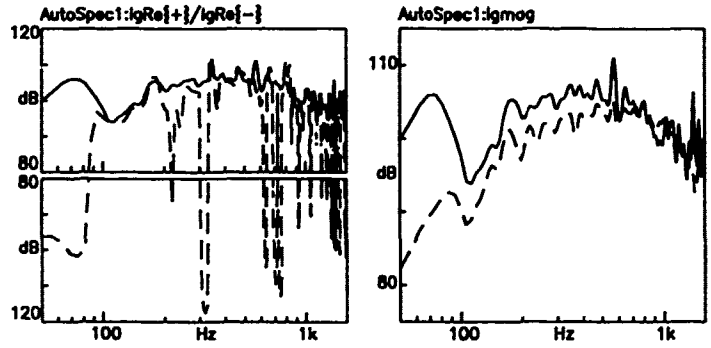

Figure 8—The incident intensity of the window, calculated with the new method, Eq. (4), ——; compared with other methods – – –. Comparison with: (left) the pointwise estimate from Eq. (3), (right) the classical hard-surface pressure estimate. Average intensities in dB re 1 $pWm^{-2}s/Hz$.

accuracy in the tested cases. The deviation found was in the correct direction; the classical method is known to underestimate the incident power at low frequencies.

Structural impedance and reflection

The estimated reflection coefficient of the beam from Eq. (14) is shown in Fig. 9. The impedances were calculated with two different methods. The first approach, Eq. (13), uses the finite difference approximations for the field quantities. The second method, Eq. (15), is based on the reflection coefficient measurement. The results are compared in Fig. 10. The main difference was that the impedance estimates based on the reflection coefficient seemed smoother; obviously because they require only one measured frequency response function.

The actual impedances at a position of the beam should vary, as functions of frequency, around the base curves of the wave impedances. This behaviour is illustrated in Fig. 9, where the force and moment impedances and the corresponding wave impedances are shown overlaid.

CONCLUDING REMARKS

The results with the acoustic impedance tests were in line with the other experiments reported in the literature: In basic, nearly ideal conditions, the two-microphone method gave an estimate which was in good agreement with those of the two conventional methods, from 200 Hz upwards. The incident intensity method was tested in two cases and compared to an independent conventional method. The results were in fair agreement in the expected frequency range. The differences were within the known inaccuracy of the conventional method and the systematic difference observed in the case of the window was in the correct direction.

Ideas based on acoustical two-microphone measurements were applied to bending wave fields in beams. Three procedures were described for estimating the impedance of bending waves. They were based either on

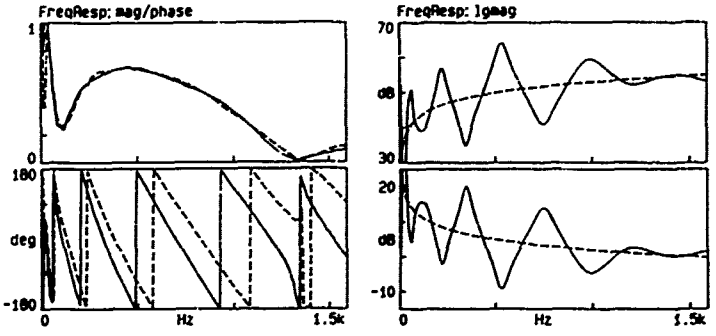

Figure 9 — (Left) Estimated reflection coefficient at positions 3 (——) and 2 (– – –), from Eq. (14). (Right) The estimated farfield impedances (——), Eq. (15) plotted together with the wave impedances (– – –), Eq. (10). Upper: force impedance, lower: moment impedance. Magnitude in dB re 1 Nm/s^{-1}.

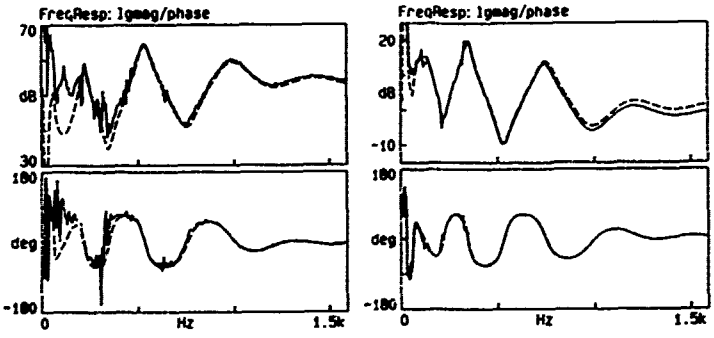

Figure 10 — (Left) Force impedance and (Right) moment impedance estimates at array midpoint, (——) from Eq. (13), and (– – –) from Eq. (15). Upper: magnitude in dB re 1 N/ms^{-1}, *lower: phase.*

finite difference approximation of four acceleration signals or on the known wave impedance and the estimated reflection coefficient. The last approach is restricted to the farfield regions but it is the simplest requiring only two acceleration signals. In the experiments it appeared to give the most reliable results.

ACKNOWLEDGMENTS

The reviewed work was carried out in the Laboratory of Heating and Ventilation and the Instrument Laboratory of the Technical Research Centre of Finland (VTT) and were mainly financed by the VTT Board.

REFERENCES

1. T Lahti, "Two channel FFT analysis applied to transmission measurements," *11th ICA*, Paris, July 1983, vol 6, 365–368.
2. T Lahti, "Application of the intensity technique to the measurement of impedance, absorption and transmission," *2nd Int. Congr. on Acoustic Intensity*, Senlis, Sept 1985, 519–526.
3. T Lahti, "Analysis methods for acoustical systems based on the FFT and intensity techniques," DTech thesis, Helsinki University of Technology. *Tech. Res. Centre of Finland, Publications* 67. Espoo 1990.
4. J Linjama and T Lahti, "Experiments of structural intensity measurements using the one-transducer frequency response method," *INTER-NOISE 88*, Avignon, Aug–Sept 1988, 595–598.
5. T Lahti and J Linjama, "Measurement of reflection and impedance in a beam by the structural intensity technique," *Tech. Res. Centre of Finland, Res. Reports* 625. Espoo 1989.
6. J Linjama and T Lahti, "Measurement of bending wave reflection and impedance in a beam by the structural intensity technique," accepted for publication in *J Sound Vib* (1992).
7. J Linjama and T Lahti, "Estimation of bending wave intensity in beams using the frequency response technique," *J Sound Vib* 151(1991)2.
8. J Y Chung and D A Blaser, "Transfer function method of measuring in-duct acoustic properties. I. Theory," *J Acoust Soc Am* 68(1980)3, 907–913.

SECOND INTERNATIONAL CONGRESS ON
RECENT DEVELOPMENTS IN AIR- AND
STRUCTURE-BORNE SOUND AND VIBRATION
MARCH 4-6, 1992 AUBURN UNIVERSITY, USA

ENERGETIC DESCRIPTION OF THE SOUND FIELD AND DETERMINATION OF THE SOURCE'S PARAMETERS BY THE SPACE INTENSITY SENSOR

Ivannikov A.N., Pavlov V.I., Holodova S.V.
Department of Acoustics
Faculty of Physics
Moscow State University
119899 Moscow
USSR.

ABSTRACT

The aim of this paper is to present the energetic description of the sound field and the first results of the experimental investigation using the space intensity sensor. We offer multi elements acoustic sensor that gives the opportunity to find the source's parameters (distance between the observer and the source, direction to the source, power of radiation, it's multipole type). It is very important for diagnoses of natural sources and technique. Method of intensity sensor calibration which allows to correct amplitude and phase inaccuracy while computer treatment in proposed. The results of the measurements of the sound multipole source's parameters are presented. The test's experimental data correspond well to the real controlled parameters.

INTRODUCTION

In the last time, due to modern equipment, methods of sound field investigation, based on determination of acoustic field's energetic parameters, spread widely [1-3]. On the one hand, the information of field's energetic structure has fundamental character, on the other hand, it is very important for diagnoses of natural noise sources and technic.

The investigation of the complicated wave field energetic structure is a new area in air- and hydroacoustics. It is called sound intensity method. With modern equipment not only sound pressure, but spatial distribution of energetic field characteristics may be measured. This possibility is based on the exploitation of the multichanal systems for informational treatment, which we shall discuss later. The cases, when the radiated wave field is the result of the wave system interference, are to be of the most importance.

These problems are connected with acoustic diagnostic of technical objects and natural sound sources, or with development of sound absorption methods, or with determination of sound characteristics.

THEORETICAL CONSIDERATION

The sound intensity method is based on the several physic preconditions [4].

The noise acoustic field is known to be described by statistical methods with using of corresponding moments of the occasional field quantities. Let us suppose that the process, that we shall regard, is established. Then the main characteristic to be measured is the paired correlation function, with which spectral densities of the acoustic field,s energetic characteristics, for example, densities of potential Π and kinetic energy K, energy flow density vector $\mathbf{S}$, are connected.

The wave field energetic structure can be characterized entirely by the moving liquids energy-momentum 4-tensor. That is why the quantities Π, K, $\mathbf{S}$ role is so fundamental.

The classical approach gives the momentary magnitudes of this tensor components:

$$\tau_{oo} = \tau^{oo} = \frac{\rho_o v^2}{2} + \frac{p^2}{2\rho_o c^2} = K + \Pi.$$

$$\tau_{\alpha\beta} = \tau^{\alpha\beta} = \rho_o v_\alpha v_\beta = T_{\alpha\beta}, \qquad (1)$$

$$\tau^{o\alpha} = -\tau_{o\alpha} = \rho v^\alpha.$$

These quantities determine acoustic noise field thin energetic structure entirely. Here the components $\tau_{o\alpha}$ are proportional to the momentum flow density vector s components ρv_α. The acoustic energy flow density is determined by $S^\alpha = \rho v^\alpha \sim c^2 \tau^{o\alpha}$. Here c - sound velocity. ρ_o - nonderturbated substance density. To synonymous characterizing of the investigating wave field it is necessary to know quantities Π, K, $\mathbf{S}$, $T_{\alpha\beta}$, as they determine the spectral densities of corresponding energetic characteristics. That is the basis of the sound intensity method, because these quantities may be determined experimentally and include the information about amplitude and phase of wave field characteristics.

Finally, let's point that the significant part of noise investigating results relates to the far sound field. Pressure level is a good description of it. In the region, where sound pressure and vibration velocity in a sampling point have the phase coincidence, there the main energetic characteristics may be determined by measuring of the pressure level under the certain direction to the source. In the close field the situation becomes essentially complicate, because of the interference effects. These effects appear due to the defined phase correlations and geometrical sources distribution influence to the field structure features. Therefore, to describe the close area sound field completely, one has to determine the acoustic pressure level, so the other field characteristics. It means that except Π, we should know the level of K, $\mathbf{S}$, $T_{\alpha\beta}$.

According to the determination, $\mathbf{S}(\omega)$ is the intensity noise field's spectral density vector and it may be written as $p(\omega)v^*(\omega)$, where asterisk is the sign of complex conjugation. Such presentation is not occasional. Since vector's components are obviously related to amplitude and phase of pressure's and velocity's Fourier-components, so their assignment can simply determine the field. The physical sense of real (active) and imaginary (reactive) $\mathbf{S}$-vector's components is quite obvious: $\mathbf{I} = Re\,\mathbf{S}(\omega)$ characterizes the process of acoustic energy propagation in medium and is normal to the sound wave constant phase surface; $\mathbf{Y} = Im\,\mathbf{S}(\omega)$, that includes the information about the potential energy field's spatial density distribution, i.e. sound pressure level, is normal to the equal level surface of the acoustic pressure. Hence it appears an interesting property which can be easily realized in close wave area: the wave field is able to create the vortex-type structures in the spatial domains, where $\mathbf{I}$ and $\mathbf{Y}$ vectors are noncolinear.

The simple analysis points that vector's components satisfy the following equations:

$$div\,\mathbf{I} = \sum W^{(i)}\delta(\mathbf{x} - \mathbf{x}_i). \qquad rot\,\mathbf{I} = 2\omega\,[\mathbf{I},\mathbf{Y}]/c^2\Pi.$$

$$div\,\mathbf{Y} = \omega(K - \Pi). \qquad rot\,\mathbf{Y} = 0. \qquad (2)$$

Here, the sound sources, characterized by power $W^{(i)}$, also as the absorbers, are supposed to be localized in the spatial regions, which are small in comparison with the characteristic spatial scale of the wave process. So they can be spatially localized by delta-functional approach.

The equations (2) show that the combined measuring of both active and reactive components of the acoustic energy's flow density vector permits effective detection of the acoustic sources.

ENERGETIC STRUCTURE OF ACOUSTIC FIELD NEAR SOURCES

We investigate the space distribution of the energy characteristics near the multipole sources, as well as we illustrate a number of typical examples of the connection of these characteristics with actual parameters of sources [5].

As we have mentioned before, the complex structure of near source field allows to use the vector of energy density flow: $\mathbf{S} = \mathbf{S}(\omega) = P(\omega)\,v^{*}(\omega) = \mathbf{I} + i\mathbf{Y}$.

Let the motion of the medium near the compact source be singularly described by the velocity potential. In accordance with the cause principle, the sound source forms in the medium a separate spherical wave of the velocity potential, and, consequently, the pressure since the potential satisfies the wave equation. Having this circumstance in mind, it is not difficult to show that there exists the correlation between the radial velocity and the pressure:

$$v(r,t) = \frac{P(r,t)}{\rho c} + \frac{1}{\rho r}\int_{\infty}^{t} dt'\, P(r,t'), \qquad (3)$$

where: ρ is the density of air, v is the velocity of sound, r is the distance between point of source and point of observation.

In eq.(3) the first member is wave component, and decreasing in accordance with the condition of radiation and equal to power flow of energy radiated from the source.

In eq. (3) the second sum describes hydrodynamics motion of the medium, not connected with the wave process of energy transference, and decreasing is comparable to r^{2}. It describes a "fur-coat" round the source. To be sure of this, one should put $c \to \infty$ in eq.(3) (i.e. hydrodynamics approximation). In this approximation, the second member in eq.(3) is non-zero, unlike the first one.

By using Fourier-transformation of eq.(3), the Fourier components of velocity and pressure are connected by

$$v(r,t) = \frac{1}{\rho c}\,P(r,t)\,\{1 + \frac{i}{kr}\}. \qquad (4)$$

where: $k = \omega/c$ is the wave number. Equation (3) shows the physical sense of phase mismatch between Fourier components of velocity and pressure. The phase mismatch also shows that there also exists non-wave component of the medium motion near the source, which is not connected with energy radiation.

Having considered P-$\mathbf{V}$ connection, following from the linear equations of hydrodynamics, $\mathbf{S}$ - vector can be presented in the form: $\mathbf{S} = \frac{i}{\rho\omega}\,P\,\mathbf{grad}\,P^{*}$. Omitting the calculations we'll demonstrate the final result. For the multipole source of noise, it yields:

$$\mathbf{S} = \frac{ik^{2}|M_{Lm}|^{2}}{\rho\omega\,[(2L+1)!!]^{2}}\left\{h_{L}^{(1)}(kr)\,Y_{Lm}(\Pi)\;\mathbf{grad}\,[h_{L}^{(2)}(kr)\,Y_{Lm}^{*}(\Pi)]\right\}. \qquad (5)$$

Here $h_{L}^{(1,2)}(kr)$ - Hankel's function of orders one and two, $Y_{Lm}(\Pi)$ - spherical functions, $\Pi = \mathbf{X}/r$ - unit-vector, M_{Lm} - debit of source.

For the aim of this work the expression is basic.

Let s use the convenient form of the $\mathbf{grad}$ - operator: i.e. $\mathbf{grad} = \mathbf{e}_{r}\partial_{r} - i[\mathbf{X}.\hat{\mathbf{L}}]/r^{2}$.

The operator of momentum of motion quantity $\hat{\mathbf{L}} = -i\,[\mathbf{X}.\mathbf{grad}]$ affects only the angle variables.

The radial component of vector $\mathbf{S}$, according to eq.(5), can be expressed in the form:

$$S_{(r)} = (\mathbf{e}_{r}\cdot\mathbf{S}) = \frac{ik^{3}|M_{Lm}|^{2}|Y_{Lm}|^{2}}{\rho\omega\,[(2L+1)!!]^{2}}\,D_{L}(kr). \qquad (6)$$

Here was used the approximation, received from the formula:

$$D_L(z) = h_L^{(1)}\,\partial_z\,h_L^{(2)} = \frac{1}{2}\,\partial_z(j_L^2 + n_L^2) - \frac{i}{z^2} \qquad (7)$$

(j_L, n_L - Bessel's and Neimann's spherical functions). The expression is correct for any meaning of the argument $z = kr$.

Now we shall calculate the component $\mathbf{S}_r$ which is orthogonal to the vector $\mathbf{X}$. Everywhere we suppose summing by repeated index from 1 to 3.

The second sum of $grad$-operator is convenient to write in components $-i\varepsilon_{\alpha\beta\gamma}\,r_\beta\,\hat{L}_\gamma\,\hat{r}^2$ where $\varepsilon_{\alpha\beta\gamma}$ is the unit of anti symmetric tensor of 3-rang. The complex fundamental 3-vectors e_μ, which give definite advantage in calculation with the spherical functions, are connected with the cartesian coordinate unit vectors by:

$$e_0 = e_z; \quad e_1 = -(e_x + ie_y)/\sqrt{2}; \quad e_{-1} = (e_x - ie_y)/\sqrt{2};$$

with the conditions: $e_\mu^* e_{\mu'} = \delta_{\mu\mu'}$; $\mu = 0, \mp 1$.

Taking into account this conditions, the relation is written:

$$\hat{L}_\mu Y_{Lm} = (-1)^\mu \sqrt{L(L+1)}\,(L, 1, m+\mu, -\mu | L, m)\,Y_{L,\,m+\mu} \qquad (8)$$

Here $(L_1, L_2, m_1, m_2 | L\ m)$ are the vector addition's coefficients or the Clebshe-Gordan coefficients. Taking into consideration $Y^*_{Lm} = (-1)^m Y_{L,-m}$ and the properties of symmetry for the Clebshe-Gordan coefficients, the expression (8) can be simplified.

Then, in view of general expression for the $\mathbf{S}$ - vector (5), as stated above expressing angle variable $grad$ - operator, and also that can be given in the form $r_\beta = \sqrt{4\pi/3}\,Y_{1\beta}$ the tangential components of vector $\mathbf{S}$ can be obtained in the following form:

$$S_{(tr)} = k^2 (-1)^{m+\mu} \sqrt{\frac{4\pi}{3}}\,|M_{Lm}|^2\,|h_L^{(1)}(kr)|^2\,\rho\omega r \cdot$$

$$\cdot \varepsilon_{\alpha\beta\gamma}\,\frac{\sqrt{L(L+1)}\,Y_{1m}Y_{1\beta}Y_{L,-m+\mu}}{\rho\omega r\,[(2L+1)\cdot 1]^2}\,(1, 1, m, -\mu, \mu | L, m). \qquad (9)$$

In this formula we suppose summing by repeated indexes. The relations (6), (9) present precise expressions for the S-vector components from the multipole source of order L.

In spite of unwieldy appearance they are highly informative.

It is not difficult to see that energy flow vector components can generally contain both real and imaginary parts. It's physical meaning was discussed earlier.

The analysis of the expressions (6), (9) shows that they contain the amount of information sufficient to determine the coordinates and the orientation of the multipole sound source in the space. First of all it is possible to solve this problem, because the real $\mathbf{I}$ and imaginary $\mathbf{Y}$ parts of the $\mathbf{S}$- vector are not collinear in any point of space observation. For example, in the spherical system of coordinates for the dipole sound source the parts are defined by:

$$\mathbf{I} = e_r \left\{\frac{M^2 k^2 \cos^2\vartheta}{16\pi^2 \rho\omega\, r^2}\right\}.$$

$$\mathbf{Y} = e_r \left\{-\frac{M^2}{16\pi^2\rho\omega}\left(\frac{k^2}{r^3} + \frac{2}{r^5}\right)\cos^2\vartheta\right\} + e_\vartheta \left\{\frac{M^2}{16\pi^2\rho\omega}\left(\frac{1}{r^2} + \frac{k^2}{r^3}\right)\sin\vartheta\cos\vartheta\right\}. \qquad (10)$$

Where $M = Ad$, d - is the distance between the point sources of the same productivity A.

The non-triviality of this type of source sound-field structure results the non-equality of $rot\mathbf{I}$ to zero:

$$Curl\ \mathbf{I} = e_{\varphi} \frac{M^2 k^2}{16\Pi^2 \rho\omega\, r^2} Sin\, 2\theta. \qquad (11)$$

It is important to note, that in such sound fields the motion of medium particles is realized by ellipse trajectory and, in other words, the velocity vector in the field presentation rotates along the ellipse plane.

It's easy to see from the equations (10), (11) that by measuring the dipole source's sound field vectorial energy characteristics magnitude and direction, one can obtain the source location in full volume. In particular, to solve his problem we can use calculation formulae determined by

$$\frac{(\mathbf{Y}\cdot e_{\theta})}{|Curl\ \mathbf{I}|} = \frac{1 + (kr)^2}{2k(kr)^2}; \quad W = \frac{4\pi}{3} \frac{|\mathbf{I}|}{Cos^2\theta}; \frac{|\mathbf{I}|}{|Curl\ \mathbf{I}|} = \frac{1}{2} r|ctg\theta|. \qquad (12)$$

where W - is the power of a the dipole source. The direction to the dipole source is defined by the direction of $\mathbf{I}$-vector, the plane, in which the source is oriented in the plane of $(\mathbf{I},\mathbf{Y})$-vectors, the distance r and the angle θ of the dipole's axis to the direction $\mathbf{I}$-vector can be found from equation (12).

An interesting supplement of the conducted general consideration is the possibility to determine the type of the source due to measuring of vectorial energy characteristics. To clarify the essence of the question, let us consider the case $z = kr < 1$. From the exact presentation (7) we can find:

$$\frac{1}{2} e_z |h_L^{(1)}|^2 \cong - \left\{ \frac{(L+1)[(2L+1)!!]^2}{z^{2L+3}} \right\} \qquad (13)$$

Then from (6) we obtain the expression for the radial component of intensity:

$$S_{(r)} = \frac{k^3 |M_{Lm}|^2 |Y_{Lm}|^2}{\rho\omega\,[(2l+1)!!]^2} \left\{ \frac{1}{z^2} - t\, \frac{(L+1)[(2L+1)!!]^2}{z^{2L+3}} \right\}. \qquad (14)$$

Further it is not difficult to see, that by the frequency dependence of the function

$$\Xi(\omega) = |Re\, S_{(r)}(z)| \,/\, |Im\, S_{(r)}(z)|. \qquad (15)$$

the useful information can be acquired about the order of multipole of the source. Really, we obtain

$$\Xi(\omega_1) \,/\, \Xi(\omega_2) = (\omega_1 \,/\, \omega_2)^{2L+1}. \qquad (16)$$

Here L - is the multipole's order ($L = 0$ -monopole source, $L = 1$ - dipole source).

It should be noted that this relation is applicable in the range of low frequencies.

METHOD OF CALCULATION

We offer multi elements acoustic intensity sensor that gives the opportunity to determine all three complex components of $\mathbf{S}$ - vector. So it is possible to find the source's parameters, that we are interested (distance between the observer and the source, direction to the source, power of it's radiation), and it's multipole type.

The acoustic intensity sensor consists of four isotropic microphones situated in the tops of tetrahedron. The results of the measuring are calculated to the center of sphere, describing the tetrahedron.

The characteristic (directivity pattern) of the sensor was proved to be isotropic in space. It means that never mind what direction we choose, the sensor determines the quantity and direction of the complex $\mathbf{S}$ - vector's components equally well.

Let the characteristic acoustic wave length fulfill the condition $\Sigma = kl \ll 1$ (l = max r_n – system size). For the four- microphones system this presentation can be written down in the form of matrix :

$$\hat{P}_m = \alpha_{mj}\,\hat{P}_{0j}, \qquad \hat{P}_{0j} = \alpha_{jm}^{-1}\,\hat{P}_m,$$
$$\hat{P}_{0j}^{T} = \left| P(r_0),\ \partial_x P(r_0),\ \partial_y P(r_0),\ \partial_z P(r_0) \right|. \tag{17}$$

where P_m - sound pressure measured by the microphone number m. α_{ij} - coefficient. that depends upon the geometry of the system.

The matrix system (17) yields the quantity of Fourier- components of sound pressure and the projections of the oscillating velocity on the coordinating axis in the point of observation. Now it can be written down in this way:

$$P(r_0) = \frac{1}{4}\,(P_1 + P_2 + P_3 + P_4),$$
$$U_x(r_0) = \frac{1}{\rho\omega}\,\partial_x P(r_0) = \frac{1}{\rho\omega\sqrt{2}d}\,(-P_1 + P_2 - P_3 + P_4),$$
$$U_y(r_0) = \frac{1}{\rho\omega}\,\partial_y P(r_0) = \frac{1}{\rho\omega\sqrt{2}d}\,(-P_1 + P_2 + P_3 - P_4), \tag{18}$$
$$U_z(r_0) = \frac{1}{\rho\omega}\,\partial_z P(r_0) = \frac{1}{\rho\omega\sqrt{2}d}\,(-P_1 - P_2 + P_3 + P_4).$$

Here d - distance between the microphones.

Having sound pressure level determined, one can obtain quantities and direction in space of vectors Re$\mathbf{S}$ and Im$\mathbf{S}$. It is possible to do with the help of corresponding algorithm [5].

The knowledge of the pointed energetic characteristics of field affords the location of source. The distance - r: the angles of the orientation - θ,φ: the power of radiation - W: multipole's type may be determined (12), (15), (16).

MEASURING COMPLEX

In order to register the energetic parameters of the acoustic field and to determine the source's parameters, measuring complex, that includes multi elements intensity sensor and computer, was assembled.

Preliminary measurements have been carried out by using the emitters of monopole's and dipole's type in the anechoic chamber of the Department of Acoustics at the Moscow State University.

Sound source has been situated in the center of the anechoic chamber. The receiving system was out in some distance from the source. The acoustic signals from the source were received by four identical microphones of the sensor. Electric signals are proportional to the acoustic characteristics of the field - pressure and signal phase. Numerical magnitudes of these electric signals were brought in the computer to calculate energetic parameters of the field and the source's characteristics.

METHOD OF CALIBRATION

It has to be noted that while intensity measurements extraordinary exact requirements on the exploited equipment are applied. That's the reason of high attention to the calibration method.

While measuring the equipment's characteristics - amplitude and phase - were controlled. Calibration of the tracts of the measuring complex and the receiving system has been done and immediately, the important role of amplitude and phase inaccuracy of receiving system microphones was cleared. This lead to the necessity of their most exact correlation. Preliminary microphones calibration was carried out by pistonphone of "Bruel & Kjer". Nevertheless, because of the limited calibration precision, there exist some amplitude and phase inaccuracy that is not inadmissible. So extra exact requirements on amplitude and phase correlation of microphones is necessary.

To compensate microphones inaccuracy, we created the computer program for calculation amplitude and phase corrections γ_n, that should be added to each microphone on each frequency. This approach is based on fact that while turning the receiving system - intensity sensor - around one of the axis (center coordinates is in the center of the tetrahedron), the $\mathbf{S}$- vector components theoretically are harmonic functions of angle turning. Received data were compared with ideal. The expression, allowing to calculate corrections γ_n:

$$C_{nm}^{-1} \langle \psi_m \rangle = \langle P_n \rangle (1 + \gamma_n) \ . \qquad (19)$$

Here C_{nm} - matrix, depending on the system geometry, ψ_n - ideal data. P_n - measured pressure. γ_n - amplitude and phase microphones corrections.

For example, fig.1 presents imaginary ($\mathrm{Im}\mathbf{S}$) parts of $\mathbf{S}$-vector components, received by intensity sensor turning around the z-axis, without and with amplitude and phase corrections (O - x-component $\mathrm{Im}\mathbf{S}$, $\Diamond$ - y-component, $\square$ - z-component). Uninterrupted line is the computer treatment result including by (19) amplitude and phase corrections.

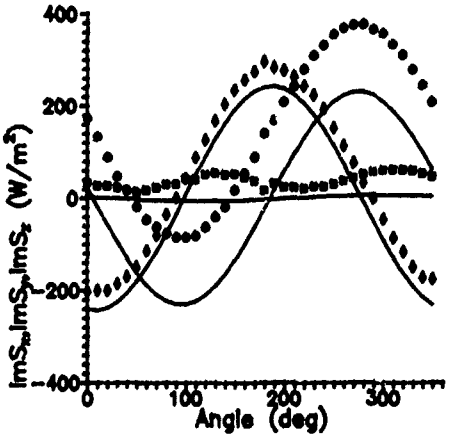

Fig.1. Imaginary parts of S-vector components are function of angle turning.

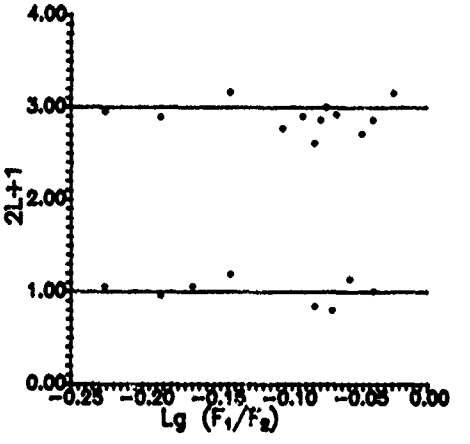

Fig.2. Determination of the source multipole type.

The suggested method of amplitude and phase correction seems to be sufficiently reliable and gives the opportunity to improve significantly the source parameters determination precision.

Ideally, in an anechoic chamber free field conditions are to be created. For us, the regions of low frequencies have been of the most interest, but in these regions the chamber doesn't realize it's function. Unfortunately, the effects that concern, for example, the reflection of the radiated waves from the chamber's walls appeared to be essential, and so on.

This made us taking into account these undesirable factors and their influence on calibration and the system's action.

Before using the sensor it was necessary to evaluate the chamber's quality, it means it's ability to imitate free field. We tested the law of pressure level's falling in the field of the monopole's type source. Declination of pressure amplitude's reverse proportionality to distance between the center of radiating source and the point of observation has been determined. These evaluations afforded to choose the suitable frequency range with minimum distortion of the sound field structure.

On the other hand it was found out that the test had to be carry out on just short enough distances from the sound source, because there the direct wave's contribution ex-

ceeds significantly corresponding the reflected wave field's contribution. To evaluate the distortion s contribution. it was found out that just near the receiving system the field's distortion was determined by the factor:

$$F \cong 1 + ikr\, e^{i2ka}\left(z_k^{-1} - 1 - (ka)^{-1}\right) < e^{ik\eta} > \qquad (20)$$

where r - distance between the source and the receiving system, a - the characteristic chamber's size. $r << a$. $kr < 1$. z_k - the wall's impedance.

The second sum in (20) describes wave's distortion because of the camber's walls: the expression in brackets means the form-factor of the chamber's configuration. that is described by η - quantity. Taking into account the diffraction corrections and corresponding experimental investigations, the range of distance to measure was chosen.

RESULTS

After the preliminary analysis had been done, the series of measurements were carried out (fig.2,3,4). On the fig.2 points correspond experimental quantities of multipole's types (L = 0 - monopole, L = 1 - dipole) and on fig.3 - distance and on fig.4 - direction to the source (for monopole). Everything was received for different frequencies.

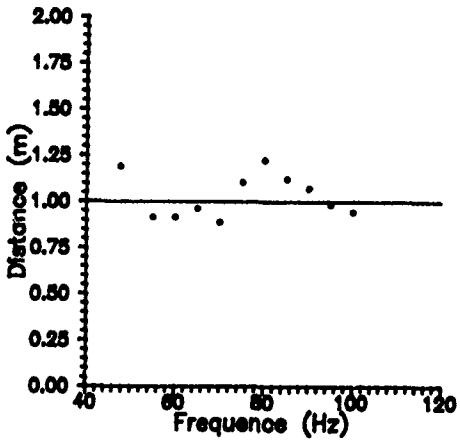

Fig.3. Determination of the distance to the source.

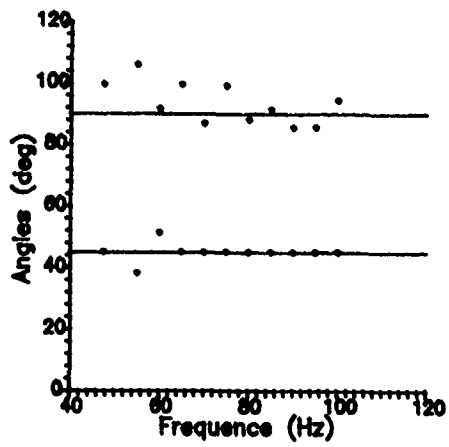

Fig.4. Determination of the direction to the source.

CONCLUSION

The test's experimental data correspond well to the real controlled parameters. So, the principles that were the base of all calculations in this situation are proved to work well. This fact bears witness of using the receiving system and the procedure of computer treatment of the received information.

REFERENCES

1. Proceedings. 2nd International congress on acoustic intensity. CETIM. Senlis (France). 1985.
2. Proceedings. 3rd International congress on intensity techniques. CETIM. Senlis (France). 1990.
3. Bruel and Kjaer. Naerum. Intensity measurements. 1988.
4. Zhukov A.N., Ivannikov A.N., Kravchenco D.I., Pavlov V.I. Distinctive features of energy fine structure of a sound field. Sov. Phys. Acoust.. 1989, vol.35, no4, p.367-369.
5. Zhukov A.N., Ivannikov A.N., Pavlov V.I. Identification of multipole sound sources. Sov. Phys. Acoust., 1990. vol.36, no3, pp.249-252.

SECOND INTERNATIONAL CONGRESS ON
RECENT DEVELOPMENTS IN AIR- AND
STRUCTURE-BORNE SOUND AND VIBRATION
MARCH 4-6, 1992 AUBURN UNIVERSITY, USA

MEASUREMENT OF STRUCTURAL INTENSITY IN THIN PLATES USING A FAR FIELD PROBE

A. Mitjavila S. Pauzin D. Biron
CERT ONERA DERMES
Toulouse FRANCE

ABSTRACT

This paper deals with structural intensity measurements. The ability of a two accelerometer probe to measure structural intensity through plates is studied. The method applies to thin homogeneous plates excited by bending waves. A finite difference approximation of a first order spatial derivative is assumed in the expression of intensity in the far field. Numerical results on infinite plate are presented; A comparison of general and far field formulations of intensity is shown; measurement errors are also studied. Capability of the probe to locate sinks and sources is demonstrated. Finally, an experiment on a clamped plate shows off specific information of structural intensity with comparison to acoustic intensity and modal analysis.

NOMENCLATURE

$\delta(O)$	Dirac function at point source	$G(x,y,f)$	cross-spectrum between x and y signals
Δ	Laplacian	$k^4 = \omega^2 \frac{m}{D}$	k wavenumber
η	displacement on z direction	$Im(u)$	imaginary part of complex u
ν	Poisson's ratio	m_s	surface mass
ω	pulsation	r	distance to source in circular coordinates
D	flexural rigidity	$Re(u)$	real part of complex u

1 INTRODUCTION

During the last few years, investigations on sound sources have been improved with the development of new measurement techniques such as acoustic intensity. Source location and noise reduction are possible, even in bad conditions of measurement: poor signal per noise ratio, multisources. The knowledge of transmission paths of mechanical energy through structures is also interesting to allow a better understanding of vibration phenomena. Vibration may cause problems in precision mechanical systems and even cracks in the structure; measurement of structural intensity is a powerful tool in the study of the path of vibration itself. Vibrations can also induce structure-borne noise, even far from vibration sources. Structural intensity can give information on sources of noise and capabilities of reducing structure-borne noise. The aim of the investigation is to study the ability of a far field method to measure structural intensity on plates in different boundary conditions. Two experiments are presented: the first one studies the ability of the method to locate sources and sinks of vibration; the second one applies to acoustic transmission through structures. Numerical simulation of measurement errors in relation with the experiments are presented.

BIBLIOGRAPHY

Formulae for structural intensity depend on the kind of structure: beam, plate, shell. Most of the periments previously published focused on beams, in part because of the simplicity of the structure. ; the moment, there are two measurement methods of structural intensity derived from mathematical pressions. The first one uses finite difference approximation, of the first order in the far field, of . second and third order for the general expression. The second one is an application of acoustic iography to structures: at the limit fluid-structure, vibrational and acoustical velocities are equal esults obtained from NAH [1] and BAHIM [2] methods are well fitted with physical phenomena and edictions. But only qualitative results can be obtained: the methods are based on evanescent wave tering. The amount of retained evanescent waves must be calculated from direct measurements. The easurement of structural intensity using high order finite difference approximations is difficult [3]. It has en pointed out [4] [5] that the method is very sensitive to measurement errors: amplitude error, phase solution, positionning of each transducer; phase mismatch, and relative positionning between sensors, fluence of reactive field on measurement. For lower order finite approximations (cf. acoustic intensity), easurement errors are not so important. Most experiments carried out in the last ten years used the pression of structural intensity in the far field, away from discontinuities. Under this assumption, oiseux [6] simplified the expression to a first order derivative and finite difference approximation. nyway, the measurement accuracy depends on measurement conditions and particularly on the choice transducers. The most practical and cheaper one to use is the piezoelectric accelerometer which has en largely used in this field. Mickol [7] found a big influence of their mass on vibration of the structure self. Strain gauges and laser techniques avoid mass addition or even contact. But the application of rain gauges to structural intensity on industrial applications is not realistic due to their cost. Errors om contact and laser techniques have been compared. The optical noises of the treatment apparatus duces errors equal or less than the first ones. For these results to be accurate, the laser must be used laboratories with well known conditions of temperature and convective flows.

THEORETICAL FORMULATION

In the case of flexural wave propagation only, intensity through a thin homogeneous plate is the m of three components: shear, flexion and torsion. Intensity depends then only on η, the transverse splacement and its spatial derivatives. Intensity in the direction x through a plate in the plane (x, y) n be written [8]:

$$I_x(x,y,t) = D[\frac{\partial(\Delta\eta)}{\partial x}\frac{\partial\eta}{\partial t} - (\frac{\partial^2\eta}{\partial x^2} + \nu\frac{\partial^2\eta}{\partial y^2})\frac{\partial^2\eta}{\partial x\partial t} - (1-\nu)\frac{\partial^2\eta}{\partial x\partial y}\frac{\partial^2\eta}{\partial y\partial t}] \quad (1)$$

oiseux [6] and Goyder [9] showed off a property of intensity expression in the case of the far field: exure and shear components become similar and twisting component tends to zero.

$$< I_x(x,y,t) >_{far\ field} = \overline{I_x(x,y,t)}_{far\ field} = 2\ D\ < \frac{\partial(\Delta\eta)}{\partial x}\frac{\partial\eta}{\partial t} > \quad (2)$$

frequency space, after a finite difference approximation, intensity is proportional to a cross spectrum.

$$< I_x >_{far\ field} \simeq -\frac{2\sqrt{Dm_s}}{\delta}\int \frac{Im(G(a1,a2,f))}{\omega^2}df \quad (3)$$

wo accelerometers, $(a1, a2)$, spaced by δ are needed to measure intensity.

SIMULATED ERRORS

In the case of a point force F_p in the z direction exciting the plate at a discrete point, the governing uation for the transverse vibration of an infinite plate is [10]:

$$\Delta(\Delta\eta(r)) - k^4\eta(r) = \delta(O)F_p e^{j\omega t}$$

ter applying boundary conditions, the solution of this equation is reduced to:

$$\eta(r,t) = \frac{-jF_p}{8Dk^2}[H_0^{(2)}(kr) - H_0^{(2)}(-jkr)]e^{j\omega t}$$

$H_0^{(2)}(kr)$: 0^{th} order Hankel function of the second kind

$H_0^{(2)}(-jkr)$: 0^{th} order modified Hankel function of the second kind

Structural intensity on thin plates is a function of η and its partial derivatives (§3). It is then possible to express intensity with Hankel functions.

We have studied the results on an infinite plate, with the same mechanical properties as the free boundary plate discribed in §5.1 with a thickness of 1.5mm. The excitation force amplitude is 10 N. In *figure 1*, different expressions of structural intensity are presented. Results are similar to beam structures. Far field intensity overestimates intensity in the very near field of the source, then lightly underestimates intensity. Finite difference error increases with frequency and spacing between transducers. The same tendency is found in acoustic intensity results. Effect of an added phase on the intensity expression has been studied. Here again, the evolution of phase errors can be compared with acoustic intensity results: phase error is higher for lower frequencies and for cases with smaller gaps between the sensors (*fig.2*). Amplitude error on intensity is a linear function of amplitude error on a transducer amplitude. Influence of a rotation of the probe between -20 and $20°$ around its normal position is shown in *figure 3*. Errors due to probe positioning are also studied (*fig.4*). Influence of measurement errors are not negligible on results values. These results allow a better understanding on frequency range of the probe in particular conditions.

5 FREE BOUNDARY CONDITION STEEL PLATE

5.1 Experimental Set-up

A steel plate with the dimensions of 0.95*0.5 m^2 and thickness 2 mm is lying on a bed of rubber elastics to simulate free boundary conditions. Its mechanical properties are known: ν =0.3, D =157.0 N/m, m_s =15.7 Kg/m^2. The exciter is a B&K 4809 electromechanic shaker which is connected to the structure (*fig.5*) using a screwrod attached at one end to the shaker and fixed at the other to the plate between two bolts A viscous damper made of plexiglass plunged in a bowl of oil is bounded to the structure through another screwrod. In order to measure input and output powers, two force transducers are placed between the screwrod and the plate. The structural intensity probe consists of two lightweight B&K 4393 accelerometers screwed on a dural base (23*15*5 mm^3). The tranducers are separated by 1.5 cm; the total weight of the probe is 7 g. The natural frequencies of the different parts of the experimental set-up are well above or below the frequency range of interest (31.5-1250 Hz) A 16 point measurement circular mesh, 6 cm from the center of the source and the sink respectively is choosen in order to measure input and output powers. A line of 10 points between them is also treated.

5.2 Results and Comments

The shaker is excited by a sine or white noise generator. The frequencies choosen for sine generation correspond to input high energy at the source and also to natural frequencies of the set-up. Sine excitation allows higher input levels than white noise excitation. The results (*fig.6*) show off good location of source. Experiments carried out on the damper show that it only works for some discrete frequencies.The 90 Hz frequency (*fig.6*) is well damped by the dashpot.At others frequencies, vortex phenomenon around the sink is observable and intensity amplitudes are lower. Comparison between powers is shown in *table 1*. Power input and output are calculated from signals obtained by a force transducer and an accelerometer. The time averaged power input $< \Pi_{input} >$ can be found from:

$$< \Pi_{input} >= \frac{1}{2} Re(Fv^*) = \int_0^\infty \frac{ImG(F,a,f)}{\omega}$$

It can also be calculated from intensity vectors $\vec{I}$ in a closed contour l around the source:

$$< \pi_{input} >= \sum \vec{I} \vec{dl}$$

The same formulae are applicable for the sink. Good agreement between the two different calculations are found at source and sink for sine excitation. Little difference is found between 8 and 16 equally spaced point calculation around source (*b and c*) and sink (*f and g*). It appears clearly that results obtained from white noise generation are not so good, probably because of low level of energy input.

In *table 1*, it is shown clearly that mechanical energy is being lost while propagating, in part due to acoustic media (between a and b or f and e columns), in part through elastics (between b and d or f and d columns).

6 CLAMPED ALUMINIUM PLATE

6.1 Experimental Set-up

The experimental apparatus used for the investigation is shown schematically in *figure 7*. A lightweight, thin aluminium plate is clamped between a diffuse room and a semi-anechoïc room. Dimensions of the plate are 0.84*0.84*0.0015 m^3. Its mechanical properties are ν =0.3, D =27.0 N/m, m_s =4.48 Kg/m^2.

The plate is excited by an acoustic white noise field generated in the diffuse room. Transmitted acoustic intensity is measured in the semi anechoïc room. Acoustic intensity measurements (*fig.8(b,c)*) are made 10 *cm* from the plate in the 3 space directions with a B&K 3519 intensity probe and a 50 *mm* spacing between the two microphones for a frequency range of measurement of 31.5 to 1250 Hz. Modal analysis is obtained from frequency responses between an impact hammer placed at different points on the structure and reference accelerometer. Structural intensity is obtained measuring the x and y components with the intensity probe described in §5.1. A 11*11 point square mesh on the plate constitutes the measurement locations.

6.2 Results and Comments

At low frequencies, analysis spectra of structural intensity show high energies only around discrete frequencies which correspond to the modes of the plate. The results presented are then calculated for narrow bands of 10 Hz around these frequencies for both structural and acoustic intensity. Our interest is focused on the first 7 modes. Results of structural intensity are presented in *fig.8-(c)*. At any frequency, structural intensity vectors at the four clamped sides have very low amplitudes. This property fits very well with the definition of clamped boundary: no mechanical energy transmitted to the edges. High amplitudes of structural intensity in the plate correspond with high amplitudes of acoustic intensity taken in the two dimensions parallel to the plane of the plate (*fig.8-(d)*). These areas of high amplitudes are located around nodal lines (*fig.8-(a)*). This behavior is noticeable at any frequency band studied. It is also interesting to point out rotational phenomena of structural intensity in the area near nodes and antinodes. These rotations are only visible in structural intensity diagrams. Mean acoustic and structural intensity levels on the plate have been compared for each frequency. The results (*tab.2*) show good agreement in variation of levels of the two quantities: non-radiating modes (low mean acoustic intensity values) correspond to low values of mean structural intensity.

7 CONCLUSION

It has been shown that measurements done with the assumption of far field are in good agreement with other measurement results, even if structural intensity measurements are not done in the far field. It has also been demonstrated that the probe is able to locate sources and sinks, for frequencies where the sink absorbs energy. The analytical model developped for infinite plates is a good tool to evaluate measurement errors. It would be interesting to study further on simulated results in order to draw a probe with a well-known range of validity. Comparison of different measuring methods (STSF, gauges, laser) would be of great interest in the better understanding of the intensity vector.

References

[1] **E.G. Williams, H.D. Dardy, et R.G. Fink**, "A technique for measurement of structure borne intensity in plates", *J. Acoust. Soc. Am.*, 78(6), 1985, pp 2061-2068.

[2] **J.C. Pascal, J.A. Loyau, et J.A. Mann III**, "Structural intensity from spatial Fourier transformation and BAIIIM acoustic holography method", Proc. 3^d *international congress on structural intensity*, Senlis, France, 1990, pp 197-206.

[3] **H. Honda**, "Structural intensity: forward and backward formulation", Proc. *Internoise*, Avignon, France, 1988, pp 569-574.

[4] **W. Redman-White**, The measurement of structural wave intensity, *Thesis*, I.S.V.R. Southampton, England, August 1983.

[5] **S.I. Hayek, M.J Pechersky, et B.C. Suen,** "Measurement and analysis of near and far field structural intensity by scanning laser vibrometry", Proc. 3^d *international congress on structural intensity*, Senlis, France, 1990, pp 281–288.

[6] **D.U. Noiseux,** "Measurement of power flow in uniform beams and plates", *J. Acoust. Soc. Am.*, 47(1), 1970, pp 238–247.

[7] **J.D. Mickol,** An investigation of energy transmission due to flexural wave propagation in lightweight, built-up structures, *Master's thesis*, Purdue University, USA, December 1986.

[8] **G. Pavic,** "Measurement of structure borne wave intensity Part 1: Formulation of the methods", *J. Sound Vib.*, 49(2), 1976, pp 221–230.

[9] **H.G. Goyder et R.G. White,** "Vibrational power flow from machines into built-up structures, 1- Introduction and approximate analyses of beam and plate-like foundations", *J. Sound Vib.*, 68(1), 1980, pp 59–75.

[10] **M. McGary,** Simulated measurement of power flow in structures near to simple sources and simple boundaries, NASA Langley, *Technical report 89124*, 1988.

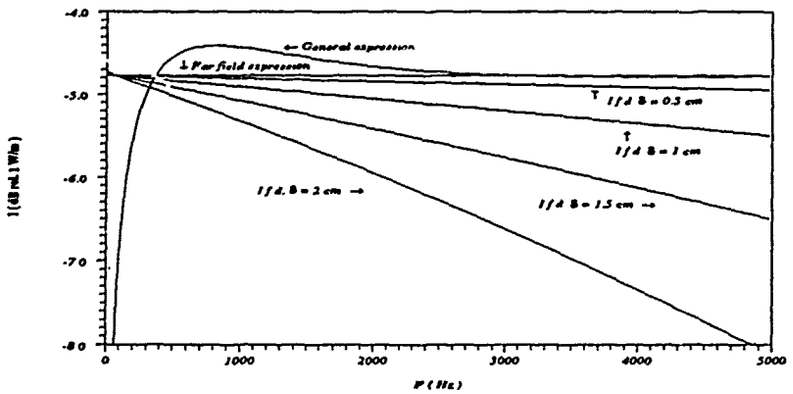

Figure 1: Comparison of three expressions of intensity on plates: general *(eq.1)*, far-field formulation *(eq.1)*, approximate finite difference formulation *(eq.3)* with different values of spacing δ. Distance from source: $r = 6cm$.

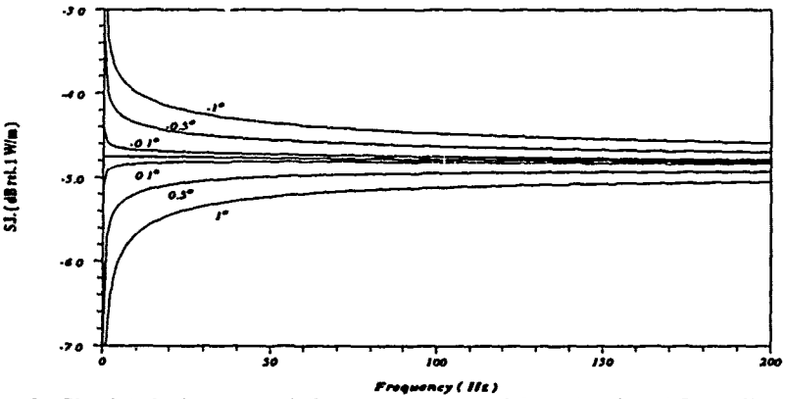

Figure 2: Simulated phase error influence on structural intensity $\delta = 1.5cm$, distance from source: $r = 6cm$

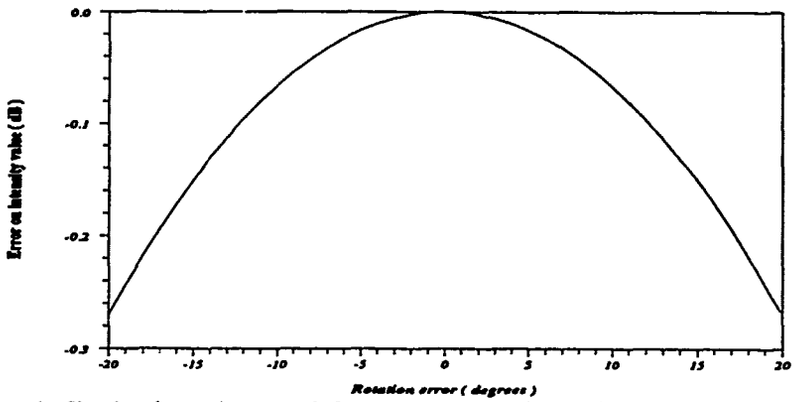

Figure 3: Simulated rotation error influence on structural intensity $\delta = 1.5cm$, distance from source: $r = 6cm$

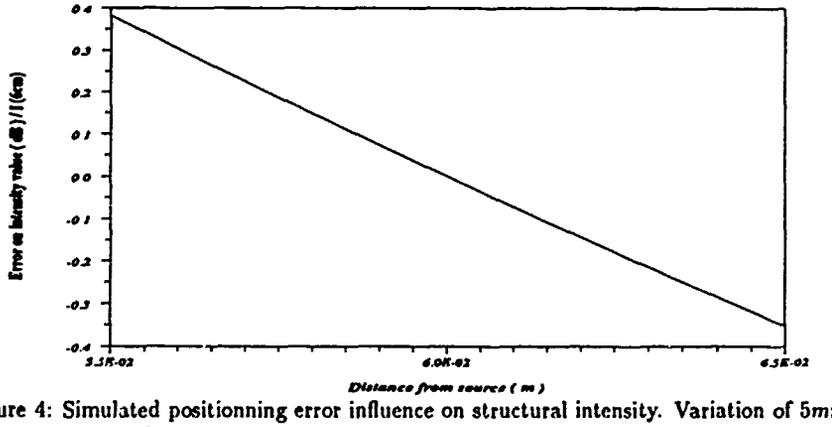

Figure 4: Simulated positionning error influence on structural intensity. Variation of $5mm$ around the reference position from the source: $r = 6cm$. $\delta = 1.5cm$

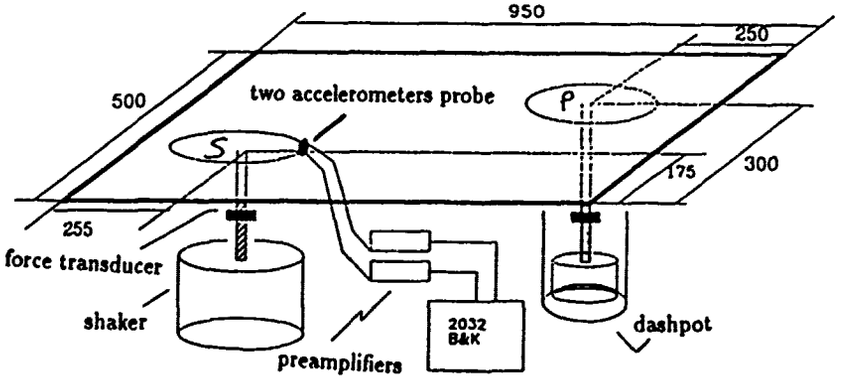

Figure 5: Measurement set up for a free boundary condition plate

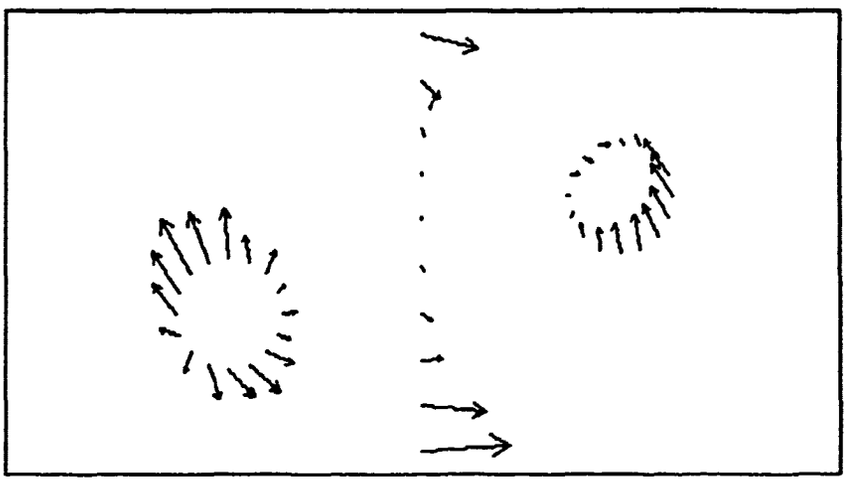

Figure 6: Intensity vectors on a free boundary plate. Sine excitation: 90 Hz

Table 1: Comparison of power calculated with different methods

Freq. band	P_S F*v	P_S $\sum \vec{I}\vec{dl}$ 8 pts	P_S $\sum \vec{I}\vec{dl}$ 16 pts	P_{line} $\sum \vec{I}\vec{dl}$ 10 pts	P_P F*v	P_P $\sum \vec{I}\vec{dl}$ 8 pts	P_P $\sum \vec{I}\vec{dl}$ 16 pts
Hz	a	b	c	d	e	f	g
Sine excitation (W/m)							
90	-0.39	-0.24	-0.236	0.296	0.201	0.107	0.103
127.5	-0.502	-0.247	-0.251	0.085	0.0047	0.0089	0.0063
134	-0.25	-0.186	-0.181	0.144	0.0051	0.104	0.104
191.5	-0.44	-0.28	-0.288	0.239	0.24	0.161	0.157
White noise excitation ($10^{-5}W/m$)							
90	-11.2	-6.06	-7.1	8.9	5.6	2.55	2.61
127.5	-14.5	-10.6	-11.5	1.5	0.55	0.385	0.421
134	-16.0	-11.5	-12.0	9.56	10.2	6.0	6.12
191.5	-18.1	-17.4	-16.4	10.4	12.6	8.38	7.38

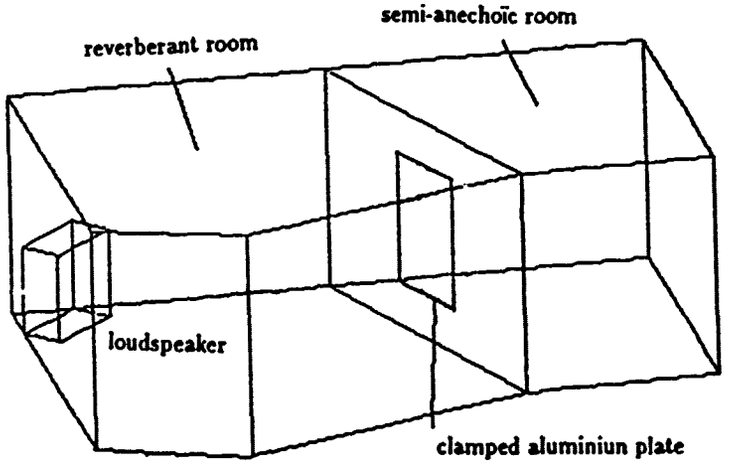

Figure 7: Measurement set-up for a clamped plate

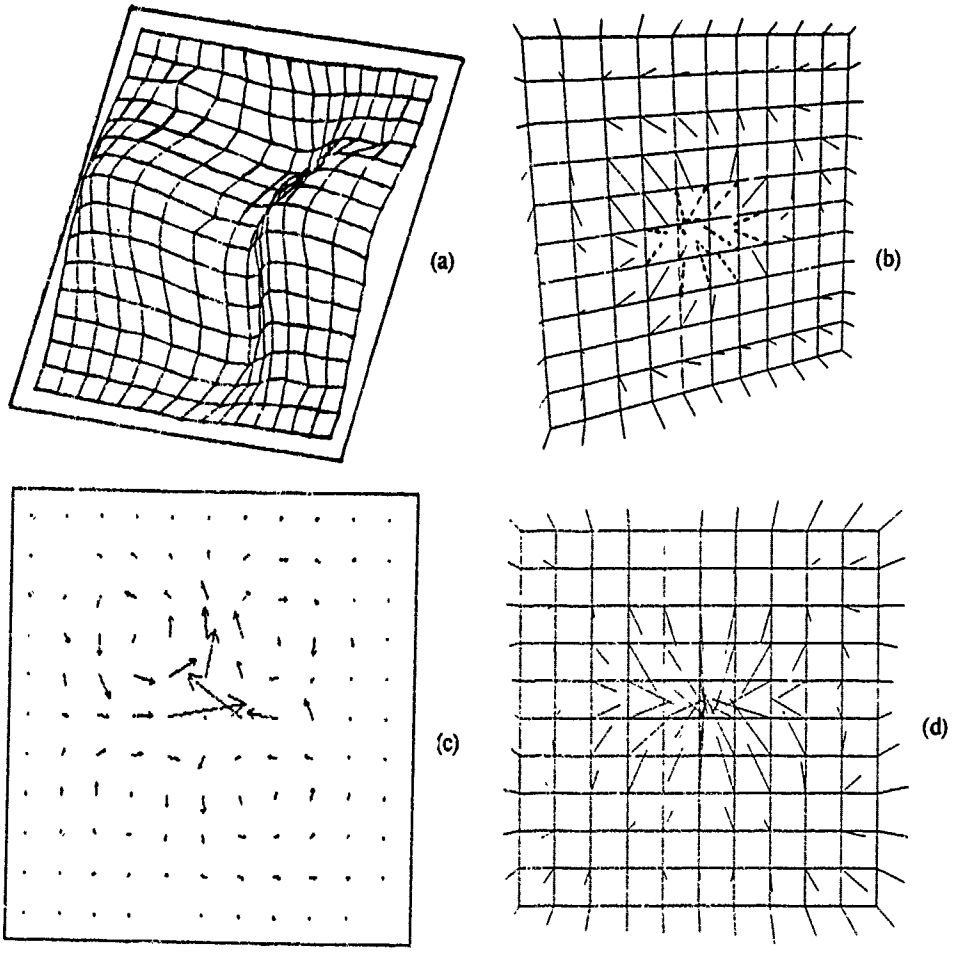

igure 8: Results on a clamped plate: (a) modal analysis (b) acoustic intensity in 3 dimensions (c) ructural intensity (d) acoustic intensity in 2 directions parallel to the plate - 4^{th} mode (70 Hz)

able 2: Comparison of mean acoustic and structural intensity. Each intensity value is the average value etween the 121 measurement points

Frequency band Hz	Acout.Int. W/m^2 rel. 10^{-12}	Struct.Int. W/m rel. 10^{-8}
17-27	67.6	92.0
37-47	67.1	86.3
55-65	57.5	57.5
65-75	69.7	79.6
85-95	68.0	93.8
105-115	69.4	63.3
115-125	59.5	83.3

SECOND INTERNATIONAL CONGRESS ON
RECENT DEVELOPMENTS IN AIR- AND
STRUCTURE-BORNE SOUND AND VIBRATION
MARCH 4-6, 1992 AUBURN UNIVERSITY, USA

FREQUENCY-WAVENUMBER ANALYSIS OF STRUCTURAL INTENSITY

J.M. Cuschieri
Center for Acoustics and Vibration
Department of Ocean Engineering
Florida Atlantic University
Boca Raton, Florida 33431, USA.

ABSTRACT

Structure–borne power flow or structural intensity components on a section of a structure represent the available vibrational power which can result in radiated or structure–borne noise. For a thick or curved structure, where in–plane and out–of–plane waves can equally exist, the distribution of the vibrational power or structural intensity between the in–plane and the out–of–plane waves would be an indication of the importance of one wave type relative to the other. Since a particular wave type can be a more efficient radiator of noise or a more efficient source for the propagation of structure–borne noise, the power imparted to that wave component, either due to external excitation or due to scattering from discontinuities in the structure, would be indicative of the potential of the structure to be an efficient source for noise radiation or for structure–borne noise. This paper described a frequency wavenumber approach to decompose the structural intensity into components which can be associated with particular wave types. For structures with both in–plane and out–of–plane waves, the frequency–wavenumber spectrum of the structural intensity will have components that represent the intensity propagated by each of these wave components. Analytic and experimentally measured frequency–wavenumber spectra of structural intensity for a thick plate and thick beam respectively, are presented that show these results. (Work Supported by ONR).

INTRODUCTION

The need to control vibration propagation is an important issue in the design of many complex mechanical structures. The conditions under which complex structures are used often require a good description and understanding of the different sources of excitation. The type of analysis or experimental measurements to be performed on these structures has to be chosen carefully in order to satisfy some specific requirements. The typical requirements and consequently the information that the analysis or measurement should provide are:

the location of the sources of vibration.

the identification of the paths of vibrational energy flow.

the identification of regions of energy absorption.

the efficiency of the structure to generate radiated sound.

The efficiency of noise radiation from a structure is very much dependent on the type of structural waves that are present in the structure. Based on the characteristics of the structure (thickness, shape, discontinuities, etc), different types of waves can propagate within the structure, these waves can be efficient sound radiators depending upon their characteristics and the characteristics of the surrounding medium. For example, under the influence of water loading, longitudinal and shear in–plane waves are efficient sound sources because their speed of propagation

is supersonic. Consequently, it would be required to differentiate between the relative contributions from the different waves propagating in the structure.

Experimental measurement of the vibrational behavior of a structure can take a number of different forms. One such measurement is the measurement of structural intensity which can yield useful information about the mechanism by which vibrational power is transmitted through the structure. From a structural intensity map, it is possible to identify the paths of significant vibrational power flow, location of vibrational sources, and areas of high energy dissipation.

The different waves that can propagate through a structure all contribute to the transmission of structural intensity. Decomposing the structural intensity into components associated with the different wave types will identify the dominant mechanisms by which the structural intensity is propagated. The total structural intensity is the sum of the contributions from the components associated with the in–plane shear waves, the out–of–plane waves and the in–plane longitudinal waves. Each of these wave types propagate through the structure with different phase velocities and therefore have different wavenumbers. Hence, it is should be possible to decompose the structural intensity into wavenumber components which correspond to the type of structural wave propagating that component of the structural intensity.

The measurement of structural intensity was first presented by Noiseux [1] who derived the expressions for the intensity flow through a unit length cross section of a thin plate. It is shown that the structural intensity due to the out–of–plane motion is based on three components related to the shear force, the bending moment and the twisting moment. Pavic' [2] introduced the use of finite differences to obtain the spatial derivatives involved in the structural intensity expressions. More recently, Redman–White [3] presents a comprehensive analysis of the structural intensity for one and two dimensional structures. These and other similar work only address the structural intensity associated with the out–of–plane vibration.

One of the first measurements of the structural intensity propagated by both out–of–plane and in–plane waves has been presented by Verheij [4]. In this work, while the technique for measuring the intensity associated with the out–of–plane waves is the same as the one used by Pavic', for the in–plane components of the intensity, an accelerometer configuration is used which measures both the longitudinal and torsional accelerations and eliminates the out–of–plane component of the acceleration. Horner and White [5], also presented measurements of structural intensity propagated by in–plane and out–of–plane waves. In this case as well, the out–of–plane and in–plane components are obtained by adjusting the orientation of the transducers to eliminate the contribution of one component or the other. Pavic' [6] used a technique for the measurement of in–plane and out–of–plane surface intensity based on the use of strain gauges and contact velocity transducers capable of measuring the in–plane and the out–of–plane velocities from which the structural intensity is computed. In all of these works, the in–plane components of the structural intensity are obtained by a separate measurement technique which is different from that used to measure the structural intensity contribution from the out–of–plane vibration.

Frequency–wavenumber analysis have been used (Chapman [7]) to measure the radiation of hull–borne energy and to correlate this energy with the wave components of the hull. Using a frequency–wavenumber analysis of the surface velocity and the radiated acoustical field, the different wave components of the hull and the contribution to the radiated field could be observed. By matching the wavenumber components of the structural waves to the wavenumber components of the radiated acoustic field, the dominant structural waves could be identified. This approach identifies in–plane and out–of–plane waves types simultaneously. The same approach can be used for the propagation of structural intensity.

BACKGROUND THEORY

The average intensity crossing a unit surface is defined as the power per unit area crossing normal to the surface. The average intensity vector at a given time instant is thus given by:

$$I(\bar{r},t) = \frac{1}{S}\int_0^S \left[\bar{F}(\bar{r},t)\ .\ \bar{V}(\bar{r},t)\right]\hat{n}_r\, dS \qquad 1.$$

where $\bar{r}$ is the position vector, $\hat{n}_r$ is the unit vector normal to the surface area S, and $\bar{F}$ and $\bar{V}$ are respectively the force per unit area and the velocity, at position $\bar{r}$. The intensity vector at a location on a plate surface represents the average intensity over the thickness of the plate and is equal to

$$I(t,x,y) = \overline{F(t,x,y)} \ . \ \overline{V(t,x,y)} \qquad 2.$$

where $\overline{F}$ in this case is the thickness average stress per unit length and $\overline{V}$ is the corresponding strain rate. Transforming equation (2) into the frequency domain,

$$I(\omega,x,y) = \frac{1}{2} Real \left\{ Force(\omega,x,y) \ Velocity^{*}(\omega,x,y) \right\} \qquad 3.$$

Both the force and the velocity may be described in terms of spatial derivatives of the plate displacements. The spatial derivatives can be approximated using finite–differences [2]. That is, the structural intensity components, as a function of frequency, can be expressed in the terms of the cross–spectra between the measurements at locations on the structure that define the finite difference approximations [3].

For the case of a thin plate structure, in–plane stresses and deflection can be neglected, and only the out–of–plane deflection of the neutral plane needs to be considered. In this case the structural intensity has components which are associated with the shear force, the bending moment and the twisting moment. The structural intensity at any point on the plate is given by the sum of these three components. The measurement of any of these components requires only a knowledge of the out–of–plane motion, since the in–plane motion can be neglected. No further processing would typically be performed after each of the three components of the structural intensity has been obtained from the measured cross–spectra.

In the case of a thick plate structure, in–plane motion and the effects of shear deformation and rotary inertia must be taken into account [8]. In this case, the structural intensity has components which are associated with the shear force, the bending moment and the twisting moment due to the out–of–plane motion, and other components associated with the longitudinal and shear forces due to the in–plane motion. Because of the different characteristics between the in–plane and the out–of–plane motions, it is generally required to measure the different intensity components. This can be accomplished using separate instrumentation to measure the in–plane or the out–of–plane components [4,5,6].

The in–plane waves also produce a transverse velocity that is proportional to the corresponding in–plane velocity due to the Poisson effect [9]. Therefore, the in–plane velocities or structural intensities can be measured from the induced out–of–plane velocity. That is, all the different components of the structural intensity can be obtained from the measurement of the out–of–plane motion of the plate. The task then is to find a way by which each of the structural intensity components, associated with different wave types, can be distinguished from each other.

Out–of–plane waves, in–plane longitudinal waves and in–plane shear waves have different propagation velocities and different wavenumbers,

$$k_T \approx \sqrt{2\pi f} \left(\frac{Eh^2}{12\varrho} \right)^{-1/4}$$

$$k_L = \frac{2\pi f}{\sqrt{\frac{E}{\varrho}}} \qquad 4.$$

$$k_S = \frac{2\pi f}{\sqrt{\frac{G}{\varrho}}}$$

where k_T, k_L, k_S, are respectively the out–of–plane, the in–plane longitudinal and the in–plane shear wavenumbers. That is, the structural intensity associated with each of these waves, propagates through the structure with different velocities. The decomposition of the structural intensity can be achieved by using spatial transform in the same way as is used for identifying different type waves [7]. From equation (3) for the structural intensity, spatial transforming this expression, an expression for the structural intensity in the frequency–wavenumber domain is obtained,

$$I(\omega,k) = \frac{1}{2} Real\ \left\{ Force(\omega,k)\ Velocity^{*}(\omega,k) \right\} \qquad 5.$$

The components of the structural intensity associated with each wave type (different wavenumber) can thus be obtained from a frequency–wavenumber spectrum.

Applying this technique to different sections of a connected structure will identify the contribution of the junctions to the way the structural intensity propagates through the complete structure. The spatial transforms however require the measurements of the forces (or equivalent derivatives) and the velocities at a number of locations. This would be very time–consuming to obtain with contacting transducers. The alternative is to use a non–contacting form of measurement such as a laser vibrometer. If finite difference techniques are used to obtain the frequency–wavenumber function of the forces, a complete set of measurements needs to be performed at every location where the intensity is measured, which, if a laser vibrometer is used, would require a multi–channel laser system.

SIMULATED RESULTS

Considering a the thick plate structure, made out of aluminium with thickness 0.0254 m, length 0.5 m and width 1.0 m, and simply supported on three edges, with a uniform load applied along the fourth edge (figure 1). In–plane and out–of–plane loads are applied at the edge of the plate to induce both in–plane and out–of–plane waves. The frequency range considered is up to 20 kiloHertz to clearly demonstrate the effect of the in–plane longitudinal and shear waves. The velocity modeshapes over the surface of the plate are calculated using the formulation in [10]. An out–of–plane motion component associated with the in–plane waves is derived from the Poisson effect for quasi–longitudinal waves [9],

$$w_{in-plane} = \left[\frac{\nu\ h\ k}{2} \right] u \qquad 6.$$

where $w_{in-plane}$ is the contribution to the out–of–plane motion due to the in–plane motion u, ν is the poisson ratio, h is the structure thickness and k is the wavenumber.

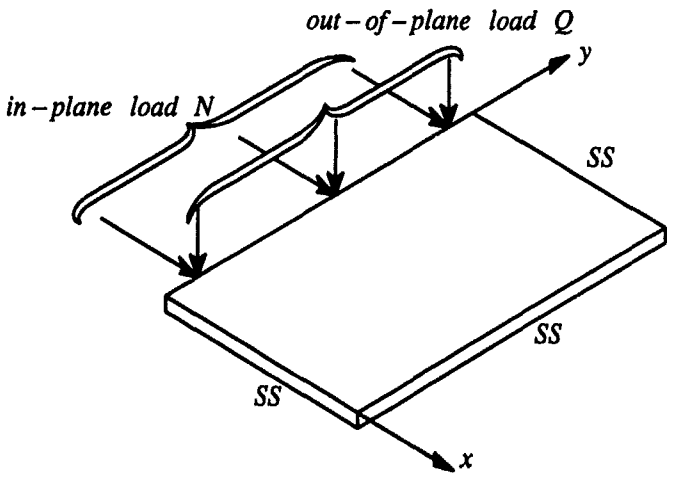

Figure 1. Thick plate structure with in–plane and out–of–plane excitation.

The analysis presented here is limited to the resonant frequencies of the structure. For each resonant frequency, after calculating the modeshapes and the cross spectra to obtain the structural intensity, two–dimensional Fourier transforms are performed at these frequencies to obtain a two–dimensional wavenumber spectrum for both

the surface motion or velocity and the structural intensity. The peaks in the wavenumber spectrum for either surface velocity or structural intensity correspond to the values of (k_x, k_y), the x and y components of the wavenumber, associated with the different wave types (figure 2). The overall frequency–wavenumber plots, (dispersion curves), are obtained by combining the values of the wavenumbers k_x and k_y at the location of the peaks in the wavenumber spectra.

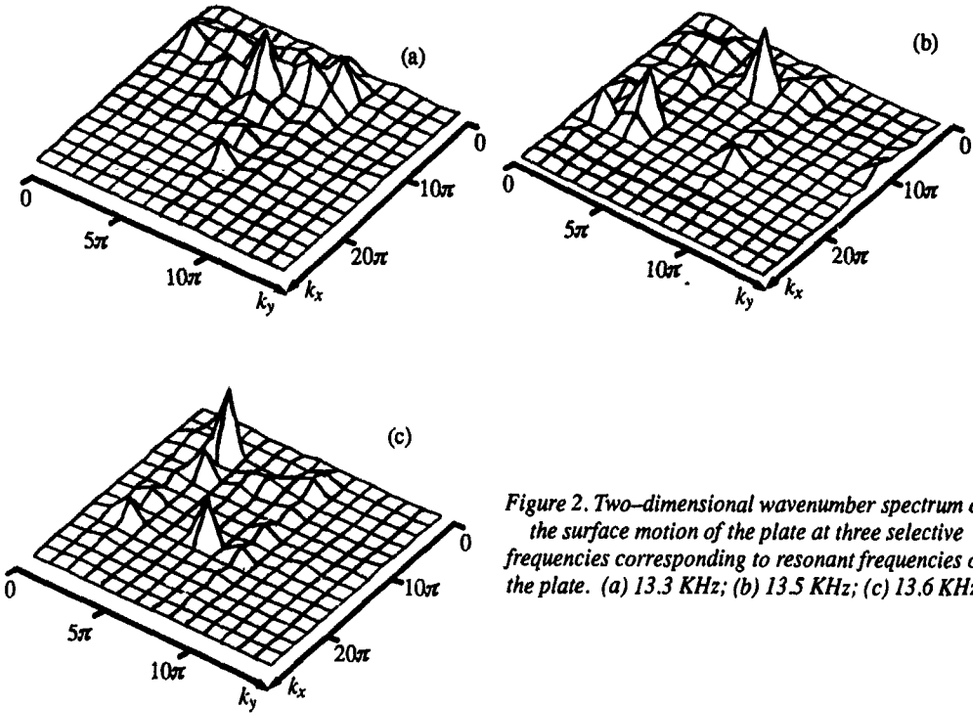

Figure 2. Two–dimensional wavenumber spectrum of the surface motion of the plate at three selective frequencies corresponding to resonant frequencies of the plate. (a) 13.3 KHz; (b) 13.5 KHz; (c) 13.6 KHz.

The results of the combined wavenumbers are shown in figure (3) for the surface velocity. The dispersion curve for the shear waves is above the dispersion curve for the longitudinal waves. The out–of–plane wavenumbers are in general larger than the shear and longitudinal wavenumbers. This is expected since the phase velocity of the out–of–plane waves is less than that of the in–plane waves. Since the analysis is performed at the resonant frequencies, at some of these frequencies, only one type of wave is present. These frequencies corresponding to either a longitudinal or shear resonance giving only one data point on the dispersion curves. For other frequencies, resonances occur for both types of waves. In this case, there are two data points.

The frequency–wavenumber results for the structural intensity are shown in figure (4). As can be observed from this result, using a frequency–wavenumber analysis, the structural intensity has components which can be associated with the in–plane longitudinal, the in–plane shear and the out–of–plane waves of the plate structure. The frequency–wavenumber curves for the structural intensity are similar to the frequency wavenumber curves for the surface velocity.

EXPERIMENTAL WAVENUMBER ANALYSIS

To verify the simulated experimental results presented in the previous section, frequency–wavenumber results for a thick beam subjected to an end load excitation are presented. In these experimental results, the presence of the in–plane and out–of–plane components of structural intensity for the thick beam can be identified.

The experimental set–up consists of a beam, 0.0254m thick, 1.17m long and 0.05m wide, made of plexiglass. One end of the beam was embedded in sand (figure 5) to provide an anechoic termination. The excitation is provided by an electrodynamic exciter which is attached to the beam at its free end. The

frequency–wavenumber spectrum is obtained by measuring the response at 32 locations, spaced 0.02 m apart. A spatial Fourier transform is performed on the measurements to obtain the wavenumber spectrum. Because of the small size of the sample record (32 points), zero padding is used to increase the size of the sample record to 128 points. With a 0.02 m spacing, the limiting wavenumber due to the Nyquist criteria to avoid spatial aliasing is given by,

$$k_{\max} < \frac{\pi}{\Delta} = \frac{\pi}{0.02} = 157 m^{-1} \qquad 7.$$

where Δ is the separation in the measurements. To satisfy this requirement, the frequency of excitation was limited to 20 KHz, for which the out–of–plane wavenumber is less than 157 m^{-1}.

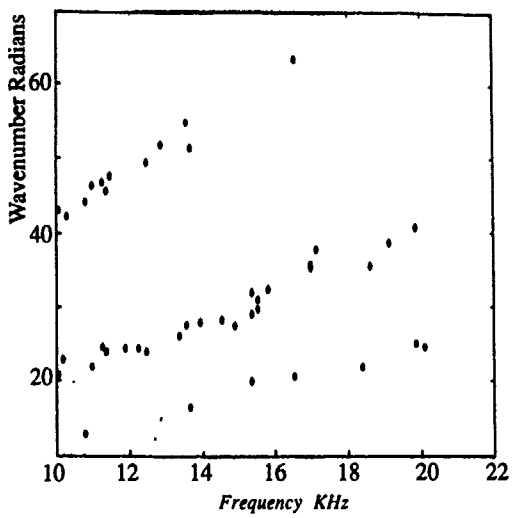

Figure 3. Frequency–wavenumber plot of the surface velocity of the thick plate. The three lines shown are for the in–plane and out–of–plane wave components contributions.

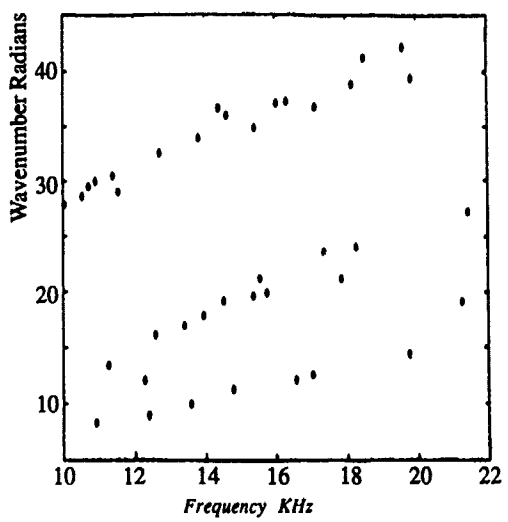

Figure 4. Frequency–wavenumber plot of the structural intensity for the thick plate. Only location of peaks in the frequency–wavenumber spectrum is shown.

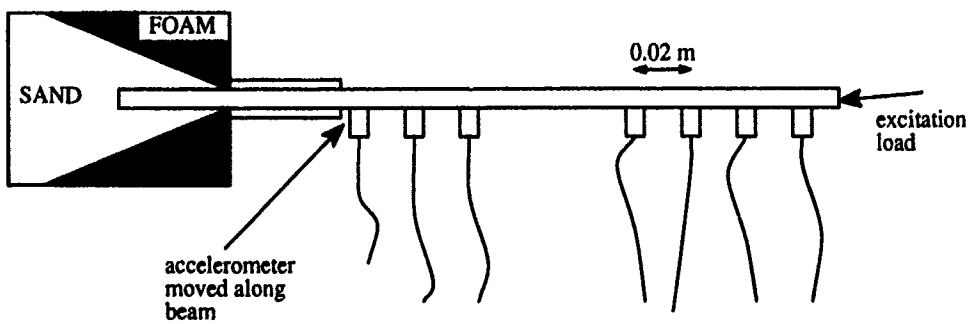

Figure 5. Experimental set–up to measure frequency–wavenumber spectrum of structural intensity.

Using a broad band frequency excitation, an estimate of the frequency response at each measurement location on the beam is obtained as a cross spectrum between the point acceleration and the input load. These frequency spectra are then spatial transformed to form the frequency–wavenumber spectra of the surface motion of

the beam. These results are shown in a contour diagram in figure (6). While the mechanical exciter was mounted in–line with the axis of the beam, due to some offset and the boundaries of the beam, both in–plane and out–of–plane waves are induced in the beam. This can be observed from figure (6) which apart from a straight line representing the linear function relating the in–plane wavenumber with frequency for longitudinal waves (equation 4), a line representing the out–of–plane waves can also be observed.

For the structural intensity, from equation (5) and using the relationship between the force and the first order derivative of the displacement [10], the frequency wavenumber spectrum of the structural intensity is obtained. The first spatial derivatives of the displacement is obtained using a finite difference approach, where for position i,

$$\left(\frac{\partial w}{\partial x}\right)_i = \frac{w_{i+1}(x,\omega) - w_{i-1}(x,\omega)}{2\Delta} \qquad 8.$$

The spatial Fourier transform using zero padding is applied separately to the velocities and to the displacement first derivatives. Using equation (5), the structural intensity is computed and the frequency–wavenumber results are shown in figure (7). The two main components of the structural intensity can be observed in this figure. One component being a linear function between frequency and wavenumber and represents the contribution of the in–plane waves to the propagation of structural intensity and the second component has a non–linear function between the wavenumber and frequency and represents the contribution to the propagation of the structural intensity due to the out–of–plane waves.

The structural intensity components are not uniform with frequency even though a semi–infinite set–up was attempted. The anechoic termination was not perfect and some resonant behavior could be observed on the beam. The results of this frequency–wavenumber analysis show that for thick structures with the right combination of the excitation, both in–plane and out–of–plane components for the structural intensity are present. The relative importance between the in–plane and the out–of–plane components is a function of excitation, frequency and structural thickness.

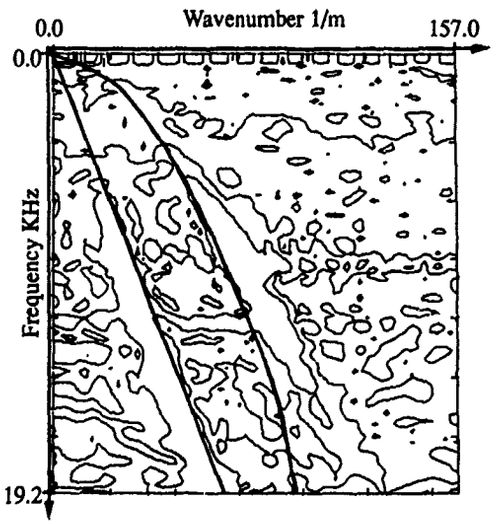

Figure 6. Experimental frequency–wavenumber plot of the surface velocity along the length of the thick beam. The two lines shown are for the in–plane and out–of–palne waves.

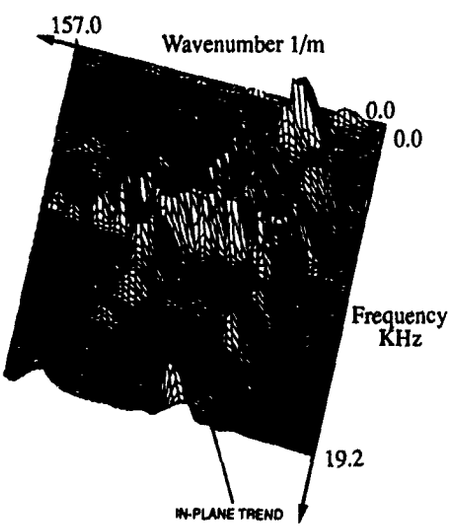

Figure 7. Experimentally measured frequency–wavenumber plot of the structural intensity for the thick beam. The two ridges in the plot correspond to out–of–plane and in–plane waves contributions.

CONCLUSION

From the results of this study it is shown that frequency–wavenumber analysis can be used to simultaneously obtain the components of the structural intensity that are associated with different structural wave components, provided the wavenumbers of the structural waves are different. Simulated experimental structural intensity measurements for a finite thick plate structure and actual experimental structural intensity measurements for a thick beam with one end embedded in sand to simulate anechoic end conditions have been performed. The results of these measurements show that in the infinite beam case two components of structural intensity are indeed obtained in the frequency–wavenumber spectrum, one components associated with the out–of–plane waves and one component associated with the in–plane longitudinal waves. No component is obtained for the in–plane shear waves because of the narrow width of the beam. In the case of the simulated structural intensity measurements for the finite plate, the results are for selected resonant frequencies. Because of the two–dimensionality of the plate, the frequency–wavenumber spectrum for the structural intensity is obtained following a two–dimensional spatial Fourier transform of the cross spectra used in the finite difference evaluation of the structural intensity. While the results obtained show the expected trends, with structural intensity components for each of the three waves types, in–plane longitudinal and shear and out–of–plane waves, some difficulty was experienced in evaluating the two–dimensional spatial transforms. Because of the limited data sets in the spatial domain, the spatial transforms are of poor resolution and further work is required in this area to improve the results and make this approach practically useful.

ACKNOWLEDGEMENT

The author would like to acknowledge the support of ONR, structural acoustics branch, for the support of this work.

REFERENCES

1. Noiseux D.U., "Measurements of Power Flow in Uniform Beams and Plates", Journal of the Acoustical Society of America, 47 (1), 238–247, 1970.

2. Pavic' G., "Measurement of Structure–borne Wave Intensity, Part I: Formulation of the Methods", Journal of Sound and Vibration, 49 (2), 221–230, 1976.

3. Redman–White W., "The Measurement of Structural Wave Intensity", Ph.D. Dissertation, University of Southampton, 1983.

4. Verheij J.W., "Cross Spectral Density Methods for Measuring Structure–borne Power Flow on Beams and Pipes", Journal of Sound and Vibration, 70 (1), 133–139, 1980.

5. Horner J.L., White R.G., "Techniques for Measuring Vibrational power Transmission in a Beam–like Structure Carrying Two Types of Waves", Proceedings of the Third International Congress on Intensity techniques, 273–280, 1990.

6. Pavic' G., "Structural Surface Intensity: An alternative approach in Vibration Analysis and Diagnostics", Journal of Sound and Vibration, 115 (3), 1987.

7. Chapman J.R., "Model–scale Measurement of the Transmission and Radiation of Hull–Borne Vibrational Energy Using Frequency–Wavenumber Analysis", Proceedings of the Shipboard Acoustics Conference, ISSA, 135–154, 1986.

8. Mindlin R.D., "Influence of Rotary Inertia and Shear on Flexural motion of Isotropic Plates", Journal of Applied Mechanics, 73, 31–38, 1951.

9. Cremer L., Heckl M., Ungar E., "Structure–Borne Sound", Springer Verlag, Second Edition, 1989.

10. McCollum M.D., "Vibrational Power Flow in Thick Connected Plates", Ph. D. Dissertation, Florida Atlantic University, 1988.

SOUND AND VIBRATION ANALYSIS

SECOND INTERNATIONAL CONGRESS ON
RECENT DEVELOPMENTS IN AIR- AND
STRUCTURE-BORNE SOUND AND VIBRATION
MARCH 4-6, 1992 AUBURN UNIVERSITY, USA

SEPARATION OF MULTIPLE DISPERSIVE STRUCTUREBORNE TRANSMISSION PATHS USING TIME RECOMPRESSION

Eric Hoenes
Alan Sorensen
Tracor Applied Sciences
Austin, TX 77825
U.S.A.

ABSTRACT

Cross-correlation techniques have been traditionally used to separate multi-path phenomena in sonar and radar processing. For these cases the propagation medium is non-dispersive implying the propagation speed and phase speed are a constant. The cross-correlation function for multi-path propagation in a nondispersive media will ideally consist of a number of delta functions at time delays corresponding to the time it takes the energy to propagate from source to receiver along each path. However, for the case of propagation in a dispersive media the peaks of the cross-correlation function of a broadband signal are smeared across a time interval. For the multi-path case where the time delay between paths are reasonably close, the effect of the dispersion can cause difficulty interpreting the results. This is also the case for the impulse response function which is often used instead of the cross-correlation to estimate time delays. A processing method for dealing with dispersive time delay measurements has been previously developed. This technique, referred to as Time Recompression, is used to compress the impulse response to sharpen time delay peaks, making it easier to discriminate adjacent peaks of multi-path propagation. This paper presents the theory and computational method, an analytical example, and an application to test data.

NOMENCLATURE

$A(x,f)$	-	complex amplitude
c_{ph}	-	phase velocity
c_g	-	propagation velocity
E	-	modulus of elasticity
f	-	frequency
f_{kq}	-	$(k_q/q)^2$ frequency array at values of k
f_{sr}	-	sample frequency
$H(f)$	-	Frequency Response Function
$H(k)$	-	Wavenumber Response Function
$h(t)$	-	Impulse Response Function
$h(l)$	-	Compressed Impulse Response Function
$hb(f)$	-	Butterworth band-pass filter coefficients
I	-	moment of inertia
$k(f)$	-	wave number of the dispersive wave
k_{sr}	-	$(f_{sr})^{1/2}$ equivalent wavenumber sample rate
k_q	-	$(q\ k_{sr}/N)$ wavenumber array for q = 0,1,2....N-1
l	-	length
l_n	-	length of path n
l_p	-	length array of p evenly spaced values
N	-	number of points in transform

S	-	cross sectional area
t	-	time
$X(f)$	-	FFT(x(t))
x	-	position of the displacement
$Y(f)$	-	FFT(y(t))
α	-	path attenuation factor
$\phi(k(f))$	-	dispersive transfer function phase (k(f)l)
$\eta(x,t)$	-	vertical displacement at x at time t
$\eta(x,f)$	-	vertical displacement at x at frequency f
θ	-	material/stiffness constant
ρ	-	mass density
ξ	-	stiffness parameter of path
ζ	-	material parameter of path

THEORY AND COMPUTATIONAL METHOD

A processing method for dealing with dispersive time delay measurements was developed in References [1] and [2] and summarized in References [3] and [4]. This technique, referred to as Time Recompression, is used to remove the effects of dispersion from a measured Impulse Response Function. The removal of dispersive effects enhances the features of the Impulse Response Function allowing easier analysis of transmission path characteristics.

To understand why recompression is necessary for processing dispersive waves, first consider dispersive propagation. For a propagating dispersive wave the displacement can be described as a function of propagation distance and time as:

$$\eta(x,t) = \mathrm{Re}\{A(x,f)e^{i(2\pi ft-k(f)x)}\} \tag{1}$$

It is important to remember that for dispersive propagation the wavenumber is a function of frequency ($k = k(f)$). Also, for a propagating wave in a physical medium, amplitude is attenuated, and in general is a function of frequency ($A(x_1,f) > A(x_2,f)$). Then the Fourier Transform of $\eta(x,t)$ becomes:

$$\eta(x,f) = \int_{-\infty}^{\infty} \eta(x,t)e^{-i2\pi ft}\,dt \tag{2}$$

or

$$\eta(x,f) = A(x,f)e^{-ik(f)x} \tag{3}$$

Now consider two points that are connected through a linear dispersive system. For a linear system the frequency response at the second point, $\eta(x_2,f)$, can be written as the frequency response at the first point, $\eta(x_1,f)$, times the Transfer Frequency Response Function, $H_{12}(f)$.

$$\eta(x_2,f) = H_{12}(f)\eta(x_1,f) \tag{4}$$

From equations 3 and 4 the Transfer Frequency Response Function in terms of a ratio of the amplitudes is:

$$H_{12}(f) = (A(x_2,f)/A(x_1,f))\ e^{-ik(f)l} \tag{5}$$

The ratio $A(x_2,f)/A(x_1,f)$ is the amount of attenuation, and $[k(f)l]$ is the relative phase angle of the propagating wave between points x_1 and x_2 separated by a distance l. For propagating waves, $c_g = dw/dk$ where c_g is the group velocity. Generally, the dispersive wavenumber is expressed as:

$$k(f) = \frac{4\pi f}{c_g} \tag{6}$$

For non-dispersive waves the group velocity is a constant, and the transformation from frequency to wavenumber is straightforward. However, for dispersive propagation, the group velocity is a function of frequency, and the conversion from frequency to wavenumber becomes more complicated. If the vibrational propagation path in a steel structure, such as a ship, is considered, the propagation of energy will typically be predominantly longitudinal and/or flexural waves. Longitudinal waves in steel are non-dispersive, and, therefore, time delay estimates between sensors can be obtained using standard cross-correlation techniques. Flexural waves, however, are dispersive and propagate at velocities that vary with frequency. A general form for the first order approximation of the group velocity of flexural waves in solids is derived in Reference [6] and expressed in Equation 7.

$$c_g = 2c_{ph} = 2(\zeta\xi)^{1/4}(2\pi f)^{1/2} \tag{7}$$

The group velocity of flexural waves expressed in Equation 7, is defined in terms of the material and stiffness parameters.

$$\zeta = E/\rho \qquad \text{and} \qquad \xi = I/S \tag{8}$$

Material and stiffness parameters have been divided for convenience since, for many cases, the material parameter will be constant. Based on these definitions, the frequency dependent dispersion relationship for flexural waves in solid structures is expressed as:

$$k(f) = \theta f^{1/2} \tag{9}$$

where θ is the material stiffness constant derived from Equations 6, 7 and 8 as:

$$\theta = (2\pi)^{1/2}\left(\frac{1}{\zeta\xi}\right)^{1/4} \tag{10}$$

In general, dispersive propagation in solid structures will have a dispersion law of the form:

$$k(f) = \theta(2\pi f)^p \tag{11}$$

where θ is a constant defined by the elastic properties of the structure. The Transfer Wavenumber Response Function from point x_1 to x_2 is expressed as:

$$H_{12}(k(f)) = \alpha_{12}\, e^{-i\phi(k(f))} \tag{12}$$

The Impulse Response Function in the length/wavenumber domain (Compressed Impulse Response Function) can be defined as the Inverse Fourier Transform of the dispersive Wavenumber Response Function.

$$h_{12}(l) = \int_{-\infty}^{\infty} H_{12}(k(f))\, e^{ikl}\, dk \tag{13}$$

However, the transfer function typically measured for a linear system is given in the frequency domain (Frequency Response Function) using Equation 14

$$H_{12}(f) = G_{12}(f)/G_{11}(f) \tag{14}$$

where $G_{12}(f)$ is the Cross Spectral Density Function between points and $G_{11}(f)$ is the Power Spectral Density Function at the first point [5]. The Impulse Response Function is then calculated from the Inverse Fourier Transform of the Frequency Response Function:

$$h_{12}(\tau) = \int_{-\infty}^{\infty} H_{12}(f)\, e^{i2\pi f t}\, df \qquad (15)$$

The Frequency Response Function is typically estimated from the Fast Fourier Transform (FFT) of the input and output using Equation 14. This implies that the Frequency Response Function values are obtained at evenly spaced intervals of f. To estimate the Inverse FFT of the Frequency Response Function to obtain the Compressed Impulse Response Function via Equation 14, Frequency Response Function values at evenly spaced values of k must be interpolated from the Frequency Response Functions. This is accomplished by computing the values of f at evenly spaced values of k using the dispersion law defined in Equation 8 and interpolating the value of the Frequency Response Function at $f(k)$. Transformation from frequency to wavenumber occurs by substituting variables so that:

$$H_{12}(k(f)) = H_{12}(f(k)) \qquad (16)$$

For a system made up of n mutually exclusive paths between points 1 and 2, the system Frequency Response Function can be defined as the linear sum of the individual Frequency Response Functions for each path.

$$H_{12}(f) = H_{12:1}(f) + H_{12:2}(f) + \ldots + H_{12:n}(f) \qquad (17)$$

From Equations 12 and 17 the Frequency Response Function for this system can be written as:

$$H_{12}(f) = \sum_{n} \alpha_n e^{-ik(f)l_n} \qquad (18)$$

where the α_n's are the attenuation factors for the n paths and l_n's are the path lengths. From Equations 12 and 13 the Compressed Impulse Response can be represented as:

$$h(l_p) = \sum_{n} \alpha_n \delta(l_p - l_n) \qquad (19)$$

where $\delta(l)$ is the Dirac delta function. This suggests that using this method would result in a Compressed Impulse Response Function with sharp peaks at lengths corresponding to the systems various path lengths.

ANALYTICAL EXAMPLE

The best documented experiment demonstrating multi-path dispersive propagation is the two beam experiment described in Reference [7] which is used as an example to explain dispersive propagation in Reference [8]. The experimental arrangement, illustrated in Figure 1, consisted of two aluminum beams, one straight and one semicircular, both with a thickness of 0.0032 meters, excited at one end. Two accelerometers were attached on the straight beam, outward of the semicircular beam attachment, providing two distinct structural paths of different length between accelerometers. In Reference [7], this multi-path problem was evaluated with band limited cross-correlation analysis to suppress the dispersion effects. This technique leads to two conflicting requirements: (1) the need for narrow bandwidth excitation and analysis to suppress dispersion; and, (2) the need for broad bandwidth analysis to suppress overlapping of adjacent peaks [8]. Time Recompression processing adjusts for dispersion and negates the need to use narrow bandwidth excitation

This problem was modeled to demonstrate the effectiveness of the Time Recompression Technique in determining dominant transmission paths in a dispersive medium. Mathematical models of the dispersive transmission paths were developed to represent the transfer of flexural energy in the system. Next a broad bandwidth signal was generated to represent an excitation source. Uncorrelated broadband random noise was introduced at the output to represent a noise environment that might be encountered in a realistic measurement scheme. An output was generated using the source excitation, the mathematical transfer function model, and the assumed broad bandwidth output noise.

A transfer function, representing a "measured" transfer function, was derived from the system model's output and input. The impulse response was calculated from this transfer function and displayed no recognizable peaks. Next, the simulated "measured" transfer function was modified using the Time Recompression Technique and the Impulse Response Function calculated. The Compressed Impulse Response Function showed sharp peaks at locations corresponding to the two dispersive path lengths at the original (before dispersion) magnitudes. Several different signal-to-noise ratios were analyzed to investigate the technique's sensitivity to low signal-to-noise ratios.

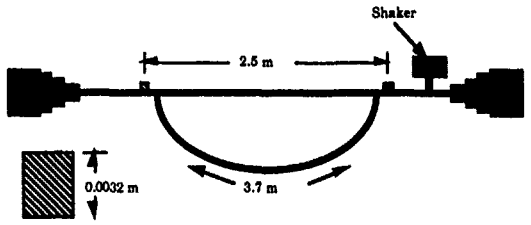

Figure 1 - Two Beam System for Multi-path Dispersion Experiment

Dispersive Two Path Transfer Function

A multipath dispersive transfer function was generated to model the transfer of flexural energy in the two beam system. The total system transfer function is assumed to be the linear sum of individual path transfer functions, as expressed in Equation 19. The phase angle (Equation 20) is defined as the wave number times the distance along a given path.

$$\phi_i(f) = 2\pi k_i(f) l_i \qquad (20)$$

As previously discussed, the flexural wavenumber (Equation 6) is defined in terms of frequency and phase velocity. Attenuation factors have no real physical significance for demonstrating time recompression. For the two beam system, the attenuation factors are arbitrarily set at $\alpha_1 = .4$, and $\alpha_2 = .6$. Both beams have the same material and stiffness parameters and the phase angle of each path's Frequency Response Function was calculated using Equation 20. With these phase angles the total system Frequency Response Function was then computed using Equation 19. This function represents the total dispersive transfer function of the two beam system. For this example the Frequency Response Function of 4096 points was calculated at a constant bandwidth of 20,000/4096 Hz from 0 to 20,000 Hz. A four-pole Butterworth band-pass filter with pass band frequency limits of 500 and 2500 Hz was used to filter the input to represent a band-limited source.

Model of Measured Transfer Function

A simple linear input/output model was developed to model the measured multipath dispersive data. For this model the output signal was a function of the input, the dispersive transfer function previously developed, and uncorrelated output noise. The input signal was generated as a zero mean Gaussian time series with a standard deviation of 1.0. The sampling rate was set at .05 milliseconds to insure that the time delay resolution was adequate to separate closely spaced time delays. The time series was then filtered using the Butterworth filter coefficients to obtain a band-pass random input time series. The band-pass time series was then transformed into the frequency domain using a FFT. A zero mean Gaussian time series with a standard deviation of 0.1 was then generated to model the output broadband noise. The output noise time series was also transformed into the frequency domain using a FFT. The output signal was then generated from the band-limited input, dispersive transfer function, and output noise. The signal-to-noise ratio of the output to output noise for the processing bandwidth was calculated to be +5 dB. Also, visible in the output signature are drop outs at frequencies where the phase angle of the two paths are 180 degrees apart, producing cancellation at the output signal. Using the generated input and calculated output, a new Frequency Response Function was generated. This Frequency Response Function represents a simulated measured Frequency Response Function. In order to further examine effects of dispersion on this typical measured Frequency Response Function, the envelope of the Impulse Response Function was calculated from the Frequency Response Function and illustrated in Figure 2. Dispersion smears the time delay peaks

significantly, making the time delay peaks unrecognizable even at this high SNR.

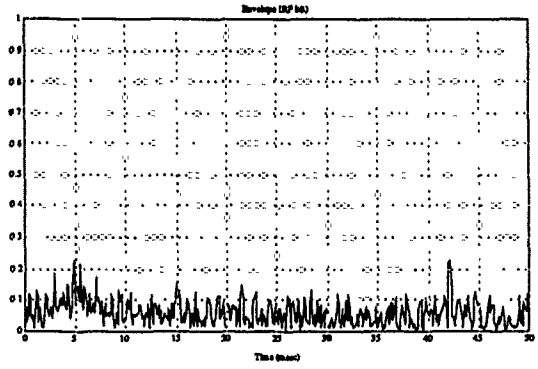

Figure 2- Envelope of the Impulse Response Function $|h_m(t)|$

This simulation again illustrates the difficulties associated with using time delay techniques in a multi-path dispersive propagation measurement and highlights the need for time recompression processing.

Wavenumber Response Function

To remove the effects of dispersion from the Impulse Response Function, the Frequency Response Function must be transformed to the Wavenumber Response Function. This is accomplished by interpolating the Frequency Response Function at values of $f(k)$ corresponding to evenly space values of $k(f)$. By defining a frequency array, f_{kq}, at evenly spaced values of k, a modified Wavenumber Response Function is obtained by interpolating $H_m(f_q)$ at frequencies f_{kq}. From Equation 16, the Wavenumber Response Function becomes the interpolated Frequency Response Function. A dispersion relationship between the wavenumber and frequency, defined in Equation 11, is used to perform the transformation. As previously discussed (Eqn's 9 and 10), for flexural waves in solid structures, the constant θ will be a function of the material and stiffness parameters and the power p will be one-half (1/2). In the multi-path case, the stiffness parameters for each path can be different. The variable θ may be set to unity without loss of generality to produce an assumed dispersion law. Either a scaled length or the stiffness parameter will be then be determined from the final calculation of the Compressed Impulse Response Function.

Compressed Impulse Response Function

Using the modified Frequency Response Function calculated with Equation 16, the Compressed Impulse Response Function was calculated by taking the Inverse FFT of the modified Frequency Response Function. Examining the magnitude of the Compressed Impulse Response Function, illustrated in Figure 3, reveals distinct peaks with amplitudes approximately equal to the attenuation factors (α's) for the two path system modeled.

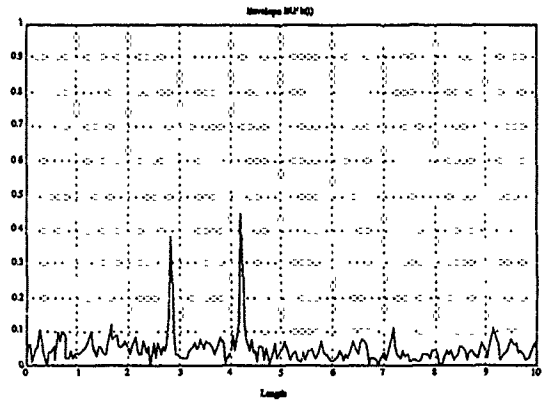

Figure 3 - Compressed Impulse Response Function $h_m(l_n)$

Interpreting Results

The Compressed Impulse Response Function produces peaks at values $l_{m:i}$ which must then be correlated to a propagation path. It is assumed that for practical cases the material properties will be known, implying that $l_{m:i}$ is a function of length and a stiffness parameter. The relationship between dispersive path parameters and lengths determined from the Compressed Impulse Response Function must be associated with actual dispersive properties and path lengths. The assumed dispersion law and measured lengths are related to the actual dispersion law and path length using the relationship between phase dispersion and length (Eqn 20). Recalling that $\theta_{m:i}$ was set to unity, this results in:

$$l_{m:i} = \theta_i \; l_i \qquad (21)$$

After determining $l_{m:i}$ a physical stiffness and length were obtained that satisfy Equation 21. For example, for the case of the two beams, the material/stiffness constant and the $l_{m:i}$'s, $l_{m:1} = 2.8$ and $l_{m:2} = 4.2$, illustrated in Figure 11 were used to calculate path lengths; $l_1 = 2.43$ m, and $l_2 = 3.65$ m.

Effect of Signal-to-Noise Ratio on Time Recompression

The previous section demonstrates Time Recompression for a relatively high output SNR. In order to further examine the effects of SNR on the calculation, the model was used with different output noise levels. Two additional cases were run with output SNR's of 0 and -5 dB over the measurement bandwidth. In both cases the peaks were easily identified in the Compressed Impulse Response Function

APPLICATION TO TEST DATA

In order to show how this technique might be applied, data from a scale model test was examined using Time Recompression. It is important to remember that the data used in this example was not taken in order to examine this technique, but was in fact taken to provide information for a separate problem. Although the source frequency was relatively low and path lengths were too short to allow much dispersion, some improvement over the regular Impulse Response Function was observed. An example set of data consisted of data from two accelerometers; one at the source and one a short distance down a section of pipe. The Impulse Response Function is illustrated in Figure 4. This figure illustrates very little dispersion as would be expected due to the relatively short length of travel, but the actual time delay is somewhat smeared. Figure 5 illustrates the envelope of the Compressed Impulse Response Function which shows the majority of the energy to be in two peaks which probably correspond to a direct path and a reflected return from a pipe elbow or pipe termination.

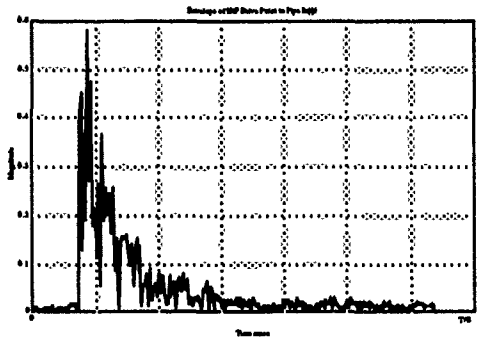

Figure 20 - Source to Pipe Envelope of IRF |h(t)|

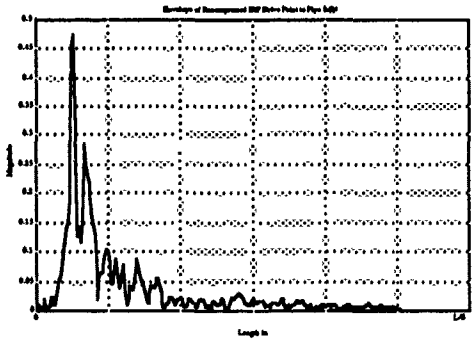

Figure 21 - Source to Pipe Envelope of Recompressed IRF |h(l)|

REFERENCES

1 Pavic, G. and White, R.G., "On the Determination of Transmission Path Importance in Dispersive Systems", Acustica Vol. 38, 1977, pp 76-80.

2 Booer, A.K., Chambers, J., Mason, I.M., "Fast Numerical Algorithm for the Recompression of Dispersed Time Signals", Electronic Letters 13, 1977, pp 453-455.

3 Brazier-Smith, P.R., Butler, D., Halstead, J.R., "The Determination of Propagation Path Lengths of Dispersive Flexural Waves Through Structures", Journal of Sound and Vibration, Vol. 75(3), 1981, pp 453-457.

4 Kalme, J.S., Uldrick, J.P., "Use of Recompressed Impulse Response to Identify Sources and Paths of Structureborne Noise in Wide Flange I-Beams and Pipes Conveying Fluid", Journal of Sound and Vibration, Vol. 95(4), 1984, pp 439-467.

5 Bendat, J.S., and A.G. Piersol, Random Data: Analysis and Measurement Procedures, Second Edition, Wiley-Interscience, New York, 1986.

6 Cramer, L., Hekl, M., Structure-borne Sound, Spring-Verlag Berlin Heidelberg New York, 1973.

7 White, P.H., "Cross-Correlation In Structural Systems: Dispersive and Non-dispersive Waves", Journal of the Acoustical Society of America, Vol. 45, 1969.

8 Bendat, J.S., and A.G. Piersol, Engineering Applications of Correlation and Spectral Analysis, Wiley-Interscience, New York, 1980.

SECOND INTERNATIONAL CONGRESS ON
RECENT DEVELOPMENTS IN AIR- AND
STRUCTURE-BORNE SOUND AND VIBRATION
MARCH 4-6, 1992 AUBURN UNIVERSITY, USA

DYNAMIC MECHANICAL PROPERTIES OF VISCOELASTIC MATERIALS

Surendra N. Ganeriwala
Philip Morris Research Center
P. O. Box 26583
Richmond, VA 23261-6583
U. S. A.

ABSTRACT

Described are a brief overview of the general viscoelastic behavior of polymeric materials, the basic theory, experimental techniques used to measure the dynamic mechanical properties, and the time-temperature superposition principle. Provided a brief discussion of the glass transition phenomenon along with its complexities and significance in governing the viscoelastic damping of polymers. Also, given are a brief description of a novel experimental technique and modeling scheme developed by us. The technique is known as Fourier Transform Mechanical Analysis (FTMA). It has many advantages over conventional methods. Our model provides a quantitative description of the glass transition phenomenon and a complete constitutive equation. The time-temperature superposition is an integral part of it.

INTRODUCTION

Viscoelastic materials are useful for isolation and control of noise and vibration because of their ability to dissipate energy. The damping ability of these materials is increasingly utilized to develop advanced composite materials such as high strength low weight aircraft structures and other engineering components. For an optimum design, dynamic analysis of viscoelastically damped structures must be performed at a design phase. A comprehensive, useful understanding of the viscoelastic damping inherent in these systems can come only from studies of mechanical properties over wide ranges of frequency (time) and temperature. If a material is moisture sensitive, the effect of moisture must be included also. The same rule also applies for plasticizers and other additives.

The mechanical behavior of most polymers and the materials that fail to crystallize when cooled from the molten state can be adequately represented by the theory of viscoelasticity. A broad classes of materials form a disordered amorphous solid structure like a glass; polymers are just a one class from the list. But because of wide uses of polymers, viscoelasticity is generally associated with polymers only. Nevertheless, it is important to note the generality of the theory of viscoelasticity. In this paper, polymers and polymeric materials will be synonymously used to designate viscoelastic materials.

Dynamic mechanical properties of polymers are generally obtained by subjecting a specimen to a single frequency sinusoidal excitation and measuring the response. The tests are then repeated over a range of temperatures and frequencies. Often the range of frequency covered by an instrument is not large enough to fully analyze the dynamic mechanical response of a material system. The principle of time-temperature superposition is then utilized to obtain master curves that presumably approximate a

mechanical response isotherm for a wide range of frequency (or time) [1-4]. Note that the effects of moisture (relative humidity) and plasticizers have not been investigated much.

The mechanical behavior of polymeric materials becomes non-linear, even at a moderately large deformation. Considering the complexities and a lack of success of any non-linear viscoelastic theory to model real materials, a meaningful discussion of the topic is beyond the scope of this article. However, an interested reader may refer to the authors paper [5]. This paper provides a brief overview of the viscoelastic behavior of polymers with a discussion of the glass transition phenomenon, the basic theory, experimental techniques used to measure the dynamic mechanical properties, and the time-temperature superposition principle. Also, given are a brief description of a novel experimental technique known as the Fourier Transform Mechanical Analysis (FTMA) [4], and a modeling scheme developed by us [6].

GENERAL NATURE OF A POLYMER MECHANICAL BEHAVIOR

Polymers are long-chain molecules made of covalently bonded atoms. They exhibit a wide spectrum of mechanical properties depending upon their chemical composition and structure, chain orientation, molecular weight, cross link density, and morphology. A distinguishing characteristic of polymers is the dependence of their mechanical properties on time, frequency, and temperature [1-3]. This is easily demonstrated by three simple tests. A constant stress applied to a polymer sample will produce an instantaneous deformation which then continuously increases with time. This process is known as creep. If a polymer sample is deformed to and held at some constant strain, then the stress required to maintain that strain continuously decreases with time. This phenomenon is known as stress relaxation. When a sinusoidally varying stress is applied to a polymer sample, the resulting strain lags behind by an angle from 0 to 90 degrees. The phase angle between stress and strain is a measure of the energy dissipated due to the internal friction or damping property of the material.

The material functions describing mechanical behavior are strong functions of temperature. Typically at low temperatures viscoelastic materials are stiff and brittle while at higher temperatures they are flexible and soft. Interestingly, the effect of temperature can also be duplicated by time or frequency, as shown in figure 1. There is a certain region of time, frequency, or temperature called the glass transition region over which the behavior changes rapidly from rubbery to glassy. In this region polymers are highly viscoelastic and useful for sound and vibration damping.

Glass Transition Phenomenon

The glass transition is probably the most important property of polymeric materials. This is evident from the fact that every time a new polymer is synthesized, the first property one determines is its glass transition temperature (T_g). It is generally believed that glass transition is a failure of a material to crystallize and settle into a thermodynamically unstable amorphous state known as a glassy structure [7,8]. Reference (7) lists 8 classes of materials such as soda lime glasses, acids, alcohols, polymers, metallic alloys, etc. which have been found to display this type of behavior. When liquids of these materials are cooled, in a certain region of temperature their viscosity precipitously increases by several orders of magnitude ($\sim 10^{13}$ Pa), probably due to molecular asymmetry. This increase in viscosity is responsible for the energy dissipation due to internal friction or the damping property of polymeric materials. Blowing of glasses, molding polymers and the like are made possible by this phenomenon.

Figure 2 shows a typical plot of damping factor versus temperature at several frequencies. The peak of damping curve shifts to a lower temperature with a decrease in frequency. Glass transition is also believed to be a consequence of the inability of a material to maintain equilibrium with the external excitation. At lower frequencies a material is able to follow the stimulus down to lower temperatures and vice-versa. Note that the peak of a damping factor curve lies approximately half way between the transition region shown in figure 1 and is not the glass transition temperature, as sometimes used in the literature.

During a glass transition many other properties such as coefficient of thermal expansion, heat capacity, compressibility, dielectric constants, refractive index, etc. also show dramatic changes. Glass

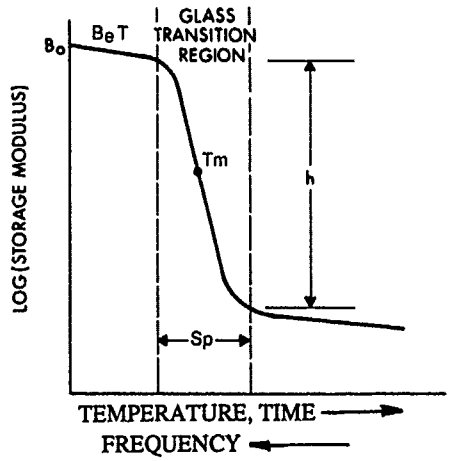

Figure 1. Typical stiffness of a polymer during a glass transition. Note frequency-temperature equivalence.

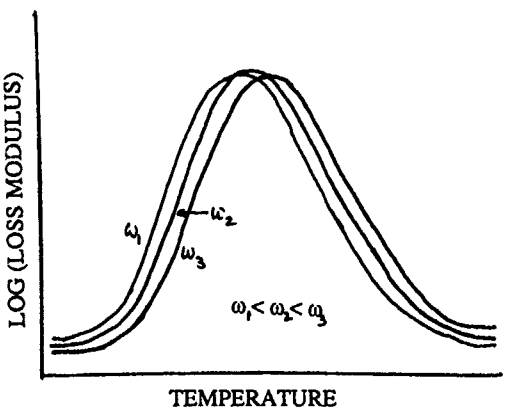

Figure 2. Typical loss modulus of a polymer in a glass transition region showing the effect of frequency.

transition temperature is generally measured by calorimetric methods. The value of T_g obtained by thermal method is usually lower than that measured by viscoelastic tests. The reason for the discrepancy is probably due to the differences in definition of glass transition temperature.

The glass transition phenomenon has several interesting as well as provocative properties. Complexities of the process can be illustrated by noting the following behavior [7,8]. Observed glass transition is a rate dependent process and the kinetics are nonlinear. Material properties (heat capacity, expansion coefficient, etc.) versus temperature curves show asymmetry and hysteresis. The deviation of a material function from the nominal value can not be modeled by a first order process even very close to thermodynamic equilibrium. Also, this deviation cannot be predicted by any known theory.

A comprehensive understanding of transition process requires a molecular interpretation [1,3,6-8]. As temperature is lowered, due to increase in viscosity molecular motion becomes sluggish. Consequently, the time required for a molecule to occupy a configuration in equilibrium with the environment increases. It is generally referred to as the molecular relaxation time. On further lowering the temperature, relaxation time gets so large that the material system starts losing equilibrium with the external changes. At temperatures approaching T_g time scales become infinitely large making it practically impossible to maintain a complete thermodynamic equilibrium in any experimental study. Such long range processes are responsible for physical aging of glassy materials and for the same reason plastics become brittle with time.

Considering the importance of glass transition, it is intriguing that the fundamental principle governing the process is not fully understood. Theoretically the problem is pursued along two lines of thought [7]. One school of thought says that the glass transition is a kinetic process and has nothing to do with thermodynamics whatsoever. While believers in thermodynamics claim that even though the observed behavior appears kinetic, the underlying fundamental principle governing the process is the second order thermodynamic transition. The second order transition designates a discontinuity in the second derivative of free energy with respect to intensive variables. In 1933 Ehrenfest argued that the second order phase transitions are thermodynamically admissible just as the first order transitions of metals, water and etc. Following his work, it has been postulated that glass transition phenomenon will mimic a second order transition in an infinitely slow approach to glass transition temperature. However, the second order transition has never been realized in any experiment.

Recently we have made an attempt to elucidate the process using a phenomenological model. Our model suggest that the underlying process for a glass transition is indeed a second order thermodynamic transition. It also indicates that practically it is impossible to attain a second order transition and that the observed behavior is kinetic. We believe that without a proper model of glass transition process it is not possible to develop a thermoviscoelastic constitutive equation.

BASIC THEORY OF LINEAR VISCOELASTICITY

A one dimensional form of constitutive equation for linear viscoelastic materials which are isotropic, homogeneous, and hereditary (non-aging) is given by [2]:

$$\sigma(t) = \int_{-\infty}^{t} G(t,t-t')\dot{\gamma}(t')dt' \qquad (1)$$

where the kernel G(t-t') is a monotonic nonincreasing function of time known as the stress relaxation modulus, $\sigma(t)$ is current stress, and $\dot{\gamma}(t')$ is the strain rate history.

For the case of sinusoidal strain history Eq. 1 can be transformed to yield an expression for the complex modulus, $G^*(j\omega)$ [2,4]:

$$G^*(j\omega) = G'(\omega) + jG''(\omega) \qquad (2)$$

where $j = \sqrt{-1}$, ω is the frequency, and $G'(\omega)$ and $G''(\omega)$ are called the storage modulus and loss modulus, respectively. G' is related to the amount of energy stored and released in a cyclic oscillation and G'' indicates the energy dissipated. In damping applications Eq. 2 is expressed:

$$G^*(j\omega) = G'(1 + j\eta) \qquad (3)$$

where η is designated as the material damping factor defined as the ratio of G'' over G'.

For a sinusoidal strain $\gamma(t) = \gamma_o \sin \omega t$ and the corresponding stress response $\sigma(t) = \sigma_o(\omega) \sin[\omega t + \delta(\omega)]$, where γ_o is strain amplitude, $\sigma_o(\omega)$ is stress amplitude and $\delta(\omega)$ is the phase angle between stress and strain, the storage and loss moduli can be written as [1-4]:

$$G'(\omega) = \frac{\sigma_o}{\gamma_o}\cos\delta \;\; ; \;\; G''(\omega) = \frac{\sigma_o}{\gamma_o}\sin\delta \qquad (4)$$

Note that $\eta = \tan\delta$. Thus, dynamic mechanical viscoelastic properties may be measured in tests with sinusoidal strain input at a fixed frequency.

METHODS FOR MEASUREMENT OF DYNAMIC MECHANICAL PROPERTIES

The many techniques and instruments used to measure the dynamic mechanical properties of polymers are shown in figure 3 [1,4]. Various methods can be classified in two main groups: methods which ignore sample inertia effects and which include them. The methods which include sample inertia effects are suitable for measuring high frequency data (generally above 1.0 kHz). The other methods can measure material properties from very low to moderate frequencies (0.01Hz to ~2.0kHz.). Each method has certain advantages and limitations

In direct stress-strain measurement methods, material properties are determined by measuring the response of the sample to a sinusoidal input. Dynamic mechanical properties are obtained over a range of frequencies and temperatures using one sample as long as wave effects in the specimen are negligible. The methods are simple, and material properties are obtained without making an assumption about the material behavior. Probably for these reasons the techniques are often preferred.

Resonance methods determine material properties at the sample resonance frequencies. A polymer sample is forced to oscillate at the resonance frequency of the system. The basic ideal is the same whether sample inertia is included or not. Several samples may be required to cover an adequate range of frequency and temperature. Also, a few questionable assumptions are made in calculations regarding the nature of material behavior. The main advantage of these techniques are that the force required to oscillate samples is relatively small.

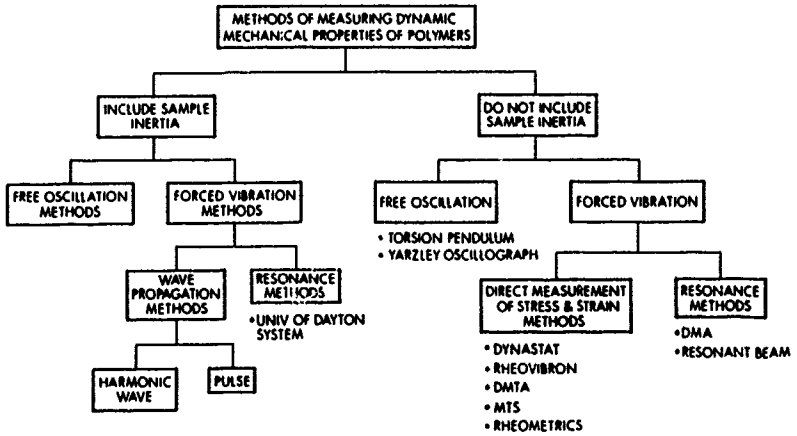

Figure 3. A classification of methods for measuring dynamic mechanical properties of polymeric materials.

The free oscillation methods require measurement of the attenuation and the natural frequency of oscillation. A sample is made to execute free oscillations. The natural frequency and amplitudes of successive peaks on one side of the mean are measured. Material properties are then determined by assuming a logarithmic dissipation mechanism. Many samples may be required to cover a range of frequency. These methods are simple to use. Again, the main idea is the same in both methods that include sample inertia and that exclude sample inertia.

Wave propagation methods are used for measurements requiring relatively high frequency material properties. A long thin strip is generally used as a sample. Travelling waves are set up by clamping one end of sample and exciting the other end by a single frequency sinusoidal wave or a short duration pulse. The attenuation factor and the phase angle of the travelling wave are measured. Material properties are then obtained solving wave equations for viscoelastic materials. Using these schemes material properties have been measured upto 100kHz.

Many instruments have been developed based on the above methods. Typically, most of these instruments measure dynamic mechanical responses to a single frequency sinusoidal input. To characterize the viscoelastic properties of a material, the tests are repeated over a range of temperatures and frequencies. This is sometimes done at a fixed frequency while the polymer specimen is heated or cooled and measurements are made periodically at different temperatures. Another method utilizes frequency variations while the temperature is held constant. In both procedures, the material is subjected to cyclic deformation over a period of time with uncontrolled temperature rise, loss of volatiles and other changes from energy dissipated in the material. These effects may be compounded by lags of sample from ambient temperature if heating is carried out at constant frequency. Another problem associated with temperature sweep is the inability of a sample to maintain the thermodynamic equilibrium at temperatures close to glass transition temperature. Thus, it is difficult to obtain truly isothermal properties using most of the commercial instruments.

Another problem with these instruments is determination of mechanical properties of moisture sensitive materials. Such materials have tendency to gain moisture when subjected to mechanical excitation at constant relative humidity and temperature. This makes single frequency tests impractical for isomoisture studies over a range of frequencies.

We have developed a novel technique known as the Fourier Transform Mechanical Analysis (FTMA) to measure dynamic mechanical properties. FTMA measures the complex moduli over a range of frequencies in one test by exciting the sample by a random signal (band limited white noise) [4]. FTMA overcomes or circumvents problems inherent in other test methods because it measures dynamic mechanical properties over a wide range of frequency with minimal temperature and moisture changes within the sample. A brief description of FTMA is provide next.

FTMA TECHNIQUE

Formulation and Measurements

Spectral analysis techniques to study the behavior of polymers subjected to dynamic mechanical loads and/or deformation are called Fourier Transform Mechanical Analysis (FTMA) [4]. If the strain $\gamma(t)$ is an arbitrary function of time, then Eq. (1) can be transformed to yield an explicit expression for the spectra of $G^*(j\omega)$ [2,4]:

$$G^*(j\omega) = \frac{\Sigma(\omega)}{\Gamma(\omega)} \qquad (5)$$

where $\Gamma(\omega)$ and $\Sigma(\omega)$ are the Fourier transforms of strain and stress, respectively. Eq. (5) can be used to determine $G'(\omega)$ and $G''(\omega)$ over a range of frequency in one test if an appropriate strain input is used. White noise would seem to be ideal since it contains all frequencies [4].

A schematic diagram of the experimental system is shown in figure 4. An impedance head is used to measure the force. A scheme known as the "mass cancellation" is used to obtain the force applied to the polymer from the total force measured by the impedance head. The shear strain is determined by twice integrating the relative accelerations between the sample mounts. To minimize the effect of bending deformation, the sample length to thickness ratio must be kept 10 or more. The ratio of shear wave length to the sample thickness must be 15 or more to avoid wave effects. FTMA provides a direct method for determining the frequency at which inertial effects become noticeable.

To study effects of temperature, the entire sensor and sample assembly is placed in a chamber with controlled temperature and humidity. A typical test takes less than 5 seconds, and tests are run at least 20 minutes apart. Thus, temperature rise due to internal friction in the test sample is minimized.

Discussion

Figure 5 shows a typical result of directly comparing three methods for determining loss modulus on the same sample. The points were determined with a commercial Rheovibron. The dashed line shows results with forced vibration using single frequency sinusoidal inputs. The solid line shows FTMA data from random noise inputs.

The primary feature of FTMA is the fact that a complete isotherm is obtained in just a few seconds. This saves time and effort and also gives better data in the case of sensitive materials, such as natural products, which may change during long exposure in a test chamber. Changes induced by energy dissipation within the sample are minimized. FTMA readily provides direct assessment of sample inertia, bending and geometry effects. This would be very difficult with single frequency instruments The Fourier transform technique is perfectly general. It may be used also to study non-linear viscoelastic properties [5].

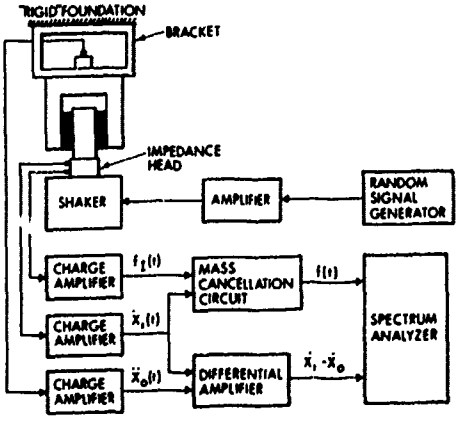

Figure 4. A schematic diagram of FTMA technique.

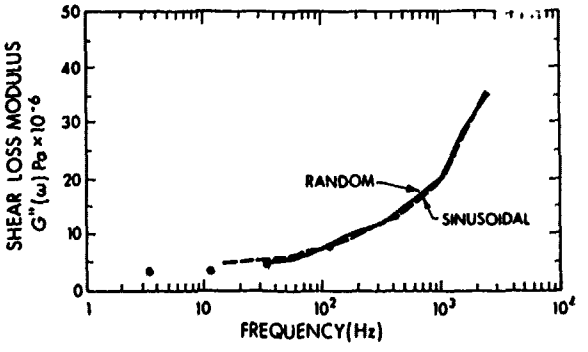

Figure 5. Comparison of NBR loss modulus obtained by three different methods. Points are Rheovibron data.

TIME-TEMPERATURE SUPERPOSITION PRINCIPLE AND MASTER CURVES

Often the range of frequency covered in a measurement is not large enough to fully analyze the dynamic mechanical response of material system. The principle of time-temperature superposition is then utilized to obtain master curves that presumably approximate a mechanical response isotherm for a wide range of frequency (or time). A master curve is a graphical representation of a viscoelastic property of the material at a given temperature. The underlying assumption is that the mechanical behavior of a material at all temperatures is governed by the same viscoelastic mechanism. This assumption has been found unsuitable in many cases. However, it is very much in use and it does provide a limited, semi-empirical perspective on the effect of frequency and temperature.

The temperature-time equivalence was first suggested by Leaderman in 1941 while studying creep recovery behavior of textile materials [9]. Then in 1945 Tobolsky and Andrews [10] developed master curves by horizontal translation on logarithmic time axis of different temperature stress relaxation data. But the procedure was popularized by Ferry and coworkers, who in 1957 gave an empirical equation for the shift factor to construct master curves [11]. It is known as the WLF (Williams, Landel, Ferry) equation and is probably the most widely used equation in polymer viscoelasticity. WLF equation is also associated with the free volume concept in polymers [7]. This concept was latter used to provide a theoretical basis of the WLF equation. It has been also used to develop kinetic theory of glass transition phenomenon [7]. In many cases, it has provided an acceptable representation of material behavior and it has failed many times also.

The equivalence of frequency (or time) - temperature implies that the effect of temperature on viscoelastic properties is to multiply (or divide) the frequency scale by a constant factor at each temperature. In construction of master curves, sometimes a vertical shift is also required. The rational behind this is that material volume changes with temperature and vertical shift factor is a correction for the change. There are also other equations that are used to model the shift factor. One of the other popular equation is Arrhenius equation [3]. Theoretical basis of the procedure is not very profound. Nevertheless, there seems to be some equivalence between frequency (or time) and temperature with respect to viscoelastic properties. However, this process is not suitable for treating the obvious effects of moisture, plasticizers, molecular weight, ect. Also, it does not provide a constitutive model. We have developed a scheme that yields a complete constitutive equation of viscoelastic materials. The time-temperature superposition is an integral part of the modeling scheme with a quantitative description of the glass transition of polymers.

CONSTITUTIVE MODEL

The model is based on postulates of generally observed temperature dependent behavior of polymers and our recent development of a new model of the glass transition phenomenon [6]. We postulate that the entire response is a sum of three distinct parts without the loss of any generality. First, all materials attain the highest modulus at absolute zero temperature. Second, the modulus of all materials decreases with increase in temperature. The third part is the glass transition region which is unique to polymers (or amorphous materials in general). It is characterized by three parameters: first, the height of transition; second, the width of transition; and third, the temperature of Tg.

We argued, on the basis of thermodynamics, that all isofrequency responses would converge at a point at low temperature [6]. This point is the second-order thermodynamic glass transition temperature. A complete temperature and frequency dependent behavior of a viscoelastic material is given as:

$$\mathrm{Log}G'(\omega,T) = B_0 + B_e(T - T_g) + h\left[1 + \tanh\left[\frac{T - (T_g + S_0 N_s \omega^{K_s})}{S_0\, \omega^{K_s}}\right]\right] \qquad (6)$$

where T = temperature in Kelvin, and B_0, B_e, h, T_m, K_s, N_s, and S_0 are modulus at T_g, slope, transition height, transition mid point, power law exponent, parameter giving the location of T_g relative to the mid point, and transition spread at one Hz (see figure 1).

Figure 6 shows polyisobutylene storage modulus versus temperature at various frequencies. The lines are model contours and the point of convergence is the thermodynamic second order glass transition temperature. To verify the model, shift factors were determined to construct a master curve. Figure 7 shows a comparison of model prediction and polyisobutylene storage modulus data at various temperatures. Excellent results were obtained for the loss modulus and loss factor by using shift factors derived from the storage modulus. Another class of polymer, NBR was also studied with good results. Our model provides a simple procedure to study the glass transition phenomenon and construct master curves.

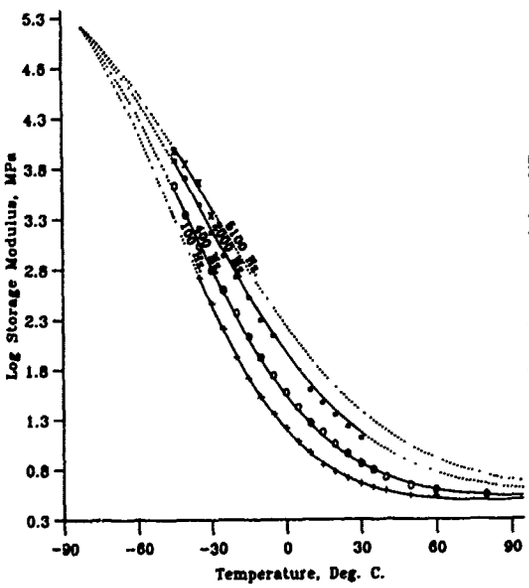

Figure 6. Convergence of polyisobutylene various frequencies G' data second order transition temperature.

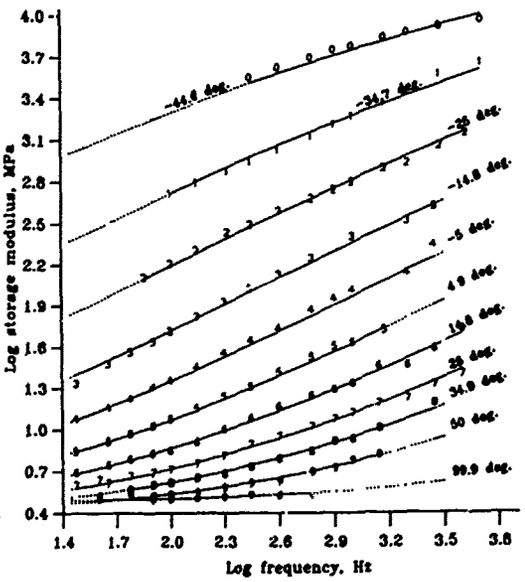

Figure 7. Comparison of model prediction with actual data of polyisobutylene G'.

REFERENCES

1. J. D. Ferry, Viscoelastic Properties of Polymers, 3rd. ed., John-Wiley & Sons Inc., New York, (1980).
2. R. M. Christensen, Theory of Viscoelasticity an Introduction, 2nd. ed., Academic Press Inc., New York, (1982).
3. I. M. Ward, Mechanical Properties of Solid Polymers, Wiley-Interscience, Inc.: New York, (1983).
4. S. N. Ganeriwala and H. A. Hartung, in Sound and Vibration Damping with Polymers, Eds. R. D. Corsaro and L. H. Sperling, ACS Symposium Series 424, American Chemical Society, Washington D. C., (1990); also, J. Acoust. Soc. Am., in Progress.
5. S. N. Ganeriwala, and C. A. Rotz, Polym. Eng. Sci., 27, 2, (1987)
6. S. N. Ganeriwala and H. A. Hartung, in Constitutive Laws for Engineering Materials: Recent Advances and Industrial and Infrastructure Applications, Eds. C. S. Desai, E. Krempl, G. Frantziskonis, and H. Saadatmanesh, ASME book Series, ASME Press, New York, (1991). and J. Chem. Phys., in Progress.
7. M. C. Shen, and A. Eisenberg, Rub. Chem. Tech., 43, (1970), 95-155.
8. C. A. Angell, D. R. MacFarlane, and M. Oguni, in Dynamic Aspects of Structural Changes in Liquids and Glasses, Eds. C. A. Angell & M. Goldstein, The New York Academy of Sciences, (1986), 241-247.
9. H. Leaderman, Textiles Research J., 11. 171, (1941).
10. A. V. Tobolsky and R. D. Andrews, J. Chem. Phys., 13, 3, (1945).
11. Williams, M. L.; Landel, R. F.; and Ferry, J. D. J. Am. Chem. Soc., 77, (1955), 3701-3707.

SECOND INTERNATIONAL CONGRESS ON
RECENT DEVELOPMENTS IN AIR- AND
STRUCTURE-BORNE SOUND AND VIBRATION
MARCH 4-6, 1992 AUBURN UNIVERSITY, USA

A NEW APPROACH TO LOW FREQUENCY AEROACOUSTIC PROBLEM DECISIONS BASED ON THE VECTOR-PHASE METHODS.

Gordienko V.A., Goncharenko B.I., Koropchenko A.A.

Department of Acoustics, Faculty of Physics,
Moscow State University, 119899, Moscow, Russia

ABSTRACT

The conception of the vector-phase methods based on simultaneous measurements of the acoustic pressure field, of three orthogonal components of the particle velocity and the differencies of phase between them in a separate points of a medium is proposed. This approach does not require potentiality condition being valid, therefore it can be used for the low sound frequency, for infrasound, during measurements in a moving media by means of the receivers of finite sizes and so on.

The methods available for determination of complicated source directivity patterns from measurements in a near field with a noise, of reflected properties of the structures or of the direction on a low frequency signal source from results of measurements in a point are observed.

The methods are confirmed by the results of experiments where three component pressure gradient receiver created by the authors has been used.

INTRODUCTION

The classic method of acoustic field description is based on using of the special function named as the velocity potential $\Phi(r,t)$:

$$\vec{V}(r,t) = - \mathit{grad}\ \Phi(r,t) \qquad (1.1)$$

The pressure field is

$$P(r,t) = \rho * \partial\Phi/\partial t \qquad (1.2)$$

where ρ denotes the density of a medium.

But using of the function $\Phi(r,t)$ as Eq.(1.1) gives an opportunity to consider only those decisions corresponding to the motion of liquid without vortexes ($\mathit{rot}\ \vec{V}(r,t) = \mathit{rot}\ (\mathit{grad}\ \Phi(r,t)) = 0$). Such a condition is not always valid for low sound frequencies, for infrasound or for moving media. The general expression for the vector $\vec{V}(r,t)$ according to the Halmholtz theorem may be written as a sum of scalar potential $\Phi(r,t)$ and vector potential $\vec{\Psi}(r,t)$

$$\vec{V}(r,t) = - \mathit{grad}\ \Phi(r,t) + \mathit{rot}\ \vec{\Psi}(r,t) \qquad (1.3)$$

The first term describes the potential component of the acoustic field, the second one describes a radiation (or reaction of the receiver on a radiation) due to hydrodynamic processes in a medium (vortexes, turbulence pulsations.) In this case we must measure at least two characteristics of the acoustic field for rigth reconstruction of the field. As we think it is the most convenient to choose the sound

pressure P(r,t) and the particle velocity V(r,t).

The approach to acoustic problems decision which does not require potentiality condition being valid and based on simultaneous measurements of the sound pressure and the particle velocity (or the pressure gradient) in some points of a medium we have named as the vector-phase methods in acoustics [1].

THEORY

In terms of the vector-phase methods we propose to use 4-d vector $\vec{P}$ (Vx,Vy,Vz, P). It is known that for a frequency $f = \frac{\omega}{2\pi}$ the first moment of P is

$$\langle P_i \rangle_\tau = \frac{1}{\tau} \int_0^\tau P_i(t)\, dt = 0 \qquad (1.4)$$

where τ is more or equal to $T = \frac{1}{f}$.

But the second moment differs from zero

$$\langle P_i^2 \rangle_\tau \equiv P_i^2 = \frac{1}{\tau} \int_0^\tau (P_i^2(t) - \langle P_i^2 \rangle_\tau)\, dt = \int_0^\tau P_i^2(t)\, dt \qquad (1.5)$$

We can write Eq.(1.5) as matrix R

$$R = \vec{P} * (\vec{P}^T)^* \qquad (1.6)$$

where $\vec{P}^T$ denotes the transposed value of $\vec{P}$,

$(\vec{P}^T)^*$ denotes the complex conjugate value of $\vec{P}^T$.

After that we have

$$R_{nm} = \frac{1}{2} P_n * P_m^* = Re (R_{nm}) + j\, Im (R_{nm}) \qquad (1.7)$$

It is clear that R_{nm} is a tensor. The expressions $\frac{1}{\rho} R_{nm}$ have dimension of acoustic power. It is convenient to express them so that the average square values be real. For that we input new tensors

$$S^{(k)} = \frac{1}{2} (R + R^*) \qquad (1.8)$$

and

$$S^{(a)} = \frac{1}{2} (R - R^*) \qquad (1.9)$$

As a result $R = S^{(k)} + j\, S^{(a)}$

The tensor $S^{(k)}$ is symmetric that is $S_{nm}^{(k)} = S_{mn}^{(k)}$; $S^{(k)} = S^{(k)T} = [S^{(k)T}]^*$. The tensor $S^{(a)}$ is antisymmetric, i.e. $S_{nm}^{(a)} = - S_{mn}^{(a)}$, $S_{nn}^{(a)} = 0$. Symmetric terms $S_{nm}^{(k)}$ determine coherent (active) part of correlation function of proper pairs of acoustic field components, antisymmetric terms $S_{mn}^{(a)}$ determine noncoherent (reactive) one. It is obvious that terms $S_{nn}^{(k)}(\omega)$ are the spectral density of pressure and of particle velocity projections. The matrix elements $S_{4m}^{(k)}$ (if m = 4) name of projections of acoustic power flux intensity on direction and denote W_{Rm}. The elements $S_{4m}^{(a)}$ correspond to components X, Y and Z of reactive density of acoustic power and denote as W_{Im}. The projection of acoustic power flux on direction r is

$$W_R = \frac{1}{2} \mathrm{Re}\,(PV^*) = \frac{1}{4}\,(PV^* + P^*V) = S^{(k)}_{4n} \qquad (1.10)$$

The full energy of acoustic field consists of active and reactive parts. It may be written in matrix notation as

$$S = \sqrt{R_{nm} \oplus R^{*T}_{nm}} \qquad (1.11)$$

Notice that the tensor $S^{(k)}_{nm}$ has 10 independent elements, the tensor $S^{(a)}_{nm}$ has only 6 ones (so as $S^{(a)}_{nn} = 0$). Therefore one can use the matrix of 16 independent elements for description of the field energy characteristics.
Note that the energy tensor contains all information about amplitude and phase characteristics of acoustic field in a point.

Very often it is useful to know the cross correlation coefficients. We can define them as

$$\rho_{nm} = S^{(k)}_{nm} / \sqrt{R_{nn} + R_{mm}} \qquad (1.12)$$

$$\rho^*_{nm} = S^{(a)}_{nm} / \sqrt{R_{nm} + R_{mm}} \qquad (1.13)$$

General Relations between Matrix Components in Homogeneous Space

Far field

Now we shall try to define the matrix elements for various cases.
Consider the particle motion in a medium without vortexes. The scalar potential for the acoustic field of N sources can be written as

$$\Phi = (Q/4\pi)\, \exp[j(\omega t - \vec{k}\vec{r} + \theta_{oi})] \qquad (1.14)$$

where θ_{oi} denotes the initial phase of a sourse,
Q denotes its productivity

If N = 1 than

$$\begin{aligned} P &= P_o \exp\,[j\,(\omega t - \vec{k}\vec{r} + \theta_o)] \\ V_x &= P_o \cos\,\phi \sin\,\alpha \exp\,[j\,(\omega t - \vec{k}\vec{r} + \theta_o)] \\ V_y &= P_o \sin\,\phi \sin\,\alpha \exp\,[j\,(\omega t - \vec{k}\vec{r} + \theta_o)] \\ V_z &= P_o \cos\,\alpha \exp\,[j\,(\omega t - \vec{k}\vec{r} + \theta_o)] \end{aligned} \qquad (1.15)$$

From Eq.(1.15) we can obtain

$$\begin{aligned} & P^2/(V_x^2 + V_y^2 + V_z^2) = 1 \\ & W_{ix} = W_{iy} = W_{iz} = 0 \\ & \rho_{xy} = \rho_{xz} = \rho_{yz} = \pm 1 \\ & \rho^*_{xy} = \rho^*_{xz} = \rho^*_{yz} = 0 \end{aligned} \qquad (1.16)$$

These relations describe a plane training wave. In this case one always can choose such a coordinate system where a wave spreads only along one axis, for example Z, and the matrix S_{nm} is

$$S_{nm} = \left|\begin{array}{c:cc} 0 & \cdots & 0 \\ \hdashline & V & 0 \\ 0 & W_{Rz} & P^2 \end{array}\right| \qquad (1.17)$$

Having N sources the displacements of particles can be written as

$$\xi = \sum_{i=1}^{N} A_i \cos\phi_i \sin\alpha_i e^{j(\omega t+\theta_i)} \equiv e^{j\omega t}\xi_o e^{j\theta_x} \qquad (1.18)$$

$$\eta = \sum_{i=1}^{N} A_i \sin\phi_i \sin\alpha_i e^{j(\omega t+\theta_i)} \equiv e^{j\omega t}\eta_o e^{jy}$$

Note Eq.(1.18) as

$$\begin{aligned} \xi &\Rightarrow x = \xi_o \cos\tau \\ \eta &\Rightarrow y = \eta_o \cos(\tau - \gamma y) \\ \vartheta &\Rightarrow z = \vartheta_o \cos(\tau - \gamma z) \end{aligned} \qquad (1.19)$$

It is clear that the particles move along elliptic orbits (if A and Q does not depend on time). These orbits are lied in plane $A_o x + B_o y + C_o z = 0$, where $A_o = \cos(\gamma_z - \gamma_y)/\xi_o$ $B_o = \cos\gamma_z/\eta_o$; $C_o = \sin\gamma_o/\vartheta_o$. In this case there is not the direction r for that $V_r = 0$. Lets choose the axis X along that amplitude of displacement is maximum. The axis Y is perpendicular to it.

After that

$$\rho_{x'y'} = 0$$

$$\rho^*_{x'y'} = 1$$

$$P^2/(V^2_{x'} + V^2_{y'}) = 1 \qquad (1.20)$$

If the field is created by a set of random sources with a homogeneous distribution on a plane or a closed surface

$$P^2/(V_x^2 + V_y^2 + V_z^2) = 1 \qquad (1.21)$$

$$\rho_{ij} = \rho^*_{ij} \approx 0$$

Near field

In the near field there is always a reactive density of acoustic energy, hence, the coefficient is less than 1 and the difference of phase between P and V differs from zero.

In the near field the relations between amplitude and phase values of pressure and particle velocity projections are determined by source type. For example, for a radial component of the particle velocity on a distance r from the source we have

$$\psi^2 = \frac{P^2}{V^2} = 1 \qquad \text{- a plane wave}$$

$$\psi^2 = (kr)^2/[(kr)^2 + 1] \qquad \text{- a concentrated monopole} \qquad (1.22)$$

$$\psi^2 = \frac{(kr)^2 + (kr)^4}{4 + (kr)^4} \qquad \text{- a concentrated dipole}$$

In case of a monopole all the particles move along the radious and the velocity of their motion is

$$V_r = \frac{P}{\rho c} - j\,\frac{P}{\rho c\, kr} \qquad (1.23)$$

For a dipole the tangencial component of velocity appears and

$$P = \frac{d}{r^2}(1 + jkr)\cos\theta\, e^{j(\omega t - kr)} \qquad (1.24)$$

$$P_r = \rho c\, V_r = \frac{P}{\rho c} - \frac{jP}{\rho c\, kr}\,\frac{(2 + jkr)}{(1 + jkr)}$$

$$P_\theta = \rho c\, V_\theta = -\frac{jP}{\rho c\, kr}\cos\theta$$

It is obvious that the particles move along ellipses and the energy flow consists of two parts: W_R and W_I. That is in a near field of a complicated source reactive component of energy appear. The function *rot* W_R does not equal to zero for elliptic motion.

DECISION OF SOME APPLIED PROBLEMS

The conception of the vector-phase methods allows us to decide a lot of acoustic problems. In this paper we consider some of them, namely, impedance measurements for various structures, the determination of the direction to a source and its classification, the determination of complicated source directivity patterns.

It is well known that the sound reflection coefficient for a plane boundary may be written as

$$V(\theta) = \frac{Z\cos\theta - \rho c}{Z\cos\theta + \rho c} \qquad (1.25)$$

where θ, Z denote the angle to the normal and the input impedance respectively.

In our experiments we used the combined receiver which consists of sound pressure receiver and the vector one. The vector receiver created by authors gives an opportunity to measure three components of the pressure gradient (or the particle velocity). Expressing the vector receiver sensitivity in units of the sound wave pressure, we can measure two signals from channels P and Z and use the formula

$$V = V(\theta) = \frac{P\cos\theta - V_Z}{P\cos\theta + V_Z} \qquad (1.26)$$

where V_Z denotes the vertical component of particle velocity. After that from frequency-angle dependencies one can say about complication of any object. In practice we used this method for determination of thickness of layers in a sea coast. The obtained results are illustrated in Fig.1 where the dependence $V(\theta)$ on a frequency has shown.

For the case of a small reflection coefficient $V(\theta)$ (for example during determination of reflecting properties of anechoic chamber walls) it is more convenient to measure the acoustic power flux. This approach allows us to determine the value of $V(\theta)$ up to 0.01 - 0.1.

The second important pecualirity of the vector-phase methods is an opportunity to reconstruct the acoustic field from measurements of its characteristics in one point. This approach is based on using of the Tailor formula

$$P(M) = P(M_o) + \frac{1}{2}\sum_{i=1}^{3}\frac{\partial P}{\partial x_i}\Delta x_i + \frac{1}{6}\sum_{i=1}^{3}\sum_{j=1}^{3}\frac{\partial^2 P}{\partial x_i\,\partial x_j}\Delta x_i\,\Delta x_j + \ldots \qquad (1.27)$$

where M_o corresponds to a point of measurements, M denotes any point of a medium where we want to define the acoustic field.

While measured all the parameters, we can determine the field. As a rule the full reconstruction is not necessary in a reality. Usually it is enough to measure only a number of first terms of this row. For example we can get information about the direction on a signal source from measurements only the pressure and its three gradient projections that is the first and the second terms in Eq.(1.26). In addition we can also determine the source type for some cases. As shown above the ratio P / V carries information about a source (Eq.(1.22)).

Besides the classification of sources is possible using measurements of the phase differency between the pressure and the particle velocity. If source directivity being independent on a frequency than after measurements of the phase differency on any two frequencies we can determine the source type.

If

$$\frac{\operatorname{tg} \Delta\phi_1}{\operatorname{tg} \Delta\phi_2} = \frac{k_2}{k_1} \qquad \text{this is a monopole} \qquad (1.28)$$

If

$$\frac{\operatorname{tg} \Delta\phi_1}{\operatorname{tg} \Delta\phi_2} = \frac{k_2^3}{k_1} \qquad \text{this is a dipole} \qquad (1.29)$$

Here k_2 and k_1 are the wave numbers for the first and the second waves respectively, $\Delta\phi_1$, $\Delta\phi_2$ denote the phase differencies.

It is useful to note that the determination of the direction on a signal source by means of the vector-phase methods is widely spread in nature. Many insests use such approach. For example a grasshopper has acoustic organs like the pressure gradient receiver disposed in his fore tarsi. It is shown in Fig.2

The vector-phase methods allow to determine directivity patterns of complicated sources. This technique is based on application of the Halmgoltz integral theorem

$$P(M) = \oint\!\!\oint_S \left\{ P(N) \frac{\partial G(N)}{\partial n} - \frac{\partial P(N)}{\partial n} G(N) \right\} dS \qquad (1.30)$$

where P(M) is a pressure in a point M, G(N) being the Green function. N denotes the points on the closed surface S.

Using of the vector receiver give an opportunity to define the directivity patterns of a source without calculations of the second term. Besides this techique is accurate and noiseproof so as additional sources and reflections from boundaries have weak influence. Lets represent the field in a point N as sum of the field P_p from the sources on the surface S and of the field P_s formed by the outside sources.

$$P(N) = P_p(N) + P_s(N)$$

$$\frac{\partial P(N)}{\partial n} = \frac{\partial P_p(N)}{\partial n} + \frac{\partial P_s(N)}{\partial n} \qquad (1.31)$$

After using of the Halmgoltz operator to the full field P(N) we have

$$L\,[P(N)] = \frac{1}{4\pi} \oint\!\!\oint_S \left\{ P(N) \frac{\partial G(N)}{\partial n} - \frac{\partial P(N)}{\partial n} G(N) \right\} dS =$$

$$= L\,[P_p(N)] + L\,[P_s(N)] = P_p(M) \qquad (1.32)$$

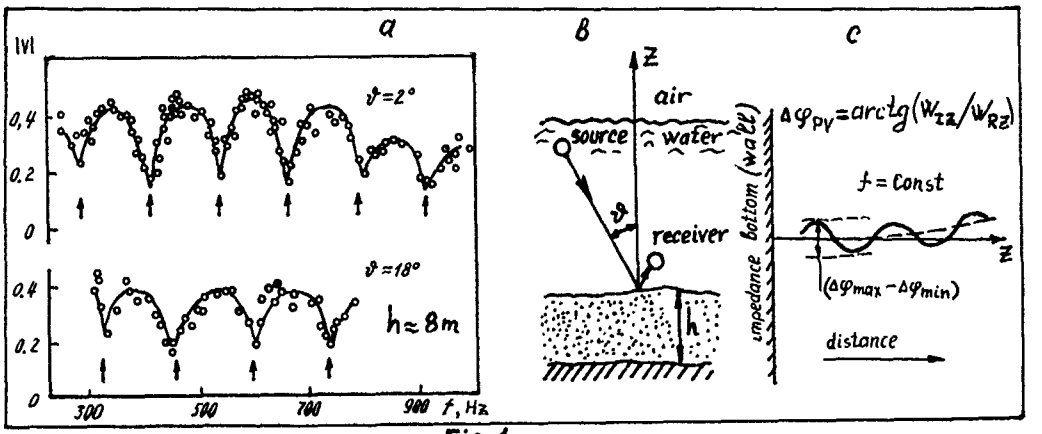

Fig. 1.

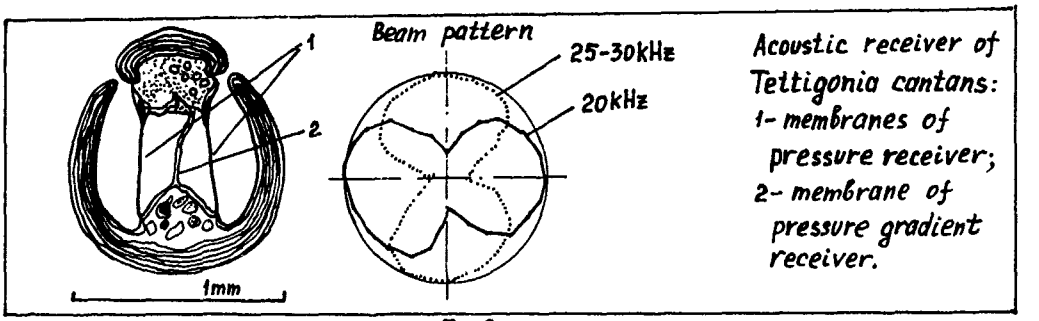

Fig.2.

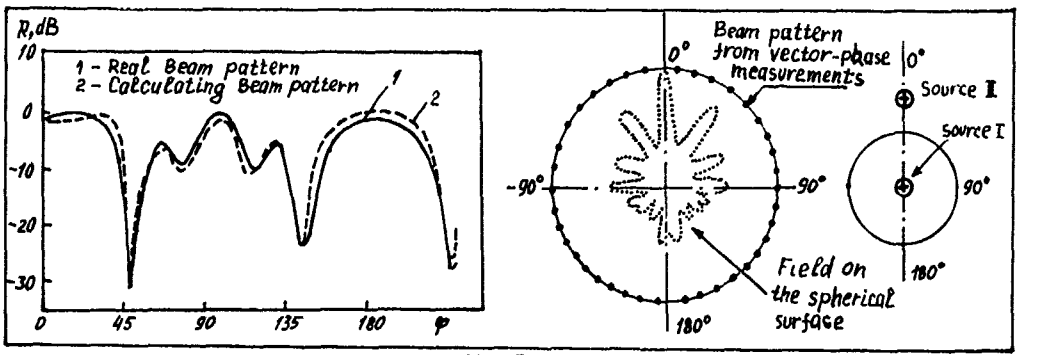

Fig. 3.

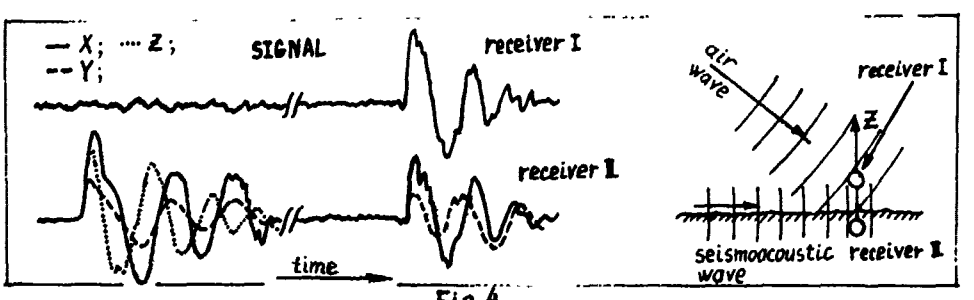

Fig. 4.

Therefore the sound field in a point M of the far field is formed by only "directed" sources being inside the volume enclosed the surface S. $L[P_s(N)] = 0$, because the points of the rest sources lie outside the volume. The reconstructed field is shown in Fig.3.

Such approach allows to use the vector receiver as the receiver of seismoacoustic signals. This is very important during measurements of sound field from a remote source in atmosphere. It is well known that sound beams deflect from the ground. As a result a shadow zone appears. The situation becames more complicated with wind. Using of proposed vector receiver allows to decrease the influence of the atmosphere conditions. Besides three component pressure gradient receiver give an opportunity to define the type of polarization wave. In the case of a sound source situated on the ground there are acoustic wave spreading in the air and seismoacoustic wave with elliptic polarization in vertical plane. From measurements of seismoacoustic waves we can define the direction on a source. This is shown in Fig.4.

CONCLUSIONS

The general approach to acoustic problems decision based on the vector-phase conception is proposed. This approach allows to explain various experimentral results from one point of view. The authors used it in aero-, hydro- and seismoacoustics. They have decided some applied tasks, for example, the determination of direction on a signal source, of reflected properties of the structures, of the directivity patterns of the sources.

REFERENCES

1. V.A.Gordienko, V.I.Ilyichev, L.N.Zakharov, "Vector-phase methods in acoustics", (Nauka, Moscow, 1989) (in Russian)

SECOND INTERNATIONAL CONGRESS ON
RECENT DEVELOPMENTS IN AIR- AND
STRUCTURE-BORNE SOUND AND VIBRATION
MARCH 4-6, 1992 AUBURN UNIVERSITY, USA

VIBRATION OF STEEL SHEETS ON THE SHEET-PILER

L.N.Kljachko, I.I.Novikov
Noise and Vibration Control Laboratory
VNIITBchermet
Chelyabinsk, USSR

ABSTRACT

Steel sheets, when transported by electromagnetic sheet-piler, radiate sound with high pressure levels. The gratest contribution is that from the back ends of the sheets. Vibration of sheet is modelled as vibration of beam with moving supports. Vibration of the back end of sheet is considered as vibration of a cantilever beam whose length is a periodic function of time. The governing equation in the last case may have both steady and unsteady solutions. The critical velocity of sheets on the piler is determind by the condition of steadiness of sheet's vibration.

Electromagnetic sheet-pilers are one of the most powerful sound sources in rolling production. Service personnel at the nearest open working places is exposed to noise with 100-105 dBA level, wich is by 20-25 dBA above the allowable one. The noise is generated by vibration of the sheets, and especially of their back ends.

As the cause of sheet's vibration was the impacts between transported sheets and carrying rollers of the piler, the first idea of noise reduction was to wrap up the rollers with elastic coating, to soften the impacts. Sound radiation from piler with rigid-rubber coated rollers was by 5-7 dBA less than radiation from piler with bare rollers. It was inexpedient to use for coating materials with better damping characteristics because of their wear and tear in short time.

Another method for noice reduction is to choose parameters of the technological process to minimize sound radiation. For this purpose, one has to investigate the sheet's vibration mathematically. From this point of view, a sheet on rollers can be considered as a beam, moving upon an infinite set of supports, located at the same distance from each other (see figure). Suppose, that there is no breaking-off sheets from rollers.

The results will be the same if the moving sistem of coordinates, connected with sheet, is introduced. Locate origin $x=0$ at the left end of the sheet, then right end will be at $x=L$. Solution of equation

$$D\frac{\partial^4 W}{\partial x^4} + m\frac{\partial^2 W}{\partial t^2} = pe^{i\omega t} \qquad (1)$$

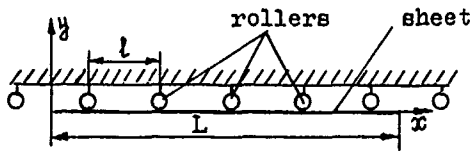

Figure. Arrangement of sheet on sheet piler.

standard for governing the free vibration of beam, with standard boundary conditions at the free ends

$$\left.\frac{\partial^2 W}{\partial x^2}\right|_{x=0,L} = \left.\frac{\partial^3 W}{\partial x^3}\right|_{x=0,L} = 0 \qquad (2)$$

should sutisfy conditions at the intermediate moving supports:

$$W(x=f_m(t)-0) = W(x=f_m(t)+0) = 0, \qquad (3)$$

$$W'(x=f_m(t)-0) = W'(x=f_m(t)+0), \qquad (4)$$

$$W''(x=f_m(t)-0) = W''(x=f_m(t)+0). \qquad (5)$$

In Eqs.(1)-(5) W is a displacement of the beam along y axis, $Pe^{i\omega t}$ - external harmonic force, applied to the beam, D - bending stiffness, m - mass per unit length of the beam. There are only $M=\left[\frac{L}{l}\right]$ supports in contact with beam simultaneously. These supports are numbered left $m=1$ to right $m=M$, this is the range for m in Eqs.(3) and (4). In a period of time $t=L/v$, the supports with numbers $2 \le m \le M$ change their numbers from m to $m-1$. $f_m(t)$ is a time-dependant, L/v - peridic function, describing the coordinate of the m-th support:

$$f_m(t) = l_0 + (m-1)l - vt, \qquad 0 \le t < \frac{L}{v} \qquad (6)$$

where l_0 is a start position of the first support on the beam at $t=0$. It should be noted, that Eqs.(5) is only an approximate interpretation for the phisical balance of the bending moments at the supports, since they pay no attention to friction and magnetic interaction between sheet and rollers.

A problem of beam on moving supports, formulated in Eqs.(1)-(5) is very difficult to solve. We could find no mention about it in literature, concerning vibration of beams. So we had to simplify problem. First of all, substitute boundary condition

$$W'(x=f_m(t)-0) = W'(x=f_m(t)+0) = 0 \qquad (7)$$

for Eqs.(4) and (5).

Now we are able to investigate the most interesting piece of the sheet-its back end - independently from next pieces. Eqs.(1), (2) for $x=0$ and (7) for $m=1$ describe vibration of a cantilever beam with time-dependant length $a(t)=f_1(t)$.

Consider an expansion of displacement $W(x,t)$ into a series

$$W(x,t)=\sum_{n=1}^{\infty} X_n(x)T_n(t) \qquad (8)$$

where $X_n(x)$ is the n-th mode of cantilever beam natural vibration, $T_n(t)$'s - unknown time-dependant functions. Eq.(8) differs from commonly used displacement's expansions because X_n's are the functions of time t also, through the beam length $a(t)$. Substitution Eq.(8) in Eq.(1) does not yields the necessary separation of variables. For the sake of further simplification, neglect the inertia forces due to the horizontal movement of sheet. It means, that

$$\frac{\partial^2 W}{\partial t^2}=\sum_{n=1}^{\infty} X_n(x,t)\,\frac{d^2T_n(t)}{dt^2} \qquad (9)$$

After this, Eq.(1) reduces to

$$a^4(t)\frac{d^2T_n(t)}{dt^2}+K_nT_n(t)=0 \qquad (10)$$

where $K_n=\frac{\alpha_n^4 D}{m}$, $\alpha_n=1.875,\ 4.694,\ldots$ - the roots of cantilever beam frequency equation. To determine the first resonant frequency, take $n=1$ and omit the subscript. Eq.(10) with L/V - periodic coefficient is of the Hill type. Its solution has a form [1]

$$T(t)=e^{i\mu t}\sum_{n=-\infty}^{\infty} g_n e^{i\lambda n t} \qquad (11)$$

where $\lambda=2\pi V/l$, μ and g_n's are constants to be found. If $\mathrm{Im}(\mu)>0$, then Eq.(10) has steady solution, if $\mathrm{Im}(\mu)<0$, then - unsteady. Values of μ and g_n's a determined from infinite system of algebraic equations:

$$g_n K-l^4\sum_{m=-\infty}^{\infty} c_{n-m}(\mu+\lambda m)^2 g_m=0,\quad n=0,\pm1,\pm2,\ldots \qquad (12)$$

where K is K_1 from (10), $C_0=\frac{1}{5}$, $C_\kappa=24\sum_{p=0}^{3}\frac{(-1)^p}{(i2\pi\kappa)^{p+1}(4-p)!}$ - coefficients of function $[a(t)/l]^4$ in the interval $0<t<l/V$, $\kappa=\pm1,\pm2,\ldots$. μ equals the root of equation

$$\Delta(\mu)=0, \qquad (13)$$

$\Delta(\mu)$ is the determinant of Eqs.(12). Our aim is to find parameters

of the process (namely the velocity V) to maintain $\mathrm{Im}(\mu) > 0$. For this purpose one has to put $\mu = 0$ in Eq.(13) and solve it for variable V . Eq.(13) with infinite determinant $\Delta(\omega)$ may be solved only approximately. But in many cases it is enough to obtain the roots of the central third order determinant [2] . Then, Eq.(13) yields for critical velocity of sheets

$$v_c = \frac{ch}{l} \frac{\alpha_1^2}{2\pi\sqrt{(C_0+|C_2|)}} \approx 0{,}31 \frac{ch}{l} \qquad (14)$$

where $c = 5300$ m/s - longitudinal wave velocity in steel, h - sheet thickness.

The sheet piler we dealt with had $l = 0{,}5$ m and $v = 1{,}5$ m/s. For 1 mm sheets $v_c \approx 3{,}3$ m/s, for 3 mm sheets $v_c \approx 9{,}9$ m/s. It is clear, that 1 mm sheets are transported with velocity closer to the critical, than 3 mm sheets. It explains, why the thinner are transposted sheets, the more sound is radiated.

REFERENCES

1. E.Kamke. Differentialgleichungen. Leipzig, 1959, v.1.
2. G.V.Bondarenko. Hill equation. Moscow, 1936 (in Russian).

SECOND INTERNATIONAL CONGRESS ON
RECENT DEVELOPMENTS IN AIR- AND
STRUCTURE-BORNE SOUND AND VIBRATION
MARCH 4-6, 1992 AUBURN UNIVERSITY, USA

VIBRATION REDUCTION IN INDEXABLE DRILLING

W. Xue and V. C. Venkatesh
Center for Manufacturing Research & Technology Utilization
Tennessee Technological University
Cookeville, TN 38505
U.S.A.

ABSTRACT

Vibrations are generated during indexable drilling and a slight unbalanced radial force makes vibration severe. Thus the shape of the roundness circle obtained from the measurement of a hole produced by an indexable drill is roughly an ellipse. To improve the roundness of the holes drilled by indexable drills, reducing the vibration of the workpiece is very important. How to reduce the vibration of the workpiece is discussed in this paper. An efficient method to reduce the vibration of the workpiece, modification of the indexable inserts of the drills, is introduced in this paper. The measurements of the dynamic responses of the workpiece before and after modification of the indexable inserts shows that the magnitude of vibration acceleration and vibration energy of the workpiece were reduced efficiently. Thus a very good roundness of the hole drilled by indexable drills can be obtained.

INTRODUCTION

After appearing several years ago, indexable drills have been widely used. Compared to traditional twist drills, indexable drills can be worked at very high drilling speeds and feed rates, and at the same time indexable drills can produce higher hole quality. Now, more and more indexable drills are used in the industries. Three typical indexable drills are shown in Figure 1. Some research shown that the values of the roundness of the holes drilled by indexable drills are much lower than that produced by twist drills, but the shape of roundness circle obtained from the measurement of a

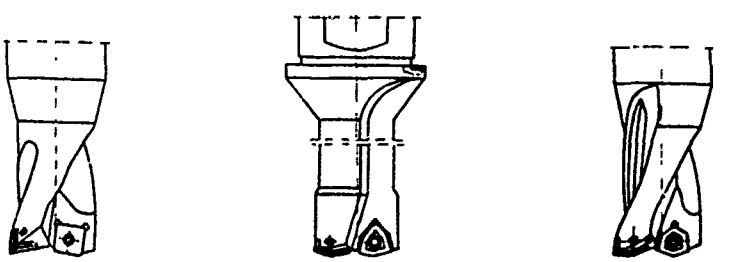

Figure 1--Schematic diagram of three typical indexable drills. (a) Indexable drill A. (b) Indexable drill B. (c) Indexable drill C.

hole produced by an indexable drill is roughly an ellipse[1] while the shape of roundness circle of the holes produced by twist drills are trigon, pentagon, and heptagon shapes[2]. Although some other research concerning indexable drills was presented[3], the ellipse shape of roundness is still a problem. This paper deals with a method to improve the roundness of the hole produced by indexable drills based on vibration reduction. Considering that the indexable drill A shown in Figure 1 is a single cutting edge tool while the other two are two cutting edge tools, only the indexable drill A shown in figure 1 is discussed here with a view to simplification.

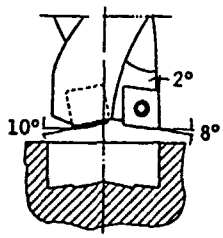

Figure 2--Differences of the side cutting edge angles of the two inserts and the radial forces on the two cutting edges.

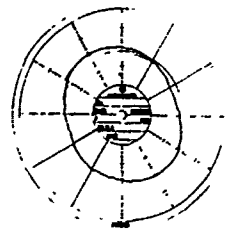

Figure 3--A typical roundness of the hole drilled by an original indexable indexable drill.

The basic drilling principle of the indexable drills is that the each insert fixed in the drill removes a volume of material along different radii of the hole while the drill is rotating. The outer insert removes the outer portion of material and the inner insert removes the inner portion (see Figure 2), thus producing a hole with a certain feed rate. In order to balance the radial forces acting on the cutting edges of the two inserts, the side cutting edge angles are different for the two inserts (shown in Figure 2). However, it is very difficult to make these two radial forces balance very well whatever be the advanced technology used in designing and manufacturing of the indexable drills if only change of cutting angles is considered. Although indexable drills work at high rotational speed and have a higher stiffness, the radial forces are rotated and are equal in all radial direction, but while the drill is rotating, there always exists a direction in which the stiffness value of the machine-tool-workpiece system is least. Thus the magnitude of vibration in this particular direction will be larger than all other directions. On the other hand, there always exists another direction in which the stiffness value of the machine-tool-workpiece system is largest. The magnitude of the vibration in this direction will be smaller than all other directions. So the center of the hole on the workpiece moves like a circle with a long axis and a short axis. This motion of the workpiece driven by the radial force will produce a hole with an elliptical roundness. This may be the main reason why the shape of the roundness circle obtained from the measurement of a hole produced by an indexable drill is roughly an ellipse. So reducing the vibration during drilling is important to improve the hole quality. Figure 3 shows the typical roundness of hole drilled by indexable drills.

VIBRATION ANALYSIS AND MEASUREMENT

Machine-tool-workpiece system is a very complicated system. Several different methods such as modal synthesis technique[4] and non-linear vibration analysis using FEM[5] were developed to solve very complicated systems like that of machine tools. Although there are several different kinds of damping in this system, it is reasonable to regard viscous damping as a main damping in a machine tool for simplifying the study. When the machine is working, an unbalanced radial force could be regarded as an

harmonic exciting force. So, the general equation of motion for this system can be expressed as[6]:

$$[M]\{\ddot{x}\}+[C]\{\dot{x}\}+[K]\{x\}=\{f\} \quad (1)$$

where

[M] = mass matrix
[C] = damping matrix
[K] = stiffness matrix
$\{x\}$, $\{\dot{x}\}$, $\{\ddot{x}\}$ = displacement vector, velocity vector, and acceleration vector, respectively
$\{f\}$ = excitation vector.

In order to reduce vibration during drilling, the values of vector $\{x\}$ or $\{\dot{x}\}$ or $\{\ddot{x}\}$ should be reduced. Generally, by changing the parameters of [M], [C], [K], and $\{f\}$ the values of the vector $\{x\}$ or $\{\dot{x}\}$ or $\{\ddot{x}\}$ in Eq. (1) can be changed. For indexable drilling, the main factor that affects the dynamic response of the system is the drilling force. Although the parameters of [M], [C], and [K] could be changed to improve the dynamic responses of the system, the best way is to limit the unbalanced radial force or reduce the excitation. To check if the dynamic responses of the system are improved by limiting the drilling force, vibration measurements were carried out. In the experiment, the workpiece (AISI 1026, ϕ 30 x 30) was clamped by a 3-jaw chuck which was fixed on the table of a Fadal 5-axis CNC machining center. Two pieze-electric accelerometers (PCB Model 302B03) were used. One was fixed in axial direction, and another in the radial direction of the drills. The vibration signals picked up by accelerometers were amplified by charge amplifiers (PCB Model 482A10), then were processed by vibration analyzer (Data Precision 6000). Finally the vibration and the results of the analysis were plotted by a plotter (HP 7475A). Figure 4 shows the schematic diagram of the set-up for vibration measurement. Figure 5 shows the measurements of the vibration during the indexable drilling at S=1000 rpm and f=0.05 mm/min.

Figure 5 shows that while several models of the system were excited during drilling, vibrations in both radial and feed directions were severe. The vibration in the radial direction results in an elliptical shape of the roundness of the hole.

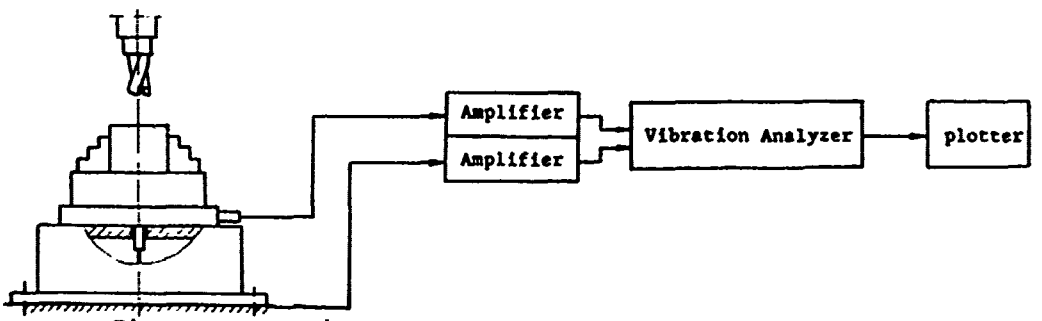

Figure 4--Experimental set-up for the vibration measurement.

MODIFICATION OF INSERTS FOR LIMITATION OF VIBRATION

To improve drilling performance and to reduce the vibration, chip-splitting grooves were introduced. The main purpose why the chip-splitting grooves are used on the two cutting edges of the inserts is to center the indexable drill during drilling. Figure 6 shows that there are several protruding rings on the bottom surface of the hole drilled by the inserts which have the chip-splitting grooves. These rings eliminate the radial

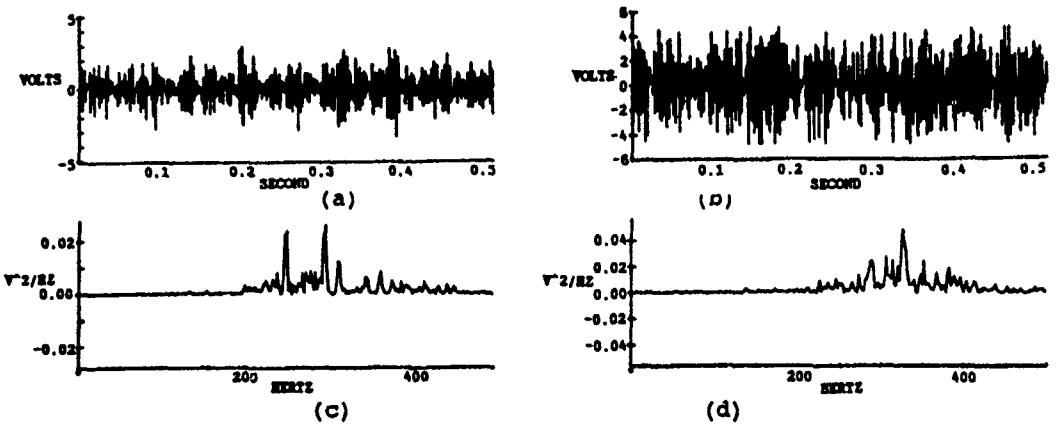

Figure 5--Vibration measurement before modification of the inserts. (a) Acceleration measurement at radial direction. (b) Acceleration measurement at feed direction. (c) Power spectrum obtained from radial direction. (d) Power spectrum obtained from feed direction.

motion of the drills, and increase the stiffness of the drill. Another advantage of the chip-splitting grooves is to split the chips when the feed rate is not very high and to improve the deformation of the chips while the feed rate is higher. Splitting the chip or improving the deformation of the chip means that the friction between chips and the tool rake faces is reduced. Because of the centering effect of the protruding rings on the bottom surface of the hole and the reduction of the friction force, the vibration is limited considerably. Figure 7 shows the results of vibration measurement when the modified inserts were used. Comparing with Figure 5, it is very clearly seen that the acceleration in both radial and feed directions is reduced. The power spectra show the difference of vibration energy expended at low frequencies (up to 400 Hz). When an unmodified indexable drill was used, the peak values of power spectra (shown in Figure 5) are up to about 0.05 V^2. However, when the modified indexable drill was used, the peak values of power spectra (shown in Figure 7) are only smaller than 0.001 V^2 at feed direction and 0.0001 V^2 at radial direction. The measurement of the roundness of the holes drilled by modified indexable drills shows that the elliptical shape of the circle of the hole roundness is very effectively reduced. Figure 8 shows a typical profile of the roundness circle of a hole drilled by a modified indexable drill.

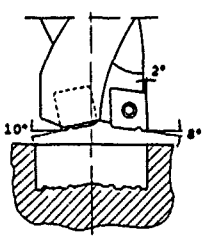

Figure 6--Protruding rings on the bottom surface of the hole.

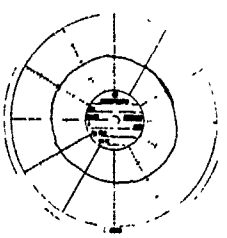

Figure 8--A typical measurement of roundness of a hole drilled by modified indexable drill.

Generally, the deeper the depth of the chip-splitting grooves, the better the quality of the holes obtained. But the depth of the grooves is limited by

the strength of the inserts, as the strength would be reduced if the depth of the grooves is too large.

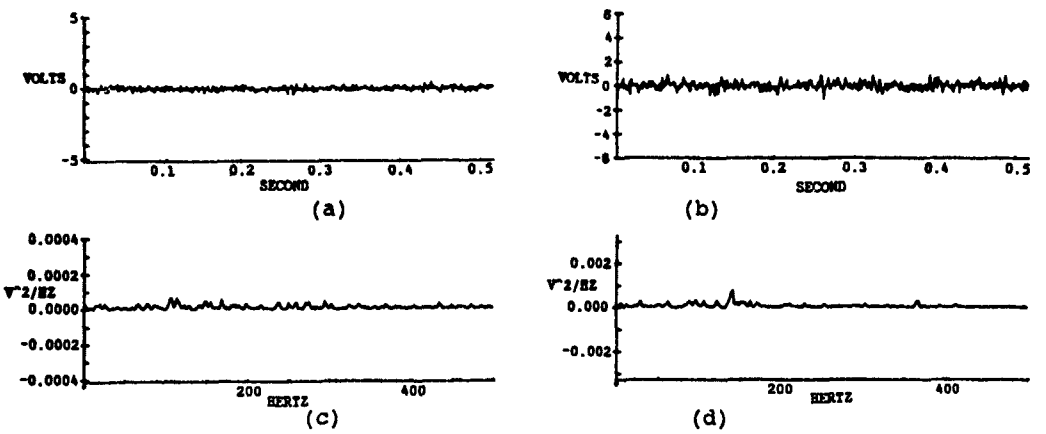

Figure 7--Vibration measurement after modification of the inserts. (a) Acceleration measurement at radial direction. (b) Acceleration measurement at feed direction. (c) Power spectrum obtained from radial direction. (d) Power spectrum obtained from feed direction.

Although the indexable drill A only was discussed in this paper, the method used for reduction of vibration can also be used for other drills. Table 1 shows the results from the three indexable drills shown in Figure 1.

Table 1--Comparison of roundness measurements produced by modified and unmodified drills (diameter of the drills is ϕ19.05 mm)

Drills	Drilling Condition		Roundness (μm)	
	S (rpm)	f (mm/rev)	Drilled by original drill	Drilled by modified drill
Drill A	1000	0.04	16.0	9.0
Drill B	1000	0.04	19.4	11.3
Drill C	1000	0.04	15.9	9.9

SUMMARY

Vibration reduction was studied in this paper to obtain a good roundness of a hole drilled by a indexable drill. The results of the study are summarized:

* There exists a distinct slightly unbalanced radial force during indexable drilling, and this force works as an excitation on the machine-tool-workpiece system. Since there always exists two directions in which the stiffness of the system is largest and least, the motion trace of the workpiece is an ellipse. Thus the vibration due to this force results in the roundness circle of the hole drilled by indexable drills becoming an ellipse.
* Modification of the indexable inserts can efficiently reduce this radial force, and thus a good roundness could be obtained.
* Vibration measurement supports this analysis to be reasonable and the modification of the indexable drill to be efficient.
* The methods of modification can be applied not only on drill A, but also on all other indexable drills.

REFERENCE

[1] V.C. Venkatesh, et al, "Performance Evaluation of Endrills." International Journal of Machine Tools and Manufacture, Vol. 28, No. 4, 1988, p341-349.

[2] S.J. Lee, et al, "An Analysis of Drill Wandering Motion," Transactions of the ASME, J. of Engineering for Industry, Vol. 109, Nov. 1987, p297-305.

[3] J.S. Agpiou, "An Evaluation of Advanced Drill Body and Point Geometries in Drilling Cast Iron," Transactions of NAMRI/SME, 1991, p79-89.

[4] Bijun Yuan, "Application of Component Mode Synthesis Techniques to the Dynamic Analysis of the Machine Tool Spindle System," 12th Biennial Conference on Mechanical Vibration and Noise, Montreal, Can, 1989, p91-94

[5] A. Shabana, and B. Thomas, "Chatter Vibration of Flexible Multibody Machine Tool Mechanisms," Mech Mach Theory, Vol. 22, No. 4, 1987, p359-369.

[6] D.J. Ewins, "Modal Testing: Theory and Practice," Research studies Press, 1984.

SECOND INTERNATIONAL CONGRESS ON
RECENT DEVELOPMENTS IN AIR- AND
STRUCTURE-BORNE SOUND AND VIBRATION
MARCH 4-6, 1992 AUBURN UNIVERSITY, USA

FREE ASYMMETRIC VIBRATIONS OF LAYERED CONICAL SHELLS BY COLLOCATION WITH SPLINES

P.V. Navaneethakrishnan
Deartment of Mathematics
College of Engineering
Anna University
Madras 600025, India

N. Ravisrinivas
Department of Mechanical Engineering
The University of Texas at Austin
Austin, Texas 78713, U.S.A.

ABSTRACT

The method of collocation with spline functions of an elegant form is used to study the free asymmetric vibrations of layered truncated conical shells. The differential equations of motion obtained in terms of the longitudinal, circumferential and transverse displacement functions are coupled. For solving them numerically, these functions are approximated by cubic and quintic spline functions. The process of collocating with them and the application of the boundary conditions lead to a generalised eigenvalue problem. Its solution yields the values of a frequency parameter and the correspondind mode shapes. Material and geometric parametric studies are made to bring out their individual and interactive effects on the vibrational behaviour of the shells. The effect of neglecting the coupling between stretching and bending and the influence of the circumferential node number on vibrations are also studied.

INTRODUCTION

In a few earlier papers by Navaneethakrishnan et al.[1,2,3] on buckling and vibrational analysis of plates and shells a spline function collocation technique was used employing one or two approximating splines. The current one is a study of free asymmetrical vibrations of conical shell frusta with laminated wall structure of constant thickness, using three spline function approximations simultaneously. A paper by Chandrasekaran and Ramamurti[4] is worth mentioning in the context of the physics of this problem, but it used an energy method based on Rayleigh-Ritz technique.

The mathematical formulation of the problem results in a two-point boundary value problem, characterised by a set of three coupled differential equations on the three displacement components of a general point on the reference surface of the shell, together with suitable boundary conditions. The equations do not have a closed form solution in general, and hence a numerical solution procedure becomes necessary. Of several numerical techniqus that could be used, the spline function technique is employed because of its attractive characteristics in convergence, accuracy and elegance of handling both analytically and computationally, brought out in the earlier papers[1,2,3]. The differential equations are modified by combining within themselves so as to admit cubic and quintic spline approximations

for the displacement functions. Collocating with these splines and imposing the boundary conditions, we have a generalised eigenvalue problem, which is solved numerically. The eigenvalues give the values of a frequency parameter. From the eigenvectors the mode shapes are constructed.

Five types of layers and three types of boundary conditions are considered for detailed analysis. The individual and interactive influence of the relative layer thickness, layer combinations, cone angle and length ratio on the frequency parameter are studied. The effect of circumferential node number is analysed. The mode shapes of vibration are presented for typical cases.

FORMULATION

The general line of procedure of Ambartsumyan[5] for the classical theory of thin shells is adopted. Love's first approximation theory is extended to layered thin shells. Each layer is of constant thickness assumed to behave as a homogeneous orthotropic and linearly elastic material with its material axes of symmetry parallel to the principal coordinate lines of the surface of the shell. Consecutive layers are assumed to be perfectly bonded together at their interface resulting in motion without slip.

The geometry of the layers and the coordinate system assumed are clarified in Fig. 1. The distance z_0 of the reference surface from the lower edge of the shell surface is given by

$$\sum_{k=1}^{K} (z_k^2 - z_{k-1}^2)\, \rho_k = 0 \tag{1}$$

where K is the total number of layers, and z_k and z_{k-1} are the distances of the outer and inner edges of the k-th layer from the reference surface.

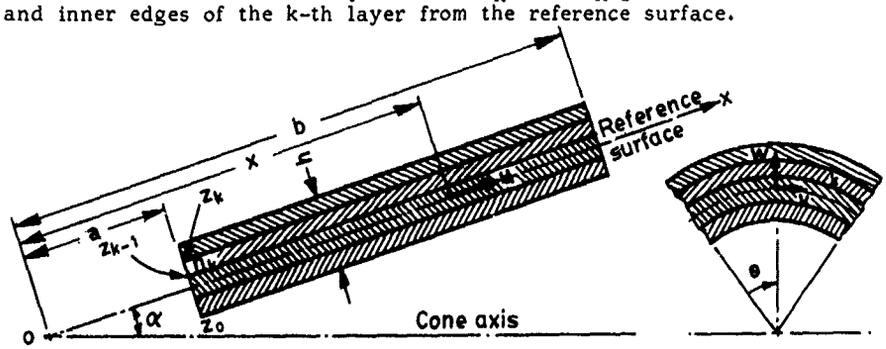

Figure 1 — Structure of the layered shell

The stress resultants and stress couples are expressed in terms of the longitudinal, circumferential and transverse displacements u,v and w, of the reference surface. Following Levy's approach, the displacements are assumed in separable form, given by

$$\begin{aligned} u(x,\theta,t) &= U(x) \cos n\theta \exp(i\omega t) \\ v(x,\theta,t) &= V(x) \sin n\theta \exp(i\omega t) \\ w(x,\theta,t) &= W(x) \cos n\theta \exp(i\omega t) \end{aligned} \tag{2}$$

Here, n is the circumferential node number, ω is the angular frequency of vibration, θ is the rotational coordinate and t is the time. Using Eqs. (2) in the constitutive equations and the resulting expressions for the stress and moment resultants in the equations of equilibrium, the governing equations of motion are obtained in the form

$$\begin{bmatrix} L_{11}^{2} & L_{12}^{1} & L_{13}^{3} \\ L_{21}^{1} & L_{22}^{2} & L_{23}^{2} \\ L_{31}^{3} & L_{32}^{2} & L_{33}^{4} \end{bmatrix} \begin{Bmatrix} U \\ V \\ W \end{Bmatrix} = \begin{Bmatrix} 0 \\ 0 \\ 0 \end{Bmatrix} \tag{3}$$

where L_{ij}^{p} are differential operators with variable coefficients, superscripts indicating the differential orders. The term $U'''(x)$ contained in the third of Eqs. (3) is inconvenient for the spline function procedure considered and hence is eliminated by differentiating the first of Eqs. (3) and using it in the third. We now have a system of three coupled differential equations, which is of order 2,2 and 4 in U, V and W, respectively.

The following non-dimensional parameters are used.

$$\lambda = \sqrt{\frac{R_0}{A_{11}}}\,, \text{ the frequency parameter} \tag{4}$$

$$\alpha = \text{semi-vertical angle of the cone} \tag{5}$$

$$\beta = \frac{a}{b}\,, \text{ the length ratio} \tag{6}$$

$$\gamma = \frac{h}{r}\,, \text{ the thickness-smallest radius ratio} \tag{7}$$

$$\delta = \frac{h_k}{h}\,, \text{ the relative thickness of the k-th layer} \tag{8}$$

$$X = \frac{x-a}{\ell}, \text{ the distance coordinate} \tag{9}$$

Here, a and b are the distances of the small and large ends of the cone from the vertex, h is the thickness of the shell, h_k is the thickness of the k-th layer, ℓ is the length of the shell, r is the radius of the shell at the small end, R_0 is the inertial coefficient of the shell and A_{11} is a familiar extensional rigidity coefficient. When there are only two layers, we write

$$\delta = \delta_1, \text{ and } 1 - \delta = \delta_2. \tag{10}$$

For any point on the shell, $a \leqslant x \leqslant b$; and hence $0 \leqslant X \leqslant 1$.

It can be noted that the case n=0 corresponds to axisymmetric vibrations, when u and w become independent of θ, and Eqs. (3) reduce to only two equations in U and W. Also, the case α=0 corresponds to that of a plate.

THE SPLINE SOLUTION

Dividing the range [0,1] of X into N subintervals at $X=X_s$, (s=1,2,..,N-1) and having these points along with the end points of the interval for knots, the displacement functions U(X),V(X) and W(X) are approximated by the spline functions

$$\begin{aligned}
U^*(X) &= \sum_{i=0}^{2} a_i X^i + \sum_{i=0}^{N-1} b_i (X-X_i)^3 H(X-X_i) \\
V^*(X) &= \sum_{i=0}^{2} c_i X^i + \sum_{i=0}^{N-1} d_i (X-X_i)^3 H(X-X_i) \\
W^*(X) &= \sum_{i=0}^{4} e_i X^i + \sum_{i=0}^{N-1} f_i (X-X_i)^5 H(X-X_i)
\end{aligned} \tag{11}$$

in which H(X) is the Heaviside step function and the coefficients $a_i,..,f_i$ are to be determined. Imposing the condition that the above splines satisfy Eqs. (3) at the knots $X=X_s$, (s=0,1,..,N), we have a system of 3N+3 field equations in 3N+11 unknown spline coefficients.

The three sets of boundary conditions imposed at the two ends of the shell are: (i) both the ends clamped (C-C), (ii) both the ends hinged (H-H) and (iii) the small end clamped and the large end free (C-F). Each set of these conditions used on the assumed spline functions yields eight more equations which, together with the field equations, constitute a generalised algebraic eigenvalue problem of the form

$$[K]\,\{q\} = \lambda^2 [M]\,\{q\} \tag{12}$$

Using an iterative technique, this equation is solved for the first few values of the

frequency parameter λ . The eigenvectors determine the spline coefficients from which the displacements are computed and mode shapes are constructed.

NUMERICAL RESULTS AND DISCUSSION

Considering the size of the matrices K and M arising in Eq. (12), computations were carried out in double precision arithmetic. After several trial runs of the computer program developed, the optimal size of N, the number of subintervals of the range of X, was chosen to be 10. Many validity checks were made by comparing the results obtained with those available in literature. An illustration is given by Table 1 in which comparison is made with the results of Irie et al.[6], for the reduced case of homogeneous shells of different length ratios, under clamped-clamped boundary conditions, for the cases of axisymmetric (n=0) and an asymmetric (n=4) vibrations. The agreements are quite good.

Table 1. Comparative Study with Irie[6]

Homogeneous Conical Shell under C-C Boundary Conditions

α =60 , γ=0.01/β, ν=0.3

n	Frequency Parameter	β		
		0.25	0.50	0.75
0	λ	0.5796	0.3863	0.2768
	λ'	0.6692	0.6690	0.9589
	λ''	0.6680	0.6685	0.9576
4	λ	0.2741	0.2545	0.2670
	λ'	0.3165	0.4408	0.9249
	λ''	0.3155	0.4298	0.9336

λ =Present value
λ'=Present value converted into Irie's parameter
$\lambda''= \lambda (\sin\alpha)/(1-\beta)$
=Irie's parameter

The materials of the layers considered were steel (St), Aluminium (Al), high-strength graphite epoxy (HSG), PRD-49-III epoxy (PRD) and S-glass epoxy (SGE). The number of layers considered in this discussion is restricted to two, since the effect of coupling between bending and stretching is most significant only for two-layered elements.

The value of the frequency parameter varies with the ratio of the thickness of the inner layer to the total thickness of the shell. Figure 2 provides two illustrations of such studies. The materials of the layers considered are Al-SGE and HSG-PRD. The boundary conditions for both are C-C. The cases δ =0 and δ =1 correspond to homogeneous shells, made up of the second material and the first material mentioned, respectively. Three meridional modes (m=1,2,3) are considered. The cotinuous and dashed curves correspond to the inclusion and omission of the coupling between bending and stretching. It is seen that the frequencies can have relative maximum and minimum values. This phenomenon is more pronounced for higher meridional modes (i.e., for larger m). It is also seen that with proper choice of δ , it is possible to achieve frequencies not only in between the frequencies of homogeneous shells of either of the two materials, but also outside the range prescribed by them. The shells are of medium length (β =0.5), with semi-vertical angle 45^0 and thickness-minimum radius ratio of 0.05. The $\lambda - \delta$ variation depends also on the materials of the layers, the end conditions and the geometric parameters. In general, the neglect of coupling raises the values of λ ; but the raise itself is not significant and hence the coupling can be ignored without much loss of accuracy, but with much gain in computational labor. Though the figure and discussion correspond to axisymmetric cases (n=0), the features described are just similar to asymmetric cases of vibrations.

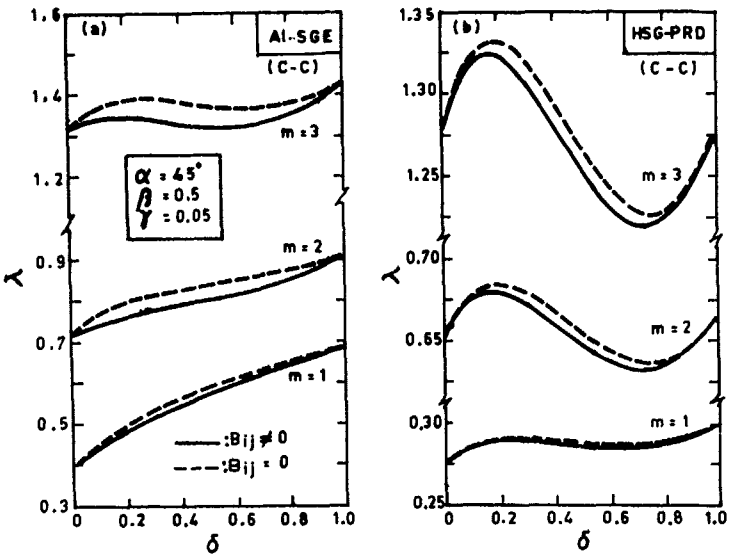

Figure 2 — Influence of relative layer thickness and coupling on frequency parameter

Since the frequency prameter is a function of the length of the cone, the study of variation of λ with β will not serve any purpose. Hence, the variation of the angular frequency ω with β is studied in Fig. 3. In Fig.(a) the variatin of the fundamental frequency ω_1 with β for different layer combinations under C-C boundary conditions is depicted. The frequencies are small for long shells (β small) and high for short shells (β large). The growth of frequencies with respect to β is almost linear and gradual upto a large value of , and then very steep. This turn occurs earliest (around β=0.6) and the 'turning value' of the frequency is also the least (between 1100 and 1600 Hz) for HSG-PRD. For smaller cone angles the almost linear part of the gradual increase is still longer. Figure 3(b) exhibits ω-β relations for the modes m=1,2,3 for two cases of asymmetric vibrations, n=4 and n=10. The characteristic shape of the curves is the same for all asymmetric vibrations and for other boundary conditions also. The steep increase in starts

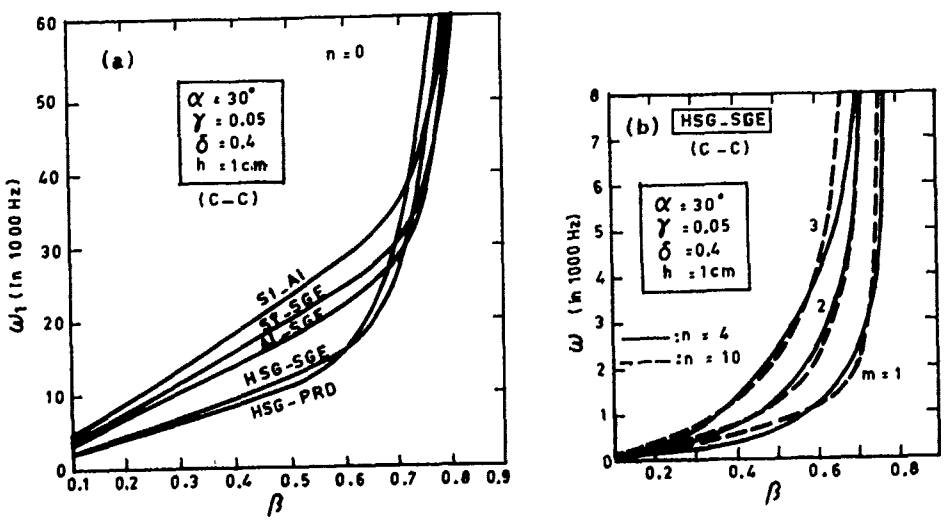

Figure 3 — Effect of length ratio on frequency

earlier for higher modes. The slope of the gradually increasing part also increases with higher modes. The steep increase in frequencies become steeper with higher values of n. With the changing boundary conditions, from C-C to H-H to C-F, the 'turning point' is pushed to the right, i.e., towards shorter lengths of the cone The percentage increase in ω_1 at β=0.5 over that at β=0.1 for HSG-SGE, for the three boundary conditions are 490, 462 and 422 %, respectively.

The dependance of the frequency parameter on the vertical angle of the cone is illustrated in Fig. 4. The other parameters take constant values as indicated. If γ is kept constant, since it is the ratio of the thickness of the shell to the minimum curvature, thickness cannot be maintained constant as α changes. Hence, instead, γ',

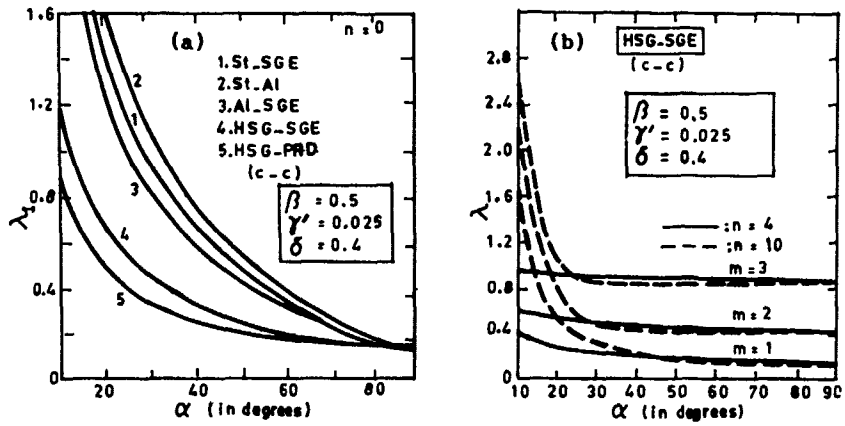

Figure 4 — Variation of frequency parameter with cone angle

the ratio h/a is held fixed. At the outset, the frequency parameter is found to decrease with increasing α. The decrease is rapid for smaller values of α and the curve is almost horizontal when the shell tends to become a plate ($\alpha \to 90°$). The rapidity with which λ tends to become constant is different for different layer combinations as can be seen in Fig. (a), which deals with the fundamental frequency parameter values for five different layer combinations, for axisymmetric vibrations. At α=90°, all the curves would have met at a common point, had δ been 0 or 1 (homogeneous plates). The frequencies for any fixed (α=90°) are distinct for the different layer combinations, assuming maximum value for St-Al and minimum value for HSG-PRD. The difference between the maximum and the minimum values of λ_1 for $10° \leq \alpha \leq 90°$, with respect to the corresponding minimum value of λ_1 is 1756 % for St-Al, and 486 % for HSG-PRD. Viewing with reference to the three types of boundary conditions imposed, it is seen that the frequencies are highest for C-C conditions and least for C-F conditions for any fixed α and β. In the C-F case, for β=0.2, HSG-SGE and St-SGE combinations (figures not presented) a kink is seen in the $\lambda_1 - \alpha$ curve around the point α=20°. This may be due to the corresponding mode shape being torsional, as also suggested by Irie. Two axisymmetric vibrational cases (n=4,10) are covered by Fig. 4(b). It is interesting to note that for certain values of n (e.g., n=4), there are no appreciable changes in values of λ with α, whereas in some other cases (like n=10, here), the changes are very rapid upto very small values of the semi-cone angle (upto α=25°, here), without much change as the cone widens further.

In Fig. 5 the nature of variation of the frequency parameter with the circumferential wave number and the effect of the length ratio and coupling are brought out. A cone of semi angle 30° of HSG-SGE lamination under C-C boundary conditions is considered. It is seen that for fairly long shells (β=0.2) the frequency parameter generally comes down in value for upto n=6 and then ascends with n. The trend is similar for shells of medium length (β=0.5) also. In the case of short shells (β = 0.8), the lower mode values of λ come down almost steadily as far as n=10. The higher mode curves begin to ascend at very small values of n. The dashed curves, which correspond to the neglect of coupling rigitities, generally closely follow the

continuous ones which correspond to the inclusion of coupling. The coupling effect is seen to be increasing with n. The effect of ignoring coupling is to raise the value of the frequency parameter. However, the percentage increase is, as already remarked, so small for all asymmetric vibrations, that coupling could be ignored without introducing appreciable errors.

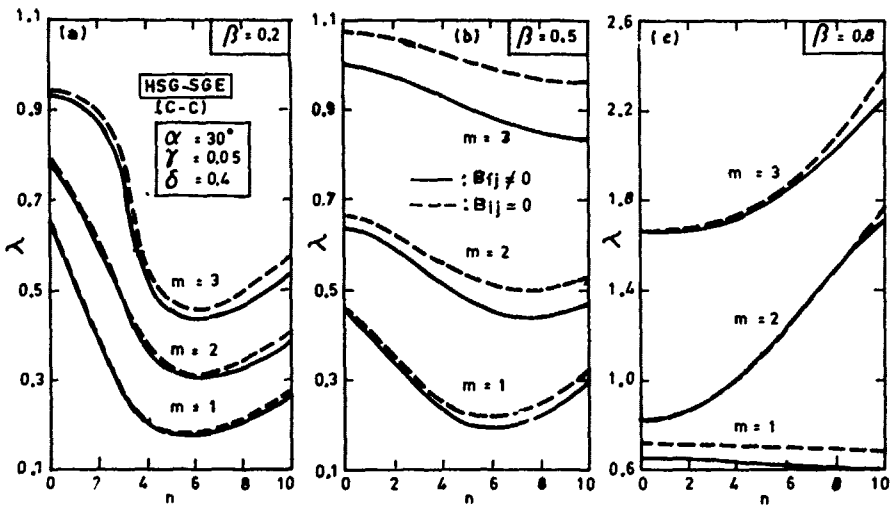

Figure 5 — Variation of frequency parameter with circumferential node number and the effect of length ratio and coupling

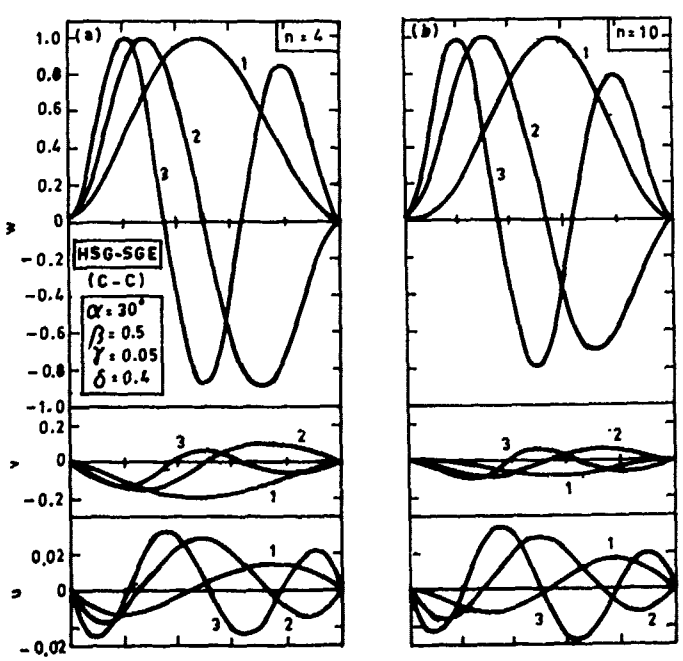

Figure 6 — Mode shapes of asymmetric vibrations

The frequency parameter values corresponding to $\delta=1$ (in which case the material becomes steel, $\nu=0.3$) is observed to come down with increasing n until n=6 and then to rise up. This trend is in agreement with what could be noted in the results of Irie et al.[6].

The U-, V- and W- mode shapes of vibration are exhibited in Fig. 6, upto three modes, for the asymmetric cases corresponding to n=4 and n=10. The displacements are normalised with respect to max(W). The transverse displacements are seen to be predomin nt, for the cases considered. The circumferential and the extensional ones follow, in that order. The longitudinal mode shapes always have one more node than what would normally correspond to the value of the mode number, for the boundary conditions considered. The general patterns of the mode shapes are the same for all n. The maximum W- and U- displacements occur at points closer to the small of the cone. With increasing n, the maximum torsional displacement comes down steadily.

REFERENCES

1. Navaneethakrishnan, P.V., "Buckling of nonuniform plates: spline method," Journal of Engineering Mechanics, ASCE, Vol. 114-5, 1988, pp.893-898.

2. Navaneethakrishnan, P.V., and Chandrasekaran, K., "A spline function analysis of axisymmetric free vibrations of layered conical shells and plates of variable thickness," Structural Vibrations and Acoustics, ASME, DE-Vol. 18-3, 1989, pp.153-159.

3. Navaneethakrishnan, P.V., Chandrasekaran, K., and Ravisrinivas, N., "Axisymmetric vibrations of layered plates of variable thickness: a spline method," Proc. International Congress on Recent Developments in Air- & Structure-born Sound and Vibration, Auburn University, Auburn, Vol.2, 1990, pp.873-880.

4. Chandrasekaran, K., and Ramamurti, V., "Axisymmetric free vibrations of layered conical shells," Trans. ASME, 81-DET-68, 1981, pp.1-10.

5. Ambartsumyan, S.A., Theory of Anisotropic Shells, NASA TTF-118, 1964.

6. Irie, T., Yamada, G., and Tanaka, K., "Natural frequencies of truncated conical shells," Journal of Sound and Vibration, Vol. 92-3, 1984, pp.447-453.

SECOND INTERNATIONAL CONGRESS ON
RECENT DEVELOPMENTS IN AIR- AND
STRUCTURE-BORNE SOUND AND VIBRATION
MARCH 4-6, 1992 AUBURN UNIVERSITY, USA

ONE OF THE METHOD OF EXPRESS-CONTROL OF THE SOUND-CAPACITY MACHINES.

V.Didkovsky, P.Markelov
Acoustic department
Kiev Politechnics
Kiev 252056
Ukraine

ABSTRACT

It is offered the method of express-control of the sound capasity machines in condition of their serial production. The method includes calculation of a possible sound-capacity of each machine by measuring vibrating velocities of it's surface in the final numbers of the control points. The conditional frequency characteristics, obtained for machines of this type before-hand, which connect vibrating velocities, mentioned above, with sound pressures of the machine acoustic field standard measuring points, are used in this case. This method is not alternative to the well-known methods of sound-capacity estimation in conditions of acoustic hindrance. The method is mostly effective in case of serial production of machines with several acoustically connected active structures, that is, in that case when sound capacity estimation standard methods application as well as application of methods, based on intensity measurements, will entail great unproductive losses of time.

The authors assumed multi-dimentional acoustic pattern based on multi-dementional linear non-parameter system, to be a machine sound-making mathematical pattern. Real sound pressures in the machine acoustic field K standard measuring points are echoes of the system. These sound pressures are used to estimate the machine sound-capacity in the surroundin space by the formula [1]

$$P = S/(K\rho c)\sum_{k=1}^{K} p_k^2 \quad , \qquad (1)$$

where p_k - measuring points sound pressures effective values, K-an amout of these points, S is a measuring surface area, ρc - is wave air resistance.

System coercions are equal to vibrating velocities in machine surfase a control points Q finite quantity. Generally such coercions are coherent to each other. That's why, in order to simplify the given system analysis it is possible to pass on to the adequate conditional multi-dimentional system, using [2] (figure). The system frequency response $L_{ki}(f)$ ($k = 1 \div K$, $i = 1 \div Q$) provides for optimum linear k-echo calculation by first coercion.

Also, $X_{1\cdot(1-1)!}(f)$, $Z_k(f)$, $N_k(f)$, $1 = 1 \div Q$, $k = 1 \div K$ -

conditional coercions realizations Fourie finite transformations, k - echo and k - echo registration hindrance correspondingly are marked in the figure. The system is symmetrical relative to the sound measuring points.

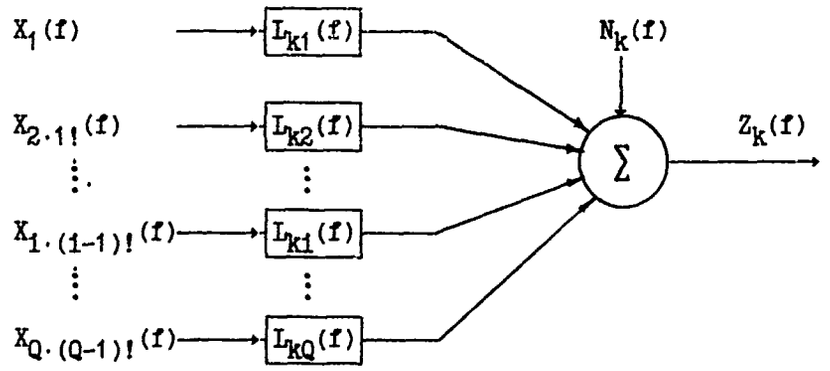

Figure. Machine vibrating and sound connection pattern.

By analysing the accepted pattern the authors became able to obtain the following ratio for sound capacity correction level calculation estimation of some machine being tested:

$$\hat{L}_p = 10\cdot\lg\left\{\Delta fS/(S_0 p_0^2\ K)\sum_{f\in(f)} 10^{0,1A(f)}\cdot\sum_{k=1}^{K}\sum_{1=1}^{Q}|\hat{L}_{k1}(f)|^2\ G_{11\cdot(1-1)!}(f)\right\}, \quad (2)$$

where p_0 - is a standard sound pressure, A(f) - frequency correction characteristic, (f) - multitude of power-consuming frequencies which are used to localize the main part of the sound capacity machine, $S_0 = 1m^2$. Besides, in (2) $G_{11\cdot(1-1)!}(f)$ -

special coherent capacity spectrum of the first coercion by all previous coercion which can be calculated by iteration method set out in [2], and $L_{k1}(f)$ - is a mean conditional frequency characteristic, that's why

$$|\hat{L}_{k1}(f)|^2 = 1/D\sum_{j=1}^{D}|{}^jL_{k1}(f)|^2 \quad (3)$$

Index j denotes individual frequency characteristic for j machine belonging to some D multitude of the same type. The method of its estimation is already described in [2].

So, the express-control method, suggested above, on the preparatory stage (on the same type machines D multitude):
- search of power-consuming frequencies multitude (f);
- search of mashine surfase control points;
- calculation of the mean conditional frequency characteristics accocrding (3).

On the propper control (stage for the machine tasted):
- vibrating velocities signal registration in control points;

- prognosis calculation according (2);
- comparing prognosis with the sound-capacity standard inherent in this type machines.

While deducing the formula (2) it has been assumed, that hindrance $n_k(t)$ has an external origin, in other words, all important formations of coercion echoes have been taken stock of. This condition is provided by a corresponding choice of control points, in particular by proximity to plurality coherence $\gamma^2_{k:x}(f)$ function unity, among every echo of the system and coercions in there points on the (f) multitude frequencies. It is advisable to choose the threshold characterizing proximity to the unity, proceeding from the analysis of concrete conditions and available experimental data. In general case the authors propose

$$\gamma^2_{k:x}(f) \geq \beta \quad , \; f \in (f) \quad , \qquad (4)$$

as a criterion for rational choice of vibration registration points.

Experimental research carried out by the authores have proved, that coeherence high level for control points remains within limits of the same type machines multitude.

The (4) criterion makes it possible to work out engineering recommendation on control points searching. It is adviseble to choose control pointe as close to sources of machine sound as possible. In general case when the sources are inaccessible to a researcher, and measuring can be carried out only on the surface around the sources, the search algoritm can be constructed on the basis of the control theory known methods, in accordance with formula (4).

The authors worked out experimentally the half division method. The successful choice of control points makes it possible to considerably improve prognostication precision.

Sound-capacity prognostication statistical mistakes are conditioned by:

1) statistical mistakes of spectral characteristics estimation connected with finite duration of analysing processes realization;
2) between plurality coeherence functios and the unity;
3) dispersing conditional frequency characteristics about the multitude of the same type objects.

The standartized quadratic mean mistake of corrected sound-capacity prognozing occasioned by statistical mistakes of spectral characteristic estimation, has been obtained by the authors by applying results [2] and is equal to:

$$\varepsilon_1 = 10 \cdot \zeta_1 / \hat{L}_p \; , \qquad (5)$$

where

$$\zeta_I = \sum_{f \in (f)} 10^{0,1A(f)} \cdot \sum_{k=1}^{K} \hat{W}_k(f) \cdot \varepsilon_0(f) \Big/ \left\{ \sum_{f \in (f)} 10^{0,1A(f)} \sum_{k=1}^{K} \hat{W}_k(f) \right\},$$

$$\varepsilon_0(f) = [2 - \gamma^2_{k:x}(f)]^{1/2} \Big/ \left[|\gamma_{k:x}(f)| (\eta + 1 - Q)^{1/2} \right],$$

$$\hat{W}_k(f) = \sum_{l=1}^{Q} |\hat{L}_{kl}(f)|^2 \, G_{11 \cdot (l-1)!}(f),$$

η - is the number of periodogram when considering spectral characteristics. When deducing formula (5) it was taken into consideration that $\lambda_a \cdot \zeta_1 \ll 1$ (λ_a -is a quantil Gaus distribution) as well as ratio (2).

To high degree the estimation error of sound-capacity correction level is conditioned by systematic composite of negative bias

$$\Delta(L_p) = 10 \cdot \lg\left\{\int_f 10^{0,1A(f)} \cdot \sum_{k=1}^{K} \hat{W}_k(f)df \Big/ \left[\sum_{f\in(f)} 10^{0,1A(f)} \cdot \sum_{k=1}^{K} \hat{W}_k(f)\right]\right\}$$

(the integration is carried out throughout the whole frequency range analysis in the numerator), which is attributed to the fact that the application of the formula (2) does not regard the whole capacity, but only the portion which is localized in power consuming frequencies. This bias is an accidental quantiti as regards the multitude of the objects of the same type and because, spectral sound-capacity power-consuming component's differ considerably with the various objects of the same type. The mean bias in the multitude of the similar objects depend on the portion of sound-capacity localized in power-consuming frequencies.

Determination of errors relative to dispertion of conditional frequency characteristics about multitude of similar objects is the most enential part of the method accurancy analysis. After we have obtained the mean optional standard to estimate conditional frequency characteristics on the muititude D and (f) - frequencies using the following formula:

$$S_{Lki}(f) = \left\{\sum_{i=1}^{D}\left[|L_{ki}(f)|^2 - |\hat{L}_{ki}(f)|^2\right]^2 / D(D-1)\right\}^{1/2},$$

we can calculate a 100 per cent principal interval for the sound-capacity veritable adjusted level of the given object obtained through (2). It will be limited by the values: $\hat{L}_p \pm \lambda_\alpha \zeta_2$, where

$$\zeta_2 = \sum_{f\in(f)} 10^{0,1A(f)} \cdot \sum_{k=1}^{K}\sum_{i=1}^{Q} S_{Lki}(f) \cdot G_{ii\cdot(i-1)!}(f) /$$

$$/\left\{\sum_{f\in(f)} 10^{0,1A(f)} \cdot \sum_{k=1}^{K}\sum_{i=1}^{Q} |\hat{L}_{ki}(f)|^2 \cdot G_{ii\cdot(i-1)!}\right\}, \qquad (6)$$

Here we take into consideration that $\lambda_\alpha \cdot \zeta_2 \ll 1$.

In such a case the normalized mean square of the object sound-capacity prognosis brought about due to dispersing frequency characteristics about the multitude of similar objects is a follows:

$$\varepsilon_2 = 10\ \zeta_2 / \hat{L}_p \qquad (7)$$

The normalized and mean square error (5) can be lenened by increasing the number of η. However, to achieve a substantial lenening of the error we should be more considerate to the criterium (4) while defining control points, in other words to the increase of β.

The mean square deviation of sound-capacity prognosies from the values obtained through applying standard method, with regard to (5) and (6), owing to irrelevance of the prognosis mistakes equals to:

$$\sigma_p = 10\ [\zeta_1^2 + \zeta_2^2]^{1/2}$$

We here regard deviation σ_p as a mean square prognosis efficiency index. It's effectivenen is in relation to the increase of β threshold in (4) if σ_p is being lenened. To great extend it depend on the coordinate and number of control points. Although the increase is being restrained by negative bias of prognosis estimation $\Delta(L_p)$ and therefore it mat-

ters greatly only in case of relatively small number of control points.

Subsequent increasing in number of control points does not make the effectivenen more substantial. The experimental studies of the method being offered hereby dealt with analysis of it's effectiveness with various number of control points. The compressors fitted into serially produced refrigirators and designed chiefly to determine noise level, were used during tests. The latter were conducted in the anembly shop of compressor producting plant, where the noise level was 80 dB, and in muffled chamber of the same plant.

The tests proved that mean square sound-capacity prognosis deviation from that obtained in the chamber was lenening with the increase of control points. Besides, the values of these deviations proved to be less than those obtained through a widely practiced method of immediate control of sound-capacity that is being done with regard to the level of vacillating velocity measured in one point on compressor's surface. A multichannelled information and control suite used with a PC of IBM type was made to perform the tests mentioned above. The tests proved the method described as effective and its theoretic assumption possible and correct.

In conclusion the authors would dare to say that the method presented hereby will have its application in measuring the noise level of complex machinery and equipment.

BIBLIOGRAPHIC REFERENCES

1. Yang S., Ellison A. Machinery Noise Measurement, Oxford University Press, 1985.
2. Bendat I., Piersol A. Random Data Analysis and Measurement Procedures. Yohn Willey Sons, 1985.

SECOND INTERNATIONAL CONGRESS ON
RECENT DEVELOPMENTS IN AIR- AND
STRUCTURE-BORNE SOUND AND VIBRATION
MARCH 4-6, 1992 AUBURN UNIVERSITY, USA

Automobile Diagnostic Expert System by Noise and Vibration

Joon Shin and Jae-Eung Oh
Dept. of Precision Mechanical Engineering
Hanyang University
Haeng dang-dong, Seong dong-ku, Seoul, 133-791
KOREA

ABSTRACT

Diagnostic prototype expert system was built using characteristics of measured sound and vibration for automobile. For the utilities of this system, 1/3 octave filter(band-pass filter) and A/D converter were used for data acquisition and then data were analyzed using signal processing technique, statistical analysis and pattern recognition using Hamming network algorithm. In order to raise the reliability of the diagnostic results fuzzy inference technique was applied by considering many operating variables and information of automobile to be diagnosed. And, the results were displayed as graphical method to help the novice in diagnostic field. The validation of this diagnostic system was checked through experiments using automobile and it showed an acceptable performance for diagnostic process. Also, for the case of wrong decision making, knowledge base of system can be extended through learning procedure. Therefore, as a result, it is expected that this system can be developed with implementing more simplicity and flexibility to the external environment.

INTRODUCTION

There has been a strong request for computer system in production line because of high speed and automation of equipment. And, the necessity of monitoring system has been increased in the diagnosis of installation. These tendency is more and more elevating in the side of shortage of expertise in the diagnostic field, prevention of industrial accident and settling of being incapability of expert due to the variety of production.[1]

Especially, automobile is a very complicate system which is composed of thousands of components, and it is one of the most important transportation device in modern society. Also, it has been developed in the face of performance and structure with the progress of the livirg environment. Besides, many expert mechanics and accumulated diagnostic techniques are required due to the increased demand and automobile variation, but the skillful mechanics and the diagnostic techniques are incapable of satisfying these demands.[2][3]

In this study, therefore, expert system for diagnosis of automobile is developed by measuring acoustic signal to supply and support the relative incapability of mechanics owing to the development of automobile. In addition, Fuzzy inference technique is applied to raise the reliability of decision making, and pattern recognition technique by Hamming network is adopted to extend the knowledge base.

The validity of the developed diagnostic algorithm and the efficiency of the expert system are verified through experiments using automobiles.

THEORY

Fuzzy Inference

Fuzzy sets deal with the uncertainty and quantify the fuzziness of a human being using membership function of real value from 0 to 1. In this study, fuzzy inference technique is applied for analysis of noisy acoustical data and vague information, and probabilistic decision is made by pattern recognition. Fig.1 represents the example of rules for fuzzy inference, and the output can be formulated by max-min composition technique as follows [4][5]

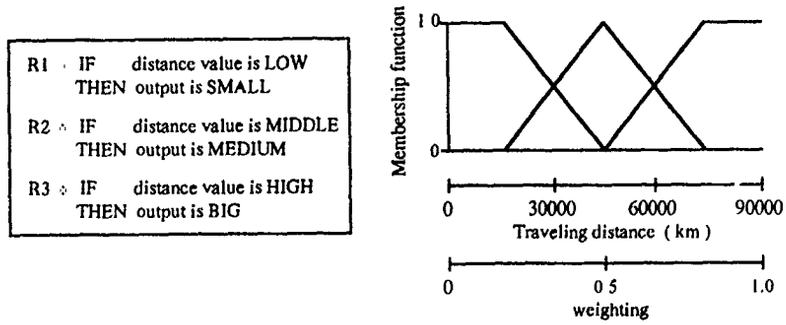

Fig.1 Example of rules and membership function

$$m(w) = \max[\min(m_A i),\ m_R(i,w))] \qquad (1)$$

where $m(w)$: Membership function for output
$m_A(i)$: Membership function for input
$m_R(i,w)$: Membership function for rule

Also, eq.(2) is used for defuzzification of output membership function.

$$w = \frac{\sum_{i=1}^{M} (\text{Action})_i (\text{Membership value})_i}{\sum_{i=1}^{M} (\text{Membership value})_i} \qquad (2)$$

Hamming Network

General Hamming network deals with binary pattern (+1, -1, or +1, 0) for inputs and weightings. But, it is difficult to use conventional Hamming network directly because the most signal is represented as continuous value at the restricted range.

Therefore, in this study, pattern recognition technique which use 1/3 octave data is proposed. In this process, measured acoustic signal is transformed to octave data and each octave data is divided with overall level data. Then, maximum value of matching score, α, is multiplied and pattern score corresponds to the input value of each input node is decided.[6]

In the diagnostic algorithm, Hamming distance, absolute value of difference of the two signals, is determined. And then, matching score can be calculated by subtracting maximum displacement from the obtained absolute value. Fig. 2 shows the application example of this method.

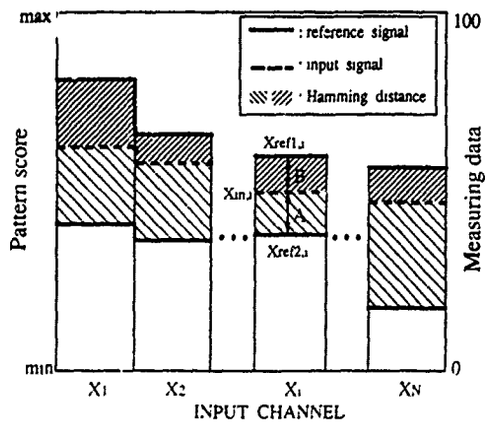

Fig.2 Concept of modified Hamming network

$$P.S = \frac{X_I}{\sum_{j=1}^{M} X_j} \times \alpha \qquad (3)$$

where P.S : Pattern score
X_I : Octave data
ΣX_j : Overall level
α : Division value

CONFIGURATION OF THE DIAGNOSTIC SYSTEM

Fig. 3 represents the inference process of developed expert system.

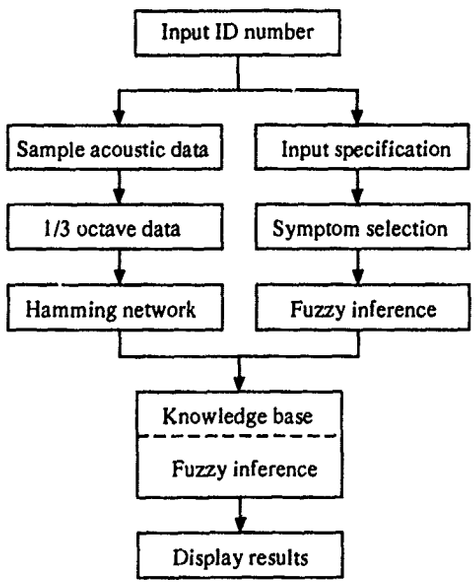

Fig.3 Diagnostic process for Neuro-Fuzzy Technique

If the system is initialized, expert system requests the specification and symptom of the automobile to be diagnosed and then sampls the acoustic data using 4 microphones. The configuration of the measuring system and data processing units are shown in Fig. 4. [7]

COMPUTER SIMULATION

Method for simulation

Fault revival simulation was carried out to evaluate the diagnostic performance of the developed software. In the first place, the automobile engine was divided to 32 points and sampled the normal data of the each measuring points. And, white noise which corresponds to 1/10 level of each normal data was added to postulate the changed measuring environment.

It was assumed that alternator had been out of order and level of 100 Hz center frequency at the alternator position was increased from once to three times. Also, level of side band center frequency to the 100 Hz was increased instanteneously from once to 1.5 times. And, each 32 points was calibrated with the proportion of the inverse distance level at the alternator position.

Results and consideration for simulation

In this simulation, three diagnostic techniques were compared.

* CASE 1 (simple diagnosis) : diagnostic result by the difference of the center frequency and overall level of the two signal at the only one point.
* CASE 2 (precision diagnosis) : diagnostic result by the difference of the center frequency and overall level of the two signal at the each 32 points.
* CASE 3 : diagnostic result by the Neuro-Fuzzy Technique.

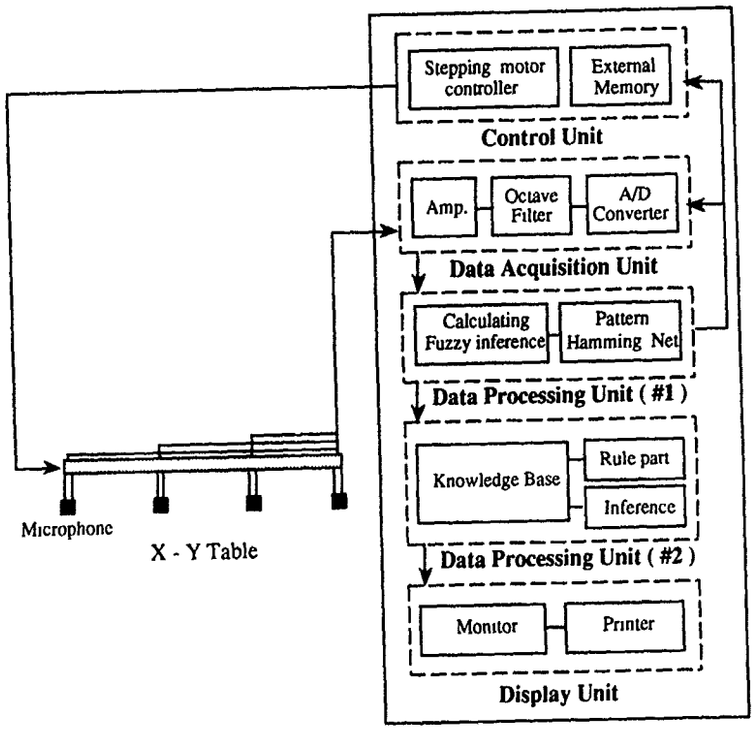

Fig.4 Configuration of the diagnostic expert system

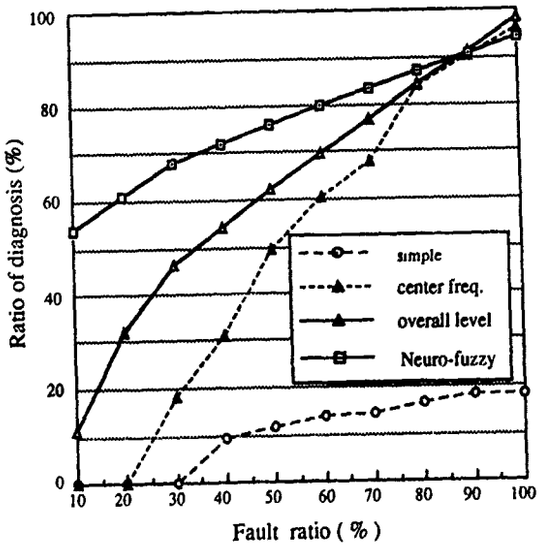

Fig.5 Ratio of diagnosis for each method according to fault ratio

From Fig. 5, in the case of simple diagnosis, it could be known that simple diagnosis was not proper to diagnose the increasement of only one certain center frequency. Also, it was shown that diagnosis by comparison of overall level was more efficient than that of center frequency, but diagnosis by overall level had some disadventage that it was not sensitive to the light fault. And in the case of Neuro-Fuzzy Technique, acceptible diagnostic result could be made by detecting slight fault signal.

EXPERIMENT

Method and apparatus for experiment

In the experiment, the automobile engine was divided to 32 points as Fig. 6 and sampled the acoustic data for normal state. For the revival of fault state, artificial faults for some kind of components were generated as Table 1.[8]

Table 1 Kind of fault types

CASE	Fault Type
I	Normal state except increasing of RPM
II	Ignition plug #1 fault
III	Ignition plug #2 fault
IV	Ignition plug #3 fault
V	Ignition plug #4 fault
VI	Coolant temperature sensor fault

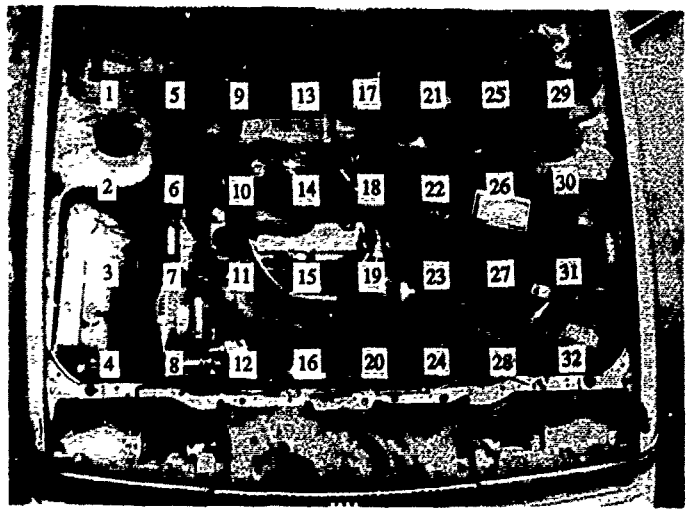

Fig.6 Measuring points of the automobile engine part

Results and consideration for experiment

Table 2 represents the expected fault component of automobile and ratio of diagnosis according to the fault type. From Table 2, it could be known that the proposed Neuro-Fuzzy Technique was superior to the conventional diagnostic method.

Table 2 Diagnostic results to each fault types

Method / CASE	Simple Diag.	Precision Diag.	Neuro-fuzzy
I	normal	normal	normal
II	fault	I P #2 fault	I.P #4 fault
III	normal	I P #2 fault	I.P #2 fault
IV	fault	distributor fault	I P #3 fault
V	normal	I P #4 fault	I.P #4 fault
VI	normal	normal	Coolant temp sensor

While wrong decision was made for the fault CASE II and it might be thought as the vicinity of the each ignition plug and decreased sound level. And, in the case of fault CASE VI, it was impossible to find the fault with the conventional method because the coolant temperature sensor does not affect to the overall sound level at all.

RESULTS

Neuro-Fuzzy Technique was proposed to diagnose the fault of automobile and diagnostic system was constructed. For the validity of the system, computer simulation was performed. And as a result it was certified that the proposed Neuro-Fuzzy Technique was superior to the conventional diagnostic method. As a result of experiments, developed system showed an about 83 % diagnostic success for the given case.

On the other hand, as the microphones are easily affected by external disturbance, counterplan is required for the noise to improve the reliability of diagnosis.

REFERENCE

1. R. A. Collacott, "Mechanical Fault Diagnosis and Conditioning Monitoring", Champman & Hall, Ltd. 1977
2. J. E. Oh, B. W. Choi, "Expert for Technique of Fault Diagnosis", J.of KSAE, Vol.10, No.1, 1988
3. M. Tomikashi, N. Kishi, et al., "Application of an Expert System to Engine Troubleshooting", SAE, No.870910, 1988
4. J. Shin, "Development of Automobile Diagnostic Expert System by Fuzzy Inference", Master's Thesis, Hanyang Univ., 1990
5. K. Hirota, "Fuzzy Reasoning and Fuzzy Control", JSME, Vol.93, No.856, 1990
6. D. G. Sohn, "Automobile Diagnosis using Neural Network", Master's Thesis, Hanyang Univ., 1990
7. "Development of On - line Diagnostic Expert System by Noise and Vibration", Research Rerort, Hanyang Univ., 1991
8. J. E. Oh, et al., "A Study on the Noise Source Identification of 4-cylinder Gasoline Engine using Sound Intensity Method", J. of KSAE, Vol.11, No.1, 1989

SECOND INTERNATIONAL CONGRESS ON
RECENT DEVELOPMENTS IN AIR- AND
STRUCTURE-BORNE SOUND AND VIBRATION
MARCH 4-6, 1992 AUBURN UNIVERSITY, USA

NOISE AND VIBRATION PROTECTION AT SOVIET COAL MINING ENTERPRISES

V.B.Pavelyev and Yu.V.Flavitsky

Skochinsky Institute of Mining
Lyubertsy, Moscow 140004
U.S.S.R.

ABSTRACT

The paper deals with noise and vibration protection at Soviet collieries and opencast mines. The authors discuss new achievements in this field and practical measures to reduce vibration by 2-3 times as well as its effect on worker's health. Certain means are developed to cut down aerodynamic and structural noise.

At present the noise and vibration pathology occupies a cardinal place within the structure of worker's professional deseases in the mining industry.

Underground about 70 per cent of working places and sites are hazardous as far as the noise and vibration levels above permissible are concerned.

The situation is still more aggravated with the specific mine conditions such as a combined attack of noise, vibration, higher temperatures, moisture, atmospheric pressure and dust factor against workers, the fact corresponding in normal microclimate to a noise intensity increased by 10-15 dB.

The principal sources of noise and vibration exceeding their permissible levels are as follows:

- hand-operated mining machinery such as augers, jackhammers and hammer drills (their total annual production in this coutry exceeds 250,000 pcs),
- roadheading and drilling equipments,
- fans, ventilators and pneumatic engines,
- machinery and equipment for opencast mining and preparation plants.

In our branch of economy work goes on to reduce and cut down the noise and vibration levels at the working places and sites; methodically it is directed by the Skochinsky Institute of Mining.

The principal developments in this field may include the following:

I. Development of jackhammers with vibration cut-down in the very source of it due to the striker mass reduction at a set strike energy and a constant force acting upon the striker. The mass is reduced due to

both shorter diameter and length of the striker and correspondingly a greater pre-striking velocity whose critical value can be determined as shown in Eq. (1):

$$V_{crit} = K\, a\, \sigma_{perm.} / E \qquad (1)$$

where $\sigma_{perm.}$ is permissible stress and strain

a is velocity of longitudinal waves

E is Young's modulus

K is striker's shape coefficient

$$K = I + (d/D)^2 \qquad (2)$$

where d is diameter of smaller section

D is diameter of greater section.

Practically in substantial constructions a pre-striking velocity of 13-14 m/s has been reached.

The jackhammers produced by the industry possess a reduced weight, require less press effort and their vibration is reduced as compared to the best specimens abroad, their energy parameters being approximately the same. At present some perforator prototypes with reduced vibration and press effort have been developed according to these very principles.

The problem of reducing the sound vibration of the impact-action machinery is rather complicated. For this purpose we have determined several regularities in forming and flying of the strike and impact processes in mono-measured elastic bodies. Based on them there has been developed an engineering method to calculate the collision momentum of stress parameters no matter what is the geometry of encountering bodies as well as the shape of contact included. The fact makes it possible to simulate the influence of design and kinematic parameters of encountering parts upon the amplitude and range of arising sound vibrations.

The vibro-isolating methods have become widely spread. They deal with the principle of mass inertia on an elastic foundation with friction avoided. So, the up-to-date perforators manufactured by the branch of economy are provided with vibro-protecting carriages where the handle and the pneumatic support are separated from the perforator's body with the help of elastic elements. The handles of jackhammers and hammer drills have been vibro-isolated from their bodies as well.

2. Development of the above-drill-bit vibration isolators for the roller-bit drilling rigs to be installed between the bit and the column. Application of the vibration isolators makes it possible to reduce the vibration load of the entire drilling rig by 2-3 times as well as the vibration level at the operator's place down to a permissible one. It also increases the drilling rate by 15...30 per cent and the durability of a drill bit by 25...50 per cent.

Specifications

(Conventional) drilling diameter, mm	200, 250, 270, 320
Mass, kg	350...500
Length, m	2.3 - 2.4
Static load, kN	250...450
Service life, running metres	25,000...30,000

The above-drill-bit vibration isolators are provided with elastic elements made of a new elastic-damping material named MR (metal-rubber). The material has made it possible to manufacture the elements of practically any shape possessing a high damping ability of operating in aggre-

ssive media and within a wide range of temperatures.

3. Development of vibration isolators on the basis of cables.

Specifications

Range of loads	$5...5 \cdot 10^5$ N
Minimum resonance frequency	2.5 Hz
Mass ratio between vibration isolator and protected object	0.01
Dynamic ability coefficient at a resonance	not more than 2.5
Serviceability in any direction under a wide range of temperatures and in corrosive media, no matter what is the type of deformation.	

4. Development of vibration isolators on the basis of center-compressed bars for chairs and platforms as well as additional springs for control cabins, etc., their minimum resonance frequency being 0.8 Hz and their serviceability remaining good within a wide range of temperatures and in corrosive media and atmosphere. The vibration isolators are used in the chair and platform designs, for cabin suspension as well as for other mining machinery.

5. Development of methods and means for reduction of acoustic noises (pneumatic engines, hand-operated pneumatic tools, ventilators) and of structural noises (impact-action machines, roadheading equipment and facilities, etc.).

6. Development of portable intrinsically-safe (with self-contained power supply) noise and vibration meter ShVD-001 type for diagnosis (for the dust and gas hazardous collieries).

Specifications for the device

Vibration acceleration measurement range	from 10^{-2} to $3 \cdot 10^3$ m/s^2 or 80-190 dB for 10^{-6} m/s^2
with automatic translation into terms of vibration rate and shift values and digital read-out	
Dynamic range without switching	40 dB
Working frequency range	0.7...12,000 Hz
Dimensions	220x250x90 mm
Mass	up to 3 kg
Digital read-out	

It provides for rms-determination in the octave frequency band from 1 to 1,000 Hz and for determination of corrected levels of both general and local vibration acceleration velocity along all the axes, dB, sound pressure level, dB, in the octave frequency band from 63 to 8,000 Hz, dB, and corrected sound level, dBA.

The vibro-acoustic diagnostics of the technical conditions of machinery and equipments is carried out due to the following:
- a narrow-band spectrum analysis with the help of four 32-unit FFTs with the frequencies of 0-22.6 Hz, 0-177 Hz, 0-1410 Hz and 0-11,600 Hz,
- determination of the peak values in the octave frequency band of 1...8,000 Hz as well as the peak factor,
- a resonance-demodulation spectrum analysis.

SECOND INTERNATIONAL CONGRESS ON
RECENT DEVELOPMENTS IN AIR- AND
STRUCTURE-BORNE SOUND AND VIBRATION
MARCH 4-6, 1992 AUBURN UNIVERSITY, USA

ADVANCED TECHNIQUES FOR PUMP ACOUSTIC AND VIBRATIONAL PERFORMANCE OPTIMIZATION

E.Carletti, G.Miccoli
Earth-Moving Machinery and Off-Road Vehicle Institute - CEMOTER
National Research Council of Italy
via Canal Bianco, 28 - 44044 Cassana (Ferrara)
Italy

ABSTRACT

The application of acoustic and vibrational research techniques to external gear pumps is explained, our attention being focused on:
a) sound power level, sound pressure, sound intensity and structural vibration measurements that allow a description of acoustic and vibrational fields due to complex sources both in space and time;
b) pump fluidborne noise and internal flow losses evaluation with a test procedure based on the use of the anechoic system and the measurement of the source characteristic impedance;
c) assessment of pump actual operating features, i.e. internal pressure distribution, as input data to finite element model computation of casing stress distribution and consequent structural modifications.

The sensitivity of these techniques has been considered for a noise optimization procedure and the achievement of the best trade-off between acoustic and functional performances.

INTRODUCTION

A gear pump consists of two meshing spur gears enclosed in a closely fitting housing. As the teeth engage on the outlet side, the volume between two meshed teeth decreases and the oil is forced out to the delivery port. As the teeth unmesh again, the volume increases and the oil is drawn into the pump. Hence the actual pumping operations take place in the meshing area where the most noise sources are concentrated.

The main causes of noise emission are primarily eccentricity or imbalance of rotating parts and pressure fluctuation and cavitation effect of the fluid.

The above events produce noise at the gear meshing frequency. Moreover, when the gear itself acts as an acoustical radiator, the radiation from gear arises. The amount of this radiated noise depends on the relationship between the excitation frequencies and the gear wheel natural frequencies.

In summary, pressure fluctuations and cavitation effects generate fluidborne noise; eccentricity or imbalance of rotating parts, as well as vibrations of structural parts, generate structureborne noise; and structural vibrations interact with the surrounding air causing airpressure fluctuations, i.e. airborne noise.

These three forms of noise are correlated by the dynamic characteristics of the system and the acoustic coupling between vibrating surfaces and surrounding medium.

In the paper gear pump case studies are presented. The airborne noise and the pump fluidborne noise are primarily considered owing to their leading positions.

PUMP AIRBORNE NOISE EVALUATION

Various constructive and working parameters influence gear pump noise emission. Tooth number, gear manufacturing, bearing block size, pump case material can change pump acoustic and functional performances significantly.

Noise influence of the following design parameters was evaluated to "optimize" noise emission of a 9 tooth gear pump:

1) type of gear set (the same geometry and tooth number, but different material and treatments);
2) type of bearing blocks.

Considering standard configuration and varying the two parameters above, pump noise emission was determined at different values of discharge pressure by the following intensity based analysis:

1) sound power calculation;
2) near field sound pressure and intensity measurements around the pump casing;
3) vibration measurements.

Procedures

The basic instrumentation consisted of an intensity analyzer equipped with 1/4" and 1/2" microphone intensity probes and delta shear piezoelectric accelerometers for vibration tests. A computer, running dedicated software packages, supervised measurements and subsequent data processing.

As the influence of gear set type on sound emission is concerned, detailed results are reported in the reference paper [1].

After having equipped the pump with the "optimal" gear set, the comparison between two couples of improved bearing blocks a and b, specifically designed to limit fluid pressure transients at gear meshing, was carried out.

* Sound power - Sound power level was derived from intensity measurements on a suitable surface enclosing the pump. Contributions of all intensity components normal to the surface were merged into the overall sound power spectrum.

Bearing block b showed average sound power level 3 dB lower than the corresponding bearing block a.

Sound power is a very useful datum that gives a first global evaluation of pump noise emission. Considering, for example, a family of pumps different only as far as displacement is concerned, the trend of the mechanical power to acoustic power ratio R vs. working pressure is an excellent index to verify constancy of pump performances as displacement increses (Tab.1). As a matter of fact, worsening of pump acoustic performances is relevant to lowering of R value as working pressure increases.

TABLE I - D: Pump Displacement(cm^3/rev) P: Working Pressure(bar);Wme: Mechanical Power(kW); Wac: Acoustic Power(μW); R: Wme/Wac

D	P	Wme	Wac	10^6 R
3.8	50	0.4	0.4	1000.0
	100	0.8	0.5	1600.0
	150	1.2	0.7	1714.3
13.0	50	1.7	5.1	333.3
	100	3.2	6.4	500.0
	150	4.8	7.6	631.6
16.0	50	2.0	6.4	312.5
	100	4.0	7.9	506.3
	150	6.0	19.9	301.5
33.0	50	4.2	13.5	311.1
	100	8.3	29.5	281.4
	150	12.5	28.8	434.0

Moreover, sound power is necessary to check whether acoustic performances lie within specified limits but it is completely insufficient to understand the origin of acoustic phenomena generation.

* Intensity maps - Near field normal intensity values were measured on an equally spaced point grid of a plane parallel to each face of the pump. In order to concentrate on effects due to the pump only, all frequencies related to the drive shaft dynamics were excluded during data processing. The same procedure was repeated for sound pressure measurements, while vibration data were carried out by stud mounting the accelerometer to the pump casing upper face.

Fig.1 compares the casing velocity maps with near field sound pressure and intensity maps, obtained on a surface parallel to the pump upper face at 200 Hz frequency and 100 bar working pressure.

The analogy between pressure level distribution and vibration pattern confirms the good fitting of structural vibratory behaviour of a surface with wave phenomenon near the surface itself. The effect of the increasing of the high pressure region along the gear enclosure is represented with an erratic velocity distribution of maxima and minima for the a couple of bearing blocks. An acoustical energy "sink" appears at the supply region for case b, being intensity, pressure and casing velocity values always lower for this couple of bearing blocks.

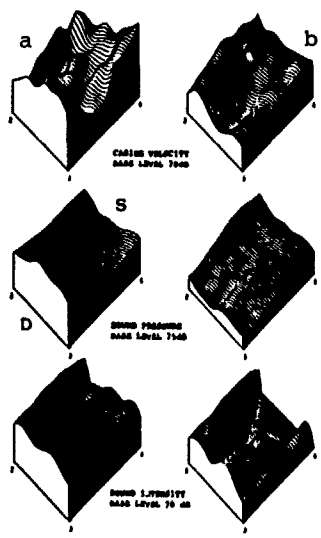

Fig.1 - Maps at 200 Hz. S=suction, D=discharge.

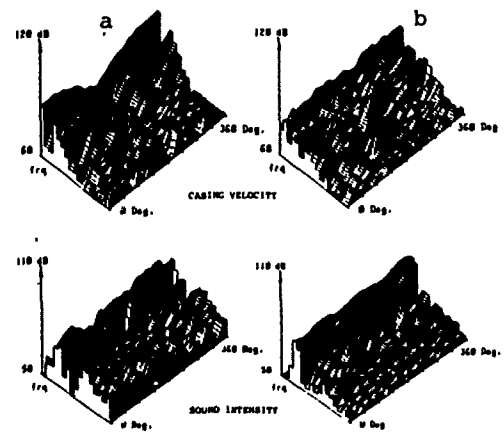

Fig.2 - Gated spectra within 200-8000 Hz frequency range.

* Gating spectra - Intensity spectra were recorded for thirty adjacent windows along the shaft revolution, each spectrum being the acoustical contribution corresponding to a different portion of revolution. For each pump configuration and discharge pressure, the intensity probe was placed over the middle of the pump upper face at a distance such as the global emission from all the surfaces of the pump could be collected. A fixed optical probe, facing the shaft, controlled the analyzer averaging process at different points of the gear revolution. The same procedure was applied for casing velocity measurements (Fig.2).

Levels at meshing frequency (220 Hz) and first harmonic are dominant. For set b these levels are relatively constant throughout the cycle, while for set a strong discontinuities can be observed either in intensity or vibration levels, both at the same angular position.

PUMP FLUIDBORNE NOISE EVALUATION

A test procedure, based on the use of the anechoic system, allows the assessment of pump source flow and equivalent source impedance. These are two fundamental complex quantities for pump noise potential evaluation, their product determining the pressure ripple along the circuit and so the main vibration source on components and connecting pipelines.

The test method characterizes entirely a pump as to its hydraulic noise. As a matter of fact, it provides the knowledge of the pump flow ripple at entry to delivery line, i.e. the pump fluidborne noise, and that of the pump internal flow losses, making the impedance a pump noise evaluation parameter.

Procedures

The reflectionless delivery line was made by a variable capacity with an adjustable diaphragm at its entrance (Fig.3). Both impedance and source flow were derived from measurements of ripples occurring when two different diameter pipes act as independent impedance values at the pump outlet port.

The harmonic analysis of pressure ripples was carried out with a digital frequency response analyzer while the complex data reduction was performed on a mainframe computer to obtain the source impedance and the flow ripple.

The reliability of the test procedure has been proved at various operating conditions on 11 gear pumps, different as displacement and gear tooth number [2].

Verified, moreover, the sensitivity of the method to source impedance and pump flow ripple variations for different geometry pump components, the fluidborne noise optimization of the gear pump has been carried out, adopting the relief groove size as design parameter. Fig.4 shows the drawing of both A and B bearing blocks, being the distance d between the edge of the suction relief grooves and the symmetry axis of the bearing block A 0.8 mm shorter.

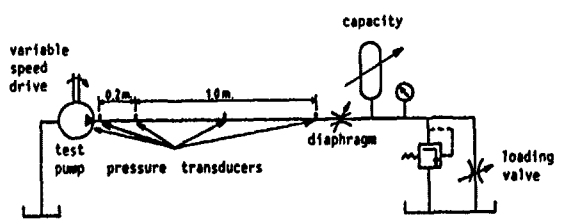

Fig.3 - Schematic diagram of the experimental set-up.

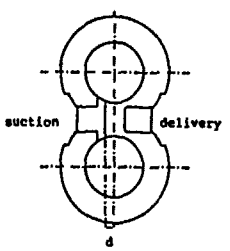

Fig.4 - Bearing blocks drawing.

The classic plane wave transmission equation, describing the form of the complex standing wave in the circuit and the pressure ripple at any point, can be considerably simplified if the circuit is so arranged that the pump is discharging into an acoustically reflectionless delivery line and the pressure ripple is measured close to the pump outlet.

Once the pump internal impedance and its ideal flow have been determined, such an anechoic system provides a useful means of knowing the pump flow ripple at entry to delivery line and the pump internal flow losses, simply by pressure ripple measurements [3].

A first qualitative evaluation of the achieved circuit reflectionless condition, main parameter for the accuracy of the results, was obtained adjusting the diaphragm with regard to the loading pressure and comparing the waveforms of the pressure signal at four different points of the delivery line (Fig.3). Transfer function measurements between two pressure

values at any two points of the line gave then the termination reflection coeffient. It allowed an easy evaluation of the termination impedance, its value coinciding with that of the line impedance, with no reflection at all.

A typical behaviour of the source impedance (Fig.5, bars) is very close to the theoretical one [4], showing an anti-resonance between 1 kHz and 2 kHz, meshing frequency being about 220 Hz, with a phase change from -90° to positive values. Fig.5 shows also the source impedance Zs behaviour (O) for this pump but with a piece of tooth cut off from one gear. A less compact pump geometry has as a consequence a shifting towards lower frequencies of the source impedance anti-resonance, what our results confirmed in agreement with the relevant phase behaviour. Pump ideal flow ripple (Fig.6) turns out from the sum, magnitude and phase, of the actual flow ripple and the internal flow losses.

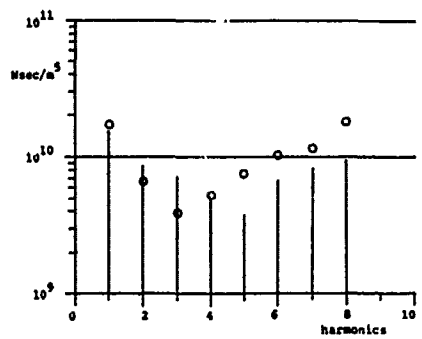

Fig.5 - Source impedance comparison.

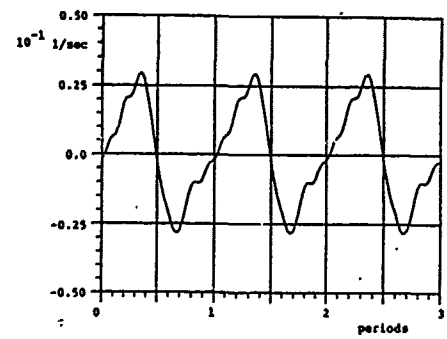

Fig.6 - Ideal flow ripple Qs.

A comparison (Fig.7) among the hydraulic noise characteristics for the pump with different couples of relief grooves shows that bearing blocks A increase the pump leakage flow Ql, without necessarily lowering the actual flow ripple Qe, measure of the pump fluidborne noise. The difference between the behaviours of the pump ideal flow rate Qs is due to the fact that they depend on both Qe and Ql and also on their phase opposition, better for relief grooves B.

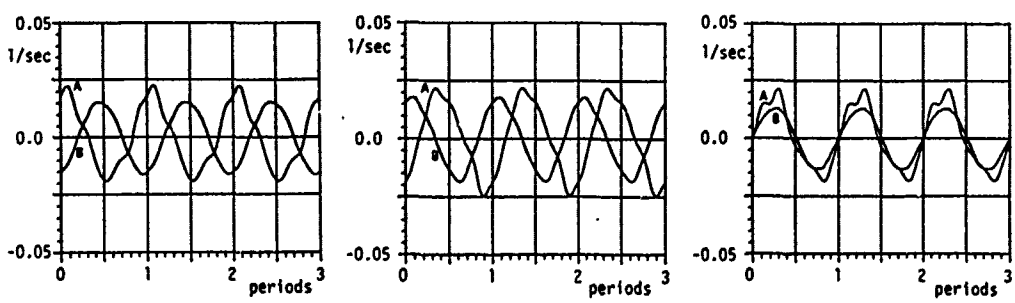

Fig.7 - Bearing blocks Ql, Qe, Qs flow ripples comparison.

Moreover, experimental data confirmed impedance meaning, a greater source value vs. harmonics pointing out a lower pump leakage flow. A value of airborne noise 3 dB(A) lower for grooves B, at test loading pressure, emphasized result accuracy.

Computer programs specialized to the experimental set-up here described and on purpose worked out provide estimates of the important flu-

idborne noise parameters, i.e. reflection factor, termination pressure value, sonic velocity, position of the actual maximum of the standing wave. They give whole system identification and allow comparison with the results obtained with the above test procedure. According to that, their application in order to characterize the fluidborne noise of a variable displacement axial piston pump located limits of the anechoic system actually used, the first being the high dissipation and pressure drop of the pipe of minor diameter [5].

For these reasons, for the sake of faster tests and more reliable results, the system optimization foresees measuring pump hydraulic noise and source impedance making use of only one line and improving computer programs in terms of system parameter sensitivity.

PUMP STRUCTURAL ANALYSES

Both experimental and theoretical techniques have been used to obtain a detailed description of the cyclic loads and forces acting on the stationary pump casing and rotating gears. Their knowledge, together with that of the overall dynamic equilibrium conditions, are prerequisite for the development of a general structural analysis of the external gear pump.

An experimental procedure with relevant computation steps has been carried out to describe the pump internal pressure behaviour and the consequent gear load distribution. A comprehensive representation of the pump casing stresses has been obtained with a 2-D finite element analysis, comparing the response to some reference pressure distributions with that for actual pump operating characteristics [6].

Procedures

A set of experimental data about the gear pump internal pressure history has been recorded with a piezoelectric transducer fixed inside the driving gear shaft and communicating with a tooth vane. That solution provides a knowledge of the pressure distribution not only on the casing inner surface but also inside the meshing zone and trapped volume. In such a way, the analysis of pressure loads on gears is exhaustive and a precise calculation of radial resultants on these possible.

For all different operating conditions, the pump had a pipe with anechoic termination as external load, such as that described above. The use of a reflectionless system is due to the fact that the analysis of the pump operating features must be carried out without introducing the effect of any external unwanted influences on the measured quantities.

Fig.8 shows a typical behaviour of the pump internal pressure ripple corresponding to a gear shaft revolution. In a vane between contiguous teeth, during fluid transfer from suction to delivery port, the pressure rises quickly from zero to delivery value. Fluid compression phenomenon for the trapped volume is represented with the maximum pressure peak corresponding to the two gear meshing angular positions. The following pressure drop occurs when trapped volume opens to suction.

The above actual pump operating features as input data allow the computation of radial load resultants on the gears.

Fig.9 is an example of the final output of the computer program on purpose worked out.

For the 2-D finite element analysis, the ANSYS code has been used. The non-linear contact between pump structure and bearing blocks has been simulated by means of a shaped rigid surface on the inner inlet side of the casing or with a finite element model of the bearing blocks, using 2-D interface elements. This second kind of solution gives a geometric configuration close as much as possible to the real one and allows to follow the deformation of the contacting surfaces.

Among the main results, the good analogy between very local stress concentration points, suggesting the possibility of fatigue crack propagation lines, and the actual fatigue failures of this type on some strain aged pumps.

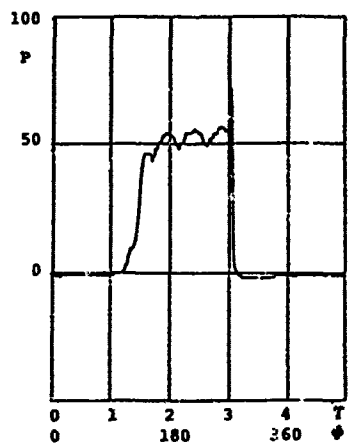

Fig.8 - Pump pressure time history. P[bar], T[0.01sec], φ[deg]. Shaft speed: 1500 rev/min. Loading pressure: 50 bar.

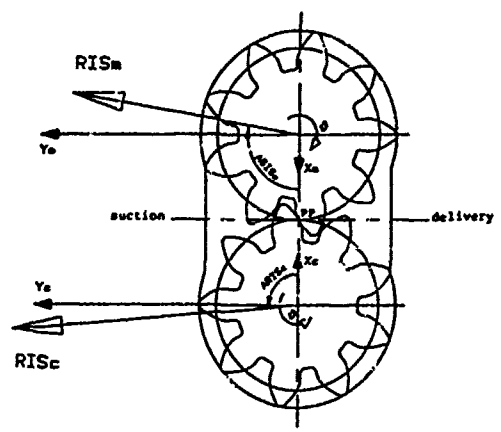

Fig.9 - Resultant forces on the gear shafts and angles. RISc,ARISc: driven gear. RISm, ARISm: driving gear.

Moreover, the radial resultant on the gear shaft, corresponding in our model to the reactions at the traslational constraints on the bearing blocks, is in very good agreement with that directly computed from the experimental results, when taking into account the absence of contact force between meshing teeth.
Fig 10 represents the pump stress behaviour using the real pressure distribution from experimental data and the finite element model of the bearing blocks. The error in both angle and magnitude evaluation is maintained within a few percent.

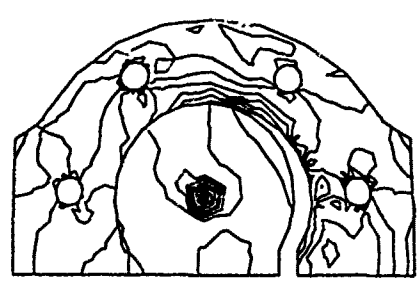

Fig.10 - Equivalent Von Mises stress distribution.Real pressure with bearing block FE model. Nine equally spaced contour lines.

CONCLUSIONS

Complementing the usual single title of merit (sound power) with multiple titles (intensity maps, gating spectra and vibration measurements) gives effective and precise ways of evaluating each design parameters in terms of minimum noise emission.

The test method for assessing fluidborne noise, being very sensitive to pump structural modifications, proved to be the basic tool for a noise optimization procedure and the achievement of the best trade-off between acoustic and functional performances.

Numeric simulation in order to evaluate the component quality at design stage together with experimental procedure allowed the computation of pump casing stress distribution, starting from pump internal pressure actual behaviour, with consequent possibility of structural modifications.

ACKNOWLEDGEMENTS

The authors wish to thank Mr.I.Vecchi and Dr.R.Paoluzzi for their helpful discussions and co-operation relevant to experimental measurements and finite element analysis.

REFERENCES

[1] Carletti E., Vecchi I.,"Acoustic Control of External Gear Pumps by Intensity Measuring Techniques", Noise Control Engineering Journal, 35(2), 1990, 53-59.

[2] Miccoli G., Bragion A.,"Gear Pump Fluidborne Noise by Source Flow and Impedance Evaluation", Noise-Con 88, West Lafayette, Indiana, 1988, 487-492.

[3] Fielding D., Taylor R., Martin M., Foster K.,"Notes on the Selection of a Standard Delivery Condition for the Theoretical Prediction and Experimental Measurement of Pressure Ripple", 5th Int. Fluid Power Symposium, Paper F1, Durham, England, 1978.

[4] Edge K.A., Johnston D.N.,"A New Method for Evaluating the Fluidborne Noise Characteristics of Positive Displacement Pumps", 7th Int. Fluid Power Symposium, Bath, England, 1986, 253-260.

[5] Miccoli G.,"Erkennen akustischer und funktioneller Leistungen von Pumpen durch Messen der Pumpenimpedanz", 10.Aachener Fluidtechnisches Kolloquium, 17-19 March, 1992, Aachen, Germany (to be published).

[6] Miccoli G., Paoluzzi R.,"Computer Aided Analysis of the Gear Pump Casing", 3rd Bath Int. Fluid Power Workshop, Bath, England, 1990, 205-226.

SECOND INTERNATIONAL CONGRESS ON
RECENT DEVELOPMENTS IN AIR- AND
STRUCTURE-BORNE SOUND AND VIBRATION
MARCH 4-6, 1992 AUBURN UNIVERSITY, USA

STATISTICAL ACOUSTICS THEORY APPLICATION FOR NOISE ANALYSIS IN TRANSPORT VEHICLES

Nickolay I.Ivanov, Georgiy M.Kurtsev
The Institute of Mechanics
Labour Safety and Environmental Protection
St. Petersburg, 198005
Russia

ABSTRACT

The authors suggest to use statistical acoustics theory for noise level predictions in vehicles (excavating machines, tractors, automobiles, loaders, moto-graders and so on).

Every vehicle is considered as a system of separate subsystems - noise sourcers, noise-protective constructions etc. The authors offers the schemes that include main designing units of the transport vehicles.

Equations being suggested allow to figure out the expected noise level of vehicles while the engineering stage. This method has been widely estimated in practice. Using this method the authors succeeded to attain much noise reduction for some vehicles. For example, noise in the cabs of wheeled vehicles has been reduced to 76 dBA, of loaders - to 77 dBA, of excavating machines - to 78 dBA, of automobiles - to 79 dBA.

This method provides several times cost saving through cutting the number of experiments because it allows to draw the task of noise of protective units into the draft designing stage. It also allows to lower the cost of noise protection facilities.

Statistical Theory has been widely used to estimate noise in Architectural Building Acoustics in the design of rooms and also with the solution of noise problems in residential areas. 1 The application of statistical theory, though being reasonably reliable for the vehicle design, is rather difficult to use because of the small volumes involved, where the sound fields are quasi-diffuse. Therefore we suggest the use of statistical acoustics theory for noise control in vehicles with several assumptions:

1. The sound field in the enclosed space (cabs, desel conpartments, and enclosures) is considered to be quasi-diffuse with the boundary frequency of : $f_B = 200 / \sqrt[3]{V}$

where - is the volume of the sound field in the space.

2. All of the numerous actual sound sources of complicated shape are considered to be reduced to five idealised ones:

- three-dimensional sound sources radiating sound in three dimensions ($a \geqslant \lambda$, $b \geqslant \lambda$, $c \geqslant \lambda$);
- plane sound sources ($a \geqslant \lambda$, $b \geqslant \lambda$)
- spherical sound sources ($D \geqslant \lambda$)
- linear sound sources ($a \geqslant \lambda$)
- point sound sources ($a \geqslant \lambda$),

where a,b,c are the characteristic dimensions of the sources, is the sound length wave.

3. Every noise protecting construction (sound isolating enclosures,cabs, acoustic shields and so on) and its components (holes, openings slots etc.) consists of a number of elemental secondary radiators, with point sound sources which are located throughout the whole area or length of the latter. The elementary sound radiators are considered to be non-coherent.

The whole variety of acoustical processes in vehicles are assumed to be reduced to the following typical estimation schemes:

- sound radiation of the enclosure components differently oriented with respect to the specified point (SP) located outside the enclosure;
- sound propagation to the cab from point, linear or tree-dimensional sound sources located outdoors under the condition of unequal sound waves distribution (attenuation) on the external cabin panels;
- sound propagation to the cab through inter-connected spaces;
- sound reflection from limited and unlimited surfaces;
-) sound penetration through a shield to a point located near the shield in the deep acoustical shadow area (with diffraction angles more than 90 grad.);
- sound radiation from the space source into free or enclosed areas with different locations of the specified point.

For the first case considered the sound intensity at the specified point depends on:

- the acoustic source power (W source);
- the factor of sound attemation from the three-dimensional source coursed by the enclosure (D enclosure);
- the average sound absorption coefficient ($\bar{\alpha}$ enclosure) being proportional to the absorption area (A enclosure);
- the location coefficient of plane the secondary sound sources (β enclosure);

- the sound conductivity of the enclosure elements (τ enclosure);
- the dimensions of the holes, slots and openings.

The intensity of the sound penetrating into the cab from a point source, located outdoors, is estimated with consideration of the following values: sound source power (W source), the distance between the cab and the sound source (R source), spatial location of the source (Ω source), A cab, the absorptive area if the cab, the cab dimensions, the cab enclosing area and their sound conductivity (τ cab) of the holes,slots and opening areas.

The intensity of the sound coming into the cab through its floor by reflection from the unlimited surface is determined with consideration of the source sound power (W source), the sound absorption coefficient (α surface), openings dimensions of the openings in the enclosure the height of the machine location above the reflective surface and absorptive τ .

The intensity of the sound penetrating through an acoustic shield (A Sh) in the deep acoustical shadow area is estimated by taking into account W source, the acoustic shield location in space (ΩA Sh), R A Sh, the distance between the shield and the specific point (d A Sh), the absorptive coefficient (α A Sh), of the area A Sh, linear dimensions of A Sh and the distance between ribs of the area A Sh and the specific point.

The analysis of the noise prediction was made for different vehicles. It was shown experimentally that the difference between the predicted and experimental data is - 3 dB in the frequency range of 50 - 8000 Hz for all the actual vehicles types (trucks, minibuses, excavators, tractors, cranes, mechanical loaders and so on).

The of theoretical and experimental results are given in TABLE 1:

Vehicle type	Sound pressure levels (dB) in the octave band with contey frequencies shown (Hz)							
	63	125	250	500	1000	2000	4000	8000
	85*	81	82	81	79	73	66	59
Minibus	103	96	86	84	80	74	65	59
Mechanical	84	84	86	82	79	75	68	64
loader	96	89	84	80	79	76	70	64
Tractor	86	90	88	84	79	76	72	69
	88	87	85	87	83	76	72	71

* Theoretical estimates are given top rows; experimental results are given in the bottom rows for each vehicle type.

Let us consider the sound peneration paths to the cab from the main vehicle noise sources (Fig. 1). As for the engine noise and that of the

cooling system fan, these sources being under the enclosure and having similar sound propagation pahts, the noise from these sources penetrates by the following three ways: through a the partition which separates the saloon cabin from the engine area; through an open enclosure apertures and, by reflections from the ground, through the saloon cabin's floor; through enclosure barriers and further through a saloon cabins panels with the exception of the partition and the floor. Exhaust noise,consi - dering the exhaust pipe location with respect to the saloon cabin, penetrates directly through the floor, underwhich it is located. The transmission noise penetrates to the cab through the floor enclosures. Noise from tires penetrates to the cab, diffraction loss accounted, through all the cab's panels with the exception of the partition. Results of airborne noise in the vehicle cab are presented in Table 2 and in Fig. 2.

Table 2.

Sound panitrating	Estimated sound pressure levels (dB), in the octave band center frequencies							
channels	63	125	250	500	1000	2000	4000	8000
from the engine	67.7	66.2	71.1	73.2	71.4	63.0	56.7	53.3
through the partition	63.1	60.6	69.4	71.5	70.7	61.1	55.3	52.6
through the floor	60.3	61.9	62.8	66.0	61.2	55.6	47.8	43.2
through the cab's pannels	64.5	61.6	63.7	64.5	57.1	55.4	47.9	40.8
from the fan	69.0	74.7	72.6	68.7	67.0	56.6	50.8	40.9
through the partition	63.1	67.1	69.7	64.7	65.7	53.1	48.1	39.2
through the floor	61.9	70.9	65.9	62.1	59.5	50.8	44.2	33.6
through the cab's pannels	66.5	70.9	67.1	61.0	55.8	51.1	44.7	81.7
from the gear box	64.6	66.8	61.6	63.1	63.6	65.0	58.6	49.1
from the exhaust	60.3	67.2	61.3	66.3	63.5	63.5	58.0	50.8
from the transmission	60.6	62.4	66.6	68.1	62.6	62.0	59.6	52.1
from tires	84.8	78.1	81.0	79.1	77.1	69.8	58.7	52.8
from all sources	85.1	80.9	82.2	80.9	79.0	72.9	65.6	59.0

Results of the method given applied to the noise estimation for some kinds of vehicles while the design stage and at the stage of experimen - tal testing are presented in Table 3.

Vehicle type	Sound levels, dB (A)	
	THE ORIGINAL STAGE	AFTER NOISE REDUSING MODIFICATIONS
Tractors	89	76
Loaders	85	77
Railway cleaning machines	95	78
Buses	86	79
Excavators	88	78

The considered method having been applied on the engineering stage, the noise level reduction by 8 - 17 dbA was successfully achieved.

REFERENCES

1. Снижение шума в зданиях и жилых районах (Г.Л.Осипов, Е.Я.Юдин, Г.Хюбнер и др.; Под ред. Г.Л.Осипова, Е.Я.Юдина) М: Стройиздат, 1987 - 558 с.
2. Иванов Н.И. Борьба с шумом и вибрациями на путевых и строительных машинах.- М: "Транспорт", 1987 - 223 с.
3. Ivanov,N. Kurtsev,G. The Theory and Practice of Construction and Transport Machine Noise Reduction / Unikeller Conference 89 - 4 p.

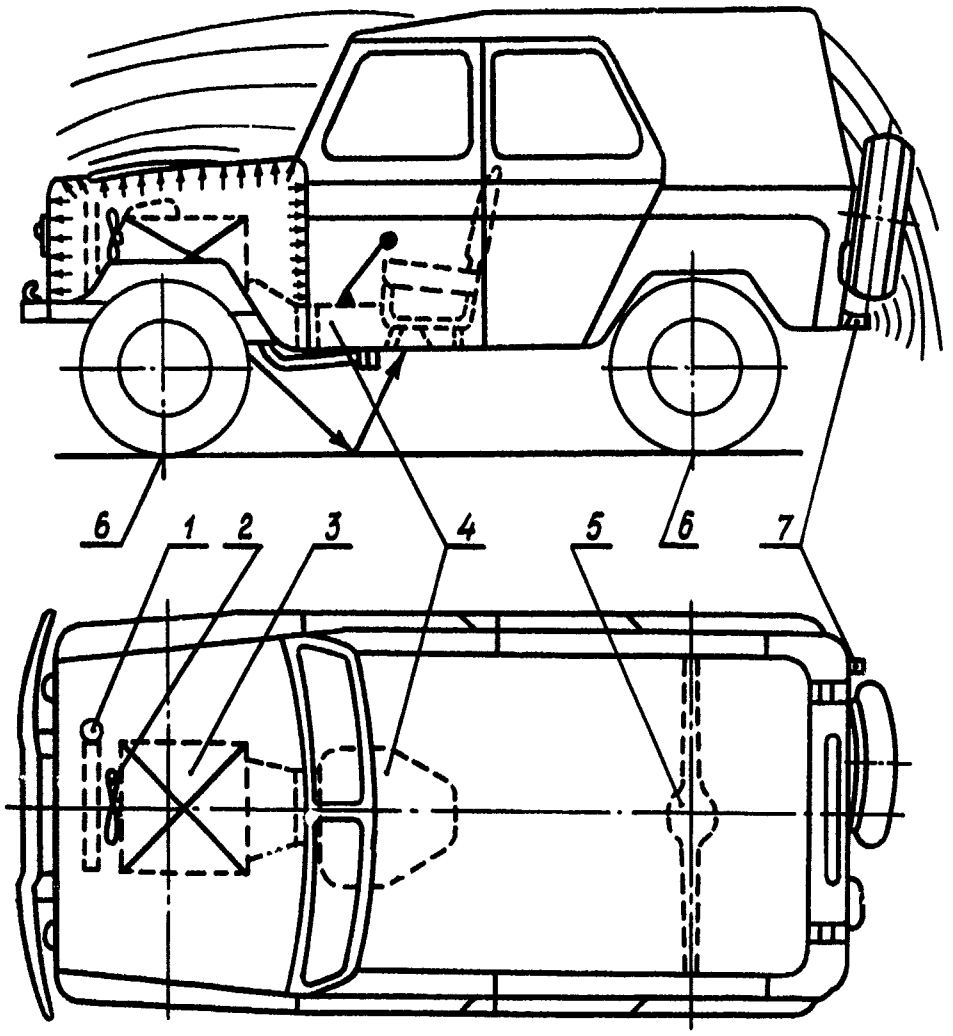

Figure 1— The Scheme of Acoustic Estimation for Vehicles.
1 - the ICE inlet; 2 - the cooling fan; 3 - the ICE coat;
4 - the gear box; 5 - the rear axle; 6 - tires; 7 - the ICE outlet.

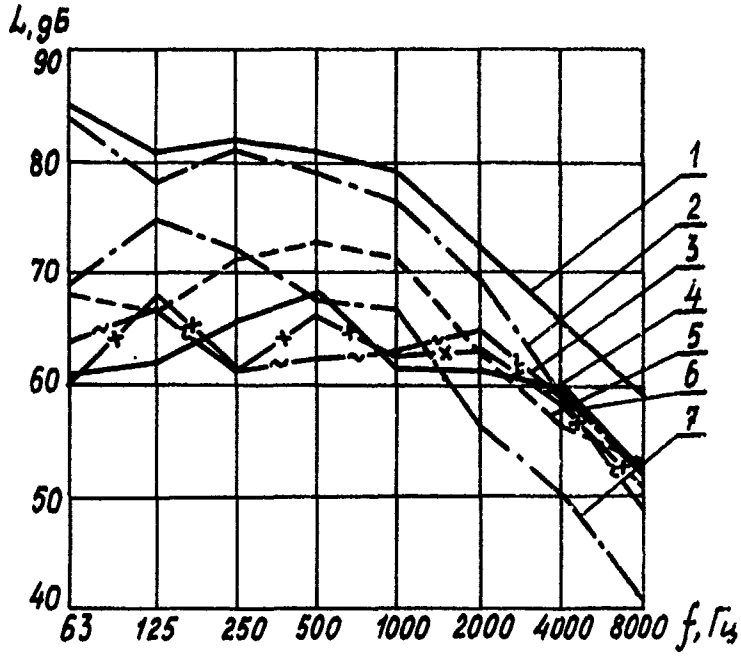

Figure 2 - - Noise estimation spectra of the vehicle cab.
1 - the total noise spectrum; 2 - the noise spectrum of tires; 3 - the noise spectrum of the gear box; 4 - the same of the exhaust; 5 - the same of the engine; 6 - the same of transmission; 7 - the same of the fan system.

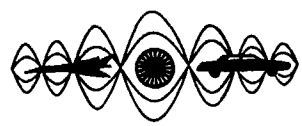

SECOND INTERNATIONAL CONGRESS ON RECENT DEVELOPMENTS IN AIR- AND STRUCTURE-BORNE SOUND AND VIBRATION
MARCH 4-6, 1992 AUBURN UNIVERSITY, USA

AUTOMATED SYSTEM FOR CALCULATING OF LIMIT ADMISSIBLE NOISE CHARACTERISTICS OF INDUSTRIAL EQUIPMENT

I.E.Tsukernikov, B.A.Seliverstov
Scientific and Industry Amalgamation "Mir"
Moscow
USSR

The composition and the possibilities of the automated system for calculating limit admissible noise characteristics (LANCh) of equipment both having been in operation already and subjected to development are described. As a basis a method of energetic composition of sound signals has been assumed. The limit admissible values of the sound power of the noise sources are being determined by means of the solution of reverse acoustic problem. The system also comprises optimization of found LANCh values, calculation of the noise chart in the room, option of the rational position of a working place and owing to it the raising LANCh values of equipment. The example of using the system for the determination of LANCh of curds production shop equipment has been given.

A limit admissible noise characteristic (LANCh) of a machine is those values of its noise characteristic (levels of sound power in octave frequency bands) which ensures the fulfilment of the noise norms at working places under typical operation conditions [1].

Preliminary calculating of the LANCh (before detailed development of a machine) makes it possible to put in noise claims corresponding to the technical level and, if it is necessary, to provide noise reduction in the process of a machine development and construction.

The method of the LANCh calculating determined by the USSR Standard [1] was worked out for conditions of even distribution of the same type equipment (equipment with approximately equal sound power level) in a production area. In a case when different types of equipment work in a production area a reverse acoustic problem should be solved: to calculate admissible values P^{ad} of sound power according to the predetermined standard values of sound intensity $I_{ad} = 10^{0.1(L_{ad} - 120)}$ (L_{ad} is the noise norm, dB, in octave frequency band) taking into account a definite order of sound sources and working places location in an industrial area [2, 3].

The problem is brought to the system of linear algebraic equations

$$\sum_{i=1}^{n} a_{ji} P_i^{ad} = I_{ad}, \quad j = 1, 2, \ldots, n_p, \tag{1}$$

where n is the number of simultaneously working sound sources; n_w is the number of working places; a_{ji} are elements of the system matrix consisting of two components:

$$a_{ji} = a_{ji}^{(dir)} + a_{ji}^{(ref)} \tag{2}$$

the first of them describes the contribution of direct sound radiated by sound source number i at working place number j, the second – the corresponding contribution of the reflected sound. Expressions for the components in Eq.(2) take into account location of the sound sources relatively to the working places and acoustic characteristics of the room and are determined by adopted model of sound spreading in the room (upon energy approach they are given in the reference book [4]).

If the information about real values of the noise characteristics of sound sources is available, the from system (1) calculated values of the P^{ad} can be optimized. For operating equipment such an information is given in the rate and technical documentation. As for the equipment under development and construction the data of noise characteristics of prototype machines may be used. An idea and procedures of optimization are given in the work [5].

If the location of working place has not been fixed due to the necessity of maintenance of the equipment, a possibility to choose an appropriate location for it in the room is available to provide maximum LANCh of the machines. An algorithm to realise such a possibility is described in the work [6].

In accordance with the above-described approach an automated system "PDHX" was developed. It includes the following computering procedures:

– calculation of limit admissible sound power levels of noise sources at the moment they are all simultaneously working, with taking into account the disposition of noise sources and working places location in an industrial area;

– optimization of the obtained LANCh values with taking into account real sound power levels of noise sources;

– calculation of sound levels in room (noise charts) and choosing of a rational position of a working place where the LANCh of the most noisy equipment have maximum values.

An enlarged block-diagram of the calculation algorithm is given in Fig. 1.

The system was realized using a personal computer IBM PC/XT/AT and an electronic computer CMriad 2.

As an example, let us consider calculation of LANCh of equipment for production of curds (cottage cheese). The composition, disposition of the equipment and the location of the working place are indicated in Fig. 2.

Table 1 shows the calculated values of the LANCh L_{pi}^{ad} in comparison with the real (measured [7]) sound power levels L_{pi}^{r} of the equipment in the octave band with the geometric mean frequency f_m = 250 Hz.

Seven sources of 15 are considered to be weak ($L_{pi}^{ad} > L_{pi}^{r}$). The numbers of thouse sources are 1–4 and 10–12. By lowering of their LANCh to the L_{pi}^{r} the LANCh of the rest powerful sources 5–9 and 13–15, for which the L_{pi}^{ad} was obtained less than L_{pi}^{r}, can be increased.

A successive procedure of optimization [5] makes it possible to increase to the required level the LANCh of the seven the powerful sources. It is impossible to reach the real value of sound power for the 15-th the most powerful source. It can not be done even in the case when all existing reserve of the sound power are used (L_{p15}^{ad} still is 4.7 dB less than L_{p15}^{r}).

Table 1 – – Comparising the LANCh and real sound power values in octave band with f_m = 250 Hz.

i	1	2	3	4	5	6	7	8	9	10	11	12	13	14	15
L_{pi}^{ad}, dB	82	81	81	80	81	82	82	82	82	82	82	82	82	82	82
L_{pi}^{r}, dB	78	78	79	72	82	84	83	86	84	72	78	78	83	84	94
Δ, dB	4	3	2	8	–1	–2	–1	–4	–2	10	4	4	–1	–2	–12

Transfering of the control station to the region with the lowerest value of sound level (Fig. 2) resulted in increasing of the LANCh from 1 to 4 dB (depending on the octave band) of the nearest to the working place sound sources 4 and 5. The LANCh of the distant sources practically did not change. Low results are connected with a great portion of reflected sound in the shop because of its small dimensions (14.5x14.0x6.0 m) and high reflecting

abilities of the surrounding surfaces. The biggest difference in the values of sound levels in the rated points was only 3 dB. It was possible to draw only five isolines with the step 0.5 dB over all space of the room (solid lines in Fig. 2). Also weak effect of optimization of the LANCh in octave bands with geometric mean frequences 500–2.000 Hz may be explained by poor acoustic characteristics of the room.

Repeated calculations under free sound field conditions (component a_{jj} in Eg.(2) is equated to zero) resulted in increasing of the LANCh by 2-5 dB for the nearest and 6-13 dB for the distant from the working place sound sources. Considerable changes in distribution of sound levels in the room took place (see the chart of sound levels in Fig. 2, dashed lines). Difference in sound levels (and sound pressure levels) was 17.8 dB. Transfer of the working place to the point with the lowerest sound level made it possible to increase the LANCh of the equipment by 12-13 dB for the sources 4 and 5 and by 2-7 dB for the rest of the sources. As a result it became possible to increase the LANCh values up to the real ones over all standardized frequency band.

The calculation proves potential effectiveness of rational choosing of the location for a working place. As far as the above-mentioned shop is concerned the necessity to cover the walls and ceiling by a sound absorbing lagging is evident. It will help considerably to decrease noise at a working place, increase equipment LANCh levels, extend abilities of their optimizing, and decrease expenditures for lowering of the acoustic activity of machines.

CONCLUSIONS

1. The system "PDHX" makes it possible to carry out optimum rationing of the noise characteristics of machines taking into account typical operation conditions. It may be considered as an element of an acoustic automated design system of industrial objects and machine building industry products used for acoustic calculations in the process of development of new equipment (machines, lines, complexes) and design of shops for industrial enterprises.

2. Application of the system on the stage of preparation of requests for a proposal makes it possible to formulate the requirements for the noise characteristics of an article under development and simultaneously with development and construction to carry out acoustic design to meet the noise requirements. A numerical experiment to determine influence of the reflected sound allowes to establish the values of noise characteristics of machines in an optimum way and to work out reasonable requirements for acoustic characteristics of rooms.

3. Application of the above-mentioned system when designing industrial areas makes it possible to choose a rational version of equipment disposition and working place location as well as to determine the requirements for noise characteristics of machines and acoustic characteristics of room to insure the fulfilment of the noise norms at working places.

REFERENCES

1. System of Standards of Labour Sofety. Noise. Methods of determining sound characteristics of stationary equipment.– GOST 12.1.023–80, Moscow, Standards publication, 1980.– 7 pages (in Russian).
2. Katsnelson M.U., Tsukernikov I.E., Segal M.E. The method of determining limit admissible noise characteristics taking into account location of the equipment in an industrial area. – Collected articles "Noise and sound vibration control", Moscow, Moscow House of Scientific and TechnicalPropaganda named after F.E. Dzerzhinsky, 1986, p. 31–36 (in Russian).
3. Tsukernikov I.E., Seliverstov B.A., Shechkova M.S. Determining of limit admissible noise characteristics of a group of machines of various types. – Acoustic ecology–90, Leningrad, Documents of the scientific and methodical conference, part 2, 1990, p. 74 – 75 (in Russian).
4. Noise control at an industrial enterprise: reference book /edited by E.J.Judin – Moscow, Mashinostroenie, 1985. – 400 pages (in Russian).
5. Tsukernikov I.E., Seliverstov B.A., Vesnina M.N. Optimization of limit admissible noise characteristics of industrial equipment. – Collected articles "Noise and sound vibration control", Moscow, Moscow House of Knowledges, 1991 (to appear).
6. Tsukernikov I.E., Seliverstov B.A. Influence of a working place location and acoustic characteristics on admissible values of noise characteristics of equipment and possibilities of their optimization. – Collected articles "Noise and sound vibration control", Moscow, Moscow House of Knowledges, 1991 (to appear).
7. Katsnelson M.U., Seliverstov B.A., Tsukernikov I.E. Noise control of food industry machines. – Moscow, Agropromizdat, 1986. – 256 pages (in Russian).

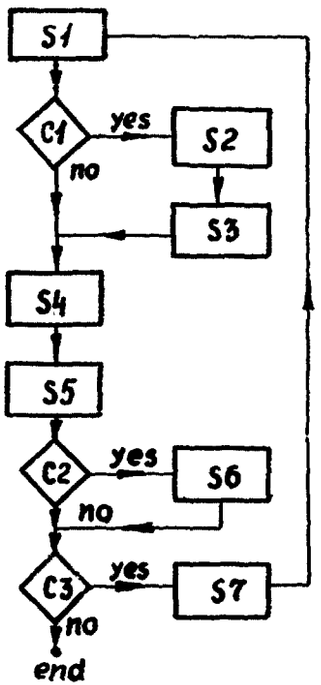

Figure 1-- Block-diagram of the calculation algorithm
S_1 — block of calculating coefficients $a_{ji}^{(dir)}$; S_2 — block of calculating acoustic characteristics of the room; S_3 — block of calculating coefficients $a_{ji}^{(ref)}$; S_4 — block of calculating coefficients a_{ji} and free members of the system; S_5 — block of calculating P_i^{ad} and L_{pi}; S_6 — block of optimization of the LANCh values; S_7 — block of selecting the rational location of a working place; C_1 — condition determining the necessity to take into account contribution of the reflected sound; C_2 and C_3 — conditions determining possibility of optimization and changing the location of the working place.

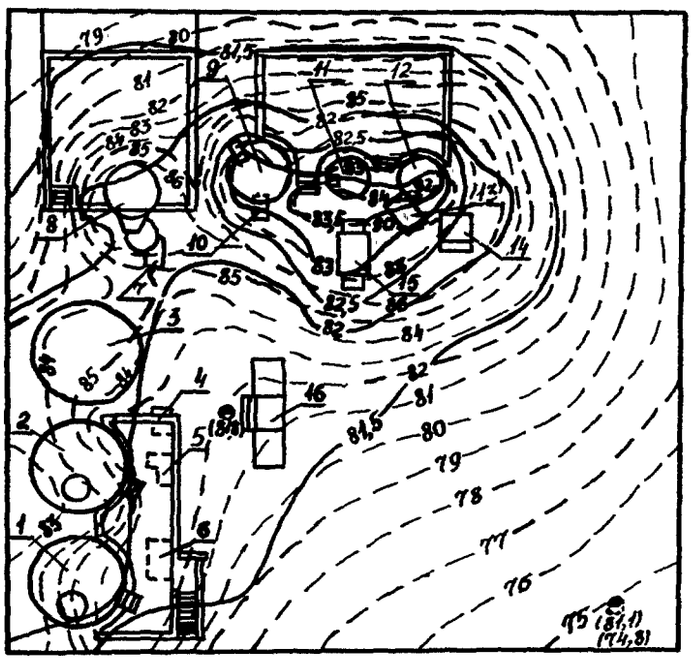

Figure 2 -- Scheme of disposition of equipment in a curds production shop
1, 2 — aseptic reservoir Б6—ОКМ/1; 4, 10 — pump 36—3Ц—3.5—10; 5 — pump П8—ОНБ; 6, 14 — pump 50—3Ц—7,1—20; 7, 13 — pump П8—ОНД; 8 — separator А1—ОДБ/3; 9 — pool for cream Б6—ОДБ/10; 11, 12 — reservoir for curds Б6—ОДБ/6; 15 — mixer Б6—ОДБ/5; 16 — control desk; ⊕, ⊕ — initial and rational location of the working place.

SECOND INTERNATIONAL CONGRESS ON
RECENT DEVELOPMENTS IN AIR- AND
STRUCTURE-BORNE SOUND AND VIBRATION
MARCH 4-6, 1992 AUBURN UNIVERSITY, USA

CALCULATION OF NOISE REDUCTION PROVIDED BY FLEXIBLE SCREENS (BARRIERS) FOR PRINTING MACHINES

Boris I. Klimov, Natalia V. Sizova
Reliability & Dynamics Department
Scientific - Research Institute
of Printing Machinery
Moscow

ABSTRACT

Flexible barriers considered in this paper were designed to provide an effective noise isolation while allowing fast access to printing machine's engine parts. The flexible barrier itself consists of a set of linear thin rigid plates joined together lengthwise into a chain. The theoretical model for calculation of the noise reduction provided by these screens, the calculation method and the experimental data are represented in this paper.

INTRODUCTION

Until now two kinds of sound protection barriers were widely applying for most printing machines. One of them is the hermetic rigid massive case, the second is the barrier with the technological openings for handling. But it is difficult to use such kinds of barriers for mechanisms which suppose to have the fast access to them. Flexible barriers were designed to provide an effective noise isolation while allowing fast access to engine parts (fig. 1a). There are flexible barriers made from fabric which used, for example, for marine's Diesel engines, but these screens are too unstable and unreliable.

The flexible barrier described below consists of a set of linear thin rigid plates joined together lengthwise into a chain (fig. 1b, c). These barriers can be mounted on variety of mechanism's shapes and also in passage ways between machine's sections.

The purpose of work was to develop a method of calculations of the noise reduction provided by different designs of flexible screens.

This method allows a choice of the design when developing.

APPROXIMATE ANALYTICAL SOLUTION

This calculation were made for barriers with the following characteristics /1/:
- small sizes of barriers - less than 1 m,
- proximity to noise source (engine) - about 0.5 m,
- remote destination (personnel) - more than 2 - 3 m,
- noise bandwidth - 63 - 8000 Hz.

The model selected is one plane containing a set of linear rectangular plates placed side-by-side, separated by narrow spaces. All plates are making flexural oscillations under the influence of evenly distributed noise pressure.

This model allows to determine parameters which are necessary to reach the best noise reduction.

It is assumed that:
- there is no vibration energy transmission from one plate to another,
- joint coupling considered as an acoustically small opening, i.e. their sizes are less than the wave length,
- plate's edges are supported,
- vibration plates phases are random.

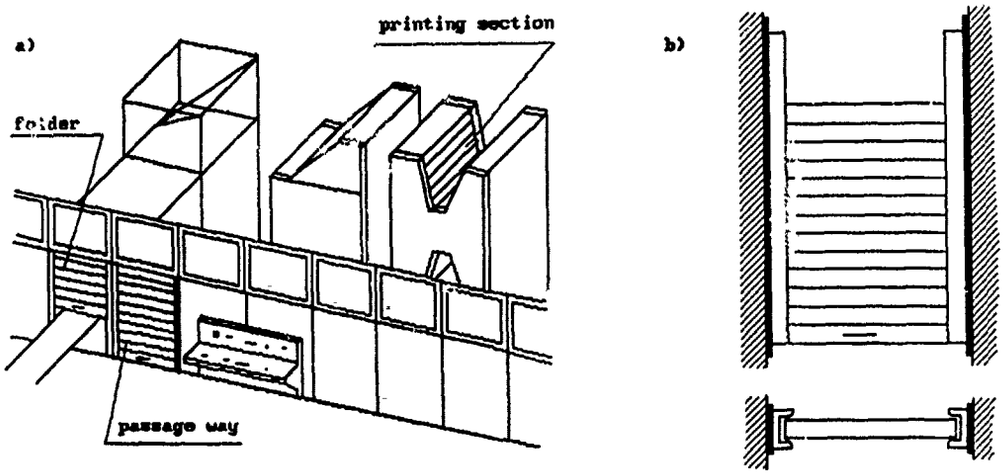

Figure 1 -- The flexible barriers for printing machines:
a) sample of placement; b) front view; c) top view.

The noise reduction was calculated as the difference between the sound pressure level at the remote point (working place) and the pressure level near to machine's engine part (inside the case).

Since the fundamental sound field equations are linear /2/, the system's sound pressure is equal to the sum of sound pressures of each source. So the total sound pressure on the central line of the system Pfb is the sum of pressures of plates and holes:

$$Pfb = \sum P + \sum Ph = k1\ (q\ P + (q - 1)\ Ph) \qquad (1),$$

where P is the sound pressure emitted by the single plate on the central line of the system, Ph is the sound pressure generated by the single hole on the central line of the system, k1 is the random phase summation coefficient, q is the number of plates.

The calculation of the noise reduction provided by the barrier (in far field) was based on the single finite plate sound pressure derivation using Huygens - Rayleigh integral /3/:

$$p = \frac{jk\rho_0 c_0}{2\pi} \int v\, d\sigma\, \frac{e^{-jkr}}{r} \qquad (2),$$

where p is the sound pressure generated by single plate, v is velocity, $d\sigma$ is the surface element, r is the distance from the surface element to the distant destination point, ρ is the air tightness, c_0 is the sound propagation speed in the air, k is the wave number, and the equation for the sound pressure determination can be written as:

$$|P| = \left| \frac{k\rho_0 c_0}{2\pi r_0}\ Vxy\ Svx\ Svy \right| \qquad (3),$$

where r_0 is the distance from the central plate to the distant destination point, Vxy is the velocity amplitude, Svx, Svy are the Fourier spectrums of the velocity distribution on the plate's surface.

The resultant pressure can be obtained by summation of the contributions of all vibration modes:

$$P = \frac{k \rho_0 c_0}{2\pi r_0} \sum_{m=1}^{\infty} \sum_{n=1}^{\infty} Vxy\ Svx\ Svy \qquad (4),$$

where m, n are numbers of vibration modes.

If the center of the plate is a point of maximal velocity, the highest possible value of velocity spectrum on the center line of the plate is equal to:

$$Svy_{max} = \frac{4\ l_1 l_2}{\pi^2\ m\ n} \qquad (5),$$

where l_1, l_2 are plate dimensions.

The sound pressure can be derived using the definition of "impedance" on the resonance frequency ω_{mn} with the loss factor η. The total sound pressure in the i-th frequency band is equal to:

$$P = \sum_{m=1}^{\infty} \sum_{n=1}^{\infty} \frac{8\ k \rho_0 c_0\ S\ Pk}{\pi r_0\ (16\ \rho_0 c_0 + \pi^2\ mn\ \rho\ h\ \omega_{mn}\ \eta_i)\ N_i} \qquad (6),$$

where N_i is the number of resonance frequencies, m, n are mode numbers, m = 1, 3, 5.., n = 1, 3, 5.., η_i is the loss factor, $S = l_1\ l_2$ is the plate area, ρ is the plate density, Pk is the applied sound pressure, ω_{mn} is the resonance frequency, h is the plate thickness. This is the expression for 2 - dimension oscillating plate. For 1 - dimension oscillation plate this expression can be written as:

$$P = \sum_{m=1}^{\infty} \frac{2\ k \rho_0 c_0\ S\ Pk}{\pi r_0\ (\ 4\ \rho_0 c_0 + \pi\ m\ \rho\ h\ \omega_m\ \eta_i)\ N_i} \qquad (7),$$

When the noise is passing through the acoustically small opening, the sound pressure in the remote point also may be obtained by using Rayleigh integral:

$$Ph = \frac{Pk}{r} \sqrt{\tau}\ \sqrt{\frac{\sigma}{4\pi}} \qquad (8),$$

where σ is the hole area, τ is the passing ratio (coefficient), r is the distance from the central hole to the distant destination point.

The analysis of the influence of different construction parameters to the noise reduction value was based on this theoretical model. The main difficulty in the definition of noise reduction was the determination of the flexible screen's loss factor. It was derived during the experiment.

THE EXPERIMENTAL DERIVATION OF THE LOSS FACTOR OF THE FLEXIBLE SCREEN

The loss factor was changing as function of thickness, width and material of plates, number of plates, dimension of a gasket. The total area of the prototype to be tested was keeping constant, was selected 550 x 450 mm. The plates thickness was changing from 1 mm to 5 mm, the number of plates was changing from 1 to 25, so their width was changing from 450 mm to 18 mm. Experiments were preformed on the specially designed prototypes where the edges of plates were fastened between two massive frames.

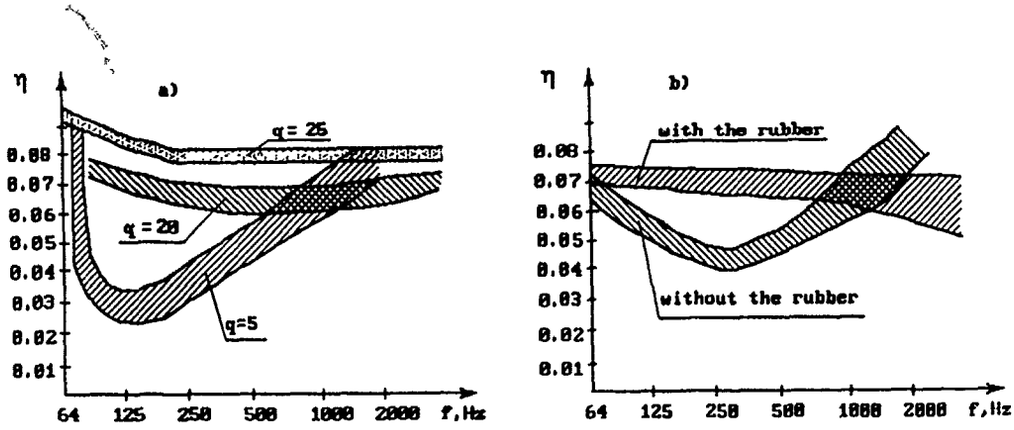

Fugure 2 -- The frequency response of the flexible barriers loss factor: a) sets having q plates; b) the set of 20 plastic plates.

Experimental data shows that boundary conditions makes the considerable influence to thin plates vibration at low modes. At frequencies higher than 4000 Hz the loss factor depends on the internal friction and almost independent on the plates thicknesses.

The loss factor of the different material plates sets is in range 0.03 - 0.12 (fig. 2). The loss factor of acrylic plastic prototypes has a more smooth functional dependence on the frequency as compare to metallic plates. Increasing of the number of plates leads to increasing of the loss factor in whole frequency band (fig. 2a). The dispersion of the results of measurements is rising in the high frequency band. When a rubber strap was located between the metallic plates loss factor was increased in the low frequency band (fig. 2b). When the rubber strap was located between the plastic plates the loss factor was increasing in average for 0.04 in whole band.

NOISE REDUCTION MEASUREMENTS OF FLEXIBLE BARRIERS

Tests were performed with sets having the different materials, thicknesses, number of plates, hole dimensions, strap diameters. The comparison of the theoretical and experimental data shows that the method described allows to obtain accurate enough results in given frequency range. Steel plates thickness changing does not influence to the noise reduction in the high frequency band. Metal plates sets have a highest noise reduction, which is equal to the isotropic plate's noise reduction in the high frequency band. In the middle frequency band the noise reduction of metal plates sets is more than the isotropic plates noise reduction on 3 - 5 dB.

Just as we had expected after theoretical calculation 3 - 7 plates sets have the best acoustical characteristics for this prototype's total area. The minimum of noise reduction is provided by 20 - 25 plates sets for this prototype area. The noise reduction of such sets is less than isotropic plate noise reduction in all frequency range.

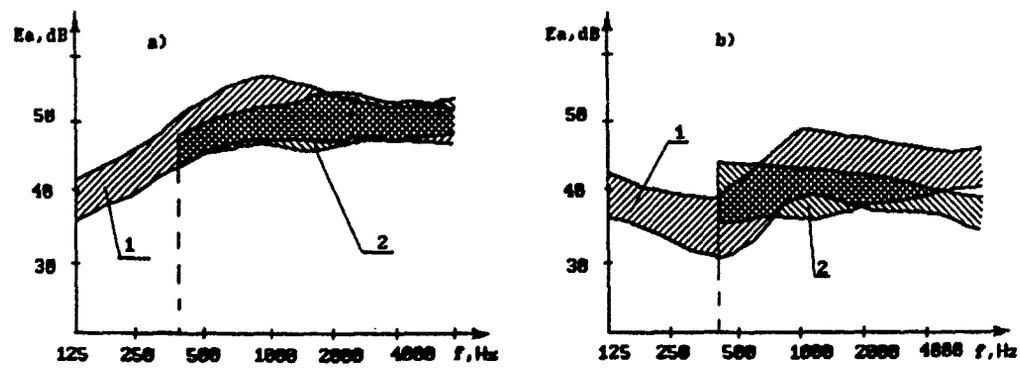

Fugure 3 -- The frequency response of the noise reduction of sets of steel plates: a) 10 plates without the hole and strap; b) 20 plates with the rubber strap (diameter 3 mm).
1- calculation results; 2- experimental results.

Experimental results are matching good with calculations performed (fig. 3a). The difference is not more than 3 dB both for wide (more than 112 mm) and narrow (less than 45 mm) plates. The difference between the theoretical and experimental data is reaching 8 - 12 dB for plates sets, having width of each plate 45 - 112 mm. Results described was obtained both for metallic and plastic plates. The presence of junctions reduces the noise reduction for 5 dB. This fact also is in a good matching with the theoretical results.

Placement of rubber strap between the metal plates leads to some falling of acoustical characteristics as compare to ones of the set without hole and rubber. Instead, the placement of rubber strap between plastic plates leads to the improvement of acoustical characteristics in whole frequency band. In this case the difference between theoretical and experimental data is too small even for 5 - 7 plates sets (fig. 3b).

APPLICATION

This theoretical model and method of calculations allow to determine the noise reduction of various designs of the flexible screen. The calculations of certain constructions based on this method were performed to determinate optimal parameters of the barriers with the given sizes and flexibility. The dependence of the noise reduction on number of plates, their thickness, rubber thickness and frequency range was found.

This method was used for designing a variety of flexible noise reducing barriers for printing machines. It also can be used for any other machines corresponding to described limitations of sizes and noise bandwidth.

REFERENCES

1. Б. И. Климов, Н.В. Сизова, Расчет акустической эффективности гибких ограждений полиграфических машин, Львов, УПИ, 1991.
2. J. W. Raleigh, The Theory of Sound, Macmillan and Co., Ltd., London, 1894, 1000 p.
3. E. J. Skudrzyk, Simple and Complex Vibratory Systems, The Pennsylvania State University Press University Park and London, 1968, 514 p.

SECOND INTERNATIONAL CONGRESS ON
RECENT DEVELOPMENTS IN AIR- AND
STRUCTURE-BORNE SOUND AND VIBRATION
MARCH 4-6, 1992 AUBURN UNIVERSITY, USA

ECONOMIC EVALUATION OF INDUSTRIAL NOISE SILENCER

OLGA A.AFONINA AND NATALYA V.DALMATOVA
ECONOMICAL DEPARTMENT
MOSCOW AVIATION INSTITUTE
MOSCOW, USSR

ABSTRACT

The object of this paper is to provide a method of cost-benefit analysis for the implanation of protection measures against industrial noise.

Protection measures against noise in national economy are aimed at achieving social effects in preserving the workers' health and qualification, creation of favourable environment, lowering the rate of traumas, illnesses and drift of man power as a result of unfavourable working.

Measures taken against noise give not only social but economic gains as well, resulting in higher labour efficiency, reduction of prime cost and greater profits.

This paper is based on the research work of O.A.Afonina and engineer N.V.Dalmatova at the Moscow Aviation Institute (MAI) under the supervision of Professor, Candidate of Science (economics) Afonina O.A.

INTRODUCTION

When the method of economic evaluation of industrial noise silencers become a realistic possibility, the loss of value in our society from industrial noise can be considerably reduced.

The data presented by the Ministry of Health show that almost 1.8 million people including 180.000 woman have been working under conditions exceeding the normal noise level; 495.000 people including 394.000 woman were subjected to excessive vibration. According to the registered morbidity data most frequent illnesses are caused by physical factors (illness due to vibration 21.6%, aural neuritis - 8.7%).

The approximate values of specific economic losses caused by vibration affecting one worker in machine building industry reach 10.500 roubles, whereas impaired hearing results in 10.000 losses.

Expected costs inus expected benefits give the expected value of social and economic effects for each year. The life and health component and rouble component of the net result are kept separate throughout the evaluation.

These figures show that a method of social and economic evaluation of industrial noise silencers is of utmost importance.

ECONOMIC EVALUATION OF JET NOISE SILENCERS

Being an externally isolated disjoined constructive part of industrial buildings, jet noise silencers have a specially designed objective and are independent operating structures.

Among such conceptions as means of labour, objects of labour and labour itself, noise silencers represent means of labour which determine the physical conditions of the industrial process and increase the efficiency of production.

Depending on the function and terms of operation jet noise silencers are the major effective means of the enterprise and therefore require capital investments.

The reproduction of noise silencers is accomplished as the reproduction of the main funds, as the process of capital construction and principal investments. Consequently the implementation of noise silencers should be planned and properly financed.

Cost accounting should be carried out for the noise silencer itself, for its operation, its effective use over the whole cycle of technical, economic and social indices which include the preservation of the worker's life, his health and qualification the lowering of trauma and illnesses rate as well as the drift of man power as a result of bad working conditions.

The social aspect of efficiency is closely connected with economical effectiveness of noise silencers application which can be quantitatively estimated.

Noise silencers being elements of modern engineering comprise part of the major active means of labour, for they are constantly updated, renovated and advancing at a rapid rate. Hence their essential likeness to machines and equipment.

Noise silencers are expensive structuren, for example, the expenditures at test stations amount to 45 - 50% of their general cost.

Noise silencers have their individual functions, definite service life, specific ways of mounting which must be done by special organizations.

They are by no means passive, taking an active part in the industrial process, affecting the efficiency of labour, the volume of production, lowering its prime cost and improving its quality.

The order and formulas of calculation

The order of calculating social and economic effectiveness is as follows:

- Formulation of a particular problem for industrial noise reduction and vibration.
- Definition of social factors.
- Determination of capital investments.
- Calculation of current expenses for a year.
- Calculation of economic effects resulting from the implementation of noise protection measures.
- Calculation of the level of economic effectiveness as a ratio of economic effects with respet to capital investments.

The following formulas may be suggested for calculating social and economic effects due to the reduction of industrial noise and vibration.

Yearly economic efficiency of production costs due to preventing industrial traumas (ϑ_{tr}) is the following.

$$\vartheta_{tr} = 1,5\ D\ W, \qquad (1)$$

where D - losses of working time because of traumas and loss of capacity for work for a day, for more days for the current year, in roubles;
W - an average daily wage of one worker, in roubles.

Yearly economical efficiency of production costs due to illnesses (ϑ_{ill}) created by unfavourable working conditions is

$$\vartheta_{ill.} = 0.25(L_v - L_p), \qquad (2)$$

where L_v, L_p - value of economic losses due to general incapacity for work, virtual and planned in roubles.

Yearly economical efficiency due to the reduction of production costs created by decreasing drift (Θ_d) of man power is

$$\Theta_{d.} = 8000\ N, \tag{3}$$

where 8000 is the average value of losses due to one worker drifting a year, in roubles;
N - the number of workers drifting due to unfavourable working conditions (industrial noise and vibration) expressed in number of men.

Yearly economical efficiency of the wage (Θ_w) fund due to the reduction of leave terms of abolishing leaves is

$$\Theta_{w.} = W\ (\Sigma 4_v D_v - \Sigma 4_p D_p), \tag{4}$$

where W - the average wage of one work a day, in roubles;
4_v, 4_p - the number of workers having additional leave due to higher noise and vibration level, virtual and planned, expressed in number of men;
D_v, D_p - the average duration of an additional leave for one worker having the right for it due to noise and vibration, virtual and planned, in days.

Analogous formulas can be suggested to determine the yearly economical efficiency as a result of payment reduction for compensation because of the decrease or annulment of higher tariff scale and shorter working day.

Expected economic losses due to professional illnesses (L) of special character

$$L_{ec} = L'\ \ N' \tag{5}$$

where L' - is specific professional losses due to certain illnesses depending on the type of production, in roubles;
N' - is the number of workers suffering from these professional illnesses - expressed in number of men.

Yearly economical efficiency of production costs due to fewer workers requiring training for a new profession because of noise and vibration, expressed in number of men.

$$\Theta_{pr} = Q_c\ \ 4_c, \tag{6}$$

where Q_c - an average costs for new professional training, in roubles;
4_c - the number of workers willing to acquire a new profession, expressed in men.

There are many other formulas for calculating social and economic effects. Global social and economic effects (expected economic losses) may be determined as a sum of above-mentioned indices.

CONCLUSIONS

The major conclusion is that the authors recommend to follow the sequence and method of calculation of social and economic effectiveness according to the suggested formulas as they have been checked up in practical work.

REFERENCES

1 Afonina O.A. Social and Economic Efficiency of Safety Measures in Industry, 1988, MAI, Moscow, USSR, p.48.

2 Recommendations on Methods of Complex Evaluation for Effective Measures of Accelerating Technical Progress. State Committee of Science and Technology, Academy of Sciences Presidium, Moscow, USSR, 1988, p.23.

SECOND INTERNATIONAL CONGRESS ON
RECENT DEVELOPMENTS IN AIR- AND
STRUCTURE-BORNE SOUND AND VIBRATION
MARCH 4-6, 1992 AUBURN UNIVERSITY, USA

SPECTRUM VARIATIONS DUE TO ARCHITECTURAL TREATMENT AND ITS RELATION TO NOISE CONTROL

O.A. Alim and N.A. Zaki
Faculty of Engineering, Alexandria University, Egypt

ABSTRACT

Exterior facades have a great influence on the noise transfer inside buildings. The aim of this paper is present and the spectral analysis of the noise inside and outside the building and also to highlight the influence of a certain kind of facade treatment, usually used as sun protection devices, which is the vertical louvers.

INTRODUCTION

A previous paper [1] reviewed different viewpoints of researchers [2,3,4,5,6,7,8], and the results concerning the effect of facades in noise control problems. The correlation between different arch-itectural treatments in the buildings' facades and the road traffic noise level was also presented [1]. That study was conducted on El Horreya Avenue, the main artery in the city of Alexandria, which runs through nearly 30% of this linear city. The facades chosen were simple, solid and void; a french window overlooking a balcony, a loggia, windows with vertical louvers, glass cladding, glazed aluminum framed facade and a window not parallel to the main road and others. In this paper the spectral analysis of the noise inside and outside the building is presented.

SITE DESCRIPTION AND MEASUREMENTS

Three sites out of the ten previous sites were chosen. They occupied the second floor of three different buildings (Figure 1). Site (1) is a window provided with a rolling shutter, existing in a facade making 30 degrees with the road. The facade has facing bricks in the solid part, while the sill beneath the void has a plaster finish. Site (2) has three windows with rolling shutters, separated by vertical concrete louvres. Each window consists of two parts, the lower being fixed. Site (3) is a typical, solid of void, facade with a wooden framed window. The measurements were carried out simultaneously on two points in each site using in each point a precise SLM and a tape recorder. The first point lies outside the window on the sill, fixing a height of 0.90 m, while the second point lies inside the room maintaining the same height and at a perpendicular distance of 1.40 m from the windows. The two points lie on the center line of the window.

FIG (1)

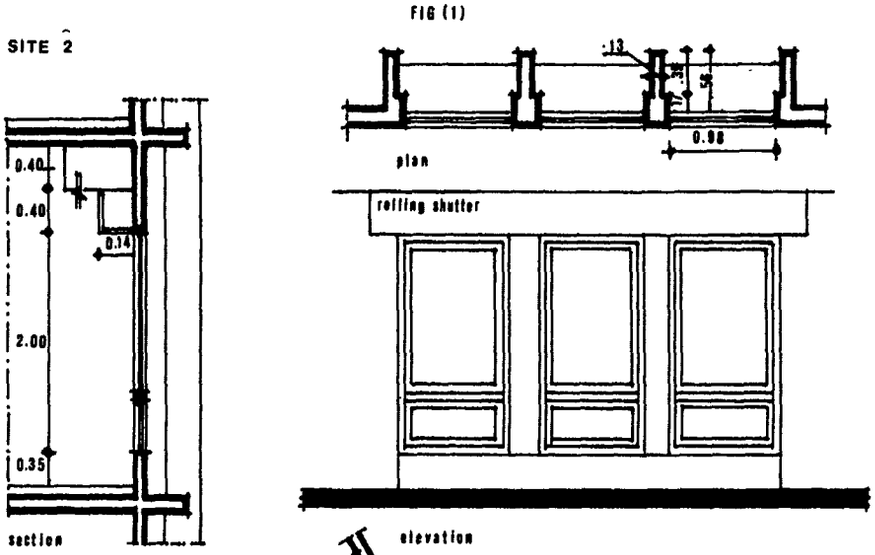
SITE 2
.13
.38
.50
0.98
plan
rolling shutter
0.40
0.40
0.14
2.00
0.35
section
elevation
SITE 1
3.00
plan
1.54
30°
SITE 3
1.50
plan
0.25
0.35
1,50
0.38
0.86
section
elevation
elevation
0.67
1.33
0.67
section

RESULTS AND DISCUSSION

1. The three spectra of the outside traffic noise in the sites (Figure 2) show the same tendency or shape. The peak value is concentrated between the range 500 Hz and 1600 Hz.

2. The reduction inside in site (1) and site (2) is greatest at 800 and 1250 Hz; also in site (3) the reduction is significant from band 800 till 1250 Hz, but at 2500 the reduction is little.

Table (1)

	Noise levels in dBA (inside)				Noise levels in dBA (outside)				
	L_5	L_{50}	L_{95}	L_{eq}	L_5	L_{50}	L_{95}	L_{eq}	ΔL_{eq}
1	64.0	56.0	48.0	58.6	91	79	71.5	82.5	23.9
2	66.0	58.0	51.0	60.2	86	78	72.5	79.8	19.6
3	67.5	58.5	51.5	61.3	95	80	72.5	84.0	22.7

FIGURE (2)

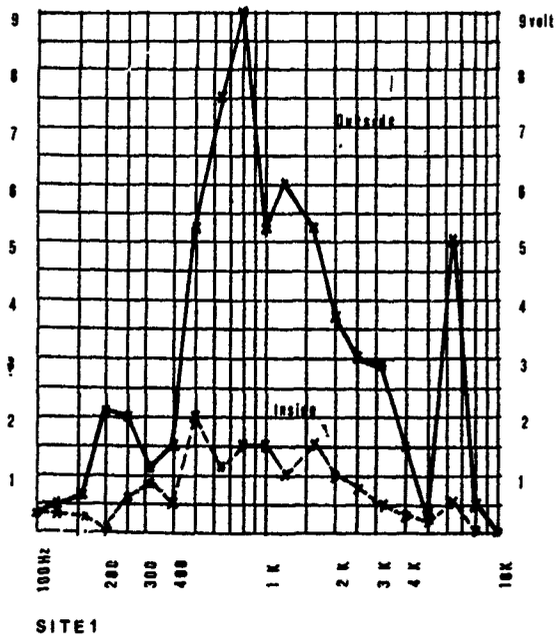

SITE1

FIGURE (2)

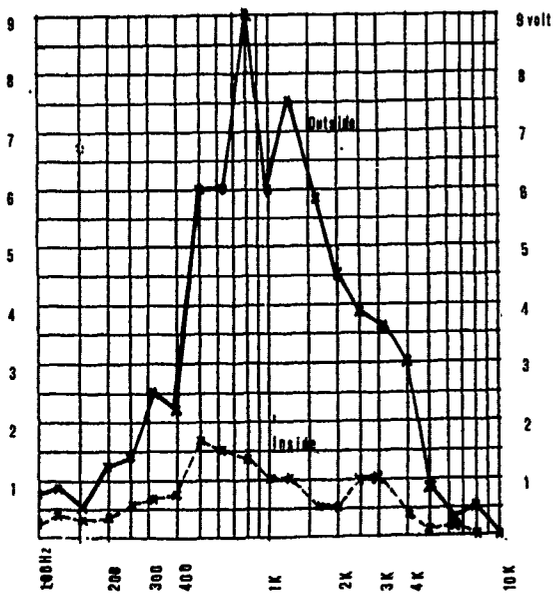

SITE 2

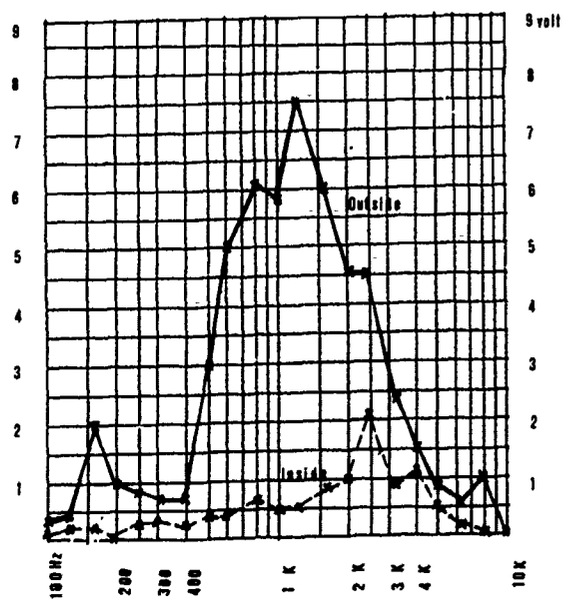

SITE 3

3. In site (1) at 500 Hz there is a peak inside; it could be due to its architectural treatment as seen from Figure (1).

4. From Figure (2) and site (3) we can observe that there is a considerable attenuation from the frequency component below 2 KHz, while above 2 KHz there are some peaks in the spectrum which may be due to its being a simple solid void, without any architectural treatment. The window is directly facing the road. Also, from Table (1) we can observe that this site possesses the highest values for both outside and inside measurements, 84 dbA, 61.3 dbA, respectively, for the same reason mentioned above .

5. From Table (1), site (1) is showing the highest ΔLeq. This is due to the window being not parallel to the road and which causes an inclined incidence of the acoustic wave and results in a minimum transmission from outside to inside. The results obtained are still in good agreement with those in [1].

6. In site (2) the path difference between the directly incident wave and the other waves reflected from the vertical louvres at A and B are comparable to the value of $\lambda/2$ in the band from 300-1000 Hz ($\lambda = c/f$; where
   λ = wave length;
   c = velocity of sound and
   f = frequency; i.e. λ = 340/800 or 340/1000);
   i.e. $\lambda/2$ = 17 & 21 cm, respectively. This may help in explaining the great value of attenuation for these frequencies as shown in Figure (2), site (2).

Conclusion

1. The architect should be supplied with accurate measurement of the traffic noise in the road, especially main arteries, before designing his building.

2. Architects, when possible, could orient their windows so as not to be parallel to the road, as this causes a loss in the transmitted noise from outside to inside.

3. The simple, solid and void reduces the effectively transmitted acoustic wave inside the building.

4. The different dimensions of the vertical louvres chosen for a certain window should not only depend on solar angles to give the best solar protection, but it could be designed as an element which could give a sufficient attenuation to traffic noise in interiors. This could be achieved if the difference between the length AY and XY of Figure (3) is in the range from 17 to 21 cm.

5. The variation in the value of the transmission loss at different frequencies from outside to inside may help in explaining the

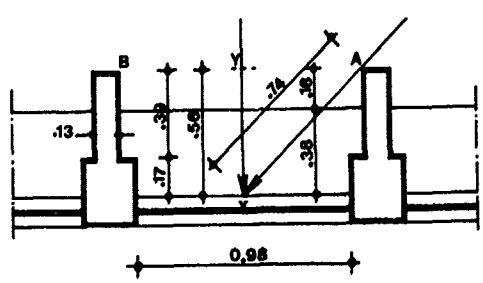

FIGURE (3)

reaction of the inhabitants due to the road traffic noise. This may be thoroughly explained by correlating subjective measurement with objective results.

REFERENCES

[1] O. Alim & N. Zaki, "Effect of Some Architectural Treatments on Road Traffic Noise", Noise-Con 90, proceedings, Ilene Busch Vishniae, Ed. (Austin, Texas, U.S.A.), 1990, pp 121-126.

[2] A Lawrance, "Variation in Individual Vehicle Noise, A Hemation Provided by a Building Facade", Internoise 79, proceedings, Stefan Czarnech, Ed. (Warszawa), Vol. II, 1979, pp 477-483.

[3] E. Gerretsen, "Calculation of the Sound Reduction by Facades", Internoise 81, proceedings, V.M.A.Pentz Aiole Bruijn, Ed. (Amsterdam, Netherlands) Vol. I, 1981, pp 405-408.

[4] S. Solberg, "Experiences From the Two First Years of a Program on Facade Insulation", Internoise 81, proceedings, V.M.A. Pentz Aiole Bruijn, Ed. (Amsterdam, Netherlands), Vol. I, 1981, pp 409-412.

[5] A. Nash, "Facade Sound Insulation - A Review of Methods", Internoise 82, proceedings, James Sechold, Ed. (San Francisco, California), Vol. II, 1982, pp 471-474.

[6] U. Ritterstadt, "The Change of Acoustical Properties of Traffic Noise at Different Distances From the Road", Internoise 83, proceedings, R. Lawrence, Ed. (Edinburgh, U.K.), Vo. II, 1983, pp 709-712.

[7] A. Nash, "Facade Sound Insulation - A Field Study" Internoise 84, proceedings, C.G. Maling, Jr., Ed. (Honolulu, Hawaii), Vo. I, 1984, pp 593-596.

[8] H. Shih, "Prediction of Outdoor-Indoor Noise Reduction by the Configuration of Building Facade", Internoise 86, proceedings, Robert Lotz, Ed. (Cambridge, Massachusetts, U.S.A.), 1986, pp 701-704.

SECOND INTERNATIONAL CONGRESS ON
RECENT DEVELOPMENTS IN AIR- AND
STRUCTURE-BORNE SOUND AND VIBRATION
MARCH 4-6, 1992 AUBURN UNIVERSITY, USA

INTERNAL COMBUSTION ENGINE STRUCTURE NOISE DECREASE OWING TO THE COEFFICIENT CHANGE OF NOISE RADIATION OF ITS ELEMENTS.

Rudolf N.Starobinsky,
the chair of the Environment protection
Polytechnical Institute, 14, Belorusskaya st.,
Togliatti, 445633, USSR.

Michael I. Fessina,
Volga Automobile associated Works, Research
and Scientific Centre, Noise and Vibration
Research Department, 16,Belorusskaya st.,
Togliatti, 445633, USSR.

ABSTRACT

There considered the problems of noise radiation decrease by the engine lamellar elements such as driving pulleys, casings, thermo-protective shields, thin-walled case elements. For radiation coefficient decrease of such elements it is offered their perforation that brings to the radiator transformation of the monopole type (e.g. air-cleaner covers) into the radiator of the dipole type. For plates, radiating sound with both sides, the perforation brings to the decrease of the equivalent moment of the dipole radiators. It is also considered (at the example of the belt driving pulley) the possibility of radiator transformation of dipole type into the quadripole radiators by the way of the acoustic mirror set near them.

The necessary perforation degree and hole situation are defined from the conditions of the minimum influence on the main function of the radiating sound elements (thermo-insulation, sound-insulation,protection from dirt, torque transfer and so on). There given some examples of the suggested method realization in the car engines.

INTRODUCTION

Noise decrease problem of the internal combustion engines as the main source of the environment noise pollution by the transport means and energetic settings continues to be actual in the conclussive ten-day period of the 20-th century. The successes in the field of noise decrease, reached by the researchers, designers and producers at present are though impressive enough, however the intensive satiation of

the planet, that continues, on by the transport means doesn't allow to take down this problem from the agenda and puts it into the category of the immediate and urgent ones.

The traditional methods of structure noise decrease of the internal combustion engines based on the mechanical impedance increase and effective vibro-insulation and vibro-damping application of the case parts evidently are exhausted at the most with the possibilities of the technological, resource and cost nature.

In the article there given attempts to research the possibilities of internal combustion engine structure noise decrease owing to the control sound radiation coefficients by the engine separate case parts which play an important role in the forming of its sound field. To such engine parts were related: a crankshaft pulley, pulleys of the engine auxiliary units, an air-cleaner cover, a drive case of the gas-distributive mechanism, a fan (ventilator) casing of the cooling system, a carburattor thermo-insulated shield.

THE WAYS OF COERCION ON RADIATION COEFFICIENTS

Mounting conditions of all the elements given abore on the engine and their dynamic conduct in the working process allow, to the definite degree of approximation, to approbate them by classic sound radiators, monopoles, dipoles, quadripoles and plane wave radiators with the control possibilities well enough by this radiation by the way of:

- radiator scale decrease (radiator characteristic dimension);

- transference in the source of a higher order (monopole into dipole, dipole into quadripole and so on);

- change of the external load on the source (nearly situated rigid or soft walls).

LAMELLAR RADIATOR PERFORATION

The well-known mean of sound radiation decrease by the oscillated plates is their perforation, bringing to sound pressure alignment on its opposite sides and radiation decrease. The more plane perforation degree, the less sound radiation at identical plane oscillation amplitudes. However, in real constructions lamellar element use with high degree of perforation is not always possible because of the breach of direct functional purpose of these elements, for example, because of the possibility of outside things getting under the casing,because of the loss of necessary durable and rigid characteristics and so on, and also because of the increase of direct sound radiation from the volumes for which these plates fulfil the role of sound insulated screens. In these cases some problems of the definition of perforation minimum degree and hole situation arise which provide with the necessary noise decrease that is radiated by the plate.

For the appreciation of radiator acoustic characteristics of the lamellar type is used a simplified model like an endless plate, performing bended oscillations (fig.1). For the estimation of plate perforation influence on the sound radiation by it an equivalent electrical scheme [1] is used which is given in fig.1. In this conductivity scheme Y is defined by the equation

$$Y = \frac{1}{F} \sum_i \frac{\xi_i^2}{\tilde{\xi}^2} \frac{1}{Z_i} \qquad (1)$$

where ξ_i is the amplitude of plate bended oscillations at the point of i-hole situation;

Z_i is rated acoustic resistance of the hole on $\rho_0 c_0$;

$\tilde{\xi}^2$ is mean square meaning of vibro-displacement amplitude;

F is plate area.

Sound radiation decrease is estimated according to the equation:

$$\Delta L = 20 \lg \left| \frac{i_s}{i} \right| = 20 \lg \left| 1 + Y (Z_{ch} + Z_1) \right| \qquad (2)$$

where $Z_{ch} = \left(j \sqrt{K^2 - K_{yz}/K^2} \right)^{-1}$;

$Z_1 = Z_{ch}$ at the absence of the wall near the oscillated plate;

$Z_1 = \left(j \sqrt{K^2 - K_{yz}^2/K^2} \cdot h \right)^{-1}$ at the presence a wall (at the distance of $h \ll \lambda$);

K_{yz} is a wave number of the plate bended oscillations.

The efficiency of the holes at the presence of the wale, as a rule, is higher than at the radiation into the unlimited space [2,3]. As an example, illustrating hole application efficiency for the radiation decrease of the vibrating plates in fig.2 are given noise spectra in the soundinsulated casing zone at the diesel engine work, competed with entire and perforated sound-insulated casing of gas-distribution mechanism.

In fig.3 sound suppression efficiency is illustrated, which is radiated by the vibrating cover of the engine air-cleaner. In spite of the fact that the cover perforation by two holes with 5 mm diameter brings to the partial unhermetization of the air-cleaner-muffler chamber, the optimum disposition and minimum holes dimensions provide with sufficient obstruction to the air- sound radiation from the chamber at the efficient suppression of low frequency sound, directly generated by the cover [4]. The measuring microphone is situated opposite the openings of the aircleaner perforated cover and thus measured air-noise radiation from the air-cleaner chamber.

The applied at the car engines thermo-insulated screens of the carburattor in the sight of cantileverly fastened steel plate can also make a valuable contribution to the engine sound field. Especially it refers to the resonance radiation conditions of these screens. In this case the perforation of the screen cantilever section by 5 holes with 5 mm diameter which were situated at the distances of 30...50 mm from the screen free edge allowed to decrease total noise levels in the screen zone up to 2 dBA [5]. Such insignificant screen perforation did not make worse direct thermo-insulated screen functions.

NOISE DECREASE FROM THE VIBRATING PULLEYS

Holes fulfilment in the rotating flat parts such as belt and chain drive pulleys, toothed wheel and some others provide with high degree of noise radiation decrease, and in particular, in the drive pulley of the internal combustion engine crankshaft, which is often known as one of the strongest radiators of internal combustion engine noise.

For estimation noise radiation decrease by the pulley at the fulfilling holes in it was approbated by the dipole radiator with dipole moment B , propotional to the oscillation mean-square velocity of the points of its surface V, pulley area S and radiator characteristic dimension L (B~V*S*L) value L was taken equal to the mean way where pressure alignment between points on the opposite surfaces of the oscillated pulley takes place. The hole presence in the pulley (L decrease) brings to quicker pressure alignment on the pulley opposite sides and to radiation decrease, propotional B^2 . At large holes doing the supplementary effect is got owing to radiator S surface decrease. Carried out researches showed that it's quite enough to perforate the crankshaft pulley of VAZ engine by six holes with 2 mm diameter which are evenly situated on the circumference, disposed between the hub external diameter and pulley outward diameter.

With this total level of sound radiation in the pulley zone (by 0,1 m from the disk surface) decreases in 3 dBA. Here it is necessary to note, that the fulfilment of the 6 holes with 2 mm diameter brings in the concrete case to decrease of the radiation area only by 0,23%. The experiments, carried out with the pulleys from different materials (cast iron, steel,polyamid) and with different thickness of the pulley disk (3 mm and 10 mm) showd: perforation diameter influenes substantially on the noise muffling magnitude. The presence of 6 holes with 8 mm diameter on the pulley ensured the greatest effect till 4 dBA (fig.4). Extreme increase of the hole diameter brings to noise muffling efficiency loss, evidently, because of the bended rigidity decrease of the pulley construction and the corresponding growth of vibration level of the pulley construction separate elements.

The greatest acoustic effect was received at the pulley use of spoke construction, realizing "the effect of big hole" [6,7]. The pulley application of the spoke construction allows in the comparison with the serial variant of the pulley construction without holes in the disk to get a substantial acoustic effect (fig.5). Thus, the radiation in the pulley zone in the frequency range 1000-2000 Hz decreases by 15 dB, total level- by 7 dBA, and total level of the external noise of cars-VAZ-by 1-1,5 dBA. Sound radiation from the pulley elements with high level of vibro-velocities can be suppressed by introduction in them small openings, dismembering them, in their turn, on smaller radiators of dipole type [8]. As the researches have shown, the fulfilment of 5 holes with 6 mm diameter in the pulley rim of the spoke construction allowed supplementary to decrease total level in the pulley zone till 2 dBA (fig.6).

In a number of cases decrease effect of the radiated by the pulley noise, reached by the perforation of its main radiating elements may appear not to be sufficient. In the connection with this it may arise the necessity of supplementary measure application on suppression of the pulley intensive noise radiation. The possibility of providing with noise decreased radiation by its more rational arranging on the engine looks very attractively.

ACOUSTIC MIRROR USE

The supplementary and highly effective mean of decrease of element measure coefficient of the oscillating pulley type is acoustic mirror use as a nearly situated rigid reflecting plate [9]. In the quality of such it can be used a casing of gas-distribution drive mechanism, situated at the corresponding distance from the side surface of the pulley disk and partially copying its contour [12]. There can be used also in the quality of reflecting surfaces separate elements of the motor-compartment (e.g. wheel splash devices settings at the diametrical disposition of the engine in the motor-compartment). It's not excluded the application of specially mounted plates, situated near the pulley side surface as from the engine side so well from the motor-compartment side.

The thooretical preconditions of practical use nearly situated sound reflecting wall of the acoustic mirror by the vertical dipole are considered by E. Skuchik [10]. If we consider the pulley as a dipole type radiator, it is useful to draw nearer maximum it to the rigid reflecting surfaces for the decrease of its radiation. It is known, that dipole radiation,situated by the absolutely rigid wall is almost competely compensated by the radiation of its imaginary picture [11].

The real wall on the constructive considerations cannot be endlesly approached to the rotating vibrating disk. Besides, it partially absorbs sound and changes the reflected wave phase. Dipole moving off influence from the ideal wall on its radiation is enough considered upon in details in [10], function F(kd/2) characterises the change of sound power N, radiated by the dipole into the semi-sphere in comparison with the power $0,5\ N_{eq}$ - radiated by it in the some semi-sphere at the wall absence (fig.7, curve 1)

$$\frac{N}{0,5N_{eq}} = F\left(\frac{kd}{2}\right) = 6\frac{1}{y^3}\left|\frac{y^3}{3} - \frac{y^2}{2}\cos 2y - \left(\frac{y^2}{2} - \frac{1}{4}\right)\sin 2y\right| \qquad (3)$$

where d/2 is distance from the wall to the dipole.

For small (kd/2) when the wall influence substantially influences upon the radiation, function F(y) is well approbated by the dependence

$$F(y) = (12/5)\,y^2 \qquad (4)$$

The real reflecting wall in contrast to the ideal one possesses some absorbtion and resility, that brings to the appearance of the supplementary unequilibration of the real dipole to be imaginary. Unequilibrated radiation bears also the dipole nature and brings in the supplementary contribution in the radiation of the reflection unideality on the radiation of the system to be considered upon.

Dipole radiation change, brought in by an unideal wall, can be estimated according to the formula [9].

$$\frac{N}{0,5N_{eq}} = \Gamma\cos\varphi \cdot F\left(\frac{kd}{2}\right) + \left|1 - \Gamma e^{j\varphi}\right| \qquad (5)$$

Where Γ and φ are ccrrespondingly modulus and phase of the radiation coefficient of the wall. The second member of this equation takes into account the reflection unideality. The dependence nature of the radiated power from and is illustrated in fig. 7. The possibility of noise decrease as a radiator of dipole type with the help of the radiated wall was experimentally researched and realized at one of the model of the car engine at the Volga Automobile Plant. The efficiency of the suggested method is illustrated in fig.8, where the comparative characteristics of radiation are given as 1/3 octave spectra of noise levels, which are registrated in the pulley zone with a reflecting wall, disposed at the distance d/2 = 40 mm from the pulley and its approximation to the pulley (d/2 = 2 mm).

Highly attractive seems an idea of the acoustic mirror using as nearly situated regid sound reflecting screens in the input zone into teeth engagement of the teeth of driving and driven pulleys and teeth of the belt of gas-distribution mechanism drive,as it was settled in the work [13] main sound radiation is formed in the engagement zone, the dimensions of this zone don't exceed 2...5 cm and the very radiation presents radiation of dipole type. In this connection there are no particular technical problems in using different screening elements of small dimensions to be situated opposite these zones at the equal distanse to the beet external surface at the distance not exceeding 0,03 Di, where Di is diameter of the corresponding pulley. The screen element area with this must be not less 0,6 of the radiation zone area to be formed with the section of the belt and pulley tooth engagement, limited by the central angle, equal to 10 with the bisector, passing through the initial point of the grasp arc an element of the corresponding acoustic mirror can appear the section of the sound-insulated casing of gasdistribution mechanism drive, the geomtry of which is specially designed in accordance with the recommendations, given abore. It is necessary also to add that in the citing work it is noticed [13] a highly efficient method (up to 20 dBA) of noise radiation suppression of the toothed-belt drives for the sake of the very driving belt perforation which represents a typical radiator of dipole type.

REFERENCE

1. Starobinsky R.N. "About some calculated models of the acoustic systems". Deposited manuscript NIIN AVTOPROM reg. N D587,Togliatti,1980,in Bl VINITI N 6,1981.

2. Starobinsky R.N. ,Fessina M.I. "About sound radiation decrease by the car vibrating elements". In the collected articles: "adaptation, modelling and diagnostics of the systems". KuAI, Kuibyshev, 1983,p.126-130.

3. Fessina M.I., A.V. Frolov, G.I.Sergeev,R.N.Starobinsky. "Gas distribution mechanism of the internal combustion engine". Author's certificate, USSR, N 1346832.

4. Fessina M.I., Starobinsky R.N., Lasarev U.P., Lyssenko E.V. "Air-cleaner for the internal combustion engine",author's certificate, USSR, N 1037700.

5. Fessina M.I., Starobinsky R.N., Lasarev U.P., Lyssenko E.V.,Afanasyev M.A. "Internal combustion engine". Author's cetificate,USSR, N 1307074.

6. Fessina M.I.,Vainshtain L.L.,Starobinsky R.N.,Malishevsky V.I. " Vibro - acoustic activity decrease of VAZ engine crankshaft pulley". Express-information "Progressive methods exchange in motor-car construction, N 10,Branch of the N11N AVTOPROM, Togliatti, 1976, p.3-12.

7. Fessina M.I., Pashin U.N., Vainshtain L.L.,Malishevsky V.I., Starobinsky R.N. "Pulley", Author certificate, USSR, N 819461.

8. Starobinsky R.N., Fessina M.I. "Pulley", Author certificate, USSR,N 934096.

9. Fessina M.I., Starobinsky R.N. "Noise decrease from the vibrating pulleys". News of Higher educational institutions, mechanical engineering, 1982, N 6, p.73-75.

10. Skuchik E. "Acoustics bases", v.2, translated from English,M.: "The Wored",1976.

11. Isakovich M.A."General acoustics",M, "Science", 1973.

12. Fessina M.I.,Starobinsky R.N. "Internal Combustion Engine". Author certificate, USSR, N 1239382.

13. Tourret J., Birembaut Y., Deschamps M. Noise Generation of Synchronous Belts Using Acoustic Intensity Mapping". Noise Control Engineering jornal /january-february, 1988, vol.30/ number 1, p.11...14.

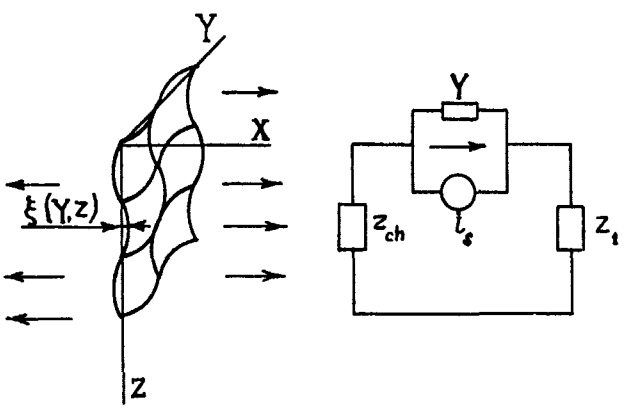

Fig.1. Endless plate and equivalent electrical scheme of sound radiation by the plate.

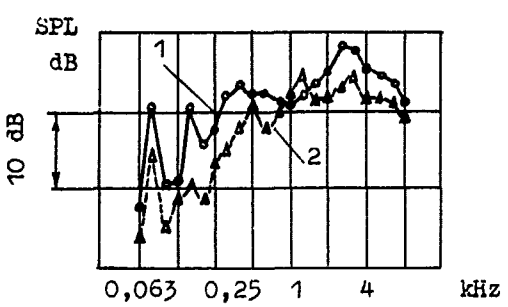

Fig.2. 1/3 octave spectrum of noise levels at 0,1 m from drive casing surface of VAZ diesel engine (V_h=1500 cm^3). Full load, n=5000 min^{-1}.
1 - drive casing (without holes)
2 - perforated casing (with 6 holes, ø 6 mm)

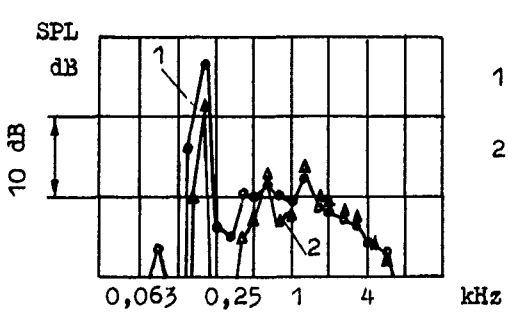

1 - air-cleaner cover (without holes)
2 - perforated cover (2 holes, diameter 5 mm)

Fig.3. 1/3 noise octave spectrum at 0,1 m from the surface of VAZ engine air-cleaner cover (V_h=1300 cm^3). Full load, n=5600 min^{-1}

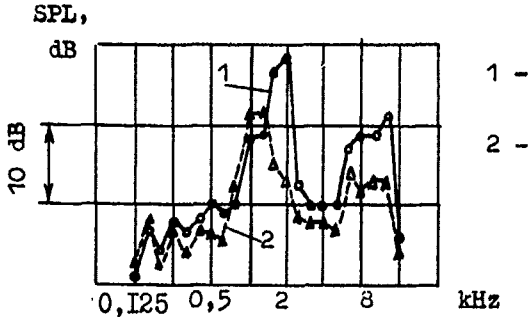

1 - pulley disk is without holes
2 - pulley disk is perforated (6 holes diameter is 8 mm)

Fig.4. 1/3 noise octave spectrum at 0,1 m from the pulley disk of VAZ engine crankshaft. V_h=1600 cm^3. Full load, n=5000 min^{-1}

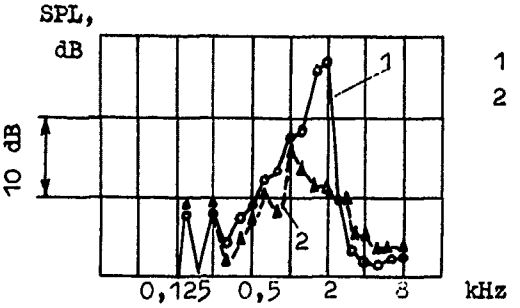

1 - pulley with entire disk,
2 - pulley of spoke construction

Fig.5. 1/3 noise octave spectrum at 0,1 m from the pulley disk of VAZ engine crankshaft (V_h=1200 cm^3). Full load, n=5000 min^{-1}

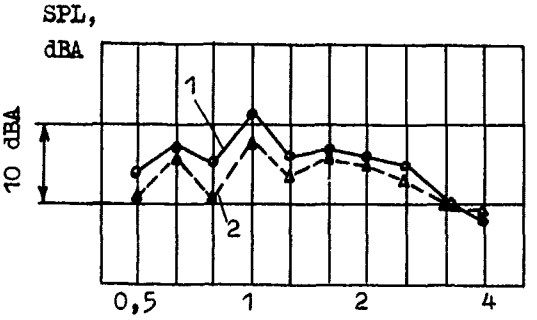

1 - pulley of spoke construction (serial),
2 - spoke pulley with perforated rim, 5 holes, diameter 6 mm

Fig.6. 1/3 octave spectrum of noise radiation at 0,1 m from the pulley rim of VAZ engine crankshaft (V_h=1600 cm^3). Full load, n=5000 min^{-1}

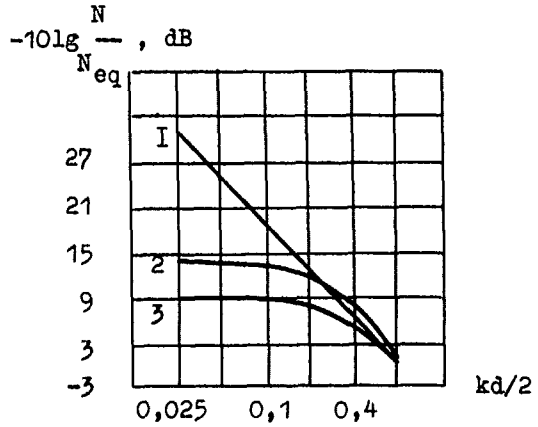

Fig.7. Dipole radiation near the reflecting wall.

1 .... r=1, φ =0;
2 .... r=0,7, φ =0;
3 .... r=1, φ =30.

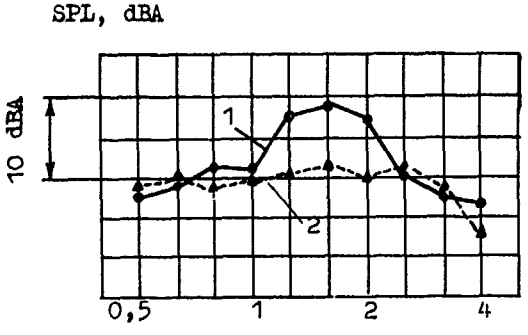

1 - sound reflecting wall at 40 mm from the pulley disk;
2 - sound-reflecting wall at 2 mm from the pulley disk.

Fig.8. 1/3 octave spectrum of noise radiation at 0,1 m from the pulley disk of VAZ engine crankshaft (V_h=1300 cm^3). The pulley with entire disk. Full load, n=5000 min^{-1}.

SECOND INTERNATIONAL CONGRESS ON
RECENT DEVELOPMENTS IN AIR- AND
STRUCTURE-BORNE SOUND AND VIBRATION
MARCH 4-6, 1992 AUBURN UNIVERSITY, USA

FORMULATION OF THE INTERIOR ACOUSTIC FIELDS FOR PASSENGER VEHICLE COMPARTMENTS

Şadi Kopuz, Y. Samim Ünlüsoy, and Mehmet Çalışkan
Mechanical Engineering Department
Middle East Technical University
06531 Ankara, Turkey

ABSTRACT

A critical examination of the Boundary Element Method (BEM) applied to the numerical solution of acoustic radiation problems governed by Helmholtz's equation is the subject of this paper. A detailed literature survey on the application of the BEM to the radiation problems concerning both the exterior and interior regions is presented. A formulation directed to the particular application of noise generation inside motor vehicle passenger compartments is developed. The solution of the problem is illustrated on the classical problem of a uniformly pulsating sphere.

INTRODUCTION

The prediction of the acoustic field due to arbitrarily shaped structures is an important research area in many disciplines. This topic has a variety of applications especially, in aerospace engineering and automotive engineering fields in determining the interior noise levels of aircraft and ground vehicles.

For the solution of the problem several different methods have been used so far; use of the finite element method, statistical energy analysis, and boundary element method (BEM) with integral formulations being the most prominent. Each method has its advantages and drawbacks depending on the particular application in hand.

In this paper, a formulation directed to the prediction of noise generation inside motor vehicle passenger compartments is introduced and a study of the boundary element method for the solution of the interior acoustic problems governed by the Helmholtz equation is presented. The ultimate aim of the study is to produce a computational tool to be used in the prediction of the acoustical characteristics for a vehicle structure for which the in-vacuo vibration characteristics are available.

SURVEY OF PREVIOUS WORK

A literature survey on the integral formulations and the use of the BEM for the solution of radiation problems concerning both the exterior and interior regions has been performed and summarized below.

Classical formulations of acoustic radiation from vibrating bodies based on integral equations started in early 1960's. In these works, exterior steady-state acoustic radiation problem for bodies of arbitrary shape was investigated. Chen and Schweikert [1] described the acoustic field

by a distribution of surface sources of unknown strength at the shell-fluid boundaries, which led to a set of integral equations. This numerical technique is named as Simple Source Formulation (SSF) in which the acoustic pressure at an exterior field point is represented in terms of a surface integral of a source density function. Computational results were given for two sample problems: (1) a piston set in a rigid sphere, and (2) a stiffened cylindrical shell of finite length in water. Chertock [2] developed a numerical method utilizing the discretized Surface Helmholtz Integral Equation (SHIE) for the solution of radiation problems involving surfaces of revolution. Another approximate method was presented by Williams et al. [3] in which the farfield pressure was approximated by a truncated series of spherical Hankel functions. The method was shown to be most accurate for radiating surfaces that are nearly spherical in shape. Copley [4] proposed a method applicable to radiation from surfaces of revolution utilizing the Interior Helmholtz Integral Equation (IHIE). All three types of integral formulations for obtaining approximate solutions of the exterior steady-state acoustic radiation problem for an arbitrary surface were discussed by Schenck [5]. Schenck proposed a Combined Helmholtz Integral Formulation (CHIEF) to overcome the deficiencies and computational difficulties present in the previous works. He showed that this formulation yielded unique solutions even at the characteristic wave numbers for which the other integral equations broke down. Meyer, Bell, and Zinn [6] investigated the development of a procedure for the exterior sound radiation problems. They were concerned with the following points: (1) the development of a numerical scheme for handling the singular integrands encountered in the application of the Helmholtz formulae, (2) the determination of the most effective procedure for handling the non-uniqueness of the radiation solution at eigenvalues of the associated internal acoustic problem, and (3) the determination of the accuracy of the resulting solutions.

The Boundary Element Method (BEM) became popular in late 1970's. Koopman and Benner [7] presented a computational method based on Helmholtz integral for assessing the sound power characteristics of machines. The accuracy of the method was demonstrated by calculating the pressure on the surface of a uniformly pulsating sphere and of an oscillating sphere. A clear explanation of the application of the BEM to exterior sound radiation problems was given by Seybert et al [8]. The BEM was used to obtain numerical solutions to the same classical radiation problems. They introduced an isoparametric element formulation in which both the surface geometry and the acoustic variables on the surface of the radiating body were represented by quadratic shape functions. Solutions to the problems encountered in the use of BEM have been suggested by Piaszczyk [9] and Brod [10]. Recently, Wu et al [11] described a BEM code for acoustic analysis, along with the process of vectorizing and parallelizing the code on a vector parallel computer and Seybert, Cheng, and Wu presented an approach to the solution of coupled interior/exterior acoustic problems using the BEM [12].

The solution of the interior noise fields of cavities having arbitrary shapes by using BEM has recently received much interest. Bell, Meyer, and Zinn [13] presented an integral solution of the Helmholtz equation for predicting acoustic properties of arbitrarily shaped bodies. They examined two-dimensional problems of a circle and rectangle together with a duct having a right-angle bend. They also investigated the acoustic properties of a sphere using an axisymmetric formulation. A master plan for prediction of vehicle interior noise was suggested by Dowell [14]. The interior noise problem was presented considering noise sources, noise effects on people and payloads, noise reduction concepts, noise transmission analysis, and interior acoustic cavities. He examined the contributions to the literature on this subject and discussed the different methods of approach to the problem. Sestieri et al [15] discussed the structural-acoustic coupling problem by using the BEM for interior volumes having complex shapes. They investigated the importance of coupling and reached the conclusion that a full coupled analysis did not seem to be justified. Seybert and Cheng [16] concerned with the application of the BEM to interior acoustics problems governed by the reduced wave (Helmholtz) differential equation. They applied the BEM formulation to an axisymmetric problem at which the surface integrals could be reduced to line integrals along the generator of the cavity and to integrals over the angle of revolution. Therefore, the surface was discretized by using line elements, not surface elements and only the generator of the cavity needed to be discretized. They illustrated the solution for the acoustic response of a spherical cavity.

Fyfe [17] discussed the application of the BEM to predict the interior acoustic mode

frequencies of an enclosed medium. He used a non-rectangular box and an automobile model to show the accuracy of the method. Cheng and Seybert [18] examined both the interior and exterior acoustic radiation problems considering the application of the BEM. The acoustical response of a spherical cavity was determined and good agreement between the BEM results and the analytical solution was obtained.

A more general investigation of the application of BEM for the numerical solution of noise problems inside a complex shaped cavity was performed by Suzuki et al [19]. A new formulation for complicated boundary conditions was proposed to solve practical noise problems inside a vehicle cabin. The acoustic effect of absorbent materials on the vibrating surfaces and the effect of leakage through an opening were considered in the analysis. They applied the method in determining the sound pressure inside a linear duct, the transmission of sound through a cavity-backed plate, and predicting the sound pressure field inside a rather simple sedan compartment model. These studies resulted in the development of a new computer code called ACOUST/ BOOM to analyze the sound pressure radiated by a vibrating structure and to calculate the acoustic resonance of the field [20].

The literature survey indicates that in spite of the continued research on the subject, the analytical and numerical problems associated with the application of the BEM to interior acoustic radiation problems have not yet been completely overcome. A complete procedure to predict acoustic parameters under realistic inputs for complicated structures is yet to be produced.

FORMULATION OF INTERIOR REGIONS

The geometry of the problem is presented in Figure 1. Problems to be considered are those dealing with behavior within cavities as shown in this figure.

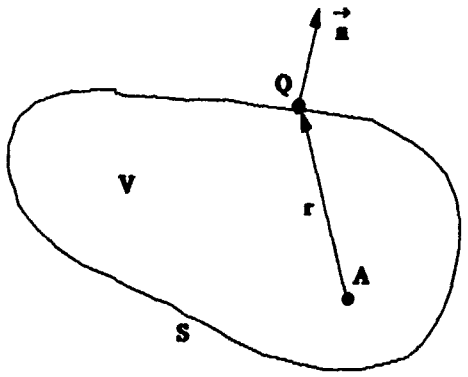

Figure 1. The Geometry of the Physical Problem.

For most practical problems a sinusoidal time dependence can be assumed so that the problem is simplified greatly. Then, the wave equation reduces to the well known Helmholtz equation:

$$\nabla^2 p + k^2 p = 0 \qquad (1)$$

where p is the acoustic pressure, k is the wave number, and c is the speed of sound in the medium.

Solution of the Helmholtz equation can be obtained by separation of variables. This method involves series expansions of the solutions in terms of eigenfunctions of the system and can only be used with special coordinate systems and boundary conditions. For arbitrarily shaped bodies, no general analytical solutions exist. Therefore, numerical methods should be used to solve the Helmholtz equation.

Applying Green's theorem together with the definition of Green's Function to the Helmholtz equation with the following substitutions, one can obtain the integral equation called the

External Helmholtz Integral Equation.

$$\int_S [\, p(Q) \frac{\partial G(A, Q)}{\partial n} - G(A, Q) \frac{\partial p(Q)}{\partial n} \,] \, dS = 0 \qquad (2)$$

where G is the free space Green's Function.

Now, consider two different cases, i.e. field point A may be inside the region V or on the surface S. The Green's function is regular inside the surface except when A ≠ Q. To remove this singularity, point A is surrounded by a small sphere or circle C of radius ε. The integral will now include a term over C, which on taking the limit as $\varepsilon \rightarrow 0$, gives the Internal Helmholtz Integral Equation:

$$p(A) = \frac{1}{4\pi} \int_S [\, p(Q) \frac{\partial G(A, Q)}{\partial n} - G(A, Q) \frac{\partial p(Q)}{\partial n} \,] \, dS \qquad (3)$$

In the case that field point A approaches surface point (source point) Q, the geometry of the problem is modified by considering a small hemisphere or half circle around point A with radius ε. The integral will now include a term over half circle, which on taking the limit as $\varepsilon \rightarrow 0$, gives the Surface Helmholtz Integral Equation:

$$p(A) = \frac{1}{2\pi} \int_S [\, p(Q) \frac{\partial G(A, Q)}{\partial n} - G(A, Q) \frac{\partial p(Q)}{\partial n} \,] \, dS \qquad (4)$$

One can write the governing equations of the internal problem after inserting the boundary conditions in a more compact form as follows:

$$c(A)\, p(A) + \int_S p(Q) [\frac{1}{r(A, Q)} + jk] \cos\gamma(A, Q) [\frac{e^{-jkr(A, Q)}}{r(A, Q)}] dS(Q) = \int_S j z k v(Q) [\frac{e^{-jkr(A, Q)}}{r(A, Q)}] \, dS(Q) \qquad (5)$$

where z is the specific acoustic impedance, v is the surface velocity, r is the distance between the points A and Q, γ is the angle between the unit normal and position vector r, and

$$c(A) = \begin{cases} 4\pi & \text{for the field points inside the body} \\ 2\pi & \text{for the field points on the surface of the body} \\ 0 & \text{for the field points outside the body} \end{cases}$$

NUMERICAL SOLUTION TECHNIQUE

In the previous section, the integral equations which describe the interior acoustic field of an arbitrarily shaped body have been developed. The numerical procedure for the BEM solution has been explained in detail in [21] and consists of the four main steps below:

1. Discretization of the boundary surface into boundary elements.
2. Numerical integration to get an algebraic system of equations.
3. Solution of the system of equations to obtain the unknown boundary surface variables.
4. Solution of the field (interior) values.

APPLICATION OF BEM TO A UNIFORMLY PULSATING SPHERE

The analytical solution for the sound pressure on the surface of a uniformly pulsating sphere is given by:

$$p = zU_o\left(\frac{jka}{1+jka}\right) \tag{6}$$

where a is the radius of the sphere and U_o is the amplitude of surface velocity in normal direction to the surface.

The magnitude and phase of the sound pressure on the surface of the sphere are obtained from both the analytical solution and the BEM. The sphere is taken with a uniform surface velocity of U_o = 1.0 m/s. For the BEM solution, the sphere is discretized into 8 quadrilateral quadratic isoparametric elements each having 8 nodes. The computer code is developed on the IBM 3090 mainframe using FORTRAN 77 and the ESSL (Engineering Scientific Subroutines Library) subroutines are used in the solution of the complex set of simultaneous equations. The results obtained from this rather rough discretization are shown in Figure 2 together with the analytical solution. The effect of internal field, which is a significant point in interior acoustics of vehicle structures, is strikingly demonstrated in the BEM solution.

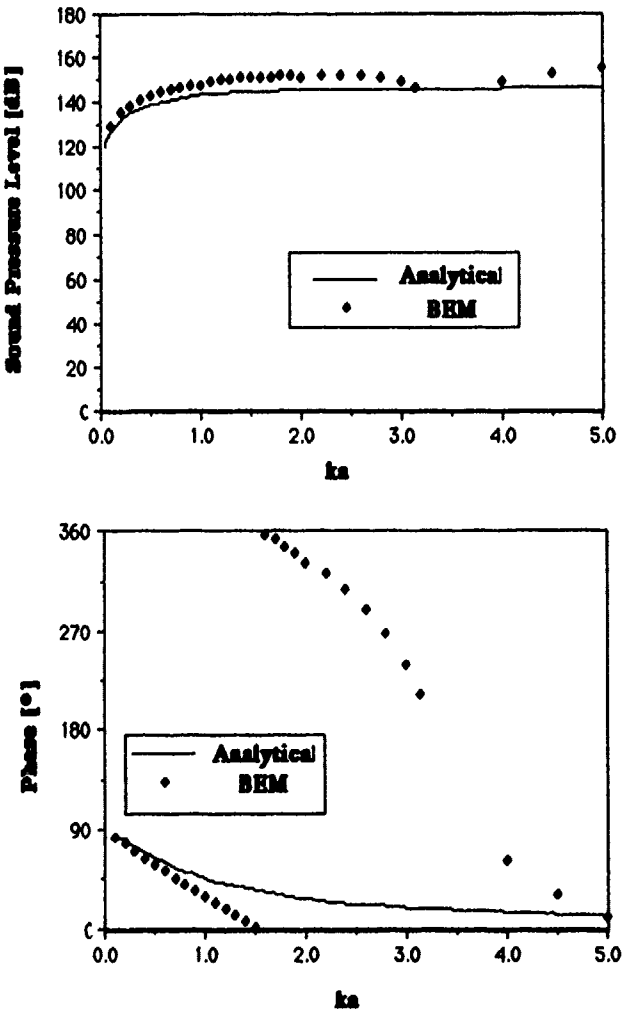

Figure 2. Surface Pressure on a Uniformly Pulsating Sphere, (a) Magnitude, (b) Phase.

CONCLUSION

In this paper the first stage of a research programme directed towards the prediction of sound pressure levels inside vehicle structures, under realistic operating conditions, is introduced. A literature survey on the application of BEM to the radiation problems concerning both the exterior and interior regions is presented. The application of the BEM to the numerical solution of acoustic radiation problems has been performed. The BEM formulation has been given for the interior acoustic radiation problems together with the numerical solution technique and illustrated on the solution of a classical acoustic problem.

ACKNOWLEDGEMENTS

Middle East Technical University Research Fund Project No. 91-03-02-02 is gratefully acknowledged for the support and the computational facilities provided.

REFERENCES

1. Chen, L.H. and Schweikert, D.G., "Sound Radiation from an Arbitrary Body", J. Acoust. Soc. Am., Vol. 35, No. 10, 1963, pp. 1626-1632.
2. Chertock, G., "Sound Radiation from Vibrating Surfaces", J. Acoust. Soc. Am., Vol. 36, No. 7, 1964, pp. 1305-1313.
3. Williams, W., et. al, "Acoustic Radiation from a Finite Cylinder", J. Acoust. Soc. Am., Vol. 36, No. 12, 1964, pp. 2316-2322.
4. Copley, L.G., "Integral Equation Method for Radiation from Vibrating Bodies", J. Acoust. Soc. Am., Vol. 41, No. 4, 1967, pp. 807-816.
5. Schenck, H.A., "Improved Integral Formulation for Acoustic Radiation Problems", J. Acoust. Soc. Am., Vol. 44, No. 1, 1968, pp. 41-58.
6. Meyer, W.L., Bell, W.A., and Zinn, B.T., "Boundary Integral Solutions of Three Dimensional Acoustic Radiation Problems", J. Sound and Vibration, Vol. 59, No. 2, 1978, pp. 245-262.
7. Koopman, G.H., and Benner, H., "Method for Computing the Sound Power of Machines Based on the Helmholtz Integral", J. Acoust. Soc. Am., Vol. 71, No. 1, 1982, pp. 78-89.
8. Seybert, A.F., et al, "Application of the BIE Method to Sound Radiation Problems Using an Isoparametric Element", ASME Paper No. 82-WA/NCA-1, 1983.
9. Piaszczyk, C.M., "Acoustic Radiation from Vibrating Surfaces at Characteristic Frequencies", J. Acoust. Soc. Am., Vol. 75, No. 2, 1984, pp. 363-375.
10. Brod, K., "On the Uniqueness of Solution for all Wavenumbers in Acoustic Radiation", J. Acoust. Soc. Am., Vol. 76, No. 4, 1984, pp. 1238-1243.
11. Wu, T.W., et al, "Vectorization and Parallelization of the Acoustic Boundary Element Code BEMAP on the IBM ES/3090 VF", International Congress on Recent Developments in Air- and Structure-Borne Sound and Vibration, Auburn University, USA, 1990.
12. Seybert, A.F., Cheng, C.Y.R., and Wu, T.W., "The Solution of Coupled Interior/exterior Acoustic Problems Using the Boundary Element Method", J. Acoust. Soc. Am., Vol. 88, No. 3, 1990, pp. 1612-1618.
13. Bell, W.A., Meyer, W.L., and Zinn, B.T., "Predicting the Acoustics of Arbitrarily Shaped Bodies Using an Integral Approach", AIAA Journal, 1977, Vol. 15, No. 6, pp. 813-820.
14. Dowell, E.H., "Master Plan for Prediction of Vehicle Interior Noise", AIAA Journal, 1980, Vol. 18, No. 4, pp. 353-366.
15. Sestieri, A., Vescovo, D.D., and Lucibello, P., "Structural-Acoustic Coupling in Complex Shaped Cavities", J. Sound and Vibration, Vol. 96, No. 2, 1984, pp. 219-233.
16. Seybert, A.F., and Cheng, C.Y.R., "Application of the BEM to Acoustic Cavity Response and Muffler Analysis", J. Vib. Ac. St. Rel. Des., Vol. 109, 1987, pp. 15-21.
17. Fyfe, K.R., "Determination of Acoustic Modal Properties from Boundary Element Modeling", Dynamic Engng., Heverlee, Belgium, 1988.
18. Cheng, C.Y.R., and Seybert, A.F., "Recent Applications of the Boundary Element Method to Problems in Acoustics", SAE Paper No. 870997, 1988, pp. 3.165-3.174.
19. Suzuki, S., Maruyama, S., and Ido, H., "Boundary Element Analysis of Cavity Noise Problems with Complicated Boundary Conditions", J. Sound and Vibration, Vol. 130, No. 1, 1989, pp. 79-91.
20. Ishiyama, S.I., et al, "The Applications of ACOUST/BOOM-A Noise Level Predicting and Reducing Computer Code", SAE Transactions Paper, 1989, pp. 4.976-4.986.
21. Seybert, A.F., et al, "An Advanced Computational Method for Radiation and Scattering of Acoustic Waves in Three Dimensions", J. Acoust. Soc. Am., Vol. 77, No. 2, 1985, pp. 362-368.

SECOND INTERNATIONAL CONGRESS ON
RECENT DEVELOPMENTS IN AIR- AND
STRUCTURE-BORNE SOUND AND VIBRATION
MARCH 4-6, 1992 AUBURN UNIVERSITY, USA

NOISE FROM LARGE WIND TURBINES: SOME RECENT SWEDISH DEVELOPMENTS

Sten Ljunggren

DNV INGEMANSSON AB
Box 47 321
S-100 74 STOCKHOLM
Sweden

ABSTRACT

This paper deals with three different aspects of wind turbine noise: the low-frequency "thumping" noise associated mainly with downwind turbines, periodic amplitude modulation of the aerodynamic broadband noise and finally mechanical noise.

It is shown from some measurement results that adverse community reaction due to the thumping noise can occur at levels substantially below those observed in laboratory experiments. Furthermore, some aspects of the corresponding sound generation are discussed.

The importance of the periodic amplitude modulation of the broadband turbine noise and in certain cases also of the random modulation is emphasized. It is shown that measurement results agree fairly well with predictions from a simple model.

The gearbox is the most important source for the mechanical noise and some aspects of the noise generation are discussed. Finally, some of the measures adopted by the Swedish industry with respect to the different noise problems are presented.

INTRODUCTION

Sweden is, compared with many other countries, sparsely populated. It could then be expected that the noise produced by wind turbines should not be a very important issue. However, the most favourable wind conditions are found in the coastal areas, where also a large number of very popular seaside resorts, vacation houses, etc, can be found. This implies that it is very difficult in practice to localize wind turbines so that the distance to adjacent dwellings is large enough for the noise level to become unimportant in practice.

Some quantitative data were given recently in an extensive parlamentary investigation. It was here concluded that if a large-scale establishment of wind power were to take place in Sweden, the maximum distance between wind turbine sites and adjacent dwellings which is possible with respect to the power output is 300 - 500 m.

On the other hand, it has been shown that the sound level due to a "first generation" wind turbine in the megawatt class is about 50-60 dB(A) at this distance. The sound level usually permitted in Sweden, for example for noise from industrial plants, is 35 - 40 dB(A). This implies that the noise from the turbines is far too high, maybe with as much as 15 - 20 dB.

Comparisons of measured indoor levels with criteria

The reason for the measurements presented in Figure 1 was vigorous complaints on the low-frequency noise. However, the levels are very low compared with the criteria proposed in Ref. [4], see Figure 2. It can also be mentioned that a number of uninfluenced persons (including the present author) visited the house during some of the measurements and that these persons commented unfavourably on the thumping noise.

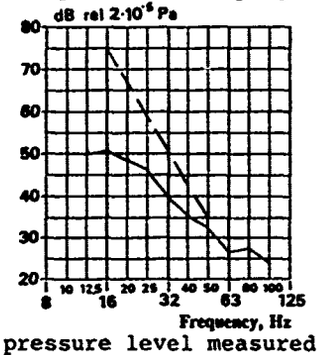

Figure 2. The sound pressure level measured inside a house at Maglarp (———) and the perception threshold (- - -) from Refs. [3-4].

MODULATION OF BROAD-BAND AERODYNAMIC NOISE

The amplitude modulation of the broad-band aerodynamic noise is clearly perceived when standing close to a unit. The main reason for this modulation is thought to be the varying distance to the sound sources during the rotation of the rotor. It should be noted, however, that if the modulation really is due to this effect, then the modulation should decrease fairly rapidly with increasing distance from the turbine.

If a two-bladed turbine is taken as an example with a hub height of uo m and the main sources situated on the blades at a distance of 30 m (70 % of the blade length) from the hub, it is seen from Figure 4 that the modulation decreases rapidly with increasing distance from the turbine. It is also seen that the modulation in the crosswind direction decreases more rapidly with distance than the modulation in the downwind direction.

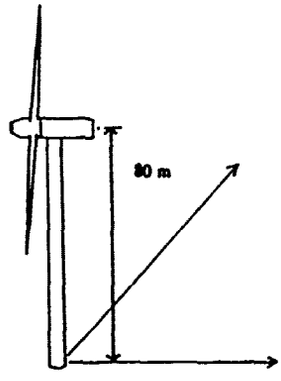

Figure 3. Configuration assumed for calculation of periodic amplitude modulation.

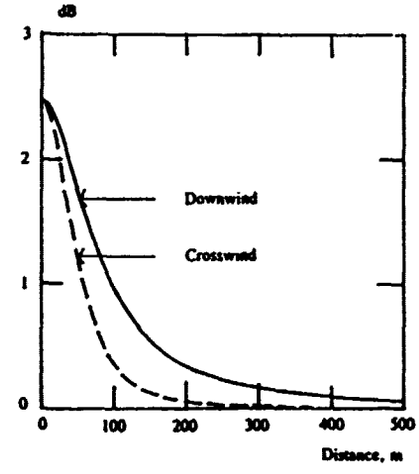

Figure 4. Calculated periodic amplitude modulation (peak-to-peak).

In practice, some random amplitude modulation will always be present due to the turbulences in the air. It could be expected that this effect should be more pronounced in the downwind direction as the sound rays then must travel through the wake of the turbine and the tower.

Results from measurements carried around at a prototype situated at Näsudden are shown in Figures 5-8. The microphone was in this case placed on the ground. These Figures apply to the broadband aerodynamic noise only; some mechanical noise in the form of pure tones were present during the measurements but have been filtered away before the analysis. The modulation spectra have been determined from the A-weighted sound pressure, and are expressed in dB re the equivalent (long-time RMS) A-weighted pressure. This implies that the Figures show the RMS-value of the modulation, not the peak-to-peak value as in Figure 4. An analysis time of 16 s was used (a longer time tends to blur the results). The measurements and the analysis procedure are discribed in detail in Ref. [5].

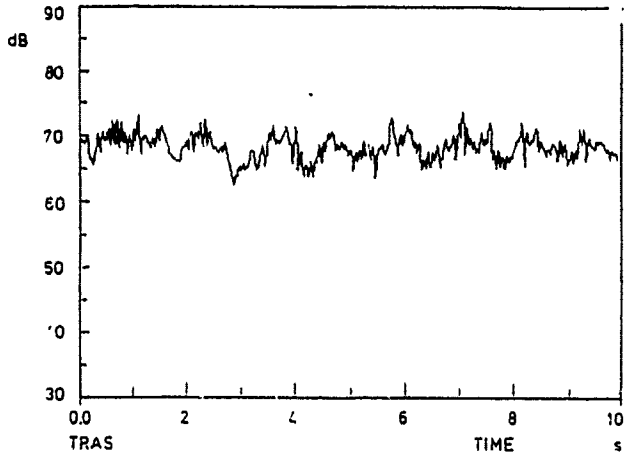

Figure 5. Measured sound level at a point 114 m downstream the wind turbine at Näsudden. Wind speed at hub height: 13 m/s.

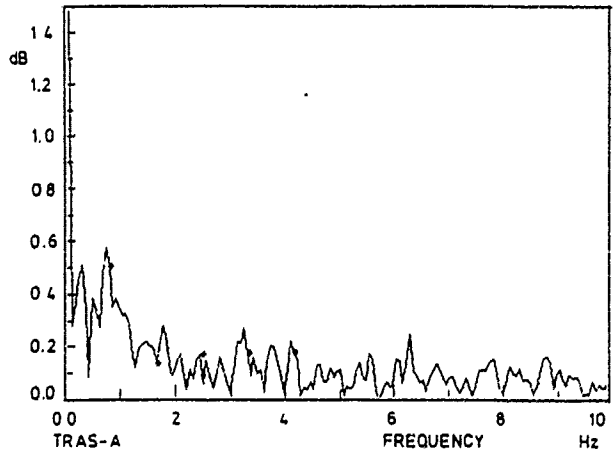

Figure 6. The modulation spectrum of the signal in Figure 5. The modulation is expressed in dB re the equivalent pressure. Analysis time: 16 s.

The results show clearly that the discrete amplitude modulation as well as the random modulation are much smaller in the crosswind direction than downstream the tower as expected.

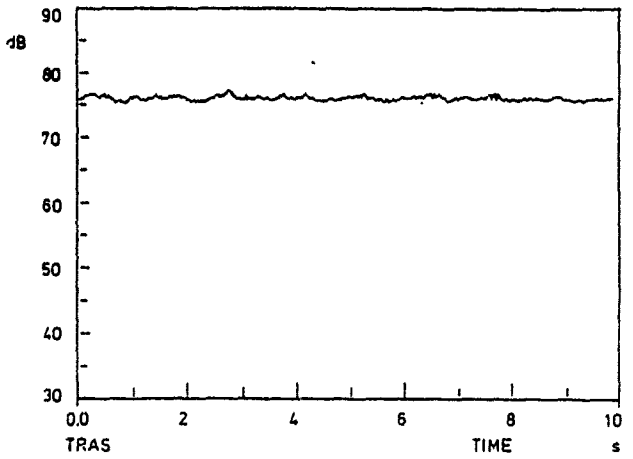

Figure 7. Measured sound level at a point 114 m from the tower at Näsudden in the crosswind direction. Wind speed at hub height: 17 m/s.

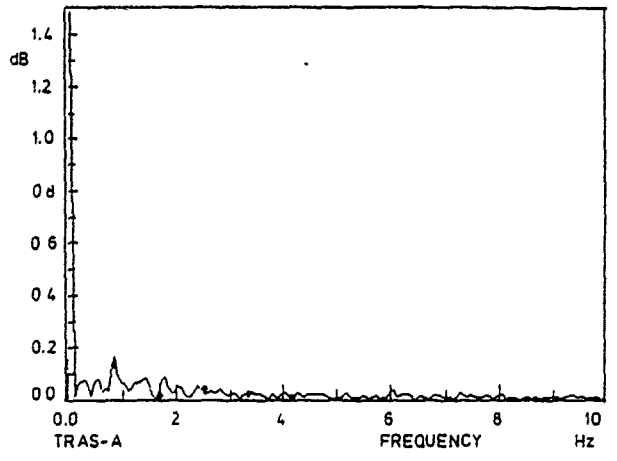

Figure 8. The modulation spectrum of the signal in Figure 7. The modulation is again expressed in dB re the equivalent pressure.

MECHANICAL NOISE

Noise sources

The mechanical noise has in many cases been found to be dominated by noise generated in the gearbox. Thus, the design and construction of the gearbox will affect the noise level inside the nacelle and hence also the needed sound insulation of the external walls of the nacelle. It should also be remembered that the structureborne sound contribution from sources of this type is often taken as proportional to the airborne sound generation. This approach seems reasonable as a first-order approximation and is very useful as source data on the structureborne sound are, in general, impossible to achieve. This implies that the type of gearbox will affect the measures against structure-borne sound as well.

A number of factors influence the sound generation of a gearbox. Among the more important ones are

- type of gearbox
- operation conditions
- the detailed design of the gearbox
- production factors
- installation

Due to the space restrictions, only the first one of these items will be discussed here; a discussion of the remaining factors can be found in Ref. [6].

The gearbox in a wind turbine unit must be able to cope with heavy loads and a high RPM increase. For this reason, planetary gears are used in the main. In the Swedish prototype at Näsudden the planetary gear is connected to a supplementary bevel gear for the last gearshift nearest to the generator, as the generator has a vertical axis.

Planetary gears are comparetively silent. The emitted air-borne sound can, as a first approximation, be taken as a function of the transmitted mechanical power alone, Ref. [7]:

$$L_{WA} = 87.7 + 4.4\log(P). \qquad (1)$$

In this empirical equation, L_{WA} is the A-weighted sound power level in dB(A) and P is the transmitted mechanical power in kW.

It should be noted that this relationship is valid only for cogs with an inclination of at least 20^{o}. Some influence of the sound radiated from the foundation (steel or concrete) is thought to be included in the formula; however, no quantitative information is known.

A comparison of the measured airborne sound generation by the gearboxes of the two Swedish prototypes at Näsudden and Maglarp with the corresponding result from equation (1) is presented in Table 1.

Table 1. The A-weighted sound power level (air-borne sound only) in comparison with the result from Eq. (1).

	Näsudden	Maglarp
Calculated	102	103
Measured	100	105

This agreement is thought to be very good in view of the many parameters not included in equation (1).

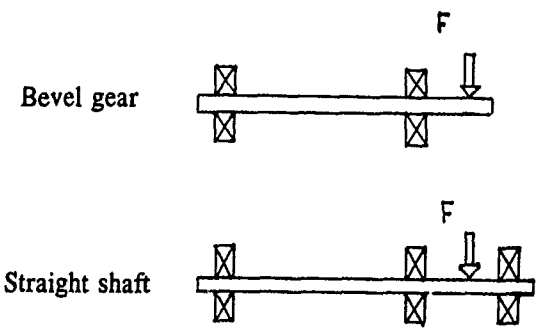

Figure 9. The mobility of the shaft of a bevel gear is higher than that of a straight shaft.

Bevel gears are used in some types of wind power units. No experimental or theoretical basis for the calculation of the generated sound power from a bevel gear has been found in the literature. However, a rough estimate of the sound generation of a bevel gear in comparison with a straight shaft is easily made. In the case of a bevel gear, one of the gearshaft ends cannot be mounted in bearings. The bending moment attached to that end is therefore transferred to the gearbox principally by radial forces on the bearings, see Figure 9.

The mechanical mobility is, for sufficiently high frequencies, four times that of the straight shaft, see e g the book by Cremer, Heckl and Ungar, Ref. [8]. This implies that the acoustic power transmitted into this shaft is also four times that in the case of a straight shaft, provided that the external force is the same. The corresponding difference in decibels is 6 dB.

Other noise sources, such as generator, hydraulic equipment and fans are comparetively easy to control with conventional measures. Some recommendations are given in Refs. [6-7].

Airborne sound insulation

Some interesting results on the airborne sound insulation of the nacelle has been obtained at the Näsudden unit. The nacelle is in this case load-bearing and consists of 15 mm steel.

These measurements were carried out on the parked unit. The interior of the nacelle was excited by a loudspeaker using pink noise, 50 - 2000 Hz. The sound pressure level inside the nacelle was measured with a rotating microphone boom. The sound pressure level outside the nacelle shell was obtained at a distance of 2 - 3 m, with the microphones mounted on rods which were held by the measuring personnel standing on the top of the roof and on a platform beside the nacelle. The sound reduction index R is evaluated as

$$R = L_i - 6 - L_o + 10\log(S_1/S_2), \qquad (2)$$

where L_i and L_o are the sound pressure levels in the generator room and outside the nacelle, respectively, and where S_1 is the area of the transmitting surface and where S_2 is the area of the measurement surface outside the nacelle.

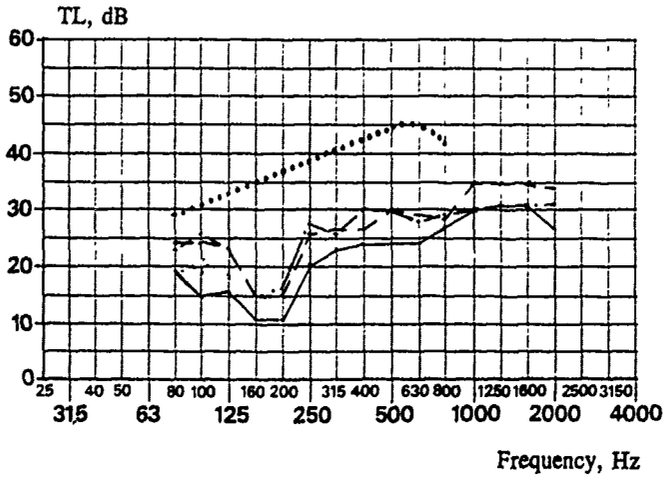

Figure 10. Sound reduction indeces. ------, from measurement points above the nacelle roof; - - -, from measurement points outside the nacelle wall; -·-·-, from measurement points below the nacelle; ·····, calculated for the forced response.

The result is given in Figure 10. The sound reduction index is here refered to the surface S_1 as seen from the interior of the nacelle. It is seen that the sound reduction index is much lower than the curve calculated for the forced response. The main reason for this discrepancy is thought to be the influence of a resonant structural response. It should also be noted that if the resonant response is important, the area of the radiating surfaces on the outside of the nacelle can be much larger than the area seen from the inside of the nacelle.

SOME MEASURES ADOPTED BY THE SWEDISH WIND POWER INDUSTRY

The main interest of the Swedish wind power industry is focused on units in the megawatt class. The noise reducing measures applied by the Swedish industry on new units and projected units can be summarized as follows (Ref. [9]):

1. Double or variable RPM are used in order to reduce the noise during low wind conditions.

2. A separate frame is used for the power line instead of a self-supporting nacelle.

3. Bevel gears are avoided.

4. High-quality gear boxes are chosen so that additional sound reducing layers on the nacelle can be avoided.

5. The interior of the nacelles are fitted with sound absorbing materials.

REFERENCES

[1] S Ljunggren: A Swedish Solution to the Noise Problem: Wind Turbines with variable RPM. Chapter 7 in D T Dwift-Hook (ed): Wind Energy and Environment. Peter Peregrinus Ltd, 1989.

[2] S Ljunggren: Airborne Sound Insulation of Thin Walls. J. Acoust. Soc. Am. 89 (5) 1991, 2324-2337.

[3] B Simonsson: Bullermätningar vid vindkraftverk Maglarp, Skåne (Noise Measurements at the Maglarp Wind Turbine). IFM Akustikbyrån TM 7.676.01, 1984 (unpublished report in Swedish).

[4] K P Shepherd: Detection of Low Frequency Impulsive Noise from Large Wind Turbine Generators. NASA CR-172511, 1985.

[5] S Ljunggren: Analysis of the Environmental Noise Situation around a Large Swedish Prototype Wind Turbine. FFA TN 1988-16.

[6] S Ljunggren and M Johansson: Measures Against Mechanical Noise from Large Wind Turbines - a Design Guide. FFA TN 1991-26, 1991.

[7] Anon: Emissionskennwerte technischer Schallquellen. VDI 2159, 1985.

[8] L Cremer, M Heckl and E E Ungar: Structure-Borne Sound. Second Edition. Springer-Verlag, 1988.

[9] B Göransson: Personal communication, 1991.

SECOND INTERNATIONAL CONGRESS ON
RECENT DEVELOPMENTS IN AIR- AND
STRUCTURE-BORNE SOUND AND VIBRATION
MARCH 4-6, 1992 AUBURN UNIVERSITY, USA

NOISE FROM WIND TURBINES, A REVIEW

H.W. Jones,
Hugh W. Jones & Associates Limited,
374 Viewmount Drive,
Tantallon N.S. B0J 3J0
Canada

ABSTRACT

This paper reviews the information presently available on wind turbine noise from both horizontal and vertical axis machines. In particular the following points are discussed: the noise sources, their origins and their measurement, the measurement and prediction of noise levels at the boundary of the turbine sites and local communities, studies of the impact of the noise on communities.

Some discussion of the work of standards groups concerning such noise problems is given.

A REVIEW OF SOME OF THE LITERATURE RELATING TO WIND TURBINES

The literature concerns itself with the following aspects of noise from wind turbines:

i) the sources of aerodynamically generated noise,
ii) the mechanical sources of noise,
iii) statements of noise measured at various wind turbine sites and attempts to correlate the noise levels with various parameters,
iv) the impact of the noise on individuals and the community, and
v) the standardization of noise measuring procedures.

Generally the literature relates to two types of turbine, the horizontal and the vertical axis types of machine. There are some differences in the special circumstances of such machines but also much that is common to both types.

SOURCES OF AERODYNAMICALLY GENERATED NOISE

The sources of aerodynamic noise can be divided into three types. The first is the aerodynamic noise due to the steady state blade loads i.e. the source of noise from the blades which is generated as if the blade was moving in an undisturbed atmosphere. This was treated by Gutin [1] originally for propeller noise and was applied to wind turbines by Martinez et.al. using the work of the authors listed in [2 through 7]. It can be shown, refer to figure 1, that the acoustical pressure is given by:

$$p(r, z_i, t) = \sum_{s=-\infty}^{\infty} P_s(r, z_i)\, e^{-i\, s\, B\, \Omega\, t} \qquad (1)$$

where P_s is the s'th harmonic of the pressure signal, B is the number of blades and Ω is their angular velocity, t being time.

A second consideration in deriving the noise pressure relates to the earth's surface boundary layer, as a result the noise source is not symmetrical about the axis of rotation. Martinez et al. derived the acoustic pressure as:

$$\Delta p(r', \gamma, t) = \sum_{q=-\infty}^{\infty} B_q^l(r')\, e^{\frac{2\pi i \gamma q}{\Gamma'}} * \sum_{s=-\infty}^{\infty} A_s(r') \exp\left[\frac{2\pi i s B(\gamma - \Omega t)}{\Gamma}\right] \qquad (2)$$

where $B_q^l(r')$ are the Fourier coefficients of the thrust at a particular radius and angle of rotation.

A third effect is associated with the tower wake, see figure 2. The passage of the blade through the wake leads to an impulsive noise which is a well recognised characteristic of wind turbine noise. The noise due to this source is given by:

$$p\left[r, \frac{z}{r}, \frac{y}{r}, \frac{r'}{r}, t\right] = \frac{iMR}{2\pi r c} \int_{-\infty}^{\infty} ds\ \ sL_o(s)\ \ D\left[s, \frac{z}{r}, \frac{y}{r}, \frac{r'}{r}\right]\ \ \exp\left[\frac{is(Mr-t)}{1-M\frac{y}{r}}\right] \qquad (3)$$

where M is $\Omega R/c_o$, R is the rotor radius, L_o is the unsteady lift amplitude due to gusts (c.f. Filotas ref [6]) and D is a directivity function.

These equations have been applied to a DOE/NASA MOD-1 wind turbine and some predictions of the theory outlined above are given in figures 3 and 4. Some detailed considerations of the factors outlined above have been given, particularly that relating to the shape of the aerofoil used in the blades. The bluntness of the trailing edge has an effect on the higher frequency noise output of the blade as is shown in figure 5, reference [8]. Figure 6 shows the contributions made by the different noise mechanisms to the overall output of the aerodynamic noise sources.

The forgoing treatment has been applied particularly to wind turbines with horizontal axis. The alternative type uses a vertical axis. The theory of Gutin and others which was referred to clearly applies directly to these machines. The detailed work required to develop computer programs for the noise prediction does not appear to have been accomplished. However noise and vibration measurements have been made in some detail on several sizes of machine (up to 500Kw [9]).

Another source associated with the aerodynamic noise arrises from geometry changes in the machine due to oscillatory bending and twisting effects [10]. Control of these effects is, of course, essential to the structural integrity of the machine but the study of the actual relation of these vibrations to noise emission does not appear to have been attempted.

MECHANICAL NOISE

Reference [12] provides an excellent example of a study of the noise arising from the gearbox of a

vertical axis machine. The gearbox with one of the most obvious noise sources. The investigation and control of such noise is a well established subject. Given that the usual practices are followed and that the manufacturing and assembly quality is satisfactory then it follows that the noise generating artifacts will be minimized. Similarly the matter of the vibration of the gear box housing needs addressing so that it does not allow significant coupling to the air. The nacelle, or in the vertical axis case the building, enclosing the machinery should be designed as an effective acoustical enclosure. As the noise levels from aerodynamic sources are well known it is quite possible to provide a total machinery noise level criterion which when applied to the housing can lead to noise immission which is less than the aerodynamic equivalent.

Mechanical vibration can be transmitted to the supporting structure and reradiated. It is therefore necessary to isolate the structure from such sources and this is well understood in engineering practice, reference to any of the publications concerned with noise control engineering will illustrate this point [13,14,15].

CORRELATION AND INTERRELATION OF EXISTING MEASUREMENTS

Papers have been written which propose methods of correlating the noise performance of wind turbines. Some of these are concerned with developing a prediction method which fits at least one set of circumstances. Reference [16] in which data from 26 different horizontal axis wind turbines is presented. An empirical relationship gives noise pressure in terms of the area of the rotor area, this equation is given below:

$$L_{wr} = 11.4 \log A_r + 73.4 \qquad (4)$$

where: L_{wr} is the source level in dBA and A_r is the area swept out by the wind vane.

The other reports [17 - 20] are based on wind turbine data prediction methods which are similar to the above, in the main with, the exception of reference [19]. In that reference Viterna describes a noise prediction method for horizontal axis wind turbines which are based on some experimental data and a "code" which is presented. Kelly et. al. in reference [17] present some interesting data because this one of the references to the swishing noise effect which is of low frequency i.e. about 2 Hz., c.f. figure 7 (after van der Borg). Sound level meters do not measure the modulation of the noise at these frequencies easily. Recently Holley and Bell [11] considered the problem of low frequency sound from wind turbine arrays. They have recommended the use of a low pass filter (for frequencies below 100Hz.) which is described in [28] and an impulsive sound measurement. Here impulsivity was defined as "the difference between the levels from standard impulse hold circuits (c.f. ANSI S1-4-1983) and the more usual C weighted rms levels". Commentary is given in Holley and Bell's paper on the application of such methods to multiple turbine sites.

Martinez et.al.,[2] presented a study of the low frequency and impulsive noise from, horizontal axis machines using the aerodynamic theory of Gutin referred to earlier. Some experimental data is presented and predictions are given for distances of 1km. from the site. It is necessary to take ground impedances effects into account in evaluating noise levels at large distances from the source [21]. It is noted that the suggestion has been made that the criterion for permissible noise levels should take account of the noise from wind in local trees and the noise in houses.

STANDARDIZATION AND NOISE MEASUREMENT PROCEDURES

Many standards probably apply to the noise measurements from such machines but this commentary has confined itself to four only [refs 22-25]. The standards are clear in their statement of the measurements to be made but in the case of references [24 and 25] in conflict with each other. Two

purposes can be supposed to be served by the standards. First, the standard can provide a method of measurement which can be used to compare the noise emission properties of different machines. Second, the standards can provide a method of measurement which allows for the assessment of the impact of noise on those who live in the neighbourhood of the machines. These are separate functions, at least in so far as their methodology is concerned. It might for example be of interest to various manufactures and operators of such machines to know of gearbox noise and the additional costs, if any, of building suitable enclosures for the generators and gearboxes. This information is not of direct interest to those concerned with town planning.

The development of standards which can provide the required information for planning has a fairly long history. The development of the I.S.O. R 1996 standard was the culmination of many years of effort and replaced an earlier standard which was considered to be inadequate by some countries. Many countries have accepted that standard and used it where appropriate as the basis of their national standard. It might be that a revision of this standard is now required to account for the low frequency and impulsive noise referred to earlier.

A comparison of some of the standards is given in table 1 below:

Table 1 -- A comparison of the standards for noise measurements for wind turbines

Standard or Draft	Microphone Height	Weight /filter	Microphone Positions	Measurement units	Comments
ISO-R1996	1.2 mtrs.	A & tonal	various	L_{eq}	The standard provides some detail on the effects of tonality and topography and refers to day and night noise levels.
CSA Z107. 53-M1982	1.2 mtrs.	A only	at site boundary	dBA	This standard is designed primarily for a walk around with a hand held sound level meter it provides a somewhat superficial survey method. Unfortunately it is the Canadian standard.
CSA F417 M1986	1.5 mtrs	A only	30mtrs or 1.5 rotor	dBA	A specification for basic sound level measurements at 1.5 m above ground level.
IEA[4] (AWEA/ ANSI)	on ground	A & 1/3 oct. & tonal	see note right	dBA, L_{Aeq}, L_{10},L_{90}, L_{95}	This draft standard is more comprehensive than any of the others. A formula for the placing the microphone is given in the document.

As has been mentioned, noise arises from two sources aerodynamic and second gearbox and related machinery noise. The methods given above give a rough and ready indication of the aerodynamic noise. It would be better however to use a measurement method which characterises the low frequency effects which have been described earlier. Information on the directivity of the sources needs to be obtained to allow predictions of noise levels appropriate to the particular site. Some sort of standardised prediction method for the treatment of the losses during transmission might also be appropriate.

The measurement of noise from the generator and gearbox housing requires different techniques and on the occasion this has been done it has included the use of sound intensity measurements around

the nacelle [26]. Such data should provide a basis for subsequent design modifications if they are felt to be required.

It may, perhaps be concluded that the present measuring protocols leave something to be desired and that the use of them does not describe the noise in a way which is useful to the future design processes.

ASSESSMENT OF THE NOISE IMPACT ON THE COMMUNITY

Briefly, there appears to be reason for supposing that the impact of noise on the community should be the subject of further study. It is noted that low frequency noise can cause vibration in dwellings and thus cause additional annoyance. The work of Kelly [17] and others e.g. [27] seems to provide a foundation for assessment work which should perhaps have a more substantial base.

CONCLUSION

This paper has attempted to review some of the major aspects of noise from wind turbines. The review has touched on aerodynamic and mechanical noise mechanisms. Some discussion of measurement techniques has been given but detailed measurements of a research nature have been omitted for reasons of brevity. A limited commentary on standards has been given. Some discussion has been given on annoyance factors and the measurement thereof.

Clearly work is needed on the latter topics and it may be that a closer liaison between wind turbine groups and the noise control engineering community might be desirable.

REFERENCES

1. L.K.Gutin N.A.C.A. TM 1195,1948
2. R.Martinez et.al. Trans A.S.M.E. 104,124-130 1982
3. P.M.Morse and K.U.Ingard."Theoretical Acoustics" McGraw Hill 1968 737-747
4. R.H.Miller Wind Energy Conversion Vol.II ASRL TR-184-8 Dept. Aero and Astronautics MIT Sept.1978
5. T.Wolf and S.E.Widnall Fluid Dynamics Res Lab. Report 78-2 MIT 1978
6. L.T.Filotas UTIAS Report 139 U.Toronto Oct. 1969
7. J.M.Savino et.al. DOE/NASA/1028-78/17 NASA TM-78853 Apr.1978
8. H.Klug et.al 1991 unascribed. Deutsches Windenergie-Institut (DEWI)
9. H.W.Jones et.al. Proc. Inter-Noise 90 Gothenburg Sweden INCE Poughkeepsie N.Y.
10. T.G.CARNE Sound and Vibration Nov.1989
11. W.E.Holley and B.F.Bell Low Frequency Noise from Wind Turbine Arrays unascribed U.S.Windpower Inc Livermore Ca.
12. G.Krishsnappa Noise Control Eng.J.22,No.1 18-24,1984.
13. Proceeding of International Conferences on Noise Control Engineering for any of the last 10 years
14. Noise Control Engineering Journal
15. L.L.Beranek Noise and Vibration Control, Inst. of of Noise Cntrl. Engrs., Poughkeepsie, N.Y. 1988.
16. N.J.C.M. van der Borg & W.J.Stam The acoustic source power of wind turbines. Petten Sept 1987.
17. N.D.Kelley et.al. Trans ASME 114/vol 104 May 1982.
18. W.G.Allen Windfarm noise issues and impacts. unascribed.
19. L.S. Viterna The NASA-LERC wind turbine sound prediction code. unascribed.
20. A de Bruin et.al. European Wind Energy Conf 1984, 889-895.
21. T.Embleton et.al. JASA 59 (1976) 267 et. seq.
22. ISO R1966

23. CSA Z107.53-M1982 PROC.FOR SURVEY OF SOUND DUE TO INDUSTRIAL INSTL.OR COMM.ACTIVITIES
24. Acoustics, measurements of noise emission from wind turbines Intl.Energy Agny. Program for R&D on wind energy conv.
25. Draft CSA standard on wind turbines
26. N.van der Borg Energy Research Foundation Petten, Netherlands. unascribed 1990.
27. A.de Bruijn et.al European Wind Energy Conf.1984 889 et. seq.
28. Proc. for Measurement of Acoustic Emissions from Wind Turbine Generator Systems. AWEA Standard 2.1. Am. Wind Energy Assn. Washington D.C.

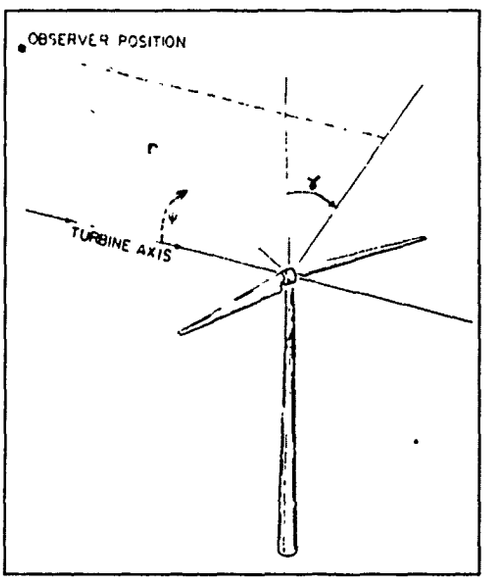

Figure1 -- Coordinate system for eqns. 1-3. (after Martinez et.al)

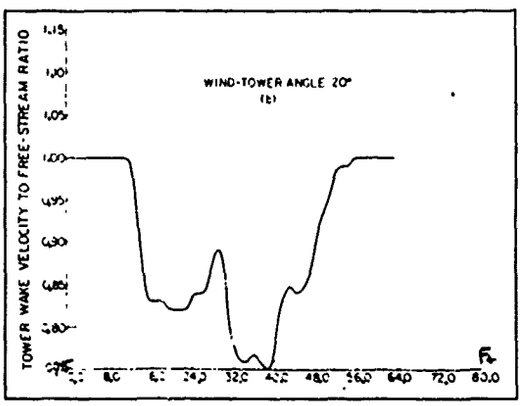

Figure 2 -- Tower wake velocity ratios v/s distance from tower for MOD 1 machine. (after Martinez et.al)

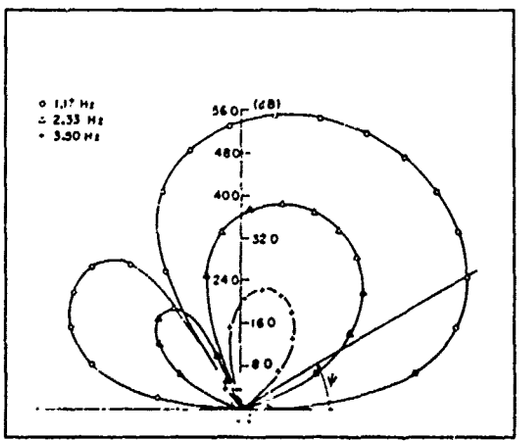

Figure3 -- Predicted sound levels for first 3 harmonics at 1Km from MOD 1 tower at varoius frequencies psi=65° linear ground shear 8mph, free stream 35 mph, cap ohmega=35 rpm. (after Martinez et.al)

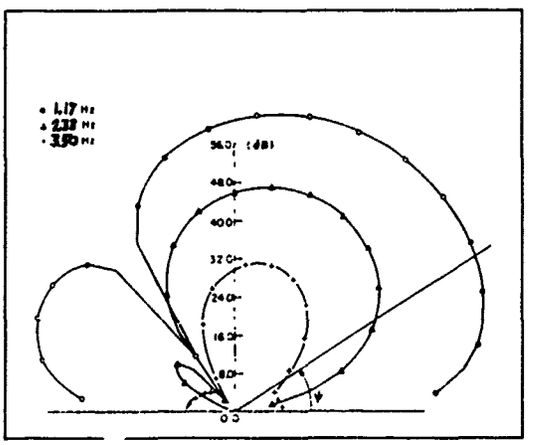

Figure4 -- Predicted sound levels for first 3 harmonics at 1Km from MOD 1 tower at various frequencies psi=65^{o} otherwise as fig. 3. (after Martinez et.al)

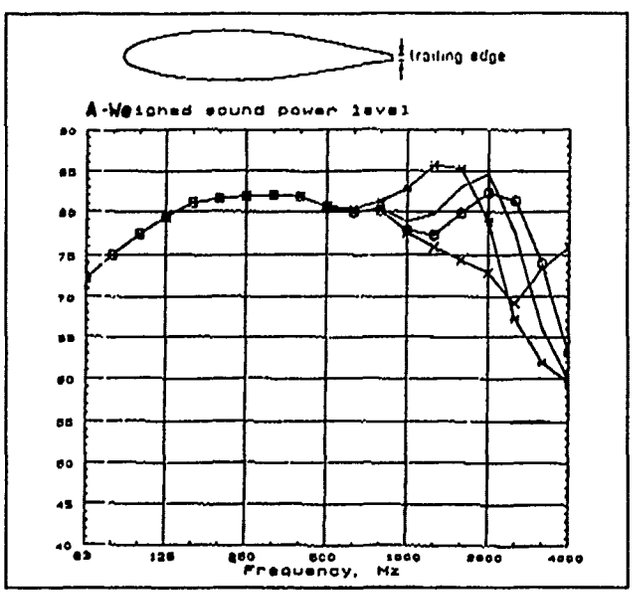

Figure 5 -- Noise profiles for an aerofoil based on 1/3 octave measurements showing effect of trailing edge bluntness.

x : 1mm.,

o : 2mm.

-- : 3mm.,

* : 4mm.

(after H.Klug et. al)

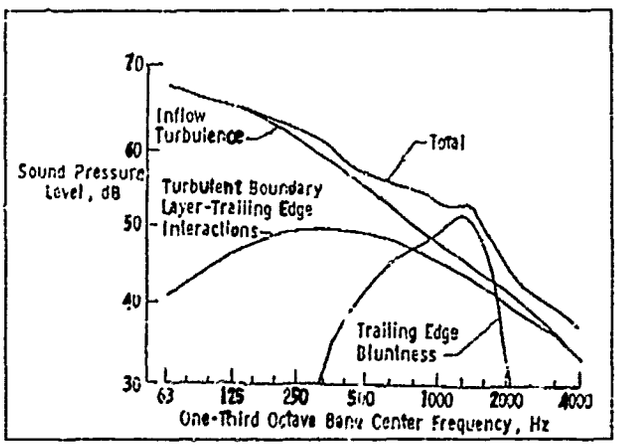

Figure 6 -- Typical contributions from various aerodynamic noise sources for an aerofoil. (after H.Klug et.al)

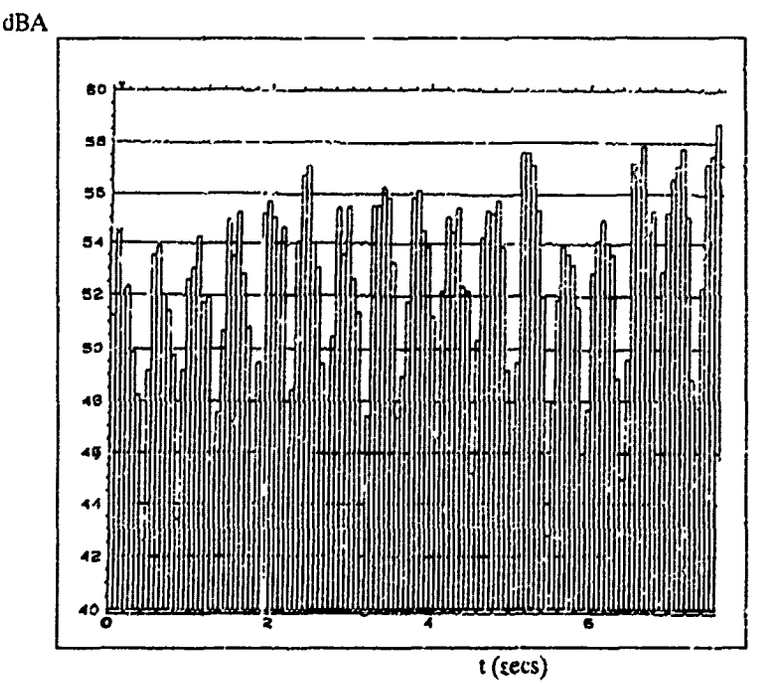

Figure7 -- Impulsive nature of sound from a wind turbine. (after van der Borg)

SECOND INTERNATIONAL CONGRESS ON
RECENT DEVELOPMENTS IN AIR- AND
STRUCTURE-BORNE SOUND AND VIBRATION
MARCH 4-6, 1992 AUBURN UNIVERSITY, USA

SOUND POWER DETERMINATION OF FANS BY TWO SURFACE METHOD

Kalman Szabo*, Gyula Hetenyi and Laszlo Schmidt
Ventilation Works
Epitesz 8. 1116 Budapest
Hungary

ABSTRACT

The paper will be focussed primarily on the measurement of sound power of fans to be tested by two surface method and in duct method. The most useful noise emission characteristic is the sound power level of the source. One of the best techniques being used now is called the two surface method. In this procedure , 1/3 octave band sound preasure leveles are measured on the surface of two hypothetical parallelepides over the machine being tested. Measuring results will be compared with other ISO method (Determination of sound power levels of ducted fans).

Introduction

A wide variety of wave phenomena can be observed in nature. There are a number of features common to all kinds of waves.
Particular attention is devoted to sound power , sound intensity, sound pressure, and decibel scale because of their importance in sound monitoring and measurement as well as understanding the two measuring methods
Determining noise source by its power level distribution was written a lot of paper including one of present authors as well.
Main goal of measurement was to reduce the noise at the refuse burning furnace near Dorog town.
Fan noise characteristics, too were measured at the testing hall of ventilation works that will be showed at the poster session.

* At present Budapest Transport Company (BKV Akacfa 15
1072 Budapest)

Sound Power Level

Employing the decibel scale, sound power level, L_W, is defined by

$$L_W = 10\log\frac{W}{W_0} \qquad (1)$$

where W is the power in watts of the sound source, and W_0 is the reference power level, usually 10^{-12} W.

Sound Intensity Level.

A sound wave may be described either in terms of the displacement of air particles produced at a point in space or in terms of the variation of air pressure at the same point. The air pressure rises above and falls below atmospheric pressure with the same frequency as the displacement. The maximum amount by which the pressure differs from atmospheric pressure is called the pressure amplitude, P. In general, P is directly proportional to the displacement amplitude and inversely proportional to the wavelength of the wave.

The power per unit area in a sound wave equals the product of the excess pressure and particle velocity. Averaging this product over one cycle, the result for the sound intensity is

$$I = \frac{P^2}{2\delta v} \qquad (2)$$

where P is the maximum pressure amplitude in N/m^2, δ is the average density of the air (1.2 kg/m^3 for air at 20 C), and v is the propagation velocity of the wave.

Sound intensity level, L_I, is defined by

$$L_I = 10\log\frac{I}{I_0} \qquad (3)$$

where I is the sound intensity in W/m^2 and I_0 is the reference intensity, usually taken as 10^{-12} W/m^2.

On this scale, the threshold of hearing ($I=I_0=10^{-12}$ W/m^2) occurs at

$$L_I = 10\log\frac{I}{I_0} = 10\log 1 = 0 \text{ dB} \qquad (4)$$

Similarly, the threshold of pain ($I=1$ W/m^2) occurs at

$$L_I = 10\log\frac{1}{10^{-12}} = 10\log(10^{12}) = 120 \text{ dB}. \quad (5)$$

Sound Presure Level.

According to Equation (2), the acoustic intensity, is directly proportional to the maximum acoustic pressure squared. Based on this relationship, sound pressure level, L_p, is defined by

$$L_p = 10 \log_{10} \frac{P^2}{P_0^2} \quad (6)$$

wher P is the maximum acoustic pressure in N/m^2, and P_0 is the reference acoustic presure.

Relationship among Sound Power, Sound intensity, and Sound Pover Level

Consider a uniform spherical wave propagating from a point source. (Most sources can be considered as point sources at distances that are large compared to the size of of the source itself.) Consider a point source of power W emitting periodic waves in three dimensions. Energy from the source is assumed to be transmitted equally in all directions. At a distance r from the source, the energy is uniformly distributed over a sphere of area $4\pi r^2$. The intensity I at this distance from the source will be

$$I = \frac{W}{4\pi r^2} \quad (7)$$

According to the above equation,

$$W = I(4\pi r^2) = IS \quad (8)$$

where S is the surface area of a sphere in m^2. Subtitution of this expression into the equation (1) leads to

$$L_W = 10\log\frac{W}{W_0} = 10\log\frac{IS}{I_0 S_0} = 10\log\frac{I}{I_0} + 10\log\frac{S}{S_0} \quad (9)$$

where S_0 is the area of a reference sphere, taken as $S_0=1m^2$. Thus,

$$L_w=L_i+10\log S \qquad (10)$$

From this relationship, the sound intensity level, L_i, can be determined at a distance r ($S=4\pi r^2$) from a source of sound power level, L_w.
The following result can be seen after the substitution

$$L_i = 10 \log \frac{p^2_{rms}}{p_{0_{rms}}} + 10 \log \frac{p_{0_{rms}}}{\delta v I_0} \qquad (11)$$

Using $p_{0_{rms}}=2*10^{-5}$ N/m^2, $\delta*v=412 \frac{kg}{m^2 sec}$ (for air at 1 atm. and 20^0C), and I_0 W/m^2, (p_{rms} a time-averaged pressure called the root-mean-square, measuring it by sound meter.)

result in

$$L_i = L_p - 0.13 \qquad (12)$$

sound pressure level are equal in magnitude under these conditions.

Sound is a highly variable component of the total human environment

As a result, a consideration of the instrumantation necessary to obtain more meaningful data about both the source and the environment is required. With respect to both simplicity and adequacy for characterizing human response, a frequency-weighted sound le- In order to use available standardized instrumentation for direct measurement, the A-frequency weighted is the only suitable choice at this time.

Measurement of the Sound Power Level.

Many state , and governments have written noise control codes listing maximum permissible sound levels crossing industrial and construction site boundaries into residential and commercial zones. They state that the maximum noise radiated by a machine must not exceed a certain level, when the noise is measured according to a prescribed test code. Permissible noise may be stated in terms of overall A-weighted sound pressure levels, octave-band sound pressure levels, one-third octave-band sound pressure levels, or a combination of these - all measured at fixed distance from the machine , under known or measurable room conditions. Alternatively, maximum noise emission may be stated in terms of sound power, or sound power level - independent of distance from the machine and independent of room environment.

These featuress make sound power an excellent way to express the noise rating of a machine.

Unfortunetly, most industrial machinery is installed in locations whereit is difficult to determine sound power. One of the best techniques now being used is called the two-surface method.

In this procedure, sound pressure levels are measured on the surfaces of two hypothetical parallelepipeds over the machine being tested.

Also, the sound pressure levels measured on the surface of S_2 will be less than those measured on surface S_1 because they are farther away from the machine. From the difference in average sound pressure levels , and the ratio of the areas of the two boxis, a correction can be determined so that sound power level can be calculated by the equation or by the diagram [1]

$$L_W = SPL_1 + 10 \log S_1 - C \qquad (13)$$

where

L_W = the sound power level re 10^{-12} watt.

SPL_1 = the average sound pressure level measured on parallelepiped S_1, in decibels re 20 mikroPa.

S_1= the area of parallelepiped S_1, in m^2.

C = the correction, from Fig wich can be seen in Ref [1, page 192]

(or according to [1] in book entitled Machinery Acoustics, Diehl George M. New York: Wiley-Interscience, 1973)

Measurement according to ISO/DIS 5136

This International Standard specifiies a method of testing ducted fans to determine the sound power radiated into an anechoically terminated duct on the inlet and / or outlet side of the equipment This International Standard may also apply to other aerodynamic sources such as boxes, dampers and throttle devices. The sound power radiated into the test duct by the fan as specified in this International Standard.

The test set-up consists of the fan to be tested, an intermediate duct, a terminating duct, if necessary, the test duct with anechoic termination, the instrumentation. Suitable provision shall also be made for maintaining and checking the operating condition of the fan. The aerodynamic performance characteristics may be measured on a separate set-up.

In the case of the suitable sampling tube it is posible to fulfill that the turbulence noise should be supressed by 10 dB at least in the frequency range of interest as compared with a noise cone. Posibilities of the sound level meter or other amplifier used to amplify the microphone signal including frequance analyser and graphic level recorder or other read-out devices should be taken into consideration the overall requirements of IEC 651.

Conclusion

Our measurements were partly performed by instrument (FFT spectrum analyzer, Typ: PSA) manufactured by Hungarian Pont Manufacturing Co (1196 Budapest Rakoczi 110 or telex 22-7783 pont h) This instrument is suitable for low cost measurements. (PSA-100

performs three main functions: narrow band analysis, constant relative bandwidth analysis (1/3, 1/1 octave) and true RMS digital voltmeter)
Old Bruel and Kjaer instruments (manufactured in Denmark) were also used for our measuring task. Measuring results were evaluated by IBM PC using Lotus program. Detailed pictures will be showed at poster session.
Results concerning the low frequency parts were different regarding the different measurin method.
It is necessary to remark that both methods can be used for evaulating the muffler designed by ventilation works.
According to result in connection with muffler it can be easily reached 10-15 dB noise reduction above 250 Hz applying the Silka product (Hungarian trademark).
Earlier, M. J. Crocker [2] measured the sound power of a vibrating cylinder using the surface intensity method and compared it with the reverberation room method and theory. F. J. Fahy [3] used correlation technique for measurement of the acoustic intensity
According to the opinion of other authors, too [4-6] all different methods implicitly assume some idealized form of sound field created by radiation from a source in order that sound pressure level measurements can be interpreted in terms of energetic quantities (power, intensity, etc). According to our experience, too, sound power and intesity measurements are the most useful methods for the noise emission investigation.

Acknowledgement

We wish to express my appreciation to Mr L. Babocsy, head of computer department (at Budapest Transport Company) for helpful support in PC program. Helpful information for Mr B. Bessenyey, sales manager of Pont Manufacturing Co is gratefully acknowledged. We have to emphasis also Mr L. Farkas and Mr G. Pekary (heads of Ventilation Works) their helpful stimulation.

References

[1] David M. Lipscomb and Arthur C. Taylor, Noise Control Handbook of Principles and Practices, Van Nostrand Reinhold Co 1978 New. York
[2] M. I. Crocker, Identification of noise sources in machines, 3rd Seminar on noise control, Szekesfehervar, Hungary Apr. 21-25, 1980.
[3] F. I. Fahy, Measurement of the acoustic intensity using the cross-spectral density of two microphone signals, J. Acoust. Soc. Am. 62, 4, (1977) p. 1057-59.
[4] G. Pleeck, Noise control in the turbine room of a power station, Noise Control Engineering, 8, 3 (1977) p. 131-36
[5] R. Guse I. Kalman and G. Mandl, Bestimmung der Schalleistung von Vielstellenmaschinen, Appl. Acoustics, Vol 12(1979) N 6 p 435-45
[6] K. Szabo, Determining noise source by its power level distribution AES 67th convention, New York, 1980 Oct. 31-Nov. 3

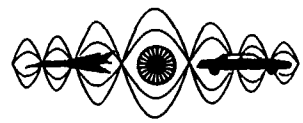

SECOND INTERNATIONAL CONGRESS ON
RECENT DEVELOPMENTS IN AIR- AND
STRUCTURE-BORNE SOUND AND VIBRATION
MARCH 4-6, 1992 AUBURN UNIVERSITY, USA

ACOUSTIC RADIATION FROM FLAT PLATES WITH CUTOUT THROUGH FE ANALYSIS

PV Ramana Murti
College of Engg.
JNTU University
Kakinada

V Bhujanga Rao
N.S.T.L.
Vigyan Nagar
Visakhapatnam

PVS Ganesh Kumar
N.S.T.L.
Vigyan Nagar
Visakhapatnam

ABSTRACT

Flat plates with cutouts of different shape and orientation are used in such applications as space, console panaling and submerged vehicles. In the present investigation, the geometry and orientation of cutouts on the acoustic radiated power of flat plates is studied. Both longitudinal and transverse, single as well as multiple, cutouts with different aspect ratios have been examined. Recourse to finite element modelling of acoustic medium is undertaken. Under the assumption of unbounded medium, the radiation efficiencies have been estimated in water medium.

Introduction

Acoustic radiation due to vibrating rigid flat plate with different sizes of cutouts (single & multiple and longitudinal and transverse) has been studied using acoustic FE analysis. This study is intended to understand the effect of cutouts on sound radiation in near and farfield distances as encountered usually in many practical applications. For illustration, in underwater acoustics, the outerhull of submersibles which is generally made of thin plates will have different type of cutouts. The near field and farfield radiation pattern of such vibrating plates is of importance from the point of view of structurally induced sonar self-noise. Similarly, some of the panellings and casings of large equipment can be modelled as plates with cutouts. A cutout in a plate of definite thickness which is assumed to be vibrating in an inviscid stationary medium influences the radiation in two different ways compared to a plate without cutouts. One direct effect is that as the surface area of radiation is decreasing due to the presence of cutout the radiating acoustic power also decreases as a function of plate area. The other effect is that there exists an acoustic coupling between the acoustic modes formed in the interior of the cutout and acoustic radiation in the unbounded space. These aspects have been discussed in this paper.

Analysis of the Problem

It is known from theory as well as from experiments that, the relation between structural vibration and radiated sound is rather complex. The general acoustic radiation problem can be formulated as boundary value problem of any arbitrarily shaped body. As boundary conditions, the normal component of velocity at any surface point of the

immersed object is given. It can be shown that a solution of this boundary value problem must satisfy the three-dimensional wave equation as well as the Sommerfeld boundary condition. In case of a plate with cutout, the exterior as well as interior boundary conditions are required to satisfy the wave equation and a superimposed solution for both exterior or interior domains is to be formulated. For any radiating surface, the well known Helmholtz Integral equation (eq (1)) gives the pressure field at any point as the surface integral of a linear combination of the surface pressure and velocity over the radiating boundary.

$$P(\bar{R}) = \int_{S_0} \left[P(\bar{R}_0) \frac{\partial}{\partial n} G\left(\bar{R} / \bar{R}_0\right) + j\omega\rho \bar{R}_0 G\left(\bar{R} / \bar{R}_0\right) \right] ds_0 \quad (1)$$

Where $G(\bar{R}/\bar{R}_0)$ is the Green's function for external and interior acoustic problem.

$V(\bar{R}_0)$ is the structural velocity.

Since the only prescribed quantity is the surface velocity, the pressure being unknown, the pressure in the acoustic field can only be determined by allowing the field point, R to approach the radiating surface and by consequently solving the resulting integral equation, i.e. Fredholm integral equation of the second kind for the unknown surface pressure $P(R_0)$. It is known that analytical solution for the general radiation problem do not exist. Several theoretical studies have been devoted to this subject and have resulted in analytical formulae which are valid only for a limited number of relatively simple source geometrics such as axisymmetric structures, cylinders, spheres and flat plates. Numerical solutions such as combined Helmholtz Integral equation (CHIEF) are conceivable but rather complex due to numerical instability problems with high demand on computer power.

Further, as with most sound radiation problems, it is difficult to evaluate the field at a distance from the source surface comparable with or much less than a source typical dimensions. The difficulty in evaluating the Helmholtz Integral for distances not comparable with source dimensions is associated with the fact that the distance, R between elementary source and the source point is generally a rather complicated function of the coordinates of the two points. This leads to errors in near field estimations. In some of the applications, as in underwater acoustics, near field radiation constitute a major source and need to be controlled. In view of these limitations, recourse is taken to acoustic FE analysis to model the flat plates with cutouts in this article.

Details of FE Analysis

The Finite Element modelling of a radiating structure can be performed by surrounding this structure with fluid domain, upon the external boundary of which a prescribed condition can be imposed. The shapes and sizes of fluid finite elements must be chosen to suit the particular geometry and frequency range being investigated.

For the purpose of present investigation, an acoustic FE package, SUNDYN (Ref. 1) developed at NSTL has been used to compute the acoustic radiation. The package essentially provides three types of acoustic finite elements, namely 1-D, 2-D and 3-D elements. The pressure is considered as nodal variable and the excitation to the acoustic model is surface acceleration. The boundary conditionsare are imposed by specifying radiation damping at the boundary surfaces. An essential restriction of this package is that the finite element size shall be limited to 0.1λ where λ is the wave length of acoustic radiation. The flat plate with cutout has been modelled using this package varying the size and orientation of the cutout. A three-dimensional acoustic finite element mesh consisting of 841 nodes and 728 elements was generated for this purpose (Fig.1). The dimensions of the plate are chosen to be 220 x 120mm. The size of the cutout was kept initially at 22 x 12mm which corresponds to 0.1 aspect ratio. Here the aspect ratio is defined as the ratio of the area of the cutout to the area of the plate. The FE analysis was repeated for various aspect ratios between 0.1 and

0.9. The direction of cutout has also been varied from longitudinal to transverse direction.for various aspect ratios. In another model of the same plate, 2 cutouts has been solved for different aspect ratios to know the effect of multiple cutouts on radiation.

In all these cases, the symmetry of the problem has been exploited by modelling only quarter of the plate and the boundary is chosen to be at a radius of 510mm. The boundary was subjected to radiation damping of the medium, i.e. water in the present case. The surface of the plate was applied with specified accelerations of 0.01 and 0.1 at frequencies of 100Hz and 1000Hz respectively which correspond to uniform velocity on the surface and the radiated pressures were computed at the two frequencies. The pressures obtained were used for estimating sound power, P and radiation Index,I using the following formulae:

$$P = \frac{\pi k^2}{\rho c} \tilde{P}^2$$

$$I = 10 \log (\sigma) \text{ where } \sigma = P/\rho c s \tilde{v}^2$$

where P is power radiated from the plate with surface area s

$\tilde{v}$ is the average root mean square velocity of the vibrating surface.

ρc is the characteristic impedance of the medium.

To check the general accuracy of the software, the noise radiated by simple geometric bodies such as pulsating sphere has been estimated and the results have shown close agreement with analytical results. During the present investigation also, pressure obtained at various radii in the far field, for which analytical solution exist for the case of a baffled plate piston, have been computed and compared with FE analysis results and discussed in succeeding paragraphs.

Results and Discussions

(a) The directivity pattern of acoustic pressure variation for both 100Hz and 1000Hz in respect of longitudinal cutouts are shown in Figs.2 to 5 as a function of aspect ratio. The theoretical value for zero aspect ratio is also plotted for the farfield case (R> L) and found to be in good ratagreement. The farfield directivity pattern at all aspect ratios is very nearly omnidirectional. In case of nearfield (R< L), the pattern snown radiation is predominantly in the tangential direction to the plane of the plate at all aspect ratios.

(b) With cutouts oriented in the transverse direction, the pattern has not changed significantly from that of longitudinal cutout (Fig.6 & 7).

(c) The variation of acoustic pressure along the central axis of the plate is plotted in Fig.8 & 9. Beyond 210mm i.e. nearly length of the plate, the intensity vary as function of inverse of square of distance as expected and is in good agreement with theoretical data in the farfield case. In case of nearfield, as there is no theory available, no comparison could be made. However, FE data in the nearfield indicate significantly high levels of acoustic pressure radiation and may constitute major source of local noise.

(d) The radiation pattern for multiple cutout is shown in figures 10 to 11. The farfield directivity pattern remains more or less same.

(e) The radiation index computed is shown in figure 12 for different aspect ratios.

(f) Considering the nodes in the inner boundary of the cutout as fixed, eigen values have been estimated and given in Table 1 with theoretical value for same boundary condition (i.e. at the inner edge). The values are in good agreement. In order

TABLE 1

EIGEN VALUES OF CUTOUT OF SIZE 500 x 250MM

Mode	Theoretical Frequency (Hertz)	Computed Frequency (Hertz)
(1,0)	1000.0	995.9
(0,1)	2000.0	1967.0
(1,1)	2236.0	2360.0

to establish any acoustic coupling of the cutout in transverse mode, FE calculations were repeated at close intervals of 2Hz from 990 to 1010Hz to see any resonance phenomenon in the near and farfield radiation. No discernible variation has been observed at first mode. Acoustic coupling at higher order modes could not be carried out due to very high computer time and fine element mesh required.

Conclusions

(a) The nearfield radiation pattern which cannot be computed using usual analytical methods indicate that local radiated noise levels constitute a major source of noise and is to be taken into account for noise control.

(b) Multiple cutouts radiate more or less same acoustic power compared to single cutout for the same aspect ratio.

Reference

1 "SONDYN" - FE Software for Acoustic Radiation due to Structural Vibration - V. Bhujanga Rao, KVVSS Murty, PVS Ganesh Kumar, B. Mamatha & Dr. SK Chaudhury, NSTL Report, June 91.

+ Professor

* Scientist

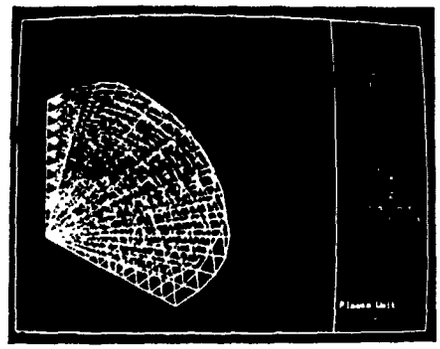

FIG.1 ACOUSTIC FE MODEL OF WATER MEDIUM AROUND FLAT PLATE

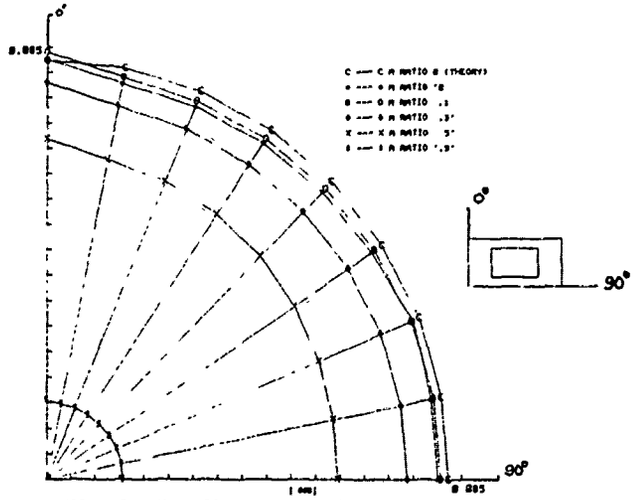

FIG. 2 FAR FIELD SINGLE CUTOUT (LONGITUDINAL) , FREQ 100 Hz.

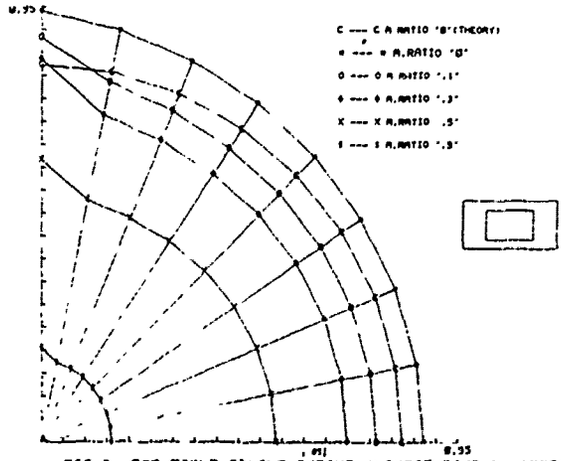

FIG.3 FAR FIELD SINGLE CUTOUT (LONGITUDINAL), 1000Hz.

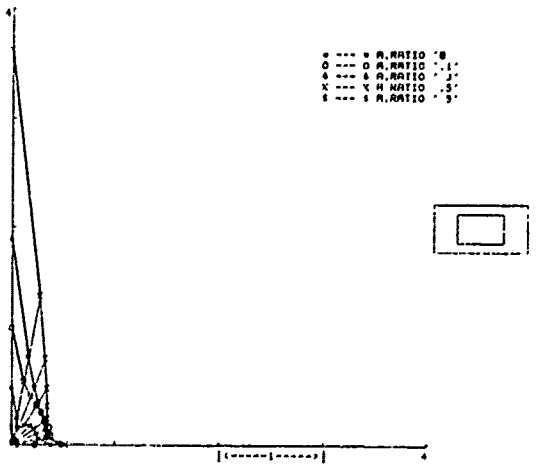

FIG.4 NEAR FIELD SINGLE CUTOUT (LONGITUDINAL), 1000Hz

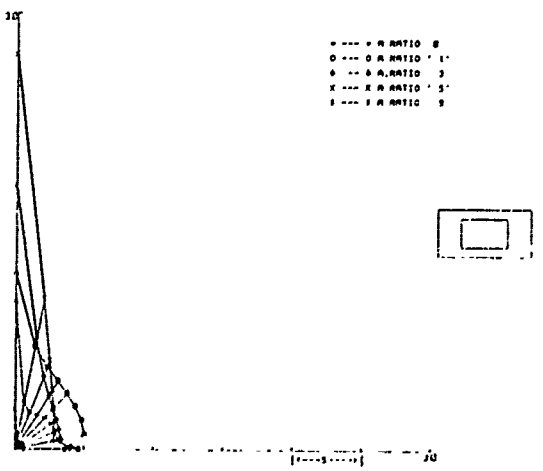

FIG 5 NEAR FIELD SINGLE CUTOUT (LONGITUDINAL), 1000 Hz

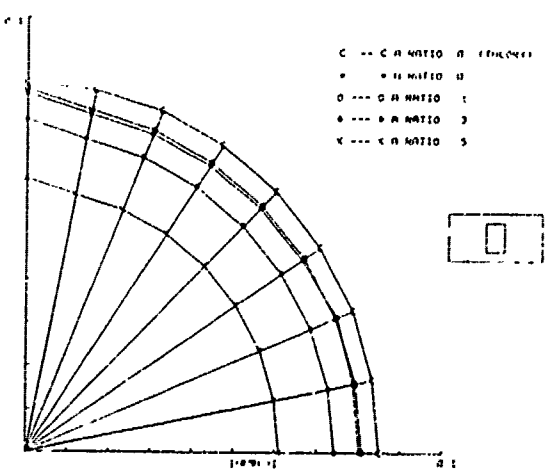

FIG 6 FAR FIELD SINGLE CUTOUT (TRANSVERSE), 1000Hz

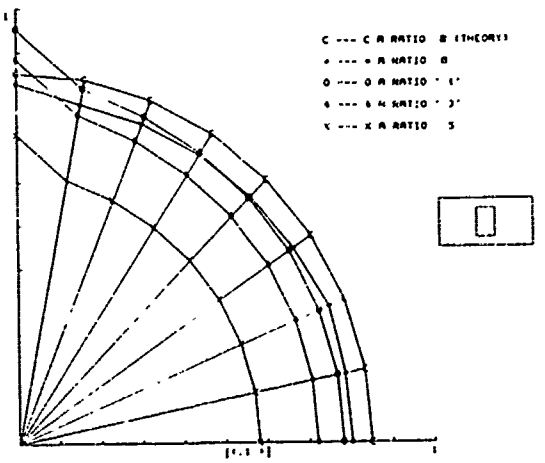

FIG 7 FAR FIELD SINGLE CUTOUT (TRANSVERSE). 1000Hz.

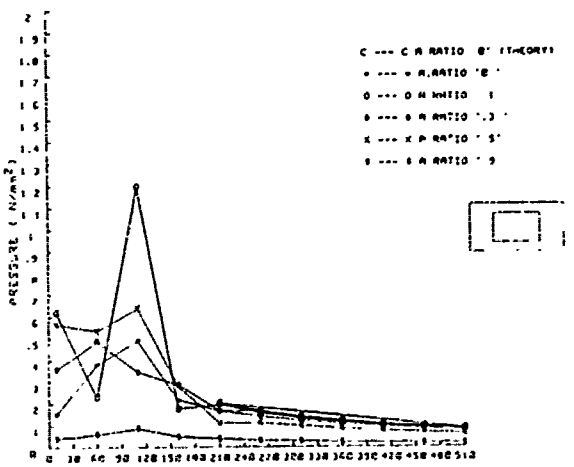

FIG 8 AXIAL PATTERN SINGLE CUTOUT. 100 Hz

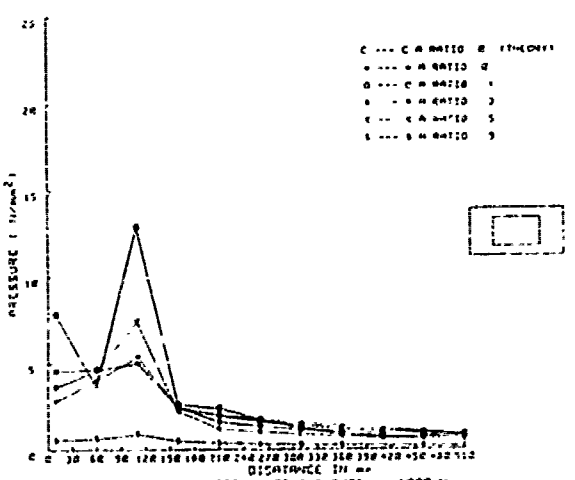

FIG 9 AXIAL PATTERN SINGLE CUTOUT. 1000 Hz

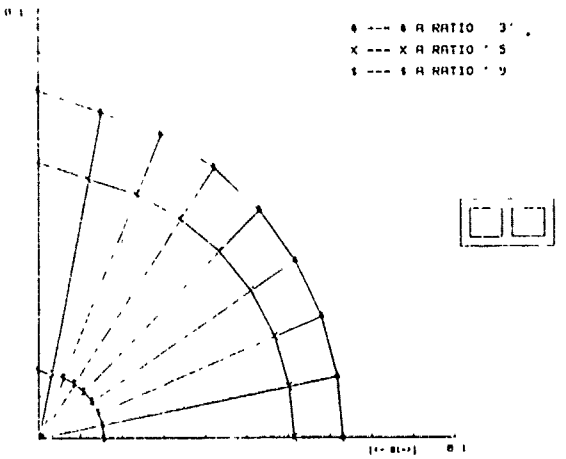

FIG 10 FAR FIELD TWO CUTOUTS , 100 Hz

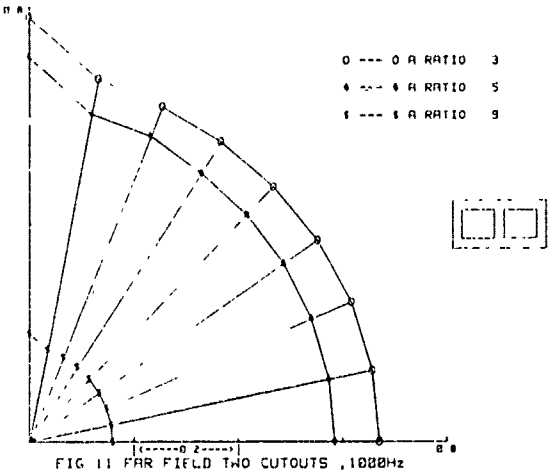

FIG 11 FAR FIELD TWO CUTOUTS ,1000Hz

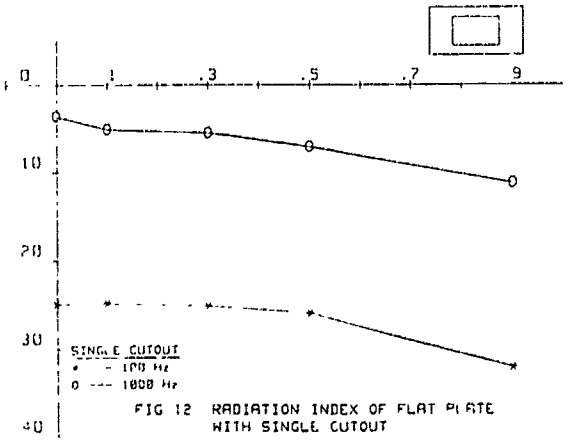

FIG 12 RADIATION INDEX OF FLAT PLATE WITH SINGLE CUTOUT

SECOND INTERNATIONAL CONGRESS ON
RECENT DEVELOPMENTS IN AIR- AND
STRUCTURE-BORNE SOUND AND VIBRATION
MARCH 4-6, 1992 AUBURN UNIVERSITY, USA

ILLUSTRATIONS OF NUMERICAL PREDICTION OF SOUND FIELDS

G. Rosenhouse
Faculty of Civil Engineering
Faculty of Architecture and Town Planning
Technion-Israel Institute of Technology, Haifa 32000

ABSTRACT

The modern numerical means for solution of various problems in acoustics allow for a better determination of sound fields in complicated material bodies. Hence, numerical analysis of acoustic problems is becoming a common and even commercial technique. In this presentation, some illustrations of numerical solutions in acoustics highlight the efficacy of these methods.

INTRODUCTION

The available theories and techniques of solving acoustic fields enable dealing with one to three dimensional domains by applying for example the FDM (including the possibility of triangular mesh generation), and by using integral methods, based mostly on variational techniques - applying BEM and FEM methods. Numerical methods may also help in animating acoustic fields, simply by taking advantage of the large memory of the new generations of computers. Problems involved with infinite domains may be treated numerically by using the theory of non-reflecting boundaries, isolating the finite domain of interest. By using the BEM the need for non-reflecting boundary conditions may be avoided in some problems. The material investigated might be either fluid or solid of any kind of constitutive relation or both. Also multi-domain acoustic problems may be treated numerically. The diversity of applications is enormous and includes, e.g., atmospheric acoustics, environmental acoustics, acoustic non-destructive evaluation (NDE), active noise control, investigation of elastic mountings with high and low Young's moduli, room acoustics (sound levels and ray tracings), flanking in buildings, mufflers and ducts analyses. Fast numerical techniques, such as FFT and LPC help in the determination of output signals and response functions, respectively. In non-linear acoustics and huge domains problems (such as in underwater acoustics) parallel computation complexities are almost the inevitable way to define the sought sound field. Many solved examples illustrate the efficacy of the numerical evaluation of problems in acoustics.

FINITE DIFFERENCE METHODS FOR PROBLEMS OF COMPLICATED GEOMETRIES

a. Rectangular array of finite differences with non-symmetrical elements

The use of non-symmetrical elements is common in the vicinity of certain boundaries or in the cases where the grid has to be

condensed - for example, near a source. The analysis used here for such elements follows [1]. A general description of a rectangular non-symmetrical finite difference element is:

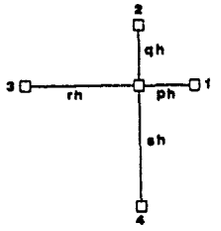

In case of discretization of Helmholtz equation.

$$\nabla^2 p + \left(\frac{\omega}{c}\right)^2 p = 0$$

Taylor expansion is done about the relevant grid point. In the x-direction the result is:

$$p = p_0 + \sum_{n=1}^{\infty} \left[\frac{1}{n!} \left(\frac{\partial^n p}{\partial x^n} \right) (x - x_0)^n \right]$$

The result in y-direction is the same as for the x-direction, x being replaced by y. Setting:

$$x = x_0 + ph \quad \text{at point 1,}$$
$$x = x_0 - rh \quad \text{at point 3,}$$
$$y = y_0 + qh \quad \text{at point 2,}$$
$$y = y_0 - sh \quad \text{at point 4;}$$

Omitting powers higher than 2, defining the finite derivatives which correspond to:

$$\frac{\partial^2 p}{\partial x^2}, \frac{\partial^2 p}{\partial y^2}$$

and finally, substituting the results in Helmholtz equation yield the discrete field equation:

$$\frac{2}{h^2}\left[\frac{p_1}{p(p+r)} + \frac{p_2}{q(q+r)} + \frac{p_3}{r(p+r)} + \frac{p_4}{s(q+s)} - \left(\frac{1}{pr} + \frac{1}{qs} \right) p_0 \right] + \left(\frac{\omega}{c} \right)^2 p_0 = 0$$

b. Mesh of elements of quadrilateral and triangular geometry

Common shapes of non-rectangular geometries are periodic and symmetric with equal sides -- such as hexagonal forms. The use of Taylor expansion allows the description of the field equations for such finite differences. Such shapes are for example [2]:

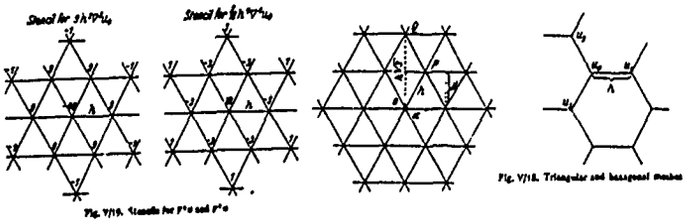

Fig. V/18. Triangular and hexagonal meshes

However, there are more flexible shapes, still using the FDM. These methods were primarily and initially developed for calculations of heat conduction. E.g., Dusinberre [3, 4] has developed arbitrarily shaped triangles which may cover rather complicated areas:

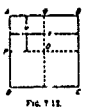
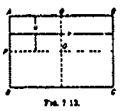
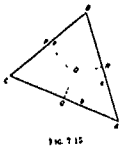
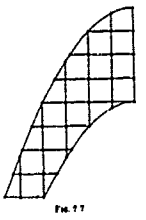
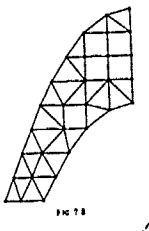

We may add our suggestion of unsymmetric rectangular elements.

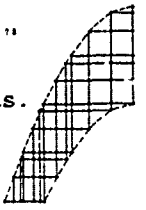

Dusinberre suggested also annular segments, with which other kinds of complicated shapes may be described:

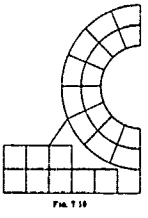
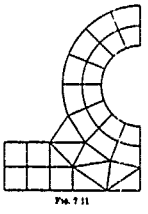
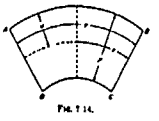
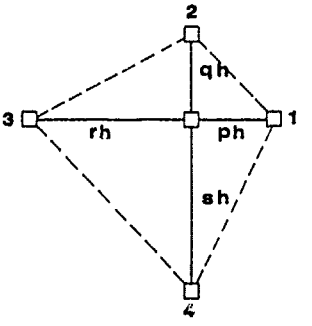

The similarity in the numerical description of derivatives is what allows for borrowing the method from the domain of heat conduction into acoustics. Bhattacharya [5,6] began also with heat conduction problems and then extended the method in order to solve problems in mechanics. His quadrilateral elements are shaped by the dashed lines in the following scheme.

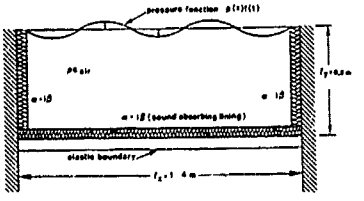

An illustration of the use of FDM for duct acoustics is given in [7], using sound absorbing boundary conditions as defined by Mechel [8].

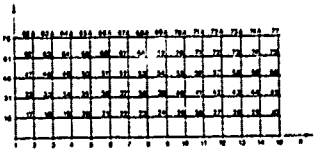
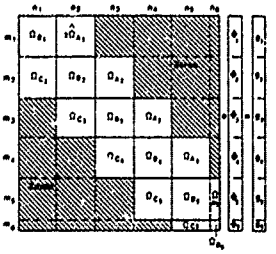
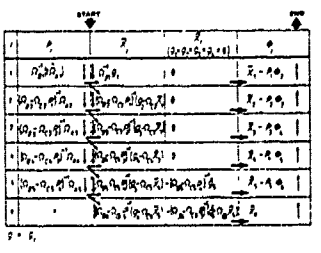
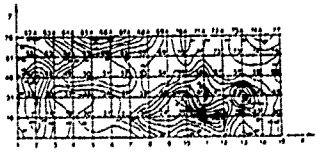

NOTES ON THE USE OF FINITE ELEMENT METHOD

The finite element method is a common way of solving local problems in acoustics where the geometry is complicated and refined mesh is necessary at the near field domain. An example was solved in [9], where the near field effect of a wide sound barrier near a low source of sound was examined by iso-parametric F.E. The results show clearly the near field fluctuation even over finite impedance surface. The results have shown a good correspondence on the average, with the wide sound barrier theory by Pierce [10]:

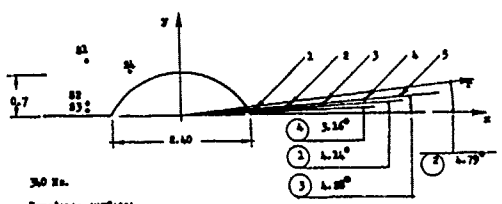

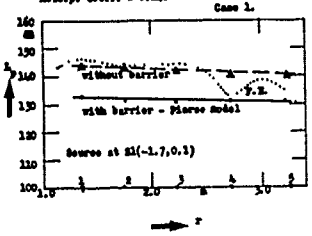

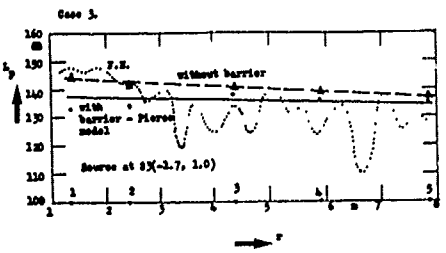

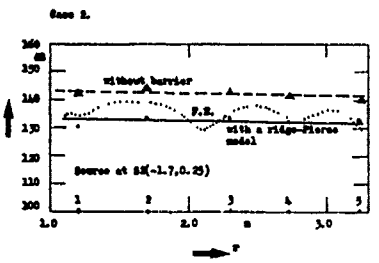

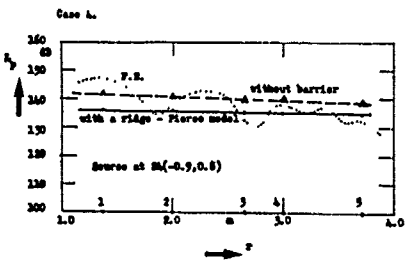

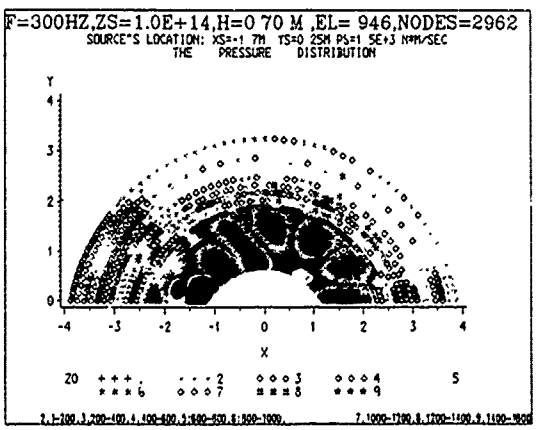

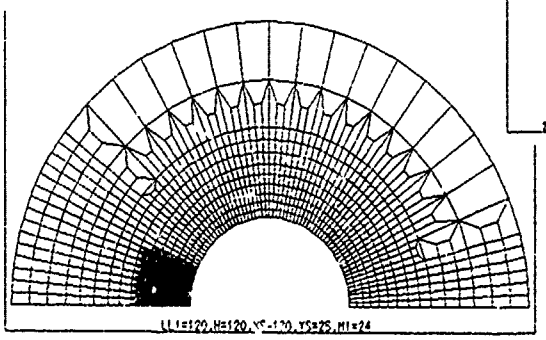

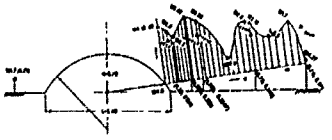

Simple non-reflecting boundary conditions for problems with infinite domains were used already in [1]. Similar but more exact boundary conditions are presented in [11,12]. In other cases, such as turbojet inlets [13], the solution is aided by both F.E. in the near field and classical acoustics solutions in the far field:

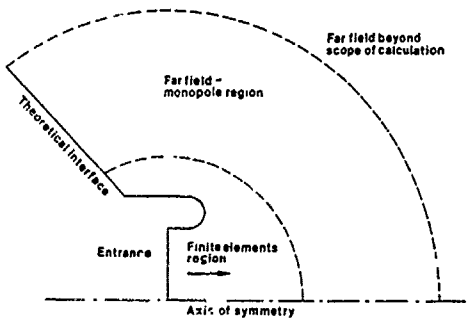

APPLICATION OF BEM IN 2-D AND 3-D DOMAINS

The BEM is based on Helmholtz integral equation. It allows for a reduction of one dimension of the problem at the cost of having instead of a sparse coefficients matrix (as in the FEM) a full one. It solves both internal and external problems. A review of the method is given rigorously in [14] and applied in [15]. The aforementionned problem of a sound barrier over a semi infinite domain was solved by the BEM as well, without need for a definition of a non reflecting boundary [16,17]. Elastic mountings, used for the isolation of sound and vibration, may be solved statically by definition of their "spring constant", which is related to the dynamic coefficient. The stress release effect by using hollow rubber blocks was analysed in [18]:

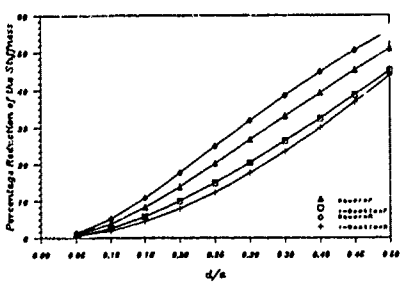

Percentage reduction of the stiffness due to square holes vs d/a

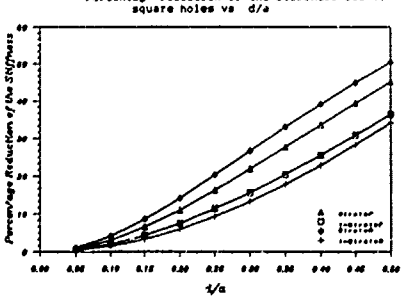

Percentage reduction of the stiffness due to circular holes vs. d/a

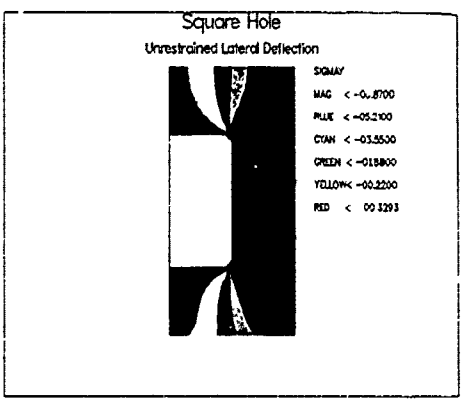

σ_{xx} stresses for case of central hole and unrestrained lateral deflection

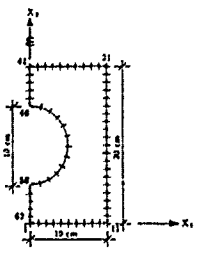

Boundary element method model

The use of BEM for 3-D problems is attractive because of the reduction of one dimension [19]. E.g., Non Destructive Evaluation of agricultural products may be aided by 3-D BEM [20].

ARCHITECTURAL ACOUSTICS

Sound level mapping in rooms was used mostly till now for estimation of sound distribution in concert halls on the one hand and for noise estimation in industrial premises on the other. Ray tracing methods were used in examinations of the effects of the shape of the room and absorption arrangement on the reverberation characteristics and decay curve, using the integrated impulse method. In this context also the Monte Carlo approach was preferred. Examining the mean free path by this last method yields very good results and it is very efficient in estimation of reverberation in arbitrarily shaped rooms [22]. Another approach is based on mapping stationary noise levels in order to define the influence domains of noise sources. Such a study of the location of open windows in living rooms is given in [22]:

Room Structure + Internal sources

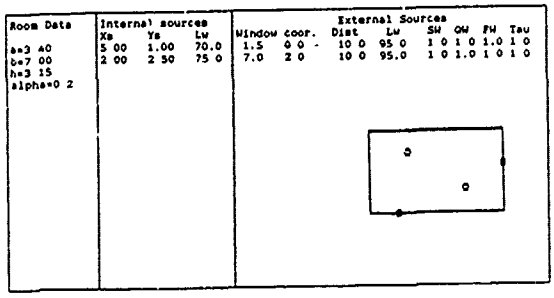

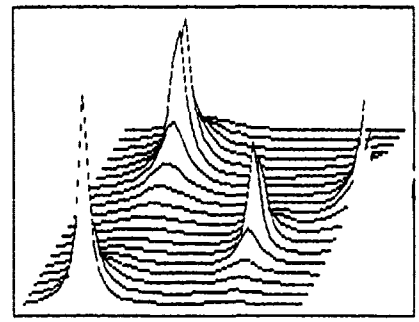

VARIATION OF ACOUSTIC FIELDS IN TIME

Computer simulation in time steps is a very effective method in order to discover some general acoustic phenomena which appear while dynamic events occur. For example, it has been found that generalization of the sound field radiated by a moving source along curved lines is involved with a clear appearance of an effect which is similar to that of the Doppler effect [23]:

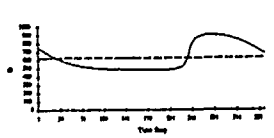

Figure 16 (a) Observed frequency at point (0,9)

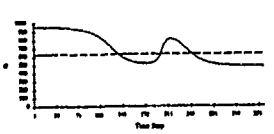

Figure 16 (b) Observed frequency at point (0,3)

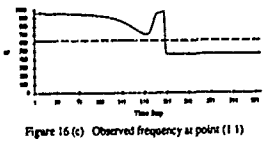

Figure 16 (c) Observed frequency at point (1 1)

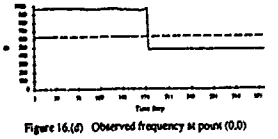

Figure 16.(d) Observed frequency at point (0,0)

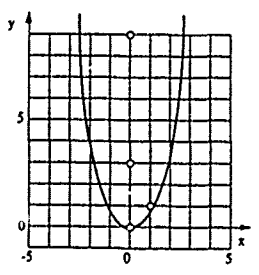

Path of source and location of control points

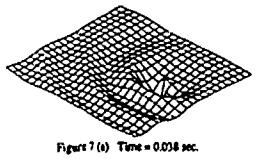

Figure 7 (a) Time = 0.038 sec.

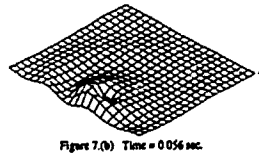

Figure 7.(b) Time = 0.056 sec.

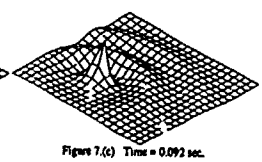

Figure 7.(c) Time = 0.092 sec.

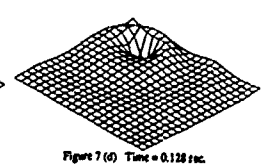

Figure 7 (d) Time = 0.128 sec.

Change in the heard frequency for a source moving along a parabolic track.

Point source of frequency 100Hz, moving along a parabolic path at a velocity of 120 m/s

THE USE OF LPC AND FFT IN SOUND TRANSMISSION ANALYSIS

[24] is an example of the application of FFT and LPC methods in speech analysis. The Fast Fourier Transform yields frequency spectra for given signals. It may represent speech output in the frequency domain for a certain duration and is a result of both the input signal and the filter (the vocal tract). On the other hand, the Linear Predictive Coding yields the response function of the vocal tract. Following is an illustration of the vowel /o/:

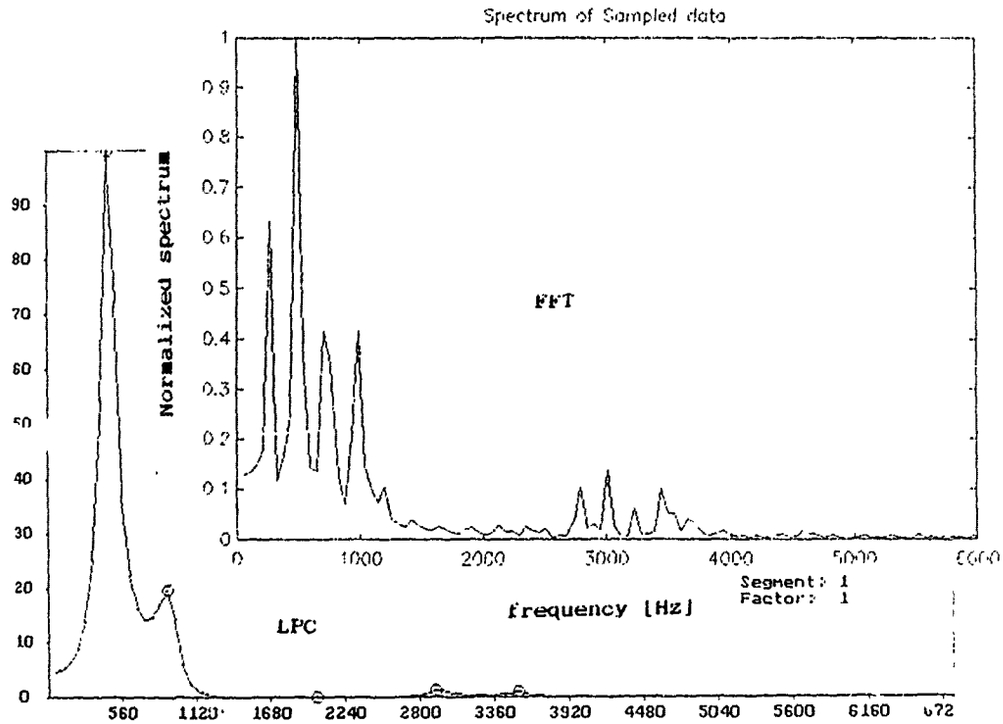

SUMMARY

A myriad of publications on numerical prediction of sound fields are already available, including commercial programs which relate to acoustics. Only a few of them were mentioned here. These developing possibilities may help a variety of problems in any dimensions. One is recommended to master those techniques in order to develop better understanding of the physical aspects of acoustics, to have more accurate solutions to sound fields and to find new applications which necessitate such exact solutions.

REFERENCES

1. Rosenhouse,G.,Cohn,G.,Numerical analysis of hyperbolic acoustic field in liquids and solids, Acustica, 59, 3, 1986, 153-166
2. Collatz, L., The Numerical Treatment of Differential Equations, Springer-Verlag, Berlin-Heidelberg, New-York, 1966, 389-395
3. Dusinberre, G. M., Numerical Analysis of Heat Flow, 1 st ed., McGraw-Hill, 1949, Ch. 9
4. Dusinberre, G. M., Triangular Grids for Heat Flow Studies, A.S.N.E., January, 1960, 61-65
5. Bhattacharya, M.C., Static and Dynamic Deflections of plates of arbitrary geometry by a new finite difference approach, JSV, 107, 3, 1986, 507-526

6. Bhattacharya, M. C., An explicit conditionally stable finite difference equation for heat conduction problems, Int. J. Num. Meth. in Engng., 21, 1985, 239-265
7. Rosenhouse, G., The application of Potters' method for 2 - D numerical analysis of acoustic fields in wave guides, IBP Mitteilung 142, Fraunhofer Inst. f. Bauphysik, Stuttgart, 1987
8. Mechel,F.P.,Schallabsorber,Band 1,Hirzel Verlag,Stuttgart, 1989
9. Frances, R, Rosenhouse, G., Analysis of steady pressure wave propagation near a vault due to a low point source by iso-parametric F.E., Vol. I, 2nd National Congress on Mechanics, Athene, 29.6-1.7.1989
10. Pierce, A., Diffraction of sound around corners and over wide barriers, Jr. Acoust. Soc. Am., 55, 5, 1974, 941-955
11. Keller,J.B.,Givoli,D.,Exact non-reflecting boundary conditions, Jr. Computational Physics, 82, 1, 1989. 172-192
12. Givoli, D., Keller, J. B., Non reflecting boundary conditions for elastic waves, Wave Motion, 12, 1990, 261-279
13. Parrett, A.V., Eversman, W., Application of finite element and wave envelope approximation to turbofan engine noise radiation including flight effects, AIAA-84 2333
14. P. Filippi(ed.),Theoretical Acoustics and Numerical Techniques, Springer Verlag Wien,1983 (pp.135-216,written by W.L. Wendland)
15. Cheng, C. Y. R., Seybert, A. F., Recent applications of the boundary element method to problems in acoustics, SAE 1987 Noise and Vibration Conference, Traverse City, MI, 28-30.4.1987
16. Holger, D. K., Kristiansen, U. R., Indirect integral equation methods for acoustic diffraction applications, 20th Midwestern Conf., 14(b), Purdue University, School of Mech. Engng, USA, 31.8-2.9.1987. 776-781
17. Hothersall, D. C., Chandler - Wilde, S. N., Hajmirzae, M. N., Efficiency of single noise barriers, JSV, 146, 2, 1991, 303-322
18. Marjieh, H., 2-D analysis of elastic mountings by the BEM,M.Sc. Thesis,Supervised by G.Rosenhouse,Technion, Haifa, Israel, 1989
19. Ahmed, S.,Manolis, G.D., Dynamic analysis of 3-D structures by a transformed boundary element method, Computational Mechanics, 2, 1987, 185-196
20. Rosenfeld, D., Rosenhouse, G., Schmulevich, I., BEM simulation of acoustic wave propagation in 3-D viscoelastic bodies, 3rd IMACS Symp. on Computational Acoustics,Harvard Univ.,Cambridge, Mass.,USA ,26-28.6.1991
21. Dorfman,P., Statistical analysis of reverberation time in halls by means of Monte Carlo Method, M.Sc. Thesis ,Supervised by G. Rosenhouse,Technion, Haifa, Israel, 1987
22. Rosenhouse, G., Rosenhouse,I., Signal to noise mapping in rooms with open windows exposed to external noise and internal sound sources, Internoise 90, Gothenburg,Sweden, 13.8.1990, 251-254
23. Peled, N., Rosenhouse, G., "Doppler effect"in motion of sound source along a curved path, 3rd IMACS Symp. on Computational Acoustics,Harvard Univ.,Cambridge, Mass.,USA ,26-28.6.1991
24. Rosenhouse,J.,Rosenhouse,G., The use of LPC and FFT in phonetic analysis, XIIth International Congress of Phonetic Sciences, University of Provence, Aix-en-Provence, France, 19-24.8.1991, Vol. 5 pp. 386-389.

SECOND INTERNATIONAL CONGRESS ON
RECENT DEVELOPMENTS IN AIR- AND
STRUCTURE-BORNE SOUND AND VIBRATION
MARCH 4-6, 1992 AUBURN UNIVERSITY, USA

ASPECTS REGARDING CAVITATION OCCURENCE DURING THE NORMAL OPERATION OF CENTRIFUGAL PUMPS

L.Comănescu[x] , A.Stan[xx]

[x] INCERC-Acoustic Laboratory,Bucharest şos.Pantelimon no.266
[xx] Academia Română,Bucharest Calea Victoriei no.125

ABSTRACT

The analysis of the noise measured in liquid,at the discharge section of some pumps aliniated to ISO 2858,working in normal conditions without cavitation,shows the appearence of some peaks of acoustical level situated at the resonance frequencies of the pump impeller.The calculations show the possibilitie that in the ventral zones,some values of the dynamic pressure components are situated under the value of the statical pressure of the fluid,this bringing to the appearence of some cavitation zones;so are confirmed the results of other authors /1/,/2/, /4/ who studied cavitation in the domain of audible frequencies,the new elements being the identification of a cavitation generating source which is not mentioned in the known literature.

INTRODUCTION

It is known that the cavitation phenomenon consists in the appearence and the implosion of some vapour bubles in a liquid,eased by the decreasing of the pressure under the level of vapourisation pressure.

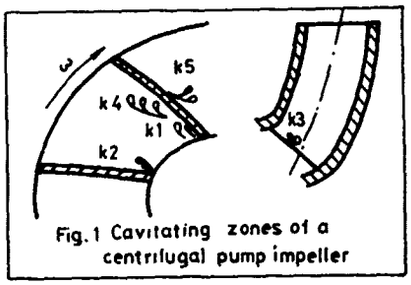

Fig.1 Cavitating zones of a centrifugal pump impeller

The local high pressure which appear, are accompanied by phenomena:mechanical, acoustical,thermical,electrical and others,bringing to the damage of the material of the wall in long of wich takes place the bubles implosion.It was found /1/,that the main zones of a centrifugal pump impeller affected by cavitation are those presented in fig.1,where k_1,k_2,k_3 are situated in the vicinity of the entrance in the impeller blades,on the: intrados,extrados and inner surface of the front disc,also k_4 and k_5 are situated the long of the blade.

The working of the pump in normal conditions,without cavitation,exept the limit of alteration of the pumping head with 3%,is conditioned by the relation:

$$NPSH_a > NPSH_r \qquad (1)$$

in which: $NPSH_a$ is the energy exprimed in meters,assured by the installation at the suction flange of the pump and $NPSH_r$ is the energy needed by the pump to work without cavitation.The values of $NPSH_r$ are proper to each pump and are experimentally established.

VIBROACOUSTICAL MEASUREMENTS

In the same time with the experimental measurements of the hydrodinamical functional parameters of a pump type TN 150-125-315 with the nominal flow of 180 m^3/h and the head of 120 m,pumping potable water at 18^0C were made recordings of the pressure oscillations. The recorded signals on magnetic tape,containing useful signal and ground noise (s+z),were analysed using Bruel & Kjaer instruments.

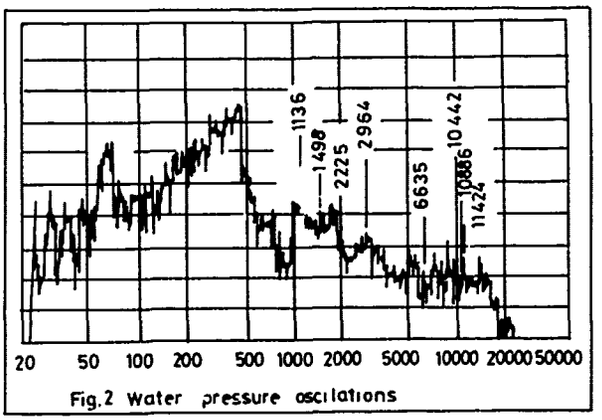

Fig.2 Water pressure oscilations

In order to obtain the useful signal (s) due to the flow, the recordings of the disturbing effect of the noise (z), originated from other sources,were corrected using the spectra difference:

$$L_s = L_{(s+z)} - L_z \qquad (2)$$

The spectrogram obtained in the mentioned conditions,accomplishing the condition (1),is presented in fig.2.

RESULTS OF MODAL ANALYSIS

Using proper instruments,were determined the own frequencies of the impeller and were identified the frequencies at which appear the resonance peaks,by excitation in the frquency domain of (2o-20k) Hz,fig.3.

The comparison of the signals contained in the spectrograms mentioned in fig.2 and 3,shows the presence of some signal peaks situated at the same values of the frequencies,this indicating the fact that these peaks of the fig.2 can be generated by the resonant behaviour of the impeller,excited by the flow itself.

For the mentioned frequencies were determined the impeller natural vibrating modes,using a laser holographical installation.

In fig.4 is presented the fringes pattern coresponding to the excitation frequency of 6635 Hz.

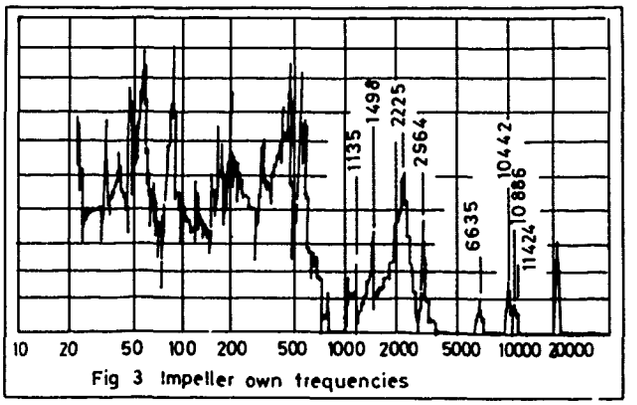

Fig 3 Impeller own frequencies

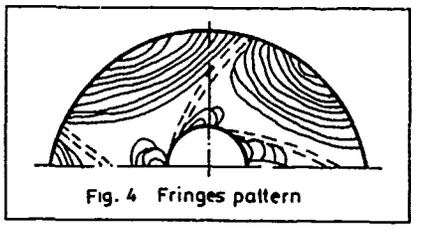
Fig. 4 Fringes pattern

THE CALCULATION OF THE MINIMAL PRESSURE

The attention was concentrated on the entrance in the impeller blades zone,situated on the front disc.Each point displacement was calculated /3/, using the relation:

$$d_n = 0{,}25.n.\lambda/(\cos\theta_1 + \cos\theta_2) \qquad (3)$$

In which: n is the order number of the fringe, λ is the laser lenght, θ_1 and θ_2 are the angles between the moving direction and the viewing direction,respectivelly the iluminating direction of the impeller in the holographical experiment.
In the liquid,these displacements generate pressure waves with the value given by the relation:

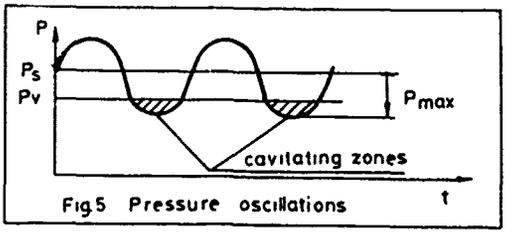

Fig5 Pressure oscillations

$$p = Z.v \qquad (4)$$

in which: Z is the mechanical impedance of the water and v is the considered point moving speed. The pressure oscillations take place around the static pressure p_s of that point, and for a given frequency f, the peak value is given by:

$$p_{max} = 2.\pi.Z.f.d_n \qquad (5)$$

So, exists the possibility of cavitation appearence in the moments in which the negative peak value of the pressure wave is under the value of the vapourisation pressure, fig.5, meaning that:

$$p_{max} \geq p_s - p_v \qquad (6)$$

Because in the pump, the inferior energetic limit admited is $NPSH_r$ and $NPSH_a = p_s$, the condition (6) can be written:

$$p_{max} \geq NPSH_a - NPSH_r \qquad (7)$$

CALCULATED VALUES

For the frequencies marked on the spectrograms, were calculated the difference values:

$$D = (NPSH_a - NPSH_r) - p_{max} \qquad (8)$$

and the results written in the table 1.
For the calculations were considered: $\theta_1=32^0$, $\theta_2=25^0$, $NPSH_a$ =10 m, $NPSH_r$ =5 m, the nominal flow 180 m^3/h, Z = 1,483.10^6 $kg.s^{-1}.m^{-2}$.

table 1

f [Hz]	1136	1498	2225	2964	6635	10442	10882	11424
p max [m]	0,47	0,75	1,3	1,99	4,46	7,9	8,29	9,6
D [m]	4,53	4,25	3,7	3,01	0,54	-2,9	-3.29	-4,6

SUMMARY

From the values contained in the table 1, it results the existence of a frequency over which it is possible the appearence of the local cavitation, even for working in normal conditions.

Increasing the flow, increases the possibilities to appear the local cavitation as a result to the increasing of $NPSH_r$.

The presented investigation method can be extended.

The authors intend to extend the investigations on other zones and also intend the demonstration by other methods of the local cavitation presence in the considered zones.

REFERENCES:
1.I.Anton, Cavitation (Ed.Academiei Romane, vol.1:1984, vol.2:1985)
2.R.Young, Cavitation (Mc Grow Hill, 1989)
3.V.I.Vlad, Introduction to Holography (Ed.Academiei Romane, 1973)
4.Gy.Sebestien, Acta Technica 66/4, Budapest, 1964
5.J.Tourret, La Houille Blanche, no.2, 1979

$$p = Z.v \qquad (4)$$

in which: Z is the mechanical impedance of the water and v is the considered point moving speed.The pressure oscillations take place around the static pressure p_s of that point,and for a given frequency f, the peak value is given by:

$$p_{max} = 2.\sqrt{\pi}.Z.f.d_n \qquad (5)$$

So,exists the possibility of cavitation appearence in the moments in which the negative peak value of the pressure wave is under the value of the vapourisation pressure,fig.5,meaning that:

$$p_{max} \geq p_s - p_v \qquad (6)$$

Because in the pump,the inferior energetic limit admited is $NPSH_r$ and $NPSH_a = p_s$,the condition (6) can be written:

$$p_{max} \geq NPSH_a - NPSH_r \qquad (7)$$

CALCULATED VALUES

For the frequencies marked on the spectrograms,were calculated the difference values:

$$D = (NPSH_a - NPSH_r) - p_{max} \qquad (8)$$

and the results written in the table 1.
For the calculations were considered: $\theta_1=32^0$,$\theta_2=25^0$,$NPSH_a$ =10 m, $NPSH_r$ =5 m,the nominal flow 180 m^3/h, Z = 1,483.10^6 $kg.s^{-1}.m^{-2}$.

table 1

f [Hz]	1136	1498	2225	2964	6635	10442	10882	11424
p max [m]	0,47	0,75	1,3	1,99	4,46	7,9	8,29	9,6
D [m]	4,53	4,25	3,7	3,01	0,54	-2,9	-3,29	-4,6

SUMMARY

From the values contained in the table 1, it results the existence of a frequency over which it is possible the appearence of the local cavitation ,even for working in normal conditions.

Increasing the flow,increases the possibilities to appear the local cavitation as a result to the increasing of $NPSH_r$.

The presented investigation method can be extended.

The authors intend to extend the investigations on other zones and also intend the demonstration by other methods of the local cavitation presence in the considered zones.

REFERENCES:

1.I.Anton,Cavitation (Ed.Academiei Romane,vol.1:1984,vol.2:1985)
2.R.Young,Cavitation (Mc Grow Hill,1989)
3.V.I.Vlad,Introduction to Holography (Ed.Academiei Romane,1973)
4.Gy.Sebestien,Acta Technica 66/4, Budapest,1964
5.J.Tourret,La Houille Blanche,no.2,1979

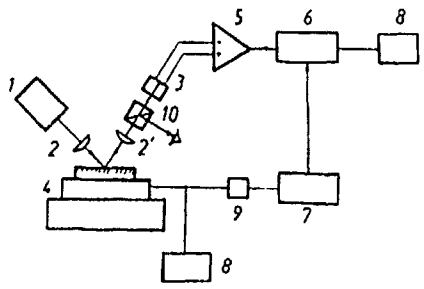

Fig. 1 Experimental set-up. 1 — He–Ne laser; 2, 2' — objectives; 3 — positionsensitive sensor; 4 — piezoelement with mirror; 5 — differential amplifier; 6 — lock-in-amplifier; 7 — generator; 8 — voltmeter; 9 — attenuator.

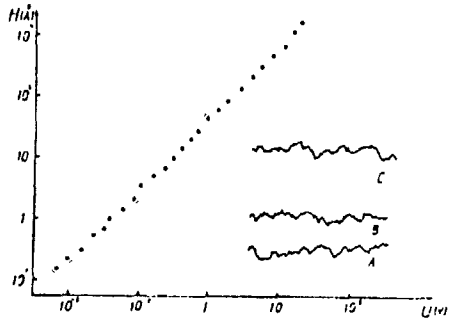

Fig 2 Experimental results. Vibration amplitude of piezoelement surface vs applying voltage The curves A — C vibration amplitudes when 0 mV, 8 mV and 18 mV applied to piezoelement, respectively. Lock-in-amplifier time constant is equal to 8 s

This signal is amplified by the low-noise differential amplifier and further goes to the lock-in-amplifier input. Constructed device could detect optical signals from any surfaces, but for good sensitivity and accuracy of the measurements it is better to use mirror-reflected surfaces.

When piezoelements were tested, a small slice of mirror was attached to it's surface. Piezoelement was excited by the generator which has output frequency 210 Hz. The experimental results are given on Fig. 2.

Amplitude vibration dependance of piezoelement on excited signal level is a linear dependance up to 30 V. The measurement result of sensitive limit is given on Fig. 2. The line A corresponds to zero signal (integration time of lock-in is 8 s), and lines B and C correspond to excited signal level 8 mV and 18 mV respectively.

We can see that signal-to-noise ratio is about 3–5 units for line B. The independent measurements have shown that vibration amplitude of tested piezoelement is 0.2 μm when supplied voltage is 100 V (f = 210 Hz). From above we can see that vibration amplitude limit is about 0.1 A (lock-in detection).

Seismic vibration and external acoustic waves are the main sources of noise disturbance. To improve the sensitivity further it is necessary to make acoustic and seismic isolation of this set-up. So this very set-up permits to make measurements of solid state surface vibration of high sensitivity and linearity.

SECOND INTERNATIONAL CONGRESS ON
RECENT DEVELOPMENTS IN AIR- AND
STRUCTURE-BORNE SOUND AND VIBRATION
MARCH 4-6, 1992 AUBURN UNIVERSITY, USA

THE OPTIMIZATION OF NONLINEAR VEHICLE SYSTEMS USING RANDOM ANALYSIS

Fangning Sun, Chengde Li, Jianjun Gao, Pamela Banks-Lee
College of Textiles
North Carolina State University
Box 8301, Raleigh, NC 27695, U.S.A.

ABSTRACT

A study on nonlinear random vibration of the vehicle system is made. First, the nonlinear element models of the leaf springs, shock absorber, jounce-stop and wheel-hop are given in this paper. The nonlinear model of the whole vehicle is obtained by the nonlinear modal synthesis technique. Also, an Improved Statistical Linearization Method ISLM is proposed. The complex modal analysis method is used to solve the ISLM equivalent equation. Calculation procedures for truck CA150 are made and a road test is made to verify the above approach.

A new optimizing procedure for nonlinear systems is developed. It reduces the design variables and computing time. Also, it can be used to solve problems where the optimal parameters vary with changing conditions.

INTRODUCTION

Investigation of the vibrations of modern vehicles concentrates nowadays into a rather broad frequency range in which the non-rigidity of their structures and components and non-linearity of their elasto-damping elements play a very important role. In fact, a vehicle system subjected to the excitation of road roughness is a nonlinear random vibration system. In solving nonlinear random vibration problems, one of the effective approximation methods, statistical linearization method-SLM, is known to have high computing efficiency and less limitation[1][2]. A lot of effort has been made towards the development of this method [3][4][5], and it is extensively used in engineering calculation. However, in the case of the presence of hysteresis damping, further modification of the Conventional statistical Linearization Method-CSLM is needed. Moreover, the optimization of linear systems, based on the SLM, is usually not easy to perform because of too many variables to optimize, non-unique solution of nonlinear parameters under a given input condition, and different linear optimal solution under different input conditions.

In order to solve these problems, in the work presented here, a nonlinear vehicle model is established, and the Improved statistical Linearization Method-ISLM is used rather than CSLM.

A new procedure for the optimization problem is given and the optimization of nonlinear vehicle vibration is performed from the standpoint of riding comfort.

THE NONLINEAR VEHICLE MODEL

Nonlinear Modal Synthesis of Vehicle Systems

In nonlinear modelling of the whole vehicle system, the following assumptions are made:

1) Each component or part is either an elastic body or a rigid mass.
2) The interconnecting elements between these components or parts are massless either nonlinear or linear two force elements. Also, they are divided into external elements which connect with external excitations and internal elements which do not connect with external excitations.
3) Only constant driving speed is considered; the road excitation is considered stationary Guassian .

The modal synthesis technique is adopted to establish the whole vehicle model. The vehicle is divided into m subsystems and the equation of motion of each subsystem is written as

$$M_i\ddot{x}_i + C_i\dot{x}_i + K_ix_i = R_i(t) - f_i(t) \qquad i=1, 2, ..., m \qquad (1)$$

where , for ith subsystem, M_i, C_i and K_i are the mass, damping and stiffness matrices ; $x_i = (x_{i1}, ..., x_{ini})^T$ is the generalized coordinate vectors ; ni the number of the generalized coordinate. $R_i(t)$ is a vector composed of zero and forces of external elements acting on ith subsystem; $f_i(t)$ is a vector composed of zero and forces of internal elements acting on ith subsystem.

The dynamic equation of the whole nonlinear vehicle system can be written as

$$M\ddot{Q} + C\dot{Q} + KQ = \Psi^T R - \Psi^T f \qquad (2)$$

where Q is the system modal coordinate vector;

$M = diag(.., M_{Qi},..); C = diag(.., C_{Qi},..); K = diag(.., K_{Qi},..); \Psi = diag(.., \psi_i,..); R = (.., R_i^T, ..)^T;$

$f = (.., f_i^T, ..)^T; \quad M_{Qi} = \psi_i^T M_i \psi_i; \quad C_{Qi} = \psi_i^T C_i \psi_i; \quad K_{Qi} = \psi_i^T K_i \psi_i;$

ψ_i is the modal matrix of ith subsystem.

The vehicle model described by Eq. (2) can be used in general cases provided the nonlinear forces and surface restriction between systems is given.

Nonlinear Models of Interconnecting Two Force Elements

In this paper, four kinds of nonlinearities are considered. These are leaf-springs and shock absorber nonlinear restoring forces, and the nonlinearities of jounce-stop and wheel-hop.

Through the testing and characteristic analysis, an exponential model of the leaf-springs is established below. As shown in Figure 1,

$$\begin{aligned} &\text{loading} \quad f(\delta, \dot{\delta}) = f_u(\delta) = F_{ENU}(\delta) - C_u(R)e^{-\beta_u(R+\delta)} && \dot{\delta} > 0 \\ &\text{unloading} \quad f(\delta, \dot{\delta}) = f_l(\delta) = F_{ENL}(\delta) + C_l(R)e^{-\beta_l(R-\delta)} && \dot{\delta} < 0 \end{aligned} \qquad (3)$$

$$
\begin{array}{ll}
C_u(R) = F_{ENU}(-R) - F_{ENL}(-R) & C_u(R) = F_{ENU}(-R) - \phi_l(-R) \\
R>\lambda & R<\lambda \\
C_l(R) = F_{ENL}(R) - F_{ENU}(R) & C_l(R) = F_{ENL}(R) - \phi_u(R) \\
F_{ENU}(d) = a_u + k_u\delta & F_{ENL}(d) = a_l + k_l\delta
\end{array}
$$

where δ and $\dot{\delta}$ are the relative displacement and velocity of the suspension; R is the amplitude of δ; $f_u(\delta)$ and $f_l(\delta)$ are the restoring forces with respect to the loading, unloading processes; β_u, β_l, a_u, a_l, k_u, and k_l are the parameters determined by curve fitting technique; $f_u(\delta)$ is the trace of the point from which $\delta > 0$ turns to $\delta < 0$ when the leaf-springs are partially locked; $f_l(\delta)$ is the trace of the point from which $\delta < 0$ turns to $\delta > 0$.

A model of the shock absorber, using power terms α and β, is set up below by experimental results of the damping property.

$$
\text{extension} \quad f_e(\dot{\delta}) = \begin{cases} a\,\dot{\delta}^{\alpha} & 0 < \dot{\delta} < \dot{\delta}_0 \\ c\,\dot{\delta} & \dot{\delta} > \dot{\delta}_0 \end{cases} \qquad \text{compression} \qquad f_c(\dot{\delta}) = \begin{cases} b\,|\dot{\delta}|^{\beta} & 0 < \dot{\delta} < \dot{\delta}_0 \\ d\,|\dot{\delta}| & \dot{\delta} > \dot{\delta}_0 \end{cases} \quad (4)
$$

where $\dot{\delta}$ is the relative velocity between two ends of the shock absorber; $\dot{\delta}_0$ is the unloading velocity; a, b, c, d, α and β are parameters determined by the regression method.

Considering the case of jounce-stop generated by the suspension bump, the restoring force model is

$$
f(\delta, \dot{\delta}) = \begin{cases} c\,\dot{\delta} + a(\delta - s) & \delta \geq s \\ 0 & \delta < s \end{cases} \quad (5)
$$

where δ and $\dot{\delta}$ are the relative displacement and velocity of the suspension; s is the spacing distance of the suspension.

The tire is approximated as a linear elasto-damping element. The nonlinearity of the wheel-hop is described by

$$
f(\delta, \dot{\delta}) = \begin{cases} k_t\delta + c_t\dot{\delta} & k_t\delta + c_t\dot{\delta} \leq P \\ P & k_t\delta + c_t\dot{\delta} > P \end{cases} \quad (6)
$$

where δ and $\dot{\delta}$ are the relative displacement and velocity of the tires; k_t and c_t are the stiffness and damping coefficients and P the static load of the tire.

NONLINEAR SYSTEM RESPONSE USING ISML

Improved Statistical Linearization Method

The idea of Conventional Statistical Linearization Method - CSLM is letting a set of linear equations with linear viscous damping and stiffness to be equivalent to the nonlinear equations. The leaf-springs possesses the hysteresis damping property. The equivalent model of hysteresis damping is given in Eq. (7). The advantage of using Eq. (7) is given in the previous work [6].

$$F_s(t) = g\,x_h = g\frac{1}{\pi}\int_{-\infty}^{+\infty} x(\tau)\frac{1}{t-\tau}d\tau \qquad x_h = H(x) \tag{7}$$

where g is called the structural damping coefficient; and H is the Hilbert transform.

Therefore, considering a nonlinear system with n DOF,

$$D1(x) = M\ddot{x} + C\dot{x} + Kx + f(x, \dot{x}) \tag{8}$$

where M, C and K are the mass, damping and stiffness matrices; $f(x, \dot{x})$ is the nonlinear force vector.

If the linear function

$$h(x, \dot{x}, x_h) = c_e\dot{x} + k_e x - g_e x_h$$

where c, k and g are the equivalent viscous damping, stiffness and structural damping, is used as the equivalence of f(x, x), then the corresponding linear system is

$$D2(x) = M\ddot{x} + C\dot{x} + Kx + c_e\dot{x} + k_e x - g_e x_h. \tag{9}$$

The difference in the two system Eqs. (8) and (9)

$$e = f(x, \dot{x}) - c_e\dot{x} - k_e x + g_e x_h.$$

By minimizing $E[e^T e]$, i.e.,

$$E[e^T e] \rightarrow \min,$$

it can be proven that

$$k_{ik} = \frac{E[L_{ik}(y_{ik}, \dot{y}_{ik})y_{ik}]}{E[y_{ik}^2]} \qquad c_{ik} = \frac{E[L_{ik}(y_{ik}, \dot{y}_{ik})\dot{y}_{ik}]}{E[\dot{y}_{ik}^2]} \qquad g_{ik} = \frac{E[D_{ik}(y_{ik}, \dot{y}_{ik})y_{hik}]}{E[y_{hik}^2]} \tag{10}$$

where $y_{ik} = x_i - x_k$ is the relative displacement of ith mass to kth mass; L_{ik} is the force of the element with viscous damping between ith and kth masses acting on ith mass; D_{ik} is the force of the element with structural damping between ith and kth masses acting on ith mass.

As shown in Eq. (10), each equivalent coefficient is the function of the response statistical characteristics. The solving process is a reiterative process.

Complex Modal Response Calculation and Verification of the Theory

The dynamic equation in the frequency domain is written as

$$[-\omega^2 M + j\omega(c_e + c) + k_e + k + jg_e\,\mathrm{sgn}(\omega)]\,X(\omega) = F(\omega) \tag{11}$$

where $F(\omega)$ is the Fourier transform of the force function. Without losing the generality, assume $c = 0$, $k = 0$. Since $X(\omega)$ possesses Hermitian property, i.e.,

$$X^*(\omega) = X(-\omega),$$

only the case of $\omega > 0$ is discussed below.

Eq. (11) is rewritten in the first order form

$$j\omega AV + BV = F_V \tag{12}$$

where $V = \begin{Bmatrix} X(\omega) \\ j\omega X(\omega) \end{Bmatrix}$, $F_V = \begin{Bmatrix} F(\omega) \\ 0 \end{Bmatrix}$, $A = \begin{bmatrix} c_e & M \\ M & 0 \end{bmatrix}$, $B = \begin{bmatrix} k_e + jg_e & 0 \\ 0 & -M \end{bmatrix}$.

By solving the eigen-problem of Eq. (12), one can obtain 2n complex eigenvalues, $\lambda_1, \lambda_2, ..., \lambda_{2n}$, and their corresponding eigenvectors $\psi_1, \psi_2, ..., \psi_{2n}$.

Setting $\Psi = [\psi_1, \psi_2, ..., \psi_{2n}] = \begin{Bmatrix} \phi_1 \\ \phi_2 \end{Bmatrix}$, $\psi^T A \psi = \bar{A}$, $\psi^T B \psi = \bar{B}$,

then,

$$X(\omega) = \phi_1 (\bar{A} j\omega + \bar{B})^{-1} \phi_1^T F(\omega). \tag{13}$$

From Eq. (13), the mean square response of each point can be obtained.

From a riding comfort point of view and based on the above vehicle nonlinear model and the solving method, a numerical program is developed. A simplified truck model of three subsystems and seven DOF as shown in Figure 2, is used to operate the simulation calculation. All parameters used are obtained by experimental measurement. The frequency range is chosen within 0.9→25 Hz.

In order to verify the model and compare the results of ISLM with CSLM, a road test of riding comfort is made. The predicted and experimental acceleration spectra using the equivalent structural damping model are given in Figure 3. It can be seen that the theoretical results agree quite well with the experimental ones so that the effectiveness of the vehicle model and the ISLM, proposed here are proven. Figure 4 gives the comparative results using the equivalent viscous damping model for suspensions. The error between predicted and experimental results for the front axle acceleration spectrum is larger when the equivalent viscous damping model is used than when the equivalent structural damping model is used. This shows that ISLM is more satisfactory in treating hysteresis damping elements than CSLM.

THE NONLINFAR PARAMETER OPTIMIZATION OF SUSPENSIONS

Difficulties always exist when the nonlinear parameters of suspensions are optimized directly based on SLM. These difficulties are in the form of too many variables to optimize, non-unique solution of nonlinear parameters under a given input condition, and different linear optimal solution under different input conditions. Therefore, a new optimization procedure is developed here, which requires first, obtaining equivalent linear parameters, and second identifying the nonlinear parameters by results of linear optimization.

Optimization of Linear Systems

The same vehicle model in Figure 2 is used and the linear mathematical model is described by Eq.(9).When considering the case without shock absorbers in rear suspensions, the design variables can be written as

$$Z = (k_f, g_f, c_f, k_r, g_r)^T \tag{14}$$

where k_f, c_f and g_f are the equivalent stiffness, viscous and structural damping of the front suspension; k_r and g_r are the equivalent stiffness and structural damping of the rear suspension

The global objective function is σ^2 and the optimization problem is given by

$$\text{minimize} \qquad \sigma^2(Z) = \sum_{i=1}^{4} (\sigma_{\ddot{x}i}^2(Z)/\gamma_{\ddot{x}i} + \sigma_{pi}^2(Z)/\gamma_{pi} + \sigma_{\delta i}^2(Z)/\gamma_{\delta i}) \tag{15}$$

$$\text{subjected to} \qquad \alpha = g(Z) < 5° \qquad Z_l \le Z \le Z_u$$

where Z_l and Z_u are the lower and upper limit vectors of design variables; $\sigma_{\ddot{x}i}^2$ is the mean square vertical acceleration of ith point of vehicle; σ_{pi}^2 is the mean square dynamic force of ith wheel; $\sigma_{\delta i}^2$ is the mean square dynamic deflection of ith suspension; $\gamma_{\ddot{x}i}$, γ_{pi} and $\gamma_{\delta i}$ are weighting factors corresponding $\sigma_{\ddot{x}i}^2$, σ_{pi}^2, and $\sigma_{\delta i}^2$; α is the body transverse angle which can be calculated from methods in the literature [7] The complex method is used for the inequality constraint problem.

The Optimal Nonlinear Parameters

After obtaining n sets of optimal equivalent linear suspension parameters Z_i for certain input conditions, system identification theory is adopted to determine the optimal nonlinear optimal parameters.

The idea is to determine the optimal nonlinear parameters by minimizing the error between estimated values of global (all input conditions) optimal linear parameters and the existing local (one input condition) linear equivalent parameters.

Assume a system shown below

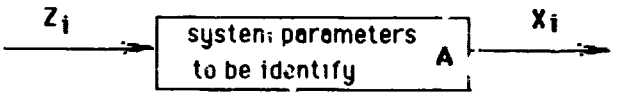

where X_i is the response statistic characteristics corresponding to Z_i and n is the number of input conditions.

From statistical linearization theory the relation between nonlinear parameters to be identify, and equivalent linear parameters is

$$Z_i = f(A, X_i) \qquad i=1, ..., n \tag{16}$$

where $A = (a_1, ..., a_m)^T$ includes the nonlinear suspension parameters to be identify. If m = n, the unique solution of A can be obtained from Eq. (16) For a general case, n > m usually be used.

Optimization Results

The optimization results of the frame (front and rear ends) acceleration mean square spectrum are given in Figure 5. It can be seen that

1) the acceleration mean square spectrum in the rear end of the frame decreases.

2) the peak values in the front end of the frame decrease.

Results of wheel dynamic forces show that both front and rear wheel mean square spectra are reduced.

CONCLUSIONS

1 The models of four kinds of nonlinear forces are established, and a vehicle nonlinear dynamic model is constructed by nonlinear modal synthesis technique

2. A Improved Statistical Linearization Method is given, which is more satisfactory to treat the hysteresis damping mechanism than CSLM

3 A new optimization procedure is developed for nonlinear parameter optimization It reduces the design variables and computing time, and also can be used to obtain the optimal nonlinear parameters for different input conditions

REFERENCES

[1] Caughey, T.K., Nonlinear Theory of Random Vibration in Advance Applied Mechanics, Vol 2, Academic Press, 1971.

[2] Roberts, J B., "Response of Nonlinear Mechanical Systems to Random Excitation, Part 2, Equivalent Linearization and Other Methods", Shock and Vibration Digest, Vol. 13, No. 5, 1981.

[3] Caughey, T K., "Equivalent Linearization techniques", J Acoust. Soc. Amer 35, 1963.

[4] Iwan, W D.and I. Yang, "Applications of Statistical Linearization Techniques to Nonlinear Multi-degree-of-freedom System", J. Appl. Mech , 39, 1972.

[5] Atalik, T.S and S Utku, "Statistic Linearization of Nonlinear Multi-degree-of-freedom Nonlinear System", Earthquake Engineering and Structural Dynamics, Vol 4, 1976

[6] Gao, J., C. Li and F Sun, "A New Model of Leaf Springs with Dry Friction", Proc. of 1989 Int. Pacific Conference on Automotive Engineering, China, 1989

[7] Lu, X etc, "A Design Procedure for the Optimization of Vehicle Suspensions", Int J. of Vehicle Design, Vol. 5, No. 1/2, 1984.

[8] Sun, F, The Research on Random Vibration of Nonlinear Vehicle Systems, Ph D Dissertation, Jilin University of Technology, 1988.

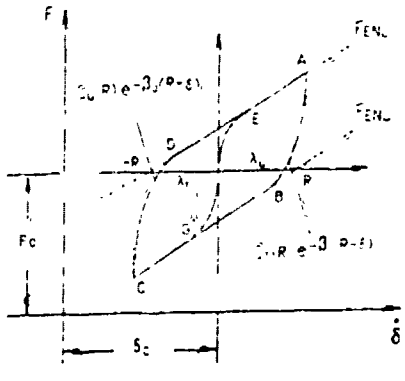

Figure 1. Leaf-springs restoring force illustration

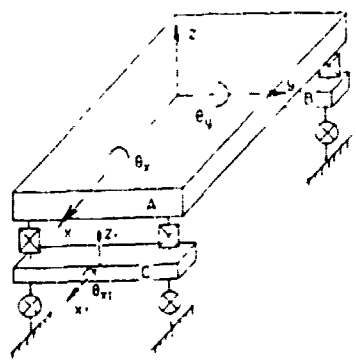

Figure 2 Vehicle riding comfort analysis model

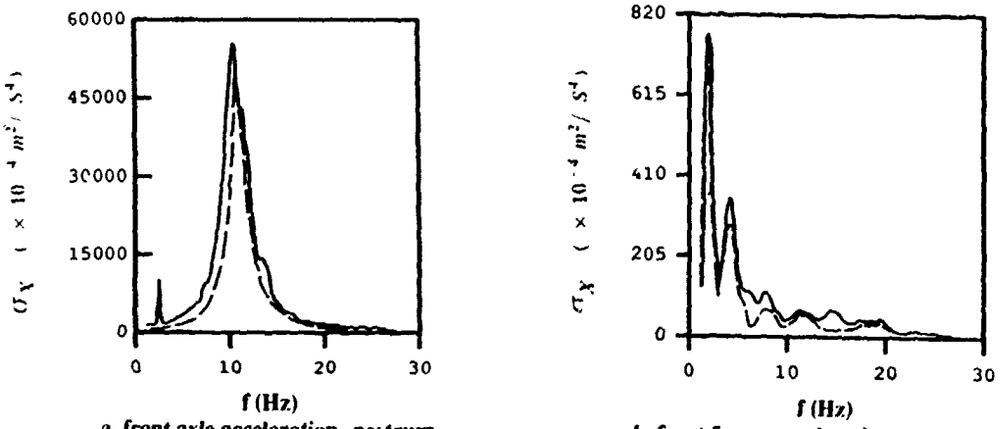

a front axle acceleration spectrum b. front frame acceleration spectrum

Figure 3. Experimental and predicted results using structural damping equivalent model

—— experimental curve ——— predicted curve

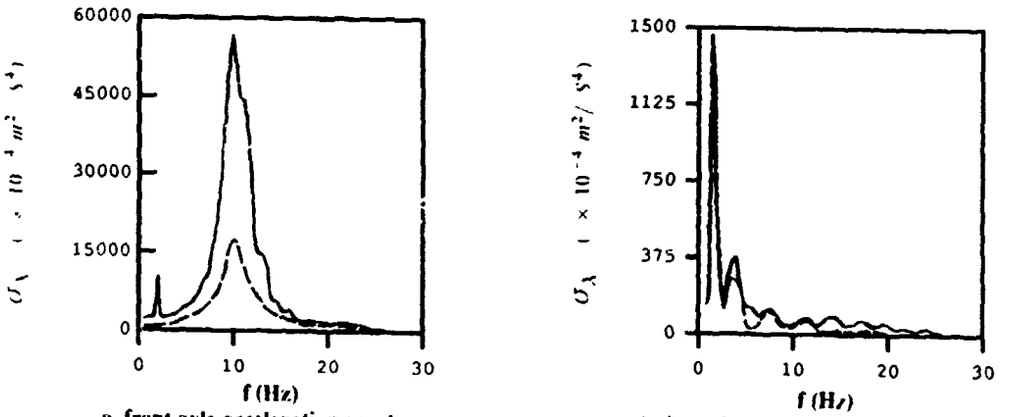

a. front axle acceleration spectrum b. front frame acceleration spectrum

Figure 4. Experimental and predicted results using viscous damping equivalent model

—— experimental curve ——— predicted curve

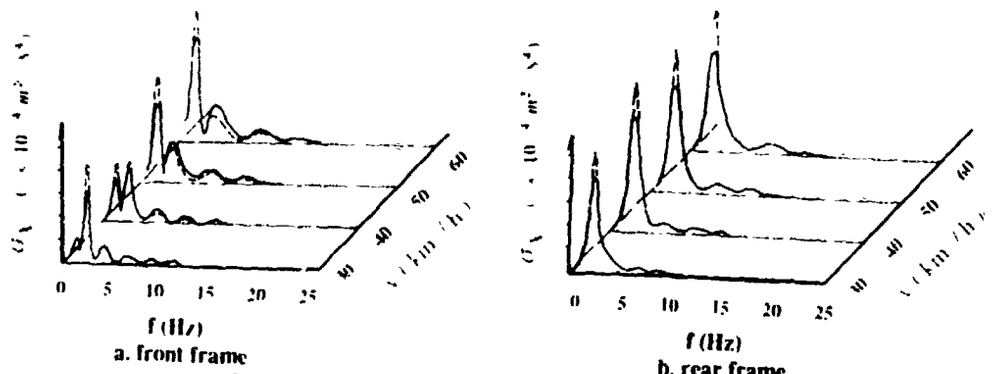

a. front frame b. rear frame

Figure 5 Optimization results of front and rear frame

——— before —— after

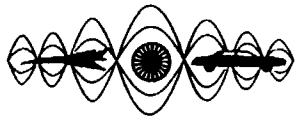

SECOND INTERNATIONAL CONGRESS ON
RECENT DEVELOPMENTS IN AIR- AND
STRUCTURE-BORNE SOUND AND VIBRATION
MARCH 4-6 1992 AUBURN UNIVERSITY USA

THE TRANSMISSION OF AERODYNAMICALLY-GENERATED NOISE THROUGH PANELS IN AUTOMOBILES

John R. Callister
Noise and Vibration Laboratory
General Motors Proving Ground
Milford, Michigan 48380-3726

Albert R. George
Mechanical and Aerospace Engineering Department
Cornell University
Ithaca, New York 14853-7501

ABSTRACT

Experimental and analytical methods were used to investigate automobile wind noise. A simplified model of an automobile side window was subjected to wind tunnel tests. The effects of window thickness and edge conditions on the transmitted wind noise level were investigated. The measurements showed that neither plate thickness nor edge conditions had much effect on the level of transmitted noise. Damping of the window edges was found to be an important parameter at low frequencies. The transmitted noise level was predicted with a Statistical Energy Analysis (SEA) model, which used an empirical expression for the fluctuating pressure on the automobile side window. The analytical prediction method was successful at predicting the frequency distribution of transmitted noise very closely, and it predicted the absolute levels to within 10 dB.

INTRODUCTION

Automobile wind noise is an old subject [1], but one that has become of more pressing interest in recent years. As automobile engines, transmissions, and tires have become quieter, wind noise has become more noticeable, particularly at higher speeds. Hence, an automobile manufacturer would like to know what design parameters affect the wind noise levels heard by the passengers. Prediction methods to date have been rather *ad hoc* in nature, and of limited success. The next level of analyses will need to consider the details of the physics at work in the generation and transmission of automobile wind noise.

The transmission of aerodynamically-generated noise through panels in automobiles consists of three parts. First, there are wall pressure fluctuations due to the flow over the exterior surface. The flow may be attached or separated. Next, these wall pressure fluctuations cause the automobile body panels to move and vibrate, the second part of the process. Third, the vibrating wall panels radiate sound into the interior of the vehicle. Actually, one could consider a fourth part to this process, the interaction of the interior of the vehicle interior cavity with the vibrating and radiating panels. It will not be accounted for here for the sake of simplicity.

This study focuses on the side window of an automobile. The automobile side window is typically a major wind noise source because it is located rather near the passenger's ears, and consists of a single, thin layer of glass. The experimental work attempted to simulate the generation and transmission of flow noise through the side window. The side window was simulated by an aluminum plate mounted in the top of an anechoic box. An analytical approach was used in an attempt to predict the noise levels measured in the experiment.

ANALYSIS

The Vibration of a Flat Plate

The side window of an automobile was simulated by a flat aluminum plate in this study. The plate was caused to vibrate by the fluctuating wall pressure exerted on one side of the plate by an external airflow. The wall pressure fluctuations are broadband; no single frequency stands out. Hence, a method to find the resonant response of a flat plate subjected to broadband forcing is needed. This can be found by using the normal mode approach, as outlined in Lin [2] and Blake [3].

The normal mode approach is rather lengthy, so only the result of Blake's [3] discussion will be mentioned here. The normal mode approach exploits the fact that the displacement of a vibrating flat plate may be arrived at by a summation or superposition of normal modes. In addition, the analysis is simplified if the eigenfunctions are assumed to be orthogonal. Fluid loading and damping can cause the modes to become physically coupled, i.e., non-orthogonal. That would complicate the analysis. In this case, where the damping is low and the only fluid loading is by air, the orthogonality assumption should hold up well. Then, following Blake's approach,

$$\langle v_{mn}^2 \rangle \approx \frac{4\,\pi^3\,\Phi_{pp}(k_1,k_2,\omega)}{m_s^2\,\omega_{mn}\,\eta\,A_p} \qquad (1)$$

where

- $\langle v_{mn}^2 \rangle$ = the mean-square velocity of the flat plate vibrating in the m,n mode.
- $\Phi_{pp}(k_1,k_2,\omega)$ = the wavenumber-frequency spectral density of the wall pressure fluctuations
- m_s = the mass per unit area of the plate
- ω_{mn} = the frequency of the vibrational mode
- η = the loss factor
- A_p = the area of the plate

The next step is to express the plate velocity in non-modal form. This could be done by considering each vibrating mode separately, and adding up all of the velocity contributions from each mode. It is more easily done by using the idea of Statistical Energy Analysis (SEA), as presented by Lyon [4]. The main idea of SEA is that of the averaging of vibrational energy over many modes. One could find an average mean-square plate velocity in a frequency band of interest by finding some average modal velocity, and multiplying by the number of modes in the frequency band. That is:

$$\langle v^2 \rangle \approx \langle v_{mn}^2 \rangle\, n(\omega)\, \Delta\omega \qquad (2)$$

where

- $\langle v^2 \rangle$ = average mean-square velocity in the frequency band, $\Delta\omega$
- $\langle v_{mn}^2 \rangle$ = the modal mean-square velocity
- $n(\omega)$ = the modal density, the number of vibrational modes per unit frequency
- $\Delta\omega$ = the width of the frequency band

The modal density of a uniform plate is [4].

$$n(\omega) = \frac{A_p}{4\pi\kappa c_l} \qquad (3)$$

where

- A_p = the area of the plate
- κ = the radius of gyration = $\sqrt{\frac{h^2}{12}}$, h = the plate thickness
- c_l = the longitudinal wave speed in the plate material

Substituting Equations (1) and (3) into Equation (2), the equation for the mean-square velocity, in a frequency band of width $\Delta\omega$, centered at the frequency ω_l, results:

$$\langle v^2 \rangle = \frac{\pi^2 \, \phi_{pp}(k_1, k_2, \omega_f) \, \Delta\omega}{m_s^2 \, \eta \, \kappa \, c_l \quad \omega_f} \tag{4}$$

The approach so far has been analytical. To solve for the mean-square velocity of the panel, values for the loss factor and the wall pressure spectrum are required. In this investigation, the loss factor was measured directly by measuring the decay of the vibration amplitude after striking the plate with a hammer. The wavenumber-frequency spectrum is derived in the next section.

Wavenumber-Frequency Spectrum of the Fluctuating Wall Pressure

The wavenumber-frequency spectrum of fluctuating wall pressure, $\phi_{pp}(k,\omega)$, gives the mean-square of the pressure exerted upon the wall, per wavevector and per frequency. The wavenumber-frequency spectrum, also known as the cross spectral density, is the Fourier transform of the cross correlation of the fluctuating wall pressure in both space and time. The formulation presented here assumes a homogeneous pressure field. That is, the correlation depends only on the separation between two points in space. While the homogeneity assumption is not strictly true, it is a reasonable approximation in many instances, and simplifies the analysis considerably.

The data of Haruna, et al [5] were used to construct an approximate model for the wavenumber-frequency spectrum for the fluctuating wall pressure beneath a separated flow. The following expression was obtained:

$$\Phi_{pp}(k_1, k_2, \omega) = \frac{1}{(2\pi)^2} \Phi_{pp}(\omega) \left[\frac{2a}{a^2 + k_1^2} \right] \left[\frac{2b}{b^2 + k_2^2} \right] \tag{5}$$

where

$$a = \frac{1.67\,\omega}{U_\infty}, \qquad b = \frac{0.25\,\omega}{U_\infty} \tag{6, 7}$$

Equation (5) is the wavenumber-frequency spectral density for the wall pressure beneath a separated flow. The frequency spectral density, $\Phi_{pp}(\omega)$, was also taken from Haruna et al [5]. A curve fit to their data gave the following relation:

$$\log_{10}(S) = -2.96 - 0.80 \left[\log_{10} \frac{fL}{U_\infty} \right] - 0.32 \left[\log_{10} \frac{fL}{U_\infty} \right]^2 \tag{8}$$

where

$S = \frac{\Phi_{pp}(\omega) U_\infty}{q^2 L}$, the non-dimensional frequency spectrum
q = the dynamic pressure based on free-stream velocity
f = the frequency
L = the average length of the separated flow region on the outside of the side window
U_∞ = the free-stream velocity

Radiation of Sound

The sound power radiated by a vibrating structure was given by Fahy [6]:

$$\Pi = \sigma \, \rho_0 \, c_0 \, S \, \langle v^2 \rangle \tag{9}$$

where

Π = the average sound power radiated by the structure
σ = the radiation efficiency
ρ_0 = the density of air
c_0 = the speed of sound in air
S = the area of the vibrating structure
$\langle v^2 \rangle$ = the mean-square velocity of the plate

Empirical expressions for the average radiation efficiency were presented by Cremer and Heckl [7]

$$\sigma = \frac{P\, c_o}{\pi^2 A_p f_c} \sqrt{\frac{f}{f_c}} \qquad \text{for } f < f_c \qquad (10)$$

$$\sigma = 0.45 \sqrt{\frac{P\, f_c}{c_o}} \qquad \text{for } f = f_c \qquad (11)$$

$$\sigma = 1 \qquad \text{for } f > f_c \qquad (12)$$

where

c_o = the speed of sound in air
f_c = the acoustic coincidence frequency
A_p = the area of the plate
P = the perimeter of the plate

Using the mean-square velocity of the plate from Equation (4), and the radiation efficiency values from Equations (10) through (12), the radiated sound power was found from Equation (9). This result was compared with the experimental results.

EXPERIMENTAL RESULTS

Description of Equipment

A sketch of the experimental set-up is shown in Figure 1. The two main components required for the experimental study were the wind tunnel, to provide the flow, and the anechoic box, in which the plate was mounted

The wind tunnel used was the Cornell University Upson Hall Low Speed Wind Tunnel. This wind tunnel was capable of speeds up to 30 meters per second. The turbulence level of the tunnel was 0.6%, with a flow uniformity of 1% [8]. The wind tunnel test section was 0 5 meters high and 0.75 meters wide The wind tunnel had both inlet and in-line silencers installed. The ambient noise level at the tunnel outlet was approximately 80 dBA.

Due to the rather high noise level of the wind tunnel, special care was taken with the construction of the anechoic box. The details of the design and construction can be found in the paper by Kost [9] The interior of the box was effectively anechoic down to 226 Hertz. The aluminum plates were mounted flush in a frame centered in the top of the box.

A microphone was mounted just above the inner floor of the box. The microphone was connected to an externally positioned General 1982 Sound Level Meter. The anechoic box was wheeled in front of the exit of the wind tunnel. As shown in Figure 1, a boundary layer scoop was added to the wind tunnel. As a result, the boundary layer on the plate was reduced to a mean thickness of 0.02 meters.

The aluminum plates tested were 3.175 and 4.76 millimeters thick. The effective radiating area of the plates was 0.25 m^2. A 3.175 mm thick plate was used in the clamped case, and the simply-supported plates were 3.175 and 4.76 millimeters thick.

Flow Obstructions to Induce Separated Flow

Mohsen [10] found that the fluctuating wall pressure was more intense behind a fence than behind a backward-facing step, so only fences were examined. Fences heights of 12.7 millimeters, 19 millimeters, and 51 millimeters were used in preliminary tests. Only the 51 millimeter fence gave a signal-to-noise ratio greater than 10 dB in the frequency bands of interest , so the 51 millimeter high fence was selected.

Next, flow visualization methods were used with the 51 millimeter fence to determine the mean reattachment point of the separated flow. A piece of sheet metal, 1.25 meters by 0.7 meters is size, was painted with a mixture of carbon black and WD-40 lubricant. The plate was fastened on the top of the box butting up to the 51 millimeter fence, with the fence positioned at the upstream edge of the plate. The wind tunnel was run for 5 minutes at an airflow velocity of 26.8 meters per second.

Five principle flow regimes were observed. Starting at the fence and moving downstream, the first region, extending from the fence a distance 0.2 meters, or 4 step heights, downstream, was one of low flow. That is, the inky mixture on the plate had not moved or formed any discernable pattern

The next region was one of backward flow This region extended from 0.2 to 0.41 meters, or 4 to 8 fence heights, downstream of the fence. The streaks of carbon black were clearly directed upstream.

The next region, dubbed the fluctuating reattachment region, emphasized that the separation was unsteady. In this region the plate had been scrubbed of quite a bit of its carbon black, due to the flow impinging on this region in an unsteady fashion. This region reached from 0.41 to 0.71 meters, or 8 to 14 fence heights, downstream.

The fourth region, the reattachment region, had been scrubbed of nearly all of its carbon black. The flow reattached most often in this region. As a result, in the mean, this region can be designated as the reattachment zone, even though the flow is unsteady and reattaches in locations varying over a large portion of the plate. The region reached from 0.71 to 0.86 meters or 14 to 17 fence heights downstream of the fence. The center of the reattachment region was a distance 15.5 fence heights (0 790 m) downstream from the fence This coincides quite well with the observations of Fricke and Stevenson [11] and Fricke [12], who found reattachment at 14 fence heights and 15 fence heights downstream, respectively.

In the fifth region, the forward flow region, the flow had clearly reattached, at least in a mean sense, and the carbon black streaks were moving downstream. This region extended from 0.86 meters or 17 fence heights downstream of the fence to the end of the painted area.

After observing the results of the flow visualization, it was decided to move the fence to a location 0.4 meters upstream of the plate This way, the plate was situated beneath the regions of fluctuating reattachment and mean reattachment, where the wall pressure fluctuations were presumably the strongest. This would also ease analysis, for an assumption of homogeneity for the wall pressure fluctuations on the plate surface would not be to outlandish

Noise Level Measurements and Results

The most important part of this investigation was the measurement of the sound level in the anechoic box when a flow was passed over the plate on top. The flow velocity was 26.8 meters per second The two flows used were a turbulent boundary layer, with an average boundary layer thickness of 0.02 meters, and a separated flow, using a 5 f millimeter high fence 0.4 meters upstream from the edge of the plate. The sound level was measured in octave bands, using a GenRad Model 1982 sound level meter

The highest overall sound level measured inside the box with the separated external flow was obtained with the 3 175 millimeter clamped-edge plate The sound level of the 3.175 millimeter simply-supported plate was 0.2 dB lower. The overall sound level with the 4 76 millimeter simply-supported plate was 0 8 dB lower than the 3.175 millimeter clamped-edge plate.

The highest overall sound level measured inside the box with the attached turbulent boundary layer external flow was obtained with the 3.175 millimeter simply-supported plate. The sound level obtained with the 3.175 millimeter clamped-edge plate was 0.4 dB lower The sound level obtained with the 4 76 millimeter simply-supported plate was 0 6 dB lower.

With both simply-supported plates, the overall sound level obtained with the separated flow was 1.5 dB higher than the sound level obtained with the turbulent boundary layer flow With the clamped-edge plate, the overall sound level obtained with the separated flow was 2.1 dB higher than the sound level obtained with the turbulent boundary layer flow.

To summarize the results, it was observed that the separated flow caused a slightly higher overall sound level at frequencies within the 500 Hertz octave band and above The effect of plate thickness on the overall sound level was observed to be small. The clamped plate gave a sound level nearly equal to the simply-supported plate with a separated flow, and somewhat lower with the turbulent boundary layer flow

COMPARISON OF EXPERIMENT AND PREDICTION

The final step was the prediction of the sound level inside the anechoic box. Only the separated flow case was considered. Three different plate conditions were considered, matching those in the experiment 3.175 mm thick simply-supported, 4.76 mm thick simply supported, and 3 175 mm thick with clamped edges

To compare the value for the sound pressure level obtained from the equations with that obtained experimentally, it was necessary to account for the distance from the plate to the microphone. That is, the calculations gave the far-field sound power right at the surface of the plate, whereas the experimental sound power measurement was made at a distance of 0.46 meters. It was assumed that the radiated sound could be considered to be non-directional. Using this assumption, the sound power

at the microphone was calculated to be 19% of the total sound power radiated by the plate. This correction was applied to the sound power calculated with Equation (9).

The results are shown in Figures 2 through 4. The 3.175 millimeter simply-supported plate results in Figure 2 show reasonably good agreement between the predicted and measured sound levels. The shape of the curve is captured rather well, but the predicted curve over-emphasizes the radiation near the acoustic coincidence frequency. The levels are within 5 to 10 dB of each other. The 4.76 millimeter, simply-supported plate in Figure 3 has better agreement at most frequencies, but the acoustic coincidence frequency octave is again the one with the greatest disparity. The analytical results clearly show the increased level at 2000 Hertz for the thicker plate, due to the reduction in the acoustic coincidence frequency. This effect shows up only slightly in the experimental results. The predicted sound levels for the clamped plate, shown in Figure 4, match the measured results quite well in terms of the shape of the two curves. The overall levels differ by less than 10 dB.

SUMMARY

The experimental portion of this investigation showed that plate thickness and edge conditions did not affect the transmitted sound level as much as one might suppose. The prediction scheme used in this investigation, while rather simple, showed promise. The prediction model incorporated some of the physics of the problem, such as the wavenumber-frequency spectral density of the wall pressure. Further refinement of the prediction model may lead to a useful noise level prediction scheme for automobile wind noise.

REFERENCES

1 Lamarque, P.V. Some Notes on Wind Noise on Cars, The Institution of Automobile Engineers, A.R.C. No. 91808, November (1939)

2. Lin, Y.K. "Probabilistic Theory of Structural Dynamics", McGraw-Hill, New York, 1967.

3. Blake, W.K "Mechanics of Flow-Induced Sound and Vibration", Academic Press, Orlando, 1986

4 Lyon, R.H. "Statistical Energy Analysis of Dynamical Systems: Theory and Applications", MIT Press, Cambridge, 1975.

5. Haruna S. Nouzawa, T Kamimoto, I and Hiroshi, S. An Experimental Analysis and Estimation of Aerodynamic Noise Using a Production Vehicle, SAE Paper 900316, Detroit (1990).

6. Fahy, F. "Sound and Structural Vibration: Radiation, Transmission, and Response", Academic Press, Orlando, 1985.

7 Cremer, I. and Heckl, M. "Structure-Borne Sound: Structural Vibrations and Sound Radiation at Audio Frequencies", Translated and revised by E E Ungar, 2nd edition. Springer-Verlag, Berlin, 1988.

8 Duell, E.G. Lift and Drag of Finite, Rotating Cylinders Near a Ground Plane, AIAA Paper 91-0191, Reno, Nevada (1991).

9. Kost, D. "Design of a Portable Anechoic Chamber", Master of Engineering Project Report, Mechanical and Aerospace Engineering Department, Cornell University, June 1991

10. Mohsen, A.M Experimental Investigation of the Wall Pressure Fluctuations in Subsonic Separated Flows, Boeing Company Report No D6-17094 (1967).

11 Fricke, F R and Stevenson, D.C. Pressure Fluctuations in a Separated Flow Region, *Journal of the Acoustical Society of America*, Vol. 44, No 5, pp. 1189-1200 (1968)

12 Fricke, F R Pressure Fluctuations in Separated Flows, *Journal of Sound and Vibration*, Vol 17, No 1, pp. 113-123 (1971)

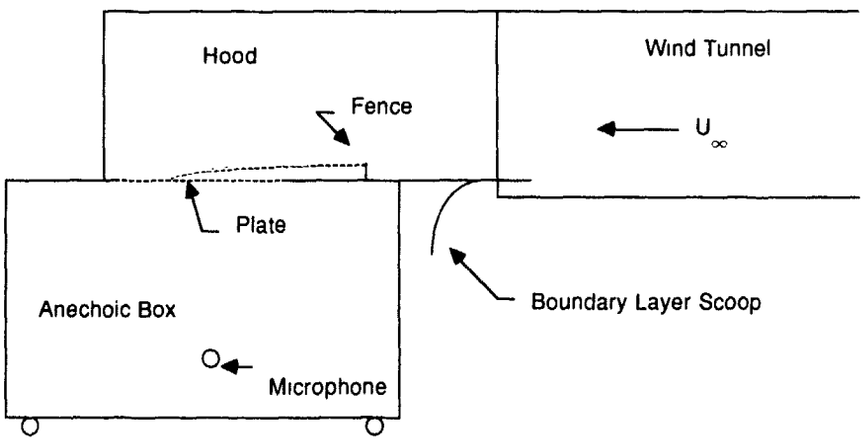

Figure 1. A Sketch of the Experimental Apparatus

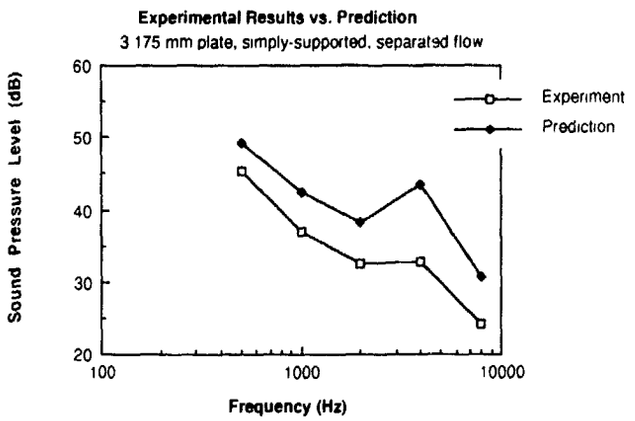

Figure 2 Sound Levels with the 3.175 Millimeter Simply-Supported Plate

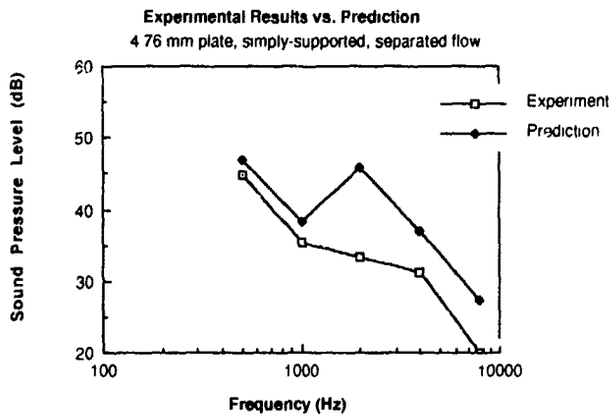

Figure 3. Sound Levels with the 4 76 Millimeter Simply-Supported Plate

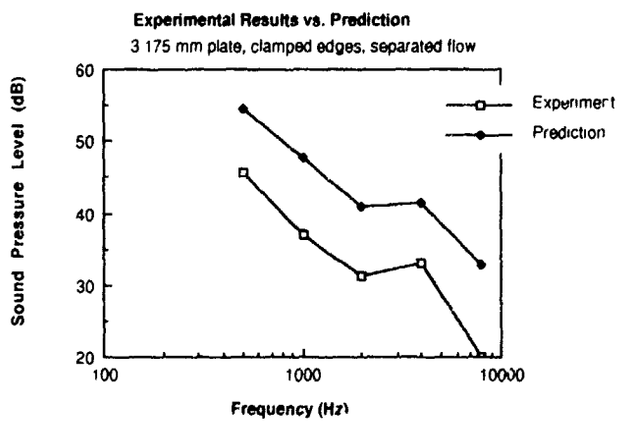

Figure 4. Sound Levels with the 3 175 Millimeter Clamped Edge Plate

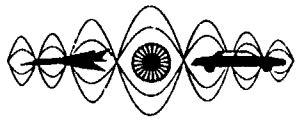

SECOND INTERNATIONAL CONGRESS ON
RECENT DEVELOPMENTS IN AIR- AND
STRUCTURE-BORNE SOUND AND VIBRATION
MARCH 4 6 1992 AUBURN UNIVERSITY USA

EXPERIMENTAL STUDY OF TRANSFER FUNCTION MEASUREMENTS USING LEAST-MEAN-SQUARE ADAPTIVE APPROACH

Jiawei Lu
United Technologies Carrier
Commercial Compressor Engineering
Syracuse, New York 13221

Malcolm J. Crocker and P.K. Raju
Department of Mechanical Engineering
Auburn University, AL 36849

ABSTRACT

This paper discusses transfer function measurements made using the least-mean-square (LMS) adaptive approaches. Experiments with transfer functions made using traditional FFT measurements and the LMS approach were conducted using computer simulation. The results for the transfer function obtained using the LMS adaptive approach are compared with the results obtained using the traditional approach in the frequency domain. The results show that an accuracy of the order of 10^{2} with respect to a measured theoretical transfer function can be obtained with a traditional 4096 point FFT measurement after fifty averages are taken and an accuracy of the order of 10^{12} is obtained by the LMS approach with fifty iterations. The measured accuracy of the transfer function and the rate of convergence to the measured function have been improved greatly by using the LMS approach. The study shows that the LMS algorithm using the FFT block processing approach can be destabilized by frequency-spectral leakage in the measurement. Some approaches to overcome this difficulty have also been investigated.

1. INTRODUCTION

Transfer function measurements are used in many engineering applications. A schematic diagram of a transfer function measurement for a SISO system is shown in Figure 1. This is usually implemented using a FFT analyzer. Increasing the number of averages is the only way to obtain an accurate measurement with the FFT analyzer. How accurate will the result be with a certain number of averages and what is the rate of accuracy improvement with increasing number of averages? The answer to this question is not well known. As seen in the results of this paper, the measurement accuracy is poor and the rate of improvement with the traditional measurement approach is very limited. However, this has not become a severe problem because there are not many engineering applications which require the measured transfer function to have a high accuracy. The measurement of damping ratio of composite materials by means of transfer function measurement is one example which requires a highly accurate measurement of the transfer function because the damping of the materials is very low. The accuracy of the damping ratio measured is limited by the accuracy of the transfer function measurement.

The Least-Mean-Square adaptive approach has been widely used in control and model identification. A transfer function measurement using the LMS approach is an essential form of model identification, as shown in Figure 4. If the LMS approach is implemented using FFT block processing in the frequency domain, the measurement system, as shown in Figure 4, can be easily realized within present commercially available FFT analyzers after a little modification. The advantages and disadvantages of using the LMS

approach for the measurements needs to be investigated. This has been the purpose of the research reported here.

2. THEORETICAL CONSIDERATION

Traditional transfer function measurements have based on the use of FFT analysis in the frequency domain. The transfer function is measured using [1]

$$H(K) = P_{xy}(K)/P_{xx}(K), \tag{1}$$

where $P_{xx}(K)$ and $P_{xy}(K)$ are the auto-spectrum of the input x and the cross-spectrum between the input x and the output y respectively, as shown in Figure 1. $P_{xx}(K)$ and $P_{xy}(K)$ are measured by

$$P_{xx}(K) = |X(K)/N|^2 \tag{2}$$

and

$$P_{xy}(K) = X^*(K)\,Y(K)/N^2 \tag{3}$$

where X(K) and Y(K) are the frequency-domain expressions for x(n) and y(n), and N is the number of sample points.

Assume that the input x(n) is a random signal with a Gaussian distribution. To improve the results measured using the traditional approach, an average can be taken of the measured results. The number of averages can be 10 or 100 for instance. The average can be executed simply from:

$$H_i(K) = (1 - 1/i)\,H_{i-1}(K) + H_{xy,i}(K)/i, \qquad i=1,2,.... \tag{4}$$

where $H_{xy,i}(K)$ is the transfer function measured at the i-th measurement.

Smoothly zero-ended windows for sample blocks can be used to reduce the effect of the Gibbs phenomenon. Although the introduction of windows in the measurement distorts the real sampled signal, this adverse effect can be averaged out by different input x(n). The accuracy of the measurement also depends on some other factors. The number of sample points is one of important factors.

Assume that the transfer function to be measured is given by

$$H(s) = 10\times\frac{\prod_{j=1}^{3}(s-z_j)(s-z_j^*)}{\prod_{j=1}^{4}(s-p_j)(s-p_j^*)}, \tag{5}$$

where the zeros z_j; z_j^* and the poles p_j; p_j^* are given in Table 1. This transfer function is abstracted from the four-degree of freedom system discussed in reference [2] where the transfer function ($H_{ul}(K)$) is required to be measured accurately in advance of the control experiments. The impulse response h(n) and the transfer function H(K) given by Eq.(5) are shown in Figures 2 and 3.

If the LMS adaptive approach is introduced into the measurement by Eqs.(1) through (3), the schematic diagram of the measurement is shown in Figure 4 The LMS algorithm is given, in the frequency domain, by

$$H_i(K) = H_{i-1}(K) + \alpha\,H_{xe,i}(K), \qquad i=1,2, \quad . \tag{6}$$

where $H_i(K)$ is the expression for h'(n) in the frequency domain and is the measured transfer function between the input x(n) and the output y(n), $H_{xe,i}(K)$ is the transfer function between the input x(n) and the error signal e(n) and α ($0<\alpha\leq 1$) is the gain constant which regulates the speed of adaptation. In Figure 4, both the input x(n) and the error e(n) are sent to a microcomputer in order to calculate $H_{xe,i}(K)$. The calculated $H_{xe,i}(K)$ is used to modify $H_i(K)$ (or h'(n)). The weights of the transfer function h'(n) are adjusted using the LMS algorithm until the error signal e(n) approaches zero and h'(n)=h(n). If the initial transfer function $H_0(K)$ is assumed to be zero and α is one, the transfer function $H_{xe,1}(K)$ obtained after the first measurement is obviously seen to be the same as $H_{xy}(K)$ given in Eq.(4). A unity gain constant α is the goal pursued in this paper because it promises to give the highest convergence speed and the widest stability margin.

To evaluate the accuracy of the measurement, the standard deviation was calculated as given by

$$S_i = \frac{1}{N/2-1}\left[\sum_{k=1}^{N/2} (|H(K)|-|H_i(K)|)^2\right]^{1/2}, \qquad i=1,2,..... \tag{7}$$

where H(K) is the theoretical transfer function, $H_i(K)$ is the measured one and N is the sample length. Because of the redundancy in $H_i(K)$ which is calculated by the Fast Fourier Transform, only half of the sample length N/2 of the spectrum is used in Eq.(7).

3. PRELIMINARY RESULTS

The experiment was first conducted using a 2048-point number of samples x(n) sampled from a random signal with a Gaussian distribution. A Hanning window was used in the measurement. The results obtained from the traditional measurement given by Eq.(4) and from the model identification using the LMS approach given by Eq.(6) are shown in Figure 5.

Fifteen averages and iterations were taken in the traditional measurement and in the measurement using the LMS algorithm. For the results shown in Figure 5, the gain constant α was chosen to be one. It can be seen that the results obtained using the LMS approach are divergent in this case. The transfer function $H_{15}(K)$ obtained using the LMS approach is shown in Figure 6. The experiment showed that as the iteration number i was increased further, the results as shown in Figure 16 drastically become much worse.

The convergent result, as shown in Figure 7, was obtained when the gain constant α was chosen to be one for the feedback of $H_{xe,1}(K)$ (i=1) and one tenth for other iterations (i>1). Fifty averages and iterations were taken in the measurement. It can be seen that the convergence of the LMS algorithm is rather slow in this case and that the convergence speed is of the same order both for the LMS approach and the traditional measurement method. The stability of the LMS algorithm has become a key to the continuation of this study. The problem of stability is investigated in the following section.

4. STABILITY OF LMS ALGORITHM

Equation (6) essentially presents a search scheme based on the Newton-Raphson method if $\alpha=1$. Newton's method will always converge provided a sufficiently accurate initial approximation is chosen. This is true because the measured transfer function $H_{xe,1}(K)$ usually gives a good approximation when $H_0(K)=0$ is assumed. Two measurement methods were used to investigate the cause of instability. The first method was considered by measuring the auto- and the cross- correlation functions directly in the time domain. The second method was considered by designing an experiment in the frequency domain which was immune to the frequency-spectral leakage. The experiments showed that the instability of the LMS algorithm is caused by the frequency-spectral leakage.

4.1 Time-Domain Measurement

If the auto- and cross- correlation functions are denoted as $C_{xx}(n)$ and $C_{xy}(n)$ respectively, the unit impulse response function h(n) can be solved by deconvolution and written as

$$h(n) = C_{xx} \odot C_{xy}, \tag{8}$$

where the symbol o is used to denote deconvolution. The solution of Eq.(8) requires that the measurements should start at the initial time t= 0 when the measured system is excited. A better approach is to solve for h(n) in the frequency domain. This requires the calculation of the spectrum functions $P_{xx}(K)$ and $P_{xy}(K)$ directly from $C_{xx}(n)$ and $C_{xy}(n)$, and then the use of Eq.(1) and the inverse Fourier transform to find h(n).

Assume that x(n) is a random signal with 1024-point samples and that the impulse response h(n) to be measured has a length of 1024-points. Thus, y(n) is the response with a length of 2047-points. $C_{xx}(n)$ and $C_{xy}(n)$ are given by

$$C_{xx}(i) = \frac{1}{N}\sum_{n=0}^{N-1} x(n)x(n+i), \quad i=0,1,2,...1023 \tag{9}$$

and

$$C_{xy}(j) = \frac{1}{N}\sum_{n=0}^{N-1} x(n)y(n+j), \quad j=0,1,2,...2046, \tag{10}$$

where x(n) and y(n) have been padded with 1023 point zeros and N=1024.

The results for H(K) obtained by using the time-domain measurement method combined with the LMS approach are shown in Figure 8. The results obtained by using the traditional measurement method (2048-point FFT) are also shown in the same figure. It can be seen that the convergence of the LMS algorithm is rather fast with $\alpha=1$ and the difference between the theoretical result H(K) and the result $H_i(K)$ measured by using this time-domain method approaches zero very rapidly.

Although the time-domain measurements are successful, the results do not directly reveal the cause of instability, and only show that the LMS algorithm with $\alpha=1$ can be stable if the measurements of $P_{xx}(K)$ and $P_{xy}(K)$ are performed in the time domain. One limitation with the time-domain method is that the input x(n) should be an incoherent time sequence. Otherwise, all the information for the measured transfer function will be lost in the measurements of $C_{xx}(n)$ and $C_{xy}(n)$. The computation of transfer functions usually takes much more time in the time domain than in the frequency domain with the FFT approach.

4.2 Frequency-Domain Measurement

The experiments were designed to examine the cause of instability. The effect of frequency-spectral leakage was the main concern of this investigation. In the experiments, a saw-tooth wave signal was used as the excitation signal, whose waveform and frequency spectrum are shown in Figures 9 and 10 respectively. The fundamental and harmonic frequency components lie at 0.49, 0.98, 1.47, 1.95, 2.44 Hz,....., while other frequency-spectral leakage can be seen explicitly. The sample length for the FFT spectrum calculation was chosen to be 1024 points with a sampling rate of 10 Hz.

The experimental results given in Figure 11 show that the algorithm in this case is divergent and the standard deviation of the measurement increases exponentially with increase of the iteration number (i). Figure 12 shows the transfer function $H_i(K)$ measured using Eq.(6) after the fourth iteration (i=4). The unstable peak can be clearly seen at the frequency f=2.07 Hz.

To eliminate the effect of frequency-spectral leakage, the experiment was tested by using a purified saw-tooth wave signal as the excitation signal. The so-called purified signal was obtained from the same signal in Figure 9 but with its frequency-spectral leakage suppressed to zero, as shown in Figure 10. Thus, the purified signal contains only the harmonic frequency components in the 1024-point frequency spectrum. The deviation of the transfer-function measurement obtained by using the purified signal is given in Figure 13 and shows that the algorithm is stable although it does not have a fast convergence rate as compared

with the results obtained using the time-domain approach as shown in Figure 8. The repeatedly identical (or invariant) saw-tooth excitation signal has resulted in the slow convergence.

5. FINAL RESULTS

Increasing the length of the Fourier transform is one way to reduce the frequency-spectral leakage. The experiment was tested using a 4096-point sample length for the FFT spectrum calculation. The experiment was the same as the experiment conducted in Section 3, except that a 4096-point random signal x(n) was used as the excitation signal in this experiment. The standard deviation of the measurement is shown in Figure 14. A large convergence rate was achieved for the results obtained using the LMS approach. This convergence rate is of the same order as the one obtained using the correlation method as shown in Figure 8.

The above experiments have only been simulated for the case when the excitation and the measurements start at the time t=0. In practice, the measurement is usually taken during any arbitrary time period after the excitation starts. This measurement procedure also can be simulated as shown in Figure 15 The excitation signal x(n) with a 5120-point sample length is used with a system represented by a 1024-point impulse response function h(n) to produce the response y(n). A length of the 4096-point response y(n) can be considered to include the effects of the x(n) history from t=0. Then, the transfer function measurement in a real measurement process can be simulated by using the response y(n) of 4096-point length and the excitation x(n) of the corresponding period as shown in Figure 15 The results obtained with the traditional measurement and the LMS approach are shown in Figure 16. Fast convergence for the LMS approach as with the previous case shown in Figure 14 was achieved.

6. CONCLUSIONS

Transfer function measurements using traditional and LMS adaptive approaches have been discussed in this paper. The results show that an accuracy of the order of 10^{-2} with respect to a measured theoretical transfer function can be obtained by a traditional 4096 point FFT measurement if fifty averages are taken and an accuracy of the order of 10^{-12} is obtained by the LMS approach with fifty iterations. The measurement accuracy of the transfer function and the rate of convergence to the measured function can be greatly improved by using the LMS approach.

The experimental study shows that the LMS algorithm using the FFT block processing approach can be destabilized by frequency-spectral leakage. One way to overcome this difficulty is to use a larger sample block with more points for the FFT.

This research work has only considered the case when the input is an independent random signal process. In principle, any response within a system can be used as an input. Such cases can be considered in further work.

ACKNOWLEDGMENTS

This work was supported and performed in the Department of Mechanical Engineering, Auburn University.

REFERENCES

1. Bruel & Kjær, Dual Channel Signal Analyzer Type 2032, Instruction Manual, Vol.2
2. J. Lu, M.J. Crocker and P.K. Raju, "Active Control of Random Vibration of a One-Dimensional Multiple Degrees of Freedom Dynamic System," Proceedings of the International Congress on Recent Developments in Air & Structure Borne Sound and Vibration held at Auburn University, Alabama, March 1990. Vol.1, 237-242

Table I Poles and Zeros of the Transfer Function H(s) Given in Eq.(5)

i	1	2	3	4
p_i, p_i^*	-0.0537±1.3876j	-1.2305±6.6473j	-2.5695±13.905j	3.8234±19.433j
z_i, z_i^*	-0.0768±1.5346j	-1.8698±8.4891j	-3.5397±17.617j	

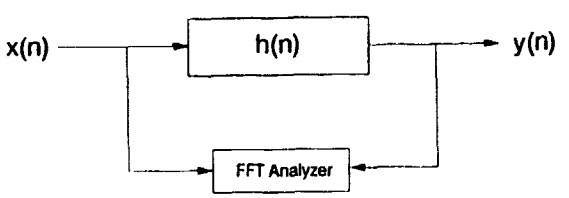

Figure 1 Schematic Diagram of the Traditional Transfer Function Measurement for a SISO System

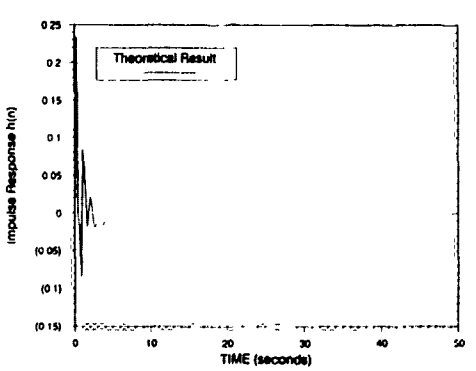

Figure 2 Impulse Response h(n) Given by Eq.(5)

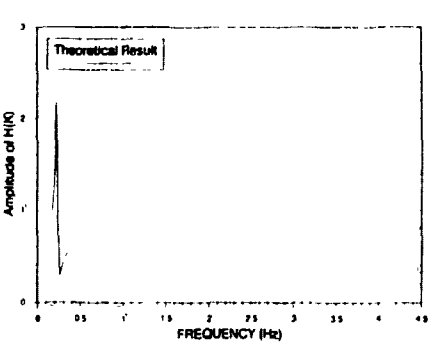

Figure 3 Transfer Function H(K) Given by Eq.(5)

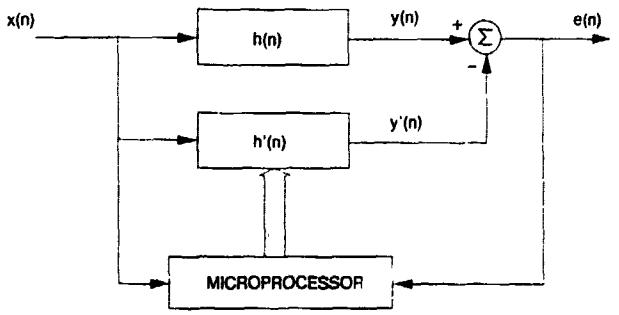

Figure 4 Transfer Function Measurement Using the LMS Approach

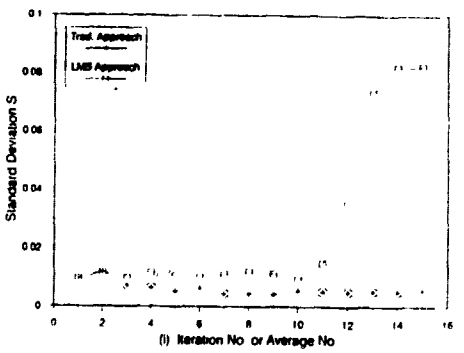

Figure 5 Standard Deviation S of the Transfer Function Measurement. Diverges for LMS Approach with Unit Gain Constant and 2048 Sample Points

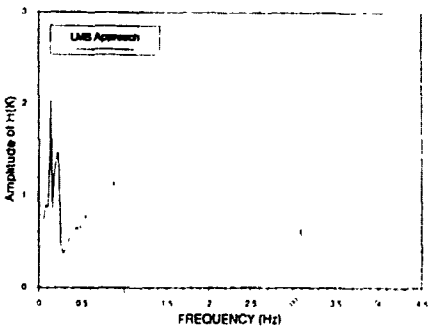

Figure 6 Measured Transfer Function H(K) Using LMS Approach after Fifteen Iterations with Unit Gain Constant and 2048 Sample Points

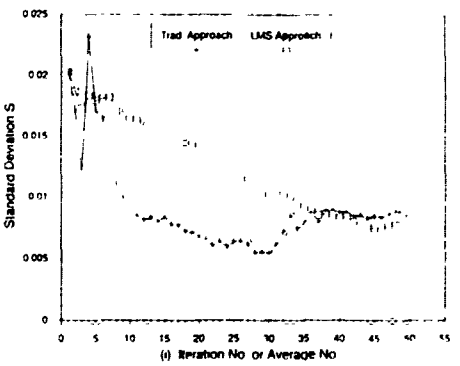

Figure 7 Standard Deviation S of the Transfer Function Measurement, 2048 Sample Points, Converges for LMS Approach with Gain Constant = 1 for the First Iteration and = 0 1 for Other Iterations

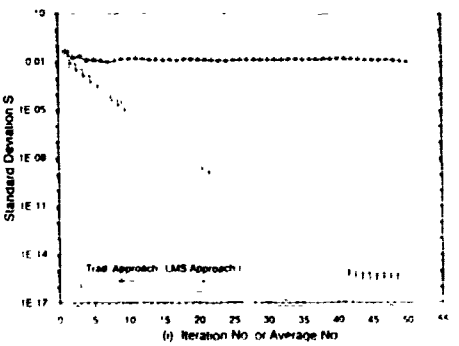

Figure 8 Standard Deviation S of the Transfer Function Measurement, Converges for LMS Approach with Unit Gain Constant by Using Correlation Method in Time Domain

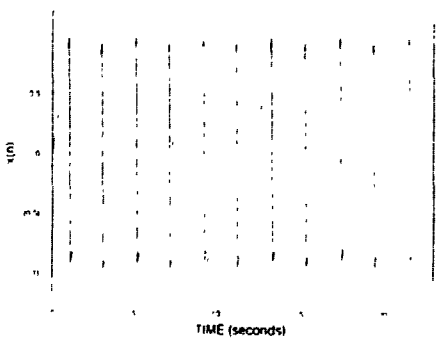

Figure 9 Saw-tooth Wave with 0 49 Hz Fundamental Frequency Sampled at a Rate of 10 Hz

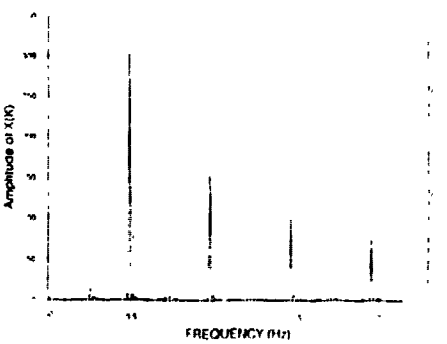

Figure 10 Spectral Amplitude of the Saw-tooth Wave with Fundamental and Harmonic Components of 0 49, 0 98, 1 47, 1 95 2 44 Hz

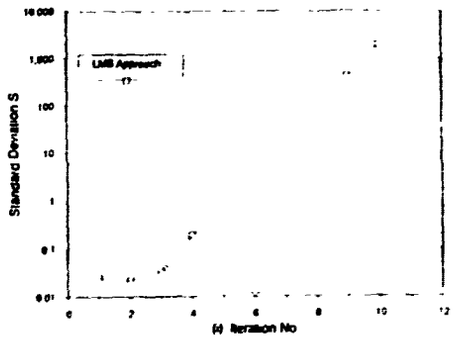

Figure 11 Standard Deviation S of the Transfer Function Measurement Using LMS Approach, Diverges with Unit Gain Constant when a Saw-tooth Signal is Used

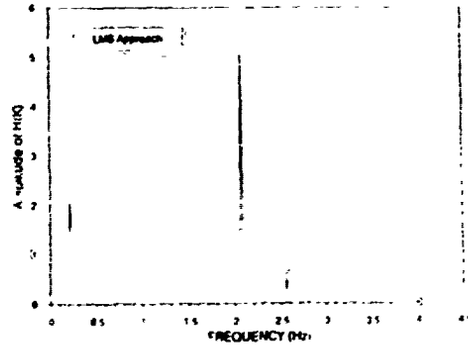

Figure 12 Measured Transfer Function H(K) Using LMS Approach after the Fourth Iteration and under Saw-tooth Wave Excitation

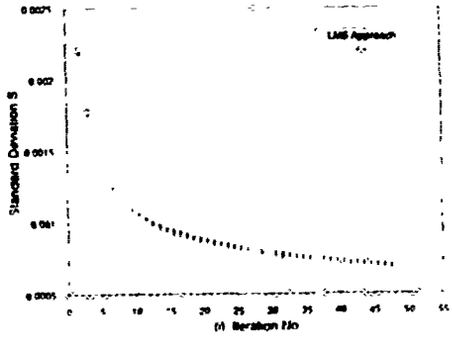

Figure 13 Standard Deviation S of the Transfer Function Measurement Using LMS Approach, Converges with Unit Gain Constant when a Purified Saw-tooth Signal is Used

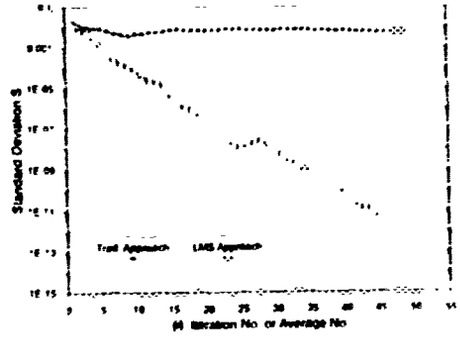

Figure 14 Standard Deviation S of the Transfer Function Measurement, Converges for LMS Approach with Unit Gain Constant and 4096 Sample Points

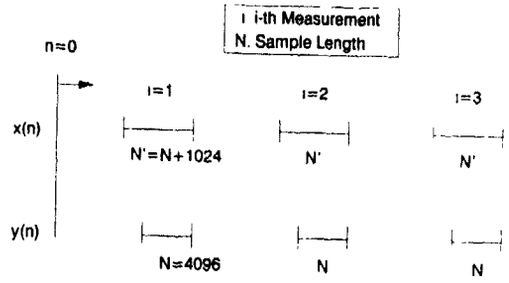

Figure 15 Schematic Diagram of the Simulation of a Real Measurement Process

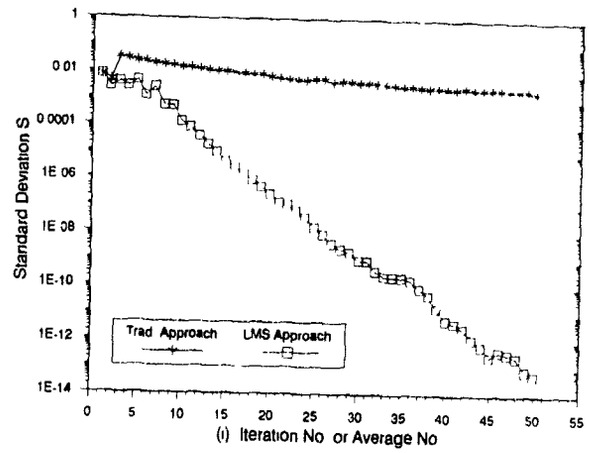

Figure 16 Standard Deviation S of the Transfer Function Measurement which is simulated for a Real Measurement Process as Shown in Figure 15

KEYNOTE ADDRESS

FUTURE DEVELOPMENTS IN EXPERIMENTAL MODAL ANALYSIS

David Brown

SECOND INTERNATIONAL CONGRESS ON
RECENT DEVELOPMENTS IN AIR- AND
STRUCTURE-BORNE SOUND AND VIBRATION
MARCH 4-6 1992 AUBURN UNIVERSITY USA

Future Developments in Experimental Modal Analysis

David L. Brown
Professor
Department of Mechanical, Industrial and Nuclear Engineering
University of Cincinnati
Cincinnati, OH 45221 USA

Abstract

This paper reviews several new developments, at the University of Cincinnati in the area of experimental modal analysis. Most of the recent advancements have been in the areas of multiple-input multiple-output measurement, signal processing and parameter estimation As the cost of transducers, data acquisition, and compute power have dropped, it has become feasible to utilize larger numbers of channels of instrumentation for modal analysis The following discussion primarily focus on new developments in multiple reference modal analysis

Introduction

In recent years there has been a significant reduction in the cost of equipment for multiple-channel modal analysis The price drop has occurred across the entire spectrum of equipment used in experimental modal analysis, that is transducers, signal conditioning, data acquisition, signal processing and data analysis equipment Much of the current research has focused on expanding measurement, signal processing and data analysis capabilities to include multiple references. This paper discusses some of the significant developments in multiple-reference modal analysis

Background

Multiple-reference modal analysis was one of the orginal techniques used in experimental modal analysis One of the first procedures developed was the tuned normal-mode testing procedure in which each mode was tuned by applying a forcing vector to a structure The forcing vector (both frequency and forcing pattern) was adjusted such that a single mode was excited The displacements at various points on the structure were then measured to determine one of the eigenvectors of the system This method was, and still is, excellent for determining the modal parameters of a system. It required a large number of simultaneously measured response channels to be practical in terms of testing time. Historically, the large numbers of data acquisition channels made this procedure cost prohibitive for most users. The method also required a high level of operator skill in tuning the normal modes Thus, the method was impractical for occasional users or for an experienced user testing a structure in which prior knowledge of the types of eigenvectors is unknown

In the late sixties and early seventies, procedures for single-input frequency response testing were developed In general, these methods were much faster than the normal-mode testing methods, particularly for cases in which only a few transducers were available It also required much lower skill levels for testing of nonstandard test objects In the mid seventies, single-input frequency response methods were used in ninety-five percent of

applications Most of these applications were associated with the trouble shooting of vibration and/or noise problems However, in the late seventies, there was an increasing demand for finite-element verification and modal model generation. Both of these applications placed severe demands on the extraction of realistic modal parameters and single input methods were not capable of extracting suitable modal parameters, except for fairly simple systems. Therefore, in this late seventies period an increased emphasis was placed upon developing multiple-input methods which could be used to increase the accuracy of the measured modal parameters

Multiple input frequency response measurement methods were subsequently developed in the late seventies and perfected in the early eighties. Also in the eighties, with the advent of the polyreference time domain method, a series of multiple-input multiple-output parameter estimation algorithms were developed In fact, algorithms are still being developed at an exponential rate

Today there is a significant effort to consolidate many of these methods into a more generalized unified theory -- a goal which is almost complete Nearly all of the multiple reference parameter estimation algorithms can be rederived in terms of a generalized Auto Regressive Moving Average (ARMA) model in the time, frequency, or LaPlace domain.

Multiple reference algorithms are very sensitive to inconsistencies within the measured data (frequency shifts, temperature dependant stiffness,damping, etc). This has restimulated a desire to measure all of the response data simultaneously to minimize effects of data inconsistencies Simultaneous measurement of the data was one of the problems associated with the normal mode testing method However by the early eighties, the technology existed to develop less expensive transducer systems The mid to late eighties, saw the develoment of relatively inexpensive transducer systems.

Transducer systems included the sensing element, signal conditioning, cabling, the identification and calibration systems were developed The availability of an arrayed transducer system triggered several new areas of development. As an example, the mounting of several hundred transducers requires a systematic approach to cabling and identification. Further discussion details several areas of development in transducer array systems

Measurement and Signal Processing

A major development in the measurement arena has been that of building integrated arrayed transducer systems which are fairly inexpensive per channel Current systems are approximately an order of magnitude less expensive than those used in the mid-sixties The cost reduction is even greater when inflation is taken into consideration.

Design philosophy is as important as cost reduction in evaluating the arrayed transducer system. Traditionally transducers were treated as individual devices In the new philosophy, the transducers are elements in an integrated system and the mounting, cabling, connectivity, identification, and calibration are important elements of this system

With the acceptance of the arrayed transducers systems, there has been increased emphasis on the development of multiple-reference signal processing In the mid eighties there were significant developments into various types of signal processing procedures for improving the computation of frequency response functions (H_1, H_2, H_v, etc) Broadband excitation procedures have been extended to cover multiple-input excitation cases. Singular Value Decomposition (SVD) or Principal Component Analysis (PCA) procedures have been developed to assess the state of the excitation and signal processing. These procedures have already been incorporated into commercial software packages for data acquisition

Broadband systems are commercially available which can process hundreds of channels of data simultaneously in real time. At the present time these systems are fairly expensive per channel, but the rapid changes in

technology promise to solve this problem. Broadband systems require considerable computer memory and disk storage to handle all of the intermediate and final functions of a multiple-input, mu'tiple-output set of frequency response functions. Computers, computer memory and disk storage costs are currently dropping substantially in cost. These reductions will have a significant effect on the cost of multiple channel systems.

There is also considerable ongoing research to develop auxiliary signal processing and parameter estimation procedures in order to determine modal parameters. These techniques compute modal parameters directly from measured input and response measurements. They utilize direct parameter estimation algorithms.

One of the data acquisition procedures which is currently being developed consists of a spatial sine testing system. This method is described in one of the following examples.

Parameter Estimation

As mentioned previously, new multiple reference parameter estimation algorithms are being developed at an exponentially increasing rate. Many of these algorithms are simply derivatives of previously developed algorithms. The major effort involves consolidation of these many techniques and methods into a general approach. This has been complicated because most of the parameter estimation procedures were developed from a curve fitting viewpoint. As a result of this historical approach, many techniques appear, from a mathematical point of view, to be quite different while in reality they are quite similar. The development and successful application of the polyreference time domain procedure by H. Vold changed the approach from a curve fitting mentality to a linear system parameter estimation process. The polyreference method was developed in the early eighties and was the first commercial application of a multiple-input parameter-estimation algorithm for modal parameter estimation.

The polyreference method illustrated the importance of spatial information in the estimation of modal parameters. Historically, the use of temporal information was emphasized. This was a natural consequence of the curve fitting of individual measurements (frequency response function, unit impulse function and/or free decays). The polyreference method was the first in which global modal parameters were estimated from a number of input reference points located at spatially-separated locations. The spatial information allowed the estimation of "repeated" or very closely coupled "pseudo-repeated" eigenvalues. This was not possible when using only temporal information or a set of response measurements taken from a single input point.

The significant advantages of the polyreference method spurred the development of a large number of similar algorithms. Procedures which had been used in controls and statistical estimation procedures for linear system identification were developed to estimate modal parameters.

These methods can easily be adapted to modal parameter estimation by relaxing several of the requirements imposed on the controls and statistics applications. Unlike the controls area a large number of input and response measurements are made and, in general, it is not necessary to estimate parameters in real time

By starting from the general parameter estimation models which have been used in the controls and statistical estimation areas, many of the modal parameter estimation procedures can be rederived from a common starting point This makes comparison of the various methods more straightforward.

The ARMA formulation is used as a common starting point. In a standard ARMA approach, the AR (auto regressive) terms are used to describe the response of the structure. The MA (moving average) terms are use to describe the system inputs and to describe noise terms in the model. In general the noise terms are nonlinear, which significantly complicates the solution. Therefore, in most of the modal applications, the influences of the noise terms are removed or significantly reduced during the measurement phase by signal processing. The remaining noise is lumped into extra AR terms. The remaining MA terms (inputs) are often eliminated by

computing frequency response or unit impulse functions and using the resulting free decay responses to estimate the AR terms.

Historically, the ARMA method was based upon using sampled time data. For the modal parameter estimation problem, it has been reformulated in the time, frequency and LaPlace domain for both discrete and continuous data.

The ARMA formulation describes the equations of motion for a mechanical system in terms of matrix polynomials. The size of the matrix polynomials and the order of the equation are determined by the number of independent measured degrees-of-freedom and the amount of spatial information. The number of degrees-of-freedom is proportional to the product of the size of the matrices and the order of the equations. If the system is completely spatially sampled (sufficient input-output measuring points), then a second order equation can be used with the matrix size being equal to the number of eigenvalue pairs. Spatial information is critical in reducing the order of the equations. In general, this is one of the main reasons, in recent years, for the dramatic emphasis on measuring a large number of input and output points.

The mathematical formulation of the ARMA is given for reference as follows:

Continuous
Time

$$[A_n]\frac{d^n x(t)}{dt^n}+[A_{n-1}]\frac{d^{n-1}x(t)}{dt^{n-1}}+\ldots+[A_0]x(t) = [B_m]\frac{d^m f(t)}{dt^m}+[B_{m-1}]\frac{d^{m-1}f(t)}{dt^{m-1}}+\ldots+[B_0]f(t) \quad (1)$$

Frequency

$$\{[A_n](j\omega)^n+[A_{n-1}](j\omega)^{n-1}+\ldots+[A_0]\}X(\omega) = \{[B_m](j\omega)^m+[B_{m-1}](j\omega)^{m-1}+\ldots+[B_0]\}F(\omega) \quad (2)$$

Laplace

$$\{[A_n]s^n+[A_{n-1}]s^{n-1}+\ldots+[A_0]\}X(s) = \{[B_m]s^m+[B_{m-1}]s^{m-1}+\ldots+[B_0]\}(F(s)+IC(s)) \quad (3)$$

Discrete

Time

$$[A_n]x_n+[A_{n-1}]x_{n-1}+\ldots+[A_0]x_0 = [B_m]f_m+[B_{m-1}]f_{m-1}+\ldots+[B_0]f_0 \quad (4)$$

Z-Domain(Laplace)

$$\{ [A_n] z^n + [A_{n-1}] z^{n-1} + \ldots + [A_0] \} X(z) = \{ [B_m] z^m + [B_{m-1}] z^{m-1} + \ldots + [B_0] \} (F(z) + IC(z)) \quad (5)$$

The standard M(mass), K(stiffness), and D(damping) model is included as a special case of the above equation sets.

Using this ARMA formulation many of the modal parameter estimation algorithms have been rederived from a common starting point. A list of the relevant algorithms are:

1. The Complex Exponential Algorithm (CE)
2. The Least Squares Complex Exponential (LSCE)
3. The Ibrahim Time Domain Method (ITD)
4. The Polyreference Time Domain Method (PTD)
5. The Eigenvalue Realization Algorithm (ERA)
6. The Polyreference Frequency Domain Method (PFD)
7. The Complex Mode Indicator Function (CMIF)

Using the ARMA model formulation many of the methods can be rederived in either the time or frequency domain. For example, a frequency domain equivalent of the ITD and the ERA method have been developed.

In the ARMA model approach the coefficients of the ARMA model are estimated from the measured input-output response data. The modal parameters are subsequently estimated from the ARMA model using a standard eigenvalue reduction. The procedures for estimating the matrix size of the coefficient terms and the order of the polynomial are important features of the different methods. The type of condensation algorithm is another important difference between the various procedures. One of the important numerical improvements has been to apply methods like Singular Value Decomposition (SVD) for condensation of the data and for estimating the model size and order.

In general, low order ARMA models are computationally more stable. However, they require considerably more computer resources. The significant improvement in computer performance and the reduced cost of memory has made lower order methods attractive. For example, the ERA method, which is one of the better new techniques, is based on a first order model. CMIF, which is a very good first-pass algorithm, is based on a zero order model. The zero order model uses only the spatial information. CMIF will be reviewed in one of the following examples

Future parameter identification algorithms will take advantage of this unified approach They will have the flexibility to handle large data sets taken in the time or frequency domain. There is currently a significant effort in this area to include the moving average terms (both input and noise) in the ARMA model formulation.

Examples:

Multiple Reference Impact Testing

Impact testing has historically been used as a simple, quick testing method to gather data for trouble shooting of vibration problems. Impact testing was often used with a simple parameter estimation procedure to extract a set of modal parameters for trouble shooting. Results could be obtained in a minimum amount of time with minimum effort. One of the fairly recent developments has been to use several reference response transducers This allows a set of simultaneous measurements which can be used with several of the new multiple reference parameter estimation algorithms to better separate
closely coupled modes.

The testing procedure involves the simultaneous measurement of the responses from several reference transducers. This requires a multiple channel data acquisition system. There are currently a number of relatively inexpensive multiple channel analyzers or PC based systems which can be used to process this type of data.

The measurements are processed in the same manner as conventional impact measurements by applying force and response windows to the data and computing frequency response functions. The impact point is roved to the measurement points on the structure and the resulting frequency response functions are used to generate a set of multiple reference data by using Maxwell's reciprocity relationships.

The resulting data set can be processed using any of the multiple reference parameter estimation algorithms. A simple algorithm which is useful for processing this type of data is the CMIF method. This method is essentially a multiple reference equivalent of the historically single degree-of-freedom algorithms. It is a spatial domain method.

The CMIF method measures an operating mode at each frequency and for each reference point. For example, if there are three reference transducers, three operating mode shapes are estimated at each spectral line. A SVD is performed on the three operating modes shapes. The operating modes shapes are put in matrix form with each mode shape being a column in the matrix. The matrix is rectangular, with the number of rows equal to the number of measured points and the number of columns equal to the number of reference points. A SVD is performed on the matrix. The SVD decomposes the matrix into the product of three matrices:

$$SVD(\Psi) = UWV^T \qquad (6)$$

where Ψ = matrix of forced modes

The U matrix is a unitary matrix whose columns are estimates of the eigenvectors. The W matrix is a diagonal matrix of singular values. The CMIF function is a plot of the elements of the singular values as a function of frequency This plot has the characteristics of a power spectrum plot with each singular value generating a separate curve. These curves peak at the frequency of the eigenvalues. This plot can be used to determine if the data has repeated or pseudo-repeated modes. The matrix V is the modal participation matrix. Each row of this matrix can be used to determine the contribution of each eigenvector at the reference point. The eigenvectors determined by CMIF are a set of orthogonal vectors If the data is weighted with the mass matrix before the CMIF computation, the CMIF eigenvectors are orthogonal with respect to the mass matrix.

Since the CMIF method only uses spatial data, it cannot estimate the eigenvalues Therefore, a second step is performed where the CMIF eigenvectors are used as weighting functions in the computation of enhanced frequency response functions. The eigenvalues are estimated by curve fitting the resulting enhanced frequency response functions.

A circular plate is used as an example of the multiple reference impact method. The plate is used since it has a number of repeated roots. In this impact test an eight channel system was used to collect the measurements. The impact hammer signal was input into one channel and seven accelerometers were input into the other channels. The accelerometer positions were chosen to determine the repeated roots. A schematic of the setup on the circular plate is shown in Figure 1.

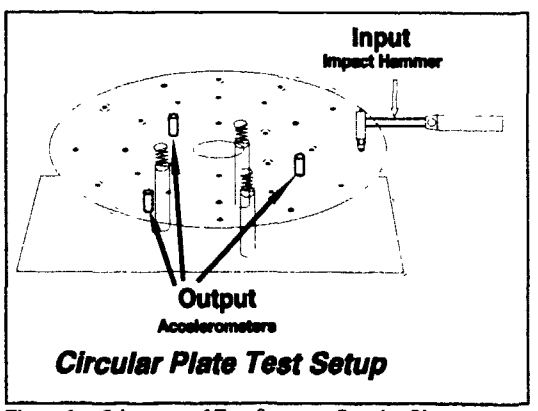

Figure 1 -- Schematic of Test Setup on Circular Plate

A typical driving point frequency response function for the circular plate is shown in Figure 2. The CMIF plot is shown in Figure 3. In order to show more detail, the plot is expanded to include the first two peaks in Figure 4. As can be seen in this figure, the CMIF function peaks at the natural frequencies of the system. For the repeated roots both the 1st and 2nd singular values peak at the natural frequencies. For the non-repeated root, only the first singular value peaks. It is relatively easy to determine the number of eigenvalues from the CMIF plot and to determine if a repeated eigenvalue exists.

In order to determine the eigenvalues, the CMIF eigenvector is used to compute a set of enhanced frequency response functions. A typical enhanced frequency response function is shown in Figure 5. The eigenvalues and the modal scale factors can be estimated by curve fitting the enhanced frequency response functions.

A typical set of eigenvectors for one of the repeated roots is shown in Figure 6.

If a multiple channel data acquisition system is available, the multiple reference impact testing method is an easy method to apply. Used with the CMIF curve fitting algorithm, it is a powerful trouble shooting method.

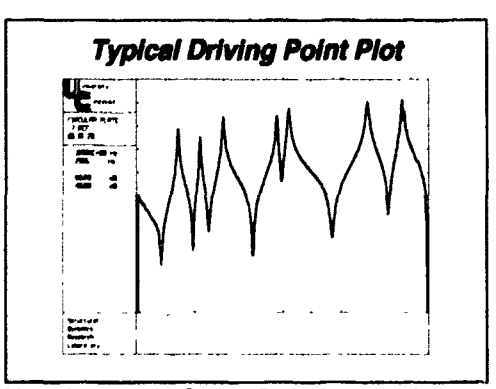

Figure 2 -- Typical Driving Point Frequency Response Function

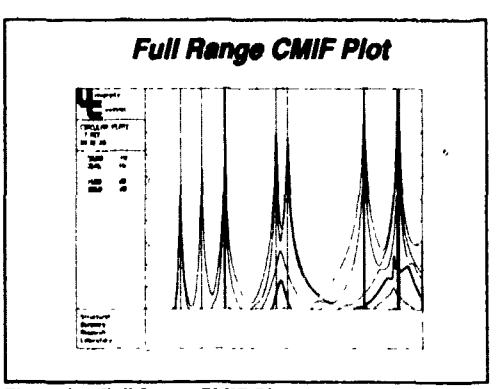

Figure 3 -- Full Range CMIF Plot

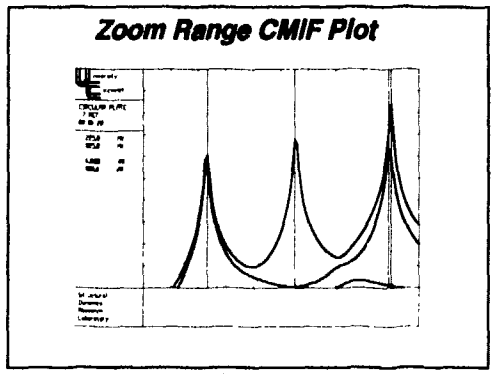

Figure 4 – Zoom Range CMIF Plot

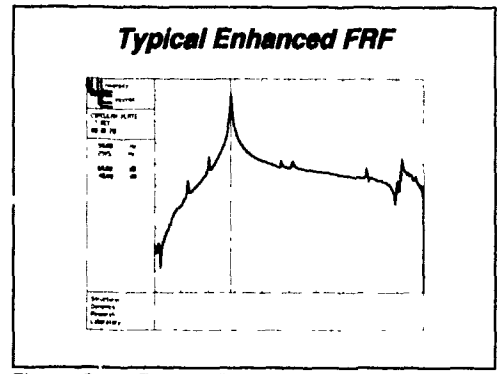

Figure 5 – Typical Enhanced Enhanced Frequency Response Plot

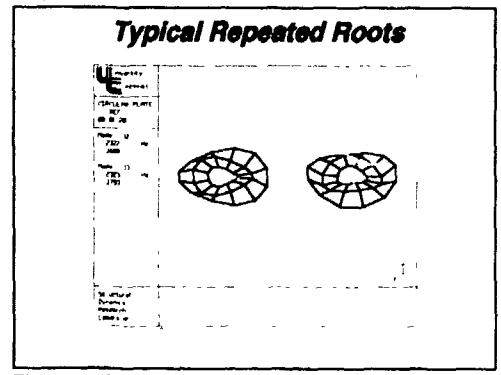

Figure 6– Typical Repeated Root Eigenvectors

Spatial Sine Testing

A spatial sine testing system is currently being developed at the University of Cincinnati. This approach uses elements of both the normal mode testing and the parameter estimation methods. The spatial sine testing system is designed to measure a large number of response and input channels simultaneously. Currently, it can handle 1024 response channels and 32 input channels.

The spatial sine method is based upon a direct parameter estimation procedure which utilizes frequency domain data to estimate system characteristic matrices which can be solved for the modal parameters. The data that are input into this procedure are measured force modes of vibration These data can be generated from measured multiple reference frequency response data or more simply from a sine test.

The sine test is similar to the test setup for a tuned normal mode test. Instead of tuning normal modes, operating mode shapes are measured by applying an arbitrary forcing vector to the structure (forcing pattern and frequency). The forced response vector of the system is measured.

The current project to develop the spatial sine testing system has been active for several years at the University of Cincinnati's Structural Dynamics Research Laboratory. The sine testing system utilizes a modified PCB Data Harvester System. The system has been modified to use a built-in signal processing capability to measure the Fourier coefficients of the response and excitation signals at the excitation frequency This data is transferred to an IBM PC which is used to control, collect and display the data in real time. The PC has a real time animation feature which displays the measured forced response vector. This PC also supplies the excitation forcing vector signal.

The PC is networked to several other computers which perform the sliding window parameter estimation task and supply the dynamic input information

The measured forced response and forcing vector are used as input into a sliding window direct parameter estimation algorithm. This method has several potential advantages.

1) The signal processing requirements are tremendously reduced. Rather than compute spectrums for each point on the structure, information is measured at a single frequency. This substantially reduces the memory requirements of the data acquisition system. At the present time this corresponds to a significant cost saving for a multiple channel system. However, as mentioned previously, the prices of various types of memory are currently changing substantially; thus, this advantage may be temporary. By the time this technology is fully developed, the memory cost may insignificant.

2) Since the direct parameter estimation works in the frequency domain, measuring data directly in the frequency domain eliminates several standard signal processing errors, such as leakage. It also allows for various types of frequency-domain weighting of the data. Variable frequency steps and adaptive averaging at selected frequencies are examples.

3) It permits the use of randomized forcing patterns in different frequency regions to investigate and/or minimize nonlinearities.

4) It allows adaptive control of the forcing conditions (step size, forcing patterns, averaging process, etc) to optimize the parameter estimation process in a sliding window.

The direct parameter estimation algorithm uses a low order ARMA model with the responses and inputs used as inputs. The moving average terms include the input data, but the noise data is handled by signal processing. The advantage of including the MA terms is that it is not necessary to compute frequency response functions. The main advantages of the frequency domain formulation is that the data can be processed in small frequency bands. This reduces the number of eigenvalues that must be included in an estimation cycle. In fact, the algorithm currently being developed will use a sliding window concept. In this concept a small frequency band of data will progressively slide over the data The size of the window, the number of forcing vectors and the size of the frequency steps will be varied to accommodate the number of significant eigenvalues in each frequency band.

The parameter estimation procedure uses the following mathematical model:

$$\{[A_n](j\omega)^n + [A_{n-1}](j\omega)^{n-1} + \ldots + [A_0]\}X(\omega) = \{[B_m](j\omega)^m + [B_{m-1}](j\omega)^{m-1} + \ldots + [B_0]\}F(\omega) \quad (7)$$

Nonlinearities will present a set of unique problems for the spatial sine testing method and this will be the basis for future studies.

Perturbed Boundary Condition (PBC) Testing

Another of the major research efforts at the University of Cincinnati over the past several years has been the development of a Perturbed Boundary Condition (PBC) testing method In this method a test article or component is tested in a number of different configurations where each configuration consists of a modification of one or more of the system's boundary conditions The primary purpose of this research has been to develop a more complete modal model of a test article with experimental data. In a standard modal testing method, a modal model is normally based upon a single testing configuration (i.e.: free-free, fixed boundary condition, etc). During the past 10 years,there has been great development in the Multiple Input Multiple Output (MIMO) measurement and parameter estimation methods. The MIMO research has significantly increased the ability to measure a modal model for a single boundary condition. The number of modes which can be extracted by these

methods consists of the 10 to 40 lowest frequency modes for the given test configuration depending on the noise, nonlinearities, damping and modal coupling, etc. In the PBC method, however, the syste- is tested in a number of drastically different configurations with the lowest 10-40 modes determined for each configuration. The boundary conditions act to filter the original modal space of the system into different subspaces. These subspaces can be used as a database to develop a more complete modal model of the system.

The recent develoments in data acquisition systems make it possible to measure a large number of test configurations in a timely fashion As a result, it is possible to collect the necessary measurements to implement a PBC test.

The current research effort is to develop methods to condense the measured subspace information into a modal model. There are three methods currently being considered:

ARMA -- In the ARMA approach the responses, the applied forces and the boundary forces are measured and input into an parameter estimation process for determining the coefficients of an ARMA model which describes the free-free component. The boundary forces are either directly measured or are measured indirectly by measuring the response of the boundary points.

Transformation Method -- In this method a modal database is measured for each PBC conditions. The stiffness and mass perturbations at the boundary points are analytically remove to obtain the free-free case for each PBC test. A transformation method such as Singular Value Decomposition (SVD) is used to condense the various estimates of the free-free system into a consistent model.

Finite Element Updating Method -- In the finite element method each PBC configuration is updated against the finite element model of the system. The procedure is the find the finite element model which best describes all configurations.

Currently , the ARMA method and the transformation method are being studied and the research effort is just starting on the finite element updating approach

Conclusions

Over the past several years there has been an increased requirement to experimentally measure a modal model. Modal models are being used to verify and update finite element models and as substructures in larger system models. This has placed increasing requirements on the testing and identification procedures.

Multiple input and output measurement methods are being developed to address the increased requirements. Large data acquisition systems have been developed in recent years and currently there is an earnest effort to develop the testing procedures and the parameter estimation methods to support these systems. These efforts will continue in the future.

References

A complete bibliography of the topics covered in this paper can be found in the Proceedings from the International Modal Analysis Conferences (IMAC).

MODAL ANALYSIS AND SYNTHESIS

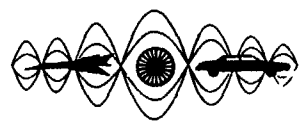

SECOND INTERNATIONAL CONGRESS ON
RECENT DEVELOPMENTS IN AIR- AND
STRUCTURE-BORNE SOUND AND VIBRATION
MARCH 4-6 1992 AUBURN UNIVERSITY, USA

DIRECT UPDATING OF NONCONSERVATIVE FINITE ELEMENT MODELS USING MEASURED INPUT-OUTPUT

S. R. Ibrahim* **W. D'Ambrogio**** **P. Salvini***** **A. Sestieri****

***Department of Mechanical Engineering and Mechanics**
Old Dominion University, Norfolk, Virginia, U.S.A.

****Department of Mechanics and Aeronautics**
Universitá di Roma "La Sapienza", Rome, ITALY

*****Department of Mechanical Engineering**
II Universitá di Roma "Tor Vergata", Rome, ITALY

ABSTRACT

A technique to directly update nonconservative Finite Element dynamic models from input-output experimental data is developed. The method totally circumvents the modal identification process and thus is advantageous in eliminating the adverse effects of a host of identification errors. In addition, the procedure requires neither the matching, or pairing, of experimental and analytical data sets nor the use of the discrepancy between values of the two sets.

In general, the theory allows any type of force input(s) and complete updating of the mass, damping and stiffness matrices is accomplished using only the response measured at two time instants. However, to avoid the simultaneous measurement of displacements, velocities and accelerations, harmonic excitation is recommended at this stage.

The system's spatial matrices are modeled using the Finite Element model submatrices. Damping mechanisms can be modeled as viscous, structural, a combination of the two, or others.

Several simulated experiments are presented in support of the proposed approach.

NOMENCLATURE

c	:	number of damping submatrices
c_{ki}	:	correction factor for stiffness proportional damping submatrix
c_k	:	a vector c_{ki}'s
c_{mi}	:	correction factor for mass proporational damping submatrix
c_m	:	a vector of c_{mi}'s
C_i	:	damping submatrix no. i

$\mathbf{C}_{mi}$	:	mass proportional damping submatrix no. i
$\mathbf{C}_{ki}$	:	stiffness proportional damping submatrix no. i
$\mathbf{C}_U$	:	updated damping matrix
f	:	excitation force vector
i	:	index or $\sqrt{-1}$
Im	:	imaginary part of a complex quantity
j	:	subscript
k	:	number of stiffness submatrices
k_i	:	correction factor for stiffness submatrix no. i
k	:	a vector of k_i's
$\mathbf{K}_U$	:	updated stiffness matrix
m	:	number of mass submatrices
m_i	:	correction factor for mass submatrix no. i
m	:	vector of m_i's
$\mathbf{M}_U$	:	updated mass matrix
n	:	number of degrees of freedom
N	:	number of excitation frequencies
Re	:	real part of a complex quantity
t	:	time
T	:	number of time measurements
u	:	real part of response vector amplitude
v	:	imaginary part of response vector amplitude
x	:	horizontal degree of freedom
x(t)	:	response vector
y	:	vertical degree of freedom

Greek Symbols

α_i	:	mass submatrix damping proportionality coefficient
β_i	:	stiffness submatrix damping proportionality coefficient
θ	:	rotational degree of freedom
ω	:	circular frequency

Special Symbols

$\dot{a}$	:	derivative of (a) with respect to time
$\bar{a}$	:	complex quantity a
a	:	boldface lower case indicates a vector quantity
A	:	boldface upper case indicates a matrix
$\mathbf{A}^+$	:	Pseudo inverse of **A**
D O.F.	:	Degree of Freedom
F.E.	:	Finite Element

1. INTRODUCTION AND JUSTIFICATION

The classical approach for dynamic design and analysis of complex structure seems to have reduced in the last decade to the following three steps:

(i) Finite Element Modeling and analysis of the structure,

(ii) Vibration testing of the full scale structure or a scaled prototype model,

(iii) Reconciliation of analysis and test data or measured, or identified, parameters.

While Finite Element modeling and vibration testing (mainly for modal parameter identification) have both advanced to a reasonably stage, there remains a host of uncertainties in the two processes[1].

The uncertainties in vibration testing and identification can be usually minimized or reduced by the application of sophisticated measurements and experimental approaches, test configuration and selection of test boundary condition, linearity checks, use of multiple techniques for data analysis or identification, . . . etc.[2] Thus, it has become an acceptable practice to use the experimental data base as a reference to which the analytical model is adjusted, optimized or updated.

Among the many possible quantities or variables to be used as the basis for comparing the test data to those of the analytical model, and subsequently use the discrepancy to adjust or update the analytical model, normal mode parameters have emerged as the most commonly used. The choice of modal parameters has only been the natural choice mainly due to the education and conditioning of vibrations engineers and scientists. The choice of normal modes versus complex modes is dictated by the lack of progress in the accurate modeling of damping mechanisms in Finite Element Models.

Majority, or approximately all, of the existing techniques in dynamic model updating fall into the modal approach; specifically normal modes. In general, the computed modal parameters from the F.E. model and the identified normal modes from a modal survey test are compared to establish the need, if any, for updating the analytical model. It must be noted here that the identified test modes are the modes corresponding to the damped structure; complex modes. Computing test normal modes from the identified ones involves some approximations[3,4] in which the errors of approximation are proportional to mode complexity.

In using the modal approach to update analytical models, it is necessary to match, or pair, analytical and test modal parameters; frequencies as well as mode shapes. Such matching process is not always easy, accurate or possible especially for structures with high modal densities. Erroneous pairing of modes can, in many cases, result in an updated model which is worse than the original one. In addition, the minimum number of mode sets, or pairs, required for optimum or unique updating remain to be a subject for further investigation. The two response approach[5] addressed these two critical points by limiting the minimum number of test modes required for "unique" updating to two modes.

Another concern in using the modal approach in model updating, and specifically when the discrepancy between the analytical and test modes is implemented in the updating algorithm, is identification errors.

Even though modal identification has reached higher levels of accuracy in recent years, in some techniques errors of as much as ten percent are not unusual[6]. These errors by themselves are of the same order of magnitude of the difference between test and analysis data.

Despite the numerous negative, or undesirable, characteristics of the normal modes based analytical model updating, the approach possesses many positive aspects. Several promising and powerful techniques exist[7-17].

An alternative to the modal approach in analytical dynamic model updating is the direct use of the input-output responses of the test structure and the analytical model as the basis for updating. The attractiveness of this concept is based on the facts that:

(i) No modal identification is performed.

(ii) Identification errors are removed from the updating process.

(iii) No matching or pairing of modes is necessary.

(iv) Outputs, or response, contain the structure's damping information.

Schematic representation of the modal and non-modal approaches in updating is shown in Figure 1.

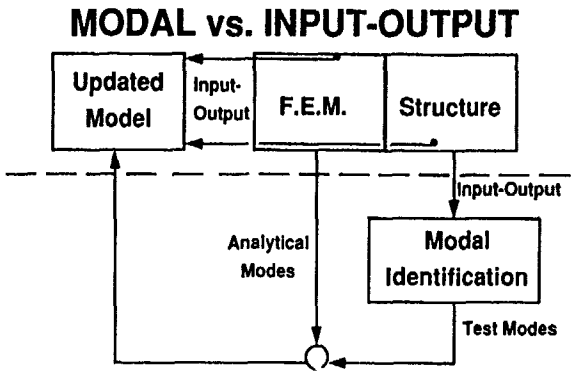

Figure 1. Modal Versus Nonmodal Approaches in Model Updating

Recognizing the merits of the input-output non-modal approach is on the increase and more literature on the subject is slowly emerging. Among the recent work on the subject is the approach presented by Lin and Ewins[18] who use the difference between the measured and analytical frequency response functions to compute mass and stiffness corrections. Lee and Dobson[19] suggested using a reduced model, containing comparable degrees of freedom, which is directly determined from measured transfer functions. Friswell and Penny[20] proposed a technique to update selected physical parameters of a F.E. model directly from measured frequency response functions. Larsson and Sas[21] addressed, in general, measurements limitation and numerical aspects of the input-output updating procedures. Natke[22] and Leuridan, Brown and Allemany[23] made early and important contributions to this subject.

The method presented here uses neither modal parameters nor frequency response functions. It requires only the measured input-output responses at a limited number of time instants to correct the entire unreduced F.E. model.

2. THEORY OF THE TECHNIQUE

The procedure is here derived to correct or update a F.E. model with n degrees of freedom. This model is represented by a mass matrix $\mathbf{M}_A$ and stiffness matrix $\mathbf{K}_A$. In addition, it is assumed that sets of submatrices $\mathbf{M}_i$, $\mathbf{C}_i$ and $\mathbf{K}_i$ are known and that the updated mass, damping and stiffness matrices are of the form:

$$\mathbf{M}_U = \sum_{i=1}^{m} m_i \mathbf{M}_i \tag{1.1}$$

$$\mathbf{C}_U = \sum_{i=1}^{c} c_i \mathbf{C}_i \tag{1.2}$$

$$\mathbf{K}_U = \sum_{i=1}^{k} k_i \mathbf{K}_i \tag{1.3}$$

where the coefficients m_i, c_i and k_i are the unity based correction factors and are equal to one if the model requires no correction. The mass and stiffness submatrices are selected from:

(1) Finite Element Model:

- at sub element level
- at element level
- at macro element level
- at component or substructure level
- at modeling parameters level

(2) special Matrices

which are any masses or springs combination that analyst or dynamistic may choose to add to compensate for F.E. modeling oversights.

The choice of the damping matrices is more difficult since most F.E. models do not usually contain any realistic damping models. At this stage the damping submatrices are selected as proportional damping at the element level. That is:

$$\begin{aligned} \mathbf{C}_i &= c_{mi}\alpha_i\mathbf{M}_i + c_{ki}\beta_i\mathbf{K}_i \\ &= c_{mi}\mathbf{C}_{mi} + c_{ki}\mathbf{C}_{ki} \end{aligned} \tag{2}$$

It is to be noted, however, that the updated damping matrix is not assumed as proportional since the coefficients c_{ki} and c_{mi} are not assumed to be the same for different damping submatrices.

In addition to the previous requirements from the analytical model, the approach assumes the availability of input force(s) to the structure and the responses measurements at the full vector of degrees of freedom of the analytical model; or the expanded and smoothed one. The method allows damping to be modeled as viscous or structural or a combination of the two. The derivation here assumes viscous damping and results can be extended to other damping mechanisms.

The structure, being assumed linear, is thus governed by the equations:

$$\mathbf{M}_U\ddot{\mathbf{x}}(t) + \mathbf{C}_U\dot{\mathbf{x}}(t) + \mathbf{K}_U x(t) = \mathbf{f}(t) \tag{3}$$

Substituting equations (1) and (2) into equation (3) gives

$$\begin{aligned} \sum_{i=1}^{m} m_i\mathbf{M}_i\ddot{\mathbf{x}}_j + \sum_{i=1}^{c} (c_{mi}\mathbf{C}_{mi} + c_{ki}\mathbf{C}_{ki})\dot{\mathbf{x}}_j \\ + \sum_{i=1}^{k} k_i\mathbf{K}_i\mathbf{x}_j = \mathbf{f}_j \end{aligned} \tag{4}$$

where the index j denotes the time t_j. Since the mass, damping and stiffness submatrices are preselected and known and the input-output responses are measured, equation (4) can be rewritten as

$$\mathbf{A}_j\mathbf{m} + \mathbf{B}_j\mathbf{c}_m + \mathbf{D}_j\mathbf{c}_k + \mathbf{E}_j\mathbf{k} = \mathbf{f}_j \tag{5}$$

or

$$[\mathbf{A}_j\ \mathbf{B}_j\ \mathbf{D}_j\ \mathbf{E}_j]\begin{Bmatrix} \mathbf{m} \\ \mathbf{c}_m \\ \mathbf{c}_k \\ \mathbf{k} \end{Bmatrix} = \mathbf{f}_j \tag{6}$$

which represents n equations in $(m + 2c + k)$ unknowns.

The time instances at which equation (6) must be repeated is T times, where T satisfies the relation:

$$nT \geq 2(m + 2c + k) \tag{7}$$

This allows for the direct solution of an overdetermined system of equations or the direct solution and the computation of uniqueness factors.

2.1 Types of Excitation and Harmonic Response

Theoretically, the previous derivation allows for any type of force input as long as the responses at t_j, $j = 1,\ldots T$ are independent. A major disadvantage, however, is the apparent need to simultaneously measure the displacement, velocity and acceleration at every selected coordinate. A practical difficulty.

To circumvent such a need, sinusoidal excitation render itself as the logical solution to this problem. If the force input is

$$\mathbf{f}(t) = \bar{\mathbf{f}}_j e^{iw_j t} \tag{8}$$

then the responses are

$$\mathbf{x}_j(t) = (\mathbf{u}_j + i\mathbf{v}_j)e^{iw_j t} \tag{9.1}$$

$$\dot{\mathbf{x}}_j(t) = iw_j(\mathbf{u}_j + i\mathbf{v}_j)e^{iw_j t} \tag{9.2}$$

$$\ddot{\mathbf{x}}_j(t) = -w_j^2(\mathbf{u}_j + i\mathbf{v}_j)e^{iw_j t} \tag{9.3}$$

and equation (6), which in this case is divided into real and imaginary, takes the form:

$$\begin{bmatrix} \mathbf{A}_j & \mathbf{B}_j & \mathbf{D}_j & \mathbf{E}_j \\ \mathbf{F}_j & \mathbf{G}_j & \mathbf{H}_j & \mathbf{I}_j \end{bmatrix} \begin{Bmatrix} \mathbf{m} \\ \mathbf{c}_m \\ \mathbf{c}_k \\ \mathbf{k} \end{Bmatrix} = \begin{Bmatrix} Re & \bar{\mathbf{f}}_j \\ Im & \bar{\mathbf{f}}_j \end{Bmatrix} \tag{10}$$

and j in this case denotes the frequency of excitation. The minimum no of frequencies required in this case is N which must satisfy:

$$nN \geq (m + 2c + k) \tag{11}$$

2.2 Solutions of Governing Equations

The previous formulation yields a set of nonhomogeneous linear algebraic equations of the form:

$$\mathbf{Q}_j\mathbf{P}_j = \mathbf{d}_j \tag{12}$$

where the vectors of the matrix $\mathbf{Q}_j$ are the products of the selected submatrices $\mathbf{M}_i$, $\mathbf{C}_{mi}$, $\mathbf{C}_{ki}$ and $\mathbf{K}_i$ and the structure's response vectors as shown in equation (4). The vector $\mathbf{p}_j$ represents the unknown coefficients and the right hand side vector $\mathbf{d}_j$ is the forces(s) input. The index j designates a time instant, equation (6), or excitation frequency, equation (10). Equation (12) can be repeated for T time instances or N frequencies.

2.2.1 Direct Solution

Equations (12) with $j = 1,\ldots T$ or $j = 1,\ldots N$ represent an over specified system of linear equations which can be solved in the least squares sense for the vector of unknown correction coefficients. Such a method of solution is useful at initial stages of updating procedure to localize modeling errors or to reduce the number of elements to be corrected. It is also possible however to use this direct solution as a one step updating.

2.2.2 Solution for Computing Uniqueness Factors

In this approach the system of equations (12) is divided into a nonhomogeneous part

$$\mathbf{Q}_1\,\mathbf{p} = \mathbf{d}_1 \tag{13}$$

and the remainder of equations is thus homogeneous and of the form:

$$\mathbf{Q}_2\,\mathbf{p} = 0 \tag{14}$$

which is then partitioned as:

$$\begin{bmatrix} \mathbf{A}_1 & -\mathbf{B}_1 \\ \mathbf{A}_2 & -\mathbf{B}_2 \end{bmatrix} \begin{Bmatrix} \mathbf{a} \\ \mathbf{b} \end{Bmatrix} = 0 \tag{15}$$

Now equation (15) is divided into two sets of equations:

$$\mathbf{A}_1\mathbf{a}_1 = \mathbf{B}_1\mathbf{b}_1 \tag{16.1}$$

and

$$\mathbf{A}_2\mathbf{a}_2 = \mathbf{B}_2\mathbf{b}_2 \tag{16.2}$$

The same unknowns **a** and **b** are noticed to be different in the two sets. To enforce uniqueness it is assumed that:

$$\mathbf{a}_1 = r\mathbf{a}_2 \tag{17.1}$$

$$\mathbf{b}_1 = s\mathbf{b}_2 \tag{17.2}$$

Thus equations (16) and (17) are reduced to:

$$\mathbf{A}_1^{+}\mathbf{B}_1\mathbf{B}_2^{+}\mathbf{A}_2 \quad \mathbf{a} = Q\mathbf{a} \tag{18}$$

which is an eigenvalue problem. The eigenvalues Q will have one of the values equal to unity for perfect or unique updating. The eigenvectors are the unscaled correction coefficients **a**. Part **b** of the unknown unscaled coefficients is obtainable from:

$$\mathbf{b} = \mathbf{B}_1^{+}\mathbf{A}_1 \quad \mathbf{a} \tag{19}$$

Now to correctly scale the correction coefficients, Equation (13) is used. Letting the scaling factor be s, then

$$s\mathbf{Q}_1 \begin{Bmatrix} \mathbf{a} \\ \mathbf{b} \end{Bmatrix} = \mathbf{d}_1 \tag{20}$$

from which s is computed.

2.3 Comments on the Condition of Solution:

The approach presented here is quite different from other approaches which require the inversion of the system's response matrix composed of responses measured at many time instances or many frequencies. In the latter, it is known that the rank of the response matrix will be equal to twice the number of modes excited in these responses.

In the method under consideration each element i, for excitation frequencies j, will have four vectors in the coefficient matrix $\mathbf{Q}_j$ of equation (12). These are:

$$-\omega_j^2 \begin{Bmatrix} \mathbf{M}_i\mathbf{u}_j \\ \mathbf{M}_{iu}\mathbf{v}_j \end{Bmatrix}, \omega_j \begin{Bmatrix} -\mathbf{C}_{mi}\mathbf{v}_j \\ \mathbf{C}_{mi}\mathbf{u}_j \end{Bmatrix}, \omega_j \begin{Bmatrix} \mathbf{C}_{ki}\mathbf{v}_j \\ \mathbf{C}_{ki}\mathbf{u}_j \end{Bmatrix}$$

and

$$\begin{Bmatrix} \mathbf{K}_i\mathbf{u}_j \\ \mathbf{K}_i\mathbf{v}_j \end{Bmatrix}$$

Hence, the condition of solution here is totally different and is function only of the selection of the system submatrices. For example if for an element with $\mathbf{K}_i$ and $\mathbf{M}_i$ proportional, which is very unlikely, singularity will occur. A favorable factor here is the fact that the system's submatrices are user's selected and the condition of solution can be controlled and/or improve by proper selection.

3. SIMULATED EXPERIMENTS

The structure which was selected to test the proposed approach is shown in Figure 2. An element j is preceded by node no. $j-1$ and terminated by the jth node. For the analytical model, six degrees-of-freedom beam elements are used in the F.E. analysis. Table 1 shows the nodal coordinates of the model. The cross-sectional area of the beam elements is 0.005 m^2, the modulus of elasticity is taken equal to 70 GPa and the density 2700 kg/m^3.

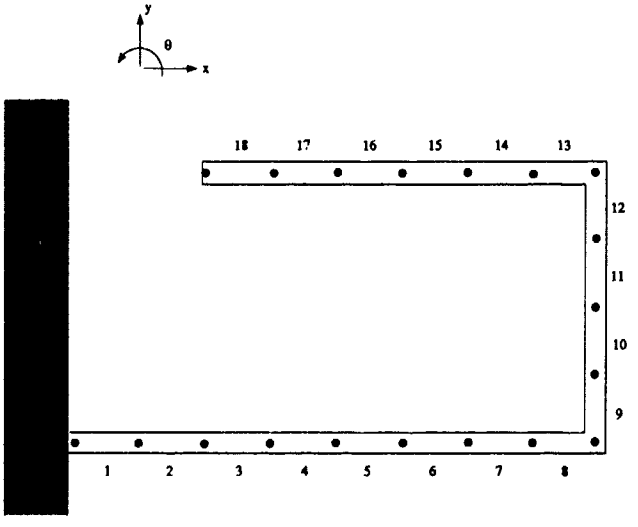

Figure 2 Test Structure

Table 1. Nodal Coordinates

Node No.	Nodal Coordinates (m)	
	x	y
1	0.	0.
2	0.125	0.
3	0.250	0.
4	0.375	0.
5	0.500	0.
6	0.675	0.
7	0.750	0.
8	0.875	0.
9	1.000	0.
10	1.000	0.075
11	1.000	0.150
12	1.000	0.225
13	1.000	0.3
14	0.875	0.3
15	0.756	0.3
16	0.675	0.3
17	0.500	0.3
18	0.375	0.3
19	0.250	0.3

Thus the structure is modeled as a 54 D.O.F. system. Each node is assigned an x, y and θ D.O.F. respectively. Table 2 shows the designated degrees of freedom. The significance of this table is to relate excitation force vectors to a particulr type of D.O.F.

Table 2. Node and D.O.F. Designation

Node	D.O.F.		
	x	y	θ
2	1	2	3
3	4	5	6
4	7	8	9
5	10	11	12
6	13	14	15
7	16	17	18
8	19	20	21
9	22	23	24
10	25	26	27
11	28	29	30
12	31	32	33
13	34	35	36
14	37	38	39
15	40	41	42
16	43	44	45
17	46	47	48
18	49	50	51
19	52	53	54

The test model is created by perturbing the properties of the elements as shown in Table 3. The responses at the 54 degrees-of-freedom were computed using a variety of sinusoidal input forces.

In order to understand and explain the selection of the input forces' frequencies, the first ten resonant circular frequencies of the analytical model are:

No.	ω(rad/s)
1	.181866E+03
2	.264177E+03
3	.973889E+03
4	.203507E+04
5	.358882E+04
6	.564278E+04
7	.725125E+04
8	981816E+04
9	.113561E+05
10	.148689E+05

Numerous updating tests we conducted with different types of excitations, damping and updating models. A summary of the tests is shown in Table 4.

Table 3. Element Perturbation Factors for Test Model

Element No	Mass	Stiffness	Damping	
			Mass Proportional	Stiffness Proportional ($x10^{-6}$)
1	1.0	1.0	1.	0.5
2	1.0	1.0	2.	1.0
3	1.4	1.4	3.	1.5
4	1.6	1.0	4.	2.0
5	1.0	1.0	5.	2.5
6	1.1	0.85	6.	3.0
7	1.0	1.0	5.	2.5
8	1.0	1.0	4.	2.0
9	1.0	1.0	3.	1.5
10	1.0	1.2	2.	1.0
11	1.0	1.0	1.	0.5
12	1.0	1.0	2.	1.0
13	1.0	1.0	3.	1.5
14	0.8	1.3	4.	2.0
15	1.0	1.0	5.	2.5
16	1.0	1.0	6.	3.0
17	1.0	1.0	5.	2.5
18	1.5	1.0	4.	2.0

In these tests, and from equation (11), the number of frequencies required N is:

$$N > \frac{18 + 2(18) + 18}{54}$$

$$N > 4/3$$

for which reason two frequencies were used in all tests.

3.1 Results

The method of solution to compute a uniqueness factor was used in all updatings.

Except for tests 10, 11, 13 and 14 uniqueness factors of unity were obtained and the computed corrections factors were the theoretical ones to six digits of accuracy.

In tests 10 and 11, the structure was viscously damped, but the updating model used had no damping. Results are shown in Table 5. It is to be noticed that while responses for test 11 were near resonance, where damping effects are maximum, those for test 10 were measured in the anti-resonance regions.

Table 5 also lists results for tests 13 and 14 in which damping was erroneously modeled in the updating procedure. While damping correction coefficients contained large errors, due to the difference in actual and modeled damping mechanisms, mass and stiffness correction coefficients were accurately identified.

Table 4. Summary of Updating Tests

Test No.	Damping Model		Force Frequency rad/s	No. of Forces and Coordinates
	Test Structure	Updating Model		
1	undamped	undamped	180.00*	4(5,17,31,38)
			2000.00*	4(5,17,31,38)
2	undamped	undamped	180.00*	1(53)
			2000.00*	1(53)
3	undamped	undamped	20.00	1(53)
			8500.00	1(52)
4	undamped	undamped	20.00	1(22)
			8500.00	1(22)
5	undamped	undamped	500.00	1(22)
			8500.00	1(22)
6	viscous	viscous	180.00*	4(5,17,31,38)
			2000.00*	4(8,20,28,53)
7	viscous	viscous	180.00*	1(17)
			2000.00*	1(53)
8	viscous	viscous	500.00	1(17)
			8000.00	1(53)
9	viscous	viscous	30.00	1(17)
			8000.00	1(17)
10	viscous	undamped	30.00	1(17)
			8000.00	1(17)
11	viscous	undamped	180.00*	1(17)
			260.00*	1(17)
12	structural	structural	180.00*	1(17)
			260.00*	1(17)
13	structural	viscous	180.00*	1(17)
			260.00*	1(17)
14	viscous	structural	180.00*	1(17)
			260.00*	1(17)
15	undamped	viscous	30.00	1(17)
			8000.00	1(17)

*Indicates a frequency close to a natural frequency.

Table 5. Test Results of Tests with Wrong Modeling[1]

	Test no.							
	10[2]		11[2]		13[3]		14[4]	
	Uniqueness Factor							
	0.995162		0.988633		1.00000		1.00002	
	Correction Coefficients for Mass and Stiffness Submatrices							
Element no j	m_j	k_j	m_j	k_j	$m_j^{(5)}$	$k_j^{(5)}$	m_j	k_j
1	996397E+00	100126E+01	.103420E+01	100569E+01	.100000E+01	.100000E+01	.993331E+00	.995782E+00
2	.996457E+00	.100126E+01	.137418E+01	.140794E+01	.100000E+01	.100000E+01	.995077E+00	.995786E+00
3	139474E+01	140177E+01	.160714E+01	.100573E+01	.140000E+01	140000E+01	.139399E+01	.139411E+01
4	.159308E+01	.100127E+01	.974067E+01	.100563E+01	.160000E+01	.100000E+01	.159272E+01	.995803E+00
5	.996068E+00	.100127E+01	.109421E+01	.854702E+01	.100000E+01	100000E+01	.996393E+00	.995805E+00
6	.109437E+01	851088E+00	.109421E+01	.100545E+01	.110000E+01	.850000E+00	.109548E+01	.846425E+00
7	.996125E+00	100103E+01	978799E+00	.100514E+01	.100000E+01	.100000E+01	.996288E+00	.995797E+00
8	997585E+00	.100156E+01	.986209E+00	100494E+01	.100000E+01	100000E+01	.995945E+00	.995786E+00
9	.989622E+00	.100259E+01	.986570E+00	100494E+01	.100000E+01	100000E+01	.995979E+00	.995790E+00
10	995480E+00	.120462E+01	996061E+00	.120580E+01	.100000E+01	.120000E+01	995637E+00	.119497E+01
11	.999280E+00	100473E+01	.996764E+00	.100482E+01	.100000E+01	.100000E+01	.995708E+00	.995840E+00
12	100170E+01	100541E+01	.997247E+00	.100487E+01	100000E+01	.100000E+01	.995658E+00	.995878E+00
13	100473E+01	.100581E+01	.987398E+00	.100485E+01	.100000E+01	.100000E+01	.996049E+00	.995907E+00
14	.801100E+00	.130855E+01	.784005E+00	130628E+01	.800000E+00	.130000E+01	.796915E+00	.129468E+01
15	101031E+01	100682E+01	.971958E+00	.100541E+01	.100000E+01	.100000E+01	.996342E+00	.995890E+00
16	.100231E+01	.100755E+01	.971048E+00	100744E+01	.100000E+01	100000E+01	.996262E+00	.995837E+00
17	.100504E+01	.101045E+01	959648E+00	.101598E+01	.100000E+01	.100000E+01	.996414E+00	.995689E+00
18	151781E+01	101224E+01	151644E+01	.102581E+01	.150000E+01	.100000E+01	.149344E+01	.995530E+00

[1] All other tests have exact results to six digits.
[2] Damped responses in undamped updating model.
[3] Structurally damped responses in viscously damped updating model.
[4] Viscously damped responses in structurally damped updating model.
[5] Equal to theoretical values. Correction factors for damping contain large errors.

4. CONCLUDING REMARKS

A technique to update a Finite Element Model's mass, stiffness and damping matrices using harmonic input-output is presented and shown to be quite effective under ideal conditions. The number of excitation frequencies is limited and is governed by the number of degrees of freedom of the model and the number of correction coefficients. In the results presented, two excitation frequencies were more than sufficient. The study of several practical considerations is underway.

5. ACKNOWLEDGEMENTS

Most of the work reported here was conducted while the first author was on a visiting professorship at the University of Rome "La Sapienza". He is indebted to many people in Rome and Italy for their generosity and collegiality. This work was supported by the Italian Space Agency (ISA).

6. REFERENCES

1. Ibrahim, S. R., "Analytical Dynamic Model Updating· The Challenge for the Nineties," Australian Transactions of Mechanical Engineering, Vol. ME16, No. 1, July 1991, pp. 17–26.

2. Brown, D. L., "New and Future Developments in Experimental Modal Analysis," Australian Transactions of Mechanical Engineering, Vol. ME 16, No. 1, July 1991, pp. 27–33.

3. Ibrahim, S. R. and Fullekrug, U., "Investigation into Exact Normalization of Incomplete Complex Modes by Decomposition Transformation," Proceedings of the 8th International Modal Analysis Conference, Union College/SEM, February 1990, pp. 205–212.

4. Sestieri, A. and Ibrahim, S. R., "Analysis of Errors and Approximations in the Use of Modal Coordinates," Planned for Presentation and Publication in September 1992.

5. Ibrahim, S. R., Stavrinidis, C.; Fissette, E. and Brunner, O., "A Direct Two Response Approach for Updating Analytical Models of Structures with Emphasis on Uniqueness," ASME Journal of Vibrations and Acoustics, Vol. 112, January 1990, pp. 107–111.

6. Niedbal, N. and Klusowski, "Optimal Exciter Placement and Force Vector Tuning Required for Experimental Modal Analysis Testing," Proceedings of the International Conference on Spacecraft Structures and Mechanical Testing, ESTEC, Noordwijk, The Netherlands, April 1991, (in print).

7. Berman, A. and Nagy, E. J., "Improvement of a Large Analytical Modal Using Test Data," AIAA Journal, Vol. 21, No. 8, 1983.

8. Caesar, B. and Peter, J., "Direct Update of Dynamic Materials Models from Modal Data," AIAA Journal, Vol. 25, November 1987, pp. 1494–1499.

9. Ewins, D. J.; He, J. and Lieven, N. A. J, "A Review of the Error Matrix Method (EMM) for Structural Dynamic Model Comparison," Proc. of an Int. Conf. by European Space Agency, pp. 55–62, October 1988.

10. Lieven, N. A. J. and Ewins, D J., "Error Location and Updating of Finite Element Models Using Singular Value Decomposition," Proceedings of the Eighth International Modal Analysis Conference, Union College/SEM, February 1990, pp. 768–773.

11. Gysin, H. P., "Attempts to Localize Finite Element Modeling Errors," Proceedings of the 13th International Seminar on Modal Analysis, Leuven, Belgium, September 1988.

12. Janter, T., Heylen, W., Sas, P., A Comparison Between Model Updating Procedures Based on the Model Optimization Parameter Set," Proceedings of the 6th IMAC, Orlando, Florida, 1988, pp. 87–92.

13. Lallement, G. and Piranda, J., "Localization Methods for Parametric Updating of Finite Element Models In Elastodynamics," Proceedings of the Eighth International Modal Analysis Conference, Union College, SEM, February 1990, pp. 579–585.

14. Link, M., "Survey on Selected Updating Procedures," Proceedings 11th International Seminar on Modal Analysis, Katholieke Universiteit, Leuven, Belgium, 1986.

15. Link, M., "Identification and Correction of Errors Using Test Data — Theoretical and Practical Bounds." Proceedings of the Eighth International Modal Analysis Conference, Union College/SEM, February 1990, pp. 570–578.

16. O'Callahan, J. C. and Leung, R., "Optimization of Mass and Stiffness Matrices Using a Generalized Inverse Technique on the Measured Modes," IMAC III, Orlando, FL, January 1985.

17. O'Callahan, J., "Determination of Analytical Model Differences Using Modal Updating," Proceedings of the Eighth International Modal Analysis Conference, Union College/SEM, February 1990, pp. 1180–1189

18. Lin, R. M. and Ewins, D. J., "Model Updating Using FRF Data," Proceedings of the 15th International Seminar on Modal Analysis, Katholic University of Leuven, Belgium, September 1990, pp. 141–162.

19. Lee, H. G. and Dobson, B. J., "The Direct Measurement of Structural Mass, Stiffness and Damping Properties," Journal of Sound and Vibration, 145(1), 1991, pp. 61–81.

20. Friswell, M. I. and Penny, J. E. T., "Updating Parameters from Frequency Data Via Reduced Order Model," Journal of Mechanical Systems, and Signal Processing, 4(5), 1990, pp. 377–391.

21. Larsson, P. O. and Sas, P., "Model Updating Based Upon Forced Vibration," Conference on Recent Advances in Structural Dynamics, Southampton, England, July 1991, pp. 95–108.

22. Natke, H. G., "Updating Computational Models in the Frequency Domain Based on Measured Data a Survey," Probalistic Engineering, 1988, Vol. 3, No. 1, pp. 28–35.

23. Leuridan, J. M.; Brown, D. L. and Allemany, R., "Direct System Parameter Identification of Mechanical Structures," Proceedings of the 23rd Structures, Structural Dynamics and Materials Conference, Paper No. 82–0767, 1982.

SECOND INTERNATIONAL CONGRESS ON
RECENT DEVELOPMENTS IN AIR- AND
STRUCTURE-BORNE SOUND AND VIBRATION
MARCH 4-6, 1992 AUBURN UNIVERSITY, USA

CURVATURE EFFECTS ON STRUCTURAL VIBRATION: MODAL LATTICE DOMAIN APPROACH

Jeung-tae Kim
Acoustics and Vibration Laboratory
Korea Standards Research Institute
P.O.Box 3, DaeDok Science Town
DaeJon, KOREA

ABSTRACT

Vibration characteristics of a shell structure with finite curvature are discussed based on the dynamic analogy between a cylinder to a flat plate. In order to understand curvature effects, the characteristics such as resonance frequencies, constant frequency loci, and number of modes in a flat plate and in a cylinder are examined. Also a simplified representation on the vibration response at the driving point is proposed.

INTRODUCTION

Although several approaches to analyze the vibration characteristics with a curvature are available in literatures, the implementation to the real engineering problems are very limited because of the high order mathematical formulation and coupled parameters. An analyst, therefore, leans to an approximate solution if a vibration estimate for a cylindrical structure is necessary. Approximate solutions available in literatures can be divided into two manifold: (i) energy minimization approach, and (ii) finite analysis approach. The former approach includes Variational integral method, Galerkins method, and Rayleigh-Ritz method[1,2,3]. The finite difference and the finite element method belong to the latter. In this study, a modal domain concept is incorporated to derive an approximate formula for a structure with curvature. The modal domain is a 2-dimensional wave space[4]. It has been has been known to be useful approach to examine the vibration level of large and complicated structures, especially when the knowledge on the vibration level of a high frequency region is necessary.

MODAL LATTICE DOMAIN ANALYSIS

Resonance frequencies of the structure can be obtained when the denominator of the mobility function vanishes. If the concept of constant frequency loci on a modal domain is employed for a cylindrical structure, we can easily calculate resonance frequencies using dynamic similarity between a plate and a cylinder.

Consider a cylinder of radius a with finite length l_1. When the boundaries are simply supported, the mode shape of a cylindrical shell becomes

$$\psi = A \sin kx \begin{pmatrix} \cos \\ \sin \end{pmatrix} n\theta \qquad (1)$$

Because of the simply supported boundary condition, k and n must be $M\pi/l_1$ and $2N\pi/l_2$, where l_1 is the height and l_2 is the circumference of the cylinder, $2\pi a$. If a 2-dimensional wave number space on the axial and the circumferential direction is considered, the modal lattice in the axial directional wave number k has a unit distance of π/l_1 . On the other hand, the circumferential directional wave space becomes doubled in the distance compared to the plate case, i.e., $2\pi/l_2$ modal lattice distance. Twice the separation of the mode into the circumferential direction is due to the fact that sine and cosine functions exist in Eq.(1). The wave number space having two crossing modal lattice are shown in Fig.1. Resonance frequencies of the structure correspond to the points where the modal lattice crosses each other on the wave number space map.

When a thin shell assumption is applied, and the lowest circumferential modes are negligible, resonance frequencies are expressed as follows[5,6]:

$$\nu^2 = (1-\mu^2)\frac{(ka)^4}{((ka)^2+n^2)^2} + \beta^2\{((ka)^2+n^2)^2 - \frac{n^2(4-\mu)-2-\mu}{2(1-\mu)}\} \tag{2}$$

where β is $\frac{h}{\sqrt{12}a}$. This equation is correct when β is smaller than 0.01 and n is bigger than 2. The first term of Eq.(2) is related to the membrane stress, and the second term to the bending rigidity because of β^2 in the term. If the vibration behavior of the resonance frequencies is compared between for a cylinder and for a plate, the dynamic similarities between those structures can be explained.

Let us consider a plate having the same dimension as a cylinder. The resonance frequency in dimensionless representation becomes

$$\nu = \beta(\pi a)^2\{(\mathsf{M}/l_1)^2 + (\mathsf{N}/l_2)^2\} \tag{3}$$

If given numbers of M and N are used in Eq.(3), the frequency ν has a circular trace with constant radius as a function of wave numbers M and N . These circles are called *constant frequency loci*. The constant frequency loci can be generated for a cylindrical structure using Eq.(2). The concept of the constant frequency loci approach becomes important when a vibration level of a certain frequency bandwidth is necessary. This concept has been developed in the area of noise prediction for a structure. The difference in frequency loci between the flat plate and the cylindrical structure is due to the membrane stress within the structure. Let a plate be wrapped to make a cylinder geometry. Since a in-plane membrane stress is built-up in the cylinder, the curvature affects the stiffness of the structure so that the travelling wave speed increases in the axial direction. As the cylinder has curvature in the radial direction, the propagating waves are subject to the stiffness effect which is due to the in-plane membrane stress. Especially the k axial wave modes are substantially affected by the curvature. The curvature effect exists until the wavelength of the membrane stress encircles the cylinder. Physically, this transition occurs at the hoop resonance, or the breathing mode. The hoop resonance is also called the ring frequency.

Therefore, the ring frequency f_r of the cylinder has to satisfy the following relation :

$$\frac{C}{f_r} = 2\pi a \tag{4}$$

If the interested frequency bandwidth is below f_r, the waves travelling in the axial direction are subject to the stiffening effect which is due to the in-plane membrane. On the other hand, the frequency band above f_r no longer has the curvature effect. As the frequency increases above the ring frequency, the speed of travelling waves becomes faster than that of in-plane membrane stress. In this region, a curvature effect of the cylindrical structure becomes negligible and the cylinder dynamics converts to a plate behavior. The boundary of the curvature effect is, therefore, the ring frequency f_r of the cylinder. Consequently, the way of analyzing the cylinder vibration can be varied depending on the frequency region compared with the ring frequency.

MODE COUNT FOR FLAT PLATE

Two different approaches to count the number of the modes for a flat plate structure are available: estimate from the geometry, and from the driving point mobility

The estimate of number of modes based on the geometry is widely known in SEA community. The modal separation δf , which is inverse to the mode number is

$$\delta f = \frac{hc_l}{\sqrt{3}A_p}. \tag{5}$$

Here, the modal separation is a function of the structural rigidity and surface area. It is independent of the frequency increment.

Another way of the mode count is to use the real part of the driving point function. When a measurement data of the flat plate is available, the direct count for resonances may not be practical due to heavy overlap of modes in most situation Instead, the average value of the real part of the mobility function can provide more precise information on the modal density. The real part of the mobility function, G_p, which is called the mechanical conductance, has a positive value always, since this component is related to a power flow from the vibration source to the structure to be excited. The averaged value of the mobility, therefore, has a certain positive value, which is related to the modal separation δf :

$$\delta f = \frac{1}{4MG_p} \tag{6}$$

Therefore, a measured driving mobility function is useful information on estimating the modal density function of the flat plate structure.

DYNAMICS OF STRUCTURE WITH CURVATURE

Instead of taking complicated mathematical analysis for a vibration estimate of a shell structure, consider a flat plate whose surface area is the same as that of a shell. When a structure is excited, the input power is transmitted through bending waves in the structure. As mentioned in the previous section, the vibration behavior resembles the plate dynamics if the frequency band is above the ring. In the case of a flat plate, the mobility function at the driving point G_p is predictable from the material properties of the structure, i.e.,

$$G_p = \frac{1}{8\rho hCa\beta}. \tag{7}$$

In order to correlate a plate and a shell dynamics, a concept of modal density is adapted. The logical parameter to modify the plate mobility into the cylinder mobility is the ratio between the plate and cylinder mode number, because the modal density within the frequency band of interest is related to the vibration power. Since any finite length of a thin shell satisfies a reverberant condition, the mean square velocity of the vibration on the surface of the structure is proportional to the received power, and each mode in the structure could have equal amount of participation in vibration power. The modal density that is directly proportional to the vibration magnitude can be a useful parameter in vibration analysis.

If the cylinder vibration behaves as in a plate, the mobility function of the driving point of a cylindrical shell G_c, therefore, may be expressed as

$$G_c = W(\nu)G_p, \tag{8}$$

where $W(\nu)$ is the correction factor and G_p is the driving point mobility of a plate. Eq.(8) correlates the plate mobility to the correction factor, $W(\nu)$, which is a function of frequency. As already mentioned, the cylinder vibrates as a plate if the frequency is above f_r. In this range, the correction factor above the ring frequency is 1. If the frequency band of interest is below the ring frequency,the correction factor, $W(\nu)$, plays a role to compensate the curvature effects on the input mobility of a plate.

Let us obtain the correction factor $W(\nu)$ below the ring frequency. Since a shell has some curvature, the membrane stress increases the bending wave speed along the axial direction so that the number of modes included within a certain frequency band becomes smaller than the same frequency band as in the plate case. When the frequency band is below f_r , the total mode number in a cylindrical shell has the form[3]

$$N_c = (0.5\gamma(0.5\pi + sin^{-1}\gamma) + \sqrt{\nu(1-\nu)})\frac{l}{2\pi a\beta}\ , \quad if \quad \nu < 1 \tag{9}$$

where γ is $2\nu - 1$. If the modal separation of the plate is converted to the mode number, N_p becomes $l\omega/2C\beta$.

The correction factor $W(\nu)$ is the ratio of the number of mode in cylinder to that in plate.

$$W(\nu) = (0.5\gamma(0.5\pi + sin^{-1}\gamma) + \sqrt{\nu(1-\nu)})/\nu \tag{10}$$

Therefore, a simplified cylinder mobility function is

$$G_c = \frac{0.5\gamma(0.5\pi + sin^{-1}\gamma) + \sqrt{\nu(1-\nu)}}{8\rho hCa\beta\nu}, \tag{11}$$

EXAMPLES

Resonance frequencies of a cylinder with $11.7cm$ in diameter, $18.1cm$ in height, and $0.32cm$ in thickness are examined at first. The structure is made of steel (ρ=7700 kg/m^3). This structure has a ring frequency of 13.8 kHz. Fig.2 shows constant frequency loci corresponding 2,4,6,8,10,12 and 14 kHz. As expected, the loci have elliptical shapes. If both dimensions of the plate are exactly the same, the loci make quarter circles. It is because directional waves travelling on the plate surface has the same bending stiffness in the case of a flat plate so that the bending wave speed of the plate with no curvature should be the same unless the frequency changes.

Let us calculate the resonance frequencies of a cylindrical structure. The constant frequency loci of the cylinder can be obtained using Eq.(2). Fig.3 shows the constant frequency loci of the cylindrical structure. Since the stiffness in the axial direction is larger than in the circumferential direction, the locus is no longer a circle. Near the horizontal axis in Fig.3, the loci have constant radii. As the frequency increases, the area covered by a constant radius increases, too. It may tell us that the dynamic property of a cylinder along the circumferential direction becomes similar to that of a plate. However, the area near the vertical axis for a cylinder is totally different from that for the plate, since the membrane stress mainly contributes the loci curve when the circumferential wave number n is small, Each grid point crossed by integer numbers along the two axes in Fig.2 and Fig.3 corresponds to the resonances of the structure. The resonance frequencies are bounded between constant frequency loci. In the case where a noise becomes an issue, a narrow frequency bandwidth between 2kHz and 4

kHz is important, since a listener is sensitive to this band. The resonance frequencies enclosed by two constant frequency loci of 2kHz and 4 kHz are shown in Fig.5. Marked positions shown in Fig.4 show resonance frequencies of the cylinder. Between 2kHz and 4 kHz, analysis reveals that 3 resonances exist:2,600 (3,1 mode), 2,925(2,1 mode), and 3,769(4,1 mode) Hz.

In order to examine the resonances obtained from the analysis, an experiment is conducted for a frequency band between 2kHz and 4 kHz. Although the analysis is not exact to the experimental data, the simplified formula is good enough to predict the resonances approximately.

Then, an estimate of the vibration level of a cylinder which is $27cm$ in diameter, $33cm$ in height, and $0.55cm$ in thickness is examined. The ring frequency of the cylinder is 5.9 kHz.

Let us examine the vibration level at the frequency band above f_r. The driving point mobility of the cylinder is identical to the case of the plate. The calculation shows that the mobility function of the plate, G_p, becomes 3.86×10^{-4} . When the value of 1 sec/kg is used as reference, the mobility of the cylindrical structure becomes -68.2 dB above the ring frequency.

For a frequency range below 5.95 kHz, the mobility function is frequency dependent, however. Comparison of the measured mobility function at the driving point to the analytical result is shown in Fig.5. The solid line represents the measured mobility function of the cylinder. The prediction calculated from the proposed formula is depicted by the dotted line. For the frequency band above 2.0 kHz, the analytical result predicts the measured data behavior quite well.

CONCLUSIONS

An approximate model predicting the vibration characteristics of the shell type structure is formulated. The proposed formula is based on the dynamic analogy between a cylinder and a flat plate. Since a cylinder converts to a flat plate dynamics for the frequency band above the ring frequency, the mobility function of the cylindrical structure has a frequency-dependent correction factor. As a way to correlate the cylinder and plate characteristics, the concept of modal density of structures is employed so that the correction factor is obtained from the ratio of the resonance frequencies of a cylinder to a plate.

In order to verify the proposed formula, experiments are conducted. Comparison of the experimental and the analytical results shows that the proposed model estimates the resonance frequencies and mobility functions pretty well. The proposed model is very simple to use and straightforward.

REFERENCES

1. Junger and Feit, *Sound, Structure, and Their Interaction,*The MIT Press, Cambridge MA, 1972
2. Leissa, A.W., *Vibrations of Shells,* NASA SP-288, Office of Technology Utilization, NASA, Washington, D.C.
3. Soedel, W., *Vibration of Shell and Plates,* Marcel Dekker, NewYork, 1981.
4. Lyon, R.H., *Machinery Noise and Diagnostics,* Butterworths, Boston, 1986.
5. Heckl, M., " Vibrations of Point-Driven Cylindrical Shells", J. Acoust. Soc. Am, 34, October 1962, pp.1553-1557.
6. Franken, P.A., " Input Impedances of Cylindrical Structures", J. Acoust. Soc. Am, 32, April 1960, pp.473-477.

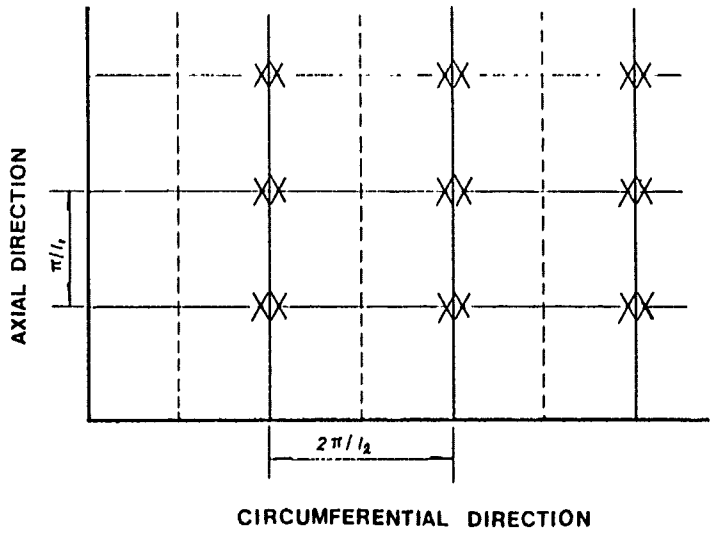

Fig. 1. Resonance frequencies on a wave number space.

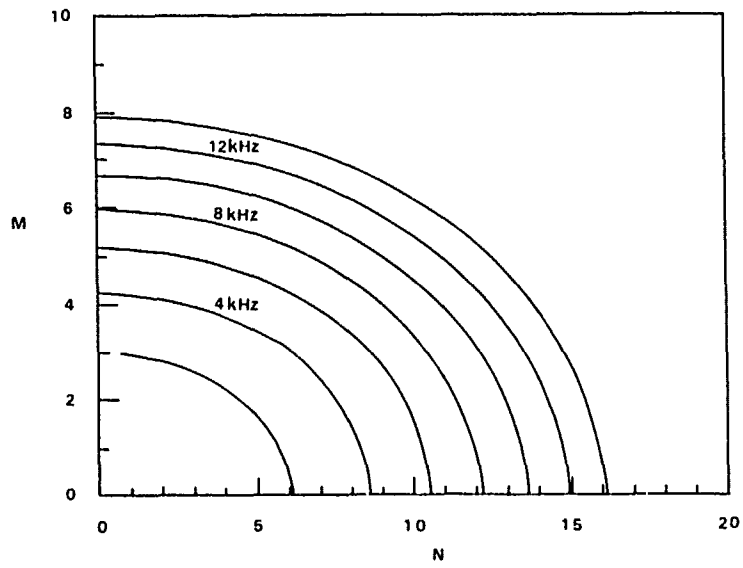

Fig.2. Constant frequency loci of a plate

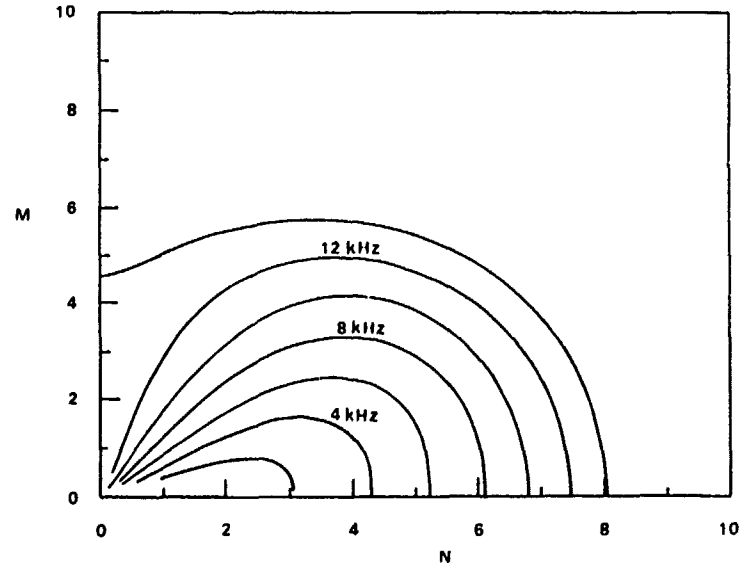

Fig.3. Constant frequency loci of a shell

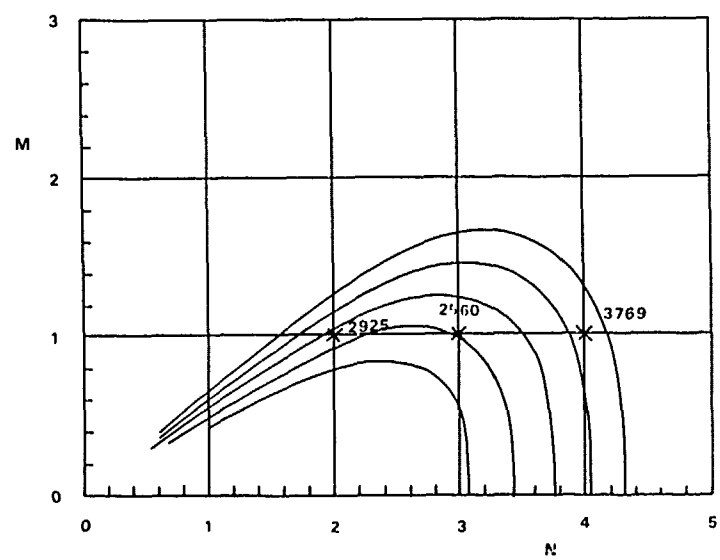

Fig.4. Narrow band frequency loci of a shell: 2 and 4 kHz frequency loci

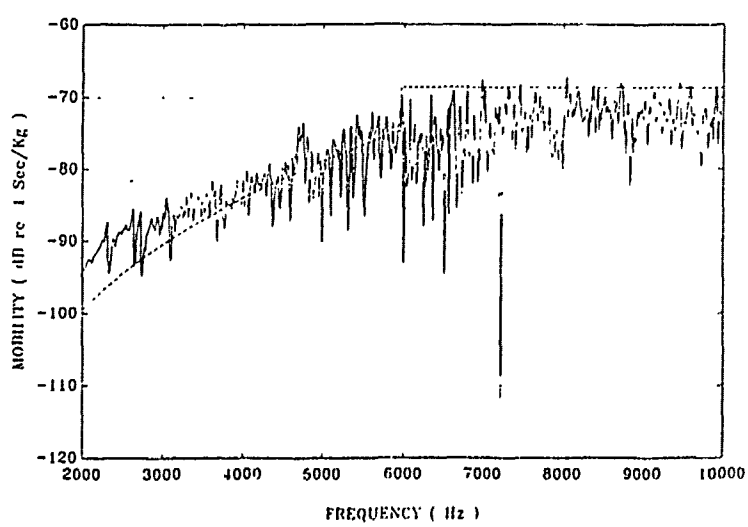

Fig.5. Driving point mobility function of the cylindrical shell.

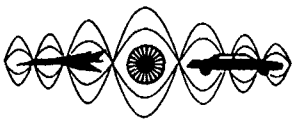

SECOND INTERNATIONAL CONGRESS ON
RECENT DEVELOPMENTS IN AIR- AND
STRUCTURE-BORNE SOUND AND VIBRATION
MARCH 4-6, 1992 AUBURN UNIVERSITY USA

THE EFFECT OF HEAVY FLUID LOADING ON EIGENVALUE LOCI VEERING AND MODE LOCALIZATION PHENOMENA

Jerry H. Ginsberg
G. W. Woodruff School of Mechanical Engineering
Georgia Institute of Technology
Atlanta, GA 30332-0405
USA

ABSTRACT

Veering of eigenvalue loci and extreme sensitivity of eigenfunctions to the value of a system parameter arise in many situations where changing that parameter causes natural frequencies to become close. Such phenomena often lead to mode localization, in which the response is restricted to a subregion. Prior investigations have mainly considered the implications for *in-vacuo* structures. The present work outlines the general theory for *in-vacuo* modes, and then extends it to acoustic radiation from submerged structures. The results of previous analyses of a two-span plate and a spheroidal shell are used to illustrate the effect of heavy fluid loading on structures that feature mode localization phenomena. These examples lead to the conclusion that such systems require special care in modelling, even though the submerged response may not actually contain regions of localized vibration.

INTRODUCTION

A large body of work exists regarding the behavior of vibratory systems in which alteration of a system parameter causes two or more natural frequencies to become close. In some cases, notably those in which the corresponding eigenfunctions belong to different symmetry groups independent of the parameter, one observes gradual changes of the modal properties as the parameter is changed, with the associated result that at some parameter value the natural frequencies become equal. However, in the circumstances of interest here, plotting the natural frequencies as a function of the parameter yields curves that deviate over a small range of that parameter, thereby avoiding intersection. When this phenomenon, which is known as eigenvalue loci veering, arises, the corresponding mode shapes show drastic changes in the veering zone, so that the system's behavior is extremely sensitive to the parameter. In addition, in many cases the mode shapes for certain values of the parameter indicate the existence of large regions of small displacement. Hence, eigenvalue veering may be accompanied by mode localization.

Numerous investigations of eigenvalue veering phenomena have been performed, and surveying them here would be prohibitive. Leissa [1] showed that this behavior could result from modelling errors, but several investigators have shown that actual manifestations are often associated with the introduction of disorder in otherwise periodic media. Pierre [2] developed criteria for the occurrence of eigenvalue veering, and Chen and Ginsberg [3] derived expressions for the mode shapes within the range of system parameters where eigenvalue veering occurs in terms of the shapes outside the veering zone.

Submarine structures feature stiffeners whose spacing is not quite constant because of functional requirements. Because they have the appearance of being nearly periodic structures, there is a strong possibility that eigenvalue veering phenomena occur. This raises significant issues for structural acoustics. If some aspects of the response are extremely sensitive to the value of a system parameter, and also might be an artifice

introduced by modelling errors, one is left to wonder about the degree to which accurate analyses can be performed. Furthermore, if mode localization is encountered, then one would expect that it would have a strong influence on acoustic radiation from the structure. These concerns must be weighed against the recognition that coupling associated with the fluid loading causes the notion of independent structural modes to lose significance.

This paper will survey some recent works by the author that have considered the effect of fluid-loading on structual dynamic systems whose *in-vacuo* response displays eigenvalue veering phenomena. It begins with a summary of the general theory for systems in which two eigenvalue loci veer, and then discusses the results for two distinctly different structures. Ginsberg and Pham [4] converted a two-span beam with interior torsional constraint, which had previously been used to illustrate eigenvalue veering, to a baffled plate as a way of introducing fluid loading. Previously, Chen and Ginsberg [5] had shown that the symmetric modes of spheroidal shells exhibit eigenvalue veering phenomena, after which they evaluated forced reponse when the shell is submerged [6]. The analyses of both systems combined the method of assumed modes and the surface variational principle (SVP) [7] for fluid-structure interaction, but the general theory is equally applicable to systems modeled by boundary element/finite element techniques.

EIGENVALUE VEERING PHENOMENA IN THE ABSENCE OF FLUID LOADING

First consider free vibration of a linear system when the system parameter has some reference value. The equations of motion are

$$\mathcal{L}(\phi_i) = \lambda_i \phi_i, \tag{1}$$

where (λ_i,ϕ_i) represents the eigensolution in the reference state. In the absence of dissipation, the operator $\mathcal{L}$ is self-adjoint, so the eigenfunctions form an orthornormal basis for the function space. When the system parameter is incremented by ϵ, the new operator $\mathcal{L}'$ is assumed to be expressible as a sum of the operator $\mathcal{L}$ and a perturbation operator $\epsilon\Gamma$. The altered eigenvalue problem,

$$(\mathcal{L} + \epsilon\Gamma)(\phi') = \lambda'\phi', \tag{2}$$

has eigensolutions (λ_i',ϕ_i'). The new eigenfunctions may be represented by a series of the original ones. In the usual circumstance covered by Courant and Hilbert [8] each eigensolution for the altered state differs from the corresponding solution in the original state by $O(\epsilon)$, being given by

$$\lambda_i' = \lambda_i + \epsilon\, h_{ii}, \quad \phi_i' = \phi_i + \epsilon \sum_{n\neq i} \frac{h_{in}}{\lambda_i - \lambda_n}\phi_n, \tag{3}$$

where self-adjointness of $\mathcal{L}$ and Γ leads to definitions of the coefficients h_{in}, which are inner products, as

$$h_{in} = h_{ni} = \langle\phi_i,\Gamma(\phi_n)\rangle. \tag{4}$$

Equations (3) breakdown if two eigenvalues, denoted λ_1 and λ_2 after reordering, become close and $\Gamma(\phi_1)$ is not orthogonal to ϕ_2. The appropriate expansion in such circumstances is

$$\phi' = c_1\phi_1 + c_2\phi_2 + \epsilon \sum_{n>2} b_n\phi_n, \tag{5}$$

where c_{i1}, c_{i2} are coefficients to be determined and ϕ_3, ϕ_4,... are eigenfunctions whose eigenvalues are well separated from λ_1 and λ_2, and each other. This expansion is substituted into Eq. (2) and appropriate inner products with respect to the original eigenfunctions are taken. The first order approximation reduces to an eigenvalue problem,

$$(\lambda_1 + \epsilon h_{11})c_1 + \epsilon h_{12}\, c_2 = \lambda' c_1, \quad \epsilon h_{21}c_1 + (\lambda_2 + \epsilon h_{22})c_2 = \lambda' c_2, \tag{6}$$

The associated matrix of this system is symmetric, so one obtains two real eigenvalues, λ_i', and two real orthogonal eigenvectors, c_{1i} and c_{2i}.

Because ϵh_{in} are small quantities, the eigenvalues λ_i' are approximately equal to λ_1 and λ_2. When plotted against ϵ, these eigenvalues form two curves called the eigenvalue loci.[2] Solving Eq. (6) shows these curves to be

$$\lambda' = \frac{1}{2}\left(\alpha_1 + \alpha_2\right) \mp \frac{1}{2}\left[(\alpha_1 - \alpha_2)^2 + 4\,\epsilon^2 h_{12}^2\right]^{1/2}, \quad \alpha_1 = \lambda_1 + \epsilon h_{11}, \quad \alpha_2 = \lambda_2 + \epsilon h_{22}. \tag{7}$$

The loci can be shown to be hyperbolas, which degenerate to their asymptotes only if $h_{12} = 0$. The minimum vertical distance between the two loci occurs when the slopes are equal, which corresponds to

$$\epsilon^* = \frac{(h_{11} - h_{22})(\lambda_2 - \lambda_1)}{(h_{11} - h_{22})^2 + 4\,h_{12}^2} \tag{8}$$

The difference between the hyperbolic curves and their asymptotes is noticeable only for a small range of system parameters close to this value. It is convenient to consider $\epsilon = \epsilon^*$ to be the unperturbed state, so the system parameter is redefined to be $\delta = \epsilon - \epsilon^*$. Because the curves have equal slope at their point of closest approach, $h_{11} = h_{22}$.

Expressions for the coefficients c_{ij} are obtained by solving Eqs. (6) corresponding to the definition of δ, subject to the requirement that the eigenfunctions for the altered state have unit magnitude. The result for $\delta h_{12}^* > 0$ is

$$\phi_i' = c_{1i}\phi_1^* + c_{2i}\phi_2^* + O(\epsilon) \; ; \; i = 1, 2, \tag{9}$$

where

$$c_{12} = \sin(\theta/2) \quad \text{and} \quad c_{22} = \cos(\theta/2) \quad \text{for the upper locus,}$$

$$c_{11} = \cos(\theta/2) \quad \text{and} \quad c_{21} = -\sin(\theta/2) \quad \text{for the lower locus.} \tag{10}$$

The quantity θ is related to the minimum difference d^* between the eigenvalues by

$$\tan\theta = 2\delta h_{12}^*/d^*, \quad d^* = \lambda_2^* - \lambda_1^*. \tag{11}$$

The corresponding eigenvalues may also be expressed in terms of θ by substituting its definition, Eq. (11), into Eq. (7), with the result that

$$\lambda' = \frac{1}{2}(\lambda_1^* + \lambda_2^*) + \delta h_{11}^* \mp \frac{1}{2}(\lambda_1^* - \lambda_2^*)/\cos\theta \tag{12}$$

Similar expressions apply when $\delta h_{12}^* < 0$.

The limit of the zone in which the veering behavior is encountered corresponds to $|\theta| \approx \pi/2$, at which $|\delta| = \delta_0 \gg d^*/2h_{12}^*$. The sensitivity of the mode shapes to the changes in the system parameter becomes apparent when one considers the situation when $|\delta| = \delta_0$. Because $|\theta| \approx \pi/2$, Eqs. (10) indicate that $|c_{2i}| \approx |c_{1i}|$, in which case one finds from Eqs. (9) that the altered modes are essentially the sum or difference of the modes at the reference state, $\delta = 0$. Thus, a small change in the system parameter results in a large change in the mode shapes. The reason for the occurrence of mode localization is less obvious. In many situations the modes associated with $\delta = 0$ have similar patterns over some of their range, and are opposite in sign over another region. Summing and differencing the modes in that case results in cancellation in some regions and reinforcement in others. This will be apparent in the example of vibration of a plate.

EFFECTS OF FLUID LOADING

The discussion shall now consider the coupled equations for surface displacement and pressure when a structure is excited by an external harmonic load. Such equations are obtained by combining structural dynamics laws and an acoustic interaction law, such as boundary elements or SVP. Let {q} denote a set of N generalized coordinates representing the structural displacement and {p} be M variables representing the surface pressure. The standard form of the system equations may be written in terms of partitioned matrices as

$$\begin{bmatrix} [k]-\omega^2[m] & [\Lambda] \\ -i\omega[\Gamma] & [A] \end{bmatrix} \begin{Bmatrix} \{q\} \\ \{p\} \end{Bmatrix} = \begin{Bmatrix} \{Q\} \\ \{0\} \end{Bmatrix}, \tag{13}$$

where $[\Lambda]$ and $[\Gamma]$ are fluid-structure coupling coefficients, and $\{Q\}$ are the generalized forces.

Presumably, an analysis of the *in-vacuo* modes has been carried out prior to addressing the submerged system. This involves finding a set of eigenvalues ω_j^2 and corresponding modes (ϕ_j) that satisfy

$$[[k] - \omega_j^2[m]](\phi_j) = (0). \tag{14}$$

In order to use the modal properties the generalized coordinates are replaced by a set of modal coordinates η_j. This is achieved by introducing the similarity transformation

$$(q) = [\phi](\eta), \quad [\phi] = [(\phi_1)\ (\phi_2)\ \cdots]. \tag{15}$$

If one determines and uses all N modes, then the foregoing is merely a change of variables. However, if a modal truncation is implemented, the number of unknowns is reduced by the foregoing from N to L.

The modes form an orthonormal set with respect to the inertia matrix [m], and they diagonalize the stiffness matrix to the respective eigenvalues. Hence, substituting the foregoing into the fluid-loaded system equations, followed by premultiplication of the first partition row by $[\phi]^T$, leads to

$$\begin{bmatrix} [D] & [\phi]^T[\Lambda] \\ -i\omega[\Gamma][\phi] & [A] \end{bmatrix} \begin{Bmatrix} (\eta) \\ (p) \end{Bmatrix} = \begin{Bmatrix} [\phi]^T(Q) \\ (0) \end{Bmatrix}, \quad D_{ij} = (\omega_i^2 - \omega^2)\delta_{ij} \tag{16}$$

Certain features of the foregoing are obvious. Although [D] is diagonal, the other matrices are generally full, so that the modal coordinates are coupled. The degree of such coupling depends on a variety of factors, but, in any event, the concept of independent modes is not meaningful. In a situation in which the localizing modes are not resonantly excited, one would not expect them to make an unusually large contribution to the overall response. However, it is reasonable to expect that appropriate tuning will lead to an excitation that strongly excites either of the localizing modes, in which case the fluid coupling should tend to excite both.

Consider such a situation, subject to the further assumption that the other modal coordinates are sufficiently small to be negligible. In that case solving the second part of Eq. (16) for (p) and substituting the result into the structural equations of motion leads to

$$(\omega_i^2 - \omega^2)\eta_i + B_{i1}\eta_1 + B_{i2}\eta_2 = (\phi_i)Q, \quad i = 1, 2, \tag{17}$$

where the coefficients B_{in} are

$$B_{in} = i\omega(\phi_i)^T[\Lambda][A]^{-1}[\Gamma](\phi_n). \tag{18}$$

The [B] array describes all modal coupling resulting from the fluid loading, because [Λ] contains the modal generalized forces associated with the pressure variables, and [Γ] represents the surface acceleration associated with the modal generalized coordinates.

Suppose the foregoing corresponds to the reference state for the veering phenomena, at which $\delta = 0$. Then alterating the system by setting $\delta \neq 0$ leads to

$$[(\omega_i')^2 - \omega^2]\eta_j' + B_{i1}'\eta_1 + B_{i2}'\eta_2' = (\phi_i')Q_i', \quad i = 1, 2. \tag{19}$$

It is reasonable to assume [A], [Λ], and [Γ] are essentially unchanged by a δ increment of the system parameter. Hence, introducing Eqs. (9) for the modes in the altered state into the definition of the coefficients B_{in}, Eq. (18), yields

$$B_{in}' = \sum_{j=1}^{2}\sum_{\ell=1}^{2} c_{ij}c_{\ell n}B_{j\ell}. \tag{20}$$

When the fluid is heavy, the coefficients B_{in} are significant to the solution for η_i. Because the coefficents c_{in} change by O(1) in the range $-\delta_0 < \delta < \delta_0$, Eqs. (20) suggest that the system of equations for the altered system are drastically different from those of the system at $\delta = 0$. Hence, it is reasonable to infer that the fluid loaded response will show extreme sensitivity to the value of the system parameter. However, because these equations govern the modal coordinates, one cannot ascertain from these equations whether localization will be observed in the resulting physical displacement components.

It is important to note that the foregoing observations are limited to situations where the two localizing modes dominate the response. Otherwise, the degree to which the response is actually sensitive to the system parameters and the issue of whether localized displacements are encountered can only be assessed by solution of the full problem, Eqs. (13) or (16).

RESULTS FOR A TWO-SPAN PLATE

A prototype for the effect of a bulkhead on a plate structure is the two-dimensional problem of a plate occupying the plane $z = 0$, pinned at ends $x = 0$ and $x = L$, and supported along a midspan line $x = L/2(1 + \delta)$ by a pin and torsional spring K_θ. The distance $\delta L/2$ from the interior support to the center point is the physical parameter associated with eigenvalue veering phenomena. The differential equations governing *in-vacuo* vibration due to a concentrated force at $x = x_f$ are

$$\frac{EI}{1 - \nu^2}\frac{\partial^4 w}{\partial x^4} + \rho A \ddot{w} = \delta(x - x_f)\exp(-i\omega t), \quad w = \frac{\partial^2 w}{\partial x^2} = 0 \text{ at } x = 0, L$$
$$w = 0, \quad \left[\frac{\partial w}{\partial x}\right] = 0, \quad EI\left[\frac{\partial^2 w}{\partial x^2}\right] = -K_\theta\left(\frac{\partial w}{\partial x}\right) \text{ at } x = \frac{L}{2} + \delta \tag{21}$$

where brackets denote jump conditions. Prior works had developed the eigensolution using a series expansion subject to an auxiliary constraint accounting for the interior support, which required 1000 terms to attain adequate accuracy. In contrast, the solution on Reference [4] was obtained by solving the differential equations on either side, and then requiring that the individual solutions satisfy the jump conditions at the support. This only required solution of a single characteristic equation, with the benefit that any mode could be obtained in an accurate, but simple, manner.

When $\delta = 0$ the *in-vacuo* modes reduce to symmetric and anti-symmetric groups. In that case, if $K_\theta L \gg EI$, the torsional restraint strongly isolates the beam segment on either side of the middle support. Hence the displacement patterns on either side are very similar between the modes, except for sign differences associated with the symmetry, being given by

$$\phi_1^* \approx \phi_2^* = f(x); \; x < L/2, \quad \phi_1^* \approx -\phi_2^* = -f(L-x); \; x > L/2. \tag{22}$$

Note that the natural frequency of the symmetric mode is always higher than that of the antisymmetric mode. The modal behavior described by Eqs. (9), according to which the mode shapes at the limits of the veering zone are a sum or difference of the modes when $\delta = 0$, results in cancellation of the modal displacement on one side or the other. The two fundamental modes of the plate for various δ are shown in Fig. 1, where it can be seen that ϕ_1 localizes to the left side, while ϕ_2 localizes to the right.

In order to investigate the coupling effects associated with fluid loading, Ginsberg and Pham [4] introduced a rigid baffle that extended the plane of the plate outward equally from both ends, with fluid considered to be situated in the upper half-plane. Equations of motion for the displacement w and surface pressure p were obtained by using an assumed modes formulation founded on a two-dimensional version of SVP and modal analysis of the plate.

The present example considers a force at $x_f = 0.75L$ when the frequency ω is swept across the natural frequencies of the two fundamental modes. If the fluid is air and $\delta = 0$, then each mode is resonantly excited in a narrow frequency range, with the peak amplitude of each mode occurring at a distinct frequency. In this frequency range the excitation of the higher modes is unimportant, as can be seen in Fig. 2, which shows $|\eta_i|$ for the first four modes. In contrast, when $\delta = 0.03$, the modes split into ϕ_1, which is localized to the left of the pin, and ϕ_2, which is localized to the right, see Fig. 1. Because the force is applied on the right span, the modal generalized force associated with ϕ_2 is much greater than that associated with ϕ_1. Thus, the frequency sweep appearing in Fig. 3 displays a very small peak at ω_1 and a large peak at ω_2.

Now consider the effect of the same excitation when the fluid is water. In general, the added-mass effect of the water resistance tends to lower the the frequency at which a peak response is encountered in comparison to the in-vacuo case. Figure 4, for $\delta = 0$, indicates that no peak is encountered in the symmetric mode, which suggest that the radiation damping of this mode overcomes the coupling effects that tend to intertwine the two low frequency modes. The picture in Figure 5, for $\delta = 0.03$, is drastically different. In this case, both modes peak at the same frequency and their amplitudes are comparable. Furthermore, the width of the peak is substantially enhanced. Because each of the two fundamental modes is associated with displacement on only one side of the interior support, it is clear that the displacement in this situation is not a localized response. Further evidence of the extreme sensitivity of the response to the location of the middle support may be found in Fig. 6, which shows the radiated power evaluated by integrating Re(p conj(v)) over the surface for several values of δ.

VIBRATION OF SPHEROIDAL SHELLS

Another aspect of the effect of eigenvalue veering was encountered in Chen and Ginsberg's analyses of axisymmetric vibration of a prolate spheroidal shell. The system parameter δ in this case is the aspect ratio L/a. Their first work [5] evaluated *in-vacuo* modal properties that are symmetric with respect to the equator. The analysis used an assumed modes formulation that included bending and membrane deformation. It was found that in several ranges of L/a the natural frequencies associated with flexural and extensional deformation became close, resulting in modes that combine both features, in the manner of Eq. (9). This interaction leads to modes that are localized, in the sense that the transverse displacement is much larger over a band at the equator than it is at the apexes. Furthermore, the modes were found to be drastically different for a comparatively small change in aspect ratio, which confirms that extreme parameter sensitivity is a corollary of veering of the eigenvalue loci. A specific case occurred for aspect ratios in the range $4 < L/a < 4.9$, where the sixth and seventh symmetric modes interact. The transverse displacement in these modes at $L/a = 4$ and 4.9 are depicted in Fig. 7. The fifth mode, which does not undergo drastic change over this range of aspect ratios is also shown in the figure for the sake of comparison.

Ginsberg and Chen [6] subsequently addressed the effect of fluid loading by using SVP to evaluate the displacement and surface pressure resulting from a harmonically varying pressure applied uniformly over the spheroid's surface. The aspect ratios described in Fig. 7 were selected for the evaluation. The frequency of the excitation was taken to be $ka = 1.8$, which is less than half the natural frequency of the pair of localizing modes. Because of the low frequency of the excitation relative to the localizing modes, this situation is distinctly different from the preceding example of the plate, in which the response is dominated by resonantly excited modes that localize.

Figures 8 and 9 show the transverse displacement and surface pressure when $L/a = 4.0$, while Fig. 10 shows the far field pressure, which was evaluated from the exterior Helmholtz integral corresponding to the surface response in Figs. 8 and 9. Four cases are shown in each figure: case (A) is the result obtained by increasing the number of basis functions until convergence is attained, case (B) is the result of a modal truncation at the seventh symmetric mode, thereby retaining both localizing modes in the representation of displacement, and cases (C) and (D) are the results obtained from modal truncations at the sixth and fifth modes, respectively. Thus, one can deduce from the figures the effect of the high frequency modes, the individual localizing modes, and the low frequency modes.

The case (A) analysis indicates that the normal displacement is unlike any one individual mode. In fact, Fig. 8 indicates that the displacement around the equator is comparable to that at the apexes of the spheroid. (Note that the axisymmetry condition, $\partial w/\partial s = 0$ at the apexes, where s is the arclength along the shape generator, is satisfied implicitly, but the scale of the figure obscures this property.) Perhaps the most important aspect of Figs. 8 and 9 is the recognition that omitting the localized modes, as is done in case (D), leads to a completely erroneous set of predictions, while including both localizing modes yields results for the surface response that are similar from an order of magnitude viewpoint to the direct SVP prediction. In addition, Fig. 10 indicates that the far field prediction obtained from such truncations is no better than the surface values.

The results for $L/a = 4.9$, which are not repeated here for reasons of brevity, do show some differences from those of Figs. 8-10. However, the degree of these differences is far less than that encountered for the mode shapes in Fig. 7. This does not disagree with the general analysis two sections previously, because the localizing modes are not resonantly excited, and therefore are not the sole contributors to the response.

CONCLUSIONS

The examples suggest that although localized displacements might occur when fluid resistance is small, they will not be observed in submerged structures. The analysis and example of a plate indicate that when the response is dominated by modes that localize, the fluid-loaded response will generally remain sensitive to the value of the system parameter. When many modes contribute, as in the case of the spheroidal shell, sensitivity to the parameter value is lessened. However, the localized modes still play an important role and must be included, even if their natural frequency is substantially higher than the excitation. Consequently, it is reasonable to conclude that direct solution of the full set of fluid-coupled equations is preferable to simplifications based on modal truncation.

ACKNOWLEDGEMENT

This work was supported by the Office of Naval Research, code 1132-SM.

REFERENCES

1. A. W. Leissa, " On a Curve Veering Aberration," *J. Appl. Math. and Phys. (ZAMP)*, Vol. 25, pp. 99-112 (1974).
2. C. Pierre, "Mode Localization and Eigenvalue Loci Veering Phenomena in Disordered Structures," *J. Sound and Vibr.*, Vol. 126, pp. 485-502, (1988).
3. P.-T. Chen and J. H. Ginsberg, "On the Relationship Between Veering of Eigenvalue Loci and Parameter Sensitivity of Eigenfunctions", *ASME J. Vibr. and Acoust.*, (forthcoming, 1992).
4. J. H. Ginsberg and H. Pham, "Mode Localization in a Fluid-Loaded Plate," 122nd Meeting of the Acoustical Society of America, Houston, TX, Nov. 4-8, 1991.
5. P.-T. Chen and J. H. Ginsberg, "Modal Properties and Eigenvalue Veering Phenomena in the Axisymmetric Vibration of Spheroidal Shells," (1991, submitted).
6. P.-T. Chen and J. H. Ginsberg, "The Effect of Mode Truncation in an Analysis of Acoustic Radiation from Spheroidal Shells," 119th Meeting of the Acoustical Society of America, Pennsylvania State University, May 21-25, 1990.
7. X.-F. Wu, A. D. Pierce, and J. H. Ginsberg, "Variational method for computing surface acoustic pressure on vibrating bodies, applied to transversely oscillating disks," *IEEE J. Oceanic Eng.* OE-12, 412-418 (1987).
8. Courant, R., and Hilbert, D., 1953, *Methods of Mathematical Physics*, Vol. 1, Interscience Publishers, Inc., pp. 343-350.

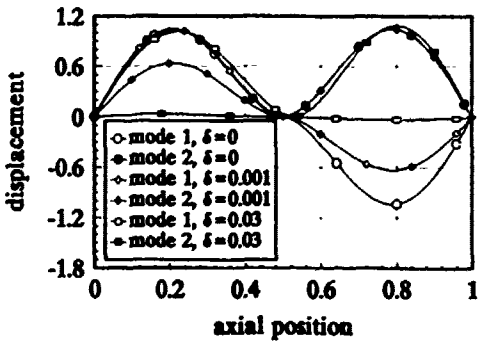

Figure 1. Mode shapes of the two-span plate, $K_\beta L/EI = 500$.

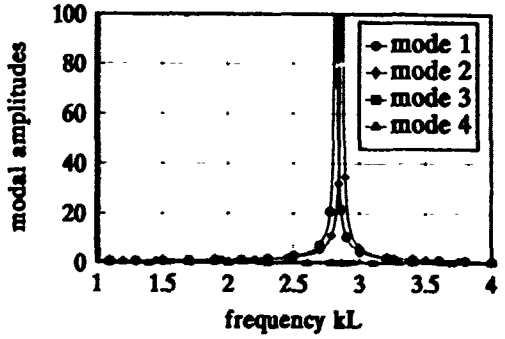

Figure 2. Modal response of the air-loaded two-span plate, $\delta = 0$.

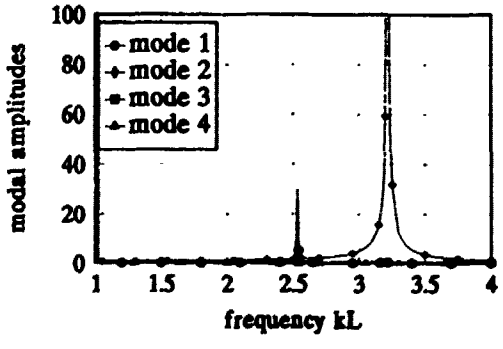

Figure 3. Modal response of the air-loaded two-span plate, $\delta = 0.003$.

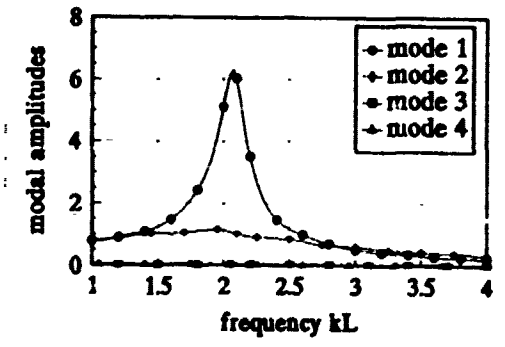

Figure 4. Modal response of the water-loaded two-span plate, $\delta = 0$.

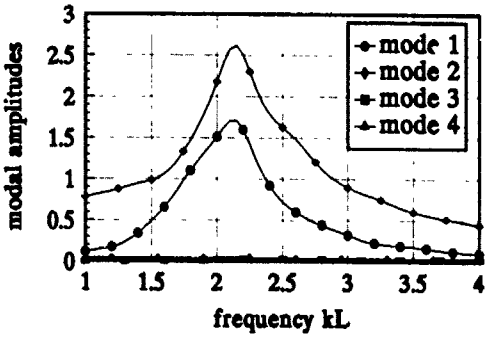

Figure 5. Modal response of the water-loaded two-span plate, $\delta = 0.003$.

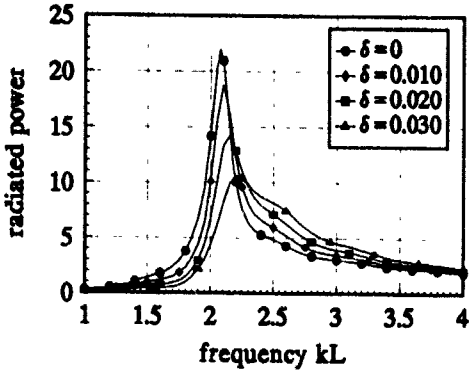

Figure 6. Power radiated from the water-loaded two-span plate.

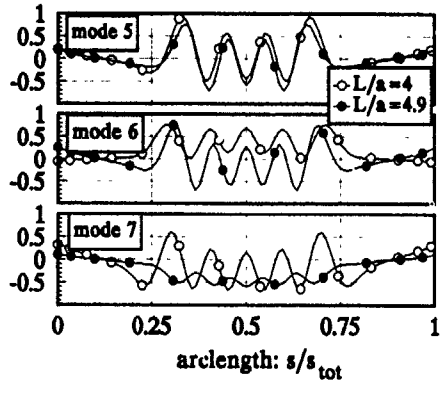

Figure 7. Selected modes of the spheroid.

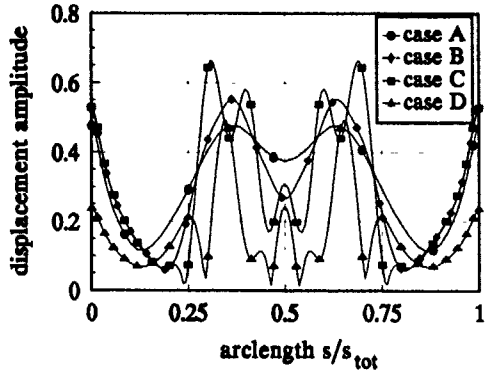

Figure 8. Transverse displacement of the spheroidal shell in water, L/a = 4, ka = 1.8.

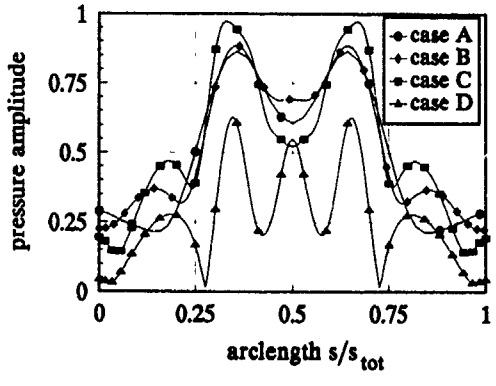

Figure 9. Pressure on the spheroidal shell in water, L/a = 4, ka = 1.8.

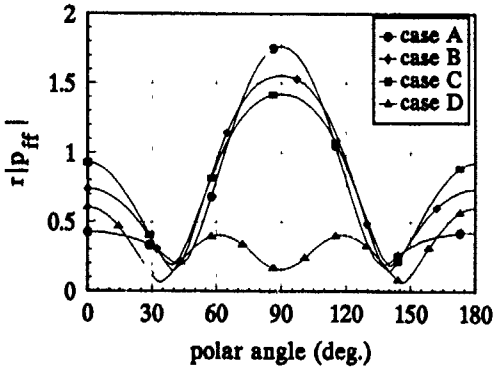

Figure 10. Far field of the sph roidal shell in water, L/a = 4, ka = 1.8.

SECOND INTERNATIONAL CONGRESS ON
RECENT DEVELOPMENTS IN AIR- AND
STRUCTURE-BORNE SOUND AND VIBRATION
MARCH 4-6, 1992 AUBURN UNIVERSITY, USA

MODAL ANALYSIS OF GYROSCOPICALLY COUPLED SOUND-STRUCTURE INTERACTION PROBLEMS

Vijay B. Bokil and U. S. Shirahatti
Mechanical Engineering & Mechanics
Old Dominion University
Norfolk, VA 23529

ABSTRACT

In many practical situations we encounter sound-structure interaction between the fluid in a cavity and the flexible walls on the boundary. In most cases, such interactions can be shown to involve gyroscopic coupling between the two systems. A direct modal analysis of these gyroscopically coupled systems is not easy to perform. The main theme of this paper is to look at an indirect technique which has been developed to perform this coupled analysis.

Here we discuss a technique of determining the modal parameters of the interacting cavity and the wall in terms of the modal parameters of the individual non-interacting systems. Results for a rectangular cavity, which has an elastic vibrating panel on one of its faces have been presented. These are compared with the experimental results obtained by previous researchers.

INTRODUCTION

Interaction between the fluid in a cavity with its flexible wall is encountered in many practical situations; for example, the aircraft cabin interacting with its fuselage and the automobile interior interacting with its flexible body. The motion of the flexible wall in such cases is due to external mechanical forces or exterior sound fields.

Various methods have been proposed to solve the above interaction problem. Exact solutions are available for simple shapes of the cavity whereas numerical methods like FEM or BEM have been used for complex shapes of the cavity [1–3]. A method based on the modal interaction of the rigid wall cavity modes and in-vacuo structural modes is discussed here.

NOMENCLATURE

A wall area
a_n velocity potential generalized coordinate
c_0 equilibrium speed of sound
F_n n th acoustic rigid wall mode
L_{nm} coupling coefficient between n th acoustic and m th wall mode
M_m mth stuctural wall generalized mass of in-vacuo mode
M_n nth acoustic gereralized mass of rigid wall mode
n unit normal to the surface, positive outward
p acoustic pressure inside the cavity
p^C acoustic pressure on the inner surface of the wall

q_m mth wall modal coordinate
t time
y_r, z_r eigenvectors corresponding to the r th eigenvalue
ζ_r, η_r generalized coordinate corresponding to y_r, z_r respectively
ρ_0 density of the acoustic medium
ρ_w structural mass per unit area
Φ acoustic velocity potential
Ψ_m mth in-vacuo wall mode
Ω natural frequency of the r th coupled system mode
ω_n^A natural frequency of the n th rigid wall acoustic mode
ω_m natural frequency of the m th in-vacuo wall mode
subscripts
F flexible
m, n modal numbers
r, s eigenvector numbers
R rigid
Bold letter denotes a matrix.

SOUND STRUCURE INTERACTION BETWEEN THE CAVITY AND THE FLEXIBLE WALL

The acoustical equations for the cavity can be derived in terms of the rigid wall modes for a prescribed motion of the wall. Similarly, the motion of the flexible wall due to external acoustic pressure can be derived in terms of the in-vacuo structural modes. When the interaction between the cavity and the wall is considered, the acoustic equations for the cavity and equations of motion for the wall can be shown to be gyroscopically coupled.

Equations For The Cavity-Wall Interaction

For a cavity occupying volume V enclosed by surface A which has a flexible portion A_F and rigid portion A_R, the acoustic velocty potential Φ satisfies the following wave equation

$$\nabla^2\Phi - \frac{1}{c_0^2}\frac{\partial^2\Phi}{\partial t^2} = 0 . \tag{1}$$

The associated boundary conditions are

$$\begin{aligned} \frac{\partial\Phi}{\partial n} &= \frac{\partial w}{\partial t} \quad \text{on} \quad A_F, \\ &= 0 \quad \text{on} \quad A_R. \end{aligned} \tag{2}$$

The velocity potential Φ can be expanded in terms of normal modes of the rigid wall cavity as

$$\Phi = \sum_{n=0}^{\infty} a_n(t)\ F_n, \tag{3}$$

and the acoustic pressure p is

$$p = \sum_{n=0}^{\infty} \dot{a}_n(t)\ F_n \tag{4}$$

The rigid wall modes F_n, n=0, 1, 2, ... satisfy the appropriate Helmholtz equation, orthogonality and boundary conditions. In order to express the motion of the flexible wall in terms of its in-vacuo modes, let the wall structure be represented by linear partial differential equation of the form

$$S\,w + \rho_w \frac{\partial^2 w}{\partial t^2} = p^C - p^E, \tag{5}$$

where S is the linear differential operator. The wall deflection w can be expressed in terms of the in-vacuo modes Ψ_m as

$$w = \sum_{m=1}^{\infty} q_m \Psi_m. \tag{6}$$

The in-vacuo normal modes Ψ_m, m=1, 2, ... satisfy

$$S\,\Psi_m - \rho_w \Psi_m \omega_m^2 = 0, \tag{7}$$

and the appropriate orthogonality and boundary conditions.

By defining

$$L_{nm} = \frac{1}{A_F} \int_{A_F} F_n\,\Psi_m\ dA, \tag{8}$$

Eq. (1) and Eq. (8) can be transformed into the following equations

$$\frac{VM_n^{\Lambda}}{A_F c_0^2} \left[\ddot{a}_n + \omega_n^2 a_n\right] - \sum_{m=1}^{\infty} \dot{q}_m L_{nm} = 0, \quad n = 0, 1, 2, \ldots \tag{9}$$

$$\frac{M_m}{\rho_0 A_F} \left[\ddot{q}_m + \omega_m^2 q_m\right] + \sum_{n=0}^{\infty} \dot{a}_n L_{nm} = -\frac{1}{\rho_0 A_F} Q_m^E, \quad m = 1, 2, \ldots \tag{10}$$

where

$$Q_m^E = -\int_{A_F} p^E\,\Psi_m\ dA. \tag{11}$$

The details of the derivation are given in reference [4]. From Eq. (9) and Eq. (10), it is clear that they are gyroscopically coupled and L_{nm} is the coupling coefficient between the nth acoustic mode and the mth structural mode of the wall.

EFFECTS OF FUNDAMENTAL ACOUSTIC MODE ON THE WALL MODES

The fundamental acoustic rigid wall mode (n = 0) has a stiffening effect on all the structural modes[4, 5]. It can be seen from Eq. (9) (with n = 0) that

$$\dot{a}_0 = \frac{A_F c_0^2}{V M_n^A} \sum_{m=1}^{\infty} q_m L_{0m} . \tag{12}$$

In the vicinity of the m th structural mode natural frequency, the only dominant term on the right hand side of Eq. (16) is $q_m L_{0m}$. Hence, near the natural frequency of the mth structural mode,

$$\dot{a}_0 = \frac{A_F c_0^2}{V M_n^A} q_m L_{0m} . \tag{13}$$

Thus we can eliminate equation corresponding to n=0 from Eq. (9) and modify Eq. (10) to write

$$\frac{V M_n^A}{A_F c_0^2} \left[\ddot{a}_n + \omega_m^2 a_n \right] - \sum_{m=1}^{\infty} \dot{q}_m L_{nm} = 0, \qquad n = 1, 2, \ldots \tag{14}$$

and

$$\frac{M_m}{\rho_0 A_F} \dot{q}_m + \left[\frac{M_m \omega_m^2}{\rho_0 A_F} + \frac{A_F c_0^2}{V M_n^A} \right] q_m + \sum_{n=1}^{\infty} \dot{a}_n L_{nm} = \frac{1}{\rho_0 A_F} Q_m^E , \qquad m = 1, 2, \ldots \tag{15}$$

Assuming that N number of acoustic modes and M number of wall structure modes are sufficient to calculate the acoustic velocity potential and the velocity of the vibrating wall to the required accuracy, Eq. (14) and Eq. (15) are written as a system of first order ordinary differential equations in matrix form

$$\mathbf{I}\,\mathbf{x}(t) + \mathbf{G}\,\mathbf{x}(t) = \mathbf{X}(t), \tag{16}$$

where

$$\mathbf{I} = \begin{bmatrix} \frac{V M_n^A}{A_F c_0^2} & 0 & 0 & 0 \\ 0 & \frac{M_m}{\rho_0 A_F} & 0 & 0 \\ 0 & 0 & \frac{V M_n^A}{A_F c_0^2} \omega_n^2 & 0 \\ 0 & 0 & 0 & \frac{M_m}{\rho_0 A_F} \omega_m^2 + \frac{A_F c_0^2}{V M_n^A} L_{0m}^2 \end{bmatrix}, \tag{17}$$

$$\mathbf{G} = \begin{bmatrix} 0 & L_{nm} & \frac{V M_n^{\Lambda}}{A_F c_0^2} & 0 \\ -L_{nm} & 0 & 0 & \frac{M_m \omega_m^2}{\rho_0 A_F} + \frac{A_F c_0^2}{V M_n^{\Lambda}} L_{0m}^2 \\ -\frac{V M_n^{\Lambda}}{A_F c_0^2} & 0 & 0 & 0 \\ 0 & -\frac{M_m \omega_m^2}{\rho_0 A_F} - \frac{A_F c_0^2}{V M_n^{\Lambda}} L_{0m}^2 & 0 & 0 \end{bmatrix}, \tag{18}$$

$$\mathbf{x} = \begin{Bmatrix} \dot{a}_n \\ \dot{q}_m \\ a_n \\ q_m \end{Bmatrix}, \quad \mathbf{X} = \begin{Bmatrix} 0 \\ \frac{1}{\rho_0 A_F} Q_m^E \\ 0 \\ 0 \end{Bmatrix} \quad \begin{matrix} n = 1, 2, \ldots, N \\ , m = 1, 2, \ldots, M. \end{matrix} \tag{19}$$

Note that $\mathbf{I}$ is a positive definite, real diagonal matrix of order 2(N+M)x2(N+M), $\mathbf{G}$ is a skew symmetric real matrix of order 2(N+M)x2(N+M), $\mathbf{x}$ and $\mathbf{X}$ are 2(N+M)x1 vectors.

It has been shown in ref.[6] that the eigenvalue problem associated with Eq. (16) can be expressed in terms of real quantities as

$$\Omega_r^2 \mathbf{I} \mathbf{y}_r = \mathbf{K} \mathbf{y}_r \ , \ \Omega_r^2 \mathbf{I} \mathbf{z}_r = \mathbf{K} \mathbf{z}_r \ , \quad r = 1, 2, \ldots (N + M), \tag{20}$$

where

$$\mathbf{K} = \mathbf{G}^T \mathbf{I}^{-1} \mathbf{G}, \tag{21}$$

is a real symmetric matrix. The solution to the eigenvalue problem in Eq. (20) consists of (N+M) repeated eigenvalues Ω_r^2 and (N+M) pairs of eigenvectors $\mathbf{y}_r$ and $\mathbf{z}_r$, r =1, 2,.. (N+M). $\mathbf{K}$ is positive definite if $\mathbf{I}$ is positive definite (as in the present case) and eigenvectors $\mathbf{y}_r$ and $\mathbf{z}_r$ are orthogonal with respect to $\mathbf{I}$. If vectors $\mathbf{y}_r$ and $\mathbf{z}_r$ are normalized to satisfy

$$\mathbf{y}_r^T \mathbf{I} \mathbf{y}_r = \mathbf{z}_r^T \mathbf{I} \mathbf{z}_r = 1 , \qquad r = 1, 2, \ldots, (N + M), \tag{22}$$

then the orthogonality relations are

$$\begin{aligned} \mathbf{y}_r^T \mathbf{I} \mathbf{y}_s &= \mathbf{z}_r \mathbf{I} \mathbf{z}_s = \delta_{rs}, \\ \mathbf{y}_r^T \mathbf{I} \mathbf{z}_s &= \mathbf{z}_r^T \mathbf{I} \mathbf{y}_s = 0 , \ r, s = 1, 2, \ldots, (N + M) , \end{aligned} \tag{23}$$

and

$$\begin{aligned} \mathbf{z}_s^T \mathbf{G} \mathbf{y}_r &= -\mathbf{y}_s \mathbf{G} \mathbf{z}_r = \Omega_r \delta_{rs} \\ \mathbf{y}_s^T \mathbf{G} \mathbf{y}_r &= \mathbf{z}_s^T \mathbf{G} \mathbf{z}_r = 0 , \qquad r, s = 1, 2, \ldots, (N + M) . \end{aligned} \tag{24}$$

Vectors $\mathbf{y}_r$ and $\mathbf{z}_r$ can be used to form basis in 2(N+M) dimensional vector space. Using

the expansion theorem given in ref.[7], vector $\mathbf{x}$ can be expressed as a linear combination of eigenvectors $\mathbf{y}_r$ and $\mathbf{z}_r$ as

$$\mathbf{x}(t) = \sum_{r=1}^{N+M} \zeta_r(t)\, \mathbf{y}_r + \sum_{r=1}^{N+M} \eta_r(t)\, \mathbf{z}_r \ . \tag{25}$$

Using Eq. (22–25), the uncoupled differential equations corresponding to Eq. (16) can be written in terms of pairs of $\zeta_r(t)$ and $\eta_r(t)$ as

$$\dot{\zeta}_r(t) - \Omega_r \eta_r(t) = \mathbf{y}_r^T \mathbf{X}(t), \quad r = 1, 2, \ldots, (N+M) , \tag{26}$$

and

$$\dot{\eta}_r(t) + \Omega_r \zeta_r(t) = \mathbf{z}_r^T \mathbf{X}(t) \ , \ r = 1, 2, \ldots, (N+M) . \tag{27}$$

For any excitation $\mathbf{X}(t)$ we can obtain $\mathbf{x}(t)$ by evaluating $\zeta_r(t)$ and $\eta_r(t)$ for given initial conditions.

From Eq. (19) it is clear that (2N+M+m)th element of vector $\mathbf{x}$ corresponds to q_m. Hence, $\dot{a}_0$ can be evaluated using Eq. (12). The cavity acoustic pressure p is then calculated using Eq. (4) and velocity of the flexible wall can be calculated from Eq. (6).

SOLUTIONS FOR RECTANGULAR CAVITY

The above method was used to calculate pressure inside the rectangular cavity which has a simply supported flexible panel on one of its faces. Four acoustic modes and nine wall modes were considered. Values of other parameters were selected to be the same as those given in reference [1] so as to compare our results with the experimental results given there. The experimental setup in reference [1] consisted of acoustically hard walled 200x200x200 mm cubical cavity with one face made up of simply supported 0.9144 mm thick brass panel which was excited with sinusoidal acoustic pressure.

Table 1 shows the natural frequencies for the above model. Generally good agreement is found between the calculated values and the experimental results. Figure [1] shows the ratio of the exterior excitation pressure at the center of the panel to the cavity pressure at the center of the back wall expressed in dB against frequency. Excellent agreement is observed between the calculated and the experimental results.

CONCLUSION

The method presented in the paper has been shown to compare favorably with the experimental results obtained by previous researchers. If the modal parameters for complex shaped cavity and wall are evaluated independently by suitable numerical schemes and if the coupling coefficient is evaluated numerically, then this method can incorporate effects of cavity-wall interaction.Further work is neccesary to model the damping of the interacting systems either in terms of individual systems or as a complete system.

REFERENCES

1. R.W.Guy and M.C. Bhattacharya, "The Transmission of Sound through a Cavity-Backed Finite Plate, " *Journal of Sound and Vibration,* Vol. 27, No. 2, 1973, pp. 207–223.
2. D. J. Nefske, J. A. Wolf, Jr. and L. J. Howell, "Structural–Acoustic Finite Element Analysis of The Automobile Passenger Compartment: A Review of Current Practice, " *Journal of Sound and Vibration,* Vol. 80, No. 2, 1982, pp. 247–266.
3. S. Suzuki, M. Imai and S. Ishiyama, "Boundary Element Analysis of Structural-Acoustic Problems, " *Boundary Elements VI, Proceedings of the 6 th International Conference on board the liner, the Queen Elizabeth 2, Southampton to New york,* July 1984, Springer-Verlag.
4. E.H.Dowell, G.F.Gorman III and D.A.Smith, "Acoustoelasticity : General Theory, Acoustic Natural Modes and Forced Response to Sinusoidal Excitation, Including Comparisions with the experiments, " *Journal of sound and Vibration,* Vol. 52, No. 4, 1977, pp. 519–542.
5. E.H.Dowell and H.M.Voss, "The Effect of a Cavity on Panel Vibrations, " *American Institute of Aeronautics and Astronautics Journal,* Vol. 1, No. 2, 1963, pp. 476–477.
6. Leonard Meirovitch, "A new method of Solution of the Eigenvalue Problem for Gyroscopic Systems, " *American Institute of Aeronautics and Astronautics Journal,* Vol. 12, No. 10, 1974, pp. 1337–1342.
7. L.Meirovitch, "A Modal Analysis for the Response of Linear Gyroscopic Systems, " *Journal of Applied Mechanics,* Vol. 42, No. 2, 1975, pp. 446–450.

Calculated	Measured (ref.[1])
87	91
390	397
702	730
860	864
1015	1034
1716	1729
1918	1923

Table 1 – – Natural frequencies (Hz) for the coupled system

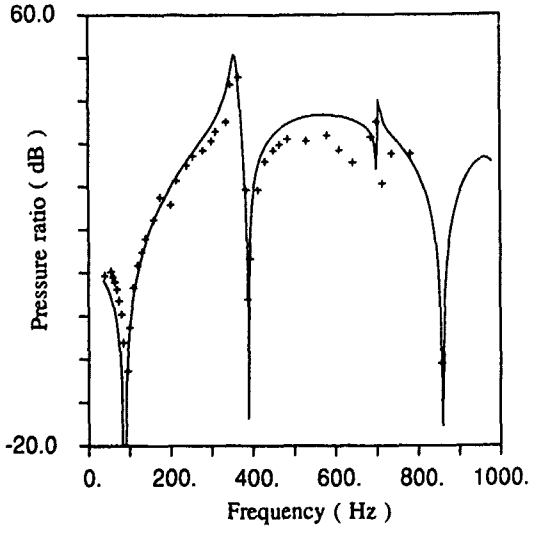

Figure 1 – – Response for the coupled system — , calculated; +, measured ref.[1]

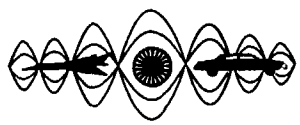

SECOND INTERNATIONAL CONGRESS ON
RECENT DEVELOPMENTS IN AIR- AND
STRUCTURE-BORNE SOUND AND VIBRATION
MARCH 4-6, 1992 AUBURN UNIVERSITY, USA

A SIMPLE METHOD OF STRUCTURAL PARAMETER MODIFICATION FOR A MDOF SYSTEM

by

Q. Chen and C. Levy
Mechanical Engineering Department
Florida International University
Miami, FL 33199
U.S.A

ABSTRACT

Vibration control is an important consideration in the design of dynamic systems. The objective of vibration control is to design the structure and its controls either to eliminate vibration completely or to reduce the response of the system to the desired level. To obtain optimal results, one must readjust the structural parameters to meet the given requirement. This paper investigates the structural parameter modification problem of a vibrating system's multiple degree of freedom (MDOF). It is assumed that when the natural frequency spectrum for an MDOF system has been initially obtained, one of the frequencies is in conflict with the system operating frequency. Simple expressions for mass and stiffness modifications required for a given frequency variation are found by means of a perturbation method. An example is given to illustrate the method and the results are compared with another method existing in the literature. It is determined that the method described herein can be very useful to the design engineer.

NOMENCLATURE

k, k_1, k_2, k_3	equivalent spring constants
k_{ij}	elements of the stiffness matrix
K	stiffness matrix of the modified system
K_0	initial system stiffness matrix
K_1	modification to stiffness matrix
M	mass matrix of the modified system
M_0	initial system mass matrix
M_1	modification to mass matrix
m, m_1, m_2	equivalent masses
m_{ij}	elements of the mass matrix
X	eigenvector matrix of the modified system
X_0	initial eigenvector matrix
$X_0^{(n)}$	nth column of X_0
X_1	modification of eigenvector matrix X_0

$X_1^{(n)}$	nth column of X_1
X_2	2nd order modification to X_0
x	degrees of freedom
$\ddot{x}$	second time derivative of x

Greek Symbols

α	undetermined parameter in X_1
ϵ^1, ϵ^2	small parameter and orders of that parameter
$\lambda_0^{(1)}$, $\lambda_0^{(2)}$	initial eigenvalues for the example
$\lambda_1^{(1)}$, $\lambda_1^{(2)}$	modifications to the eigenvalues of the example
A	eigenvalue matrix of the modified system
A_0	initial eigenvalue matrix
$A_0^{(n)}$	nth column of the initial eigenvalue
A_1	modification to A_0
$A_1^{(n)}$	nth column of matrix, A_1
A_2	2nd order modification to A_0

Superscripts

T	transpose
-1	inverse

INTRODUCTION

Vibration control is an important consideration in the design of dynamic systems. The objective of vibration control is to design the structure and its controls either to eliminate vibration completely or to reduce the response of the system to the desired level. To obtain optimal results, one must readjust the structural parameters to meet the given requirements. The reanalysis for modified structures can be achieved in several ways. In general, either an analytical model is used throughout the analysis or the measured response of the original structure is employed in the structural modification algorithm.

There is a vast literature on numerous different analysis techniques and their application to structural variations. Baldwin and Hutton [1] presented a detailed review of structural dynamics modification techniques that existed until 1984. Since that time much work has been done to improve the methods or to obtain new methods. Ram et al. [2] dealt with the theoretical basis for the approximation of a modified structure eigensystem based on the Rayleigh-Ritz approximation. The structural modification method based on Rayleigh Quotient Iteration was also presented by To and Ewins [4]. Wei [5] discussed the coupling between changes in mass and stiffness matrices. Kabe [6] introduced a procedure that used the mode data and structural connectivity information to optimally adjust deficient stiffness matrices. The sensitivity problems encountered by the previous methods were investigated [7,8]. Besides, a new algorithm for structural redesign by perturbation techniques was developed [9]. It allowed for large changes between baseline and objective structures. In order to significantly limit the computational effort, right-hand-side modifications [3] via control forces were introduced. The determined control forces were then related to changes in the design or system matrices.

It is clear from the above studies that investigations have focused on the establishment of the relationship between characteristic changes and structural parameter modification. The solution obtained in these studies required a lot of computational effort. Many methods to reduce computation have been presented. But there has been no explicit and unique expressions for the modifications of mass and stiffness required for the change of frequency. In this paper, the structural parameter modifications problem is investigated. Simple expressions of mass and stiffness modifications required for a given frequency variation is obtained by means of perturbations method. An example is given to illustrate the method.

STRUCTURAL MODIFICATION

For the purposes of the analysis several assumptions have been made. The structure is assumed to be approximated by a discrete system, linear and undamped. The system is assumed to be positive definite with no equal or closely located eigenvalues. Also, a small modification assumption is made. Under these assumptions, the eigenvalue problem can be expressed as:

$$K X = MX A \tag{1}$$

where K, M, and A are stiffness, mass, and eigenvalue matrices of the system, respectively, and X is a matrix composed of the eigenvectors. To establish the relationship between the changes of mass, stiffness, and the changes of eigenvalues, the perturbation method was used. Assuming the original mass and stiffness matrices to be M_0 and K_0, the new mass and stiffness matrices may written as:

$$M = M_0 + \epsilon M_1 \tag{2a}$$

$$K = K_0 + \epsilon K_1 \tag{2b}$$

where ϵ is a small parameters, M_1 is the perturbed mass matrix, K_1 is the perturbed stiffness matrix. According to perturbation theory, the general solution of Eq. (1) may be expressed in a power series with respect to small parameter, ϵ, i.e.

$$A = A_0 + \epsilon A_1 + \epsilon^2 A_2 + \ldots \tag{3a}$$

$$X = X_0 + \epsilon X_1 + \epsilon^2 X_2 + \ldots \tag{3b}$$

where A_0 and X_0 are eigenvalues and eigenvectors matrices of the original system. A_1, X_1, are the first order modifications. A_2 and X_2 are the second order modifications, and so on.

$$X_0 = (X_0^{(1)} \vdots X_0^{(2)} \vdots \text{---} \vdots X_0^{(n)}) \tag{4a}$$

$$A_0 = \text{diag}\,(\lambda_0^{(1)}, \lambda_0^{(2)}, \text{---}, \lambda_0^{(n)}) \tag{4b}$$

$$X_1 = (X_1^{(1)} \vdots X_1^{(2)} \vdots \text{---} \vdots X_1^{(n)}) \tag{4c}$$

$$A_1 = \text{diag}\,(\lambda_1^{(1)}, A_1^{(2)} \text{---}, A_1^{(n)}) \tag{4d}$$

where $X_0 = (X_0^{(1)} \vdots X_0^{(2)} \vdots \ldots \vdots X_0^{(n)})$ represent a matrix whose columns are $X_0^{(1)}, X_0^{(2)} \ldots, X_0^{(n)}$. $A_0 = \text{diag}\,(\lambda_0^{(1)}, \lambda_0^{(2)}, \ldots, \lambda_0^{(n)})$ represents a matrix whose diagonal entries are $\lambda_0^{(1)}, \lambda_0^{(2)}, \ldots, \lambda_0^{(n)}$.
Substituting Eqs. (2) and (3), into Eq. (1) yields.

$$(K_0+\epsilon K_1)\,(X_0+\epsilon X_1 + \epsilon^2 X_2 \text{---}) = (M_0+\epsilon M_1)\,(X_0+\epsilon X_1+\epsilon^2 X_2)\,(A_0+\epsilon A_1+\epsilon^2 A_2 \text{---}) \tag{5}$$

Rearranging Eq. (5) and equating like coefficients of ϵ^0, ϵ^1 ---, we obtain

$$K_0X_0 = M_0X_0A_0 \tag{6}$$

$$K_0X_1 + K_1X_0 = M_0X_0A_1 + M_0X_1A_0 + M_1X_0A_0 \ . \tag{7}$$

We normalize the system with respect to the mass matrix, i.e.,

$$X^T MX = I \tag{8}$$

$$X^T KX = A \tag{9}$$

where I is the identity matrix. By defining M, K, A, and X using Eqs. (2) and (3), we obtain the following relationship,

$$X_0^T M_0 X_0 = I \tag{10a}$$

$$X_0^T M_0 X_1 + X_1^T M_0 X_0 + X_0^T M_1 X_0 = 0 \tag{10b}$$

Also,

$$X_0^T K_0 X_0 = \Lambda_0 \tag{11a}$$

$$X_0^T K_1 X_0 + X_0^T K_0 X_1 + X_1^T K_0 X_0 = \Lambda_1 \tag{11b}$$

The problem will now be solved for two specific cases. The first case we tackle is that of mass modifications. It is assumed that only the mass matrix will be modified and the stiffness matrix remains the same, i.e., $K_1 = 0$. The other case is stiffness modification only and lets $M_1 = 0$.

Case 1 Mass Modification ($K_1 = 0$)

In this case, Eqs. (10b) and (11b) may be written as:

$$X_0^T M_1 X_0 + X_1^T M_0 X_0 + X_0^T M_0 X_1 = 0 \tag{12}$$

$$X_1^T K_0 X_0 + X_0^T K_0 X_1 = \Lambda_1 \tag{13}$$

Equation (7), which also involves M_1, reduces to Eq. (6) when (12) and (13) are employed; it is not an independent equation. From Eq. (12), we have:

$$M_1 = -(X_1 X_0^{-1})^T M_0 - M_0(X_1 X_0^{-1}) \tag{14}$$

Generally, X_1 may be solved from Eq. (13) if Λ_1 is known. With this X_1, M_1 may be obtained from Eq. (12).

Case 2 Stiffness Modification ($M_1 = 0$)

In this case, Eqs. (10b) and (11b) may be written as:

$$X_0^T M_0 X_1 + X_1^T M_0 X_0 = 0 \tag{15}$$

$$X_0^T K_1 X_0 + X_0^T K_0 X_1 + X_1^T K_0 X_0 = \Lambda_1 \tag{16}$$

From Eq. (16), we have:

$$K_1 = (X_0^T)^{-1} \Lambda_1 X_0^{-1} - K_0(X_1 X_0^{-1}) - (X_1 X_0^{-1})^T K_0 \tag{17}$$

In the above equation, X_1 may be determined from Eq. (15). Baldwin and Hutton's discussion [1] assumes X_1 to be zero for the change of the eigenvalue, Λ_1, and use the original eigenvector in Rayleigh's equation. From Eqs. (13) and (15), it can be seen that this assumption is not applicable to these cases.

ILLUSTRATIVE EXAMPLE

A simple example to demonstrate the main ideas of the paper is presented. The example chosen is an undamped two degree of freedom system shown in Fig. 1.

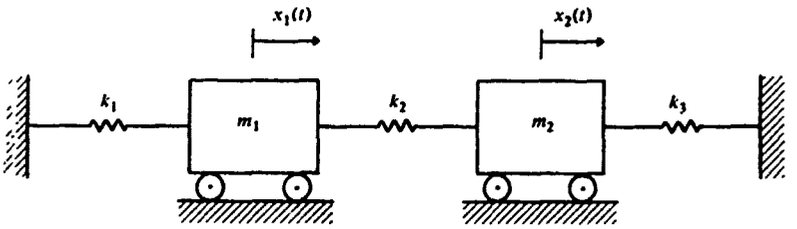

Fig. 1 Two Degree of Freedom System

The differential equations of motion of the system are:

$$\begin{bmatrix} m_1 & 0 \\ 0 & m_2 \end{bmatrix} \begin{Bmatrix} \ddot{x}_1 \\ \ddot{x}_2 \end{Bmatrix} + \begin{bmatrix} k_1+k_2 & -k_2 \\ -k_2 & k_2+k_3 \end{bmatrix} \begin{Bmatrix} x_1 \\ x_2 \end{Bmatrix} = \{0\} \tag{18}$$

The eigenvalues of the above system can be found to be [10]:

$$\lambda_0^{(1)}, \lambda_0^{(2)} = \frac{m_1 k_{22} + m_2 k_{11}}{2 m_1 m_2} \mp \frac{1}{2} \sqrt{\left(\frac{m_1 k_{22} + m_2 k_{11}}{m_1 m_2} \right)^2 - 4 \frac{k_{11} k_{22} - k_{12}^2}{m_1 m_2}} \tag{19}$$

where $k_{11} = k_1 + k_2$, $k_{12} = k_{21} = -k_2$, $k_{22} = k_2 + k_3$. If a system has following parameters $m_1 = m$, $m_2 = 2m$, $k_1 = k_2 = k$, $k_3 = 2k$, the eigenvalues are:

$$\begin{matrix} \lambda_0^{(1)} \\ \lambda_0^{(2)} \end{matrix} = \begin{Bmatrix} \frac{k}{m} \\ \frac{5k}{2m} \end{Bmatrix} \tag{20}$$

and

$$X_0 = \frac{1}{\sqrt{3m}} \begin{bmatrix} 1 & \sqrt{2} \\ 1 & -\frac{1}{\sqrt{2}} \end{bmatrix} \tag{21}$$

Case 1 Mass Modification ($K_1 = 0$)

Let us assume $\lambda_0^{(1)}$ is the eigenvalue where the exciting frequency matches. If the exciting frequency cannot be altered, the system parameters must be changed in order to avoid resonance. If we choose the value of $\lambda_1^{(1)}$ from experiment, for example, $\lambda_1^{(1)} = (\sqrt{2} - 1)\ \lambda_0^{(1)}$ and keep $\lambda_1^{(2)} = 0$, then from Eq. (13), the eigenvector matrix modification is:

$$X_1 = \begin{bmatrix} \frac{1}{3}\left(\frac{0.359}{\sqrt{m}} - 1.697\alpha\right) & \alpha \\ \frac{\sqrt{2}}{15}\left(3\alpha - \frac{1.269}{\sqrt{m}}\right) & \alpha \end{bmatrix} \tag{22}$$

The solution is not unique, depending on a variable, α. However, it is noted that X_1 is not equal to zero. If $\alpha = 1/\sqrt{3m}$ is chosen to make X_1 have the same form as X_0, then

$$X_1 = \frac{1}{\sqrt{3m}} \begin{bmatrix} -0.358 & 1 \\ 0.076 & 1 \end{bmatrix} \tag{23}$$

With this X_1, the mass modification can be obtained from Eq. (14) to be:

$$M_1 = m \begin{bmatrix} 0.704 & -0.284 \\ -0.284 & 1.682 \end{bmatrix} \tag{24}$$

For the general case where α is any value, the mass modification is:

$$M_1 = -m\sqrt{\frac{m}{3}} \begin{bmatrix} \frac{0.24}{\sqrt{m}} + 1.697\alpha & 0.848\alpha \\ 0.848\alpha & -3.394\alpha - \frac{0.96}{\sqrt{m}} \end{bmatrix} \tag{25}$$

We will now compare our value of A_1 to that of [1] for the same M_1.

Using Eq. (6) of reference [1], the following relationship from the mass modification can be obtained:

$$\lambda_1^{(i)} = -(X_0^i)^T M_1 X_0^{(i)} \lambda_0^{(i)} \qquad i = 1,2 \tag{26}$$

Substituting Eq. (25) into Eq. (26) gives:

$$\lambda_1^{(1)} \doteq 0.138\, \lambda_0^{(1)} \tag{27}$$

$$\lambda_1^{(2)} = 0.0\, \lambda_0^{(2)} \tag{28}$$

In our case, $\lambda_1^{(2)}$ is assumed to be zero. This is confirmed by Eq. (28). It is noted that the calculated $\lambda_1^{(1)}$ given by Eq. (27) is less than the given value ($(\sqrt{2}-1)\lambda_0^{(1)}$). This is a direct result of the fact that X_1 is not zero. Normally, the "cross terms" would be minimized; i.e., the non-diagonal terms of M_1 would be made zero. In such a case, α would be taken to be zero; yet it is noted that X_1 is still non-zero.

Case 2 Stiffness Modification ($M_1 = 0$)

In this case, M_1 is set to zero. If the same values, $\lambda_1^{(1)} = (\sqrt{2}-1)\lambda_0^{(1)}$ and $\lambda_1^{(2)} = 0$ are used, then

$$X_1 = \alpha \begin{bmatrix} -\sqrt{2} & 1 \\ \frac{\sqrt{2}}{2} & 1 \end{bmatrix} \tag{29}$$

where α is a variable. It can be seen that the solution for X_1 is not unique. But if α is chosen to be zero, then $X_1 = 0$. In this situation, Baldwin and Hutton's [1] assumption holds. If $\alpha = 0$, then

$$K_1 = \frac{(\sqrt{2}-1)k}{3}\begin{bmatrix}1 & 2\\ 2 & 4\end{bmatrix} \tag{30}$$

For the general case when α is non-zero, we have

$$K_1 = \frac{k}{3}\begin{bmatrix}(\sqrt{2}-1)+3\sqrt{6m}\,\alpha & 2(\sqrt{2}-1)+\frac{3}{2}\sqrt{6m}\,\alpha\\ 2(\sqrt{2}-1)+\frac{3}{2}\sqrt{6m}\,\alpha & 4(\sqrt{2}-1)-6\sqrt{6m}\,\alpha\end{bmatrix} \tag{31}$$

Our value of A_1 may now be compared to that of reference [1], assuming the same K_1.

In the same way as in Case 1, by using Eq. (6) of reference [1], the relation between K_1 and A_1 may be obtained.

$$\lambda_1^{(i)} = (X_0^{(i)})^T K_1 X_0^{(i)} \lambda_0^{(i)} \qquad i = 1,2 \tag{32}$$

Substituting Eq. (31) into Eq. (32) yields:

$$\lambda_1^{(1)} = (\sqrt{2}-1)\lambda_0^{(1)} \tag{33}$$

$$\lambda_1^{(2)} = 0.0\,\lambda_0^{(2)} \tag{34}$$

It can be seen that Baldwin and Hutton's [1] method gives exact results in this case (i.e., when $\alpha = 0$).

If the "cross-terms" of K_1 are minimized (i.e., K_1 is diagonalized), $\alpha = -\,4(\sqrt{2}-1)/(3\sqrt{6m})$ would be chosen. This would be equivalent to changing springs, k_1 and k_3 in Fig. 1. Generally speaking, changes in k_1, k_2, and k_3 may be deduced from Eq. (31). Either all three springs are simultaneously changed, or k_1 and k_3 are changed, and k_2 is left unchanged. It is not possible to change the value of k_2 alone.

It should be noted that we are solving an inverse problem and we must determine the coefficients of M_1 and K_1. For an n degree of freedom system, n^2 coefficients must be determined and require n^2 equations to be solved. Thus, this method will require use of a computer for large numbers of degree of freedom.

CONCLUSION

The structural parameter modification problem has been studied in this paper. By means of a perturbation method, simple expressions for the mass and stiffness modifications required for a given frequency variation are derived. Thus, for a design engineer, from a given frequency spectrum, the modification for the system can be deduced. This method is very useful for engineering applications in which variations of the frequency spectrum is the input. A comparison between the present method and a previous method has been performed in the paper. The results show that the present method will give a better approximation for the modification of the system.

ACKNOWLEDGMENT

The authors gratefully acknowledge the help of the Department of Energy whose grant DEFG0390ER18-715 provided partial support for this work.

REFERENCES

[1] J. F. Baldwin and S. G. Hutton, "Natural Modes of Modified Structures," *AIAA Journal*, Vol. 23, No. 11, 1985, pp. 1737-1743.

[2] Y. M. Ram, S. G. Brown, and J. Blech, "Structural Modifications in Trancated System by the Rayleigh-Ritz Method," *J. Sound and Vib.*, Vol. 125, No. 2, 1988, pp. 203-209.

[3] H. Baier and A. Rausch, "On Right-Hand-Side Modifications for the Solution of Inverse Problems in Structural Dynamic Response," *Mechanical Systems and Signal Processing*, Vol.4, No. 3, 1990, pp. 187-194.

[4] W. M. To and D. J. Ewins, "Structural Modifications Analysis Using Rayleigh Quotient Iteration," *Int. J. Mech. Sci.*, Vol. 32, No. 3, 1990, pp. 169-179.

[5] F. S. Wei, "Mass and Stiffness Interaction Effects in Analytical Model Modification," *AIAA J.*, Vol. 28, No. 9, 1990, pp. 1686-1688.

[6] A. M. Kabe, "Stiffness Matrix Adjustment Using Mode Data," *AIAA Journal*, Vol. 23, 1985, pp. 1431-1436.

[7] R. T. Haftka and R. K. Kapania, "Sensitivity of Actively Damped Structures to Imperfections and Modeling Errors," *AIAA J.*, Vol. 27, No. 10, 1989, pp. 1434-1440.

[8] R. T. Haftka and R. K. Kapania, "Sensitivity of Control-Augmented Structure Obtained by a System Decomposition Method," *AIAA J.*, Vol. 29, No. 2, 1991, pp. 264-270.

[9] M. M. Bernitsas and B. Kang, "Admissible Large Perturbations in Structural Redesign," *AIAA J.*, Vol. 29, No. 2, 1991, pp. 404-413.

[10] L. Meirovitch, *Elements of Vibration Analysis*, McGraw-Hill Book Company, 1986.

SECOND INTERNATIONAL CONGRESS ON
RECENT DEVELOPMENTS IN AIR- AND
STRUCTURE-BORNE SOUND AND VIBRATION
MARCH 4-6, 1992 AUBURN UNIVERSITY, USA

Application of Localized Modes in Vibration Control

Daryoush Allaei[1]
Senior Scientist
QRDC, Inc.
108 Glen Eagle Rd.
Oxford, MS 38655

ABSTRACT

There are numerous engineering application problems that deal with vibration analysis and control of elastic linkages, frames, space structures, rotating shaft and turbine blades. In particular, vibration control of such systems becomes even more important when they are subjected to a severe vibratory environment. In this project, the feasibility of developing a more efficient and a more precise vibration control methodology based on phenomenon, such as loci veering and mode localization, is investigated. In particular, these vibration phenomenon are enforced on structures so that the undesired vibrations are confined to a specified region and therefore easier to detect and control. For demonstration purposes, localized vibrations of a three bar frame, and a nonuniform ring are presented. It is shown that localization of modes is possible in both cases.

INTRODUCTION

Machines do not function properly [1], and structures do not respond in the predicted manner by the designer and analyst unless their part have the correct size and shape relative to one another. However, it is not possible to make a part of any exact size or shape. Due to unavoidable manufacturing processes, even if a number of parts are made with the same process, their dimensions will vary. Such variations are known as tolerances. The amount of variations due to manufacturing can be reduced, but the cost will accordingly increase. Therefore, the analyst and the designer must carefully plan the amount of variation that is acceptable in the system, to gain the best possible balance between cost and function.

Tolerances can not be reduced to zero, and therefore must not be avoided in the design, analysis, and control of vibratory structures. A small increase in the complexity of parts that fit together can result in tolerance accumulations. It will make the designer's life more pleasant if the parts do not fit or the material do not have the required characteristics, and they are returned for redimensioning or rebuilding before they are assembled. Costly failure and time-downs will result if the parts fit, but they have the correct dimensions to cause drastic changes in the dynamic response (i.e., loci veering and crossing, and mode localization and transition) of the entire assembly.

Irregularity in periodic and symmetric structures have also been reported [2-14,24-27] to be the cause of frequency curves crossing and veering, and mode localization and transition. Examples of such cases are asymmetric rings due to the localized mass and stiffness nonuniformities [5-7], nonuniform tires [4], differences in the individual blades of turbine and compressor rotors [10,11], irregularities in nearly periodic structures [12-14] which have been used in space applications, and continuous plates with unevenly spaced supports [19]. These and many other structures experience drastic changes in their dynamic response if the irregularities are within a specified range. Such changes in their dynamic characteristics will cause either rapid failure, improper functions, and/or increased vibrations and noise.

---

[1] Also program manager of the Sound and Vibration Engineering Technology, HTC, Hutchinson, MN 55350

Finally, fasteners, adhesives, welded joints, and bolts and nuts could be another source of causing the localization of the modes of vibration. To the best of the author's knowledge, no report, that addresses the effect of joints and adhesives on the frequency curves crossing and veering, and mode localization and transition, has been appeared in the open literature. There is certainly a need for studying the relation between the interfaces of the parts, variations in the type of joints, and other relevant parameters, and the above-mentioned vibration phenomenons.

All the possible factors: tolerances, structural irregularities, material nonuniformities, fasteners, adhesives, welded joints, and bolts and nuts need to be studied. Their role and contributions to the above mentioned dynamic characteristics is being identified and classified according to the type and the magnitude of influence they may have on such vibration phenomenon. Also, a methodology is being developed to integrate the contributing factors in the design procedures and manufacturing processes.

Historical Background

It was back in 1958 when P.W. Anderson [22] identified a phenomena called localization of energy (often referred to as Anderson localization) with applications in solid state physics. At that time, no one related his findings to mechanical systems, even though there is a possibility that people had been observing the phenomena and not reporting it. A set of papers by Lisa, Abraham, Pierre, Hodges, and Allaei [2-23] have shown the occurrence of the phenomenon in mechanical systems.

In 1974, Leisa reviewed some of the relevant papers and he argued that curve veering occurs when an approximation method is used. He stated that the curve veering may imply coupling when there is none. In 1981, it was discussed in reference [27] by Kuttler and Sigillito that the curve veering could be an actual phenomenon of the mathematical model, and it is not necessarily caused because of the use of an approximation method in the analysis.

In 1984, a paper by Azimi et al [19] demonstrated that mode localization occurs in the case of continuous rectangular plates with evenly spaced rigid supports. However, not only he did not explain the observed characteristics, but also he did not show the frequency curves. So, it is not clear whether the frequency curves cross or veer away when the modes are localized. His analysis was based on the receptance method.

In 1986, Pierre et al [10,11] published a paper on the mode localization of multi-span beams. His analysis was based on a modified perturbation method. He showed that the modes of a two-span beam become localized in a certain range of parameters of interest. In 1987, Ibrahim [13] published a review on a number of topics pertaining to structural dynamics with parameter uncertainties. In particular, his paper includes the results of experimental study of the mode localization and its effect on flutter and force response characteristics of structures.

Two papers by Allaei et al [4,6] have shown that these phenomenons also occur in ring and tire type structures. The parameters that he considered were number, magnitude, and relative location of nonuniformities around rings or tires. In his second paper, for the first time, he showed that these vibration characteristics occur in real structures such as tires. In the case of tires, both small mass and stiffness nonuniformities were considered. An in-depth investigation of the mode localization and transition, and frequency curves crossing and veering phenomenon in structures is being conducted at QDRC, Inc. It is expected that a systematic methodology be established to incorporate such characteristics in the design process and analysis of structures in order to better predict and reduce their undesired vibrations and noise.

CASE STUDY

Free Vibration of Frame Structures

Recently, Labadi and Allaei [28] have shown that these phenomenon may occur in non-periodic structures such as frames and linkages. Their results indicate that the modes of vibration of the frames are localized in a certain range of controlling parameters.

Figure 1 shows one example of the type of structures that they studied. The frame is composed of two bars pinned to knife edge supports. Both bars are allowed to vibrate in their axial and transverse (i.e., along and perpendicular to the long axis of the beams) directions. All the three joints are constrained by linear elastic springs. The parameters of intersest in this study are the angle between beam one and the fixed x-axis (θ), the stiffnes of the connected springs (k), the length and thickness of the bars (L,h), and the material properties of the beams. In this paper, the case of varrying the angle θ is presented for discussion purposes.

Figure 2 shows the frequency curves of the lowest four natural frequencies vs. the angle θ which varries from 0^+ to 90^-. It is observed that the frequency curves 1 and 2, and 3 and 4 cross each other when $\theta=6^+$ and $\theta=12.5^+$ degrees, respectivey. Figure 3 shows a zoomed version of figure 2 in the vicinity of the intersection of ω_3 and ω_4 curves. In this figure, it is clearly shown that the two curves cross.

How the mode shapes behave before, at, and after the crossing point is also of interest. Figure 4 shows the third and fourth mode shapes before, almost where, and after their frequency curves intersect. It is observed that not only the modes are localized in the vicinity of the crossing point, but also they go through a transiosion after the intersection. In other words, the third mode appears at a higher frequency than the forth one, and vice versa. Theso localizations and transisions are very impotant in experimental

work and forced vibration of the strucutres. If the experimentalist is aware of the occurance of such phenomenon, the sensors can be effectively places, and the resulting measured data are much easier to interpret. Furthermore, the forced response of the strucutre is drastically changed in this range of parameters.

Free Vibrations of Asymetric Rings

In a series of papers by Allaei, at al, [4-8] it is shown that these phenomenons occur in nonuniform ring type structures (i.e. tires). The controling parameters are number, magnitude, and relative location of non uniformities around tires. Both ring-on-elastic-foundation, and a finite element model of tires are utilized. In the case of the ring model, the closed form solutions are used to generate the natural frequencies and mode shapes of the uniform ring. In the second case, an axisymetric finite element model of the tire is used to produce the free vibration characteristics of the uniform tire. Next, the receptance method is utilized to add the nonuniformity element around the tire, and the natural frequencies and mode shapes of the nonuniform tire are detemined. Some of the results associated with the ring model are presented here.

Figures 5a-c show the frequency curves of the first three modes of a ring on an elastic foundation with two localized stiffness irregularities around it. The first characteristic that should be noted is that the irregularities have doubled the number of modes of the ring. The later has been only reported in rotating rings. An increase in the separation angle α, has stiffening effect on one set of modes (i.e. frequencies increase) while it has softening effect on the other modes (i.e. the frequencies decrease). It should also be observed that at certain values of the separation angle, there are pair of modes with the same frequencies (i.e., crossing points, for example: n=2, α=45°, K/M=100) but different mode shapes . Furthermore, the number of crossing point is eqaul to the value of n as expected, and the crossing pints are moved to higher range of the separation angle, α, as the magnitude of the nonuniformities are increased. Finally, mode transision occurs for ceratain range of the parameters (i.e., the frequency curves cross their upper limit and enter the range of the next mode) .

Figures 6a-c represent the corresponding mode shapes. For some values of the nonuniformities and seperation angle, the modes are localized {(n=1, α=20,45,70°, K/M= 10^5), (n=2, α=70°, K/M= 10^5)}. As it is shown in figure 6 when (n=3, α=60 and 120°, K/M= 10^5), the second pair of the third mode has crossed its upper limit and it is no longer classified as the third mode. Therfore, it is not shown in figure 6. In the case of (n=3, α=160°, K/M= 10^5), the mode shapes are localized.

Loci veering has not been observed in any of the cases except when the nonuniformity elements are placed at eqaul separation angles. In this case, frequency curves either veer away after coming close together or cross as shown in figures 7-8, respectively. In the case of two eqaully placed stiffness nonuniformities, only veering is observed in the frequecy curves (see figure 7), and the mode shapes go through a transision of resembling higher modes after the veering range (see figure 9). However, modes are never localized. On the contrary, in the case of three equally spaced stiffness elements, both loci veering and crossing occurs (see figure 8). As it is observed in figure 10, the mode shapes also undergo both localization and transision. Finally, the degenrated mode shapes, for the case of three equally space springs, are shown in figure 11. All these mode shapes must be included in the forced vibration in order to have a correcte solution.

The occurance of these phenomenon in rings and tires is important since in practice no ring or tire is precisely uniform. It may happen that the nonuniformity parameters cause such effects which will substantially invalidate the predicted response of a theoretical model in which the nonuniformities are neglected. Also, the measured damping factors may be seriously in error [14] since mode localization has similar effect as damping does on the forced response of strcutures. One should be aware that the energy injected into the tire from an external source (such as ground contact forces) can not propagate far away from the source when the modes are localized. Therefore, the energy is built up around the source until the total rate of dissipation in that region matches the rate of energy input [14]. Practical implications of energy build-up in nonuniform tires near the input source due to localization need more in depth investigation which is under way at QRDC, Inc..

Discussion

One implication of occurrence of such phenomenon in structures and vibrating parts is that the assumptions of simple mode shapes made in approximate methods would not be valid in the vicinity of loci veering and crossing, or mode localization and transition. Therefore, numerical models will be in error if the same modes are used for entire range of parameters of interest. Another important point is that during the occurrence of loci veering, and nodal patterns are known to undergo rapid changes. Such rapid changes in the mode shapes are likely to significantly change the flutter characteristics.

The mode localization has its own implications in propagation of vibrational energy. As it is pointed out by reference [13], in the case of localization of the mode shapes, the vibration energy is confined to a local region and does not propagate to large distances. The conventional method of controlling the propagation of vibration is to introduce some sort of damping to dissipate the energy. Under certain conditions, mode localization has shown to have similar effects by confining the energy instead of dissipating it. In his paper, Hodges [14] uses the coupled pendular arranged on a chain, and a vibrating string constrained with masses and springs to demonstrate the phenomenon.

SUMMARY, CONCLUSIONS, AND FUTURE WORK

It was the aim of this project to study these vibration phenomenon in order to draw a link between all four characteristics, and classify them on the basis of their effect on the vibration response of structures. The main focus of this work has been to investigate the feasibility of applying these vibration phenomenons to better undrestand, and therefore control the dynamics of structures.

After an overview of the literature was presented, occurance of the phenomenon in frame and ring structures was discussed. It was shown that loci veering and crossing, and mode localization and transision do occur in both type of structures. Therefore, if the parameters of the system are properly tuned, one may be able to force the vibrational energy to be confined to a specified region, thus easier to monitor and control.

A better understanding of the above mentioned vibration phenomenons is the key to more effectively applying them to reduce the undesired vibrations in components and structures. The link between all mode localization cases , as well as the significant parameters should be established. Finally, an investigation of the forced vibration of localized structures need to be conducted.

ACKNOWLEDGMENT

The support of this work by funds from QRDC, Inc. is grealtfully acknowledged.

REFERENCES

[1] Edwards, Jr., K.S., and McKee, R.B., "Fundamentals of Mechanical Component Design," *McGraw-Hill Book Company*, 1991.

[2] Shih, T.S., and Allaei, D., "On The Free Vibration Characteristics of Annular Plates With Ring-Type Elastic Attachments," *Journal of Sound and Vibration*, Vol. 140 (2), 1990, pp. 239-257.

[3] Allaei, D., and Shih, T.S., "Vibration Analysis of Annular Plates Carrying Cocenter Circular Dynamic Elements," *Applied Mechanics and Engineering Science Conference*, full presentation and published abstract, June 20-22, 1988.

[4] Allaei, D., Soedel, W., and Yang, T.Y., "Vibration Analysis of Non-axisymmetric Tires," *Journal of Sound and Vibration*, Vol. 122, No. 1, 1988, pp. 11-29.

[5] Allaei, D., Soedel, W., and Yang, T.Y., "The Problem of Non-uniformities of Tires," presented at the *7th Annual Meeting and Conference on Tire Science and Technology*, March 1988.

[6] Allaei, D., Soedel, W., and Yang, T.Y., "Eigenvalues of Rings With Radial Spring Attachments," *Journal of Sound and Vibration*, Vol. 121, No. 3, 1987, pp. 547-561.

[7] Allaei, D., Soedel, W., and Yang, H.T.Y., "Free Vibration of Rolling Structures Carrying Local Non-uniformities by the Receptance Method," *Twentieth Midwestern Mechanics Conference*, presentation and proceeding publication, September 1987, pp. 1347-1353.

[8] Allaei, D., "Vibration Analysis of Circular Plates Using Axisymmetric Finite Element," *Twentieth Midwestern Mechanics Conference*, presentation and proceeding publication, September 1987, pp. 330-336.

[9] Allaei, D., Soedel, W., and Yang, H.T.Y., "Natural Frequencies and Modes of Rings that Deviate From Perfect Axisymmetry," *Journal of Sound and Vibration*, Vol. 111, No. 1, 1986, pp. 9-27.

[10] Pierre, C., and Dowell, E.H., "Localization of Vibrations by Structural Irregularity,"*Journal of Sound and Vibration*,Vol.114(3),87,pp. 549-564.

[11] Pierre, C., "Mode Localization and Eigenvalue Loci Veering Phenomena in Disordered Structures," *Journal of Sound and Vibration*, Vol. 126 (3), 1988, pp. 485-502.

[12] Bendiksen, O.O., "Mode Localization Phenomena in Large Space Structures," *AIAA Journal*, Vol. 25(9), September 1987.

[13] Ibrahim, R.A., "Structural Dynamics with Parameter Uncertainties," *Applied Mech. Rev.*, Vol. 40(3), March 1987.

[14] Hodges, C.H., "Confinement of Vibration by Structural Irregularity," *Journal of Sound and Vibration*, Vol. 82 (3), 1982, pp. 411-424.

[15] Bishop, R.E.D., and Johnson, D.C., "The Mechanics of Vibration," Cambridge: Cambridge University Press, 1960.

[16] Soedel, W., "Vibrations of Shells and Plates," New York: Marcel-Dekker, Inc., 1981.

[17] Wilken, I.D., and Soedel, W., "The Receptance Method Applied to Ring-Stiffened Cylindrical Shells, Analysis of Modal Characteristics," *Journal of Sound and Vibration*, Vol. 44, No. 4, 1976, pp. 563-576.

[18] Soedel, W., and Prasad, M.G., "Calculations of Natural Frequencies and Modes of Tires in Road Contact by Utilizing Eigenvalues of the Axisymmetric Non-Contacting Tire," *Journal of Sound and Vibration*, Vol. 70, No. 4, 1980, pp. 573-584.

[19] Azimi, S., Hamilton, J.F., and Soedel, W., "The Receptance Method Applied to the Free Vibration of Continuous Rectangular Plates," *Journal of Sound and Vibration*, Vol. 93, No. 1, 1984, pp. 9-29.

[20] Azimi, S., "Natural Frequencies and Modes of Cylindrical Polygonal Ducts Using Receptance Method," *Journal of Sound and Vibration*, Vol. 109, No. 1, 1986, pp. 79-88.

[21] Allaei, D., and Krousgrill, C.M., "Finite Element Analysis of Flow Induced Oscillations of Tubes Conveying Fluids," presentation at *21st Annual Meeting of the Society of Engineering Science* and published in the Official proceedings of the Meeting, October 1984.
[22] Anderson, P.W., "Absence of Diffusion in Certain Random Lattices," Physical Review 109, 1958, pp. 1492-1505.
[23] Allaei, D., "Vibration Analysis of Circular Plates Using Axisymmetric Finite Element, *Twentieth Midwestern Mechanics Conference* presentation and proceeding publication, September 1987, pp. 330-336.
[24] Leissa, Arthur W., "On Curve Veering Aberration," *Journal of Applied Mathematics and Physics*, Vol. 25, 1974.
[25] Nair, P.S., and Durvasula, S., "On Quasi-Degeneracies in Plate Vibration Problems," *Int. J. Mech. Sci.*, Vol., 25, 1973, pp. 975-986.
[26] Claasen, R.W., and Thorne, C.J., "Vibration of a Rectangular Cantilever Plate," J. Aerospace Sci., Vol. 29, 1962, pp. 1300-1305.
[27] Kuttler, J.R., and Sigillito, V.G., "On Curve Veering," Journal of Sound and Vibration, Vol. 75 (4), 1981, pp. 585-588.
[28] Labadi, M., and Allaei, D., "Loci Veering and Mode Localization in Elastic Linkages and Frames," accepted for presentation at SECTAM XVI, April 12-14, 1992.

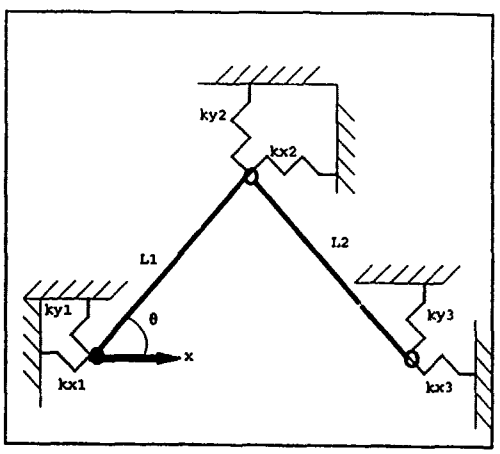

Figure 1 A two-bar frame with elastically supported joints

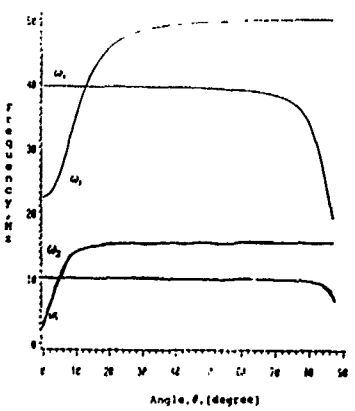

Figure 2 Lowest four frequency curves of a two bar frame

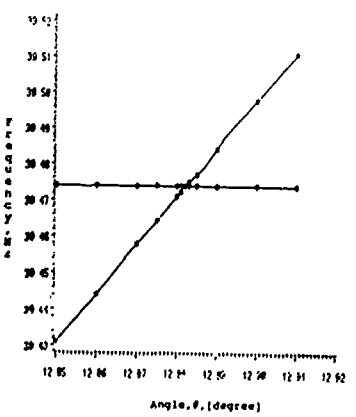

Figure 3 The enlarged frequency curve of the third an[3] fourth mode in the vicinity of their crossing point

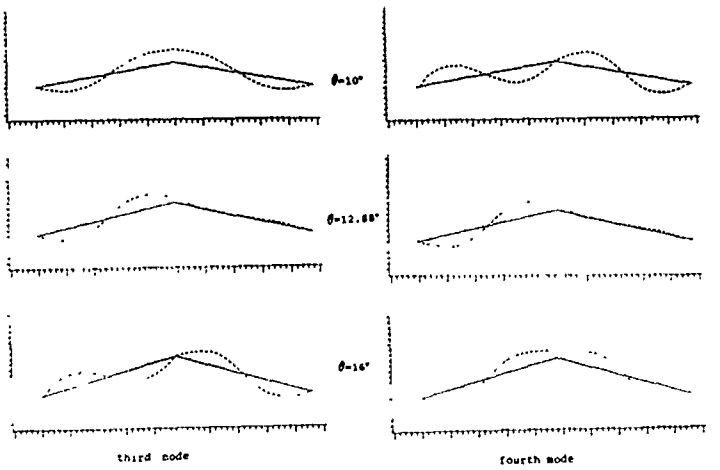

Figure 4 The third and fourth mode shapes of the frame in the vicinity of their crossing point

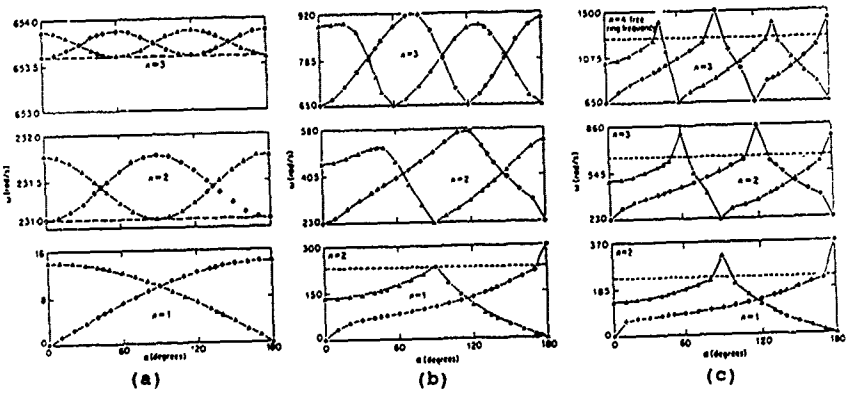

Figure 5 The lowest three frequency curves of a ring on an elastic foundation with two localized stiffness nonuniformities located at an separation angle, α, (a) k/M=100, (b) $k/M=10^5$, (c) $k/M=10^6$ rad/s^2

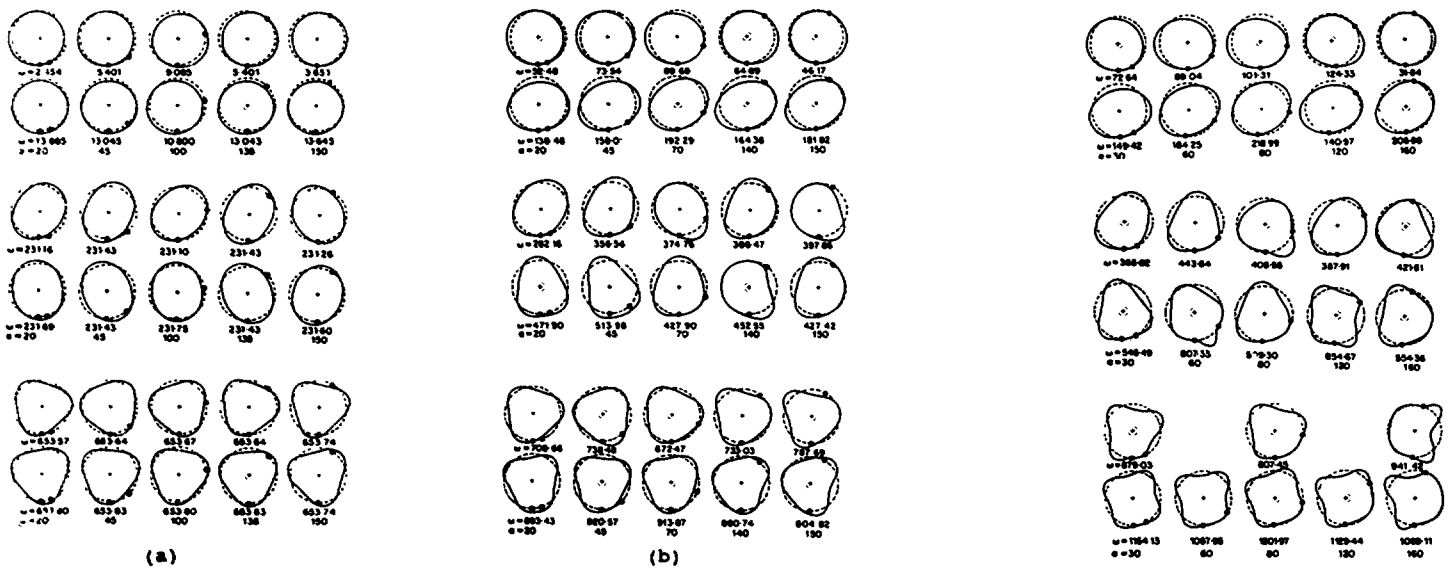

Figure 6 The lowest three mode shapes of a ring on an elastic foundation with two localized stiffness nonuniformities located at an separation angle, α, (a) k/M=100, (b) k/M=10^5, (c) k/M=10^6 rad/s^2

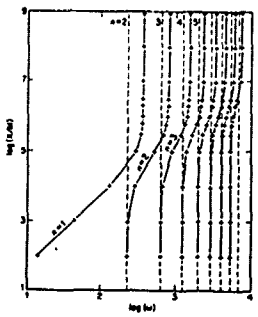

Figure 7 The natural frequency curves of a ring on an elastic foundation with two equally spaced stiffness nonuniformities, α=180°, --- uniform ring, _ nonuniform ring

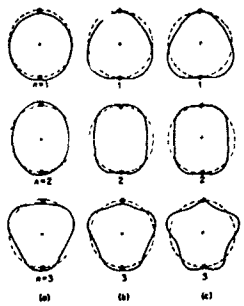

Figure 9 The mode shapes of a ring on an elastic foundation with two equally spaced stiffness nonuniformities, (a) k/M=1E04, (b) k/M=3E05, (c) k/M=1E06 rad/s²

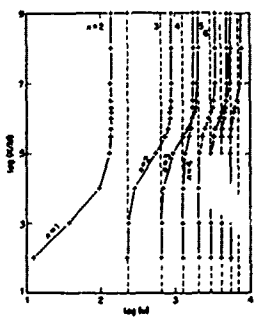

Figure 8 The natural frequency curves of a ring on an elastic foundation with three equally spaced stiffness nonuniformities, α=120°, --- uniform ring, _ nonuniform ring

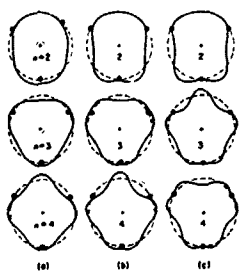

Figure 10 The mode shapes of a ring on an elastic foundation with three equally spaced stiffness

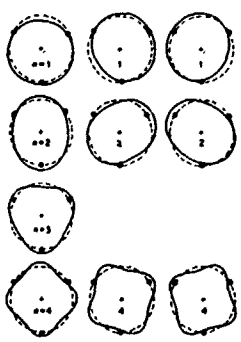

Figure 11 The degenerated mode shapes of a ring on an elastic foundation with three equally spaced stiffness nonuniformities

SECOND INTERNATIONAL CONGRESS ON
RECENT DEVELOPMENTS IN AIR- AND
STRUCTURE-BORNE SOUND AND VIBRATION
MARCH 4-6, 1992 AUBURN UNIVERSITY, USA

MODAL ANALYSIS AND SYNTHESIS OF CHAMBER MUFFLERS

Rudolf N. Starobinsky
Labor and Environment Protection Department
Toqliatti Polytechnical Institute
Belorusskaya st.,14 Toqliatti,445667
USSR

ABSTRACT

Expansion chambers are the main elements of noise mufflers. The main principle of their work is the reflection of the incident wave sound energy back to the inlet pipe. In low frequency range their characteristics depend on chamber volume and chamber efficiency increases together with the noise frequency. In the middle and high frequencies regions chamber efficiency depends very much on resonance excitation of sound in its cavity and it decreases when excitation is near to chamber natural frequencies.

Efficient ways of resonance transmissions decreasing and chamber protection characteristics improving are synthesis of chamber oscillation modes and their connections with the pipes. In these cases sound transmission decreasing is reached by means of weakening of connections between pipes and the most dangerous modes; selective increasing of sound energy dissipation of some modes, interdependent compensation of transmitting by modes having divisible natural frequencies. Independent compensation of sound oscillation running into outlet pipe from different points of the chamber is used too.

Some examples of using of these ways for intake and exhaust mufflers creation are given.

INTRODUCTION

Chamber mufflers are usually used for noise transmission decreasing at frequencies for which half of sound wavelength is more than connection pipes sectional dimension. Noise transmission decreasing, particularly for low frequencies is reached mainly owing to a buffer (accumulation) effect. This effect is proportional to the chamber volume and noise frequency and it doesn't depend on a chamber shape. At high frequencies for which half of sound wavelength is compared with chamber size, chamber characteristics depend on the wave phenomena in their cavity. They depend on the chamber volume and shape as well.

At frequencies which are near to natural frequencies of chamber cavity, resonance phenomena increasing the sound transmission and decreasing their protection characteristics are typical. Modal analysis of these phenomena, their mathematical description, possible ways of chamber efficiency increasing, methods of chamber synthesis are considered in this paper.

MODAL ANALYSIS OF SOUND FIELD IN CHAMBER CAVITY

Principal scheme of chamber excitation by incident wave and sound transmission through chamber used for transmission losses definition is given on fig.1. On fig.2 equivalent electric circuit describing the chamber by an incident wave a_1 is given. For calculation transmitted wave b_2 amplitude one supposes tension source intensity $u_2 = 2a_1$. In this case b = U. In this circuit the resistances Z_{a1} and Z_{a2} describe characteristic impedances of inlet and outlet pipes. Chamber characteristics are described by means of impedance matrix having elements $Z_{jk} = u_j/i_k$ Their values are described by means of modal expansions

$$Z_{jk} = \frac{1}{Y_c}\left(1+\sum_{N=1}^{\infty}\frac{\varphi_j\varphi_{nk}}{\bar{\varphi}_N^2}\frac{f^2}{f^2-f_N^2}\right) = \frac{1}{Y_c}\left(1+\sum_{N=1}^{\infty}Z_{jk}^N\right) \qquad (1)$$

where f are natural frequencies of chamber cavity, limited with inner surface of chamber walls, outer surface of pipe inner parts and imaginary surface of hard covers closing open pipe ends (on fig. 1a this volume is limited with dotted line); φ_{nk} are average meanings of mode φ_N on imaginary covers 1 and 2; $\bar{\varphi}_N^2$ is an average meaning of mode φ_N in volume; $Y_c = j\omega V/\rho c^2$ is cavity conductivity; V is chamber volume; ρ and c are gas density and sound velocity.

Chamber transmission characteristics depend mainly on transfer impedance Z_{21}. It defines sound pressure near outlet 2 if the chamber is excited by volume velocity at inlet 1. With the help of modal expansion (1) Z is described as sum of transfer impedances of unconnected modes. One can regulate full transfer impedance value by separate action to each of modal impedances Z_N^{21}.

When the chamber is excited by running wave (see fig.2) oscillations of separate modes in the cavity turn out to be connected through resistances Z_{a1} and Z_{a2}, however, out of the resonance oscillation zone this connection doesn't influence much on sound transmission. As chamber synthesis is done particularly for this zone, sound transmission analysis with the help of transfer resistance values is very productive for solving problems of designing of chamber of high effectiveness.

THE WAYS OF IMPROVING OF CHAMBER MUFFLER EFFECTIVENESS.

One can substantially improve chamber muffler effectiveness owing to the suppression (even partial) of resonance sound transmissions at lower natural frequencies. In such a way chamber TL - characteristics in the frequency zone where resonance transfer are suppressed approach to characteristics of ideal buffer cavity, having transfer impedance $Z_{21} = Y_c^{-1}$. For realization of such Kind of chambers there are used the methods including the following:

- increasing of the first natural frequency owing to approaching of the chamber shape to spherical one, cubic one or similar to them;
- selective increasing of oscillation decrements of some modes owing to the active resistance situation in the pressure nodes (in the velocity loops) and active pliabilities in pressure loops of the suppressed modes;
- chamber excitation and sound transfer decreasing owing to the pipe open ends situated in the pressure modes of lower modes (in this case meaning in formula 1 decreases);
- interdependent compensation of the transferring oscillations with the modes with each other.

To do it chamber shape and dimension are chosen in such a way that in the spectrum of its natural frequencies identical (divisible) frequencies corresponding to the different modes should be present. The compensation is reached with the choice of inner pipe open ends in chamber placing, providing pressure summing at outlet pipe open end from the modes with divisible natural frequencies with the opposite signs.

- selective interferation oscillation from some points of cavity at natural frequencies owing to pressure phase difference in that points or different transformation of the phase in branched pipes;
- selective suppression of transmission at natural frequencies owing to using of narrowband resonators.

PRINCIPAL SCHEMES OF CHAMBER WITH HIGH EFFECTIVENESS.

Some possible variants of constructive schemes of the chambers made according to above written principles are given on fig. 3, 5, 6, 7. For cubic chamber given on fig.3 transmission decreasing is reached owing to inner pipe open ends placing in nodes of lower modes with n, m, l = 1,2,3. TL - characteristic of this chamber (full line on fig. 4) are compared with TL - characteristic of standard cylindrical chamber without inner pipes and with the division length to diameter (L:D=2).

Chamber scheme with suppression transmission by mode with n =4 by means of transversal partition is given on fig.5. The partition is placed in node surface of the mode with n=4. In the chamber given on fig.6 the transfers by the modes and suppress each other. The interferention principle is illustrated by the chamber given on fig. 7. In this chamber sound transmission by radial mode φ_{100} is suppressed with the help of the interferention sound signals from this mode came from points A and B to point C.

CONCLUSION

Given above examples illustrate wide opportunities of supposing methods of chamber synthesis. These methods are successfully used for many constructions of automobiles intake and exhaust mufflers.

REFERENCE

Starobinsky R.N. Theory and synthesis of mufflers for intake and exhaust systems of internal combustion engine, Doct. diss. Togliatti,1982, 333p (Russian).

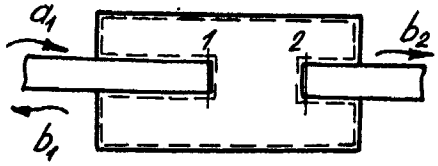

Fig.1. Scheme of chamber exitation by incindent wave

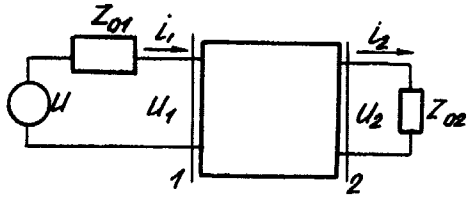

Fig2. Equivalent electric circuit

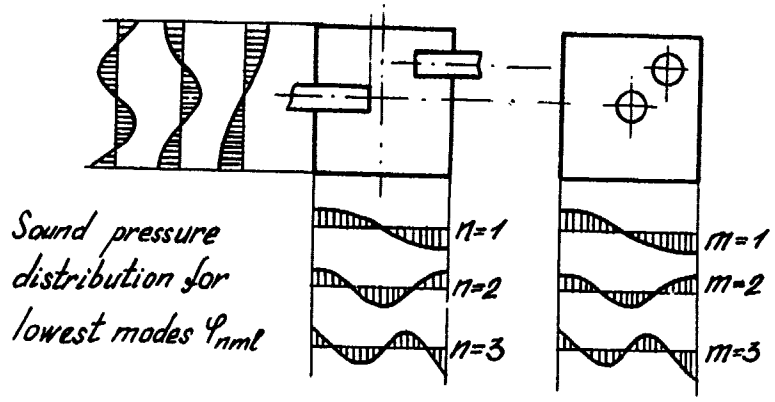

Fig.3. Cubic chamber with inner pipes

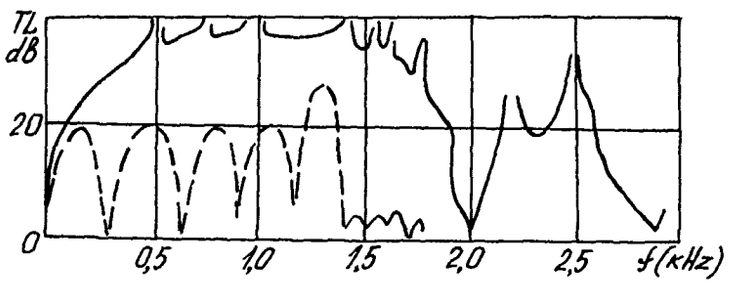

Fig. 4. Compared characteristics of cubic camber (fig. 3) with inner pipes (—) and standart cilindrical camber without inner pipes (---)

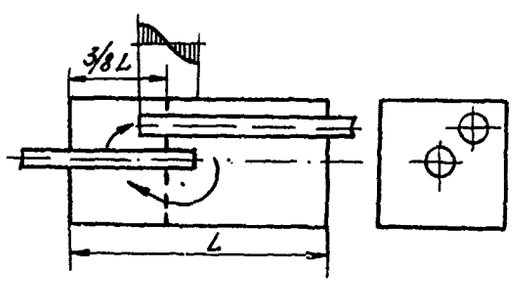

Fig 5. Chamber with partition

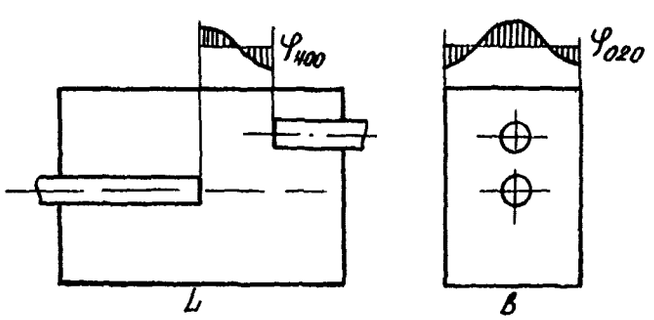

Fig. 6. Chamber with compensation of transmission (L = 2B)

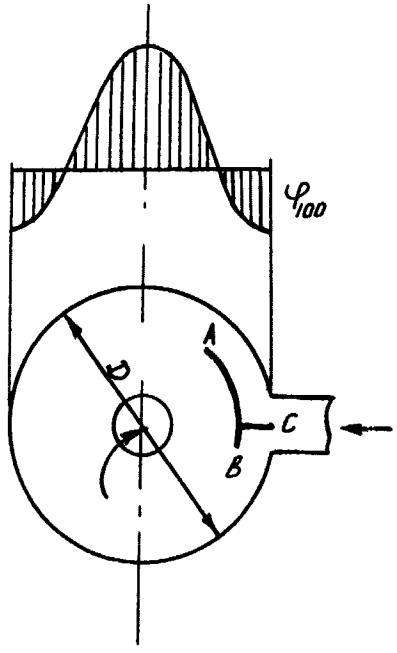

Fig 7. Aircleaner chamber with interferation

LATE PAPERS

SECOND INTERNATIONAL CONGRESS ON
RECENT DEVELOPMENTS IN AIR- AND
STRUCTURE-BORNE SOUND AND VIBRATION
MARCH 4-6, 1992 AUBURN UNIVERSITY, USA

Evaluation of Adaptive Filtering Techniques for Active Noise Control

J. C. Stevens†
K. K. Ahuja††
Georgia Institute of Technology
GTRI/Aerospace Laboratory
Atlanta, GA 30332-0800
U. S. A.

ABSTRACT

An overview of several digital adaptive filtering techniques is given. The methods range from a simple least-mean-squares (LMS) approach to fast transversal and adaptive infinite impulse filtering algorithms. An evaluation is performed to determine which of the several adaptive filter algorithms are particularly suited to active noise control applications. Each method is then tested in a computer simulation of an active noise control problem. Considerations for the implementation of an active noise control system are discussed.

NOMENCLATURE

n	Discrete time or sample index	N	Dimension of vector
$e(n)$	Instantaneous error signal	$d(n)$	Instantaneous system output
$\hat{d}(n)$	Instantaneous system estimate	$\varepsilon(n)$	Instantaneous mean square error
$w_i(n)$	ith filter weight	$x(n)$	Instantaneous system input value
$\mathbf{w}_N$	Filter weight vector of length N	$\mathbf{x}_N$	Input sample vector of length N
$\mathbf{p}_N$	Cross-correlation vector of output, $d(n)$, and input vector, $\mathbf{x}_N$	$\mathbf{R}_{NN}$	Autocorrelation matrix of input
μ	Step size for adaptive algorithms	α	Alternate step size for adaptive algorithms, $\alpha = 2\mu$
λ	Forgetting factor for RLS filter	$e(i\|n)$	Conditional error used in RLS algorithm
$\mathbf{X}_{0,N}\cdot(n)$	Data matrix for FTF algorithm	$\pi(n)$	Unit time vector used in FTF algorithm
$a_m(n)$	Autoregressive filter weights in IIR filter	$b_m(n)$	Moving average filter weights in IIR filter

INTRODUCTION

The first part of this paper will provide an overview of the principles and techniques of digital adaptive filtering. The next several sections will cover various adaptive filtering algorithms. The equations necessary for each algorithm will be provided. While this material is not new, it has been included in the interest of completeness. A complete derivation of all the algorithms used will not be given. The notation style used and most of the equation derivations are from reference 1. Additional derivations and general digital filtering information has been gathered from references 2, and 3.

After the algorithms have been presented, they will be compared on a basis of algorithmic complexity, execution time and stability characteristics. A brief description of the methods of active noise control will be given. Then, the necessary considerations for an adaptive filter implementation of active noise control will be discussed. The algorithmic analysis and the specific requirements of active noise control will then be used to determine which algorithms are best suited to the active control of sound and vibration. Finally, the results of simulations and actual tests will be presented.

†*Research Engineer at GTRI and Graduate Student in the Georgia Tech School of Electrical Engineering*
††*Head: Acoustics Branch, GTRI/AERO and Professor: School of Aerospace Engineering*

OVERVIEW OF ADAPTIVE FILTERING

Adaptive filtering can perhaps best be explained as a feedback control system. An input, x, is fed through a digital filter and an output, $\hat{d}$ is produced (See Figure 1). The n in the figures and equations is the index to the particular time sample in the signal.

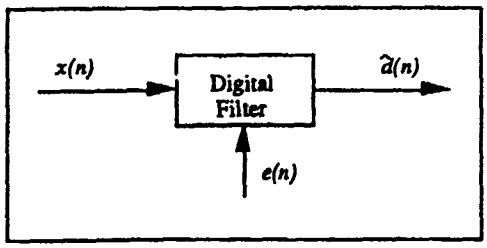

Figure 1. Adaptive digital filter.

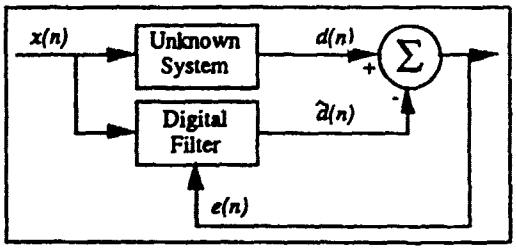

Figure 2. System identification application.

The parameters of the filter are continually adjusted as the filtering algorithm uses the error input, e, to determine filter performance. Adaptive filtering algorithms use various methods in an attempt to reduce the feedback error signal to zero. The particular application will dictate how the error signal is determined.

A typical application for adaptive filtering and the one most commonly used in active noise control is system identification. In this application, the adaptive filter is attempting to estimate the output, d, of an unknown system. A block diagram of a system identification application is shown in Figure 2. A review of the work done in active noise control with this and other system models can be found in reference 4. More extensive information about recent work in active noise control can be found in reference 5.

Clearly, the error in this application will be generated by determining the difference between the system output and the filter output. The simplest difference measure is a simple subtraction. This error is known as the prediction error.

$$e(n) = d(n) - \hat{d}(n) \tag{1}$$

It is often convenient to use an error measure that equally weighs positive and negative errors. This is easily accomplished by squaring the prediction error.

$$e^2(n) = \left[d(n) - \hat{d}(n)\right]^2 \tag{2}$$

In most real systems, there is some noise. This noise is usually modeled as a stochastic process. Since the system output has stochastic noise, the error signal is also modeled as a stochastic process. The stochastic noise is handled by taking the ensemble average or mean of the squared error. This is called the mean squared error measure (MSE) and is defined as

$$\varepsilon(n) = E\left\{e^2(n)\right\} \tag{3}$$

where $E\{\cdot\}$ is the statistical expectation.

The task of digital filtering is to produce an estimate of the system output that will be used to determine the error function. The filter produces this output, $\hat{d}$, by convolving the input stream, x, with a vector of filter weights, $\mathbf{w}_N$. This convolution, which can also be calculated as the vector dot product of the weight vector and a vector of input samples (in the case of a finite impulse response filter), is shown in equation (4). The equation for the more complex infinite impulse response filter will be given later. The filter is completely specified by its weight vector, $\mathbf{w}_N$. More accurate filters can be built using longer weight vectors. (For a detailed description of digital filtering see references 6 and 7.) The "T" in equation (4) and subsequent equations is the matrix and vector transpose operator.

$$\hat{d}(n) = \sum_{i=0}^{N-1} w_i(n)x(n-i) = \mathbf{w}_N^T(n)\mathbf{x}_N(n) \tag{4}$$

where

$$\mathbf{w}_N^T(n) = \left[w_0(n), \ldots, w_{N-1}(n)\right],$$
$$\mathbf{x}_N^T(n) = \left[x(n), \ldots, x(n-N+1)\right] \tag{5}$$

The problem of adaptive filtering then, is to determine the appropriate values for the weight vector, $\mathbf{w}_N$. If we substitute equation (4) into equation (2) and in turn substitute equation (2) into equation (3) we get (after some algebra):

$$\varepsilon(\mathbf{w}_N) = E\{d^2(n)\} - 2\mathbf{w}_N^T E\{d(n)\mathbf{x}_N(n)\} + \mathbf{w}_N^T E\{\mathbf{x}_N(n)\mathbf{x}_N^T(n)\}\mathbf{w}_N \tag{6}$$

We define the cross-correlation vector, $\mathbf{p}_N$, as

$$\mathbf{p}_N = E\{d(n)\mathbf{x}_N(n)\}, \tag{7}$$

and the autocorrelation matrix, $\mathbf{R}_{NN}$, as

$$\mathbf{R}_{NN} = E\{\mathbf{x}_N(n)\mathbf{x}_N^T(n)\}. \tag{8}$$

Then, by substituting equations (7) and (8) into equation (6) we get the MSE in the form

$$\varepsilon(\mathbf{w}_N) = \sigma_d^2 - 2\mathbf{w}_N^T\mathbf{p}_N + \mathbf{w}_N^T\mathbf{R}_{NN}\mathbf{w}_N. \tag{9}$$

The MSE surface, $\varepsilon(\mathbf{w}_N)$, will look something like an N dimensional bowl. Hence it will have only one extremum and that extremum will be a minimum point. This point can be located by taking the partial derivatives of $\varepsilon(\mathbf{w}_N)$ with respect to each element, w_i, of $\mathbf{w}_N$ and setting the derivatives equal to zero. These equations can be represented by the matrix equation

$$\mathbf{R}_{NN}\mathbf{w}_N^* = \mathbf{p}_N, \tag{10}$$

where $\mathbf{w}_N^*$ denotes the optimal filter weight vector. The optimal filter weight vector solution is then

$$\mathbf{w}_N^* = \mathbf{R}_{NN}^{-1}\mathbf{p}_N, \tag{11}$$

where $\mathbf{R}_{NN}^{-1}$ is the inverse of the autocorrelation matrix. As N increases, it becomes increasingly time consuming and difficult to calculate $\mathbf{R}_{NN}^{-1}$. Therefore, most adaptive filtering algorithms do not calculate $\mathbf{R}_{NN}^{-1}$ directly.

This is the basic derivation upon which all adaptive filtering algorithms are based. In the following sections, individual algorithms will be presented and analyzed.

FINITE IMPULSE RESPONSE METHODS

A finite impulse response filter (FIR), as the name implies, will have a finite output response to an impulsive input. Mathematically, it means that the output can be computed from the input alone. There are no recursive inputs being fed back from the output. Finite impulse response (FIR) filters have the form

$$\hat{d}(n) = \sum_{i=0}^{N-1} w_i(n)x(n-i) = \mathbf{w}_N^T(n)\mathbf{x}_N(n). \tag{12}$$

Each of the following algorithms computes the optimal value of the filter weights, $\mathbf{w}_N^*$, for an FIR filter. The solutions found will depend on the error function chosen and the convergence method. The simplest of these algorithms is called the steepest descent algorithm.

Steepest Descent Algorithm

The steepest descent algorithm can perhaps best be understood by visualizing the MSE surface defined by equation (9) for a two dimensional weight vector, $\mathbf{w}_2$. This surface will look like a bowl in three dimensions (see Figure 3).

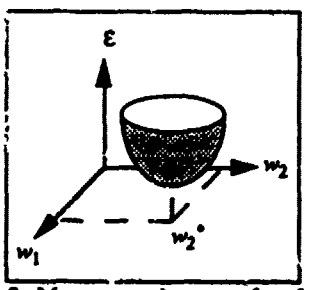

Figure 3. Mean squared error surface for $\mathbf{w}_2$.

Assume we have an initial weight vector, $\mathbf{w}_2(0)$, somewhere on the surface of the bowl, but not at the minimum. On the next iteration, $\mathbf{w}_2(1)$, we can get closer to $\mathbf{w}_2^*$ by taking a step towards $\mathbf{w}_2^*$. By taking enough steps, we should eventually get a good approximation of $\mathbf{w}_2^*$. This is the idea behind the steepest descent algorithm.

It is necessary, then, to determine the direction towards $\mathbf{w}_2^*$. This direction can be found by taking the gradient of the error surface of equation (9) at position $\mathbf{w}_2(n)$. The gradient is defined as

$$\nabla_{\mathbf{w}}[\varepsilon] = \frac{\partial \varepsilon}{\partial \mathbf{w}_N}, \tag{13}$$

where $\nabla[\cdot]$ is the gradient operator.

The size of the step, μ, will depend upon the constraints of the application. With a smaller step size the algorithm will converge to the optimal weight vector more slowly, but probably more accurately. The weight vector update equation then becomes

$$\mathbf{w}_N(n+1) = \mathbf{w}_N(n) - \mu \nabla_{\mathbf{w}}[\varepsilon(n)]. \tag{14}$$

If we substitute the definition of $\varepsilon(\mathbf{w}_N)$ from equation (9) into equation (14) and calculate the gradient, we get

$$\mathbf{w}_N(n+1) = \mathbf{w}_N(n) + 2\mu\left[\mathbf{p}_N - \mathbf{R}_{NN}\mathbf{w}_N(n)\right]. \tag{15}$$

Available data is used to compute estimates of $\mathbf{p}_N$ and $\mathbf{R}_{NN}$ and a reasonable choice is made for the constant μ. In a typical application, a new input sample, $x(n)$, is taken and the input vector is filtered using equation (4). A new weight vector, $\mathbf{w}_N(n+1)$, is computed using equation (15) and the process begins again. If the estimates of $\mathbf{p}_N$ and $\mathbf{R}_{NN}$ are accurate, the filter output, $\hat{d}(n)$, will converge to the desired response.

Least Mean Squares Algorithm

One of the problems of the steepest descent algorithm is that it requires that estimates of $\mathbf{p}_N$ and $\mathbf{R}_{NN}$ be known. Calculation of these statistics might take considerable time. Even if time is not a problem, the data to be filtered must be stationary in order to avoid significant errors.

The least mean squares (LMS) algorithm avoids these problems because it doesn't require the second order statistics (expectations of the product of two random variables), $\mathbf{p}_N$ and $\mathbf{R}_{NN}$. The LMS algorithm uses an estimate for the gradient (equation (13)) in the weight update equation. The gradient can be written as

$$\nabla_{\mathbf{w}}[\varepsilon(n)] = -2E\left\{e(n)\mathbf{x}_N(n)\right\}, \tag{16}$$

and hence, the gradient estimate can be written as

$$\hat{\nabla}_{\mathbf{w}}[\varepsilon(n)] = -2\hat{E}\left\{e(n)\mathbf{x}_N(n)\right\}. \tag{17}$$

A reasonable estimate of the expected value is

$$\hat{E}\left\{e(n)\mathbf{x}_N(n)\right\} = e(n)\mathbf{x}_N(n), \tag{18}$$

so the filter weight update equation becomes

$$\mathbf{w}_N(n+1) = \mathbf{w}_N(n) + \alpha e(n)\mathbf{x}_N(n), \tag{19}$$

where $\alpha = 2\mu$ with no loss of generality. The LMS algorithm has the advantage that it is the simplest of the algorithms in terms of computational complexity and storage requirements. The essential difference between the steepest descent algorithm and the LMS algorithm is that the steepest descent algorithm is deterministic while the LMS algorithm uses a stochastic approximation of the gradient as it converges to the optimal weight vector, $\mathbf{w}_N^*$.

Recursive Least Squares Algorithm

Unlike the LMS algorithm, the recursive least squares (RLS) algorithm produces filters that are exactly optimal for the data acquired rather that statistically optimal. This is accomplished by minimization of the cumulative squared error

$$\varepsilon(n) = \sum_{i=1}^{n} \lambda^{n-i} e^2(i|n), \tag{20}$$

rather than the mean squared error of equation (3). The conditional error, $e(i|n)$, is defined as

$$e(i|n) = d(i) - \mathbf{x}_N^T(i)\mathbf{w}_N(n) \tag{21}$$

The constant, λ, is called the forgetting factor and is typically used to weight recent data samples more heavily. If the data is stationary, λ can be set to 1. Otherwise, a value between 0.95 and 0.9995 is usually a good choice for tracking nonstationary signals.

We now define the sample autocorrelation matrix as

$$\mathbf{R}_{NN}(n) = \sum_{i=1}^{n} \lambda^{n-i}\mathbf{x}_N(i)\mathbf{x}_N^T(i) \tag{22}$$

and the sample cross-correlation vector as

$$\mathbf{p}_N(n) = \sum_{i=1}^{n} \lambda^{n-i} d(i)\mathbf{x}_N(i) \tag{23}$$

$\mathbf{R}_{NN}(n)$ and $\mathbf{p}_N(n)$ approximate the second order statistics and $\lim_{n\to\infty}(1/n)\mathbf{R}_{NN}(n) = \mathbf{R}_{NN}$, where $\mathbf{R}_{NN}$ without the index is the true autocorrelation matrix. Thus, the filter weight vector can be found using a matrix equation similar to the normal equation (11) used previously.

$$\mathbf{w}_N(n) = \mathbf{R}_{NN}^{-1}(n)\mathbf{p}_N(n) \tag{24}$$

A recursive relationship can be used to compute $\mathbf{R}_{NN}^{-1}(n)$ from $\mathbf{R}_{NN}^{-1}(n-1)$ as follows:

$$\mathbf{R}_{NN}^{-1}(n) = \frac{1}{\lambda}\left[\mathbf{R}_{NN}^{-1}(n-1) - \frac{\mathbf{R}_{NN}^{-1}(n-1)\mathbf{x}_N(n)\mathbf{x}_N^T(n)\mathbf{R}_{NN}^{-1}(n-1)}{1+\mu(n)}\right], \tag{25}$$

where $\mu(n)$ is the scalar

$$\mu(n) = \mathbf{x}_N^T(n)\mathbf{R}_{NN}^{-1}(n-1)\mathbf{x}_N(n) \tag{26}$$

Finally, assigning

$$\mathbf{g}_N(n) = \mathbf{R}_{NN}^{-1}(n)\mathbf{x}_N(n) \tag{27}$$

we get the RLS filter weight update equation

$$\mathbf{w}_N(n) = \mathbf{w}_N(n-1) + \mathbf{g}_N(n)e(n|n-1) \tag{28}$$

The RLS algorithm is significantly more complex than the LMS algorithm, but provides for a solution based on all the data rather than just the current data. The RLS algorithm is also known as the Kalman algorithm.

Fast Transversal Filter Algorithm

The fast transversal filter (FTF) algorithm is actually an algorithm which uses a collection of four transversal filters; (1) the least squares prediction filter, (2) the forward prediction error filter, (3) the backward prediction error filter, and (4) the gain transversal filter. The first filter is the (1) least squares filter developed above. However, the least squares prediction must now be done with a transversal filter. In the FTF algorithm a geometric approach is taken. The mean squared error described earlier is a sum of squared error terms. This is also the definition of the vector inner product

$$\varepsilon(n) = \left\langle \mathbf{e}(n|n), \mathbf{e}(n|n) \right\rangle \tag{29}$$

where $\langle\cdot\rangle$ is the vector inner product operator. The least squares problem, then, is simply a minimization of the vector norm of the error vectors. The minimum can be found by taking the derivative with respect to the weight vector and setting it equal to zero

$$\frac{\partial}{\partial w_m(n)}\left\langle \mathbf{e}(n|n), \mathbf{e}(n|n) \right\rangle = 0 \tag{30}$$

Substituting and solving for $\mathbf{w}_N(n)$ yields the following vector equation for the least squares prediction filter weights

$$\mathbf{w}_N(n) = \left\langle \mathbf{X}_{0,N-1}(n), \mathbf{X}_{0,N-1}(n) \right\rangle^{-1} \mathbf{X}_{0,N-1}^T(n)\mathbf{d}(n) \tag{31}$$

where $\mathbf{X}_{0,N-1}(n)$ is the data matrix defined by

$$\mathbf{X}_{0,N-1}(n)=\begin{bmatrix} x(1) & 0 & \cdots & 0 \\ x(2) & x(1) & \cdots & 0 \\ \vdots & \vdots & \ddots & \vdots \\ x(n-1) & x(n-2) & \cdots & x(n-N) \\ x(n) & x(n-1) & \cdots & x(n-N+1) \end{bmatrix}. \tag{32}$$

Due to space limitations, the other three filter algorithms will be explained, but not derived. A complete derivation can be found in reference 1. The second filter used in the FTF algorithm is the (2) forward prediction error filter. The forward prediction error is the difference between the current data value $x(n)$ and an estimate of the current data value $\hat{x}(n)$ based on previous data values.

The third filter is the (3) backward prediction error filter. The backward prediction error is the difference between the delayed data vector, $z^{-N}\mathbf{x}(n)$, and the estimate of the delayed data vector, $\hat{\mathbf{x}}_b(n-N)$. The backward prediction error is necessary in the development of the least squares FTF algorithm.

The final transversal filter required in the FTF algorithm is the (4) gain transversal filter. The gain transversal filter quantifies the change in angle between successive data samples in time. The corresponding error vector is the difference between the unit time vector $\pi(n)$ and the least squares prediction of the unit time vector $\hat{\pi}(n)$.

These filters are interrelated in the formulation of the FTF algorithm. In the algorithm, each of the filters assumes an update form in which the filter weights are adjusted during each iteration to reduce the errors for each filter described above. The principle benefit of the FTF algorithm is that it is comparatively insensitive to the correlation properties of the data. A highly correlated input can significantly increase the convergence rate of gradient-based algorithms such as the LMS algorithm, but the FTF algorithm still converges quickly. In addition, the convergence factor δ has little effect on the convergence speed of the FTF algorithm.

Gain Normalized Fast Transversal Filter Algorithm

An additional O(N) (where O(N) denotes "order of N") operations can be conserved using a variation of the FTF algorithm known as the gain-normalized fast transversal filter (GNFTF). This reduction is accomplished by normalizing the gain vector by dividing it by its angle parameter

$$\mathbf{c}_N(n)=\frac{\mathbf{g}_N(n)}{\gamma_N(n)}. \tag{33}$$

The angle parameter is calculated directly from the data and the gain vector. The reduction in the number of computations is particularly due to a simplification in the calculation of the backward prediction error. After some substitution and simplification, equation (33) can be reduced to the scalar equation

$$e^b(n|n-1)=m(n)\varepsilon^b(n-1), \tag{34}$$

where

$$m(n)=\frac{e^b(n|n)}{\varepsilon^b(n-1)\gamma_N(n)}. \tag{35}$$

By reducing equation (34) from a vector to a scalar equation, approximately O(N) operations are conserved. This reduces the number of operations for each iteration of the algorithm from O(8N) in the FTF case to O(7N).

INFINITE IMPULSE RESPONSE METHODS

Infinite impulse response (IIR) digital filters differ from FIR filters in that an autoregressive or recursive element is added to the equation. An IIR filter has the form

$$\hat{d}(n)=\sum_{m=1}^{M-1}a_m(n)d(n-m)+\sum_{m=0}^{M-1}b_m(n)x(n-m) \tag{36}$$

where $a_m(n)$ and $b_m(n)$ are the filter weights for the recursive and non-recursive parts of the IIR filter respectively.

In a systems-identification application, the IIR filter will be better able to identify systems that are inherently autoregressive. In addition, IIR filters are often capable of superior performance with fewer filter weights than FIR filters. This is due to the fact that the IIR filter can generate an infinite impulse response with only a finite number of filter weights.

Feintuch Algorithm

The Feintuch algorithm is a gradient based IIR approach. It is analogous to the FIR LMS algorithm with the addition of a recursive element. There are separate update equations for the recursive and non-recursive parts

$$\mathbf{a}_N(n+1) = \mathbf{a}_r(n) + \alpha e(n)\mathbf{d}_N(n) \tag{37}$$

and

$$\mathbf{b}_N(n+1) = \mathbf{b}_N(n) + \alpha e(n)\mathbf{x}_N(n) \tag{38}$$

The output equation then becomes

$$\hat{d}(n) = \mathbf{a}_N^T(n)\mathbf{d}_N(n) + \mathbf{b}_N^T(n)\mathbf{x}_N(n) \tag{39}$$

The Feintuch algorithm relies on the statistical properties of the error signal. Like the LMS algorithm, the instantaneous error is used as an estimate of the mean squared error. In order for the algorithm to converge, the expected value of the error and signal terms must be zero. Otherwise, the convergence point will not be an actual minimum. This is true even if a unique minimum exists.

Recursive Prediction Error Algorithm

The recursive prediction error (RPE) algorithm is also a gradient based IIR algorithm. It attempts to simplify the mean squared error $\varepsilon(n)$. Since the MSE is not readily available, it is estimated by the instantaneous squared error $e^2(n)$. The RPE algorithm updates the weight vector in the direction of the gradient defined by

$$\nabla_{w_N} e^2(n) \equiv \frac{\partial e^2(n)}{\partial w_N(n)} = e(n)\nabla_{w_N} e(n) = -e(n)\nabla_{w_N} y(n) \tag{40}$$

where the gradient $\nabla_{w_N} y(n)$ is defined by the vector

$$\nabla_{w_N} y(n) = \left[\frac{\partial y(n)}{\partial a_1(n)}, \ldots, \frac{\partial y(n)}{\partial a_{N-1}(n)}, \frac{\partial y(n)}{\partial b_0(n)}, \ldots, \frac{\partial y(n)}{\partial b_{M-1}(n)}\right]^T. \tag{41}$$

Using a development similar to that of the recursive least squares algorithm, an estimate of the inverse of the autocorrelation matrix is calculated based upon the previous autocorrelation matrix. Defining the vector $\phi(n)$ to be the combined input and output vectors

$$\phi(n) = [y(n-1), \ldots, y(n-N+1), x(n), \ldots, x(n-M+1)]^T \tag{42}$$

the filter weight update equation becomes

$$\mathbf{w}_N(n) = \mathbf{w}_N(n-1) + \alpha \mathbf{R}^{-1}(n)\phi(n)e(n) \tag{43}$$

One of the problems of the RPE algorithm is that the recursive part of the filter may become unstable during adaptation. This can happen if one of the poles of the filter moves outside the stability region of the unit circle during the adaptation process. If this happens, the output can grow without bound. There are various methods for determining if the filter is unstable (see reference 3) and these can be used if stability becomes a problem.

ALGORITHM COMPLEXITY COMPARISONS

We will now analyze the described algorithms for complexity. In this analysis, the order is the number of additions and multiplications. Only the highest order term is indicated in the table. It should be noted that these order estimates are based upon the particular implementations of the algorithms used in our tests.

Algorithm	Order of Operations
Least Mean Squares	4N
Recursive Least Squares	N^2
Fast Transversal Filter	8N
Gain-Normalized (FTF)	7N
Feintuch (IIR)	3N
Recursive Prediction Error (IIR)	$5N^2$

Table 1. Algorithmic complexity comparisons.

ALGORITHM EXECUTION TIME COMPARISONS

In this section, results are provided of computer simulations of the various algorithms as performed by the authors. The simulations were performed on Macintosh computers with the MatLab® matrix manipulation software. The algorithm execution time comparisons tabulated below are intended to indicate the actual algorithm performance for an active noise cancellation experiment. To that end, the time to convergence (relative to the number of samples) was considered as well as the required execution time for a data stream of 400 samples. Each algorithm was tested on a time delayed, attenuated, noise corrupted random(white) signal. Thus, the system could be almost (except for additive noise) perfectly identified by an FIR filter of sufficient length. All the filters simulated had 20 filter weights, which is plenty for an accurate identification of the system.

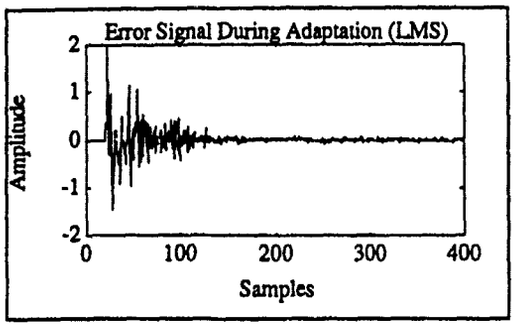

Figure 4. LMS algorithm convergence.

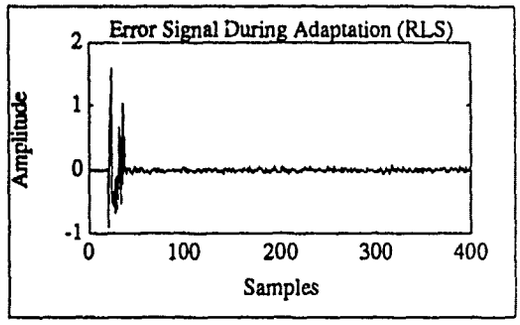

Figure 5. RLS algorithm convergence.

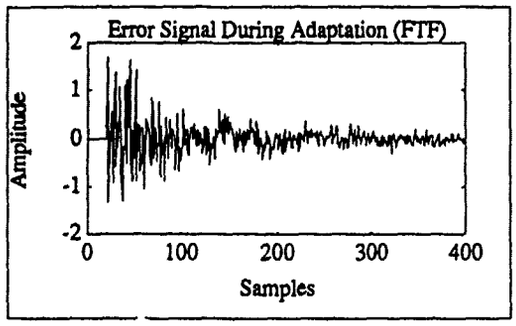

Figure 6. FTF algorithm convergence.

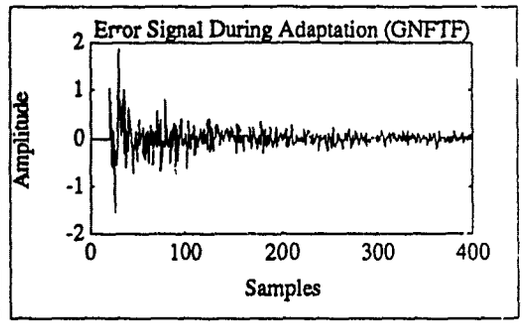

Figure 7. GNFTF algorithms convergence.

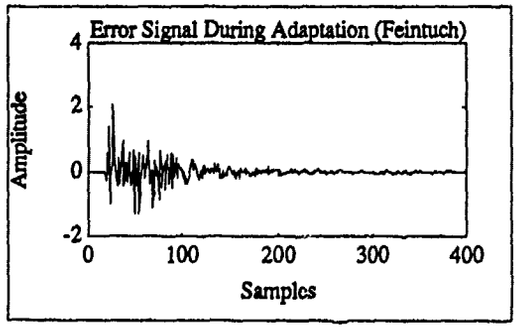

Figure 8. Feintuch algorithm convergence.

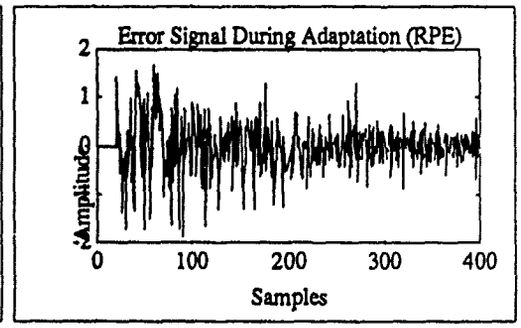

Figure 9. RPE algorithm convergence.

Figures 4 through 9 show graphically how the various algorithms converge for the active noise control simulation. In our tests, the recursive least squares algorithm converged much more quickly with respect to the samples than the other algorithms. The recursive prediction error algorithms was the slowest. This may be due to the fact that the IIR gradient is not well-suited to modeling simple FIR systems. The Feintuch algorithm, on

the other hand performed rather well using an IIR approach. This can be explained by the fact that the Feintuch algorithm separates the recursive and non-recursive parts of the IIR filter and solves them separately. For this experiment, as long as the recursive part of the IIR filter converges to approximately zero, the non-recursive part will handle the system identification. The fast transversal filters are perhaps not as fast as their name would imply. The results of the simulation are tabulated below in table 2 for comparison.

Algorithm	Number of Data Samples Before Convergence	Comparative Execution Time (in seconds)	Adjusted Convergence Score (lower is faster)
Recursive Prediction Error Filter (IIR)	>400	295.58	>118232.00
Fast Transversal Filter	225	24.52	5517.00
Gain-Normalized Fast Transversal Filter	200	18.57	3714.00
Recursive Least Squares	50	68.33	3416.50
Least Mean Squares	150	11.17	1675.50
Feintuch Filter (IIR)	150	8.85	**1327.50** (fastest)

Table 2. Execution time comparisons for the algorithms tested.

As a better indicator of the performance of the algorithms, we have included an adjusted convergence score for the algorithms tested. This value is calculated by multiplying the number of data samples before convergence by the comparative execution time of each test. A lower score indicates a faster time for convergence.

As can be seen, the best convergence score was achieved by the Feintuch (IIR) algorithm. While the LMS algorithm converged as quickly with respect to data samples, the algorithmic complexity of the Feintuch algorithm was less. The RLS algorithm converged very quickly with respect to data samples, but the algorithm was the second slowest. It earned the third lowest convergence score.

The slowest algorithm by far was the recursive prediction error filter. The execution time was particularly slow because it requires calculation of the inverse of the autocorrelation matrix. Additionally, the IIR gradient approach for both the recursive and non-recursive parts of the filter was not well suited to a simple non-recursive system. The RPE algorithms got the worst score in both speed categories.

The fast transversal filters were not as fast as some of the other methods, but the expected improvement in performance was observed for the gain-normalized FTF over the regular FTF algorithm.

It should be noted that these results are for a single test paradigm. Different input signals, systems and constants can vary the performance of each of the algorithms. The purpose of this test, however, was to determine the performance of various adaptive filter algorithms in a typical active noise control experiment.

CONSIDERATIONS FOR ADAPTIVE FILTERS IN ACTIVE NOISE CONTROL

There are several factors that need to be considered when implementing an adaptive filter in an active noise control application. The following is a list of typical tasks required.

- Determine a model for the active noise control system. A signal flow diagram can be useful in identifying the operation of the system and can aid in the selection of an appropriate algorithm.
- Choose an algorithm that matches the system model/geometry. Once the system has been identified, an algorithm must be selected to model the system. If the system is recursive, an IIR filtering method should probably be selected.
- Consider the data rates, signal frequency band and processor speed. The convergence score tabulated above is a good measure of algorithm performance if the data is sampled at a rate just slow enough that the algorithmic calculations can be performed between sample times. If there is plenty of time for the algorithm to execute between samples, perhaps a filter should be selected which has higher complexity but quicker convergence with respect to the samples.
- Consider parallelism and modularity issues. In most active noise control applications, a single filter does not provide satisfactory performance. Usually several canceling sources and microphones are necessary. This may require independent filters or an algorithm capable of reducing an ensemble averaged error for several microphones.
- Determine the target architecture. Adaptive digital filters can be implemented with general purpose computers, but often this is overkill. Reasonably simple specialized circuits can be developed to

provide cheaper and more modular solutions. Digital signal processing (DSP) chips can be used to improve speed performance of the algorithms.

- Select the transducers. Transducers need to be selected which are capable of providing the required performance. While adaptive filters can compensate for deficiencies in the transducers, the more accurate the transducer the better the system will work.

CONCLUDING COMMENTS

The research and experiments described in this paper were done in order to determine which algorithms perform well in an active noise control application. We considered a system identification model of a delayed, attenuated, and noise-corrupted signal. All the algorithms tested were capable of performing the task, but the best algorithm in terms of time to convergence was the Feintuch IIR algorithm. This is encouraging because the IIR method also handles recursive systems.

We considered only six adaptive filter algorithms in this paper. There are many more. One significant class of filters, adaptive lattice filters, was not investigated due to time and paper length constraints. Reference 1 contains the development of some of these algorithms. Neural networks, which are essentially parallel and highly interconnected adaptive filters, have also been used in active noise control applications. Adaptive filters and active noise control continue to be very active areas of research.

We intend to continue the investigation of adaptive filtering algorithms in active noise control applications. We are currently testing the algorithms in experiments with various configurations of noise sources and microphones and will report on our findings when more quantitative results are available.

ACKNOWLEDGMENTS

The authors gratefully acknowledge the support of the Georgia Tech Research Institute Senior Technical Guidance Council.

REFERENCES

1. S. Thomas Alexander, *Adaptive Signal Processing Theory and Applications*, Springer-Verlag, New York, 1986.
2. B. Widrow and S. D. Stearns, *Adaptive Signal Processing*, Prentice-Hall, New Jersey, 1985.
3. John S. Shynk, "Adaptive IIR Filtering," *IEEE ASSP Magazine*, April, 1989, pp. 4-21.
4. J. C. Stevens and K. K. Ahuja, "Recent Advances in Active Noise Control," *AIAA Journal*, Vol. 29, No. 7, July 1991, pp. 1058-1067.
5. C. A. Rogers and C. R. Fuller, Editors, "Recent Advances in Active Control of Sound and Vibration, Technomic, Lancaster, PA, 1991.
6. Alan V. Oppenheim and Ronald W. Schafer, *Digital Signal Processing*, Prentice-Hall, New Jersey, 1975.
7. Athanasios Papoulis, *Signal Analysis*, McGraw-Hill, New York, 1977.

SECOND INTERNATIONAL CONGRESS ON
RECENT DEVELOPMENTS IN AIR- AND
STRUCTURE-BORNE SOUND AND VIBRATION
MARCH 4-6, 1992 AUBURN UNIVERSITY, USA

EFFECT OF CYLINDER LENGTH ON VORTEX SHEDDING SOUND IN THE NEAR FIELD

J. T. Martin*
K. K. Ahuja**
Georgia Institute of Technology
GTRI/AERO and School of Aerospace Engineering
Atlanta, Georgia 30332-0800
U. S. A.

ABSTRACT

A study was conducted on the effect of changing the length of a constant diameter circular cylinder on the discrete tone sound associated with its vortex shedding. A microphone, fitted with a nose cone, was used to measure the near field sound. Two cylinder configurations were used. In the first configuration, the cylinder was anchored from the test section floor. The cylinder length was changed by pushing the antenna up through an opening in the test section floor and then secured. The microphone remained fixed in the mid-plane of the test section. In the second configuration, the cylinder was suspended by two helically wrapped welding rods that kept the cylinder centered between upper and lower walls. The microphone in this case was always located in the plane bisecting the cylinder. These measurements were made in an acoustically treated test section of a closed-loop wind tunnel. All measurements were made at a flow speed of 33.53 m/sec (75 miles/hour). It is shown that, the noise produced by the vortex shedding behind a cylinder first increases with length, and then reaches a fixed value at about length over diameter (L/D) ≅ 64.

NOMENCLATURE

C_0	Ambient Speed of Sound
C_l	Root-Mean-Square Sectional Lift Coefficient
D	Cylinder Diameter
f	Frequency
I	Intensity of the Far Field Radiation
L	Cylinder Length
L/D	Non-Dimensional Length
l_c	Correlation Length ($\equiv 2\int_0^{\infty} R(\xi)d\xi$)
r	Microphone Distance from Cylinder Axis
r/D	Non-dimensional Microphone Distance
$R(\xi)$	Spatial Correlation Coefficient
SPL	Sound Pressure Level
St	Strouhal Number (≡ fD/U)
U	Free stream Velocity

---

* *Graduate Student, School of Aerospace Engineering*
** *Head: Acoustics Branch, GTRI/AERO and Professor: School of Aerospace Engineering*

γ Correlation Centroid ($\equiv \frac{2}{l_c}\int_0^{\infty}\xi R(\xi)d\xi$)

ρ Density

θ Angle Measured from the Flow Direction in the Plane Normal to the Cylinder Axis

INTRODUCTION

Much of the published research on the effects of vortex shedding from a constant diameter circular cylinder has been for the far field, where the microphone distance is much larger than the cylinder length. There exist a number of published theoretical and experimental studies on this topic. A summary, given by Blevins [1] is particularly noteworthy. One of the theoretical models mentioned by Blevins gives meaningful insight to the experimental data in the far field and can be used to predict sound pressure levels given cylinder geometry, flow parameters, and empirical data. However, there are situations where the vortex shedding noise needs to be quantified in the near field. Automobile roof rack or antenna noise affecting the passengers are two examples of near field vortex shedding noise.

This paper is an attempt to examine the dependence of near field noise associated with the vortex shedding from a cylinder on its length. Noise data taken from cylinders of various lengths and at various microphone distances are presented.

DESCRIPTION OF THE EXPERIMENT

The Experimental Arrangement

These experiments were conducted in a closed-loop wind tunnel at the Georgia Tech Research Institute. The test section is lined with 10.16-cm (4-inch) thick polyurethane sound-absorbing foam and has the inner dimensions of 0.762 x 0.762 x 2.438 m (30 x 30 x 96 inches). The test section is shared by a cut-out section of a Mercury Sable automobile, which occupies the left half (with respect to the direction of the flow), and the cylinder, occupying the right half (see Figure 1). The cut-out extends at most 31.75 cm (12-1/2 inches) into the tunnel at the cross-section containing the axis of the cylinder. The cylinder was placed at 19.05 cm (7-1/2 inches) from the right wall and was held in place by mounts outside the test section. A Bruel and Kjaer condenser microphone (type 4135), fitted with a nose cone, was mounted in the mid-plane of the tunnel (indicated in Figure 1), between the cylinder and the right hand side wall. The noise levels at the microphone location (with the cylinder removed) with and without the cut-out were the same and the discrete tone sound pressure levels (SPL's) associated with the vortex shedding were dominant and not affected by any noise produced by the cut-out in the test section. The cut-out was present for all measurements. The microphone signals were recorded on a TEAC W-410 2-channel cassette tape recorder and analyzed on a Macintosh IIcx, with a real time digital signal processor installed, from which plots were obtained (see Figure 2). The signal processing parameters were set so $\Delta f = 15.625$ Hz (where Δf is the difference between two consecutive frequencies of the Fast Fourier Transform).

Cylinder Test Arrangements

Two cylinder arrangements were used, referred to here as Arrangements A and B, and are shown in Figures 3 and 4, respectively.

Arrangement A. In this arrangement, a 4.763 mm (3/16 inch) diameter cylinder was used. The cylinder was anchored from the test section floor and held tightly by a 0.3969 mm (1/64 inch) diameter cable connected to the test section ceiling (see Figure 3). The tone associated with the cable used produced a much higher frequency than that by the cylinder and also had a much lower amplitude because of its small diameter.

In the course of the experiment, the cylinder was set to the proper length, mounted to the floor, and tightened by the attached cable. The microphone boom, which was mounted through the side of the test section, was positioned so that it was in the mid-plane of the wind tunnel test section. Thus in this case, even though the cylinder length was changed, the location of the observer, i.e., the microphone, remained fixed. This test configuration simulated a situation where the driver of an automobile is fixed in space, and the antenna length above the antenna/car body junction is increased.

Arrangement B. In Arrangement B, a 6.35 mm (1/4 inch) diameter cylinder was used (see Figures 4 a and b). The cylinder was mounted in the mid-plane between the ceiling and floor of the test section by two spiral-wrapped welding rods. As shown in Figure 5, The cylinder consisted of several smaller length segments that were joined by small threaded rods. Each cylinder segment was bored and threaded along the axis on both ends so that the threaded rod could be completely enclosed between the two joined segments. The welding rods had a 3.175 mm (1/8 inch) diameter and were also threaded to fit into the cylinder and hold it securely. The part of each welding rod that was exposed to the flow was wrapped with 0.7938 mm (1/32 inch) diameter wire with 2.54 cm

span per turn (1 inch per turn). The purpose of wrapping the welding rods helically with wire was to destroy the coherence of vortex shedding over the rod and reduce the discrete tone noise produced by the rod so that only the noise produced by the main cylinder would be measured.

The Experimental Program

At the beginning and end of a set of test runs, a microphone signal calibration was performed. For each run, the cylinder length and the microphone position were appropriately set, the flow was set to 33.53 meters/second (75 miles/hour), and the narrow band sound pressure levels obtained. A typical measured spectrum is presented in Figure 6. From the spectra obtained, the frequency and amplitude for the vortex shedding sound for each test cylinder were tabulated. Table 1 contains some of the test data from Arrangement B, where cylinder length and microphone distance from the axis were varied. The discrete tones corresponded to an average Strouhal number, St = 0.2.

RESULTS

It should be pointed out before presenting these results that we were unable to locate literature on that detailed the near field noise data from cylinders in flow. A number of interesting results were obtained in our study. These results are presented below under two categories: (1) The Effect of Cylinder Length and (2) The Effect of Microphone Distance in the Near Field.

The Effect of Cylinder Length

The effects are described first for the microphone fixed in space with respect to the base of the cylinder and the cylinder length increasing (i.e., Arrangement A). Then, the effects for the microphone always located in a plane bisecting the cylinder (i.e., Arrangement B) are described.

Effects of Cylinder Length on Near Field Noise With Microphone at a fixed Distance with Respect to the Base of the Cylinder (Arrangement A)

In this arrangement, the microphone was kept in the mid-plane of the wind tunnel test section (a distance of 81 diameters from the base of the cylinder) and the cylinder was pushed up through the bottom of the test section to the desired length and then secured. The results, plotted in Figure 7, show that the SPL increases about 25 dB between L/D of 27 and 117, and then levels off to a constant value within a measurement accuracy of +/- 1 dB for larger non-dimensional lengths.

Effects of Cylinder Length on Near Field Noise With Microphone at a fixed Distance with Respect to the Center of the Cylinder (Arrangement B)

In this arrangement, the microphone received noise contribution from the cylinder portion above and below the mid-plane, unlike Arrangement A, where a contribution from above the mid-plane was not always present. As in Arrangement A, the noise in Arrangement B first increased with increasing cylinder length, but after L/D greater than 64, the noise leveled off to a constant value. This is shown in Figure 8. A further comparison is made in Figure 9 for the SPL's produced by the two cylinder arrangements. It is found that for the same cylinder length, a maximum, constant SPL is obtained if the microphone is in the plane bisecting the cylinder. This constant value was only a few dB higher than that reached by the Arrangement A.

Effect of Cylinder Length on Near Field Noise with Respect to Far Field Theory

The equation for noise from a cylinder in the far field as given by Leehey and Hanson [2] is as follows:

$$I(r) = \frac{\rho \cos^2 \theta \, C_l^2 \, U^6}{16 \, C_o^3 \, r^2} [L - \gamma] \, l_c \qquad (1)$$

It is seen from this equation that the noise from a cylinder in the flow should increase with increasing cylinder length. Indeed, this is also observed in the near field. The equation contains a correlation length, l_c, and the term γ, which is the correlation centroid of the cylinder. For the Reynolds number used in the tests (about 10^4), this value is estimated, from the data in Reference [2], to be 2.5 cylinder diameters. To examine if our data of SPL variation with L/D (at least up to the value of L/D after which there was little change in noise radiation) followed this relationship, the data at r/D = 14 was replotted as a function of 10 Log[(L - γ)/D] in Figure 10. For comparison, the plots of SPL versus 10 Log(L/ D) are also superimposed on this figure. If the above equation holds good in the near field, a slope of 1 is expected in the plot shown in Figure 10 after accounting for the correlation centroid. The slope is found to be 1.85. Thus, it appears that the equation derived for the near field needs to be modified for application to the near field. Additional on-going work at Georgia Tech by the authors is expected to shed further light on this topic in the near future.

The Effect of Microphone Distance in the Near Field

After acquiring the data shown above, which were acquired at a microphone distance of r/D = 14, additional data were acquired at six distances, which are r/D = 27, 23, 19, 15, 11, and 7. For each r/D, six cylinder lengths were tested. These cylinder lengths were: L/D = 8, 16, 28, 40, 64, and 120. In each case, the cylinder diameter was constant and was equal to 6.35 mm (1/4 inch). For each L/D, the plots of SPL versus 10 Log(L/D) were examined to study if the trend seen in the last three figures was obtained at all microphone distances. Typical results are shown for r/D = 27, 23, 19, and 11 in Figures 11 (a) through (d), respectively. In each plot, the data for r/D = 15 are also superimposed. (Note that this is close to the distance for which data shown in Figures 7 through 9 were acquired. The reference data for r/D = 15 is used here only for convenience. These data were acquired and analyzed along with the data for all the other distances mentioned above. Also, these data are very similar to those obtained at r/D = 14.)

It is seen in these plots that at each r/D, the variation with L/D is almost identical. It is also noticed that it is not until r/D = 15 (10 Log(r/D) ≅ 11) that the noise levels are found to increase with decreasing distance from the cylinder. As shown later, it is likely that the data at the higher values of r/D is contaminated by reflections from the wind tunnel wall. As shown in Figure 12, where the data for r/D = 7 are compared with those for r/D = 15, as one gets closer to the cylinder, a definite increase in the noise levels is seen. Here the noise has increased by as much as 10 dB for each cylinder length.

To examine the distance scaling in the near field, the sound pressure levels correspondir g to the vortex shedding tones were plotted as a function of 10 Log(r/D) for each cylinder. This is shown in Figures 13 (a) through (f) for L/D = 8, 16, 28, 40, 64, and 120, respectively. The slopes of the distance scaling for the SPL are approximately -3.8, -3.5, -3.3, -2.8, -2.9, and -1.8 for the non-dimensional lengths of L/D = 8, 16, 28, 40, 64, and 120, respectively.

It is noticed that in each plot of Figure 13, the slope starts to rise at r/D ≅ 19. This increase in slope for r/D greater than 19 could be due to the proximity of the microphone to the test section wall. Although the wall is lined with foam, there was a patch of tape over the foam near the microphone in this position. The tape was used to cover cavities in the wall from other unrelated tests. In these tests, the further the microphone was from the cylinder, the closer it was to the patch of tape. The most extreme case was at the r/D = 27, where the microphone was only 4 diameters away from the tape.

In the far field, Eq. (1) predicts that the SPL versus 10 Log(r/D) curve should have a slope of m = -2 . The results of Figure 13 show that for r/D less than or equal to 19, this value of m is approached in the near field for the larger cylinder lengths. This is rather surprising and no explanation is available as to why this should be so in the near field. Values closer to -4 are expected in the near field, which are obtained in the present experiment for the smallest value of L/D tested. A simple formulation for the near field noise as a function of cylinder length is needed. This formulation must account for the vortex shedding coherence and the fact that for smaller cylinders, the coherence of this shedding will be substantially modified by the end effects.

CONCLUDING COMMENTS

These results of near field noise from the cylinder have two very important practical implications. The results of the first test with Arrangement A imply that for a fixed relative location between an observer and the base of the antenna, as is the case between a radio antenna of a car and the driver, the noise levels can be reduced by as much as 20 dB by reducing the antenna length from L/D = 120 to 75. It also implies that once a critical length is exceeded, if the reception performance of a radio antenna is enhanced by increasing the antenna length, one can safely increase the antenna length without increasing the acoustical noise further.

The implications of the results of the second test with Arrangement B relate to the wind tunnel testing of the ranking of the acoustic performance of various antennas or other cylindrical bodies. Often wind tunnels available to a number of researchers are not large enough to make acoustic measurements in the far field. In fact, most wind tunnels are too small even for adequate near field acoustic measurements. Sometimes it is desirable to make measurements in the wind tunnel at as few locations as possible to obtain the most representative data. For example, the second author had the opportunity of conducting a comparative acoustic evaluation of a number of cellular telephone antennas which varied in length by at least a factor of three. The first question in a situation like this that comes to mind is: where should the microphone be placed in the test section with respect to the antenna center so that a reasonably good estimate of the relative acoustic performance of antennas of different lengths could be obtained without acquiring an inordinate amount of acoustic data or without resorting to complex acoustic power measurements? Clearly, as shown in Figure 9, it would be desirable to keep the microphone in a plane passing through the center of the antennas to determine the highest levels produced by a given cylinder. It is further demonstrated in Figure 9 that during a noise ranking exercise, the maximum noise produced by an antenna can easily be misrepresented if the microphone is not placed in the plane passing through the center of the antenna.

ACKNOWLEDGMENTS

The authors are grateful of the Ford Motor Company for supporting this effort.

REFERENCES

1. Blevins, R. D., "Review of sound induced by vortex shedding from cylinders," *Journal of Sound and Vibration*, Vol. 92, No. 4, 1984, pp. 455-470.

2. Leehey, P. and Hanson, C. E., "Aeolian tones associated with resonant vibration," *Journal of Sound and Vibration*, Vol. 13, No. 4, 1971, pp. 465-483.

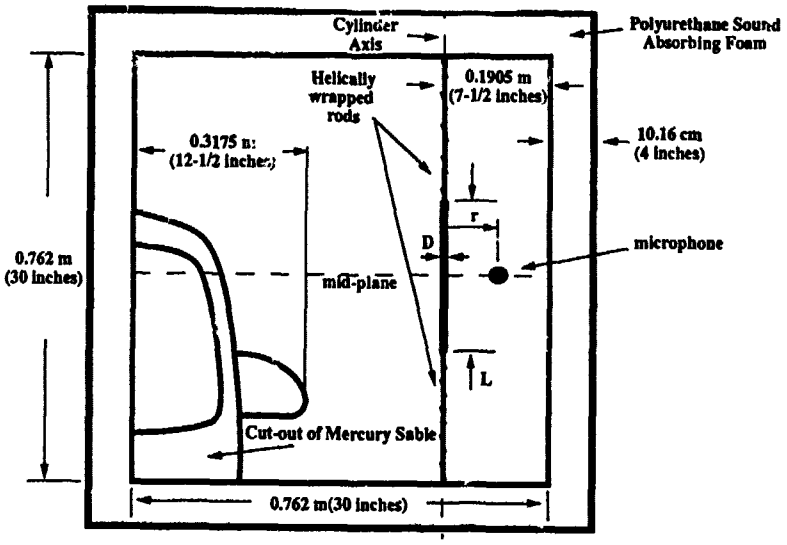

Figure 1 --Cross sectional view of the test section at the cylinder axis.

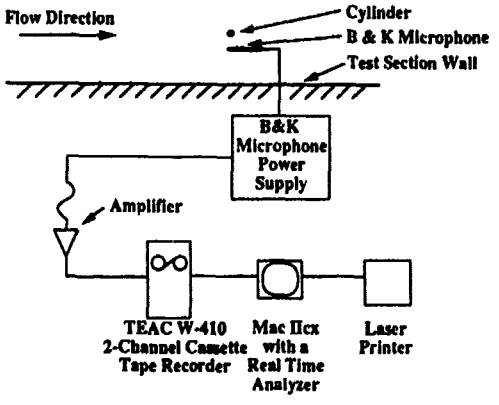

Figure 2 --Acoustic data acquisition and analysis set-up.

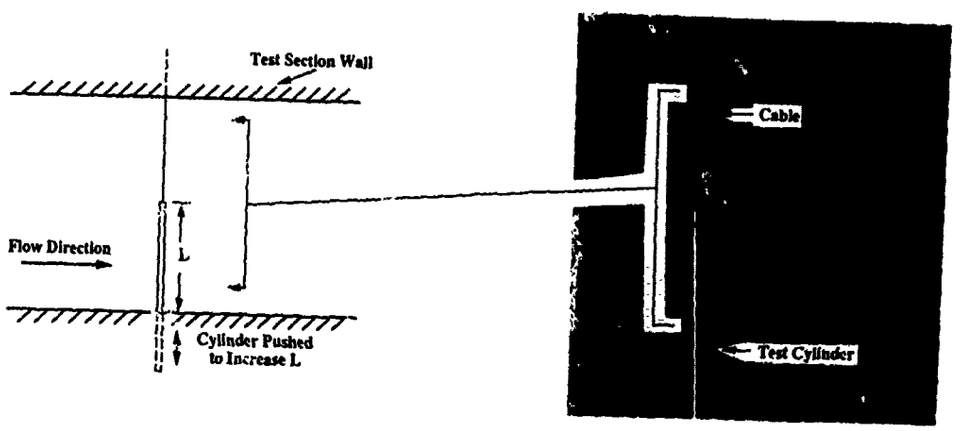

Figure 3 --Cylinder used in Arrangement A.

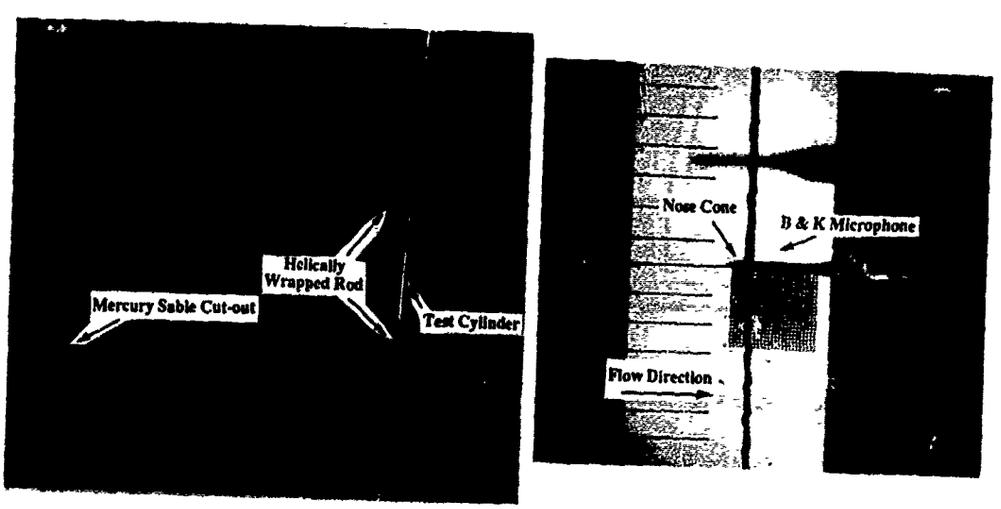

(a) (b)

Figure 4 --Test section: (a) view from the flow direction, (b) side view

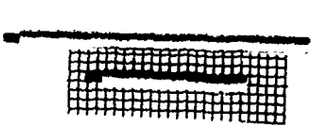

Figure 5 --Cylinder segments used in Arrangement B to increase total cylinder length.

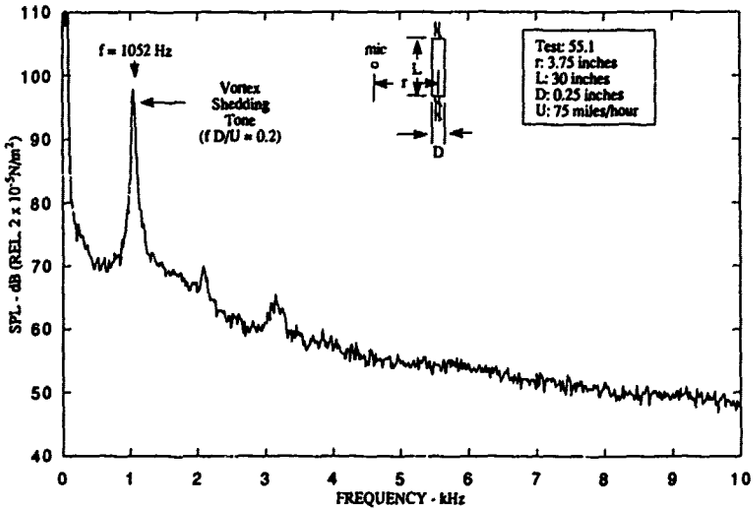

Figure 6 --A typical noise spectrum.

Table 1 --Vortex shedding Strouhal numbers and SPL's as a function of cylinder length and microphone distance.

Cylinder Diameter		6.35 mm (0.25 inches)			
Flow Velocity		33.53 m/sec (75 miles/hour)			
L/D	r/D	Strouhal Number	SPL (dB)	Amb. Press. (KPa.)	Tunnel Temp. (°C)
8	7	0.179	83.4	99.05	31.8
8	15	0.179	70.8	99.05	36.4
16	7	0.204	98.8	98.04	34.1
16	15	0.204	87	98.04	37.9
16	23	0.204	85.7	98.04	39.6
28	7	0.207	103.4	97.12	35.8
28	7	0.204	102.6	98.04	30.3
28	15	0.207	91.8	98.04	33.5
28	23	0.207	91.6	98.04	35.3
40	7	0.204	100.5	97.22	39.8
40	15	0.204	93.5	97.22	43.2
40	23	0.204	92.2	97.22	43.0
40	7	0.200	102.1	98.04	41.8
40	23	0.200	93.7	98.04	39.0
40	7	0.197	105.1	99.05	26.2
40	11	0.197	97.7	99.05	31.9
40	15	0.200	94.4	99.05	35.0
40	19	0.204	92.9	99.05	37.5
40	23	0.204	92.3	99.05	41.3
40	27	0.200	94.6	99.05	42.7
64	7	0.197	104.7	96.88	38.2
64	15	0.197	95.8	96.88	36.2
64	23	0.200	96.7	96.88	31.7
64	7	0.197	106.4	97.12	34.7
120	7	0.197	104.6	98.51	40.0
120	11	0.197	101.1	98.51	39.7
120	15	0.197	97.9	98.51	38.1
120	19	0.197	96.5	98.51	41.8
120	23	0.197	98.1	98.51	42.6
120	27	0.197	100.1	98.51	42.2

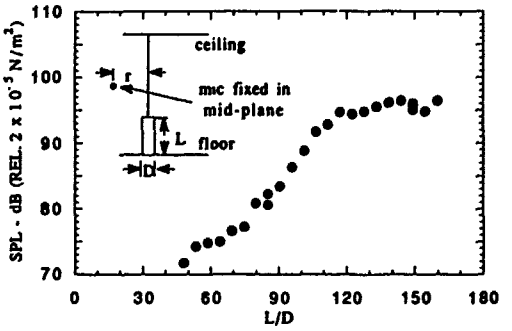

Figure 7 --Vortex shedding tone amplitude increases with cylinder length for microphone fixed with respect to the cylinder base. (D = 0.1875 inches, r/D = 14, U = 75 miles/hour, Arrangement A)

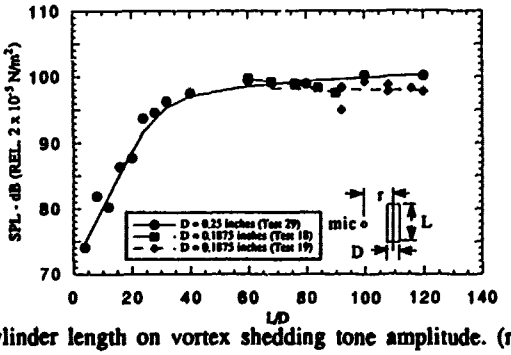

Figure 8 --Effect of cylinder length on vortex shedding tone amplitude. (r/D = 14, U = 75 miles/hour, Arrangement B)

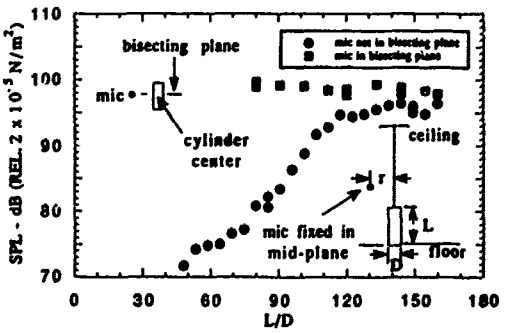

Figure 9 --Vortex shedding tone amplitude comparison for Arrangements A and B. (D = 0.1875 inches, r/D = 14, U = 75 miles/hour)

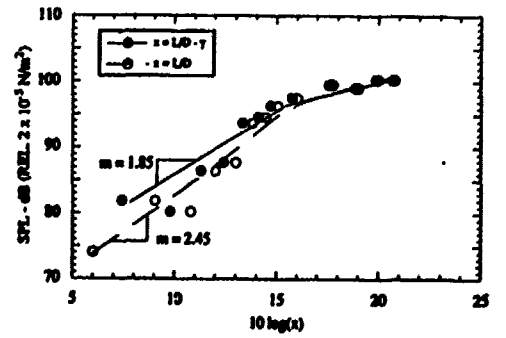

Figure 10 --The effect of using the approximate correlation centroid in representing the cylinder length scale. (γ = 2.5 D, U = 75 miles/hour)

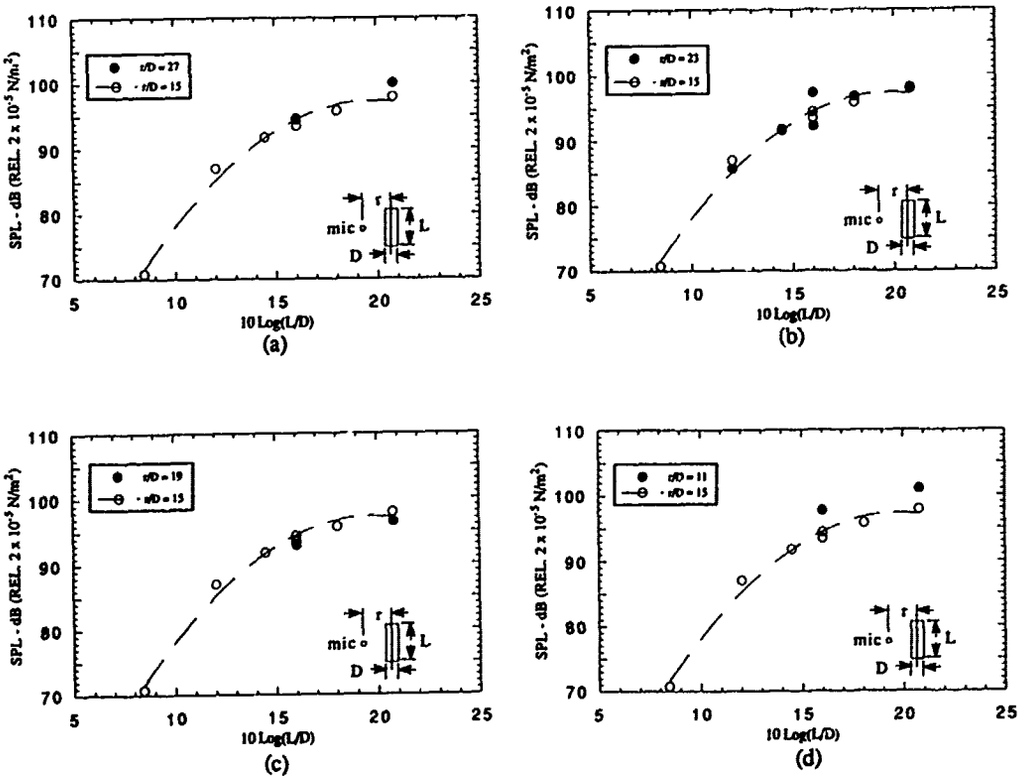

Figure 11 --Effect of cylinder length on vortex shedding tone amplitude. r/D: (a) 27, (b) 23, (c) 19, (d) 11.

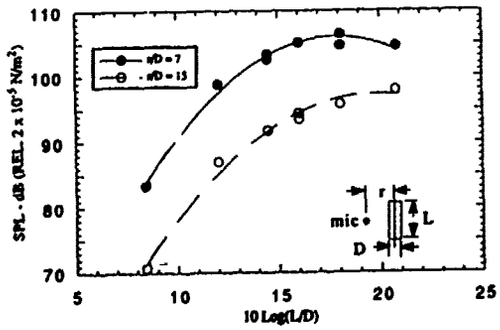

Figure 12 - Tone amplitudes at r/D = 7 versus those at r/D = 15.

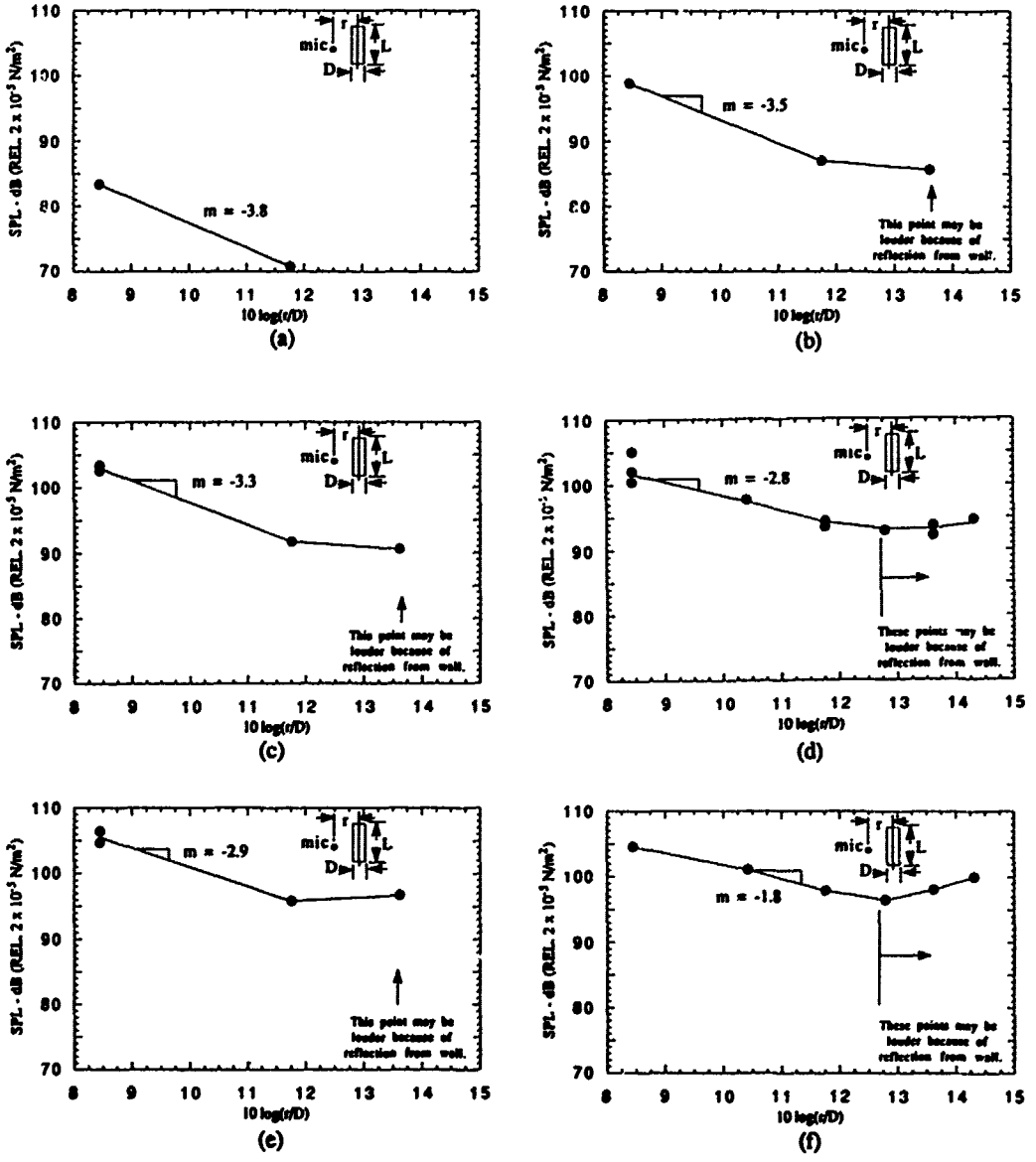

Figure 13 --Vortex shedding tone amplitude variation with microphone distance. L/D: (a) 8, (b) 16, (c) 28, (d) 40, (e) 64, (f) 120.

SECOND INTERNATIONAL CONGRESS ON
RECENT DEVELOPMENTS IN AIR- AND
STRUCTURE-BORNE SOUND AND VIBRATION
MARCH 4-6, 1992 AUBURN UNIVERSITY, USA

SCATTERING FROM INHOMOGENEOUS PLANAR STRUCTURES

William K. Blake and David Feit
Ship Acoustics Department
Carderock Division, Naval Surface Warfare Center
Bethesda, MD 20084-5000
U.S.A.

ABSTRACT

A plane acoustic wave incident on a spatially homogeneous elastic surface reflects as a specular wave. When the surface properties vary, i.e. the surface is spatially inhomogeneous, the reflected wave is no longer specular. This work systematically examines how the spatial scales of the surface impedance inhomogeneity determine the wavenumber-frequency characteristics, and hence the directivity-frequency magnitude of the scattered field. Both the surface wave field and scattered sound field are examined, the latter being derived from the former. Using three dimensional or color displays of the wavenumber-frequency spectra or angle-frequency magnitudes of the surface and scattered fields resulting from various classes of inhomogeneities, we show how the inhomogeneities affect the wave fields by introducing resonance and aliasing effects. The resonance effects manifest themselves as a modulation in frequency while the aliasing effects are revealed through angular modulation. Depending on the ratios of the ensonifying wavelength and the scales of the surface impedance, the surface may appear to be acoustically "smooth" with little spectral broadening or acoustically "rough" with significant spectral broadening. We also examine the conditions under which a finite length inhomogeneity can be modelled as an infinite system of periodically spaced similar inhomogeneities.

INTRODUCTION

In certain classes of inverse problems in structural acoustics, we are concerned with the interpretation of scattered acoustic transients in order to both localize and identify the mechanisms of the individually contributing components of complex scattering fields. When the structure is spatially non-homogeneous, the reflected waves are nonspecular because of wave vector redirection (conversion) of both pressure and velocity waves induced on the surface; these redirected waves thus control much of the directivity-frequency

characteristics of the scattered field. In complex structures, multiple scattering mechanisms and scattering sites co-exist so that the resulting scattered fields are determined by a superposition of these mechanisms. The role of the inversion technique is, therefore, to unravel this superposition thus allowing a physically meaningful diagnosis of the body. Not only does the inversion process have obvious application in the location and classification of acoustically significant structures, but it can also provide insight into the scattering performance of engineering designs. It is also useful to the design of post-processing schemes for the analysis of large scale computed acoustic response of complex structures.

We concern ourselves here with the physical interpretation of scattered sound rather than the mathematical analysis of the formal inverse problem. Signal processing techniques provide very indispensable tools for this interpretation because both spatial and temporal processing may be used to elucidate wave-like behavior in both the surface motion of the structure and pressures reradiated to the exterior acoustic medium. Since signal processing algorithms are analytically defined operations, signal patterns resulting from isolated structural acoustic mechanisms may be illustrated clearly by simulation. Furthermore, broad band transient response of the simulated mechanism associated with short pulse acoustic ensonification is especially useful in providing multipath separation of identified reflection events. In the present context, then, the simulations are made by revisiting certain classical problems for which known solutions are available. Superposition of these mechanisms is then made for hypothesized structural complexes, the simulated signal behavior may then be compared with identically-conducted physical experiments. The simulations, actually, are useful on various levels. They allow us to separate the component "events" in a given complex of superimposed mechanisms; they allow us to understand, in a detailed way how specific features of spatial inhomogeneity influence (or control) the wave conversion process. Furthermore, they can be used to design the signal processing algorithm that best adapts to the situation under study.

The objective of the paper, for which a synopsis is given here, is to describe the results of analytic simulations that are currently forming the basis of experimental work.

SIMPLE MECHANISM REPRESENTATIONS

Inhomogeneities in the surface properties of a scattering body may occur in the form of geometric or elastic features. In either case, the interaction of the surface initially involves a space-time filtering of the incident pressure; assumed to be plane wave prior to interaction with the body but generating a surface pressure field that is wave-vector distorted due to the shaping of the body. Motion of the surface involves further filtering, but now made more complex by the propagation of acoustically coupled elastic waves which also undergo a series of wave-vector distortions due to unique shape and orientation of surface impedance variations on the surface. The simulations carefully examine how the surface wave field that controls reradiation is affected by various classes of surface impedance inhomogeneity.

In order to focus this paper to illustrate some generally relevant points on the behavior of single structural elements, we revisit the example problem of the scattering from a plate window in an otherwise rigid plane. Ensonification by plane waves parallel to one of the generating axes of the window allows us to consider this problem as a one dimensional plate-like strip. This problem relates to more general problems, such as that of an elastic plate with repeated line discontinuities, in illustrating the separate influences of resonances and wave vector aliasing that is characteristic of such systems.

By using the Fourier transformation technique in space and time we can simultaneously solve the Bernoulli-Euler plate and acoustic wave equations for the acoustic response of the resonant modes of the plate [1]. The resulting velocity of the plate is then expressed as a summation over its invacuo modes with simply supported edges. This is a particularly convenient form for interpretation because the response of each mode is expressed as a product of spectral functions in frequency and wave number. The impedance function of the surface controls resonances; the modal shape function (in this case the modal shape function is the Fourier transform of the mode shape) expresses the effect of finite boundary in determining the aliasing behavior. This clearly identifies the resonant behavior of the modes in the plate window distinctly from the spatial aliasing characteristics of the mode shape of the window. The resonance behavior is natural to the strip and the frequencies of resonance are not dependent on the incidence angle of the sound. The resonant response, however, is determined by the trace matching of the incident wave with the characteristic wave number of the surface and coincidence with a plate wave number at a resonant frequency can occur. The resonant response of the strip is relatively weakly dependent on the incidence angle of the sound except near the coincident resonant frequencies. The wave vector filtering of the mode shape is more strongly dependent on the angle of incidence and, accordingly, dominates the angular dependence of the nonspecularly reflected sound because it describes the interference of edge sources.

These features are clearly shown in three dimensional presentations of the angle-frequency or wave number-frequency spectra of plate response using color as the third dimension to display amplitude. The frequency-angle polar pattern of scattered far field pressure is thus determined by three intersecting frequency-wave number characteristics as determined by the pattern of allowed resonances, the dispersion characteristics of the plate, and the aliasing lobes of the mode shape function. The intersections of these characteristic trajectories describe the net pattern in frequency-wave number of peaks in the system response. These loci, then determine the frequency-angle pattern of the scattered sound through trace wave matching.

FEATURES IN THE TIME DOMAIN AND LOCALIZATION

Inverse Fourier transformation of the frequency-angle results can be used to disclose certain pathological features of reflected transient wave forms. We consider the cases of equal incidence and reflection angles and develop a finely populated array in frequency-angle over which one and two dimensional Fourier transform inversion is possible. Inverse transformation in frequency of the pulsed reflections from the window at a given incidence/reflection angle,

assuming a band-limited ensonification pulse, gives time histories of received pulses. If we display these temporal responses in an angle-time relationship with amplitude described by color, we can view the characteristic behavior of the surface as a function of trace wave matching. The characteristics have identifiable angle-time patterns that depend on the relationships between spatial scales of discontinuities of the surface compared with the wave length of incident sound, and the existence of resonance or of acoustic coincidence within the range of angle-frequency. Thus the angle-time domain behavior patterns disclose the characteristic resonance and multipath features of the target, existence of critical coincidence angles. By systematically shifting the center frequency of the incident pulse, the resulting series of angle-time patterns can be developed to permit the tracking of acoustic coincidence behavior that may be distinct from localized response resonances in the structure.

The second inverse transformation of the measurement arrays, now taken over specific angle apertures, allows a localization of the scattering origins along a coordinate that is perpendicular to the line of sight within the angular aperture from the source to the scattering structure. This coordinate is called the cross range. The result of this transformation now yields a spatial distribution of the reflected signals at specific times and the display in cross range and time may be interpreted as a spatial resolution of the reflectivity of the surface. The method is borrowed from the radar technique [2,3]. Thus, the two dimensionally transformed angle-frequency pattern allows simultaneously both a cross range localization and temporal characterization of the scattering body. The simulations show how the cross range-time characteristics depend on whether resonances and acoustic coincidences occur in the measurement band of angle-frequency.

Returning to the theoretical descriptive model of the scattering structure in terms of its modal shape and resonance functions, we can now see that the cross range-time description of these functions allow recognition of specific features of the scattering body. Specifically, the temporal response is principally governed by the wave mechanical nature of the surface, while the cross range features are governed principally by the discontinuity interference pattern as determined by the acoustic spatial scale of the geometric system of line surface discontinuities.

STUDIES OF RELATIVE SPATIAL INHOMOGENEITY SCALES IN SCATTERING

Certain important limiting values of spatial scale dimension relative to the acoustic and elastic wave lengths have evolved from our studies of the elastic strip and of arrays of line discontinuities. These limits are:

a) The acoustic responses internal members of a finite distribution of discontinuities appears as that of an array of infinite number when the number of elements exceeds 2π divided by the loss factor of the structure. This means that the system resonances of a finite array may be estimated as virtually infinite under this condition.

b) A finite or infinite array of line discontinuities appears as a "smooth" reflector, with no identifiable internal interference effects, when the

discontinuity spacing is less than an acoustic trace wavelength. The converse is true in the opposite limit. Similarly, elastic interferences are to be neglected when the characteristic elastic wave length is large compared with the interstitial spacing. These are simply statements of the classical Rayleigh criterion.

c) A stronger limit is that bending wave interactions between nearest neighbor line discontinuities are minimal when the spacing exceeds a bending wave length divided by π.

d) In cases of scattering from a patch consisting of continuously distributed mass inhomogeneities on an otherwise homogeneous elastic plate, and satisfying the conditions (b) for smoothness, the scattered field is controlled by the edges of the patch [4]. The interference pattern so determined is reduced as the lower order spatial derivatives of the area mass density are reduced or made equal to zero. That is, these patterns are reduced by smooth taper.

e) In cases of large interstitial spacings, conforming to the conditions (a) and (c), useful good analytical approximations to the diffraction field utilize functions that model the discontinuity set as an acoustic array of line sources/receivers.

CONCLUSION

These analytical studies of revisited problems are proving useful at developing insights for the interpretation of the behavior of more complicated problems. The approach being taken is to build up our ability of assembling and superimposing known (and often previously examined) mechanisms to explain complex structural systems. The use of signal processing techniques, together with this built-up mechanistic understanding will also allow the development of post processing algorithms for interpreting the results of large scale computations of complex structures and for the support of experimental evaluations.

REFERENCES

1. Junger,M.C. and Feit, D. "Sound Structures and Their Interaction," 2nd ed, M.I.T. Press, 1986

2. Wehner, D.R. "High Resolution Radar," Artech House, 1987

3. Blake, W.K., Le,T., Peoples, J.R. "Target Interpretation Using Synthetic Aperture Sonar Techniques," 122nd Meeting of the Acoustical Society of America, 4-8 Nov. 1991

4. Feit, D.,"Scattering by a Mass Inhomogeneity on a Fluid-loaded Elastic Plate," 122nd Meeting of the Acoustical Society of America, 4-8 Nov. 1991, Manuscript submitted to JASA for publication, Feb. 1991

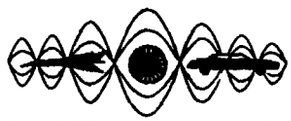

SECOND INTERNATIONAL CONGRESS ON
RECENT DEVELOPMENTS IN AIR- AND
STRUCTURE-BORNE SOUND AND VIBRATION
MARCH 4-6, 1992 AUBURN UNIVERSITY, USA

An Inferential Treatment of Resonance Scattering from Elastic Shells

M.F. Werby
NRL, Numerical Modeling Branch, Stennis Space Center, MS 39529
and
H. Überall
The Department of Physics, The Catholic University of America, Washington D.C. 20064

Abstract

One can extract both the existence and nature of resonances on elastic shells by direct measurement of surface vibrations or one may infer this information by examining various aspects of far field scattering via back scattered echo's and residual bistatic angular distributions. The origin of the inferential method is contained in the prodigious work of Überall[1,2] over the past decades. In this study the later technique is taken and an analysis for recently studied resonances is presented. Use is made of the recently formulated acoustic background for elastic shells[3-5] which makes it possible to examine residual back scattered echo's characterized by pure resonance effects. One observes the lowest order symmetric and antisymmetric model or Lamb resonances as well as water borne and pseudo-Stoneley resonances[6] and the higher order Lamb modes A_i and S_i where i=1,2,3.. Use of partial wave analysis will be made to investigate several relevant cases which infer the nature of the resonances.

Introduction

A direct approach advocated by Hickling[7] to examine the nature of resonances pertains to measurement of the vibrations on the surface of an object. Such measurements are generally not feasible especially for remote targets so that a systematic method has been worked out that enables researchers to infer information from certain features from the far field scattered signal. Our aim here is to discuss some of the methodology used to extract information concerning resonances and in particular to discuss observations of recently studied phenomena. A discussion of a resonance scattering theory in the time domain[8,9] is outlined since we will make use of it in what follows. The correct acoustical background for an elastic shell has been developed[3-5] and it now allows one to make proper use of partial wave analysis to determine the nature of specific resonances and so a limited discussion of the new background is presented here with examples. A partial wave analysis is then used to interpret the resonances. We will focus on water borne resonances observed at coincidence frequency (pseudo-Stoneley resonances) both in the time and frequency domains and on other kinds of water borne waves that occur on elastic shells particularly at higher frequencies. We will emphasize the pseudo-Stonely resonances which are narrow in ka space and occur over a limited frequency region about coincidence frequency, the point at which the flexural resonances begin to manifest themselves. The flexural resonances are very broad and fairly weak at inception though they become narrower and increase in magnitude with increasing frequency. We illustrate, in addition, that there are also other water borne waves that increase in importance with increasing frequency and are also more significant for lower material densities and thinner shells.

The correct acoustical background for elastic shells

In several works Überall and colleagues[1,2] determined that in the absence of a resonance an elastic solid behaves like a rigid scatterer. This was referred to as the " background " for the elastic solid. Subsequently Überall et. al.[10,11] employed that background for elastic shells although such a choice is not in general adequate. It has been

demonstrated that for shells a rigid background is adequate for high frequencies while a soft background is adequate for very thin shells at the lower frequency end.[12,13] However, for a large number of circumstances, neither is adequate. The correct background for shells has recently been published[3-5] and is based on implementing relevant conservation principles, use of entrained mass and a postulate that determines the surface displacement on a shell in the absence of a resonance. We will demonstrate the effectiveness of the new background for an Aluminum shell of 2% thickness calculated for a ka from 0 to 120. Fig. 1a illustrates the back scattered response for the shell. Fig. 1b is the response minus a soft background which is a reasonable background for the very low frequency region but inadequate otherwise. Fig. 1c is the response minus the rigid background which is never very good in terms of isolating the resonances though it improves with increasing frequency. Finally, the new background is illustrated in Fig. 1d and is clearly very good through out the frequency range. In the figures there is a large return centered about ka=72. This is the region about coincidence frequency. In the next section we will use a partial wave analysis for a similar scatterer to show the presence of two types of waves.

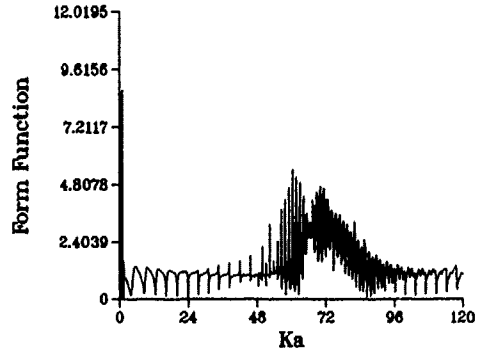

Fig. 1a Backscatter from 2% Al Shell,

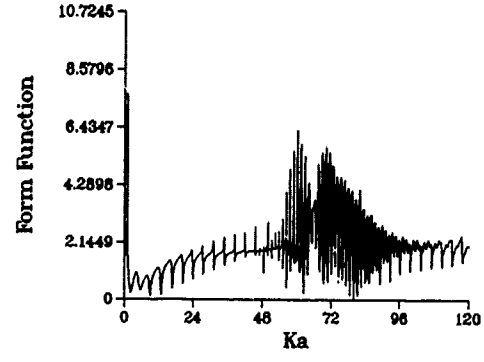

Fig. 1b Backscatter minus soft background.

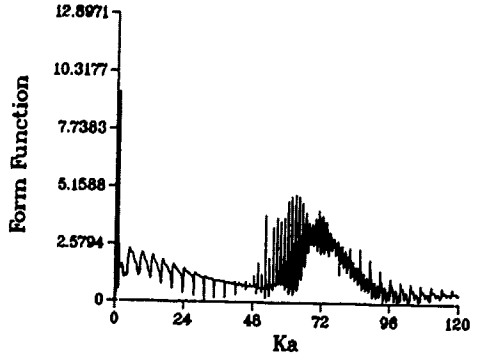

Fig. 1c Backscatter minus rigid background.

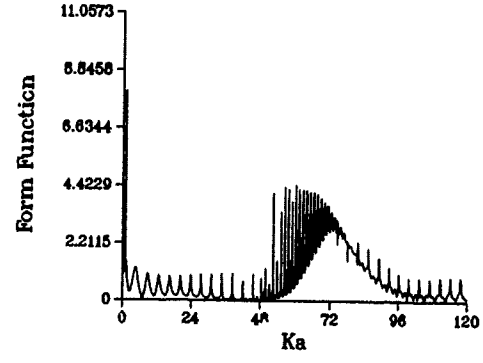

Fig. 1d Backscatter minus new background.

Partial wave analysis

If one subtracts the correct background from the elastic response then by definition one is left with the "pure" resonance response. Resonances excited on bodies of canonical shape usually correspond to circumferentially excited waves which for spheres have a unique wave number. To be sure, this fact can be obscured by, for example, broadly overlapping partial waves; but none the less by plotting the residual partial wave components-which is here referred to as a partial wave analysis-can be very revealing. There are two ways to perform a partial wave analysis: one can fix the mode number N and plot the residual response with respect to ka. On the other hand one can fix ka and plot the partial wave form function with respect to mode number N. The first of these approaches is the most commonly used but it will be demonstrated that the second approach offers a very powerful interpretative tool. The second approach will be referred to as a full partial wave analysis (FPWA) to distinguish it from the first case and because it involves all the partial waves for any fixed value of ka. We now

examine back scatter signals from a 2.5% thick steel shell for ka=20 to 60. Fig. 2a illustrates mainly the region about coincidence frequency centered about ka=44. We can better understand what is happening be subtracting the new background to leave Fig. 2b which illustrates a series of spikes as well as what appears to be an envelop of some sort. We can determine what is happening be performing a FPWA at one of the lower spikes at Ka=31, an intermediate value at ka=37 and a higher value at ka=51. The analysis is illustrated in Fig. 3a, 3b, and 3c respectively. In each of the figures we see the presence of two waves. In the lowest two cases we observe a sharp well defined subsonic wave, and a weak broad sonic wave. Since we know that this takes place at about coincidence we infer that the broad wave represents the inception of a flexural resonance. We know from scattering from flat plates evacuated on one side and fluid loaded on the other that water borne waves (subsonic) exist at coincidence frequency and are referred to as Stoneley waves[15]. Thus we infer (in analogy with the flat plate case) that that subsonic sharp peak is associated with a Stoneley wave on a flat plate and thus is a pseudo-Stoneley resonance. We see from Fig. 3c that at some point the waves seem to merge but actually what happens is that the pseudo-Stoneley wave dissipates as it reaches the speed of sound of the fluid and another type of water borne wave begins to grow and to maintain prominence with increasing frequency. We will discuss the case below. We can also perform a study of the phase velocities of the two waves. The results are illustrated in Fig.4 (associated with the pseudo-Stoneley resonance) and Fig. 5 (the phase velocity associated with a flexural resonance). Note that the pseudo-Stoneley wave is of limited range and is mainly subsonic.

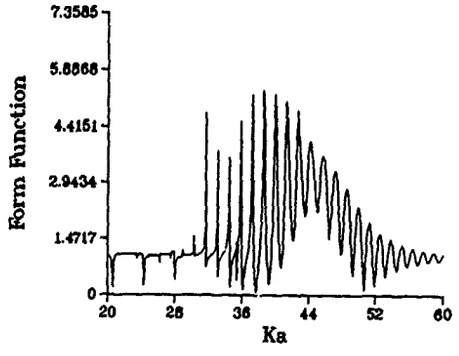

Fig. 2a Backscatter from 2.5% steel shell.

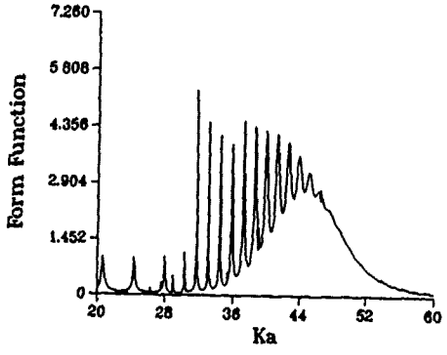

Fig. 2b Backscatter minus new background.

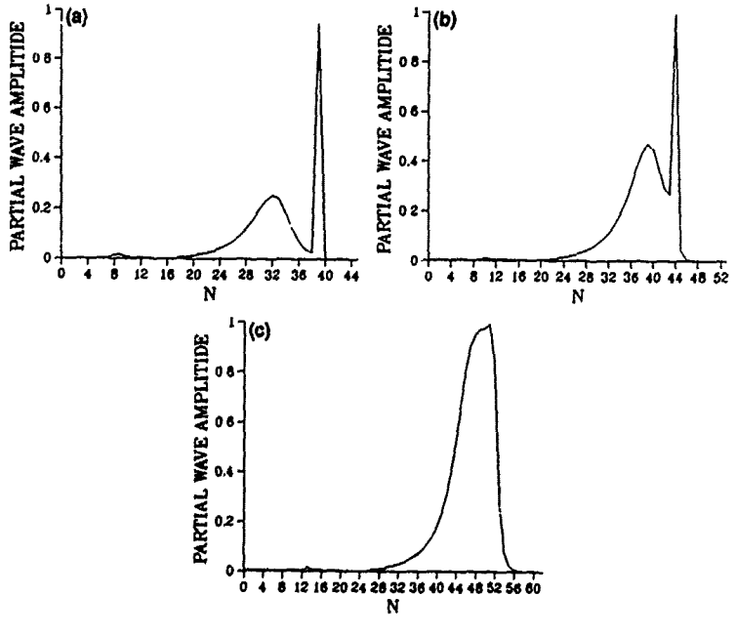

Fig. 3 Partial wave analysis for ka a) 31, b) 36, c) 51

Time Domain Resonance Scattering Theory

The partial wave series that emerges from normal mode theory for separable geometries can be represented in distinct partial waves or modes. It has been shown[1,2] that a representation due to a distinct mode{n} can be written in the form

$$f_n(\theta) = \frac{2}{ka} e^{2i\xi_n^{(r)}} \{ \frac{(\frac{1}{2})\Gamma_n^{(r)}}{\chi - \chi_n^{(r)} + (\frac{i}{2})\Gamma_n^{(r)}} + e^{-i\xi_n^{(r)}} \mathrm{Sin}\xi_n^{(r)} \} \qquad (1)$$

where $\chi = ka$, $\chi_n^{(r)}$ is the nth resonance and $(\frac{1}{2})\Gamma_n^{(r)}$ the half − width.

Where $e^{2i\xi_n^{(r)}} = -\frac{h_n^{(2)'}(x)}{h_n^{(1)'}(x)}$

Here, the factor 2n+1 is absorbed in the expansion coefficient. For the pulse form a continuous wave (cw) ping is used which corresponds to a very broad frequency range. For each time domain modal component one has that

$$\mathrm{Re} \int_{-\infty}^{\infty} \frac{(\frac{1}{2})\Gamma_n^{(r)}}{\chi - \chi_n^{(r)} + (\frac{i}{2})\Gamma_n^{(r)}} e^{-ixs} dx = 2\pi(\frac{1}{2})\Gamma_n^{(r)} \mathrm{Sin}(\chi_n^{(r)} s) e^{-(\frac{1}{2})s\Gamma_n^{(r)}} . \qquad (2)$$

That is, at a resonance the time domain solution is simply the product of the half-width times a sinuosoidal function times an exponential damping factor. From the time domain solution for a nest of resonances (N-m) for a cw ping, one obtains the form

$$p(s) \approx 2\pi \sum_{n=m}^{N} (\frac{1}{2})\Gamma_n^{(r)} \mathrm{Sin}(\chi_n^{(r)} s) e^{-(\frac{1}{2})s\Gamma_n^{(r)}} . \qquad (3)$$

The remaining contributions from backscatter are small due to phase averaging.

It is assumed that calculations are performed in a resonance region for which the resonance widths are fairly constant and the resonance spacing is fairly uniform[8,9]. This assumption leads to the important expression

$$P(s) \approx 2\pi 2^M (\mathrm{Sin}(\chi_{ave}^{(r)} S) \{\mathrm{Cos}(\Delta\chi_{ave}^{(r)} s / 2)\}^M e^{-s\Gamma/2}, \qquad (4)$$

where $\chi_{ave}^{(r)} = \frac{1}{2M} \sum_{i=n}^{n+2M} \chi_i^{(r)}$.

Here one sets n-m=2M. It is seen from the above expression that the half-width is associated with the decay of the response in the time domain solution. When the number of adjacent resonances (2M) sensed increases, the return signal becomes more sharply defined and the envelope function (the beats) are more enhanced and clearly defined Finally, for larger carrier frequencies, the signal is more oscillatory within the envelope.

Time Domain Back Scatter at Coincidence Frequency

Flexural waves do not yield resonances from fluid-loaded shells until the phase velocity of the flexural wave is about equal to the speed of sound in the ambient fluid. The value in frequency for which this happens is referred to as the coincidence frequency ; however, some subsonic fluid-borne waves produce sharp [8,9,14,15] resonances below coincidence frequency. These waves are referred to as pseudo-Stoneley waves and the related

resonances as pseudo-Stoneley resonances.[8,15] The pseudo-Stoneley resonances are well defined in partial wave space; they usually correspond to only one partial wave mode number and a very narrow half-width with a dispersive phase velocity, which approaches the speed of sound in the fluid with increasing frequency. The pseudo-Stoneley resonances diminish in significance at the point where the flexural resonances begin to dominate. It can be determined that a phase change occurs in the pressure field in the transition region from subsonic to supersonic. This change accounts for the envelope of the resonance curve at coincidence frequency where the waves are in phase until coincidence and are out of phase afterwards. Our interest here is in examining the time domain response, since one expects the conditions previously described to be partially met over a broad frequency range and thus to yield a strong coherent response with a carrier frequency in the neighborhood of the frequency at coincidence. Accordingly, the case of cw pings for two examples - for which coincidence resonances are expected to arise - is examined. This is certainly suggested by the strong responses in Figs. 6b and 7b at the ka values 113 and 87, respectively, for steel and WC. Further, in this analysis the Mindlin-Timoshenko [16] thick plate theory is used to determine the value for which the flexural phase velocity will equal the speed of sound in water. The phase and group velocities are determined from flat plate theory which proves to be quite reliable in predicting the phase velocity for the curved surfaces of the spheres at coincidence frequency.

The time domain calculations are now examined. The first example is a steel shell of 1% thickness. In this case a well-defined envelope (illustrated in Fig. 6a) with pronounced oscillations within the envelope is consistent with Eq. 4. The enhancement due to the factor 2^M is obvious. The group velocity can be obtained from the peak-to-peak distance of the adjacent envelopes. The result leads to a value of 2.23 km/sec. Both flexural and pseudo-Stoneley resonances compete in this region. A mixture of pseudo-Stoneley waves, as well as flexural waves must be leaking into the fluid. For flexural waves, the group velocity is 2.53 km / sec at coincidence frequency with a range between 2.44 and 2.68 km / sec. over the ka range of 100-140, where the strong flexurals are significant. In that range the phase velocity varies from 1.37 to 1.58 km/sec. The values of the extracted group velocity does not agree well with the flexural group velocity ; the discrepancy is 12%. This variation suggests that in the time sequence the flexural resonances are of little importance for the time sequence presented here. The group velocity of the pseudo-Stoneley waves for this case has been determined[14] to be 2.16 km / sec based on plate theory. The phase velocity is in the range from 88% to 98% of the speed of sound in the fluid. This value of group velocity is within 3% of the extracted value from the time domain solution. Moreover the pseudo-Stoneley resonances have very narrow widths while the flexural resonances are quite large. The conditions in the previous section would indicate that the flexural resonances would rapidly dampen due to the large half-widths while the pseudo-Stoneley resonances would attenuate slowly in time. Thus, based on the similarity of the extracted group velocity and that of the pseudo-Stoneley wave and the conditions in the previous section on level widths, one may conclude that the time domain calculations in Fig. 6a represent pseudo-Stoneley resonances. A similar argument holds for WC for Fig. 7a.

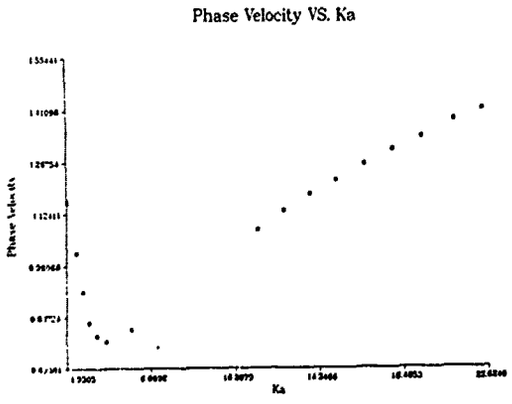

Fig. 4 Phase velocity for pseudo-Stoneley resonance.

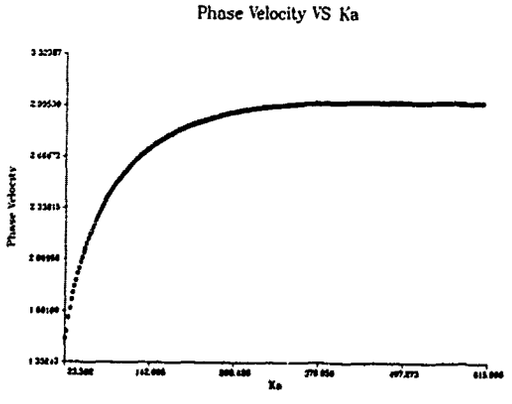

Fig. 5 Phase velocity for flexural resonance.

Pure Water borne Waves

The above analysis dealt with pseudo-Stoneley waves. There is another phenomenon due to waves that have phase velocities that correspond to about the speed of sound in water. They are not, however, sharply defined in partial wave space, nor are they associated with the flexural wave at coincidence frequency. They are associated with the density of the material, and the thickness (really just the mass of the target) and the frequency. Their importance increases with frequency and they do not manifest themselves as sharp resonances in the form function

but rather wash-out other resonances such as the S_0 and A_0 resonances. Thus for light material and thin shells such as Aluminum and at high frequency one does not observe sharp resonances due to this wash out effect. Figs. 8 and 9 illustrate this effect in partial wave space for Aluminum of 2.5%, and an Aluminum shell of 5% at a ka of 250. It is clear that there is a prominent contribution in each case corresponding to a phase velocity equal to the speed of sound in water (it is centered about 250 indicative of a slightly subsonic wave). The other peaks correspond to the Lamb waves. Clearly, the effect is more pronounced for thinner (lighter materials) shells. In Fig. 10 we illustrate a plot of the phase velocity of this wave for the 5% steel case. An extensive study of this phenomena is to be presented in a future work including the sensitivity to material properties and the overall effect on the form function.

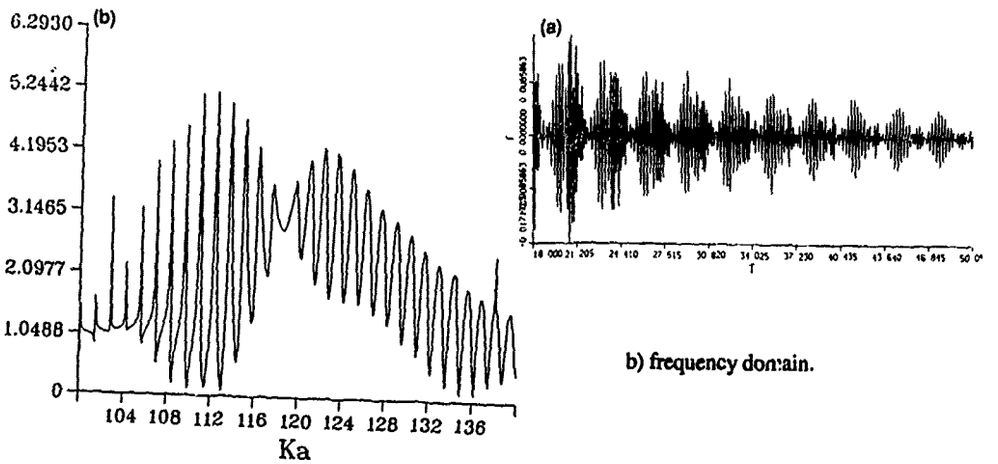

b) frequency domain.

Fig. 6 Scattering from 1% steel shell a) Time domain,

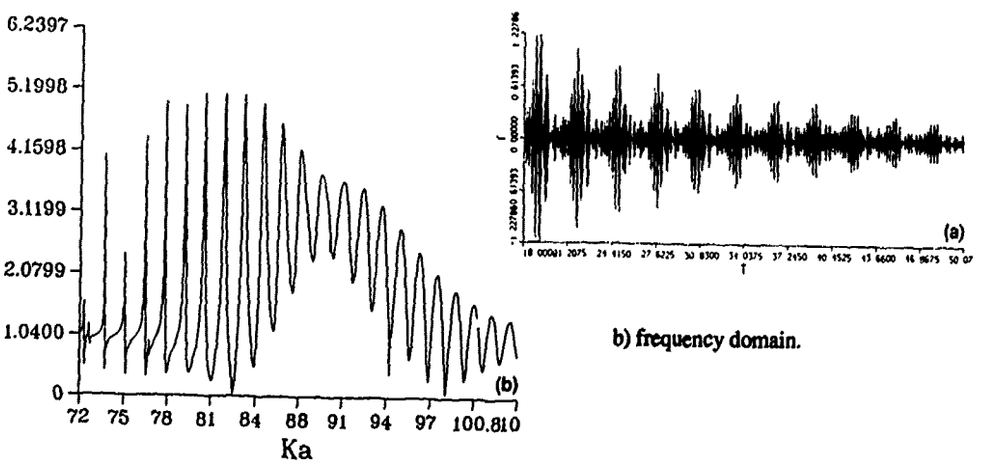

b) frequency domain.

Fig. 7 Scattering from 1% WC shell a) Time domain,

Conclusions

We have used the new acoustic back ground for an elastic shell, partial wave analysis and a time domain version of re[illegible] scattering theory to discuss several interesting resonances recently under study. One can see how use of these [illegible] along with analogies with flat plate results enable one to infer the nature of such complicated phenomena. The fact that several competing events can occur in the same frequency region perhaps renders the direct measurement of surface vibrations less useful then an inferential approach. On the other hand an inference does not guarantee that that inferred is always the correct interpretation.

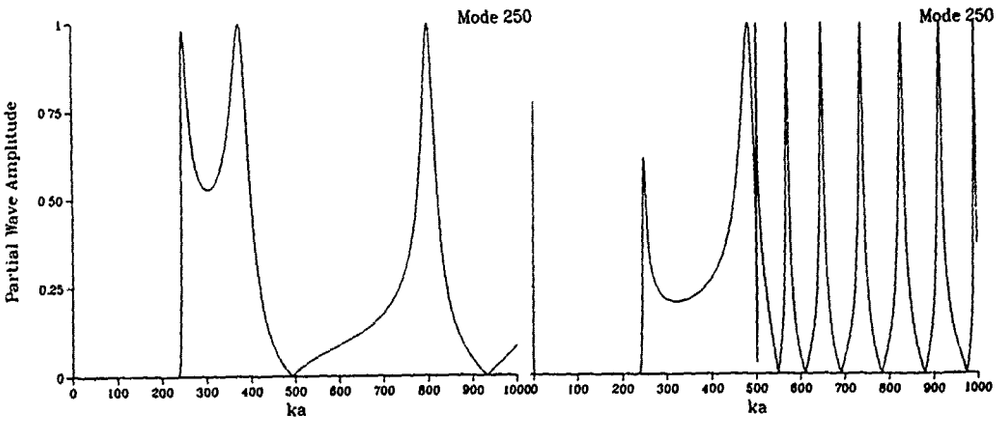

Fig. 8 Full partial Wave Analysis for 2.5% Aluminum Shell.

Fig. 9 Full partial Wave Analysis for 5% Aluminum Shell.

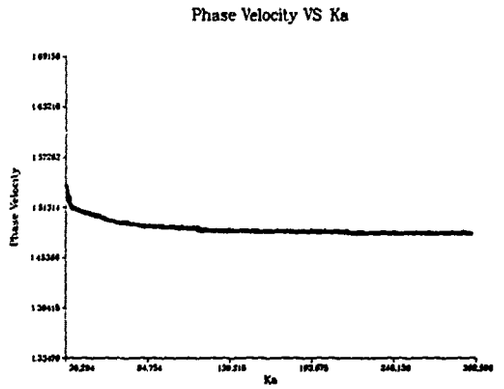

Fig.10 Phase velocity for pure water borne resonance.

Acknowledgments One of us (MFW) wishes to thank NRL management at Stennis Space Center for their continued support and in particular PE 0601153n and Dr E. Franchi. NRL contribution number PR 92:052:221.

References

1. H. Überall, " Model and surface-wave resonances in acoustic-wave scattering from elastic objects and in elastic-wave scattering from cavities,", p. 239-263, in Proceedings of the IUTAM Symposium: Modern Problems in Elastic Wave Propagation", Northwestern Univ., Evanston, Il. Sept. 12-15, 1977, edited by J. Miklowitz and J. D. Auchenbach, Wiley Interscience , New York, (1978)

2. L. Flax, L.R. Dragonette, and H. Überall, " Theory of elastic resonance excitation by sound scattering ", J. Acoust. Soc. Amer. 63, 723-731, (1978)

3. M.F. Werby, " The Isolation of Resonances and the Ideal Acoustical Background for Submerged Elastic Shells", Acoustics Letters Vol. 15, No.4 (1991) pp. 65-69

4. M.F.Werby, "The Acoustical Background for a Submerged Elastic Shell", J. Acoust. Soc. Amer. 90, 3279-3287, (1991)

5. M. F. Werby, "Recent Developments in Scattering from Submerged Elastic and Rigid Targets", in Proceedings on " Resonance Scattering Theory " at the Conference in May, 1989 at Catholic University of America, Editor, H. Überall, in press

6. M. F. Werby and H. Überall, " The Excitation of Waterborne waves at the Interface of evacuated shells and pseudo-Stoneley Resonances", Deuxième Congrès Français d'Acoustique, Arcachon, France, 14-17 April, 1992.

7. R. Hickling, Private Communication.

8. M.F. Werby and H.B. Ali, " Time Domain Scattering from the Frequency Domain: Applications to Resonance Scattering from Elastic Bodies", Computational Acoustics Vol. 2, D. Lee, A. Cakmak, R. Vichnevetsky (Editors), Elsevier Science Publications B. V. (North Holland) IMACS, 1990, pp. 133-148

9. M. F. Werby and J. Dicky, " Transient scattering from Elastic Targets", in Proceedings on " Resonance Scattering Theory " at the Conference in May, 1989 at Catholic University of America, Editor, H. Überall, in press

10. Murphy J.D., E.D. Breitenback and Überall,H.," Resonance Scattering of Acoustic Waves from Cylindrical Shells", J. Acoust. Soc. Am. 64(1978),677

11. E.D. Brietenback, Herbert Überall and Kwang-Bock Yoo, " Resonance Acoustic Scattering from elastic cylindrical shells ", J. Acoust. Soc. Am. 74 (1883) 1267

12. M.F. Werby and G.C. Gaunaurd, " Transition from soft to rigid behavior in scattering from submerged thin elastic shells' , Acoustics Letters, Vol. 9, No. 7, pp. 89-93 (1986)

13. M. F. Werby and L. H. Green, " A comparison of Acoustical Scattering from fluid loaded elastic shells and Sound-soft objects", J. Acoust. Soc. Amer. 76 (1984) 1227

14. Maryline Talmant, H. Überall, R.D. Miller, M.F. Werby and J.W. Dickey, " Lamb waves and Fluid-Borne Waves on Water-Loaded , Air filled thin Spherical Shells", To Appear in J. Acoust. Soc. Amer. 1989

15. Gerard Quentin and Maryline Talmant, " The Plane Plate Model Applied to Scattering of The Ultrasonic Waves From Cylindrical Shells", in Proceedings of the Int. Conf. on Elastic Wave Propagation, M.F. McCarthy, M.A. Hayes (Editors) Elsevier Science Publishers B.V. (North-Holland), 1989

16. M. F. Werby and G. C. Gaunaurd, " Critical Frequencies for large scale resonance signatures from elastic bodies", SPIE Conference on "Automatic Object Recognition", Proceedings, Paper # 1741-01, April, 1991 (in press)

SECOND INTERNATIONAL CONGRESS ON
RECENT DEVELOPMENTS IN AIR- AND
STRUCTURE-BORNE SOUND AND VIBRATION
MARCH 4-6, 1992 AUBURN UNIVERSITY, USA

SOUND POWER DETERMINATION OF A MULTINOISE SOURCES SYSTEM USING SOUND INTENSITY TECHNIQUE

Mirko Čudina
University of Ljubljana
Faculty of Mechanical Engineering
Murnikova 2, 61000 Ljubljana
SLOVENIA

ABSTRACT

With an IC engine running of and the bus being at standstill on a peaceful site, noise in the bus interior is generated only by the heating, ventilating and airconditioning (HVAC) systems. In order to minimize the noise originating from the HVAC systems it is necessary to separate the different sound components and determine their sound power. For the sound sources identification and their power determination the sound intensity measurement method was applied. This paper presents the results of sound intensity measurements which have been carried out on HVAC system operating in situ (with quasi reverberant sound field in the bus) and in a free field (in an anechoic room), by the discrete point method and scanning method at different measurement distances.

INTRODUCTION

In the case of a system with multiple noise sources, such as the HVAC system in a bus interior, beside the interference between the sources, the reactivity of the sound field would influence their identification and sound power determination. The reliability of the sound power determination from intensity measurements depends also on many other factors, such as radiation characteristics, sampling techniques (discrete points or scanning method), measurement distance, shape of measurement surface and so on. The purpose of this investigation was to evaluate and rank the noise sources in the HVAC system and find out the effect of the acoustic field in which the HVAC system was measured, as well as the effects of the measurement distance and techniques of sampling on the reliability of sound power determination.

The HVAC system contains components which take in the cold air from the bus interior or exterior and lead it through a heat exchanger, pressing the thus warmed air by means of fans into the bus interior. Here the particular sound sources are the fans, the heat exchanger and intake and exhaust openings. This paper should answer a question of how much sound power radiates from the particular components of the HVAC system. The results are presented for only two noisiest parts of the HVAC system: the heater in front of the driver and the underfloor heater, Fig. 1, /1/.

TEST PROCEDURE

A HVAC system in a tourist bus TAM 260 A 11U T was used for the tests, /2/. To determine the sound power of particular noise sources inside the HVAC systems two test series were performed. The first test series were performed in situ in the conditions of the IC engine running of and the bus being at standstill on a peaceful site, whereas the second test series were carried out in a free field - in an anechoic room in which a reflective floor was made of concrete panels. In both cases the HVAC systems were operated at highest power or speed at 24 Volts.

sound-power measurements, for diagnostic design work, and to get the standard necessary for engineering grade measurement.

Averaging Time. Using the discrete points method in each measurement position the averaging time was 14 s (100 averaging). In the case of the scanning method, different scanning speeds were investigated from 0.05 m/s, 0.08 m/s to 0.1 m/s. For all speed rates similar measurement results were obtained, being also similar to the measurement in discrete points, therefore a fast scanning speed of 0.1 m/s was chosen for further measurements as it was easier to control it. The same scanning speed was used for measurement in the far field as well as in the near field.

Measurement Surface was prepared according to ISO/DIS 9614 standard. Considering the purpose of the investigation, the measurement surface may be farther away in a far field and close to the source in a near field. In the case of the total sound power determination of the heater as the whole source, the measurement surface was prepared as an imaginary cubical enclosure around the source in a far field.

For the sound power determination of particular components of the multiple noise source and sound distribution location over a multiple source, the measurement surface was taken close to the source surface in a near field.

On each measuring surface in the far field, the normal sound intensity was measured using two different sampling techniques: in discrete points at the centre of each segment of the measurement surface and by the manual scanning method over the contour of the measurement surface, making sure that the probe was always pointed towards the measurement surface.

Distance to the Measurement Surface. In situ the distance between the source surface and measurement surface was limited by the geometrical obstruction of passenger seats in the bus interior, whereas in the anechoic room there were no limitations. The distance between the source surface and the measuring surface is dictated by measuring accuracy, i.e. by the number of measurement points and by the air flow velocity that should be smaller than 1 m/s. In situ measurements, the distance between the source surface and the measurement surface was for the heater in front of the driver 0.5 m and for the underfloor heater 0.13 m.

In free field measurements (in an anechoic room), the measurement surface was a cubic enclosure of 1 m side length set around the sound source.

The distance between the source surface and the measuring surface in near field was constant over the entire surface and was determined by the physical dimension of the intensity probe with a windscreen (approximately 5 cm). The foam windscreen on the intensity probe was used to minimize pressure disturbances at the microphones in the case of high air flow velocity.

Number of Measurement Positions. The approach of sampling at discrete points allows the accuracy of the sound power estimate to be determined from the individual intensity measurements. This is true however, only when a sufficient number of measurements are made. The size of the mesh segments on the measurement surface was fixed in accordance with the field non-uniformity indicator F_4 and formula determining a minimum number of measurement positions $N_{min} \geq C.F_4^2$ (C is constant, defining the precision in ISO/DIS 9614, for the frequency range from 160 to 5000 Hz C = 28) guarantying given uncertainty limits. When the measuring points are many, the measurement time becomes longer, so the appropriate measuring points should be determined by the accuracy required. The number of microphone positions is in close relation to the measurement distance from the source. For high accuracy the smaller number of microphone positions demands the larger measurement distance. In band without significant extraneous noise a smaller number of measurement points is needed at the greater distance.

In the measurements which were made in the anechoic room on dismantled heaters in absence of the undesirable extraneous sound, the values of the indicator F_4 are smaller and number of measurement positions could be lesser. In the case of in situ measurements, the number of microphone positions for the heater in front of the driver was 123 and for the underfloor heater 35, whereas in free field measurements (in anechoic chamber) it was 80 in both cases.

The measurement surface in far field was divided into segments in the form of a mesh according to the number of measurement positions needed. In situ, the measurement surface for heater in front of the driver was divided into segments of 10 x 10 cm and

The sound intensity was measured with equipment consisting of a B & K p-p type 3519 probe, fitted with 1/2 inch diameter phase-matched microphones. The spacer between the microphones was 12 mm for a frequency range from 160 Hz to 5 kHz. The middle of the spacer runs through the measurement surface. The pressure signals from the microphones were fed to the dual channel signal analyzer B & K Type 2032. The analyzer directly computed the spectrum of sound intensity, using the cross spectrum between the two input sound pressure signals. This spectrum was postprocessed using a HP-3852A computer so that the output from the computer could be sent to a printer or a plotter. The microphones were calibrated using a pistonphone.

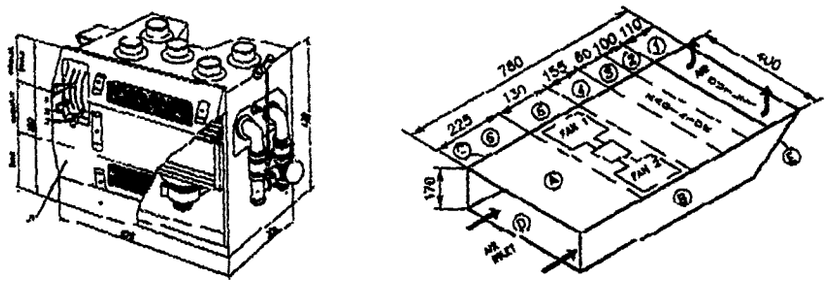

a) b)

Fig. 1. a) Heater in front of driver, b) Underfloor heater.

SOUND INTENSITY MEASUREMENT

Two main advantages of sound intensity measurement are: the ability to measure the acoustic power of the sound source in situ giving access to the quantitative radiation, and the ability to estimate the partial acoustic power related to some of the source's components. A necessary precondition to distinguish acoustic power radiated by various parts or buildings components of the studded source is a sufficiently wide space between the noisy components to be estimated. The total sound intensity of the HVAC system and its particular components was measured in situ and in the anechoic room.

The sound intensity measurements were carried out according to ISO/DIS 9614 and ANSI S 12.12-1987, and the sound power levels were calculated according to the same standards. The sound intensity level and sound pressure level were measured simultaneously and then the sound field indicators were calculated. But, beforehand, we have to make a selection of the measurement parameters such as: the actual measurement surface with the number and array of measurement positions, the type of spatial averaging (discrete point vs. scanning method), measurement distance and performance of measurement equipment (required frequency range, frequency resolution, microphone spacing, time integration, etc.).

Frequency Resolution may be narrow band, 1/3 or 1/1 octave band and wide band. The narrow band is very time consuming, therefore, for the total sound power estimation from the positive-going sound intensity (which represents the sound energy coming from the test source), the wide band resolution was chosen, /1/.

Spatial Averaging. Sound intensity measurements may be made in discrete points on a grid and as a space-time average by scanning with the SI probe during data acquisition. In principle, the scanning method can give a more accurate estimate of the source sound power with fewer measurements than a discrete point method. The scanning method also saves measurement time in general. But, determination of sound power using the intensity technique according to ISO/DIS 9614 standard is based on discrete point measurements. The scanning method is not considered, as no means of evaluating the spatial variance is proposed, and it is thereby not possible to determine the accuracy class of the measurement. In the proposed ANSI S 12.12 there is a procedure to evaluate the results using scan measurements.

The discrete points method is used to determine the overall radiation of the particular surface and to providing more information on the radiation patterns of the surface under consideration. The scanning method is used to provide information on the overall radiation through the surface. The scanning method is suitable for quick total

for the underfloor heater into segments of 10 x 6.5 cm. In the anechoic room the measurement surface was divided into 16 segments of 25 x 25 cm areas.

The measurement surface in near field was also divided into imaginary segments which cover a size of a significant source inside the multiple noise source (see Fig. 1). In near field measurements it is not necessary to make a grid. On each measuring surface over the contour of the sound source in the near field, the normal sound intensity was suitably measured only by the scanning method. In this case the total sound power of the particular components of the multiple noise source could be determined.

Multiple Source Interaction. Sound intensity provides a measure of the net flow of acoustic energy through a surface, defining both the magnitude and direction of this quantity. The sound power level can be obtained by calculations from the product of the area of the measurement surface and the mean value of the normal sound intensity component. Therefore, theoretically, sound power evaluation should be independent of environment or interference out of the measurement surface. But in practice the errors can appear because of errors in the intensity measurement caused by the interference or standing waves and directivity of the SI probe. In the reactive sound field in the bus interior at low frequencies standing waves may exist and sound intensity probe will not account for this energy as there is no net energy flow. The error in the measurement is not well established if the source under test has large surfaces which may absorb or reflect the sound that enters the measurement surface from outside.

When the acoustic field of primary source is unwerely interfered by a secondary source (so-called active interference) or boundary reflections (so-called passive interference) additional field errors due to interference are expected. As the intensity field is a vector field, any interference (either active or passive) will introduce changes in magnitude and in directivity pattern of the acoustic field of the primary source. The interference depends on the location of a field point with regard to the primary and parasitic source, distances among the sources and the measurement points to the sources, source strengths and its directivity path, phase differences among sources and acoustic frequency, radiation characteristics of the sources, diffraction, etc. Diffraction occurs in the near field of the source and can distort the radiation characteristics of the source. The surrounding structure holding the IS probe may cause diffraction which is detrimental to the radiation pattern.

To determine the effects of interference due to presence of background (extraneous) noise, the pressure-intensity or interference indicator F_2 is used. In a general sound field there are always two components, the direct sound and diffuse sound. The diffuse sound has great influence on sound pressure whereas the direct sound has an influence on sound intensity. If the primary sound source is superposed by a diffuse extraneous sound interference descriptor $F_2 = F_3$, and if parasitic noise is incidenting directly into the measurement surface, then $F_2 < F_3$. Only the measurement of an anomalously low or even negative value for intensity indicates the presence of strong extraneous noise. The pressure-intensity indicator F_2 is used to check data validity allowing invalid data points to be repeated. As a basic guide-line, indicator F_2 should not exceed 10 dB for engineering accuracy.

The sound intensity method is not affected by background noise when the external noise is steady noise and when sound field indicators (according to ISO/DIS 9614) are satisfied. In the other cases modifications of the measurement field must be done. In situ measurements (in the bus) were of this kind, therefore, efforts were made to eliminate the undesirable extraneous sound field (with eliminating negative-going components of the intensity spectrum) on the measurement surface. This method can be used only for sources radiating broad band noise and if the estimated parameter is the total sound power level of the source. The checking of the frequency feature of the source is necessary every so often. The elimination of the strong directly incidencing sound was achieved by wrapping the disturbing extraneous sound sources (e.g. in the case of operating of two opposite installed underfloor heaters which correlated) and by introducing additional sound absorption. Alternative methods to this would be a longer distance between the source and the measurement surface, if it is possible, and a longer measurement time.

Measurement Uncertainty Origin. The both kinds of the measurement surfaces (in far field and in near field) and both kinds of the spatial averaging (discrete point and scanning method) were used in situ in the bus as well as in an anechoic room. Different results or at least their uncertainty could be expected. The differences may have origin in the different measurement conditions such as: the nature of the sound field

(interference, standing waves, etc.), shape and distance of the measurement surface around the noise source in the bus and in the anechoic room, variability in the acoustic output of the source, excessive levels (and/or variability) of background noise, SI probe directivity, lesser measurement accuracy for a scanning approach vs. discrete points method and so on.

In the bus the sound field is diffuse with quasi reverberant characteristics, whereas in an anechoic room a quasi free field with absorptive surrounding walls was created. In situ measurement free surfaces, which radiate the main noise from the source (heater) in the bus interior is only surface A in Fig. 1a and surface D in Fig. 1b, whereas in the measurements in anechoic room the measured source radiates noise in all directions (without the sound path damping or disturbing).

EXPERIMENTAL RESULTS AND DISCUSSION

Heater in Front of the Driver

A sketch of the heater is shown in Fig. 1a. It consists of two axial fans below, a heat exchanger in the middle, and exhaust pouts above. The heat exchanger is out of operation during the measurements. The speed of the fans was maximal.

Results of the First Test Series in Situ. In situ, the measurement surface was built in front of the heater (in front of the surface A) at a distance of 0.5 m. The measurement surface was divided by threads into meshes with an area of 0.01 m^2. The centres of these areas were used as microphone positions. The sound intensity

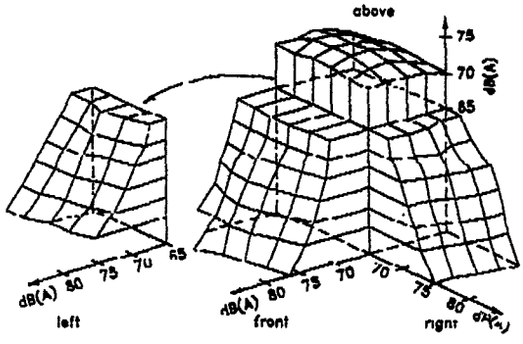

a)

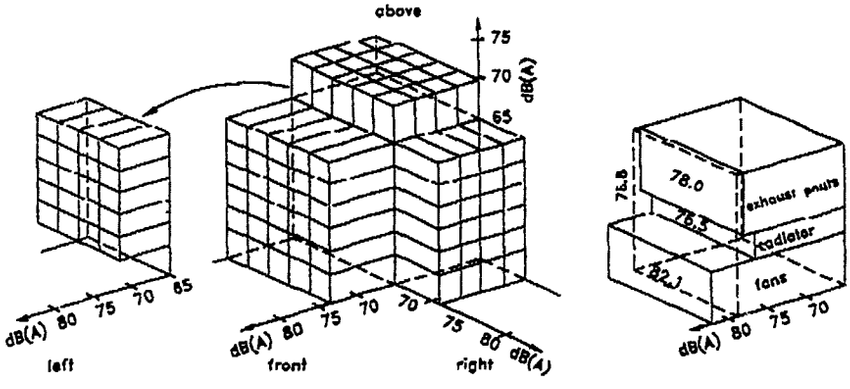

b) c)

Fig. 2. 3-D presentation of normal sound intensity on the heater in front of driver, measured in situ: a) by discrete points in far field, b) by scanning method in far field, c) by scanning method in near field.

Table 1. Comparison of the sound intensities measured in situ using discrete points and scanning method.

Surface	left	front	right	above	total
in discrete points	70.9	73.1	71.8	71.7	72.1
by scanning method	71.6	72.2	71.1	70.7	71.2
difference	+0.7	-0.9	-0.7	-1.0	-0.9

measurement results obtained by the discrete points method are shown in Fig. 2a in 3-D presentation. Fig. 2b presents sound intensity distributions on the measurement surface made by the scanning method. Integrated values of the sound intensity on the particular surfaces are presented in Table 1 to compare the results obtained by the discrete points to those obtained by scanning method.

Differences in Table 1 between the integrated results over the control surfaces obtained by discrete points and the scanning method are due to a larger distance (by 5 cm) in case of the scanning method. But the differences between the results shown in Fig. 2a and 2b are qualitative. From Fig. 2a the sound intensity distribution is evident whereas from Fig. 2b it is not. The scanning method thus gave less information than the discrete points method, but the scanning method can be improved by forming smaller integrated areas close to the source surface in near field. The measured results in near field using the scanning method are shown in Fig. 2c. It can be seen that the scanning method used in near field can give more information than the discrete points method in far field. Total sound power, however, for all three measurement approaches does not differ much from one another, see Table 2.

Table 2. Comparison of the sound power measured in situ using discrete points and scanning method.

Measurement method	discrete points in far field	scanning method in far field	scanning method in near field
Sound power	75.0 dB(A)	74.7 dB(A)	74.0 dB(A)

From Fig. 2a and 2c we can see that the main noise source of the heater in front of the driver is emitted from the fans below. Fig. 2c shows that the noise source second in strength is exhaust pouts above and not the radiator as it seems from Fig. 2a. That means that the scanning method used in the near field can give more information than the discrete points method in the far field. The discrete method used in the near field is time consuming and less accurate than the scanning method owing to diffraction existing in the near field.

Results of the Second Test Series in an Anechoic Room. In the case of in situ measurement, the heater in front of the driver is examined only in front of surface A (see Fig. 1a), because other surfaces are hidden in a bus chassis. In an anechoic room, however, radiated noise could be measured, also in near field, in all directions of the dismantled heater. But information about noise sources from surface A are most important. Table 3 presents the results measured in the anechoic room in the far field and in the near field.

Table 3. Comparison of the sound power measured in anechoic room using discrete points and scanning method.

Measurement conditions	discrete points in far field	scanning method in far field	scanning method in near field
Sound power	78.0 dB(A)	77.9 dB(A)	78.2 dB(A)

From Table 3 it can be seen that the total sound power is nearly independent on measurement method used. The sound intensity of the particular sources (fans, radiator and exhaust ports) was measured in the near field in the anechoic room too. Their sound powers and reciprocal relation were very similar to those in Fig. 2c.

Underfloor Heater

A sketch of the underfloor heater is presented in Fig. 1b. It consists of a duplex centrifugal fan, a heat exchanger (radiator) and a casing with an inlet and outlet air flow opening.

Results of the First Test Series in Situ. The measurement surface was built at a distance of 0.13 m in front of the heater (in front of surface D). The measurement surface was divided by threads into meshes with an area of 0.0065 m^2. The centres of these areas were used as microphone positions. The sound intensity measurement results obtained by the discrete points method are shown in Fig. 3a in 3-D presentation. Integrated values of the sound intensity on the particular measurement surfaces are presented in Table 4 to make a comparison between the discrete points and the scanning method.

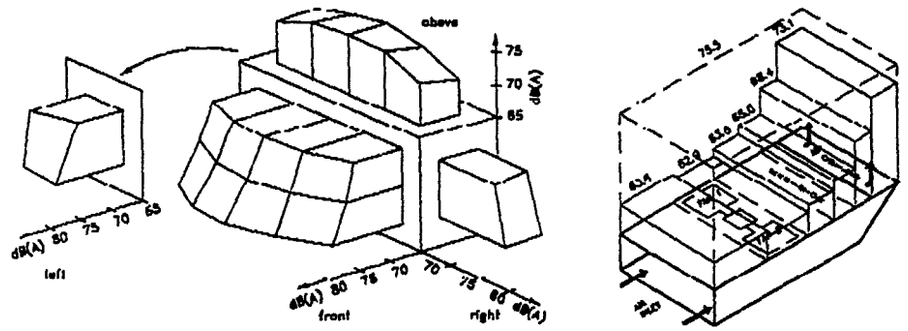

Fig 3: a) Normal sound intensity of the underfloor heater measured by discrete points method in the far field in situ, b) sound power distribution alongside the underfloor heater measured by the scanning method in the near field in free field.

Table 4. Comparison of the sound intensities measured in situ using discrete points and scanning method.

Surface	left	front	right	above	total
in discrete points	74.6	77.7	74.7	72.8	76.0
by scanning method	73.3	76.5	74.2	71.5	74.8
difference	-1.3	-1.2	-0.5	-1.3	-1.2

In Table 4 the differences between the sound intensities measured by discrete points and the scanning method are higher than those in Table 1. The reason for this is a relatively longer measurement distance to the probe centre in the case of the sweeping method. Certain effect is exerted also by the sound field reactivity in narrow space in front of the heater. The calculated sound power is the same for both cases and similar to that obtained by scanning method in the near field, see Table 5.

Results of the Second Test Series in an Anechoic Room. In the case of in situ measurement, the underfloor heater was examined in front of the air inlet opening because only from this side the underfloor heater radiates the main part of the noise into the bus interior. But the results obtained so could not be used to noise control of the underfloor heater. For this reason, more information has to be acquired.

Table 5. Comparison of the sound power measured in situ using discrete points and scanning method.

Measurement method	discrete points in far field	scanning method in far field	scanning method in near field
Sound power	69.2 dB(A)	69.2 dB(A)	69.8 dB(A)

Measurements in an anechoic room on a dismantled underfloor heater would be able to give more information about noise sources inside the heater. The measurements of the sound intensity of the heater in the far field, at a distance of 1 m, do not give a proper answer to it. Therefore, sound intensity measurements in the near field must be made. Fig. 3b presents sound intensity distributions alongside the heater measured in the near field by the scanning method. It can be seen that the main noise source originates from the air outlet opening and the minimum sound power radiates from the part representing the air moving device. The noise generated by the duplex fan, which is at the top side damped by a cover plate, is transmitted by air as aerodynamic noise through an outlet opening and to a smaller extent in the air inlet opening.

With sound intensity measurement on the dismantled underfloor heater in the anechoic room in the far field it is only the total sound power that could be determined exactly. But it should not be compared with the sound power determined in situ, because in situ sound is radiated in the bus interior only at air inlet side of the heater, whereas in the anechoic room sound is radiated from all surfaces of the heater. Therefore, a comparison should be made between the results of in situ measurements with the corresponding results recorded at the air inlet side (surface D) of the heater in the anechoic room in the far field as well as in the near field. These comparisons are presented in Table 6. The results are in very good agreement.

Table 6. Comparison of the sound power measured in situ and in anechoic room using discrete points and scanning method.

Measurement conditions	scanning method in far field in anechoic room	scanning method in near field in anechoic room	scanning method in far field in situ	scanning method in near field in situ
Sound power	70.2 dB(A)	69.6 dB(A)	69.2 dB(A)	69.5 dB(A)

CONCLUSIONS

The total sound intensity of a HVAC system operating in the bus interior and the sound power of individual components were measured in situ and in the free field using two different measuring methods, the discrete points and the scanning method. The measurement results were analyzed and compared. In none of the cases the sound field in which the measurement were carried out was ideal. In the narrow closed space in the bus there exists a very high diffuse field whereas in the anechoic room there isn't any ideal free field. In both acoustic fields there exist, in the acoustic near field, not only reactivity of the sound field but also the sound pollution from every part of the measured surface. This is not the case in the acoustic far field. In spite of these facts, comparisons of the results made in different sound fields and with different sampling methods have shown good agreement. It can also be concluded that the sound power measurement can be made with high accuracy by the manual scanning method in the near field of the source. Intensity measurement is also a powerful tool in separating the acoustic radiation parts of the system running under nominal conditions. The total output power can be determined, along with the output power of individual components of a source.

REFERENCES

1) M., Čudina, E., Železič: Identification of the Bus Interior Noise Using Sound Intensity Measurement Method. NOISE CON 91, Tarrytown, New York 1991, page 561-568.

SECOND INTERNATIONAL CONGRESS ON
RECENT DEVELOPMENTS IN AIR- AND
STRUCTURE-BORNE SOUND AND VIBRATION
MARCH 4-6, 1992 AUBURN UNIVERSITY, USA

CALCULATION METHOD OF SOUND FIELD IN INDUSTRIAL HALLS

V.I. Ledenyov and A.I. Antonov
Tambov Institute of Chemical Machine Building
Leningradskaya Str., 1
Tambov 392620
Russia

Summary

On the basis of statistical energy approach a new impulse calculation method of sound fields in industrial halls is proposed by the authors. The calculation relations received with sufficiently high accuracy describe both stationary and nonstationary sound fields.

The technique used is based on the principle that for quasi-diffusion sound fields there exists a relation between the resultant energy $\bar{q}$ flux and density gradient of reflected energy $\mathcal{E}$ homogenized in analysis frequency band. The above mentioned relation may be formulated in the form of

$$\bar{q} = -\chi \, grad(\mathcal{E}), \tag{1}$$

where χ - coefficient of energy transfer.

On the basis of extensive calculation and experimental material it was determined that in halls with scattered sound reflection for almost all practically important cases the following equation holds good

$$\chi \approx 0{,}5 \, c \bar{\ell}, \tag{2}$$

where c - sound velocity, $\bar{\ell}$ - mean free path of reflected sound waves.

Based on (1) a mathematical model of non-stationary reflected sound waves in halls has been formulated in the form of differential equation

$$0{,}5 \, c \bar{\ell} \nabla^2 \mathcal{E} - \frac{\partial \mathcal{E}}{\partial t} - m_B c \mathcal{E} = 0 \tag{3}$$

with boundary conditions of the third type

$$\left. \frac{\partial \mathcal{E}}{\partial n} \right|_S = - \left. \frac{\alpha_S}{(2-\alpha_S)\bar{\ell}} \cdot \mathcal{E} \right|_S , \tag{4}$$

where m_B - spatial coefficient of acoustic absorption in air, α_S - diffusion sound absorption coefficient of enclosure.

The distribution of sound energy impulse over a hall immediately after its radiation is taken as initial conditions

$$\mathcal{E} = \frac{P(1-\alpha)\,d\tau}{\int_{V_{uc}} dV}; \quad x_j \in V_{uc} \qquad (5)$$

$$\mathcal{E} = 0; \quad x_j \notin V_{uc}$$

where V_{uc} - sufficiently small, as compared with a hall volume, range of the original impulse energy distribution, P- acoustic source strenght.

By means of separation of variables there has been received a solution which expresses distribution over a hall and damping of a single impulse

$$\mathcal{E}_{uuu} = P(1-\alpha) \sum_m \sum_n \sum_q \frac{\varphi_m \varphi_n \varphi_q \varphi_m^\circ \varphi_n^\circ \varphi_q^\circ}{B_m B_n B_q} \cdot \exp\left[-u_{mnq}(t-\tau)\right] d\tau, \qquad (6)$$

where t - time of energy impulse observation; $\varphi_m, \varphi_n, \varphi_q$ - the system of orthogonal trigonometric eigenfunctions; $\varphi_m^\circ, \varphi_n^\circ, \varphi_q^\circ$ - the values of eigenfunctions in a source point having coordinates $x_1^\circ, x_2^\circ, x_3^\circ$; u_{mnq} - damping coefficient of particular solution amplitudes. Eigennumbers are selected in such a way that φ_i functions would correspond to boupdary conditions (4). Rating cofactors are defined from the expression

$$B_i = \int_0^{\ell_j} (\varphi_i)^2 \, dx_j, \qquad (7)$$

where ℓ_j - dimension of a hall in the direction of x_j axis (j =1; 2; 3.).

The total sound energy density during the period of source action [τ_1 ; τ_2] is defined as

$$\mathcal{E} = \int_{\tau_1}^{\tau_2} \mathcal{E}_{uuu}. \qquad (8)$$

Formula (8) permits to calculate sound energy density in non-stationary as well as in stationary conditions of sound energy radiation.

For calculation of stationary sound fields in halls with constant acoustic strenght sources there has been derived an expression in the form of a triple alternating rapid-convergent series $\tau_2 - \tau_1 = \infty$; $\tau_2 = t - r/c$

$$\mathcal{E} = P(1-\alpha) \sum_m \sum_n \sum_q \frac{\varphi_m \varphi_n \varphi_q \varphi_m^\circ \varphi_n^\circ \varphi_q^\circ}{B_m B_n B_q u_{mnq}} \cdot e^{-u_{mnq} r/c}, \qquad (9)$$

where r - the distance between the source and the point of reception.

It should be noted that the first member of the series in (9) is equal to the mean with respect to a hall density of reflected sound energy defined according to the diffusion field techniques.The subsequent sign-variable members show the non-uniformity of reflected energy distribution over a hall. The value of the mean with respect to a hall energy density in (9) depends on the position of sound source in a hall and its distance from the sound absorbing enclosures.

The data calculated according to (9) have been compared with the experimental data obstained for 65 technical halls of various proportions, volumes and acoustic charactestics. The deviations of calculation results do not exceed 3 dB at confidence probability 0.9 and 1 dB at confidence probability 0.6.

The technique used permits to analyze the non-stationary sound fields. There have been devised an algorithm and computer program for calculation of the general case of non-stationary problems described in (7) and (8). The parameters dependent on time are acoustic source strenght as well as coordinates of calculation point and sound source. Functional time dependence of the parameters is assigned by analytical expressions.

There have been performed calculations of sound fields formed in halls having non-stationary sources of sound with variations in acoustic strenght. The figure given below shows the example of sound level variations at the distance of 15 m from a sound source in a hall with the following dimensions 198x15x12.5 m.

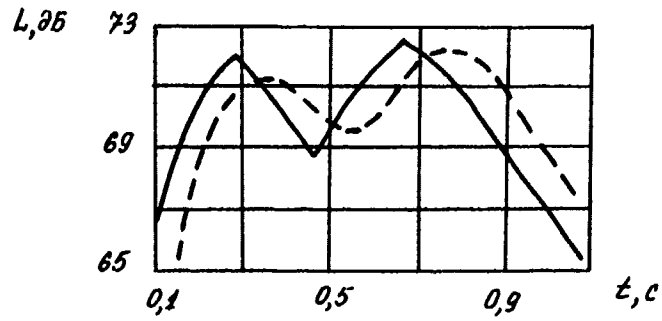

Diagrams of level modifications of reflected sound energy affected by impulse sound source: ——— for a rectangular impulse shape, — — for a sinusoidal one.

SECOND INTERNATIONAL CONGRESS ON
RECENT DEVELOPMENTS IN AIR- AND
STRUCTURE-BORNE SOUND AND VIBRATION
MARCH 4-6, 1992 AUBURN UNIVERSITY, USA

AN APPROXIMATE MODAL POWER FLOW FORMULATION FOR LINE-COUPLED STRUCTURES

Paul G. Bremner, Paris Constantine and David C. Rennison

Vibro-Acoustic Sciences Limited, Level 5, 15 Orion Road, Lane Cove, N.S.W. 2066 Australia

ABSTRACT

It is often desirable to compute mode-to -mode power flow between finite flexural substructures. Indeed it is necessary, when low modal populations in the analysis bandwidth cause excessive variance in Statistical Energy Analysis (SEA) predictions of vibrational energy levels. An important class of such problems occurs for flexural structures connected along continuous line junctions. This paper proposes an approach which uses a complimentary set of constrained and free uncoupled modes to obtain approximations for the power flow between the coupled sub-structures.

INTRODUCTION

The flow of vibratory energy between connected substructures is of considerable interest in the field of structural acoustics. A statistical approach is a natural way to reduce the complexity of the problem. It involves averaging over time and spatial sub-domains and across resonant mode distributions in analysis frequency bands. However, even the original proposers of statistical energy methods (Lyon,[1]) recognised the need for more deterministic "mode-to-mode" power flow estimates when low modal populations in the analysis bandwidth cause excessive variance in statistical predictions of energy levels.

A modal power flow formulation of this kind has been proposed by Pope & Wilby,[2] for the case of sound transmission through a flexural panel subsystem, into an enclosure. The spatial and frequency characteristics of each (uncoupled) panel mode are used to obtain better estimates of the input power and power flow to the connected acoustic subsystems. The method yields estimates for both resonant and non-resonant power in the lower frequency bands, and asymptotes smoothly to statistical (modal) formulations in higher frequency bands.

A similar approach is required for low frequency power flow between two finite flexural substructures. However, there are some important differences. We note that flexural systems will transmit power via both forces and moments, (Cremer & Heckl,[4]). Furthermore, it may not be reasonable to use Pope & Wilby's assumption of "weak coupling", which in the acoustic case

allows one to neglect changes in the modal parameters of the flexural panel, due to loading effects of the connected acoustic fluid, and visa versa.

This paper explores Pope & Wilby's quasi- statistical formulation, applied to power flow between two co-planar, line-connected flexural plates. No boundary motion restraints are implied for the coupled plate system, so that power flows via both forces and moments at the junction. External power input is considered as a quite general, spatially-distributed and phase-correlated pressure field. The weak coupling analogy with the structure-acoustic case suggests the use of "blocked" modal force in one flexural plate, and free modal response of the coupled plate, to compute power flow.

FLEXURAL POWER FLOW

The time-averaged, band-integrated power flow from one flexural subsystem to another, through a line connection of length L_c is: [2]

$$\Pi_{1,2}(\Delta\omega) = \int_{\Delta\omega} d\omega \int_{L_c} dx_c \, Re\left\{ \lim_{T\to\infty} \left(\frac{2}{T}\right) \left(\frac{d\omega}{2\pi}\right) E\left(f_2^*(x_c,\omega,T)\, q_2^{\bullet}(x_c,\omega,T)\right)\right\} \quad (1)$$

where q_2 is a vector of motional degrees of freedom accepting power, which for flexural waves can be expressed in terms of transverse displacement w_2;

$$q_2^{\bullet} = \Gamma_{w_2} . w_2^{\bullet}(x,\omega,T); \qquad \Gamma_{w_2} = \left[\frac{1}{\frac{\partial}{\partial x_n}}\right]; \quad (2)$$

and f is the vector of actions (forces and moments per unit length), acting on plate 2 at the coupling boundary. For the special case of thin plate bending (Liessa,[6]),

$$f_2 = \begin{bmatrix} \left(Q_n + \frac{\partial M_{nt}}{\partial x_t}\right) \\ M_n \end{bmatrix} = \Gamma_f . w_2(x_c,\omega,T); \quad (3)$$

Q is the transverse shear force and M are edge moments. Subscripts t,n denote tangential directions and normal to the coupling boundary, respectively.
From the analysis of strain and Hooke's Law, the force operator is defined as;

$$\Gamma_f = -D_2 \begin{bmatrix} \left\{\frac{\partial}{\partial x_n}\nabla^2 + (1-\mu_2)\frac{\partial}{\partial x_t}\left(\frac{\partial^2}{\partial x_t \partial x_n}\right)\right\} \\ \left\{\frac{\partial^2}{\partial x_n^2} + \mu_2 \frac{\partial^2}{\partial x_t^2}\right\} \end{bmatrix} \quad : (4)$$

where D_2 is the flexural stiffness of plate 2, and μ is Poissons ratio.

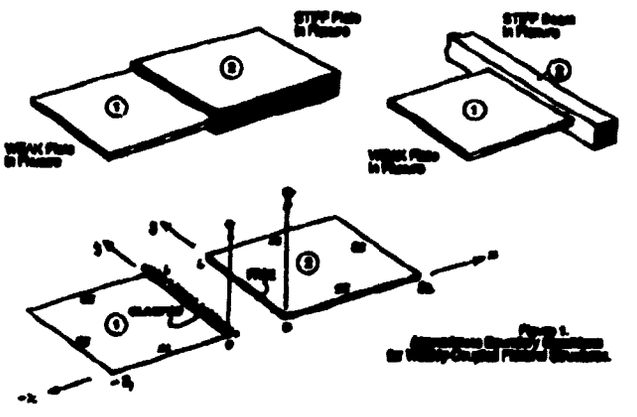

APPROXIMATE WEAK / STRONG INTERACTION FORMULATION

The motions and actions at the coupling boundary can be determined explicitly when the displacement compatibility and force equilibrium conditions are enforced. Consider the special case of power flow from a flexurally weak plate to a flexurally more rigid plate, as shown schematically in Figure 1. The structural interaction can be approximated in the modal expansion of the two uncoupled plates, by considering the weak plate 1 "CLAMPED", and the strong plate 2 "FREE", at the coupling boundary.

Let the coupling action vector $\underline{f}_2$ be estimated by an uncoupled mode expansion of the restraint forces (and moments) at the clamped boundary of plate 1;

$$\underline{f}_2(\underline{x}_c,\omega,T) = -\underline{f}_1(\underline{x}_c,\omega,T) = \sum_{m,n} \gamma_{1,mn}(\omega,T)\,\underline{\Gamma}_c\,\Phi_{1,mn}(\underline{x}_c) \qquad :(5)$$

where $\Phi_{1,mn}$ are the eigenfunctions (mode shapes) for plate 1 CLAMPED at the coupling boundary, with nodal indices m,n in x,y directions respectively. $\gamma_{1,mn}$ is the modal displacement of plate 1, which is a function of frequency only. Using modal co-ordinates, the coupling force in this approximation is determined by the external forcing function p_1, acting on plate 1.

$$\gamma_{1,mn}(\omega,T) = -\frac{\int_{A_1} p_1(\underline{x}_1,\omega,T)\Phi_{1,mn}(\underline{x}_1)\,d\underline{x}_1}{M_{1,mn}\,Y_{1,mn}(\omega)} \quad ; \quad (6a)$$

The modal mass is defined using the plate mass per unit area m_1, over the plate surface A_1,;

$$M_{1,mn} = \int_{A_1} m_1(\underline{x}_1)\,\Phi^2_{1,mn}(\underline{x}_1)\,d\underline{x}_1 \qquad :(6b)$$

and modal receptance is defined by;

$$Y_{1,mn}(\omega) = \left\{\omega^2_{mn}(1+j\eta_{mn}) - \omega^2\right\} \qquad :(6c)$$

where ω_{mn} is the natural frequency, and η_{mn} is the modal damping loss factor.

Now let $\underline{f}_2^*$ in equation (1) be approximated by the uncoupled response of plate 2, under the action of plate 1 boundary restraint forces and moments (5) acting on plate 2, along $\underline{x}_c$

$$\underline{f}_2^*(\underline{x}_c,\omega,T) = \sum_{r,s} \gamma^*_{2,rs}(\omega,T)\,\underline{\Gamma}_c\,\Phi_{2,rs}(\underline{x}_c) \qquad :(7a)$$

Here $\Phi_{2,rs}$ are the plate 2 FREE edge mode shapes, and $\gamma_{2,rs}$ are its modal displacements, which can be described by;

$$\gamma^*_{2,rs}(\omega,T) = \frac{\int_{L_c} \underline{f}_2^{*T}(\underline{x}'_c,\omega,T)\,\underline{\Gamma}_c\,\Phi_{2,rs}(\underline{x}'_c)\,d\underline{x}'_c}{M_{2,rs}\,Y^*_{2,rs}(\omega)} \qquad :(7b)$$

where $M_{2,rs}$ and $Y^*_{2,rs}$ are the modal mass and receptance of plate 2, defined as in (6b) and (6c) with interchange of subscripts r,s for m,n. Note that the ω_{rs} natural frequencies, are for plate 2 uncoupled with FREE edge conditions at the coupling boundary.

Approximations for motions in equation (7), and actions in equation (6) at the coupling boundary can be substituted into equation (1) to yield the mechanical power flow for the weak/strong interaction case, this then becomes a function of the following variables;

$$\Pi_{12}(\Delta\omega) = f(M_{1,2},\ Y_{1,2},\ G_p,\ \Phi_{1,2},\ \omega,\ \xi) \qquad (8)$$

In equation (8) above, G_p is the Cross Spectral Density of the excitation pressure field acting

on plate 1

$$G_p(\underline{x};\underline{x}',\omega) = \lim_{T\to\infty}\left(\frac{2}{T}\right)\left(\frac{1}{2\pi}\right)E\langle p_1(\underline{x},\omega,T)\,p_1^{*}(\underline{x}',\omega,T)\rangle \qquad (9)$$

A measure of the input power accepted by each plate 1 mode from the excitation pressure can be represented by the modal joint acceptance function;

$$\int_{A_1}\int_{A_1} d\underline{x}_i\,d\underline{x}'_i\,.\,\Phi_{1,mn}(\underline{x}_i)G_p(\underline{x}_i;\underline{x}'_i,\omega)\Phi_{1,pq}(\underline{x}'_i)\cdot$$

$$\begin{cases} j^2_{mn}(\omega) & ;\ pq = mn \\ 0 & ;\ pq \neq mn \end{cases}$$

; (10)

For diffuse acoustic field excitation it is convenient to normalise the joint acceptance by the auto pressure spectrum magnitude;

$$j^2_{mn} = \frac{\int_{A_1}\int_{A_1} d\underline{x}_i\,d\underline{x}'_i\,.\,\Phi_{mn}(\underline{x}_i)G_p(\underline{x}_i;\underline{x}'_i,\omega)\Phi_{mn}(\underline{x}'_i)}{A_1^2 G_p(\underline{x}_i;\underline{x}_i,\omega)} \qquad (11)$$

so by substituting equations (6), (7) and (11) into (1) the approximate modal power flow formulation can be simplified to;

$$\Pi_{1,2}(\Delta\omega) \approx A_1^2 \sum_{m,n}\sum_{r,s}\frac{B^2_{mn,rs}\eta_{2,rs}\omega^2_{2,rs}}{M^2_{1,mn}M_{2,rs}}\int_{\Delta\omega} d\omega \frac{\omega j^2_{mn}(\omega)\,G_p(\omega)}{|Y_{1,mn}|^2|Y_{2,rs}|^2} \qquad (12)$$

where the Modal Coupling Co-efficients $B^2_{mn,rs}$, between plate 1 and plate 2, are defined by;

$$B^2_{mn,rs} = \left\{\int_{L_c} d\underline{x}_c\left[\underline{\Gamma}_f\,\Phi_{1,mn}(\underline{x}_c)\right]^{T}\underline{\Gamma}_n\,\Phi_{2,rs}(\underline{x}_c)\right\}^2 \qquad (13)$$

We note that the modal power flow formulation in equation (12) is equally applicable to analytic modal descriptions of simple substructures, or to discrete numerical modal descriptions, using finite element methods. Indeed, an analytical modal subsystem can be connected in a completely consistent manner to a numerical modal subsystem. The coupling co-efficient (13) and joint acceptance function (10) become numerical integrals and for quite arbitrary line connections, invoke the interpolation or "Shape" functions assumed for finite element subsystems.

INPUT POWER ESTIMATION

Input power has been estimated previously[8] by the authors based on the uncoupled modal response of plate 1. It was shown that this approximation can imply non-physical power transfer ratios in narrow bands corresponding to resonances in plate 2.

Another approximation for input power $\Pi^i(\Delta\omega)$ is evaluated here. It uses the same weak coupling assumption as equation (12) to include the effect on the connected plates of lightly damped resonant behavior in plate 2, as follows;

$$\Pi^i(\Delta\omega) \equiv \int_{\Delta\omega} d\omega \int_{A_1} d\underline{x}_i Re\left\{\lim_{T\to\infty}\left(\frac{2}{T}\right)\left(\frac{j\omega}{2\pi}\right)E\langle p_1(\underline{x}_i,\omega,T)\,(w_{1,1}^{*}(x_i,\omega,T) + w_{1,2}^{*}(x_i,\omega,T))\rangle\right\} \qquad (14)$$

where $w_{1,1}(\underline{x}_i,\omega,T)$ is plate 1 displacement, based on its uncoupled modal response to pressure $p_1(\underline{x}_i,\omega,T)$; and $w_{1,2}(\underline{x}_i,\omega,T)$ is the additional plate 1 displacement due to the uncoupled resonant motions $q_r(\underline{x}_c,\omega,T)$ of plate 2 in equation (7a), which are enforced on the coupling

boundary of plate 1.

The first term $w_{1,1}(\underline{x}_i,\omega,T)$ can be written in terms of only the plate 1 clamped modes,

$$w_{1,1}(\underline{x}_i,\omega) = \sum_n \frac{\Phi_n(\underline{x}_i)}{M_n Y_n(\omega)} \int_A p_1(\underline{x}_i',\omega)\Phi_n(\underline{x}_i')\,d\underline{x}_i' \tag{15}$$

where for simplicity the two-dimensional nodal indices m,n and r,s are abbreviated hereafter with mode number indices n,r respectively.

It is then convenient to describe $w_{1,2}(\underline{x}_i,\omega,T)$ in terms of a "static" (stiffness-controlled) component $w_0(\underline{x}_i,\omega,T)$, and a "dynamic" (resonance-controlled) component $w_d(\underline{x}_i,\omega,T)$, as follows;

$$w_{1,2}(\underline{x},\omega) = w_0(\underline{x},\omega) + w_d(\underline{x},\omega) \tag{16}$$

Assuming that the static deflection component w_0, can be described by separable influence functions[7] δ_w and δ_θ in x and y directions, we can then write w_0 as;

$$w_0(\underline{x},\omega) = \underline{D}^T \underline{\Gamma}_m w_2(\underline{x},\omega) \tag{17}$$

where $\underline{D}^T$ is given by;

$$\underline{D}^T(\underline{x};x_c) = \begin{bmatrix} \delta_w(\underline{x};x_c) \\ \delta_\theta(\underline{x};x_c) \end{bmatrix} \tag{18}$$

To obtain the relative dynamic deflection $w_{1,2}$ we substitute equation (16) into the equation of motion of the plate;

$$D\left(\nabla^2\,\nabla^2\, w_{1,2}(\underline{x},\omega)\right) - \omega^2 m'(w_{1,2}(\underline{x},\omega)) = 0 \tag{19}$$

Which yields the relative dynamic deflection;

$$w_{1,2}(\underline{x},\omega) = \underline{D}^T \underline{\Gamma}_m w_2(\underline{x},\omega) + \sum_p \frac{\Phi_p(\underline{x})}{m_p Y_p} \int_A K_f \underline{D}^T(\underline{x};x_c)\,\underline{\Gamma}_m w_2(\underline{x},\omega)\Phi_p(\underline{x})\,d\underline{x} \tag{20}$$

where

$$K_f = \omega^2 m' - D\left(\frac{\partial^4}{\partial y^4} + \frac{\partial^2}{\partial y^2}\frac{\partial^2}{\partial x^2}\right) \tag{21}$$

The new approximate input power estimate is obtained by substituting equations (15) and (19) into (14) to give;

$$\Pi_i(\omega) = \frac{1}{2A} Re\left(\sum_n \frac{j\omega\Lambda_n}{M_n Y_n^*} J_n^2 A^2 G_{pp}(\omega) + \begin{array}{l} \sum\sum_{n\ r} \frac{j\omega B_{nr}}{M_n M_r Y_n^* Y_n} H_{nr} J_n^2 A^2 G_{pp}(\omega) + \\ \sum\sum_{n\ r} \frac{j\omega B_{nr}\Lambda_n}{M_n^2 M_r |Y_n|^2 Y_n^*} \Delta_{nr} J_n^2 A^2 G_{pp}(\omega) \end{array} \right) \tag{22}$$

where Λ_n is the normalization constant

$$\Lambda_n = \int_A \Phi_n^2(\underline{x})\,d\underline{x} \tag{23}$$

H_{nr} the static input coupling coefficient is given by;

$$H_{nr} = \int_A \Phi_n(\underline{x}) D^T(\underline{x};x_c)_{1,m} \Phi_r(x_c)\, d\underline{x} \tag{24}$$

the dynamic input coupling coefficient is given by;

$$\Delta_{nr} = \int_A \Phi_n(\underline{x}) K_f D^T(\underline{x};x_c) \Gamma_m \Phi_r(x_c)\, d\underline{x} \tag{25}$$

EVALUATION PROCEDURE

A thorough evaluation of this approximate formulation requires detailed experimental and numerical calculation of narrow band power flow between finite plates. As a first step, equation (12) is integrated across octave bands to compare against the SEA estimate[1] of power flow at high modal densities.

Analytical modal solutions[3] for two rectangular plates of different thickness and areas 0.080 and 0.062 sq.m. respectively, are considered as shown in Figure 1. Plate 1 has a CLAMPED edge boundary condition and plate 2 has a FREE edge boundary condition along the connection line; all other edges have simply-supported boundary conditions.A unit mean-squared force spectrum is input as a point source, acting on plate 1.

The total power flow is predicted from equation (12) as a continuous function of frequency, by summing over the resonant and non-resonant modal power contributions. Figure 4 compares the input power to a 2 mm plate/5mm plate system with the transmitted power from the 2 mm plate to a 5 mm plate. Figure 2 shows the power transmitted by moments compared with the power transmitted by transverse shear forces.

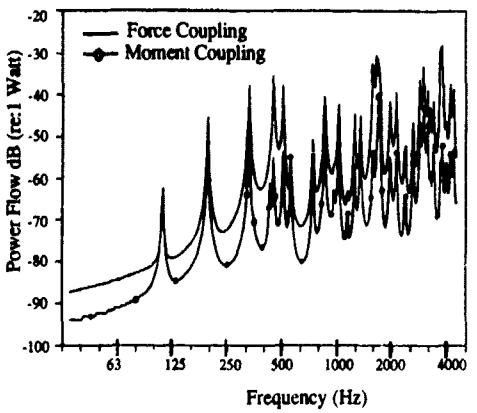

Figure 2: Force and Moment power flow for plates (h1=2mm, h2=10mm DLF 1,2=0.01)

A power transmission efficiency or "Power Ratio" is computed by dividing the band-integrated transmitted power by the band-integrated input power, over standard octave bands. The Power Ratio is then compared with the SEA estimate[6] of Power Ratio

$$\frac{\Pi_{1,2}}{\Pi_i}(\Delta\omega) = \frac{\bar{\eta}_2\eta_{12}}{(\bar{\eta}_1\bar{\eta}_2 + \bar{\eta}_1\eta_{21} + \bar{\eta}_2\eta_{12})} \tag{26}$$

Figures 3 presents results for three different non-driven plate thicknesses.

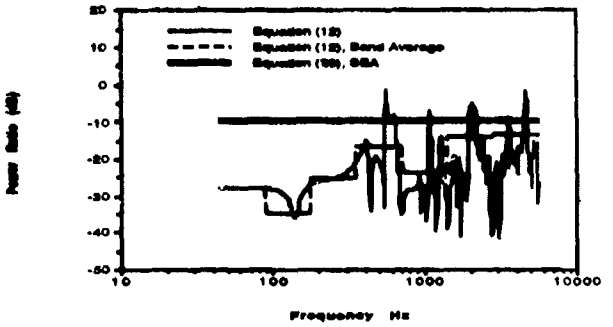

Figure 3 (a) 2mm/10mm Plates, Power Ratio

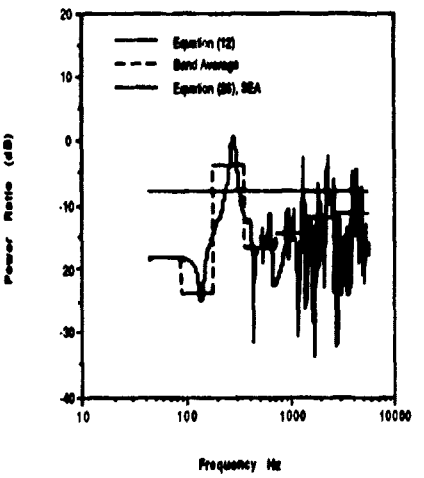

Figure 3 (b) 2mm/5mm Plates, Power Ratio

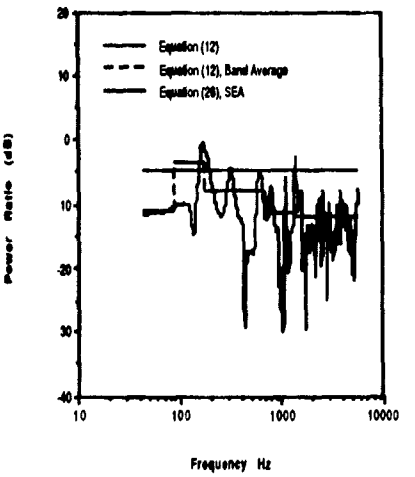

Figure 3 (c) 2mm/3mm Plates

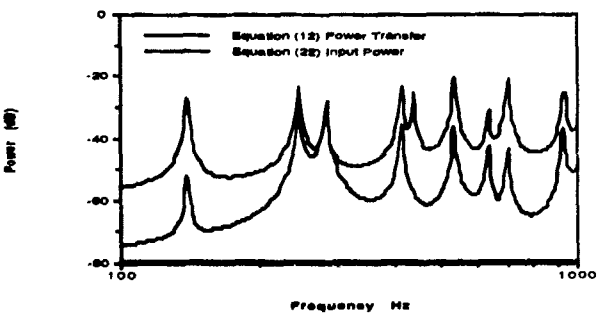

Figure 4 Input Pow - versus Transmitted Power, 2mm/5mm Plates

A number of observations can be made:

(i) Equation (12) and equation (22) generally converge at higher modal densites but with considerable variances, +/- 12 db being common. The input power always exceeds the transmitted power, as required, where we note that without the contributions defined in equation (22), this may not be the case.

(ii) As flexural rigidities of the two connected plates approach each other the weak coupling assumption in eqn (12) does generate larger variance in Power Ratio, when compared with SEA predictions.

(iii) Power Ratio's lower than the SEA estimate are predicted for frequencies below the first resonance.

For the 2 - 10mm plate example, four other statistically independent input power locations were simulated and averaged. Results presented in Figure 5 show a reduction in the variations calculated from 16db to less than 5db, above the first resonance in Plate 2. This is consistent with direct measurement of point-excited, coupled plates, as demonstrated by others[5].

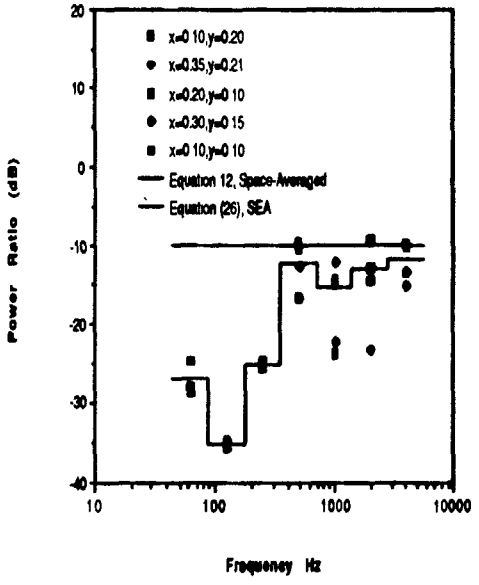

Figure 5.(Space Averaged Power Ratio 2mm / 10mm Plates)

CONCLUSION

Only interim conclusions can be drawn at this stage on the validity and usefulness of this weak/strong coupling approximation for modal power flow between structures. These are:

(i) The method is mathematically consistent with and converges at high modal density to the method of Statistical Energy Analysis (SEA).

(ii) The method appears to yield an improved estimate of the structural power flow at lower frequencies (and low modal densities) where SEA is less accurate. This includes resonant and non-resonant power flow components, to be compared in future formulations.

(iii) The accuracy of the method needs further validation at the narrow band level, using both experimental and numerical methods.

REFERENCES

(1) R H Lyon 1975 Statistical Energy Analysis of Dynamical Systems: Theory and App. The MIT Press.

(2) L D Pope and J F Wilby 1977 Journal of Acoustical Society of America G2, 906 - 911. Band-Limited power flow into enclosures.

(3) A W Leissa 1969 NASA SP-160. Vibration of Plates.

(4) L.Cremer,M.Heckl and E.Ungar 1973 Structure-Borne Sound, Springer-Verlag.

(5) D.Bies and S.Hamid 1980 Journal of Sound and Vibration, 70 (2) In-situ Determination of Loss and Coupling Loss Factors by the Power Injection Method.

(6) Z. M. Cushieri 1991 Journal of Acoustical Society of America 87,1159-1165. "Structrural power flow analysis using a mobility approach of an L-shaped plate."

(7) S.Timoshenko,"Vibration Problems in Engineering" 1974 Wiley & Sons.

(8) P.G.Bremner, et .al., An Approximate Mode-to-Mode Power Flow Formulation for Line-coupled Structures, Presented at 120th Meeting of ASA, San Diego, 1990.

SECOND INTERNATIONAL CONGRESS ON
RECENT DEVELOPMENTS IN AIR- AND
STRUCTURE-BORNE SOUND AND VIBRATION
MARCH 4-6, 1992 AUBURN UNIVERSITY USA

NONDESTRUCTIVE EVALUATION OF CARBON-CARBON COMPOSITES

U.K.Vaidya, P.K.Raju, M.J.Crocker, and J.R.Patel
Department of Mechanical Engineering
Auburn University, Auburn, AL 36849

ABSTRACT

Carbon-Carbon (C/C) composites are found useful in the aerospace industry in the area of high temperature applications. In the fabrication of this composite, the first carbonization cycle is crucial, as the mechanical properties of the composite are completely altered at this stage. Some predominant effects of the first carbonization process are delamination, fiber breaks, distributed porosity, and transverse crack formation in the matrix. These effects of carbonization are to some extent beneficial during latter processing however excessive occurrence of any of these defects is undesirable. Keeping this in view, the present study focuses on the application of acoustic emission (AE) technique for studying the failure modes of C/C composites at the processing stages. Acoustic emission (AE) has been used to study the failure modes of the composite at the*as-cured* and *carbonized* stages using parameters such as the peak amplitude distribution event duration, and energy content of the AE signals. These parameters have been related to effects such as delamination, fiber breakage, and matrix cracking which occur in the composite in the *as-cured* and *carbonized* stages.

INTRODUCTION

A carbon-carbon composite differs from a conventional composite due to the presence of two phases of the element carbon, a carbon fiber reinforcement and a carbonaceous matrix. Figure.1 represents the schematic of the fabrication cycle of a C/C composite. The C/C composite undergoes a complex manufacturing process, beginning with impregnation of carbon fibers with a matrix precursor, i.e. a resin to form the base composite. This stage is referred to as the *as-cured* stage. The composite is then subjected to carbonization i.e. heat treatment at high temperatures (1000°C). This is referred to as the *carbonized* stage. In this process the matrix in the composite is pyrolyzed to yield a secondary porous carbon phase. The composite at the stage of first carbonization is highly porous and inferior in terms of its mechanical properties and density [1]. In order to improve the mechanical property, it is then subjected to a densification process, during which time, the pores formed during pyrolysis are densified using a chemical vapor deposition process or a liquid impregnation process [1]. Due to the complexities involved in the fabrication of a C/C composite, each stage of the fabrication cycle plays an important role in the performance of the final composite. Hence, it is important to have a knowledge not only of the mechanical properties of the composite at each stage of its fabrication, but also to have a clear idea of the prominent failure mechanisms, which occur at each of these stage. In this study such an investigation was undertaken.

The acoustic emission technique, a powerful nondestructive tool was chosen in the present study due to its sensitivity to flaw growth in materials. AE refers to stress waves that are generated due to dynamic processes occurring during the loading of a structural material. These stress waves in the case of composites are caused by fiber, matrix or interface related failures. Several investigators have reported the application of AE to graphite/epoxy composite materials [2-5] for classification of failure mechanisms such as matrix cracking, fiber breakage, and delamination. The present study utilizes amplitude, energy, and event duration distribution of AE signals to differentiate failure mechanisms.

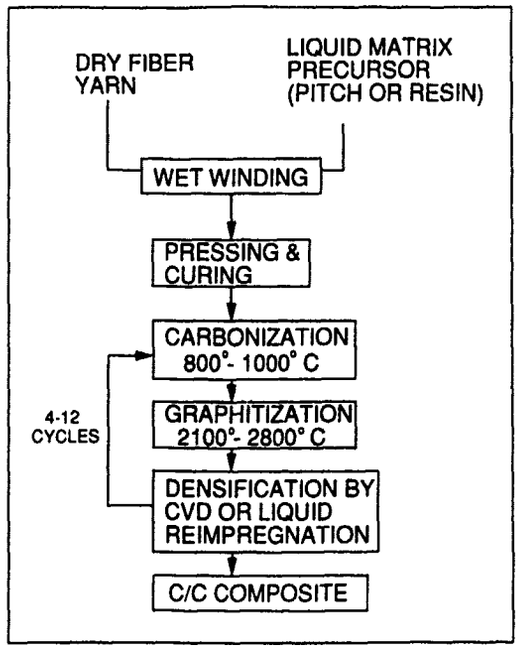

Figure 1. Fabrication cycle of carbon-carbon composites

SPECIMEN FABRICATION

Ten layers of graphite fabric, Style 193*A (Supplier Hercules Inc.) were impregnated with phenolic resin MXR-6055 (Supplier Fiberite Inc.) using hand lay-up technique. Phenolic resin was chosen due to its high carbon yield ~55%. The hand lay-up was subjected to a compression molding process at 140°C for one hour to obtain the *as-cured* composite laminate. Five tensile specimens of dimensions 7.5"X 0.5"X 0.05" were machined from these laminates. End tabs made of tapered glass epoxy were attached to the specimens for mechanical testing. Another set of five specimens from the same laminate were subjected to the carbonization process. In this process the specimens were placed in a high temperature oven and were subjected to pyrolysis by heating them to a temperature of 800°C in an inert atmosphere of nitrogen gas. End tabs were then attached to these specimens for mechanical testing.

EXPERIMENTAL

The mechanical testing was performed at room temperature (23°C) on an Instron testing machine (Model 1125) equipped with a 20,000 lb load cell. All the specimens tested were loaded to failure under tension. A crosshead speed of 0.01inch/minute was maintained for all the tests. A LOCAN system (Mfr-Physical Acoustics Corp.) acoustic emission system was used for data acquisition. A 150 kHz resonance frequency AE sensor (Reference level 0 dB at 1 μV at sensor output) was attached to the specimen at its center using a constant force spring clamp and silicon grease couplant (Dow Corning Stopcock Grease). The output from the sensor was fed to a 40-60 dB preamplifier (set at 40 dB), with a plug-in filter of 100-300 kHz bandwidth from which the signal was fed to the AE Locan system. For all the tests, the threshold and gain settings on the Locan were set at 40 dB and 20 dB respectively. The load-time history was recorded on the strip chart recorder on the Instron machine. The AE signals were recorded on the disk drive of the LOCAN. The data files were then converted from CP/M to DOS format (eventually into ASCII files) and then incorporated into SASGRAPH, a module of the Statistical Analysis System (SAS). Three-dimensional (3D) and other plots were then generated using SASGRAPH.

RESULTS AND DISCUSSION

Visual observation of the failed specimens indicate that the *as-cured* composite failed by extensive delamination resulting in clean separation of the individual plies with very little fiber breakage or fiber pullout. In contrast, the failure mode of the *carbonized* composite was found to be a combination of broken fibers, fiber pullout and complete matrix failure. Only a small portion of the failed specimens showed indications of delamination. The failure of the *as-cured* composite occurred in a progressive manner while the *carbonized* composite failed in a brittle fashion. The *as-cured* composite failed at a stress value of 483 MPa, while the *carbonized* composite failed at a stress of only 10% of this value, at 46 MPa.

The distribution of AE event intensities of the specimens at the *as-cured* and *carbonized* stage was completely different. Usually, the AE test parameters are represented by two dimensional (2D) histograms, but the 3D plots generated in this study, provide an excellent means of visualization of the failure process. Figure 2 shows the 3D plot of time, amplitude, energy distribution of the AE signals for the duration of a test, for an *as-cured* specimen. The amplitude distribution lie in three ranges: 40-60 dB, 60-85 dB and 85-100 dB respectively. Events in the amplitude range 40-60 dB were observed to start at very low stress values (25 MPa). Events in the amplitude range 60-85 dB occurred around a stress value of 60 MPa. AE activity was continuously observed from then on in both these ranges until the failure of the specimen. The high amplitude events i.e in the range 85-100 dB always either preceded or coincided with a load drop. This was observed on the load-displacement chart. Subsequently, there was an advance of delmaination. Fig. 2 illustrates the energy distribution of AE signals at a stress value of 240 MPa. This was in the low and medium amplitude ranges (i.e 40-60 and 60-85 dB). A sudden increase in the energy value is seen to occur

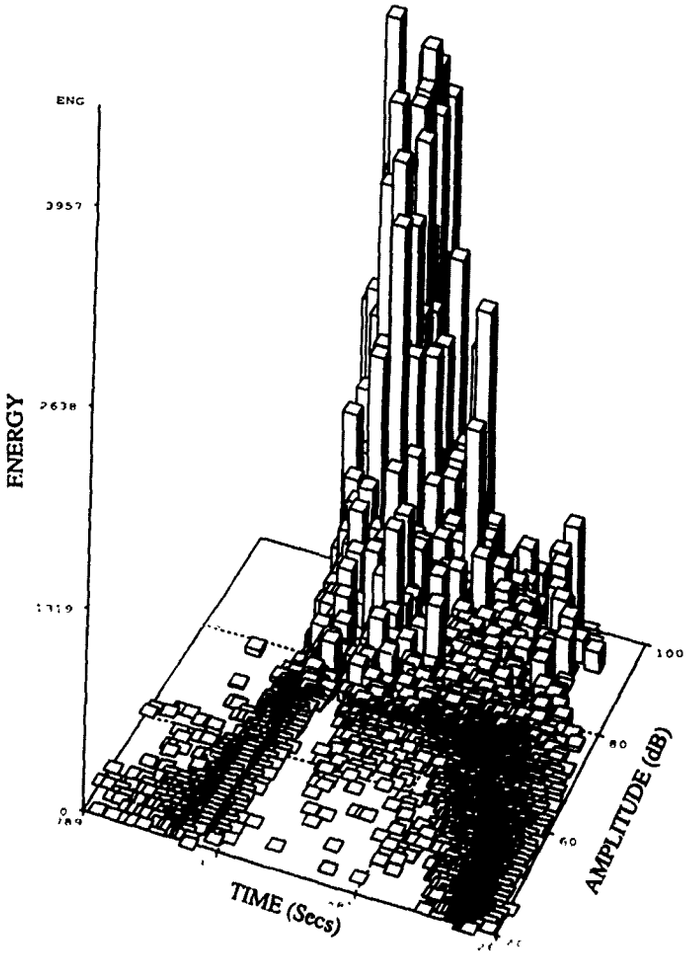

Figure 2. AE distribution histogram of time (secs) vs amplitude (dB) vs energy for an *as-cured* stage composite specimen

illustrates the energy distribution of AE signals at a stress value of 240 MPa. This was in the low and medium amplitude ranges (i.e 40-60 and 60-85 dB). A sudden increase in the energy value is seen to occur at this stress level. The first evidence of delamination and its advance coincided with this increase in energy From a stress level of 240 MPa to failure, energy distribution is seen to lie in three ranges, low, medium, and high. With successive delaminations occurring in the *as-cured* composite, the number of high energy events continued to dominate the later portion of the energy emission distribution histogram. High values of energy as observed from Fig. 2, always coincided with the high amplitude range (85-100 dB) of the histogram, while low energy events had low amplitudes (40-65 dB). The total number of AE events in the case of the *as-cured* specimen were 7740.

Figure 3 represents the 3D plot of time vs amplitude vs energy distribution of AE signals for a *carbonized* specimen. The number of high amplitude events (85-100 dB) were few (5% of the total events) for this specimen. The distribution of low and medium amplitude events was similar to the *as-cured* specimen, except that they were fewer in number. From Fig. 3 it can be seen that the low and medium amplitude events (40-60 & 60-85 dB) had lower energy levels. The last segment of the test, close to failure

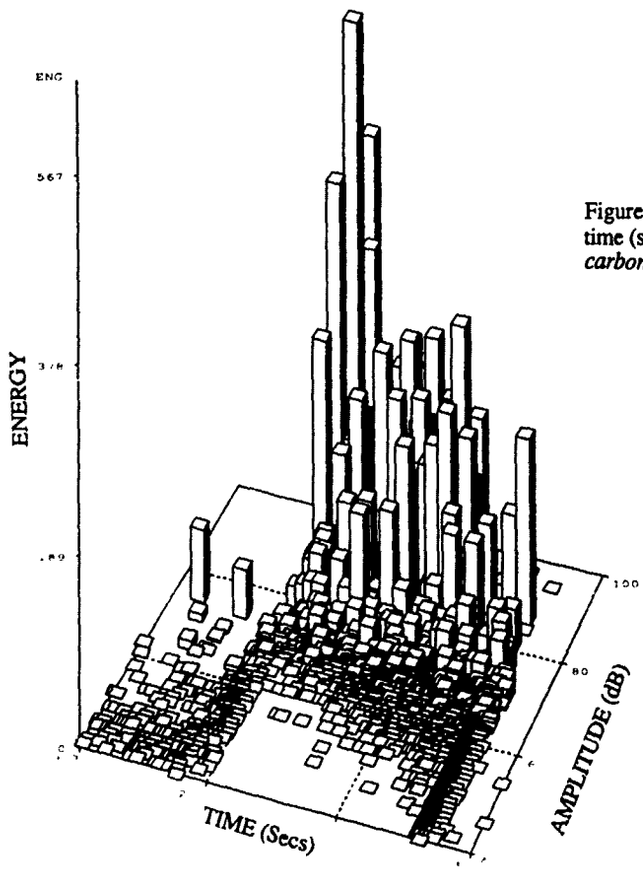

Figure 3. AE distribution histogram of time (secs) vs amplitude (dB) vs energy for a *carbonized* stage composite specimen

resulted in higher energy event distributions. The overall energy distribution for the *carbonized* specimen contained lower energy levels when compared to the *as-cured* composite. A total of 2660 events occurred in case of the *carbonized* composite. Figures 4 and 5 represent the 3D plot of time vs amplitude vs duration distribution of the AE signals for the *as-cured* and *carbonized* specimen respectively. It can be observed from Fig. 4, for the *as-cured* composite, the event durations were in the low and medium range (< 1000, 1000-10,000), prior to a stress level of 240 MPa, and increased sharply to higher durations coinciding with the first delamination. The event duration values remained high with every successive delamination, until the specimen failed. In the case of the *carbonized* composite, as seen from Fig. 5, the event duration levels were high (> 10,000) only at the very last segment of the test, just prior to failure of the specimen. Medium and low amplitude level events occurred over a major portion of the test.

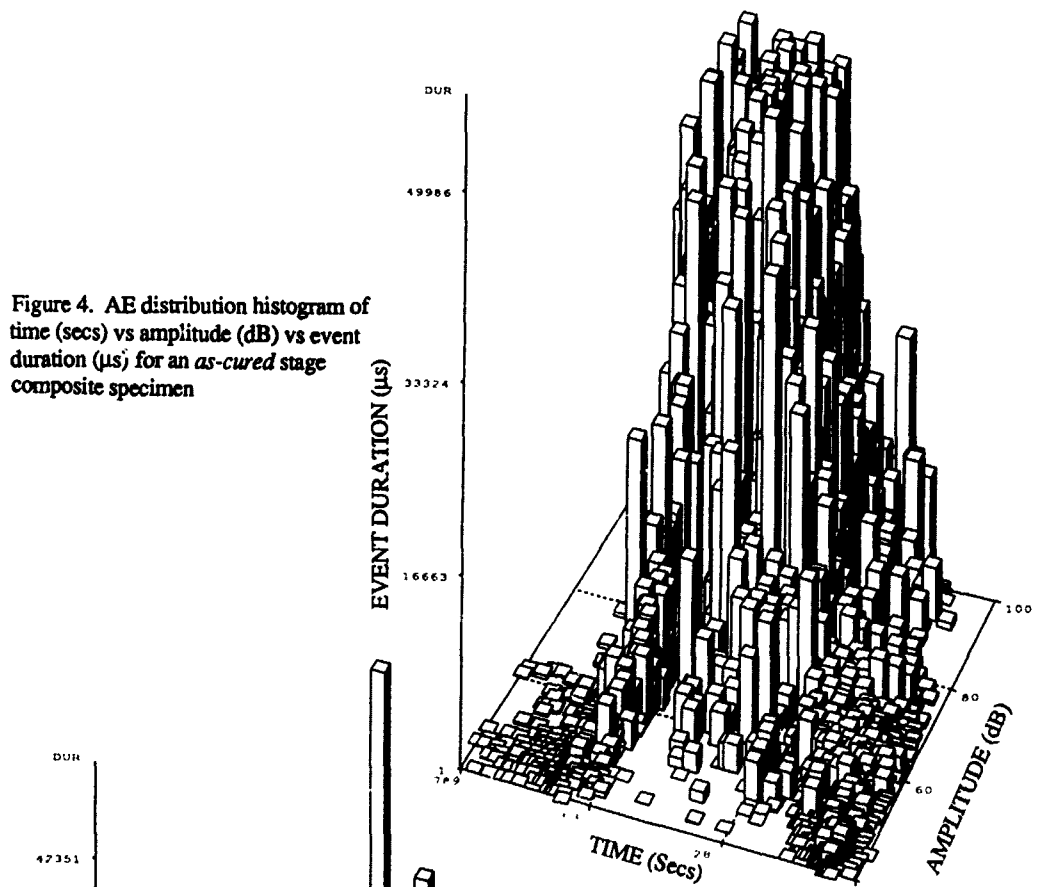

Figure 4. AE distribution histogram of time (secs) vs amplitude (dB) vs event duration (µs) for an *as-cured* stage composite specimen

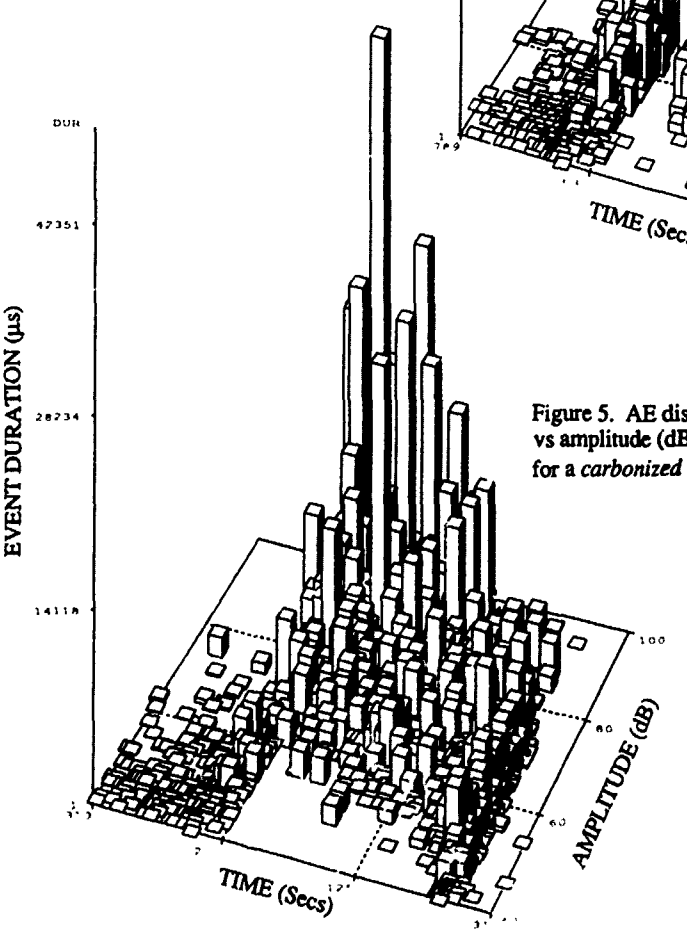

Figure 5. AE distribution histogram of time (secs) vs amplitude (dB) vs event duration (µs) for a *carbonized* stage composite specimen

DISCUSSION

From the 3D plots of time, amplitude, energy and the event distribution histograms (Figs.2 and 4), there is an indication that failure modes for the *as-cured* composite start at lower load levels and continue throughout the loading cycle. The failure modes are due to matrix cracks, interfacial debonding, random fiber failure, and other frictional mechanisms. Events in lower amplitude level range of 40-60 dB are predominant for this type of specimen and occur throughout the loading process. This range of levels i.e. 40-60 dB, is attributed to matrix microcracks and individual random fiber failure. They correspond to lower energy and event duration of the signals in this amplitude range. Both these processes, matrix microcracking and individual fiber failure are random in nature and can occur at low load levels. Higher number of events are observed in the range of amplitude levels corresponding to 60-85 dB for both *as-cured* and *carbonized* specimens. Matrix microcracking at higher loads evolves into macrocracks that run both across and parallel to the fibers. Fiber bundles then start fracturing at this higher load. Moreover, both these processes are interdependent and do not occur individually [3]. The presence of low and medium amplitude level of events at lower stress levels before failure are a result of this continuing process. A large population of fiber failures and matrix cracking in a localized region results in the loss of stiffness and onset of delamination in the specimen. The delamination then advances from this weak spot to form successive delaminations in other layers. This explains the presence of high duration events prior to a load drop. Significant amount of frictional energy causes these high duration events. The energy is dissipated in the formation and advanceof the delamination.

In the *carbonized* composite (Figs. 3 and 5), the process of carbonization resulted in weakening of the material. Microstructural analysis revealed an increase of distributed porosity, interfacial debonds and transverse crack formation in the matrix [6]. The weak spots formed due to carbonization, resulted in a much lower failure stress for the material. The absence of significant delamination can be related to poor matrix strength. The matrix failure across the width of the specimen occurs prior to the initiation and advance of delamination in the direction of loading. In doing so, the fibers that were present in the path of the failing matrix, were pulled out from the surrounding matrix. As is observed the matrix failure is the main contributor to AE events in this case resulting in a large number of low and medium level amplitude events (i.e 40-60 & 60-85 dB respectively). Only towards the end, a single delamination that results, contributes tc the high level amplitude, energy and duration events. Clearly, the 85-100 dB level amplitude region corresponds to the advance of delamination.

CONCLUSIONS

The failure modes of carbon-carbon composites in the first two stages of their fabrication are seen to be distinctly different. The *as-cured* composite fails in a progressive manner, withstands a higher failure stress, while the *carbonized* composite fails in a brittle manner at a much lower failure stress. The failure mechanisms of the *as-cured* composite are matrix cracking, fiber failure and delamination, while the *carbonized* composite exhibits little delamination, but fails by fiber pull-out and rupture in addition to extensive matrix cracking. Acoustic Emission analysis reveals three regions of amplitude distribution levels associated with these failures 1) a 40-60 dB level range corresponding matrix microcracks & random individual fiber failure 2) a 60-85 dB level range corresponding to matrix macrocracks, fracture of fiber bundles and onset of delamination 3) an 85-100 dB level range relating to advancing delaminations. The last of these regions is significantly suppressed in the *carbonized* stage composite. 3D plots of energy & event duration with time and amplitude gave an excellent means of visualization of the failure process.

REFERENCES

1. Fitzer, E., "The Future of Carbon-Carbon Composites," *Carbon*, Vol. 25, No. 2, pp 163-190, 1987.
2. Valentin, D., "A Critical Analysis of Amplitude Histograms Obtained During Acoustic Emissions Tests on Unidirectional Composites with an Epoxy and a PSP Matrix,"*Composites*, Vol. 16, No. 3, pp 225-230, July 1985.
3. Madhukar and Awerbuch, "Monitoring Damage Progression in Center Notched Boron Aluminum Laminates through Acoustic Emission," *ASTM STP 893*, pp 337-367.
4. Fuwa, M., Bunsel, A. R., and Harris, B., "The Tensile Failure Mechanisms in Carbon Fiber - Epoxy Composites," *Journal of Materials Science*, Vol. 10, pp 2062-2070, 1975.
5. Raju, P. K., Vaidya, U. K., Crocker, M. J., and Valaire, B. T., "Nondestructive Evaluation of Graphite Epoxy Composites using Acoustic Technology," *NDE*, ASME Winter Annual Meeting, San Francisco, California, Ed. P. K. Raju, Vol. 6, Dec 10-15, 1989.
6. Vaidya.U.K., Raju.P.K. and Kowbel.W., " Material Damping Studies on Carbon-Carbon Composites," *Carbon*, 1991 (In Press).

SECOND INTERNATIONAL CONGRESS ON
RECENT DEVELOPMENTS IN AIR- AND
STRUCTURE-BORNE SOUND AND VIBRATION
MARCH 4-6 1992 AUBURN UNIVERSITY, USA

ACOUSTIC WAVES EMISSION AND AMPLIFICATION IN FERROELECTRIC CERAMIC LAYER WITH NONSTATIONARY ANISOTROPY INDUCED BY THE ROTATING ELECTRIC FIELD

Semchenko I.V., Serdyukov A.N., Khakhomov S.A.
Department of Physics
Gomel State University
named after F.Skorina
Soviet. st.,104, 246699, Gomel
Republik Byelarus

The propagation of the circularly polarized acoustic wave in the centrosymmetrical crystal with strong deformation dependence of permittivity, a layer of wich is affected by the rotating electric field is investigated. The resonance interaction when tne frequences and rotation directions of the electric field coincide with those of the displacement vector of acoustic waves is considered. In this emission of reversed and amplification of passed acoustic waves can take place. It is shown that if the electric field exceeds same threshold value, ultrasonic waves absorption suppression effect is possible. For the rotating coordinate system accompanying the electric field, the proper acoustic eigenmodes of crystal layer have a form of standing waves with real wave numbers. As a result of that the attenuation of these waves doesn't occur in crystal despite the viscosity of the medium. Boundary-value problem is solved and intensities of reversed and passed acoustic waves taking into account ultrasonic waves reflection from the border of the layer with rotating anisotropy are found. The conditions when the reversed and passed acoustic waves intensities have extreme values are defined.

Lately, an interest to researches of acoustic waves interaction with alternating electric fields in crystals [1-5] increases greatly. In the book [1], for example, acoustic electromagnetik interactions in ferroelectic resonators from potassium tantalate are regarded as a basis of ultrasonic waves excitation. In article [2] non-linear electroacoustic interaction in lithium niobatum is considered as a method of phase conjugation of acoustic waves. In the book [6] a possibility of rotating acoustic anisotropy forming in crystals with strong deformation dependence of the permittivity under outside electric field influence is shown. The effects of ultrasonic waves frequences transformation, amplification and generation of the reversed acoustic wave, appearance of electroacoustic memory of the crystal are studied; and advantages of space-uniform rotating electric field are grounded. Detailed study of the medium viscosity influence on acoustic properties of the crystal with rotating anisotropy is given in the book [7]. In the giveh work, the suppression effect of the acoustic waves absorption and their resonance interaction with rotating electric field in the crystal layer with abnormally high permittivity

is studied. Acoustic waves propagation through this layer taking into account ultrasonic waves reflection from the border of the layer is also the matter of this study. The reversed and passed waves intensities dependence from thickness of the layer with rotating anisotropy is studied.

Let's consider a crystal with strong deformation dependence of permittivity (for example, centrosymmetric ferroelectric ceramic on the basis of barium titanatum), central part of which is placed in rotating round the axis Z (unit vector $\underline{c}$) electric field. A considerable change in crystal acoustic properties takes place; as a result the equation of elastic wave propagation will be as follows

$$\rho \frac{d^2 u_i}{dt^2} = \Lambda(t) \frac{d^2 u_i}{dz^2} + B(t) \frac{d}{dt} \frac{d^2 u_i}{dz} \qquad (1)$$

where $\underline{u}$ - displacement vector, ρ -medium density,

$$\Lambda(t) = U(t)(\Lambda_{22} + (\Lambda_{11} - \Lambda_{22})\underline{a}\cdot\underline{a})U^{-1}(t) \qquad (2)$$

$$B(t) = U(t)(B_{22} + (B_{11} - B_{22})\underline{a}\cdot\underline{a})U^{-1}(t) \qquad (3)$$

-tensors of elastic constants and viscosity, taking into account nonstationary influence of outside electric field,

$$U(t) = \exp(\Omega t c^{*}) \qquad (4)$$

-matrix of turning round axis Z at an angle $\phi = \Omega t$ [8]. In expressins (2)-(4) the following designations are used:

$\Lambda_{11} = \bar{\Lambda} + \delta$, $\Lambda_{22} = \bar{\Lambda} - \delta$, $\bar{\Lambda} = c_{44} + (\alpha_{155} + \alpha_{144})E_0^2/2$,

$\delta = (\alpha_{155} - \alpha_{144})E_0^2/2$, $B_{11} = \bar{B} + æ$, $B_{22} = \bar{B} - æ$,

$\bar{B} = \eta_{44} + (\beta_{155} + \beta_{144})E_0^2/2$, $æ = (\beta_{155} - \beta_{144})E_0^2/2$,

E_0 and Ω -amplitude and outside electric field rotation frequency,

α and β -tensors, taking into account electrostriction influence of field $\bar{E}$ onto elastic constants and medium viscosity, $\underline{a}$, $\underline{b}$ and $\underline{c}$ - orthes of Decart system of axes, point between the vectors denominates their direct (diad) product, c^{*} - antisymmetrical tensor dual to vector $\underline{c}$.

To solve the motion equation (1), introduce vector

$$\underline{u}' = \overset{-1}{U}(t)\underline{u} \tag{5}$$

characterising elastic displacement of the medium particles in rotating system of axes accompanying outside electric field turning. In this system of axes, unlike the laboratory one, the tensors of elastic constants and the medium viscosity do not depend on time. That lets to seek the solution of the motion equation in the form of flat monochromatic waves

$$\underline{u}' = \underline{u}_0' \exp\{i k(\omega')z - i\omega' t\} \tag{6}$$

with frequency ω' and wave number $k(\omega')$. In laboratory system of axes wave displacement vector (6) can be represented as two interconnected flat monochromatic waves [9]

$$\underline{u} = U(t)\underline{u}' = \{A_+ \underline{n}_+ \exp[-i(\omega'-\Omega)t] + \underline{A}_- \underline{n}_- \exp[-i(\omega'+\Omega)t]\}\exp[ik(\omega')z] \tag{7}$$

having equal wave numbers $k(\omega')$, different frequences $\omega \pm \Omega$ and opposite circular polarizations set by the vectors $\underline{n}_\pm = (a \pm ib)/\sqrt{2}$
By using the connections between vectors u and u', the motion equation (1) can be written in the rotating system of axes as follows:

$$\{\rho[\Omega^2(\underline{c}\cdot\underline{c} - 1) - 2i\omega'\Omega c^* - \omega'^2] + k^2[\Lambda + B(\Omega c^* - i\omega')]\}\underline{u}' = 0 \tag{8}$$

Let's consider the case when on the crystal border in z=0 circular-polarized acoustic wave is excited

$$\underline{u}_0 = u_0^- \underline{n}_- \exp[-i\omega_0 t] \tag{9}$$

elastic displacement vector of which has the same rotation direction in time as the outside electric field. From the condition of vector $\underline{u}$ continuity on the border, it follows that $\omega_0 = \omega' + \Omega$, i.e. $\omega' = \omega_0 - \Omega$
If the ultrasonic waves frequency ω_0 coincides with the electrical field Ω frequency (case of resonance interaction), the correspondence $\omega' = 0$ is correct, and proper eigenmodes (6) of acoustic field have form of standing waves with wave numbers:

$$k_{1,2} = \left[\frac{\rho\Omega^2 \bar{\Lambda} \pm \left[\rho^2\Omega^4[\delta^2 - (\bar{B}^2 - \varkappa^2)\Omega^2] \right]^{1/2}}{\bar{\Lambda}^2 - \delta^2 + (\bar{B}^2 - \varkappa^2)\Omega^2} \right]^{1/2} \tag{10}$$

As follows from the equation (10), when anisotropy of elastic constants $\hat{\delta}$ tensor and anisotropy of viscosity $\hat{\varkappa}$ tensor increase, imaginary parts of wave numbers monotonuously decreases up to zero. Starting from threshold values of parameters $\hat{\delta}$ an $\hat{\varkappa}$, determ ed by the condition

$$\delta^2 + \varkappa^2\Omega^2 = B^2\Omega^2 \tag{11}$$

wave numbers (10) become real, and proper eigenmodes of acoustic field cease to damp in the crystal. As the numeral estimations show, for crystal with abnormally high permittivity execution of threshold condition (11) is achieved when electric field intesity is several kV/cm.

($\bar{\Lambda}\sim10^{11}$ N/m^2, $\delta\sim10^{9}$ N/m, $\bar{B}\sim100$ units SI, $\varkappa\sim5$ units SI, $\Omega\sim10^{7}$Hz[10-12])

Boundary-value Problem Solution

As a result of propagation in the crystal ultrasonic waves interaction with rotating electric field, amplification of the passed wave at the frequency ω_0

$$\underline{u}_\tau = u_\tau^- \underline{n}_- \exp[-i\omega_0 t + ik_0 z] \tag{12}$$

and generation of the reversed wave at the frequency $2\Omega - \omega_0$ can take place.

$$\underline{u}_c = u_c^+ \underline{n}_+ \exp[-i(\omega_0 - 2\Omega)t + ik_0^c z] \tag{13}$$

As a result of ultrasonic waves reflection from the border of the layer with rotating anisotropy, the reflected wave at the frequency ω_0

$$\underline{u}_r = u_r^- \underline{n}_- \exp[-i\omega_0 t - ik_0 z] \tag{14}$$

and the passed wave at the frequency $2\Omega - \omega_0$ can also appear

$$\underline{u}_{c\tau} = u_{c\tau}^+ \underline{n}_+ \exp[-i(\omega_0 - 2\Omega)t - ik_0^c z] \tag{15}$$

Representing according to [7] the acoustic field in the layer with rotating anisotropy in the form of the superposition of four proper modes with amplitudes A_m ,from the conditions of continuity of wave elastic displacement vectors (9,12-15) and continuity of tensions σ tensor components on the borders of the layer [13] ,we have the system of eight equations

$$\sum_{m=1}^{4} A_m = u_r^- + u_o^-$$

$$\sum_{m=1}^{4} A_m \xi_m^{-1}(\omega_o - \Omega) = u_c^+$$

$$\sum_{m=1}^{4} A_m \exp[\imath k_m(\omega_o - \Omega)L] = u_\tau^- \exp[\imath k_o L]$$

$$\sum_{m=1}^{4} A_m \xi_m^{-1}(\omega_o - \Omega)\exp[\imath k_m(\omega_o - \Omega)L] = u_{c\tau}^+ \exp[-\imath k_c^o L]$$

$$\sum_{m=1}^{4} \{[\imath\bar{\Lambda} + \bar{B}\omega_o] + [\imath\delta + æ(\omega_o - 2\Omega)]\xi_m^{-1}(\omega_c - \Omega)\}k_m(\omega_o - \Omega)A_m =$$
$$= k_o(\imath c_{55} + \eta_{55}\omega_o)(u_o^- - u_r^-) \qquad (16)$$

$$\sum_{m=1}^{4} \{[\imath\bar{\Lambda} + \bar{B}(\omega_o - 2\Omega)]\xi_m^{-1}(\omega_o - \Omega) + [\imath\delta + æ\,\omega_o]\}k_m(\omega_o - \Omega)A_m =$$
$$= k_o^c(\imath c_{55} + \eta_{55}(\omega_o - 2\Omega))u_c^+$$

$$\sum_{m=1}^{4} \{[\imath\bar{\Lambda} + \bar{B}\omega_o] + [\imath\delta + æ(\omega_o - 2\Omega)]\xi_m^{-1}(\omega_o - \Omega)\}k_m(\omega_o - \Omega)A_m \exp[\imath k_m(\omega_o - \Omega)L] =$$
$$= k_o(\imath c_{55} + \eta_{55}\omega_o)u_\tau^- \exp[\imath k_o L]$$

$$\sum_{m=1}^{4} \{[\imath\bar{\Lambda} + \bar{B}(\omega_o - 2\Omega)]\xi_m^{-1}(\omega_o - \Omega) + [\imath\delta + æ\,\omega_o]\}k_m(\omega_o - \Omega)A_m \exp[\imath k_m(\omega_o - \Omega)L] =$$
$$= -k_o^c(\imath c_{55} + \eta_{55}(\omega_o - 2\Omega))u_{c\tau}^+ \exp[-\imath k_o^c L]$$

There k_o, k_o^c are wave numbers depending on waves frequency and undisturbed parameters of density ρ, elasticity c_{55} and viscosity η_{55} of the crystal layers bordering when $Z = 0$ and $Z = L$ with the layer put into the rotating electric field.

$$k_{1,2}(\omega) = - k_{4,3}(\omega) \qquad (17)$$

$$\xi_{1,2}(\omega) = \xi_{3,4}(\omega) \qquad (18)$$

wave numbers and ellipticity of the proper modes of the acoustic field [7].

In fig.1 and 2 presented diagrams of all waves intensities dependence on the thickness of the layer with rotating anisotropy acquired in the result of numerical solution of the system (16). Calculations were made with the same values of parameters and

$$\rho = 5.7\times10^{3} \text{ kg/m}^3 \ , \ E_0 = 400 \text{ kV/m} \ , \ c_{55} = 9.38\times10^{10} \text{ N/m}^2 \ ,$$

$$\eta_{55} = 93.8 \text{ SI units} \ , \ \omega_0 = 10^7 \text{ Hz}$$

Diagrams analysis led us to the conclusion about the character of dependence of coefficients of reflection, passage and amplification from the thickness of the region with induced anisotropy. All diagrams have periodically repeated resonance on condition

$$[k_1(\omega_0 - \Omega) - k_2(\omega_0 - \Omega)]L_s = \psi_1 - \psi_2 + 2\pi s \qquad (19)$$

where ψ_1 and ψ_2 are arguments of complex ellipticities $\xi_1(\omega_0 - \Omega)$ and $\xi_2(\omega_0 - \Omega)$ (18), parameter S takes values from number of whole number. When carring out condition (19), n.malized intensities of the passed and reversed waves can reach gigantic values of order 10^5. At the same time the generation and amplification of the ultrasonic waves in critical points are unstable, because the coefficients of amplification of passage and reflection decrease very quickly if the condition (19) is slightly violated. When the layer thickness corresponds to the correlation

$$[k_1(\omega_0 - \Omega) - k_2(\omega_0 - \Omega)]L_s = 2\pi s \qquad (20)$$

the reversed wave intensity takes minimal values.

REFERENCES

1.Belokopytov G.V., Ivanov A.V., Chistyaev V.N. Parametrical striction excitation of ultrasonic waves in dielectric resonators of microwave range.// Acoust. Mag. 1989.V.35.No 2.p.218-222.

2.Ohno Masahiro. Generation of acoustic phase conjugate waves using nonlinear electroacoustic interaction in $LiNbO_3$.// Appl. Phys.Lett.1989.V.54.No 20.p.1979-1980.

3.Belokopytov G.V.,Ivanov A.V.,Semenenko V.N. and others. Thermal disturbances influence on conditions of appearance of ultrasonic waves striction parametrical generation.// Mag. of Techn Phys. 1989. V.59. No 4.p.182-184.

4.Ohno Masahiro. Wave front reversal in acoustic phase conjugation by nonlinear electroacoustic interaction in $LiNbO_3$. // Appl.Phys.Lett.1989.V.55.No 9.p.832-833.

5.Bajak Ivan L. Nonlinear interaction of acoustic vibrations and frequenyelectric field. // Wiss. Beitr. M.,Luter-Univ. Halle-Wittenberg 0. 1989.No 26.p.83-90.

6.Bely V.N.,Sevruk B.B.Rarametrical electroacoustic effects in the crystal with induced outside electric field of rotating acoustic anisotropy. // Mag. of Techn. Phys.1987.V.57.No 2.p.336-340.

7.Semchenko I.V.,Serdyukov A.N.,Khakhomov S.A. Medium viscosity influence on amplification of the acoustic waves in the crystal in presence of the rotating electric field. // Crystallografy.1991.V.36. No 2.p.298-303.

8.Fedorov F.I. Gyrotropic Theory.Minsk:Nauka i Tehnika.1976

9.Semchenko I.V.,Serdyukov A.N. Light propagation in the medium with rotating cholesterical structure of anisotropy.// Mag.of Appl. Spectroscopy.1985.V.41.No 5.p.827-830.

10.Pekar S.I.,Demidenko A.A.,Zdebski A.P. and others. Researches of electrostriction constants of the first and the second order in the substances with big permittivity. // Reports of the USSR Science Academy.1976.V.230.p.1089.

11.Zhabitenko N.K.,Kucherov I.Y.Researches of electric field influence on the speed of elastic waves propagation in isotropic solid bodies // Ukr.Phys.Mag.1978.V.23.No 2.p.263.

12.Rybyanets A.N.,turik D,V.,Dorokhova N.V. and others. Constant electric field infuence on propagation of surface acoustic waves in ferroelectric of CTS system. // Mag. of Techn. Phys.1986. V.56. No 12. 2371-3275.

13.Sirotin Y.I.,Shaskolskaya M.P. Crystal Physics Basics. Moscow: Nauka.1979.

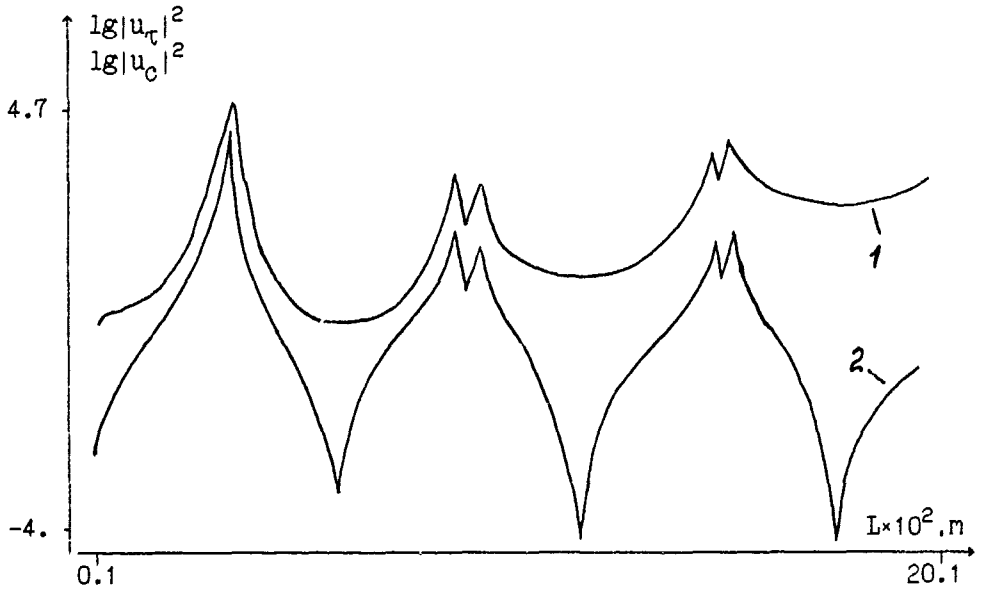

FIG. 1. The passed at frequency ω_0 and the reversed waves intensities dependence on the thickness of the layer with rotating anisotropy.

$1-lg|u_\tau|^2$, $2-lg|u_c|^2$

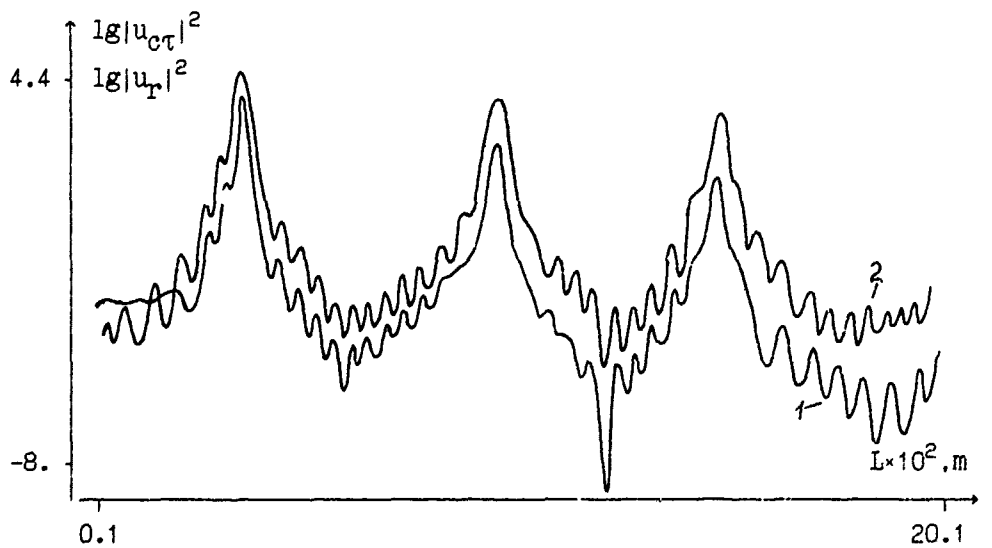

FIG. 2 . The passed at frequency $2\Omega - \omega_0$ and reflected waves intensities dependence on the thickness of the layer with rotating anisotropy.

$1-lg|u_{c\tau}|^2$, $2-lg|u_r|^2$

AUTHOR INDEX